frontiers | Research Topics

Coal and rock dynamic disasters: Advances of physical and numerical simulation in monitoring, early warning, and prevention, volume II

Edited by
Jingjing Meng, Jia Lin, M. Younis Khan and Zhibo Zhang

Published in
Frontiers in Earth Science
Frontiers in Ecology and Evolution
Frontiers in Environmental Science

ISSN 1664-8714
ISBN 978-2-8325-4867-7
DOI 10.3389/978-2-8325-4867-7

About Frontiers

Frontiers is more than just an open access publisher of scholarly articles: it is a pioneering approach to the world of academia, radically improving the way scholarly research is managed. The grand vision of Frontiers is a world where all people have an equal opportunity to seek, share and generate knowledge. Frontiers provides immediate and permanent online open access to all its publications, but this alone is not enough to realize our grand goals.

Frontiers journal series

The Frontiers journal series is a multi-tier and interdisciplinary set of open-access, online journals, promising a paradigm shift from the current review, selection and dissemination processes in academic publishing. All Frontiers journals are driven by researchers for researchers; therefore, they constitute a service to the scholarly community. At the same time, the *Frontiers journal series* operates on a revolutionary invention, the tiered publishing system, initially addressing specific communities of scholars, and gradually climbing up to broader public understanding, thus serving the interests of the lay society, too.

Dedication to quality

Each Frontiers article is a landmark of the highest quality, thanks to genuinely collaborative interactions between authors and review editors, who include some of the world's best academicians. Research must be certified by peers before entering a stream of knowledge that may eventually reach the public - and shape society; therefore, Frontiers only applies the most rigorous and unbiased reviews. Frontiers revolutionizes research publishing by freely delivering the most outstanding research, evaluated with no bias from both the academic and social point of view. By applying the most advanced information technologies, Frontiers is catapulting scholarly publishing into a new generation.

What are Frontiers Research Topics?

Frontiers Research Topics are very popular trademarks of the *Frontiers journals series*: they are collections of at least ten articles, all centered on a particular subject. With their unique mix of varied contributions from Original Research to Review Articles, Frontiers Research Topics unify the most influential researchers, the latest key findings and historical advances in a hot research area.

Find out more on how to host your own Frontiers Research Topic or contribute to one as an author by contacting the Frontiers editorial office: frontiersin.org/about/contact

Coal and rock dynamic disasters: Advances of physical and numerical simulation in monitoring, early warning, and prevention, volume II

Topic editors

Jingjing Meng — Luleå University of Technology, Sweden
Jia Lin — Curtin University, Australia
M. Younis Khan — University of Peshawar, Pakistan
Zhibo Zhang — University of Science and Technology Beijing, China

Citation

Meng, J., Lin, J., Khan, M. Y., Zhang, Z., eds. (2024). *Coal and rock dynamic disasters: Advances of physical and numerical simulation in monitoring, early warning, and prevention, volume II*. Lausanne: Frontiers Media SA.
doi: 10.3389/978-2-8325-4867-7

Table of contents

frontiers | Frontiers in Earth Science

TYPE Original Research
PUBLISHED 31 May 2023
DOI 10.3389/feart.2023.1204989

OPEN ACCESS

EDITED BY
Xuelong Li,
Shandong University of Science and Technology, China

REVIEWED BY
Chaoxuan Zhang,
Institute of Rock and Soil Mechanics (CAS), China
Yu Xuguang,
Tangshan Vocational and Technical College, China

*CORRESPONDENCE
Ruiyuan Zhang,
1532272557@qq.com

RECEIVED 13 April 2023
ACCEPTED 19 May 2023
PUBLISHED 31 May 2023

CITATION
Li X, Zhang R, Yang Z, Chen P, Ji F and Wen B (2023), Mechanical behavior analysis and bearing capacity calculation of CFG pile composite foundation on coral sand site.
Front. Earth Sci. 11:1204989.
doi: 10.3389/feart.2023.1204989

Mechanical behavior analysis and bearing capacity calculation of CFG pile composite foundation on coral sand site

Xiaobin Li[1,2], Ruiyuan Zhang[1]*, Zhao Yang[1], Peishuai Chen[1], Fuquan Ji[1] and Bing Wen[3]

[1]CCCC Second Harbor Engineering Co, Ltd., Wuhan, China, [2]First Engineering Co, Ltd. of CCCC Second Harbor Engineering Bureau, Wuhan, China, [3]Design Institute of the First Construction Engineering Co, Ltd. of China Construction Third Engineering Bureau, Wuhan, China

Coral sand foundation formed by hydraulic fill often faces the problem of poor bearing capacity. This paper proposed for the first time to apply CFG pile composite foundation to coral sand sites to verify the feasibility of this scheme and understand its mechanical characteristics. Firstly, taking on-site coral sand as the research object, a pile sand interface shear test was conducted to clarify the mechanism of pile side friction. At the same time, the ultimate bearing capacity of CFG pile and its composite foundation was measured through *in-situ* static load tests. Then, based on the strength parameters of the pile sand interface revealed by indoor tests, numerical simulations were conducted to analyze the bearing characteristics of CFG piles and their composite foundations. Finally, a method for calculating the vertical bearing capacity of rigid piles in composite foundation considering interface parameters was proposed. The results showed that the bearing capacity characteristic values of single pile and composite foundation meet the design requirements; The interface friction angle and cohesion together increased the ultimate side friction by 64.41%; The load is mainly borne by the pile tip resistance, and the increase of the interface friction angle will make the proportion of the side friction load first increase and then decrease more obviously; The pile soil stress ratio first increased and then tended to stabilize as the interface strength increased. Compared with the field static load test results, the rationality of the calculation method for composite foundation rigid piles was verified. This study may have reference significance for the design and construction of coral sand foundation treatment in offshore island and reef projects.

KEYWORDS

coral sand, CFG pile composite foundation, interface strength parameters, static side pressure coefficient, bearing characteristics

1 Introduction

Coral sand (Wang et al., 2020) is a kind of rock and soil mass formed by the remains of coral groups under geological action, it is characterized by irregular shape (Liu and Wang, 1998; Smith and Cheung, 2003), many pores (Chang-qi et al., 2016; Xu et al., 2022), easy cementation (Meng et al., 2014), easily broken (Hu, 2008; Donohue et al., 2009), and its engineering mechanical properties are quite different from those of ordinary continental sediments (JIANG et al., 2015; Wang et al., 2017). As the construction site gradually extends

to the sea, more and more reclamation projects are being built. Due to the characteristics of high cohesion, large internal friction angle and high residual strength, coral sand has become a good blowing filler and is widely used in island and reef engineering (Wang et al., 2011; Wang et al., 2021); However, due to its engineering characteristics of high porosity, large compressibility, and easy crushing of particles (Coop, 1990; Ma et al., 2022), untreated coral sand foundation often has problems such as large uneven settlement and low foundation bearing capacity (Rittirong et al., 2008), which brings great threats to the engineering construction (Ohno et al., 1999). Therefore, proper foundation treatment measures are suggested be taken.

At present, driven piles and bored piles were mostly used in coral sand sites (Dean, 2009). In the earliest period, Angemeer et al. (1973) used the field static load test to study the bearing characteristics of the driven pile in the coral reef stratum, and it was found that the side friction resistance of the steel pile was very low; through the test of driving pile with openings, the ultimate side friction measured by Dutt and Cheng, (1984) was only 9.2 kPa at the lowest level; Datta et al. (1980) evaluated the bearing capacity of pile foundation in calcareous sand, and they found that the surface friction might be overestimated in the project because that the end bearing may not be fully utilized. During the piling process of the driven pile, the coral sand particles around the pile are damaged to a large extent, which will make the bearing capacity decrease, and even cause pile sliding (Poulos, 1988); Based on the deep mixing technology, Igoe et al., 2014; Spagnoli et al. (2015) proposed a new type of cast-in-place pile with steel casing inside, and systematically studied its bearing capacity. Although the cast-in-place pile can significantly increase the side friction resistance of the pile (Lee and Poulos, 1991) and has little impact on the shape of coral sand around the pile, it has the disadvantages offs high cost and long period. Compared with the construction scheme of above pile foundations, the CFG pile (i.e., pile constructed by granular materials of cement, fly-ash and gravel) composite foundation has many advantages such as small disturbance, small settlement, low cost, etc., but so far, its application in the coral reef site is rarely reported. The mechanism of the pile-soil interface is the key influencing factor for the bearing capacity of pile foundation and has been studied by scholars. By conducting the sand-steel interface shear test, Zhang et al. (2021) studied the shear behavior of this interface under different roughness and compactness. Similarly, Chen et al. (2022) studied the influence of roughness and relative density on the mechanical properties of the sand-concrete pile interface through the interface shear test. Uesugi et al. (1990) found that the maximum friction coefficient of the sand-concrete interface is closely related to the interface roughness and the average diameter of sand. Based on the sand-steel interface shear test, Kou et al. (2021) studied the interaction mechanism between coral sand and steel pipe pile interface under the geological conditions of coral reef. Wang et al. (2022) analyzed the macroscopic shear characteristics and particle crushing characteristics. For the interface of the concrete pile, Li et al. (2022) carried out large-scale direct shear tests to study the shear failure characteristics of coral reef limestone-concrete interface. Aiming to study the bearing capacity of pre-drilled rock-socketed concrete piles on the coral reef debris layer, Liu et al. (2021) conducted the direct shear test on the pile-coral reef debris interface under the condition of constant normal stiffness and analyzed the friction mechanism and shear expansion characteristics of the pile-rock interface. To sum up, the mechanical properties of the interface between continental ordinary sand and steel pipe piles or concrete piles. For the coral reef stratum, some scholars carried out research on the impact mechanism of steel pipe piles on coral sand, except for the action mechanism of concrete piles, while only reef limestone and its clastic layer were involved, and fully classified coral sand (gravel sand, coarse sand, medium sand, fine sand, and silt) was not taken into account.

This article based on a high-rise residential project, which was designed on a hydraulic fill coral sand site in Hulumale Island, Maldives. Based on the special engineering properties of coral sand, the shear characteristics of the interface between the fully classified coral sand and the CFG pile were revealed through the indoor shear test, and a large number of on-site static load tests were conducted on the single pile and composite foundation to evaluate the application effect of this composite foundation. The influence of the interface strength parameters (cohesion and friction angle) on the bearing characteristics of the CFG pile composite foundation was clarified through numerical simulation. Furthermore, it also proposed a calculation method for the bearing capacity of rigid piles in the composite foundation considering the interface strength.

2 Project overview

This high-rise residential project in Hulumale Island, Maldives, is designed in the land area formed by coral sand reclamation and is the largest residential building in this area. This site is mainly distributed by coral sand from top to bottom, and the pile end has quasi-reef limestone. The specific geological overview is introduced in Table 1. In this project, the CFG pile was used for foundation treatment; The pile diameter is 0.4 m, the pile spacing is 1.3 m, and the pile body is made of C30 concrete. These piles were arranged rectangular and drilled using the long spiral, as shown in Figure 1. The pile end entered into the bearing

FIGURE 1
Construction of CFG pile.

TABLE 1 Geological overview.

Geotechnical no. And name	Morphological description	Average standard penetration number
①Hydraulic fill sand	Loose~slightly dense, calcareous, uneven particles	11
②-2 Coral sand	Local clumping and stickiness between particles	4
③Parareef limestone	The skeleton is mostly 0.5–1.0 cm, with weak cementation between particles and high hammering strength	30

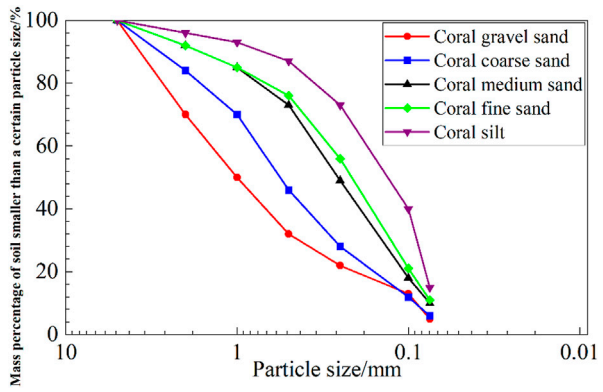

FIGURE 2
Particle grading curve of sample.

layer of the quasi-reef limestone for 50 cm, the design bearing capacity of the single pile and the composite foundation is 420 kN and 370 kPa, respectively.

3 Bearing characteristic test

3.1 Indoor direct shear test on interface

After sampling and analyzing the coral sand at the project site for several times, the grain size distribution of the reclaimed coral sand is found to be wide, which can be divided into coral gravel sand, coral coarse sand, coral medium sand, coral fine sand and coral silty sand according to Code for Geotechnical Investigation of Water Transport Engineering (Partial Revision)—Geotechnical Investigation of Coral Reef (General Revision) in Table 2. The strength parameters of the interface bewteen different graded coral sand and piles will directly affect the side friction resistance of CFG piles, and furtherly affect the bearing characteristics of CFG pile composite foundation.

3.1.1 Experiment scheme

In this paper, five kinds of coral sand were taken as the research object to carry out the indoor interface shear test, so as to clarify the shear strength parameters of the interface between coral sand and concrete pile. The particle analysis test results of typical samples are shown in Figure 2.

According to the particle grading curve in Figure 2, parameters of the restricted particle size d_{60}, medium particle size d_{30}, average particle size d_{50}, effective particle size d_{10}, nonuniformity coefficient C_u and curvature coefficient C_c were all calculated and shown in Table 3.

Due to the large and uneven particle size of coral sand, a large special direct shear instrument for coral sand was invented, as shown in Figure 3. The cutting box size is 15 × 15 × 15 cm, and the measurement range is 0–50 kN with an accuracy of 0.01 kN while using this special direct shear equipment to carry out mechanical test of pile-sand interface, the sample was processed into the size of 15 cm × 15 cm, and the density is 1.65 g/cm ^{3}. Besides, the normal stress of the test was set as 25, 50, 100, 200, 400 and 800 kPa, and the shear rate was 1 mm/min.

The specific test steps are as follows.

(1) Prefabricated the size to 15× 15 × 7.5 cm concrete block was placed inside the sample box, with the top surface of the concrete block located exactly at the shear plane position;
(2) According to the experimental design density (1.65 g/cm^3) and volume (15 × 15 × 7.5 cm) weighed a certain mass of coral sand sample;
(3) Divided the weighed coral sand sample into three parts and placed it in the upper half of the sample box. Vibrated according

TABLE 2 Classification of coral sand.

Coral reef detritus		Particle grading
Coral sandy soil	Coral gravel sand	Percentage of the particle with the diameter of more than 2 mm is 25%–50%
	Coral coarse sand	Percentage of the particle with the diameter of more than 0.5 mm is 50%
	Coral medium sand	Percentage of the particle with the diameter of more than 0.25 mm is 50%
	Coral fine sand	Percentage of the particle with the diameter of more than 0.075 mm is 85%
	Coral silty sand	Percentage of the particle with the diameter of more than 0.075 mm is 50%

TABLE 3 Grading parameters of coral sand.

Parameter	Coral gravel sand	Coral coarse sand	Coral medium sand	Coral fine sand	Coral silty sand
d_{10}	0.09	0.09	0.08	0.08	0.08
d_{30}	0.45	0.28	0.16	0.14	0.09
d_{50}	1.00	0.58	0.26	0.22	0.15
d_{60}	1.50	0.80	0.36	0.30	0.20
Nonuniformity coefficientC_u	16.67	8.70	4.80	4.00	2.67
Curvature coefficientC_c	1.50	1.07	0.95	0.87	0.54
Gradation	Good	Good	bad	bad	bad

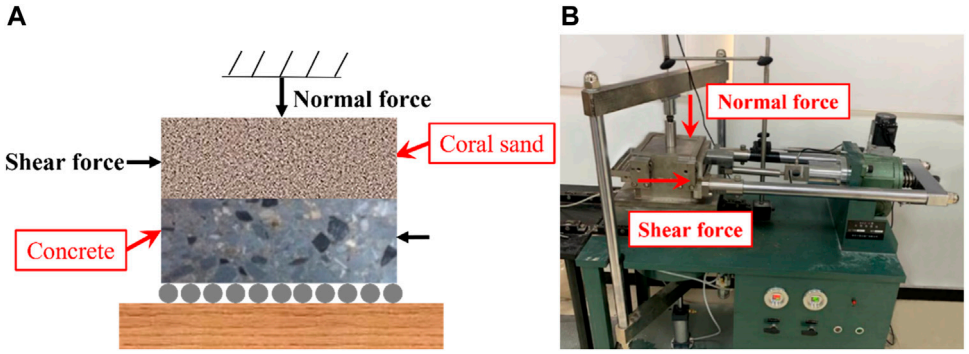

FIGURE 3
Large-scale direct shear test of Pile-coral sand interface **(A)** Schematic diagram of the large-scale direct shear test; **(B)** The equipment large direct shear test.

to the height of the layers, so that the coral sand sample just filled the upper half of the sample box;

(4) Started the instrument and applied normal stress through the cylinder;

(5) Started the lateral pushing device, so that the lower part of the shear box began to shear and move, from which the interface shear strength between the concrete block and the coral sand sample can be obtained.

3.1.2 Experiment results

Figure 4–Figure 8 shows the interface shear curves and the change rule of strength with normal stress. From Figure 4A–Figure 8A, it can be seen that with the increase of shear strain, the shear stress on the coral sand-concrete interface first increased and then basically remained unchanged; this characteristic is similar to the ideal elastoplastic model. Moreover, the interface strength of coral sand-concrete increased with the side pressure. Draw the curve of normal stress and shear strength, Figure 4B–Figure 8B shows the slope of the curves between the interface strength and the normal stress was different under different normal stress, that is, these curves were broken lines, and the inflection point was about 100 kPa. After fitting the collected data, the friction angle and cohesion of the coral sand-concrete interface under different normal stresses are shown in Table 4. It can be seen that the variation of shear stress on the coral sand-concrete interface with the normal stress showed a broken line, with an inflection point of about 100 kPa. When the normal stress was less than 100 kPa, the interface cohesion was between 13.1 and 23.4 kPa, and the friction angle was between 17.2 and 27.7. When the normal stress was greater than 100 kPa, the interface cohesion was close to 0, and the friction angle was between 28.4 and 34.1.

By summarizing the results of the coral sand concrete interface shear test, it can be found that due to the natural multiple edges and irregular shapes of coral sand, these irregular shapes have significant impact on the interface strength when it shears with concrete. Especially under low normal stress, irregularly shaped coral sand will generate significant biting force at the interface and inside the sand, The reason is that the edges and corners between particles are embedded and occluded with each other, forming a strong whole, exhibiting greater biting force than conventional terrestrial sand. At this time, coral sand cannot be simply treated as conventional sand; At the same time, due to the fragility of coral sand, under high normal stress, the irregular edges and corners of coral sand will be broken to varying degrees, and the particle roundness will continue to increase. The embedding and interlocking effect between particles will gradually weaken, and the interfacial interlocking force displayed will continue to decrease, approaching 0. At this time, the cohesive force between coral sand particles is becoming closer to conventional terrestrial sand.

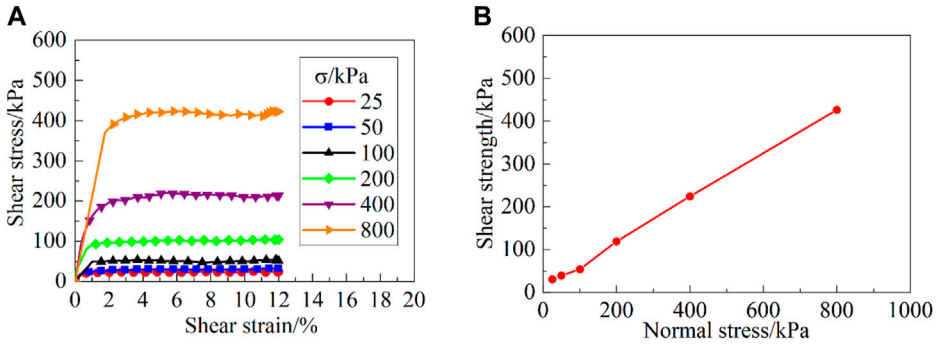

FIGURE 4
Coral gravel sand. **(A)** Relation curve between shear strain and shear stress; **(B)** Strength curve.

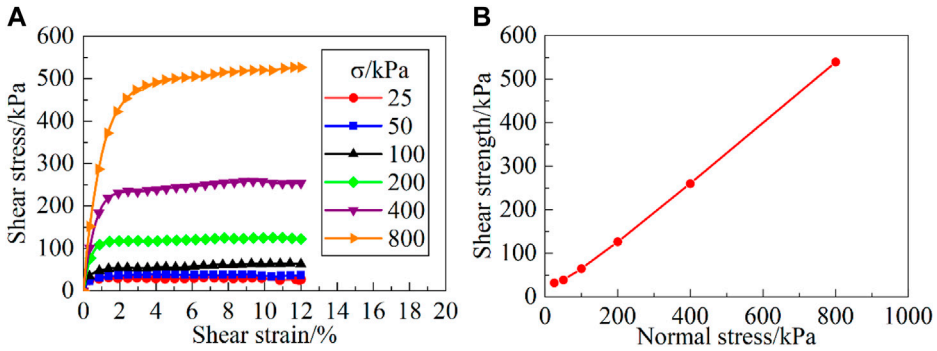

FIGURE 5
Coral coarse sand. **(A)** Relation curve between shear strain and shear stress; **(B)** Strength curve.

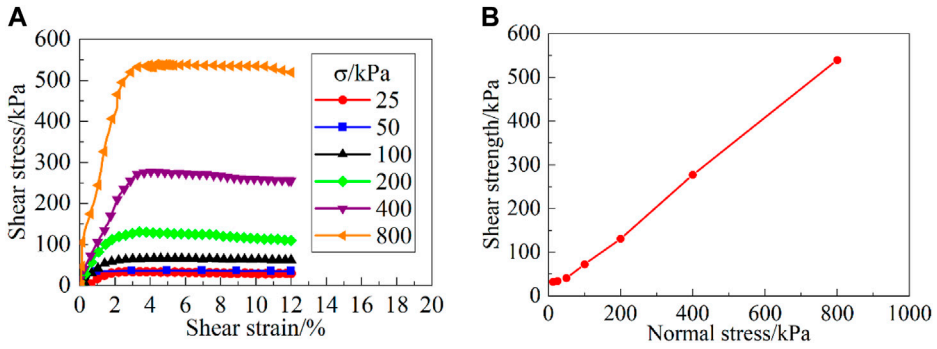

FIGURE 6
Coral medium sand. **(A)** Relation curve between shear strain and shear stress; **(B)** Strength curve.

During the process of normal stress variation, coral sand itself undergoes a dynamic change process, resulting in a large range of fluctuations in interface bite force. Coral sand and concrete also exhibit different interface strengths, which in turn affect the lateral friction resistance of the pile foundation and have different effects on the bearing characteristics of the pile foundation.

3.2 Site static load test

3.2.1 Static load test results of single pile

A total of 48 single pile static load tests were conducted on site, and the static load test results of two test piles were used as examples to illustrate. The test pile is 14 m long and 0.4 m in diameter. During the static load test of single pile, a ceratin low

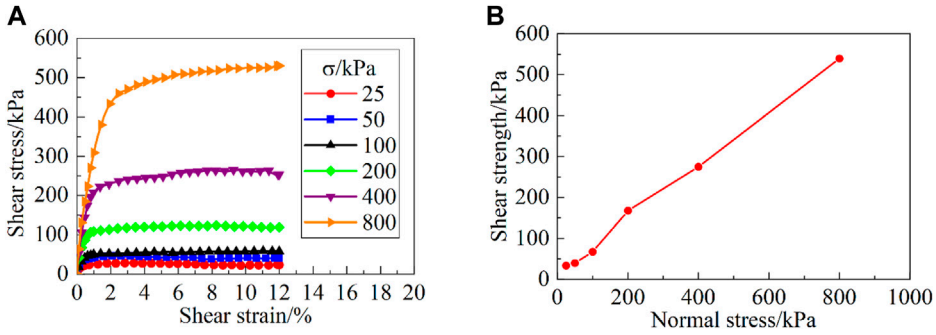

FIGURE 7
Coral fine sand. **(A)** Relation curve between shear strain and shear stress; **(B)** Strength curve.

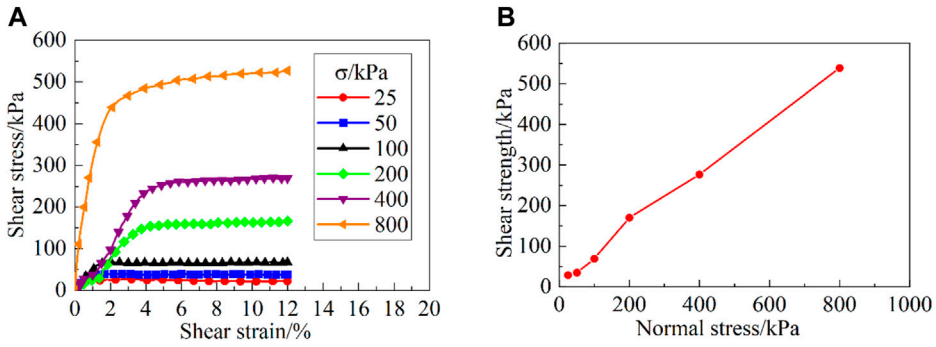

FIGURE 8
Coral silty sand. **(A)** Relation curve between shear strain and shear stress; **(B)** Strength curve.

TABLE 4 Statistical table of interface mechanical parameters.

Interface sand type	Low normal stress		High normal stress	
	Cohesion/kPa	Interface friction angle/°	Cohesion/kPa	Interface friction angle/°
Coral gravel sand	23.4	17.2	0	28.4
Coral coarse sand	19	24.1	0	33.7
Coral medium sand	18.3	27.7	0	34.1
Coral fine sand	16	26.6	0	33.6
Coral silt	13.1	23.2	0	32.2

speed was kept to sustain the load. The maximum stacking load is 1000 kN and is divided into 8 levels, the loading amount of each level is set as 1/10 of the estimated limit load. The 1st level load is applied by 2 times the graded loading amount, and the field loading is shown in Figure 9. As Q-S curves of a single pile shown in Figure 10, after applying the first eight levels of loading, the settlement was observed to be relatively stable. When the load was increased to the 9th level of 1000 kN, there was a significant steep drop in the pile top, indicating that the pile has been damaged; thus, the ultimate bearing capacity of a single pile was taken as 900 kN, and its characteristic value of the vertical bearing capacity was taken as 450 kN, which meets the design and specification requirements.

3.2.2 Static load test of composite foundation

A total of 48 single pile composite foundation static load tests were conducted on site, and the results of the composite foundation static load tests on two test piles were used as an example to

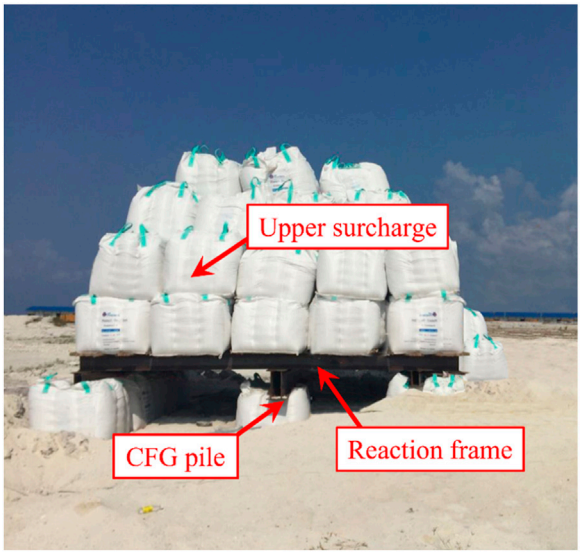

FIGURE 9
Static load test.

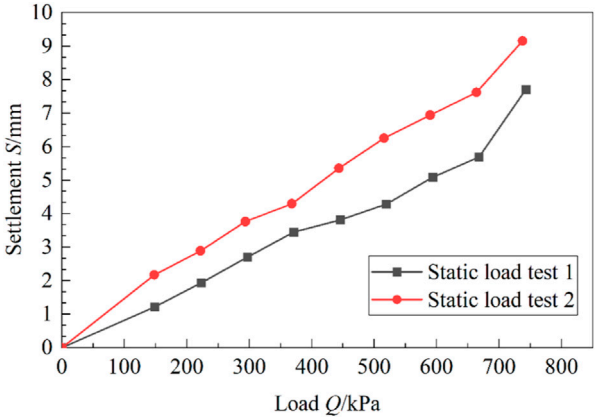

FIGURE 11
Q-S curve of composite foundation.

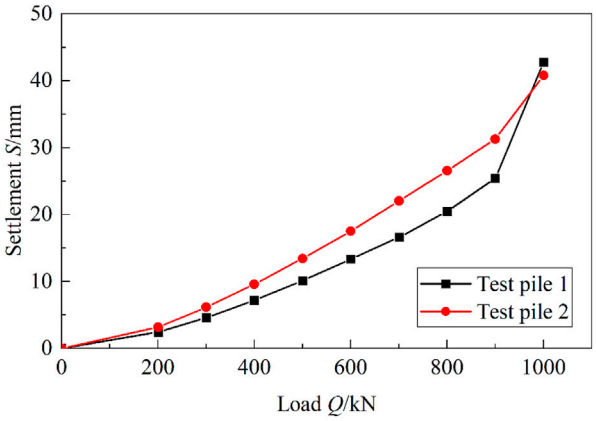

FIGURE 10
Q-S curve of single pile.

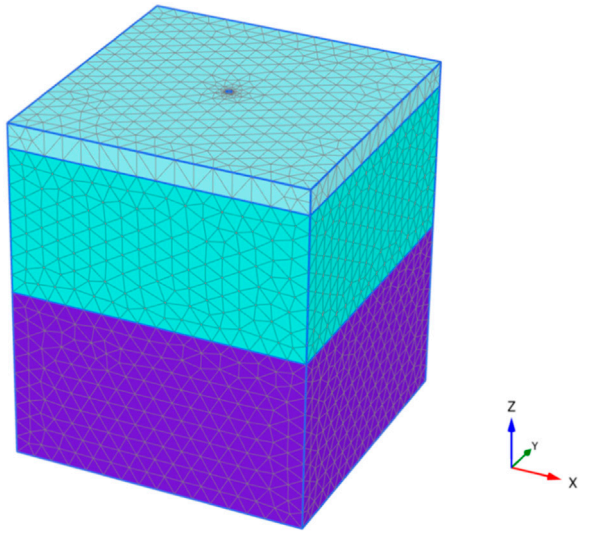

FIGURE 12
Numerical grid model.

illustrate. The length, diameter and spacing of the test pile is 14 m, 0.4 m, and 1.3 m, respectively; the size of the pressing plate is 1.30 m × 1.30 m. During the test, a ceratin low speed was kept to sustain the load, the maximum load on the pile was set as the ultimate bearable load, which was divided into 9 levels, the loading amount of each level was set as 1/10 of the estimated limit load, and the 1st level of loading took 1/5 of the maximum load. Figure 11 shows the Q-S curve of the composite foundation. It can be seen that the increasing rate of settlement obviously became larger after the last level of the load was applied. According to the key points of the composite foundation static load test, the limit load was taken as 740 kPa, and the characteristic value of the composite foundation bearing capacity was taken as 370 kPa to meet the requirements.

4 Numerical simulation research

4.1 The establishment of numerical model

The numerical model was established with PLAXIS 3D software, as shown in Figure 12. The pile length was 14 m and the pile diameter was 0.4 m. The side dimension of soil was set as 60 times the pile diameter, and the verticle dimension was set as 2 times the pile length. The horizontal displacement of soil around the pile was fixed, and the bottom was fixed. In this model, 29451 elements were generated and with 45406 nodes in total. The solid element was adopted for CFG pile, and the linear elastic model was selected; Based on the Mohr Coulomb criterion, a hardening soil constitutive model considering small strain

TABLE 5 Mechanical parameters of pile and soil.

Material	Elastic modulus	Poisson's ratio	Cohesion	Friction angle	Expansion angle
	MPa		kPa	(°)	(°)
Pile	25000	0.2	—	—	—
Coral sand	5	0.3	34.5	41.5	10
Medium-coarse sand	10	0.3	23	44	10
Parareef limestone	35	0.2	34.5	23	10
Cushion layer	15	0.3	0	40	10
Interface material	9	0.25	0、4、8、12、16、20、24	0、17、20.5、24、27.5、31、34.5	10

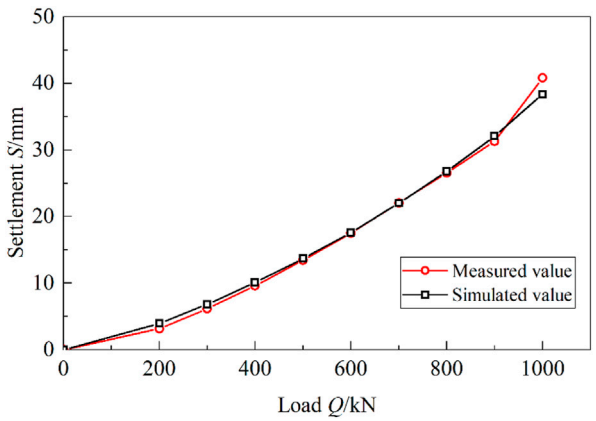

FIGURE 13
Comparison of Q-S curves of single pile.

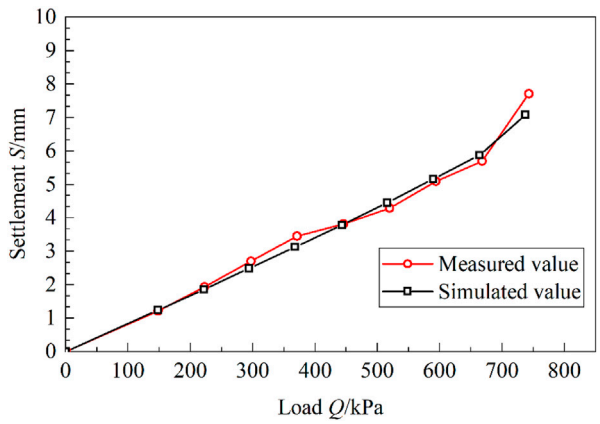

FIGURE 14
Q-S curve comparison of composite foundation.

stiffness was adopted for the soil layer. The contact interface between piles and soil was set to simulate the real contact between piles and soil, and this interface was regarded as an independent material, and its material parameters were input separately. The specific operation method is to set up a layer of interface unit between the pile and sand when establishing the model. The interface unit does not have actual thickness, and the material properties of the interface unit were customized. By inputting the designed cohesion and internal friction angle values in the material properties, accurate simulation of different interface strengths can be achieved, simulating the interface interaction between the pile and sand, Further results can be obtained on the impact of different interface strengths on the bearing characteristics of pile foundations. The mechanical parameters of all these materials are shown in Table 5.

4.2 Model validation and analysis

To verify the rationality of the numerical model, the load-displacement curves obtained from numerical simulation and bearing capacity tests of single pile and composite foundation on site were compared, as shown in Figures 13, 14. From Figure 13, it can be seen that in the initial stage of loading, the trend of the two load displacement curves was consistent, and the displacement increased linearly with the load. The slope of the load displacement curve obtained from numerical simulation was larger, and the displacement is greater under the action of primary load; After the primary load, there was a significant change in the slope of both curves, and the on-site measured curves performed more significantly; When the load reached its ultimate bearing capacity, the slope of the curve increased, and then the two showed an approximate linear relationship. The on-site measured load displacement curve showed a sharp drop, indicating that the pile had undergone certain damage and reached its ultimate bearing capacity. However, the slope change of the load displacement curve obtained from numerical simulation was not significant. In the primary and ultimate load stages, there was a deviation between the two curves, especially in the ultimate load stage, where there was a certain deviation in the ultimate bearing capacity obtained by the two curves. However, overall, the calculated values of the two curves were in good agreement with the measured values, verifying the rationality of the numerical simulation.

From Figure 14, it can be seen that in the initial stage of loading, the displacement in the two curves increased linearly with the load. After loading to the primary load, the on-site measured load

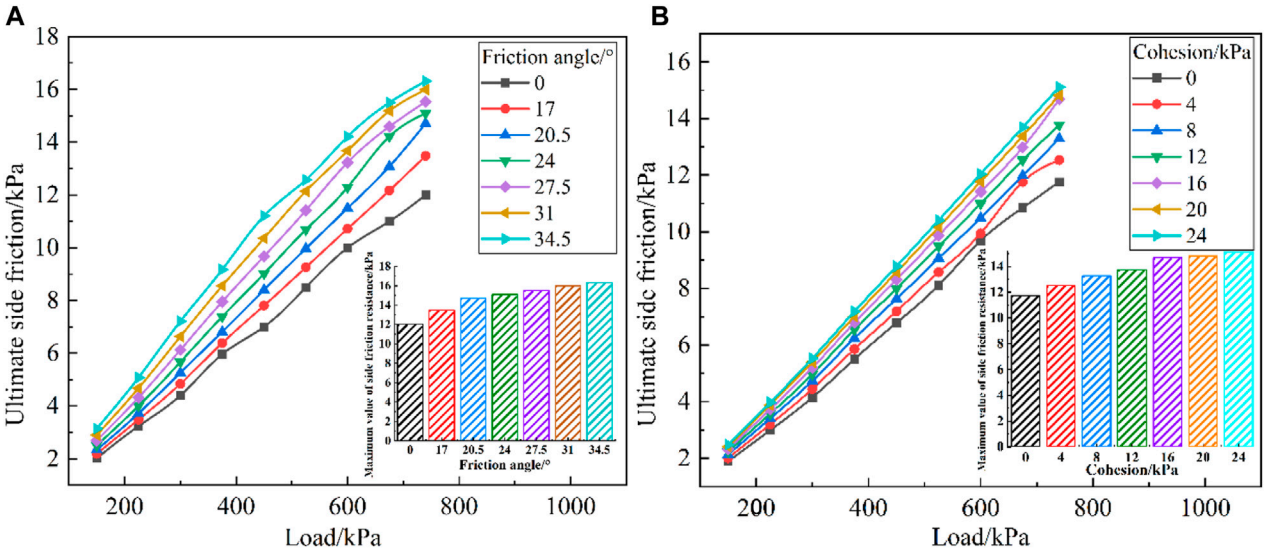

FIGURE 15
Influence of interface strength parameters on ultimate side friction under different loads **(A)** Influence of interface friction angle on ultimate side friction; **(B)** Influence of interface cohesion on ultimate side friction.

displacement curve showed different amplitude fluctuations, leading to a certain deviation in the two curves. When the load reached the ultimate bearing capacity, the slope of the curve increases, and then the two showed an approximate linear relationship. The slope of the on-site measured load displacement curve showed a significant change, indicating a certain degree of damage within the composite foundation and reaching the ultimate bearing capacity. However, the slope change of the load displacement curve obtained from numerical simulation was relatively small, and there was a certain deviation in the ultimate bearing capacity values obtained from the two curves. However, overall, the calculated values were in good agreement with the measured values, verifying the rationality of the numerical simulation.

4.3 Influence of interface strength parameters on bearing capacity of composite foundation

The strength parameters of the pile-sand interface have a direct impact on the pile side friction, which furtherly affects the bearing capacity of the pile foundation. Therefore, in this research, the interface strength parameters obtained from the indoor shear test were input in the software as interface parameters to study the impact of different interface strength parameters on the vertical bearing capacity of the pile foundation.

4.3.1 Influence of interface strength parameters on ultimate side friction

The influence of interface strength parameters on the ultimate side friction is shown in Figure 15. It can be seen from Figure 15A that with the increase of interface friction angle, the ultimate side friction increased continuously, and when the interface friction angle was 0, 17, 20.5, 24, 27.5, 31 and 34.5, the corresponding limit side friction was 12, 13.48, 14.71, 15.09, 15.53, 15.99 and 16.31 kPa respectively; it was noticed that when the friction angle was 34.5, the limit side friction resistance increased by 35.92%. It can be seen from Figure 15B that the increase in cohesion led to an increase of ultimate side friction. When the interface cohesion was 0, 4, 8, 12, 16, 20 and 24 kPa, the corresponding limit side friction was 11.76, 12.53, 13.29, 13.77, 14.68, 14.82 and 15.11 kPa respectively. When the cohesion was 24 kPa, the limit side friction increased by 28.49%. The interface friction angle and cohesion together increased the ultimate side friction by 64.41%, indicating that the interface strength parameters are key factors affecting the ultimate side friction, and also indicating that the interface strength parameter is only one influencing factor.

4.3.2 Influence of interface strength parameters on pile load sharing ratio

The ratio of pile side friction Q_s and pile end resistance Q_p with load Q is shown in Figure 16. It can be seen from Figure 16A that in the coral sand foundation, the pile end resistance plays a major role in the bearing capacity of the pile foundation. The proportion of side friction increased first and then decreased with the increase in load. As the load increased, the pile side friction gradually played its role and the share proportion gradually increased; then, as the load continued to increase, the impact of pile side friction was fully used and became stable. As the share proportion of pile end resistance gradually increased, the corresponding share of side friction decreased, so the load was mainly sustained by the pile end resistance. This phenomenon became more and more obvious with the increase of interface friction angle. It can be seen from Figure 16B that with the increase of cohesion, the proportion of pile side friction gradually increased, while the proportion of pile end resistance decreased; but their changing amplitudes were small, and the load proportion tended to a stable level.

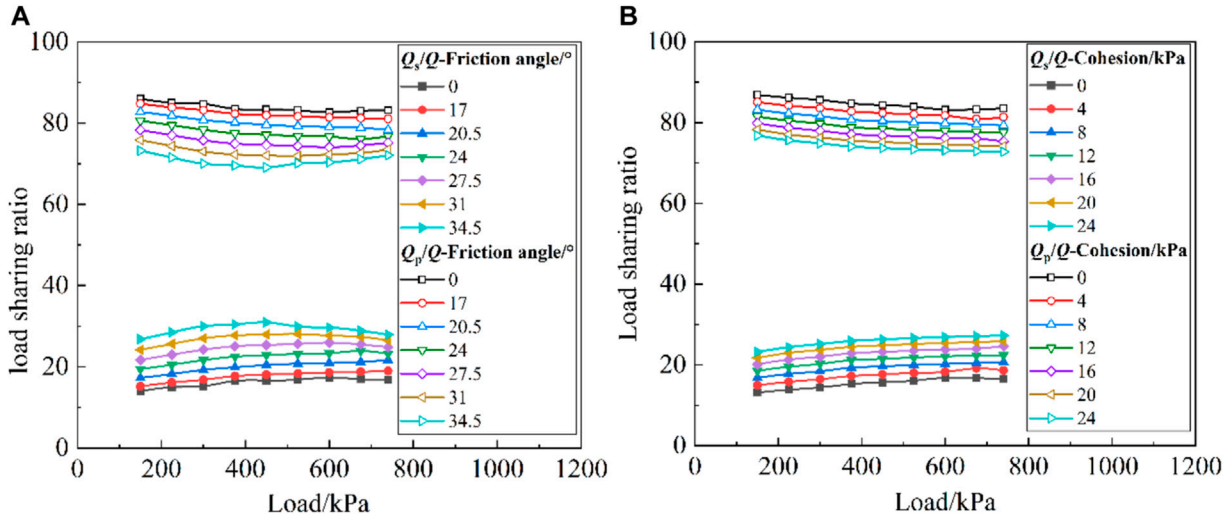

FIGURE 16
Influence of interface strength parameters on load sharing ratio of piles under different loads **(A)** Influence of interface friction angle on load sharing ratio; **(B)** Influence of interface cohesion on load sharing ratio.

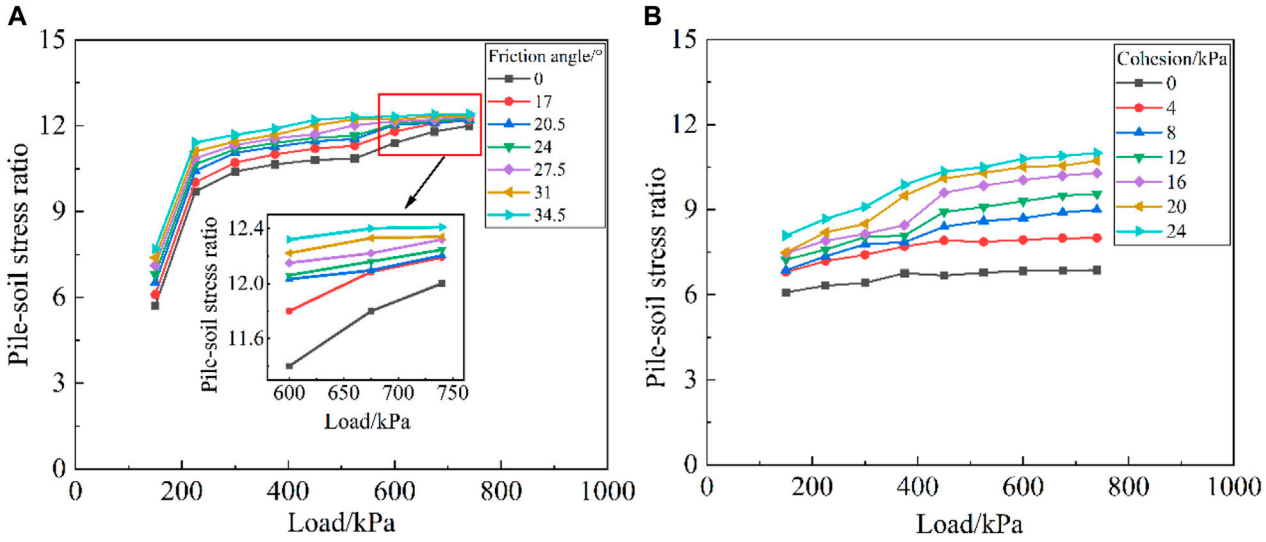

FIGURE 17
Influence of interface strength parameters on pile-soil stress ratio under different loads **(A)** Influence of interface friction angle on pile-soil stress ratio; **(B)** Influence of interface cohesion on pile-soil stress ratio.

4.3.3 Influence of interface strength parameters on pile-soil stress ratio

The influence of interface strength parameters on the pile-soil stress ratio is shown in Figure 17. It can be seen that with the increase of interface friction angle and cohesion, the pile-soil stress ratio gradually increased, but the increase ratio gradually slowed down to a stable value; this indicated that with the increase of the upper load, the load sustained by soil between piles gradually decreased, and the pile body sustained more load, reflecting the bearing characteristics of the rigid pile composite foundation.

5 Formula correction of the characteristic value of single pile bearing capacity

According to the Technical Code for Building Foundation Treatment, the characteristic value of the vertical bearing capacity of composite foundation reinforcement single pile can be estimated as follows; Based on the indoor test and the vertical compressive static load test of single pile, the calculation formula of the characteristic value of the vertical

TABLE 6 The determination of parameter value.

Parameter	Pile diameter(m)	k_0	Interface friction anglle δ (°)	Interface cohesion c (kPa)	Gravity (kN/m^3)	Calculation depth(m)	End resistance coefficient c_1	Uniaxial compressive strength f_{rk} (MPa)
Value	0.4	0.23	30	0	18	6.5	0.4	3.375

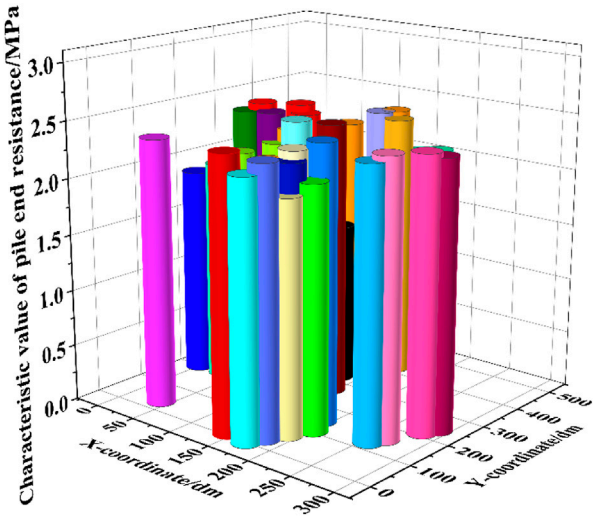

FIGURE 18
The characteristic value of pile end resistance in the static load test.

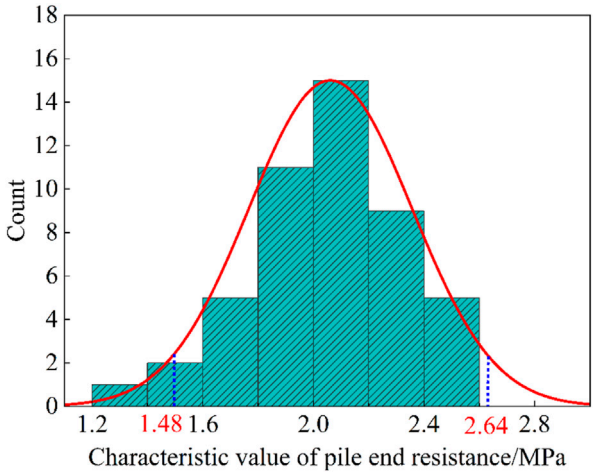

FIGURE 19
Characteristic value interval of pile end resistance with 95% confidence interval.

bearing capacity of composite foundation rigid single pile is proposed:

$$[R_a] = u_p \sum_{i=1}^{n} q_{si} l_{pi} + c_1 f_{rk} A_p \quad (1)$$

Where the pile end bearing capacity is determined by the uniaxial compressive strength f_{rk} and development coefficient of pile end resistance c_1 related to the integrity of rock mass. u_p is the perimeter of the pile m); l_{pi} is the thickness of the layer of soil within the range of pile length m); A_p is the sectional area of the pile (m^2); α_p is the development coefficient of pile end resistance; q_p is the characteristic value of pile end resistance (kPa).

The characteristic value of pile side friction is related to the horizontal effective stress and interface strength parameters, which can be calculated according to the following formula:

$$q_{si} = c + \sigma_n' \tan\delta = c + k_0 \sigma_v' \tan\delta \quad (2)$$

Where σ_n' is the horizontal effective stress of the soil at the pile side, δ is the interface friction angle, c is the interface cohesion, k_0 is the static lateral pressure coefficient of the soil, σ_v' is the vertical effective self-weight stress of the soil at the pile side.

5.1 The determination of parameter value

Based on the field static load test of the single pile, the ultimate bearing capacity of each pile was obtained, and its half value was taken as the characteristic value of the vertical bearing capacity of a single pile. Assuming the stratum only distributes medium-coarse sand, q_{si} was calculated to be 15.6 kPa according to the parameters in Table 6.

5.2 Comparison of characteristic values of pile end resistance

After substituting all characteristic values of the bearing capacity of single pile obtained from the field static load test into Formula (2), the characteristic values of pile end resistance are shown in Figure 18.

By comparing the characteristic value of pile end resistance obtained from the field static load test of the single pile with that from the modified formula $c_1 f_{rk}$, it was found in Figure 19 that the confidence interval of the characteristic value of pile end resistance corresponding to 95% confidence in the field test results was 1.48–2.64 MPa, the calculated value of $c_1 f_{rk}$ was 1.35 MPa and was less than the measured value, with a small error, indicating that the proposed calculation method of composite foundation rigid pile is reliable.

6 Discussion

Currently, there are few engineering reports on the application of CFG pile composite foundation to coral sand foundation. In this

study, it was found that the maximum cohesive force at the pile coral sand interface is 23.4 kPa, which is consistent with the research conclusion that the coral sand bite force is relatively large (Feng et al., 2020; Liu and Li, 2022). At the same time, this study showed that the pile end resistance in coral sand foundation plays a major role in the bearing capacity of CFG piles, with the load sharing of pile side frictional resistance accounting for about 20%, while the remaining 80% of the load is borne by the pile end resistance. The variation law of pile soil stress ratio is basically consistent with that of pile soil stress ratio in general terrestrial strata (Chen et al., 2008; Liu et al., 2023). The difference is that the pile in coral sand foundation always bears a large load, which is due to the relatively poor bearing capacity of coral sand formation formed by hydraulic fill, and the pile end bearing layer is quasi reef limestone, with a large characteristic value of pile end resistance (Zhang et al., 2022). This provides an important reference for the design of similar projects in coral sand foundation. The first point is to pay attention to the design of the vertical bearing capacity of the pile itself, and the pile always bear the main load; The second point is that the design of pile length in composite foundation should be embedded in rock, and the design of pile end resistance should be strengthened (Li et al., 2023). The limitations of the research work in the article are explained as follows: The contact interface between CFG piles and coral sand during on-site construction is rough and complex, and the shear test of coral sand concrete interface failed to consider the influence of interface roughness. The grading range of coral sand listed in the article is limited, and in-depth research is needed on the interfacial shear characteristics of other graded coral sand. Because coral sand is brittle and anisotropic, the influence of these characteristics on the bearing characteristics of pile foundation has not been fully considered in the numerical simulation (Zhang et al., 2023).

7 Conclusion

In this paper, a series of studies have been carried out on the bearing characteristics of CFG pile composite foundation in the reclaimed coral sand site, and the following conclusions can be drawn.

(1) By conducting the shear test on the interface between the concrete pile and coral sand, it is shown that under the low normal stress, the corner bite effect of coral sand is obvious, while the corner is damaged and the bite effect becomes unobvious under the high normal stress. It is also revealed that when the normal stress of pile-sand is less than 100 kPa, the interface cohesion is between 13.1 and 23.4 kPa, and the interface friction angle is between 17.2 and 27.7; When the normal stress of pile-sand is greater than 100 kPa, the interface cohesion is close to 0, and the interface friction angle is between 28.4 and 34.1.
(2) Aiming to the reclamation coral sand site, the treatment method of CFG pile composite foundation was proposed for the first time. The results of the field static load test of single pile and composite foundation show that both the limit bearing capacity and settlement of the pile meet the specification and design requirements, which verifies the reliability and rationality of this foundation treatment. Furthermore, the practical engineerings show that the application of the CFG pile composite foundation in the hydraulic fill coral sand foundation is feasible.
(3) The numerical simulation results show that with the increase of interface strength parameters, the ultimate side friction resistance of the pile increases gradually. With the increase of the interface friction angle, the proportion of the side friction resistance increases first and then decreases more obviously. At the same time, the increase of the interface cohesion leads to a slight increase in the proportion of the side friction resistance of the pile, and the pile end resistance bears the most of load. With the increase of interface strength parameters, the pile-soil stress ratio gradually increases and tends to be stable, reflecting the bearing characteristics of rigid pile composite foundation.
(4) Based on the field load test results, the rationality of the calculation formula of the vertical bearing capacity of composite foundation reinforcement single pile considering the interface strength parameters is verified.

Suggestions for future research work are as follows.

(1) It is recommended to conduct coral sand concrete interface shear tests considering interface roughness to improve the accuracy of testing interface strength parameters;
(2) It is recommended to carry out on-site monitoring of CFG pile composite foundation in coral sand sites, monitor the stress characteristics of the pile foundation during the bearing process, and verify and revise the numerical simulation research results.
(3) Due to the high porosity of coral sand, it is recommended to conduct research on the post grouting technology of CFG piles to enhance the bearing capacity of pile foundations.

Data availability statement

The original contributions presented in the study are included in the article/supplementary material, further inquiries can be directed to the corresponding author.

Author contributions

Methodology, XL and RZ; validation, RZ; formal analysis, RZ and ZY; writing—original draft, RZ; writing—review and editing, RZ; supervision, ZY and PC; project administration, FJ and BW. All authors contributed to the article and approved the submitted version.

Conflict of interest

Authors XL, RZ, ZY, PC, and FJ were employed by CCCC Second Harbor Engineering Co., Ltd. XL was employed by First Engineering Co, Ltd. of CCCC Second Harbor Engineering Bureau. BW was employed by Design Institute of the First Construction Engineering Co, Ltd. of China Construction Third Engineering Bureau.

Publisher's note

References

Angemeer, J., Carlson, E. G., and Klick, J. H. (1973). Techniques and results of offshore pile load testing in calcareous soils. *Proc. Offshore Technol. Conf.* 1984, 1. doi:10.4043/1894-MS

Chang-qi, Z., Hai-feng, L., and Bin, Z. (2016). Micro-structures and the basic engineering properties of beach calcarenites in South China Sea. *Ocean. Eng.* 114, 224–235. doi:10.1016/j.oceaneng.2016.01.009

Chen, C., Yang, Q., Leng, W., Dong, J., Xu, F., Wei, L., et al. (2022). Experimental investigation of the mechanical properties of the sand–concrete pile interface considering roughness and relative density. *Materials* 15, 4480. doi:10.3390/ma15134480

Chen, Q.-n., Zhao, M.-h., Zhou, G.-h., and Zhang, Z.-h. (2008). Bearing capacity and mechanical behavior of CFG pile composite foundation. *J. Central South Univ. Technol.* 15, 45–49. doi:10.1007/s11771-008-0434-8

Coop, M. (1990). The mechanics of uncemented carbonate sands. *Géotechnique* 40, 607–626. doi:10.1680/geot.1990.40.4.607

Datta, M., Gulhati, S. K., and Rao, G. V. (1980). An appraisal of the existing practice of determining the axial load capacity of deep penetration piles in calcareous sands. *Proc. Offshore Technol. Conf.* 3836, 1. doi:10.4043/3867-MS

Dean, E. (2009). *Offshore geotechnical engineering*.

Donohue, S., O'sullivan, C., and Long, M. (2009). Particle breakage during cyclic triaxial loading of a carbonate sand. *Géotechnique* 59, 477–482. doi:10.1680/geot.2008.t.003

Dutt, R., and Cheng, A. (1984). Frictional response of piles in calcareous deposits. *Proc. Offshore Technol. Conf.* 4838, 1. doi:10.4043/4838-MS

Feng, Z.-k., Xu, W.-j., and Meng, Q.-s. (2020). Mechanical behaviors of interaction between coral sand and structure surface. *J. Central South Univ.* 27, 3436–3449. doi:10.1007/s11771-020-4557-x

Hu, B. (2008). *Research on the particle breakage mechanical characteristics and constitutive model of calcareous sand under triaxial conditions*. Wuhan, China: Institute of Rock and Soil Mechanics, Chinese Academy of Sciences.

Igoe, D., Spagnoli, G., Doherty, P., and Weixler, L. (2014). Design of a novel drilled-and-grouted pile in sand for offshore oil&gas structures. *Mar. Struct.* 39, 39–49. doi:10.1016/j.marstruc.2014.06.001

Jiang, L., Fan, J., Wang, Z., and Huo, Z. (2015). Mechanical property of calcareous sand under action of compaction. *Glob. Geol.* 18, 183–187. doi:10.3969/j.issn.1673-9736.2015.03.05

Kou, H.-l., Diao, W.-z., Zhang, W.-c., Zheng, J.-b., Ni, P., Bo-An, J., et al. (2021). Experimental study of interface shearing between calcareous sand and steel plate considering surface roughness and particle size. *Appl. Ocean Res.* 107, 102490. doi:10.1016/j.apor.2020.102490

Lee, C., and Poulos, H. G. (1991). Tests on model instrumented grouted piles in offshore calcareous soil. *J. geotechnical Eng.* 117, 1738–1753. doi:10.1061/(asce)0733-9410(1991)117:11(1738)

Li, D.-j., Shi, C., Ruan, H.-n., Li, B.-y., Li, W.-y., and Yao, X.-c. (2022). Study on shear behavior of coral reef limestone–concrete interface. *Mar. Georesources Geotechnol.* 40, 438–447. doi:10.1080/1064119x.2021.1906365

Li, X., Zhang, X., Shen, W., Zeng, Q., Chen, P., Qin, Q., et al. (2023). Research on the mechanism and control technology of coal wall sloughing in the ultra-large mining height working face. *Int. J. Environ. Res. Public Health* 20, 868. doi:10.3390/ijerph20010868

Liu, C., and Wang, R. (1998). Preliminary research on physical and mechanical properties of calcareous sand. *Rock Soil Mech.* 19, 32–37. doi:10.16285/j.rsm.1998.01.006

Liu, H., Zhu, C., Wang, R., Cui, X., and Wang, T. (2021). Characterization of the interface between concrete pile and coral reef calcarenite using constant normal stiffness direct shear test. *Bull. Eng. Geol. Environ.* 80, 1757–1765. doi:10.1007/s10064-020-02039-8

Liu, S., and Li, X. (2022). Experimental study on the effect of cold soaking with liquid nitrogen on the coal chemical and microstructural characteristics. *Environ. Sci. Pollut. Res.* 30, 36080–36097. doi:10.1007/s11356-022-24821-9

Liu, S., Sun, H., Zhang, D., Yang, K., Li, X., Wang, D., et al. (2023). Experimental study of effect of liquid nitrogen cold soaking on coal pore structure and fractal characteristics. *Energy* 275, 127470. doi:10.1016/j.energy.2023.127470

Ma, W., Qin, Y., Zhao, K., and Chen, G. (2022). Comparisons on liquefaction behavior of saturated coral sand and quartz sand under principal stress rotation. *Mar. Georesources Geotechnol.* 40, 235–247. doi:10.1080/1064119X.2021.1882627

Meng, Q.-S., Yu, K.-F., Wang, R., Qin, Y., Wei, H.-Z., and Wang, X.-Z. (2014). Characteristics of rocky basin structure of yongshu reef in the southern south China sea. *Mar. Georesources Geotechnol.* 32, 307–315. doi:10.1080/1064119x.2013.764553

Ohno, S., Ochiai, H., and Yasufuku, N. (1999). Estimation of pile settlement in calcareous sans. *Eng. calcareous sediments*, 1–6. ISBN:90-5809-041-8.

Poulos, H. G. *The mechanics of calcareous sediments*. Australian Geomechanics 1988: John Jaeger Memorial Address.

Rittirong, A., Shang, J. Q., Mohamedelhassan, E., Ismail, M. A., and Randolph, M. F. (2008). Effects of electrode configuration on electrokinetic stabilization for caisson anchors in calcareous sand. *J. geotechnical geoenvironmental Eng.* 134, 352–365. doi:10.1061/(asce)1090-0241(2008)134:3(352)

Smith, D. A., and Cheung, K. F. (2003). Settling characteristics of calcareous sand. *J. Hydraulic Eng.* 129, 479–483. doi:10.1061/(asce)0733-9429(2003)129:6(479)

Spagnoli, G., Doherty, P., Murphy, G., and Attari, A. (2015). Estimation of the compression and tension loads for a novel mixed-in-place offshore pile for oil and gas platforms in silica and calcareous sands. *J. Petroleum Sci. Eng.* 136, 1–11. doi:10.1016/j.petrol.2015.10.032

Uesugi, M., Kishida, H., and Uchikawa, Y. (1990). Friction between dry sand and concrete under monotonic and repeated loading. *Soils Found.* 30, 115–128. doi:10.3208/sandf1972.30.115

Wang, R., Guo, J., Lei, S., Wang, X., Rong, W., Yu, Z., et al. (2022). A spike-trimer protein-based tetravalent COVID-19 vaccine elicits enhanced breadth of neutralization against SARS-CoV-2 Omicron subvariants and other variants. *Mar. Georesources Geotechnol.*, 1–13. doi:10.1007/s11427-022-2207-7

Wang, X.-Z., Jiao, Y.-Y., Wang, R., Hu, M.-J., Meng, Q.-S., and Tan, F.-Y. (2011). Engineering characteristics of the calcareous sand in nansha islands, south China sea. *Eng. Geol.* 120, 40–47. doi:10.1016/j.enggeo.2011.03.011

Wang, X.-Z., Wang, X., Jin, Z.-C., Zhu, C.-Q., Wang, R., and Meng, Q.-s. (2017). Investigation of engineering characteristics of calcareous soils from fringing reef. *Ocean. Eng.* 134, 77–86. doi:10.1016/j.oceaneng.2017.02.019

Wang, X., Ding, H., Meng, Q., Wei, H., Wu, Y., and Zhang, Y. (2021). Engineering characteristics of coral reef and site assessment of hydraulic reclamation in the South China Sea. *Constr. Build. Mater.* 300, 124263. doi:10.1016/j.conbuildmat.2021.124263

Wang, X., Wu, Y., Cui, J., Zhu, C. Q., and Wang, X. Z. (2020). Shape characteristics of coral sand from the South China Sea. *J. Mar. Sci. Eng.* 8 (10), 803. doi:10.3390/jmse8100803

Xu, L.-J., Wang, X.-z., Wang, R., Zhu, C.-q., and Liu, X.-p. (2022). Physical and mechanical properties of calcareous soils: A review. *Mar. Georesources Geotechnol.* 40, 751–766. doi:10.1080/1064119x.2021.1927270

Zhang, J., Li, X., Qin, Q., Wang, Y., and Gao, X. (2023). Study on overlying strata movement patterns and mechanisms in super-large mining height stopes. *Bull. Eng. Geol. Environ.* 82, 142. doi:10.1007/s10064-023-03185-5

Zhang, L., Shen, W., Li, X., Wang, Y., Qin, Q., Lu, X., et al. (2022). Abutment pressure distribution law and support analysis of super large mining height face. *Int. J. Environ. Res. Public Health* 20, 227. doi:10.3390/ijerph20010227

Zhang, P., Ding, S., and Fei, K. (2021). Research on shear behavior of sand–structure interface based on monotonic and cyclic tests. *Appl. Sci.* 11, 11837. doi:10.3390/app112411837

frontiers | Frontiers in Earth Science

TYPE Original Research
PUBLISHED 08 June 2023
DOI 10.3389/feart.2023.1225287

OPEN ACCESS

EDITED BY
Xuelong Li,
Shandong University of Science and Technology, China

REVIEWED BY
Liang Zhang,
Xihua University, China
Shaojie Zuo,
Guizhou University, China

*CORRESPONDENCE
Meng Yang,
603894673@qq.com
Jianzhong Chen,
chenjianzhong@cmhk.com

RECEIVED 19 May 2023
ACCEPTED 29 May 2023
PUBLISHED 08 June 2023

CITATION
Cao S, Yang M, Hu J and Chen J (2023), Advanced perception and control method of harmful gas during construction period of coal tunnel based on DeepAR.
Front. Earth Sci. 11:1225287.
doi: 10.3389/feart.2023.1225287

Advanced perception and control method of harmful gas during construction period of coal tunnel based on DeepAR

Shengye Cao[1], Meng Yang[2,3]*, Juyi Hu[2,3] and Jianzhong Chen[2,3]*

[1]Qinghai Province Huangyuan Highway Engineering Construction Co., Ltd., Qinghai, China, [2]China Merchants Chongqing Transportation Research and Design Institute Co., Ltd., Chongqing, China, [3]National Engineering Research Center of Highway Tunnel, Chongqing, China

Effective real-time treatment and control of harmful gases are key to ensuring the safety of tunnel construction workers. Currently, the monitoring ability of harmful gases is insufficient to match the processing needs, which poses significant risks to the safety of tunnel construction workers. This paper proposes an advanced perception and treatment method for harmful gases during tunnel construction, utilizing the DeepAR algorithm. Real-time monitoring of the concentration and diffusion of harmful gases is conducted, and a harmful gas concentration prediction model is established using the DeepAR algorithm, achieving advanced perception of harmful gases during tunnel construction. The harmful gas treatment plan is developed in advance, and the effectiveness of the proposed method is demonstrated by simulation testing under realistic field scenarios and comparing with other prediction models. The method was applied in a coal mine tunnel in Qinghai Province, achieving an accuracy rate of 94.3%, which is higher compared to those obtained using RNN and LSTM algorithms. Moreover, the computational time is less than 60 s. The method provides timely perception of the concentration distribution of harmful gases in the tunnel and proposes targeted treatment measures, verifying the effectiveness of the prediction model from the perspective of practical engineering application.

KEYWORDS

highway tunnel, harmful gas, DeepAR, advance forecast, tunnel construction

1 Introduction

With the continuous development of modern transportation facilities, more and more underground tunnels, subway passages and underground spaces have been built and utilized. In modern tunnel construction, due to the complexity of construction methods and geological environment (Fei et al., 2010; He et al., 2017; Su et al., 2020), the concentration and diffusion law of harmful gases produced by different coal seam structures are different under coal-penetrating geological conditions (Zhang et al., 2023a; Liu et al., 2023), and the generation and aggregation characteristics of toxic and harmful gases such as gas and hydrogen sulfide need to be sensed in advance, which will effectively protect the health of tile workers in tunnel construction (Cao et al., 2016; Zhao et al., 2020; Gong et al., 2022). Excessive inhalation of harmful gases has a great negative impact on human respiratory system, circulatory system and nervous system, especially under continuous exposure to high concentration of harmful gases, workers may lose consciousness and even die. Therefore, how to effectively warn and control the

concentration of harmful gases during tunnel construction, adopt effective methods to forecast harmful gases and take countermeasures in advance is of great practical significance to tunnel engineering practice (Kang et al., 2010).

Current toxic and harmful gas monitoring and detection methods rely on real-time sensing devices to monitor gases and take prompt action to prevent harm to construction workers and nearby environmental conditions (Chen et al., 2020). Nonetheless, the

Assessment and identification of dangerous gases during tunnel construction is greatly influenced by the location of sensor placement, the work conditions, and the number of sensors utilized in the process. Meanwhile, a range of geological factors contribute to differing amounts of toxic gases, their fluctuations, and overall trends during excavation, all of which pose formidable challenges for the real-time management and control of these gases, thereby endangering the wellbeing of construction personnel.

With the development, and application of deep-learning and artificial intelligence technology, using deep-learning-based time-series prediction models to make real-time predictions of noxious gas concentrations has shown extensive potential applications (Gong et al., 2015a; Zhang and Yang, 2017a; Wu and Fan, 2020). DeepAR, a deep-learning algorithm specially designed for the prediction of time-series data, holds high flexibility and prediction accuracy and has been widely applied across domains, including transportation, electricity, and finance (Salinas et al., 2020). However, pertinent research on the prediction and evaluation of noxious gas concentrations during tunnel construction lacks an adequate experimental foundation and having improvement schemes implemented.

This article presents a proactive approach to monitoring and mitigating the risks associated with harmful gases during tunnel construction, utilizing the DeepAR algorithm for effective prediction and control of gas concentrations. Firstly, existing technologies for monitoring and controlling harmful gases are extensively reviewed, including a detailed description of the data preprocessing process. Following this, various time series prediction algorithms are compared and analyzed to provide a comprehensive assessment of their respective advantages and limitations. The DeepAR-based model for predicting harmful gas concentrations is subsequently presented, with simulated results obtained from actual field scenarios compared and contrasted with other prediction models. Finally, a comprehensive discussion is made on the effectiveness of the DeepAR approach in mitigating harmful gas concentrations. The proposed method provides a new and promising means of minimizing harmful gas exposure during tunnel construction.

2 Overview of relevant work

The monitoring and early detection of hazardous gases has always been a crucial aspect of construction site safety. In China, the predominant method for mountain tunnel excavation is the drilling and blasting technique. This method boasts simple, versatile, and economically efficient equipment and facilities that can adapt to a wide range of geographical conditions and has been widely employed in China's mountain-tunnel excavation processes. However, the use of drilling and blasting for excavation produces hazardous gases (Zhang et al., 2023b; Liu et al., 2023), which are more prone to accumulation in the relatively enclosed spaces of the tunnels. As a result, large-scale excavation works in tunnel construction lead to a buildup of hazardous gases on the tunnel surface, severely impacting the construction workers' health. Therefore, it is imperative to address this issue promptly by effectively monitoring hazardous gases, predicting their diffusion and development laws in real-time during construction periods, and implementing appropriate countermeasures.

TABLE 1 Allowable concentration of harmful gases in tunnel construction site.

Country	Harmful gas	Allowable exposure limits	
		Ppm	mg/m^3
China	CO	24	30
	NO_2	5	5
	H_2S	6.6	10
United States	CO	50	55
	NO_2	5	9
	H_2S	20	25
Germany	CO	30	33
	NO_2	5	9
	H_2S	10	14
Japan	CO	50	57
	NO_2	5	9
	H_2S	5	7

Domestic scholars have developed relevant standards and specifications to alleviate the construction of tunnels, and have made relevant regulations on the tunnel construction environment (Industry Standards of the People's Republic of China, 2002; Indus try Standards of the People's Republic of China, 2009; Industry Standards of the People's Republic of China, 2000). For the CO concentration in the tunnel, it must not exceed 20 mg/m^3 and in special conditions, when the time does not exceed 15 min, the concentration of CO must not exceed 30 mg/m^3. CO_2 calculated by volume should not be less than 0.5%; NO_2 in nitrogen oxides should not be less than 5 mg/m^3. At the same time, relevant standards and specifications also specify the highest allowable concentration of harmful gases during tunnel construction, time-weighted average allowable concentration and short-term exposure allowable concentration. Foreign standards for tunnel construction research have started relatively early, and Germany, the United States, and Japan have specified the concentration of carbon monoxide, nitrogen dioxide, and hydrogen sulfide during tunnel construction in Table 1.

According to the table, it is clear that China implements more rigorous standards. However, the ventilation method on tunnel construction sites still follows the traditional approach of "real-time monitoring before forced ventilation" which leads to poor effectiveness in treating harmful gas due to the inadequate awareness of gas diffusion patterns and range. Numerous studies have been conducted by domestic and international experts and scholars on the monitoring and treatment of harmful gases in tunnels.

Matsumoto et al. built a numerical model to analyze the comprehensive impact of structural, geological, and environmental factors (Matsumoto et al., 1998). Liu et al. conducted numerical simulations to investigate the diffusion of harmful gases during tunnel excavation under press-in ventilation conditions, revealing the patterns and changes in the spread of these gases (Liu et al., 2009). Additionally, Liu et al. (2014) used Fluent simulations to explore the distribution of harmful gases during the rock breaking process at tunnel exits and to investigate the wind field characteristics and harmful gas distribution in the tunnel cavity during this process. Klemens et al. (2001) investigated the movement of tunnel dust and optimized the current ventilation methods based on this understanding of dust distribution patterns. Chen and Su, 2019 analyzed the features of harmful gases in tunnels and drew upon experiences and data from similar underground projects in geochemically comparable areas to provide a reference for studying harmful gases in metamorphic and magmatic rock areas. Lastly, Huo et al. (2023) applied the key stratum theory, fluid mechanics, and other theories to propose conditions for the failure of harmful gases in Jurassic goaf and establish a multi-parameter control equation for harmful gas discharge from Jurassic goaf to the coal seam working face.

During tunnel construction, various harmful gases are released, and their prediction and treatment is essential. Gong et al., 2015b addressed the problem of detecting multiple harmful gases by using the particle swarm optimization (PSO) algorithm to optimize the weights and thresholds of the BP neural network. They proposed a method that combined a sensor array with the BP neural network for monitoring multiple harmful gases. Fu, 2022 suggested corresponding preventive measures for gas outburst at different positions in the tunnel and developed a gas outburst prediction model based on the exponential smoothing method. Li (Li, 2017) proposed a wireless network technology that enables the transmission of video and audio data using 2.4G wireless signals and gas data using 470 MHZ wireless signals, thereby freeing the system from cable constraints. Ding, 2011 analyzed the factors affecting coal and gas outbursts, established two tunnel gas concentration prediction models using the exponential smoothing and curve trend prediction methods, and monitored the short-term gas concentration of the tunnel. Li (Li et al., 2022) tackled the problem of single control means, control lag, low efficiency, and poor effects of ventilation systems, and proposed a novel method using the fuzzy PID control technology based on an improved fuzzy logic theory for comprehensive treatment of various harmful gases. Wang, 2022 pointed out the drawback of using harmful gas content prediction technology based on quality sensors, which overly relies on sensor sensitivity and thus lowers the accuracy of harmful gas content prediction. They proposed a harmful gas content prediction technology based on sensitivity infrared sensors. Finally, to address the high cost of numerous geological drills used in previous studies that seriously affected construction progress, Zhang and Yang, 2017b used a comprehensive projection calculation method of tunnel-rock relationship to predict the occurrence location of harmful gases in the tunnel for the next phase.

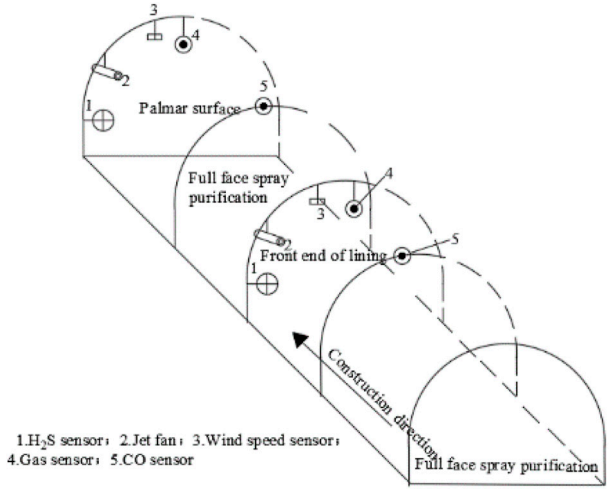

FIGURE 1
Monitor section distribution.

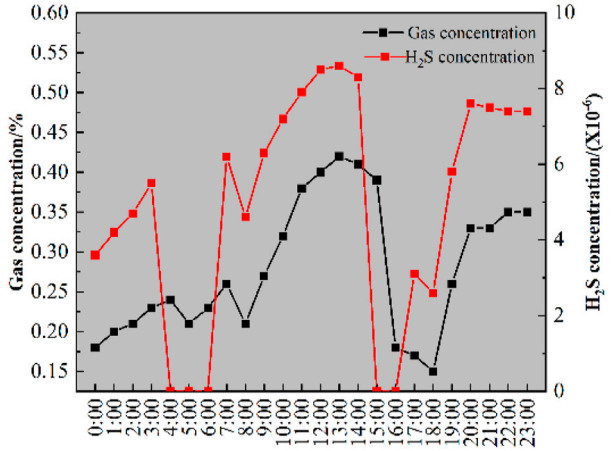

FIGURE 2
Abnormal result of data collection.

3 Data preprocessing

During tunnel construction, harmful gases such as hydrogen sulfide, methane, and carbon monoxide are monitored using gas-collection sensors. Wind-speed sensors are used for information control and monitoring. To track the diffusion of gas, sensors are placed in various sections such as the leading end of the lining, the return air outlet, and the face of the excavation area. Figure 1 displays the distribution of these sensors.

Four types of monitoring sensors are used to continuously monitor gas concentrations inside the tunnel in two states, traditional ventilation diffusion and system purification through dilution and spraying. These sensors are programmed to automatically collect data every 5–60 s, which are then transmitted via a network to a central PC for storage.

The data collected from sensors are subject to limitations imposed by the operating environment. These limitations may result in erroneous, missing or duplicate data during the data collection process. Thus, data must be cleared and repaired to ensure their

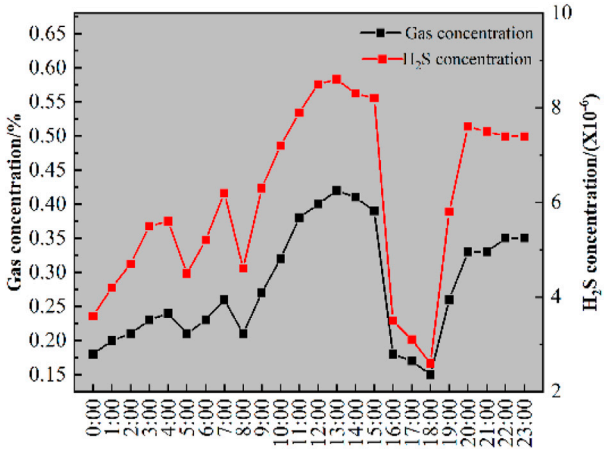

FIGURE 3
Data patch results.

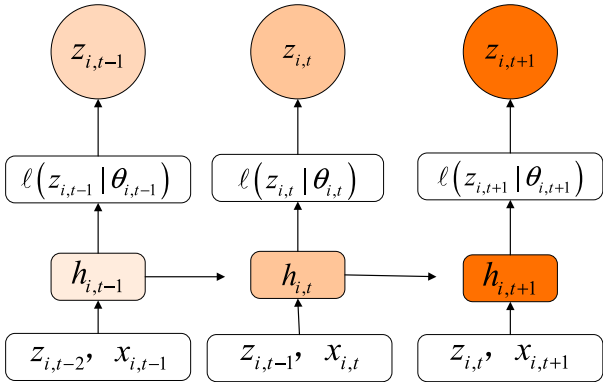

FIGURE 4
Model training process.

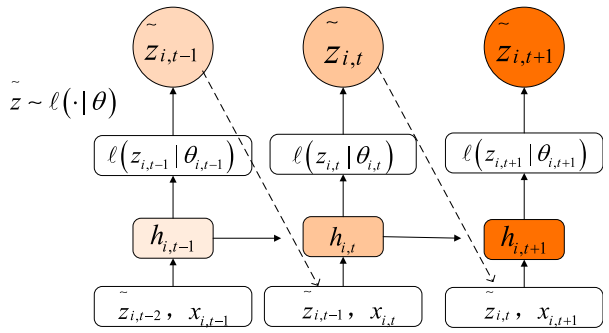

FIGURE 5
Model prediction process.

quality and reliability. In this study, we adopted the method of identifying harmful gas data anomalies to explore the original data and remove erroneous values. By drawing the time series graph of harmful gases, we were able to easily identify the exceptional data. For example, as shown in Figure 2, the hydrogen sulfide concentration and the methane variation of a collected data segment suddenly drop to zero, while adjacent data change normally, indicating data loss during the data collection of hydrogen sulfide concentration. Therefore, the data of this time period needs to be patched.

The collected raw data exhibits certain patterns. To address missing data, we employed time series analysis. Specifically, we utilized the sulfur dioxide data as a time series and employed the weighted mean method to estimate and fill in the missing data. As a result, we obtained a more comprehensive and reasonable trend of the data, as depicted in Figure 3. Similarly, after identifying all outliers in the raw data, we filled them in using time series analysis, thereby maintaining the integrity of our dataset.

When dealing with large volumes of raw data or data with high dimensionality, computing distances between different data can be extremely difficult. Additionally, utilizing random sampling to process data poses a risk of producing biased results, while still being unable to guarantee data completeness. To overcome these issues, data normalization becomes necessary, especially when dealing with data that possess varying dimensions. This paper utilizes the z-score method to normalize raw data. The z-score method ensures that data errors resulting from varying dimensions are eliminated. In the case of a data set on harmful gases, the z-score expression is utilized.

$$y = \frac{x_i - \bar{x}}{\sqrt{\frac{1}{n}\sum_{j=1}^{n}\left(x_j - \bar{x}\right)^2}}$$

In the equation, y is the normalized value of harmful gases, $\bar{x}$ is their respective mean. The normalized result falls within the range of [-1, 1].

4 Prediction model based on DeepAR

4.1 Model building

Predicting changes in harmful gas concentrations during tunnel construction can aid in the early formulation of effective treatment plans and ensure the health and safety of workers. The gas concentration data is time-dependent, and can be viewed as time-series data. A wide range of time prediction algorithms are available, including the traditional statistical methods of ARIMA and exponential smoothing models. With the development of artificial intelligence, deep learning methods such as RNN, LSTM, and DeepAR have gradually been applied to time series prediction. Compared to traditional models, DeepAR is a self-autoregressive recurrent neural network-based time series probability prediction method. It can handle complex scenarios such as periodic and multi-variable time series, accurately predict the probability of large-scale time series through learning similar data, and is therefore used in this study to predict harmful gas in the tunnel construction period. Figure 4 and Figure 5 shows the training and prediction process, which comprises the following steps.

TABLE 2 Raw data result.

Date	Gas/%	$H_2S/(x10^{-6})$
2021–04-20 00:00:00	0.18	3.6
2021–04-20 00:02:00	0.3	4.2
2021–04-20 00:04:00	0.21	4.7
2021–04-20 00:06:00	0.23	5.5
2021–04-20 00:08:00	0.24	5.6
2021–04-20 00:10:00	0.21	4.5
2021–04-20 00:12:00	0.23	5.2
...	...	...

Step1: the harmful gas data during the tunnel construction period was preprocessed, and the results were divided into training and testing sets. 70% of the data was used for the training set, and 30% for the testing set.

Step2: the preprocessed harmful gas data was transformed into DeepAR data format, which is a JSON file consisting of the following attributes: "start" representing the starting time of the time series, "target" representing the time series that meets the conditions, "cat" indicating the classification variables related to the time series, and "dynamic_feat" representing the non-classification features associated with the time series.

Step3: we configured the hyperparameters and the model structure of the DeepAR model. The hyperparameters included the length of predicted time series, the number of LSTM layer neurons, the number of LSTM layers, the Dropout regularization rate, the loss function, the optimizer, and other hyperparameters.

Step4: the DeepAR model was trained using a training dataset. During the training process, at each time step t, the network takes the input of harmful gases, the previous value $z_{i,t-1}$, and the previous state $\vec{h}_{i,t-1}$. The current state $\vec{h}_{i,t} = h(\vec{h}_{i,t-1}, z_{i,t-1}, x_{i,t-1})$ is calculated first, and then the parameter $\theta_{i,t} = \theta(\vec{h}_{i,t})$ for the likelihood $l(z|\theta)$ is derived. Finally, the prediction result is obtained using maximum likelihood estimation. The expression for this prediction is as follows:

$$\ell = \sum_i \sum_t \log l\left(z_{i,t} | \theta\left(\vec{h}_i, t\right)\right)$$

Step5: After comparing the predicted and actual values, the error function E is calculated. If the loss function E is less than the predetermined threshold, the training is considered complete. Otherwise, the weights and biases in the neural network are updated using gradient descent, and the computation returns to step 4 for recalculation.

Step6: After the training process is completed, a model for predicting the concentration of harmful gases at the tunnel construction site is obtained.

4.2 Model evaluation

To evaluate the outcomes of the model, this paper introduces the Root Mean Square Error (RMSE) as the metric. The equation to calculate RMSE is presented below.

$$RMSE = \sqrt{\frac{1}{n}\sum_{i=1}^{n}(y_i - \hat{y}_i)^2}$$

The equation takes the form of y_i and $\hat{y}_i$, which represent the actual and predicted values, respectively.

5 Model application and result analysis

5.1 Data source

A certain tunnel, spanning 6,044 m, is located in a frigid and high-altitude area. In accordance with the requirement of geological forecast for advanced tunnel construction, the geological drilling of the left tunnel face was carried out in front of the construction plant while crossing geological formations such as coal seams. When the drilling was done at a distance of 2 m from the floor, the concentration of hydrogen sulfide and gas reached as high as 0.010% and 2.5%, respectively, after the drilling depth reached 2.5 m. The analysis of onsite detection data shows that the coal geological structure of the tunnel excavation is more likely to produce a large amount of harmful gas, of which methane and hydrogen sulfide are the main ones. Based on expert experience and field judgment evaluation, it is necessary to monitor and perceive harmful gases in real time and take corresponding control measures to ensure the safety of personnel during the tunnel construction, as there is still about 1,500 m of coal geological structure for the subsequent tunnel section, which could be even longer. The sampling interval of the harmful gas monitoring sensor is sufficiently frequent, but since there are a lot of monitoring data and the monitoring duration exceeds 24 h, only the harmful gas concentration values before and after the detonation and in the front end of the lining before the initial data selection were chosen. Preliminary screening and analysis of the initial data shows that the gas concentration changes are significant only before and after the detonation, while at other times, they did not exceed the limit value and tended to be stable. The data results are shown in Table 2.

4.2 Model parameter optimization

The prediction of harmful gas concentration in tunnels using AI algorithms commonly uses mean squared error (MSE) or mean absolute percentage error (MAPE) as the loss function. However, MSE is sensitive to outlier values, and handling them may compromise the integrity of actual data. Hence, this paper uses MAPE as the loss function.

The DeepAR model was employed to construct a predictive model for harmful gas concentration at a tunnel construction site. The optimal parameters of the model were iteratively calculated. Based on the data from April 2022 at a tunnel construction site in Qinghai, the model was optimized by varying the number of hidden

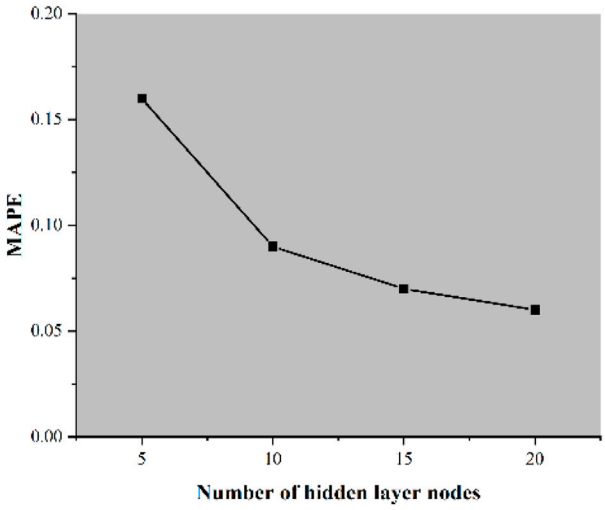

FIGURE 6
Calculation of MAPE values for different hidden layer nodes.

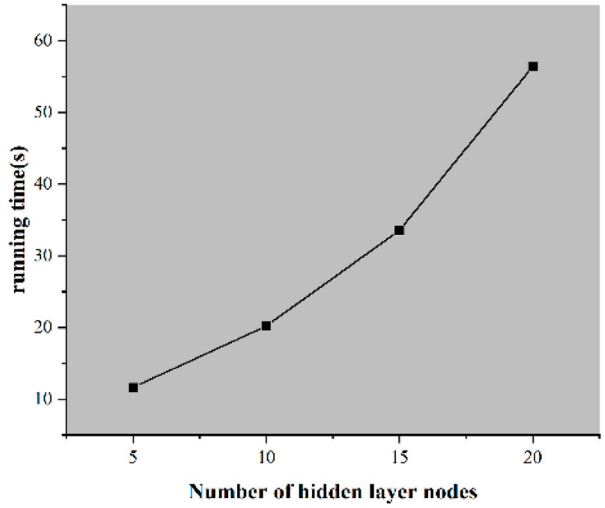

FIGURE 7
Running time of different hidden layer nodes.

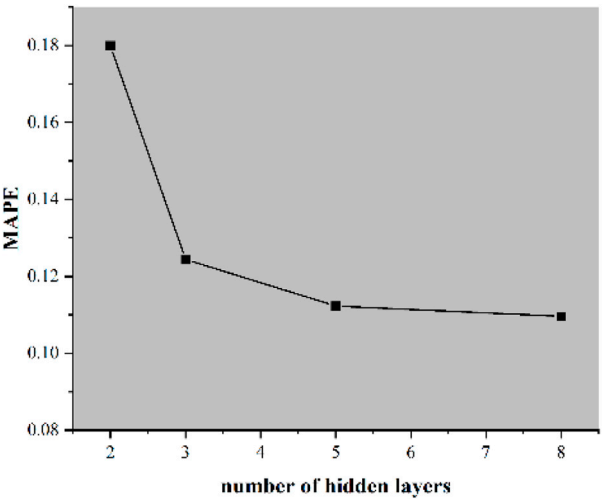

FIGURE 8
Calculation of MAPE values for different hidden quantities.

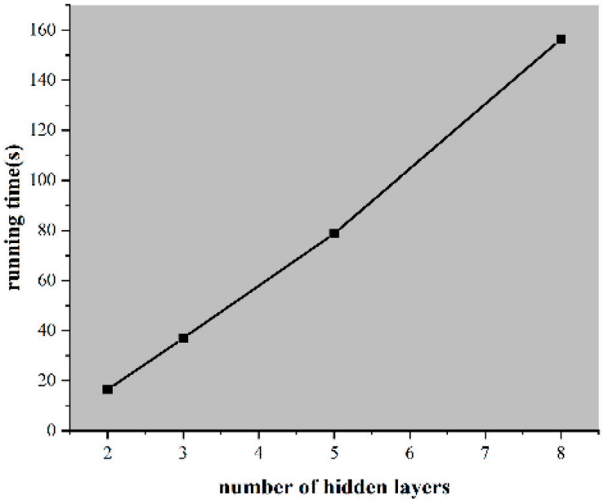

FIGURE 9
Running time for different hidden quantities.

layer nodes, the number of hidden layers, and the optimizer used. Specifically, the DeepAR predictive model for 5, 10, 15, and 20 hidden layer nodes were separately optimized using 100 iterations. The resulting MAPE values and run times for different parameters are presented in Figure 6 and Figure 7.

The MAPE values obtained from the DeepAR predictive models for different structures suggest that the MAPE values decrease as the number of hidden layer nodes increases and then stabilize, indicating an increase in the accuracy of the model's output. However, an exponential increase in the running time of the model accompanies the gradual increase in the number of hidden layers. Therefore, to reduce the running time of the model while maintaining its accuracy, the model with 10 nodes in the hidden layer was selected as the baseline parameter to build the predictive model. The DeepAR predictive models for 2, 3, 5, and 8 hidden layers were separately optimized using 100 iterations. The resulting MAPE values and run times for different parameters are presented in Figure 8 and Figure 9.

Based on the MAPE values obtained from the DeepAR predictive models of different structures, an increase in the number of hidden layers led to an improved model accuracy. However, as the number of hidden layers increased to 5, the improvement in the model's accuracy reduced significantly while the model's running time increased drastically. Therefore, in this study, a hidden layer size of five was selected as the baseline parameter for the predictive model.

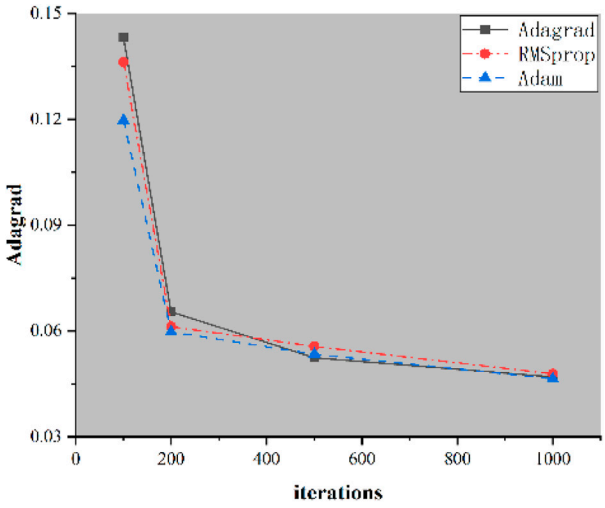

FIGURE 10
Calculation of MAPE values for different hidden quantities.

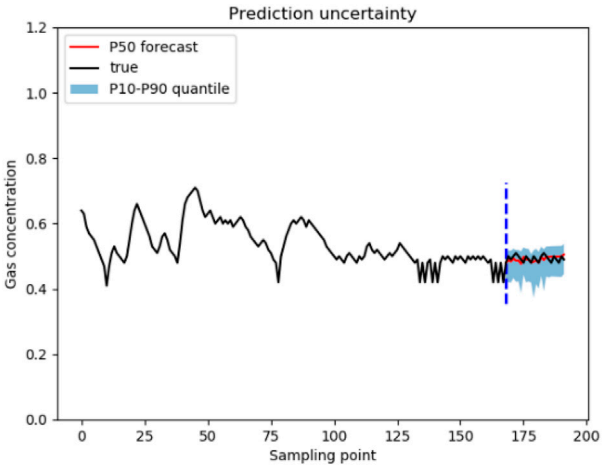

FIGURE 11
shows the model prediction results.

TABLE 3 Predictive model parameters.

Indicator type	Parameter result
Number of hidden layer nodes	10
Number of hidden layers	5
Optimizer	Adam

We conducted a comparative analysis of Adagrad, Adadelta, and Adam optimization algorithms, utilizing a learning rate of 10. The corresponding results of our training are presented in Figure 10.

Based on the MAPE results obtained from the DeepAR forecast model with various structures, the MAPE values for the models under every optimizer decrease continually with increasing iterations. Among them, the MAPE values for the models that use Adagrad and Adam as optimizers decrease at the fastest rates. When the model is iterated 1,000 times, the MAPE value of the model that uses Adam as the optimizer is 0.064, which is relatively the lowest. Thus, we chose Adam as the optimizer for the tunnel construction site's harmful gas early warning model that we constructed based on DeepAR. The corresponding parameters can be found in Table 3.

4.3 Result analysis

This paper presents a case study on gas sampling during a tunnel construction site. We selected the monitoring data of the past 7 days to forecast the gas concentration in the tunnel 72 h ahead. Then, we utilized the data in the advanced perception model for harmful gases during the tunnel construction period. The prediction result is shown in Figure 11.

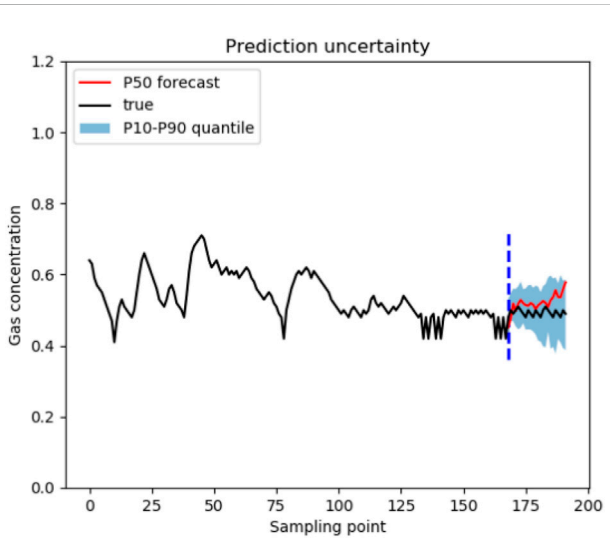

FIGURE 12
RNN model prediction results.

As shown in Figure 11, the predicted results are consistent with the trend of actual values, with relatively small errors, indicating that the model has good forecasting results.

To ensure the accuracy of the harmful gas advanced perception model during tunnel construction based on DeepAR, this paper performs a comparison between Recurrent Neural Networks (RNN) and Long Short-Term Memory (LSTM) models. The prediction results of both models are shown in Figure 12 and Figure 13, and their RMSE values and run times are listed in Table 4.

After comparing the results obtained from different models, it can be concluded that the DeepAR model is a more effective tool for predicting harmful gases concentration at highway tunnel construction sites compared to RNN and LSTM models. The RMSE for the DeepAR model is relatively smaller, and its

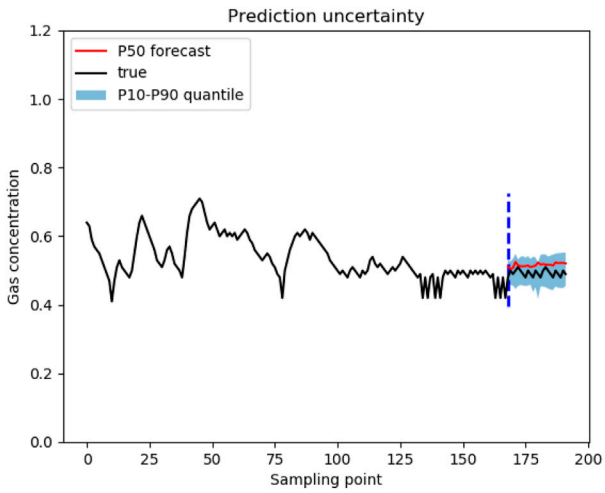

FIGURE 13
LSTM model prediction results.

TABLE 4 Comparison of calculation results of different models.

Model	RMSE	Running time (s)
DeepAR	2.67	58.46
RNN	6.59	34.17
LSTM	3.79	39.62

accuracy has reached 94.3%. These results demonstrate that the DeepAR model's predicted values are closer to actual values. However, the DeepAR model takes longer time to run compared to other models, albeit still within 60s. Nevertheless, the model's prediction time fully satisfies the daily working requirements.

5 Discussion on harmful gas control methods in tunnels

Road tunnel construction sites are prone to harmful gas diffusion, which poses a significant threat to the health and safety of workers. In this study, we use real-time sensors installed at construction sites to preprocess and analyze harmful gas data. By implementing artificial intelligence algorithms, we can predict and anticipate the concentration and distribution of harmful gases. This method enables us to effectively track the development and spread of harmful gases.

Traditional methods of treating harmful gas during tunnel construction involve enhancing ventilation and spraying diluting fluids to purify the tunnel's air. However, it is currently common practice to intensify ventilation only after conducting real-time gas monitoring at construction sites. This practice may lead to mismatched connections between the concentration and range of harmful gases, and the effectiveness of ventilation or dilution. Consequently, ventilation and dilution may not occur on time, be imprecise, and unsafe. By accurately perceiving and predicting harmful gases in advance, we can provide a basis for ventilation or dilution efficacy during tunnel construction. Using advanced fuzzy PID control technologies, we can open the fans early and regulate the wind volume, speed, and pressure inside the tunnel. This will ensure that harmful gases remain within the acceptable range for worker health, guarantee their physical wellbeing, and simultaneously maintain construction progress.

This study proposes a DeepAR-based method for accurately anticipating harmful gases during tunnel construction. By leveraging real-time sensor data and considering harmful gas diffusion characteristics, this approach enables advanced perception and prediction of harmful gases, which can ensure effective remediation and providing accurate data. The harmful gas prediction data obtained from this method can be utilized by remediation equipment such as fans and atomizers, to implement intelligent control measures. By setting up the necessary index parameters for harmful gas remediation in advance, an appropriate working environment can be secured within the tunnel while reducing material and resource waste incurred by ineffective ventilation or atomization, reducing tunnel construction costs.

6 Conclusion

In the context of constructing coal tunnels, there exist concerns regarding the safety of workers due to exposure to three types of toxic and harmful gases: gas, hydrogen sulfide, and carbon monoxide. To address this issue, this paper proposes a method for forecasting and managing hazardous gases during tunnel construction based on the DeepAR model. The proposed method has been verified through actual tunnel monitoring data, demonstrating its capability to precisely predict changes in gas concentration and facilitate effective synchronous treatment of hazardous gases. These findings contribute to enhancing the safety of tunnel construction. The primary research conclusions are summarized below.

(1) Superior advance perception and advance handling of hazardous gases in tunnel construction sites are of significant importance for the safety of the construction process. As tunnel excavation progresses, different layers contain varying concentrations and changes of harmful gases which, when anticipated and treated in advance, guarantee the safety of the construction process. By perceiving and processing harmful gases ahead of time, accidents during tunnel construction can be prevented or reduced.
(2) Combining real-time monitoring data of harmful gases in the tunnel, a method for predicting the concentration variation of harmful gases at the construction site ahead of time is proposed. This method enables the prediction of the concentration change of harmful gases within the next 72 h. The Root Mean Square Error (RMSE) of this method is superior to that of both the Recurrent Neural Network (RNN) model and the Long Short-Term Memory (LSTM) model, demonstrating an accurate prediction of the changes in harmful gas concentrations in the tunnel. The prediction speed is within 60 s, allowing for

sufficient time to develop effective and timely treatment solutions for harmful gases in the tunnel.

(3) The tunnel harmful gas prediction method proposed in this study can sense the changes of harmful gas at the tunnel construction site in advance, and also provides an effective and accurate data basis for the control parameters of the treatment equipment, which can save costs and increase construction efficiency while ensuring construction safety.

Data availability statement

The original contributions presented in the study are included in the article/Supplementary Material, further inquiries can be directed to the corresponding authors.

Author contributions

SC wrote the original manuscript and designed algorithm. MY, JH, and JC proposed the idea, supervised the research work, and revised the manuscript. SC and MY discussed and analyzed the results. All authors contributed to the article and approved the submitted version.

Funding

This work was supported by the Chongqing Natural Science Foundation (Distinguished Youth Fund) Project (No. cstc2021jcyjjqX0012), the Qinghai Provincial Science and Technology Plan (No. 2023-SF-128), and the Qinghai Transportation Science and Technology Project (No. 2020-01).

Conflict of interest

Author SC is employed by the Qinghai Province Huangyuan Highway Engineering Construction Co., Ltd; Authors MY, JH, and JC were employed by the China Merchants Chongqing Transportation Research and Design Institute Co., Ltd.

Publisher's note

References

Cao, Z., Yang, Q., and Guo, C. (2016). Hazardous gas migration characteristics during construction of railway tunnels in high altitude areas [J]. *J. Central South Univ. Nat. Sci. Ed.* 47 (11), 3948–3957. doi:10.11817/j.issn.1672-7207.2016.11.044

Chen, D., and Su, P. (2019). Research on the characteristics and hazards of harmful gases in the Kanglin section of the Sichuan-Tibet Railway [J]. *J. Railw. Eng.* 36 (6), 18–22. doi:10.3969/j.issn.1006-2106.2019.06.005

Chen, Z., Su, P., and Lu, H. (2020). Research on harmful gas monitoring and protection technology of hongdoushan tunnel 1~# inclined shaft [J]. *Mod. Tunn. Technol.* 57 (4), 178–184. doi:10.13807/j.cnki.mtt.2020.04.024

Ding, Y. (2011). *Research on gas outburst mechanism and prediction and early warning of highway tunnel [D]*. Chengdu: Chengdu University of Technology.

Fei, L., Chen, D., and Zhu, Y. (2010). Engineering design research of pengbu station-jianhua station section of hangzhou metro line 1 passing under harmful gas soil layer[J]. *Railw. Stand. Des.* 582 (10), 108–113.

Fu, X. (2022). Gas emission prediction and prevention measures of high risk Long shale gas tunnels [J]. *Railw. Constr. Technol.* 354 (9), 189–192+197. doi:10.3969/j.issn.1009-4539.2022.09.037

Gong, X., Liu, P., and Jiawen, J. (2015a). Multiple harmful gas detection system based on PSO algorithm integrated neural network [J]. *J. Sens. Technol.* 28 (6), 938–942. doi:10.13873/J.1000-9787(2015)02-0154-03

Gong, X., Xu, J., and Sun, S. (2015b). Application of PSO-BP neural network in multiple harmful gas detection [J]. *Sensors Microsystems* 34 (2), 154–156+160. doi:10.3969/j.issn.1004-1699.2015.06.027

Gong, S., Cai, N., and Liu, Z. (2022). Influence of shallow harmful gas accumulation characteristics on tunnel construction [J]. *Sci. Technol. Eng.* 22 (26), 11630–11637.

He, C., Zhang, J., and Chen, Z. (2017). Cause analysis and treatment measures of harmful gas in milin tunnel of lalin railway [J]. *Railw. Constr.* 57 (10), 78–80. doi:10.3969/j.issn.1003-1995.2017.10.21

Huo, B., Jin, J., and Hu, Y. (2023). Discussion on the quantitative relationship of harmful gas release in the overlying goaf of multi-coal seam mining [J/OL]. *J. Saf. Environ.* 1-12. doi:10.13637/j.issn.1009-6094.2022.0064

Industry Standards of the People's Republic of China (2009). *JTG F60-2009. Technical specifications for road tunnel construction [S]*. Beijing: People's Communications Publishing House.

Industry Standards of the People's Republic of China (2000). *JTG/T D70/2-01-2014. Detailed rules for road tunnel ventilation design [S]*. Beijing: People's Communications Publishing House.

Industry Standards of the People's Republic of China (2002). *TB 10204-2002/) 163-2002. Construction specifications for railway tunnels[S]*. Beijing: China Railway Press.

Kang, X., Xu, M., and Ding, R. (2010). Preliminary study on risk assessment of tunnel gas disasters [J]. *J. Railw. Eng.* 27 (5), 39–42. doi:10.3969/j.issn.1006-2106.2010.05.010

Klemens, R., Sinski, P. K. O., Wolanski, P., Korobeinikov, V., Markov, V., Menshov, I., et al. (2001). Numerical study of dust lifting in a channel with vertical obstacles. *J. Loss Prev. Process Industries* 14 (6), 469–473. doi:10.1016/s0950-4230(01)00035-3

Li, K., Li, P., and Cai, S. (2022). Research on harmful gas treatment technology in tunnel based on fuzzy control [J]. *Tunn. Constr. Chin. Engl.* 42 (1), 120–127. doi:10.3973/j.issn.2096-4498.2022.S1.014

Li, Y. (2017). *Research on "dynamic control" monitoring technology and construction management system of highway high gas tunnel [D]*. Chongqing: Chongqing Jiaotong University.

Liu, Z., Chai, J., and Jia, X. (2009). Numerical simulation of concentration diffusion of harmful gas in heading face with forced ventilation[J]. *Rock Soil Mech.* 30 (2), 536–539. doi:10.16285/j.rsm.2009.s2.038

Liu, D., Gan, R., Zhang, C., and Li, B. (2014). Research and application of CO concentration monitoringand simulation under tunnel mucking process[J]. *J. Railw. Sci. Eng.* 11 (5), 90–95. doi:10.3969/j.issn.1672-7029.2014.05.016

Liu, S. M., Sun, H. T., Zhang, D. M., Yang, K., Li, X., Wang, D., et al. (2023). Experimental study of effect of liquid nitrogen cold soaking on coal pore structure and fractal characteristics. *Energy* 275 (7), 127470. doi:10.1016/j.energy.2023.127470

Matsumoto, K., Sakait, K., Horinchi, K., Takahashi, H., and Okamoto, S. (1998). Advanced air quality simulation model for road tunnel portals in complex terrain. *Veh. Des.* 20, 71–77. doi:10.1504/ijvd.1998.001830

Salinas, D., FlunkertGasthaus, J., and Januschowski, T. (2020). DeepAR: Probabilistic forecasting with autoregressive recurrent networks. *Int. J. Forecast.* 36 (3), 1181–1191. doi:10.1016/j.ijforecast.2019.07.001

Su, P., Cao, J., and Shu, H. (2020). The genetic mechanism and migration model of harmful gases in non-coal formation tunnels in structurally complex areas [J]. *China Railw. Sci.* 41 (2), 91–98. doi:10.3969/j.issn.1001-4632.2020.02.11

Wang, X. (2022). Prediction and analysis of harmful gas content in gas tunnels using sensitive infrared sensors [J]. *J. Jiangsu Inst. Archit. Technol.* 22 (3), 17–20. doi:10.19712/j.cnki.jsjyxb.2022.03.001

Wu, Z., and Fan, Y. (2020). Design of toxic and harmful gas monitoring system based on machine learning method [J]. *Fire Sci. Technol.* 39 (11), 1550–1553.

Zhang, Z., and Yang, R. (2017). Prediction method of harmful gas in tianping tunnel of chongqing-guizhou railway [J]. *Tunn. Constr.* 37 (5), 618–621.

Zhang, Z., and Yang, R. (2017). Harmful gas forecasting method for tianping tunnel of yuqian railway [J]. *Tunn. Constr.* 37 (5), 618–621. doi:10.3973/j.issn.1672-741X.2017.05.014

Zhang, J. C., Li, X. L., Qin, Q. Z., Wang, Y., and Gao, X. (2023). Study on overlying strata movement patterns and mechanisms in super-large mining height stopes. *Bull. Eng. Geol. Environ.* 82 (3), 142. doi:10.1007/s10064-023-03185-5

Zhang, L. B., Shen, W. L., Li, X. L., Wang, Y., Qin, Q., Lu, X., et al. (2023). Abutment pressure distribution law and support analysis of super large mining height face. *Int. J. Environ. Res. Public Health* 20 (1), 227. doi:10.3390/ijerph20010227

Zhao, L., Zhao, Y., and Su, P. (2020). Research on safety management of toxic and harmful gas construction in non-coal measures stratum tunnel [J]. *Mod. Tunn. Technol.* 57 (1), 1168–1171. doi:10.13807/j.cnki.mtt.2020.S1.160

frontiers | Frontiers in Earth Science

TYPE Original Research
PUBLISHED 14 June 2023
DOI 10.3389/feart.2023.1189129

OPEN ACCESS

EDITED BY
Jingjing Meng,
Luleå University of Technology, Sweden

REVIEWED BY
Gang Huang,
Wuchang University of Technology, China
Xu Qian,
Changzhou University, China

*CORRESPONDENCE
Chenglong Yu,
ycl19880228@126.com

RECEIVED 18 March 2023
ACCEPTED 09 May 2023
PUBLISHED 14 June 2023

CITATION
Yu C, Shi X, Gao Q, Zhang X and Wang F (2023), Research on the evolution law of the seismic wave field based on the explosive source parameters.
Front. Earth Sci. 11:1189129.
doi: 10.3389/feart.2023.1189129

Research on the evolution law of the seismic wave field based on the explosive source parameters

Chenglong Yu[1]*, Xunxian Shi[1], Quan Gao[1], Xingkai Zhang[1] and Fengnian Wang[2,3]

[1]China Academy of Safety Science and Technology, Beijing, China, [2]Shanxi Transportation Technology Research and Development Co., Ltd., Taiyuan, China, [3]School of Earth Sciences and Engineering, Hohai University, Nanjing, China

We present a numerical model for blast-induced seismic waves. This model is based on the transformation mechanism of the seismic wave field, and the process of the seismic wave's generation is divided into two stages. The first stage is the generation of elastic waves. Due to the plastic deformation of the geotechnical medium in this stage, we have established the Euler model to describe it. The second stage is the prorogation of the elastic waves; we have established the Lagrange models to describe this stage. Finally, the influence of the main parameters of the explosive sources (detonation pressure and expansion index) on the seismic wave is analyzed by the established model. The results show that the proposed model in this paper can reasonably predict the evolution law of the seismic wave field based on the explosive source parameters.

KEYWORDS

explosive source, seismic wave, numerical model, seismic exploration, transformation mechanism

1 Introduction

It is essential to improve seismic resolution, since the seismic exploration has challenges in exploring the smaller, deeper, and thinner targets.

For a long time, physicists have been expected to explain the corresponding relationship between the elastic wave caused by the explosion and the initial conditions, such as the explosive performance and dynamic characteristics of the soil medium, by establishing an equivalent model. Jeffreys (1931) first introduced the operator symbol and operator to solve the one-dimensional cavity vibration problem. The particle displacement caused by the body wave (P wave) and surface wave (S wave) in the spherical impact propagating in the medium changes with time, and the displacement analytical solution of the two waves is obtained. In 1942, Sharpe (1942) observed and recorded the time travel curve of the particle vibration velocity at different positions through a large-scale explosion test in soil and clarified the relationship between some characteristics of the recorded results and the characteristics of explosive seismic sources. According to these experimental results, the equivalent model of the "equivalent cavity" elastic medium was proposed, and many studies conducted later were based on this equivalent cavity model. Goldsmith and Allen (1955) assumed that the elastic medium is isotropic, there is a spherical cavity with a certain radius inside, and the cavity is subjected to the pulse stress in the exponential attenuation form. The function equations of particle displacement, velocity, normal stress, and shear stress with respect to space and time are derived to reflect the propagation law of stress waves in the elastic medium. Friedman et al. (1965) calculated the one-dimensional stress–wave propagation during the expansion

of the medium cavity, obtained the analytical expression of the elastic region with respect to time and spatial location parameters, and calculated the particle disturbance caused by the elastic unloading near the cavity when the pressure on the cavity wall decayed exponentially with the spatial location parameter by a "jump" difference scheme. However, the method he proposed becomes unstable as the distance increases. Achenbach and Sun (1966) also studied the effect of the initial cavity size on the explosion in the medium under the assumption that the medium is an elastomer. The stress fields when the cavity wall is not moving and the cavity radius increases with the time parameter alignment are calculated, and the propagation of the stress wave after the cavity stops expanding is discussed. Garg (1968a) changed the pressure load on the cavity under the premise of Friedman operation and gave a more complicated pressure form to calculate the particle stress and particle vibration velocity distribution in the plastic region near the cavity. The results obtained by this method can clearly reflect the spatial distribution of the particle stress and particle vibration velocity near the cavity in a short time. However, this method still requires a complex boundary processing method. In another research by Garg (1968b), the start-up conditions of the computation procedure were improved, which simplified the boundary condition process, and a new pressure attenuation load was applied. The numerical solution obtained by the theoretical method is only applicable to particles with a small time parameter and near the cavity. No detailed calculation methods are given for the more distant medium.

On the basis of the elastic medium, considering the destruction and compression of the soil medium caused by an explosive high-pressure effect, it is very meaningful to introduce the elastic–plastic medium. Ghosh (1968) took the large underground explosion as the premise, assumed that the medium around the cavity was an elastomer, and pointed out that the medium near the cavity should exhibit plastic properties, and there was a plastic wave that propagates outward from the cavity boundary after the elastic wave. Elastoplastic region boundaries also propagated outward at a certain speed. In his article, he assumed two situations: first, the propagation velocity of the elastoplastic boundary is constant, and the pressure load on the cavity boundary is under normal pressure; second, the propagation velocity of the elastoplastic boundary and the pressure load of the cavity boundary decay exponentially with time. The corresponding analytical expression is obtained by solving the displacement field in these two cases. Lyakhov (1964) and LyakhovPolyakova (1967) obtained the relationship between peak overpressure and distance by the closed explosion test of the TNT spherical charge in sand. The results show that the larger the air-to-volume ratio, the smaller the moisture content and the larger the overpressure attenuation velocity. The peak overpressure in the unsaturated soil may be 1/100th of the peak overpressure in the saturated soil. The explosives in unsaturated soil produce a stable shock wave, and the shock wave attenuation becomes the elastic–plastic wave when the overpressure attenuation is 4–12 kg/cm^2. Kawasumi and Yosiyama (1935) solved the displacement field of the cavity wall when the spherical pressure load is given by the Fourier's integral and proved that the simplest reason for the seismic wave is the existence of the initial strain potential energy. It is pointed out that the cavity is subjected to different loads, and the excited damping oscillation form still maintains a certain degree of similarity. G. N. Bycroft (1966) solved the cavity-expansion problem of the semi-infinite space analytically, taking into account the free-surface particle vibration caused by the seismic wave returning to the cavity wall after free-surface reflection and re-reflecting. The particle displacement solution of the free surface with the known expansion velocity of the cavity wall is calculated.

In addition, the pressure time function of the point source is determined according to the far-field vibration waveform and spectral characteristics, and this kind of inversion is also an effective seismic source model to interpret the explosive seismic wave. The pressure load of the equivalent seismic source is the difference between the true stress and the linear elastic model stress, which is essentially different from the "ideal cavity" model. Heelan (1953) proposed a point-source moment model to explain linear explosion, and the theoretical prediction results are close to the experimental results. Aboudi (1972) used the finite difference method to calculate the stress and displacement fields during the explosion of shallow-buried deep explosives. The numerical calculation is carried out for two different cases of cavity non-expansion and cavity expansion velocity constants. Thiruvenkatachar derived the series form the transient solution of the semi-infinite elastic space problem using the iterative method (Thiruvenkatachar and Viswanathan, 1965) and proved its convergence. Considering the complexity of the series solution, the analytical approximation (Thiruvenkatachar and Viswanathan, 1967) was made on the steady-state solution using the saddle-point method, and the approximate solution of three emissions between the chamber wall and the free surface is obtained. At the same time, the transient solution is also calculated for the case where the pressure load on the chamber wall is subjected to an

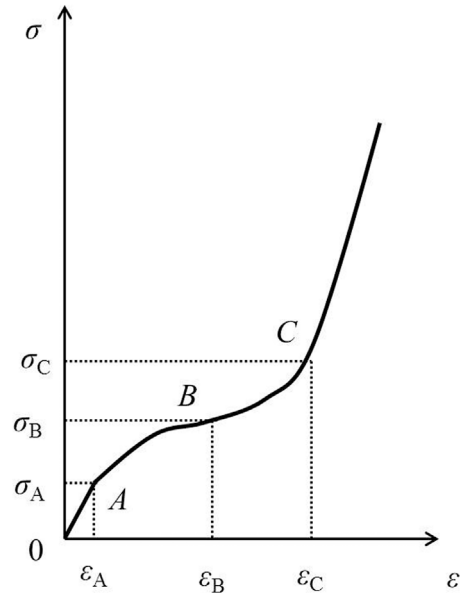

FIGURE 1
Stress–strain relationships of the soil medium (Henrych, 1979).

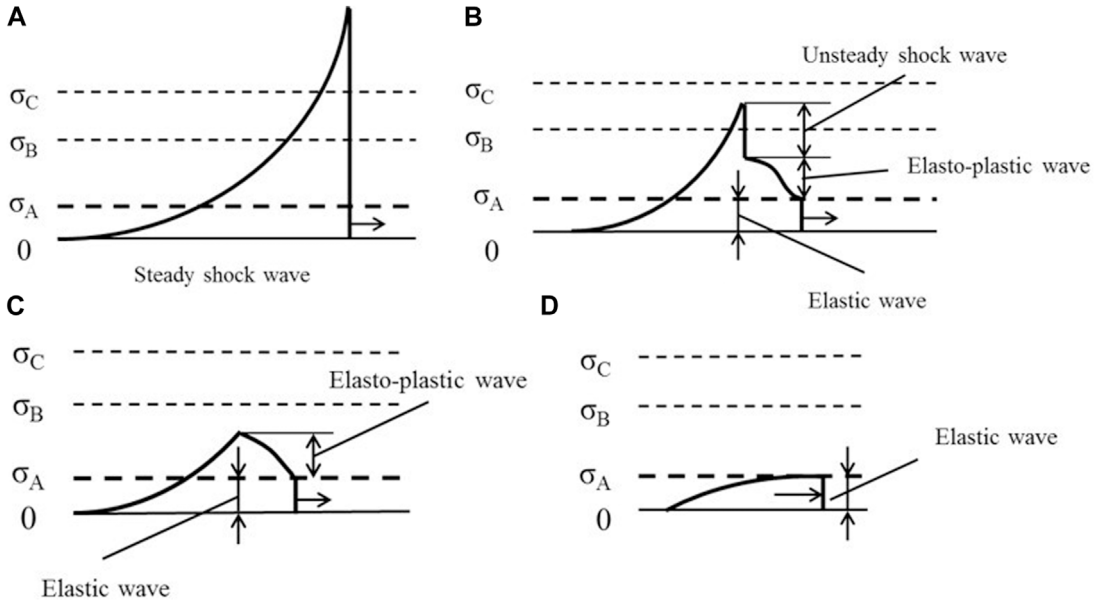

FIGURE 2
Evolution of explosion waves (Henrych, 1979). **(A)** steady shock wave, **(B)** unsteady shock wave, **(C)** plasticity, **(D)** elasticity.

exponential decay law with time. Pekeris (1955) studied the problem of free-surface vibration caused by the impact pressure under the one-dimensional column model and solved the displacement of the free-surface particle of horizontal and vertical directions caused by the action of a single impact pressure (impact pressure only related to the time parameter) on the semi-infinite elastic medium. Based on the Heelan model, Blair proposed a class of models that can calculate infinite linear explosion (Blair, 2007) and finite linear explosion (Blair, 2010).

However, all these methods focus on the destruction of the medium rather than the propagation of explosion waves. The solutions of non-wave dynamic expansion and elastic wave propagation are independent.

In this study, we propose a numerical model that describes the whole process from the explosion of explosive sources to the propagation of seismic waves. Based on our model, the blast-induced seismic waves can be predicted. The influence of the main parameters of the explosive sources (detonation pressure and expansion index) on the seismic wave is briefly discussed. The model shows that the frequency spectrum of seismic waves can be enhanced by lowering the initial explosion pressure of explosive sources or increasing the adiabatic exponent. This model would help us to predict seismic waves, which are generated by explosion, and control the seismic waves for a specific exploration target.

2 Transformation mechanisms of the seismic wave field

There are four stages of the explosion process involved during the blast-induced seismic wave's generation: hydrodynamics, crushing of soil mediums, dynamic expansion, and elastic-wave propagation outside the destructed zone (Opjiehko, 2011).

These four stages and the evolution of explosion waves are illustrated by the stress–strain relationship of the soil media in Figure 1 (Henrych, 1979), and the evolution process of the explosion wave profile is illustrated in Figure 2 (Henrych, 1979). The complete transformation mechanisms are illustrated in our previous research results (Chenglong et al., 2018) (Chenglong et al., 2017). At the same time, the medium is subject to different intensities in the process of

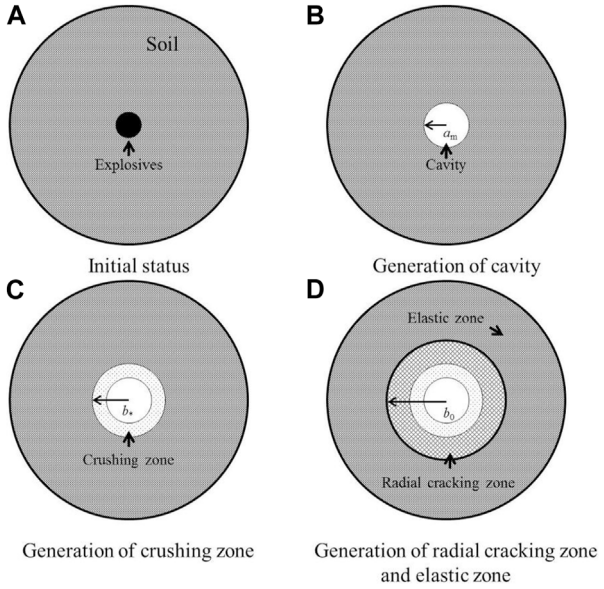

FIGURE 3
Response regions in a spherical explosive (Favreau, 1969).

stress–wave propagation, and different deformation areas will be generated after the seismic wave propagation, as shown in Figure 3 (Favreau, 1969).

In order to find the key influencing factors of explosive seismic wave propagation, specific propagation stages need to be divided. According to Ding's research, the seismic signals are produced from the vibration of the elastic cavity, rather than being decided by the non-elastic properties of a medium (Ding and Zheng, 2002), and the whole process of the explosion wave's evolution could be considered in two parts. They are the dynamic expansion of blast-induced cavities and the propagation of elastic waves. These two parts are associated with the condition of the elastic zone's boundary (Drukovanyi et al., 1976).

According to the seismic wave field transformation theory mentioned previously, the whole process of the explosive source-excited seismic wave can be categorized into the formation of seismic waves of the close-in blasting zone and propagation of the seismic wave in elastic regions. As the two processes differ vastly in the range and scale, the numerical simulation method of the multiscale seismic wave field is adopted to establish models to conduct the research.

3 Excitation model of explosion seismic waves

The formation of the initial seismic wave is simulated by the Euler model. Due to the high-pressure load in the vicinity of the explosion, the Euler method is applied to manage large deformation problems. With the simulation of the close-in explosion area, this paper grasps the explosive source parameters, elastoplastic boundary, and the relationship between the pressure load characteristics on the boundary and extracts the pressure load as the conditions of loading in the simulation of far explosion zones.

3.1 Control equation

The simulation of the close-in explosion area is aimed at addressing problems such as large deformation in very short time periods and finite strain transient. Such problems are described in terms of mass, momentum, energy conservation equation, and the equations of continuous mechanics made of equations that describe the behavior of the material.

In order to simplify the problem, the following assumptions are usually made.

3.1.1 Continuum assumption

It is assumed that the substance is composed of a large number of micelles, and the size of the micelles is negligible compared with the discussed flow field. However, it is much larger than the molecular free path and the size of the solid crystal structure. The micelles are processed statistically and on average to obtain corresponding macroscopic variables, thus leading to the natural conclusion that matter is a continuous composition of micelles with microscopic quantities.

3.1.2 Assumption of local heat balance

It is assumed that each micelle in the substance is in a thermal equilibrium state, and there exists a statistically averaged thermodynamic quantity in each micelle. All the conclusions of equilibrium thermodynamics can be applied to any micelle. Ignoring the dissipative process in micelles, it is considered that micelles have instantaneously reached heat balance, and then, an energy balance relation can be established for the material micelle.

3.1.3 Material homogeneity and isotropy assumption

It is assumed that each material micelle is composed of the same species, the physical and mechanical properties of which are the same in any direction.

The processes of non-steady flows such as seismic source-explosive detonation, product expansion, and deformation of the soil medium depend not only on the time variable t but also on spatial variables r and z. In a 2D rectangular coordinate system ($\alpha = 0$) or an axisymmetric cylindrical coordinate system ($\alpha = 1$), without considering external force, external source, and heat conduction, the conservative form of the partial differential equations of Euler fluid elastoplastic dynamics is as follows.

Mass-conservation equation:

$$\frac{\partial \rho}{\partial \tau} + \frac{\partial}{\partial z}\left(\rho u_z\right) + \frac{1}{r^\alpha}\frac{\partial}{\partial r}\left(r^\alpha \rho u_r\right) = 0. \tag{1}$$

Momentum-conservation equation:

$$\begin{aligned}
&\frac{\partial \rho u_z}{\partial \tau} + \frac{\partial}{\partial z}\left(\rho u_z^2\right) + \frac{\partial}{r^\alpha \partial r}\left(r^\alpha \rho u_z u_r\right) = -\frac{\partial P}{\partial Z} + \frac{\partial S_{zz}}{\partial Z} + \frac{\partial\left(r^\alpha S_{rz}\right)}{r^\alpha \partial r},\\
&\frac{\partial \rho u_r}{\partial \tau} + \frac{\partial}{\partial z}\left(\rho u_z u_r\right) + \frac{\partial}{r^\alpha \partial r}\left(r^\alpha \rho u_r^2\right) = -\frac{\partial P}{\partial r} + \frac{\partial S_{rs}}{\partial Z} \frac{\partial\left(r^\alpha S_{rr}\right)}{r^\alpha \partial r} - \alpha \frac{S_{\theta\theta}}{r}.
\end{aligned} \tag{2}$$

Energy-conservation equation:

$$\begin{aligned}
\frac{\partial(\rho E)}{\partial \tau} + \frac{\partial\left(\rho E u_z\right)}{\partial Z} + \frac{\partial\left(r^\alpha \rho E u_r\right)}{r^\alpha \partial r} = \frac{\partial\left(S_{rz} u_r\right)}{\partial Z} + \frac{\partial(-P + S_{ss})}{\partial Z}\\
+ \frac{\partial r r^\alpha u_r\left(-P + S_{rr}\right)}{r^\alpha \partial r} + \frac{\partial\left(r^\alpha S_{rz} u_z\right)}{r^\alpha \partial r}.
\end{aligned} \tag{3}$$

3.2 Physical model

3.2.1 Geotechnical medium models and parameters

The geomaterial model in the finite-element model is an elastoplastic model, and the equation of state in the model is in the linear equation of state, which is expressed as follows (Blake, 1952):

$$p = K\left(\frac{\rho}{\rho_0} - 1\right), \tag{4}$$

where K is the bulk modulus of the geomaterial, and the intensity model of the geomaterial is the von Mises model (Forrestal and Tzou, 1997).

$$(\sigma_1 - \sigma_2)^2 + (\sigma_2 - \sigma_3)^2 + (\sigma_3 - \sigma_1)^2 = 2\sigma_s^2 = 6G^2, \tag{5}$$

TABLE 1 Soil parameters (Chenglong et al., 2018) (Chenglong et al., 2017).

Density (kg/m^3)	Bulk modulus (MPa)	Shear modulus (MPa)	Yield strength (MPa)
2000	32.1	14.8	10

TABLE 2 Parameters of the JWL equation of state for TNT explosives (Yixin et al., 2013).

C_1(Pa)	C_2 (Pa)	r_1	r_2	ω	ρ (kg/m^3)	D (m/s)	E (J/m^3)	P_{CJ} (Pa)
3.737×10^{11}	3.747×10^{9}	4.15	0.90	0.35	1,630	6,930	6.0×10^{9}	2.1×10^{10}

where σ_s is the yield strength of the medium and G is the shear modulus of the medium. The engineering elastic constants of the soil are determined by the triaxial and light-gas gun tests, as shown in Table 1.

3.2.1 The equation of state and parameters for detonation products of explosives

JWL model is used to describe the effects of explosives. It should be noted that this model is a simplified model. When the type and shape of explosives change, the calculation results will be different. For TNT, the equation of state commonly taken for the ideal explosive detonation products is the JWL equation of state (Yixin et al., 2013).

$$P = C_1\left(1 - \frac{\omega}{r_1 v}\right)e^{-r_1 v} + C_2\left(1 - \frac{\omega}{r_2 v}\right)e^{-r_2 v} + \frac{\omega}{v}, \quad (6)$$

where e is the C–J detonation energy and C_1, C_2, r_1, r_2, and ω are the experimentally determined parameters (Figure 2). The values of these parameters are listed in Table 2.

3.3 Geometric model

A one-dimensional wedge soil model is established, and the numerical simulation of the dynamite scheme calculated by the analytical model in the second section is carried out to obtain the variation of each area and the main factors affecting the elastic-wave pressure. The model and the status of each area after the explosion are presented in Figure 4.

3.4 Simulation results and analyses

The explosion of 1 kg TNT in silty clay is calculated, and the motion of the damage area by explosion is calculated through the one-dimensional model, as shown in Figure 4:

From the simulation results in Figure 5, it can be seen that an explosive cavity is formed in the medium in direct contact with the explosive and shows a fluid state. With the attenuation of the pressure peak, a plastic range with a certain width is formed between the explosive cavity and the elastic zone. With the spread of the explosive stress wave, the cavity and the plastic range gradually expand. After a certain time, when the stress in the medium tends to be stable, the cavity radius and the elastoplastic boundary stop expanding. By documenting the development of the cavity and the elastic–plastic range, the curve of development time of the two boundaries is obtained, as shown in Figure 6.

In Figure 6A, the blasting cavity radius is formed after the dynamite blast increases with time, and the size of the blasting cavity gradually tends to a certain value near the position of 2 ms. The region of the explosion cavity in this method is 0.36 m (Chenglong and Wang, 2017), and the region which is calculated by a quasi-static

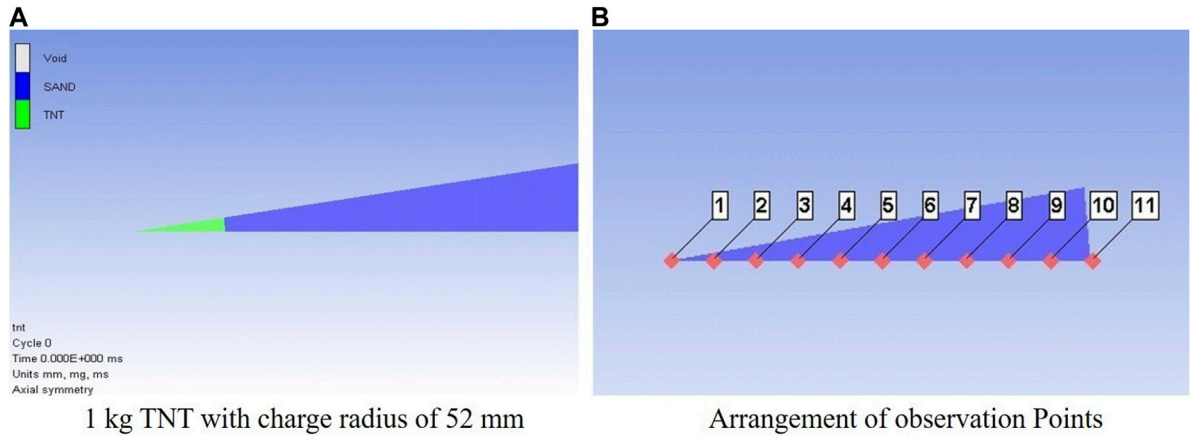

FIGURE 4
One-dimensional wedge calculation model.

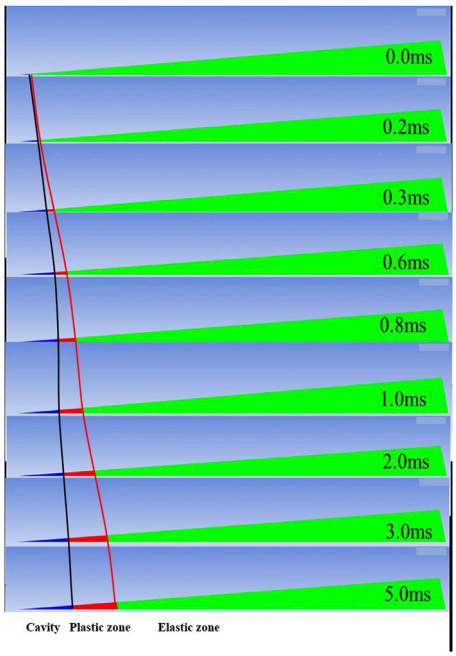

FIGURE 5
Movement of the explosion-damaged area.

model is 0.37 m. The regions we obtained through experiments are 0.38 m (Chenglong and Wang, 2017). In Figure 6B, it is obvious that the plastic range formed after the dynamite blast begins to develop almost at the same time as the cavity and expands outward at the same time. When the pressure reaches the limit of yielding of geomaterials, the plastic range stops developing and approaches a certain value, which is the elastoplastic boundary after the final stabilization.

The initial pressure load generated by the explosion (Figure 7) and the pressure load on the elastoplastic boundary (Figure 8) are extracted, respectively. It can be seen from the change in the pressure load that the peak value of the pressure load drops rapidly from 3 GPa to 2.5 MPa, and the duration also increases from 0.02 ms to 2 ms.

4 Propagation model of explosive seismic waves

The Lagrange model is adopted to simulate the propagation of the initial elastic wave in geomaterials. Since the pressure peak of the initial elastic wave is basically consistent with the yield condition of the geomaterial, under the loading condition of the initial elastic wave, the medium will not experience large deformation. By changing the load of the initial elastic wave, the whole process of the seismic wave field excited by the explosive source is simulated.

4.1 Control equations

When the initial elastic wave is formed, its pressure peak is less than the limit of yielding of the medium. Hence, it will not cause large deformation in the geomaterial. In this regard, the Lagrange method is applied to simulate the propagation process of seismic waves, and the governing equations include the mass-conservation equation, the momentum-conservation equation, and the energy-conservation equation in the following form.

Mass-conservation equation:

$$\rho = \frac{\rho_0 V_0}{V} = \frac{m}{V}. \tag{7}$$

Momentum-conservation equation:

$$\rho\ddot{x} = \frac{\partial \sigma_{xx}}{\partial x} + \frac{\partial \sigma_{xy}}{\partial y} + \frac{\partial \sigma_{xz}}{\partial z}, \rho\ddot{y} = \frac{\partial \sigma_{yx}}{\partial x} + \frac{\partial \sigma_{yy}}{\partial y} + \frac{\partial \sigma_{yz}}{\partial z}, \rho\ddot{z} = \frac{\partial \sigma_{zx}}{\partial x} + \frac{\partial \sigma_{zy}}{\partial y} + \frac{\partial \sigma_{zz}}{\partial z}. \tag{8}$$

Energy-conservation equation:

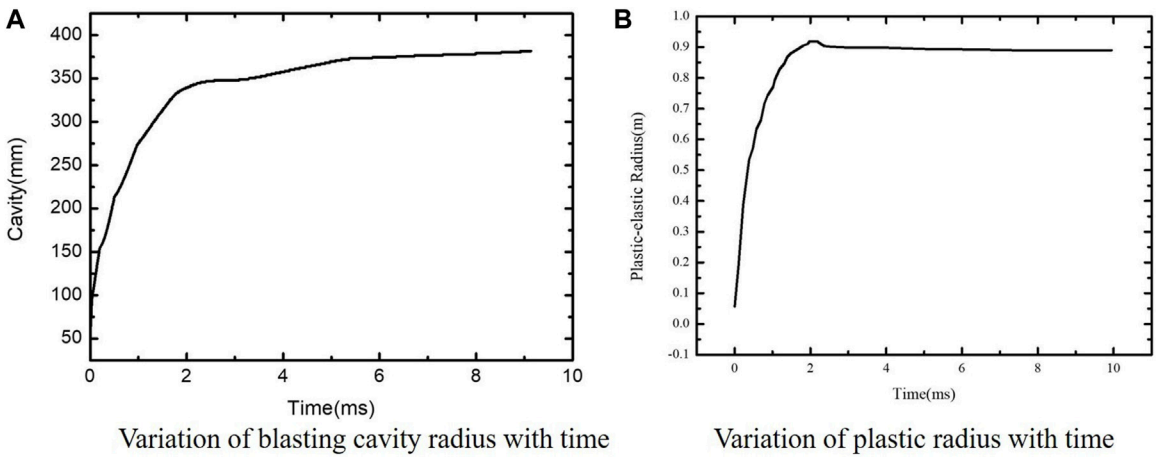

FIGURE 6
Time-dependent movement of the boundary of different blasting areas.

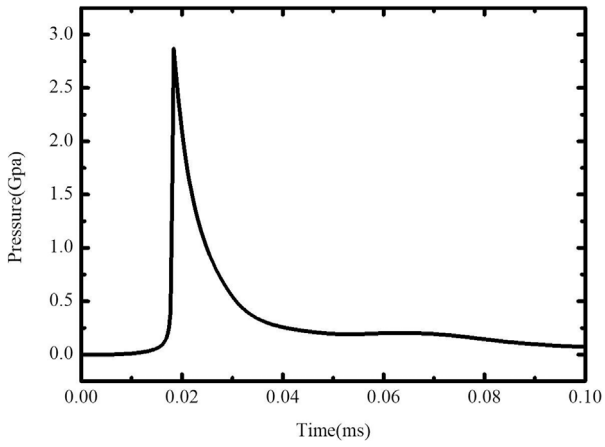

FIGURE 7
Initial pressure elastic–plastic boundary.

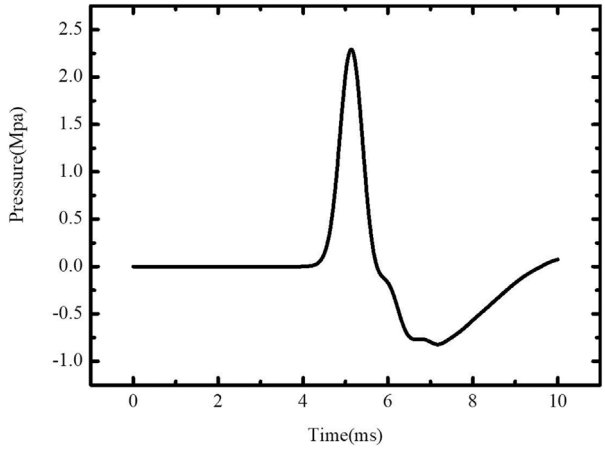

FIGURE 8
Pressure on the elastic plastic boundary.

$$\dot{e} = \frac{1}{\rho}\left(\sigma_{xx}\dot{\varepsilon}_{xx} + \sigma_{yy}\dot{\varepsilon}_{yy} + \sigma_{zz}\dot{\varepsilon}_{zz} + 2\sigma_{xy}\dot{\varepsilon}_{xy} + 2\sigma_{yz}\dot{\varepsilon}_{yz} + 2\sigma_{zx}\dot{\varepsilon}_{zx}\right). \quad (9)$$

4.2 Physical model

By simulating the formation of the blasting seismic wave, the radius of the elastoplastic boundary and the pressure curve on the elastoplastic boundary are obtained. When the curve is applied to the viscoelastic medium models in the initial condition, the propagation process of seismic waves can be simulated.

For the geomaterial in the propagation process of the seismic wave, the viscoelastic medium model is adopted, in which the linear equation of state is selected. The linear viscoelastic model is adopted for the intensity model of geomaterials. The long-term behavior of this model is described by the elastic shear modulus G, and the viscoelastic behavior is introduced by the instantaneous shear modulus (G_0) and the viscoelastic attenuation constant (β). The viscoelastic deviatoric stress at the time increment n + 1 is calculated from the viscoelastic stress at the time increment n and is expressed as follows (Ricker, 1953):

$$\sigma'_{n+1} = \sigma' n^{e^{-\beta\Delta t_n}} + 2(G_0 - G)\frac{\left(1 - e^{-\beta\Delta t_n}\right)}{\beta}\frac{\Delta\varepsilon'_n}{\Delta t_n}. \quad (10)$$

For the effect of the explosive source, we extract the data curve of the blasting seismic wave formation simulation in the previous step and load the corresponding explosive source.

4.3 Geometric model

The calculation model is shown in Figure 9.

The observation points (Gaussian point) are set at the free surface of the geomaterial and below the explosive source, with a burial depth of explosives of 15 m as measured by the observation points. The variation of the seismic wave excited by the explosive source on the surface and the downward direction is analyzed. The

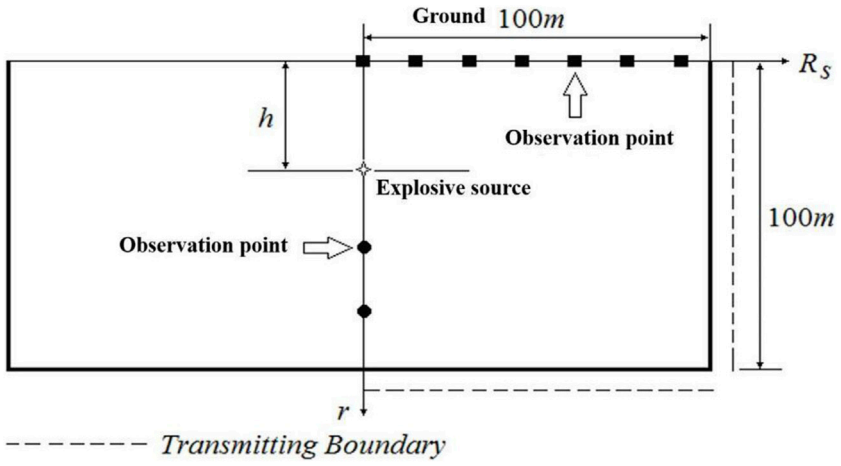

FIGURE 9
Calculation model diagram.

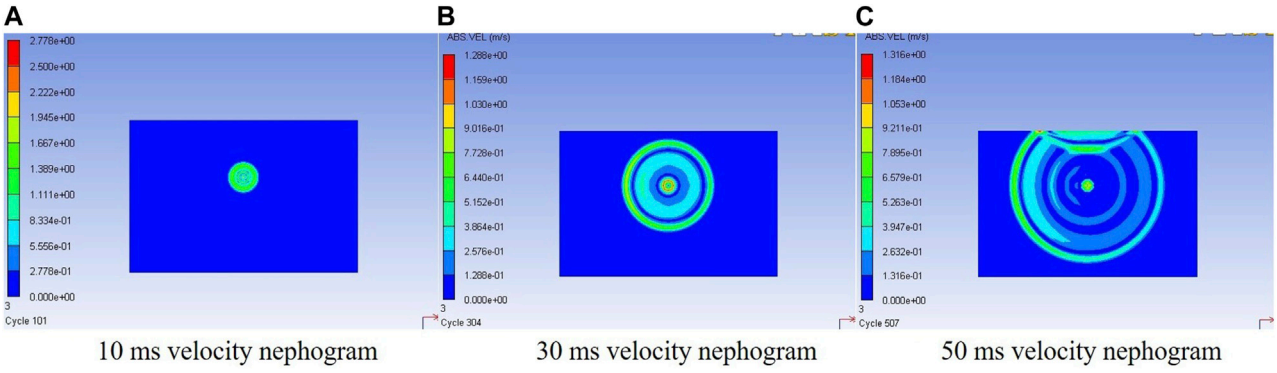

FIGURE 10
Seismic wave velocity nephogram at different times.

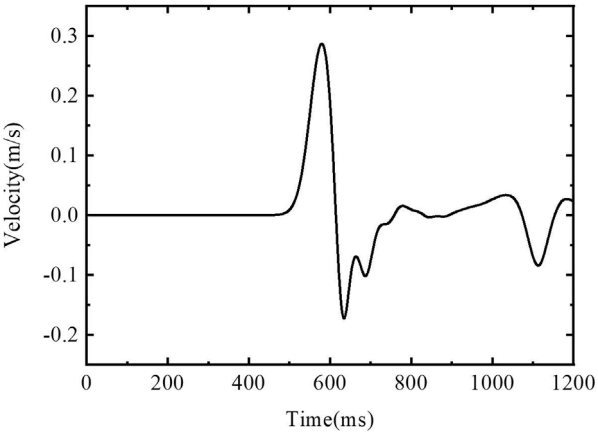

FIGURE 11
Comparison of particle vibration velocities obtained by numerical simulation.

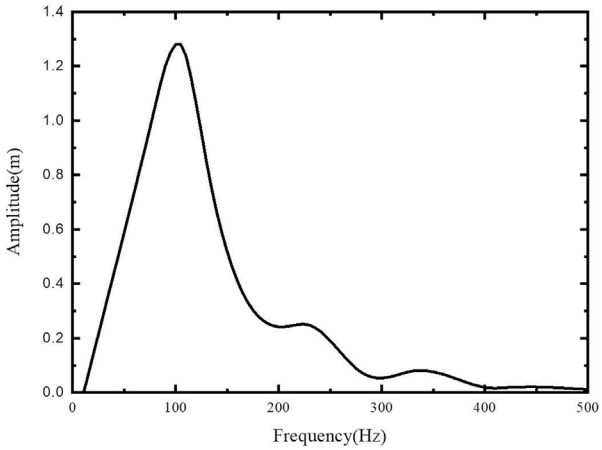

FIGURE 12
Spectrum features of particle vibration.

overall computational domain is 200 m × 100 m, and the free boundary is selected on the surface of the soil medium, while the transmitting boundary is adopted for other boundaries. These boundary conditions do not reflect the stress wave propagating along these boundaries.

4.4 Calculation results

We simulated the aforementioned case using a dual-core CPU (Intel Xeon Silver 4210 R Processor) and calculated each scenario for 10 h, resulting in the following results. By simulating the propagation process of the seismic wave, Figure 10 reveals the vibration velocity nephogram of seismic waves excited by 1 kg TNT at 10 ms, 30 ms, and 50 ms. Qualitative analysis is adopted on the nephogram of different particle vibration velocities. At 10 ms, the seismic wave excited by the explosive takes the explosive source as its center and radiates spherical stress waves to the surrounding area. As the stress wave propagates, stress waves with different peaks are gradually formed in the medium. It is easily seen from the velocity contours of 30 ms and 50 ms that although the detonation products of the explosive source have already been completed at this time, the particle velocity of the explosion center is higher than the external vibration velocity, indicating that the blasting cavity generated by the explosive source is still moving after the explosion. This is the main cause of the subsequent seismic wave, which is the same as Ding Hua's conclusion that the seismic wave signal is due to the cavity vibration.

The results of the particle velocity at 30 m from the explosion center are shown in Figure 11, and by Fourier analysis on the vibration velocity, we obtained Figure 12:

Through the numerical simulation of the explosive source excitation seismic wave process, the explosive cavity, plastic range, particle velocity, and spectrum features at different distances can be obtained. As a result, the relation between parameters of explosive-source characteristics and amplitude-

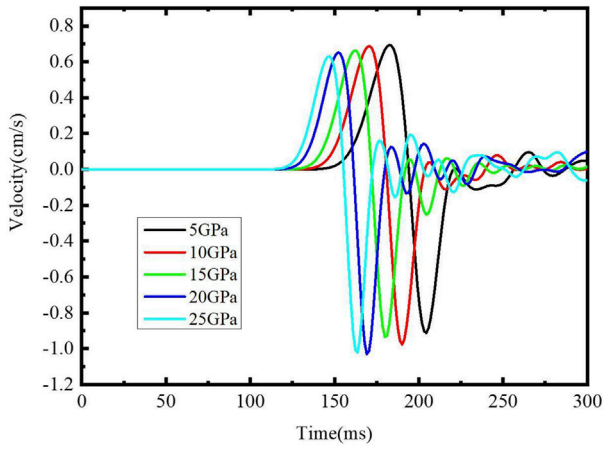

FIGURE 13
Particle velocity at 15 m from the explosion center at different distances of explosion pressure.

frequency characteristics of the seismic wave field can be deeply analyzed.

5 Influence of parameters of explosive source characteristics on amplitude frequency characteristics of seismic waves

Through the theoretical study on seismic waves stimulated by explosive sources, when the geotechnical medium parameters are determined, the detonation pressure of explosive sources and the expansion index of explosion products are the main factors that affect the amplitude frequency characteristics of seismic waves. The following are respective studies on the patterns of how different detonation pressures and product expansion indexes affect the amplitude frequency characteristics of seismic waves.

We continue to use the numeric simulation scheme propagated by blasting seismic waves as described previously to change the bursting pressure of explosive sources so that the detonation pressure can vary in the range of 5–25 GPa. A monitoring point on the surface directly above the explosive source is selected 15 m away from the explosive source, and the particle velocity caused by different detonation pressures at this point is shown in Figure 13.

By extracting the particle vibration velocity peak under different detonation pressures, the influence law of the detonation pressure on the particle vibration velocity peak is obtained, as shown in Figure 14A; *PPV* in this figure is the peak particle velocity. Through Fourier transform on the velocity curve in Figure 13, the influence law of the detonation pressure on the dominant frequency of the seismic wave is acquired, as shown in Figure 14B:

Figure 14 proves that the particle vibration velocity peak value increases with the increase in the detonation pressure. Both the particle vibration velocity peak value and the particle vibration amplitude are parameters representing the seismic wave energy. The law of energy increasing with the increase in the bursting pressure obtained by the numerical method is consistent with the conclusion of the theoretical model of the seismic wave by the explosive source. The increase in the explosive pressure leads to the expansion of the damage area by the media and more loss on high-frequency parts, lowering the master frequency of seismic waves. The detonation pressure of the explosive source in the numerical simulation scheme remains unchanged, and the expansion index of the explosion products of the explosive source varies from 1.0 to 4.0. Then, the calculated attenuation law is obtained as shown in Figure 15:

Figure 15 shows that the particle vibration velocity peak decreases with the expansion index of detonation products, and the dominant frequency of the seismic wave increases with the increase in the product expansion index. The process of explosive source exploding and forming a damage area is very fast, which is considered as an adiabatic process.

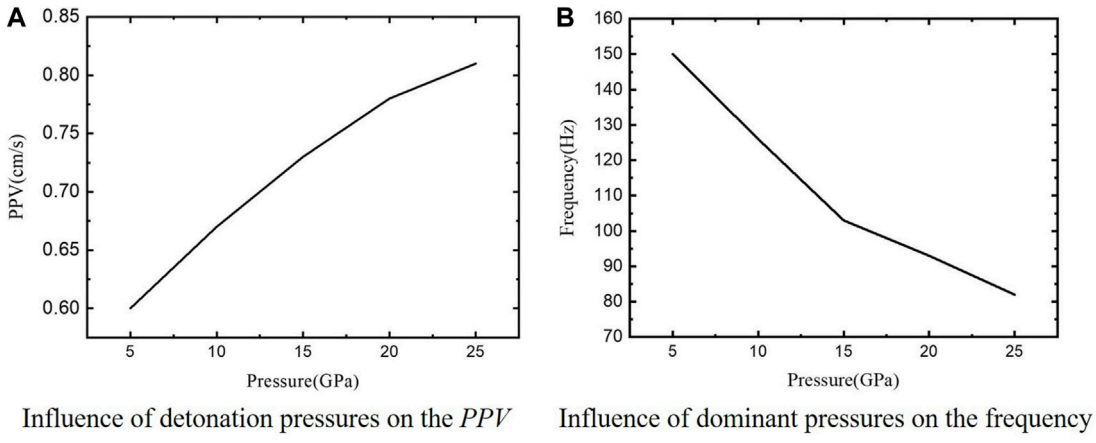

FIGURE 14
The influence law of seismic wave field characteristics under different detonation pressures.

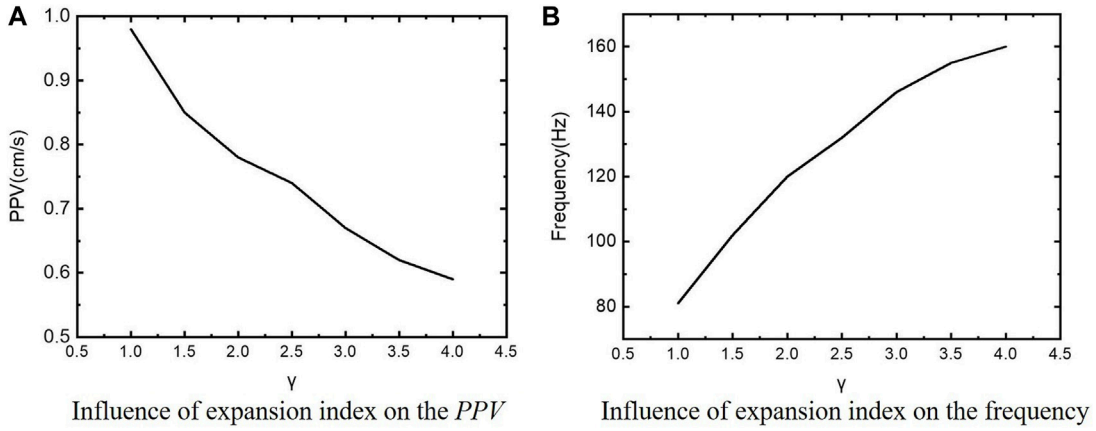

FIGURE 15
Influence of the expansion index of different explosion products on the characteristics of seismic wave field.

According to the adiabatic law, when the product expansion index increases, the damage area decreases by explosion, the energy decreases, but the main frequency increases.

6 Conclusion

Based on the numerical simulation of the characteristics of the explosive source and the relation of the wave field, the development process of the explosive cavity and elastic–plastic boundary is collected along with the variation rule of seismic wave amplitude frequency characteristics with distance.

The formation of seismic waves is simulated by the Eulerian method. During the formation of seismic waves, along with the development of explosive cavities and elastoplastic range, the boundaries between the three zones almost expand simultaneously along the explosion center until the explosive cavity, plastic range, and elastic zone are formed in turn.

The Lagrange method is applied to simulate the propagation process of seismic waves, extract the numerical simulation data curve of the formation process of seismic waves, and load it into the two-dimensional Lagrange model. The vibration velocity of the particles at different positions can be acquired, and the Fourier transform can be adopted to obtain the spectral features of the particle vibration.

Finally, the influence law of the explosive source detonation pressure and the expansion index of explosion products on the particle vibration velocity peak and the dominant frequency of the seismic wave are analyzed. The detonation pressure and expansion index of explosive sources exert opposite effects on the energy and dominant frequency of seismic waves, and the change law between the energy of the seismic wave and the master frequency is often the opposite, and this conclusion was calculated by our prediction model for amplitude–frequency characteristics of blast-induced seismic waves (Chenglong et al., 2018). While the energy of the seismic wave increases, the master frequency of the seismic wave decreases. To finally realize the control of the seismic wave field and improve the seismic exploration accuracy, it is vital to comprehensively consider the influence law of the explosion pressure of the blasting source and product expansion index on the amplitude and frequency of seismic waves and adjust the amplitude and frequency characteristics of seismic waves to a certain extent, so as to improve the seismic exploration accuracy.

Data availability statement

The raw data supporting the conclusion of this article will be made available by the authors, without undue reservation.

Author contributions

CY finished writing the manuscript. XS completed the numerical calculation. QG completed the data processing. XZ completed the translation of the thesis. FW completed the typesetting and modification of the paper. All authors listed made a substantial, direct, and intellectual contribution to the work and approved it for publication.

Funding

This work was supported by the National Natural Science Foundation Young Investigator Grant Program (No. 41904131).

Conflict of interest

FW was employed by the company Shanxi Transportation Technology Research and Development Co., Ltd.

The remaining authors declare that the research was conducted in the absence of any commercial or financial relationships that could be construed as a potential conflict of interest.

Publisher's note

References

Aboudi, J. (1972). The response of an elastic half-space to the dynamic expansion of an embedded spherical cavity. *Bull. Seismol. Soc. Am.* 62 (1), 115–127. doi:10.1785/BSSA0620010115

Achenbach, J. D., and Sun, C. T. (1966). Propagation of waves from a spherical surface of time-dependent radius. *J. Acoust. Soc. Am.* 40 (4), 877–882. doi:10.1121/1.1910160

Blair, D. P. (2007). A Comparison of heelan and exact solutions for seismic radiation from a short cylindrical charge. *GEOPHYSICS* 72 (2), E33–E41. doi:10.1190/1.2424543

Blair, D. P. (2010). Seismic radiation from an explosive column. *Geophysics* 75 (1), E55–E65. doi:10.1190/1.3294860

Blake, F. G. (1952). Spherical wave propagation in solid media. *J. Acoust. Soc. Am.* 24 (2), 211–215. doi:10.1121/1.1906882

Bycroft, G. N. (1966). Surface displacements due to an underground explosion. *Bull. Seismol. Soc. Am.* 56 (4), 877–888. doi:10.1785/bssa0560040877

Chenglong, Y., and Wang, Z. (2017). Quasi-static model for predicting explosion cavity with spherical charges. *Explos. Shock Waves* (02), 249–254.

Chenglong, Y., Zhongqi, W., and Wengong, H. (2018). A prediction model for amplitude-frequency characteristics of blast-induced seismic waves. *Geophysics* 83 (3), 5MJ–Z13. doi:10.1190/geo2017-0228.1

Chenglong, Y., Zhongqi, W., and Wengong, H. (2017). A prediction model for frequency spectrum of blast-induced seismic wave in viscoelastic medium. *Geophys. Prospect.* 66 (S1), 87–98. doi:10.1111/1365-2478.12601

Ding, H., and Zheng, Z. M. (2002). Source model for blasting vibration. *Sci. China (Series E:Technological Sci.* (4), 395–407. doi:10.1360/02ye9046

Drukovanyi, M. F., Kravtov, V. S., Chernyavskii, Y. E., Shelenok, V. V., Reva, N. P., and Zver'kov, S. N. (1976). Calculation of fracture zones created by exploding cylindrical charges in ledge rocks. *Soviet Min. Sci.* 12 (3), 292–295. doi:10.1007/bf02594873

Favreau, R. F. (1969). Generation of strain waves in rock by an explosion in a spherical cavity. *J. Geophys. Res.* 74 (17), 4267–4280. doi:10.1029/jb074i017p04267

Forrestal, M. J., and Tzou, D. Y. (1997). A spherical cavity-expansion penetration model for concrete targets. *Int. L Solids Struct.* 34 (31-32), 4127–4146. Nos. doi:10.1016/s0020-7683(97)00017-6

Friedman, M. B., Bleich, H. H., and Parnes, R. (1965). Spherical elastic plastic shock propagation. *J. Eng. Mech. Div.* 91 (3), 189–203. doi:10.1061/jmcea3.0000623

Garg, S. K. (1968). Numerical solutions for spherical elastic-plastic wave propagation. *Z. fur Angew. Math. Phys. (ZAMP)* 19 (5), 778–787. doi:10.1007/bf01591008

Garg, S. K. (1968). Spherical elastic-plastic waves. *Z. fur Angew. Math. Phys.* 19 (2), 243–251. doi:10.1007/bf01601469

Ghosh, M. L. (1968). On the propagation of spherical waves due to large underground explosion. *Pure Appl. Geophys.* 72 (1), 22–34. doi:10.1007/bf00875689

Goldsmith, W., and Allen, W. A. (1955). Graphical representation of the spherical propagation of explosive pulses in elastic media. *J. Acoust. Soc. Am.* 27 (1), 47–55. doi:10.1121/1.1907495

Heelan, P. A. (1953). Radiation from a cylindrical source of finite length. *Geophysics* 18 (8), 685–696. doi:10.1190/1.1437923

Henrych, J. (1979). *The dynamics of explosion and its use*. Amsterdam, Netherlands: Elsevier Scientific Publishing Company.

Jeffreys, H. (1931). On the cause of oscillatory movement in seismograms. *Roy. Astr. Soc. Geophys.suppl.* 2 (2), 407–416. doi:10.1111/j.1365-246x.1931.tb04462.x

Kawasumi, H., and Yosiyama, R. (1935). On an elastic wave animated by potential energy of initial strain. *Bull. Earthq. Res. Inst. Tokyo Imp. Univ.* 13, 496–503. doi:10.3390/computation11020015

Lyakhov, G. M. (1964). *Principles of explosion dynamics in soils and in liquid media*. Москва, Russia: Недра.

LyakhovPolyakova, G. M. N. (1967). *Waves in compact media and loading of structures*. Москва, Russia: Недра.

Opjiehko, L. P. (2011). *Explosion physics*. Beijing, China: Science press. SUN Cheng-wei.

Pekeris, C. L. (1955). The seismic surface pulse. *Proc. Nat. Acad. Sei. U.S.A.* 41, 469–480. doi:10.1073/pnas.41.7.469

Ricker, N. (1953). The form and law of propagation of seismic wavelets. *Geophysics* 18, 10–40. List of symbols. doi:10.1190/1.1437843

Sharpe, J. A. (1942). The production of elastic waves by explosion pressures. *Geophysics* 7 (7), 311–321. doi:10.1190/1.1445016

Thiruvenkatachar, V. R., and Viswanathan, K. (1967). Dynamic response of an elastic half-space to time-dependent surface tractions over an embedded spherical cavity. *Proc. Roy. Soc. Lond. A* 300, 159–186. doi:10.1098/rspa.1965.0196

Thiruvenkatachar, V. R., and Viswanathan, K. (1965). Dynamic response of an elastic half-space to time-dependent surface tractions over an embedded spherical cavity. *Proc. Roy. Soc. Lond. A* 287, 549–567. doi:10.1098/rspa.1965.0196

Yixin, Z., Chunhua, B., Chen, J., and Zhongqi, W. (2013). Simulations of seismic waves stimulated by aluminized explosive. *Chin. J. High Press. Phys.* 027 (006), 872–876.

Nomenclature

List of symbols

σ_A, σ_B, and σ_C	Critical stresses of different deformation characteristics of the medium under the stress loading
ε_A, ε_B, and ε_C	Corresponding strains of the medium under different stress loadings σ_A, σ_B, and σ_C
a_m	Radius of the expanding cavity
b_*	Inner boundary of the elastic zone
b_0	Radius of the crushed zone
p	Pressure on the medium
ρ	Density of the medium
ρ_0	Initial density of the medium
e	C–J detonation energy
K	Bulk modulus of the geomaterial
σs	Yield strength of the medium
G	Shear modulus of the medium
G_0	Instantaneous shear modulus
β	Viscoelastic attenuation constant

frontiers | Frontiers in Earth Science

TYPE Original Research
PUBLISHED 15 June 2023
DOI 10.3389/feart.2023.1191049

OPEN ACCESS

EDITED BY
Zhibo Zhang,
University of Science and Technology Beijing, China

REVIEWED BY
Yang Xiao,
Xi'an University of Science and Technology, China
Bo Tan,
China University of Mining and Technology, China
Chunliu Liu,
Anhui University of Technology, China
Ge Huang,
Liaoning Technical University, China

*CORRESPONDENCE
Jiafeng Fan,
symkyfjf@163.com

RECEIVED 21 March 2023
ACCEPTED 31 May 2023
PUBLISHED 15 June 2023

CITATION
Fan J (2023), Effects of CO_2 injection factors on preventing spontaneous coal combustion in coal mine gobs: a simulation approach.
Front. Earth Sci. 11:1191049.
doi: 10.3389/feart.2023.1191049

Effects of CO_2 injection factors on preventing spontaneous coal combustion in coal mine gobs: a simulation approach

Jiafeng Fan*

State Key Laboratory of Coal Mine Safety Technology, China Coal Technology and Engineering Group Shenyang Research Institute, Shenfu Demonstration Zone, Fushun, China

The spontaneous combustion of residual coal in the gob seriously threatens the safety of coal mining. Injecting CO_2 into the gob not only prevents the residual coal from spontaneous combustion but also realizes CO_2 storage in the mined areas. Injection flux and burial depth of the port are crucial for CO_2-preventing fire in coal mine gobs. In this study, the distribution of the oxidation zone in the Tanyaoping coal mine was field-measured, and the coal oxidation kinetic model was built by the adiabatic test. Then, a 3-D mathematical model was constructed based on the conditions of the 5011 working face by COMSOL Multiphysics. Furthermore, the coupled effects of the two factors on the distribution of the oxidation zone were investigated. Increases in both injection flux and burial depth result in a decrease in the oxidation zone volume. The reasonable ranges of the injection flux and burial depth are 540–720 $m^3 h^{-1}$ and 30–40 m, respectively. These results provide some guidelines on how to prevent the spontaneous combustion of residual coal in mine gobs.

KEYWORDS

coal, spontaneous combustion, CO_2 injection, oxidation zone, oxidation kinetic model

1 Introduction

China is the largest producer of coal in the world. Coal mining normally faces several types of accidents that can cause environmental disruption, fatalities, and equipment loss (Zhang et al., 2021; Li et al., 2022). The reaction between coal and O_2 at low temperatures usually results in spontaneous combustion and uncontrolled coal fires (Zhang et al., 2023). During underground coal mining, spontaneous combustion of residual coal in the mine gob often leads to a wide range of secondary disasters, such as methane explosions, carbon monoxide generation, and ventilation disorders. The oxidation process of residual coal in the gob is extremely complex. High-mechanized technology, especially coal caving mining, results in considerable coal resources left in the gob. However, it is necessary to keep enough fresh air through the airways and working face for human survival and methane dilution. Therefore, the residual coal in the gob is exposed to continuous O_2 and has the possibility of spontaneous combustion. The hazardous areas of self-ignition in the gob depend on many factors, such as air leakage, thickness of residual coal, and the advanced rate of the working face (Zhu and Wen, 2023). Normally, the "three zones" (the cooling zone, oxidation zone, and suffocation zone) in the gob are determined based on the distribution of O_2 concentration in the gob area (Ma et al., 2020).

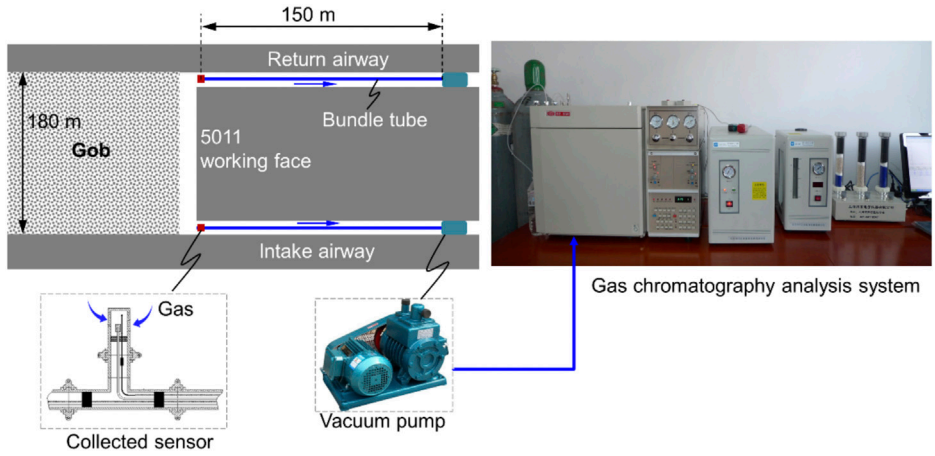

FIGURE 1
Measurement of O_2 concentration in the gob.

Spontaneous combustion of coal is influenced by coal oxidation reactions, heat accumulation, and the characteristics of porous media (Si et al., 2021). Therefore, many technical solutions were presented to prevent coal from spontaneous combustion and inhibit coal fire, which normally focus on two aspects: isolating coal active sites from O_2 and cooling the temperature (Dou et al., 2022). The present strategies can be broadly classified as uniform pressure ventilation (Lu et al., 2017), grouting (Zhang et al., 2018), spray inhibitors (Lu et al., 2020; Sun et al., 2022), pumping inert gas (Zhu and Wen, 2023), and injecting gel foam or gel (Lu et al., 2018; Lu et al., 2021; Han et al., 2022; Huang et al., 2022). CO_2 is an inert gas and can dilute the O_2 concentration and protect the coal from heat release. Furthermore, broken coal can absorb CO_2 and thus saved from oxidation (Guan et al., 2018). With the advancement of the working face, the volume of the mine gob increases. The resistance of internal airflow is small, and the porosity is large. Thus, the coal mine gob is an ideal location for storing CO_2. Injecting CO_2 into the gob can achieve the dual benefits of fire prevention and CO_2 storage.

This study is based on the actual conditions of the 5011 working face of the Tanyaoping coal mine. To achieve the fire prevention of residual coal in the gob by injecting CO_2, the oxidation zone was calculated by mathematical simulation using COMSOL Multiphysics. This simulated result without CO_2 injection was verified to be reasonable by comparing it with the field measurement. By studying the effect of the injection flux and burial depth of the injection port on the oxidation zone, the superior injection parameters were determined.

2 Overview of the 5011 working face

The Tanyaoping coal mine is located in Lvliang city, China. The recoverable coal seams consist of 5# and 10# coal seams. The 5011 working face is in coal seam 5# and adopts the "U" ventilation method. Coal seam 5# is the main production seam

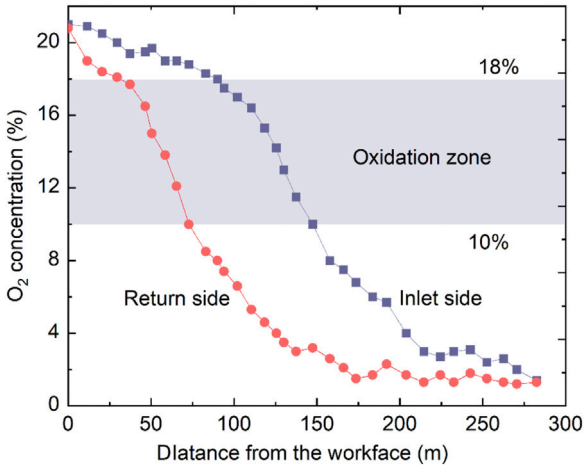

FIGURE 2
O_2 concentration of measured points in the intake and return airways.

and is around 4.4 m thick. The width and design length are 180 and 2,000 m, respectively. The width and height of the intake and return airways are 5 and 4.5 m, respectively. The thickness of the residual coal that remains in the mined area, that is, the gob, is about 0.4 m. The mined coal has a spontaneous combustion tendency.

As shown in Figure 1, two sensors were fixed in the intake and return airways to collect the gas. The monitoring system was based on the measurement of bundle tubes. With the advancement of the working face, O_2 concentrations at different buried depths were drawn out through the bundle tubes using a vacuum pump. A gas chromatography analysis system was used to analyze the O_2 concentrations of the collected bags. Figure 2 shows the measured O_2 concentration values in the intake and return airways. The O_2 concentrations at the observation points decrease with increasing buried depth. According to the actual

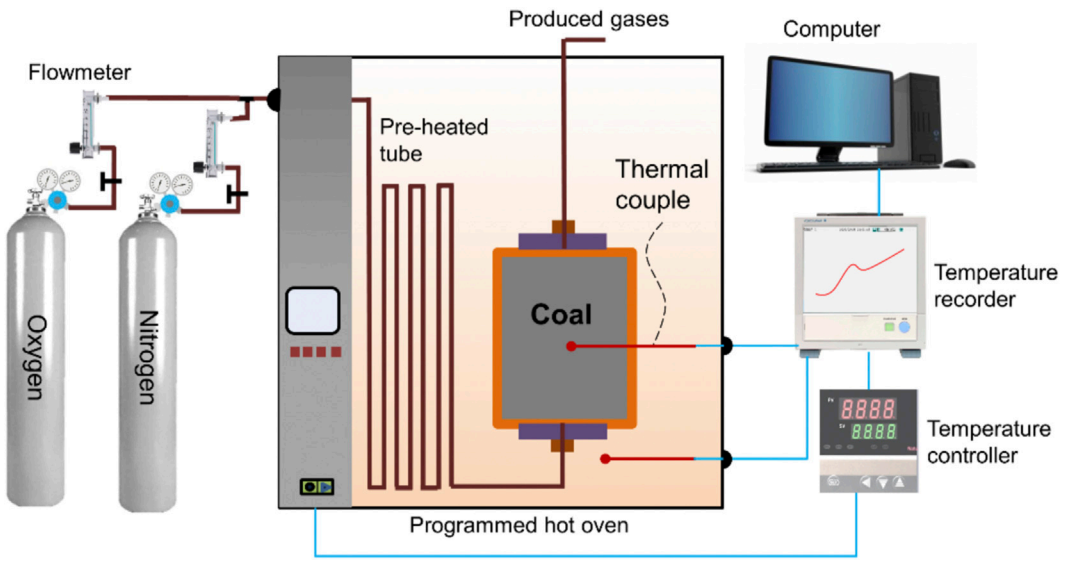

FIGURE 3
Schematic representation of the adiabatic oxidation test.

condition and other studies, the "three zones" were divided by using an O_2 concentration of 10%–18% (Ma et al., 2020). The O_2 concentration at the point in the intake airway decreased to 18% and 10% at 90 and 147 m, respectively. For the measured point in the return airway, the buried depths of O_2 concentrations of 18% and 10% are 30 and 73 m, respectively. Normally, there are three parameters to determine the "three zones" in the gob: the air leakage velocity, O_2 concentration, and heating rate (Deng et al., 2018). However, the O_2 concentration is the most accessible and was, therefore, applied in this study to judge the oxidation zone.

3 Coal oxidation kinetic model

Coal exothermic processes under low temperatures include three forms: physical adsorption, chemical adsorption, and chemical reactions (Liang et al., 2021). Chemical adsorption and chemical reactions are recognized as the main reasons for promoting the self-heating of coal under low temperatures (Zhang et al., 2019; Qu et al., 2023). Although partially active functional groups are self-reacting, a significant amount of heat will be released from the coal–O_2 reaction. Therefore, a linear relationship between the O_2 consumption rate and heat generation rate is generally considered to exist, expressed as follows:

$$q = r\Delta H, \tag{1}$$

where q is the heat generation rate of the coal reaction ($W{\cdot}m^{-3}$); ΔH is the coal oxidation heat ($J{\cdot}mol^{-1}$); and r is the O_2 consumption rate ($mol{\cdot}m^{-3}{\cdot}s^{-1}$).

Based on the coal oxidation dynamics theory, another major influence on coal oxidation is temperature, which increases, causing the activation of functional groups, i.e., the exothermic intensity increases with increasing temperature. Most of the models on O_2 consumption in the previous studies were based on the Arrhenius equation, expressed as follows:

$$r = Ac_o \exp\left(-E/RT\right), \tag{2}$$

where A is the pre-exponential factor (s^{-}); E is the activation energy ($J{\cdot}mol^{-1}$); R is the gas constant ($8.314\ J\ mol^{-1}{\cdot}K^{-1}$); c_o is the O_2 concentration (%); and T is the temperature (K). The kinetic parameters in Equation 2 are normally obtained from the adiabatic oxidation test.

As shown in Figure 3, the coal sample was mined from the 5011 working face of the Tanyaoping coal mine. Moisture, ash, volatile matter, and fixed carbon of coal are 7.64, 2.21, 26.24, and

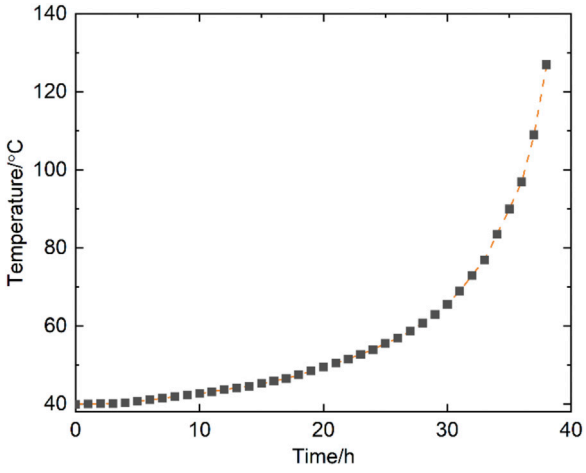

FIGURE 4
Temperature profile versus time under adiabatic conditions.

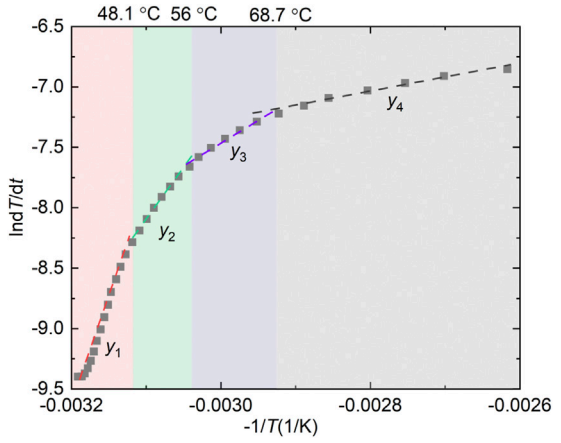

FIGURE 5
Fitting of lndT/dt versus $-1/T$.

63.19, respectively. Elements of C, H, O, and N of coal are 63.61, 4.86, 0.81, and 30.69, respectively. Approximately 220 g of coal particles (0.2–0.45 mm) were prepared and naturally filled into the reaction vessel. The sample was dried in N_2 at 105°C for 5 h and then cooled to 40°C under a N_2 atmosphere (Wang et al., 2010). Once the temperature was stable, the mixed gases with 21% O_2 were injected into the reaction vessel at 10 mL min^{-1}. It should be ensured that the oven temperature is synchronized with the coal temperature using the temperature controller. The change in coal temperature over time was recorded using the recorder for later analysis. Figure 4 shows the temperature profile versus time of the adiabatic oxidation test.

Under the adiabatic conditions, the coal sample was subjected to accelerated self-oxidation so that the heat released in the last step was completely converted to internal energy, which can be described by Equation 3 as follows:

$$q = \rho_c C_{pc} \frac{dT}{dt} = r\Delta H = \Delta H A c_o \exp(-E/RT), \tag{3}$$

where ρ_c is the density of coal (kg·m^{-3}) and C_{pc} is the specific heat capacity of coal (J·kg^{-1}·K^{-1}). Equation 4 can be rearranged by taking the natural logarithm, which is expressed as follows:

$$\ln \frac{dT}{dt} = \ln \frac{\Delta H A c_o}{\rho_c C_{pc}} - \frac{E}{R} \cdot \frac{1}{T}, \tag{4}$$

$$y = \begin{cases} y_1 = -17230x + 45.476 & R^2 = 0.9796 \quad (x < 48.1), \\ y_2 = -6910.4x + 13.353 & R^2 = 0.9933 \quad (48.1 < x < 56), \\ y_3 = -3955.9x + 4.3786 & R^2 = 0.9937 \quad (56 < x < 68.7), \\ y_4 = -2343.1x - 0.3393 & R^2 = 0.9974 \quad (x > 68.7). \end{cases} \tag{5}$$

The relationship between lndT/dt and $-1/T$ shown in Figure 5 is a nonlinear positive correlation, which does not follow the standard Arrhenius equation, and this phenomenon also appears in other studies (Zhang et al., 2020; Yoruk and Arisoy, 2022). It is difficult to fit the curve with one or two straight lines. The curve was divided into four stages with three break points of 48.1, 56, and 68.7°C. In each stage, lndT/dt and $-1/T$ exhibit good linearity, as shown in Equation 1. The slope of the fitting line in each stage presents the value of -E/R, and the intercept is the value of ln$\Delta HAc_0/\rho_c C_{pc}$. The apparent activation energies of the four stages are 143.25, 57.45, 32.89, and 19.48 kJ mol^{-1}, respectively. Accordingly, the pre-exponential factors of the coal sample are 2.53×10^{20}, 2.83×10^{6}, 358.31, and 3.2 s^{-1}, respectively. In the numerical calculation, different E and A are invoked based on the coal temperature for the heat generation model.

4 Numerical simulation

The process of spontaneous combustion of residual coal in the gob area will involve heat transport and generation, O_2 consumption and transport, CO_2 emission and migration, and gas airflow. As shown in Figure 6, all the involved equations are interrelated based on the fluid-solid-thermal coupling (Xia et al., 2016; Zhang et al., 2019; Qi et al., 2021). The continuity equation and the momentum conservation equation are as follows:

$$\frac{\partial(\varepsilon\rho_g)}{\partial t} + \nabla(\rho_g \mathbf{U}) = 0, \tag{6}$$

$$\frac{\partial(\varepsilon\rho_g \mathbf{U})}{\partial t} + \nabla \cdot (\varepsilon\rho_g \mathbf{U}\mathbf{U}) = -\varepsilon\nabla p + \nabla \cdot (\varepsilon\boldsymbol{\tau}) + \varepsilon\mathbf{F} - \frac{\varepsilon^2\mu}{K}\mathbf{U}, \tag{7}$$

where ρ_g is the density of air (kg·m^{-3}); ε is the porosity of gob; t is the time (s); $\mathbf{U}$ is the seepage air velocity vector (m·s^{1}); p is the static pressure (Pa); $\boldsymbol{\tau}$ is the stress tensor (Pa); μ is the air viscosity (Pa s); K is the permeability (m^2); and $\mathbf{F}$ is the gravitational body force (N·m^{-3}).

The relationship between porosity and permeability is expressed as

$$K = \frac{d\varepsilon^3}{150(1-\varepsilon)^2}, \tag{8}$$

where d is the particle size (mm). With the working face advanced, the stress status of overlying strata is damaged, and the roof-bed formation collapses. The overlying strata are vertically divided into a caving zone, fissure zone, and bent deformation zone based on the differences in the balance status and re-compaction degree of the damaged strata (Qin et al., 2016). Therefore, it is a significant challenge to build mathematical models with reasonable permeability and porosity in the gob area. According to the observation of the mine pressure, the compaction bulking factor, k, of the gob follows the law (Xia et al., 2015):

$$\varepsilon = 1 - \frac{1}{k}, \tag{9}$$

$$k = k_{p,\min} + (k_{p,\max} - k_{p,\min}) \cdot \exp\{-a_1 d_1 \cdot [1 - \exp(\xi_1 \cdot a_0 d_0)], \tag{10}$$

where $k_{p,\min}$ and $k_{p,\max}$ are the initial bulking factors before and after compacting in the gob area, respectively, (1.15 and 1.5). a_0 and a_1 are the decay ratios of the bulking factor in the dip and strike directions of the working face, respectively, (0.268 and 0.0368 m^{-1}). d_0 and d_1 are the distances between the point (x,y) in the gob and the working face and coal pillar, respectively. ξ_1 is the adjustment factor controlling the distribution pattern of the model, 0.233.

The local thermal non-equilibrium is considered in the energy equation of conservation, which is given by

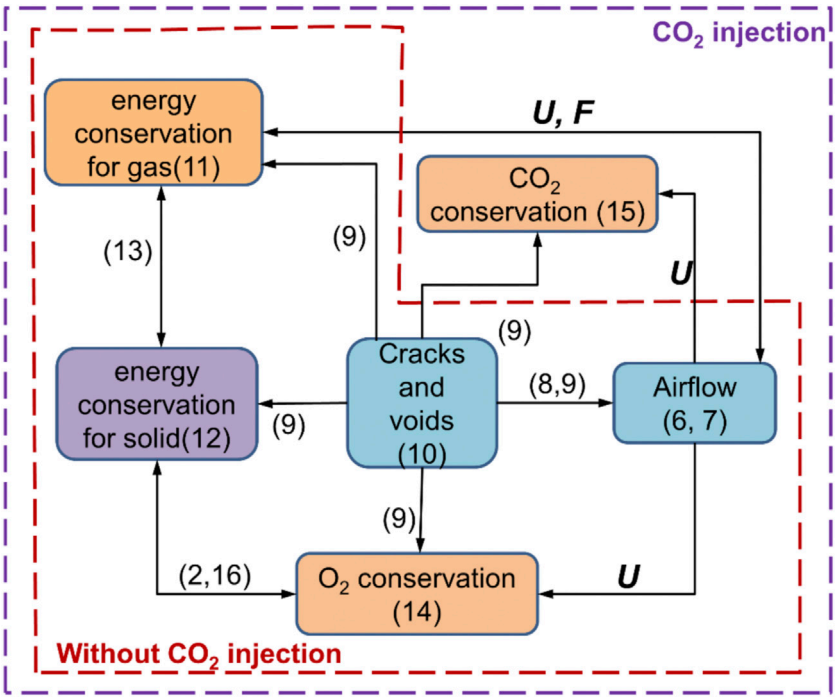

FIGURE 6
Main conservation equations of modeling.

$$\text{For gas, } \varepsilon\rho_g C_{pg}\frac{\partial T_g}{\partial t} + \rho_g C_{pg}\mathbf{U}\nabla T_g = \varepsilon\nabla\left(\lambda_g \nabla T_g\right) + q_{gc}, \tag{11}$$

$$\text{For solid, } (1-\varepsilon)\rho_c C_{pc}\frac{\partial T_c}{\partial t} = (1-\varepsilon)\nabla(\lambda_c \nabla T_c) - q_{gc} + (1-\varepsilon)q_o, \tag{12}$$

where C_{pg} is the specific heat capacity of air (J·kg^{-1}·K^{-1}); λ_g and λ_c are the thermal conductivities of air and coal, respectively (W·m^{-1}·K^{-1}); T_g and T_c are the temperatures of air and coal, respectively (K); q_o is the heat generation rate of coal (W·m^{-3}) obtained using Equation 3; q_{gc} is the solid–gas heat exchange around coal particles (W·m^{-3}), which has

$$q_{gc} = h_{gc}a\left(T_c - T_g\right), \tag{13}$$

where h_{gc} is the convective heat transfer coefficient (W·m^{-2}·K^{-1}), indicating the heat exchange between coal and pore air; a is the specific surface area, that is, the exposed area of coal particles per unit volume (m^{-1}).

O_2 conservation is a unique consideration without CO_2 injection. However, we must consider the conservation of O_2 and CO_2 for fire prevention by injecting CO_2 into the gob, which is expressed as follows:

$$\varepsilon\frac{\partial c_o}{\partial t} + \nabla(\mathbf{U}c_o) = \nabla(\varepsilon D\nabla c_o) + r_o, \tag{14}$$

$$\boldsymbol{\varepsilon}\frac{\partial c_m}{\partial t} + \nabla(\mathbf{U}c_m) = \nabla(\varepsilon D\nabla c_m) + r_m, \tag{15}$$

where c_m is the concentration of CO_2 (mol·m^{-3}); D_o and D_m are the effective diffusivities of O_2 and CO_2, respectively (m^2·s^{-1}); and r_o is the O_2 consumption rate (mol·m^{-3}·s^{-1}). r_m is the CO_2 generation rate (mol·m^{-3}·s^{-1}) of coal oxidation, whose ratio to r_o is 0.1 (Taraba et al., 2014). The oxidation reaction of residual coal in the gob is affected by working face advance. Based on Equation 2, r_o can be expressed as

$$r_o = wr, \tag{16}$$

where w is the influence coefficient of working face advance.

In addition, to ensure the normal operation of modeling, the following main assumptions are supplemented (Ma et al., 2020; Zhang et al., 2022):

(i) The effects of moisture transport and evaporation are not considered.
(ii) Thermal conductivity and heat capacity of coal and gas are independent of other parameters.
(iii) The transfer of heat in the gob merely involves convection and conduction, and the radiative transfer is not taken into account.
(iv) The gas in the gob is incompressible.

According to the actual conditions of the 5011 working face, the corresponding geometric model has been established. COMSOL Multiphysics software was applied to simulate the oxidation process of residual coal in the mine gob. The whole model consists of four parts: the mining area, the inlet airway, the return airway, and the working face. The cross-sectional area of both the inlet and return airways is 22.5 m^2, and the cross-sectional area of the working face is 25 m^2. The length of the inlet and return airways is 5 m. The length of the working face is set as 220 m, and

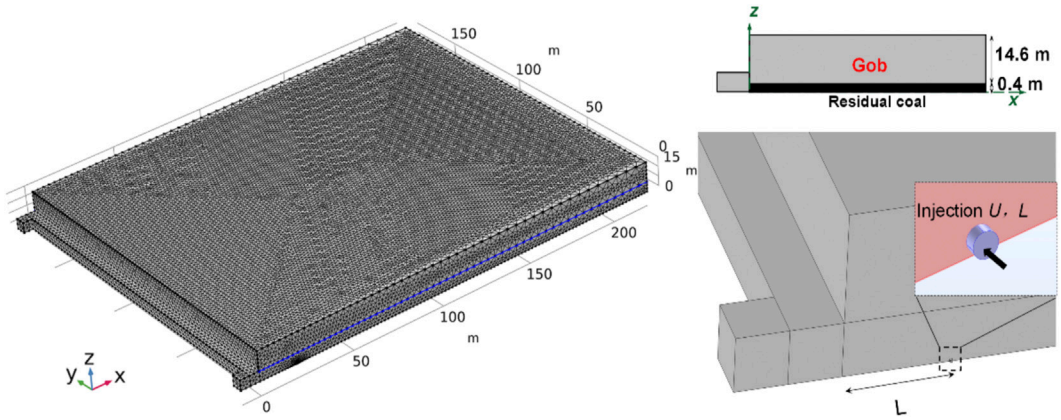

FIGURE 7
Geometric model and meshing.

TABLE 1 Main parameters applied in the numerical simulation.

Parameter	Item	Value	Unit
A_0	Pre-exponential factor	40	kJ·mol^{-1}
E	Apparent active energy	320	s^{-1}
ρ_a	Density of air	1.225	kg·m^{-3}
ρ_c	Density of coal	1300	kg·m^{-3}
c_a	Specific heat capacity of air	1007	J·kg^{-1}·K^{-1}
c_c	Specific heat capacity of coal	1210	J·kg^{-1}·K^{-1}
λ_a	Thermal conductivity of air	0.02	W·m^{-1}·K^{-1}
λ_c	Thermal conductivity of coal	0.21	W·m^{-1}·K^{-1}
μ	Viscosity	1.87×10^{-5}	Pa·s
D_o	O_2 diffusion coefficient	1.76×10^{-5}	m^2·s^{-1}
D_m	CO_2 diffusion coefficient	1.6×10^{-5}	m^2·s^{-1}
h_{gc}	Convective heat transfer coefficient	11	W·m^{-2}·K^{-1}
ΔH	Coal oxidation heat	380,000	J·mol^{-1}
w	Influence coefficient of working face advance	0.9	-

the length and height of the gob area are 180 and 15 m, respectively. For the condition without CO_2 injection, grid independence was checked by carrying out three sets of grids. Eventually, after considering the CPU time and the sensitive parameter, 34,954 mesh blocks are divided among this model, including 32,389 mesh blocks in the gob area. The mesh blocks of the models for CO_2 injection were slightly larger than those without CO_2 injection. The time step was set as 1 h. As shown in Figure 7, the CO_2 injection port was a round tube with a radius of 0.2 m and a length of 0.2 m. Two parameters, injection flux (U, m^{3}h^{-1}) and injection port burial depth (L, m), were considered to investigate the performance of CO_2 injection in preventing residual coal fires. The parameters used in the simulations are listed in Table 1. The boundary and initial conditions used in the mathematical model are illustrated in Table 2.

5 Results and discussion

5.1 Analysis of the oxidation zone without CO_2 injection

As shown in Figures 8A, B, the porosities and permeabilities of the gob near the working face and pillars are larger than those of the

TABLE 2 Boundary and initial conditions of the mathematical model.

	Types	Positions	Values
Boundary conditions	Inlet	x = −5 m	Velocity: 0.7 m s^{-1} (1050 m^3 min^{-1})
		y = 0–5 m	Temperature: 20°C
		z = 0–5 m	O_2 concentration: 9.7 mol m^{-3}
		x = L	Velocity: U
		y = −0.2 m	Temperature: 20°C
		z = 0.1 m (circle)	CO_2 concentration: 44.6 mol m^{-3}
	Outlet	x = −5 m	Free outflow
		y = 115 m–120 m	
		z = 0–5 m	
	Wall	Other surfaces	Temperature: 20°C
Initial conditions	Temperature	Entire domain	20°C
	(Seepage) velocity		0
	CO_2 concentration		0
	O_2 concentration		9.7 mol m^{-3}

inner zone due to the mining process. Fresh air enters the working face from the inlet airway with a velocity of 0.7 m s^{-1}, and more than 90% of the ventilation flux passes through the working face and then flows into the return airway. The airflow streamlines in the gob area, normally from the windward zone near the inlet airway to the zone near the return airway. The airflow velocity near the working face is larger than that in the inner zone due to the smaller forced-convection resistance.

With the deepening of the gob, the O_2 concentration gradually decreases. As shown in F8(e), on the side of the inlet airway, the fresh air from the intake airway enters the gob and flows toward the deep. However, gases with low O_2 concentrations flow from the deep to the return airway. Therefore, the O_2 concentration near the side of the return airway shows a more rapid decline than that of the intake airway.

This distribution of the oxidation zone has been observed in many other field measurements and simulations (Xia et al., 2015; Chu et al., 2019; Xu et al., 2020). Coal near the working face undergoes a strong oxidation reaction because of the abundant O_2, accompanied by the release of heat. We can find that the high-temperature zone is located on the windward side of the oxidation zone, as shown in Figure 8C. It is due to the fact that O_2 was consumed in the high-temperature zone, causing fewer O_2 molecules to enter the interior of the gob. Therefore, it is difficult to transport enough O_2 to the inner zone, resulting in a low concentration of O_2 within the area. The distribution of CO_2 in the gob is the opposite of the distribution of O_2 because most of the CO_2 in the gob is derived from low-temperature oxidation of residual coal, as shown in Figure 8D. The overall CO_2 values are much lower than those of O_2. The CO_2 concentration near the working face is lower than that in the inner zone due to the dilution of airflow seepage.

Figure 8E is a three-dimensional distribution of O_2 concentration in the gob area. The O_2 concentration in the upper area in the same vertical direction is slightly higher than that in the lower area. The volume of the oxidation zone without CO_2 injection is calculated to be 121,000 m^3. The average width of the oxidation band is 45 m. Figure 8F shows the range comparison of the oxidation zones (z=0.2 m) between the field measurement and simulation. The two results show good alignment. It indicates that the numerical simulation can reflect the performance of the self-ignition of the residual coal in the gob.

5.2 Analysis of the base case with CO_2 injection

The base case of U = 540 m^3 h^{-1} and L = 20 m was calculated, and the distributions of O_2, CO_2, and temperature in the gob area are shown in Figure 9. CO_2 injection has the properties of a displacement effect on the air leakage, a dilution effect on the O_2 distribution, and a cooling effect on the high-temperature zone. Therefore, the spontaneous combustion of residual coal is delayed or prevented. CO_2 injection can dilute the O_2 concentration. CO_2 concentration is much higher than O_2 concentration downstream of the injection port. The oxidation zone on the inlet airway side moved significantly toward the injection port, and the width of the oxidation zone decreased significantly. CO_2 was continually mixed with leaked O_2, and the dilution effect on the O_2 distribution was gradually attenuated. The high-temperature zone under CO_2 injection was a smaller area than that without CO_2 injection. CO_2 also suppresses the maximum temperature in the gob. It indicates that CO_2 can restrict the self-ignition of coal. In addition, the area of the oxidation zone for CO_2 injection on the surface z = 0.2 m is 1300 m^2, much smaller than that without CO_2

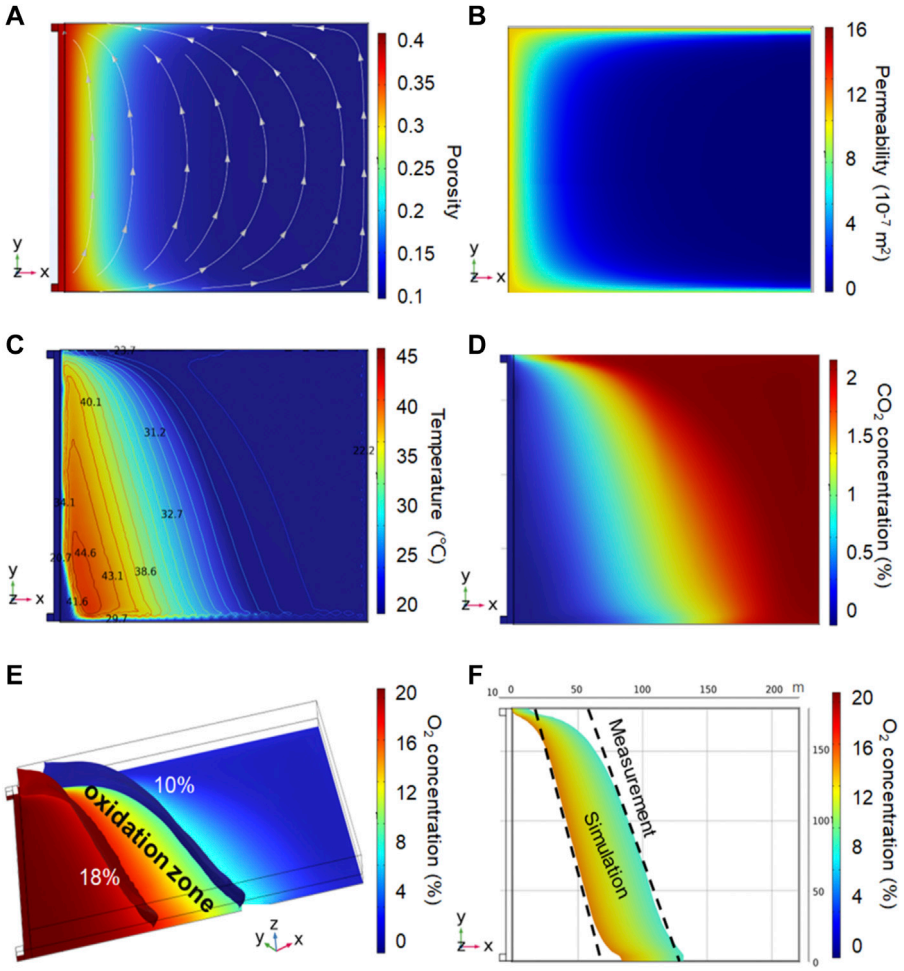

FIGURE 8
Numerical simulation without CO_2 injection: **(A)** porosity and airflow seepage at z=0.2 m, **(B)** permeability distribution at z=0.2 m, **(C)** temperature distribution at z=0.2 m, **(D)** CO_2 distribution at z=0.2 m, **(E)** 3-D oxidation zone, and **(F)** oxidation zone at z = 0.2 m.

injection, which is 7400 m^2. However, the volumes of the oxidation zone with and without CO_2 injection are 63,000 m^3 and 121,000 m^3, respectively. The injection port is located near the bottom, causing a large amount of CO_2 cluster in the lower area and, therefore, not easily diluting O_2 in the upper area. As a result, the width of the oxidation zone in the upper area is much greater than that of the lower area.

5.3 Effect of the CO_2 injection flux

Based on the base case and the corresponding simulation without CO_2 injection, the effects of the CO_2 injection flux on the prevention of residual coal fires were analyzed. The assumed CO_2 injection fluxes are 180, 360, 540, 720, 900, and 1080 m^3 h^{-1}, respectively. Figure 10 shows the oxidation zone in the gob for different CO_2 injection fluxes at L=20 m. An increase in the injection flux weakens the O_2 concentration in the gob and increases the displacement effect. When $U \geq 180$ m^3 h^{-1}, the higher pressure of the intake airway and gravity suppress the injected CO_2, which flows along the lower side of the gob in the direction of airflow seepage, as shown in Figure 11. At U= 180 and 540 m^3 h^{-1}, CO_2 concentrations in the upper zone of the gob are much lower than those in the bottom zone. Because the CO_2 injection fluxes (≤1080 m^3 h^{-1}) are smaller than the air flux from the intake airway (1050 m^3 min^{-1}). CO_2 injection hardly affects the air leakage streamlines, and thus, the high CO_2 areas at different U values are extremely similar. With the increase in CO_2 injection flux, the overall distribution of the oxidation zone moves toward the working face. The oxidation zone in the lower gob area moves toward the upwind side of the injection port when $U \geq 0$. As wind speeds increase, the distance between the iso-surfaces increases by 10% to 18%, reducing the volume of the oxidation zone. The volumes of the oxidation zone at U = 180, 360, 540, 720, 900, and 1080 m^3 h^{-1} are 89,000, 62,500, 43,000, 2,950, 24,000, and 23,000 m^3 at L=20 m, respectively. Therefore, when $U <$ 900 m^3 h^{-1}, the volume of the oxidation zone decreases with the injection flux, and when $U >$ 900 m^3 h^{-1}, the volume changes little as flux increases. This phenomenon also appears in other cases with different L values.

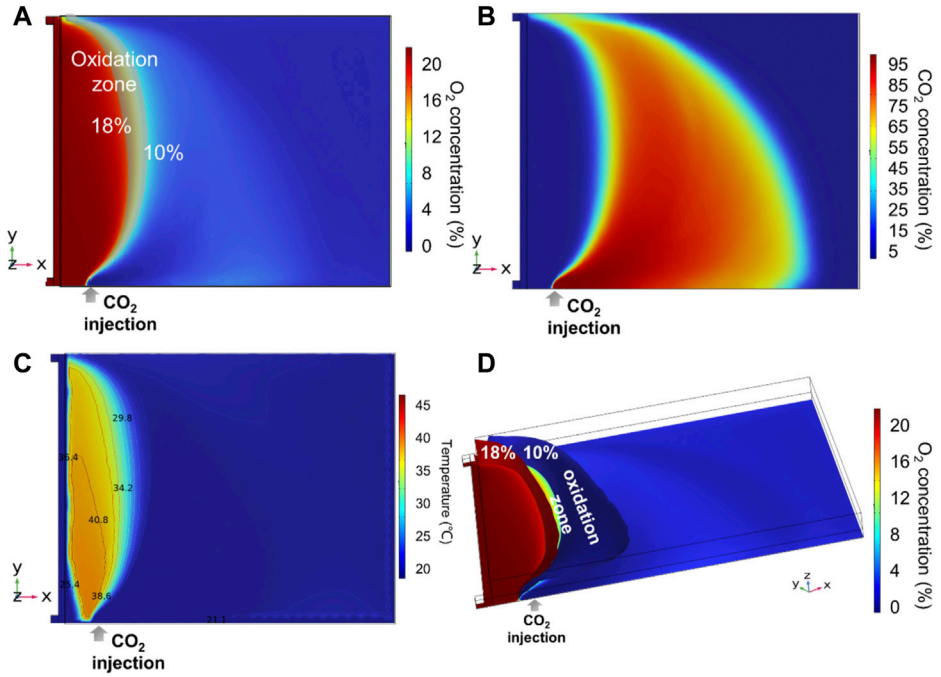

FIGURE 9
Numerical simulation with CO_2 injection (L = 20 m and U = 540 $m^3\ h^{-1}$): **(A)** oxidation zone at z = 0.2 m, **(B)** CO_2 distribution at z = 0.2 m, **(C)** temperature distribution at z = 0.2 m, and **(D)** 3-D oxidation zone.

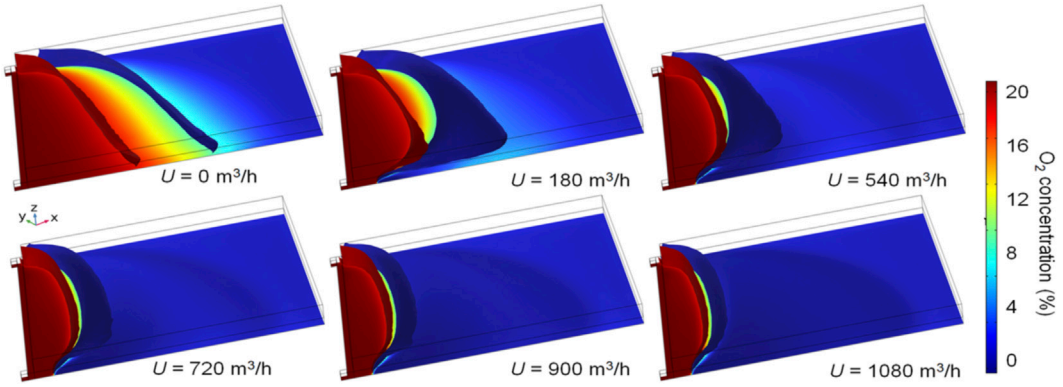

FIGURE 10
Simulated oxidation zone with different injection fluxes at L = 20 m.

5.4 Effect of the CO_2 injection location

Figures 12, 13 show O_2 and CO_2 distributions in the gob with different burial depths at U = 540 $m^3\ h^{-1}$. Once CO_2 is injected, the oxidation zone on the inlet side is significantly reduced. This is because the high CO_2 concentration near the injection port effectively dilutes O_2. The closer the inlet port is to the working face, the closer the oxidation zone on the inlet side is to the working face, and the weaker the effect of the O_2 concentration in the upper area of the inlet side being displaced by CO_2. It is due to the high leakage strength near the working face and a large amount of fresh air that suppresses CO_2 diffusion by the dilution effect. Therefore, as shown in Figure 13, the smaller L is, the lower the CO_2 concentration within the gob. At L = 10, 20, and 30m, the CO_2 concentration in the upper area of the gob is low. Moreover, as the burial depth of the injection port increases, the airflow leakage from the working face is small, and CO_2 can migrate to the upper area without high resistance. The volumes of the oxidation zone at L= 10, 20, 30, 40, 50, and 60 are 65,000, 43,000, 27,000, 23,000, 19,200, and

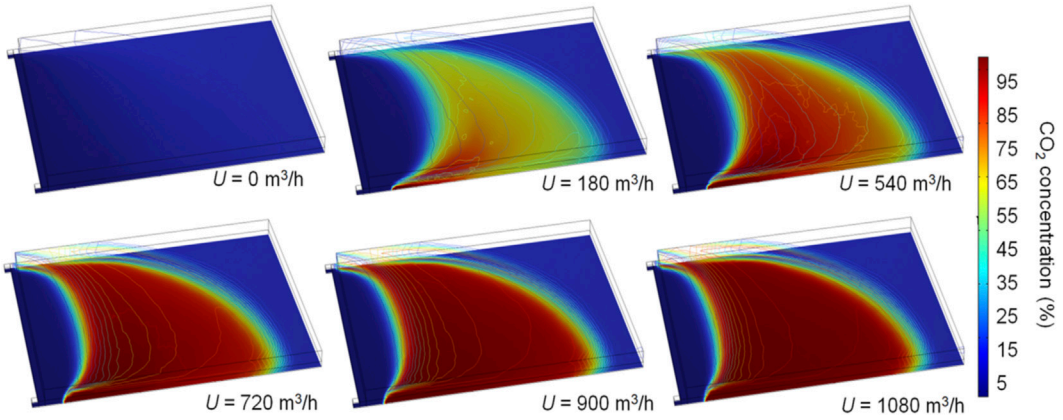

FIGURE 11
Simulated CO_2 distribution with different injection fluxes at L = 20 m.

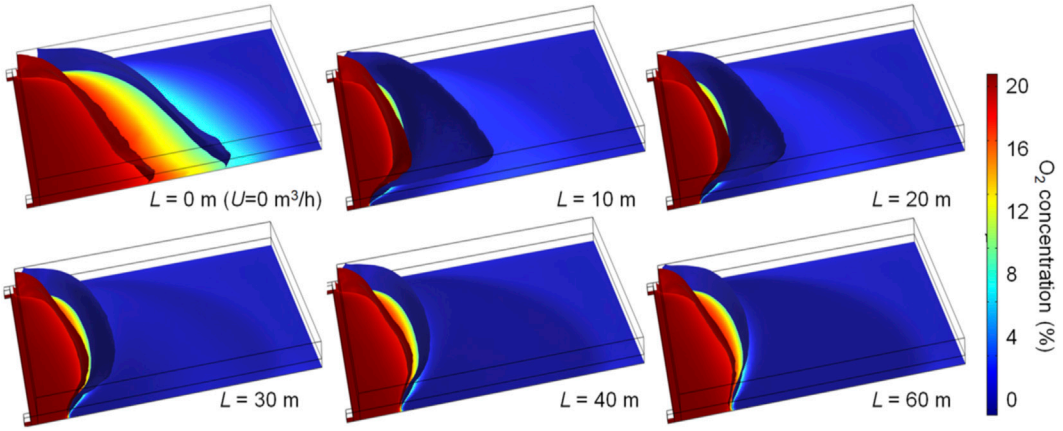

FIGURE 12
Simulated oxidation zone with different burial depths at U = 540 m^3 h^{-1}.

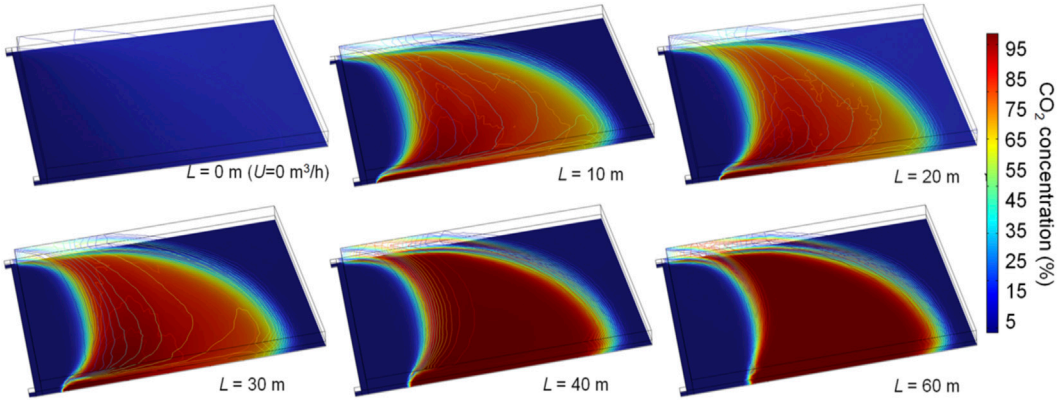

FIGURE 13
Simulated CO_2 distribution with different burial depths at U = 540 m^3 h^{-1}.

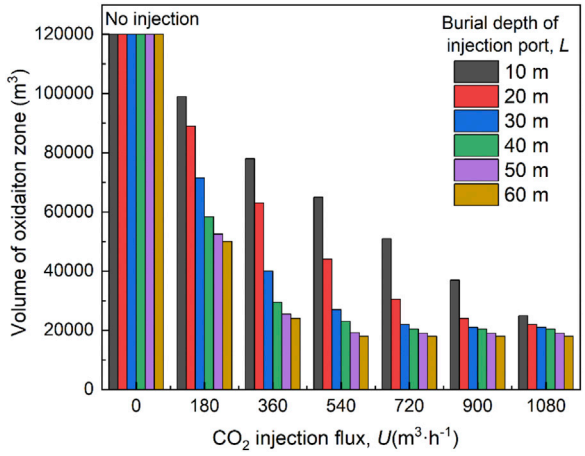

FIGURE 14
Predicted volume of the oxidation zone at different *L* and *U* values.

18,500 m^3 at Q=540 $m^3\ h^{-1}$, respectively. As L increases, the width of the oxidation zone in the upper area decreases rapidly. The volumes of the oxidation zone are almost identical at L = 50 and 60 m. In addition, the change in the burial depth of the injection port has little effect on the distribution of the oxidation zone on the return side.

5.5 Comprehensive analysis of coupling the CO_2 injection flux and location

Figure 14 shows the effects of coupling factors, that is, the CO_2 injection flux and location, on the predicted volume of the oxidation zone. A decrease in the CO_2 injection volume or burial depth of the port will reduce the volume of the oxidation zone. When U < 720 $m^3\ h^{-1}$, an increase in the burial depth significantly reduces the volume of the oxidation zone, especially at a lower injection flux. When U=1080 $m^3\ h^{-1}$, the change in the position of the injection port does not have a significant effect on the distribution of the oxidation zone. At L = 10 m, the volume of the oxidation zone decreases linearly with the injection flux. However, when L > 30 m, the volume dramatically reduces with increasing U from 0 to 540 $m^3\ h^{-1}$, but changes little as flux continues increasing. In practice, longer gas injection lines are avoided, which can make operations difficult. Smaller U values can save costs and reduce CO_2 concentrations in the upper corner and working face when achieving similar effects of suppressing coal spontaneous combustion for different U values. Therefore, based on the simulation results, the parameters of U = 540–720 $m^3\ h^{-1}$ and L = 30–40 m are recommended for the 5011 working face.

6 Conclusion

To accurately predict the effectiveness of CO_2 injection on spontaneous combustion in the coal mine gob. A mathematical simulation by COMSOL Multiphysics was applied in this study.

According to the conditions of the 5011 working face in the Tanyaoping coal mine, a 3-D mathematical model considering fluid-solid-thermal inter-relationship was established. The coal oxidation kinetic model was derived from the adiabatic oxidation test, where four stages were considered in the model. The apparent activation energies of the four stages are 143.25, 57.45, 32.89, and 19.48 kJ mol^{-1}, respectively. A good agreement between the field measurement and numerical simulation indicates the rationality of the mathematical model. CO_2 injection can dilute the O_2 concentration and prevent spontaneous combustion of coal. The coupling effects of injection flux, U, and the burial depth of the injection port, L, on the oxidation zone were investigated. The oxidation zone volume decreased with increasing U and L. When U or L is small, the upper width of the oxidation zone is wider, and as U or L increases, the upper width gradually decreases until it is no longer sensitive to parameter changes. An optimum injection plan is to keep the volume of the oxidation zone at a lower value in consideration of economic viability and operational parameters. The injection parameters of U = 540–720 $m^3\ h^{-1}$ and L = 30–40 m are recommended after considering the activity of the 5100 working face. The volume of the oxidation zone was estimated to be 18,500–23000 m^3.

Data availability statement

The original contributions presented in the study are included in the article/supplementary material, further inquiries can be directed to the corresponding author.

Author contributions

Investigation, methodology, writing—original draft, formal analysis, and final draft were completed by the author FJ.

Conflict of interest

The author declares that the research was conducted in the absence of any commercial or financial relationships that could be construed as a potential conflict of interest.

Publisher's note

References

Chu, T., Li, P., and Chen, Y. (2019). Risk assessment of gas control and spontaneous combustion of coal under gas drainage of an upper tunnel. *Int. J. Min. Sci. Technol.* 29 (3), 491–498. doi:10.1016/j.ijmst.2018.05.002

Deng, J., Lei, C., Xiao, Y., Cao, K., Ma, L., Wang, W., et al. (2018). Determination and prediction on "three zones" of coal spontaneous combustion in a gob of fully mechanized caving face. *Fuel* 211, 458–470. doi:10.1016/j.fuel.2017.09.027

Dou, G., Liu, J., Jiang, Z., Jian, H., and Zhong, X. (2022). Preparation and characterization of a lignin based hydrogel inhibitor on coal spontaneous combustion. *Fuel* 308, 122074. doi:10.1016/j.fuel.2021.122074

Guan, C., Liu, S., Li, C., Wang, Y., and Zhao, Y. (2018). The temperature effect on the methane and CO_2 adsorption capacities of Illinois coal. *Fuel* 211, 241–250. doi:10.1016/j.fuel.2017.09.046

Han, C., Nie, S., Liu, Z., Liu, S., Zhang, H., Li, J., et al. (2022). A novel biomass sodium alginate gel foam to inhibit the spontaneous combustion of coal. *Fuel* 314, 122779. doi:10.1016/j.fuel.2021.122779

Huang, Z., Quan, S., Hu, X., Zhang, Y., Gao, Y., Ji, Y., et al. (2022). Study on the preparation and inhibition mechanism of intumescent nanogel for preventing the spontaneous combustion of coal. *Fuel* 310, 122240. doi:10.1016/j.fuel.2021.122240

Li, J., Li, X., Liu, C., and Zhang, N. (2022). Study on the air leakage characteristics of a goaf in a shallow coal seam and spontaneous combustion prevention and control strategies for residual coal. *Plos one* 17 (6), e0269822. doi:10.1371/journal.pone.0269822

Liang, Y., Tian, F., Guo, B., and Liu, Z. (2021). Experimental investigation on microstructure evolution and spontaneous combustion properties of aerobic heated coal. *Fuel* 306, 121766. doi:10.1016/j.fuel.2021.121766

Lu, W., Cao, Y. J., and Tien, J. C. (2017). Method for prevention and control of spontaneous combustion of coal seam and its application in mining field. *Int. J. Min. Sci. Technol.* 27 (5), 839–846. doi:10.1016/j.ijmst.2017.07.018

Lu, W., Guo, B., Qi, G., Cheng, W., and Yang, W. (2020). Experimental study on the effect of preinhibition temperature on the spontaneous combustion of coal based on an $MgCl_2$ solution. *Fuel* 265, 117032. doi:10.1016/j.fuel.2020.117032

Lu, W., Zhang, X., Yuan, Y., Qi, G., Hu, X., Li, J., et al. (2021). Study on the characteristics and mechanism of a new type of antioxidant gel foam for coal spontaneous combustion prevention. *Colloids Surfaces A Physicochem. Eng. Aspects* 628, 127254. doi:10.1016/j.colsurfa.2021.127254

Lu, X., Zhu, H., Wang, D., Hu, C., Zhao, H., and Huo, Y. (2018). Flow characteristic investigation of inhibition foam used for fire extinguishment in the underground goaf. *Process Saf. Environ. Prot.* 116, 159–168. doi:10.1016/j.psep.2018.02.005

Ma, L., Guo, R., Wu, M., Wang, W., Ren, L., and Wei, G. (2020). Determination on the hazard zone of spontaneous coal combustion in the adjacent gob of different mining stages. *Process Saf. Environ. Prot.* 142, 370–379. doi:10.1016/j.psep.2020.06.035

Qi, Y., Wang, W., Qi, Q., Ning, Z., and Yao, Y. (2021). Distribution of spontaneous combustion three zones and optimization of nitrogen injection location in the goaf of a fully mechanized top coal caving face. *Plos one* 16 (9), e0256911. doi:10.1371/journal.pone.0256911

Qin, B., Li, L., Ma, D., Lu, Y., Zhong, X., and Jia, Y. (2016). Control technology for the avoidance of the simultaneous occurrence of a methane explosion and spontaneous coal combustion in a coal mine: A case study. *Process Saf. Environ. Prot.* 103, 203–211. doi:10.1016/j.psep.2016.07.005

Qu, L., Liu, L., Chen, J., and Wang, Z. (2023). Molecular model construction and optimization study of gas coal in the huainan mining area. *Processes* 11, 73. doi:10.3390/pr11010073

Si, J., Li, L., Cheng, G., Shao, H., Wang, Y., and Li, Z. (2021). Characteristics and Safety of CO_2 for the fire prevention technology with gob-Side entry retaining in goaf. *ACS Omega* 6 (28), 18518–18526. doi:10.1021/acsomega.1c02836

Sun, L., Zhan, M., Zhang, C., Shi, Q., Huang, Q., and Wang, W. (2022). Experimental study on prevention of spontaneous combustion of coal by ionic surfactant solution injection in coal seam. *Energy* 260, 125079. doi:10.1016/j.energy.2022.125079

Taraba, B., Michalec, Z., Michalcová, V., Blejchař, T., Bojko, M., and Kozubková, M. (2014). CFD simulations of the effect of wind on the spontaneous heating of coal stockpiles. *Fuel* 118, 107–112. doi:10.1016/j.fuel.2013.10.064

Wang, D., Zhong, X., Gu, J., and Qi, X. (2010). Changes in active functional groups during low-temperature oxidation of coal. *Min. Sci. Technol.* 20 (1), 35–40. doi:10.1016/s1674-5264(09)60157-5

Xia, T., Wang, X., Zhou, F., Kang, J., Liu, J., and Gao, F. (2015). Evolution of coal self-heating processes in longwall gob areas. *Int. J. Heat Mass Transf.* 86, 861–868. doi:10.1016/j.ijheatmasstransfer.2015.03.072

Xia, T., Zhou, F., Wang, X., Zhang, Y., Li, Y., Kang, J., et al. (2016). Controlling factors of symbiotic disaster between coal gas and spontaneous combustion in longwall mining gobs. *Fuel* 182, 886–896. doi:10.1016/j.fuel.2016.05.090

Xu, Y., Li, Z., Liu, H., Zhai, X., Li, R., Song, P., et al. (2020). A model for assessing the compound risk represented by spontaneous coal combustion and methane emission in a gob. *J. Clean. Prod.* 273, 122925. doi:10.1016/j.jclepro.2020.122925

Yoruk, B., and Arisoy, A. (2022). Development of a mathematical model for simulating the self-heating behavior of moist coal. *Combust. Sci. Technol.* 194 (13), 2674–2692. doi:10.1080/00102202.2021.1885388

Zhang, C., Wang, E., Xu, J., and Peng, S. (2021). A new method for coal and gas outburst prediction and prevention based on the fragmentation of ejected coal. *Fuel* 287, 119493. doi:10.1016/j.fuel.2020.119493

Zhang, H., Sasaki, K., Zhang, X., Sugai, Y., and Wang, Y. (2019). Numerical simulations on the self-heating behaviours of coal piles considering aging effect. *Combust. Theory Model.* 23 (6), 1169–1190. doi:10.1080/13647830.2019.1644378

Zhang, H., Wang, Y., Zhang, X., Sasaki, K., Sugai, Y., Han, F., et al. (2023). Experimental study of moisture effects on spontaneous combustion of Baiyinhua lignite from individual particles to stockpile. *Fuel* 334, 126774. doi:10.1016/j.fuel.2022.126774

Zhang, H., Zhang, X., Wang, Y., Dong, W., Fan, J., and Sasaki, K. (2022). Application of aging effect model in numerical simulation for predicting spontaneous combustion of coal stockpiles. *J. Therm. Analysis Calorim.* 147, 13847–13860. doi:10.1007/s10973-022-11708-7

Zhang, J., An, J., Wen, Z., Zhang, K., Pan, R., and Akter Al Mamun, N. (2020). Numerical investigation of coal self-heating in longwall goaf considering airflow leakage from mining induced crack. *Process Saf. Environ. Prot.* 134, 353–370. doi:10.1016/j.psep.2019.12.025

Zhang, Q., Hu, X. M., Wu, M. Y., Zhao, Y. Y., and Yu, C. (2018). Effects of different catalysts on the structure and properties of polyurethane/water glass grouting materials. *J. Appl. Polym. Sci.* 135 (27), 46460–46511. doi:10.1002/app.46460

Zhu, X., and Wen, H. (2023). Numerical simulation study on the influence of air leakage on oxygen concentration in goafs of fully mechanized caving mining with shallow buried and large mining height. *Front. Earth Sci.* 11, 281. doi:10.3389/feart.2023.1138925

frontiers | Frontiers in Earth Science

TYPE Original Research
PUBLISHED 26 June 2023
DOI 10.3389/feart.2023.1222920

OPEN ACCESS

EDITED BY
Xuelong Li,
Shandong University of Science and Technology, China

REVIEWED BY
Rulong Bn,
Guilin University of Technology, China
Junlong Sun,
Kunming University of Science and Technology, China

*CORRESPONDENCE
Junwei Qiao,
qiaojunwei@xust.edu.cn

RECEIVED 15 May 2023
ACCEPTED 13 June 2023
PUBLISHED 26 June 2023

CITATION
Qiao J, Zhang Y, Li W and Tan J (2023), IPSO-ELM intelligent prediction of landslide displacement in complex and unstable area of karst landform. *Front. Earth Sci.* 11:1222920. doi: 10.3389/feart.2023.1222920

IPSO-ELM intelligent prediction of landslide displacement in complex and unstable area of karst landform

Junwei Qiao[1,2,3]*, Yu Zhang[1], Weibo Li[4] and Jieqing Tan[5]

[1]College of Geology and Environment, Xi'an University of Science and Technology, Xi'an, China, [2]Geological Research Institute for Coal Green Mining, Xi'an University of Science and Technology, Xi'an, China, [3]Shaanxi Provincial Key Laboratory of Geological Support for Coal Green Exploitation, Xi'an, China, [4]Shaanxi Institute of Geological Survey, Xi'an, China, [5]Sichuan Institute of Geological Survey, Chengdu, China

In southern China, the karst landform areas possess a complex geological and topographic environment, a fragile ecosystem, poor surface stability, and frequent occurrences of landslides and other geological disasters. To effectively monitor and predict such events, it is crucial to process landslide monitoring data and establish reliable prediction models. This paper presents an IPSO-ELM displacement prediction model that integrates the improved particle swarm optimization algorithm (IPSO) and extreme learning machine (ELM). The proposed coupling model predicts decomposed displacement subsequences individually, which are then reconstructed to obtain the total displacement prediction value. In this study, displacement monitoring data from a typical landslide in the karst landform area between 2007 and 2012 were selected. Various prediction and verification scenarios were established to validate the accuracy and stability of the prediction model. The MAPE of the IPSO-ELM model is 0.18%, which outperforms the ELM and BPNN models with MAPEs of 0.56% and 0.65%, respectively, in predicting landslide displacement in karst landform areas. This study provides a solid theoretical foundation and practical value for landslide displacement prediction.

KEYWORDS

complex and unstable area of karst, improved particle swarm optimization algorithm, landslide, displacement prediction, extreme learning machine (ELM)

1 Introduction

Karst of China are widely distributed in mountainous areas with complex geological and topographical environments, fragile ecosystems and poor surface stability. The typical landslide disaster in this paper is located in the area with the most active karst landform in China. The karst activities on the underground surface are very frequent, resulting in the very active micro-movement of the underground surface and frequent geological disasters. The prediction of landslide displacement in this area is helpful to predict natural disasters such as landslides (Li et al., 2023; Liu et al., 2023a; Liu et al., 2023b; Liu et al., 2023c; Zhang et al., 2023a; Liu et al., 2022; Zhou et al., 2022; Li et al., 2021).

Landslides seriously damage to the natural environment, and cause social property losses. How to use the landslide monitoring data to predict the deformation of landslide and disaster is an important scientific subject in the research of geological disaster prevention.

The formation of most landslides is a gradual accumulation process, so the long-term deformation monitoring data of landslides is an important basis for landslide deformation prediction at present. There are many prediction methods for landslide deformation based on the monitoring data of landslide cumulative deformation. The mainstream method is to decompose the time series of landslide cumulative displacement into trend, periodic, and random items, and use different methods to carry out targeted prediction. For example, Peng et al. and Zhang et al. decomposed the landslide deformation based on time series and ignored the influence of random items (Peng et al., 2013; Zhang LB. et al., 2023). Qiu et al. used the grey model to solve the trend term, and ignored the random term and then used the AR model to solve the periodic term (Qiu et al., 2020). Guo et al. used the reverse order method to calculate the trend and trigonometric functions to fit the periodic term (Guo et al., 2018). Jiang et al. used the variational mode to decompose the accumulated deformation of the landslide, and then used different methods to solve it respectively (Jiang et al., 2022). Huang et al. used the moving average method to decompose the cumulative displacement into trend term and periodic term displacement, and used the support vector machine model to predict the landslide deformation (Huang et al., 2014). Li et al. and Huang et al. established an autoregressive moving average time series model and used support vector machines, neural networks and other algorithms to predict landslides (Huang et al., 2018; Li et al., 2018).

The research shows that the deformation of landslides is often affected by many factors, and different methods and models are used to decompose the cumulative deformation, and different decomposition results will reduce the accuracy of data fitting. For the prediction of cumulative deformation under the influence of multiple variables, Duan et al. and others used different smoothing parameters to predict the deformation of landslides under different monthly rainfall conditions, but the selection of models and the weight of different factors have a great impact on the results (Duan et al., 2016). Yang et al. used short-term and short-term memory neural networks to predict landslides, proving the feasibility and high accuracy of using neural networks to predict landslides (Yang et al., 2019). Genetic algorithm is used to optimize the structure of BP neural network, and a nonlinear synergetic bifurcation model is established to predict the deformation of single variable (Guo et al., 2011). Cai et al., 2019 and others used FA algorithm to optimize the selection of neural network structure, but the same network structure will also lead to different training effects due to the random selection of initial value (Cai et al., 2019). The above results have been well applied in the study of deformation prediction using long-term monitoring data of landslides, but there are still some areas for improvement in the accuracy of the prediction results. Zhou et al. proposed a new extreme gradient boost (XGBoost) and Hodgrick Prescott (HP) filtering coupling method to predict landslide displacement (Zhou et al., 2022). Tang et al. developed a progressive landslide displacement prediction model driven by Semantic information, which includes the identifier of the displacement stage and the predictor of acceleration stage (Tang et al. . 2022). Miao et al. took the Baishui River landslide as the research object and decomposed the landslide displacement into three parts (trend term, periodic term, and random term) through variational mode decomposition (VMD), introduced a data mining algorithm to select the triggering factors of periodic displacement, and applied the fruit fly optimization algorithm backpropagation neural network to train and predict periodic and random displacement (Miao et al., 2022). Long et al. applied the multi-feature fusion transfer learning method to the Baijiapu landslide scene to obtain sufficient monitoring data and laws, improving landslide prediction ability (Long et al., 2022). Zheng et al. proposed a displacement prediction method based on multi-source domain transfer learning, and used the optimal variational mode decomposition model based on minimum sample entropy to decompose the cumulative displacement into trend component, periodic component and random component (Zheng et al., 2023). The trend component is predicted by the autoregressive model, and the cycle component is predicted by the long-term and short-term memory. For random components, a combination of Wasserstein-generated adversarial networks, and multi-source domain transfer learning is used for prediction to improve prediction accuracy.

Therefore, the difficulty of landslide displacement prediction research lies in the scientific and reasonable analysis of the original data and improving the accuracy of the prediction model as much as possible. On the basis of previous research results, this paper adopts the variational modal decomposition algorithm to decompose the landslide displacement sequence, which can avoid modal aliasing in the process of decomposition and can control the number of sub-sequences. The improved particle swarm optimization algorithm is used to optimize the ELM parameters, and IPSO-ELM is constructed. The model is used to predict the decomposed displacement subsequences respectively, and the prediction results of each subsequence are reconstructed to obtain the predicted value of landslide cumulative displacement. On the basis of the above work, the displacement prediction values obtained by the model used in this paper are compared with those obtained by the traditional ISPO-ELM, extreme learning machine (ELM), and back propagation neural network (BPNN) models. The mean square error (MSE), mean absolute error (MAE) and mean absolute percentage error (MAPE) of these models are calculated, respectively. Thus, the prediction accuracies of these three models were quantitatively compared, and the models with the highest prediction accuracy were indicated.

2 Principle and algorithm of variational mode decomposition (VMD)

The landslide displacement sequence is a nonlinear and non-stationary time series. If the prediction is made directly on the basis of the original cumulative displacement monitoring data, it is easy to produce large errors. In relevant research, the method of decomposing the original displacement sequence using a decomposition algorithm (i.e., decomposing first and then predicting) is widely used, and the landslide displacement prediction based on this method has achieved good prediction results. By decomposing the original sequence, on the one hand, the complexity of the data is reduced, on the other hand, the information of the original monitoring data is fully utilized, and the prediction accuracy is improved. Typical sequence decomposition algorithms include wavelet analysis, empirical mode decomposition (EMD), ensemble empirical mode decomposition (EEMD), etc (Shihabudheen, 2017; Miao et al., 2022).

Variational mode decomposition (VMD) can convert the original signal into non-recursive VMD mode. Compared with EMD algorithm and EEMD algorithm, VMD algorithm has an

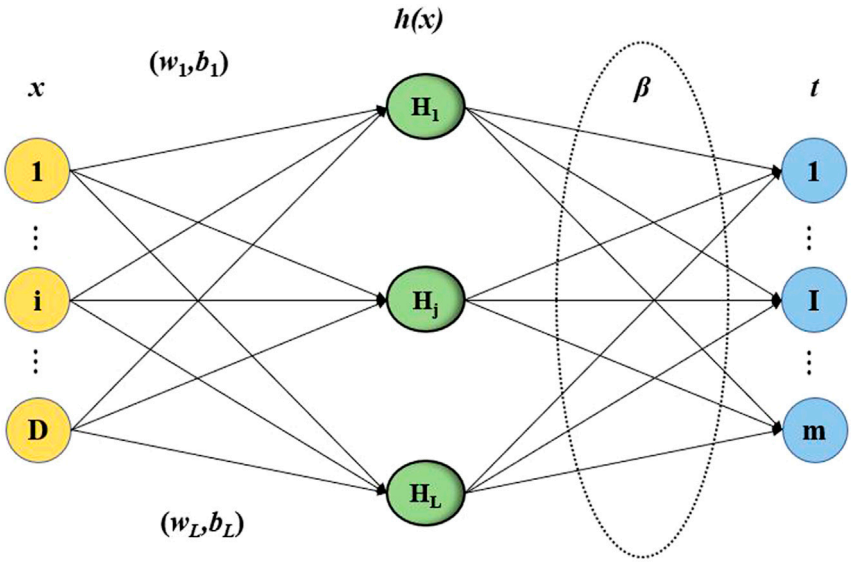

FIGURE 1
The Schematic of extreme machine learning.

excellent performance in anti-noise. In addition, the VMD algorithm controls the convergence conditions and the number of decompositions reasonably, and the number of modes obtained after decomposition is also less than EMD and EEMD. Therefore, VMD has the advantages of solid mathematical foundation and fast calculation speed, which is extremely beneficial to reduce the workload of later prediction.

The overall idea of VMD algorithm is to construct a variational problem first, and then decompose a real value signal S into a discrete number of modes $S_k(t)$, $k = 1, 2, \cdots, K$ by solving the variational problem, and assume that each mode is approximately compact around the center pulse. Wiener filter, Hilbert transform and frequency mixing in signal analysis are the important basis of VMD algorithm.

3 Improved particle swarm optimization extreme learning machine (IPSO-ELM)

3.1 Extreme learning machine (ELM)

The extreme learning machine was proposed in 2004. Because of its simple structure, less parameters and fast learning speed, many scholars have studied and applied the algorithm (Huang et al., 2006; Marti et al., 2011; Xue et al., 2020; Panghal et al., 2021). The principle of extreme machine learning is shown in Figure 1.

In a single hidden layer neural network, it is assumed that there are N samples (x_i, y_i), where $x_i = [x_{i1}, x_{i2}, x_{i3}, \cdots, x_{in}]^T \in R^n$, $y_i = [y_{i1}, y_{i2}, y_{i3}, \cdots, y_{im}]^T \in R_m$, when in a single hidden layer neural network, the output samples can be expressed as:

$$y_i = \sum_{i=1}^{l} \beta_i g(\omega_i g x_i + b_i) \tag{1}$$

Where, β_i is the output weight; $g()$ is the activation function; ω_i is the input weight; b_i is the offset of hidden layer nodes; $\omega_i \cdot x_i$ is the inner product of ω_i and x_i.

The purpose of using ELM model is to minimize the output error value. Assume that when the error value is 0, the output of the existence, and make formula β_i, ω_i and b_i is equal to the actual output, and the following matrix can be established:

$$\begin{cases} \boldsymbol{Y} = \boldsymbol{\beta H} \\ \boldsymbol{Y} = (y_1, y_2, \cdots, y_i) \\ \boldsymbol{\beta} = (\beta_1, \beta_2, \cdots, \beta_i) \\ \boldsymbol{H} = \begin{cases} g(\omega_1 \cdot x_1 + b_1) \ldots g(\omega_1 \cdot x_i + b_1) \\ \boldsymbol{M} \qquad\qquad \boldsymbol{M} \\ g(\omega_i \cdot x_1 + b_i) \ldots g(\omega_i \cdot x_i + b_i) \end{cases} \end{cases} \tag{2}$$

To sum up, calculate the minimum value $\|\mathbf{H\beta} - \mathbf{Y}\|^2$, where $\mathbf{Y}$ is the actual output; $\mathbf{H}$ is determined according to the value of ω_i and b_i, from which it can be concluded that the prediction model is established.

3.2 Improved particle swarm optimization (IPSO)

Particle swarm optimization algorithm (PSO) is an evolutionary computing technique derived from the study of bird swarm predation behavior. The algorithm was originally inspired by the regularity of bird cluster activity and then a simplified model using swarm intelligence. Each particle represents different possible solutions. The quality of the particle's position is judged according to the fitness function value. Through continuous learning from the global optimization and individual optimization, the particle's position and speed are updated to achieve the optimization purpose.

Assume that in the dimensional space, it represents the position of particles and the speed. Under this condition, $X_i = (X_{i1}, X_{i2}, \cdots, X_{id})$

indicates the position of particles, $V_i = (V_{i1}, V_{i2}, \cdots, V_{id})$ indicates speed, its position and speed are updated according to formulaunder this condition:

$$X_{id}^{t+1} = X_{id}^{t} + V_{id}^{t+1} \tag{3}$$

$$V_{id}^{t+1} = \omega \cdot V_{id}^{t} + c_1 r_1 \left(p_{id}^{t} - X_{id}^{t}\right) + c_2 r_2 \left(p_{gd}^{t} - X_{id}^{t}\right) \tag{4}$$

Where, ω is inertia weight; p_{id}^{t} is the best individual under this condition; p_{gd}^{t} is the corresponding global optimum; c_1, c_2 is the sub-factor of students; r_1, r_2 is a random number with a value range of [0 1].

In particle swarm optimization, inertia weight ω, as one of the important parameters, plays a vital role in the search effect. The value of ω determines the global search ability of PSO. The larger the value of ω, the stronger the global search ability of PSO; otherwise, the stronger the local search ability of PSO. In order to achieve higher search efficiency, the random weight method is introduced to optimize this algorithm in the optimization process. When optimizing based on this method, the PSO algorithm is considered to be random. The advantages of this setting are:

(1) When the initial position is close to the global optimum, the random value obtained is small, which is beneficial to improve the convergence speed.
(2) Overcome the limitation that the algorithm cannot converge to the best point caused by linear decline.

The inertia weight is modified based on the following expression:

$$\begin{cases} \omega = \mu + \sigma \times N(0,1) \\ \mu = \mu_{\min} + (\mu_{\max} - \mu_{\min}) \times r \text{ and } (0,1) \end{cases} \tag{5}$$

Where, $N(0,1)$ represents the random number of the standard state distribution, and $r\mathrm{and}(0,1)$ represents the random number between [0 1].

The calculation steps of random weight method are as follows.

(1) Initializes the speed of particles.
(2) Calculate and determine the fitness of each particle, save its position and fitness information in p_{best}, and compare and analyze all of p_{best} to get the best individual value and then store it in g_{best}.
(3)The displacement and velocity are updated by the following expression:

$$x_{i,d}(t+1) = x_{i,d}(t) + v_{i,d}(t+1) \tag{6}$$

$$v_{i,d}(t+1) = \omega \cdot v_{i,d}(t) + c_1 r_1 \left[p_{i,d} - x_{i,d}(t)\right] + c_2 r_2 \left[p_{g,d} - x_{i,d}(t)\right] \tag{7}$$

(4) Update the inertia weight according to the formula.
(5) Compare the current position and the best position of particles, and replace the latter with the current position in the case of proximity. Compare all p_{best} and g_{best} and update g_{best}.
(6) If the algorithm meets the stop condition, the iteration operation is ended and the result is output. On the contrary, return to step (3).

3.3 IPSO-ELM model

The random weight method is applied to the PSO algorithm, which overcomes the shortcomings of the PSO algorithm that the global search ability and local search ability are poor due to the improper value of inertia weight. The improved particle swarm optimization algorithm (IPSO) is used to globally optimize the connection weight and hidden layer threshold of the extreme learning machine (ELM), and thus IPSO-ELM model is constructed for landslide displacement prediction.

4 Landslide displacement prediction process

The steps of landslide displacement prediction based on VMD and IPSO-ELM coupling model are as follows, Figure 2 shows the flow of landslide displacement prediction.

5 Engineering case analysis

5.1 Typical landslide engineering geology and monitoring overview

A typical landslide selected for this project case analysis is located on the south bank of the Yangtze River in the Three Gorges Reservoir area, 56 km away from the dam site of the Three Gorges Dam. The landslide is an old landslide, which has repeatedly occurred bedding sliding in history. The landslide mass is located in the broad valley section of the Yangtze River, a monoclinic bedding slope, high in the south and low in the north, and is distributed in a stepped manner towards the Yangtze River. The rear edge elevation of the landslide is 410 m, bounded by the geotechnical boundary, and the front edge is about 70 m, which has not been below the reservoir water level, the eastern and western sides are bounded by the bedrock ridge, with an overall slope of about 30°.

The deformation of typical landslide mainly occurs in the early warning area of the sliding mass, and the deformation of other parts of the sliding assembly obvious could be clearer. There are currently 6 GPS monitoring points in the early warning area. The monitoring data shows that in 2011, the cumulative horizontal displacement of GPS monitoring points M1, M2, and M3 for the whole year was 182.2, 128.5, and 145.8 mm, respectively, with an average rate of 15.2, 10.7, 12.2 mm/month; The cumulative horizontal displacement of the whole year in 2012 was 239.6, 113.0, and 113.6 mm respectively, with the average rate of 20.0, 9.4, and 9.5 mm/month respectively.

5.2 Prediction of landslide displacement

Reasonable selection of landslide displacement influencing factors is of great significance to the rationality and prediction accuracy of displacement prediction. Based on the previous research experience, the monthly rainfall, reservoir water level value, bimonthly rainfall, inter-monthly reservoir water level variation, bimonthly reservoir water

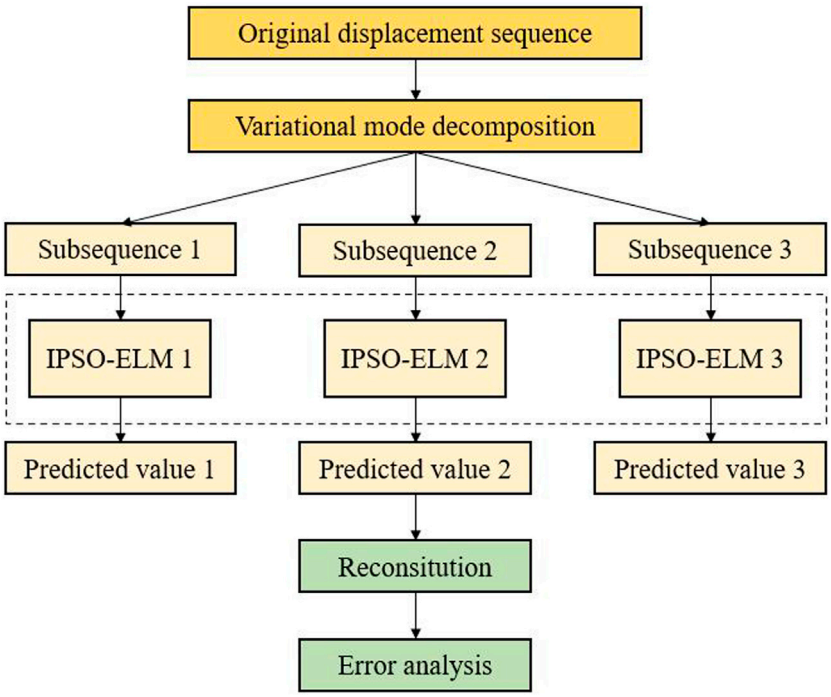

FIGURE 2
Flow chart of landslide displacement prediction.(1) VMD is used to decompose the original cumulative displacement sequence to obtain the subsequence components.(2) IPSO is used to optimize the parameters of ELM, and IPSO-ELM coupling model is established.(3) The IPSO-ELM coupling model is used to predict the subsequences obtained from VMD decomposition.(4) Reconstruct the prediction results of each displacement subsequence to obtain the total displacement prediction value of the monitoring point.(5) Error analysis. In error analysis, the degree of dispersion of prediction results and the degree of deviation between prediction value and actual value are taken as careful consideration, and MSE, MAE and MAPE are selected as accuracy evaluation indicators.

level variation and monthly displacement increment are considered the displacement influencing factors system.

Under the conditions of engineering practice, the prediction model must have strong adaptability to the dynamic monitoring data to accurately and stably output the prediction results. To verify the validity and stability of the proposed model, the monitoring data of this typical landslide monitoring point is divided into two datasets to train and test the model. Select the monitoring data from 2007 to 2010 as the training set, and the monitoring data from 2011 as the corresponding test set.

5.2.1 Selection of mode number

Before the VMD decomposition of the original displacement sequence, the number of decomposition subsequences needs to be set first. In order to facilitate the subsequent prediction, the cumulative displacement sequence of the monitoring point from 2007 to 2011 is decomposed, and the modal number is set as K=2, 3, 4.

According to the previous test, the first sub-sequence (the main component of the cumulative displacement sequence) obtained by decomposition is obviously inconsistent with the original series in the trend when K=4, and it is considered that there is over-decomposition. Therefore, K=3 is more appropriate. To maximize the use of the information of the original data, the original cumulative displacement sequence is decomposed into three sub-sequences, and the three modes are obtained by decomposition.

TABLE 1 Accuracy comparison of three models.

Error index	IPSO-ELM	ELM	BPNN
MSE	115.23	496.21	762.12
MAE	4.95	15.36	20.14
MAPE	0.18%	0.56%	0.65%

5.2.2 Sub-sequence displacement prediction

According to the landslide displacement prediction flow, the three subsequences obtained from the decomposition of the original displacement sequence are modelled and predicted, respectively, and three groups of corresponding displacement prediction values are obtained.

5.2.3 Sub-sequence prediction displacement reconstruction

The final total landslide displacement prediction value is obtained by superposition of three groups of prediction values, and compared with the actual monitoring value. The prediction accuracy results of the prediction model were obtained by the

validation of the displacement data in 2011. The comparison of prediction accuracies is shown in Table 1.

The comparison results show that.

(1) Both ELM and BPNN have prediction effects only in a particular range, but the prediction accuracy in a more extensive range is very low, indicating that the robustness and generalization ability of these two models are relatively poor.
(2) The prediction accuracy of BPNN depends on the training of large data samples. For the prediction of small samples similar to this paper, BP neural network's prediction accuracy and generalization ability the are worse than ELM.
(3) The IPSO-ELM model proposed in this paper can adapt to the changing data environment. Displacement data from different scenarios were used for stability testing of the IPSO-ELM model. The displacement data from 2007 to 2011 as training set and the 2012 data as test set. The results show slight differences in prediction accuracy in different scenarios, but high accuracy, indicating the good stability.

6 Conclusion

This paper studies the landslide displacement prediction based on VMD and IPSO-ELM coupling model. In the landslide displacement prediction, the original displacement sequence is decomposed into three sub-sequences, and then predicted separately is an effective method to make full use of the limited data information. On the basis of VMD, IPSO algorithm is used to optimize the parameters of ELM, which can effectively solve the problem of premature particle swarm optimization algorithm. It is easy to fall into the problem of local optimization, and it also retains the advantages of particle swarm optimization algorithm itself, such as fast convergence speed.

The verification results of typical landslide examples show that the coupling model can accurately predict the displacement value of landslides, with good accuracy and stability, and has high application value in landslide displacement prediction. When using IPSO-ELM coupling model based on VMD. When predicting landslide displacement, the K value of VMD can be set manually. When the appropriate K value is selected, the prediction effect of the model is perfect.

Data availability statement

The datasets presented in this article are not readily available because the data used to support the findings of this study are available from the corresponding author upon request. Requests to access the datasets should be directed to qiaojunwei@xust.edu.cn.

Author contributions

JQ wrote and modified this paper; YZ provided algorithm processing for it; WL collected and processed the data in the paper; JT collected on-site data for the paper. All authors contributed to the article and approved the submitted version.

Conflict of interest

The authors declare that the research was conducted in the absence of any commercial or financial relationships that could be construed as a potential conflict of interest.

Publisher's note

References

Cai, Shuling, Li, Erbing, and Liang, Chen (2019). Research on temporal prediction of tunnel surrounding rock deformation based on FANAR dynamic neural network. *Chin. J. Rock Mech. Eng.* 38, 3346–3353. (in chinese). doi:10.1007/s00366-019-00894-y

Duan, Gonghao, Niu, Ruiqing, and Zhao, Yannan (2016). Rainfall-induced landslide prediction based on dynamic exponential smoothing model. *J. Wuhan Univ.* 41 (7), 958–962. (in chinese). doi:10.13203/j.whugis20140276

Guo, H. Q., Liu, Y., and Deng, A. (2011). The GA improved ANN-synergy-bifurcation model method on slope slide forecasting. *Geotech. Spec. Publ.* 216, 149–156. doi:10.1061/47627(406)20

Guo, Zizheng, Yin, Kunlong, and Huang, Faming (2018). Landslide displacement prediction based on combined model of surface monitoring data and nonlinear time series. *Chin. J. Rock Mech. Eng.* 37 (1), 3392–3399. (in chinese). doi:10.13722/j.cnki.jrme.2016.1534

Huang, Faming, Yin, Kunlong, and Jiang, Shuihua (2018). Landslide susceptibility evaluation based on cluster analysis and support vector machine. *Chin. J. Rock Mech. Eng.* 37 (1), 156–167. doi:10.1016/j.geomorph.2008.02.011

Huang, G. B., Zhu, Q. Y., and Siew, C. K. (2006). Extreme learning machine: Theory and applications. *Neurocomputing* 70 (1–3), 489–501. doi:10.1016/j.neucom.2005.12.126

Huang, H., Yi, W., and Song, K. (2014). Influence of parameters on support vector machine for landslide displacement prediction in Three Gorges Reservoir. *New Front. Geotechnical Eng.* Geo-Shanghai 2014, 160–168. doi:10.1061/9780784413456.017

Jiang, Yuhang, Wang, Wei, and Zou, Lifang (2022). Research on dynamic prediction model of landslide displacement based on PSOVMD, NARX and GRU. *Rock Soil Mech.* 43 (1), 601–612. doi:10.156800/IJIRCCE.2016

Li, H., Xu, Q., He, Y., and Deng, J. (2018). Prediction of landslide displacement with an ensemble-based extreme learning machine and copula models. *Landslides* 15 (10), 2047–2059. doi:10.1007/s10346-018-1020-2

Li, X. L., Chen, S. J., Liu, S. M., and Li, Z. H. (2021). AE waveform characteristics of rock mass under uniaxial loading based on Hilbert-Huang transform. *J. Central South Univ.* 28 (6), 1843–1856. doi:10.1007/s11771-021-4734-6

Li, X. L., Zhang, X. Y., Shen, W. L., Wang, Y., Qin, Q., and Lu, X. (2023). Abutment pressure distribution law and support analysis of super large mining height face. *Int. J. Environ. Res. Public Health* 20 (2), 227. doi:10.3390/ijerph20010227

Liu, H. Y., Zhang, B. Y., Li, X. L., Liu, C., Wang, C., and Wang, F. (2022). Research on roof damage mechanism and control technology of gob-side entry retaining under close distance gob. *Eng. Fail. Anal.* 138 (5), 106331. doi:10.1016/j.engfailanal.2022.106331

Liu, S. M., and Li, X. L. (2023a). Experimental study on the effect of cold soaking with liquid nitrogen on the coal chemical and microstructural characteristics. *Environ. Sci. Pollut. Res.* 30 (3), 36080–36097. doi:10.1007/s11356-022-24821-9

Liu, S. M., Sun, H. T., Zhang, D. M., Yang, K., Li, X., and Wang, D. (2023c). Experimental study of effect of liquid nitrogen cold soaking on coal pore structure and fractal characteristics. *Energy* 275 (7), 127470. doi:10.1016/j.energy.2023.127470

Liu, S. M., Sun, H. T., Zhang, D. M., Yang, K., Wang, D., and Li, X. (2023b). Nuclear magnetic resonance study on the influence of liquid nitrogen cold soaking on the pore structure of different coals. *Phys. Fluids* 35 (1), 012009. doi:10.1063/5.0135290

Long, J., Li, C., Liu, Y., Feng, P., and Zuo, Q. (2022). A multi-feature fusion transfer learning method for displacement prediction of rainfall reservoir-induced landslide with step-like deformation characteristics. *Eng. Geol.* 297, 106494. doi:10.1016/j.enggeo.2021.106494

Marti, P., Manzano, J., and Royuela, A. (2011). Assessment of a 4-input artificial neural network for ET0 estimation through data set scanning procedures. *Irrigation Sci.* 29 (3), 181, doi:10.1007/s00271-010-0224-6

Miao, F., Xie, X., Wu, Y., and Zhao, F. (2022). Data mining and deep learning for predicting the displacement of "step-like" Landslides. *Sensors* 22 (2), 481. doi:10.3390/s22020481

Panghal, S., and Kumar, M. (2021). Neural network method: Delay and system of delay differential equations. *Eng. Comput.* 38 (2), 2423–2432. doi:10.1007/s00366-021-01373-z

Peng, Ling, Niu, Ruiqiu, and Wu, Ting (2013). Landslide displacement prediction by time series analysis and support vector machine. *J. Zhejiang Univ.* 47 (9), 1672–1679. (in chinese).doi:10.3390/ijerph19042077

Qiu, Mao, Dong, Jianhui, and Zhao, Jianjun (2020). Prediction of landslide displacement based on time series analysis:taking the revival of Jianshanying ancient landslide as an example. *Sci. Technol. Eng.* 20 (30), 12361–12366. (in chinese). doi:10.3390/ijerph19042077

Shihabudheen, K., and Peethambaran, B. (2017). Landslide displacement prediction technique using improved neuro-fuzzy system. *Arabian J. geosciences* 10 (22), 502. doi:10.1007/s12517-017-3278-4

Tang, F., Tang, T., Zhu, H., Hu, C., and Jiang, H. (2022). A semantic information-driven stepwise landslide displacement prediction model. *Environ. Monit. Assess.* 194: 836, 1–23. doi:10.1007/s10661-022-10417-w

Xue, J. K., and Shen, B. (2020). A novel swarm intelligence optimization approach: Sparrow search algorithm. *Syst. Sci. &Control Eng.* 8 (1), 22–34. doi:10.1080/21642583.2019.1708830

Yang, B., Yin, K., Lacasse, S., and Liu, Z. (2019). Time series analysis and long short-term memory neural network to predict landslide displacement. *Landslides* 16 (4), 677–694. doi:10.1007/s10346-018-01127-x

Zhang, J. C., Li, X. L., Qin, Q. Z., Wang, Y., and Gao, X. (2023a). Study on overlying strata movement patterns and mechanisms in super-large mining height stopes. *Bull. Eng. Geol. Environ.* 82 (3), 142. doi:10.1007/s10064-023-03185-5

Zhang, L. B., Shen, W. L., Li, X. L., Wang, Y., Qin, Q., and Lu, X. (2023b). Abutment pressure distribution law and support analysis of super large mining height face. *Int. J. Environ. Res. Public Health* 20 (1), 227. doi:10.3390/ijerph20010227

Zheng, H. Q., mHu, L. N., Jin, S. Y., and Zhang, Y. (2023). Slope displacement prediction based on multisource domain transfer learning for insufficient sample data. *Appl Geophys* 20 (1), 1–9. doi:10.1007/s11770-022-1003-x

Zhou, L. S., Fu, Y. H., and Berto, F. (2022). Prediction of landslide displacement by the novel coupling method of HP filtering method and extreme gradient boosting. *Strength Mater.* 54 (5), 942–958. doi:10.1007/s11223-022-00470-8

Zhou, X. M., Wang, S., Li, X. L., Meng, J., Li, Z., and Zhang, L. (2022). Research on theory and technology of floor heave control in semicoal rock roadway: Taking longhu coal mine in Qitaihe mining area as an Example. *Lithosphere* 2022 (Special 11), 3810988, 1–17. doi:10.2113/2022/3810988

frontiers | Frontiers in Earth Science

TYPE Original Research
PUBLISHED 27 June 2023
DOI 10.3389/feart.2023.1201946

OPEN ACCESS

EDITED BY
Jingjing Meng,
Luleå University of Technology, Sweden

REVIEWED BY
Zhaolin Li,
Anhui University of Science and Technology, China
Tong Zhao,
Taiyuan University of Technology, China

*CORRESPONDENCE
Ruimin Du,
857196702@qq.com

RECEIVED 07 April 2023
ACCEPTED 13 June 2023
PUBLISHED 27 June 2023

CITATION
Guo Y, Gu S, Du R and Shen J (2023), Multi-parameter comprehensive early warning of coal pillar rockburst risk based on DNN.
Front. Earth Sci. 11:1201946.
doi: 10.3389/feart.2023.1201946

Multi-parameter comprehensive early warning of coal pillar rockburst risk based on DNN

Ying Guo[1,2], Shitan Gu[3], Ruimin Du[3]* and Jianbo Shen[4]

[1]Key Laboratory of Deep Coal Resource Mining (Ministry of Education), School of Mines, China University of Mining and Technology, Xuzhou, China, [2]Baodian Coal Mine, Yankuang Energy Group Co, Ltd, Zoucheng, China, [3]College of Energy and Mining Engineering, Shandong University of Science and Technology, Qingdao, Shandong, China, [4]Shandong Jining Mine Luneng Coal Power Company Limited, Wenshang, China

A multi-parameter comprehensive early warning method for coal pillar-type rockburst risk based on the deep neural network (DNN) is proposed in this study. By utilizing preprocessed data from the surveillance of coal pillar impact hazards in Yangcheng Coal Mine, this study incorporates training samples derived from three distinct coal pillar-type impact hazard monitoring methodologies: microseismic monitoring, borehole cutting analysis, and real-time stress monitoring. The data characteristics of the monitoring data were extracted, evaluated, classified, and verified by monitoring the data of different working faces. This method was applied to develop the depth of multi-parameter neural network comprehensive early warning software in engineering practice. The results showed that the accuracy of the depth for burst monitoring data processing is improved by 6.89%–16.87% compared to the traditional monitoring methods. This method has a better early warning effect to avoid the occurrence of coal pillar rockburst hazard.

KEYWORDS

deep neural network, rockburst, model training, hazard monitoring, comprehensive early warning

1 Introduction

Currently, most impact risk monitoring data processing methods are directly obtained and classified according to warning values or processed by statistical machine learning methods based on shallow models. In the feature selection process, these methods rely more on human subjective factors, which affects the accuracy of impact risk assessment. The rockburst hazard monitoring data are processed by deep learning feature extraction methods to avoid the shortcomings of the traditional shallow learning models in feature selection (Ji et al, 2003; Jiang et al, 2014; Chen et al, 2015; He et al, 2022; Wang, 2022; Li et al, 2023).

The deep learning algorithm is derived from an artificial neural network, known as a deep neural network (DNN), which is a multilayer perceptron with multiple hidden layers. The algorithm can learn, adjust, improve, and understand huge data contents and independently find the optimal solution from data changes (Ren, 2016; Zheng, 2022; Wang et al, 2023). The rockburst hazard monitoring data are enormous, and the drilling chip method generally requires drilling multiple holes to judge the rockburst hazard of a specific roadway or working face while driving and mining (Chen et al, 2013; Zhang, 2020; Li et al, 2022). Microearthquake monitoring requires arranging 6-8 groups of measuring points. Each group of measuring points acquires and records monitoring data every 10 seconds,

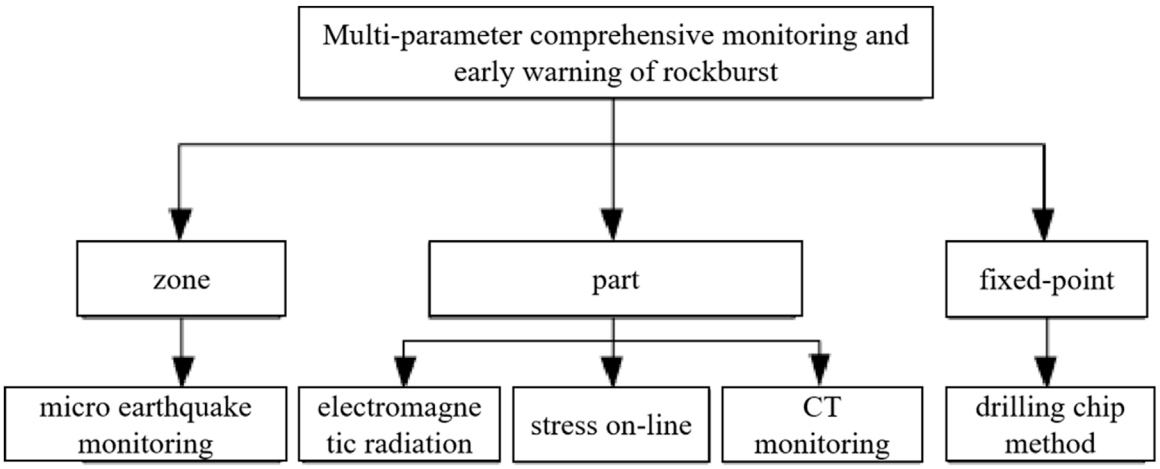

FIGURE 1
Comprehensive early warning technology application diagram.

stress online monitoring is utilized to arrange more than a dozen groups of measuring points and record data every few seconds, and a large number of impact hazard monitoring data are obtained in actual mining scenarios. However, there are great deficiencies in the application and processing of data, especially in the in-depth mining processing of monitoring data feature information (Yuan et al, 2018; Bao et al, 2019; Ai et al, 2020). Therefore, Chen et al (2020) proposed the integrated high-precision intelligent microseismic monitoring technology based on the high-precision time synchronization strategy of PTP. In general, the velocity model database was used to match the micro-source location algorithm, and these technologies were integrated. Many chaotic initial data were abstracted into distinguishing feature information, evaluated, and classified through the DNN to ensure that the precursor information of rockburst hazard monitoring can be accurately identified in the subsequent monitoring and early warning (Pan, 2003; Bosch et al, 2007; Sun et al, 2013; Lu et al, 2021; Yin, 2022; Zhang et al, 2023).

2 Monitoring method of rockburst hazard

2.1 Monitoring technology

Rockburst hazard monitoring mainly includes drilling chip method monitoring, microearthquake monitoring, stress online monitoring, and electromagnetic radiation (Jiang and Zhao, 2015; Lan and Zhang, 2022).

Among them, the drilling chip method monitoring mainly monitors the discharge amount of drilling cuttings, the change in particle size of drilling cuttings, and the change in drilling noise and strength and judges the crushing zone range, plastic zone, and elastic zone in the coal body using a number of drilling cuttings. The rockburst hazard of the coal pillar is judged by the dynamic effect during drilling to identify the stress state of the coal body (Zhu et al, 2014; Jia et al, 2019). Generally, a rockburst hazard occurs when the average pulverized coal amount per meter exceeds the critical pulverized coal amount. When the pulverized coal increases first and then decreases with the increase in the drilling depth, it is considered that there is no impact hazard but stress concentration. The dynamic properties, such as drilling suction and sticking, are based on the dynamic characteristics of the rockburst. This is more obvious from the increase in drill cuttings' particle size of pulverized coal.

Microearthquake monitoring is mainly used to monitor the whole mine according to microseismic sensors, determine the location and energy of the seismic source, compare it with the energy calculated according to the minimum energy principle, and adjust the early warning energy combined with the actual monitoring experience of the mine to determine the monitoring indicators within the monitoring coal pillar. The driving and mining speed affect the evolution process of strata fracture movement. The determination of an early warning value for microearthquake monitoring should fully reflect the influence of tunneling and mining, with the early warning value of microearthquake monitoring for a single event being set to 10^5 J (Tan et al, 2022; Wang et al, 2014; Liu et al, 2022; Zhang et al, 2023).

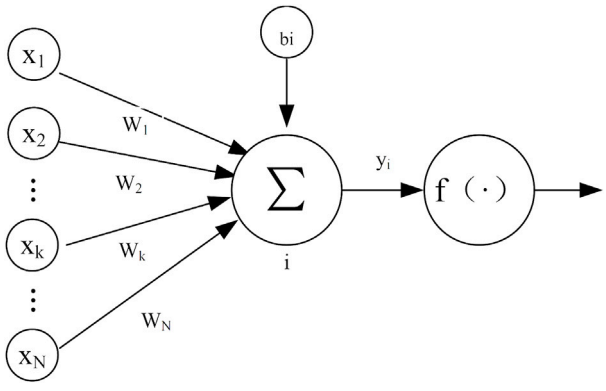

FIGURE 2
Activation function structure diagram.

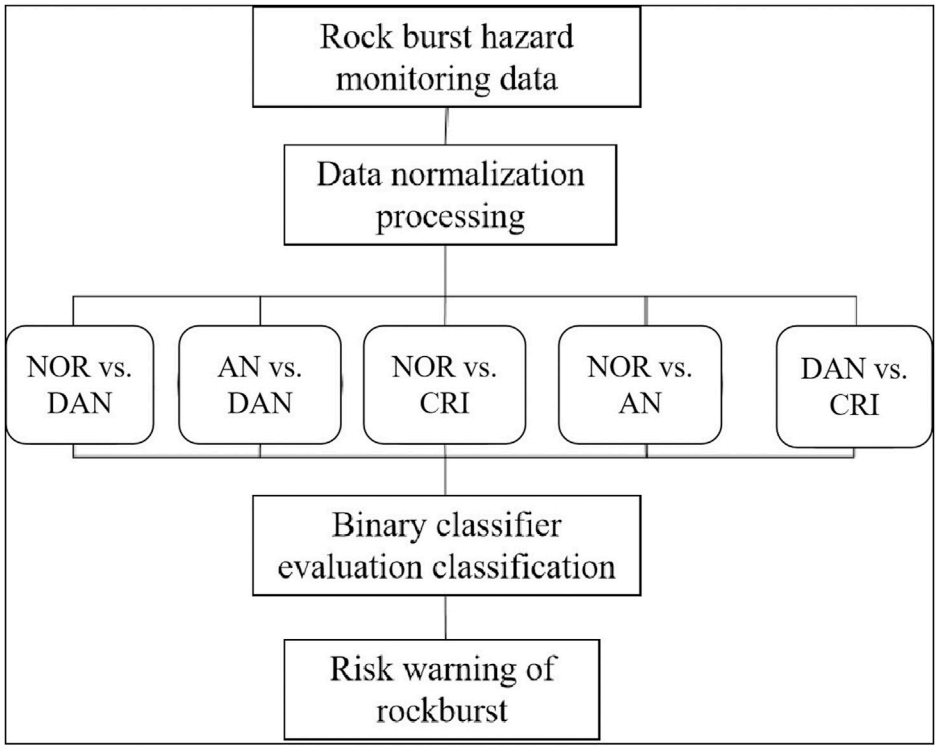

FIGURE 3
SVM classification process.

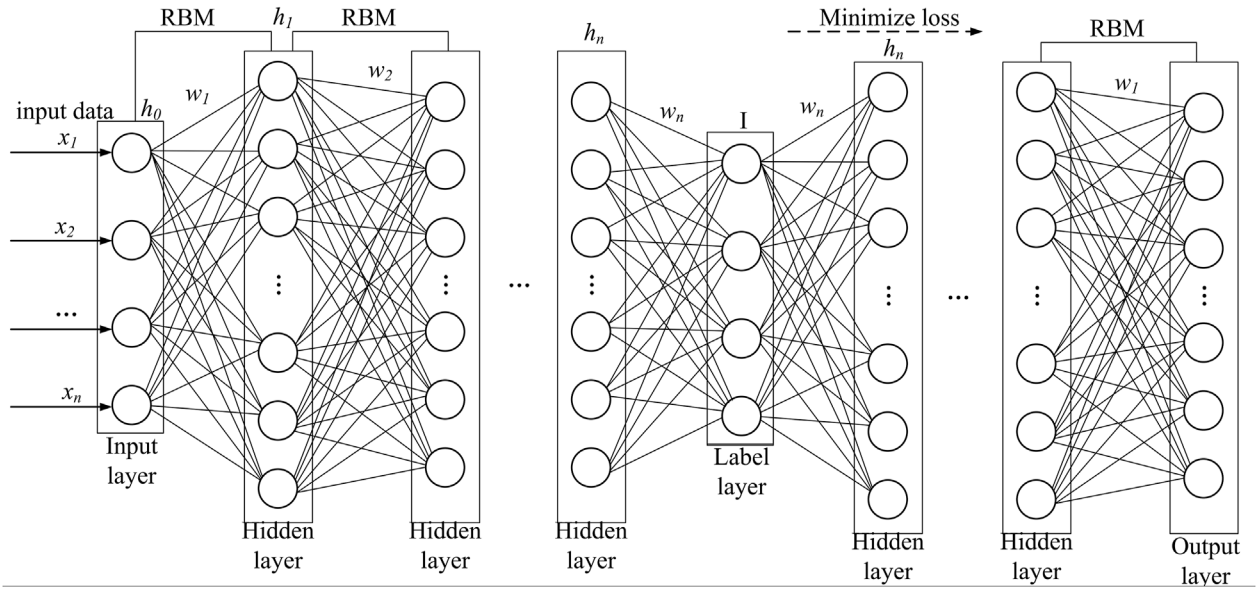

FIGURE 4
Evaluation of the neural network structure by an impact ground.

Stress online monitoring takes coal stress increment as the rockburst hazard evaluation index. Before a rockburst hazard occurs, there will be a gradual increase in stress, and only when the stress reaches the coal failure's ultimate stress, the rockburst will be caused. At the same time, the stress state in the coal pillar can be reflected by stress online monitoring, and the safety factor of the coal

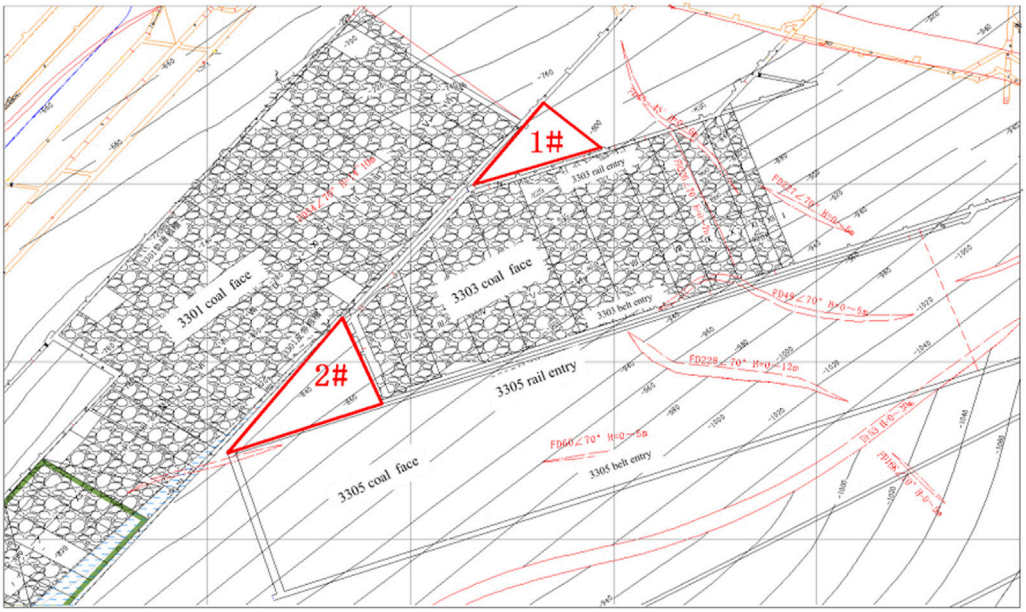

FIGURE 5
Position of the working face and geological condition.

pillar can also be obtained by the coal pillar strength. The early warning of coal pillar impact hazard can be obtained based on the change in stress increment (Wang et al, 2015; Dou et al, 2020).

2.2 Multi-parameter comprehensive early warning

The impact monitoring methods are becoming complicated, with the increase in monitoring data. When monitoring is equipped with multiple monitoring systems, especially when the monitoring data are contradictory, it is a common problem to rely on one of the monitoring methods or comprehensively evaluate multiple monitoring methods simultaneously (Jiang et al, 2011; Luo et al, 2013; Lv et al, 2013; Wang et al, 2018; Liu and Li, 2023).

Microearthquake monitoring is a means of regional rockburst hazard monitoring, which has a wide monitoring range and is suitable for large-scale regional rockburst monitoring. The position and level of energy events are reflected and confirmed through microearthquake monitoring. Hence, microearthquake monitoring is an effective means of regional rockburst monitoring. The earthquake, quantity, frequency, intensity, density, scale, and properties of rock mass fracture can be monitored by microseismic monitoring. Stress online monitoring has the advantages of good continuity and the capability of monitoring stress change in the coal pillar while reflecting its stress change. Hence, it is suitable for continuous monitoring of long-term impact hazards. The position of the stress peak in the coal body and whether the supporting pressure of the coal body reaches its limit strength are based on the relationship between the drilling chip's monitoring value obtained by the drilling chip method and the stress state and damage degree of the working face and coal pillar. The stress in coal mass is reflected by the amount of drilling chips, which effectively monitors the rockburst risk at a fixed point. The application of comprehensive multi-parameter monitoring and early warning technology of rockburst is shown in Figure 1.

For coal pillar rockburst, due to many influencing factors, rockburst has different stress characteristics and energy variation laws, and it is difficult to effectively monitor the rockburst hazard by using a monitoring method. Therefore, an appropriate monitoring method should be selected based on the expected rockburst performance characteristics (Jia et al, 2014; Zhang, 2021; Wang et al, 2022; Liu et al, 2023a; Liu et al, 2023b).

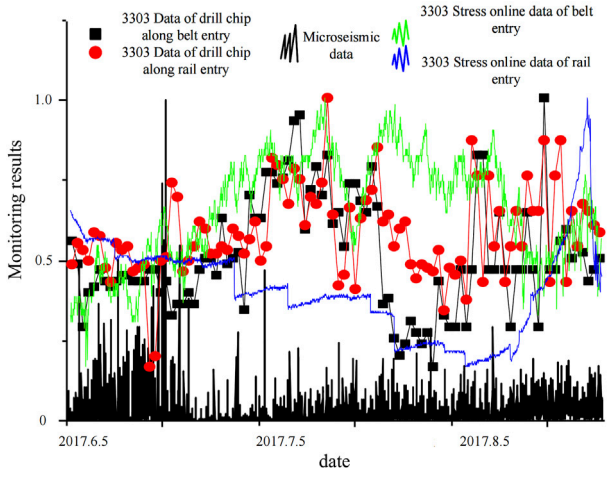

FIGURE 6
Normalization of monitoring data.

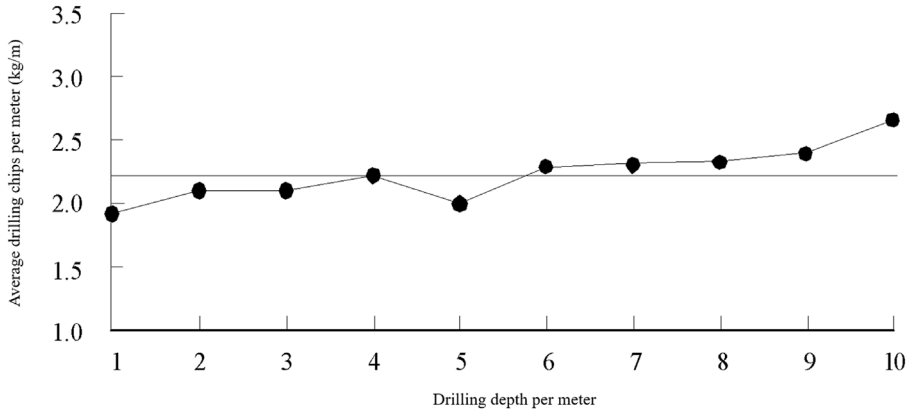

FIGURE 7
Early warning index of the critical coal quantity.

3 Deep learning analysis of monitoring data

3.1 DNN

The DNN model structure includes an input layer and several hidden layers. The difference between DNN and BP neural networks is the number of hidden layers, where DNN has many hidden layers that might exceed 10 in some cases. The data enter the network from the input layer and passes through L hidden layers: $H^{(1)}$, $H^{(2)}$, $H^{(3)}$, and $H^{(L)}$, to perform data abstraction and feature extraction step by step. $H^{(L)}$ is the desired representation, and this process is the representation learning of DNN.

The basic unit in DNN is the node which comprises an input, a state function, and an activation function, wherein the input includes an input value and a connection weight. The input value is the same as the output value of the upper node, and the weight adjusts the node's connection strength. The state function is the linear accumulation of the input values and weights, and the node state is controlled by an offset term. The general state function form is provided in Eq. 1, while the state function's matrix is given in Eq. 2. The activation function is the number used to select a linear, non-linear, continuous, discrete, numerical, or probability function to control the output range (Zhang et al, 2015), as shown in Figure 2.

$$y_i = \sum_{k=1}^{N} x_k w_k + b_i, \tag{1}$$

$$y_i(x) = x^T \times w + b_i, \tag{2}$$

where x_k is the kth input value of the upper layer of the network, including energy x_1, frequency x_2, drilling powder x_3, deep hole stress x_4, and shallow hole stress x_5; W_k is the connection strength between the node and x_k; and b_i is the bias term.

Support vector machine (SVM) plays a critical role in classification and linear regression. This method uses statistical learning theory to establish a decision surface and maximize the isolation between different results. In this paper, the early warning identification results of coal pillar rockburst hazards are divided into four situations: danger (DAN), probable danger (CRI), probable danger (AN), and safety (NOR). The support vector machine classifier is extended from binary classification to a multi-class classifier. The classifier is constructed with $n(n-1)/2 = 6$ based on the one-to-one method. Hence, six binary SVMs must be constructed. The specific classification process is shown in Figure 3.

The DNN constructed in this paper adopts the greedy initialization method, and the data representation of the neural network is obtained by iteration of input values. The network's internal parameters are initialized to obtain a better initial value that reduces the possibility of the network falling into the local limit value. The DNN model adopts greedy initialization layer by layer to obtain a better training effect, or the optimal value, so that the low-level network can be fully trained. First, the deep network is built by restricted Boltzmann machine (RBM), and the marked data and unlabeled data are used to find the network space W.

A fully connected directional multilayer neural network is established. The input layer h^0 includes energy, frequency, powder drilling amount, deep-hole stress value, and shallow-hole stress value. The label layer contains four units: danger, probable danger, probable danger, and safety. The number of hidden layers and nodes in each hidden layer are selected through an iterative approach. In the training process, one hidden layer is trained first, this layer is fixed next, then two hidden layers are trained, and multiple hidden layers are trained according to the second method. Thereafter, the spatial parameter w of the multilayer network is found through label data. The gradient descent method is used to train the deep structure based on the exponential loss function, and the parameter space is further optimized using the labeled data. The structure of the rockburst evaluation neural network is shown in Figure 4.

According to the DNN characteristics, if the number of nodes in each layer is enough, each hidden layer's output value contains the input data's complete information. Thus, each hidden layer represents the input data, but the specific form is different.

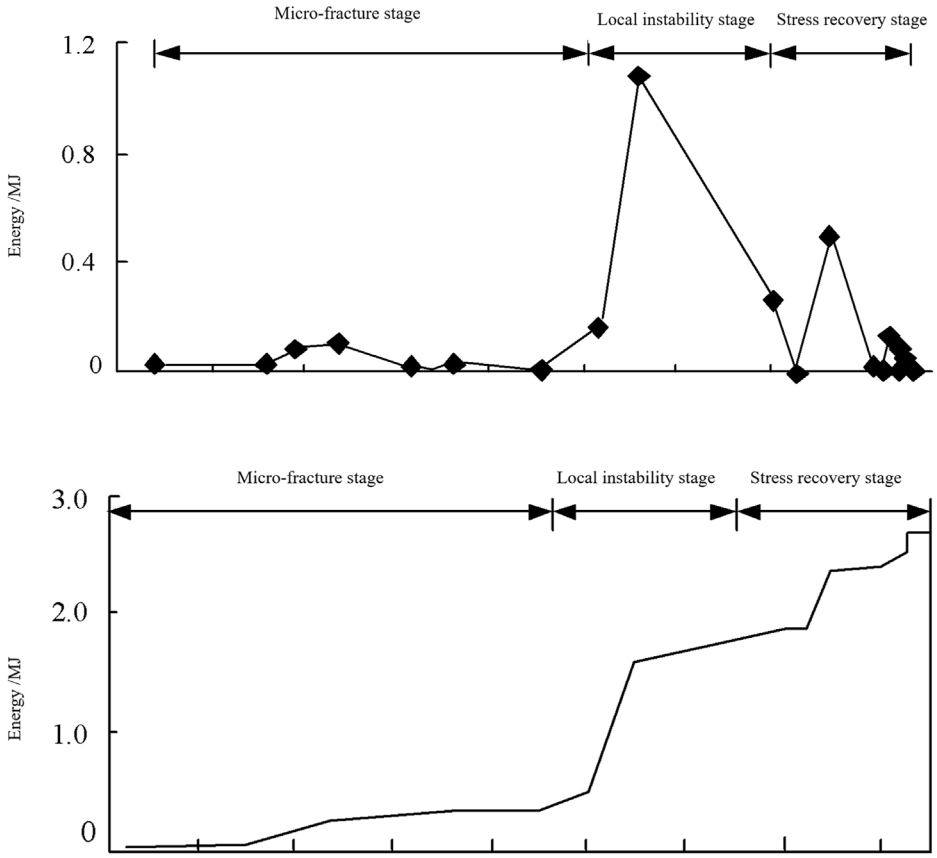

FIGURE 8
Daily energy and cumulative energy release curves of typical microearthquakes.

3.2 Sample data

The monitoring data of the drilling cutting method, microseismic monitoring data, and stress online monitoring data are analyzed based on the monitoring methods and conditions of the rockburst in Yangcheng Coal Mine. The monitoring data of rockburst hazards during mining in the 3303 working face of Yangcheng Coal Mine were collected and used as training data to develop the neural network. The layout of the 3303 working face of Yangcheng Coal Mine is shown in Figure 5.

Before using the DNN model to train the impact monitoring and early warning data, it is necessary to preprocess the mine

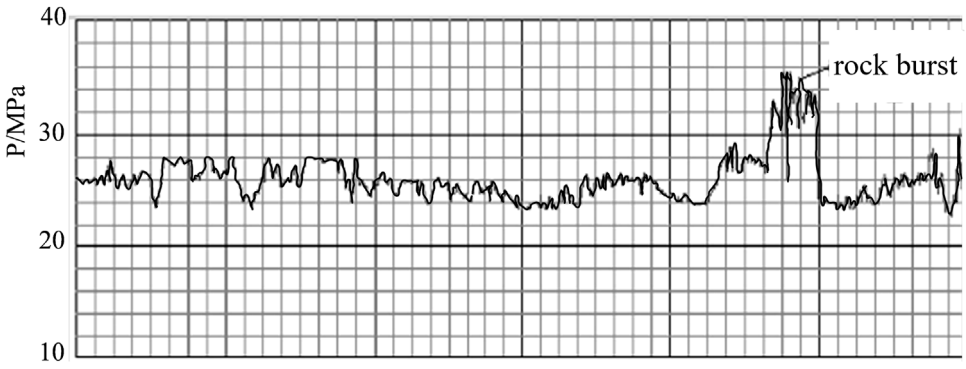

FIGURE 9
Typical stress monitoring curve.

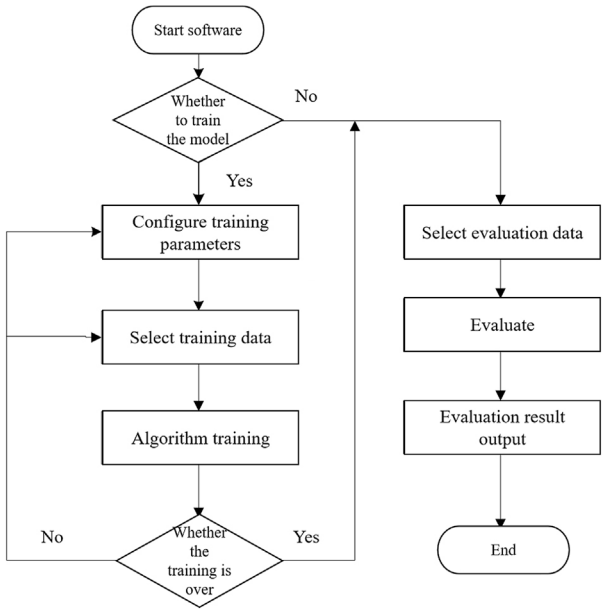

FIGURE 10
Multi-parameter integrated flowchart.

impact monitoring data and correct and deal with some missing and obvious errors to ensure data reliability. Preprocessing of rockburst hazard monitoring data mainly checks the data's completeness and accuracy. The specific processing methods include removing the inaccurate data, trimming the missing data, and rearranging the out-of-order monitoring data. The microseismic monitoring system extracts, records, and saves microseismic events and continuously saves energy signals. The errors in microseismic monitoring are mainly related to timing and wave velocity. However, because data processing software of the microseismic system itself has good data judgment and extraction ability, the preprocessing of microseismic monitoring data only requires checking the integrity. Online stress monitoring data errors are mainly caused by problems such as initial pressure, pipeline length, and inner diameter, so it is necessary to eliminate and correct the measuring points with abnormal initial stress and the wrong points. The problems of drilling cutting monitoring data are mainly data discontinuity, errors caused by construction conditions, and data loss caused by untimely records. Therefore, the processing of drilling cutting monitoring data needs to complete the monitoring data and eliminate the wrong parts. The rockburst hazard monitoring training samples are selected,

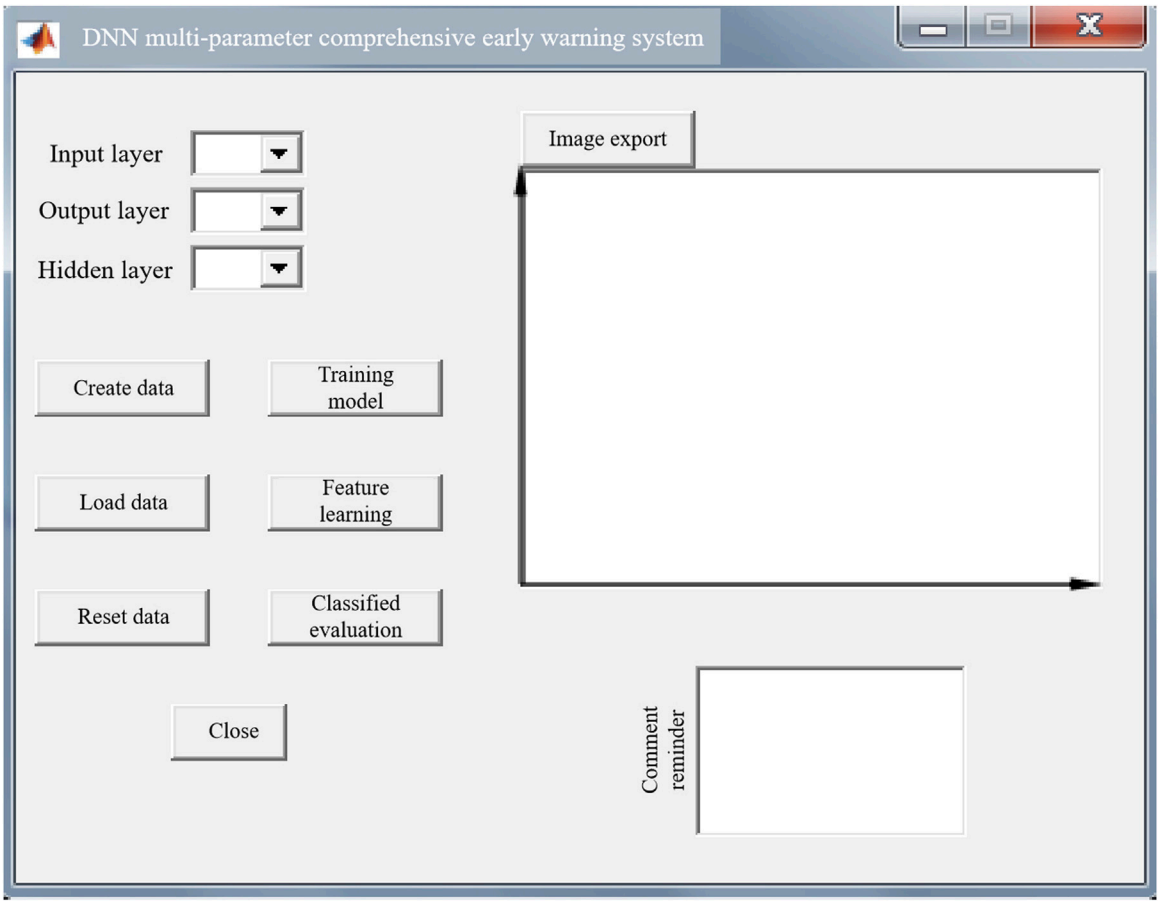

FIGURE 11
DNN multi-parameter integrated early warning system.

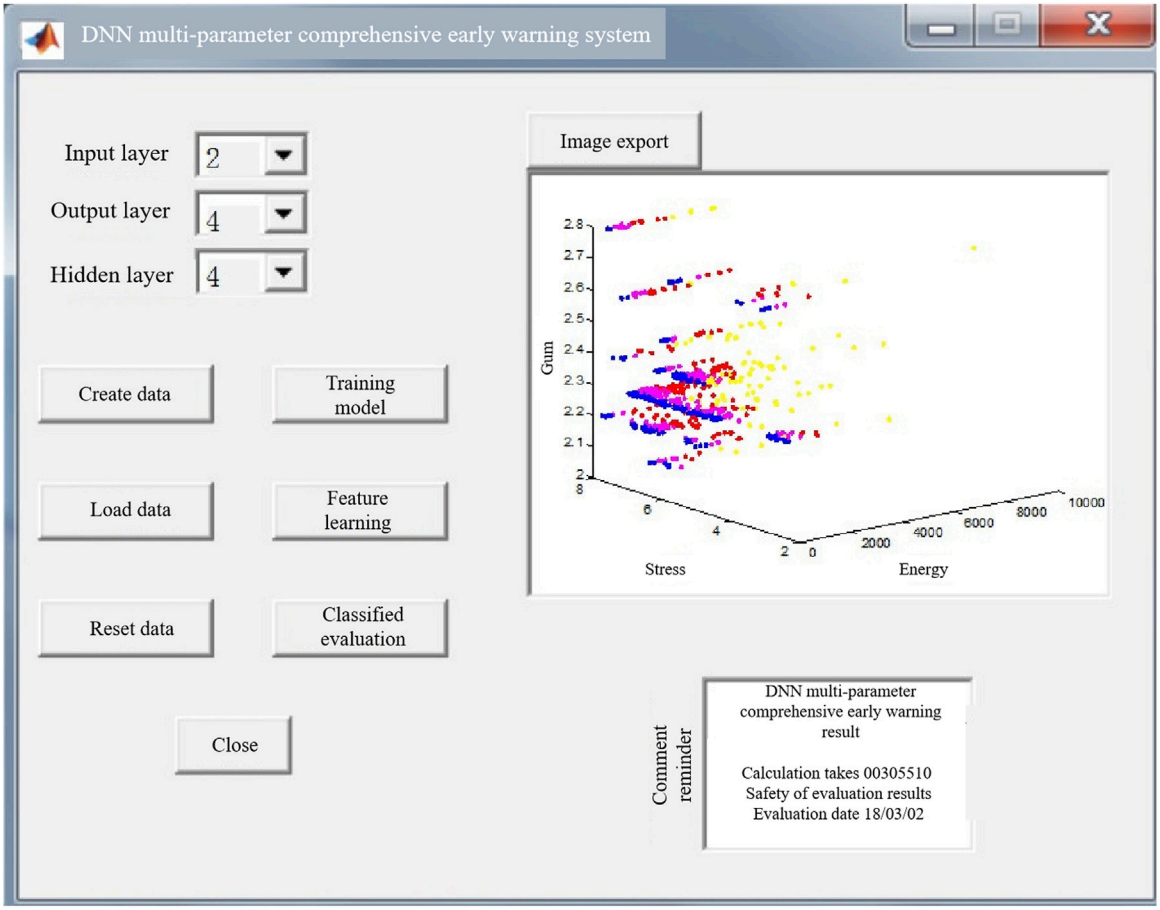

FIGURE 12
Schematic diagram of DNN multi-parameter comprehensive early warning.

and the data are normalized by the mapminmax function. The processing results are shown in Figure 6.

3.3 Classification index

Determining the monitoring and early warning index of the drilling cutting method is performed to calculate the amount of pulverized coal in the area without impact danger and discard the first 1 m of pulverized coal. Under normal circumstances, the pulverized coal per m is *G*, the drilling rate index is K, the correction coefficient α is 1.1, and the critical pulverized coal amount is $Gi = G \cdot K \cdot \alpha$. According to test results, the critical pulverized coal amount of the early warning index is calculated, the rockburst danger in the monitored area is judged, and the impact danger monitoring data sample is selected. The coal powder early warning index of Yangcheng Coal Mine is shown in Figure 7.

The laws of early warning of impact hazards summarized from the microseismic monitoring site include total energy active high-frequency sub-vibration type, vibration silence maintaining high-frequency sub-vibration type, typical strong impact hazard early warning, monitoring daily energy release curve, and cumulative energy characteristic curve, as shown in Figure 8.

According to the monitoring experience of Yangcheng Coal Mine, early warning is required when the stress increment reaches 2 MPa, the stress of 8 m measuring point reaches 11 MPa, or the stress of 14 m measuring point reaches 12.5 MPa. High-stress concentration and sudden change are the necessary conditions to induce a rockburst, so before a rockburst occurs, the stress values of the surrounding rock all change greatly. Therefore, analyzing the borehole stress gauge reveals the change in surrounding rock stress, and when the stress changes greatly, the rockburst is warned. The typical rockburst stress monitoring curve is shown in Figure 9.

3.4 Model training

After data preprocessing, the data of microseismic monitoring, online stress monitoring, and drilling cutting monitoring are selected as experimental samples. The data are further corresponded according to timepoints to obtain input vectors, and the sample data are divided into training and verification data. The microseismic data include energy and frequency, online stress monitoring data include deep hole stress and shallow hole stress, and the drilling cutting monitoring data include the number of drilling cuttings.

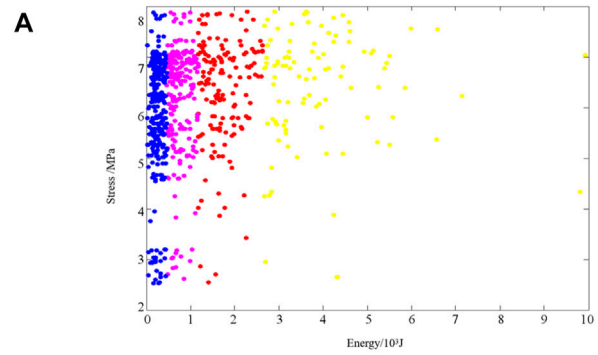

Two-dimensional view of coal pillar impact hazard monitoring data classification

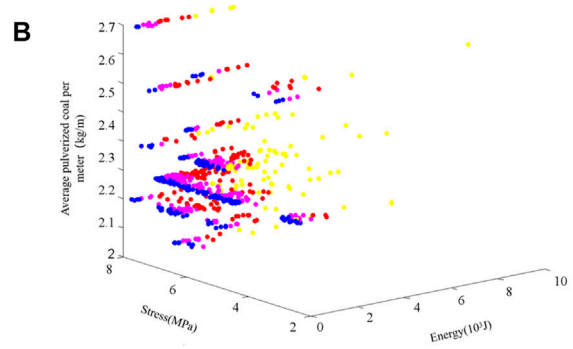

Three-dimensional view of coal pillar impact hazard monitoring data classification

FIGURE 13
Classification results of impact ground pressure evaluation. **(A)** Two-dimensional view of coal pillar impact hazard monitoring data classification. **(B)** Three-dimensional view of coal pillar hazard monitoring data classification.

In the DNN model, the performance may be improved with the deepening of the network layers, but there may also be over-fitting. For the DNN, there may be a small gradient near the input layer and a large gradient near the output layer. When the model's learning rate is constant, the learning rate near the input layer will be slow, while that near the output layer will be too fast, which may lead to local minimum. For such problems, the neural network is generally optimized by changing the activation function or the learning rate. Using the ReLU activation function instead of sigmoid activation function solves the training gradient vanish problem, and the output of the ReLU activation function is calculated as $max(0, x^T w + b)$.

After preprocessing the data, five-dimensional parameters corresponding to the pulverized coal amount, energy, frequency, shallow hole stress, and deep hole stress can be obtained. The standard sample output divides the impact hazard monitoring results into four levels: danger, probable danger, probable danger, and safety. This paper uses the early warning information of rockburst hazards extracted from the monitoring data of 1310 and 3303 working faces in Yangcheng Coal Mine as

TABLE 1 Multi-source information early-warning number table.

System name	DAN/time	CRI/time	False alarm/time	Accuracy/time	Accuracy/%
Microearthquake	12	266	42	236	75.88
Stress	17	309	68	258	82.95
Drill chips	14	293	52	255	83.06
Comprehensive early warning of microearthquake stress	6	248	36	218	85.86
Multi-parameter comprehensive early warning	10	266	20	256	92.75

training samples. According to the data characteristics, types, and quantities of judgment results, it is determined that in the pre-training stage, the number of iterations for each layer is 30, the learning rate is 0.1, and the initial impulse ν is set to 0.5. In the training stage of supervised learning, the conjugate gradient descent method is used, and the number of training steps is 3,325.

4 Evaluation classification model and its application

4.1 Multi-parameter comprehensive early warning software

The procedure for establishing DNN multi-parameter comprehensive early warning is shown in Figure 10. The early warning process of the impact hazard using multiple parameters includes the following: when the model has not been trained, train the model by configuring training parameters to select sample data and basic algorithms; when the training is completed, directly select the data to be evaluated and import the data into the trained model to obtain the evaluation result. This method evaluates and classifies the output based on the rockburst hazard monitoring data characteristics and obtains the rockburst hazard grade.

Based on the characteristics of coal pillar rockburst monitoring data, it is determined that the functional modules of the DNN multi-parameter comprehensive early warning model include the graphic module, data loading module, and algorithm analysis module. The graphic module mainly displays data and early warning results. The data loading module is used to create new data or extract stored data and classify the data. The algorithm module is used to select the basic parameters of the neural network model, and its DNN multi-parameter comprehensive early warning software interface is shown in Figure 11.

The real-time database is established through the monitoring data obtained by the drilling chip method, microearthquake monitoring, and stress online monitoring. In addition, the continuous numerical curves of different impact hazard monitoring data are drawn, and the data are preprocessed. Intelligent identification method for coal pillar rockburst hazard monitoring finds the characteristics of monitoring data, including the relationship between indicators and causality or correlation between indicators and evaluation targets. Studying the data and mining the data characteristics are needed to establish an evaluation model. Using the DNN multi-parameter comprehensive early warning model, the imported information of rockburst hazard monitoring is evaluated, and conclusive information on the safety status of the rockburst hazard is obtained. Data processing is carried out in the multi-parameter comprehensive early warning system to obtain the interface information, as shown in Figure 12.

4.2 Early warning result analysis

The DNN model is used to evaluate and classify the test data. Two groups of stress online monitoring and microearthquake monitoring data are selected for training to obtain two-dimensional stress and energy classification results. Three groups of microearthquake, stress, and drill chip data are selected for training to obtain three-dimensional classification stress, pulverized coal, and energy results, where yellow indicates danger, red indicates probable danger, pink indicates probable danger, and blue indicates safety. The evaluation and classification results of the test data are shown in Figure 13.

Pre-training abstractly extracted feature information of impact hazard monitoring data, learning impact hazard monitoring data through DNN, and evaluating and classifying different data groups. The node's output value reflects the feature extraction result of the input data by the neural network in this layer structure to obtain new data representation. When the output value of a node is large, that is, closer to 1, the role and position of the node in representation are great, and conversely, the output value is small, and its importance is negligible. Hence, the situation of feature learning can be judged according to the node's output value.

In the early warning mode of multi-parameter comprehensive early warning, comprehensive monitoring information is obtained through different monitoring means. However, there is a lack of an effective, comprehensive evaluation method when there is a contradiction in monitoring data, and the daily obtained monitoring data are not used deeply enough. Thus, the monitoring data are not mined. The DNN model is used to extract the features of the monitoring data, then evaluate and classify the monitoring data, and make early warnings of rockburst hazards according to the classification results. The DNN SVM classification method is used to judge the accuracy of the rockburst hazard. Compared to the traditional monitoring and early warning methods, this approach fully uses the monitoring data and has a better early warning effect. The specific comparison results are shown in Table 1 (Qin et al, 2022; Zhang et al, 2022).

5 Conclusion

(1) The coal pillar rockburst model is established based on the DNN analysis using the drilling chip method, stress online, and comprehensive microearthquake monitoring. The energy, stress, and pulverized coal data recorded in the mining process of Yangcheng Coal Mine are used for training, and the precursor characteristic information of rockburst hazard monitoring data is extracted to realize the evaluation and classification of rockburst hazard monitoring results, and a multi-parameter comprehensive early warning system based on DNN is designed to perform the comprehensive monitoring and early warning of the coal pillar rockburst hazard.

(2) The DNN model can learn data features independently. The DNN model is trained by the collected rockburst hazard monitoring data. The features with discrimination are extracted from the monitoring data by greedy layer-by-layer training methods. The unsupervised learning model is optimized by the symmetric hidden layer method. The supervised learning model is optimized by adding a single-layer algorithm to obtain the standard output value, which improves the data processing ability of the model.

(3) Multi-parameter comprehensive early warning based on DNN improves the early warning accuracy of rockburst risks. Compared with traditional microseismic monitoring, drilling cuttings method, online stress monitoring, and comprehensive microseismic stress early warning, the accuracy of this method is improved by 16.87%, 9.8%, 9.69%, and 6.89%, respectively. This study provides a new method for rockburst monitoring and early

warning and introduces a new research idea for rockburst monitoring and early warning.

Data availability statement

The original contributions presented in the study are included in the article/Supplementary Material; further inquiries can be directed to the corresponding author.

Author contributions

YG: writing—original draft, validation, formal analysis, and methodology. SG: visualization, software, and investigation. Corresponding author: writing—editing, funding acquisition, resources, and project administration. JS: resources, validation, and investigation. All authors contributed to the article and approved the submitted version.

Conflict of interest

Author YG was employed by Baodian Coal Mine, Yankuang Energy Group Co., Ltd, Zoucheng, China. Author JS was employed by Yangcheng Coal Mine, Shandong Jining Mine Luneng Coal Power Company Limited, wenshang, China. The remaining authors declare that the research was conducted in the absence of any commercial or financial relationships that could be construed as a potential conflict of interest.

Publisher's note

References

Ai, D. H., Li, C. W., Zhao, Y. C., and Li, G. Y. (2020). Study on microseismic, electromagnetic radiation and crack propagation characteristics of coal under static load failure. *Rock Soil Mech.* 41 (6), 2043–2051. doi:10.16285/j.rsm.2019.0899

Bao, X. Y., Ma, F., and Han, D. Y. (2019). Risk analysis of rock burst in mining face based on online stress monitoring. *Shandong Ind. Technol.* (11), 73–75. doi:10.16640/j.cnki.37-1222/t.2019.11.063

Bosch, A., Munoz, X., and Marti, R. (2007). Which is the best way to organize/classify images by content? *Image Vis. comput.* 25 (6), 778–791. doi:10.1016/j.imavis.2006.07.015

Chen, B. R., Feng, X. T., Fu, Q. Q., Wang, B., Zhu, X. H., Li, T., et al. (2020). Integration and high precision intelligence microseismic monitoring technology and its application in deep rock engineering. *Rock Soil Mech.* 41 (7), 2422–2431. doi:10.16285/j.rsm.2019.1062

Chen, F., Pan, Y. S., Li, Z. H., Wang, A. W., and Xu, L. M. (2013). Analysis and evaluation of effects of borehole pressure relief measures by drilling cutting method. *Chin. J. Geotech. Eng.* 35, 266–270. S2.

Chen, Z., Xia, J. B., Bai, J., and Xu, M. (2015). Feature extraction algorithm based on evolutionary deep learning. *Comput. Sci.* 42 (11), 288–292. doi:10.11896/j.issn.1002-137X.2015.11.059

Dou, M., Wang, S. C., Gong, S. Y., Cai, W., and Li, X. L. (2020). Cloud platform for intelligent identification, monitoring and early warning of rock burst risk. *J. Coal Sci.* 45 (6), 2248–2255. doi:10.13225/j.cnki.jccs.ZN20.0318

He, S. Q., He, X. Q., Song, D. Z., Li, Z. L., Chen, J. Q., Xue, Y. R., et al. (2022). Multi-parameter integrated early warning model of rock burst and intelligent identification cloud platform. *J. China Univ. Min. Technol.* 51 (5), 850–862. doi:10.13247/j.cnki.jcumt.001440

Ji, H. G., Wang, J. A., and Cai, M. F. (2003). Relativity and unity of physical and geometrical characteristics of rockbursting events. *J. China Coal Soc.* 28 (1), 31–36. doi:10.3321/j.issn:0253-9993.2003.01.007

Jia, B. X., Chen, H., and Pan, Y. S. (2019). Research on multi-parameter comprehensive index rock burst prediction technology. *J. Disast. Prev. Mitigat. Eng.* 39 (2), 330–337. doi:10.13409/j.cnki.jdpme.2019.02.019

Jia, R. S., Sun, H. M., Fan, J. C., Wu, C. F., and Qiu, T. (2014). Multiparameter precursor information identification model and method for rockburst. *Chin. J. Rock Mech. Eng.* 33 (8), 1513–1519. doi:10.13722/j.cnki.jrme.2014.08.001

Jiang, F. X., Qu, X. C., Yu, Z. X., and Wang, C. W. (2011). Real time monitoring and measuring early warning technology and development of mine pressure bumping. *Coal Sci. Technol.* 39 (2), 59–64. doi:10.13199/j.cst.2011.02.64.jiangfx.011

Jiang, Y. D., Pan, Y. S., Jiang, F. X., Dou, L. M., and Ju, Y. (2014). State of the art review on mechanism and prevention of coal bumps in China. *J. China Coal Soc.* 39 (2), 205–213. doi:10.13225/j.cnki.jccs.2013.0024

Jiang, Y. D., and Zhao, Y. X. (2015). State of the art: Investigation on mechanism, forecast and control of coal bumps in China. *Chin. J. Rock Mech. Eng.* 34 (11), 2188–2204. doi:10.13722/j.cnki.jrme.2015.1076

Lan, J. G., and Zhang, H. J. (2022). Research on roadway ground pressure monitoring method based on fiber grating sensor. *Coal Technol.* 41 (2), 121–124. doi:10.13301/j.cnki.ct.2022.02.030

Li, X. L., Zhang, X. Y., Shen, W. L., Zeng, Q. D., Chen, P., Qin, Q. Z., et al. (2023). Research on the mechanism and control technology of coal wall sloughing in the ultra-large mining height working face. *Int. J. Environ. Res. Publ. Health* 20 (1), 868. doi:10.3390/ijerph20010868

Li, Z. Q., Zhang, L., Shao, S. H., Qiao, M. G., Cao, S. X., and Ma, J. K. (2022). On-the-spot practice of monitoring coal stress and impact danger by drilling cuttings method. *Coal Technol.* 41 (5), 137–141. doi:10.13301/j.cnki.ct.2022.05.033

Liu, Q., Wei, J. H., Meng, Q. R., Cao, M., Feng, J., Huang, H., et al. (2022). Clinical characteristics and vaccine effectiveness against SARS-CoV-2 Omicron subvariant BA.2 in the children. *Coal Technol.* 41 (8), 203–207. doi:10.1038/s41392-022-01023-w

Liu, S. M., and Li, X. L. (2023). Experimental study on the effect of cold soaking with liquid nitrogen on the coal chemical and microstructural characteristics. *Environ. Sci. Pollut. Res.* 30 (3), 36080–36097. doi:10.1007/s11356-022-24821-9

Liu, S. M., Sun, H. T., Zhang, D. M., Yang, K., Li, X. L., Wang, D. K., et al. (2023a). Experimental study of effect of liquid nitrogen cold soaking on coal pore structure and fractal characteristics. *Energy* 275 (7), 127470. doi:10.1016/j.energy.2023.127470

Liu, S. M., Sun, H. T., Zhang, D. M., Yang, K., Wang, D. K., Li, X. L., et al. (2023b). Nuclear magnetic resonance study on the influence of liquid nitrogen cold soaking on the pore structure of different coals. *Phys. Fluids* 35 (1), 012009. doi:10.1063/5.0135290

Lu, X. G., Yu, X. M., and Meng, Z. H. (2021). Study on borehole strain monitoring and early warning of dynamic disasters in disturbed mining areas. *Coal Technol.* 40 (12), 174–178. doi:10.13301/j.cnki.ct.2021.12.041

Luo, H., Pan, Y. S., and Xiao, X. C. (2013). Multi-parameter risk evaluation and graded early warning of mine dynamic disaster. *China Saf. Sci. J.* 23 (11), 85–90. doi:10.16265/j.cnki.issn1003-3033.2013.11.020

Lv, J. G., Jiang, Y. D., and Zhao, Y. X. (2013). Hierarchical monitoring for coal bumps and its study and application of early warning methods. *J. China Coal Soc.* 38 (7), 1161–1167. doi:10.13225/j.cnki.jccs.2013.07.023

Pan, L. Y. (2003). *Identification and application of omen information of rockburst*. Qingdao, China: Shandong University of Science and Technology.

Qin, M., Liu, C., Wang, Q., Wang, X., Song, Y., Hu, J. W., et al. (2022). Analysis and research on microseismic monitoring and early warning parameters of ground pressure disasters in mining plants. *Min. Res. Dev.* 42 (10), 180–186. doi:10.13827/j.cnki.kyyk.2022.10.020

Ren, S. (2016). *A feature extraction algorithm for handwritten digits based on deep learning*. Changsha, China: Hunan Normal University.

Sun, Z. J., Xue, L., and Xu, Y. M. (2013). Marginal Fisher feature extraction algorithm based on deep learning. *J. Electr. Inf. Technol.* 35 (4), 805–811. doi:10.3724/SP.J.1146.2012.00949

Wang, C. Q., Jiang, B. Y., Gu, S. T., Tan, T. L., Wang, R. C., and Huang, R. F. (2014). Study of precursor information recognition and multiparameter early warning before rockburst of island fully mechanized caving face. *Rock Soil Mech.* 35 (12), 3523–3530. doi:10.16285/j.rsm.2014.12.023

Wang, D. B., Wang, Q., Li, S. C., Wang, F., Guo, N., Wang, B., et al. (2015). Stress distribution characteristics of deep mine in fully-mechanized sublevel caving face based on microseismic and online stress monitoring system. *J. Min. Saf. Eng.* 32 (3), 382–388. doi:10.13545/j.cnki.jmse.2015.03.006

Wang, H. L. (2022). *Risk warning and prevention decision of rock burst based on cost-sensitive machine learning*. Beijing, China: University of Science and Technology Beijing.

Wang, J. Y., Wang, Z. G., Chen, Y. M., and Gao, J. H. (2023). Deep artificial neural network in seismic inversion. *Progr. Geophys.* 38 (1), 298–320. doi:10.6038/pg2023FF0467

Wang, Y., Liu, J. H., Wang, Y. L., and Wei, Q. D. (2018). Study on multi-parameter monitoring and warning platform for rock burst. *Coal Eng.* 50 (4), 19–21. doi:10.11799/ce201804006

Wang, Z. D., Liu, G. L., Cui, Y., Jiang, T., Zheng, Y. C., Liang, W. Z., et al. (2022). Study on multi-parameter correlation of rock burst monitoring in deep isolated island structure area. *Coal Technol.* 41 (12), 63–66. doi:10.13301/j.cnki.ct.2022.12.015

Yin, L. X. (2022). Research on safety monitoring and early warning system of coal mine heading face. *Energy Energy Sav.* (7), 136–138. doi:10.16643/j.cnki.14-1360/td.2022.07.062

Yuan, L., Jiang, Y. D., He, X. Q., Dou, L. M., Zhao, Y. X., Zhao, X. S., et al. (2018). Research progress of precise risk accurate identification and monitoring early warning on typical dynamic disasters in coal mine. *J. China Coal Soc.* 43 (2), 306–318. doi:10.13225/j.cnki.jccs.dy20.0272

Zhang, C. P. (2020). Application of drill cuttings method to evaluate rock burst risk in mining face. *Energy Environ. Prot.* 40 (12), 20–23. doi:10.19389/j.cnki.1003-0506.2020.12.004

Zhang, J. C., Li, X. L., Qin, Q. Z., Wang, Y. B., and Gao, X. (2023). Study on overlying strata movement patterns and mechanisms in super-large mining height stopes. *Bull. Eng. Geol. Environ.* 82 (4), 142. doi:10.1007/s10064-023-03185-5

Zhang, L. (2021). Construction of intelligent anti-scour system in deep area of coal mine. *China Coal Ind.* (7), 68–70. doi:10.3969/j.issn.1673-9612.2021.07.026

Zhang, L., Shen, W. L., Li, X. L., Wang, Y. B., Qin, Q. Z., Lu, X. T., et al. (2022). Abutment pressure distribution law and support analysis of super large mining height face. *Int. J. Environ. Res. Pub. Health* 20 (1), 227. doi:10.3390/ijerph20010227

Zhang, Y. Y., Huo, J., Yang, W. Q., Gao, Y., and Shi, Y. H. (2015). The second generation ID card heterogeneous face verification algorithm of Deep Belief Network. *J. Intell. Syst.* 10 (2), 193–200.

Zheng, J. H. (2022). *Random load identification method based on deep neural network*. Guangzhou, China: Guangzhou University.

Zhu, L. Y., Li, Z. H., and Xu, L. M. (2014). Measuring stress and strength of coal by drilling cutting torque method. *Chin. J. Geotech. Eng.* 36 (11), 2096–2102. doi:10.11779/CJGE201411016

frontiers | Frontiers in Earth Science

TYPE Original Research
PUBLISHED 04 July 2023
DOI 10.3389/feart.2023.1227154

OPEN ACCESS

EDITED BY
Xuelong Li,
Shandong University of Science and Technology, China

REVIEWED BY
Lei Shi,
China University of Mining and Technology, Beijing, China
Yu Xuguang,
Tangshan Vocational and Technical College, China

*CORRESPONDENCE
Changjian Wang,
changjian_wang66@163.com

RECEIVED 22 May 2023
ACCEPTED 26 June 2023
PUBLISHED 04 July 2023

CITATION
Qiao J, Wang C, Su G, Liang X, Dong S, Jiang Y and Zhang Y (2023), Application research on the prediction of tar yield of deep coal seam mining areas based on PSO-BPNN machine learning algorithm. *Front. Earth Sci.* 11:1227154. doi: 10.3389/feart.2023.1227154

Application research on the prediction of tar yield of deep coal seam mining areas based on PSO-BPNN machine learning algorithm

Junwei Qiao[1,2,3], Changjian Wang[1]*, Gang Su[4], Xiangyang Liang[1], Shenpei Dong[1], Yi Jiang[1] and Yu Zhang[1]

[1]College of Geology and Environment, Xi'an University of Science and Technology, Xi'an, China, [2]Geological Research Institute for Coal Green Mining, Xi'an University of Science and Technology, Xi'an, China, [3]Shaanxi Provincial Key Laboratory of Geological Support for Coal Green Exploitation, Xi'an, China, [4]Shaanxi Shanmei Caojiatan Mining Co., Ltd., Yulin, China

There are abundant deep coal resources in northern Shaanxi, but the fragile natural environment in this area hinders the large-scale exploitation of oil-rich coal. *In-situ* thermal conversion of deep coal to oil and gas will become an environmentally friendly technology for oil-rich coal mining. Accurate prediction of oil-rich coal tar yield in various regions is a prerequisite. Based on a particle swarm optimization algorithm and two machine learning algorithms, BP neural network and random forest, a prediction model of tar yield from oil-rich coal is constructed in this paper. Combined with the particle swarm optimization method, the problem of slow convergence speed and possibly falling into local minimum value of BP neural network is solved and optimized. The results showed that the PSO-BP had a convergence speed about five times faster than that of the BP neural network. Furthermore, the predicted value of the PSO-BP was consistent with the measured value, and the average relative error was 4.56% lower than that of the random forest model. The advantages of fast convergence and high accuracy of the prediction model are obviously apparent. Accurate prediction of tar yield would facilitate the research process of *in-situ* fluidized mining of deep coal seams.

KEYWORDS

particle swarm optimization (PSO), BP neural network, machine learning, oil-rich coal, tar yield prediction

1 Introduction

Tar-rich coal is a resource that integrates coal, oil, and gas attributes, and it has received significant attention due to its high tar yield (Ju et al., 2021; Du and Li, 2022). When the coal is subjected to pyrolysis (500°C–700°C) and Gray-King assay, coal with a tar yield of more than 7% and less than or equal to 12% is classified as tar-rich coal (Jiang et al., 2020; Shi et al., 2022). This type of coal is an important way to increase oil and gas supply (one tonne of tar-rich coal can yield approximately 10% oil and 500 m^3 of combustible gas (Marshall et al., 2015; Chen et al., 2017; Li et al., 2022; Ma et al., 2022), thereby realizing clean and efficient utilization of coal resources. Specifically, China is rich in tar-rich coal resources but faces the pressure of "poor oil and gas" energy, which

has promoted the development of the coal-to-liquids industry (Wang et al., 2020; Wang et al., 2021; Liu et al., 2023a; Liu et al., 2023b; Liu and Li, 2023). The subversive idea of deep fluidization mining is to realize the local fluidization of solid resources in deep earth, form liquefied, gasification, electrochemical, biological, and mixed fluidization resources, and efficiently and intelligently transfer them to the surface in the form of fluidization. The subversive theory and technical conception of deep-ground fluidized mining break through the limitation of the traditional mining depth of coal solid mineral resources, and fundamentally subvert the mining mode of reliable resources. Oil-rich coal's oil and gas properties ensure *in-situ* conversion in fluidized mining technology. The fluidized mining technology of deep coal seams has also been deeply studied (Zhang et al., 2023; Zhang et al., 2023; Li et al., 2023). Oil-rich coal has been one of the important ways to guarantee national energy security in China. However, more than 80% of coal is directly combusted for power generation, result in a massive wastage of precious oil resources (Xu et al., 2015; Ju et al., 2021). Moreover, only a few coal samples were tested for tar production during past geological explorations, limiting the study and large-scale development of tar-rich coal (Fu et al., 2023; Wang et al., 2023). Thus, it is essential to explore the mathematical relationship between tar yield and the geological evaluation index of tar-rich coal to predict the tar yield.

In the study of the tar-rich coal in oil-rich coal mining areas, some scholars have summarized the mathematical relationship between tar yield and coal seam thickness, industrial analysis, macrolithotype and micro-composition, ash content, actual density (Shi et al., 2022). Furthermore, a prediction model for the tar yield of low-rank coal in Shenfu Southern mining area was established using multiple linear regression and other mathematical methods, and the multiple correlation coefficient reached 0.8 (Guo et al., 2021). A general relationship exists between tar yield and these parameters, but the Pearson correlation coefficient is low, indicating a complex nonlinear relationship. Thus, a machine learning method is suitable for investigating the relationship between tar yield and other geological evaluation indices of coal. With the progress of science and technology, the technique of machine learning is more and more applied to the geological coal industry such as gas outburst prediction (Wu et al., 2020; Gao et al., 2023; Zhu et al., 2023), coal ash softening temperature prediction (Liang et al., 2020), coal gangue identification (Wang et al., 2022), coal dust wettable identification (Zheng et al., 2023), coal seam impact risk assessment (Zhang et al., 2022), etc. It has become a new research hotspot in coal geological engineering practice to mine the relationship between various nonlinear big data through machine learning algorithms to realize data prediction. Based on the geological data, coal quality testing data and geophysical logging data of Huangling mining area in the past geological exploration stage, the relationship between tar-rich coal tar yield and geophysical logging data has been studied, and the calculation model of tar-rich coal tar yield and logging compensation density value has been established (Yan et al., 2022). Using logging data, BP neural network technology has been applied to predict coal tar yield (Zhao et al., 2021).

Although the above study can get a particular-pattern of tar yield, it is only a rough estimate. The research using the BP neural network method to predict the tar yield is still in the beginning stage. There are some problems, such as slow convergence speed and easy falling into the local optimum, so it can not realize the accurate prediction of the tar yield of the coal that has been mined before but has not been tested (Zhang et al., 2022; Li et al., 2022). In this paper, we established the prediction model of PSO-BP, which combines the PSO algorithm and BP neural network based on the geological evaluation index of tar-rich coal. In this paper, the particle swarm optimization algorithm (PSO) is used to optimize the BP network connection weights and thresholds to overcome the defects of BP network. Based on the measured coal quality data in the past, the PSO-BP tar yield prediction model was established to predict the coal tar yield. The convergence speed and prediction accuracy are significantly improved compared with the traditional BP network.

2 Materials and methods

2.1 Experimental data

Samples of coal were obtained from coal seam 2^{-2} in oil-rich coal mining areas, which have high calorific value, rich tar, low ash, low sulfur, and low phosphorus. The coals were analyzed according to ISO 17247:2013 (Coal-Ultimate analysis) and ISO 17246:2010 (Coal-Proximate analysis). Proximate analysis used an automatic analyser to determine the moisture (M_{ad}), ash (A_d), volatile matter (V_{daf}), and fixed carbon (FC_{ad}) content of coal samples. The ultimate analysis of coal was performed to determine the elemental content of C,H and S. The seven geological evaluation indices [volatile matter (V_{daf}), ash (A_d), moisture (M_{ad}), fixed carbon (FC_{ad}), Sulfur ($S_{t,d}$), hydrogen (H_{daf}) and carbon (C_{daf})] and tar yield values of 52 coal samples were used for this research. These seven coal quality indicators are the external manifestation of the essential nature of coal. From the analysis results of these seven coal quality indicators, the types of coal, processing and utilization ways and mining technologies can be related and corresponding policies can be adopted for efficient mining.

Some studies show that with the increase of volatile matter, the coal tar yield shows a weak, increasing trend. The moisture content in coal decreases with the increase in coal grade, and the moisture content also affects the tar yield. The effect of ash content on tar yield is reflected in that clay minerals in ash composition are positively correlated with tar. In contrast carbonate minerals are negatively correlated with tar yield (Du and Li, 2022). Tar yield is also closely carbon structure of the carbon in coal. Carbon content (C_{daf}) and hydrogen content (H_{daf}) determine the H/C atomic ratio of coal, which indicate the key hydrogen-rich structure or the distribution type of hydrogen and oxygen elements in coal (Liu et al., 2016; Li et al., 2022), which plays a more critical role in tar yield. The migration of sulfur content ($S_{t,d}$) during pyrolysis also affects the tar yield. In addition, as the most widely tested items in coal, these seven indices have been generally recorded in the previous exploration results. The selection of these seven indices to predict the coal tar

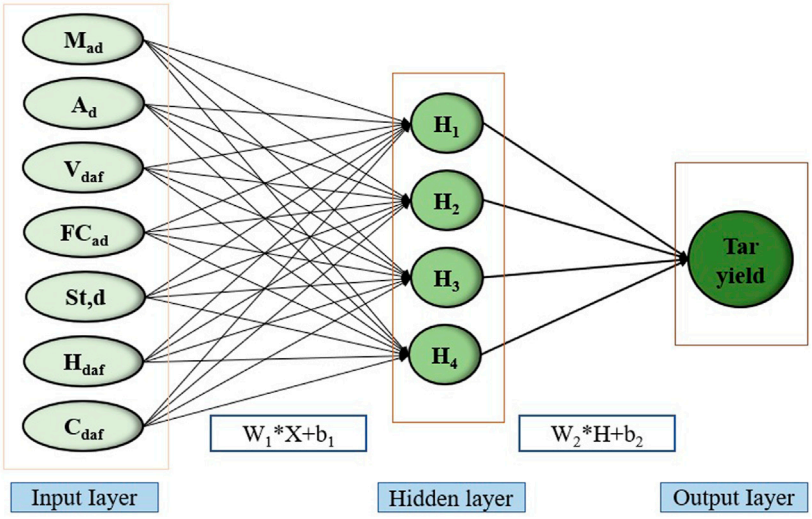

FIGURE 1
BP neural network structure for predicting tar yield.

yield of great significance to realize the full utilization of the previous exploration results.

2.2 BP neural network

The BP network has a simple structure, is easy to use, and has broad applicability (Hinton et al., 2006). The design of the BP neural network is shown in Figure 1, which is composed of an input layer, a hidden layer and an output layer. The layers are fully connected to each other (Wu et al., 2020; Wang et al., 2022). The input layer is the normalized value of each coal geological evaluation index, and the output layer is the value of tar yield to be predicted.

2.3 Particle swarm optimization (PSO) algorithm

Although BP neural network has excellent self-learning, high fault tolerance, good generalization performance, and other advantage, but could be better, there are some things that could be improved. Given the main defect of slow convergence speed, many researchers focus on combination with other intelligent algorithms. The combination with different intelligent algorithms is mainly combined with genetic algorithm (GA) and Particle Swarm Optimization (PSO) algorithm. We introduce PSO to improve the convergence speed and accuracy of the tar yield prediction model.

Based on previous research, the PSO algorithm can obtain the optimal global value and assign it to the weight and threshold of the BP neural network, which can overcome some of the defects of the BP neural network (Li et al., 2022; Zhu et al., 2023). PSO is an algorithm that searches for the best solution by simulating the movement and flocking of birds. The algorithm randomly initializes a flock of birds over the search space, where each bird is called a "particle." These "particles" fly with a certain velocity and find the best global location after some iterations. The steps of the PSO algorithm are as follows (Moazen et al., 2023; Song et al., 2023; Yin et al., 2023).

Step 1. Initialize the particle swarm (there are n particles): assign a random initial location and velocity to each particle.

Step 2. Calculate the fitness value according to the objective function of the optimization problem.

Step 3. Compare the fitness value of the particle's current location with its historical best location (pbest). If the fitness value of the current location is better, the place location is replaced.

Step 4. Compare the fitness value of the particle's current location with its global best location (gbest). If the fitness value of the current location is better, the gbest is replaced.

Step 5. Update the velocity and location of each particle according to Eq. 1 and Eq. 2.

$$v_{id}^{k} = wv_{id}^{k-1} + c_1 r_1\left(pbest_{id} - x_{id}^{k-1}\right) + c_2 r_2\left(gbest_d - x_{id}^{k-1}\right) \quad (1)$$

$$x_{id}^{k} = x_{id}^{k-1} + v_{id}^{k-1} \quad (2)$$

v_{id}^{k} represents the d-dimensional component of the velocity vector of particle i in the K-th iteration; x_{id}^{k} represents the d-dimensional component of the position vector of particle i in the K-th iteration; c_1 and c_2 represent the acceleration constant and are used to adjust the maximum learning step length; r_1 and r_2 represent two random parameters with a value range of [0,1] to increase the randomness of search. Inertia weight w represents the non-negative parameter and is used to adjust the search range of the solution space.

Step 6. The global optimum is output if the stopping criteria are achieved, Otherwise, the algorithm goes back to Step 2.

2.4 Random forest regression

Random forest is a supervised machine learning method that integrates decision trees as individual learners. It further introduces randomness into the training process of decision trees, so that it has excellent anti-overfitting and anti-noise ability. The random forest algorithm performs the following steps.

1) Extract a training set from the original sample. Each round uses Bootstrapping to extract n training examples from the original sample set (with replacement sampling). A total of k extractions are made.
2) One training set obtains a model at a time, resulting in k models from k training sets.
3) For the regression problem, calculate the mean of the above model as the final result.

3 The establishment of a tar yield prediction model

3.1 Structure design of BP neural network

Firstly, the node number of the input and output layers of the BP network is determined according to the actual problem. Then the most appropriate hidden layer number and node number are determined on the premise of ensuring the accuracy of the algorithm. As for the number of hidden layers, the three-layer BP network of a single hidden layer can complete the nonlinear mapping of any dimension (Hinton et al., 2006; Liang et al., 2020; Zhang et al., 2022). Thus, the network structure of a single hidden layer is adopted. As for the number of nodes in the hidden layer, too many nodes may lead to a massive amount of computation, while too few nodes may reduce the model's accuracy (Tang et al., 2023; Xie et al., 2023). Thus, the number of hidden layer nodes is usually determined according to the empirical formula, as shown in Eq. 3:

$$H = \sqrt{I + O} + b \tag{3}$$

Where H, I and O are the nodes of the network's hidden layer, input layer and output layer respectively. B is a natural number from (0,10).

3.2 The structure of particles and populations

Based on the particle population of training sample data, the mapping relationship between the weight and threshold of the BP network and the particle dimension of PSO is established. Suppose the number of neurons in the input layer, hidden layer and output layer of the BP network is I, H and O respectively, the spatial dimension of PSO particles is $d=I\times H+H\times O+O$, which corresponds to the number of weights and thresholds in the BP neural network.

3.3 Construction of fitness function

The mean square error calculation formula of BP neural network output is used as the fitness function of PSO algorithm, as shown in Eq. 4.

$$F = MSE = \frac{1}{n}\sum_{i=1}^{n}\left(y_i - y_i^{'}\right)^2 \tag{4}$$

Where y_i is the i-th actual output value of the network; $y_i^{'}$ is the expectation value of the i-th.

3.4 Design of PSO-BP neural network model

The steps of weight and threshold of BP neural network optimized based on particle swarm optimization are as follows. The algorithm flow of the PSO-BP model is shown in Figure 2.

Input: Training sample set.

Step 1. Initialize network parameters.

1) Set the learning parameters of the BP network. These include the activation function, training function, learning rate (lr), goal error (goal), and maximum iterations (epochs), which are determined based on the training sample data.
2) Set the parameters of the PSO algorithm. The parameters in the particle swarm are initialized, including the number(n) of particles, their initial location (x_i) and velocity (v_i) of particles, acceleration constants (c_1, c_2), inertia weight (w), optimal personalized value (pbest) and global optimal value (gbest).

Step 2. Iteratively update particle locations, velocities, individual optimal values, and global optimal values.

1) Calculate the fitness value F(x) of each particle based on Eq. 4, and then calculate the pbest and gbest.
2) Update the location and velocity of particles based on Eq. 1 and Eq. 2, and then update the pbest and gbest.

Step 3. Evaluate whether one of the following conditions is met. If yes, go to Step 4; otherwise, Step 2.

1) The training errors of the network meet the accuracy requirements.
2) The training frequency of the network reaches the maximum number of iterations.

Step 4. Output the global optimum (gbest) and assign the weight and threshold to the network. The algorithm ends.

Output: A trained BP neural network. This illustration belongs to 3.5.

3.5 The structure of random forest

The establishment of random forest model is inseparable from the combination of decision trees. Similar to the flowchart of the tree

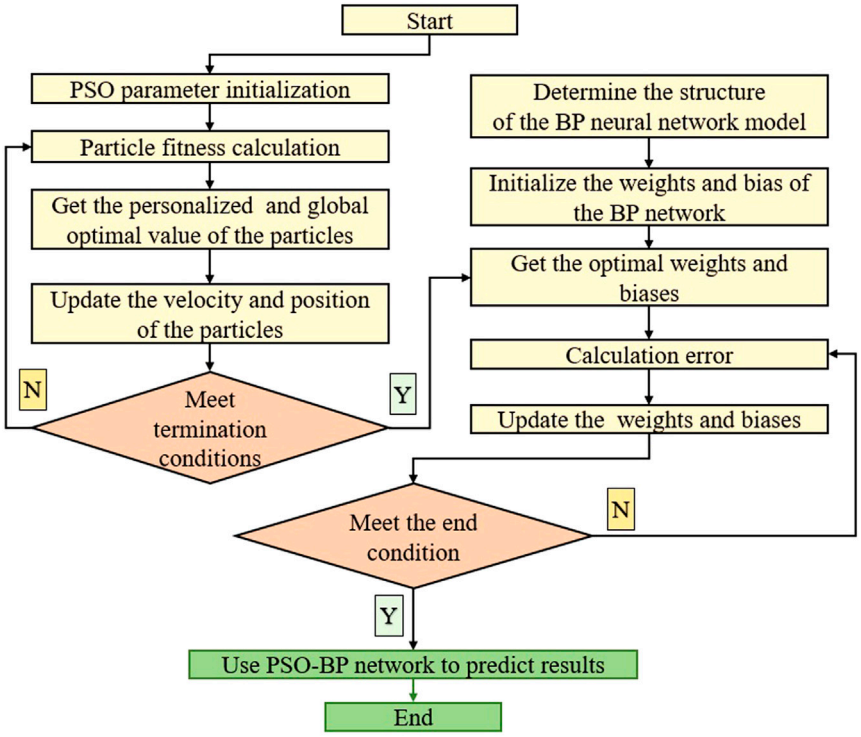

FIGURE 2
Flow of PSO-BP model algorithm.

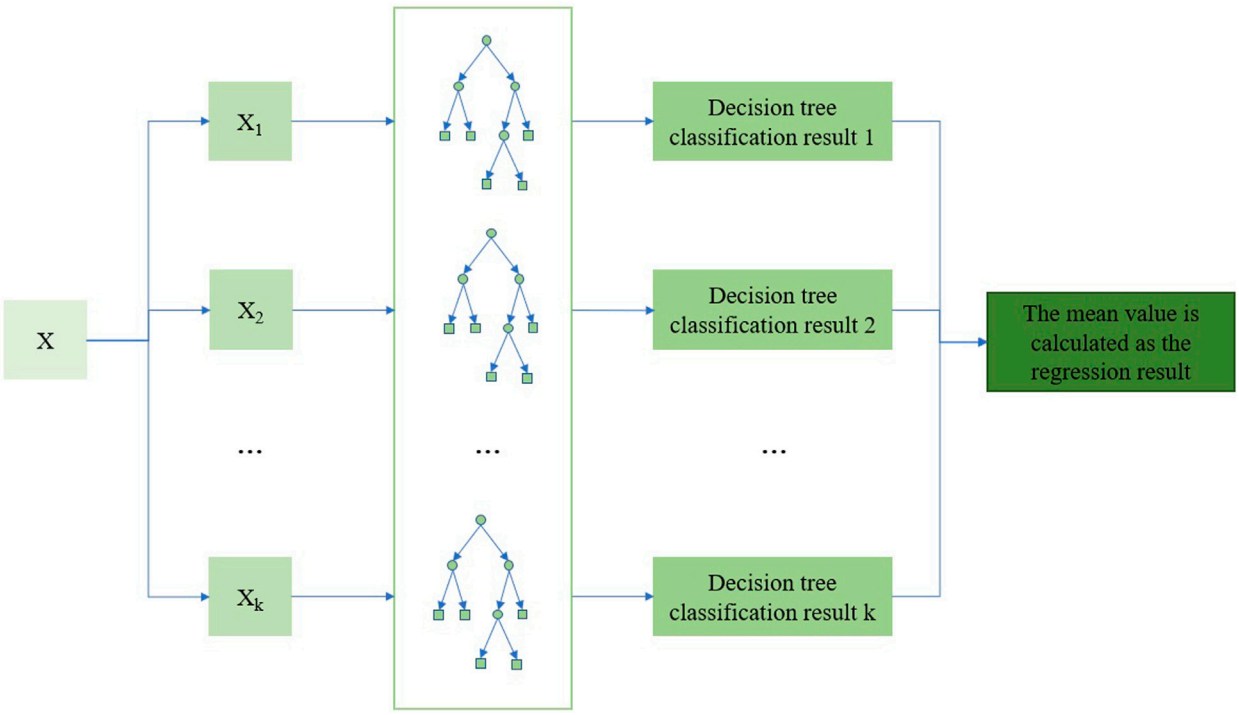

FIGURE 3
Random forest principle for predicting tar yield.

TABLE 1 Original training sample data (partial data).

Serial number	Moisture (M_{ad})%	Ash (A_d)%	Volatile matter (V_{daf})%	Fixed carbon (FC_{ad})%	Sulfur ($S_{t,d}$)%	Carbon (C_{daf})%	Hydrogen (H_{daf})%	Tar yield (Tar.d)%
1	6.76	4.49	36.78	56.3	0.34	83.4	4.68	9.4
2	6.19	9.19	35.65	54.82	0.87	81.38	4.12	7.8
3	5.34	10.79	37.31	52.94	0.43	81.53	4.7	9.2
4	5.71	9.97	37.73	52.86	0.47	81.67	4.88	11.1
5	5.18	10.97	36.99	53.19	26.72	0.51	81.53	4.8
6	5.93	7.25	37.66	54.39	27.94	0.45	81.81	4.86
7	6.07	7.24	37.69	54.29	27.82	0.49	81.83	4.83
8	5.73	7.47	36.62	55.29	27.83	0.57	82.2	4.65
9	4.59	18.9	37.12	48.66	23.62	0.86	80.51	4.28
10	5.62	18.57	36.17	49.05	23.67	0.65	80.82	4.33
11	5.74	10.84	37.34	52.66	26.08	0.94	81.06	4.27
...	...	...	...	...	...	...	...	...

TABLE 2 Statistical data of various coal quality indicators.

Indicators	Average	Variance	Kurtosis	Skewness	Correlation coefficient
Moisture (M_{ad})%	6.32	1.31	1.20	0.44	0.08
Ash (A_d)%	9.84	73.38	19.93	3.80	−0.18
Volatile Matter (V_{daf})%	38.08	10.76	0.05	0.25	−0.11
Fixed Carbon (FC_{ad})%	52.31	34.43	8.81	−2.22	0.20
Sulfur ($S_{t,d}$)%	0.68	0.20	11.43	2.86	−0.45
Carbon (C_{daf})%	80.98	3.01	5.01	−1.85	0.16
Hydrogen (H_{daf})%	4.47	0.13	−0.02	−0.15	0.23
Tar Yield (Tar.d)%	8.02	1.71	0.48	−0.18	1.00

structure, a decision tree is a recursive process from top to bottom. It starts from the tree's root node, selects the optimal features in different internal nodes, determines the corresponding branch according to the test output, and the final result comes from the nodes of the leaf of the decision tree (Figure 3).

4 The studying and training of the tar yield prediction model

4.1 Learn parametric sample selection

We collected 52 coal quality analysis data of coal seam 2^{-2} in oil-rich coal mining areas, and used the data set random partition function in the python language sci-kit-learn machine learning library to take 40 coal quality analysis data as the training data set of the model, and the other 12 coal quality analysis data as the test data set of the model. The industrial analysis and elemental analysis data of 40 groups of coal samples are used as training dataset for the model. The dataset includes seven geological evaluation indices [volatile matter (V_{daf}), ash (A_d), moisture (M_{ad}), fixed carbon (FC_{ad}), Sulfur ($S_{t,d}$), Hydrogen (H_{daf}), and carbon (C_{daf})] and tar yield values of 40 coal samples used as the model output parameters. Part of the original training sample data is shown in Table 1. The statistical data of the actual training sample and the correlation coefficients with the tar yield are shown in Table 2.

4.2 Preprocessing training data

If the geological evaluation indices of coal with significant differences are directly input to the model, the prediction accuracy will be reduced and the convergence speed will be slow. Therefore, the z-score standardized method was adopted to map the input sample data to the same magnitude, as shown in Eq. 5:

$$z_{ij} = \frac{x_{ij} - \bar{x}_j}{s_j} \ (i = 1, 2, \cdots, n, j = 1, 2, \cdots, m) \tag{5}$$

Where X_{ij} represents the data of the i-th sample and j-th variable before standardization; Z_{ij} is the standardized data; $\bar{x}_j$ and s_j are the average and variance values in the data series.

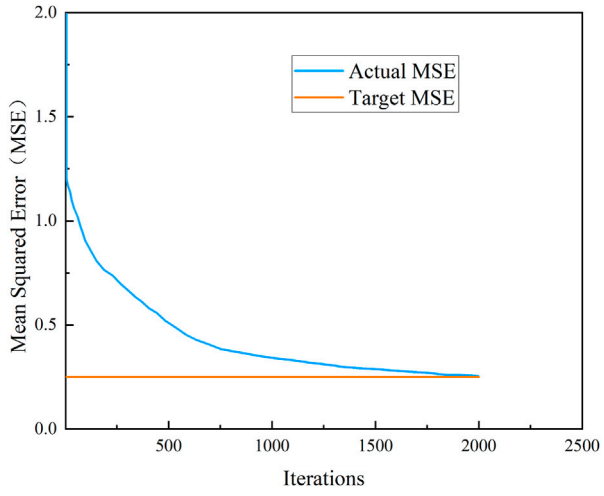

FIGURE 4
BP neural network iterative training optimization process.

4.3 Select and set model parameters

4.3.1 Select studying and training parameters of BP networks

Based on the practical problem, the number of nodes in the input and output layers of the BP neural network was determined to be 7 and 1 respectively. These values were then substituted into Eq. 3 to calculate that H ranged from 2 to 13. After repeated tests, the optimal number of hidden layer nodes was determined to be 4. The target error goal was 0.25, the learning rate was set to 0.005, and the maximum number of iterations was set to epochs = 3000. The activation function for the hidden layer was selected as the Sigmoid function, a smooth function biased towards derivative and can map any input to the range of [0,1]. The BP neural network's iterative training and optimization process is shown in Figure 4.

4.3.2 Set the PSO algorithm parameters

The number of particles generally ranges from 20 to 200. A large number of particles leads to a robust global optimization ability of the algorithm but also increases the amount of computation and slows down the convergence speed. Thus, based on the complex nonlinear relationship between the input and output of the model, the number of particles was set to 50 to obtain the global optimum.

The inertia weight w affects the global and local search ability of particles. The more oversized w is, the more conducive it is to global search; the smaller w is, the more conducive it is to local search. Therefore, the value of w was set to 0.1.

The acceleration constants c_1 and c_2 are the weights that adjust the role of their experience and social experience in their motion. The fixed c_1 and c_2 are only limited to the application of some problems and cannot be generalized to all problem domains. In general, $c_1 + c_2 \leq 4$, and $c_1 = c_2 = 1.49445$ is commonly used.

To balance the algorithm's running speed and the practical problem's needs, the maximum of iterations was set to 30 (Li et al., 2022).

4.3.3 Set the random forest parameters

To establish a reliable tar yield prediction model, it is necessary to adjust the parameters of the random forest regression algorithm to obtain the optimal algorithm parameters.

The most crucial algorithm parameter is the number of decision trees. A small number of decision trees will not make the effect of the model entirely play, and a large number of decision trees will not only reduce the training and prediction speed of the model, but also cause the problem of over-fitting. In this problem, when the number of decision trees is greater than 50, the accuracy performance of the model almost stops improving. Therefore, the value 50 is selected as the optimal this paper's random forest regression algorithm in this paper.

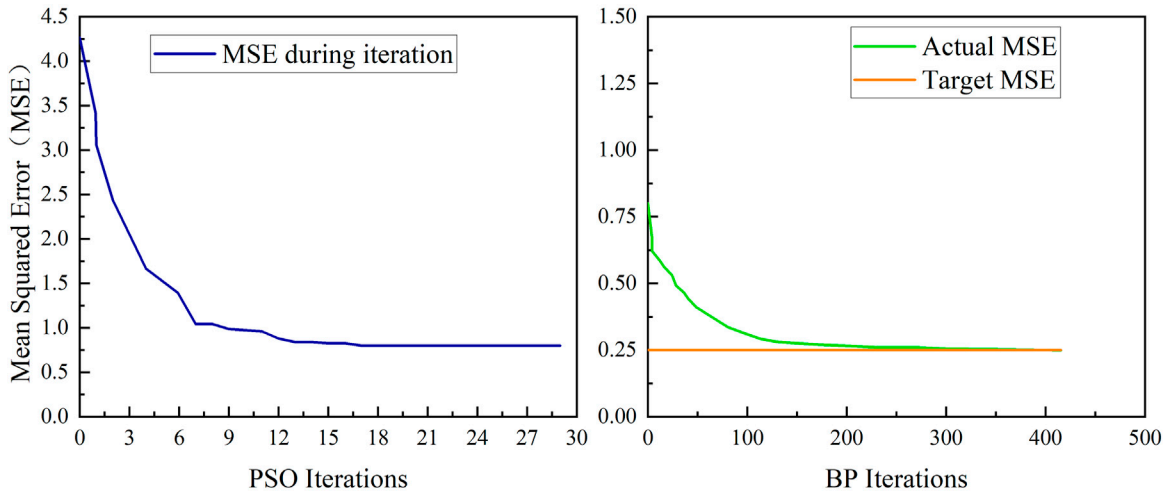

FIGURE 5
PSO-BP neural network iterative training process.

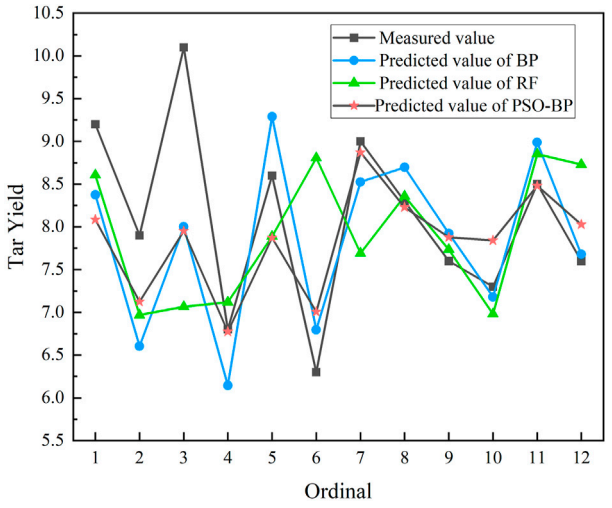

FIGURE 6
Comparison of predicted values and measured values of tar yield in each model.

Parameters such as max tree depth, max min leaf nodes, and max number of features have little impact on the random forest regression model, and we keep the default Settings in the scikit-learn machine learning library.

4.4 Comparison of model training speed

The original training data in Table 1 were imported into the BP and PSO-BP models for training after standardized processing. The training times required for both models to achieve the target accuracy requirements were obtained. The iterative training process of the PSO-BP neural network is shown in Figure 5. The random forest model is not iterative, so we don't compare its training speed.

It can be seen from Figure 5 that the PSO-BP prediction model needs about 400 iterations to meet the accuracy requirements, while the BP neural network prediction model needs about 2000 iterations. Therefore, the training speed of the PSO-BP prediction model was about five times faster than the BP prediction model when meeting exact same accuracy requirements. It indicates that the BP network optimized by the PSO algorithm overcomes the problem of slow convergence speed, and improves the training speed.

5 Practical engineering project

In engineering practice, the model's generalization ability is more important than the fitting performance. To test the prediction performance and universality of the tar yield prediction model, we used three models of BP neural network, PSO-BP, and random forest to predict the tar yield values of the 12 test set data mentioned above and compared them with the measured values.

The test set data are standardized and then imported into BP model and PSO-BP model respectively. Since the random forest model is not sensitive to the numerical magnitude, the test set brought into the random forest model does not need to be standardized. The comparison between the predicted and measured values of each model is shown in Figure 6, and the corresponding error is shown in Table 3.

Figure 6 shows deviations between the predicted values of the three predictive models and the measured values. Notably, the

TABLE 3 Analysis of tar yield prediction deviation.

NO.	Actual value (%)	BP prediction (%)	Relative error (%)	PSO-BP prediction (%)	Relative error (%)	Rf prediction (%)	Relative error (%)
1	9.2	8.37	8.97	8.08	12.12	8.60	6.47
2	7.9	6.60	16.42	7.12	9.83	6.97	11.79
3	10.1	8.00	20.79	7.95	21.27	7.07	30.03
4	6.8	6.14	9.64	6.77	0.37	7.12	4.68
5	8.6	9.29	7.99	7.87	8.48	7.89	8.29
6	6.3	6.80	7.88	7.01	11.21	8.81	39.79
7	9	8.52	5.28	8.87	1.44	7.69	14.56
8	8.3	8.70	4.77	8.23	0.86	8.36	0.70
9	7.6	7.92	4.25	7.88	3.65	7.73	1.75
10	7.3	7.18	1.62	7.84	7.43	6.98	4.36
11	8.5	8.99	5.73	8.48	0.24	8.85	4.14
12	7.6	7.68	1.02	8.03	5.62	8.73	14.85
AVG	8.1	7.85	8.17	7.84	7.17	7.90	11.73

PSO-BP network model is more accurate than the BP network and random forest model, with a better fitting effect and the predicted values are closer to the measured values. As shown in Table 3, the relative errors of the PSO-BP network model are minor. Compared with the BP network model, the PSO-BP tar yield prediction model has a more stable nonlinear fitting ability and more vital generalization ability. Compared with the random forest model, the results of the PSO-BP model are more accurate. The model is a simple and effective method for predicting the tar yield, indicating the nonlinear relationship between the geological evaluation index (industrial analysis and elemental analysis) and the tar yield index of coal.

6 Conclusion

Based on the three machine learning algorithms, a tar yield prediction model was constructed for seven geological evaluation indices of tar-rich coal in oil-rich coal mining areas. Following conclusions were drawn.

(1) The convergence speed of the PSO-BP model was about five times faster than that of the traditional BP network, thus overcoming the disadvantage of slow convergence speed of the BP network.
(2) The coal tar yield of the 2^{-2} coal seam in oil-rich coal mining areas was predicted, and verified, demonstrating the model's easy implementation, high prediction accuracy, and strong generalization ability.
(3) The practical engineering project showed that the predicted values of the PSO-BP model were close to the measured values. The relative error of the PSO-BP model was smaller than that of the random forest model, and the average relative error of the 12 test samples was reduced by 4.56%. Therefore, the prediction accuracy and universality of the PSO-BP model were significantly improved compared to the random forest model, providing reliable data support and a new technical approach for coal tar yield prediction.

In conclusion, the PSO-BP prediction model provides reliable data support and a new technical approach for predicting coal tar yield.

Data availability statement

The original contributions presented in the study are included in the article/supplementary material, further inquiries can be directed to the corresponding author.

Author contributions

JQ: resources, investigation, supervision, project administration, funding acquisition, writing—review and editing. CW: methodology, coding, investigation, data processing, validation, visualization, writing—original draft, writing—review and editing. GS: Sample collection and data analysis. XL: investigation, data processing. SD: data processing. YJ: data processing. YZ: data processing. All authors contributed to the article and approved the submitted version.

Funding

The study was supported by the Science and Technology Research Program of Shaanxi Coal and Chemical Industry Group Co., Ltd. (No. 2021SMHKJ-A-J-0702).

Conflict of interest

Author GS was employed by Shaanxi Shanmei Caojiatan Mining Co., Ltd. The authors declare that this study received funding from Shaanxi Coal and Chemical Industry Group Co., Ltd. The funder had the following involvement in the study: sample collection and data analysis.

Publisher's note

All claims expressed in this article are solely those of the authors and do not necessarily represent those of their affiliated organizations, or those of the publisher, the editors and the reviewers. Any product that may be evaluated in this article, or claim that may be made by its manufacturer, is not guaranteed or endorsed by the publisher.

References

Chen, J., Deng, C., Wang, H., and Sun, X. (2017). Main oil generating macerals for coal-derived oil: A case study from the jurassic coal-bearing turpan basin, NW China. *Org. Geochem.* 111, 113–125. doi:10.1016/j.orggeochem.2017.05.004

Du, Z. H., and Li, W. (2022). The catalytic effect from alkaline elements on the tar-rich coal pyrolysis. *Catalysts* 12, 376. doi:10.3390/catal12040376

Fu, D., Yu, Z., Gao, K., Duan, Z., Wang, Z., Guo, W., et al. (2023). Thermodynamic analysis on *in situ* underground pyrolysis of tar- rich coal: Secondary reactions. *Acs Omega* 8, 12805–12819. doi:10.1021/acsomega.2c08033

Gao, Y., Yu, Z., Chen, W., Yin, Q., Wu, J., and Wang, W. (2023). Recognition of rock materials after high-temperature deterioration based on SEM images via deep learning. *J. Mater. Res. Technol.* 25, 273–284. doi:10.1016/j.jmrt.2023.05.271

Guo, C., Wang, S. Q., Shi, Q. M., Qiao, J. W., Li, H. T., Zhang, W. G., et al. (2021). Chemical compositions and technological properties of low-rank coals in the south Shenfu mining area: Characteristics, relationship and practice. *Coal Geol. Explor.* 49, 87–99. doi:10.3969/j.issn.1001-1986.2021.01.009

Hinton, G. E., Osindero, S., and Teh, Y. W. (2006). A fast learning algorithm for deep belief nets. *Neural Comput.* 18, 1527–1554. doi:10.1162/neco.2006.18.7.1527

Jiang, H. X., Wang, M. Y., Li, Y., Jin, L. J., and Hu, H. Q. (2020). Integrated coal pyrolysis with steam reforming of propane to improve tar yield. *J. Anal. Appl. Pyrolysis* 147, 104805. doi:10.1016/j.jaap.2020.104805

Ju, Y., Zhu, Y., Zhou, H., Ge, S., and Xie, H. (2021). Microwave pyrolysis and its applications to the *in-situ* recovery and conversion of oil from tar-rich coal: An overview on fundamentals, methods, and challenges. *Energy Rep.* 7, 523–536. doi:10.1016/j.egyr.2021.01.021

Li, H. T., Cao, D. Y., Zou, X. Y., Zhu, Z. R., Zhang, W. G., and Xia, Y. (2022a). Raman spectroscopic characterization and surface graphitization degree of coal-based graphite with the number of aromatic layers. *Spectrosc. Spectr. Analysis* 42, 2616–2623. doi:10.3964/j.issn.1000-0593(2022)08-2616-08

Li, S. X., Shao, L. Y., Liu, J. S., Qin, L. Z., Kang, S. L., Eriksson, K. A., et al. (2022b). Oil generation model of the liptinite-rich coals: Palaeogene in the xihu sag, east China sea shelf basin. *J. Petroleum Sci. Eng.* 209, 109844. doi:10.1016/j.petrol.2021.109844

Li, X. L., Zhang, X. Y., Shen, W. L., Zeng, Q., Chen, P., Qin, Q., et al. (2023). Research on the mechanism and control technology of coal wall sloughing in the ultra-large mining height working face. *Int. J. Environ. Res. Public Health* 20 (2), 868. doi:10.3390/ijerph20010868

Li, Y., Zhou, L., Gao, P., Yang, B., Han, Y., and Lian, C. (2022c). Short-term power generation forecasting of a photovoltaic plant based on PSO-BP and GA-BP neural networks. *Front. Energy Res.* 9, 824691. doi:10.3389/fenrg.2021.824691

Liang, W., Wang, G., Ning, X., Zhang, J., Li, Y., Jiang, C., et al. (2020). Application of BP neural network to the prediction of coal ash melting characteristic temperature. *Fuel* 260, 116324. doi:10.1016/j.fuel.2019.116324

Liu, P., Le, J., Wang, L., Pan, T., Lu, X., and Zhang, D. (2016). Relevance of carbon structure to formation of tar and liquid alkane during coal pyrolysis. *Appl. Energy* 183, 470–477. doi:10.1016/j.apenergy.2016.08.166

Liu, S. M., and Li, X. L. (2023). Experimental study on the effect of cold soaking with liquid nitrogen on the coal chemical and microstructural characteristics. *Environ. Sci. Pollut. Res.* 30 (3), 36080–36097. doi:10.1007/s11356-022-24821-9

Liu, S. M., Sun, H. T., Zhang, D. M., Yang, K., Li, X., Wang, D., et al. (2023b). Experimental study of effect of liquid nitrogen cold soaking on coal pore structure and fractal characteristics. *Energy* 275 (7), 127470. doi:10.1016/j.energy.2023.127470

Liu, S. M., Sun, H. T., Zhang, D. M., Yang, K., Wang, D., Li, X., et al. (2023a). Nuclear magnetic resonance study on the influence of liquid nitrogen cold soaking on the pore structure of different coals. *Phys. Fluids* 35 (1), 012009. doi:10.1063/5.0135290

Ma, L., Mao, Q., Wang, C. a., Duan, Z., Chen, M., Yang, F., et al. (2022). Investigation of pyrolysis and mild oxidation characteristics of tar-rich coal via thermogravimetric experiments. *Acs Omega* 7, 25613–25624. doi:10.1021/acsomega.2c02786

Marshall, C., Large, D. J., Meredith, W., Snape, C. E., Uguna, C., Spiro, B. F., et al. (2015). Geochemistry and petrology of Palaeocene coals from Spitsbergen - Part 1: Oil potential and depositional environment. *Int. J. Coal Geol.* 143, 22–33. doi:10.1016/j.coal.2015.03.006

Moazen, H., Molaei, S., Farzinvash, L., and SabaeiPSO-Elpm, M. (2023). PSO-ELPM: PSO with elite learning, enhanced parameter updating, and exponential mutation operator. *Inf. Sci.* 628, 70–91. doi:10.1016/j.ins.2023.01.103

Shi, Q. M., Wang, S. M., Wang, S. Q., Guo, C., Cai, Y., Du, F. P., et al. (2022). Multi-source identification and internal relationship of tar-rich coal of the Yan'an Formation in the south of Shenfu. *J. China Coal Soc.* 47, 2057–2066. doi:10.13225/j.cnki.jccs.2021.1046

Song, Q., Yu, L., Li, S., Hanajima, N., Zhang, X., and Pu, R. (2023). Energy dispatching based on an improved PSO-aco algorithm. *Int. J. Intelligent Syst.* 2023, 1–17. doi:10.1155/2023/3160184

Tang, X., Xu, B., and Xu, Z. (2023). Reactor temperature prediction method based on CPSO-RBF-BP neural network. *Appl. Sciences-Basel* 13, 3230. doi:10.3390/app13053230

Wang, D., Ni, J., and Du, T. (2022). An image recognition method for coal gangue based on ASGS-CWOA and BP neural network. *Symmetry-Basel* 14, 880. doi:10.3390/sym14050880

Wang, S. M., Sun, Q., Qiao, J. W., and Wang, S. Q. (2020). Geological guarantee of coal green mining. *J. China Coal Soc.* 45, 8–15. doi:10.13225/j.cnki.jccs.YG19.1758

Wang, S., Shi, Q., Wang, S., Shen, Y., Sun, Q., Cai, Y., et al. (2021). Effects of glycated glutenin heat-processing conditions on its digestibility and induced inflammation levels in cells. *J. China Coal Soc.* 46, 1365–1377. doi:10.3390/foods10061365

Wang, Z., Yang, F., Fu, D., Ma, L., Duan, Z., Wang, Q., et al. (2023). Economic and heating efficiency analysis of double-shell downhole electric heater for tar-rich coal *in-situ* conversion. *Case Stud. Therm. Eng.* 41, 102596. doi:10.1016/j.csite.2022.102596

Wu, Y., Gao, R., and Yang, J. (2020). Prediction of coal and gas outburst: A method based on the BP neural network optimized by gasa. *Process Saf. Environ. Prot.* 133, 64–72. doi:10.1016/j.psep.2019.10.002

Xie, Y., Gao, C., Wang, P., Zhou, L., Zhang, C., and Qu, X. (2023). Research on vibration fatigue damage locations of offshore oil and gas pipelines based on the GA-improved BP neural network. *Shock Vib.* 2023, 1–18. doi:10.1155/2023/2530651

Xu, J., Yang, Y., and Li, Y. W. (2015). Recent development in converting coal to clean fuels in China. *Fuel* 152, 122–130. doi:10.1016/j.fuel.2014.11.059

Yan, H., Duan, Z., and Wang, J. (2022). Study on the relationship model between oil-rich coal tar yield and compensation density in huangling mining area. *Coal Geol. China* 34, 25–30. doi:10.3969/j.issn.1674-1803.2022.10.05

Yin, S., Jin, M., Lu, H., Gong, G., Mao, W., Chen, G., et al. (2023). Reinforcement-learning-based parameter adaptation method for particle swarm optimization. *Complex and Intelligent Syst.* doi:10.1007/s40747-023-01012-8

Zhang, H., Niu, F., Zhang, J., and Yu, X. (2022a). Prediction of three-dimensional fractal dimension of hematite flocs based on particle swarm optimization optimized back propagation neural network. *Min. Metallurgy Explor.* 39, 2503–2515. doi:10.1007/s42461-022-00684-z

Zhang, J. C., Li, X. L., Qin, Q. Z., Wang, Y., and Gao, X. (2023b). Study on overlying strata movement patterns and mechanisms in super-large mining height stopes. *Bull. Eng. Geol. Environ.* 82 (3), 142. doi:10.1007/s10064-023-03185-5

Zhang, K., Zhu, J., He, M., Jiang, Y., Zhu, C., Li, D., et al. (2022b). Research on intelligent comprehensive evaluation of coal seam impact risk based on BP neural network model. *Energies* 15, 3292. doi:10.3390/en15093292

Zhang, L. B., Shen, W. L., Li, X. L., Wang, Y., Qin, Q., Lu, X., et al. (2023a). Abutment pressure distribution law and support analysis of super large mining height face. *Int. J. Environ. Res. Public Health* 20 (1), 227. doi:10.3390/ijerph20010227

Zhao, J., Yan, H., Wang, J., and Wang, S. (2021). The Research on coal tar productivity prediction method based on logging information. *Prog. Geophys.* 2021, 1–10.

Zheng, H., Shi, S., Jiang, B., Zheng, Y., Li, S., and Wang, H. (2023). Research on coal dust wettability identification based on GA-BP model. *Int. J. Environ. Res. Public Health* 20, 624. doi:10.3390/ijerph20010624

Zhu, J., Zheng, H., Yang, L., Li, S., Sun, L., and Geng, J. (2023). Evaluation of deep coal and gas outburst based on RS-GA-BP. *Nat. Hazards* 115, 2531–2551. doi:10.1007/s11069-022-05652-w

frontiers | Frontiers in Earth Science

TYPE Original Research
PUBLISHED 06 July 2023
DOI 10.3389/feart.2023.1216667

OPEN ACCESS

EDITED BY
Xuelong Li,
Shandong University of Science and Technology, China

REVIEWED BY
Xiaoping Zhou,
Chongqing University, China
Gang Lei,
Yibin University, China
Yuezheng Zhang,
University of Science and Technology Beijing, China

*CORRESPONDENCE
Kuikui Hou,
houkuikui@sd-gold.com
Yingjie Hao,
haoyingjiell@sd-gold.com
Yantian Yin,
yinyantian@sd-gold.com
Long An,
anlong@mail.neu.edu.cn

RECEIVED 04 May 2023
ACCEPTED 12 June 2023
PUBLISHED 06 July 2023

CITATION
Hou K, Zhu M, Hao Y, Yin Y and An L (2023), Stability analysis and evaluation of surrounding rock of ultra-deep shaft under complicated geological conditions.
Front. Earth Sci. 11:1216667.
doi: 10.3389/feart.2023.1216667

Stability analysis and evaluation of surrounding rock of ultra-deep shaft under complicated geological conditions

Kuikui Hou[1,2]*, Mingde Zhu[1,2], Yingjie Hao[1,2]*, Yantian Yin[1,2]* and Long An[3]*

[1]Deep Mining Laboratory of Shandong Gold Group Co, Ltd., Laizhou, China, [2]Shandong Key Laboratory of Deep-sea and Deep-earth Metallic Mineral Intelligent Mining, Jinan, China, [3]Key Laboratory of Ministry of Education for Safe Mining of Deep Metal Mine, Northeastern University, Shenyang, China

The construction of deep underground engineering is greatly influenced by complex geological conditions such as high stress, faults, and fracture zones, which significantly affects the stability of the project. Taking the construction of 1,915-m-deep shaft in Sanshandao Gold Mine as the engineering background, which passes through many different strata and multiple fracture zones, the stability evaluation and failure zone prediction during its excavation under the influence of high stress, uneven strata, and fault structure are studied. Results show that the range of the failure zone increases significantly when the shaft passes through the fracture zone or different lithologies, and the maximum depth is 5.28 m. When the distance between the rock mass in the borehole and the excavation face is greater than 48 m, the disturbance superposition effect basically disappears. This paper provides theoretical and data support for the design and construction of the kilometer-deep shaft in Sanshandao Gold Mine.

KEYWORDS

deep shaft, uneven strata, surrounding rock stability, fault, damage proximity

1 Introduction

With the depletion of shallow resources, metal mines at domestic and abroad have gradually entered the stage of deep mining. As the first project of deep mining, the construction of deep shafts has become the primary problem to be solved. Overviewing the deep mining activities at domestic and abroad, many deep shafts with a depth of over 2,000 m have been built and operated in South Africa, Canada, the United States, and Russia. The deep shafts that have been built in China include the main and auxiliary shafts of Sishanling Iron Mine of Jianlong Group, with depths of 1,505 and 1,503.9 m, respectively, the No. 3 shaft of Huize lead–zinc mine in Yunnan Province, with a depth of 1,526 m, and the new main shaft of Xincheng Gold Mine in the Shandong Gold Group, with the depth of 1,527 m. However, there are few engineering examples of shafts deeper than 1,500 m (Zhao, 2018; Tan et al., 2021). The deep shaft, with a depth of over 1,000 m, passes through multi-layer non-uniform complex strata, faults, and fracture zones of different scales during the construction process. Therefore, due to the influence of high stress and complex geological conditions, there are obvious regional differences in the mechanical response characteristics of the surrounding rock on the shaft wall during its construction, bringing difficulties to the stability control of the rock mass during the construction process (Kaiser et al., 1983; Gao

et al., 2009; He et al., 2009; Wang et al., 2009; Qian and Zhou, 2018; Zhang and Zhou, 2020; Wang et al., 2022; Li et al., 2023; Zhang et al., 2023).

Experts in the field of shaft construction and rock mechanics have carried out many research studies on borehole stability when shafts or tunnels pass through rock mass of different strata (Liu et al., 2016; Song et al., 2018; Walton et al., 2018; Cheng et al., 2020; Li and Wang, 2020; Huang et al., 2022). Sun et al. (2020) utilized UDEC software combined with surface subsidence monitoring to analyze the stress and displacement meter damage changes in rock mass of a shaft of Jinchuan Group at different mining stages of the ore body and pointed out that as the mining activities pass through the upper and lower parts of the fault, it will be activated in different ways, and suggestions were made for the stability of the shaft during the operation. Gao et al. (2021) analyzed the stress distribution of the surrounding rock in granite and homogeneous mixed rock strata using FLAC3D and demonstrated clear requirements for the strengthening of the lining concrete, aiming at the wall cracking of the west second auxiliary shaft of Longshou Mine in the Jinchuan mining area. Feng et al. (2012) pointed out that the instability and failure of the tunnel mostly occurred in the contact zone of soft and hard rocks and studied the stress distribution during excavation using FLAC3D. It was concluded that there is obvious stress concentration and uneven distribution in the soft and hard rock foundation zone after tunnel excavation. The stress is concentrated in hard rock, whereas a certain degree of stress release occurs in the soft rock area. The plastic zone of soft rock is significantly larger than that of hard rock. Yassaghi and Salari-Rad (2004) illustrated that the stress concentration occurs when the tunnel passes through the fault zone. The convergence value of the roadway near the fault zone is approximately 3% higher than that of the normal area. The deformation of the tunnel gradually stabilizes after 1 month of excavation. Sun et al. (2018) used 3DEC to analyze the deformation characteristics of rock mass and borehole when the shaft passes through different lithologies and pointed out that shear stress concentration occurs in the contact zone of soft and hard rocks, where the depth of the plastic zone is the largest, forming a pressure relief zone.

The aforementioned research studies analyze the deformation law and instability mode of surrounding rock and supporting system when the shaft or tunnel passes through different strata or fault zones at different angles. However, in view of the lack of systematic research on crossing multi-layer non-uniform complex strata during construction, this paper uses FLAC3D to analyze stability and evaluate failure zone prediction of the 1,915-m auxiliary shaft of Sanshandao Gold Mine, which is the deepest shaft in China and the fourth deepest shaft in Asia. First, the failure proximity index is introduced for rock mass stability analyzation. Meanwhile, the size characteristics and variation law of the failure zone are predicted. The study provides theoretical and foundation data support for shaft construction and its long-term stability.

2 Engineering background

On the purpose of the construction of a 1,915-m auxiliary shaft in Sanshandao Gold Mine, a 2,017-m prospecting hole was drilled in the center of the shaft; the wellhead elevation was 15 m. During the drilling process, the core investigation, *in situ* stress test, and rock mechanics experiments were carried out simultaneously, which obtained the distribution of strata, the variation law of *in situ* stress, and the mechanical parameters of rock mass in this deep shaft, respectively. According to the results of the *in situ* stress test, its three-dimensional variation law (Hou et al., 2022) is shown in Eq. 1. The investigation results showed that the auxiliary shaft of Sanshandao Gold Mine passes through seven different lithologies and six obvious fracture structures during its construction. Based on the results of rock mechanics experiment and rock mass quality classification, the whole length of the geological exploration borehole was divided into 18 areas with the lithology boundary and fault as the interface, as shown in Figure 1. According to the results of engineering exploration, it can be seen that the 1,915-m auxiliary shaft of Sanshandao Gold Mine is affected by the combined action of complex geological conditions such as uneven strata, high stress, and fault structure, which inevitably leads to the deformation and failure characteristics of borehole rock mass showing significant regional differences.

$$\begin{cases} \sigma_H = 0.030H + 10.142, \\ \sigma_h = 0.020H + 7.986, \\ \sigma_v = 0.027H - 0.019, \end{cases} \tag{1}$$

where H is the depth of rock mass, σ_H is the maximum horizontal principal stress, σ_h is the minimum horizontal principal stress, and σ_v is the vertical principal stress.

3 Numerical simulation of the deep shaft excavation process under uneven stratum conditions

3.1 Numerical calculation model and scheme

According to the results of the rock mass quality investigation and *in situ* stress test of the exposed strata, a refined numerical calculation model of the auxiliary shaft of Sanshandao Gold Mine was established, and the corresponding rock mechanics parameters were assigned to the 18 rock mass regions. The excavation response characteristics of rock mass under the combined influence of stress state, uneven strata, and faults were analyzed, and the stability of surrounding rock was evaluated. Since the design diameter of this shaft section was 10.5 m, the diameter of this model was set to 10.5 m, as shown in Figure 2. In order to eliminate the boundary effect of the model, its scale was set to 3–5 times of the engineering scale. Meanwhile, the model size was 100 m × 100 m × 2,200 m, and the single excavation footage of this model was 5.0 m.

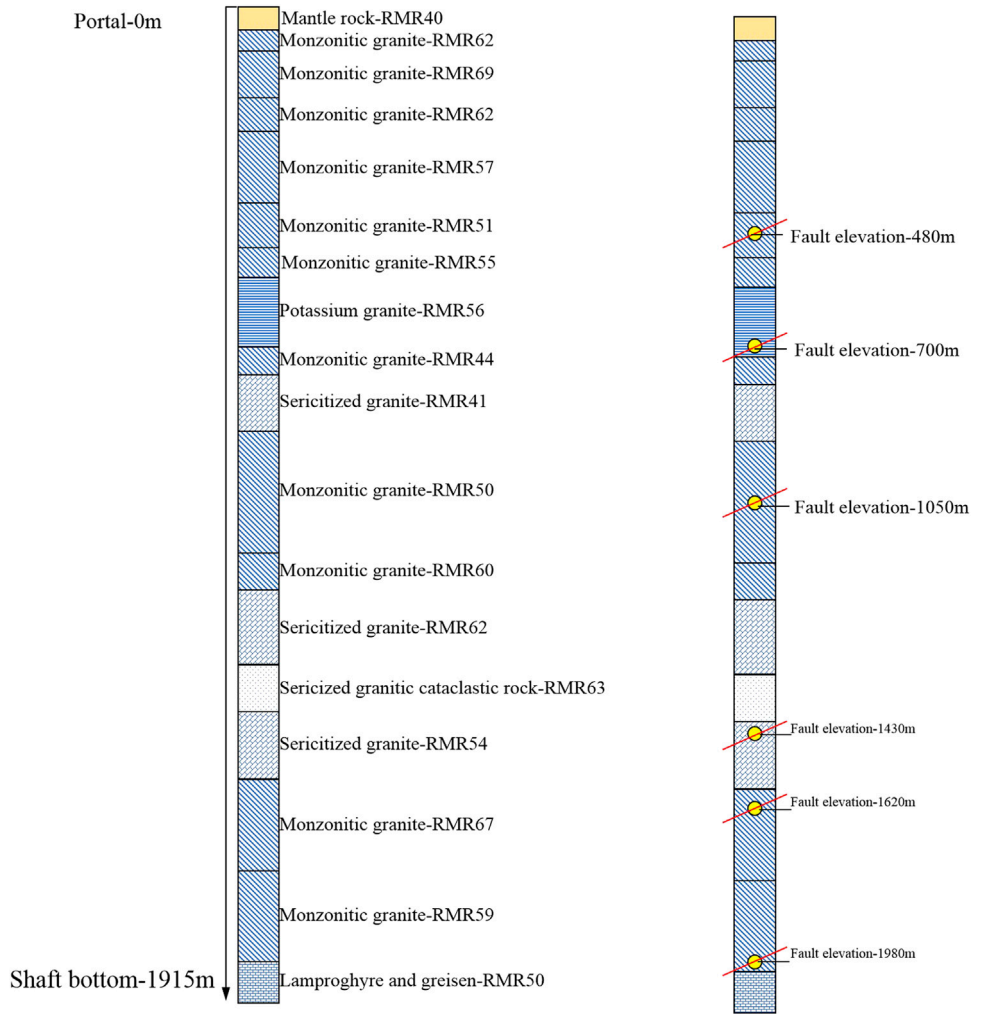

FIGURE 1
Diagram of the shaft crossing different strata.

3.2 Boundary conditions and assignment parameters

In this paper, the Hoek–Brown criterion (Sun et al., 2011; Hoek and Brown, 2019; Renani and Cai, 2021) was used to carry out numerical simulation. The boundary conditions were the normal displacement constraints on the left, right, front, back, and upper boundaries of the model and the three-way fixed displacement constraints at the bottom. The stress conditions of the model were set according to the *in situ* stress results, and the calculation expression of rock mechanical parameters is given as follows:

$$\begin{cases} c = \sigma_{ci}[1 + 2a + (1-a)m_b\sigma_{3n}]f_c \Big/ \left[f_a\sqrt{1 + \dfrac{f_b f_c}{f_a}}\right], \\ \varphi = \sin^{-1}\left[f_b f_c/(2f_a + f_b f_c)\right], \\ \sigma_T = -s\sigma_{ci}/m_b, \end{cases} \tag{2}$$

where φ represents the internal friction angle of rock mass, c represents cohesion, and σ_T represents the tensile strength of rock mass. $f_a = (1 + a)\ (2 + a)$ and $f_b = 6am_b$, $f_c = (s + m_b\sigma_{3n})^{a-1}$, where $\sigma_{3n} = \sigma_{3max}/\sigma_{ci}$, $\sigma_{3max} = 0.47\sigma_{cm}\ [\sigma_{cm}/\gamma H]^{-0.94}$, and σ_{cm} represents the rock mass strength, $\sigma_{cm} = \sigma_{ci}[m_b + 4s\text{-}a\ (m_b\text{-}8s)\ (m_b/(4+s))^{a-1}]/2f_a$. Furthermore, a, s, and m_b represent Hoek–Brown material parameters related to rock damage.

$$\begin{cases} s = \exp\left[(GSI - 100)/(9 - 3D)\right], \\ a = 0.5 + 1/6\left[\exp(-GSI/15) - \exp(-20/3)\right], \\ m_b = m_i \exp\left[(GSI - 100)/(28 - 14D)\right]. \end{cases} \tag{3}$$

The value m_i in the aforementioned formula is the empirical parameter of rock dimension, which is obtained using the following empirical formula (Zhang et al., 2019):

$$\sigma_{ci}/|\sigma_t| = 0.81m_i + 7. \tag{4}$$

GSI is a geological strength index, which can be estimated from the *RMR* (rock mass classification index) value. The empirical

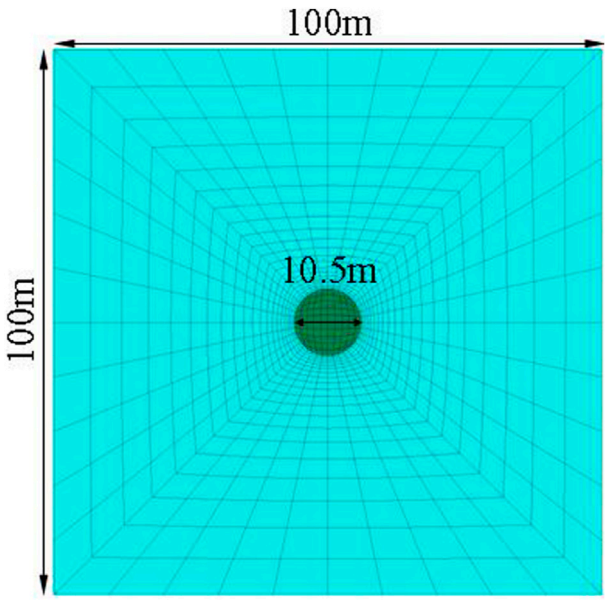

FIGURE 2
Section of numerical calculation model.

relationship between *RMR* and *GSI* is obtained from Zhang et al. (2019) as follows:

$$RMR = 0.827GSI + 15.394. \quad (5)$$

D is the coefficient of the disturbance degree of blasting or stress release to rock mass, and its value ranges from 0 (not disturbed) to 1 (the maximum disturbance), and the disturbance parameter *D* is 0.2. Parameters obtained from the aforementioned formulas are summarized in Table 1.

3.3 Evaluation method of the surrounding rock failure zone based on the failure proximity index

The plastic zone obtained according to the current failure criterion can only determine the range of the damage zone and cannot further quantify its damage degree. Therefore, the damage proximity index (Liu et al., 2009; Zhang et al., 2011) is used to evaluate the failure of the rock mass. *FAI* is a comprehensive quantitative evaluation index of risk degree, and its calculation expression is given as follows:

$$FAI = \begin{cases} \omega, & 0 \le \omega < 1, \\ 1 + FD & \omega = 1, FD \ge 0, \end{cases} \quad (6)$$

where *FD* is the degree of failure and ω is the complementary parameter of yield approachability *YAI*, given as $\omega = 1 - YAI$, where *YAI* is the yield approachability function. The formula of yield

TABLE 1 Material assignment parameters.

Model assignment range	*RMR*	Compressive strength/MPa	Elastic modulus/GPa	Poisson ratio	m_b	*s*	*a*
0< Z <−10 m	48	34.43	24.87	0.24	1.711	0.003	0.505
−10< Z <−50 m	60	42.72	23.81	0.20	1.094	0.017	0.502
−50< Z <−200 m	69	139.0	56.80	0.15	5.680	0.052	0.501
−200< Z <-370 m	62	87.87	45.69	0.16	4.739	0.020	0.502
−370< Z <−550 m	57	96.89	69.19	0.25	4.272	0.011	0.503
−550< Z <−650 m	51	126.67	60.33	0.21	2.922	0.005	0.504
−650< Z <−780 m	55	60.79	53.02	0.21	1.732	0.009	0.503
−780< Z <−970 m	56	72.99	47.63	0.21	2.665	0.011	0.503
−970< Z <−1,020 m	44	104.87	39.62	0.28	2.182	0.002	0.507
−1,020< Z <−1,060 m	41	117.53	56.51	0.19	1.885	0.001	0.508
−1,060< Z <−1,150 m	50	152.51	72.25	0.20	6.163	0.005	0.504
−1,150< Z <−1,350 m	60	128.25	52.24	0.27	5.260	0.016	0.502
−1,350< Z <−1,680 m	62	82.76	27.21	0.18	4.672	0.020	0.502
−1,680< Z <−1,730 m	63	49.70	22.80	0.19	2.951	0.023	0.502
−1,730< Z <−1,750 m	54	98.63	47.70	0.15	2.623	0.008	0.503
−1,750< Z <−1,840 m	67	129.0	49.07	0.20	5.002	0.040	0.501
−1,840< Z <−1,970 m	59	114.0	50.86	0.19	3.480	0.015	0.502
−1,970< Z <−2,200 m	50	104.93	56.73	0.18	2.475	0.004	0.504

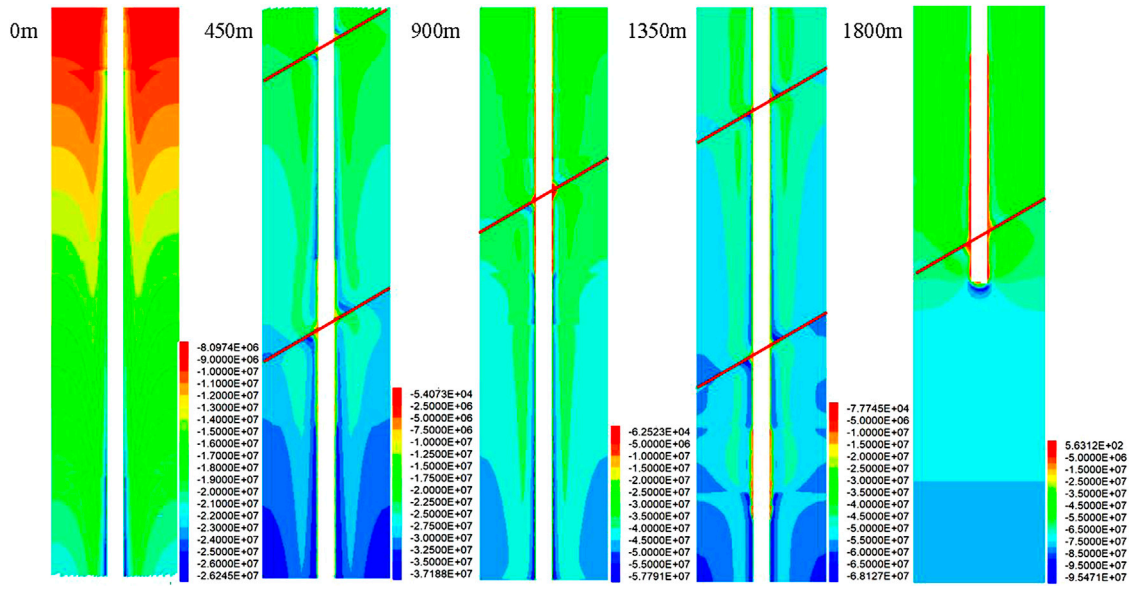

FIGURE 3
Cloud diagram of the maximum principal stress of the surrounding rock after deep shaft excavation.

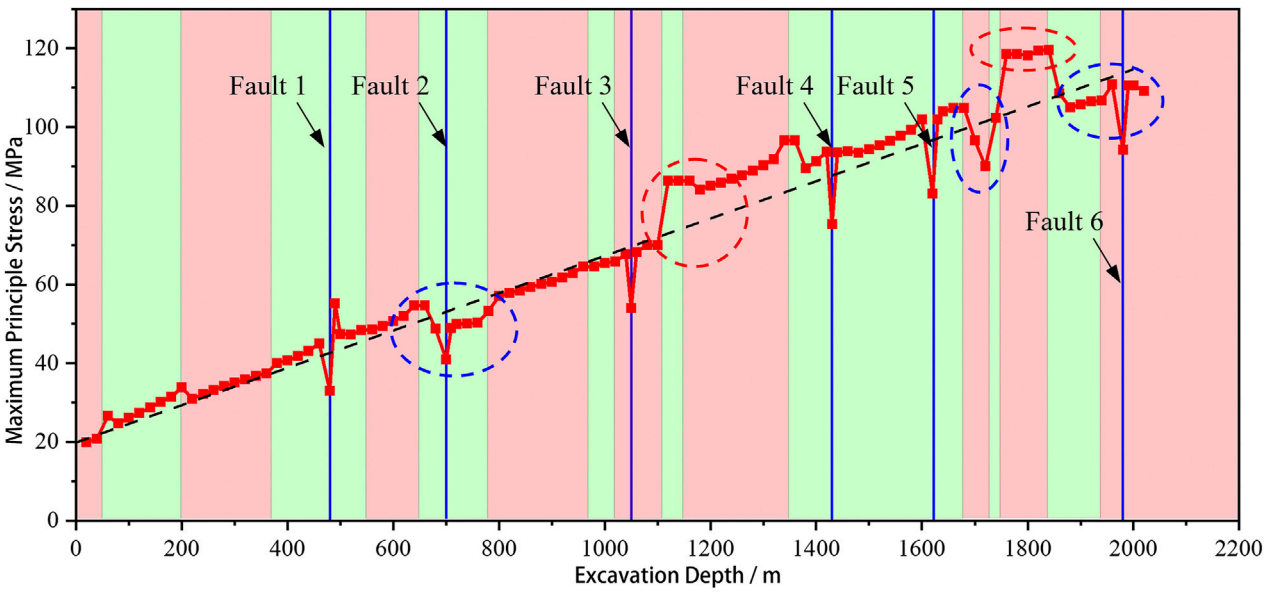

FIGURE 4
Variation law of maximum principal stress with excavation depth.

approachability function based on the Hoek–Brown criterion is as follows:

$$YAI = \begin{cases} \dfrac{-\beta\tau_\pi}{\alpha_{hb}\sigma_\pi + \gamma_{hb}} & \dfrac{\sigma_1+\sigma_3}{2} \le \sigma_{Rhb}, \\ \dfrac{\sigma_1-\sigma_{Rhb}}{\sigma_L-\sigma_{Rhb}} & \dfrac{\sigma_1+\sigma_3}{2} > \sigma_{Rhb}, \end{cases} \tag{7}$$

$$\beta = \left(\cos\theta_\sigma - \sin\theta_\sigma \sin\varphi/\sqrt{3}\right)/\sqrt{2}, \tag{8}$$

$$\alpha_{hb} = f_a f_b/\left(2\sqrt{3}\, f_a + \sqrt{3}\, f_b f_c\right), \tag{9}$$

$$\sigma_{Rhb} = \left[\sigma_r\left(4f_a + f_b f_c\right) + \left(2f_b f_c\right)\gamma_{hb}\right]/\left(4f_a\right), \tag{10}$$

$$FD = \bar{\gamma}_p/\bar{\gamma}_p^r, \tag{11}$$

where θ_σ is the stress lode angle; σ_π and τ_π are normal stress and shear stress components of the plane, respectively; γ is the rock mass density; H is the depth of embedment; $\bar{\gamma}_p$ is the plastic shear strain, $\bar{\gamma}_p = \sqrt{\frac{1}{2}e_{ij}^p e_{ij}^p}$, where plastic deviatoric strain

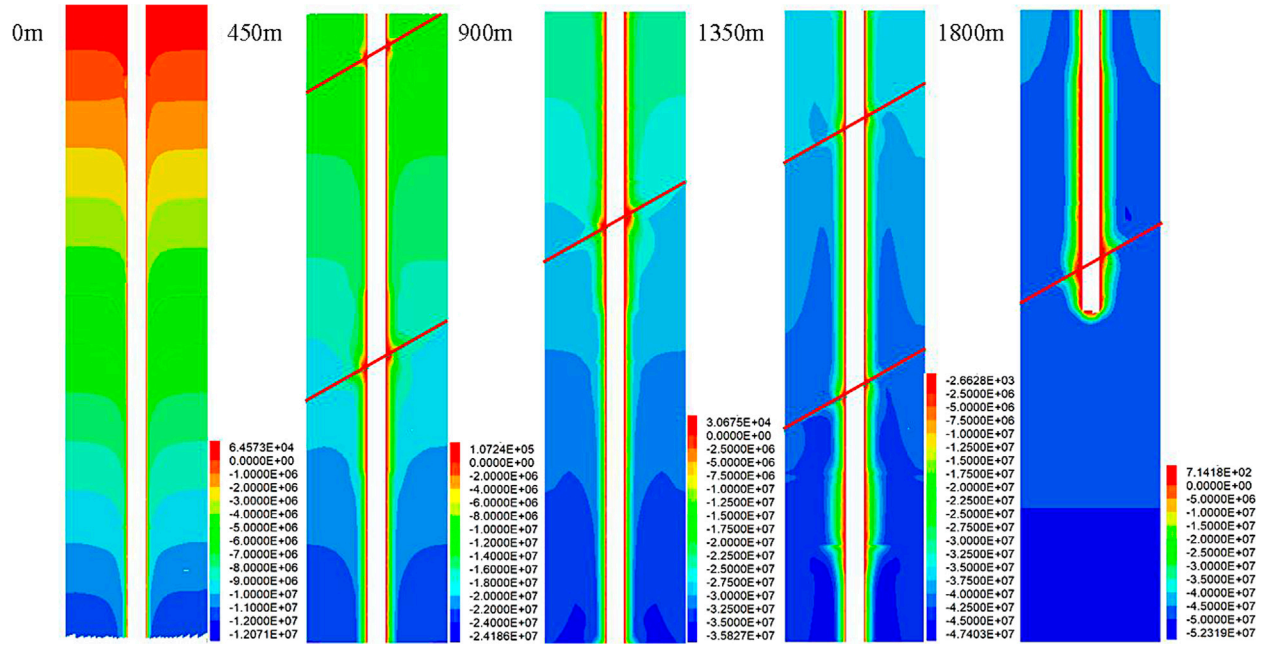

FIGURE 5
Cloud diagram of the minimum principal stress of the surrounding rock after deep shaft excavation.

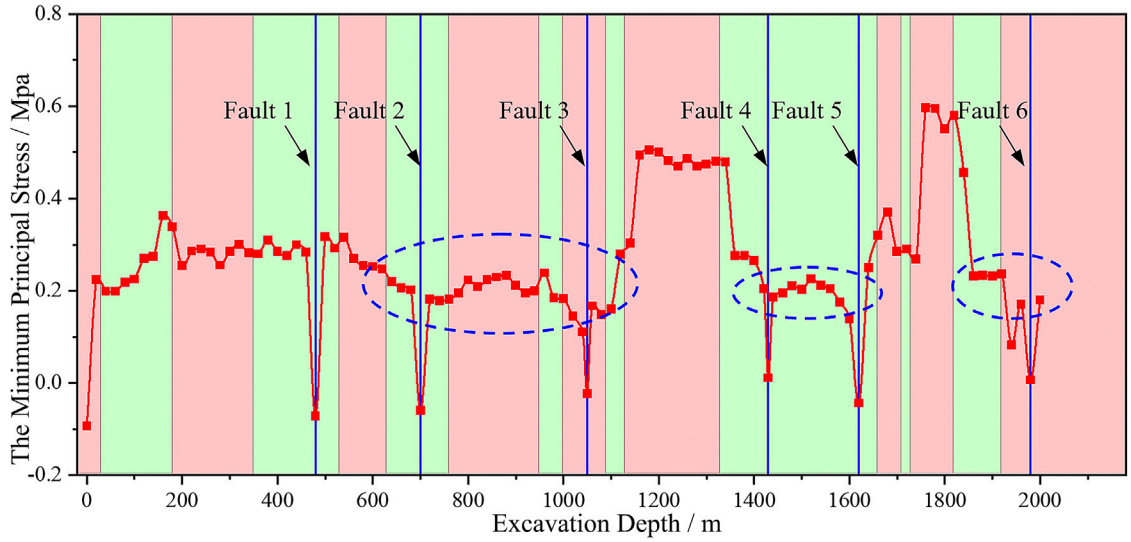

FIGURE 6
Variation in minimum principal stress with excavation depth.

$e_{ij}^p = \varepsilon_{ij}^p - \varepsilon_m^p \delta_{ij}$; and $\bar{\gamma}_p{}^r$ is the calculation of the plastic shear strain of materials.

In summary, the *FAI* index can be used to characterize the rock failure degree intuitively and quantitatively. Moreover, it can predict the distribution and size of the rock failure zone after shaft excavation. When $FAI \geq 2.0$, the rock is seriously broken and failure occurs. In this paper, the area with $FAI \geq 2.0$ is defined as the instability zone.

4 Numerical simulation results

4.1 Distribution characteristics of the surrounding rock stress field

As shown in Figures 3, 4, with the increase in buried depth, the maximum principal stress of the surrounding rock also increases. However, due to the influence of uneven strata, the maximum

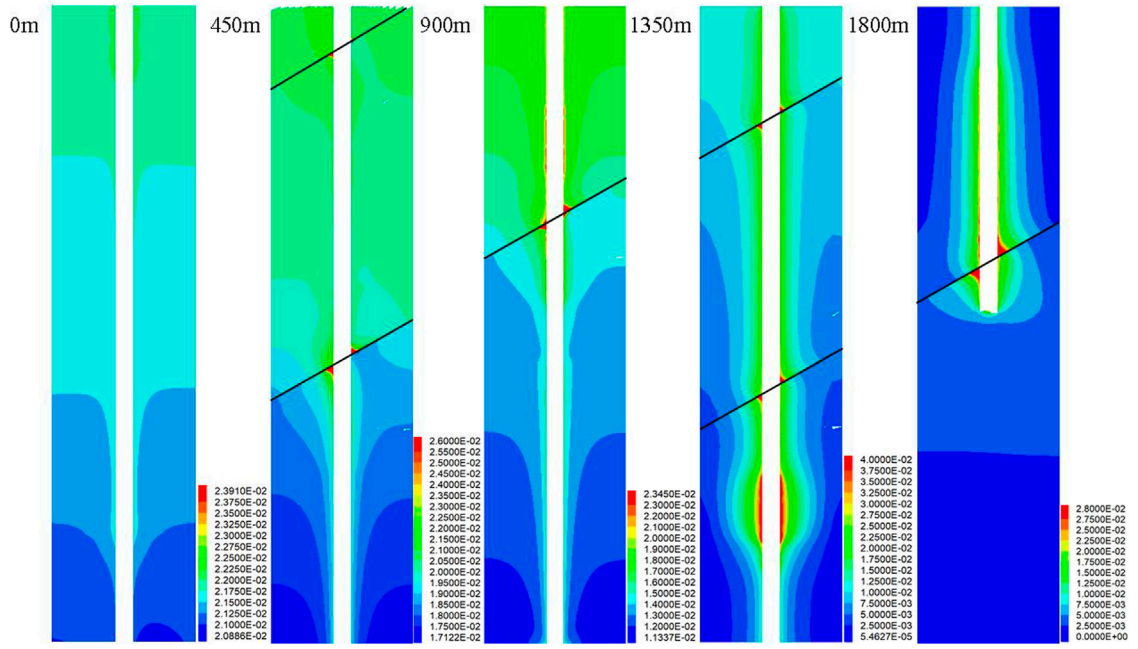

FIGURE 7
Cloud image of surrounding rock displacement after deep shaft excavation.

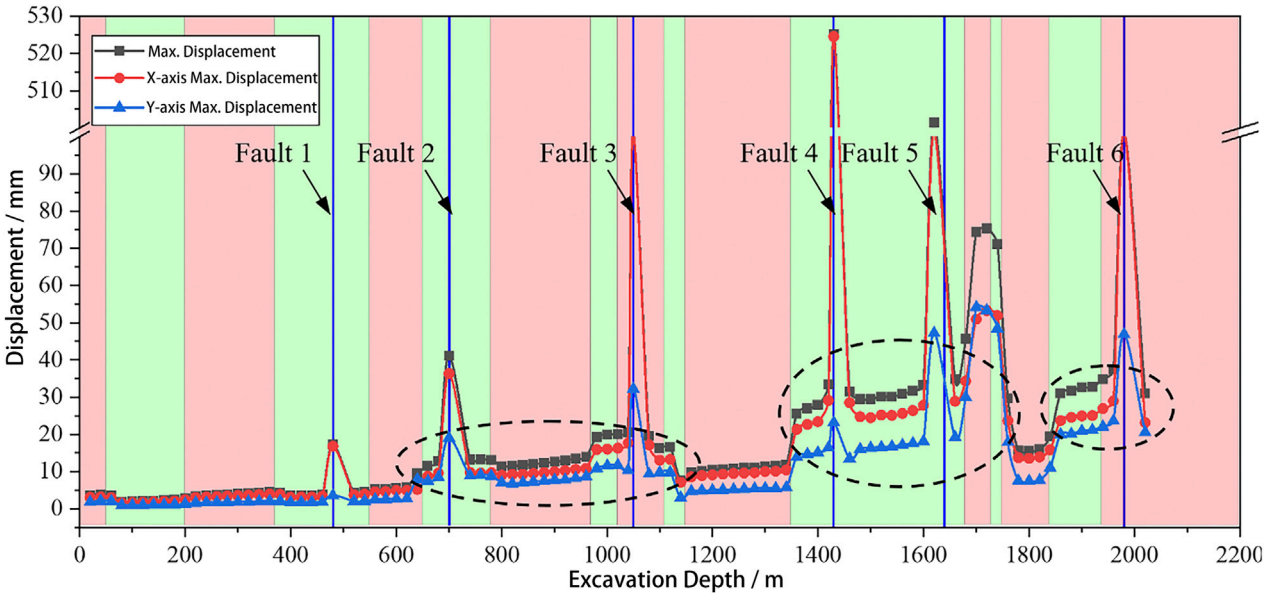

FIGURE 8
Variation in surrounding rock displacement with excavation depth.

principal stress changes non-linearly with the increase in buried depth, and it experiences a significant increase or decrease in some areas. It shows a critical decrease at the depth from −680 to −780 m, −1,680 to −1,750 m, and −1,820 to −2,050 m. The comparative analysis shows that the mechanical properties of the rock mass corresponding to these three areas are lower than those of the adjacent strata and the rock mass is weak and broken, which indicates that the reduction degree of the maximum principal stress is critically influenced by the difference in mechanical properties between adjacent strata. The maximum principal stress increases strongly in the two areas of buried depths from −1,050 to −1,350 m and −1,750 to −1,850 m. The rock mass in the aforementioned two areas is relatively complete and hard, whereas the stress concentration effect on the surrounding

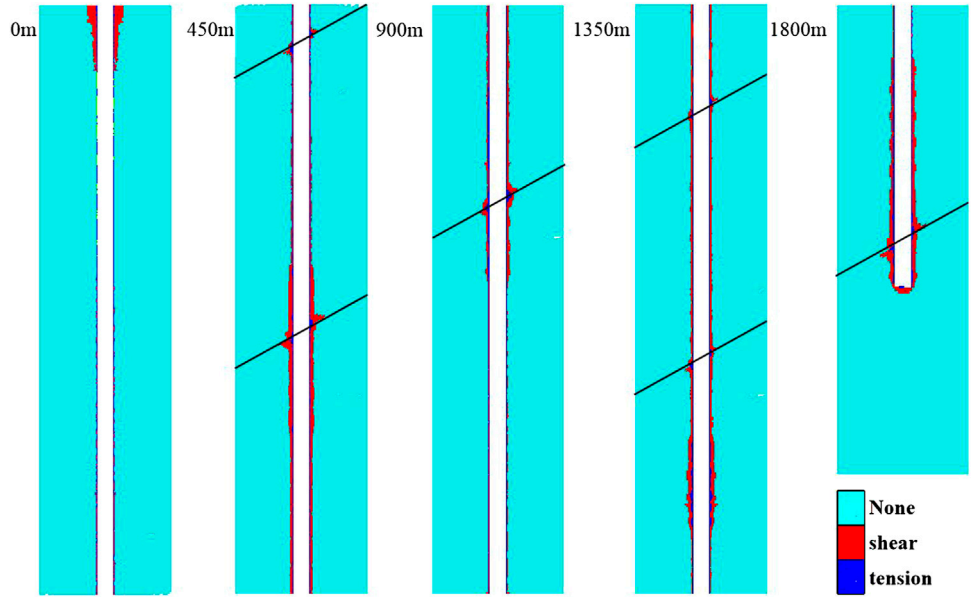

FIGURE 9
Plastic zone distribution of the surrounding rock after deep shaft excavation.

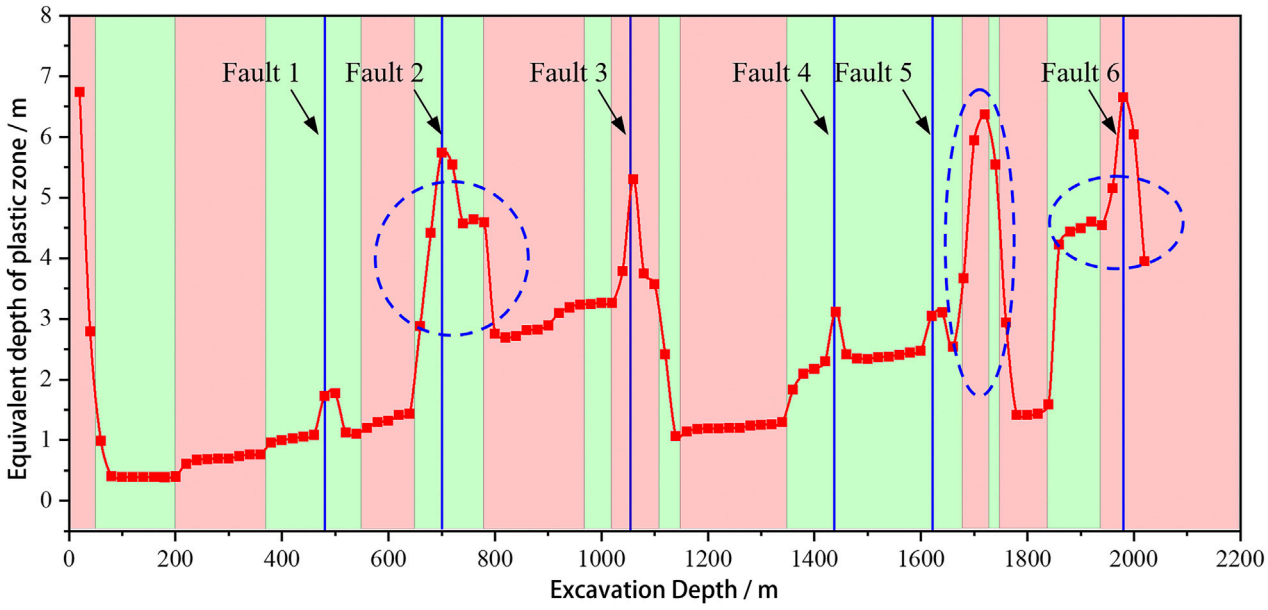

FIGURE 10
Variation in plastic zone depth with the excavation depth of the shaft section.

rock is significant. The maximum principal stress value at the fault reduced obviously, and its reduction value differs with the increase in buried depth. When the buried depth is less than 500 m, the reduction value caused by the fault is 10 MPa. Compared with the buried depth from 500 to 1,200 m, its value is 15 MPa. When the buried depth is greater than 1,200 m, it could reach 20 MPa. Therefore, with the increase in buried depth, the initial *in situ* stress increases, and the unloading effect at the fault caused by shaft excavation is significant, which indicates that the support should be strengthened.

Figures 5, 6 show that the pressure relief zone is generated near the borehole, and the depth of the pressure relief zone at the fault position is obviously increased. According to the distribution of the minimum principal stress, it is obviously reduced from −650 to −1,150 m, −1,350

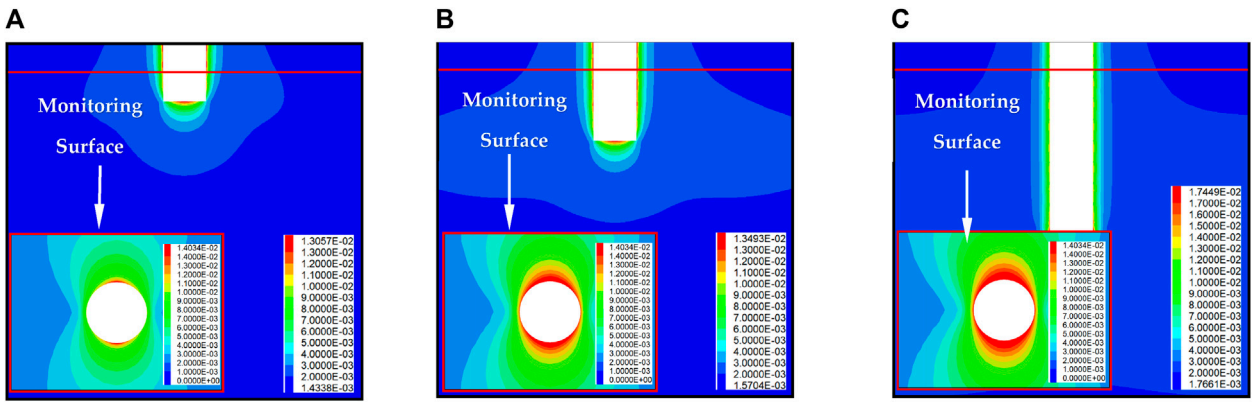

FIGURE 11
Displacement variation in the monitoring surface with excavation depth: **(A)** 6 m between excavation and monitoring face; **(B)** 18 m between excavation and monitoring face; and **(C)** 48 m between excavation and monitoring face.

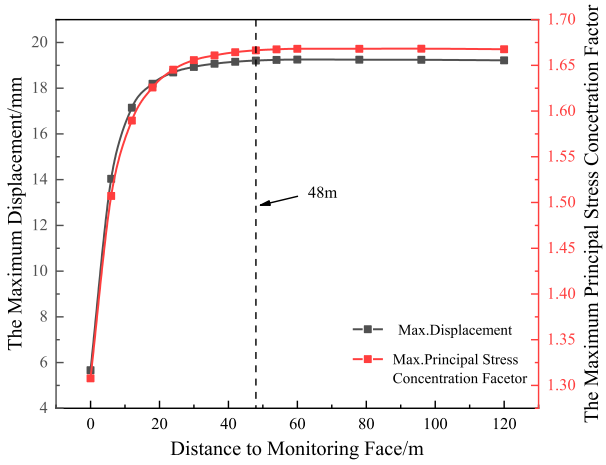

FIGURE 12
Maximum displacement and maximum principal stress concentration coefficient of the monitoring surface varying with the distance from the excavation surface.

to −1,650 m, and −1,850 to −1,980 m, respectively, with a critical unloading phenomenon, which demonstrates the support system on the borehole should be strengthened, and the forced state of the borehole is changed from compression to tension due to the existence of fault. It further aggravated the risk of borehole caving.

4.2 Distribution characteristics of the surrounding rock displacement field

As shown in Figures 7, 8, with the increase in buried depth, the displacement of the borehole shows an increasing trend. Affected by uneven strata, the displacement of surrounding rock increases sharply in some areas. The displacement increases sharply in the depth from −650 to −1,050 m, −1,350 to −1,750, and −1,850 to −1,950 m. Among the non-fault areas from −1,680 to −1,720 m, it reaches the maximum value of 75.75 mm. By analyzing the distribution law of the initial maximum principal stress direction, the minimum principal stress direction, and the displacement of rock mass in the area without the interface between the fault and the lithology, it can be seen that the displacement value in the maximum principal stress direction is greater than that in the minimum principal stress direction, and the displacement difference in those two directions gradually increases with the increase in the buried depth. It reaches 10 mm when the excavation depth is between 1,400 and 1,700 m. Moreover, the displacement in the direction of the maximum principal stress at the fault is seven times more than that in the direction of the minimum principal stress. For example, at a depth of −480 m, the displacement value in fault is 13.17 mm higher than that in rock mass near the borehole, and this difference increases to 29.23 mm at −700 m, 103.06 mm at −1,050 m, 495.90 mm at −1,430 m, 467.28 mm at −1,620 m, and 139.78 mm at −1,980 m. It can be seen that the influence of fault on surrounding rock displacement is more significant than that of excavation depth and stratum condition.

Through the analysis of displacement, it demonstrates that displacement increases from −650 to −1,050 m, −1,350 to −1,750 m, −1,850 m to −1,950 m, and six fault zones. It experiences a significant increase below −1,000 m due to the comprehensive influence of high stress and discontinuity structure. Timely and strong support measures should be considered, such as long anchor cables and lining concrete.

4.3 Distribution characteristics of the plastic zone

From Figures 9, 10, it can be concluded that the failure type of the shaft is mainly shear failure (Li and Wang, 2020). When the buried depth is shallow, tensile failure and shear–tensile mixed failure appear in the borehole rock mass. With the increase in buried depth, the *in situ* stress increases and the depth of the plastic zone also increases. However, due to the influence of uneven rock strata, the plastic

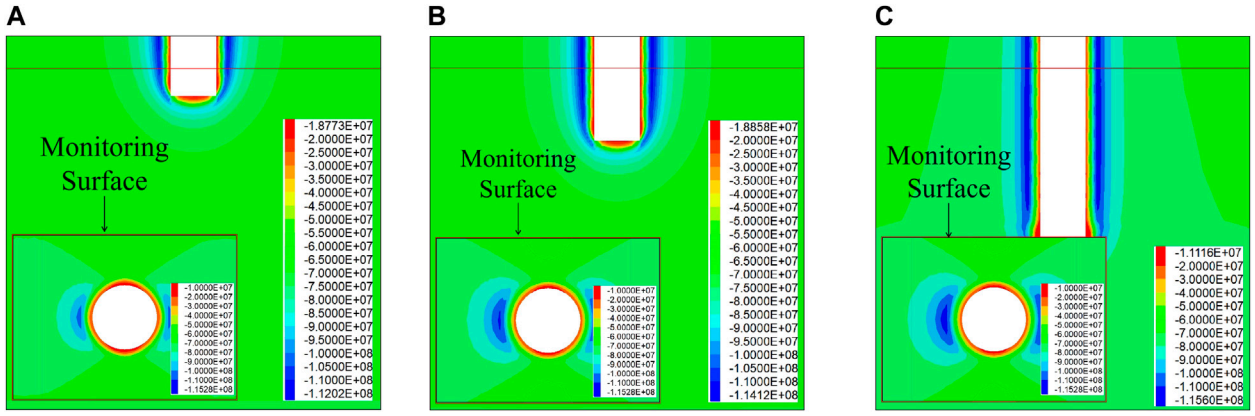

FIGURE 13
Nephogram of maximum principal stress of the monitoring surface with excavation depth: **(A)** 6 m between excavation and monitoring face; **(B)** 18 m between excavation and monitoring face; and **(C)** 48 m between excavation and monitoring face.

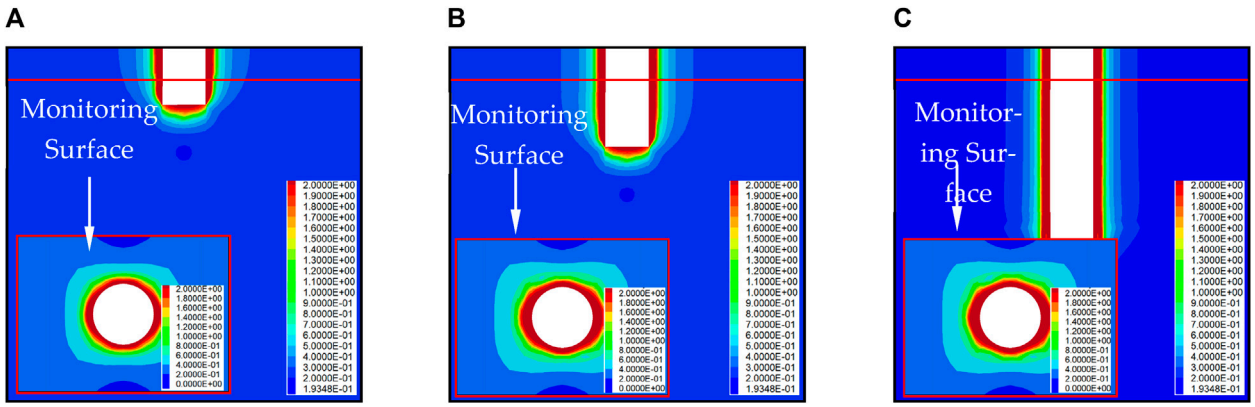

FIGURE 14
Variation rule of the monitoring surface with the depth of the excavation failure zone: **(A)** 6 m between excavation and monitoring face; **(B)** 18 m between excavation and monitoring face; and **(C)** 48 m between excavation and monitoring face.

zone in the local area fluctuates. From −650 to −1,150 m, −1,680 to −1,750 m, and −1,900 to −2,000 m, the equivalent depth of the plastic zone increases significantly, resulting in the deterioration of rock mass mechanical parameters. Among them, it has the most critical increase from −680 to −780 m and −1,680 to −1,750 m, which are 5.73 and 6.38 m, respectively. In the region of buried depth from −1,080 to −1,350 m, the equivalent depth of the plastic zone decreases significantly due to the strengthening mechanical parameters of the rock mass. In addition, the plastic zone of the surrounding rock at the fault increases obviously, and there are more shear–tensile mixed failure in the rock mass near the fault.

Meanwhile, the equivalent depths of the plastic zones in the fault area buried at −480 , −700, −1,050, −1,430, −1,620, and −1,980 m are, respectively, 0.64, 1.42, 2.58, 0.78, 0.58, and 1.89 m higher than those of the surrounding rock near the fault. It can be obtained that the variation in the plastic zone caused by faults at different buried depths differs due to the influence of uneven strata, and its variation law is affected by faults, ground *in situ* stress, and geomechanical characteristic.

5 Stress release rule and damage superposition characteristics of surrounding rock in deep shaft excavation

The stress release and deformation of surrounding rock during shaft excavation will be constrained by the excavation face. Therefore, the stress during shaft excavation is released step by step, and its damage is affected by the distance from the excavation face. In this section, the shaft section at the buried depth of 1,900 m is used as the monitoring surface to analyze the stress release and damage evolution law of surrounding rock with the increase in the shaft excavation depth.

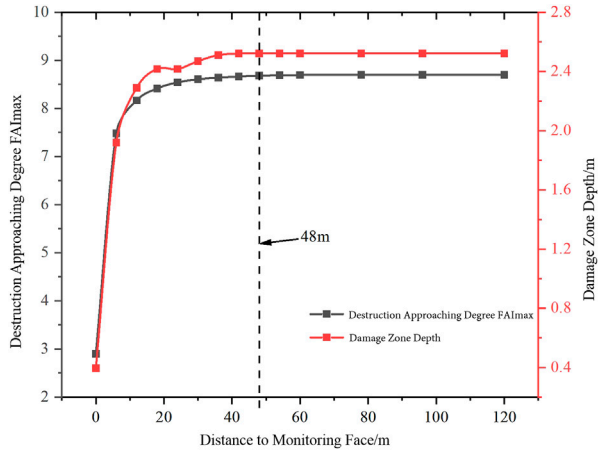

FIGURE 15
Variation in the failure zone on the monitoring surface with distance from the excavation surface.

Figures 11, 12 show that the distance between the monitoring surface and the excavation surface increases, and the displacement shows an increasing trend followed by a stable tendency. When excavating to the monitoring surface, due to the influence of the upper excavation, a displacement of 5.66 mm has been generated. With the first step of excavation, the displacement increases rapidly to 14.03 mm. As the excavation depth continues to increase, the displacement of the surrounding rock continues to increase, and its increment decreases. When the excavation depth reaches 48 m, the displacement increases by 19.21 mm, and it no longer increases and tends to be stable with the further increase in excavation depth.

Figures 12, 13 show that they have a similar displacement variation law. Due to the influence of the upper excavation, the maximum principal stress on the monitoring surface is 90.47 MPa, and the stress concentration factor is 1.31. With the first step of excavation, the stress is rapidly released, and the stress concentration occurs on both sides of the borehole. The maximum principal stress of the monitoring surface increases to 104.27 MPa, and the stress concentration factor increases to 1.51. With the increase in excavation depth, the degree of stress concentration continues to increase, and the increase in stress concentration decreases. When the excavation depth reaches 48 m, the stress concentration degree of the monitoring surface tends to be stable. At this time, the maximum principal stress of the monitoring surface increases to 115.28 MPa, and the stress concentration factor increases to 1.666.

Figures 14, 15 show that the displacement variation law is similar to the maximum principal stress variation tendency. Due to the influence of the upper excavation, the destruction approaching degree FAI_{max} of the monitoring surface is 2.89, and the depth of the failure zone is 0.39 m. With the first step of excavation, the surrounding rock around the monitoring surface is rapidly destroyed, the destruction approaching degree FAI_{max} of the monitoring surface increases rapidly to 7.48, and the depth of the damage zone increases to 1.92 m. As the excavation depth continues to increase, the depth of the failure zone and the degree of damage continue to increase, whereas the depth of the failure zone decreases. When the excavation depth reaches 48 m, the depth of the failure zone and the degree of damage to the monitoring surface basically tend to be stable. At this time, the destruction approaching degree FAI_{max} of the monitoring surface is 8.69, and the depth of the failure zone increases to 2.52 m.

In summary, with the increase in the distance between the working face and the monitoring section, the constraint effect of the working face is gradually weakened, and the stress is fully released. The displacement, the maximum principal stress concentration factor, the maximum value of destruction approaching degree, and the depth of the failure zone increase, indicating the expansion of the rock damage range and the increase

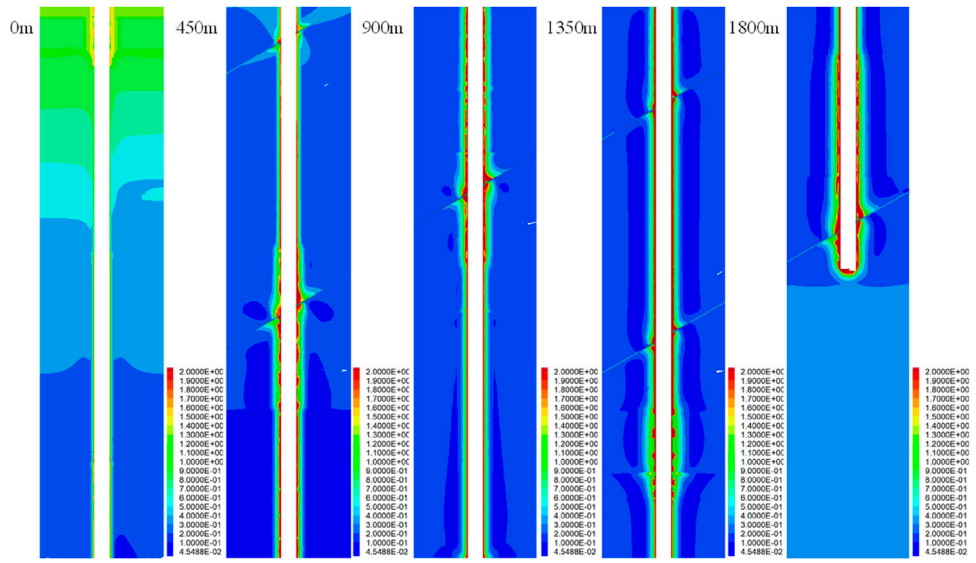

FIGURE 16
Variation in the failure area of shaft section distribution with excavation depth (including faults).

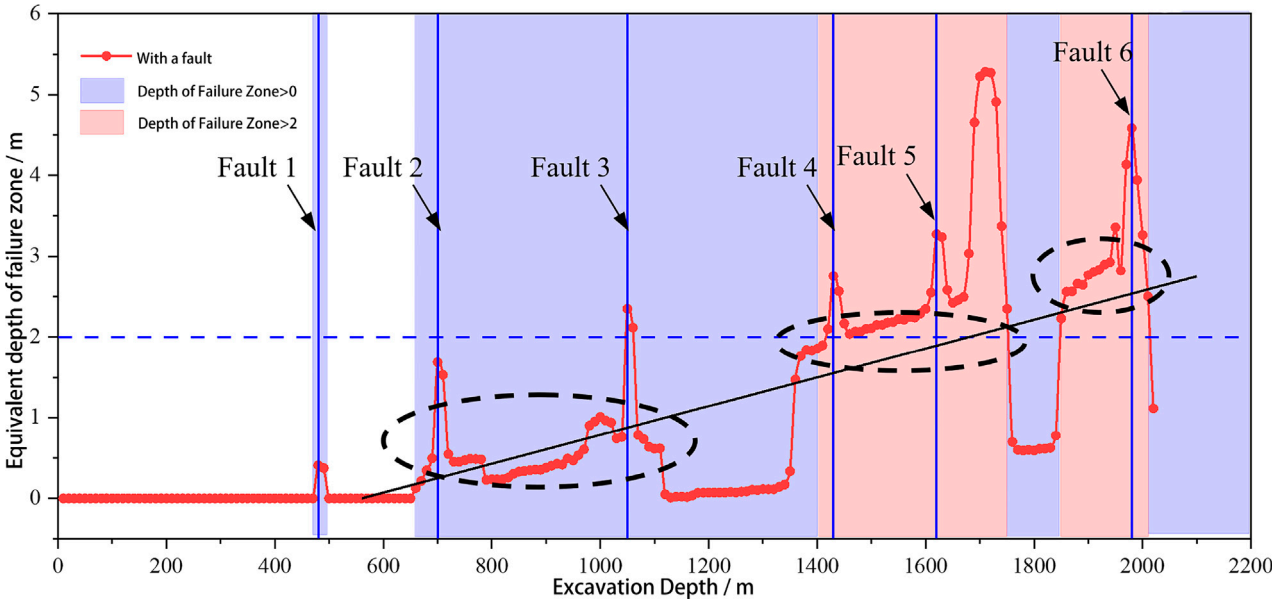

FIGURE 17
Variation rule of the equivalent depth of the failure zone with excavation depth.

in the degree of fragmentation. When the monitoring section is 48 m away from the excavation surface, the deformation of the surrounding rock is released by stress, and the changes in each evaluation index tend to be stable.

6 Failure range evaluation of the 1,915-m-deep shaft in Sanshandao Gold Mine

As shown in Figures 16, 17, with the increase in buried depth, there is no damage zone in the shallow rock mass. The first and only damage zone is located at the fault buried at −480 m. When passing through the fault, with the increase in excavation depth. When the excavation depth exceeds −660 m, the borehole begins to produce a damage zone. With the increase in excavation depth, the damage zone shows an increasing trend, but it is affected by the uneven stratum. There is a significant increase in the surrounding rock in the local area. The depth of the failure zone increases significantly in the three regions of −650 to −1,050 m, −1,350 to −1,750 m, and −1,850 to −2,016 m. Among them, the depth of the failure zone increases slightly in the region of −650 to −1,050 m, whereas it increases greatly from −1,350 m to −1,750 m. Particularly, in the region of −1,680 m to −1720 m, the damage reaches the peak (5.68 m). The change rule is consistent with the reduction zone of the minimum principal stress. It shows that the support strength of the surrounding rock should be strengthened in the aforementioned three areas during construction, and there are two serious damage areas in the whole shaft construction area, which locate at −1,400 to −1,750 m and −1,850 to −2,016 m. The depth of the serious damage area of the surrounding rock in the aforementioned two areas is more than 2 m. Similar to the aforementioned analysis of displacement and plastic zone, due to the existence of the discontinuous structure of the fault, the depth of the failure zone is significantly increased compared with the depth of the surrounding rock failure zone in the borehole. At the same time, when the buried depth reaches −480, −700, −1,050, −1,430, −1,620, and −1,980 m, the equivalent depth of the failure zone increases by 0.41, 1.34, 1.75, 0.72, 0.98, and 1.79 m, respectively.

Through the analysis of the failure zone, it will be generated at the depth of −480 m fault and more than −660 m area, and the stability of the surrounding rock should be paid attention to in the area where the failure zone will be generated. Moreover, a corresponding support plan should be formulated. Particularly, in the two areas of −1,400 to −1,750 m and −1,850 to −2,016 m, the depth of the failure zone exceeds 2 m. The traditional bolt support will no longer be able to meet the requirements of stability control in these two areas.

7 Results and conclusion

1) Through the analysis of stress, displacement, and plastic zone, with the increase in excavation depth and the decrease in rock mass quality, the maximum principal stress concentration value, displacement, and plastic zone area increase. The stress reduction zone, the deformation zone of rock mass, and the

increase in the area of the plastic zone are consistent: 650 to −1,050 m, −1,350 to −1,750 m, and −1,850 to −1,950 m. Particularly, in the area of −1,680 to −1,720 m, the displacement reaches a maximum value of 75.75 mm, with a 6.38 m plastic zone. The maximum displacement at fault reaches 525.06 mm, with a 6.64 m plastic zone.

2) Through the analysis of the stress release law and damage superposition characteristics of the surrounding rock during the shaft excavation, it is concluded that with the increase in the distance between the working face and the monitoring section, the constraint effect of the working face is gradually weakened, and the stress release is sufficient. When the distance between the monitoring section and the excavation face reaches 48 m, the deformation of the surrounding rock is released as stress, and the change in each evaluation index tends to be stable.
3) Through the analysis and prediction of the failure zone, except for the fault, there is no failure zone when the buried depth is less than 660 m. The depth of the failure zone is more than 2 m at the buried depth of −1,400 to −1,750 m and −1,850 to −2,016 m, and the depth of the failure zone reaches a maximum of 5.28 m.

Data availability statement

The original contributions presented in the study are included in the article/supplementary material; further inquiries can be directed to the corresponding authors.

Author contributions

KH: responsible for drafting the main text of the manuscript and for designing and conducting the experiments; YH and YY: software; MZ and LA: validation. All authors contributed to the article and approved the submitted version.

Funding

This research was funded by the National Science Foundation of Shandong Province, China (grant number ZR2021ZD36).

Acknowledgments

The authors would like to thank the research team members for their contributions to this work.

Conflict of interest

Authors KH, MZ, YH, and YY were employed by the company Deep Mining Laboratory of Shandong Gold Group Co., Ltd., Laizhou, China.

The remaining author declares that the research was conducted in the absence of any commercial or financial relationships that could be construed as a potential conflict of interest.

Publisher's note

All claims expressed in this article are solely those of the authors and do not necessarily represent those of their affiliated organizations, or those of the publisher, the editors, and the reviewers. Any product that may be evaluated in this article, or claim that may be made by its manufacturer, is not guaranteed or endorsed by the publisher.

References

Cheng, Q., Yi, D., Yuan, Q., Liu, T. X., Lei, H., and Wang, F. (2020). Large deformation analysis of tunnel-surrounding rock along the expressway from Wenchuan to Maerkang, China. *IOP Conf. Ser. Earth Environ. Sci.* 570 (5), 052058. doi:10.1088/1755-1315/570/5/052058

Feng, W. K., Huang, R. Q., and Li, T. B. (2012). Deformation analysis of a soft–hard rock contact zone surrounding a tunnel. *Tunn. Undergr. Space Technol. incorporating Trenchless Technol. Res.* 32, 190–197. doi:10.1016/j.tust.2012.06.011

Gao, M. S., Dou, L. M., Xie, Y. S., Gao, J., and Zhang, L. S. (2009). Latest progress on study of stability control of roadway surrounding rocks subjected to rock burst. *Procedia Earth Planet. Sci.* 1 (1), 409–413. doi:10.1016/j.proeps.2009.09.065

Gao, Y. L., He, Q. Y., Li, C. P., Wang, M., Han, X. L., Ma, B., et al. (2021). Analysis of shaft failure mechanism in the 1240m-1120m range of xier auxilisry shaft in Longshou mine of jinchuan deposit[J]. *Sicence Technol. Eng.* 21 (23), 9814–9822. doi:10.12404/j.issn.1671-1815.2023.23.03.00991

He, M. C., Gong, W. L., Li, D. J., and Zhai, H. M. (2009). Physical modeling of failure process of the excavation in horizontal strata based on IR thermography. *Min. Sci. Technol.* 19 (6), 689–698. doi:10.1016/s1674-5264(09)60128-9

Hoek, E., and Brown, E. T. (2019). The Hoek–Brown failure criterion and GSI – 2018 edition. *J. Rock Mech. Geotechnical Eng.* 11 (03), 445–463. doi:10.1016/j.jrmge.2018.08.001

Hou, K. K., Wu, Q. Z., Zhang, F. P., Peng, C., Liu, H. X., Liu, X. Q., et al. (2022). Application of different *in-situ* stress testing methods in 2005 meterss haft-building area of Sanshandao gold mine and the distribution law of *in-situ* stress [J]. *Geotech. Mech.* 43 (04), 1093–1102. doi:10.16285/j.rsm.2021.1172

Huang, J., Wei, X., Luo, Y., Gong, H., Liu, T., and Li, X. (2022). Analysis of the deformation characteristics of the surrounding rock mass of a deep tunnel during excavation through a fracture zone. *Rock Mech. Rock Eng.* 55 (12), 7817–7835. doi:10.1007/s00603-022-03056-7

Kaiser, P. K., Maloney, S., and Morgenstern, N. R. (1983). "The time dependent properties of tunnel in highly stressed rocks," in Proceedings of the 5th Congress ISRM (D), Melbourne, Australia, April 10–15, 1983. (A.A. Balkema), 329–335.

Li, H. H., and Wang, X. D. (2020). Deformation and failure law and control technology of surrounding rock in deep shafts[J]. *Metal. Mine* 533 (11), 11–18. doi:10.19614/j.cnki.jsks.202011002

Li, X. L., Zhang, X. Y., Shen, W. L., Wang, Y., Qin, Q., Lu, X., et al. (2023). Abutment pressure distribution law and support analysis of super large mining height face. *Int. J. Environ. Res. Public Health* 20 (2), 227. doi:10.3390/ijerph20010227

Liu, M., Zhang, J. M., Zhou, Z. P., and Xiang, Z. B. (2016). Analysis of the surrounding rock stability and supporting time of a soft rock tunnel in the red bed area[J]. *Saf. Environ. Eng.* 23 (03), 146–151+162. doi:10.13578/j.cnki.issn.1671-1556.2016.03.025

Liu, Q. Y., Zhu, Z. Q., Zhong, Z. Q., and He, X. Q. (2009). Yield proximity analysis of tunnel surrounding rock based on Hoek-Brown criterion [J]. *Geotech. Mech.* 30 (08), 2447–2451. doi:10.19713/j.cnki.43-1423/u.2008.05.008

Qian, Q. H., and Zhou, X. P. (2018). Failure behaviors and rock deformation during excavation of underground cavern group for Jinping I hydropower station. *Rock Mech. Rock Eng.* 51 (8), 2639–2651. doi:10.1007/s00603-018-1518-x

Renani, H. R., and Cai, M. (2021). Forty-year Review of the Hoek–Brown failure criterion for jointed rock masses. *Rock Mech. Rock Eng.* 55 (1), 439–461. doi:10.1007/s00603-021-02661-2

Song, Z. Y., Mao, A. Q., and Yi, S. S. (2018). Deformation analysis of surrounding rocks in weak and broken zone under high water[J]. *Transp. Sci. Technol.* 287 (02), 87–93. doi:10.3963/j.issn.1671-7570.2018.02.022

Sun, C., Zhang, X. D., and Zhang, J. J. (2011). Stability analysis of vertical shaft surrounding rock and supporting system in deep fracture [J]. *J. Chian Coal Soc.* 36 (4), 914–920. doi:10.13225/j.cnki.jccs.2013.04.019

Sun, Q. H., Ma, F. S., Guo, J., Li, G., and Feng, X. (2020). Deformation failure mechanism of deep vertical shaft in jinchuan mining area [J]. *Sustainability* 12 (6), 2226. doi:10.3390/su12062226

Sun, X. M., Li, G., Zhao, C. W., Liu, Y., and Miao, C. (2018). Investigation of deep mine shaft stability in alternating hard and soft rock strata using three-dimensional numerical modeling. *J. Process.* 7 (1), 2–17. doi:10.3390/pr7010002

Tan, J., Liu, Z. Q., Song, C. Y., Liu, Q. H., Long, Z. Y., and Ning, F. B. (2021). The status and development trend of shaft sinking technology in mines in China [J]. *Metal. mines* 539 (05), 13–24. doi:10.19614/j.cnki.jsks.202105002

Walton, G., Kim, E., Sinha, S., Sturgis, G., and Berberick, D. (2018). Investigation of shaft stability and anisotropic deformation in a deep shaft in Idaho, United States. *Int. J. Rock Mech. Min. Sci.* 105, 160–171. doi:10.1016/j.ijrmms.2018.03.017

Wang, J. X., Lin, M. Y., Tian, D. X., and Zhao, C. l. (2009). Deformation characteristics of surrounding rock of broken and soft rock roadway. *Min. Sci. Technol.* 19 (2), 205–209. doi:10.1016/s1674-5264(09)60039-9

Wang, S. K., Zhu, Z. G., Yu, Y. S., Cheng, Y., and Liu, J. M. (2022). Stability analysis and support optimization of shaft wall with deep high stress[J]. *Min. Res. Dev.* 42 (04), 38–44. doi:10.13827/j.cnki.kyyk.2022.04.028

Yassaghi, A., and Salari-Rad, H. (2004). Squeezing rock conditions at an igneous contact zone in the taloun tunnels, tehran-shomal freeway, Iran: A case study. *Int. J. Rock Mech. Min. Sci.* 42 (1), 95–108. doi:10.1016/j.ijrmms.2004.07.002

Zhang, C. Q., Zhou, H., and Feng, X. T. (2011). An index for estimating the stability of brittle surrounding rock mass: FAI and its engineering application. *Rock Mech. Rock Eng.* 44 (4), 401–414. doi:10.1007/s00603-011-0150-9

Zhang, J. Z., and Zhou, X. P. (2020). AE event rate characteristics of flawed granite: From damage stress to ultimate failure. *Geophys. J. Int.* 222 (2), 795–814. doi:10.1093/gji/ggaa207

Zhang, J. C., Li, X. L., Qin, Q. Z., Wang, Y., and Gao, X. (2023). Study on overlying strata movement patterns and mechanisms in super-large mining height stopes. *Bull. Eng. Geol. Environ.* 82 (3), 142. doi:10.1007/s10064-023-03185-5

Zhang, Q., Huang, X. B., Zhu, H. H., and Li, J. (2019). Quantitative assessments of the correlations between rock mass rating (RMR) and geological strength index (GSI). *Tunn. Undergr. Space Technol.* 83, 73–81. doi:10.1016/j.tust.2018.09.015

Zhao, X. D. (2018). The basic theory and development trend of ultra-deep shaft construction [J]. *Metal. mines* 502 (04), 1–10. doi:10.19614/j.cnki.jsks.201804001

frontiers | Frontiers in Earth Science

TYPE Original Research
PUBLISHED 13 July 2023
DOI 10.3389/feart.2023.1239495

OPEN ACCESS

EDITED BY
Xuelong Li,
Shandong University of Science and Technology, China

REVIEWED BY
Lei Shi,
China University of Mining and Technology, China
Yu Xuguang,
Tangshan Vocational and Technical College, China

*CORRESPONDENCE
Mingming Cao,
707360021@qq.com

RECEIVED 13 June 2023
ACCEPTED 05 July 2023
PUBLISHED 13 July 2023

CITATION
Cao M, Huang W, Liu G and Wu Z (2023), Study on the dynamic response characteristics of roadbed and pavement under the humidity and season factors in the hilly area of Southwest China. *Front. Earth Sci.* 11:1239495. doi: 10.3389/feart.2023.1239495

Study on the dynamic response characteristics of roadbed and pavement under the humidity and season factors in the hilly area of Southwest China

Mingming Cao[1]*, Wanqing Huang[1], Guoming Liu[2] and Zhiyong Wu[1]

[1]Sichuan Communication Surveying and Design Institute Co., Ltd., Chengdu, China, [2]School of Civil Engineering, Sichuan Vocational and Technical College of Communications, Chengdu, China

The environment of the roadbed and pavement often has a significant impact on its dynamic performance. The stability of the strata in the Hilly Area is poor, and long-term complex environmental impacts will cause significant damage to the pavement. This article tests the dynamic response characteristics of semi rigid and inverted asphalt pavement through road load tests, and measures the humidity data of the roadbed during on-site rainfall. In addition, the variation of pore water pressure in the transition layer under the coupling effect of humidity and dynamic load was analyzed, revealing the influence of seasonal factors on the dynamic response of the pavement and roadbed. The test results indicate that the humidity inside the roadbed is greatly influenced by seasonal factors, and the humidity conditions of the roadbed and pavement vary significantly due to differences in measurement point depth, season, and rainfall. Graded crushed stone cushion is beneficial for improving the humidity conditions of the roadbed. The pore water pressure of the graded crushed stone transition layer did not show significant pore water reabsorption throughout the entire loading process. Meanwhile, the thickness of the surface layer and the magnitude of the load have a significant impact on the measurement of pore water pressure in the transition layer. The measured values of the dynamic response indicators of the pavement are greatly influenced by seasonal factors. The research in this article will provide theoretical and guiding significance for the dynamic response characteristics of pavement under the influence of multiple factors in the southwestern hilly area.

KEYWORDS

pore water pressure, dynamic response, seasonal factor, the hilly area, graded crushed stone

1 Introduction

The dynamic modulus, viscoelasticity and damping characteristics of asphalt mixtures are all-sensitive to temperature. The strength and permanent deformation characteristics of graded crushed stone and soil foundation are greatly affected by the dry and wet conditions, and the environment has a significant impact on the material properties and the response behavior of the pavement.

The research on the dynamic response of temperature to asphalt pavement has two main parts. 1) The dynamic modulus has temperature-dependent characteristics. When the

dynamic modulus of the asphalt mixture is higher at low temperature than that is at high temperature, the influence of the research temperature on the bottom strain of the asphalt layer and the vertical earth pressure on the top surface of the subgrade is studied. 2) Temperature fluctuations in the asphalt mixture cause temperature shrinkage and expansion, and temperature strain is formed at the bottom of the asphalt layer (Garg and Hayhoe, 2001; Al-Qadi et al., 2004; Islam and Tarefder, 2013; Assogba et al., 2020; Gao, et al., 2023). However, it is not reasonable to use the temperature index to characterize the seasonal variation on the dynamic response of asphalt pavement. Meanwhile, there has been relatively little research on the dynamic response of asphalt pavement to seasonal temperature changes. This article studies the dynamic response characteristics of asphalt pavement under different seasonal temperature changes.

The humidity conditions inside the pavement structure change with the seasons, and there are significant differences in the internal humidity conditions of the pavement structure in different seasons. The inverted asphalt pavement is particularly obvious. The difference in dynamic response of pavement under different season conditions is the combined effect of temperature and humidity changes in the pavement structure. It is unreasonable to use the temperature index to characterize the seasonal variation in the literature (Ai et al., 2017; Chen et al., 2019; Zhang et al., 2023). The research on the dynamic response characteristics of the inverted asphalt pavement is mainly limited to the response characteristics of the asphalt layer and the soil foundation. There is little research on the response characteristics of the graded crushed stone transition layer based on the on-site vehicle loading test. In addition, the graded crushed stone belongs to the porous composite material. Under the load of the vehicle, the moisture in the transition layer of the graded crushed stone generates transient pulsating water pressure, changes the internal force condition, and forms a coupled stress field of load and pore water pressure, which forms the fatigue coupling load (Li, 2013; Liu et al., 2023a). The research on the influence factors and distribution law of the pore water pressure of the asphalt pavement is mainly based on numerical simulation (Dong et al., 2007), and its field test has mainly focused on the inside of the asphalt layer (Jiang et al., 2012). However, due to the differences in rainfall in different seasons, the humidity of the roadbed varies significantly, which has a significant impact on the dynamic response characteristics of asphalt pavement and roadbed.

Seasonal changes lead to significant changes in temperature and humidity inside asphalt pavement. More and more attention has been paid to the impact of temperature on road bearing capacity, with less attention paid to the changes in humidity. However, the impact of humidity on the dynamic response of the road surface is significant, and previous research has not focused on testing under coupling of hydrodynamic pressure and axle load. At the same time, there are relatively few studies on changes in hydraulic stress response indicators of the graded crushed stone transition layer under different speed and axle weight. In view of this, based on the design of the asphalt load response test and the monitoring system, the internal humidity of the subgrade and pavement in the rainfall process is tested. In this paper, the variation of pore water pressure in the transition layer under the coupling of humidity and dynamic load is studied, and the influence of seasonal variation on the dynamic response of the pavement structure is discussed. The analysis improves the adaptability of modified semi-rigid base asphalt pavement in the hilly area of eastern Sichuan.

2 Test plan layout of test section

2.1 Test section pavement structure

There are three pavement structures in the dynamic response test section of the asphalt pavement of the Sui-guang Expressway, including a traditional semi-rigid asphalt pavement (S1) and two inverted asphalt pavements (S2 and S3), which are mainly distributed in the excavated section. The composition is shown in Figure 1. The inverted asphalt pavements are that flexible graded crushed stone transition layer is arranged between asphalt layer and cement stabilized macadam base layer. The S1 is the original design document for the pavement structure, while S2 and S3 are designed with inverted asphalt pavement structures that are more suitable for the characteristics of the southwest hilly area based on the characteristics of the roadbed and rainfall. The inverted asphalt pavement adds a graded crushed stone transition layer between the base layer and the asphalt surface layer, which significantly reduces the reflection cracks of the asphalt pavement and eliminates internal moisture.

2.2 Sensor component layout

6 types of sensing elements are installed in the dynamic response test section of the asphalt road of Sui-guang Expressway, including horizontal asphalt strain gauges (transversal and longitudinal), vertical large deformation strain gauges, earth pressure gauges, temperature sensors, pore water pressure gauges and soil moisture sensors. The specific layout scheme is shown in Figures 2A–C (taking structure S3 as an example (Cao et al., 2022). Among them, the horizontal asphalt strain gauges are arranged in a 3×4 matrix form, 12 horizontal asphalt strain gauges are embedded in each pavement structure, and the strain amplitude is the sum of the absolute values of tensile and compressive strains (Dong et al., 2008; Dong et al., 2013; Liu et al., 2023b). The structural S2 and S3 transition layer two vertical large deformation strain gauges are arranged with wheel tracks positions, and one vertical large deformation strain gauge is arranged at the central position of the traffic lane. Two dynamic earth pressure gauges are arranged along the wheel track on the top surface of each structural soil foundation. There are 4 dynamic earth pressure gauges arranged on both sides of the bottom wheel of the graded crushed stone transition layer of structures S2 and S3. The soil moisture sensor is set at the 30 cm below the soil base of the structure S1, the middle part of the structural S2 transition layer, the middle part of the cushion layer, at the 30cm and 50 cm below the soil foundation. At the same, the soil moisture sensor is arranged at 30 cm below the structural S3 soil foundation and in the middle of the transition layer. Seven soil moisture sensors were buried in the test section. Two pore water pressure gauges are arranged along the wheel track in the middle of the structural S2 and S3 transition layers. The temperature sensors are placed in the middle of upper

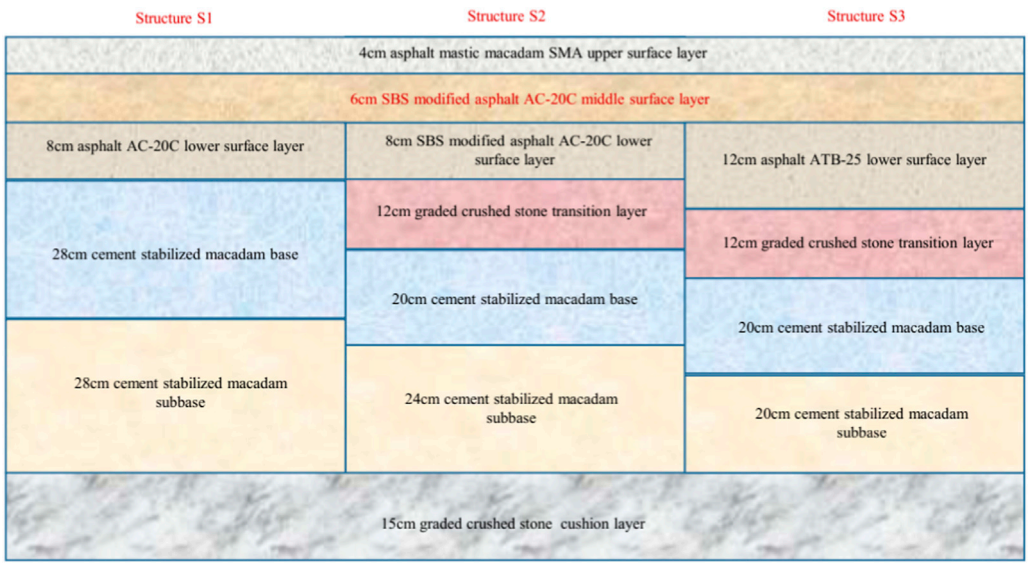

FIGURE 1
The structure of test section pavement.

TABLE 1 Test trucks parameters.

Vehicle model	Description	Number of rear axles/piece	Front axle wheel pressure/MPa	Rear axle wheel pressure/MPa
3-type	Type 12 truck	1	0.7	1.1
4-type	Type 15 truck	2	1.2	1.2

surface layer, middle surface layer and lower surface layer. It should be noted that the strain or stress values used in the analysis below refer to the peak value of the corresponding axial position on the time history curve unless otherwise specified.

2.3 Testing vehicles

Different types of vehicles are driving on the road. Different models have different natural frequencies. Large-duty trucks have more damage to road surface than cars. The load response characteristics of pavement structures under different vehicle loads are different. The two models are loaded and tested on different pavement structures. The vehicle parameters are shown in Table 1; Figures 3A, B.

3 Coupling response analysis of humidity to dynamic load of inverted asphalt pavement

3.1 Overview of the field test process

The rebound modulus of the subgrade soil and transition layer graded crushed stone is very sensitive to the internal humidity of the corresponding structural layer (Li and Selig, 1994; Cao, 2007; Zhou, 2014). Therefore, while the road surface dynamic response tested, the typical layer moisture conditions inside the pavement structure were observed to investigate the effect of rainfall on the change of the humidity status of the new pavement graded crushed stone transition layer, cushion, and subgrade soil. The stress and strain state of pavement structure provides basis and reference.

The humidity test data of subgrade and graded crushed stone layer are shown in Table 2. The volumetric water content of the subgrade with the depth of 20 cm in the asphalt pavement structure tested in May 2016 is about 30%± 5%, which is higher than when the sensor is buried (On the 29th of December 2015), the initial volumetric water content of the test (5–10%). The volumetric water content of the soil foundation at 40 cm depth of the subgrade is 1.9–2.0 times of the depth of the subgrade at 20cm, and the volumetric water content of the graded crushed stone cushion tested before the rain is 7.0–7.5%.

On May 18th of 2016, the day was cloudy, and on the 18th, there was 20 h of rain from 20:00 to 19:00, and the peak of rainfall was concentrated within 12 h from the early morning to noon on the 19th, with a rainfall of 10 mm. In the meantime, the humidity variation data of the graded crushed stone transition layer was recorded every half hour by i500-ES. It was found that the volumetric water content in the middle of the structural S2 graded crushed stone transition layer was stable at around 5.9%, and the water content of the structural S3 was stable at about 4.7%. There is no obvious fluctuation, because the test

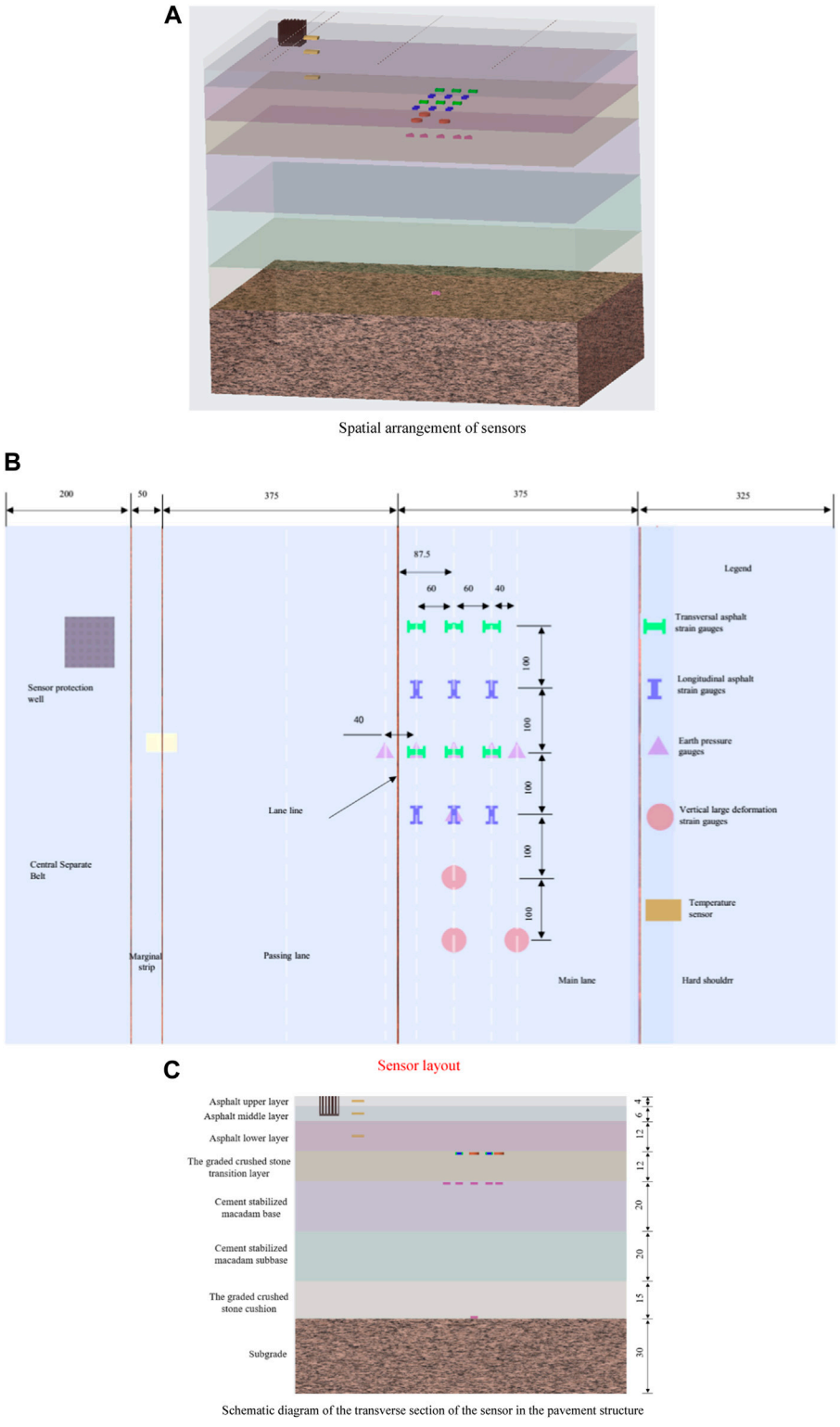

FIGURE 2
Schematic diagram of structure S3 sensing element (unit: cm).

section is a new highway, the asphalt surface layer is basically not water seepage, the road surface water cannot penetrate into the inner pavement. The cement stabilized macadam layer blocks the groundwater ascending channel. Therefore, the transition layer is a self-contained relatively closed system, and the water content has relatively less affected by environmental factors.

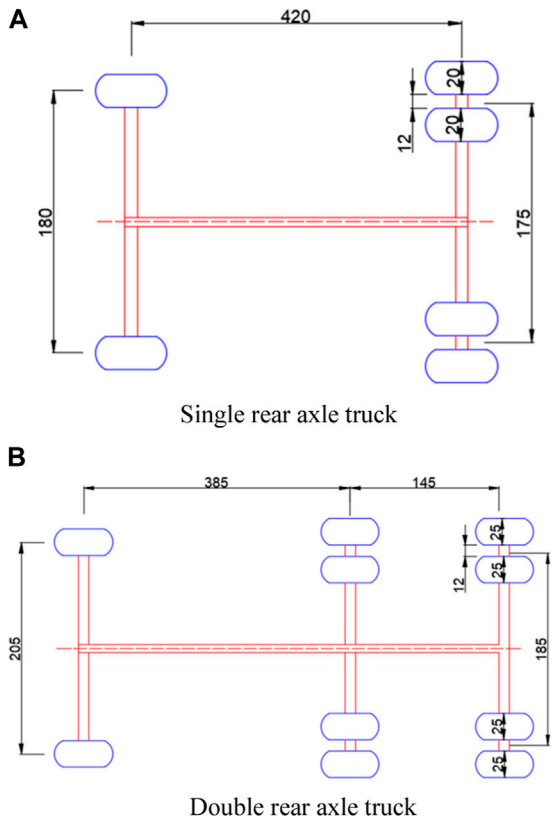

FIGURE 3
Schematic diagram of test trucks (unit: cm).

As for the subgrade, before the rainy season, the rainfall has no significant effect on the internal humidity of the subgrade. The volumetric water content at 20 cm below the subgrade is 26.6–27%, and the volumetric water content at 40 cm below the subgrade is 52.1%. Obviously, before the rainy season, due to no heavy rainfall or long-term continuous rainfall, the water content of the subgrade soil is stable for a long period, and the humidity of the subgrade soil will not fluctuate significantly due to short-term rainfall or a small amount. At this time, the impact of rainfall on the moisture content of the subgrade soil is relatively small. Conversely, in the rainy season, the fluctuation of the water content of the subgrade soil is greatly affected by rainfall (Jiang, 2014).

In contrast, the effect of rainfall on the humidity of the graded crushed stone cushion is more obvious. The volumetric water content of the graded crushed stone cushion tested before rain, during rain (close the stop of the rain) and after rain (within 24 h) respectively at 7.1%, 16.2%, and 18.9%, the volumetric water content of the graded crushed stone cushion during and after the rain was about 2.3 times and 2.7 times that before the rain, respectively. The volumetric water content of the graded crushed stone cushion is still rising within 24 h after the rain stop, but the increase is less than that during the rainfall process. The graded crushed stone cushion effectively improves the internal humidity of the subgrade and has a good drainage effect. The literature (Liu et al., 2012) draws the same conclusions through an indoor model test.

3.2 Basic characteristics of dynamic response of pore water pressure in transition layer

For the structure S2, under the condition that the volumetric water content of the graded crushed stone transition layer is 5.9%, when the 10t single rear axle and the 23t double rear axle load pass the test section at a speed of 20 km/h, the pore water pressure stress in the transition layer is measured. The time history curve is shown in Figure 4.

Analysis test data is visible: the pore water pressure field has the same wave propagation characteristics as the displacement field under the action of dynamic load, consistent with literature results (Dong et al., 2009). As the wheel-loaded adjacent pore water pressure timing, the pore water pressure stress inside the graded crushed stone increases sharply, and it quickly reached the peak and then quickly dissipated. Due to the test error, the pore water pressure measured fluctuated near 0 o'clock, but overall, it was not found that the pore water re-absorbed due to vacuum negative pressure suction, resulting in negative pores water pressure, which proves the good drainage performance of the inverted asphalt pavement graded crushed stone transition layer and realizes the basic intention of the design. In addition, the weight difference between the front and rear axles of the single-rear axle truck is large, and the difference of the mechanical response index is obvious, but the load assigned to

TABLE 2 Measured humidity value.

Sensor	Structure	NO.	Position	Initial value/%	Volumetric water content test value in May/%				
					12th	13 th	18 th	19 th	20 th
Hygrometer	structure S1	B1-L1-S1	Subgrade 20 cm deep	9.4	35.1	35.2	33.9	—	—
	structure S2	Z1-L1-S1	Subgrade 20 cm deep	5.5	30.5	30.4	27	26.6	27.9
		Z1-L1-S2	Subgrade 40 cm deep	3.7	58.5	58.4	52.1	52.1	53.5
		Z1-D1-S3	Middle of cushion	2.8	7.5	7.3	7.1	16.2	18.9
		S1-4	Middle of transition layer	4.3	5.7	5.7	5.9	5.9	5.8
	structure S3	Z2-L1-S1	Subgrade 20 cm deep	5.4	31.2	31.4	—	—	31.7
		S2-4	Middle of transition layer	3.7	4.7	4.7	—	—	4.7

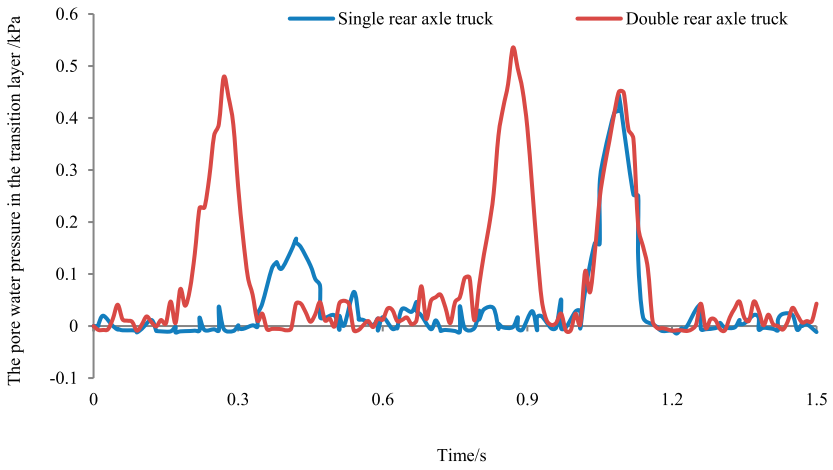

FIGURE 4
Dynamic time history curve of pore water pressure.

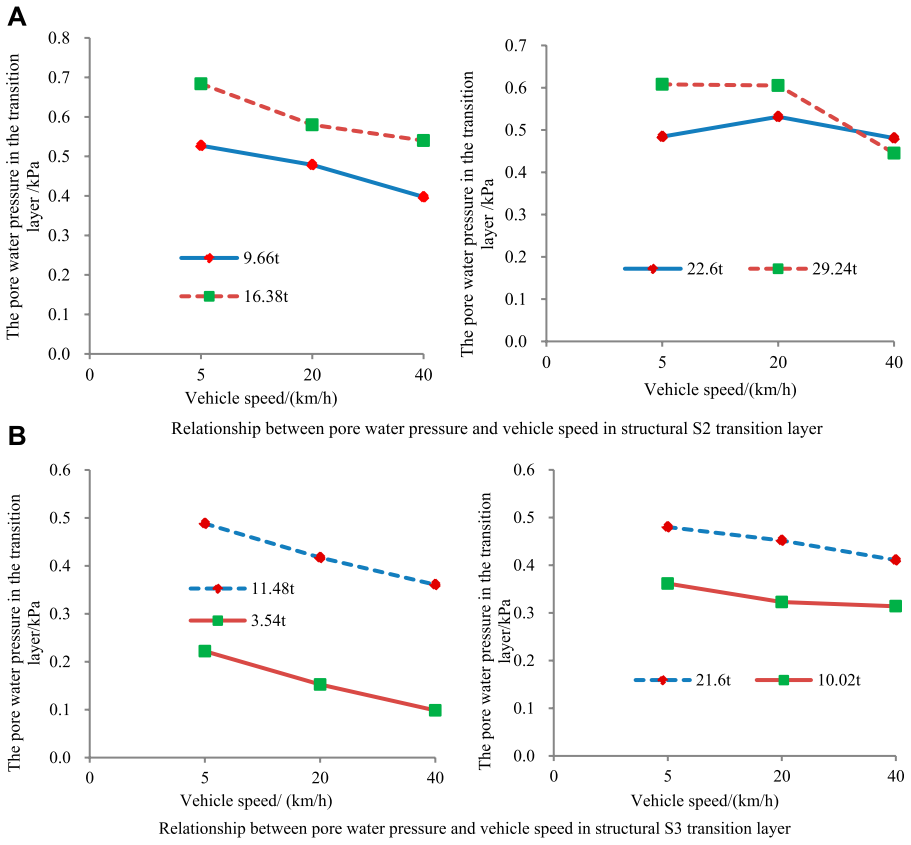

FIGURE 5
Relationship between pore Water pressure and Speed in transition layer (left: single rear axle truck, right: double rear axle truck).

each front axle tire by the double rear axle truck is slightly larger than the load on each tire of the rear axle. Therefore, the amplitude difference among the shafts before and after the pore water pressure of the rear axle truck graded crushed stone transition layer is small, and the rear axle amplitude may be smaller than the front axle.

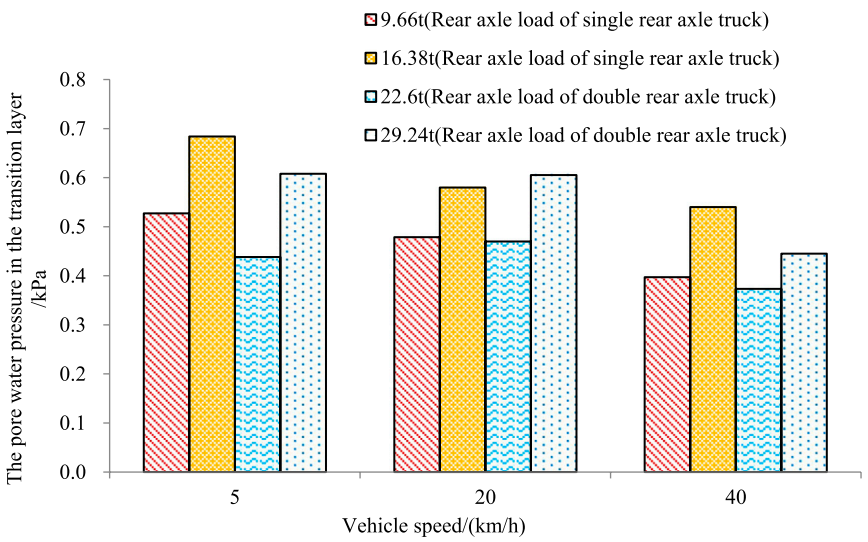

FIGURE 6
Relationship between pore water pressure and axle load in structure S2 transition layer.

3.3 Analysis of driving speed and load sensitivity of pore water pressure in transition layer

Under the driving load, the measured pore water pressure in the transition layer of the inverted structure S2 and S3 is shown in Figures 5A, B. It can be concluded that the pore water pressure decreases with the growth of the traveling speed regardless of the structure S2 or the structure S3. Taking the test of structure S2 with 10t and 16t single rear axle trucks as an example, when the driving speed is increased from 5 km/h to 40 km/h, the pore water pressure caused by the rear axle and decreased by about 21–26%. Further, when the comparison vehicle is traveling at a speed of 40 km/h, the structure S2 is at 22.6 t (rear axis, the same below) and the structure S3 is under the action of 21.6 t axle load, and the structure S2 is at 9.66 t and the structure S3 is at 11.48 t axle load. Under the difference of the pore water pressure in the transition layer of the two pavement structures, it is found that the difference is mainly due to the difference in the applied load. It is noted that the structure S2 and the structure S3 adopt different ways (surface layer reinforcement or thickening) to compensate for the influence of the thickness of the cement stabilized macadam layer on the bearing capacity of the pavement structural. Therefore, it is reasonable to speculate that the performance of the diffusion load is enhanced, resulting that the deformation of the gradation gravel transition layer is smaller; the more effectively reduce the pore water pressure in the transition layer and reduce the erosion or seepage erosion of the graded crushed stone by the pore water.

It is worth noting that in this test, the graded crushed stone of the transition layer is far from saturated, resulting in a very small amount of pore water pressure, which is less than 1% of the vertical pressure (see Figure 6). The transition layer can effectively reduce the damage degree of water seepage to the pavement structure.

4 Analysis of seasonal influence factors in field test

The field test eliminates the distortion of the test results caused by the material scale effect, which reproduces the pavement structural response to the driving load. However, in the test under the changing conditions of the natural environment, the detection data is bound to produce large dispersion, especially the extremely sensitive temperature of the pavement material. The significant variability of the acquisition index is inevitable, and the reasonable definition of the experimental environment parameters is therefore more important (Ovik et al., 2000; Drumm and Meier, 2003). Most studies have adopted the temperature in the middle of the asphalt layer to establish the relationship between temperature and strain (Priest and Timm, 2006; Willis, 2009). The literature (Mateos and Snyder, 2002) considers that the average temperature of the asphalt layer is more representative. Considering the nonlinear distribution of the pavement temperature along the depth, the equivalent temperature of asphalt layer calculated in the pavement surface, the middle of the asphalt middle surface layer and of the asphalt lower surface layer of this paper. A field comparison test was conducted in two seasons, and in the deep winter (January 2016, equivalent temperature about 11 ˚C) and early summer (May 2016, the equivalent temperature is about 46 ˚C). The test uses a single rear axle truck (rear axle weight 6t), and is carried out at a travel speed of 30–35 km/h, and the test data shown in Figures 7A–E, 8A, B. The results showed that.

1) At the same measuring point, the detection values of the structural response indicators of the summer pavement are higher than the winter detection values, and the difference between them can be as high as several times. Taking the strain amplitude at the bottom of the asphalt layer as an example, the measured value in summer is about 1.4–3.9 times of the measured value in winter. The trend of strain response is further analyzed. It is found that the variation

10.3389/feart.2023.1239495

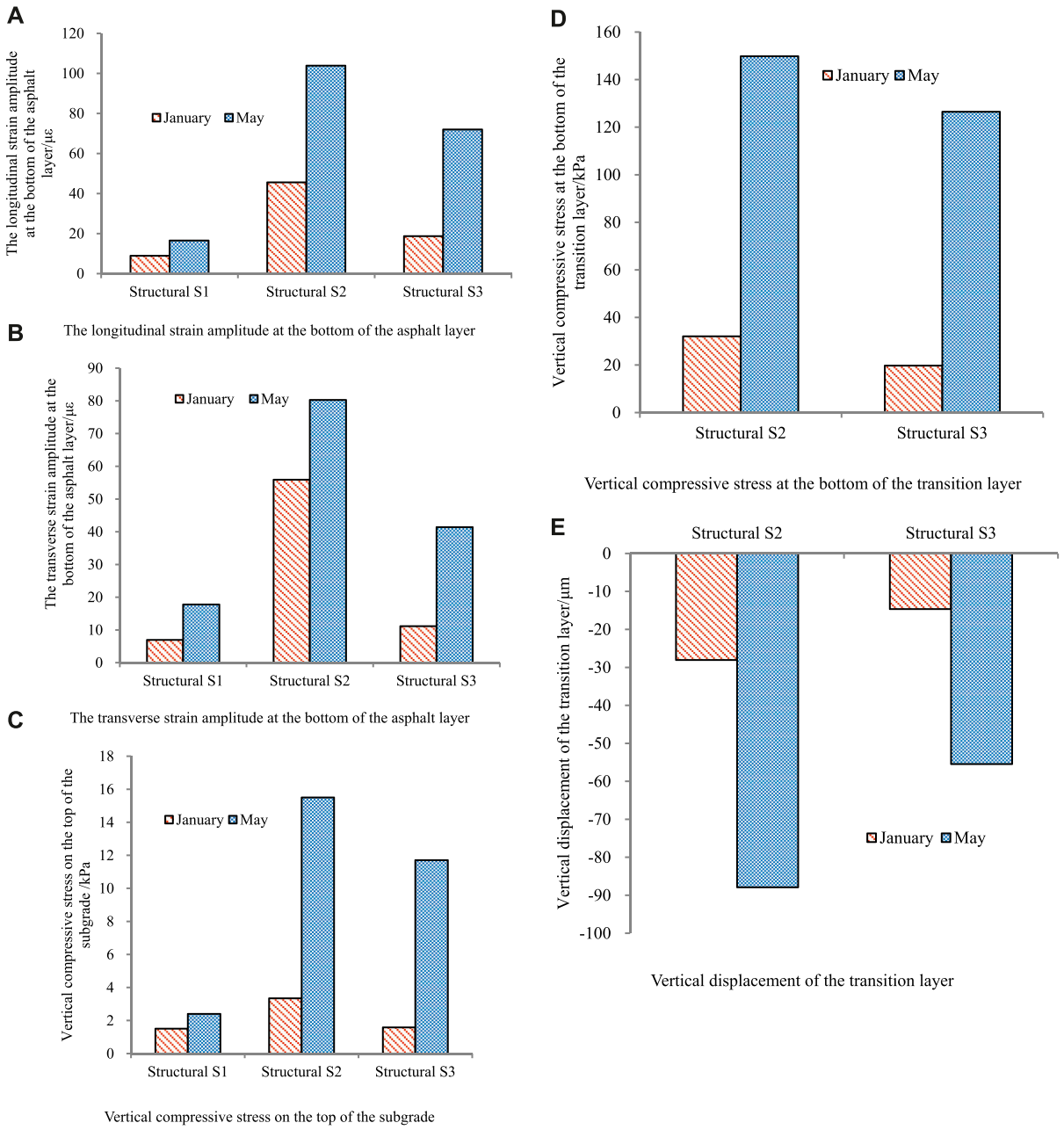

FIGURE 7
Influence of season on pavement mechanical response.

of longitudinal and transverse strain along the road is different after the temperature rises. Among them, along the longitudinal direction, the tensile strain and compressive strain at the bottom of the asphalt layer increase greatly. While in the transversal direction, the tensile strain at the bottom of the asphalt layer increases with temperature, and the compressive strain hardly increase in magnitude, which stay near zero.

2) Due to the difference in water content between the graded crushed stone cushion and the subgrade in January and May, especially the water content of the subgrade soil is quite different. In January, the atmosphere is dry and the water content is low. The cushion and the subgrade strength are both relatively high. While the rainfall in May increased significantly, the water content of the subgrade and the cushion was relatively large, and its strength was relatively low. The mechanical response of the pavement under load was relatively severe, so the vertical compressive stress on the top surface of the subgrade was affected by seasonal factors. The measured value in May is larger about 1.5–7.5 times than that is in January. The seasonal variation performance of the cushion and subgrade will inevitably affect the load response of the superstructure, hence, a vertical compressive stress at the bottom of the graded crushed stone

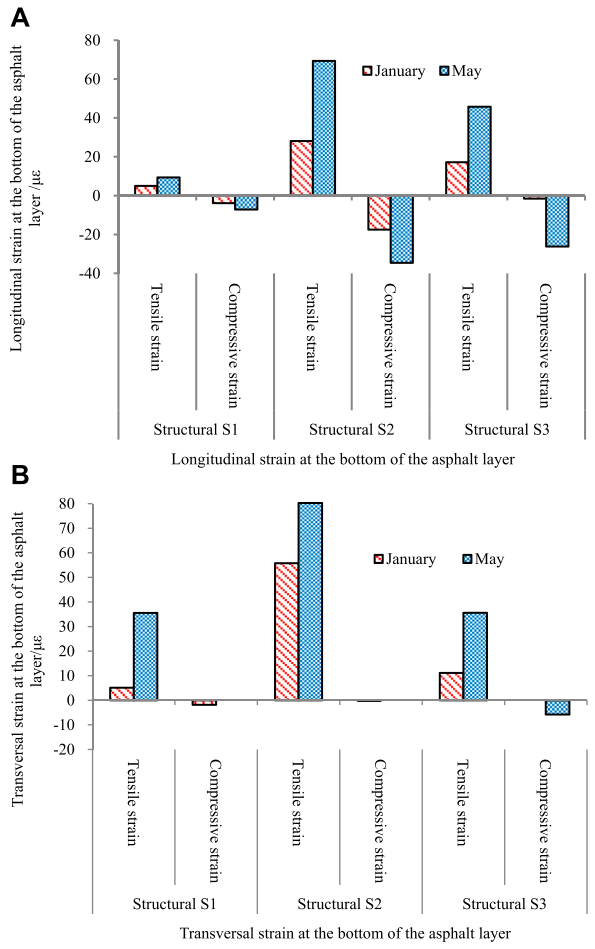

FIGURE 8
Effect of season on strain composition at the bottom of the asphalt layer.

transition layer increased by 3.5–5.5 times in May compared with January, and the vertical displacement increase by 2–3 times.

3) The sensitivity of the three pavement structures to seasonal factors is different. Overall, the sensitivity of the structure S1 to the season is lower than that of the structure S2 and the structure S3, and the structure S3 is most sensitive to the season. The structure S1 is a semi-rigid asphalt pavement, and the main bearing structure layer is a cement stabilized gravel layer. The temperature is higher, the inter-layer strain transmission performance is worse between the asphalt layer and the cement stabilized macadam, and the load transmitted to the top surface of the subgrade is small. The thickness of the asphalt layer is thinner. The influence of temperature on the mechanical response of the pavement structure is also lower than that of the structure S3. However, the upper 30 or 34 cm of the inverted asphalt pavement is a flexible structural layer. The mechanical properties of the asphalt mixture are greatly affected by the temperature, and the mechanical properties of the graded crushed stone are greatly affected by the water content, which leads to the seasonal sensitivity of the inverted structure more than the semi-rigid structure. The thickness of the structural S3 asphalt surface layer is larger than the structure S1 and the structure S2, and the mechanical response characteristics are relatively more affected by the season and temperature.
4) The summer temperatures in the eastern Sichuan region are relatively high (with the highest temperature reaching 41.6°C in recent years), the climate is hot, and the rainfall is large (with an average precipitation of 1,014–1,282 mm in Guang'an for many years, and the maximum annual rainfall is 1,485 mm). The continuous rain time is long, and the roadbed filler is mainly shale, which will sharply reduce its strength under rainwater immersion. In addition, some roads have high traffic volume, which requires high performance requirements for asphalt pavement resistance to water damage and high-temperature deformation. In view of this, it is recommended to install a graded crushed stone cushion under the pavement structure in the eastern Sichuan region to regulate the humidity of the roadbed and extend the service life of the asphalt pavement. Meanwhile, the inverted asphalt pavement structure has good adaptability in the hilly areas of eastern Sichuan.

4 Conclusion

1) The rainwater is blocked from entering new pavement transition layer by the upper and lower structural layers, so the volumetric water content in the middle part of the transition layer of the asphalt pavement has no obvious fluctuation during the rainfall process. At the same time, the rainfall has a great influence on the water content of the subgrade soil (excavated section) during the rainy season. The fluctuation range is different due to the different depth of the subgrade layer. The water content at the middle of cushion fluctuated significantly during the rainfall process, and the fluctuation peak lags behind the rainfall peak. The addition of the cushion layer helps to improve the humidity inside the subgrade.
2) There is a wave propagation characteristic of the pore water pressure in the transition layer, and the measured value increases with the growth of the axle weight, and decreases with the growth of the driving speed. However, the good drainage performance makes the pore water pressure in the transition layer of graded crushed stone small in magnitude. It eliminates the time-dependent effect of the pore water pressure caused by the axle load, and the pore water-sucking phenomenon caused by the vacuum negative pressure suction. Especially for new pavements, the water content of the transition layer is relatively weakly affected by rainfall with the participation of the surface layer and the underlying cement stabilized macadam base. Largely, the erosion or seepage erosion of the graded crushed stone by the pressurized water is alleviated.
3) Seasonal changes have significant influence on the dynamic response of asphalt pavement, which is affected by the difference of temperature and water content in different seasons. The bottom strain amplitude of asphalt layer, the vertical compressive stress of top surface of subgrade, the vertical compressive stress at the bottom layer of graded crushed stone transition layer and the vertical displacement of the graded crushed stone transition layer of the summer are 1.4–3.9 times, 1.5–7.5 times, 4.5–6.5 times and 3–4 times of the winter, respectively, and the sensitivity of the inverted asphalt pavement to the season is greater than semi-rigid asphalt pavement.

Data availability statement

The original contributions presented in the study are included in the article/Supplementary material, further inquiries can be directed to the corresponding author.

Author contributions

MC: methodology, formal analysis and Writing—Original Draft; WH: data Curation, Writing—Review and Editing; GL: investigation, visualization; ZW: Writing—Review and Editing, visualization. All authors contributed to the article and approved the submitted version.

Funding

This study was supported by the Sichuan transportation science and technology project (grant number 2015 from 4-1, 2019-ZL-13), the Sichuan Province Science and Technology Planning Project (Application Fundamental Research) (grant number 2020YFS0362), and supported by Sichuan Science and Technology Program (grant number 2022YFG0048).

Conflict of interest

Authors MC, WH, and ZW were employed by the Sichuan Communication Surveying and Design Institute Co., Ltd.

The remaining author declares that the research was conducted in the absence of any commercial or financial relationships that could be construed as a potential conflict of interest.

Publisher's note

References

Ai, C., Rahman, A., Xiao, C., Yang, E., and Qiu, Y. (2017). Analysis of measured strain response of asphalt pavements and relevant prediction models. *Int. J. Pavement Eng.* 18 (12), 1089–1097. doi:10.1080/10298436.2016.1149836

Al-Qadi, I. L., Loulizi, A., Elseifi, M., and Lahouar, S. (2004). The Virginia Smart Road: The impact of pavement instrumentation on understanding pavement performance. *J. Assoc. Asphalt Paving Technol.* 73 (3), 427–465.

Assogba, O. C., Tan, Y., Zhou, X., Zhang, C., and Anato, J. N. (2020). Numerical investigation of the mechanical response of semi-rigid base asphalt pavement under traffic load and nonlinear temperature gradient effect. *Constr. Build. Mater.* 235, 117406. doi:10.1016/j.conbuildmat.2019.117406

Cao, C. (2007). "Study on the humidity condition and moduli adjustment coefficient of Subgrade,". Doctoral dissertations (Shanghai: Tongji University).

Cao, M., Huang, W., and Wu, Z. (2022). Influence of axle load and asphalt layer thickness on dynamic response of asphalt pavement. *Geofluids* 2022, 1–16. doi:10.1155/2022/9592960

Chen, J., Wang, H., and Xie, P. (2019). Pavement temperature prediction: Theoretical models and critical affecting factors. *Appl. Therm. Eng.* 158, 113755. doi:10.1016/j.applthermaleng.2019.113755

Dong, Z., Cao, L., and Tan, Y. (2009). Time history analysis of dynamic response for saturated asphalt pavement. *J. Wuhan Univ. Technol. Transp. Sci. Enginee ring)* 33 (6), 1033–1036. doi:10.3963/j.issn.1006-2823.2009.06.003

Dong, Z., Zhang, Y., and Peng-Min, L. V. (2013). Fatigue performance of asphalt mixture under tensile-compressive alternating loading. *China J. Highw. Transp.* 26 (2), 15–19.

Dong, Z., Zhang, Z., and Peng-Min, L. V. (2008). Experiment study on the influence of the vehicle velocity on the asphalt pavement dynamic response. *J. Zhengzhou Univ. Eng. Sci.* 29 (2), 123–126.

Dong, Z. J., Tan, Y. Q., Cao, L., et al. (2007). Research on pore pressure within asphalt pavement under the coupled moisture-loading action. *J. Harbin Inst. Technol.* 10, 1614–1617. doi:10.3321/j.issn:0367-6234.2007.10.024

Drumm, E. C., and Meier, R. (2003). *LTPP data analysis: Daily and seasonal variations in insitu material properties*. Washington, DC: Transportation Research Board, National Research Council.

Gao, Y., Yu, Z., Chen, W., Yin, Q., Wu, J., and Wang, W. (2023). Recognition of rock materials after high-temperature deterioration based on SEM images via deep learning. *J. Mater. Res. Technol.* 25, 273–284. doi:10.1016/j.jmrt.2023.05.271

Garg, N., and Hayhoe, G. F. (2001). "Asphalt concrete strain responses at high loads and low speeds at the national airport pavement test facility (NAPTF)," in *Advancing airfield pavements* (Chicago, Illinois: Springer), 1–14.

Islam, M. R., and Tarefder, R. A. (2013). Measuring thermal effect in the structural response of flexible pavement based on field instrumentation. *Int. J. Pavement Res. Technol.* 6 (4), 274–279. doi:10.6135/ijprt.org.tw/2013.6(4).274

Jiang, Z., Gao, J., Ji, T., et al. (2012). Research on piezo-electric sensor measuring pavement hydrodynamic pressure. *Transducer Microsyst. Technol.* 31 (4), 17–19.

Jiang, Z. (2014). "Research on existent subgrade moisture condition and stability evaluation for expressway,". Master's degree thesis (Xi'an: Xi'an of Chang'an University).

Li, D., and Selig, E. T. (1994). Resilient modulus for fine-grained subgrade soils. *J. geotechnical Eng.* 120 (6), 939–957. doi:10.1061/(asce)0733-9410(1994)120:6(939)

Li, R. (2013). "Study on unsaturated hydraulic asphalt concrete pavement internal hydrodynamic pressure distribution,". Master's degree thesis (Chongqing: Chongqing Jiaotong University).

Liu, J., Yao, H., Hu, M., et al. (2012). Study of moisture dynamic response and underground drainage test of subgrade model under water level fluctuation. *Rock Soil Mech.* 33 (10), 2917–2922.

Liu, S. M., Sun, H. T., Zhang, D. M., Yang, K., Li, X., Wang, D., et al. (2023a). Experimental study of effect of liquid nitrogen cold soaking on coal pore structure and fractal characteristics. *Energy* 275 (7), 127470. doi:10.1016/j.energy.2023.127470

Liu, S. M., Sun, H. T., Zhang, D. M., Yang, K., Wang, D., Li, X., et al. (2023b). Nuclear magnetic resonance study on the influence of liquid nitrogen cold soaking on the pore structure of different coals. *Phys. Fluids* 35 (1), 012009. doi:10.1063/5.0135290

Mateos, A., and Snyder, M. (2002). Validation of flexible pavement structural response models with data from the Minnesota road research project. *Transp. Res. Rec. J. Transp. Res. Board* 1806, 19–29. doi:10.3141/1806-03

Ovik, J. M., Birgisson, B., and Newcomb, D. (2000). *Characterizing seasonal variations in pavement material properties for use in a mechanistic-empirical design procedure*. United States: University of Minnesota.

Priest, A. L., and Timm, D. H. (2006). *Methodology and calibration of fatigue transfer functions for mechanistic empirical flexible pavement design (No NCAT Report 06-03)*. United States: Auburn University.

Willis, J. R. (2009). *Field-based strain thresholds for flexible perpetual pavement design*. United States: Auburn University.

Zhang, J. C., Li, X. L., Qin, Q., Wang, Y., and Gao, X. (2023). Study on overlying strata movement patterns and mechanisms in super-large mining height stopes. *Bull. Eng. Geol. Environ.* 82 (3), 142. doi:10.1007/s10064-023-03185-5

Zhou, Y. (2014). *Research on subgrade moisture distribution and stiffness of humidity dependence in hot and humid areas*. Master's degree thesis (Changsha: Institutes of technology of Changsha).

frontiers | Frontiers in Earth Science

TYPE Original Research
PUBLISHED 17 July 2023
DOI 10.3389/feart.2023.1206252

OPEN ACCESS

EDITED BY
Xuelong Li,
Shandong University of Science and Technology, China

REVIEWED BY
Yiming Liu,
Hubei University of Technology, China
Junxin Liu,
Southwest University of Science and Technology, China
Feezan Ahmad,
Dalian University of Technology, China

*CORRESPONDENCE
Wang Guangjin,
wangguangjin2005@163.com

RECEIVED 15 April 2023
ACCEPTED 03 July 2023
PUBLISHED 17 July 2023

CITATION
Chunlin J, Guangjin W, Shujian L, Fuqi K, Binting C and Lei Z (2023), Study on dynamic strength and liquefaction mechanism of silt soil in Castor earthquake prone areas under different consolidation ratios.
Front. Earth Sci. 11:1206252.
doi: 10.3389/feart.2023.1206252

Study on dynamic strength and liquefaction mechanism of silt soil in Castor earthquake prone areas under different consolidation ratios

Jiang Chunlin[1], Wang Guangjin[1,2]*, Li Shujian[3], Kang Fuqi[1], Cai Binting[3] and Zhao Lei[3]

[1]Faculty of Land Resources Engineering, Kunming University of Science and Technology, Kunming, China, [2]Yunnan International Technology Transfer Center for Mineral Resources Development and Solid Waste Resource Utilization, Kunming, China, [3]Yunnan Phosphate Group Co., Ltd., Kunming, China

Under the Castor earthquake, there is a risk of liquefaction instability of saturated tailings, and the evolution of dynamic pore pressure can indirectly reflect its instability process. Before applying dynamic loads, the static stress state of soil is one of the main factors affecting the development of soil dynamic strength and dynamic pore pressure, and there are significant differences in soil dynamic strength under different consolidation ratios. This paper conducted dynamic triaxial tests on saturated tailings silt with different consolidation ratios, and analyzed the dynamic strength variation and liquefaction mechanism of the samples using the discrete element method (PFC3D). The results showed that 1) as the Kc′ gradually increased, and there was a critical consolidation ratio Kc′ during the development of the dynamic strength of the sample. The specific value of Kc′ was related to the properties and stress state of saturated sand. The Kc′ in this research was about 1.9. When Kc < 1.9, dynamic strength was increased with the increase in Kc; when Kc > 1.9, dynamic strength was decreased with the Kc. 2) Under the impact of cyclic load, when samples were normally consolidated (Kc =1), the pore water pressure would tend to be equal to the confining pressure to cause soil liquefaction. In the case of eccentric consolidation (Kc > 1), the pore water pressure would be less than the confining pressure, thus, the soil liquefaction would not be induced, and the pore pressure value would decrease with the increase of consolidation ratio. This paper provides engineering guidance value for the study of dynamic strength and liquefaction mechanism of tailings sand and silt in Castor earthquake prone areas under different consolidation ratios.

KEYWORDS

Castor earthquake area, saturated tailings sand soil, consolidation ratio, dynamic triaxial test, particle flow simulation

1 Introduction

As is well known, The pre-earthquake action of the on-site soil unit has vertical effective force force σ_v and horizontal effective stress $K_0\sigma_v$ (K_0 is the coefficient of static earth pressure), the earthquake will cause repeated cyclic action of the dynamic shear stress $\pm \tau_d$, while the normal stresses remain constant. Any indoor dynamic test instrument should simulate such a stress state where there is a constant normal stress and a reciprocal shear stress acting on a plane of the soil sample. In the dynamic triaxial test, the stress state in the specimen the stress state in the 45° plane is simulated: for horizontal ground, the initial shear stress $\tau_0 = 0$, using isobaric consolidation K_c, i.e., equal consolidation pressure is applied on the specimen force $\sigma_{1c} = \sigma_{3c} = \sigma_0$, the normal stress in the 45° plane is σ_0, the tangential stress $\tau_0 = 0$. The pre-earthquake stress state can be simulated; for inclined ground, the initial shear stress $\tau_0 \neq 0$, and the bias consolidation $K_c \neq 1$ (K_c is the consolidation stress ratio). The static stress state of the soil before the dynamic load is applied determines the consolidation condition of the indoor.

As shown in Figure 1, The Karst landform area in southwestern China is prone to earthquakes. The dynamic instability of the tailings dam during the earthquake has gradually been paid attention to (Yan-Qiang et al., 2016); besides, most of the tailings dams are in the state of anisotropic consolidation, so it is important to study the dynamic characteristics of sand with different consolidation ratios (wang and Zhou, 2001).

At present, scholars have studied dynamic strength and the evolution law of dynamic pore water pressure of soil different consolidation ratios K_c, and some representative results have been obtained. Through the undrained dynamic triaxial test, Konstadinou, M. (Konstadinou and Georgiannou, 2013). found that the cyclic strength of Ottawa sand increased with the increase of consolidation stress ratio, and obvious stress dependence of sand was observed under high consolidation stress ratio. Through conducting dynamic triaxial tests on Yunlin sand samples with different consolidation ratios ($K_c = 1.0, 1.5, 2.0, 2.5, 3.0$), Chien, LK (Chien et al., 2000) found that liquefaction strength will decrease with the increase of consolidation stress ratio, and under low consolidation ratio ($K_c = 1.5$), the liquefaction strength is very close; when the strain amplitude is small, the influence of K_c tends to be less. Bao Chenyang (Chen-Yang et al., 2006) studied Yunnan silt samples under different consolidation ratios, and found that the dynamic strength curves had the highest point, and this point corresponded to $K_c = 2.1$ and $K_c = 2.01$ respectively when $\sigma_3 = 200kPa$ and $\sigma_3 = 100kPa$. By conducting dynamic triaxial tests on Fujian standard sand under different consolidation ratios of $K_c = 1.0, 1.25, 1.5, 2.0, 2.5, 3.0$, Ma Meiying (Mei-Ying, 1988) concluded that the dynamic strength of sand increases with the increase of K_c in a certain range of K, but the increase of dynamic strength gradually decrease, and the dynamic strength decreases When $K_c = 3.0$. By analyzing the dynamic triaxial test results of unsaturated fly ash, Zhang Jianhong et al. (Zhang and Chang-Rong, 1994) found when $K_c = 1.5$, the dynamic strength was increased compared to that when $K_c = 1.0$, the dynamic strength has shown a downward trend when $K_c = 2.0$. He Changrong et al. () used the Pubugou dam foundation sand to carry out dynamic triaxial tests under consolidation stress ratios of $K_c = 0.43 \sim 2.0$, and it was indicated that the dynamic strength had been increasing. Liao Hongjian et al. (Hong-Jian et al., 1998; Liao et al., 2001) conducted dynamic triaxial tests on Pozzolanic clay under consolidation stress ratios of $K_c = 1.0, 1.5, 2.0, 3.0$, and it was concluded that the dynamic strength tended to be stable with the consolidation ratio. Hu Yuanfang (Hu, 1996) conducted dynamic triaxial tests on Beba power plant fly ash under different consolidations of $K_c = 0.4 \sim 3.0$, and the results showed that the dynamic strength reached the maximum value when $K_c = 2.167$. Through the strength test of saturated sand and gravel materials for the earth-rock dam foundation, Zhang Ru (Zhang et al., 2006) believed that when the anisotropic consolidation $K_c = 0.7 \sim 1.3$, the final pore pressure of the test soil can reach the confining pressure; when $K_c \geq 1.5$, the final pore pressure reachs the confining pressure when the dynamic stress σ_d is greater than the principal stress difference $\sigma_1 - \sigma_3$. Yu Lianhong et al. (Lian-Hong and Wang, 1999) conducted an experimental study on the relationship between the dynamic pore water pressure and the consolidation ratio K_c of saturated silty soil, and concluded that the dynamic pore pressure may still rise to the confining pressure when the K_c is greater than 1.0 and less than a certain value. Nie Shouzhi et al. (Shou-Zhi, 1980) conducted liquefaction tests on saturated sandy soils under different consolidation conditions and proposed a series of indexes such as pore water pressure and dynamic strength, and also analyzed and explained the “notch” in the crest of the dynamic pore water pressure process line. Zhang Kexu et al. (Ke-Xu, 1984)proposed round-trip shear action functions under different consolidation and gave a unified interpretation of

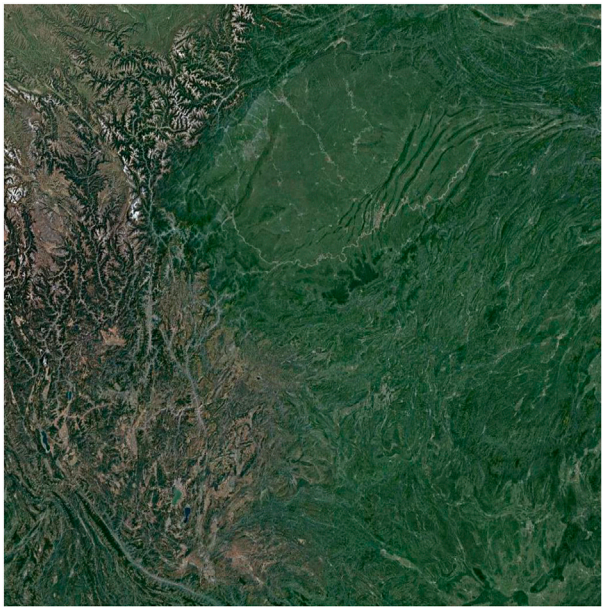

FIGURE 1
Karst landform area.

FIGURE 2
KTL-DYN10 dynamic triaxial equipment.

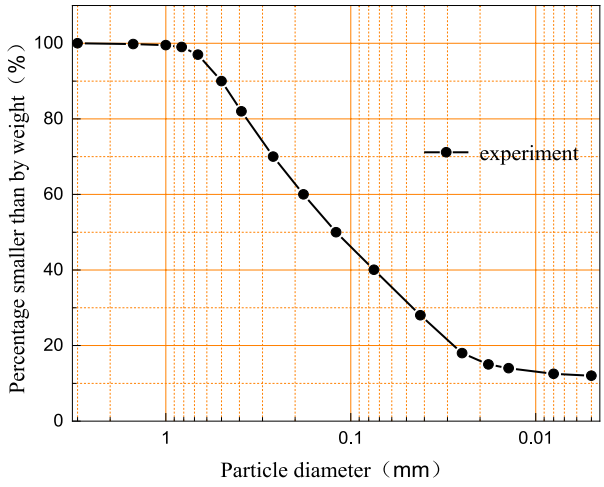

FIGURE 3
Particle size distribution of Tailing silty sand.

the results of several existing liquefaction tests. Wang Yuanzhan et al. (Wang et al., 2015)analyzed the pore pressure development law and undrained shear strength weakening law under the effect of different stress combinations by indoor dynamic triaxial tests with surrounding pressure, initial static deflection stress, cyclic dynamic stress and number of cycles as the test variables, taking Yantai port *in situ* silty powder clay as the research object.

However, during studying ynamic characteristics of soil, the dynamic pore pressure evolution of tailings under different consolidation conditions has not been paid enough attention. In practical projects, the dynamic failure process and dynamic pore pressure evolution law of tailings under different consolidation conditions also have certain differences (ZHANG et al., 2018). Therefore, in this paper, the influence of different consolidation ratios K_c on soil dynamic characteristics was mainly studied. On the basis of existing research, through dynamic triaxial test and discrete element simulation (DAI et al., 2013; KONG et al., 2013; SHEN et al., 2015; JIANG et al., 2020), the macro mechanical behavior and micro mechanical properties of saturated tailing silt were carefully studied according to the macro and micro results; moreover, the test of tailing silt was designed to discuss the influence of K_c on the dynamic strength and dynamic pore pressure of soil samples, and made a reasonable explanation.

2 Experiment scheme

2.1 Experiment apparatus and material

As shown in Figure 2, KTL-DYN10 dynamic triaxial equipment was selected for this experiment, and its hardware system consists of axial loading equipment, a controlling chamber of dynamic confining pressure, a back pressure controller, 8-channel high-speed control and acquisition equipment; The software system is a DSP high-speed digital control system with a maximum operating frequency of 10 Hz and a maximum dynamic stress amplitude of ±10 kN.

In this research, the tailings silty sand was taken from an iron tailings pond in Sichuan, and it is the main damming material of the tailings dam. Figure 3 shows the grading analysis of the tailings

FIGURE 4
Test sample.

samples, the sample used in this test is Void ratio e =0.69, Specific Gravity G=2.725, The dry density of the sample after consolidation is controlled as ρ_d =1.63 g/cm^3.

2.2 Sample preparation

In the process of sample preparation, according to the《Code for Geotechnical Test: GBT 50123-2019》(General Institute of Water Resources and Hydropower Planning and Design, 2019), the drying temperature was determined to be 110°C. In this test, a cylindrical sample with a diameter of 50 mm and a height of 105 mm was processed, which was compacted in four layers; at the same time, the sample density was controlled according to the dry density, and the dry density of samples was determined to be 1.63 g/cm^3 according to the deposition law of the tailings pond. Then, prepared samples were installed as shown in Figure 4.

2.3 Test procedure and scheme

After the sample preparation, the first action was to use the back-pressure controller to test its air impermeability, and then the CO_2 saturation, water head saturation, and back-pressure saturation were subsequently performed to improve the sample saturation. After the sample saturation reached 98% (B>0.98), it was consolidated under the corresponding conditions; After that, the cyclic load with fixed frequency was applied for the test under the undrained condition.

In this test, the load frequency was set as 1 Hz, the dynamic stress was set as 70 kPa, the consolidation confining pressure was kept to be 100 kPa, and the cyclic load was subjected using the method of equal stress amplitude. For the isotropic consolidation (K_c = 1), the consolidation stress was loaded at one time; for the anisotropic consolidation (K_c > 1), the consolidation stress was loaded step-wise. The effect of different consolidation ratios on the dynamic characteristics of saturated tailing silty sand was studied by applying different axial static stresses, and the test scheme is shown in Table 1. In order to facilitate analysis and comparison, the failure strain was taken as the criterion for terminating the test in this paper: the failure strain of isotropic consolidation (K_c = 1) was defined as 5% of the dynamic strain (ε_d = 5%), and that of anisotropic consolidation (K_c > 1) ws defined as 5% of the total strain (including residual strain and dynamic strain)(ε = 5%) (Mei-Ying, 1980), while the limit equilibrium failure criterion was adopted in the theoretical analysis.

3 Analysis of test results

3.1 The influence of K_c on soil dynamic strength

As shown in Figure 5, When K_c = 1.0 ~ 1.9, the higher the K_c, the more vibration times the sample needs to meet the failure standard; When K_c = 1.9 ~ 2.6, the changing rule was opposite to the above; Therefore, it can be seen that the influence of the consolidation ratio K_c on the dynamic strength of soil samples is very obvious. When K_c = 1.0 ~ 2.6, the value of 1.9 was the turning point; when K_c < 1.9, dynamic strength gradually increased; when K_c > 1.9, dynamic strength first increased and then decreased. Thus, the existence of critical consolidation ratio is proved. When K_c = 1, the initial shear stress was zero, the reverse shear stress was the maximum, and the soil particle skeleton was in a certain equilibrium state. The cyclic load made the direction of the large principal stress axial rotated 90°, and the cyclic shear stress made the pore space uniformly distributed, which resulted in the occurrence of plastic compaction, and the increase in pore pressure due to the sliding of particle skeleton. When 1 < K_c < 1.9, the initial shear stress increased with K_c, and the shear effect was induced during the test, which made the sand particles be rearranged and the deformation of the soil particle skeleton in a more stable state due to the disturbance of shear on the sand particle skeleton. The reverse shear stress slowly decreased with K_c, its influence on the change of pore space and volume of samples decreased gradually during vibration, as well as the deformation rate and amplitude, thus the seismic stability and liquefaction resistance became higher. As shown in Figure 6, I, II and III represent stress circles under different consolidation ratios, ①, ②, ③ represents the distance between consolidation stress circle and strength envelope; It can be seen that ③<②<①. This indicates that when K_c > 1.9, the greater the difference between σ_1 and σ_3, the larger the initial shear stress, the larger the diameter of the molar circle during static consolidation, and the less the distance from the Mohr-Coulomb envelope. For larger K_c, even if a periodic load with small amplitude σ_d was applied, the soil sample would also be

TABLE 1 Test scheme.

Test number	Confining pressure/kPa	Consolidation ratio	Frequency/Hz	Dynamic stress/kPa
1	100	1	1	70
2		1.3		
3		1.5		
4		1.7		
5		1.8		
6		1.9		
7		2.0		
8		2.2		
9		2.4		
10		2.6		

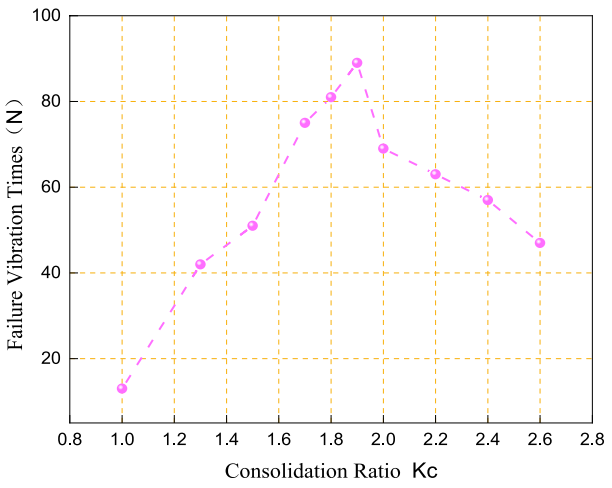

FIGURE 5
Failure Criteria-Vibration Times N-Consolidation Ratio K_c relation curve.

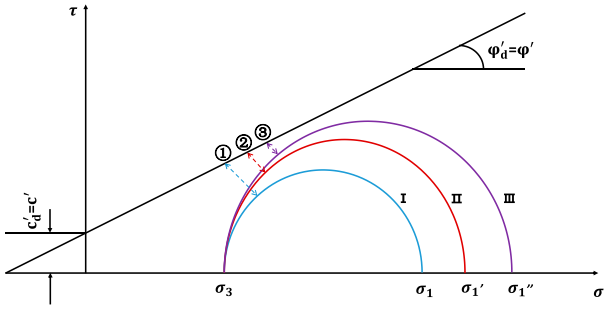

FIGURE 6
Consolidation Stress stress Circle.

deformed or damaged quickly; even without the dynamic load, the specimen would also occur shear failure as the static load was continuously applied by increasing σ_1.

3.2 The influence of K_c on soil dynamic pore pressure

Figure 7 shows development curves of dynamic pore water pressure of the sample under different consolidation ratios K_c, it can be seen that when $K_c = 1$, the pore pressure would finally reach the confining pressure and realize complete liquefaction; When $K_c > 1$, the pore pressure would always be less than the confining pressure, and the initial liquefaction would not be caused; besides, the larger the consolidation ratio, the smaller the pore pressure.

In order to analyze the influence of different consolidation ratios on the evolution of dynamic pore pressure of tailing silty sand, this paper used the limit equilibrium criterion to analyze the pore water pressure of materials under the limit equilibrium state, namely, the critical pore water pressure u_{cr} (Ding-Yi et al., 1981; Li et al., 2021a; Liu et al., 2022; Zhou et al., 2022). It was assumed that the static limit equilibrium condition was also applicable to the dynamic test, and their Mohr-Coulomb failure envelopes were the same, which means the dynamic effective cohesion $c_d^{'}$ and internal friction angle $\varphi_d^{'}$ was respectively equal to static effective cohesion c' and internal friction angle φ' as shown in Figure 7. The stress circle ① represents the stress state of the sample before vibration, and the stress circle ② represents the maximum stress circle during dynamic load application, that is, the dynamic stress was equal to the instantaneous stress circle with an amplitude of σ_d. During the process of dynamic loading, the pore water pressure in the sample would develop continuously, and the stress circle ② would move towards the strength envelope; when the pore water pressure reached the critical value u_{cr}, the stress circle was tangent to the strength envelope, suggesting that the tailing silty sand reached the failure state according to the limit equilibrium condition.

According to the geometric conditions shown in Figure 8, the pore water pressure at the limit equilibrium state can be deduced as follows.

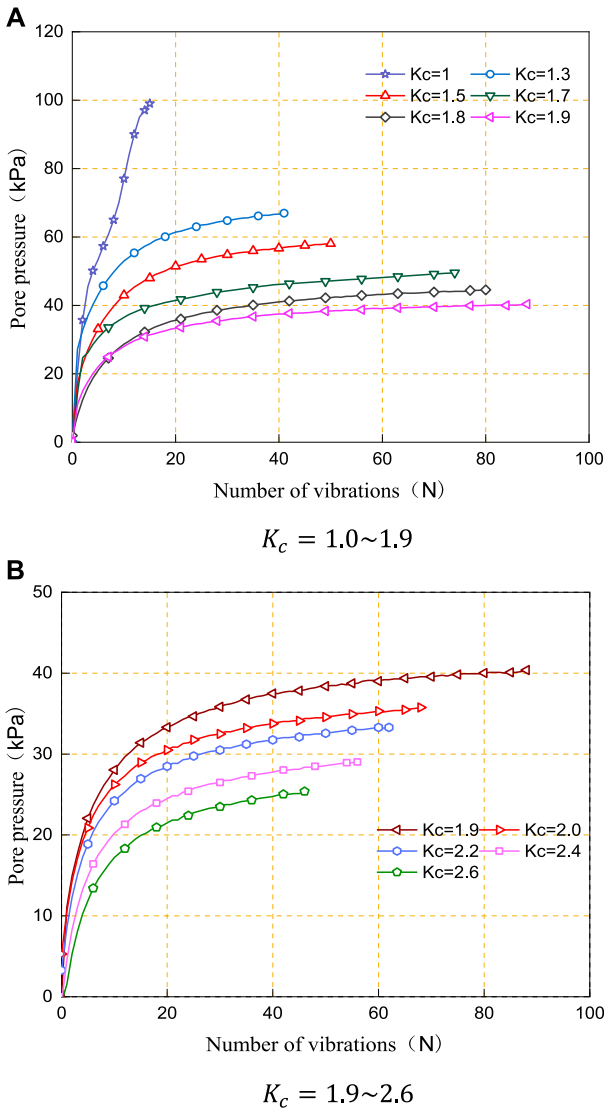

FIGURE 7
The evaluation of pore pressure under different K_c **(A,B)**.

$$u_{cr} = \frac{\sigma_1 + \sigma_3}{2} + \frac{c'}{tan\,\varphi'} - \frac{\sigma_1 - \sigma_3 + \sigma_d(1 - sin\,\varphi')}{2\,sin\,\varphi'} \quad (1)$$

Where: c' and φ' is the static effective cohesion and static effective internal friction angle of soil samples; σ_d is the dynamic stress amplitude; σ_1 and σ_3 represents axial pressure and confining pressure respectively.

Setting $\sigma_1 = K_c\sigma_3$, it can be obtained:

$$u_{cr} = \left(\frac{K_c + 1}{2} + \frac{K_c - 1}{2\,sin\,\varphi'}\right)\sigma_3 + \frac{c'}{tan\,\varphi'} + \frac{\sigma_d(sin\,\varphi' - 1)}{2\,sin\,\varphi'} \quad (2)$$

making

$$\lambda = \frac{K_c + 1}{2} + \frac{K_c - 1}{2\,sin\,\varphi'} \quad (3)$$

λ is the critical pore pressure ratio

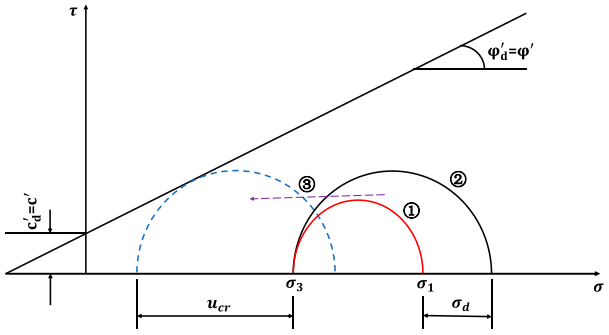

FIGURE 8
Critical pore water pressure under limit equilibrium state.

$$\Delta\sigma = \frac{c'}{tan\,\varphi'} + \frac{\sigma_d(sin\,\varphi' - 1)}{2\,sin\,\varphi'} \quad (4)$$

then

$$u_{cr} = \lambda\sigma_3 + \Delta\sigma \quad (5)$$

For common tailings, when $\sigma_d = 30kPa$, $\Delta\sigma \approx 0$; when $\sigma_d > 30kPa$, $\Delta\sigma < 0$, and it decreased with the increase in σ_d.

When $K_c = 1$, by substituting, $u_{cr} = \sigma_3 + \Delta\sigma$; when $K_c > 1$, aftering substituting $\lambda = 1$, the following can be gotten:

$$\lambda = \frac{K_c + 1}{2} + \frac{K_c - 1}{2\,sin\,\varphi'} = \frac{1 + sin\,\varphi'}{2\,sin\,\varphi'} - \frac{1 - sin\,\varphi'}{2\,sin\,\varphi'}K_c \quad (6)$$

Because $0 < sin\,\varphi' < 1$, the critical pore pressure ratio λ decreased with the increase of consolidation stress ratio K_c. After substituting Eq. 6, When $K_c > 1$, the critical pore pressure ratio $\lambda < 1$, and

$$u_{cr} < \sigma_3 + \Delta\sigma \quad (7)$$

Therefore, for a given dynamic stress amplitude, the pore water pressure will approach the confining pressure during isobaric consolidation, and during anisotropic consolidation, the critical pore pressure will be e less than the confining pressure, and the larger the consolidation ratio, the smaller the critical pore pressure.

4 Microscopic analysis

4.1 The introduction of simulation

In this paper, PFC 3D was used to simulate the standard indoor undrained dynamic triaxial test of saturated tailing silty sand, and the simulated effective confining pressure was controlled to be 100 kPa; the test was carried out using the loading method of equal stress amplitude. The upper and lower walls are loaded uniformly by the control program, and when the bias stress reaches the set stress amplitude q_{cyc}, the upper and lower walls reverse and continue to move until they reach the set stress amplitude q_{cyc} in the opposite direction and then reverse again.

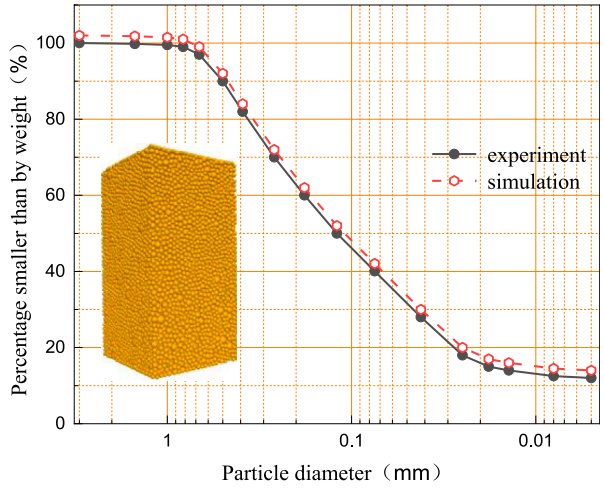

FIGURE 9
Gradation curve of discrete element sample.

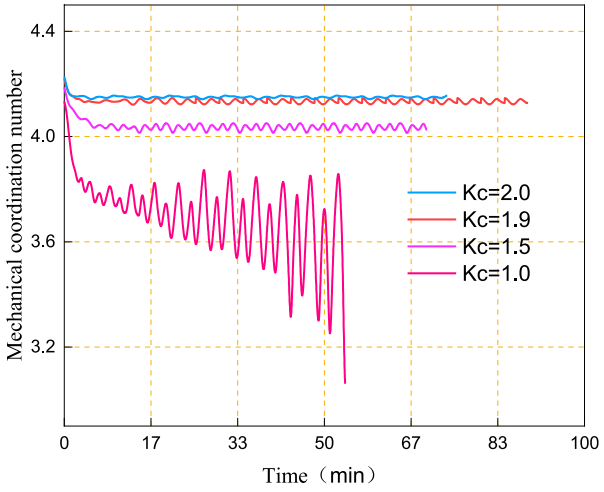

FIGURE 11
Mechanical coordination number curves under different consolidation conditions.

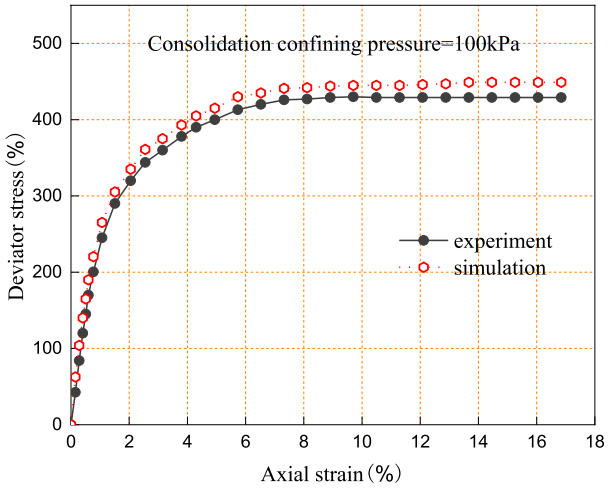

FIGURE 10
Stress-strain relationship curve.

TABLE 2 Parameters of the discrete element model.

Microscopic parameter	Value
Stiffness modulus	1×10^8
Stiffness ratio	1.0
Friction coefficient	0.5
density	2650
Anti-rotation coefficient	0.5

During the loading process, the lateral strain ε_1 is equal to the axial strain $-\varepsilon_2$ by adjusting the movement rate of the lateral walls, at which time the specimen volume is kept constant, and this constant volume condition is comparable to the undrained condition in the conventional cyclic triaxial test.Based on the constant volume condition, the liquefaction characteristics of the sample were simulated (ZHOU et al., 2009). The advantage of particle flow numerical simulation is the ability to observe the evolution of the meso fabric parameters in the sample at different cyclic loading times while modelling macroscopic mechanical performance of sample liquefaction; thus, the internal relationship between the change of meso fabric and the macroscopic mechanical response in the process of sand liquefaction can be analyzed, so as to further explore the meso-mechanical mechanism of sand liquefaction (Yang et al., 2007; Liu et al., 2020). In this simuation, situations under K_c = 1.0, K_c = 1.5, K_c = 1.9, K_c = 2.0 were taken as examples to analyze the coordination number and energy under different consolidation conditions. In this paper, the particle grading of the discrete element sample was determined first, as shown in Figure 9. After that, the stress-strain curve simulated by PFC triaxial shear test was comapred to the results of indoor triaxial shear test to calibrate the reasonable contact model parameters (AHMAD et al., 2019a; Yao-Hui et al., 2021), and these calibtared parameters were adopted for the subsequent dynamic triaxial test simulation and microscopic property analysis (JIANG, 2019). The comparison between numerical simulation and the indoor triaxial shear test is shown in Figure 10, and calibrated physical parameters of numerical model are shown in Table 2.

4.2 Analysis of mechanical coordination number

The mechanical coordination number refers to the average number of contacts per particle in the sample (MAHMOOD et al., 2020; AHMAD et al., 2021), excluding suspended particles with contact numbers less than or equal to 1. For granular

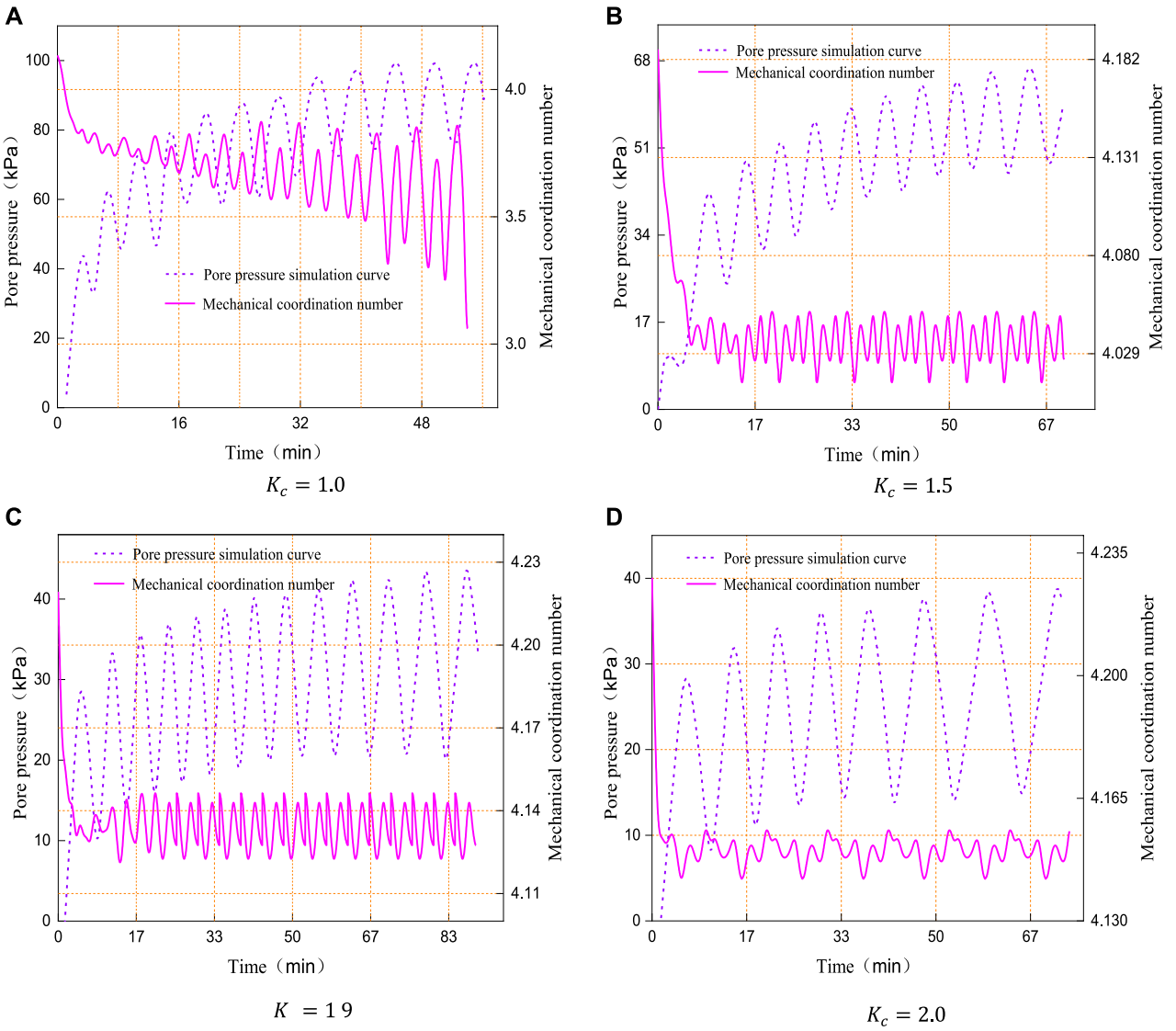

FIGURE 12
Pore pressure simulation and mechanical coordination curves under different consolidation conditions **(A–D)**.

materials, their mechanical properties are mainly affected by the density, which is affected by the indirect contact density of particles at the microscopic level (Thornton, 2000; Li et al., 2021b), which can be expressed by the mechanical coordination number of particles.

It can be seen from Figure 11 that with the increase of the consolidation ratio, the initial value of the mechanical coordination number became larger, as well as the number of particle contacts and the compactness of the sample, at the initial stage of cyclic loading, the mechanical coordination number of the sample continued to decrease. Figure 12 shows the changing curve of the instantaneous dynamic pore water pressure and corresponding mechanical coordination number curve while meeting the failure criteria under different consolidation ratios K_c; it can be seen from Figure 12A, when $K_c = 1$, when the "initial liquefaction" was initiated, and the mechanical coordination number decreased to about 3, which was reflected by the increase of pore water pressure under the undrained condition at the macroscopic level. At this time, the pore water pressure reached the confining pressure. According to Figures 12B–D, it can be seen that when $K_c = 1.5$, $K_c = 1.9$, $K_c = 2.0$, with the increase of the consolidation ratio, the decreasing amplitude of the mechanical coordination number decreased gradually during the cyclic loading of the sample. When the pore water pressure was stable, the mechanical coordination number did not fluctuate significantly, and the pore water pressure failed to reach the confining pressure. As the consolidation ratio increased from $K_c = 1$, $K_c = 1.5$ to $K_c = 1.9$ the time required for the sample to occur liquefaction became longer r; And from $K_c = 1.9$ to $K_c = 2.0$, with the increase in consolidation ratio, the time required for the sample to reach the failure standard became shorter.

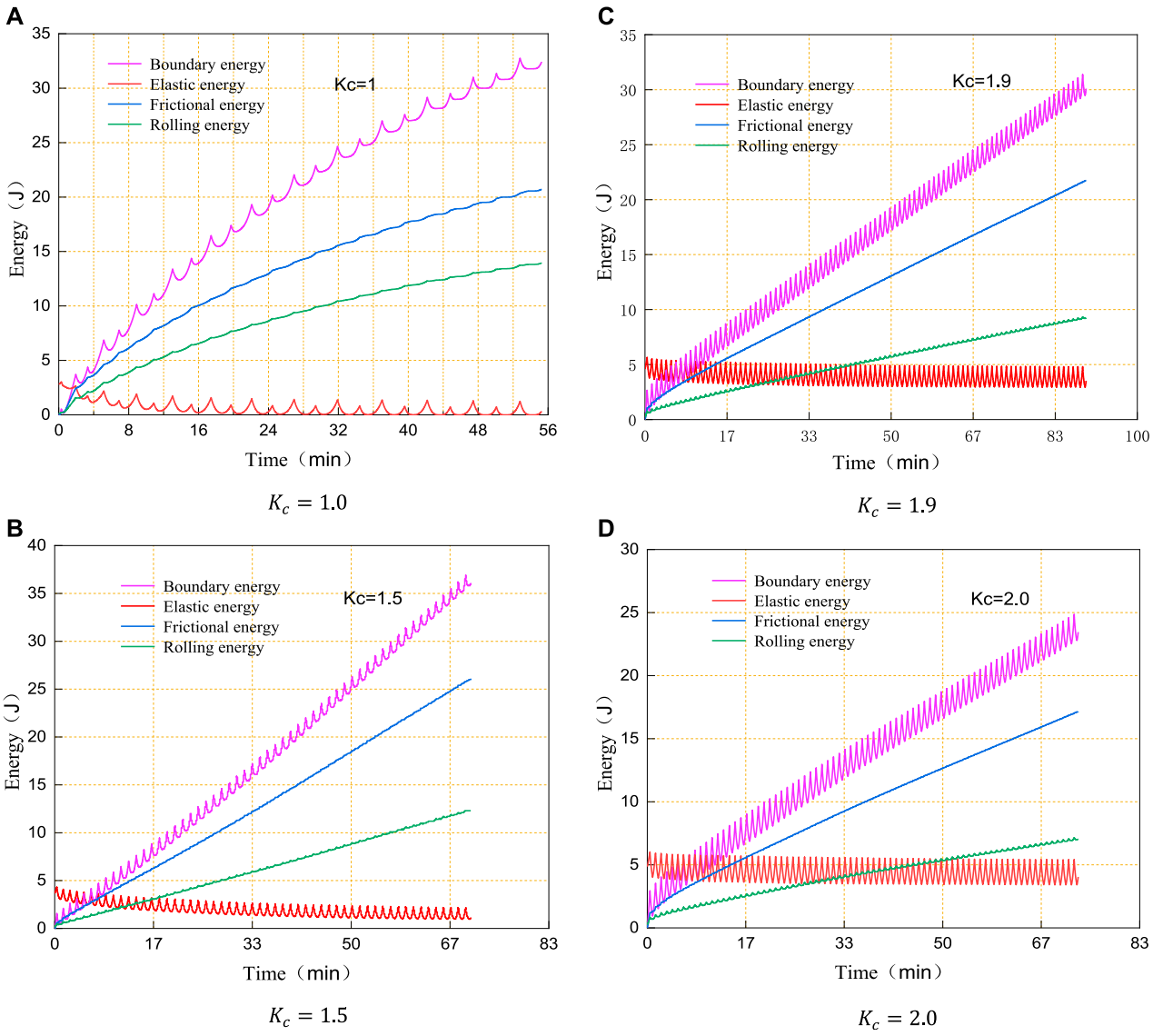

FIGURE 13
Energy curves under different consolidation conditions **(A–D)**.

4.3 Energy analysis

The energy storage and dissipation of particles during the loading process can represent their macroscopic mechanical response to a certain extent, and their failure actually experienced the evolution process of energy dissipation and instability (AHMAD et al., 2019b; AHMAD et al., 2020). The following will focus on the evolution law of The evolution law of elastic energy of particles (refers to the energy stored in the contact area of particles to deform the particles), particle friction (Bolton et al., 2008; Li et al., 2023), rolling energy dissipation (refers to the energy dissipated by sliding friction and anti-rolling between particles respectively) and boundary energy (refers to the energy generated by wall driving) (AHMAD et al., 2019c; Gao et al., 2023).

Figure 13 shows the energy evolution curves of the saturated tailing silty sand samples. it can be seen when the wall was subjected to cyclic loading and unloading, the wall would generate a certain amount of energy named boundary energy. At the same time, there was a certain amount of elastic energy stored at the contact of particles, and it increased and decreased successively with the loading and unloading process, but the decreasing amplitude was greater than the increasing amplitude so that the elastic energy was gradually released. In addition, under the effect of cyclic load, relative sliding (friction energy consumption) occurred between particles, which was followed by different degrees of rolling between particles (rolling energy consumption).

At the initial state, the elastic energy of particles increased with the increase of the consolidation ratio. As shown in Figure 13A, when K_c = 1, as the cyclic loading was subjected, the elastic energy of particles became 0, and the slope of particle friction dissipation energy and particle bending dissipation energy gradually decreased to approach 0; At this time, the sample began to occur initial

liquefaction. As shown in Figures 13B–D, when $K_c = 1.5, K_c = 1.9, K_c = 2.0$, the particle elastic energy did not decrease to 0, while the particle friction dissipation energy and particle bending dissipation energy continued to increase, without showing signs of initial liquefaction. Moreover, with the increase of the consolidation ratio, the elastic energy of the remaining particles became larger, which was the liquefaction of the sample when $K_c = 1$ on the macro level and pore water pressure reached confining pressure, and when $K_c > 1$, the sample did not occur liquefaction, and the pore water pressure decreased with the increase of consolidation ratio.

5 Conclusion

In this paper, in order to study the dynamic strength and liquefaction mechanism of tailings sand in karst seismic prone areas under different static stress states, a series of dynamic triaxial tests were conducted on saturated tailings fines in an iron tailings pond in Sichuan, and combined with discrete element simulations to further explore the dynamic properties of the fines under different consolidation ratios. The main conclusions are as follows.

(1) The critical consolidation ratio K_c' was proved by dynamic triaxial test and particle flow simulation, and its specific value is related to the properties and stress state of saturated sand. In this research, the critical consolidation stress ratio K_c' was about 1.9.
(2) The variation of dynamic strength showed different trends before and after reaching the $K_c' = 1.9$. When $K_c < 1.9$, the dynamic strength of the sample increased with the K_c; when $K_c > 1.9$, the dynamic strength of the sample decreased with the K_c. (3) The limit equilibrium theory and particle flow simulation were used to explain the phenomenon that for the isobaric consolidation $K_c = 1$, the pore water pressure tended to the confining pressure and induced complete liquefaction. For anisotropic consolidation ($K_c > 1$), the pore water pressure was less than the confining pressure and failed to initiate liquefaction, and decreased with the increase of consolidation ratio.
(3) The limit equilibrium theory and particle flow simulation were used to explain the phenomenon that for the isobaric consolidation $K_c = 1$, the pore water pressure tended to the confining pressure and induced complete liquefaction. For anisotropic consolidation ($K_c > 1$), the pore water pressure was less than the confining pressure and failed to initiate liquefaction, and decreased with the increase of consolidation ratio.

Data availability statement

The original contributions presented in the study are included in the article/Supplementary material, further inquiries can be directed to the corresponding author/s.

Author contributions

JC: Writing—review and editing WG: Conceptualization LS: Methodology KF: Software CB: Validation ZL: Formal analysis. All authors contributed to the article and approved the submitted version.

Conflict of interest

The authors LS, CB, and ZL were employed by Yunnan Phosphate Group Co., Ltd.

The remaining authors declare that the research was conducted in the absence of any commercial or financial relationships that could be construed as a potential conflict of interest.

Publisher's note

All claims expressed in this article are solely those of the authors and do not necessarily represent those of their affiliated organizations, or those of the publisher, the editors and the reviewers. Any product that may be evaluated in this article, or claim that may be made by its manufacturer, is not guaranteed or endorsed by the publisher.

References

Ahmad, M., Tang, X. W., Qiu, J. N., Gu, W-J., and Ahmad, F. (2020). A step forward towards a comprehensive framework for assessing liquefaction land damage vulnerability: Exploration from historical data. *Front. Struct. Civ. Eng.* 14 (6), 1476–1491. doi:10.1007/s11709-020-0670-z

Ahmad, M., Tang, X. W., Qiu, J. N., Gu, W-J., and Ahmad, F. (2021). Application of machine learning algorithms for the evaluation of seismic soil liquefaction potential. *Front. Struct. Civ. Eng.* 15 (2), 490–505. doi:10.1007/s11709-020-0669-5

Ahmad, M., Tang, X-W., Qiu, J-N., and Ahmad, F. (2019a). Evaluating seismic soil liquefaction potential using bayesian belief network and C4.5 decision tree approaches. *Appl. Sci.* 9 (20), 4226. doi:10.3390/app9204226

Ahmad, M., Tang, X-W., Qiu, J-N., and Ahmad, F. (2019b). Interpretive structural modeling and MICMAC analysis for identifying and benchmarking significant factors of seismic soil liquefaction. *Appl. Sci.* 9 (2), 233. doi:10.3390/app9020233

Ahmad, M., Xiaowei, T., and Jiangnan, Q. (2019c). Response and tolerability of sofosbuvir plus daclatasvir in elderly patients with chronic hepatitis-C. *IEEE 14th Int. Conf. Intelligent Syst. Knowl. Eng. (ISKE) Proc.* 31, 527–529.

Bolton, M. D., Nakata, Y., and Cheng, Y. P. (2008). Micro- and macro-mechanical behaviour of DEM crushable materials. *Geotechnique* 58 (6), 471–480. doi:10.1680/geot.2008.58.6.471

Chang-Rong, H. E. (1998). Compression and extrusion elongation characteristics of the dynamic triaxial test[J]. *Sichuan United Univ. Sci. Ed.* 2(04), 49–54. doi:10.15961/j.jsuese.1998.04.009

Chen-Yang, B. A. O., Xiang-Juan, Y., and Gao, Z. B. (2006). Experimental study on the dynamic properties of Yunnan chalk soil[J]. *J. Disaster Prev. Mitig. Eng.* 26 (03), 321–325. doi:10.13409/j.cnki.jdpme.2006.03.015

Chien, L. K., Oh, Y. N., and Chang, C. H. (2000). "In the effects of anisotropy consolidation on liquefaction strength and deformation for reclaimed soil," in *10th international offshore and polar engineering conference (ISOPE-2000)*. Seattle,Wa; International Society Offshore& Polar Engineers. 594–599. Seattle, Wa May 28-Jun 02.

Dai, B. B., Yang, J., and Zhou, C. Y. (2013). Numerical simulation of unstable behavior of loose sand[J]. *Chin. J. Geotechnical Eng.* 35 (09), 1737–1745.

Ding-Yi, X. I. E., Zhi-Hui, W. U., and Yao-Tang, G. U. O. (1981). Application of limit equilibrium theory in the analysis of dynamic instability process of saturated sand[J]. *China Civ. Eng. J.* 14 (04), 17–28. doi:10.15951/j.tmgcxb.1981.04.003

Gao, Y., Yu, Z., Chen, W., Yin, Q., Wu, J., and Wang, W. (2023). Recognition of rock materials after high-temperature deterioration based on SEM images via deep learning. *J. Mater. Res. Technol.* 25, 273–284. doi:10.1016/j.jmrt.2023.05.271

General Institute of Water Resources and Hydropower Planning and Design (2019). "Ministry of water Resources, nanjing Institute of water Resources science," in *Geotechnical test procedures: Gbt 50123 -2019[S]* (China Plan Press.

Hong-Jian, L., Mao-Hong, Y., and Qi-Ming, W. A. I. (1998). Study of dynamic shear strength of loess-like soils and volcanic ash clayey soils[J]. *J. Xi'an Jiaot. Univ.* 32 (10), 73–77.

Hu, Y. F. (1996). *Engineering properties and stability analysis of fly ash dam construction*. Sichuan United University.

Jiang, M. J., Sun, R. H., and Tao, L. I. (2020). CFD-DEM simulation of undrained cyclic triaxial shear of microbial treated sand[J]. *Chin. J. Geotechnical Eng.* 42 (01), 20–28. doi:10.11779/CJGE202001002

Jiang, Y. X. (2019). *Study on the vibration liquefaction characteristics of gravelly sandy soil and rubbery sandy soil[D]*. China University of Mining and Technology.

Ke-Xu, Z. (1984). Liquefaction stress condition of saturated sand[J]. *Earthq. Eng. Eng. Vib.* 4 (1), 99–109. doi:10.13197/j.eeev.1984.01.009

Kong, L., Liang-Liang, J. I., and Cao, J. F. (2013). Meso-mechanism of the effect of stress path and particle size on sand deformation[J]. *Chin. J. Rock Mech. Eng.* 32 (11), 2334–2341.

Konstadinou, M., and Georgiannou, V. N. (2013). Cyclic behaviour of loose anisotropically consolidated Ottawa sand under undrained torsional loading. *Geotechnique* 63 (13), 1144–1158. doi:10.1680/geot.12.p.145

Li, X. L., Chen, S. J., Liu, S. M., and Li, Z. H. (2021a). AE waveform characteristics of rock mass under uniaxial loading based on Hilbert-Huang transform. *J. Central South Univ.* 28 (6), 1843–1856. doi:10.1007/s11771-021-4734-6

Li, X. L., Chen, S. J., Wang, S., Zhao, M., and Liu, H. (2021b). Study on *in situ* stress distribution law of the deep mine taking Linyi Mining area as an example. *Adv. Mater. Sci. Eng.* 9 (4), 5594181–5594211. doi:10.1155/2021/5594181

Li, X. L., Zhang, X. Y., and Shen, W. L. (2023). Abutment pressure distribution law and support analysis of super large mining height face. *Int. J. Environ. Res. Public Health* 20 (2), 227. doi:10.3390/ijerph20010227

Lian-Hong, Y. U., and Wang, Bo (1999). Experimental study of vibratory pore water pressure in saturated powder soils[J]. *J. Dalian Univ.* | *J Dalian Univ* 20 (4), 59–64.

Liao, H. J., Song, L., and Zheng, Y. A. N. G. (2001). Experimental study on the strength of cohesive soils under reciprocal loading and the criteria for taking values[J]. *Rock Soil Mech.* 2001 (01), 1620. doi:10.16285/j.rsm.2001.01.004

Liu, H. Y., Zhang, B. Y., Li, X. L., Liu, C., Cheng, W., Feng, W., et al. (2022). Research on roof damage mechanism and control technology of gob-side entry retaining under close distance gob. *Eng. Fail. Anal.* 138 (5), 106331. doi:10.1016/j.engfailanal.2022.106331

Liu, S. M., Li, X. L., Wang, D. K., and Zhang, D. (2020). Investigations on the mechanism of the microstructural evolution of different coal ranks under liquid nitrogen cold soaking. *Energy Sources, Part A Recovery, Util. Environ. Eff.*, 1–17. doi:10.1080/15567036.2020.1841856

Mahmood, A., Tang, X-W., Qiu, J-N., Gu, W-J., and Ahmad, F. (2020). A hybrid approach for evaluating CPT-based seismic soil liquefaction potential using Bayesian belief networks. *J. Central South Univ.* 27 (2), 500–516. doi:10.1007/s11771-020-4312-3

Mei-Ying, M. A. (1988). Effect of initial consolidation shear stress on the dynamic strength of saturated sandy soils[J]. *Water Resour. Water Transp. Sci. Res.* 2 (1), 63–68. doi:10.16198/j.cnki.1009-640x.1988.01.007

Mei-Ying, M. A. (1980). Several problems of standard sand liquefaction test[J]. *Chin. J. Geotechnical Eng.* 2 (4), 46–54.

Shen, Y., Tao, M. A., and Guo-Jian, X. U. (2015). PFC numerical experimental study on dynamic collapse characteristics of silt under stress control mode[J]. *Chin. J. Geotechnical Eng.* 37 (12), 2280–2285.

Shou-Zhi, N. E. I. (1980). Liquefaction and strength of saturated sand under dynamic load[J]. *Chin. J. Geotechnical Eng.* (03), 64–73.

Thornton, C. (2000). Numerical simulations of deviatoric shear deformation of granular media. *Geotechnique* 50 (1), 43–53. doi:10.1680/geot.2000.50.1.43

Wang, X. H., and Zhou, H. L. (2001). Influence of consolidation ratio on liquefaction of saturated sand[J]. *China Railw. Sci.* 22 (6), 121–126.

Wang, Y. Z., Pan-Bo, Y. A. N. G., and Sun, Xi-Ping (2015). Study on strength weakening of soft clay under cyclic load and its dynamic calculation application[J]. *Chin. J. Geotechnical Eng.* 37 (05), 821–828. doi:10.11779/CJGE201505007

Yan-Qiang, D. U., Chun-He, Y. A. N. G., and Shang-Wei, W. U. (2016). Pore water pressure characteristics of tailings silt undercyclic loading[J]. *J. Northeast. Univ. Sci.* 37 (04), 583–588. doi:10.3969/j.issn.1005-3026.2016.04.027

Yang, L. I. U., Zhou, J., and Wu, S. C. (2007). Fine view numerical simulation of sandy soil deformation under cyclic loading I:Loose sand test results[J]. *Chin. J. Geotechnical Eng.* 29 (7), 1035–1041.

Yao-Hui, G. U. O., Peng, Z., and Tian, Y. K. (2021). Numerical simulation of particle flow in triaxial compressionof tailings from a metal mine[J]. *Min. Res. Dev.* 41 (05), 118–123. doi:10.13827/j.cnki.kyyk.2021.05.021

Zhang, J. H., and Chang-Rong, H. E. (1994). Liquefaction strength and pore pressure law of unsaturated sandy soils under reciprocal loading[J]. *J. Chengdu Univ. Sci. Technol.* (01), 1–8.

Zhang, Ru, Chang-Rong, H. E., Wen-Ping, F. E. I., and Mingzhong, G. A. O. (2006). Effect of consolidation stress ratio on the development pattern of dynamic strength and dynamic pore pressure of soil samples[J]. *Chin. J. Geotechnical Eng.* (01), 101–105.

Zhang, X. Z., Shang-Wei, W. U., and Zhang, Chao (2018). Evolution of dynamic pore pressure in tailings under different consolidation conditions[J]. *Rock Soil Mech.* 39 (03), 815–822. doi:10.16285/j.rsm.2016.0921

Zhou, J., Yang, Y. X., and yang, L. I. U. (2009). Numerical simulation of granular flow with sandy soil liquefaction characteristics under cyclic loading[J]. *Rock Soil Mech.* 30 (04), 1083–1088. doi:10.16285/j.rsm.2009.04.053

Zhou, X. M., Wang, S., Li, X. L., Meng, J., Zhang, L., Pu, D., et al. (2022). Research on theory and technology of floor heave control in semicoal rock roadway: Taking longhu coal mine in Qitaihe mining area as an Example. *Lithosphere* 2022 (11), 3810988. doi:10.2113/2022/3810988

frontiers | Frontiers in Earth Science

TYPE Original Research
PUBLISHED 19 July 2023
DOI 10.3389/feart.2023.1235674

OPEN ACCESS

EDITED BY
Xuelong Li,
Shandong University of Science and Technology, China

REVIEWED BY
Chaoxuan Zhang,
Chinese Academy of Sciences (CAS), China
Cheng Lyu,
Sichuan University, China

*CORRESPONDENCE
Rui Yang,
yr_swjtu@outlook.com

RECEIVED 06 June 2023
ACCEPTED 05 July 2023
PUBLISHED 19 July 2023

CITATION
Yang R, Kong Q, Ren M, Ji F and Li D (2023), Statistical and numerical analysis on characteristics and influence factors of construction cracks of large-diameter underwater shield tunnel: a case study. *Front. Earth Sci.* 11:1235674. doi: 10.3389/feart.2023.1235674

Statistical and numerical analysis on characteristics and influence factors of construction cracks of large-diameter underwater shield tunnel: a case study

Rui Yang[1,2]*, Qian Kong[1,2], Meng Ren[1,2], Fuquan Ji[1,2] and Dejie Li[1,2,3]

[1]CCCC Second Harbour Engineering Co., Ltd., Wuhan, China, [2]CCCC Highway Bridge National Engineering Research Centre Co., Ltd., Beijing, China, [3]Hohai University Institute of GeoEnvironmental, Nanjing, China

Tunnel excavation is prone to segment cracks, which may lead to serious safety accidents. This work aims to investigate the type, location and occurrence time of cracks in a large-diameter underwater shield tunnel and also ascertain the causes of the cracks. The correlations between crack characteristics and shield tunneling parameters were analyzed. The effect of jack deflection and poor assembly on cracks were investigated using a refined finite element model of two consecutive rings with consideration of the assembly clearance and the constraint effect of the shield machine. The results confirmed that 93% of the cracks were formed between the current ring and the last ring jacking stage. Positive cracks induced by jack deflection occurred during the current ring jacking stage, while the lengths of the cracks, proportional to the constraint of the boring machine on the segments, remained constant during the subsequent construction process. The cracks caused by poor assembly quality arose during the current and next ring jacking stages. Furthermore, the cracks generated in the current ring jacking stage would propagate during the subsequent construction process. The type, length, and number of cracks were influenced by the assembly clearance. The inverted V-shape longitudinal joints caused more cracks than any other assembly defects. The finding of this study results and conclusions are expected to contribute to the reduction of cracks at the jacking stage of the large-diameter underwater shield tunnels with eccentricity force transfer platforms.

KEYWORDS

segment cracks, shield tunneling parameters, statistical analysis, numerical modeling, jack deflection, assembly defects

1 Introduction

Large-diameter shield tunnels have already become the most popular solution to relieve the pressure of the crosse river transportation. For such tunnels, segment lining cracks are one of the primary structural safety issues. These cracks may occur at various stages such as segment transportation, segment hoisting, tunnel construction and operation, while most of them are produced during the shield tunneling process (Chen and Mo, 2009; Shayanfar et al., 2017). Segment cracks not only affect the appearance of tunnels but also lead to hazards and

reduce the functionality and durability of tunnels. Developed cracks can even threaten the safety of the tunnels (Sugimoto, 2006; Xu et al., 2019). Therefore, it is essential to study the causes of cracks, so as to prevent the occurrence of cracks in the segment linings.

The most common segment cracks can be classified as longitudinal, corner, U-shaped and circumferential cracks (Gruebl, 2006; Sugimoto, 2006; Chen and Mo, 2009; Shayanfar et al., 2017; Xu et al., 2019). The causes of longitudinal cracks include jack eccentricity, jack deflection, uneven support, uneven thrust, inconsistent jacking speeds, assembly angles, and uneven regional pressures of the upper and lower jacks (Burgers et al., 2007; Cavalaro et al., 2011; Lu et al., 2017; Lu et al., 2018.; Sharghi et al., 2021). When the jack boot is eccentric or the jack is at a deflection angle to the segment, a bending moment toward the outer arc of the segment would be generated, which may loosen the longitudinal joints and lead to joint openings. The joint openings lead to uneven support, causing tension on the front end of the segment (Burgers et al., 2007; Sharghi et al., 2021), which results in positive longitudinal cracks between the two jack boots (Lu et al., 2018). In addition, inconsistent jacking speed, uneven regional pressures in the upper and lower jacks, and the presence of there is a longitudinal moments at the front end of the segment, can lead to temporary or permanent positive cracks (Koyama, 2003; Xu and Zhang, 2013; Lu et al., 2017; Lorenzo, 2021). During the construction of shield tunnels, the segment at the unsolidified position of the grouting behind the wall can be considered as a simply supported beam that is restrained by the shield machine in the front and by the completed tunnel in the rear. When the difference in regional pressure between the upper and lower or left and right jacks is too large, a bending moment on the transverse axis of the tunnel would be generated at the rear of the shield machine (Liu et al., 2023a). As a result, the segments in the weakly constrained region are under tensile stress, and form the circumferential cracks (Mo and Chen, 2008). Corner cracks are generally attributed to the loose bolts or wide longitudinal (radial) joints, which could lead to collisions or uneven contacts between segments during the assembly process (Burgers et al., 2007; Cavalaro, 2009). U-shaped cracks are usually located between the end face and the handhole. These U-shaped cracks occur when adjacent segments are not aligned with each other due to the rotation, which may lead to compression between segments and the compression of the bolt rod against the bolt hole (Chen and Mo, 2009). Besides small shield tail clearance, improper shield posture, poor assembly quality and change in the longitudinal slope of the tunnel can also lead to cracks in the segment linings, despite the fact that it is still not clear which kind of cracks are subjected to these causes (Mo and Chen, 2008; Cavalaro, 2009; Yang et al., 2018; Ahmadi and Molladavoodi, 2019; Liu et al., 2020; Dai et al., 2022). Macroscopic or microscopic experimental tests, deep learning-based method, and numerical simulations are effective approaches to investigate the cracks (Liu et al., 2023b; Gao et al., 2023; Liu and Li, 2023). However, the mechanical conditions of the segments inside the shield machine are very complicated, which poses challenges to fully consider various factors during experimental testing. Therefore, many experimental studies have focused on the single factor, such as jack eccentricity and limit thrust (Hemmy, 2001; Plizzari and Tiberti, 2007; Li et al., 2015; Nogales and Fuente, 2020). Due to the simplicity of the numerical simulations, more factors like the effect of rotation between segments, uneven support, uneven thrust, jack eccentricity, and jack deflection, have been selected for investigation in the scientific literatures (Mohtadinia et al., 2020; Krahl et al., 2021; Tian et al., 2021).

It should be noted that most of previous studies on segment cracks were performed on the premise that the tunnel was completed, whereas the crack data obtained during the shield tunneling were limited. Hence, there is missing information on the detailed occurrence time of the cracks was lacking. Numerical simulations on segment generally concentrated on a specific ring assembling or jacking stage. These studies assumed the cracks of the segment rings only occurred during the construction of the selected ring and failed to consider the effect of subsequent construction as well as the cracking behaviors of adjacent rings on the crack generation. In addition, the influence of the joint clearance and the restraint of the shield tail on the segments were also not taken into account.

In present study, 927 cracks in 1225 ring segments of a large-diameter shield tunnel with the eccentric force transfer platforms in Bangladesh were examined in terms of the type, quantity, location and occurrence time. Based on the selected tunneling parameters and a refined model of two consecutive segment rings considering the assembly clearance, the type, distribution, expansion, and occurrence time of segment cracks in the scenarios of shield attitude adjustment and poor assembly during the process of jacking two consecutive rings were investigated. The findings are expected to provide some guidelines for reduction of cracks at the jacking stage of large-diameter underwater shield tunnels with segment eccentric force transfer platforms.

2 Background

2.1 Project overview

The Karnapuri River tunnel is located in Chittagong, Bangladesh and connects the east and west banks of Karnapuri River at the estuary. The shield tunnel is 2450 m long and is assembled with 1225 ring segments. The tunnel depth ranges from approximately 7–32 m, with a maximum water pressure of about 4 bar. The stratigraphic distribution of the tunnel site is shown in Figure 1.

2.2 Design of segment and shield tail

The outer diameter of the tunnel is 10.8 m, and the thickness of the segment is 0.5 m, and the width of the segment is 2 m. Each ring lining consists of 1 K segment, two adjacent segments (L1, L2), and five standard segments (B1–B5). The longitudinal joints are connected by Class 8.8 M30 bolts, while the circumferential joints are connected by Class 8.8 M36 bolts. The central angle of the adjacent segments and the standard segments is 46.9°, and the central angle of the K segment is 31.7°. Each adjacent and standard segment has three force transfer platforms, and the K segment has two force transfer platforms. The thickness of the force transfer platform is 4 mm.

The dimensions of the segments, as well as the dimensions and positions of the force transfer platform, hand holes, and bolt holes as shown in Figure 2. It is worth noting that there was a 32-mm

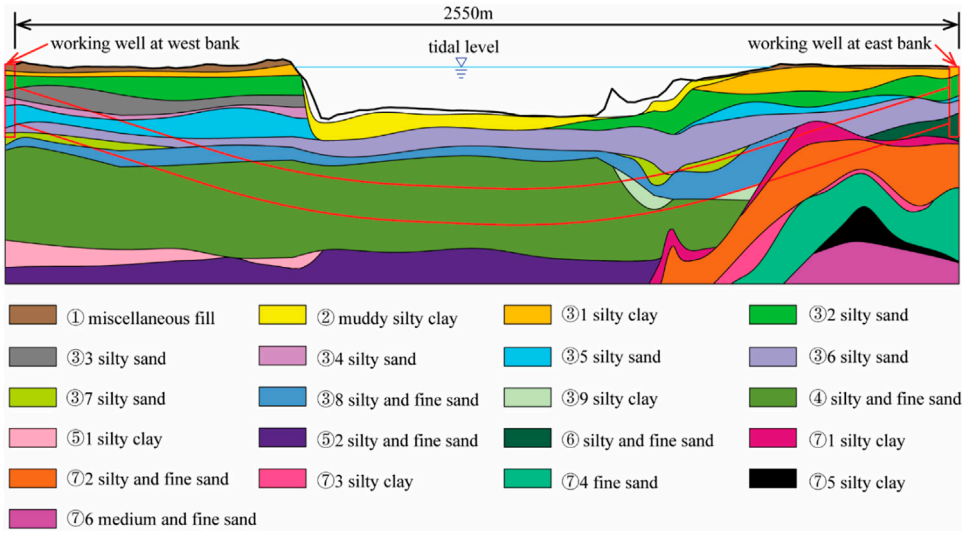

FIGURE 1
Geological profile of the tunnel.

deviation between the center lines of the force transfer platforms and the center line of the segment (Figure 2B). As the positions of the force transfer platforms are the same as those of the jacks, the forces acting on the segment is always eccentric during the jacking process.

The shield machine is equipped with 23 jacks, which are divided into four zones. Jacks No. 21–23 and No. 1–3, No. 4–8, No. 9–15, and No. 16–20 are in the upper, right, lower and left zones, respectively. The central angles of the upper, lower, left, and right zones are 94°, 110°, 78°, and 78°, respectively (Figure 3A).

Guide bars are installed at the tail of the shield machine to avoid excessive jack deflection angles. The dimensions of the guide bars are 30 mm in height, 50 mm in width, 2795 mm in length and they are arranged in a circumferential direction, with a central angle of 8° between adjacent guide bars. The distance between the guide bar and the jack is 300 mm. There are four shield tail brushes at machine tail. The distances from the end of the guide bars for the four tail brushes are 200, 650, 1050, and 1500 mm, respectively (Figure 3B).

3 Statistical analysis of segment cracks

3.1 Segmental cracks in shield tunnel

A total of 927 cracks were identified in the left tunnel, and the segment rings with cracks accounted for 47.7% of the total number of segment rings. The cracks could be divided into five types: positive, backward, handhole, corner and circumferential cracks. The handhole cracks started from the end of the bolts and developed obliquely (Figure 4).

The proportion of each crack type is illustrated in Figure 5. Positive cracks accounted for the largest proportion, followed by the backward and circumferential cracks. These three types of cracks accounted for 95% of the total cracks. The focus of the work was therefore on the causes of the longitudinal and circumferential cracks.

Considering that the dominant loads acting on segments were the thrust of the jacks before the segments were pushed out from the shield tail, the number of longitudinal cracks at locations of the 23 jacks was counted (Figure 6). The longitudinal cracks occurred mainly in the down zone of the jacks, followed by the left zone. Cracks in the lower and left zones accounted for 76% and 16.21% of the total cracks, respectively. Of the 23 jacks, the largest proportion of longitudinal cracks was found at jacks 13 and 14, which were mainly in the down zone closest to the left zone of the jack.

To investigate the relationship between the cracks and segment type, eight segments were divided into 23 zones (labelled as A–W), with the boundary of the adjacent zones being the bisector between the two force transfer platforms (Figure 7A).

Figure 7B lists the numbers of longitudinal cracks in each zone of the different segments. The largest proportion of longitudinal cracks was in zone J, followed by zone V. The segment with the most longitudinal cracks was B5, followed by L1, and the K segment had the least longitudinal cracks. For each segment, the zone with the largest proportion of cracks was the force transfer platform in the middle part, followed by the force transfer platform on the left.

The segments were assembled with staggered joints. Therefore, the segments could be divided into two types, namely, i.e., Type A and Type B according to the positional of the longitudinal joints of the front and rear rings in relation to and the segment of the objective ring, with the exception of the K segment. The proportion of longitudinal cracks in each type of segment is shown in Figure 8. Overall, 73.5% of the longitudinal cracks were observed in Type-A segments.

Figure 9 displays the distribution of the occurrence time of the longitudinal cracks. The current ring jacking indicates that the cracks were produced in the n-th segment when the n-th segment was jacked. The last ring jacking represents that the cracks were generated in the n-th segment when the (n+1)-th segment was jacked. The third ring jacking denote that the

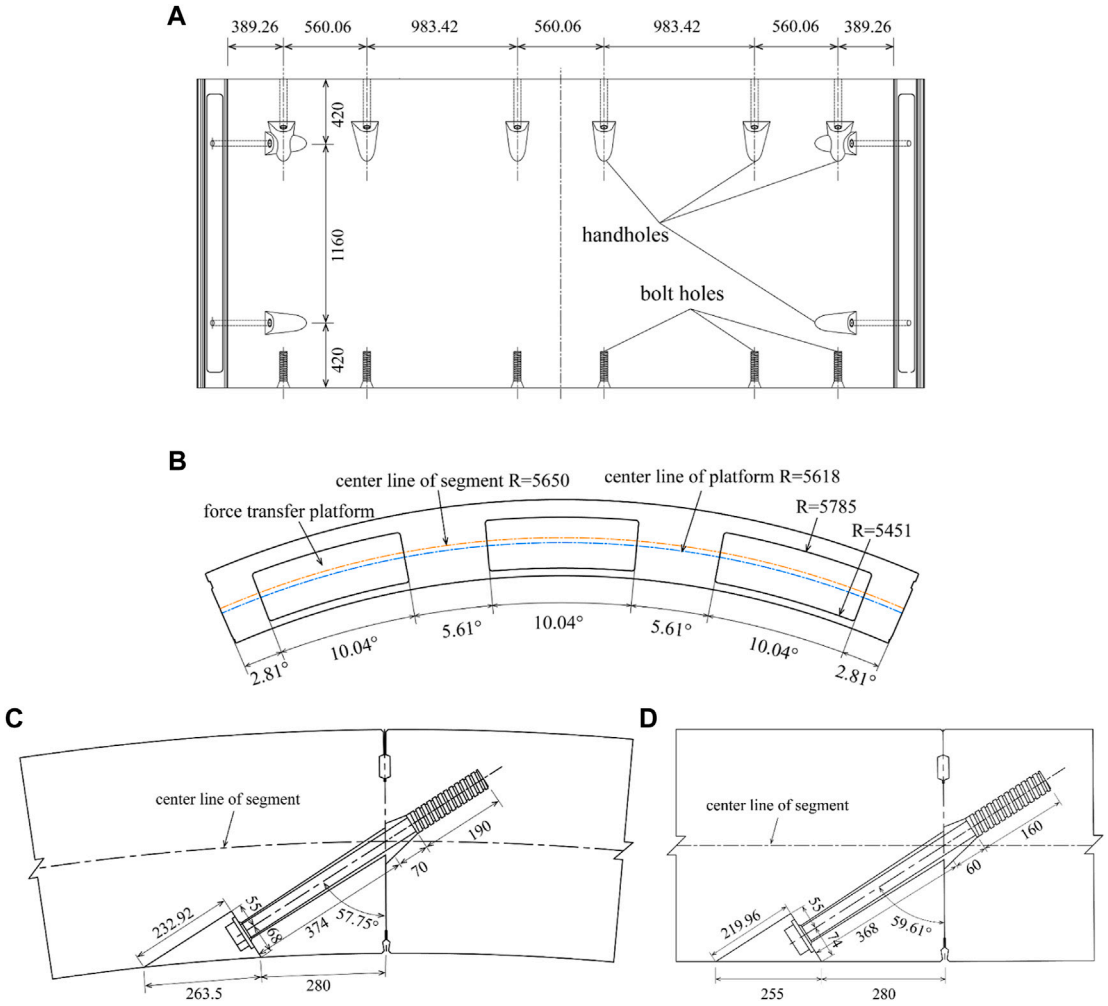

FIGURE 2
(A) Unfolded drawing of the inner curved surface of the segment **(B)** Drawing of the force transfer lug position and dimension **(C)** Drawing of the longitudinal seam joint **(D)** Drawing of the circumferential seam joint (unit: mm).

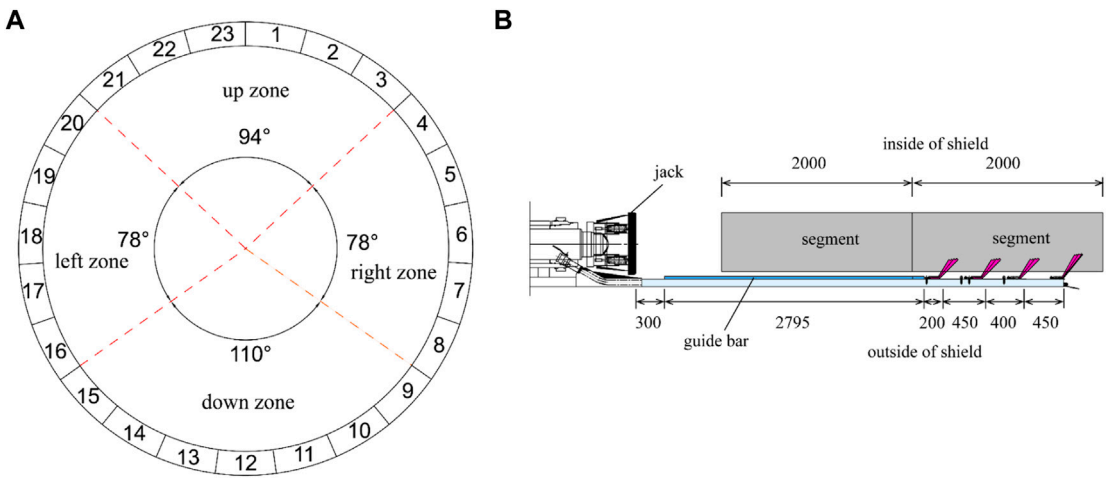

FIGURE 3
(A) Serial number and partition of jack **(B)** side view of shield tail (unit: mm).

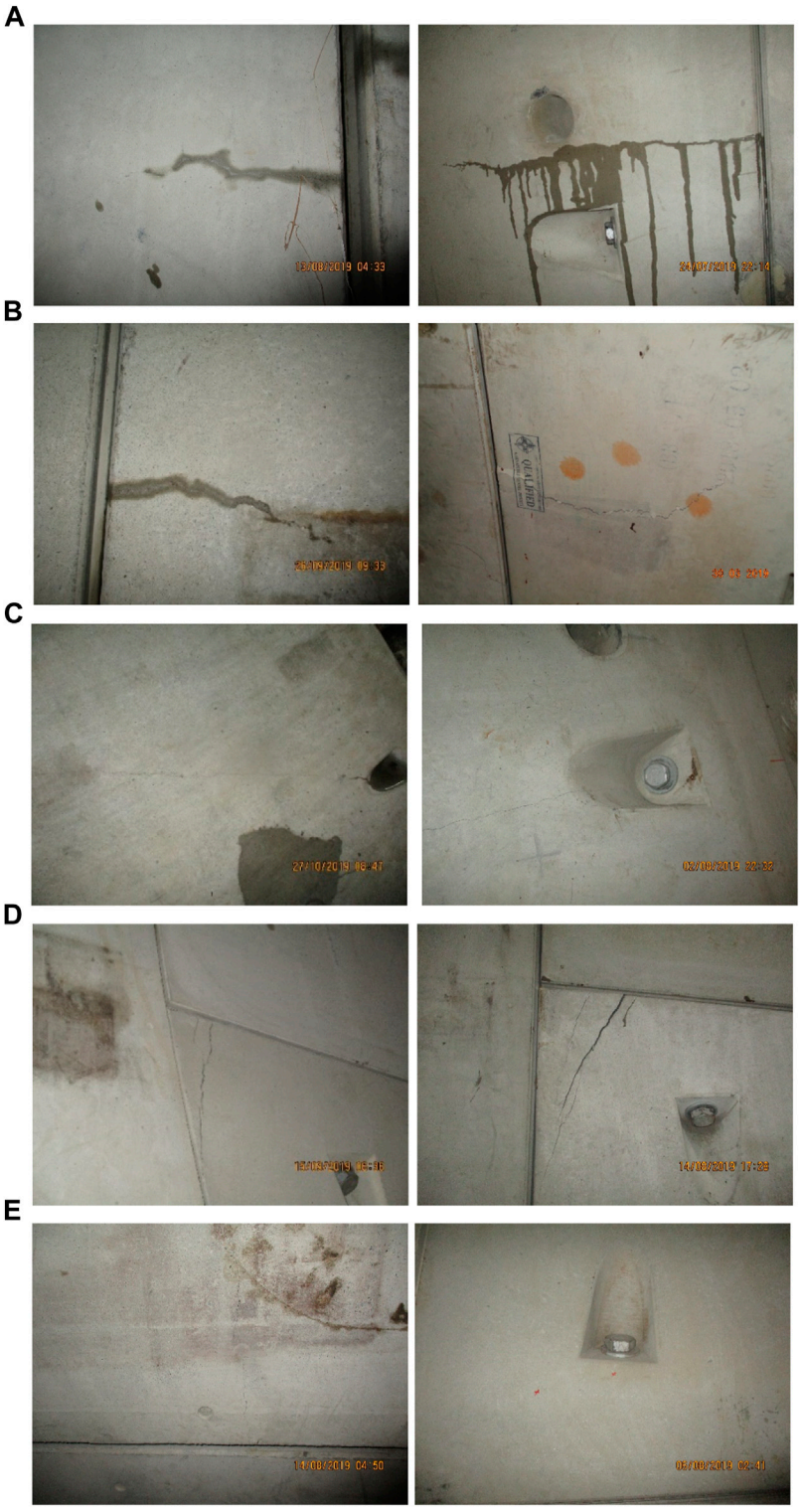

FIGURE 4
Typical cracks: **(A)** positive crack, **(B)** backward crack, **(C)** bolt crack, **(D)** corner crack, and **(E)** circumferential crack.

cracks were developed in the n-th segment when the $(n+2)$-th segment was jacked.

Figure 9, demonstrates that more than half of the cracks were formed during the current ring jacking stage. However, unlike different from previous studies, 38% of the cracks were formed during the last ring jacking stage. Considering that 93% of the cracks were formed in the current and last ring jacking stages, this study only concentrated on the cracks developed in these two jacking stages.

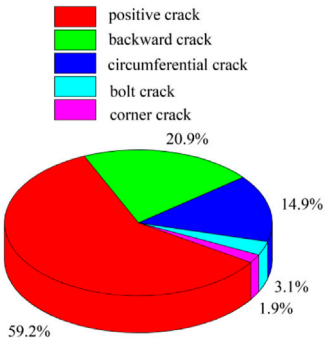

FIGURE 5
Proportions of different types of cracks.

3.2 Statistical analysis of segmental cracks

Since the segment cracks were primarily longitudinal, the main causes of the segment cracks were considered to be the same. Previous studies have linked formation of cracks to the thrust, torque, jacking speed, and posture of the shield machine. Therefore, the values of these tunneling parameters were utilized to analyze the causes of cracks. The equation for calculating the shield attitude adjustment could be given as:

$$\Delta = \sqrt{\left(\left|y_{f,n} - y_{f,n-1}\right| + \left|y_{t,n} - y_{t,n-1}\right|\right)^2 + \left(\left|x_{f,n} - x_{f,n-1}\right| + \left|x_{t,n} - x_{t,n-1}\right|\right)^2} \quad (1)$$

where Δ is the adjustment amount of the shield attitude between two segment rings; $y_{f,n}$ and $y_{f,n-1}$ are the vertical deviations of the shield head of the nth and $(n-1)$-th segments, respectively; $y_{t,n}$ and $y_{t,n-1}$ are the vertical deviations of the shield tail of the nth segment and the $(n-1)$-th segments, respectively; $x_{f,n}$ and $x_{f,n-1}$ are the horizontal deviations of the shield head of the nth and the $(n-1)$-th segments, respectively; $x_{t,n}$ and $x_{t,n-1}$ are the horizontal deviations of the shield tail of the nth and the $(n-1)$-th segments, respectively.

The average shield thrusts and cutter torques of the segments with and without cracks are indicated in Figure 10A. It can be seen that the average thrusts and cutter torques of the segments with cracks were lower than those without cracks, demonstrating that excessive thrusts and cutter torques were not the main causes of cracking in the segments.

The average tunneling speeds and attitude adjustment values of the segments with and without cracks are displayed in Figure 10B. It is indicated which shows that the average tunneling speed for the segments with cracks were lower than those without cracks. Hence, the large tunneling speed was not the main cause of cracking in the segments. However, the attitude adjustment value of the segments with cracks was 1.64 times higher than that without cracks, implying the attitude adjustment of the shield machine may be the cause of cracking in the segments.

For an individual segment ring, the jacking pressure in different zones and the shield tail clearance may cause cracks in the segments. As can be seen from Figure 10C, the largest average jacking pressure was found in the down and left zones. Excessive jacking pressure may have contributed to the cracking in the segments as the cracks in the down and left zones accounted for 76% and 16% of total cracks, respectively.

It can be seen from Figure 10D that the lower and left zones of the jacks with larger shield tail clearance values had a greater proportion of cracks compared to the up and right zones, indicating that the shield tail clearance was not the cause of cracking in the segments.

4 Numerical simulation

The above analysis suggested that the adjustment of the shield attitude and the high jacking pressure in the down and left zones may be the two main causes of the longitudinal cracks in the shield segments of the Karnapuri River in Bangladesh. However, the above analysis can only reflected the correlation between the parameters

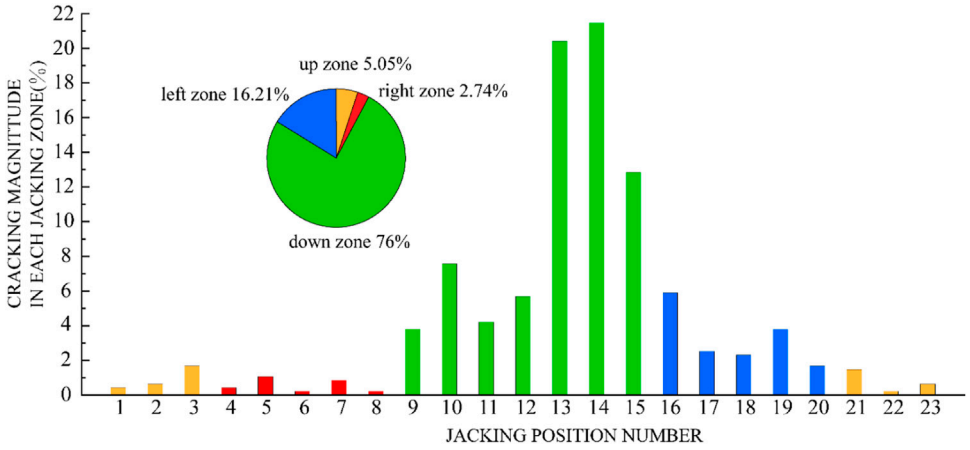

FIGURE 6
Cracking magnitudes in different jacking zones.

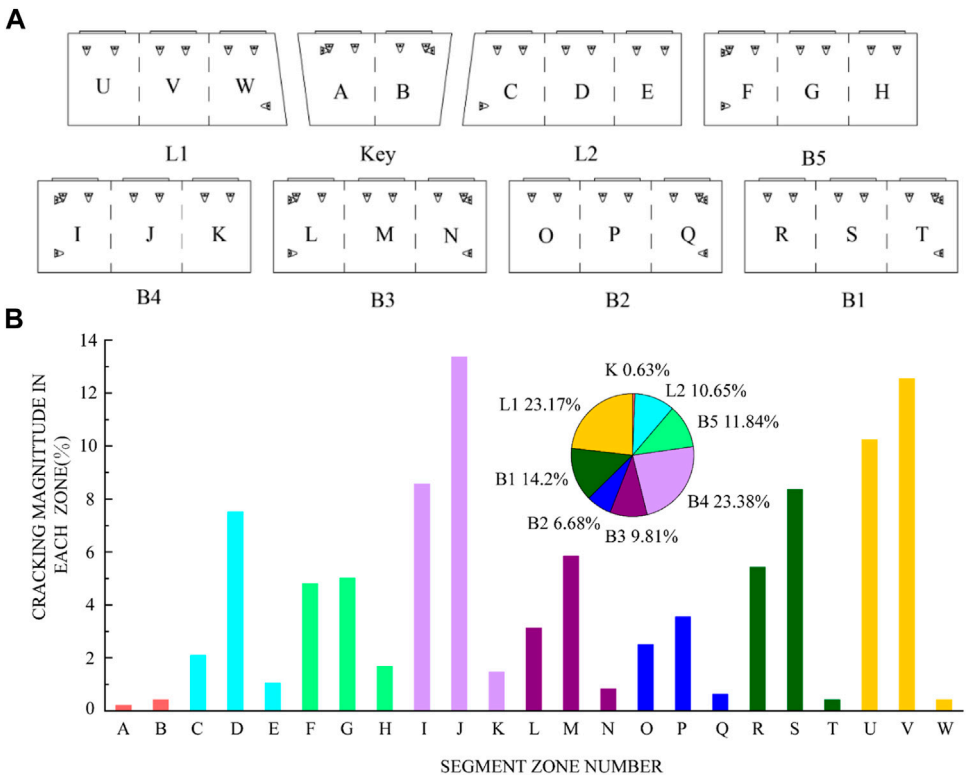

FIGURE 7
(A) Zoning of the segmental linings for statistical examination **(B)** Cracking magnitude in different segment zones.

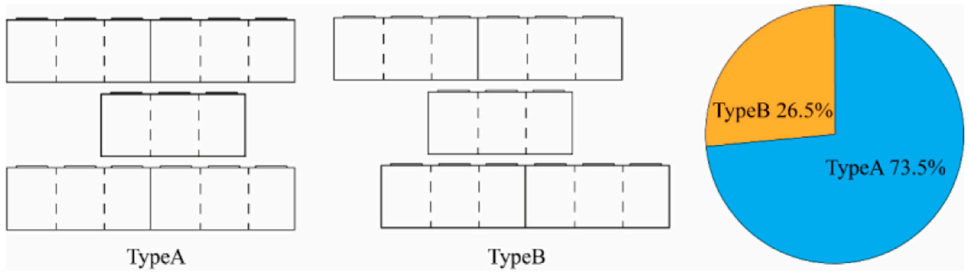

FIGURE 8
Different types of segment positional relationships between the front and last ring.

and crack formation but failed to identify the mechanisms of the cracking. Moreover, investigation on cracks caused by poor assembly were not involved. Therefore, in this section, numerical simulations were performed to further analyze the causes of longitudinal cracks in the segments.

4.1 Finite element model

The analysis from the data in the previous sections, the B4 segment had the largest number of cracks. The positional of the segment ring with cracks and its front and rear rings was Type-A. Moreover, most cracks occurred in the current and the last ring jackings stage. Therefore, these two rings containing B4 segments were chosen for the further study. The *n*-th segment was divided into B3*n*, B4*n*, and B5*n*, while the (*n*+1)-th segments was divided into B3*n*+1 and B4*n*+1.

Figure 11 illustrates the finite element model constructed in this study. In order to simulate the interactions between the segments, circumferential pedestals were built for B3*n*, B5*n*, B3*n*+1, and B4*n*+1, and longitudinal pedestals were created for B3*n*, B4*n*, and B5*n*. For the B4*n* segment, there were two longitudinal pedestals, S and H, to simulate the uneven longitudinal support and assembly angles of the segments. Guide bars were set on the outer arc surfaces

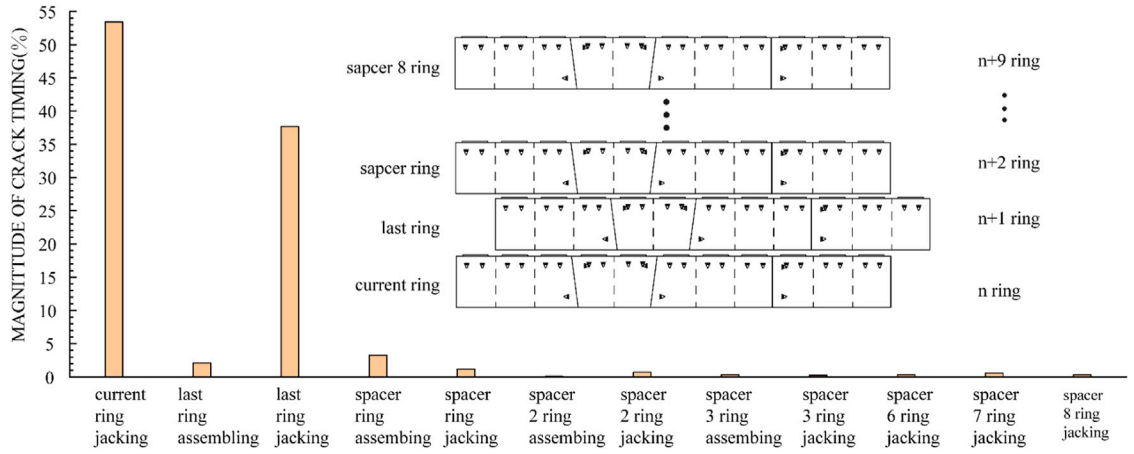

FIGURE 9
Magnitude of crack occurrence time.

of the segments. Longitudinal bolts were adopted for the longitudinal and circumferential joints of the segments, and the clearance between the bolt and bolt hole was neglected. The handholes were simplified to be of a rectangle cross section. Steel rebars were placed in the segments of B4n, B3n+1, and B4n+1. In the numerical model, the solid elements were employed to simulate segments, bolts and pedestals, while the Truss elements were utilized to simulate the steel rebars (Zhang LB. et al., 2023a; Zhang JC. et al., 2023b).

The pedestals and guide bars were fully constrained, and Coulomb friction was assigned between the longitudinal and circumferential joints, as well as between the segments and the guide bars. The coefficient of friction was 0.5 between the longitudinal and circumferential joints (Zhang et al., 2021), and was 0.2 between the segments and the guide bars. The steel rebars and bolts were embedded in the model (Li et al., 2023).

The model was run in three phases (Figure 12). In the first phase, the n-th segment was jacked. The (n+1)-th segment and the corresponding bolts in the longitudinal and circumferential joints were not activated. In the second phase, the (n+1)-th segment was just assembled and was about to be jacked. In the third phase, the jacking of the (n+1)-th segment was completed, and the n-th segment was thrust out from the shield tail.

The loads applied to the segment are depicted in Figure 13. The designed pre-tightening forces of the longitudinal, and the circumferential bolts were 150 kN and 100 kN, respectively. The calculated handhole stresses of the longitudinal and circumferential bolts were 12.9 and 8.6 MPa, respectively. The jacking pressures in the down and left zones were similar, and the same was true for up and right zones, so the average pressures in the down zone (i.e., 23 MPa) and the up zone (i.e., 14.5 MPa) were taken as the jacking pressures. When the shield tail clearance was 110 mm (i.e., 0.5 MPa), the pressure in the down jacking zone was taken as the shield tail brush pressure for the n-th segment of the second phase and the (n+1)-th segment of the third phase (Wei, 2021). The shield tail sealing grease was set to 0.6 MPa based on actual practical conditions. In the third phase, when the n-th segment was thrust out from the shield tail, and the water and soil pressure of 0.45 MPa was at its maximum for the duration of the shield construction.

The above analysis confirmed that the shield attitude adjustment and poor assembly were two possible causes of the segment cracks, and they were which therefore selected for the further analysis. Attitude adjustment may cause jack eccentricity and deflection of the jack, while the transform platform lead to a 32-mm eccentricity of the boot (Figure 2B). Hence, the additional eccentricity was not studied. Six deflection angles (0°–5°) were studied in the sensitivity analysis of attitude adjustment. The distances between the segment and the guide bar in three cases were varied between 0 mm and 8 mm (Figure 14A). The clearance in the longitudinal and circumferential joint was not considered in the sensitivity analysis of attitude adjustment.

The assembly quality was reflected by the uneven longitudinal supports and V-shaped openings of the longitudinal joints. The uneven longitudinal support was at a distance of 1 mm, and the assembly angle of the longitudinal joint was 0.1°. The assembly clearance values of circumferential joints ranged from 0 to 4 mm. In this study, assembly clearance values of 0 and 4 mm were investigated. As shown in Figure 14B, the simulation scenarios included the uneven longitudinal support, V-shaped longitudinal opening, inverted V-shaped longitudinal opening, and continuous uneven longitudinal support. The jack pressures for the shield attitude adjustment conditions were set at 23 and 14.5 MPa, respectively. The jack deflection was not considered in the sensitivity analysis of assembly condition, while the jacking pressure was fixed at 23 MPa, and the distance between the segment and the guide bar was kept at 50 mm.

4.2 Constitutive model and parameters

Although concrete damage is not necessarily manifested in the form of cracks, damage evolution is a precondition for the development of the cracks (Behnam et al., 2018). Hence, the concrete damage plasticity (CDP) model was introduced to evaluate crack development. When the tensile damage coefficient D_t or the compressive damage coefficient D_c were 1, the concrete

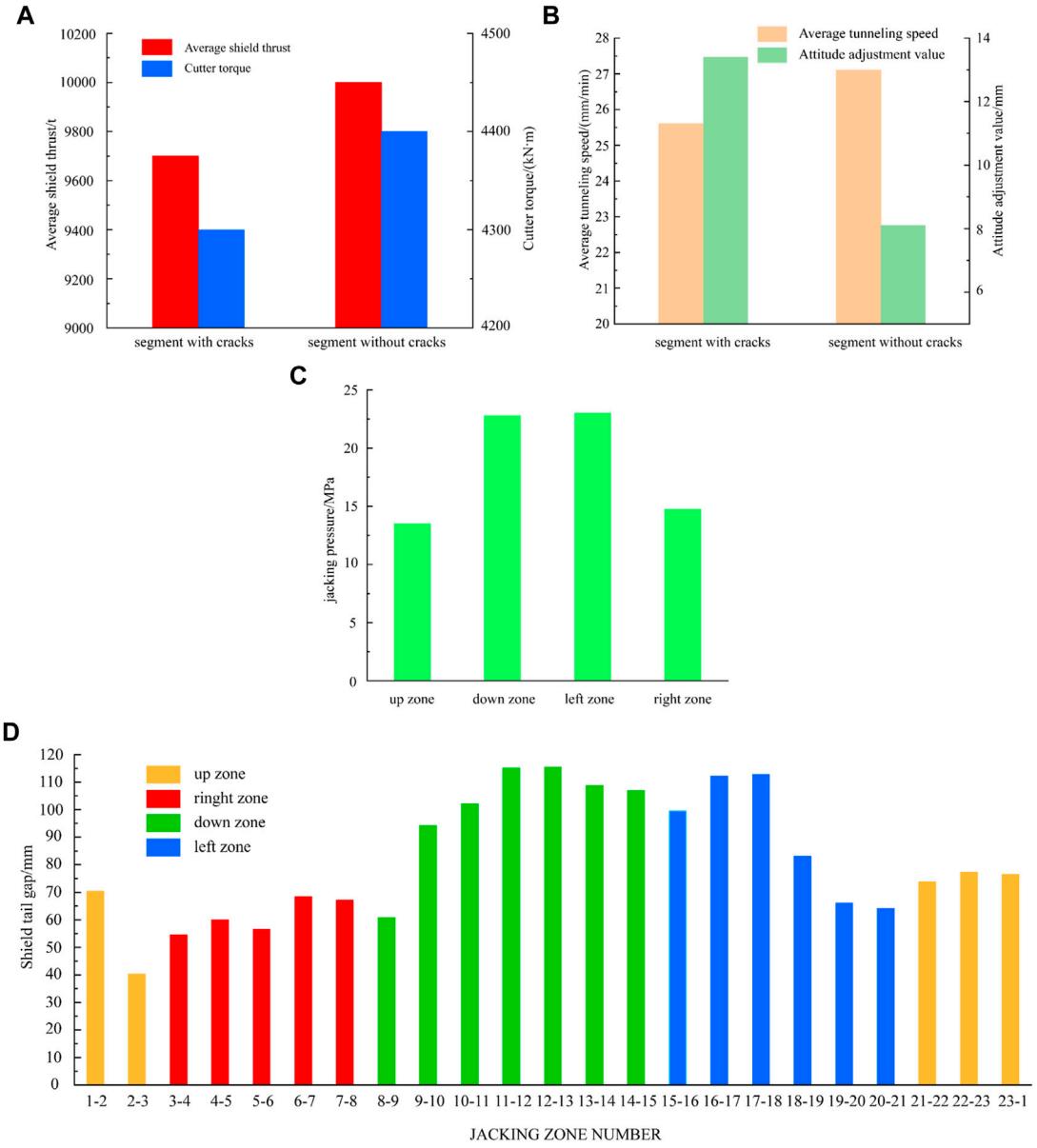

FIGURE 10
Statistics of **(A)** average shield thrust and cutter torque **(B)** average tunneling speed and attitude adjustment value **(C)** jacking pressure of each zone **(D)** Average value of shield tail clearance.

was completely damaged, and when D_t or D_c becomes 0, the concrete was in an elastic state (Lubliner et al., 1989). The ratio of the biaxial yield stress to the uniaxial yield stress σ_{b0}/σ_{c0} was set to 1.16. The expansion angle $\psi(\theta - f_i)$ and the change of expansion angle $\varepsilon(\theta - f_i)$ under hydrostatic pressure condition were 35° and 0.1, respectively. The ratio of the tensile to the compressive stress was a constant with a value of 0.667, and the concrete viscosity parameter was 0.0005 (Jiang et al., 2020).

The stress-strain relationship of concrete under compression is determined by Eqs 2–6 (China Architecture and Building Press, 2010).

$$\sigma_c = (1 - d_c)E_c\varepsilon_c \tag{2}$$

$$d_c = \begin{cases} 1 - \dfrac{\rho_c n}{n - 1 + x^n} & x \le 1 \\ 1 - \dfrac{\rho_c}{\alpha_c (x-1)^2 + x} & x > 1 \end{cases} \tag{3}$$

$$\rho_c = \frac{f_{cr}}{E_c\varepsilon_{cr}} \tag{4}$$

$$n = \frac{E_c\varepsilon_{cr}}{E_c\varepsilon_{cr} - f_{cr}} \tag{5}$$

$$x = \frac{\varepsilon}{\varepsilon_{cr}} \tag{6}$$

In the equations, σ_c is the concrete compressive stress, ε_c is the concrete compressive strain, E_c represents the concrete elastic modulus, d_c

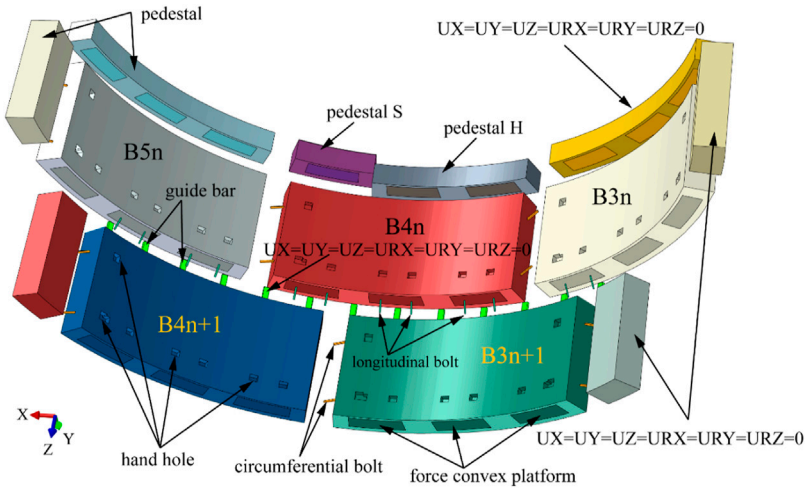

FIGURE 11
Numerical model and boundary conditions.

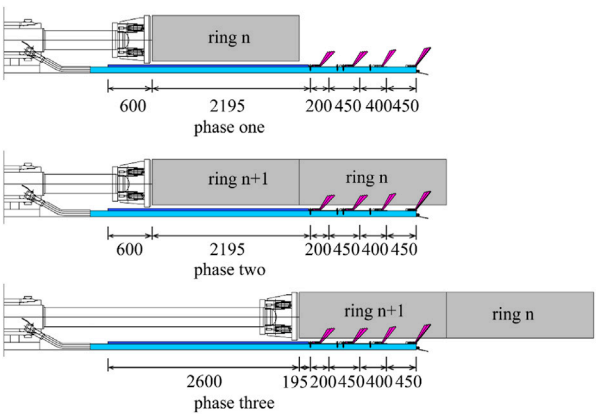

FIGURE 12
Calculation phase.

is a uniaxial compressive damage evolution parameter, α_c denotes the parameter of the descending segment of the concrete's uniaxial stress-strain curve, f_{cr} is the standard uniaxial compressive strength of concrete, and ε_{cr} represents the peak compressive strain of concrete corresponding to f_{cr}.

The stress-strain relationship of concrete under tension is determined by Eqs 7–10 (China Architecture and Building Press, 2010).

$$\sigma_t = (1 - d_t)E_c\varepsilon_t \tag{7}$$

$$d_t = \begin{cases} 1 - \rho_t\left(1.2 - 0.2x^5\right) & x \le 1 \\ 1 - \dfrac{\rho_t}{\alpha_t(x-1)^{1.7} + x} & x > 1 \end{cases} \tag{8}$$

$$\rho_t = \frac{f_{tr}}{E_c\varepsilon_{tr}} \tag{9}$$

$$x = \frac{\varepsilon}{\varepsilon_{tr}} \tag{10}$$

where σ_t is the tensile stress of concrete, ε_t is the tensile strain of concrete, d_t is the damage evolution parameter of concrete under uniaxial tension, α_t is the parameter value of the descending section of the stress–strain curve of concrete under uniaxial tension, f_{tr} is the standard uniaxial tensile strength of concrete, and ε_{tr} is the peak tensile strain of concrete corresponding to f_{tr}.

Due to the linear stress-strain relationship of concrete in CDP, which is inconsistent with the specifications, it is necessary to manually set the yield points of concrete under compression and tension. If the yield points of tension and compression are set to $\sigma_{to} = 0.8f_{tr}$ and $\sigma_{co} = 0.6f_{cr}$, respectively, the corresponding strains are $\varepsilon_{to} = \sigma_{to}/E_c$ and $\varepsilon_{co} = \sigma_{co}/E_c$, respectively (Figure 15).

Once the modified stress-strain curve of concrete is obtained, the tensile damage factor and compression damage factor of concrete can be calculated based on the energy loss (Krajcinovic and Lemaître, 1007) as shown in Table 1.

$$D_t = 1 - \frac{\int \sigma_t d\varepsilon_t}{E_c\varepsilon_t^2/2} \tag{11}$$

$$D_c = 1 - \frac{\int \sigma_c d\varepsilon_c}{E_c\varepsilon_c^2} \tag{12}$$

The elastic modulus and Poisson's ratio of the concrete were taken as 36 GPa and 0.2, respectively. , and the concrete Poisson's ratio was 0.2. Reinforcement and bolts adopted a double-line constitutive law. The elastic modulus and the Poisson's ratio of steel were 206 GPa and 0.31, respectively. The yield stress and plastic strain of the steel rebars and bolts are displayed in Table 2. The CDP model was adopted to describe the B4*n*, B4*n*+1, and B3*n*+1 segments. The elastic concrete model was applied to B5*n*, B3*n*, and the pedestals. A steel elastic model was assigned to the guide bars.

4.3 Results and analyses

As segmental cracks could only be observed inside the tunnel, the analysis in this section concentrated on the cracks occurred on the segment inner surface. Figure 16 illustrates the damage results of the B4*n* segment in the first phase under various shield attitude adjustment

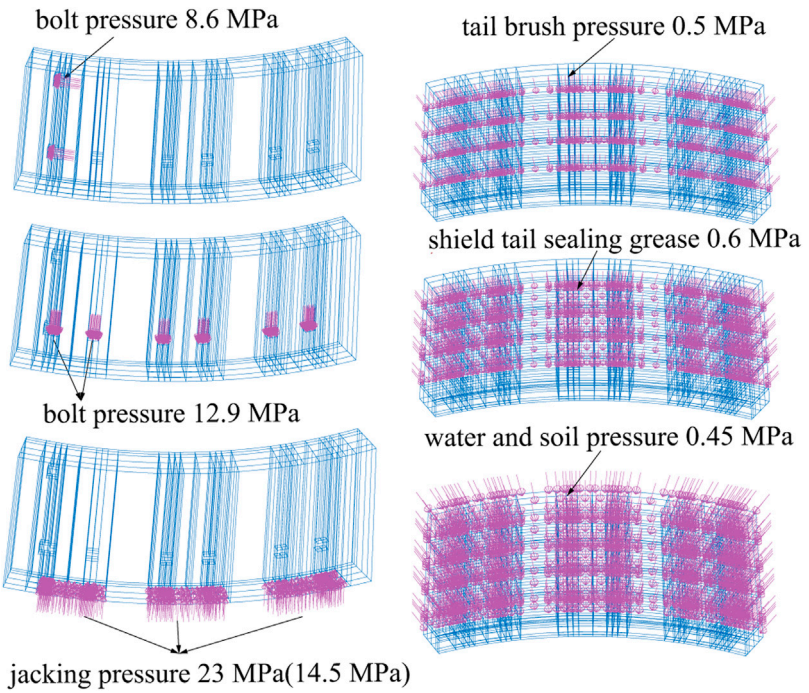

FIGURE 13
Loads applied to each segment.

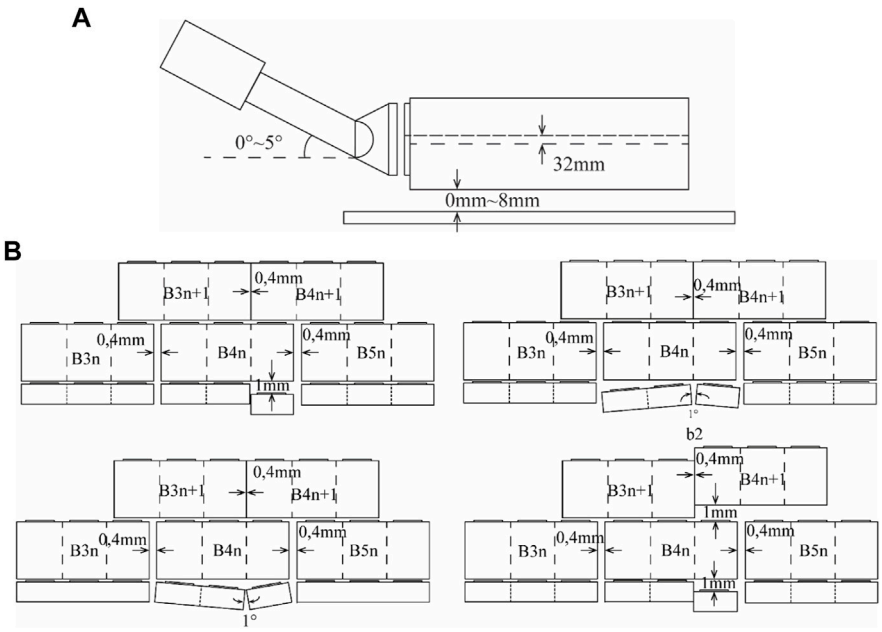

FIGURE 14
Simulation of **(A)** attitude adjustment and **(B)** inaccurate assembly.

conditions. The DAMAGET threshold for crack occurrence was defined as 0.95. Two major tensile cracks occurred in all the studied scenarios regardless of the deflection angle, while the crack lengths increased with the increasing deflection angle. Figure 17 shows the influence of the spacing between the guide bar and segment as well as the and deflection angle on the crack length.

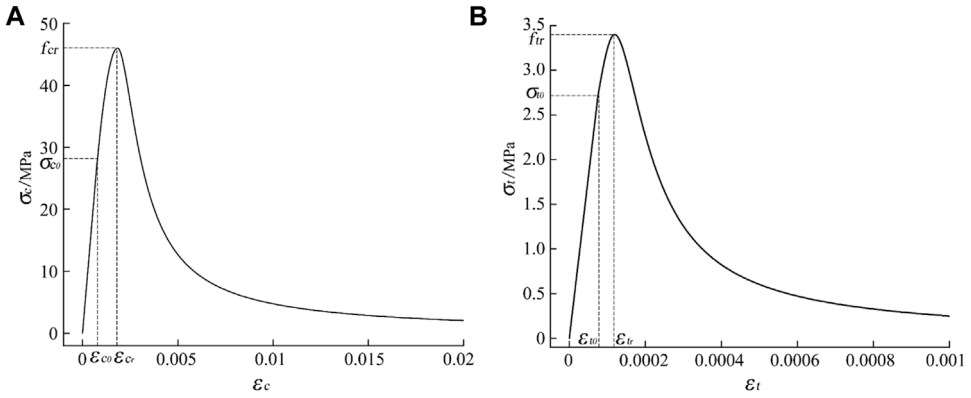

FIGURE 15
(A) Compressive stress-strain curve for concrete **(B)** tensile stress-strain curve for concrete.

TABLE 1 Constitutive model parameters of concrete.

Compressive behavior		Compressive damage	Tensile behavior		Tensile damage
Yield stress (MPa)	Inelastic Strain	Dc	Yield stress (MPa)	Inelastic Strain	Dt
27.6	0	0	2.72	0	0
39.2	1.12E-04	0.027	3.40	2.44E-05	0.06
46.0	5.63E-04	0.129	2.54	1.12E-04	0.28
39.1	1.32E-03	0.256	2.37	1.28E-04	0.32
32.1	1.91E-03	0.351	1.52	2.22E-04	0.53
27.5	2.33E-03	0.4199	1.00	3.21E-04	0.68
22.8	2.84E-03	0.495	0.49	5.69E-04	0.86
18.2	3.48E-03	0.580	0.32	8.04E-04	0.92
13.6	4.42E-03	0.679	0.15	0.002	0.95
8.9	6.06E-03	0.791			
4.3	0.01	0.914			

TABLE 2 Constitutive model parameters of steel and bolt (Wang et al., 2021).

Steel		Bolt	
Yield stress (MPa)	Plastic strain	Yield stress (MPa)	Plastic strain
400	0	640	0
600	0.97	800	0.18

When the jack deflection was 0°, the crack length remained constant regardless of the spacing between the guide bar and the segment, which was caused by the eccentricity of the platform. There was an upper limit to the crack length for each case of deflection angle. This was due to the outward bending moment of the segment induced by the jack deflection. Since the outer surface of the segment was constrained by guide bars, the segment did not deform towards the outer arc surface, thus preventing positive cracks from occurring. However, the restraining effect of guide bars was weakened when the distance between the outer arc surface of the segment and the guide bars became larger. The segment was constrained by the adjacent segments and bolts. On the other hand, the formation of cracks was inhibited when the spacing between the guide bar and the segment was small enough to restrain the deformation.

Figure 18 presents the crack lengths in three phases, where the positive cracks in the B4*n* segment caused by the jack deflection did not develop in the second and third phases. Therefore, the positive cracks caused by jack deflection mainly occurred during the current ring jacking stage, and subsequent tunneling contributed little to the development of positive cracks.

As shown in Figure 19, the crack lengths decreased significantly when the jacking pressure was 14.5 MPa, and the positive cracks were no longer obvious when the jack deflection angle was less than 3°.

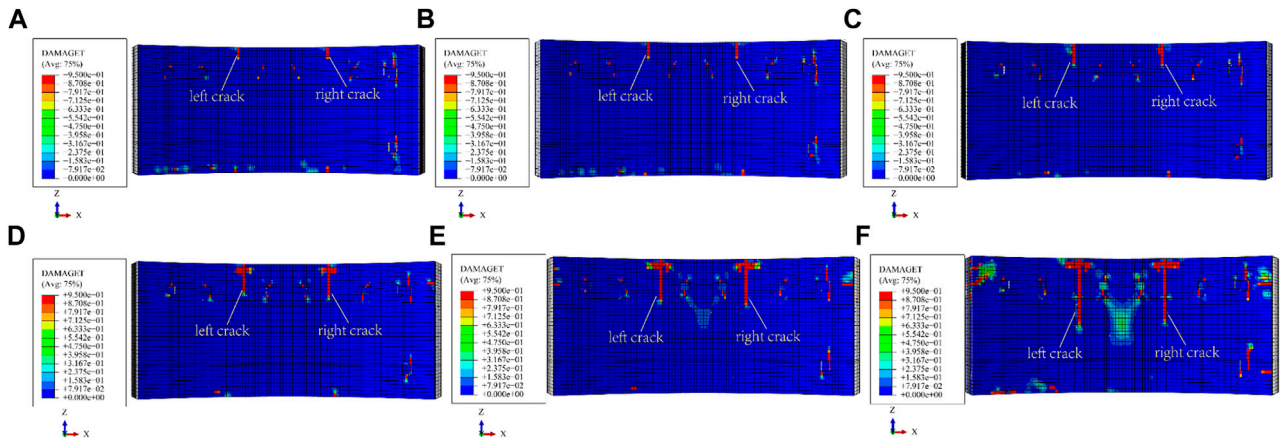

FIGURE 16
Damage of B4*n*, jack pressure of 23 MPa, 8 mm between guide bar and segment, deflection angle: **(A)** 0° **(B)** 1° **(C)** 2° **(D)** 3° **(E)** 4° **(F)** 5°.

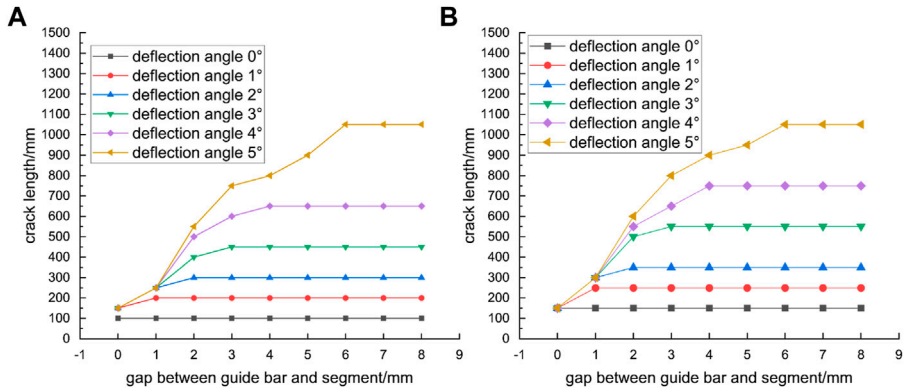

FIGURE 17
Crack lengths with different segment clearances and deflection angles, jack pressure of 23 MPa **(A)** left crack **(B)** right crack.

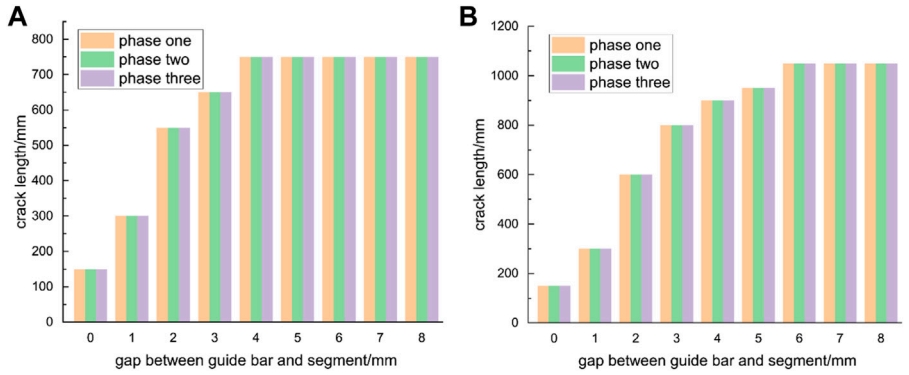

FIGURE 18
Crack lengths in the three phases with deflection angles of **(A)** 4 and **(B)** 5°.

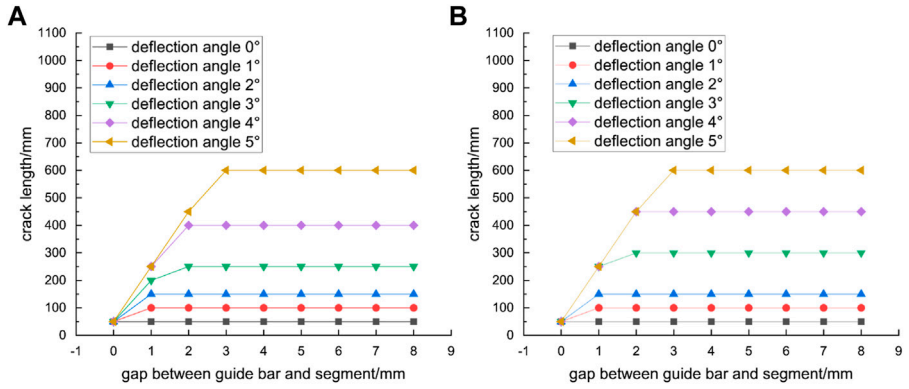

FIGURE 19
Crack lengths with different segment spacings and deflection angles, with jack pressure of 14.5 MPa **(A)** left crack **(B)** right crack.

Figure 20 presents the simulation results of a single-ring segment with the presence of uneven longitudinal support. When the assembly clearance was 0 mm, the right end of the B4*n* segment was deformed in the negative Z-axis direction during the jacking of the *n*-th segment, causing the tension on the end face and the formation of positive tensile cracks. Moreover, due to friction of the right-side segment and the constraint of the bolts, there was shear at the rear end of the uneven support, which resulted in backward shear cracks. During the jacking of the (*n*+1)-th segment, the positive cracks did not propagate, the length of the backward crack increased by 150 mm, and there were no cracks in the B3*n*+1 and B4*n*+1 segments. All cracks were formed in the current jacking stage, and the total number of cracks was 2. When the assembly clearance was 4 mm, the maximum length of the positive cracks was 600mm, which was an increase of 350 mm compared to the case of the tense assembly model. Meanwhile, during the last ring jacking stage, two positive tensile cracks developed on B4*n*+1, one backward shear crack developed on all B4*n*, B3*n*+1, and B4*n*+1 and one circumferential tensile crack developed on both B4*n* and B4*n*+1 the total number of cracks increased to 14.

Figure 21 shows the results of a single-ring segment with a V-shaped opening in the longitudinal joint. When the assembly clearance was 0 mm, the front end of B4*n* was under tension during the jacking of the *n*-th segment. Consequently, a positive tensile crack formed in the middle segment. The left end of B4*n* was subjected to the friction from the adjacent segment and the constraint from the bolts during deformation, which resulted in a circumferential tensile crack. During the jacking of the (*n*+1)-th segment, there was a clearance between B4*n* and pedestal H, and the left end of B4n continued to deform in the negative Z-axis direction. Due to frictional constraint at the left end, the length of the circumferential crack increased by 300 mm, and a new backward shear crack generated at the rear of B4*n*. The total number of cracks was 9. When the assembly clearance was 4 mm, the both ends of B4*n* were only constrained by the bolts, and the deformed in the negative Z-axis direction and were in contact with pedestals S and H. The maximum length of the positive cracks was 850mm, whereas in the tense assembly model the length was only 300 mm. Meanwhile, during the last ring jacking stage one positive tensile crack developed on B4*n*+1, one backward shear crack developed on B4*n*+1, two backward shear crack developed on B3*n*+1, and one circumferential tensile crack developed on B4*n*, the total number of cracks increased to 18.

Figure 22 presents the results of a single-ring segment with an inverted V-shaped opening in the longitudinal joint. When the assembly clearance was 0 mm, B4*n* was a simply supported beam that was restrained at both ends during the jacking of the *n*th segment. The rear end was under tension, so that multiple longitudinal shear and tensile cracks formed in the middle part of the segment. During the jacking of the (*n*+1)-th segment, the backward crack did not propagate and there were no cracks developed on the B3*n*+1 and B4*n*+1 segments due to the friction constraints on both ends of B4*n*. One positive tensile crack on B3n+1 occurred in the last ring jacking stage, and the total number of cracks was 7. When the assembly clearance was 4 mm, the length of the backward crack during jacking of the *n*-th segment was 250 mm longer than that when the assembly clearance was 0 mm due to the lack of friction constraints. The maximum length of the backward tensile crack was 1300 mm, while in the tense assembly model the length was 700 mm. Meanwhile, one positive tensile crack on B3*n*+1 and two backward shear cracks on B4*n* formed in the last ring jacking stage, the total number of cracks increased to 12.

Figure 23 shows the segment cracks formed due to the continuous uneven support. Compared with Figure 20, when the assembly clearance was 0 mm, the front and rear rings on the right end of B4*n* were not sufficiently restrained during the jacking of the (*n*+1)-th segment. The pressure on the segment led to the shear on the uneven platform and a new backward shear crack was formed. The left end of B4*n*+1 was deformed in the negative Z-axis direction, and one backward shear crack was generated due to the friction of the B3n+1 segment and the constraint of the bolts. One backward shear crack on B3*n*+1 occurred in the last ring jacking stage and the total number of cracks was 7. When the assembly clearance was 4 mm, the maximum length of the positive tensile crack was 500 mm, while in the tense assembly model the length was 200 mm. Meanwhile, one positive tensile crack developed both on B3*n*+1 and B4*n*+1, and one circumferential tensile crack developed on B4*n* in the last ring jacking stage, the total number of cracks increased to 12.

5 Discussion

The deviation angle of the hydro-cylinder can cause damage and cracks to the pipe segments (Mohtadinia et al., 2020; Dai et al., 2022). Dai et al. (2022) mainly focused on segment damage caused

10.3389/feart.2023.1235674

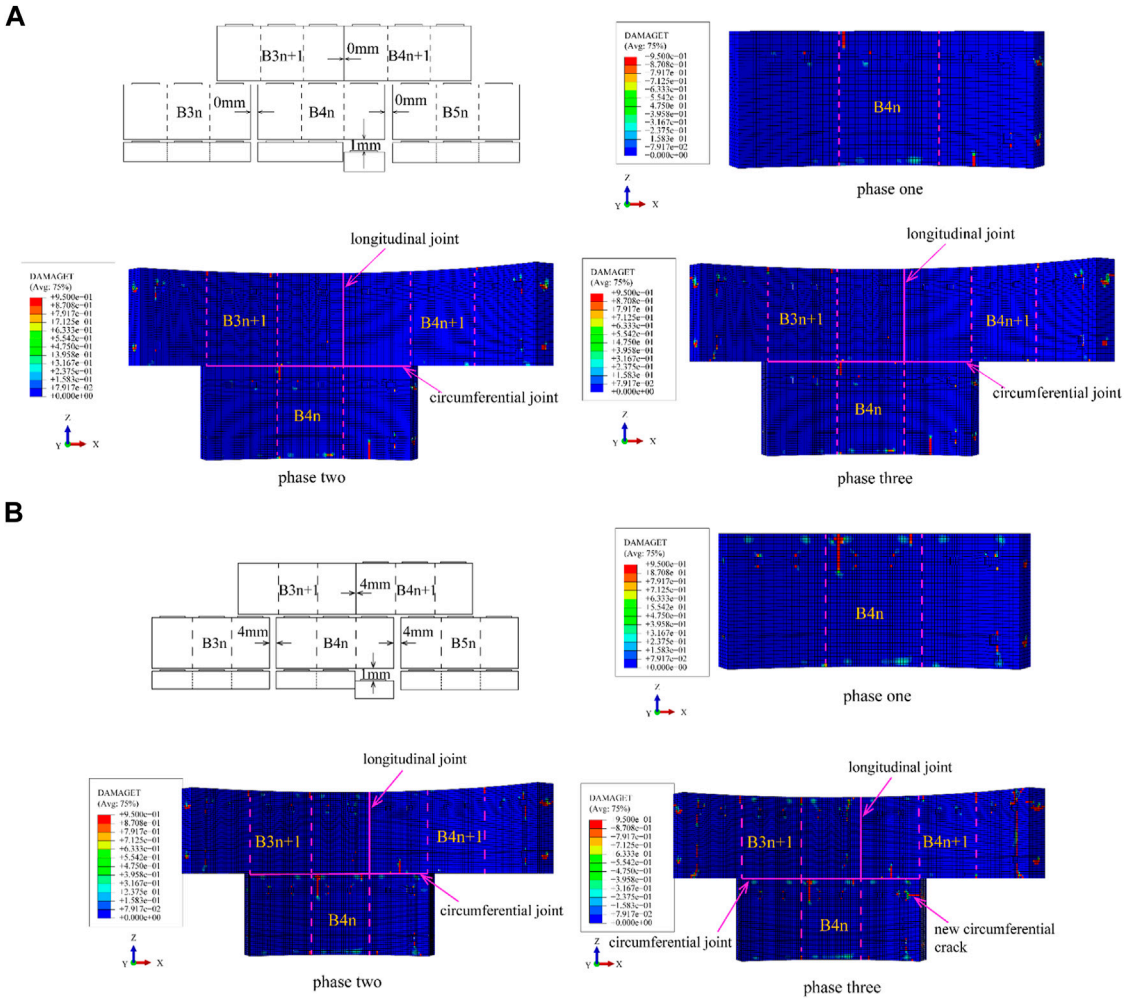

C

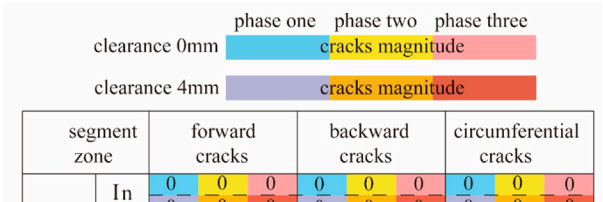

segment zone		forward cracks			backward cracks			circumferential cracks		
B4n	In	0	0	0	0	0	0	0	0	0
		0	0	0	0	0	0	0	0	0
	Jn	1	1	1	1	1	1	0	0	0
		2	2	2	0	0	0	0	0	0
	Kn	0	0	0	0	0	0	0	0	0
		0	0	0	0	1	1	0	0	1
B4n+1	In+1	\	0	0	\	0	0	\	0	0
		\	0	0	\	1	1	\	1	1
	Jn+1	\	0	0	\	0	0	\	0	0
		\	1	2	\	0	0	\	0	0
	Kn+1	\	0	0	\	0	0	\	0	0
		\	0	1	\	0	1	\	0	1
B3n+1	Ln	\	0	0	\	0	0	\	0	0
		\	1	1	\	0	1	\	0	0
	Mn	\	0	0	\	0	0	\	0	0
		\	1	1	\	0	0	\	0	0
	Nn	\	0	0	\	0	0	\	0	0
		\	0	0	\	0	0	\	0	0

FIGURE 20
Formation of cracks due to longitudinal dislocation: **(A)** S pedestal dislocation with a longitudinal assembly clearance of 0 mm and **(B)** S pedestal dislocation with a longitudinal assembly clearance of 4 mm **(C)** cracks magnitude of longitudinal dislocation.

10.3389/feart.2023.1235674

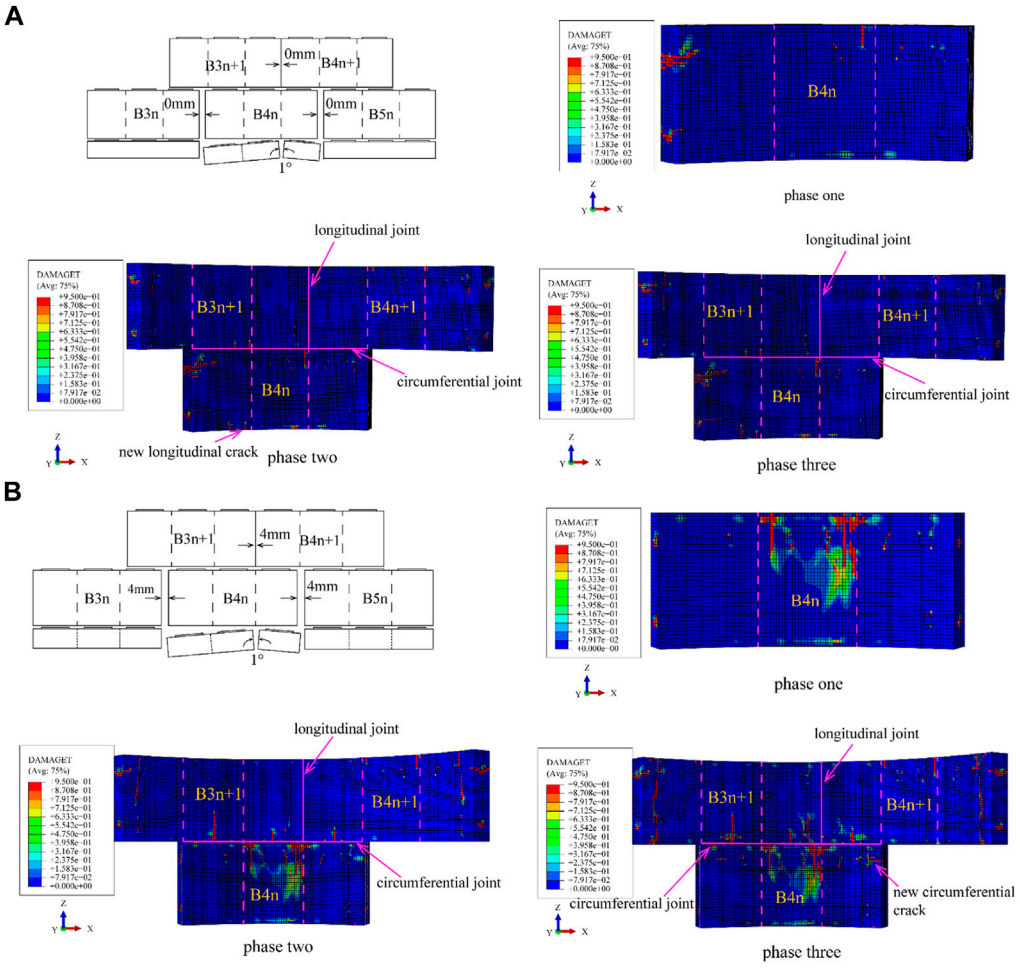

C

phase one phase two phase three

clearance 0mm cracks magnitude

clearance 4mm cracks magnitude

segment zone		forward cracks			backward cracks			circumferential cracks		
B4n	In	0	0	0	0	2	2	3	3	3
		0	0	0	0	0	0	0	0	0
	Jn	1	1	1	0	0	0	0	0	0
		4	4	4	0	0	0	0	0	0
	Kn	0	0	0	0	0	0	0	0	0
		1	1	1	0	0	0	0	0	1
B4n+1	In+1	\	0	0	\	1	1	\	0	0
		\	0	0	\	1	1	\	1	1
	Jn+1	\	1	1	\	0	0	\	0	0
		\	1	2	\	0	0	\	0	0
	Kn+1	\	0	0	\	0	0	\	0	0
		\	1	1	\	0	1	\	0	0
B3n+1	Ln	\	0	1	\	0	0	\	0	0
		\	1	1	\	0	1	\	1	1
	Mn	\	0	0	\	0	0	\	0	0
		\	0	0	\	1	1	\	0	0
	Nn	\	0	0	\	0	0	\	0	0
		\	0	0	\	1	2	\	0	0

FIGURE 21
Formation of cracks due to V-shaped longitudinal joint: **(A)** S and H pedestals with inverted V-shapes and a longitudinal assembly clearance of 0 mm and **(B)** S and H pedestals with inverted V-shapes and a longitudinal assembly clearance of 4 mm **(C)** cracks magnitude of longitudinal joint V-shaped.

by incorrect assembly angles during the assembly process, which mainly occurs at the joints and is different from the simulated working conditions in this article. Mohtadinia et al. (2020) suggest that when the cylinder deflection angle is 5°, cracks will appear when the cylinder thrust reaches over 5 MPa, and the cracks are mainly distributed in the middle of a single pipe segment, which is

10.3389/feart.2023.1235674

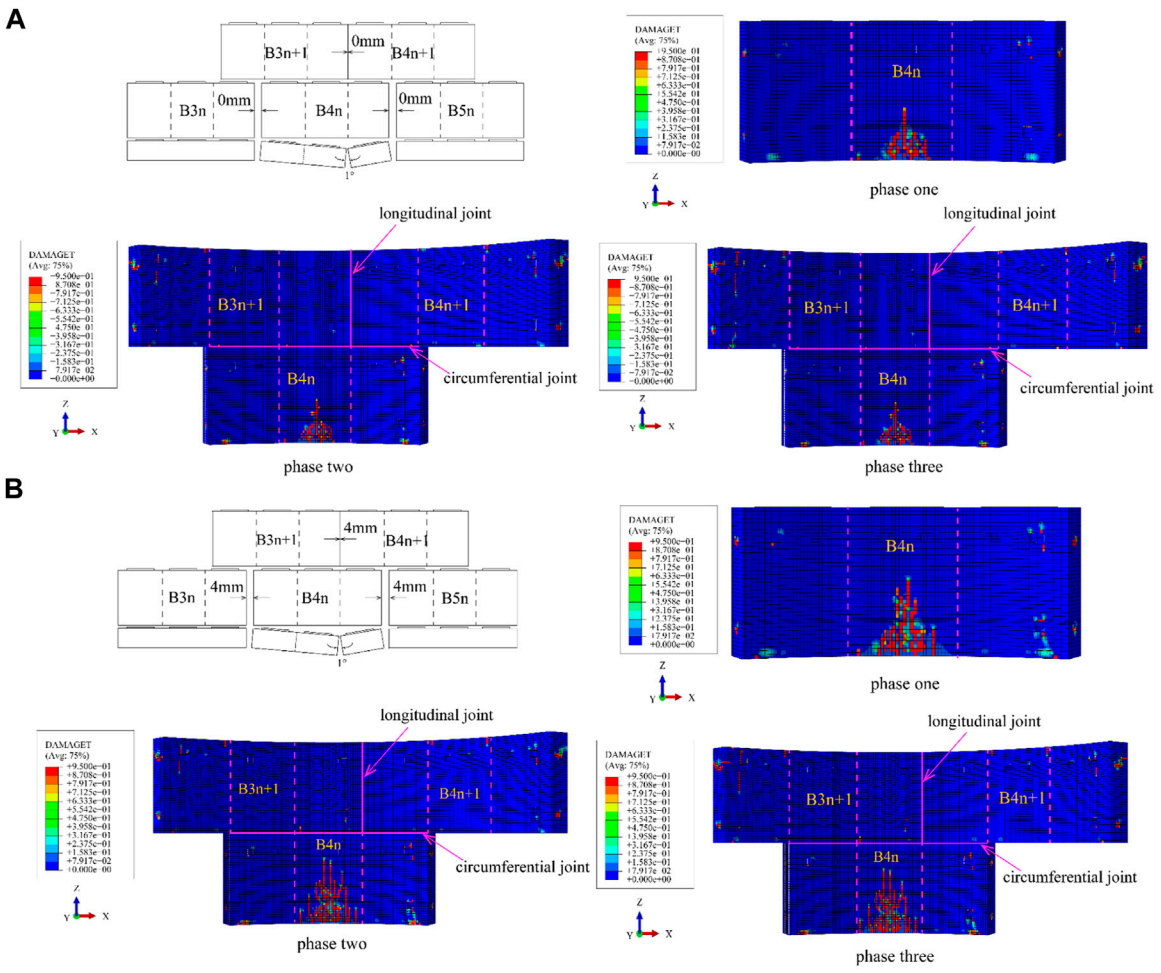

segment zone		forward cracks			backward cracks			circumferential cracks		
B4n	In	0	0	0	0	0	0	0	0	0
		0	0	0	0	0	0	0	0	0
	Jn	0	0	0	4	4	4	0	0	0
		0	0	0	6	8	8	0	0	0
	Kn	0	0	0	0	0	0	0	0	0
		0	0	0	0	0	0	0	0	0
B4n+1	In+1	\	0	0	\	0	0	\	0	0
		\	0	0	\	0	0	\	0	0
	Jn+1	\	1	1	\	0	0	\	0	0
		\	2	2	\	0	0	\	0	0
	Kn+1	\	0	0	\	0	0	\	0	0
		\	0	0	\	0	0	\	0	0
B3n+1	Ln	\	1	2	\	0	0	\	0	0
		\	1	2	\	0	0	\	0	0
	Mn	\	0	0	\	0	0	\	0	0
		\	0	0	\	0	0	\	0	0
	Nn	\	0	0	\	0	0	\	0	0
		\	0	0	\	0	0	\	0	0

FIGURE 22
Formation of cracks due to longitudinal joint with inverted V-shape: **(A)** S and H pedestals with inverted V-shapes and a longitudinal assembly clearance of 0 mm and **(B)** S and H pedestals with inverted V-shapes and a longitudinal assembly clearance of 4 mm **(C)** cracks magnitude of longitudinal joint with inverted V-shape.

consistent with the crack distribution in the numerical simulation results of this paper. The present work considers the constraint effect of the guidance bar on the pipe segment, and one should note that the front cracks generated by the hydro-cylinder deflection angle only occurred in the pushing stage of the current ring. This is consistent with the statistics of crack characteristics, where 53% of

10.3389/feart.2023.1235674

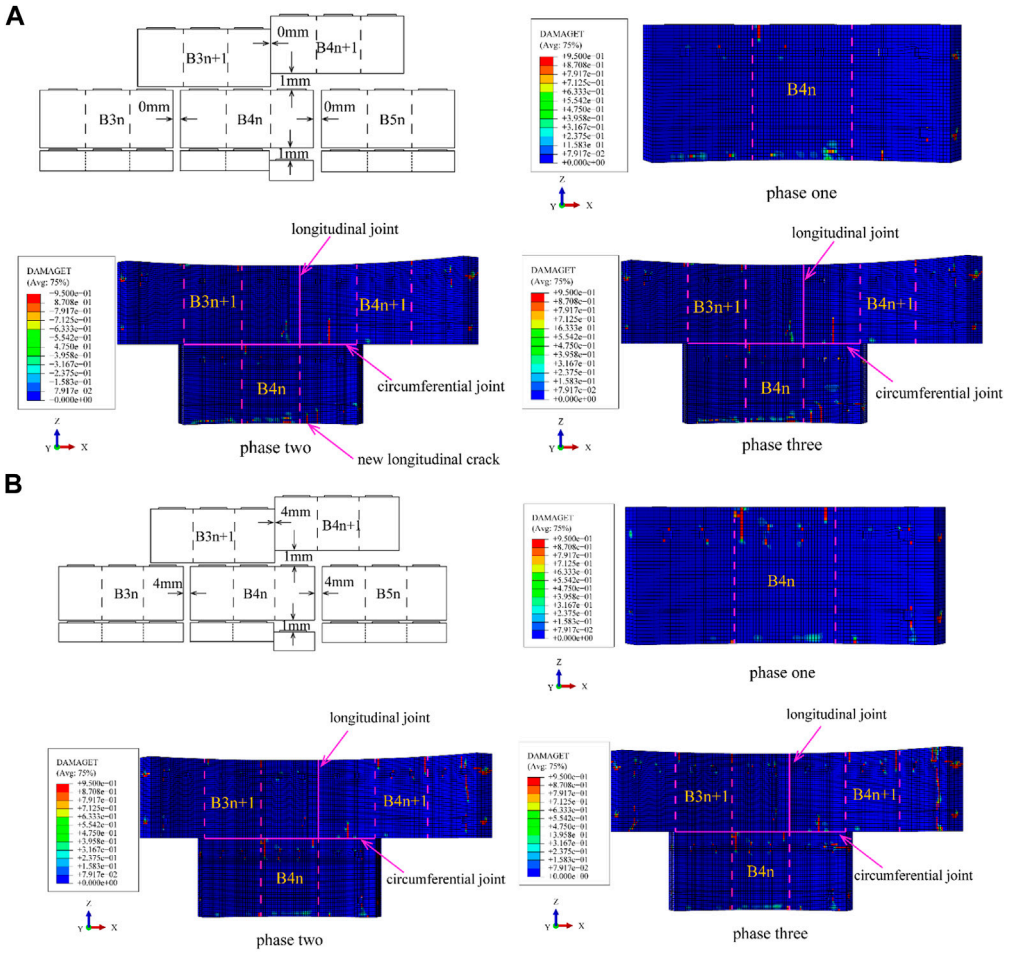

segment zone		forward cracks			backward cracks			circumferential cracks		
B4n	In	0	0	0	0	0	0	0	0	0
		0	0	0	0	0	0	0	0	0
	Jn	1	1	1	0	0	0	0	0	0
		2	2	2	0	0	0	0	0	0
	Kn	0	0	0	1	2	2	0	0	0
		0	0	0	0	0	0	0	0	1
B4n+1	In+1	\	0	0	\	1	1	\	0	0
		\	0	0	\	1	1	\	0	0
	Jn+1	\	0	0	\	2	2	\	0	0
		\	0	0	\	0	0	\	0	0
	Kn+1	\	0	0	\	0	0	\	0	0
		\	1	1	\	0	1	\	0	0
B3n+1	Ln	\	0	0	\	0	0	\	0	0
		\	0	0	\	0	1	\	0	0
	Mn	\	1	1	\	0	0	\	0	0
		\	2	2	\	0	0	\	0	0
	Nn	\	0	0	\	0	0	\	0	0
		\	0	0	\	0	0	\	0	0

FIGURE 23
Formation of cracks due to serial longitudinal dislocation: **(A)** S pedestal and B4n+1 dislocation with a longitudinal assembly clearance of 0 mm and **(B)** S pedestal and B4n+1 dislocation with a longitudinal assembly clearance of 4 mm **(C)** cracks magnitude of serial longitudinal dislocation.

cracks were generated in the pushing stage of the current ring. This indicates that the hydro-cylinder deflection angle is one of the main reasons for cracks during tunnel construction. The cracks caused by the deviation angle are mainly affected by the radial component force generated by the hydro-cylinder force, so they have no direct correlation with the total thrust force. According to the statistical results, the adjustment amplitude of the shield tunnelling posture of the segment with cracks is greater than that of the segment without

cracks, indicating that the angle between the hydro-cylinder and the segment during the pushing process is highly likely caused by posture adjustment, and the angle adjusted by posture is likely to exceed 3°. In the vast majority of cases, the clearance between the shield tail was above 50 mm, and the value of the clearance cannot reflect the contact between the pipe segment and the guidance bars. Therefore, there is little correlation between the occurrence of cracks in the pipe segment and the clearance between the shield tail.

When the quality of pipe segment assembly is poor, front cracks, back cracks, and circumferential cracks will occur, and these cracks will expand in the subsequent construction process. This is consistent with Krahl et al. (2021) conclusion that splitting, peeling, back cracks, and cracks at longitudinal joints will occur when the longitudinal assembly is staggered [(Plizzari and Tiberti, 2007; Krahl et al., 2021),43]. However, Krahl et al. (2021) only analyzed the working conditions during the longitudinally staggered assembly of the current ring during the pushing stage, without analyzing the cracks caused by other poor assembly quality modes and the impact of subsequent construction stages on these cracks. In addition, they did not consider the assembly clearance of longitudinal joints and bolts [43]. Some cracks caused by poor assembly quality did not appear during the pushing stage of the current ring but appeared during the pushing stage of the adjacent ring, accounting for 38% of its cracks. In addition, the length, type, and quantity of cracks caused by poor assembly quality of adjacent segments are related to the constraints between segments.

Among all types of pipe segments, the K block has the least number of cracks, which may be due to the smaller arc length of the K block compared to adjacent blocks and standard blocks. The constraints of both sides and adjacent ring bolts make it difficult for the K block to be affected by the hydro-cylinder. In addition, most assembly points are selected when the K block is located in the upper half of the tunnel, where the hydro-cylinder force is relatively small. The cracks generated after the segment detaches from the shield tail only account for 7% of the total number of cracks. This is because, under the action of water and soil pressure, the axial force on the segment increases, and the clearance between the longitudinal joints of the segment decreases. Compared to being located inside the shield machine, detaching from the shield tail increases the stiffness of the longitudinal joints of the segment and decreases the pushing force of the cylinder on the segment (SHI et al., 2021).

6 Conclusion

Previous studies regarding shield tunnel cracks usually neglect the formation time of crack, stage of crack propagation and their influence by assembly clearance. In this study, based on the crack characteristics collected during a boring process, cracks caused by jacking deflection and assembly defects were investigated via sensitivity analyses of tunneling parameters and a continuous construction 3D finite element model. The length, number, propagation and occurrence time of cracks were discussed considering TBM constraints on segments and the different longitudinal assembly clearances. The following conclusions are obtained:

1) The cracks in the shield tunnel segments were dominated by longitudinal cracks, which were mainly distributed in the lower and left zones of the jacks. For each segment, the highest proportion of cracks appeared in the middle part. And 53% of the cracks were formed during the current ring jacking stage, while 40% of the cracks occurred during the last ring jacking stage.
2) The constraints on both sides of the segment and the outward jacking deflection angle led to an uneven outward deformation in the segment. Two positive cracks were formed in the middle part of the segment during the current ring jacking stage, and their lengths remained constant during the subsequent construction process. The crack formation was suppressed when the distance between the guide bar and the segment was small enough to restrain the deformation. The crack length was directly related to the magnitude of the jacking force and deflection angle.
3) Assembly defects led to positive, backward and circumferential cracks, and most cracks propagated during the subsequent construction process. A proportional of cracks were formed in the last ring jacking stage rather than the current ring jacking. The inverted V-shape longitudinal joint with an was the most severe assembly defect, which caused dense backward cracks in the middle part of B4 segment. The V-shape or inverted V-shape longitudinal joint should be avoided during construction.
4) Lateral constraints on segments suppressed the cracks generation and their length developed. The 4 mm longitudinal assembly clearance resulted in more than two times the average number and length of crack for all assembly defects compared to seamlessly assembled longitudinal joints. Considering that the longitudinal joints were compressed under water and Earth pressure, only 7% of the segment cracks occurred after the segment detached from the shield tail.

Data availability statement

The original contributions presented in the study are included in the article/supplementary material, further inquiries can be directed to the corresponding author.

Author contributions

RY: conceptualization, methodology, formal analysis QK: writing—Original draft MR: writing- reviewing and editing FJ: data curation DL: numerical simulation. All authors contributed to the article and approved the submitted version.

Conflict of interest

Authors RY, QK, MR, FJ, and DL were employed by the company CCCC Second Harbour Engineering Co., Ltd.

Publisher's note

References

Ahmadi, M. H., and Molladavoodi, H. (2019). A micromechanical sliding damage model under dynamic compressive loading. *Period. Polytech. Civ. Eng.* 63 (1), 168–183. doi:10.3311/PPci.13249

Behnam, H., Kuang, J. S., and Samali, B. (2018). Parametric finite element analysis of RC wide beam-column connections. *Comput. Struct.* 205, 28–44. doi:10.1016/j.compstruc.2018.04.004

Burgers, R., Walraven, J., Plizzari, G. A., and Tiberti, G. (2007). "Structural behavior of SFRC tunnel segments during TBM operations," in *World tunnel congress ITA-AITES* (London: Taylor & Francis), 1461–1467.

Cavalaro, S. H. P., Blom, C. B. M., Walraven, J. C., and Aguado, A. (2011). Structural analysis of contact deficiencies in segmented lining. *Tunn. Undergr. Space Technol.* 26 (6), 734–749. doi:10.1016/j.tust.2011.05.004

Cavalaro, S. H. P. (2009). *Evaluación de aspectos tecnológicos en túneles construidos con tuneladora y dovelas prefabricadas de hormigón*. Barcelona, Spain: Dissertation, Universidad Politécnica de Cataluña.

Chen, J. S., and Mo, H. H. (2009). Numerical study on crack problems in segments of shield tunnel using finite element method. *Tunn. Undergr. Space Technol.* 24 (1), 91–102. doi:10.1016/j.tust.2008.05.007

China Architecture and Building Press (2010). *GB50010 code for design of concrete structures*. Beijing, China: China Architecture and Building Press.

Dai, Z., Li, P., Wang, X., Liu, J., Fan, J., and Kou, X. (2022). Asymmetric force effect and damage analysis of unlooped segment of large diameter shield under synchronous propulsion and assembly mode. *Appl. Sci.* 12, 2850. doi:10.3390/app12062850

Gao, Y., Yu, Z., Chen, W., Yin, Q., Wu, J., and Wang, W. (2023). Recognition of rock materials after high-temperature deterioration based on SEM images via deep learning. *J. Mater. Res. Technol.* 25, 273–284. doi:10.1016/j.jmrt.2023.05.271

Gruebl, F. (2006). Segmental rings (critical loads and damage prevention). *Int Symposium Undergr Excav Tunn*.

Hemmy, O. (2001). *Investigation on tunnel segments without curvature*. Germany: University of Braunschweig.

Jiang, T., Wu, Z., Huang, L., and Ye, H. (2020). Three-dimensional nonlinear finite element modeling for bond performance of ribbed steel bars in concrete under lateral tensions. *Int. J. Civ. Eng.* 18 (5), 595–617. doi:10.1007/s40999-019-00488-1

Koyama, Y. (2003). Present status and technology of shield tunneling method in Japan. *Tunn. Undergr. Space Technol.* 18 (2-3), 145–159. doi:10.1016/S0886-7798(03)00040-3

Krahl, P. A., Palomo, I. I., Almeida, S. J. de C., Henrique Siqueira, G., Pinto Junior, N. de O., and Vieira Junior, L. C. M. (2021). Tolerances for TBM thrust load based on crack opening performance of fiber-reinforced precast tunnel segments. *Tunn. Undergr. Space Technol.* 111, 103847. doi:10.1016/j.tust.2021.103847

Krajcinovic, D., and Lemaître, J. *Continuum damage Mechanics theory and application*. Berlin, Germany: Springer. doi:10.1007/978-3-7091-2806-0

Li, X. L., Zhang, X. Y., Shen, W. L., Zeng, Q., Chen, P., Qin, Q., et al. (2023). Research on the mechanism and control technology of coal wall sloughing in the ultra-large mining height working face. *Int. J. Environ. Res. Public Health* 20 (2), 868. doi:10.3390/ijerph20010868

Li, X., Yan, Z., Wang, Z., and Zhu, H. (2015). Experimental and analytical study on longitudinal joint opening of concrete segmental lining. *Tunn. Undergr. Space Technol.* 46, 52–63. doi:10.1016/j.tust.2014.11.002

Liu, M. B., Liao, S. M., Xu, J., and Men, Y. Q. (2020). Analytical solutions and *in-situ* measurements on the internal forces of segmental lining produced in the assembling process. *Transp. Geotech.* 27, 100478. doi:10.1016/j.trgeo.2020.100478

Liu, S. M., and Li, X. L. (2023). Experimental study on the effect of cold soaking with liquid nitrogen on the coal chemical and microstructural characteristics. *Environ. Sci. Pollut. Res.* 30 (3), 36080–36097. doi:10.1007/s11356-022-24821-9

Liu, S. M., Sun, H. T., Zhang, D. M., Yang, K., Li, X., Wang, D., et al. (2023a). Experimental study of effect of liquid nitrogen cold soaking on coal pore structure and fractal characteristics. *Energy* 275 (7), 127470. doi:10.1016/j.energy.2023.127470

Liu, S. M., Sun, H. T., Zhang, D. M., Yang, K., Wang, D., Li, X., et al. (2023b). Nuclear magnetic resonance study on the influence of liquid nitrogen cold soaking on the pore structure of different coals. *Phys. Fluids* 35 (1), 012009. doi:10.1063/5.0135290

Lorenzo, S. G. (2021). *In situ* behaviour of an instrumented ring subjected to incipient TBM steering around a curve. *Eng. Struct.* 249, 113–124. doi:10.1016/j.engstruct.2021.113124

Lu, D., He, C., and Wang, S. (2017). Emergency medicine faculty are poor at predicting burnout in individual trainees: An exploratory study. *J. South West Jiaot. Univ.* 52, 75–78. doi:10.1002/aet2.10017

Lu, D., Sun, W., and Su, A. (2018). Statistics and analysis of cracking disease in segment lining for shield tunnel in construction stage. *J. Railw. Eng. Soc.* 35 (6), 59–66. doi:10.3969/j.issn.1006-2106.2018.06.012

Lubliner, J., Oliver, J., Oller, S., and Onate, E. (1989). A plastic-damage model for concrete. *Int. J. Solids Struct.* 25 (3), 299–326. doi:10.1016/0020-7683(89)90050-4

Mo, H. H., and Chen, J. S. (2008). Study on inner force and dislocation of segments caused by shield machine attitude. *Tunn. Undergr. Space Technol.* 23 (3), 281–291. doi:10.1016/j.tust.2007.06.007

Mohtadinia, M., Ahmadi, M. H., Fasaghandis, M. M., Dibavar, B. H., and Davarpanah, S. M. (2020). Statistical and numerical study of chipping and cracking in segmental lining. *Period. Polytechnica-Civil Eng.* 64 (3), 869–886. doi:10.3311/PPci.16037

Nogales, A., and Fuente, A. de L. (2020). Crack width design approach for fibre reinforced concrete tunnel segments for TBM thrust loads. *Tunn. Undergr. Space Technol.* 98, 103342. doi:10.1016/j.tust.2020.103342

Plizzari, G. A., and Tiberti, G. (2007). "Structural behavior of SFRC tunnel segments," in *FraMCos-6. Catania* (Brescia, Italy: University of Brescia).

Sharghi, M., Chakeri, H., Afshin, H., and Dias, D. (2021). Analysis of the possible cracking and damages of tunnel lining segments during installing stage. *Soil Mech. Found. Eng.* 58, 287–294. doi:10.1007/s11204-021-09741-z

Shayanfar, M. A., Mahyar, P., Jafari, A., and Mohtadinia, M. (2017). Classification of precast concrete segments damages during production and transportation in mechanized shield tunnels of Iran. *Civ. Eng. J.* 3, 412–426. doi:10.28991/cej-2017-00000101

Shi, X. Y., Yao, Y., Wang, L., and Zhang, C. (2021). The influence of CDP model parameters based on the numerical simulation of uniaxial loading test. *Build. Struct.* 51, 999–1007.

Sugimoto, M. (2006). Causes of shield segment damages during construction. *Int. Symposium Undergr. Excav. Tunn. Eff. Groundw. Tunn. Stab.*, 67–74.

Tian, L., Wang, X., and Cheng, Z. (2021). *Numerical study on the fracture properties of concrete shield tunnel lining segments*, 2021–11. doi:10.1155/2021/9975235*Geofluids*

Wang, F., Huang, H., Soga, K., and Li, Z. (2021). 3D modelling of concrete tunnel segmental joints and the development of a new bolt-spring model. *Tunn. Undergr. Space Technol.* 110, 103835. doi:10.1016/j.tust.2021.103835

Wei, L. (2021). Experimental study on mechanical behavior of wire brushes on shield tail. *Tunn. Constr.* 41 (2), 206–211. doi:10.3973/j.issn.2096-4498.2021.02.006

Xu, G., He, C., Lu, D., and Wang, S. (2019). The influence of longitudinal crack on mechanical behavior of shield tunnel lining in soft-hard composite strata. *Thin-Walled Struct.* 144, 106282. doi:10.1016/j.tws.2019.106282

Xu, M., and Zhang, Z. (2013). Cause analysis and treatment of segment damage of large diameter shield tummel. *Chin. J. Undergr. Space Eng.* 9, 1705–1712.

Yang, Y., Zhou, B., Xie, X., and Liu, C. (2018). Characteristics and causes of cracking and damage of shield tunnel segmented lining in construction stage–a case study in Shanghai soft soil. *Eur. J. Environ. Civ. Eng.* 22, 213–227. doi:10.1080/19648189.2017.1356243

Zhang, J. C., Li, X. L., Qin, Q. Z., Wang, Y. B., and Gao, X. (2023b). Study on overlying strata movement patterns and mechanisms in super-large mining height stopes. *Bull. Eng. Geol. Environ.* 82 (3), 142. doi:10.1007/s10064-023-03185-5

Zhang, L. B., Shen, W. L., Li, X. L., Wang, Y., Qin, Q., Lu, X., et al. (2023a). Abutment pressure distribution law and support analysis of super large mining height face. *Int. J. Environ. Res. Public Health* 20 (1), 227. doi:10.3390/ijerph20010227

Zhang, W. X., De Corte, W., Liu, X., and Taerwe, L. (2021). Optimization study on longitudinal joints in quasi-rectangular shield tunnels. *Appl. Sci.* 10, 573. doi:10.3390/app11020573

frontiers | Frontiers in Ecology and Evolution

TYPE Original Research
PUBLISHED 20 July 2023
DOI 10.3389/fevo.2023.1222676

OPEN ACCESS

EDITED BY
Xuelong Li,
Shandong University of Science and Technology, China

REVIEWED BY
Shufeng Pei,
North China University of Water Conservancy and Electric Power, China
Yaxiong Peng,
Hunan University of Science and Technology, China
Yun Lin,
Central South University, China
Gang Wang,
Shaoxing University, China
Hailiang Jia,
Xi'an University of Science and Technology, China

*CORRESPONDENCE
Shaobo Chai
shbchai@chd.edu.cn

RECEIVED 15 May 2023
ACCEPTED 07 July 2023
PUBLISHED 20 July 2023

CITATION
Chai S, Liu H, Song L, Li X, Fu X and Zhou Y (2023) Static pressure and dynamic impact characteristics of filled jointed rock after frozen-thaw cycle damage.
Front. Ecol. Evol. 11:1222676.
doi: 10.3389/fevo.2023.1222676

Static pressure and dynamic impact characteristics of filled jointed rock after frozen-thaw cycle damage

Shaobo Chai[1,2*], Huan Liu[1], Lang Song[1], Xianpeng Li[1], Xiaodong Fu[3] and Yongqiang Zhou[3]

[1]School of Civil Engineering, Chang' an University, Xi'an, China, [2]Key Laboratory of Hydraulic and Waterway Engineering of the Ministry of Education, Chongqing Jiaotong University, Chongqing, China, [3]State Key Laboratory of Geomechanics and Geotechnical Engineering, Institute of Rock and Soil Mechanics, Chinese Academy of Sciences, Wuhan, China

In the construction project, rock mass is often destroyed from the joint plane, and the jointed rock mass is easy to be eroded by freeze-thaw environment. Therefore, the damage mechanical properties of filled jointed rock mass under freeze-thaw action are very important for construction disaster prevention, engineering safety evaluation and reinforcement. In order to research the effect of the freeze-thaw cycle on the mechanical deterioration properties and damage characteristics of filled jointed rocks, prefabricated filled jointed rock samples are tested with different numbers of freeze-thaw cycles under the temperature range of -20°C~20°C. Then the wave velocity test, static compression test and SHPB impact test are conducted on the rock samples after freeze-thaw. Based on the test results, the change regularity of wave velocity degradation, static compression mechanical properties and dynamic compression mechanical properties of filled jointed rocks under the effect of freeze-thaw cycles were analyzed. The results show that the wave velocity, static compressive strength and dynamic compressive strength of the filled jointed rocks all show a downtrend with the increase of the number of freeze-thaw cycles, and each parameter is positively correlated with the strength of the filling materials. Among them, the decrease in the wave velocity of the rock sample after 30 freeze-thaw cycles is greater than 30%, and the strength loss of the static peak compressive strength exceeds half of its initial strength. The static peak strain rises exponentially with the increase of the number of freeze-thaw cycles while the dynamic peak strain does not show a clear trend. The dynamic peak strain is about 1/10 to 1/5 of the static peak strain. Under the same freeze-thaw action, the lower the strength of filling material, the more serious the damage.

KEYWORDS

filled jointed rock, freeze-thaw cycles, compressive mechanical properties, damage deterioration, dynamic properties

1 Introduction

With the development needs of human construction, more and more engineering projects need to be constructed in high-altitude and cold regions. Among them, a large number of engineering activities, such as water conservancy and hydropower engineering, nuclear power engineering, deep underground engineering, rock mass tunnel engineering, etc., will inevitably involve the rock mass affected by freezing and thawing. There are a large number of filled joints in natural rock mass. The low strength and large deformation characteristics of filling joints will change the strength of the whole rock mass and increase the instability of engineering rock mass (Singh et al., 2002). In practical engineering, the stress wave generated by dynamic loads such as blasting and earthquake will cause the normal and tangential deformation along the filled joint surface when acts on the filled jointed rock mass, resulting in obvious changes in the mechanical properties of the jointed rock mass (Li and Ma, 2009). The damage and deterioration of filled jointed rock subjected to freeze-thaw cycle for a long time will pose a great threat to the dynamic stability of rock mass engineering. Therefore, it is of great significance to study the mechanical properties of rock filled with joints under freeze-thaw cycles and the propagation law of stress waves in jointed rock mass for stability evaluation and safety protection of rock mass engineering in cold regions.

At present, freeze-thaw cycling tests mainly focus on intact and fractured rocks on their mechanical and degradation characteristics, such as the influencing factors of rock freezing-thawing damage, deterioration mode of rock damage, and microstructure of freezing-thawing rock and mechanical properties of rock. For example, in view of the huge differences in the properties of various rocks, some researchers have carried out experimental study on the effects of different rock types on freeze-thaw damage, and obtained the conclusion that the freeze-thaw durability of igneous rock, sedimentary rock and metamorphic rock is generally reduced in turn (Matsuoka, 1990; Yang et al., 2021). Besides, the freeze-thaw durability of the same rock has been confirmed to decrease with the aggravation of weathering (Deng et al., 2014a). As for the influence of freeze-thaw action on rock characteristics, the research results show that with the increase of freeze-thaw cycle times, the damage of rock will accumulate continuously, but the cumulative damage of rock with high strength is not obvious (Nicholson and Nicholson, 2000; Tan et al., 2011; Qiao et al., 2021).

A number of researches on rock freeze-thaw failure show that the damage and deterioration modes can be roughly divided into falling mode, crack mode and particle loss mode (exfoliation mode) (Xu, 2006; Tan et al., 2011; Li et al., 2017; Deng et al., 2014b). Further analysis shows that the rocks with low strength and high porosity, such as red sandstone and silty mudstone, mostly show the falling mode under the influence of freeze-thaw. Rocks with high strength and low porosity, such as shale, diabase and granite, are mainly show the crack mode. Rocks whose surface is easily softened by water, such as argillaceous siltstone and dolomitic limestone under acidic conditions, show the particle loss mode. In terms of micro view, researchers have conducted experimental exploration on the relationship between rock freezing-thawing damage and porosity by means of scanning electron microscopy, CT scanning and nuclear magnetic resonance (Li et al., 2022; Zhang et al., 2022; Liu et al., 2023; Jiang et al., 2019; Mousavi et al., 2020; Wang et al., 2020). The results show that the more freeze-thaw cycles, the greater the porosity and damage degree of rock samples.

The research on the damage mechanical properties of rock under freeze-thaw cycle is mainly based on the static mechanical tests. For example, through uniaxial or triaxial compression experiments on rock samples under freeze-thaw cycle, it has been found that the compressive strength, peak strain, elastic modulus and other mechanical parameters of rocks show an exponential function or quadratic function attenuation trend with the number of freeze-thaw cycles (Tan et al., 2011; Li et al., 2017; Deng et al., 2019; Lu et al., 2019; Fan et al., 2020; Mousavi et al., 2020). Based on these, some researchers have established a constitutive model with the number of freezing-thawing cycles and strain as control variables on the basis of damage mechanics theory (Zhang and Yang, 2010; Bayram, 2012; Huang et al., 2018; Li et al., 2021a).

In terms of dynamic mechanical properties, the dynamic test of the rock after freezing and thawing is mainly carried out by using the split Hopkinson compression bar device which is suitable for the study of dynamic mechanical properties of various brittle materials at high strain rate (Li et al., 2021b; Liu et al., 2022; Zhao et al., 2022). For example, Wang et al. (2016a) and Wang et al. (2016b) explored the dynamic characteristics of freezing-thawing red sandstone under different strain rates through SHPB test. The results show that the decrease of peak strength and dynamic elastic modulus under the impact test gradually with the increase of freeze-thaw action, while the peak strength and shear strength are positively correlated with the strain rate. In addition, the compressive strength and elastic modulus decrease more obviously under dynamic impact than under static load. For homogeneous sandstone, Zhou et al. (2015) carried out experimental study by nuclear magnetic resonance test and SHPB impact test to reveal that the higher the porosity, the more serious the dynamic strength degradation will be under freezing-thawing action, and the relationship between porosity and dynamic peak strength is polynomial. Yi et al. (2020) found that the dynamic mechanical indexes of sandstone deteriorated after freezing-thawing cycles, and the cumulative damage inside rock samples grew slowly when the number of freezing-thawing cycles is large. In addition, some scholars have observed the failure characteristics of rock samples during dynamic impact with the help of high-speed cameras. For example, Zhou et al. (2018) used high-speed cameras to study the crack propagation and failure mode of intact sandstone samples after dry-wet cycles during dynamic tensile process. Su et al. (2021) found that the final failure modes of sandstone with different dip angles were different in the dynamic compression test of filling weak through jointed sandstone by means of high-speed camera. With the increase of joint dip angle, the failure order of the sample changed from the first failure of filling weak joints in the middle to the first failure of rocks on both sides.

At present, there are many studies on the mechanical properties of intact or fractured rocks under freeze-thaw cycle, but there are few studies on the mechanical properties of jointed rocks under freeze-thaw cycle. Moreover, the influence of external factors such

as freeze-thaw cycle has not been considered in the study of dynamic characteristics and wave propagation law of filled rock joints. In recent years, more and more attention has been paid to the research on dynamic characteristics of filled rock joints. The static and dynamic characteristics, stress wave propagation law, energy loss and other important characteristics of filled joints are gradually revealed by wave propagation theory, numerical simulation and rock test (Li et al., 2014; Huang et al., 2015; Liu et al., 2017; Chai et al., 2020a; Chai et al., 2020b; Jia et al., 2021). In terms of experimental research, Chai et al. (2020a) studied the mechanical properties of filled jointed rock under cumulative impact, including static and dynamic characteristics, and comprehensively considered the effects of filling materials and joint thicknesses. Based on this, the cumulative damage characteristics of filled joints under multiple impacts and the energy dissipation law under dynamic loading were studied by means of a self-made cumulative impact device (Chai et al., 2020b). However, the damage characteristics of filled jointed rock under environmental action such as freeze-thaw cycle have not been studied yet.

In view of the unclear mechanical characteristics of freeze-thaw damage of filled joints, on the basis of previous studies (Chai et al., 2020a; Chai et al., 2020b), this paper presents static and dynamic compression experimental study on prefabricated artificial jointed rock samples pretreated under different freeze-thaw cycles. The variation law of static and dynamic mechanical parameters and failure characteristics of filled jointed rock samples under the action of freeze-thaw cycle are studied and analyzed, and the propagation characteristics of stress wave in filled rock samples are further analyzed.

2 Test profile

2.1 Sample preparation

Due to the complex distribution and varying thickness of filled joint layer in natural rock mass, it is difficult to prepare the same type of rock samples in batches, which is not conducive to the single factor analysis. Therefore, in this test, the granite with good lithology and the mortar with similar properties to the joint filling layer are used to prepare the filled jointed rocks by artificial combination. As the weak layer of rock mass, the physical and mechanical properties of joint layer are generally lower than that of rock blocks on both sides. In the previous research work of our research group (Chai et al., 2020a; Chai et al., 2020b), four kinds of filling joint rock samples with different filling materials, cement mortar, lime mortar, gypsum mortar and sediment mortar, were prepared to simulate the filling joints with different characteristics in practice. In this paper, only the filling joint rock with lime mortar is selected as the object for research. In order to reflect the diversity of the filling layer, three filling mortars with different mix proportions are used in this test. The mortar proportion and the mortar strength are shown in Table 1.

The preparation method of the filled jointed rock samples remained the same as in the previous studies (Chai et al., 2020b). In the preparation process, firstly, the granite is processed into cylindrical test blocks with a diameter of 50 mm and a height of 15 mm, and one end of each test block is polished to ensure that the roughness of the end faces of each test block is the same. At the same time, six grooves are cut at equal spacing on this end to form three horizontal and three vertical grooves with a depth of 1 mm and a width of 2 mm. Then the filling mortar is prepared according to the mortar proportion in Table 1. Finally, the two test blocks are placed face-to-face with the grooves aligned with each other and filled with the filling mortar with a thickness of 5 mm. After the sample preparation, a wave velocity tester is used to screen the rock samples and eliminate those with large differences in wave velocity. In addition, in order to reduce the influence of external factors on the rock samples, parallel tests are used for each part of the process, and three samples are used as one group.

The prepared filled jointed rocks are maintained under standard curing conditions for 28 days. The cured rock samples are dried in an oven at 60°C for 12 h, and then immersed in a distillation tank for 12 h until the rock samples are naturally saturated. After that, the water-saturated rock samples are put into a rapid freeze-thaw cycle test chamber for the freeze-thaw cycle test. The freeze-thaw cycle test parameters are set as follows: -20°C freezing for 4 h, 20°C thawing for 4 h. Under this condition, 0, 1, 5, 10, 15, 20 and 30 freeze-thaw cycles are carried out in groups, as shown in Figure 1.

2.2 Experimental equipment

After the freeze-thaw cycles of the rock samples, the NN-4B nonmetallic ultrasonic testing analyzer is used to test the wave velocity of the filled jointed rock after different freeze-thaw cycles. The wave velocity tester is shown in Figure 1. During the measurement, Vaseline is applied to the surface of both sides of the rock sample. Multiple wave velocity tests are conducted to eliminate the results with large variance, and the average of three

TABLE 1 Physical and mechanical parameters of rock and joint filling materials.

Fillings	Mix proportion		Strength(MPa)
I	Water: Lime: Sand	1:1:3	1.62
II	Water: Lime: Sand	1:1.54:1.54	1.12
III	Water: Lime: Soil:Sand	1:0.7:0.3:3	2.31
Rock on both sides	Granite	—	67

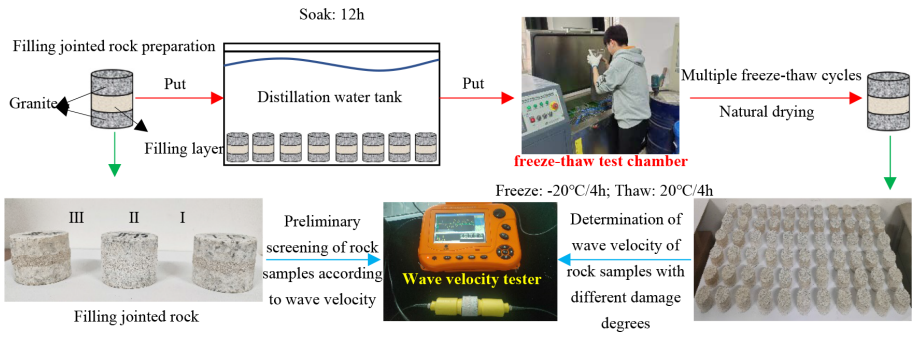

FIGURE 1
Fabrication and freeze-thaw cycle test process of jointed rock samples of three filling materials.

valid wave velocity values is taken as the effective measurement result of wave velocity.

In order to find out the change regularity of mechanical properties of rock samples after freeze-thaw cycles, the WAW31000 microcomputer-controlled electro-hydraulic servo universal testing machine and SHPB testing device are used to conduct static compression tests and dynamic impact tests on rock samples under the accumulated damage of different freeze-thaw cycles, as shown in Figure 2. The static compression test is performed by controlling the load to achieve compression damage to the rock samples at a rate of 50 N/s. The dynamic impact test is performed with a Split Hopkinson Pressure Bar (SHPB), which is mainly composed of an incident bar, a transmission bar and an absorption bar. The diameter of the bars is 50 mm, the elastic modulus is 210 GPa, Poisson ratio is 0.25, the longitudinal wave speed is 5172 m/s, and the density is 7800 kg/m^3. The length of the impact bar, the incident bar and the transmission bar respectively are 0.3 m, 3.7 m and 2.5 m, respectively. In order to reduce the superposition effect of the incident and reflected waves, the strain gauges on the incident and transmission bars are pasted at 1 m and 0.5 m away from the surface of the sample, and the method of symmetrical pasting is adopted to improve the test accuracy. The dynamic impact pressure is set to 0.15 MPa, and 0.15mm thick copper sheet is used as pulse shaper. The FASTCAM Mini UX high-speed camera is used to record the damage process of the rock samples during the dynamic impact.

3 Analysis of test results

3.1 Damage regularity of filled jointed rocks under the freeze-thaw action

Under the action of freeze-thaw cycles, the pores and fractures inside the filled jointed rocks continue to develop and expand, causing irreversible damage to the rocks. The macroscopic performance of the cumulative damage is the deterioration of wave velocity, elastic modulus, density, strain and other parameters of rock samples. In this study, the wave velocity is used as a macroscopic parameter to describe the damage and deterioration of the filled jointed rocks. The average wave velocity values are shown in Table 2.

It can be seen from Table 2 that with the increase of the number of freeze-thaw cycles, the wave velocity values of the filled jointed rocks continue to decrease. The wave velocities of the three types of filled rock samples have decreased by 34.02%, 42.03% and 30.95% respectively after 30 freeze-thaw cycles, indicating that the freeze-thaw cycles have a greater impact on the damage and deterioration of the filled jointed rocks. This is because under the freeze-thaw action, a large number of fissures and cracks are produced inside the filled jointed rocks, which leads to a more complex ultrasonic wave propagation path and reduces the wave propagation velocity.

Under the action of the same freeze-thaw cycles times, the wave velocity relationship of the three types of filled jointed rocks is $v_{III}>v_I>v_{II}$. Considering the initial strength of the filling materials, it is found that the wave velocity value of the filled jointed rocks is positively correlated with the strength of the filling materials. The main reason is that the greater the strength of the filling materials is, the better the overall stability of the rock samples, and the slower the deterioration rate of the rock samples under the action of the same freeze-thaw cycles, as well as the higher the wave velocity. To further analyze the damage and deterioration regularity of freeze-thaw cycles on the filled jointed rocks, the damage degree D_n from the reference was cited as (Chai et al., 2020b):

$$D_n = 1 - v_n^2/v_0^2 \quad (1)$$

where v_n is the wave velocity value of the filled jointed rock after n times freeze-thaw cycles, and v_0 is the wave velocity value of the rock samples without the freeze-thaw cycles. By substituting the wave velocity values in Table 2 into Eq. (1), the accumulated damage of three types of filled jointed rocks under different freeze-thaw cycles times can be calculated, as shown in Figure 3.

As shown in Figure 3, the cumulative damage degree of the three types of filled jointed rocks increases nonlinearly with the increase of the number of freeze-thaw cycles, indicating that the damage caused by the freeze-thaw action of the jointed rock sample is a continuous cumulative process. This is mainly due to the fact that water inside the pores of water-saturated rock samples freezes into ice under low-temperature conditions, and the frost heaving force generated by the water-ice phase change react on the pores and fractures. When the frost heaving force exceeds the tensile strength of the rock matrix, it will promote the further development of pores and cracks, and the migration of free water in the new

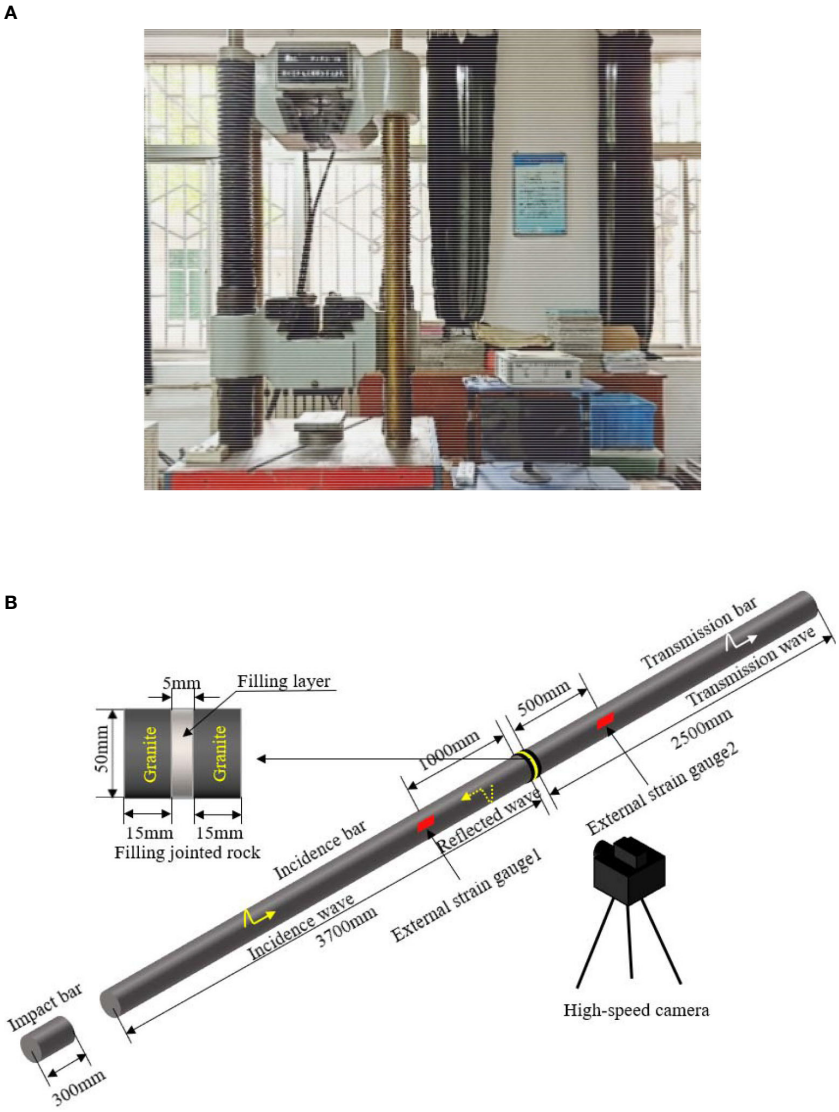

FIGURE 2
Static and dynamic compression mechanical characteristic test instrument: **(A)** WAW31000 universal testing machine; **(B)** diagram of SHPB test device.

cracks during the melting process will lead to the further expansion of cracks. The jointed filling layer is formed by the weathering of rocks, and the number of internal pores and fissures is much more than that of the rocks on both sides. Hence, the water content in the filling layer in the saturated state is more than that of the rocks on both sides. During the freeze-thaw cycle, the frost heaving force generated by the water ice phase change in the filling layer is greater than that of the rocks on both sides. The frost heaving force in the filling layer partially promotes the development of cracks, and partially acts on the rocks on both sides, further leading to the reduction of the integrity of the joint layer and even damage.

In addition, the slope of the curve in the Figure 3 is greater in the early stage than in the middle and late stage, showing a gradual decreasing trend, indicating that the damage and deterioration rate of the jointed rock samples in the early stage of the freeze-thaw is greater than in the middle and late stage. It reflects the rapid

TABLE 2 Wave velocity of jointed rock under different freeze-thaw cycles.

Filling type	Wave velocity values of rock samples after different freeze-thaw cycles(m/s)						
	0	1	5	10	15	20	30
I	2945	2734	2454	2123	2074	1986	1943
II	2734	2494	2136	1823	1764	1713	1685
III	3438	3281	2973	2707	2455	2402	2374

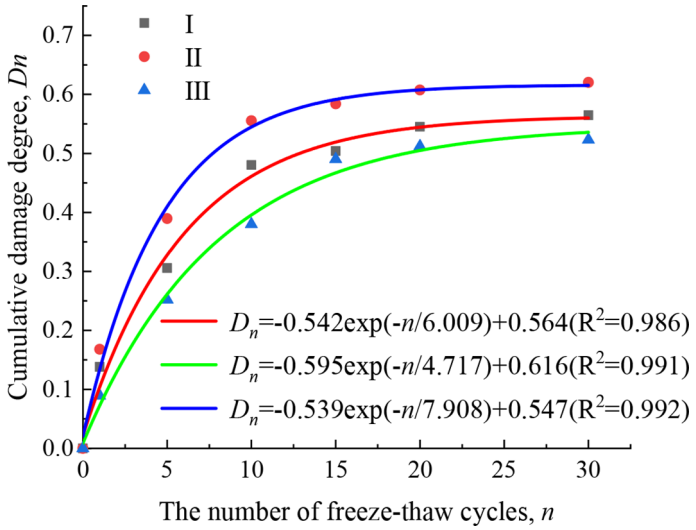

FIGURE 3
Cumulative damage changes of jointed rock under different freeze-thaw cycles.

development of pores and fractures in the rock samples at the early stage of the freeze-thaw, accelerating the damage and deterioration of the filling layer. However, the sensitivity of the rock samples to the damage and deterioration gradually decrease in the middle and late stage of the freeze-thaw.

By fitting the curves, it is found that the fitting function is the same as the damage function in the reference (Chai et al., 2020b), and the curve fitting degree is high, indicating that the model is applicable to the evaluation of accumulative damage of filled jointed rocks under the freeze-thaw action, expressed as:

$$D_n = \alpha - \beta\exp(-n/\gamma) \quad (2)$$

where α, β, γ are fitting coefficients, and n is the number of freeze-thaw cycles. According to the change rule of each value of the curve, it is found that α, β and γ in the formula are related to the filling materials. More specifically, α and β are negatively correlated with the filling strength, while γ is positively correlated with the filling strength. According to this formula, the damage degree of the filled jointed rocks under the action of different number of freeze-thaw cycles can be calculated.

3.2 Analysis of the static uniaxial compressive strength deterioration

The static stress-strain curves of the rock samples can be obtained by the uniaxial compression test on the filled jointed rocks under different times of freeze-thaw cycles, as shown in Figure 4.

From Figure 4, it can be seen that the stress-strain curves of the three filled jointed rocks have similar trends, and the curves move downward to the right with the increase of the number of freeze-thaw cycles. Based on the previous research results (Chai et al., 2020b), the static compression process of rock samples is divided into four stages: the compaction stage, the elastic stage, the plastic yielding stage, and the destruction stage. For the rock samples with same filling material, with the increase of the number of freeze-thaw cycles, the compaction stage of the curve gradually lengthens, and the slope in the elastic stage of the curve gradually decreases. At the same time, there is an obvious plastic yielding stage, and the decline rate in the destruction stage becomes slower.

To further study the static properties of the filled jointed rocks under the freeze-thaw, the static peak compressive strength corresponding to each condition is obtained from Figure 4, and the results are shown in Table 3. From the Table 3, it can be seen that the compressive strength of rock samples corresponding to the same number of freeze-thaw cycles is: Type III > Type I > Type II. This is because the filling layer, as the weak layer of the rock samples, has a "barrel effect" on the compressive strength of the rock samples. From a material perspective, the filling materials of type I and type II both are mixed with lime, sand and water, and under the premise of consistent lime content, the sand content of type I is greater than that of type II. The combination of fine sand as a fine aggregate material and a cementitious material (lime) greatly increases the friction between material particles, so the stability of Type I filling material is higher than that of Type II filling material. For the jointed rock samples of type I and type III, on the condition of the same sand content, the filling materials of type III contain part of clay, which enhances the cohesion among the particles of each material, so the stability of type III is higher than that of type I and type II.

The decreasing trend of static peak compressive strength of the three types of filled jointed rocks is similar: first decreasing sharply and then decreasing at a slower rate. For example, after 15 freeze-thaw cycles, the strength of type II filled jointed rock decreased the most by 51.1%; type I is the followed by 39.7%; type III has the smallest strength loss rate of 38.4%, accounting for 3/4 of the strength loss during the its full freeze-thaw cycle. After 30 freeze-thaw cycles, the peak compressive strengths of the three types of filled jointed rocks are respectively 45.8%, 33.4%, and 47.9% of those before the freeze-thaw cycles, with strength loss rates greater

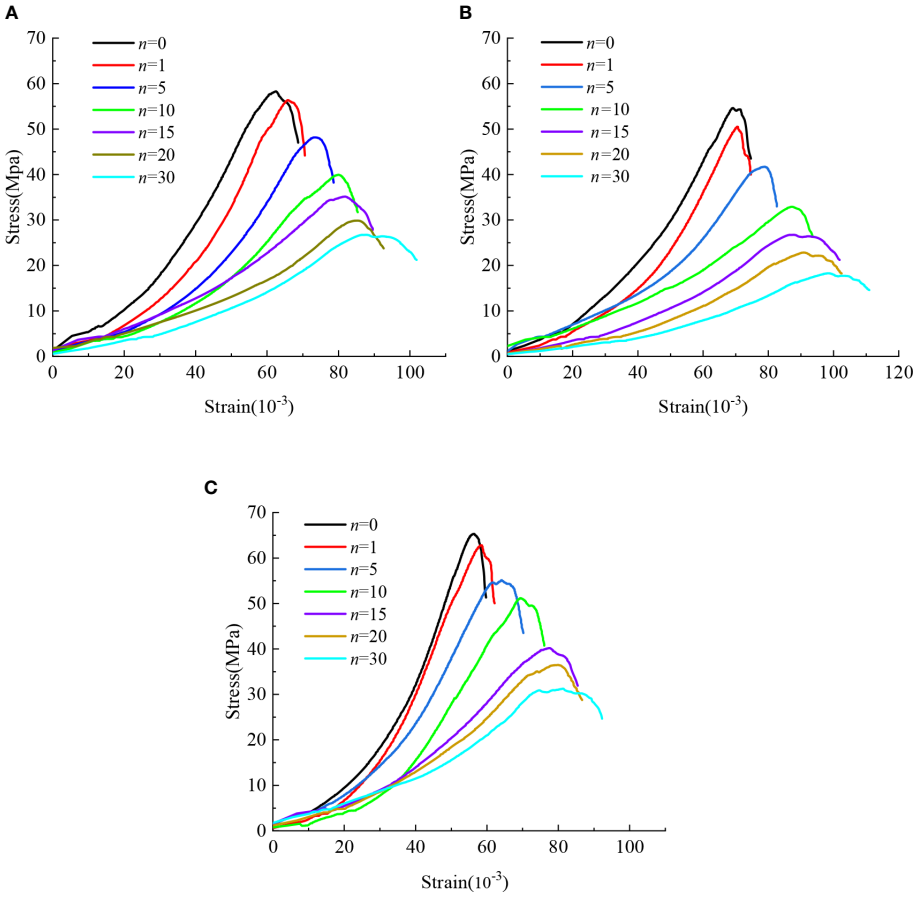

FIGURE 4
Static stress-strain curves of three kinds of jointed rock: **(A)** type I filling jointed rock; **(B)** type II filling jointed rock; **(C)** type III filling jointed rock.

than 50%. To better present the change regularity of compressive strength with the number of freeze-thaw cycles, the freeze-thaw coefficient is adopted and is expressed as:

$$K_f = R_f / R_s \tag{3}$$

where R_s and R_f are the uniaxial saturated compressive strengths (MPa) of the filled jointed rocks before and after the freeze-thaw cycles, respectively. The results of freeze-thaw coefficients were compared and analyzed as shown in Figure 5.

As shown in Figure 5, the freeze-thaw coefficient of the rock samples decreases nonlinearly with the increase of the number of freeze-thaw cycles, indicating that the peak compressive strength of the filled jointed rocks is deteriorating continuously. The decreasing trend of the curve can also show the damage and deterioration rate of the rock samples at each stage of the freeze-thaw.

The static peak strain shows different trends, and all three types of rock samples show an increase in peak strains of more than 40% after 30 freeze-thaw cycles. The curve fitting of the peak strain under various freeze-thaw cycles is shown in Figure 6. The peak strains of the rock samples increase with the increase of the number of freeze-thaw cycles, and the growth rate of peak strains is greater in the early stage of the freeze-thaw than that in the middle and late stage. With the increase of freeze-thaw times, the deformation of the rock samples gradually tends to stabilize, and the rock samples show a trend of decreasing brittleness and increasing ductility.

The curve of static peak strains with the number of freeze-thaw cycles shown in Figure 6 can be fitted as:

TABLE 3 The static compression strength of the filled jointed rock.

Filling type	Compressive strength value of rock samples after different freeze-thaw cycles(MPa)						
	0	1	5	10	15	20	30
I	58.29	56.36	48.16	39.93	35.15	29.87	26.73
II	54.63	50.51	41.69	32.93	26.73	22.84	18.27
III	65.30	62.79	55.13	51.19	40.20	36.49	31.27

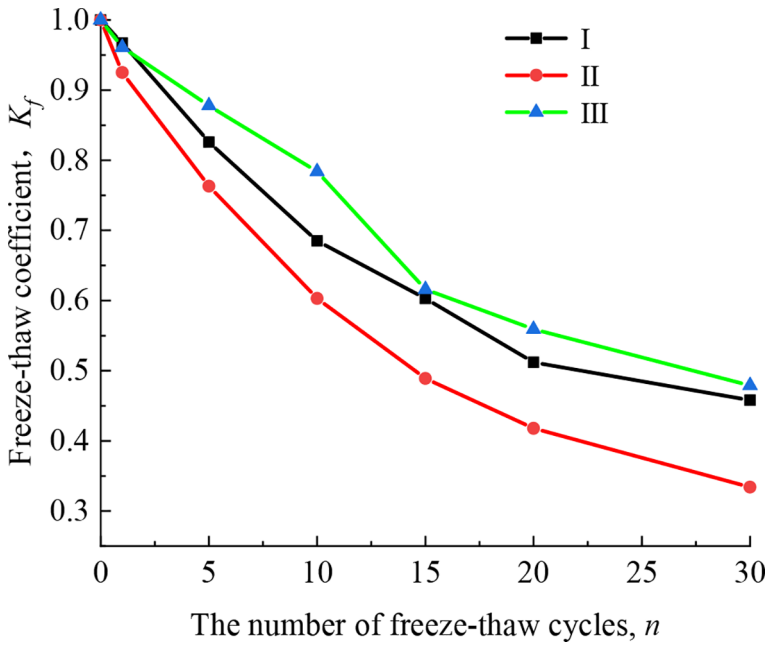

FIGURE 5
The relationship between freeze-thaw coefficients and freeze-thaw cycle times.

$$\varepsilon_b = a \cdot n^b \quad (4)$$

where ϵ_b is the static peak strain; n is the number of freeze-thaw cycles; a and b are the fitting coefficients. In Eq. (4), it can be seen that the peak strains of all the three types of filled jointed rocks increases exponentially, and the fitting parameter b is greater than 0 and less than 1, indicating that the peak strains increases with the increase in the number of freeze-thaw cycles. However, with the continuous increase in the number of freeze-thaw cycles, the rising trend of peak strains becomes slower, indicating that the fracture development is gradually completed and stable after the rock samples undergoes a certain number of freeze-thaw cycles, i.e., the

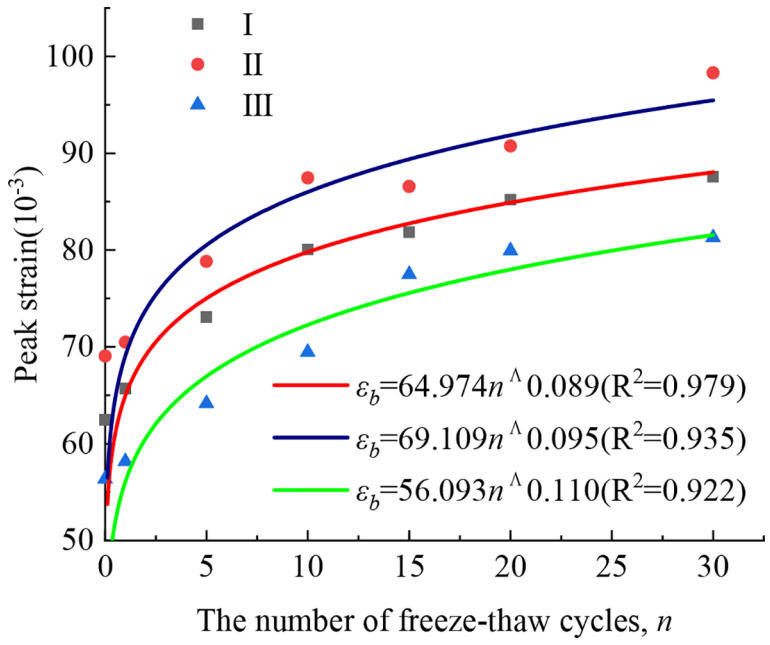

FIGURE 6
The relationship between the peak strain and freeze-thaw cycle times.

filled jointed rocks will not be in an endless deterioration process. By comparing the curve fitting coefficients, it is found that the coefficient *a* is negatively correlated with the strength of the filling layers.

From Section 4.1, it can be seen that the filled jointed rocks are in the process of continuous cumulative damage under the action of freeze-thaw cycles. The continuous deterioration of rock samples under the freeze-thaw action is further confirmed by the change regularity of static parameters of rock samples in this section. To illustrate the inherent relationship between the strength eterioration and cumulative damage, Figure 7 shows the change regularity of static peak stress and peak strain with the change of cumulative damage degree. The certain accumulated damage threshold in the Figure 7 can divide the curve into two zones (Region A and Region B) with different trends. The data points before this damage threshold are relatively discrete, and the results of the rock samples with three filling materials show significant differences. However, beyond this threshold, the results of the three types rock samples tend to be similar. Therefore, it can be inferred that the joint filling layers have been damaged after reaching this damage threshold and lost their contributions to the overall strength and deformation. Subsequently, the change regularity of peak stress and strain with the damage degree of rock samples is mainly determined by the rocks on both sides. The damage threshold in this test is about D'_n=0.5.

By fitting the curve of Figure 7, the relationship between the peak stresses in Region A and Region B and the cumulative damage degree can be obtained as:

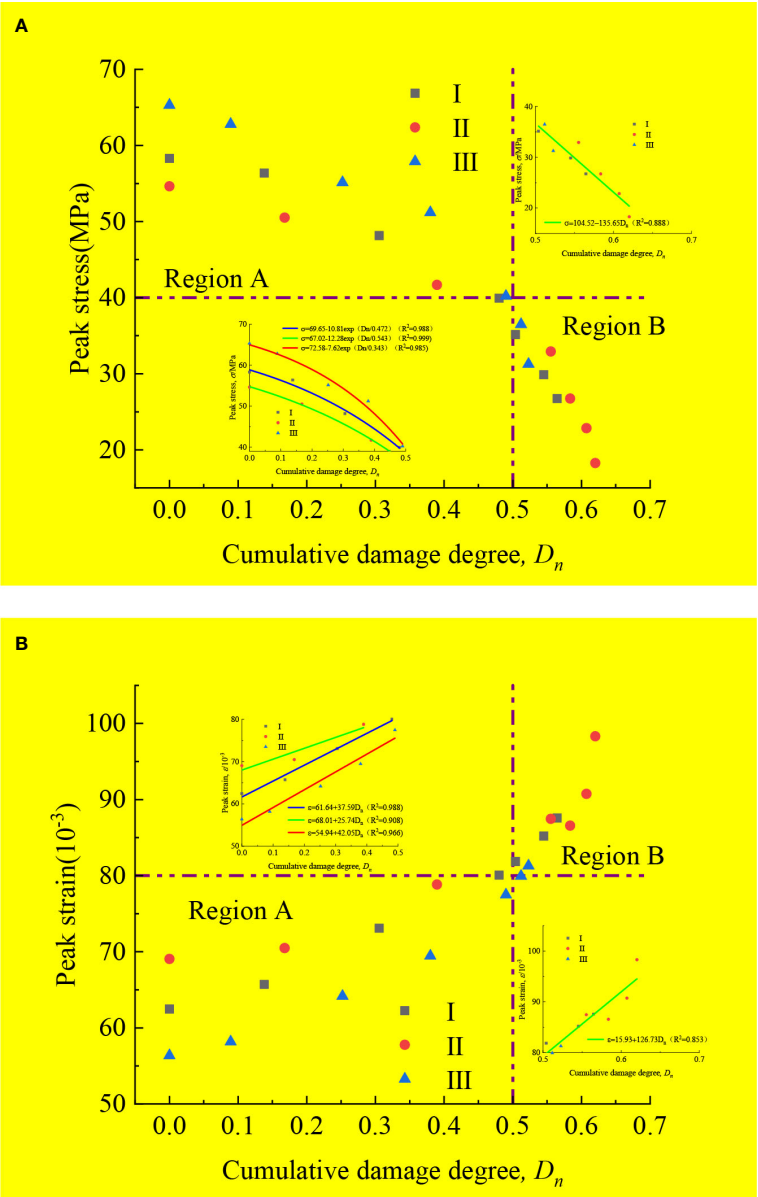

FIGURE 7
Variation of static peak stress and strain with cumulative damage degree: **(A)** peak stress-cumulative damage degree; **(B)** peak strain-cumulative damage degree.

$$\sigma_p = \begin{cases} \alpha' - \beta' \cdot \exp\left(D_n/\gamma'\right), \left(D_n \le D_n'\right) \\ \eta' - \zeta' D_n, \left(D_n > D_n'\right) \end{cases} \quad (5)$$

The fitting relations of peak strain and cumulative damage degree in the two zones are:

$$\varepsilon_p = \begin{cases} a' + b' D_n, \left(D_n \le D_n'\right) \\ c' + d' D_n, \left(D_n > D_n'\right) \end{cases} \quad (6)$$

The fitting parameters are shown in Table 4.

Obviously, the fitting coefficients of the curve in Region A are related to the filling material properties, and α' and b' in this test are positively correlated with the strength of the filling layers, while β', γ' and a' are negatively correlated with the strength of the filling layers. The fitting coefficients in Region B are only related to the properties of the rock on both sides.

From the perspective of failure state, after undergoing multiple freeze-thaw cycles of damage, the rock sample exhibits a trend from splitting failure to shear failure due to decreased strength and increased strain. Figure 8 shows the final damage morphology of type III rock samples with 0 and 30 freeze-thaw cycles. It is obvious that the rock sample after 30 cycles exhibits oblique cracks in a shear failure pattern.

3.3 Analysis of dynamic impact results

The SHPB device is used to conduct impact tests on rock samples after freezing and thawing. Referring to the three-wave method used by Bayram (Bayram, 2012), the electrical signals collected from the impact tests are converted into the stress, strain, and strain rate of the rock samples, and the dynamic stress-strain curves of each filled jointed rock under freezing and thawing cycles are further calculated, as shown in Figure 9. Compared to the static pressure curve shown in Figure 4, the slope of the dynamic stress-strain curve in the initial stage is relatively larger, mainly because the SHPB test belongs to high strain rate compression, and the impact process is completed in an instant. The deformation of the filling layers is slower than the transfer of stress. In the elastic stage, the slope of the curve (i.e., dynamic compression modulus) tends to decrease with increasing freeze-thaw action. Similarly, the slope of the curve in yielding stage decreases with increasing freeze-thaw times, indicating that the ductility of the rock samples is increasing under the freeze-thaw action.

As can be seen from Figure 9 that the dynamic stress-strain curves of the three types of filled jointed rocks have similar trends. With the increase of the number of freeze-thaw cycles, the dynamic peak compressive strength of the jointed rock samples gradually decreases. The dynamic peak strain of the rock samples changes in an unclear way, and there are fluctuations. The dynamic compressive strength of the rock samples is in continuous deterioration process under the action of freeze-thaw cycles, and the strength damage continues to accumulate with the increase of the number of freeze-thaw cycles. The regularity of dynamic strength of the three types of rock samples under the action of the same freeze-thaw cycles is consistent with that of static compressive strength. According to the analysis of Section 3.1, the macroscopic damage of rock samples under the freeze-thaw action can be manifested as wave velocity deterioration. In order to explore the relations between strength damage and wave velocity damage,

TABLE 4 Fitting parameter table.

	Peak stress parameters					Peak strain parameters			
	α'	β'	γ'	η'	ζ'	a'	b'	c'	d'
I	69.65	10.81	0.472	104.52	135.62	61.64	37.59	15.93	126.73
II	67.02	12.28	0.543			68.01	25.74		
III	72.58	7.62	0.343			54.94	42.05		

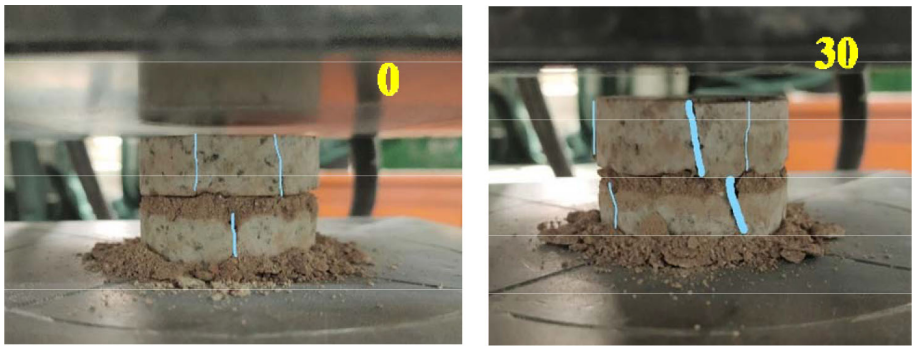

FIGURE 8
Static compression failure diagrams of type III rock samples with 0 and 30 freeze-thaw cycles.

the dynamic peak compressive strength of each condition is fitted with the corresponding wave velocity, as shown in Figure 10.

It can be seen from Figure 10 that the wave velocities of the three types of rock samples have a good correlation with the dynamic peak compressive strength. The dynamic compressive strength of the rock sample shown in the figure decreases nonlinearly with the attenuation of the wave velocity. From the change regularity of the fitting curve of strength versus wave velocity, it can be seen that if the wave velocity value v_n of the filled jointed rocks after the freeze-thaw is measured, the corresponding dynamic compressive strength σ_{pn} can be calculated by the formula $\sigma_{pn} = a\}\ exp(^{-v_n}/_{b^n}) + c\}$ where a''、b''、 c'' are the fitting coefficients.

Comparing the static peak strain in Figure 6, it is found that the amplitude and range of dynamic peak strain changes are much smaller than the static peak strain. Compared with the change trend of static peak strain, the dynamic peak strain has a certain discreteness with the change of freeze-thaw times. As shown in Figure 11, the value of dynamic peak strain ranges from 0.01 to 0.013, which is approximately 1/10 to 1/5 of the static peak strain. This is mainly due to the fact that uniaxial compression belongs to a low strain rate test, while dynamic impact is a kind of high strain rate test. The latter acts on the rock samples for an extremely short time, causing the rock samples to be damaged by compression in a very short time, which results in smaller dynamic peak strain values and a more complex change regularity of the rock samples.

3.4 Analysis of impact failure

Figure 12 shows the failure process of each rock sample after 10 freeze-thaw cycles recorded by a high-speed camera. Based on the stress-strain curves, it is found that the impact process of the filled jointed rock sample after freeze-thaw damage contains filling layer compaction, overall elastic compression, crack growth, filling layer splash and rock sample destruction. From Figure 12, it can be seen that the filling layers are firstly destroyed by compaction under the impact load, and its filling layer destruction appears as granular clasts splash due to the lowest filling layer strength of type II, while the filling layers of type I and III are compressed and slightly lateral expansion occurs. As the impact continues, the filling layer emits joint debris around under the impact load, and the rocks on both sides bear the impact load to generate cracks. Under the impact load, the cracks gradually develop, penetrate, and thicken, ultimately leading to complete destruction of the rocks on both sides.

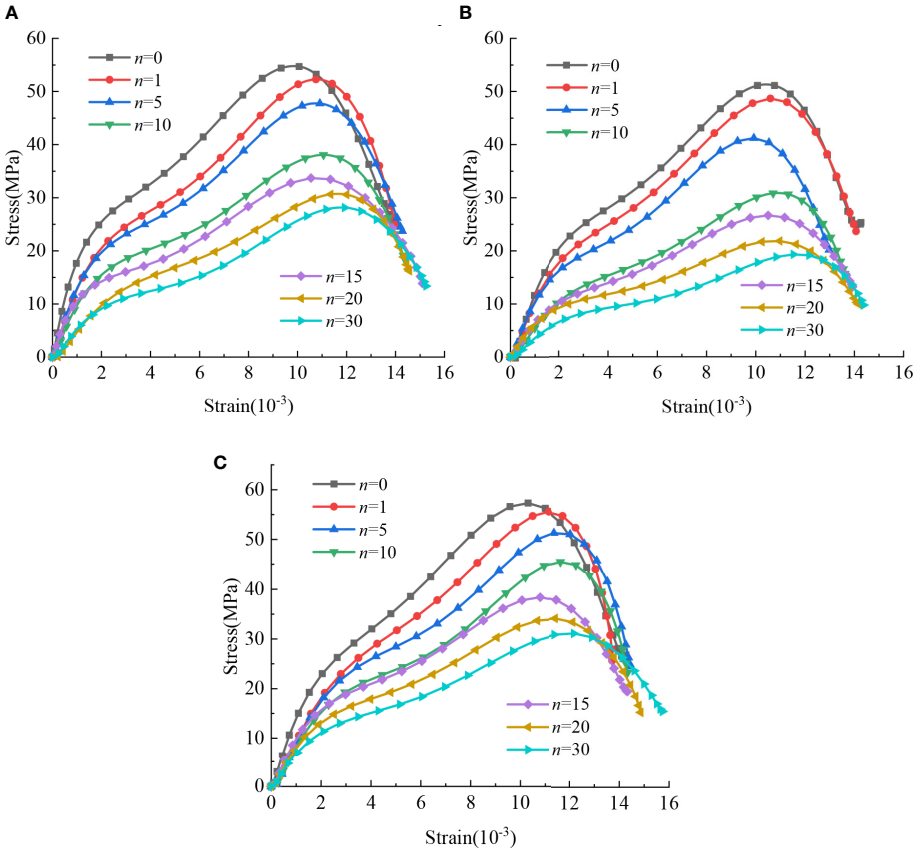

FIGURE 9
Dynamic stress-strain curves of three kinds of jointed rock: **(A)** type I filling jointed rock; **(B)** type II filling jointed rock; **(C)** type III filling jointed rock.

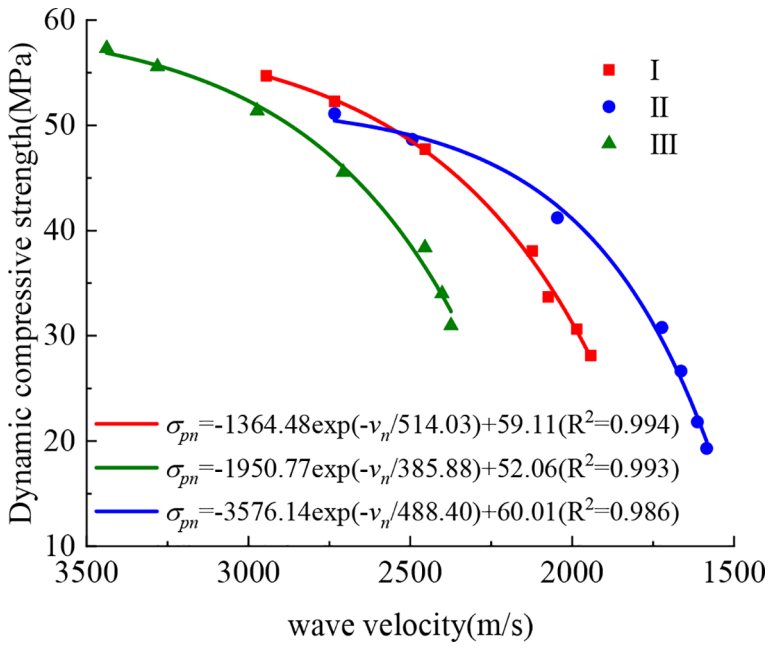

FIGURE 10
Relation curve between dynamic compressive strength and wave velocity.

3.5 Effect of freeze-thaw cycles on wave propagation characteristics in filled jointed rocks

This SHPB test is performed by controlling the impact pressure (0.15 MPa) to maintain the initial velocity of the impact bar to ensure consistent amplitude values of the incident wave. Figure 13 shows the waveform curves of reflected and transmitted in filled jointed rocks after 0, 5, 10, 15, 20 and 30 freeze-thaw cycles. Due to the consistent shape of the incident wave, it is not reflected in this figure. As shown in Figure 13, as the number of freeze-thaw cycles increases, the amplitude of the reflected wave continuously increases, while the amplitude of the transmitted wave decreases. This is mainly due to the fact that the filled jointed rocks are in the process of continuous freeze-thaw damage and deterioration, and the pores and fractures in the jointed layers are increasing, which leads to the continuous decrease of the overall density and the increase of the average wave impedance of rock samples. According to the relation between reflection coefficient R and wave impedance z_p in the reference (Chai et al., 2020b), Eq. (7) shows that the average impedance of the rocks increases and the reflected wave amplitude keeps rising and the transmitted wave amplitude keeps decreasing.

$$R = (z_{p1} - z_{p2})/(z_{p1} + z_{p2}) \tag{7}$$

where z_{p1} is the wave impedance of the bar and z_{p2} is the wave impedance of the rock sample.

It can also be seen from Figure 13 that the change of the amplitude of transmitted and reflected waves with the freeze-thaw cycles is larger before 15 freeze-thaw cycles. As the freeze-thaw cycles continue, the change gradually decreases. Based the analysis of the dynamic mechanical properties of rock samples, it is shown that the deterioration rate of the rock samples in the early stage is faster than in the later stage. In addition, the fluctuation regularity of transmitted waves in each rock sample is good in the early stage of the freeze-thaw, but it is gradually complex with the increase of freeze-thaw times, which indicates that the transmitted wave propagation path is gradually complex, further indicating that the freezing and thawing caused the development of pores and fractures in the filled jointed rock in multiple directions.

To further study the influence of freeze-thaw action and filling materials on the transmitted and reflected effect of stress wave propagation of the filled jointed rocks, the transmitted and reflected wave amplitudes of each rock sample were compared and analyzed, as shown in Figure 14.

From Figure 14, it can be seen that the freeze-thaw action and the filling joint materials jointly affect the stress wave transmission and reflection law of the filled jointed rocks. Under the condition of the same filling material, the peak value of reflected wave increases with the increase of the freeze-thaw cycle times, while the peak value of the transmitted wave decreases. Under the condition that the freeze-thaw action is the same, the amplitude of reflected wave is negatively correlated with the strength of the filling materials, while that of transmitted wave is positively correlated with the material strength. This indicates that the filling materials and the freeze-thaw action have different effects on the transmitted and reflected mechanism of stress waves, which shows that the lower the strength of filling materials is and the more freeze-thaw cycle times are, the weaker the reflected ability of stress waves is and the stronger the transmitted ability is.

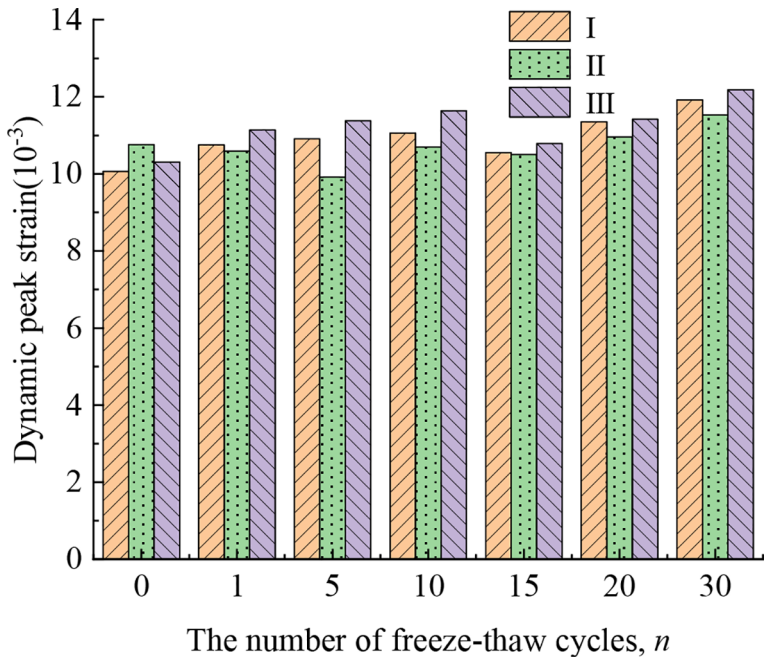

FIGURE 11
Dynamic peak strain histogram of jointed rock under freeze-thaw cycle.

3.6 Analysis of energy dissipation of dynamic impact damage

The impact process of filled jointed rocks is driven by external energy to complete the damage. According to the one-dimensional stress wave theory, the incident energy W_i, reflected energy W_r and transmitted energy W_t of the rock samples under each operating condition can be calculated from the cross-sectional area of the pressure bar A, the elastic modulus E, the stress wave velocity C_0 and the corresponding strain, expressed as:

$$W_{m|m=i,r,t} = A \cdot E \cdot C_0 \int_0^t \varepsilon_m^2 dt \tag{8}$$

where ε_m (m=i, r, t) are respectively the incident strain, reflected strain and transmitted strain, which can be directly calculated by the three-wave method when obtaining the dynamic stress-strain curve. The corresponding dissipation energy W_s can also be calculated according to the law of energy conservation:

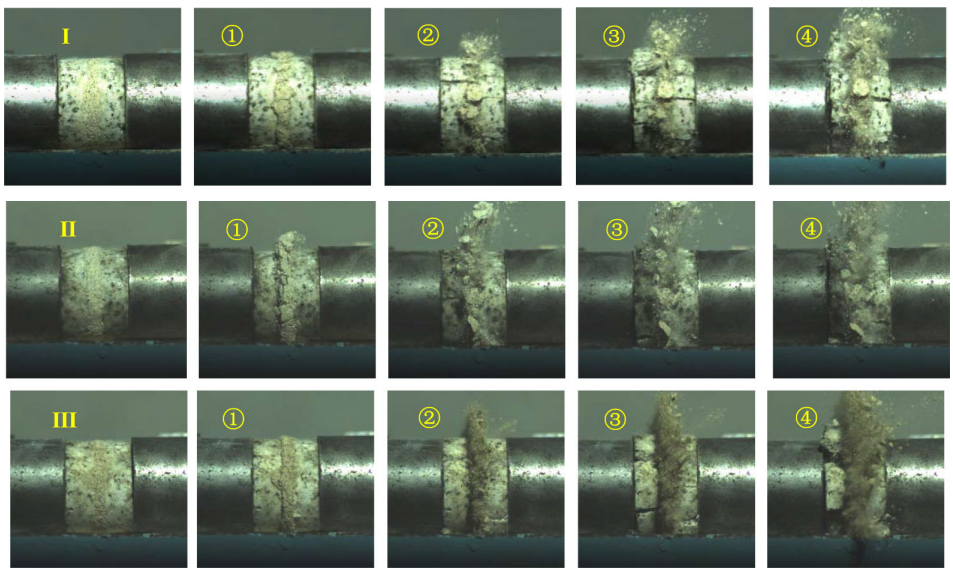

FIGURE 12
Failure patterns of three kinds of jointed rocks after 10 freeze-thaw cycles.

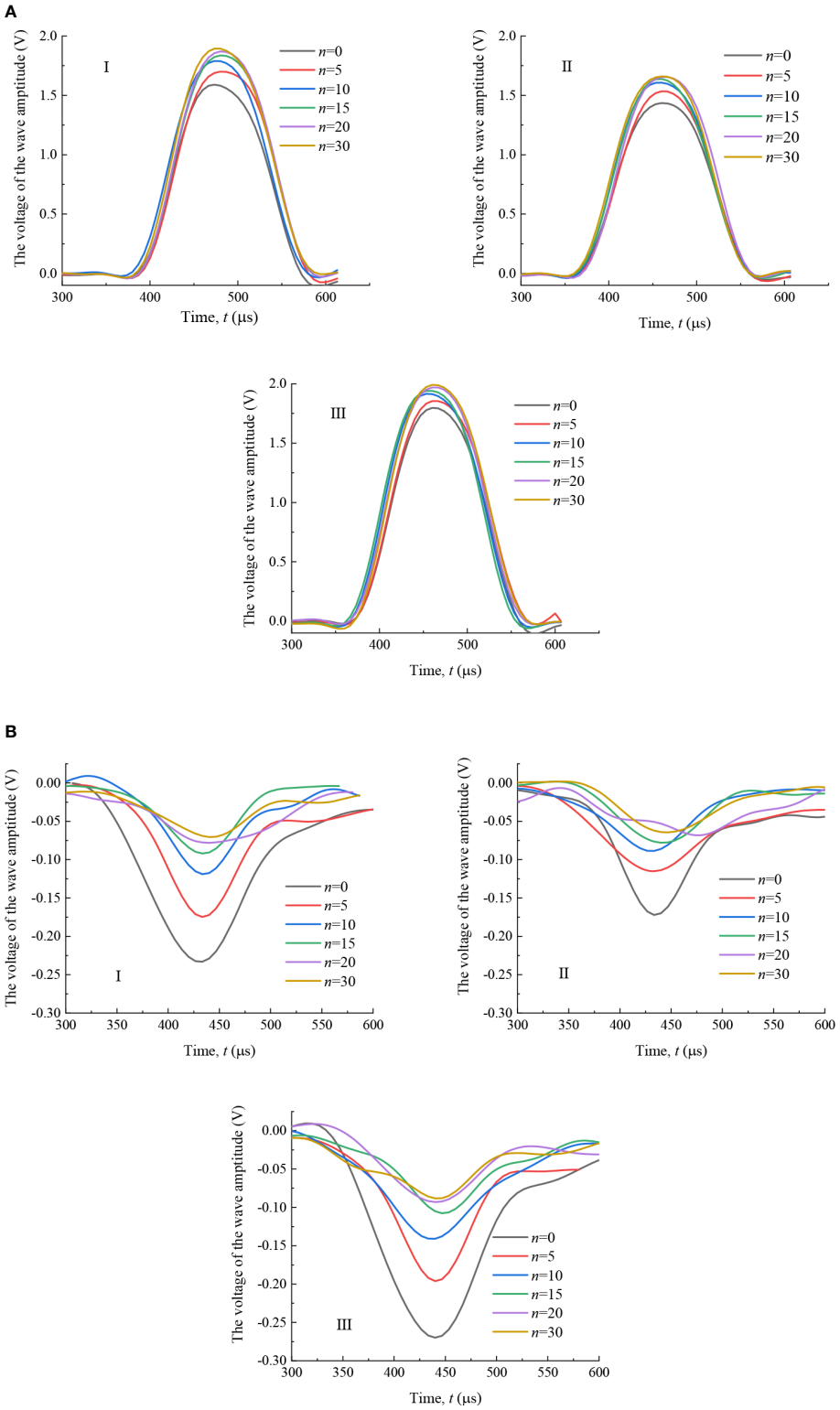

FIGURE 13
Reflection and transmission waveform curves of jointed rock under freeze-thaw cycle: **(A)** reflected wave; **(B)** transmitted wave.

$$W_s = W_i - W_r - W_t \quad (9)$$

Accordingly, the energy dissipation rate W_s/W_i can be used to analyze the energy dissipation regularity of the stress wave of the filled jointed rocks under the freeze-thaw action. The energy dissipation rate of different filling materials under different number of freeze-thaw cycles can be obtained from the calculation results, as shown in Figure 15.

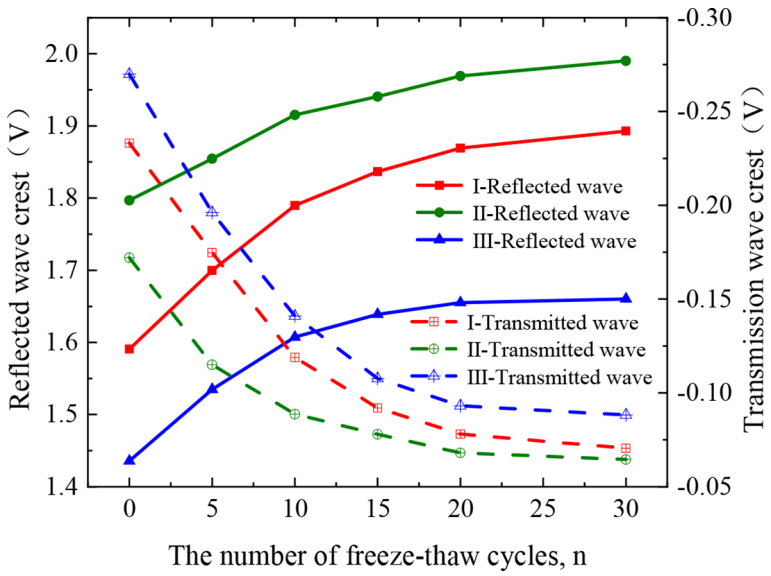

FIGURE 14
Transmission and reflection wave peaks of jointed rock under freeze-thaw cycle.

From Figure 15, it can be seen that the energy dissipation rate of rock samples is positively correlated with the strength of the filling materials, indicating that the stronger the filling material, the greater the energy consumed by the rock sample to undergo failure after undergoing the same freeze-thaw cycles. Considering the accumulated damage of each rock sample, it can be found that under the same freeze-thaw cycle times, the higher the strength of the filling layers is, the smaller the accumulated damage is and the larger the energy dissipation rate during impact damage is. This is mainly due to that the higher density of the filling layer with higher strength requires more energy for destruction. In addition, the energy dissipation rate of the same filled jointed rocks gradually decreases with the increase of freeze-thaw cycle times, and the rate of in energy dissipation rate decreases with the continuous effect of freeze-thaw action.

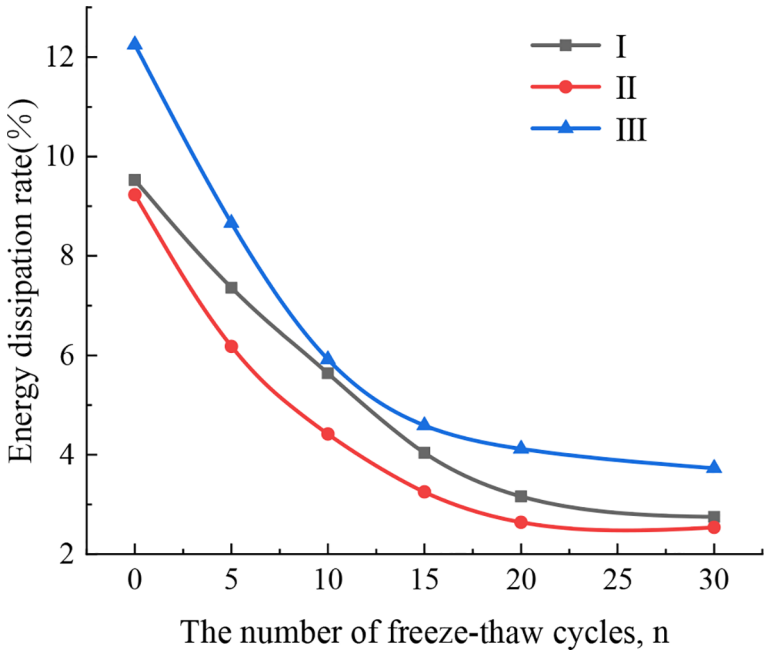

FIGURE 15
Energy dissipation rate of filled jointed rock under freeze-thaw cycle.

4 Conclusions

In this paper, the experimental study on the static and dynamic compression characteristics of filled jointed rock samples under different freeze-thaw cycles are carried out, and the corresponding failure characteristics are accordingly analyzed. The main conclusions are as follows:

(1) With the increase of freeze-thaw cycles, the wave velocity of the filled jointed rock deteriorates continuously. After 30 freeze-thaw cycles, the wave velocity of the jointed rock decreases by more than 30%, and the wave velocity of the rock mass with lower filling material strength decreases more. This indicates that the wave velocity value of the filled jointed rocks is positively correlated with the strength of the filling materials. The fitting formula of freeze-thaw cumulative damage evolution model is $D_n = \alpha - \beta\exp(-n/\gamma)$.

(2) The static and dynamic peak compressive strength of the filled jointed rock decrease continuously with the increase of freeze-thaw cycles, and the strength loss rate of the static peak compressive strength of the rock sample is greater than 50% after 30 freeze-thaw cycles, indicating that the freeze-thaw action has a significant impact on the strength deterioration of the filled jointed rocks, and the freeze-thaw damage has a continuous accumulation process. The dynamic and static peak compressive strengths of the jointed rock decrease with the decrease of the filling layer strength under the same number of freeze-thaw cycles.

(3) The static peak strain of the filled jointed rocks shows an obvious rising trend with the increase of freeze-thaw cycle times and is much larger than the dynamic peak strain in numerical value. The trend of dynamic peak strain change is not obvious, and the numerical range is 0.01 ~ 0.013. This is mainly due to the fact that dynamic impact belongs to high strain rate tests, the rock is compressed and destroyed in a very short time, and the impact process undergoes obvious splashing of broken rock debris. Therefore, the dynamic peak strain change law is complex and the value is small.

(4) Under freeze-thaw cycles, there is a damage accumulation threshold for the filled jointed rock samples, and the damage accumulation threshold for this filled jointed rock sample is 0.5. After reaching the threshold, the joint filling layer has been destroyed, and the damage deterioration is basically complete. The filling layer will lose its contribution to the subsequent freeze-thaw process of overall strength and deformation, and the strength and peak strain will be determined by the rocks on both sides.

(5) Under the same freeze-thaw condition, the peak value of reflected wave amplitude and energy dissipation rate increases with the increase of filling material strength. Under the same filling material condition, the peak value of reflected wave amplitude and energy dissipation rate decreases with the increase of freeze-thaw times.

Data availability statement

The original contributions presented in the study are included in the article/supplementary material. Further inquiries can be directed to the corresponding author.

Author contributions

All authors listed have made a substantial, direct, and intellectual contribution to the work and approved it for publication.

Funding

The work described in this paper was supported by the National Natural Science Foundation of China (No. 42172302 & No.41902277), the Natural Science Basic Research Plan in Shaanxi Province, (No. 2023-YBGY-085), Key Laboratory of Hydraulic and Waterway Engineering of the Ministry of Education, Chongqing Jiaotong University (SLK2021A04), and Fundamental Research Funds for the Central Universities, CHD (No. 300102282201), and for which the authors are very thankful.

Conflict of interest

The authors declare that the research was conducted in the absence of any commercial or financial relationships that could be construed as a potential conflict of interest.

Publisher's note

References

Bayram, F. (2012). Predicting mechanical strength loss of natural stones after freeze–thaw in cold regions. *Cold. Reg. Sci. Technol.* 83-84, 98–102. doi: 10.1016/j.coldregions.2012.07.003

Chai, S. B., Wang, H., Yu, L. Y., Shi, J. H., and Abi, E. (2020a). Experimental Study on Static and Dynamic Compression Mechanical Properties of Filled Rock Joints. *Lat. Am. J. Solids. Stru.* 17, 1–15. doi: 10.1590/1679-78255988

Chai, S. B., Wang, H., Jing, Y. L., and Jia, N. (2020b). Experimental study on dynamic compression characteristics of rock with filled joints after cumulative damage. *Chin. J. Rock Mech. Eng.* 39, 2025–2037. doi: 10.13722/j.cnki.jrme.2020.0310

Deng, H. W., Dong, C. F., Li, J. L., Zhou, K. P., Tian, W. G., and Zhang, J. (2014a). Experimental Study on Sandstone Freezing-Thawing Damage Properties under Condition of Water Chemistry. *Appl. Mech. Mater.* 3207, 556–562. doi: 10.4028/www.scientific.net/AMM.556-562.826

Deng, J. H., Wang, X. C., and Wu, A. J. (2014b). Experiment of Freezing-Thawing Cycles and Analysis of Damage Characteristics for Argillaceous Dolomite. *Adv. Mater. Res.* 1065-1069, 1884–1893. doi: 10.4028/www.scientific.net/AMR.1065-1069.1884

Deng, H. W., Yu, S. T., Deng, J. R., Ke, B., and Bin, F. (2019). Experimental Investigation on Energy Mechanism of Freezing-Thawing Treated Sandstone under Uniaxial Static Compression. *Ksce. J. Civ. Eng.* 23, 2074–2082. doi: 10.1007/s12205-019-1278-5

Fan, L. F., Xu, C., and Wu, Z. J. (2020). Effects of cyclic freezing and thawing on the mechanical behavior of dried and saturated sandstone. *B. Eng. Geol. Environ.* 79, 755–765. doi: 10.1007/s10064-019-01586-z

Huang, S. B., Liu, Q. S., Cheng, A. P., and Chen, Y. Z. (2018). A statistical damage constitutive model under freeze-thaw and loading for rock and its engineering application. *Cold. Reg. Sci. Technol.* 145, 142–150. doi: 10.1016/j.coldregions.2017.10.015

Huang, X. L., Qi, S. W., Williams, A., Zou, Y., and Zheng, Y. (2015). Numerical simulation of stress wave propagating through filled joints by particle model. *Int. J. Solids. Struct.* 69-70, 23–33. doi: 10.1016/j.ijsolstr.2015.06.012

Jia, S. L., Wang, Z. L., Wang, J. G., Lu, Z. T., and Wang, H. C. (2021). Experimental and theoretical study on the Propagation Characteristics of stress wave in Filled Jointed Rock Mass. *PloS One* 16, e0253392. doi: 10.1371/journal.pone.0253392

Jiang, H. B., Li, K. N., and Jin, J. (2019). The variation characteristics of micro-pore structures of underground rocks in cold regions subject to freezing and thawing cycles. *Arab. J. Geosci.* 13, 86–93. doi: 10.1007/s12517-019-4936-5

Li, J. L., Zhu, L. Y., Zhou, K. P., Chen, H., Gao, L., Lin, Y., et al. (2021a). Non-linear creep damage model of sandstone under freeze-thaw cycle. *J. Cent. South. Univ.* 28, 954–967. doi: 10.1007/s11771-021-4656-3

Li, Y., Cheng, X. W., Ma, Z. L., Li, X. H., and Wang, M. (2021b). Dynamic response and damage evolution of Zr-based bulk metallic glass under shock loading. *J. Mater. Sci. Technol.* 93, 119–127. doi: 10.1016/j.jmst.2021.03.052

Li, J. C., Li, H. B., Jiao, Y. Y., Liu, Y. Q., Xia, X., and Yu, C. (2014). Analysis for oblique wave propagation across filled joints based on thin-layer interface model. *J. Appl. Geophys.* 102, 39–46. doi: 10.1016/j.jappgeo.2013.11.014

Li, J. C., and Ma, G. W. (2009). Experimental study of stress wave propagation across a filled rock joint. *Int. J. Rock Mech. Min. Sci.* 46, 471–478. doi: 10.1016/j.ijrmms.2008.11.006

Li, B., Zhang, G. H., Ma, W., Liu, M. H., and Li, A. Y. (2022). Damage mechanism of sandstones subject to cyclic freeze-thaw (FT) actions based on high-resolution computed tomography (CT). *B. Eng. Geol. Environ.* 81, 374. doi: 10.1007/s10064-022-02872-z

Li, J. L., Zhou, K. P., Liu, W. J., and Deng, H. W. (2017). NMR research on deterioration characteristics of microscopic structure of sandstones in freeze–thaw cycles. *Trans. Nonferrous Metals Soc China.* 26, 2997–3003. doi: 10.1016/S1003-6326(16)64430-8

Liu, T. T., Li, X. P., Li, J. C., Li, H. B., Zheng, Y., and Luo, Y. (2017). Numerical study on s-wave transmission across a rough, filled discontinuity. *Arab. J. Geosci.* 10, 249. doi: 10.1007/s12517-017-3030-0

Liu, G. J., Peng, Y. X., Zuo, Q. J., Su, Y., and Wu, L. (2022). Comparative study on tunnel blast-induced vibration for the underground cavern group. *Minerals.* 12, 1246. doi: 10.3390/min12101246

Liu, S. M., Sun, H. T., Zhang, D. M., Yang, K., Wang, D. K., Li, X. L., et al. (2023). Nuclear magnetic resonance study on the influence of liquid nitrogen cold soaking on the pore structure of different coals. *Phys. Fluids.* 35, 012009. doi: 10.1063/5.0135290

Lu, Y. N., Li, X. P., and Chan, A. (2019). Damage constitutive model of single flaw sandstone under freeze-thaw and load. *Cold. Reg. Sci. Technol.* 159, 20–28. doi: 10.1016/j.coldregions.2018.11.017

Matsuoka, N. (1990). Mechanisms of rock breakdown by frost action: An experimental approach. *Cold. Reg. Sci. Technol.* 17, 253–270. doi: 10.1016/S0165-232X(05)80005-9

Mousavi, S. Z. S., Tavakoli, H., Moarefvand, P., and Rezaei, M. (2020). Micro-structural, petro-graphical and mechanical studies of schist rocks under the freezing-thawing cycles. *Cold. Reg. Sci. Technol.* 174, 103039. doi: 10.1016/j.coldregions.2020.103039

Nicholson, D. T., and Nicholson, F. H. (2000). Physical deterioration of sedimentary rocks subjected to experimental freeze–thaw weathering. *Earth Surf. Process. Landf.* 25, 1295–1307. doi: 10.1002/1096-9837(200011)25:12<1295::AID-ESP138>3.0.CO;2-E

Qiao, C., Wang, Y., Tong, Y. J., Yang, H. P., Li, C. H., and Qian, C. (2021). Deterioration Characteristics of Pre-flawed Granites Subjected to Freeze-Thaw Cycles and Compression. *Geotech. Geol. Eng.* 39, 5907–5916. doi: 10.1007/s10706-021-01904-x

Singh, M., Rao, K. S., and Ramamurthy, T. (2002). Strength and Deformational Behaviour of a Jointed Rock Mass. *Rock Mech. Rock Eng.* 35, 45–64. doi: 10.1007/s006030200008

Su, Q. Q., Ma, Q. Y., Ma., D. D., and Yuan, P. (2021). Dynamic mechanical characteristic and fracture evolution mechanism of deep roadway sandstone containing weakly filled joints with various angles. *Int. J. Rock Mechanics Min. Sci.* 137, 104552. doi: 10.1016/j.ijrmms.2020.104552

Tan, X. J., Chen, W. Z., Yang, J. P., and Gao, J. J. (2011). Laboratory investigations on the mechanical properties degradation of granite under freeze–thaw cycles. *Cold. Reg. Sci. Technol.* 68, 130–138. doi: 10.1016/j.coldregions.2011.05.007

Wang, Y., Han, J. Q., and Li, C. H. (2020). Acoustic emission and CT investigation on fracture evolution of granite containing two flaws subjected to freeze–thaw and cyclic uniaxial increasing-amplitude loading conditions. *Constr. Build. Mater.* 260, 119769. doi: 10.1016/j.conbuildmat.2020.119769

Wang, P., Xu, J. Y., Liu, S., Liu, S. H., and Wang, H. Y. (2016a). A prediction model for the dynamic mechanical degradation of sedimentary rock after a long-term freeze-thaw weathering: Considering the strain-rate effect. *Cold. Reg. Sci. Technol.* 131, 16–23. doi: 10.1016/j.coldregions.2016.08.003

Wang, P., Xu, J. Y., Liu, S., Wang, H. Y., and Liu, S. H. (2016b). Static and dynamic mechanical properties of sedimentary rock after freeze-thaw or thermal shock weathering. *Eng. Geol.* 210, 148–157. doi: 10.1016/j.enggeo.2016.06.017

Xu, G. M. (2006). *Study on mechanical charateristics of rock at low temperature, damage due to freezing and thawing and mutiphysical coupling problems of rock in cold regions* (Wuhan, China: Chinese Academy of Science).

Yang, C., Zhou, K. P., Xiong, X., Deng, H. W., and Pan, Z. (2021). Experimental investigation on rock mechanical properties and infrared radiation characteristics with freeze-thaw cycle treatment. *Cold. Reg. Sci. Technol.* 183, 103232. doi: 10.1016/j.coldregions.2021.103232

Yi, L. C., Qu, D. X., Gang, W., Li, X. P., and Zhang, G. (2020). Degradation model of the dynamic mechanical properties and damage failure law of sandstone under freeze-thaw action. *Soil. Dyn. Earthq. Eng.* 132, 106094. doi: 10.1016/j.soildyn.2020.106094

Zhang, J. F., Xu, R. P., Liu, Y., and Zhang, H. M. (2022). Study on micro-pore evolution law and shear mechanical behavior of grouting fractured rock mass under freeze-thaw cycle. *Chin. J. Rock Mech. Eng.* 41, 676–690. doi: 10.13722/j.cnki.jrme.2021.0568

Zhang, H. M., and Yang, G. S. (2010). Research on damage model of rock under coupling action of freeze-thaw and load. *Chin. J. Rock Mech. Eng.* 29, 471–476. Available at: http://rockmech.whrsm.ac.cn/EN/abstract/abstract19977.shtml.

Zhao, S. P., Feng, Z. D., Li, L. X., Zhao, X. J., Lu, L., Chen, S., et al. (2022). Dynamic mechanical properties, deformation and damage mechanisms of eutectic high-entropy alloy AlCoCrFeNi2.1 under plate impact. *J. Mater. Sci. Technol.* 134, 178–188. doi: 10.1016/j.jmst.2022.05.060

Zhou, Z. L., Cai, X., Ma, D., Chen, L., Wang, S. F., and Tan, L. H. (2018). Dynamic tensile properties of sandstone subjected to wetting and drying cycles. *Construction And Building Materials* 182, 215–232. doi: 10.1016/j.conbuildmat.2018.06.056

Zhou, K. P., Li, B., Li, J. L., Deng, H. W., and Bin, F. (2015). Microscopic damage and dynamic mechanical properties of rock under freeze–thaw environment. *Trans. Nonferrous Metals Soc China* 25, 1254–1261. doi: 10.1016/S1003-6326(15)63723-2

frontiers | Frontiers in Earth Science

TYPE Original Research
PUBLISHED 25 July 2023
DOI 10.3389/feart.2023.1221404

OPEN ACCESS

EDITED BY
Xuelong Li,
Shandong University of Science and Technology, China

REVIEWED BY
Dan Ma,
China University of Mining and Technology, China
Geng Jiabo,
Jiangxi University of Science and Technology, China

*CORRESPONDENCE
Huafen Sun,
154221644@qq.com

RECEIVED 12 May 2023
ACCEPTED 07 July 2023
PUBLISHED 25 July 2023

CITATION
Niu X, Sun H and Hou K (2023), Uniform thickness in the process of ore-mixed characteristics of particles passing through experimental research. *Front. Earth Sci.* 11:1221404. doi: 10.3389/feart.2023.1221404

Uniform thickness in the process of ore-mixed characteristics of particles passing through experimental research

Xiangdong Niu[1,2], Huafen Sun[1,2]* and Kepeng Hou[1,2]

[1]Faculty of Land and Resources Engineering, Kunming University of Science and Technology, Kunming, China, [2]Yunnan Key Laboratory of Sino-German Blue Mining and Utilization of Special Underground Space, Kunming, China

The nature of fine particulate matter is caused by the deterioration of the lean ore loss index and the important influence factors of a mine disaster accident. In this paper, fine moraine particles and coarse-grained ore from the Pulang Copper Mine are studied. The flow of fine particles in mixed particles under the condition of uniform ore drawing was studied by using the laboratory 3D physical model test method. This experiment explored the flow of hybrid particles in the system and characteristics of the particle size of fine particles passing through, and suggested a transit index to quantify the draining effect of fine particles. The experimental results show the following: ①Hybrid particles in the flow system of fine particulate matter under their own gravity use mixed ore particles flow in the process of formation of the pore to implement down through sports. ②The fine particles with the particle sizes of 2.5–1.25 mm, 1.25–0.63 mm, 0.63–0.315 mm, and 0.315–0.16 mm all have the flow-through characteristics, and the smaller the particle size, the more significant the flow-through degree. ③The cumulative ore drawing height of fine particles with different particle sizes increases, while the permeability index of the appropriate discharge decreases. ④The relative motion of coarse and fine particles is the internal control factor that leads to the flow of fine particles. The more significant the relative motion of coarse and finely mixed particles is, the more pores are randomly generated in the particle flow system and the larger the pores are, resulting in the more obvious fine particle flow effect. This study provides some theoretical reference value for revealing the flow-through characteristics of the fine particulate matter in the mixed particle flow system. At the same time, it has practical engineering significance for ore lean loss index control and mine disaster accident prevention and control in caving mining.

KEYWORDS

uniform ore drawing, mixed particle flow, cross-flow characteristics, quantification method, physical model test

1 Introduction

Mixed particles refer to particle aggregates composed of two-phase or multi-phase particles, and are randomly and disorderly arranged in the particle flow system (Li et al., 2021; Rong et al., 2021; Xing et al., 2022; Xu et al., 2022). The phenomenon of flow-through of mixed particles widely exists in nature and industries. It not only occupies an important position in metallurgy, ceramics, powder, and other industries (Ma et al., 2020; Ma et al., 2022; Ma et al., 2023) but also has extremely important significance in the study of mine disaster accidents and ore loss control.

In the caving method, mines in some special areas have the surface covering layer composed of fine granular material. During the mine production process, the fine particles of the surface covering layer are continuously mixed into the caving ore layer to form a two-phase or multi-phase mixed particle flow system (Huang et al., 2020; Niu et al., 2020; Zhang et al., 2023). In mines that switch from open-pit to underground mining, a particulate material covering layer is often formed on the isolation pillar to form a buffer cushion. During the production process, the covering layer particulate material will also be mixed into the ore at the ore–rock interface to form a mixed particle flow system (Zhang and Cheng, 2017; Lu et al., 2021; Zhang and Gao, 2021; Li et al., 2023). The flow characteristics of the fine particles of the overburden layer in the caving ore directly affect the ore loss and dilution index, and even cause the underground debris flow disaster, which belong to the research category of mixed particles.

At present, scholars at home and abroad have paid attention to the related research on the mixed particle flow. Scholars in different research fields have carried out related research on this issue using indoor physical experiments and numerical simulation methods. Pierce et al. (1994) and Pierce et al. (2019) studied the phenomenon of small particle permeation in the ore-drawing process by the numerical simulation method. When the ore drawing is disturbed, the small particles will flow through the pores between the large particles. Hashim (2011) used Kvapil A's physical model to study the effects of particle shape, particle size, density of states, and other factors on the particle flow. Ketterhagen et al. (2008) studied the flow-through behavior of coarse and fine particles under the action of gravity, and carried out quasi-3D model simulation-related research from factors such as particle material parameters, particle contact coefficients, and particle construction methods in the model. Based on the non-Newtonian fluid theory, Christopher (2009) studied the relationship between displacement and velocity of a fine-grained medium flowing through the ore drawing process from the perspective of theoretical mechanics. Li et al. (2016) used discrete element software to discuss the seepage law of fine particles during the overburden of waste rock during the ore-drawing process. The results show that the seepage rate of fine particles is higher than that of coarse particles. Hou et al. (2016) used indoor ore-drawing experiments to explore the flow rule of fine particles and found that the flow phenomenon of fine particles was obvious during the ore-drawing process. Jin et al. (2020) studied the flow characteristics of particles with uneven particle size distribution, and the results showed that particle inhomogeneity has a significant effect on the flow-through of fine particles. Ren et al. (2020) used high-speed camera technology to study the flow characteristics of tailings in the collapse area under the condition of ore drawing. By constructing the spatial distribution model of the particle size of overburden, the influence of rock mixing is studied by You and Zhang (2016). The downward motion of the particle is faster than that of the larger particles. Li (2020) simulated the "Cross-flow" phenomenon of fine particles in the ore-drawing process by numerical simulation software. The simulation results show that the larger the overburden block, the more obvious the fine particle migration. The application of 60 cm–80 cm waste rock overburden can effectively slow down the flow of fine particles in the ore-drawing process. Wang et al. (2019) used PFC3D discrete element software to investigate fine particle migration in the backfill. The results show that fine particle migration is more likely to occur in the 30 cm–70 cm block backfill during ore drawing. The fragmentation of overburden and backfill has a significant effect on fine particle migration, and the effect of the overburden bulk is highly significant.

Although scholars at home and abroad have achieved certain research results on the flow-through characteristics of mixed particles, most of them use numerical simulation methods, and most of the physical models are limited to the two-dimensional single-bucket ore-drawing model, which cannot fully reflect the flow-through of real particles. In addition, although scholars at home and abroad have studied the flow-through of fine particles, but also a consistent conclusion, that is, fine particles in the ore-drawing process, there are certain cross-flow phenomena. However, what is the extent of fine particles flowing through the ore during ore drawing? What is the amount of fine particles passing through? What indicators are used to measure the degree of penetration of fine particles? The problems raised by the aforementioned authors have not been studied in-depth. Therefore, in view of the deficiency of the research methods on the fine particle flow-through characteristics and the unstudied problems on the fine particle flow-through characteristics at present, this paper conducts a deep research on the fine particle flow-through characteristics. In this paper, using the indoor three-dimensional physical model test method, taking the fine-grained moraine and coarse-grained ores of various particle sizes in the surface overburden of the Pulang Copper Mine as the research object, the experimental study on the flow-through characteristics of mixed particles under the condition of multi-bucket uniform ore drawing was carried out. The characteristics and laws of the flow of fine particles of each size in the coarse and finely mixed particle flow systems were explored.

2 Indoor physical experiment model

2.1 Engineering background introduction

The Plan Copper Mine, which belongs to Yunnan Diqing Non-ferrous Metal Co., Ltd., is a thick, large and low-grade porphyry copper deposit. The mine uses natural caving and has an annual production capacity of 12.5 million tons. Figure 1 shows that the height of the bottom structure is 16 m, the spacing of the ore-drawing and vein-crossing roadways is 30 m, the spacing of the ore-drawing route is 15 m, and the size of the ore-drawing exit (width × height) is 4.2 m × 4.2 m. In order to avoid the moraine particles from the Quaternary system mixing into the caving ore bed prematurely, a uniform ore-drawing management model is adopted in the production process. The average thickness of the ore bed overlying the bottom structure of the mine is about 80 m, and the average thickness of quaternary moraine is about 15 m. The indoor 3D physical model was designed and fabricated using a 1:100 similarity ratio.

2.2 Overview of the experimental model

In order to facilitate the observation of the flow characteristics of fine moraine particles in the mixed particle flow system during the test, the test device uses a transparent acrylic sheet material. The indoor 3D physical model test device mainly includes an acrylic plate frame, a bottom structure, and camera system, as shown in Figure 2. The size of the ore-drawing test model is 75 cm × 45 cm × 150 cm (length x width x height). The bottom structure of the model

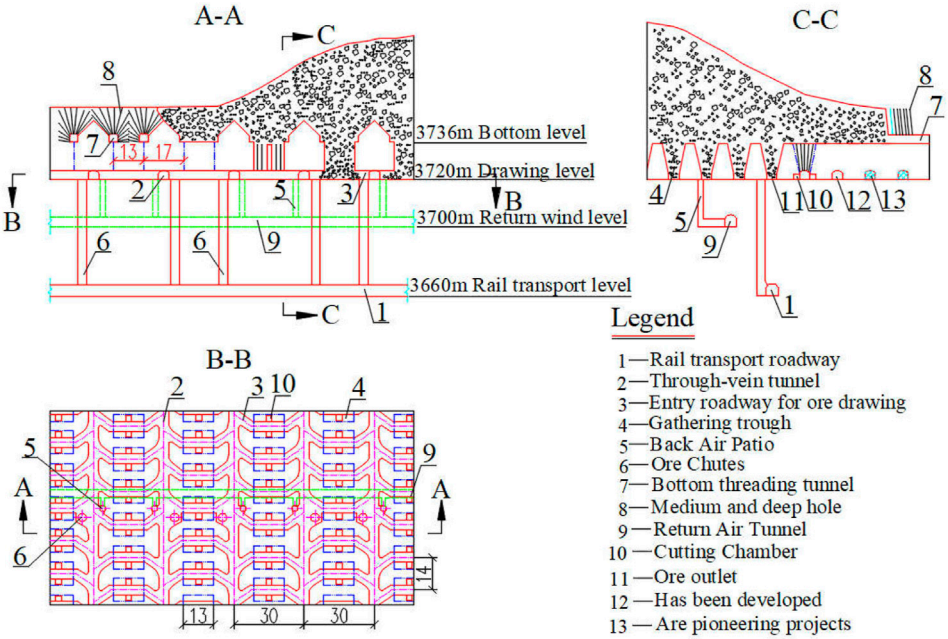

FIGURE 1
Mining method map of the Plan Copper Mine (unit: m).

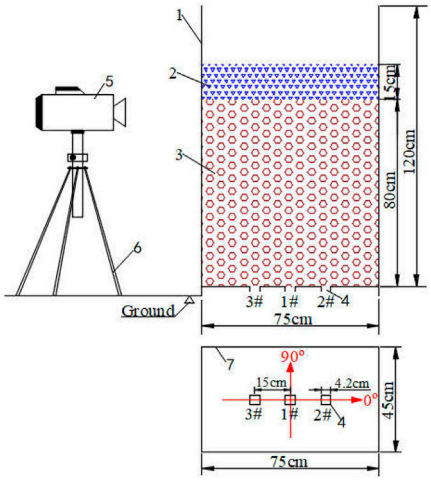

1-Transparent test device, 2-Fine grain moraine, 3-Coarse grain ore,
Mine drawing port, 5-High-speed camera, 6-Camera bracket, 7-Bottom structure

FIGURE 2
Design of the indoor 3D physical model test device.

is arranged with three ore-drawing ports (1#, 2#, and 3#), and the size of the ore-drawing port is 4.2 cm × 4.2 cm.

2.3 Test granular media

The Pulang Copper Mine is mined by the natural caving method, and the caving ore is drawn under the Quaternary moraine particle covering layer on the surface. During the mine production process, the fine moraine particles in the surface covering layer are continuously mixed into the caving ore layer, and a two-phase or multi-phase mixed particle flow system has been formed. Therefore, the coarse- and fine-grained media (fine-grained moraine and coarse-grained ores) used in this experiment are all obtained from the sampling material at the Pulang Copper Mine site. Photographs of field sampling are shown in Figure 3.

The particulate medium used in the test was obtained by sieving the sampled particulate matter with a standard sieve (implementation standard JGJ52-2006). Table 1; Figure 4 show the gradation of the experimental coarse and finely mixed particle media. The characteristic particle size parameters of the coarse and fine granular media are shown in Table 2. From the analysis of Table 2, it can be seen that the coefficient Cu=18.75 > 5 of the coarse and fine particles is uneven, and the curvature coefficient Cc=6.16 ∉(1,3) is discontinuous. It shows that the particles after highly discrete particles mixing belong to coarse and fine. In addition, fine moraine is easy to fill in the pores formed by the coarse ore. The mixture particles selected in the experiment can realize the cross-flow behavior.

In addition, the natural angle of repose and the Water Content Index of the mixed particles used in the experiment have an important effect on the cross-flow of fine particles. The natural resting angle is the maximum angle at which the bulk can keep the natural stable state when stacked. The average natural resting angle of the mixture particles was 36°. The average moisture content of the mixture particles was 5%.

2.4 Experiment process

The ore-drawing process of the test is carried out in sequence according to the 1#→2#→3# ore-drawing openings. Until the mixed

FIGURE 3
Site sampling photographs of the Pulang Copper Mine.

TABLE 1 Statistical table of particle size and the mass ratio of experimentally mixed granular media.

Coarse particle size/mm	Mass ratio of the coarse particle size	Fine particle size/mm	Mass ratio of the fine particle size (%)
20 ~ 16	15%	5 ~ 2.5	5
16 ~ 10	25%	2.5 ~ 1.25	5
10 ~ 5	35%	1.25 ~ 0.63	5
—	—	0.63 ~ 0.315	5
—	—	0.315 ~ 0.16	5

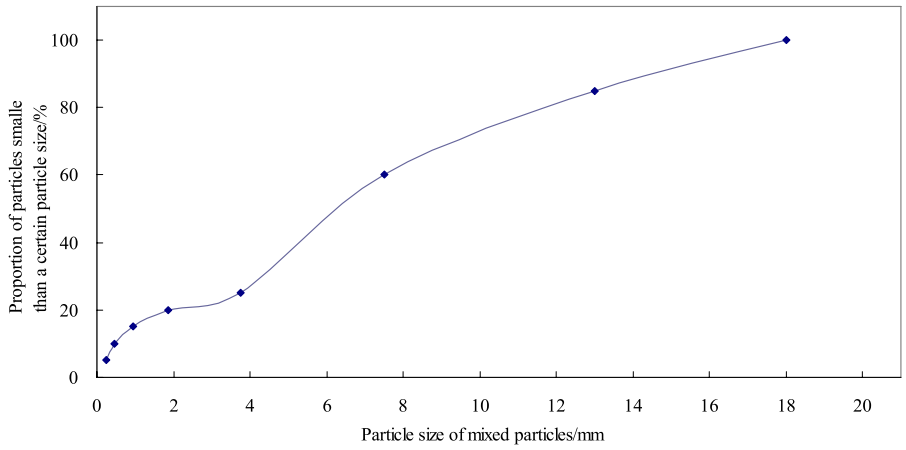

FIGURE 4
Test coarse and finely mixed particle gradation curve.

TABLE 2 Parameter table of characteristic particle size of coarse and fine granular media.

Characteristic particle size/mm				Particle characteristic index	
Controlling particle size d_{60}	Average grain diameter d_{50}	d_{30}	Effective grain size d_{10}	Uneven coefficient Cu	Curvature coefficient Cc
7.5	6.2	4.3	0.4	18.75	6.16

$Cu=d_{60}/d_{10}$, where $Cu<5$ represents uniform particles; $Cc=d_{30}^2/(d_{60}*d_{10})$; and $1<Cc<3$ is graded continuously.

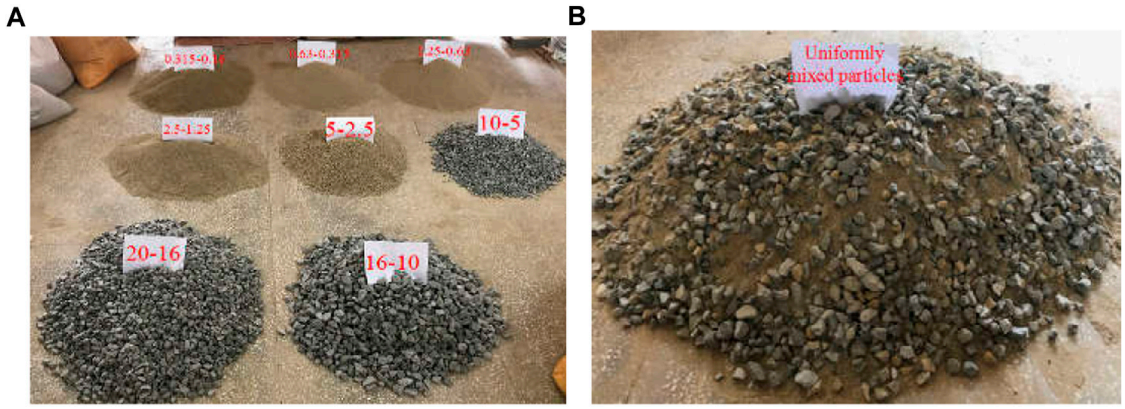

FIGURE 5
Fine-grained moraine and coarse-grained ore test media. **(A)** Test particle media with different particle sizes after sieving. **(B)** Homogeneous mixing of test particles.

granular medium in the model device is completely discharged, the discharge amount of each ore-drawing port remains basically the same so as to achieve a simulated uniform ore-drawing environment. The specific test process is as follows:

①A standard sieve is used to screen the sampled particulate matter. Figure 5A shows fine moraine and coarse ore with different particle sizes after screening.

②Proportion in accordance with the mass ratio of particles with different particle sizes is shown in Table 1. Moreover, fully and uniformly proportioned particles are mixed. The uniformly mixed particles are shown in Figure 5B.

③The coarse and finely mixed particles were loaded into the physical test model by the central quadrant method (Penfound, 1963; Raj and Thakur, 2016). In the filling process of mixed particles, in order to ensure the uniformity of mixed particles in each filling, a multiple-loading method is adopted. In the model test, the loading height of the mixed particles was 80 cm. The test model of the mixed particles after loading is shown in Figure 6.

④After the aforementioned test steps are completed, the ore-drawing stage begins. Then, 2# and 3# ore-drawing ports are closed, and 1# ore-drawing port and drawing ore are opened. When ore drawing at No.1 ore-drawing hole is finished, the discharged particulate matter shall be screened immediately, the screened particulate matter with different particle sizes shall be weighed, and the quality of each particle size discharged at this time shall be recorded.

⑤Then, 1# and 3# ore-drawing ports are closed, and 2# ore drawing port and draw ore are opened. When ore drawing at No.1 ore-drawing hole is finished, the discharged particulate matter shall be screened immediately, the screened particulate matter with different particle sizes shall be weighed, and the quality of each particle size discharged at this time shall be recorded.

⑥Thereafter, 1# and 2# ore-drawing ports are closed, and 3# ore-drawing port and draw ore are opened. When ore drawing at No.1 ore-drawing hole is finished, the discharged particulate matter shall be screened immediately, the screened particulate matter with different particle sizes shall be weighed, and the quality of each particle size discharged at this time shall be recorded.

FIGURE 6
Packed mixed particle test model.

⑦Then, 1#→2#→3# ore-drawing hole is called an ore-drawing cycle when all ore-drawing holes are finished once. Steps ④ ~ ⑥ are repeated until all the particles in the physical test model are released. Four cycles of ore drawing were carried out in the whole experiment.

2.5 Physical test hypothesis

During the uniform ore-drawing test, the movement of the moraine and ore particles is extremely complicated. In order to avoid the influence of other factors on the test results during the model test ore drawing, this experiment explains some possible influencing factors and makes the following assumptions: ①In order to ensure that the test particle medium has good fluidity, the moraine and ore particles used in the test have been air-dried and there is no cohesion between the particles. ②Due to the high strength of ore particles, the effect of secondary crushing is ignored in the process of uniform ore drawing. ③The cent quartering method is adopted to load the test particles in different times, and the flow of fine particles did not occur during the filling process, ignoring the influence of artificial filling.

3 Analysis of test results

3.1 Method for quantifying the effect of cross-flow

After each release of the coarse and finely mixed particles, immediately a standard sieve is used to sieve the released mixed particles, and weigh them, respectively, to obtain the mass of the coarse and fine particles released at that time. There is a slight difference in the amount released each time. The "Normalization Method" of formula (1) is used to process the test data to obtain the mass ratio of the coarse and fine particles released in the current time (Xu and Li, 2020; Wang et al., 2023).

$$\alpha = m_i / \sum m_i \times 100\%. \quad (1)$$

Formula: α—mass ratio of the coarse particles or fine particles released each time;
m_i—mass of coarse particles or fine particles released each time;
$\sum m_i$—sum of the mass of coarse particles and fine particles released each time.

In order to compare the flow-through effect of fine particles with different sizes more intuitively, a preliminary quantification method for the flow-through characteristics of fine particles with different sizes in the process of ore drawing is proposed. To quantify the significant degree of permeation of fine particles of each particle size by the permeation flow, the permeation degree is expressed as follows:

$$\gamma = \frac{\alpha}{\beta}. \quad (2)$$

Formula: γ—permeability of fine particles of a certain size;
α—percentage of fine particles with this particle size in the current discharge;
β—percentage of particles with this particle size in the mixed particles before ore drawing.

FIGURE 7
Whole test process of four ore-drawing cycles.

The degree of flow through can quantify the significant degree of flow through of the fine particles of each size in the mixed particles. The larger the value of flow-through, the more obvious the flow of fine particles. When the permeation degree $\gamma > 1$, it means that the fine particles have permeated in the pores of the mixed particles during the ore-drawing process. The fine particles migrate downward in preference to other particles, and as the ore-drawing time continues, the concentration of the fine particles becomes greater.

3.2 Characteristics and laws of cross-flow

The cycle of ore-drawing ore in sequence according to the 1#→2#→3# ore-drawing opening is called an ore-drawing

TABLE 3 Current discharge flow-through of the fine particles of each particle size in the mixed particles.

Number of ore-drawing times	Number of ore-drawing holes	Ore-drawing height	Permeability of fine particles of each particle size				
			5–2.5 mm	2.5–1.25 mm	1.25–0.63 mm	0.63–0.315 mm	0.315–0.16 mm
1	1#	10	0.77	0.96	1.14	1.30	1.72
2	2#	15	0.88	1.12	1.32	1.52	1.90
3	3#	20	0.99	1.25	1.54	1.77	2.18
4	1#	25	0.87	1.14	1.40	1.72	2.14
5	2#	30	0.97	1.28	1.56	1.92	2.37
6	3#	35	1.11	1.40	1.66	1.95	2.39
7	1#	40	0.69	0.90	1.14	1.36	1.61
8	2#	45	0.86	1.02	1.30	1.55	1.84
9	3#	50	1.17	1.36	1.61	1.81	2.00
10	1#	55	1.30	1.13	0.93	0.81	0.76
11	2#	60	1.69	1.49	1.28	1.16	0.95
12	3#	65	1.46	1.27	1.11	0.94	0.81

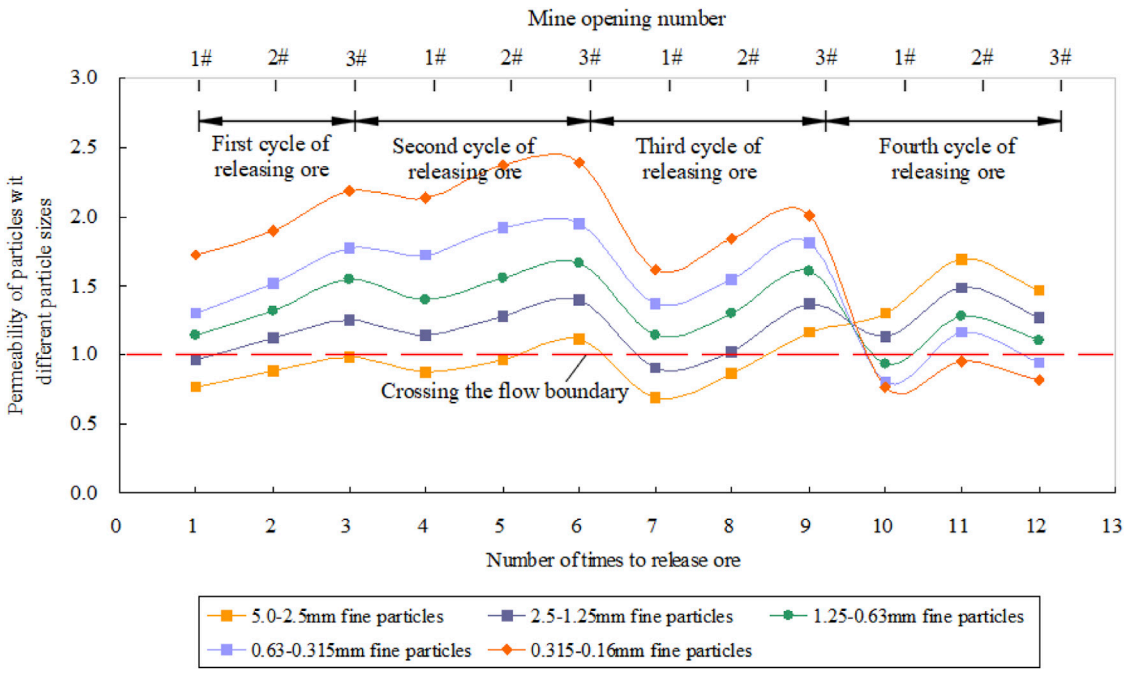

FIGURE 8
Relationship between the current penetration of fine particles of each particle size and the number of ore drawings.

cycle. A total of four ore-drawing cycles were carried out in the whole test process, as shown in Figure 7. Table 3 shows the current release flow-through of the fine particles of each particle size in the mixed particles. Figure 8 shows the relationship between the current discharge flow rate of fine particles of each particle size and the number of times of ore drawing.

Analysis of Figure 8 shows that the current penetration of fine particles of 5.0–2.5 mm in the first to the third ore-drawing cycles fluctuates around the boundary line 1 of the penetration. It is basically below the flow boundary 1, and its flow degree is less than 1. It shows that 5.0–2.5 mm fine particles do not have flow-through characteristics in the pores of 5–20 mm coarse-grained medium. For fine particles of 2.5–1.25 mm,

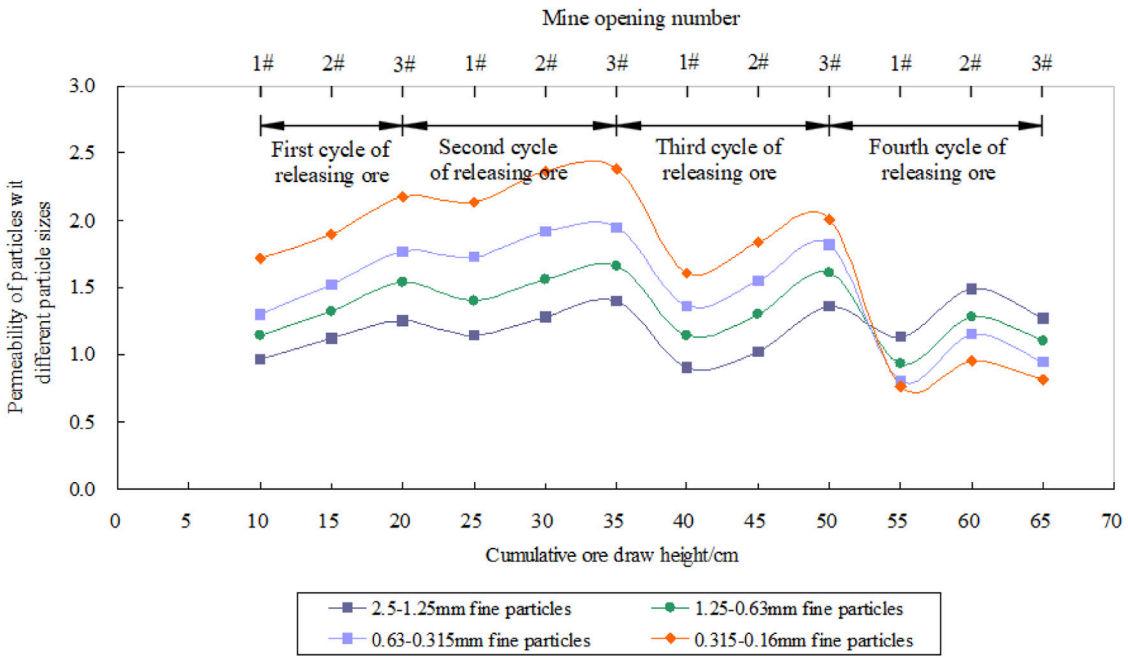

FIGURE 9
Relationship between the current penetration value of the fine particles of each particle size and the cumulative drawing height.

1.25–0.63 mm, 0.63–0.315 mm, and 0.315–0.16 mm, the current penetration values of the first ore-drawing cycle to the third ore-drawing cycle are basically at the penetrating boundary line 1 above. It shows that it has the characteristics of flow-through, and the smaller the particle size of fine particles, the larger the index of flow-through and the more obvious is the degree of flow-through.

Figure 8 also shows that 2.5–1.25 mm, 1.25–0.63 mm, 0.63–0.315 mm, and 0.315–0.16 mm are fine particles with flow-through characteristics. During the flow process of each particle size, fine particles from the first ore-drawing cycle to the third ore-drawing cycle; with the increase of the times of ore-drawing cycles, the value of cross-flow increases first and then decreases. In the fourth ore- drawing cycle, with the continuous release of the medium and fine particles in the coarse particles, the fine particles are continuously reduced and there is no continuous replenishment, resulting in a continuous increase in the amount of released coarse particles. Therefore, there is a phenomenon that when the medium with coarse particles is released, the permeability value is larger than that of fine particles.

According to the characteristics and rules of the flow of fine-grained media with different particle sizes in Figure 8, the four ore-drawing cycle test processes for uniform ore drawing are divided into the following four stages: the first ore-drawing cycle is the downward flow stage of fine particles, the second ore-drawing cycle is the fine particle flow and convergence stage, the third ore-drawing cycle is the continuous flow stage of fine particles, and the fourth ore-drawing cycle is the coarse particles' late release stage.

3.3 Effect of ore-drawing height on fine particle cross-flow

Figure 9 shows the relationship between the current penetration value and the cumulative drawing height of fine particles of 2.5–1.25 mm, 1.25–0.63 mm, 0.63–0.315 mm, and 0.315–0.16 mm. It can be seen that during the flow of fine particles from the first ore-drawing cycle to the third-ore drawing cycle, the current discharge flow rate of each particle size and fine particle increases first and then decreases with the cumulative ore-drawing height changing trend. Among them, in the second ore-drawing cycle, the value of permeation is the largest and the phenomenon of permeation is the most obvious.

Before ore drawing, the coarse and fine particles in the test model are distributed uniformly in theory. With the continuous ore drawing, the cumulative height of ore drawing increases gradually. The test model of the mixture of coarse and fine particles was continuously released during the process. At first, the fine particles flew down the pores of the coarse particles, which makes the fine particles move before the bottom of the coarse particles model and converge continuously, and finally release from the ore-drawing mouth. As a result, during the first and second ore-drawing cycles, the permeability of fine particles increases with the ore-drawing height. When the third and fourth ore-drawing cycles were reached, the fine particles in the upper part of the test model were gradually reduced and no fine particles in the upper part of the test model were continuously replenished. The permeability of fine particles decreases with the increase in the ore-drawing height. The process of the aforementioned analysis is the explanation of the mechanism that the penetrability of fine particles first increases and then decreases with the cumulative ore-drawing height.

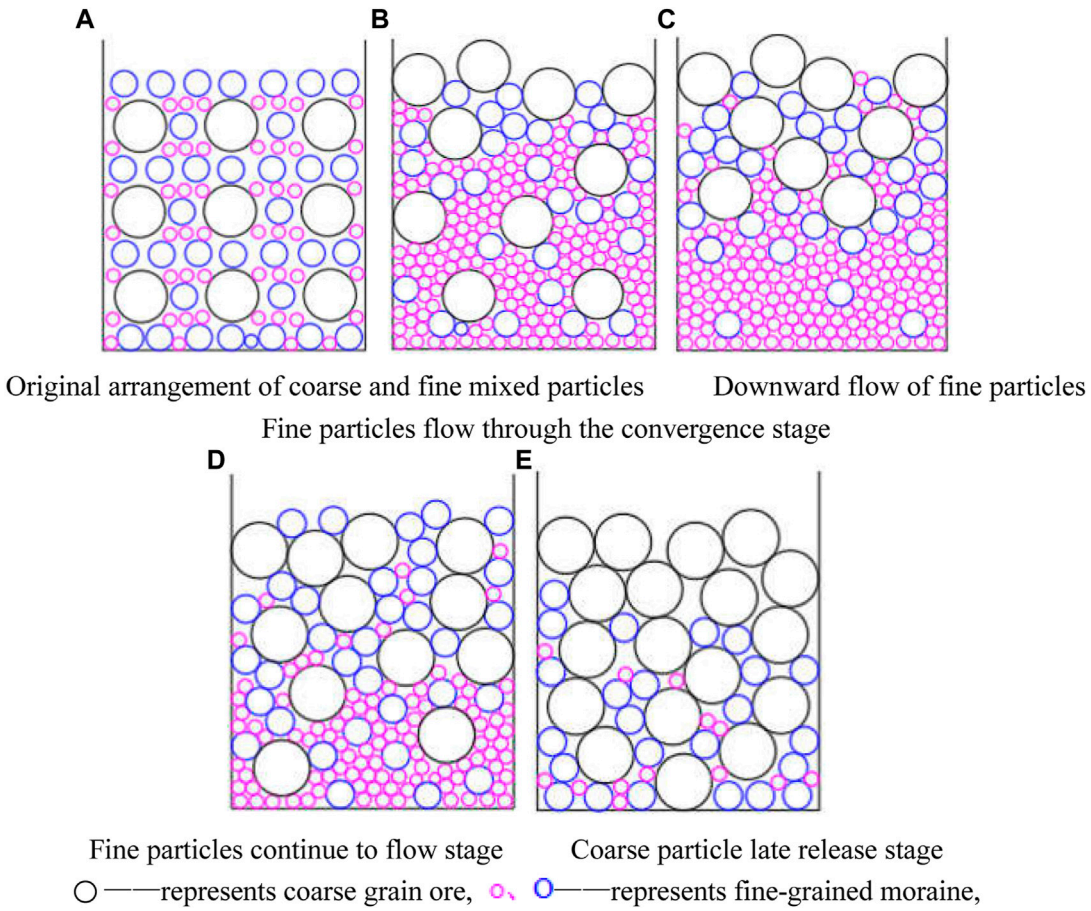

FIGURE 10
Schematic diagram of the flow mechanism of fine particles in mixed particles. **(A)** Original arrangement of coarse and finely mixed particles. **(B)** Downward flow of fine particles. **(C)** Fine particles flow through the convergence stage. **(D)** Fine particles continue to the flow stage. **(E)** Coarse particles in the late release stage.

4 Cross-flow mechanism of fine particles

Figure 10 shows the schematic diagram of the fine particle flow mechanism in different draw cycles in the coarse and finely mixed particles. Figure 10A shows the original arrangement state of the coarse and finely mixed particles in the physical model before ore drawing. Figure 10B shows the process of the downward flow of fine particles in the first draw cycle. Figure 10C shows the process of the fine particle flow and the convergence stage of the second ore-drawing cycle. Figure 10D shows the process of the continuous flow of fine particles in the third ore-drawing cycle. Figure 10E shows the process of the later stage of coarse particles in the fourth ore-drawing cycle.

Figures 10, 10A show the uniform arrangement of coarse and fine particles in the mixed particles before ore drawing. With the progress of uniform ore drawing, in the process of the first ore-drawing cycle, fine particles take precedence over coarse particles to flow downward, showing that there are more and more fine particles at the bottom of the model, as shown in Figure 10B. In the second ore-drawing cycle, a large number of fine-grained media in the upper part of the test model flowed downward and converged, and the most fine-grained medium accumulated at the bottom of the model. Moreover, in this ore-drawing stage, the current discharge amount of fine particles has the largest permeability value, as shown in Figure 10C. In the third ore-drawing cycle, most of the fine particles in the test model have flowed to the bottom to be continuously released, and only a small amount of fine particles in the pores of the coarse particles continued to flow downward. During the ore-drawing process, the upper coarse particles also moved downward, and the coarse particles at the bottom of the test model began to gradually increase, as shown in Figure 10D. In the fourth ore-drawing cycle, as the medium of coarse particles and fine particles is further discharged through the flow, and there is no replenishment of fine particles, the material released in this later stage is mainly coarse particles, as shown in Figure 10E.

In the process of uniform ore drawing, the flow of fine particles in the mixed particles of coarse and fine particles is a process in which the fine particles preferentially move downward in the flow pores of the mixed particles under certain gravity conditions. According to the results of "ore-drawing theory," if the particle size of fine particles is 1/3–1/2 of the particle pore, the piercing behavior will occur (Penfound, 1963; Xu and Li, 2020; Wang et al., 2023). At the same time, according to the movement track of fine moraine in particle pores during the ore-drawing test, the law and

characteristics of cross-flow movement of fine moraine during uniform ore drawing are revealed. The relative motion of coarse and fine particles is the intrinsic controlling factor leading to the flow of fine particles. The more significant the relative motion of coarse and fine particles is, the greater the number of randomly generated pores in the particle flow system and the larger the pores, and the more obvious the flow of fine particles.

5 Conclusion

In this paper, the indoor 3D physical model test method is used to study the fine-grained moraine and coarse-grained ores of various particle sizes in the surface overburden of the Pulang Copper Mine. The experimental study on the flow characteristics of mixed particles under the condition of uniform ore drawing was carried out, the characteristics and laws of the flow of fine particles in the mixed particle flow system were obtained, the mechanism of the flow of fine particles was briefly discussed, and the following main conclusions were obtained:

(1) The cross-flow characteristics of fine particles in mixed particles are studied. In this paper, the authors propose to quantify the cross-flow effect of fine particles by using the index of the cross-flow degree. The index can be used to measure the cross-flow degree of fine particles quantitatively.
(2) Under the action of its own gravity, the fine particle medium in the mixed particle flow uses the pores formed in the process of the mixed particle ore-drawing flow to achieve the downward flow. The fine particles of 2.5–1.25 mm, 1.25–0.63 mm, 0.63–0.315 mm, and 0.315–0.16 mm have significant permeation characteristics, and the smaller the particle size of the finer particles, the more significant the degree of permeation. The relative motion of coarse and fine particles is the intrinsic controlling factor leading to the flow of fine particles. The more significant the relative motion of coarse and fine particles is, the greater the number of randomly generated pores in the particle flow system and the larger the pores, and the more obvious the flow of fine particles.
(3) The current penetration value of fine particles of each particle size shows a variation law of first increasing and then decreasing with the number of ore-drawing times and the cumulative ore-drawing height. Among them, in the second ore-drawing cycle, the value of permeation is the largest, and the phenomenon of permeation is the most obvious. In addition, the variation regularity of fine particle penetration with a cumulative ore-drawing height is explained from the mechanism.

Data availability statement

The original contributions presented in the study are included in the article/supplementary material. Further inquiries can be directed to the corresponding author.

Author contributions

Conceptualization, XN and KH; methodology, KH; software, XN and KH; validation, XN and HS; writing—original draft preparation, XN and HS. All authors contributed to the article and approved the submitted version.

Acknowledgments

The authors would like to thank all the reviewers who participated in the review, as well as MJEditor (www.mjeditor.com) for providing English editing services during the preparation of this manuscript.

Conflict of interest

The authors declare that the research was conducted in the absence of any commercial or financial relationships that could be construed as a potential conflict of interest.

Publisher's note

References

Chen, Q. F., Qin, S. K., and Chen, Q. L. (2019). Stress analysis of ore particle flow behaviour under the influence of a flexible barrier. *Arabian J. Geosciences* 12 (15), 1–13. doi:10.1007/s12517-019-4658-8

Christopher, R. L. (2009). *Development of a computational framework coupling the non-Newtonian lattice Boltzmann method and the discrete element method with application to block caving*. Swansea: Swansea University.

Hashim, M. H. M. (2011). *Particle percolation in block caving mines*. Sydney: The University of New South Wales. School of Mining Engineering. 102–126.

Hou, K. P., Liang, W., and Wen, Y. M. (2016). Simulation experimental study on fine particles percolation in process of ore drawing. *J. Kunming Univ. Sci. Technol. (Nat. Sci. Ed.* 41 (1), 25–30.

Huang, H. T., Luo, G. P., Wang, H., Zeng, X. T., and He, X. (2020). Research and application of mud inrush control in stope of Block Caving method. *World Non-Ferrous Met.* (10), 55–56.

Jin, A. B., Chen, S. J., Sun, H., Zhao, Y. Q., Tan, X., Ju, Y., et al. (2020). Characteristics of particle percolation based on inhomogeneous particle size distribution. *J. Central South Univ. Sci. Technol.* 51 (6), 1673–1680.

Ketterhagen, W. R., Curtis, J. S., Wassgren, C. R., and Hancock, Bruno. C. (2008). Modeling granular segregation in flow from quasi-three-dimension-al, wedge-shaped hoppers. *Powder Technol.* 179 (03), 126–143. doi:10.1016/j.powtec.2007.06.023

Li, D. F. (2020). *Study on the crushing characteristics and fine particle migration law of the filling body above the caving stope*. Wuhan: Wuhan University of Science and Technology.

Li, R., He, Z. H., Shen, Y. H., Yang, S. N., Han, H., Yan, D., et al. (2021). In-hospital complication-related risk factors for discharge and 90-day outcomes in patients with aneurysmal subarachnoid hemorrhage after surgical clipping and endovascular coiling: A propensity score-matched analysis. *J. Hubei Univ. Educ.* 38 (02), 1–12. doi:10.3171/2021.10.JNS211484

Li, T., Wu, A. X., Han, B., Feng, Y. T., and Sun, W. (2016). Discrete element method study on the percolation process of fine particles in ore drawing by the block caving method. *Chin. J. Eng.* 38 (11), 1509–1514. doi:10.13374/j.issn2095-9389.2016.11.001

Li, X. L., Zhang, X. Y., Shen, W. L., Zeng, Q. D., Chen, P., Qin, Q. Z., et al. (2023). Research on the mechanism and control technology of coal wall sloughing in the ultra-large mining height working face. *Int. J. Environ. Res. Public Health* 20 (01). doi:10.3390/IJERPH20010868

Lu, Z. Y., Li, X. J., and Xu, F. (2021). Research on air leakage control technology of overburden in an iron ore open-pit to underground mining. *Mod. Min.* 37 (08), 84–87.

Ma, D., Duan, H. Y., Li, W. X., Zhang, J. X., Liu, W. T., and Zhou, Z. L. (2020). Prediction of water inflow from fault by particle swarm optimization-based modified grey models. *Environ. Sci. Pollut. Res.* 27 (33), 42051–42063. doi:10.1007/s11356-020-10172-w

Ma, D., Duan, H. Y., Zhang, J. X., and Bai, H. B. (2022). A state-of-the-art review on rock seepage mechanism of water inrush disaster in coal mines. *Int. J. Coal Sci. Technol.* 9 (01), 50. doi:10.1007/S40789-022-00525-W

Ma, D., Li, Q., Cai, K. C., Zhang, J. X., Li, Z. H., Hou, W. T., et al. (2023). Understanding water inrush hazard of weak geological structure in deep mine engineering A seepage-induced erosion model considering tortuosity. *J. Central South Univ.* 30 (02), 517–529. doi:10.1007/S11771-023-5261-4

Mao, S. L., and Ming, J. (2019). *Theory and application of ore drawing*. Beijing: Metallurgical Industry Press.

Niu, X. D., Xie, J. Y., Hou, K. P., Li, Z. R., Wang, D. W., and Liang, W. (2020). Experimental study on rainfall threshold and outbreak time of downhole debris flow induced by the prang copper mine. *Nonferrous Met. Eng.* 10 (07), 100–106.

Penfound, W. T. (1963). A modification of the point-centered quarter method for grassland analysis. *Ecology* 44 (01), 175–176.

Pierce, M., Leyronas, X., and Chevy, F. (2019). Few versus many-body physics of an impurity immersed in a superfluid of spin 12 attractive fermions. *Phys. Rev. Lett.* 123 (8), 080403. doi:10.1103/PhysRevLett.123.080403

Pierce, M., Stuart, J., Pungor, A., Dryden, P., and Hlady, V. (1994). Adhesion force measurements using an atomic force microscope upgraded with a linear position sensitive detector. *Langmuir ACS J. surfaces colloids* 10 (09), 3217–3221. doi:10.1021/LA00021A053

Raj, R., and Thakur, D. G. (2016). Qualitative and quantitative assessment of microstructure in Al-B 4 C metal matrix composite processed by modified stir casting technique. *Archives Civ. Mech. Eng.* 16 (04), 949–960. doi:10.1016/j.acme.2016.07.004

Ren, F. Y., Liu, Y., He, R. X., and Zhang, J. (2020). Flow-through features of tailings in subsidence area under ore drawing conditions. *J. Northeast. Univ. Nat. Sci.* 41 (6), 858–862.

Rong, W. J., Qin, D. Y., Li, B. K., and Feng, Y. Q. (2021). Experimental study on particle mixing process in rotating drum. *J. Northeast. Univ. Nat. Sci.* 42 (01), 49–54.

Wang, J. R., Tang, R. L., Jiang, Y. Z., Liu, M., and Li, Z. L. (2023). A practical method for angular normalization of global MODIS land surface temperature over vegetated surfaces. *ISPRS J. Photogrammetry Remote Sens.* 199, 289–304. doi:10.1016/J.ISPRSJPRS.2023.04.015

Wang, P., Li, D. F., Cheng, A. P., Zeng, W. X., Zhang, Y. S., Tan, T., et al. (2019). Integrated RNA-seq and ChIP-seq analysis reveals a feed-forward loop regulating H3K9ac and key labor drivers in human placenta. *Metal. Mine* 76 (12), 40–50. doi:10.1016/j.placenta.2019.01.010

Xing, X., Zhang, C., Jiang, B., Sun, Y., Briens, C., and Zhang, L. (2022). A study of solids mixing in a bubbling fluidized bed using the TFM method. part I. particle travel time distribution. *J. Eng. Thermophys.* 31 (01), 132–143. doi:10.1134/S1810232822010106

Xu, L. M., and Li, M. J. (2020). A data preprocessing method in dynamic comprehensive evaluation. *Engl. J. Manag. Sci.* 28 (01), 162–169. doi:10.16381/j.cnki.issn1003-207x.2020.01.014

Xu, Y., Li, R., Xiu, W. z., Chen, Q., Sun, Q. c., and Yang, H. (2022). Six new species of aspidophorodon verma, 1967 (Hemiptera, aphididae, aphidinae) from China. *Mech. Eng.* 44 (01), 1–55. doi:10.3897/zookeys.1106.77912

You, X., and Zhang, G. J. (2016). Effect of particle size space distribution in coverage rocks on rocks mixture. *J. Northeast. Univ. Nat. Sci.* 37 (11), 1605–1608.

Zhang, J. C., Li, X. L., Qin, Q. Z., Wang, Y. B., and Gao, X. (2023). Study on overlying strata movement patterns and mechanisms in super-large mining height stopes. *Bull. Eng. Geol. Environ.* 82 (3), 142. doi:10.1007/S10064-023-03185-5

Zhang, X. F., Tao, G. Q., and Zhu, Z. H. (2019). A gravity flow model of fragmented rocks in longitudinal sublevel caving of inclined medium-thick ore bodies. *Archives Min. Sci.* 64 (03), 533–546. doi:10.24425/ams.2019.129367

Zhang, Y. G., and Gao, F. (2021). Study on reasonable gradation and thickness of overburden based on air leakage characteristics. *China Min. Mag.* 30 (04), 115–119.

Zhang, Y. W., and Cheng, Z. H. (2017). Analysis of particle gradation of an iron mine from open-pit to underground overburden. *West. Prospect. Eng.* 29 (01), 171–173.

frontiers | Frontiers in Earth Science

TYPE Original Research
PUBLISHED 28 July 2023
DOI 10.3389/feart.2023.1207110

OPEN ACCESS

EDITED BY
Xuelong Li,
Shandong University of Science and Technology, China

REVIEWED BY
Anquan Xu,
Tianjin University, China
Chaoyu Chang,
Institute of Disaster Prevention, China

*CORRESPONDENCE
Cheng Li,
licheng@hebnetu.edu.cn
Dewen Liu,
civli_liudewen@sina.com
Weiwei Sun,
3259145086@qq.com

RECEIVED 17 April 2023
ACCEPTED 05 June 2023
PUBLISHED 28 July 2023

CITATION
Xiao S, Li C, Liu D, Sun W and Lei M (2023), Research on irregular plane mid story isolation structures in castor earthquake prone areas considering SSI effect. *Front. Earth Sci.* 11:1207110. doi: 10.3389/feart.2023.1207110

Research on irregular plane mid story isolation structures in castor earthquake prone areas considering SSI effect

Shuai Xiao[1], Cheng Li[2,3]*, Dewen Liu[1]*, Weiwei Sun[1]* and Min Lei[4]

[1]College of Civil Engineering, Southwest Forestry University, Kunming, Yunnan, China, [2]Discipline Inspection and Supervision Office, Hebei Open University, Shijiazhuang, China, [3]School of Traffic and Transportation, Shijiazhuang Tiedao University, Shijiazhuang, China, [4]School of Civil Engineering, Southwest Jiaotong University, Chengdu, Sichuan, China

The rock composition of karst area is mainly limestone, which is easy to be eroded and dissolved by water, forming a complex and fragile tectonics. Under the action of earthquake, the instability of stratum is aggravated. The mid story isolation structure is a new type of isolation structure developed from the basic isolation structure, and irregular mid story isolation buildings are highly susceptible to adverse seismic conditions. Previous studies have mostly adopted the assumption of rigid foundations, neglecting the influence of soil on irregular structures. In order to study the seismic response of isolated structures in irregular planes in karst earthquake prone areas considering soil structure interaction, a finite element model of isolated structures in irregular planes considering soil component interaction was established, and the seismic response of the structure under rigid foundation was calculated. Soft and hard soil foundations were studied, and compared with structures without considering SSI effect. Research shows that when considering the SSI effect, the seismic response of the structure increases and the damage to the structure intensifies; When considering SSI, the seismic response of soft soil is greater than that of hard soil, and the softer the soil, the more obvious it becomes; After considering the SSI effect, the torsional effect caused by the irregularity of the plane increases; The design of building structures should fully consider the adverse effects of soil layers on the seismic response of structures under plane interlayer seismic irregularities. In the design of building structures, it is necessary to fully consider the adverse effects of irregular planes on the seismic response of the structure. This consideration is particularly important in the design of soft soil high-rise buildings in karst earthquake areas to prevent unsafe designs and consider the SSI effect in actual seismic resistance.

KEYWORDS

SSI effect, castor earthquake zone, planar irregularity, mid story isolation structure, seismic wave

1 Introduction

The rock composition of karst area is mainly limestone, which is easy to be eroded and dissolved by water, forming a complex and fragile tectonics. Under the action of earthquake, the instability of stratum is aggravated. The mid-story isolated structure is a new type of seismic isolated structure developed on the basis of the base isolated structure, while the mid-

story isolated structure with an irregular plan is extremely prone to adverse seismic conditions. Previous studies have mostly adopted the assumption of rigid foundations and ignored the impact of soil on the structure with an irregular plan. The research on the structure with an irregular plan considering soil-structure interaction (SSI) effect is mainly focused on seismic and base isolated structures, and there is less research on the mid-story isolated structure with an irregular plan considering SSI effect of SSI.

Losanno et al. (2021) conducted a meticulous study of the base isolated system and demonstrated that the base isolated system can effectively protect buildings from damage during earthquakes. Luis et al. (2021) conducted a study of the base isolated structure considering SSI effects and demonstrated that the base isolated structure can effectively control the damage to the structure caused by the SSI effect and can extend the fixation period of the superstructure. Vasiliki (2022) revealed the validity boundary and impact of the research on soil-structure interaction. Jean and Keri (2020) performed a coupling analysis of mass floor vibration and mass eccentricity for irregular buildings and proposed modifications. Repapis and Zeris (2020) made static prediction and dynamic analysis of the irregular in plan frame structure, exhibiting excitation and irregularity forming dependent failure mechanism. Kosmopoulos and Fardis (2008) performed inelastic seismic analysis of the 3D model of the bidirectionally eccentric multi-storey RC buildings, and presented a simple bar model, demonstrating that static eccentricity is an important parameter for controlling torsional effects. Sahar et al. (2022) carried out a seismic performance analysis of a multi-storey concrete frame shear asymmetric building considering SSI effects, and the results showed that there is an adverse effect on the structure at the limit state when SSI effects are considered. Zeshan et al. (2021) analyzed the damage to a planar irregular structure, which was mainly attributed to the coupled torsional vibration, and drew the conclusion that the design of the irregular in plan structure needed a lot of design redundancy and special structural details to resist rare earthquakes. Mohammed et al. (2022) carried out a simulation of a seismically isolated building with triple friction pendulum bearings considering SSI effects, which would amplify the displacement and acceleration of the structure, and calculated the response of the model to the soil. The SSI effect amplifies structural displacements and accelerations, and the response of the calculated model is sensitive to the damping ratio, Poisson's ratio of the soil and the foundation dimensions. Ferj and Lopez (2022) conducted several limit analysis studies on hospitals with concrete frame isolated structures and concluded that hospitals with isolated structures are more able to perform in the seismic limit state, increasing the threshold of structural resistance to earthquakes. Soheil and Mansour (2017) evaluated the social and economic aspects of the project of the isolated structure. The results show that vibration isolation results provide the optimal criteria from a global perspective, and is especially important for the hospital. The ability to meet the required structure of earthquake demand in the countries with high growth rate using the value-based design method is lower than that in the low growth rate areas. Ryan and Earl (2010) explored the location of the seismic isolated layers of the mid-story isolated structure, indicating that the mid-story isolated structure has a good damping effect on the upper part of the isolated layer, but a poor damping effect on the lower part of the structure, and discussed the actual effect of the damping effect of the mid-story isolated structure. Faming et al. (2020) made a prediction and analysis of soil landslide based on machine learning and statistics. Chang et al. (2020) compared unsupervised machine learning of landslides based on remote sensing images and GIS. Huang et al. (2020) used self-coding neural network to predict landslide susceptibility. Huang et al. (2020) used perceptron to predict susceptibility of soil landslide. Jiang et al. (2018) studied the variability model of shear strength of the slope.

Jianbing et al. (2007) studied three cases of foundation seismic isolation structures for magnitude eight multiple earthquakes, rigid base mega-structures for magnitude seven multiple earthquakes, and foundation seismic isolation structures for magnitude eight rare earthquakes, combining physical stochastic ground motion models and probability density evolution methods to perform. The results of the study show that the first mode shape of the structure dominates the response under strong earthquakes, while the response of higher order modes can be ignored, and the stochastic seismic response analysis and reliability assessment can provide more objective indicators for decision making. Christos et al. (2020) upgraded the seismic performance of the five-story frame reinforced concrete building. With the addition of an isolated layer, the seismic performance of the building was improved greatly. Hitesh and Sandip (2022) proposed a detailed numerical framework for seismic analysis of liquid storage tanks considering soil-structure interaction (SSI), demonstrating the considerable influence of soil on structural isolation systems. Jaya et al. (2008) studied the influence of parameters such as the relative stiffness of the site layer, soil layer thickness and foundation embedding on the interaction behavior between soil and structure, indicating that the seismic response has a strong correlation with the relative stiffness of the site and the depth of the soil layer to the bedrock. Yazdan et al. (2021) proposed a simple method for studying soil-structure interaction problems, which can obtain higher mode frequencies and responses for superstructures on flexible foundations, which is very useful for modal analysis including SSI effects. Sekhar et al. (2017) studied the vertical irregular structure and obtained the research result that the reinforcement bar strength near the vertical irregularity can improve the overall seismic performance of the irregular structure. Muberra and Ibrahim (2013) discussed the response of multi-storey structures considering SSI affect under seismic excitation, and conducted analysis on site conditions with different hardness. Considering that the strength reduction coefficient of buildings under SSI is less than the design strength reduction coefficient, the structure design will be unsafe. Devis et al. (2020) used a fluid viscous damper to dissipate part of the input seismic energy and convert the structural weakness into an energy dissipation device. Yongbo et al. (2022) studied the isolation effect of sliding implant magnetic bearing (IMB), and the results showed that IMB had good isolation effect. After the Kobe earthquake in Japan. Bujar et al. (2002) introduced the isolation technology to Japanese houses, and the research results showed that the isolation technology could effectively reduce the damage to houses caused by earthquakes. Castaldo and Tubaldi (2018) studied the Influence of ground motion characteristics on the optimal single concave sliding bearing properties for base-isolated structures, The results show that the optimization of foundation isolation is very effective under different

earthquake effects. Giovanni et al. (2008) carried out the isolation transformation of existing buildings, and the results showed that the existing buildings could be ensured to have a comparable seismic level after the transformation. Liu SM et al. (2020) studied the microstructures of the mediocrity under cold leaching of liquid nitrogen. Zhou XM et al. (2022) conducted an in-depth study on the semi-coal rock of Longhu Coal Mine in Qitaihe Mining area. Li et al. (2021b) studied the characteristics of different rock masses. Li et al. (2021a) took Linyi Mining area as an example to study the distribution law of ground stress in deep mines. Liu et al. (2022) conducted an in-depth study on the failure mechanism and control technology of roadway retention roof in close goaf. Li et al. (2023) conducted an in-depth study on the mechanism and control technology of coal wall shedding in super-high working face.

Attanasi and Auricchio (2011) conducted research on the basis of a new type of isolation device made of super elastic material components made of shape memory alloy, which can effectively dissipate earthquake energy and ensure the safety of structures. Diana et al. (2022) applied the spacer seismic system to irregular masonry buildings, carried out detailed design and analysis, and put forward some design standards. Shi-Shuenn et al. (2019) studied the structure method based on iterative wave propagation (WP), which can more effectively study the influence of the soil layer below the structure on the structure. Micozzi et al. (2021) based on the Italian seismic code, the failure rate of the isolation system of the frame structure is analyzed, and the comparative analysis of the failure rate under the new design is obtained. Mohammed et al. (2021) in the damage function, the results obtained from static and dynamic analysis will be compared and discussed, and recommendations for future research and seismic regulations will be provided. Peter et al. (2005) carried out nonlinear dynamic analysis of planar irregular structures and showed that the torsion of planar irregular structures increased significantly. Taskin and Khan (2020) seismic response analysis of multi-storey masonry filled concrete (RC) frames can effectively guide structural designers to design structures in a reasonable way to make them safer. Sahar et al. (2022) studied the seismic performance of multi-storey asymmetric structures considering SSI using a probabilistic performance-based method, and the results showed that the irregular results under SSI effect had adverse effects in the limit state. Johanes and Philippe (2019) conducted centrifugal test analysis on the nonlinear soil-structure interaction and the interaction between soil and structure. The study showed that the existence of buildings would strongly change the nonlinear soil response, and discussed the simplified relationship between the overall soil-structure system response. Kyoung et al. (2021) used nonlinear dynamics to analyze vertical irregular structures and adopted a simplified method to study the seismic response of vertical irregular structures, which can effectively save time for the structural calculation. Kosmopoulos and Fardis (2008) proposed a simple model and carried out 3D inelastic seismic analysis of bidirectional eccentric multi-storey RC buildings. The study showed that the structural torsion was correlated with the static eccentricity of the structure. Didier et al. (2007) studied the residual deformation of irregular structures after an earthquake. The torsion of structures is quite limited in the current methods, because the current methods do not clearly define how seismic elements are affected by inelastic torsional reactions.

Previous studies on structures with an irregular plan considering SSI effect have mainly focused on seismic and base isolated structures, with less attention given to mid-story isolated structures with an irregular plan. Therefore, this paper aims to address this research gap by establishing a model of a mid-story isolated structure with an irregular plan, and studying its seismic response under the consideration of SSI effect. Additionally, we conduct a comparative analysis with the mid-story isolated structure without considering SSI effect, providing important reference for future research on mid-story isolated structures with an irregular plan.

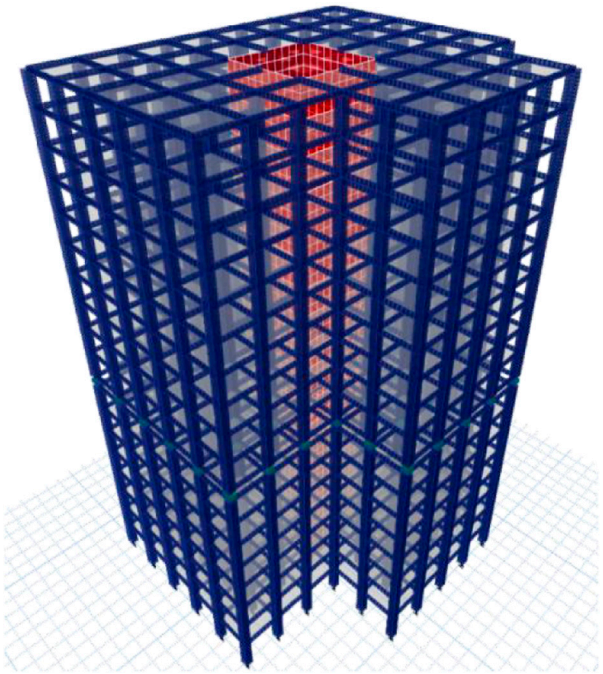

FIGURE 1
3D view of the mid-story isolated structure.

2 Materials and methods

2.1 Project overview

According to Chinese norms, the concave plane size should be greater than 30% of the total size of the corresponding projection direction. In this study, an 18-story frame-core tube structure with an irregular plan was constructed using the mid-story isolated system, with an intensity level of 8 degrees (0.20 g). The site category is Class II and the seismic design group is Group II. The seismic isolated layer is positioned at the top of the 8th storey. The vertical members of the first five floors are made of C40 concrete, the next five floors use C35 concrete, and the remaining floors use C30 concrete. The wall thickness of the core tube is 300 mm and the column frame has a section size of 800 mm × 800 mm. The frame beam adopts C30 concrete, with a cross-section size of 300 mm × 700 mm. The longitudinal reinforcement of the beam and column is HRB400, and the hoop is HRB400 as well. The 3D diagram of the structure can be seen in Figure 1. Vibration isolation support data in Table 1.

10.3389/feart.2023.1207110

TABLE 1 Parameters of lead-core rubber vibration isolated bearings.

Model	LRB700	LRB800	LRB900
Effective diameter of vibration isolated pad (mm)	700	800	900
Shear modulus G (Mpa)	0.392	0.392	0.392
Equivalent damping ratio ζ (%)	24	23	23
Diameter of central hole (mm)	120	130	150
First shape factor S1	≥15	≥15	≥15
Second shape factor S2	≥5	≥5	≥5
Vertical pressure limit (kN)	4,616	6,029	7,630
Vertical stiffness Kv (kN/mm)	2,600	2,900	3,500
Equivalent horizontal stiffness Keq (kN/mm)	1.87	2.05	2.37
Design strains	100%	100%	100%
Extreme shear strain	≥400%	≥400%	≥400%
Stiffness before yielding Ku (kN/mm)	15.19	17.35	19.67
Stiffness after yielding Kd (kN/mm)	1.17	1.33	1.51
Total thickness of rubber layer (mm)	130	149	167
Yield force Qd (kN)	90	106	141
Total height of support (mm)	266.5	302	353

TABLE 2 Subsoil parameters of the foundation.

Soil type	Soft soil	Hard soil
Shear wave speed/(m·s^{-1})	150	300
Density (kg·m^{-3})	1750	2000
Damping ratio	0.2	0.2
ξ/(kg·m^{-1}·s^{-1})	1.48 x 106	4.20 x 106
k_T/(N·m^{-1})	1.21 × 109	5.54 × 109
C_T/(N·s·m^{-1})	3.40 × 107	7.90 × 107
k_φ/(N·m^{-1})	3.11 × 1,010	1.42 × 1,011
c_φ/(N·s·m^{-1})	1.96 × 108	4.47 × 108

2.2 Modeling

The finite element software ETABS was used to model the mid-story isolated structure with an irregular plan, using LRB700, LRB800, and LRB900 lead-core rubber isolation bearings. The bearings were model led using Isolation units; the concrete used Takeda hysteresis type; and the reinforcement used Kinematic hysteresis type. Fibre P-M2-M3 hinges were used for all frame columns, and M3 hinges were used at the ends of the frame beams and the connecting beams. The foundations of the topside structure are buried in the soil layer, and a layered foundation model that is more in line with the characteristics of the foundation soil is used. The soil parameters of the foundation are shown in Table 2.

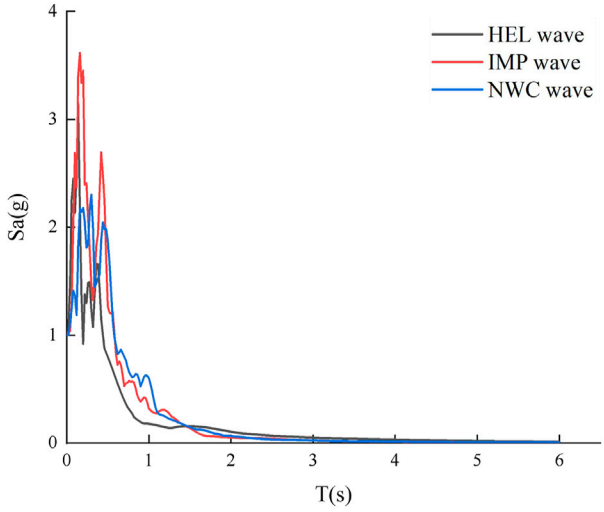

FIGURE 2
Acceleration wave response spectrum.

2.3 Earthquake wave selection

According to the code of seismic design of Chinese buildings. In this paper, the seismic intensity of this area was selected as 8 degrees, and the average value of the shear force at the bottom of the structure calculated according to the three time curves selected from the code was greater than 80% of the result of the vibration decomposition response spectrum

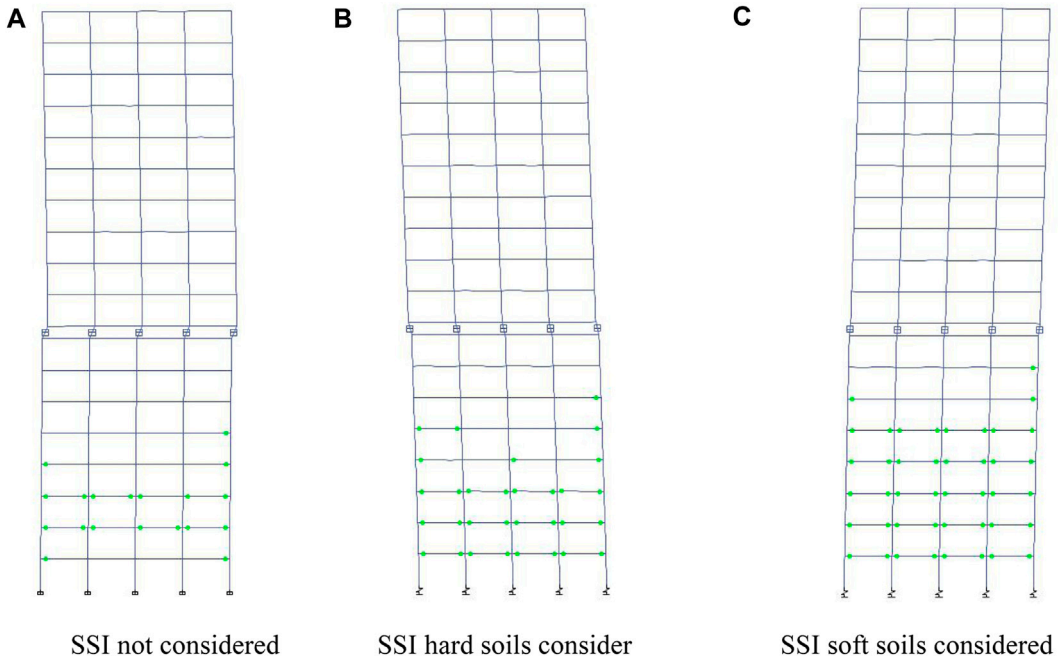

FIGURE 3
Structural plastic hinge. **(A)** SSI not considered. **(B)** SSI hard soils consider. **(C)** SSI soft soils considered.

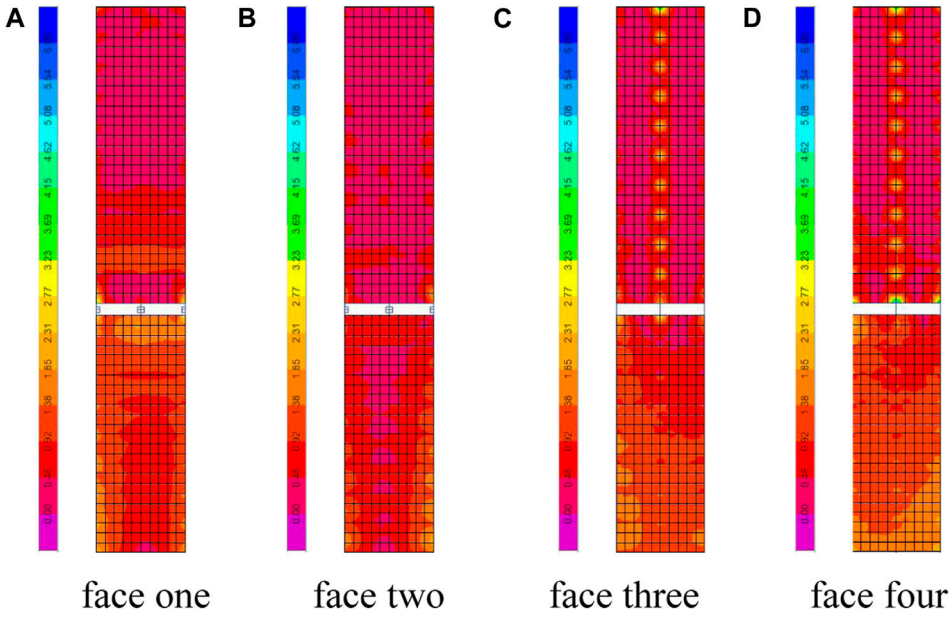

FIGURE 4
Structural damage not considering SSI effects. **(A)** face one. **(B)** face two. **(C)** face three. **(D)** face four.

method, and the acceleration response spectrum was selected from HEL, IPM, and NWC waves through the US Pacific Seismic Centre as shown in Figure 2. The peak acceleration of the seismic wave is adjusted to 400 cm/s^2, which corresponds to the peak acceleration at a basic seismic intensity of 8 degrees under a rare earthquake.

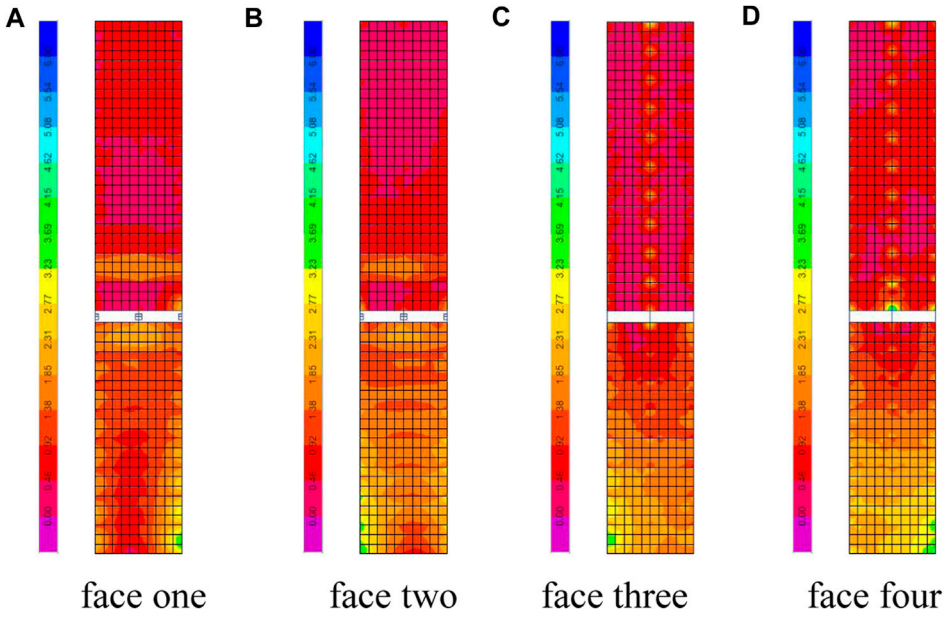

FIGURE 5
Structural damage of the hard soil considering SSI. **(A)** face one. **(B)** face two. **(C)** face three. **(D)** face four.

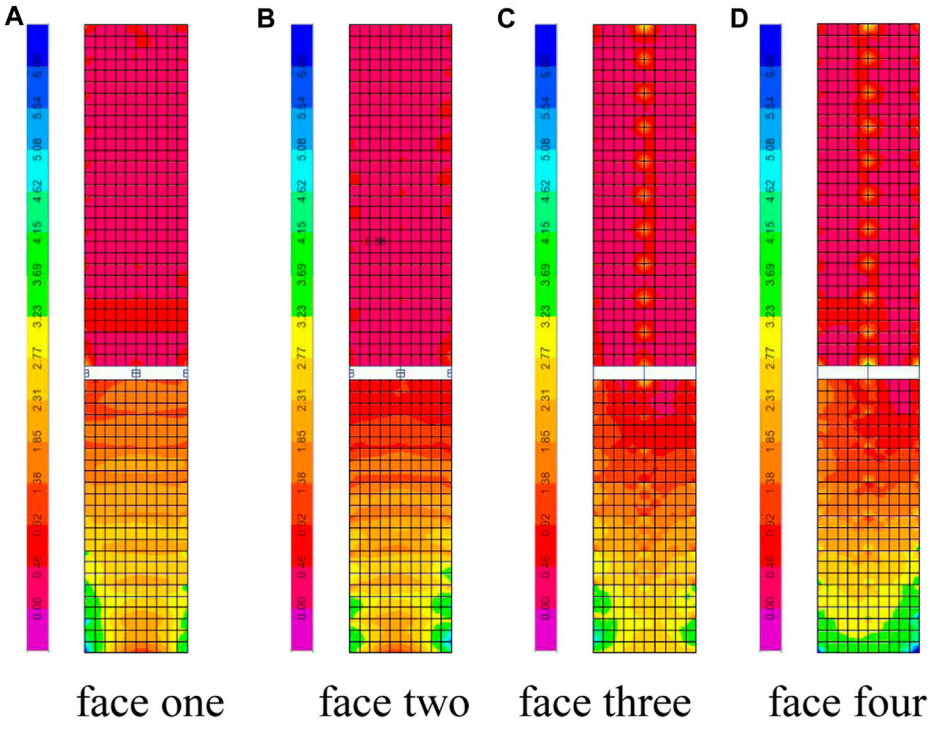

FIGURE 6
Structural damage of the soft soil considering SSI. **(A)** face one. **(B)** face two. **(C)** face three. **(D)** face four.

2.4 Results of structural damage

The dynamic elastic-plastic time-history analysis method was carried out on the structure and The results of the plastic hinge are shown in Figures 4–6, and the results of the structural damage of the core tube are shown in Figure 3.

From Figures 3–6, it can be seen that under the action of earthquakes, the structural plastic hinge state of the mid-story isolated structure with an

TABLE 3 Modal period of the first 6 orders of the structure for different properties of the substrate.

Number of steps	SSI is not considered/s	Consider SSI (hard soil)/s	Consider SSI (soft soil)/s
1	2.749	2.998	3.148
2	2.160	2.490	2.615
3	1.647	1.701	1.786
4	0.658	0.726	0.762
5	0.579	0.710	0.746
6	0.464	0.531	0.558

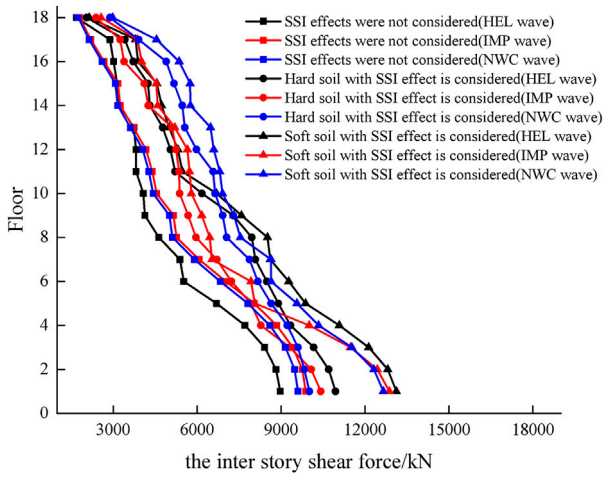

FIGURE 7
Comparison of the inter story shear forces.

irregular plan considering SSI effect are all in the yielding stage (green dots in Figure 3), and the number and stress value of the structural plastic hinge are both greater than that without considering SSI effect.

3 Analysis of the shock absorption effect

3.1 Modal period

As can be seen from Table 3, the period of the mid-story isolated structure with an irregular plan increases when the SSI effect is taken into account, and the increase of the period is slightly greater when the foundation is a soft soil than a hard soil. This is due to the interaction between the soil and the structure softening the stiffness of the structure. Therefore, the structure becomes more flexible and the period is extended.

3.2 Seismic damping performance

When different properties of soil are used in the substrate, HEL, IPM, and NWC waves are input as excitation of the mid-story isolated structure and the seismic response analysis is carried out to obtain the comparison of the inter story shear force and the base shear force of the structure as shown in Figures 7, 8.

As can be seen from Figure 7, the inter-storey shear force of the main body of the mid-story isolated structure with an irregular plan decreases layer by layer under the action of ground shaking. Considering the SSI effect, the inter-storey shear force of the mid-story isolated structure is significantly greater than that of the structure without considering SSI. Considering the SSI effect, the inter story shear force of the soft soil in the base is slightly larger than that of the hard soil in the substrate. This is because the stiffness of the structure is softened when considering the SSI effect, and the softer the soil is, the more obvious this effect is.

As can be seen from Figure 8, the shear force of the base of the mid-story isolated structure with an irregular plan considering the SSI effect under earthquake action is slightly larger than that without SSI effect. Although the change is relatively small, due attention should be paid to the structure design.

3.3 Torsional effects

The structure with an irregular plan are very prone to generate torsional effects under earthquake action, amplifying earthquake damage to the building. Seismic response analysis was carried out when the substrates with different properties are used for this structure, and the torsional displacement ratio (the maximum inter-storey displacement/average inter-storey displacement) was obtained as shown in Figure 9, and the torsional coefficients (torsional ratio column under modal analysis) are shown in Table 4.

From Figure 9 and Table 4, it can be seen that the torsional displacement ratio and torsional coefficient of the mid-story isolated structure with an irregular plan considering the SSI effect are greater than those without the SSI effect, and the soft soil substrate brings greater torsional displacement ratio and torsional coefficient to the structure than the hard soil substrate. This is due to the fact that the filling of the substrate reduces the stiffness of the bottom of the structure, which increases the torsional effect of the structure and makes it more susceptible to torsional damage and increases the adverse effects of earthquakes on the upper structure, therefore, the adverse effects of the lower soil layer on the torsion of the structure should be fully considered when designing the structure with an irregular plan.

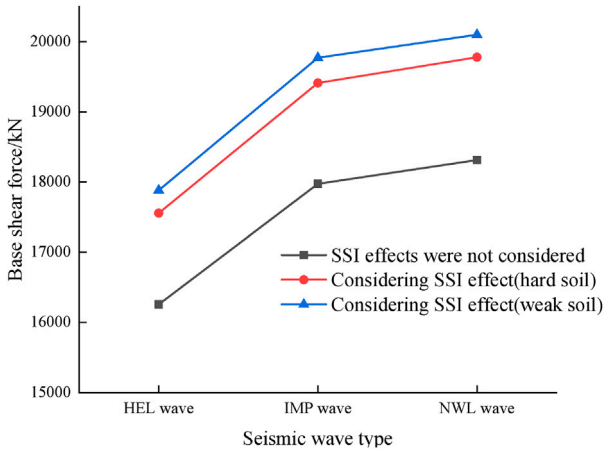

FIGURE 8
Comparison of shear forces at the base of the structure.

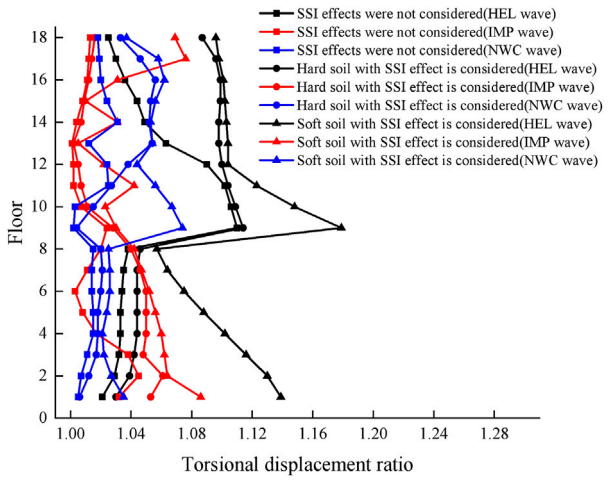

FIGURE 9
Comparison of torsional displacement ratios of structures.

4 Discussion and conclusion

4.1 Discussion

In this paper, the finite element analysis software ETABS is used to analyse the seismic response of the mid-story isolated structure with an irregular plan, and the seismic response analysis and damage of the structure are studied in terms of seismic wave selection, inter-layer shear force, structural damage, etc. It is concluded that the mid-story isolated structure with an irregular plan has good seismic isolation effect under ground shaking.

The research in this paper also allows for further research in the following areas.

(1) The model in this paper is a mid-story isolated structure with an irregular plan, which is limited by the calculation time and the calculation operation equipment, so the number of calculations for the typical ground shaking condition is small and not universal. Fabio and Alfonso (2009) studied the adverse effects of near-fault earthquakes on base-isolated frame structures using European norms, and drew the conclusion that preventive measures should be taken for near-fault earthquakes, especially for base-isolated structures located on soft soil. In the next step, we should screen the typical ground shaking in different regions of the world and compare them with each other, calculate a few more conditions and draw lessons from them.

(2) There is a lack of research and analysis on vertical ground vibration of super tall conjoined structures. Trishna and Hemant (2020) carried out a vulnerability analysis of vertically irregular buildings, which could effectively predict the actual damage of such buildings observed in past earthquakes. The next step is to compare the vertical vibration comfort evaluation standards of various countries and recommend a relatively practical comfort evaluation standard suitable for conjoined structures.

(3) The parameters of seismic isolation bearings, BRBs and viscous dampers in the damage control scheme for interval seismic structures with planar irregular layers are less studied in this paper. Raz and Gopal (2018) investigated the effectiveness of tuned mass dampers (TMD) in dynamic soil-structure interaction systems. In the future, more in-depth studies can be conducted on the influence of more dampers parameters on the damage control and seismic performance of the structure, and a universal design method for the selection of dampers parameters can be established, and the reasonable between the stiffness of the dampers and the stiffness of the connected body, and between the stiffness of the dampers and the stiffness of the strengthened layer The influence of the stiffness values on the response of the structure under strong earthquakes requires more research and discussion.

(4) In this paper, the seismic response analysis of the mid -story isolated structure with an irregular plan is mainly based on the horizontal earthquake, and does not consider the different foundation size. Dao and Ryan (2022) studied the seismic response of structures under 3D earthquakes, showing that the response of the computational model is very sensitive to the hysteresis damping ratio of soil, Poisson's ratio of soil and the foundation size. Further studies are needed to investigate the isolation effect of the plane irregular layer spacer structure under the actual earthquake action including vertical earthquake action.

(5) The mid-story isolated system adopted in this paper is the traditional lead-core rubber isolated bearing system. Mohammad et al. (2022) studied the new multi-directional isolation (MDSI) system, which can effectively reduce the damage to the structure caused by earthquake compared with the basic isolated system. Further study is needed to determine whether the better isolation effect can be achieved by using different isolation systems and different foundation size.

4.2 Conclusion

In conclusion, a model of a mid-story isolated structure with an irregular plan has been developed and analyzed using non-

TABLE 4 Torsional coefficients for different properties of substrate structures.

Number of steps	Torsion factor not considering SSI	Torsion factor considering SSI (hard soil)	Torsion factor considering SSI (soft soil)
1	0.073	0.091	0.113
2	0.040	0.067	0.082
3	0.734	0.802	0.830
4	0.052	0.066	0.084
5	0.012	0.020	0.073
6	0.668	0.774	0.841

linear time analysis under seismic action with SSI effect. The analysis of the seismic response of the mid-story isolated structure with an irregular plan when different properties of soil substrates are used has been compared, and the following conclusions can be drawn.

(1) The seismic response of the mid-story isolated structure with an irregular plan considering SSI effect increases under the action of earthquakes. The seismic response of soft soil considering SSI is greater than that of hard soil, and the softer the soil, the more obvious the effect. Therefore, attention should be paid to the design of high-rise building structure in a soft soil layer.
(2) Compared with the rigid foundation, the hard soil increased the first three periods of the structure period by 0.249 s, 0.330 s, and 0.054 s. The soft soil increased the first three periods of the structure period by 0.399 s, 0.455 s, and 0.139 s. After considering the SSI effect, the base shear increases by about 10%, and the structural plastic hinge and stress damage also increase. Therefore, designers should pay attention to these effects in the design.
(3) Under the action of earthquakes, the torsional displacement ratio and torsional coefficient of the mid-story isolated structure with an irregular plan considering SSI effect increase, which amplifies the torsional effect of the structure. The softer the soil, the more obvious the amplification. Therefore, designers should fully consider this effect when constructing the structure with an irregular plan in a soft soil layer to avoid unsafe designs in actual seismic resistance without considering SSI effect.

Data availability statement

The original contributions presented in the study are included in the article/supplementary material, further inquiries can be directed to the corresponding authors.

Author contributions

SX wrote the article as a whole and established the research content; CL drew the pictures and tables of the article; DL calculated the data of the article; WS gave important opinions on the research methods of the article; ML conducted an effective review of the article. All authors contributed to the article and approved the submitted version.

Conflict of interest

The authors declare that the research was conducted in the absence of any commercial or financial relationships that could be construed as a potential conflict of interest.

Publisher's note

All claims expressed in this article are solely those of the authors and do not necessarily represent those of their affiliated organizations, or those of the publisher, the editors and the reviewers. Any product that may be evaluated in this article, or claim that may be made by its manufacturer, is not guaranteed or endorsed by the publisher.

References

Attanasi, G., and Auricchio, F. (2011). Innovative superelastic isolation device. *J. Earthq. Eng.* 15(1), 72–89.

Bujar, M., Mitsumasa, M., Masanori, I., and Masayoshi, I. (2002). Seismic behavior of a newly developed base isolation system for houses. *J. Asian Archit. Build. Eng.* 1 (2), 17–24. doi:10.3130/jaabe.1.2_17

Castaldo, P., and Tubaldi, E. (2018). Influence of ground motion characteristics on the optimal single concave sliding bearing properties for base-isolated structures. *Soil Dyn. Earthq. Eng.* 104, 346–364. doi:10.1016/j.soildyn.2017.09.025

Chang, Z., Du, Z., Zhang, F., Huang, F.*, Chen, J., Li, W., et al. (2020). Landslide susceptibility prediction based on remote sensing images and GIS: Comparisons of supervised and unsupervised machine learning models. *Remote Sens.* 12, 502. doi:10.3390/rs12030502

Christos, G., and Dimitrios, K.Associate Professor Constantinos Repapis (2020). Seismic isolation: An effective technique for the seismic retrofitting of a reinforced concrete building. *Struct. Eng. Int.* 30 (1), 43–52. doi:10.1080/10168664.2019.1678449

Dao, N. D., and Ryan, K. L. (2022). Soil–structure interaction and vertical-horizontal coupling effects in buildings isolated by friction bearings. *J. Earthq. Eng.* 26 (4), 2124–2147. doi:10.1080/13632469.2020.1754969

Devis, S., Andrea, P., and Marco, C. (2020). Seismic retrofit of an industrial building using damping devices. *Struct. Eng. Int.* 30 (1), 53–63. doi:10.1080/10168664.2019.1635975

Diana, F., Bruno, C., and Elena, M. (2022). Seismic retrofit of existing masonry buildings through inter-story isolation system: A case study and general design criteria. *J. Earthq. Eng.* 26 (4), 2051–2087. doi:10.1080/13632469.2020.1752854

Didier Pettinga, J., Nigel Priestley, M. J., Pampanin, S., and Christopoulos, C. (2007). The role of inelastic torsion in the determination of residual deformations. *J. Earthq. Eng.* 11(1), 133–157.

Fabio, M., and Alfonso, V. (2009). Nonlinear response of RC framed buildings with isolation and supplemental damping at the base subjected to near-fault earthquakes. *J. Earthq. Eng.* 13 (5), 690–715. doi:10.1080/13632460802632302

Faming, H., Zhongshan, C., Shui-hua, J., Chuangbing, Z., Zizeng, G., and Guo, Z. (2020). Landslide susceptibility prediction based on a semi-supervised multiple-layer perceptron model. *J. Landslides* 17, 2919–2930. doi:10.1007/s10346-020-01473-9

Ferj, M., and Lopez-Garcia, D. (2022). Comparative seismic fragility analysis of conventional and base isolated hospital buildings having different structural systems. *J. Earthq. Eng.* 26 (5), 2491–2513. doi:10.1080/13632469.2020.1767229

Giovanni, C., Antonio De, L., and Elena, M. (2008). Design aspects in seismic isolation: Application to retrofit churches. *Int. J. Archit. Herit.* 2 (3), 247–273. doi:10.1080/15583050802063741

Hitesh, K., and Sandip Kumar, S. (2022). Effects of soil-structure interaction on seismic response of fixed base and base isolated liquid storage tanks. *J. Earthq. Eng.* 26 (12), 6148–6171. doi:10.1080/13632469.2021.1911887

Huang, F., Jing, Z., Chuangbing, Z., Yuhao, W., Jinsong, H., and Li, Z. (2020). A deep learning algorithm using a fully connected sparse autoencoder neural network for landslide susceptibility prediction. *Landslides* 17 (01), 217–229. doi:10.1007/s10346-019-01274-9

Jaya, V., Dodagoudar, G., and Boominathan, A. (2008). Seismic soil-structure interaction analysis of tall slender structures. *Int. J. Geotechnical Eng.* 2 (4), 381–393. doi:10.3328/ijge.2008.02.04.381-393

Jean, C. G. P., and Keri, L. R. (2020). Slab vibration and horizontal–vertical coupling in the seismic response of low-rise irregular base-isolated and conventional buildings. *J. Earthq. Eng.* 24 (1), 1–36. doi:10.1080/13632469.2017.1387197

Jianbing, C., Weiqing, L., Yongbo, P., and Jie, L. (2007). Stochastic seismic response and reliability analysis of base-isolated structures. *J. Earthq. Eng.* 11 (6), 903–924. doi:10.1080/13632460701242757

Jiang, S. H., Huang, J., Huang, F., Yang, J., Yao, C., and Zhou, C. (2018). Modelling of spatial variability of soil undrained shear strength by conditional random fields for slope reliability analysis [J]. *Appl. Math. Model.* 63, 374–389.

Johanes, C., and Philippe, G. (2019). Nonlinear response of soil–structure systems using dynamic centrifuge experiments. *J. Earthq. Eng.* 23 (10), 1719–1741. doi:10.1080/13632469.2017.1398692

Kosmopoulos, A. J., and Fardis, M. N. (2008). Simple models for inelastic seismic analysis of asymmetric multistory RC buildings. *J. Earthq. Eng.* 12 (5), 704–727. doi:10.1080/13632460701673126

Kosmopoulos, J., and Fardis, M. N. (2008) Simple models for inelastic seismic analysis of asymmetric multistory RC buildings,*J. Earthq. Eng.* 12(5), 704–727. doi:10.1080/13632460701673126

Kyoung, M. R., Min, S. K., and Young, H. L. (2021). A simplified approach to modeling vertically irregular structures for dynamic assessment. *J. Asian Archit. Build. Eng.* 21, 2320–2329. doi:10.1080/13467581.2021.1971682

Li, X. L., Chen, S. J., Liu, S. M., and Li, Z. H. (2021a). AE waveform characteristics of rock mass under uniaxial loading based on Hilbert-Huang transform. *J. Central South Univ.* 28 (6), 1843–1856. doi:10.1007/s11771-021-4734-6

Li, X. L., Chen, S. J., Wang, S., Zhao, M., and Liu, H. (2021b). Study on *in situ* stress distribution law of the deep mine taking Linyi Mining area as an example. *Adv. Mater. Sci. Eng.* 9 (4), 5594181–5594211. doi:10.1155/2021/5594181

Li, X. L., Zhang, X. Y., Shen, W. L., Zeng, Q., Chen, P., Qin, Q., et al. (2023). Research on the mechanism and control technology of coal wall sloughing in the ultra-large mining height working face. *Int. J. Environ. Res. Public Health* 20 (2), 868. doi:10.3390/ijerph20010868

Liu, H. Y., Zhang, B. Y., Li, X. L., Liu, C., Wang, C., Wang, F., et al. (2022). Research on roof damage mechanism and control technology of gob-side entry retaining under close distance gob. *Eng. Fail. Anal.* 138 (5), 106331. doi:10.1016/j.engfailanal.2022.106331

Liu, S. M., Li, X. L., Wang, D. K., et al. (2020). *Investigations on the mechanism of the microstructural evolution of different coal ranks under liquid nitrogen cold soaking, Energy Sources, Part A: Recovery, Utilization, and Environmental Effects*, 1–17.

Losanno, D., Ravichandran, N., Parisi, F., Calabrese, A., and Serino, G. (2021). Seismic performance of a Low-Cost base isolation system for unreinforced brick Masonry buildings in developing countries. *Soil Dyn. Earthq. Eng.* 141, 106501. doi:10.1016/j.soildyn.2020.106501

Luis E Pérez, -R., Javier, A-L., and Arturo, T-C. (2021). Base isolation for mid-rise buildings in presence of soil-structure interaction. *Soil Dyn. Earthq. Eng.* 151, 2021.

Micozzi, F., Flora, A., Viggiani, L. R. S., Cardone, D., Ragni, L., and Dall'Asta, A. (2021). Risk assessment of reinforced concrete buildings with rubber isolation systems designed by the Italian seismic code. *J. Earthq. Eng.* 26, 7245–7275. doi:10.1080/13632469.2021.1961937

Mohammad, M. P., James, B. P. L., Iman, H., and Daniel, M. (2022). Multi-directional base isolation system for coupled horizontal and vertical seismic excitations. *J. Earthq. Eng.* 26 (3), 1145–1170. doi:10.1080/13632469.2020.1713925

Mohammed, H., Miloud, H., and Djamel, N. (2021). Vulnerability of asymmetric multi-storey buildings in the context of performance-based seismic design. *Eur. J. Environ. Civ. Eng.* 25 (5), 813–834. doi:10.1080/19648189.2018.1548380

Muberra, E. A., and Ibrahim, E. (2013). Soil–structure interaction effects on seismic behaviour of multistorey structures. *Eur. J. Environ. Civ. Eng.* 17 (8), 635–653. doi:10.1080/19648189.2013.810177

Peter, F., Damjan, M., and Iztok, P. (2005). Torsional effects in the pushover-based seismic analysis of buildings. *J. Earthq. Eng.* 9 (6), 831–854. doi:10.1080/13632460509350568

Raz, N. J., and Gopal, S. P. M. (2018). Tuned mass damper positioning effects on the seismic response of a soil-MDOF-structure system. *J. Earthq. Eng.* 22 (2), 281–302. doi:10.1080/13632469.2016.1224743

Repapis, C. C., and Zeris, C. A. (2020). Performance investigation of existing RC buildings with height irregularity using the IDA procedure. *J. Earthq. Eng.* 24 (12), 1944–1974. doi:10.1080/13632469.2018.1488777

Ryan, Keri L., and Earl, Curtis L. (2010). Analysis and design of inter-story isolation systems with nonlinear devices. *J. Earthq. Eng.* 14 (7), 1044–1062. doi:10.1080/13632461003668020

Sahar, M. O., Hamzeh, S., and Ghyslaine, M. (2022). Optimal performance-based configurations of stiffness and strength centers in multi-story wall-frame asymmetric buildings including soil–structure interaction effects. *J. Earthq. Eng.* 26 (11), 5978–6014. doi:10.1080/13632469.2021.1911881

Sekhar, C. D., Pranab, K. D., and Piyali, S. (2017). Seismic behaviour of irregular structures. *Struct. Eng. Int.* 27 (4), 526–545. doi:10.2749/222137917x14881938989765

Shi-Shuenn, C., Jun-Yang, S., and Yi-Ying, W. (2019). Numerical damage localisation for building systems including dynamic soil-structure interaction. *Struct. Infrastructure Eng.* 15 (3), 362–375. doi:10.1080/15732479.2018.1552711

Soheil, R., and Mansour, Z. (2017). A value-based design approach for base-isolated structural systems. *Civ. Eng. Environ. Syst.* 34 (1), 34–52. doi:10.1080/10286608.2017.1297802

Taskin, A., and Khan, M. A. (2020). Seismic response of randomly infilled reinforced concrete frames with soft ground storey. *Aust. J. Civ. Eng.* 18 (2), 153–163. doi:10.1080/14488353.2020.1745617

Trishna, C., and Hemant, B. K. (2020). Component level fragility estimation for vertically irregular reinforced concrete frames. *J. Earthq. Eng.* 24 (6), 947–971. doi:10.1080/13632469.2018.1453413

Vasiliki, G. T. (2022). Statistical analyses on the degree of influence of various assumptions in soil-structure interaction studies. *Eng. Struct.* 252, 113750. doi:10.1016/j.engstruct.2021.113750

Yazdan, H., GholamReza, H., Abolfazl, E., and Matteo, F. (2021). *3D soil-structure interaction analysis with a combined substructure-FEM under external forces and seismic waves, Mechanics of Advanced Materials and Structures*.

Yongbo, P., Tianchen, H., and Jianbing, C. (2022). Experimental study of seismic isolated structures with sliding implant-magnetic bearings. *J. Earthq. Eng.* 26 (5), 2514–2545. doi:10.1080/13632469.2020.1767230

Zeshan, A., Li, S., Chunwei, Z., Zhongxin, S., and Bijan, S. (2021). Experimental and numerical investigation on the complex behaviour of the localised seismic response in a multi-storey plan-asymmetric structure. *Struct. Infrastructure Eng.* 17 (1), 86–102. doi:10.1080/15732479.2020.1730914

Zhou, X. M., Wang, S., Li, X. L., Meng, J., Li, Z., Zhang, L., et al. (2022). Research on theory and technology of floor heave control in semicoal rock roadway: Taking longhu coal mine in Qitaihe mining area as an Example. *Lithosphere* 2022 (11), 3810988. doi:10.2113/2022/3810988

frontiers | Frontiers in Earth Science

TYPE Original Research
PUBLISHED 03 August 2023
DOI 10.3389/feart.2023.1237280

OPEN ACCESS

EDITED BY
Xuelong Li,
Shandong University of Science and Technology, China

REVIEWED BY
Cai Peichen,
Chang'an University, China
Junbiao Yan,
Chinese Academy of Sciences (CAS), China
Peichao Li,
Shanghai University of Engineering Sciences, China

*CORRESPONDENCE
Jiachao Zhang,
jiach66zhang@163.com

RECEIVED 09 June 2023
ACCEPTED 24 July 2023
PUBLISHED 03 August 2023

CITATION
Xu Y, Zhang J, Liu Z and Cui P (2023), Study on the consolidation behavior of horizontal drainage foundation under complex aquifer formation conditions in karst regions.
Front. Earth Sci. 11:1237280.
doi: 10.3389/feart.2023.1237280

Study on the consolidation behavior of horizontal drainage foundation under complex aquifer formation conditions in karst regions

Yunbo Xu[1], Jiachao Zhang[1,2]*, Zhongyu Liu[2] and Penglu Cui[3]

[1]College of Civil Engineering, Henan University of Engineering, Zhengzhou, China, [2]School of Hydraulic and Civil Engineering, Zhengzhou University, Zhengzhou, China, [3]College of Civil Engineering, Hunan University, Changsha, China

Introduction: The consolidation behavior of horizontal drainage foundation under complex aquifer conditions in karst areas is a hot topic in the field of geotechnical engineering.

Methods: This paper presents a modified piecewise-linear model for plane-strain consolidation. In this model, the distributed drainage boundary was used to describe the drainage performance of soil layer boundaries, and the UH model considering the time effect was selected to reflect soil's rheological property. Through comparison with existing research, the validity of the calculation model in this paper was verified. Then several examples were used to analyze the consolidation behavior of the foundation under the combined action of rheological effect and distributed drainage boundaries.

Results and discussion: Numerical studies show that the phenomenon of the increase of excess pore pressure exists in the foundation of the distributed drainage boundary after considering the rheology in the early stage of consolidation. Moreover, the larger the secondary consolidation coefficient and the initial over-consolidation parameter, or the smaller the pave rate and the thickness-width ratio, the above phenomenon is more obvious. In terms of the dissipation of the pore water pressure, the larger the secondary consolidation coefficient and the initial over-consolidation parameter, the slower the pore pressure dissipation, and the smaller the pave rate or the thickness-width ratio can achieve the above effects. In terms of the impact on settlement, the above-mentioned parameters are consistent, that is, the larger the corresponding parameter, the larger the corresponding settlement value.

KEYWORDS

karst regions, consolidation, plane-strain, piecewise-linear, distributed drainage boundary

1 Introduction

In recent years, engineering safety protection has become a hot topic in geotechnical engineering. To achieve this goal, scholars have conducted corresponding research work from different perspectives. For example, many scholars (Liu and Li, 2023a; Liu et al., 2023b; Liu et al., 2023c) explored the mechanical properties of rock or soil through experimental methods, in order to provide valuable basic data for engineering safety development. In addition, some scholars (Gao et al., 2023; Zhang et al., 2023a; Li et al., 2023; Zhang et al., 2023b) studied the working mechanism of rock or soil from a

theoretical perspective. It is worth noting that the drainage and consolidation of foundation in karst areas is a branch of the above research. Among many drainage consolidation methods, laying horizontal drainage bodies has become the focus of attention in recent years. In this regard, many scholars (Nagahara et al., 2004; Liu, 2008; Chen et al., 2016a) carried out related research. Some scholars have conducted research on horizontal drainage materials (i.e., sand cushion (Nagahara et al., 2004; Chai et al., 2014), geotextiles (Chen et al., 2016b), and some scholars (Liu, 2008; Xu and Lei, 2016; Xu and Lei, 2017) conducted corresponding discussions on the optimization of horizontal drainage. Among them, the optimization of drainage channels has attracted the attention of many scholars. Regarding the optimization problem of the drainage channel, it can be attributed to the drainage boundary problem in the consolidation process in essence (Chen et al., 2020b). In this regard, highly recognized drainage boundaries include completely permeable boundaries (Terzaghi et al., 1996), mixed drainage boundaries (Gray, 1944), semi-permeable boundaries (Liu and Lei, 2013) and continuous drainage boundaries (Mei et al., 2022). It is worth noting that the above-mentioned research work is based on the full deployment of drainage bodies. Relevant studies (Chen et al., 2020a; Chen et al., 022b) have shown that most of the drainage process of foundation is concentrated in the early stage of consolidation, and it is not obvious in the middle and late stages of consolidation which the engineers are concerned about. In order to solve this problem, some scholars (Fan and Mei, 2016) proposed a method of distributed horizontal drainage. Since this method was proposed, scholars have started from a theoretical perspective to discuss the consolidation problem under the distributed drainage boundary. Some scholars have successively discussed the consolidation of single-layer (Chen et al., 2020b) and multi-layer foundations (Chen et al., 2020a) under distributed drainage boundaries based on Terzaghi's consolidation theory, and some scholars (Yao et al., 2019) applied Biot's consolidation theory to explore the distributed drainage boundary problem. However, the above researches ignore the inherent characteristics of the soft soil, that is, the nonlinear of deformation, especially the rheological characteristics.

Many experiments (Zhou and Chen, 2006; Joseph, 2014; Gui et al., 2015; Chen et al., 2016a) show that the deformation process of cohesive soil has significant rheological characteristics. To reflect this characteristic, scholars have proposed many constitutive relations. Among them, one type is composed of component models, which include Kelvin model (Wang et al., 2017), Nishihara model (Yan et al., 2017), Voigt model (Liu et al., 2015), Merchant model (Ding et al., 2022), and so on. The other is based on elastic-viscoplastic theory, such as the EVP model (Zhou et al., 2020) and the UH constitutive model considering time effects (Yao et al., 2020). In order to observe the effect of rheological properties on the consolidation process, scholars successively introduced the above constitutive model into the classic Terzaghi consolidation equation, and analyzed the consolidation behavior of soil considering the rheological effect. However, most of these studies are based on the classic Terzaghi consolidation theory. When solving related problems, users need to construct corresponding partial differential equations according to corresponding conditions. Moreover, the complexity of partial differential equations will be further strengthened according to the increase of consideration factors. This undoubtedly adds a lot of difficulty to the solution process. In order to optimize the consolidation calculation process, Fox and Beries. (1997) proposed a piecewise-linear consolidation method. This method does not require the construction of complex partial differential equations, and has a modular feature. At present, this method has been used by many scholars to study consolidation problems. For example, considering the multi-layered nature of the soil (Fox et al., 2014), the viscosity of the soil (Liu et al., 2020), the soil's structure (Shi et al., 2021), and the permeability of soil's boundary (Liu et al., 2021).

In view of the existing research status, this paper presents a modified plane-strain consolidation model, called MPSC model, based on piecewise-linear consolidation method (Deng and Zhou, 2016a; Deng and Zhou, 2016b). In MPSC model, the distributed drainage boundary (Fan and Mei, 2016) is used to reflect the drainage state of the soil, and the UH constitutive model considering the time effect (Yao et al., 2020) is used to describe the deformation process of the soil. By comparing with existing researches, the validity of the model in this paper is verified. Then, some calculation examples are applied to analyze the influence of the rheological properties of the soil under the distributed drainage boundary on the consolidation process.

2 Model description

2.1 Distributed drainage boundary

Relevant research (Chen et al., 2020a; Chen et al., 2020b) has showed that the drainage volume in the middle and late stages of consolidation that engineers were concerned about was less. In order to achieve the purpose of drainage and resource conservation, scholars (Fan and Mei, 2016) proposed the method of distributing drainage bodies. The corresponding schematic diagram is shown in Figure 1. Among them, Figure 1A is a model diagram of distributed drainage boundary, and Figure 1B is a characteristic element obtained based on symmetry.

In Figure 1A, the drainage material is arranged on the top surface of the foundation at equal intervals. Among them, the width of the paved area is $2L$, and the distance between adjacent paved areas (that is, the unpaved area) is $2D$. In this way of laying the drainage body, the pore water in the foundation first flows horizontally from the undistributed area to the distributing area, and then flows vertically within the distributing area, and finally drains out of the foundation. In essence, the problem of ground consolidation under the distributed drainage boundary (Fan and Mei, 2016) can be attributed to the plane strain problem.

2.2 Basic assumption

When establishing the MPSC model, the following assumptions are introduced here:

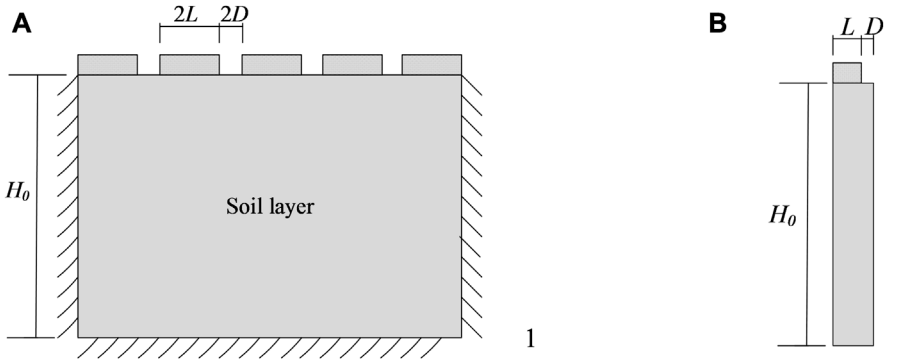

FIGURE 1
The model for the distributed drainage boundary: **(A)** the diagram of distributed drainage boundary; **(B)** the characteristic element.

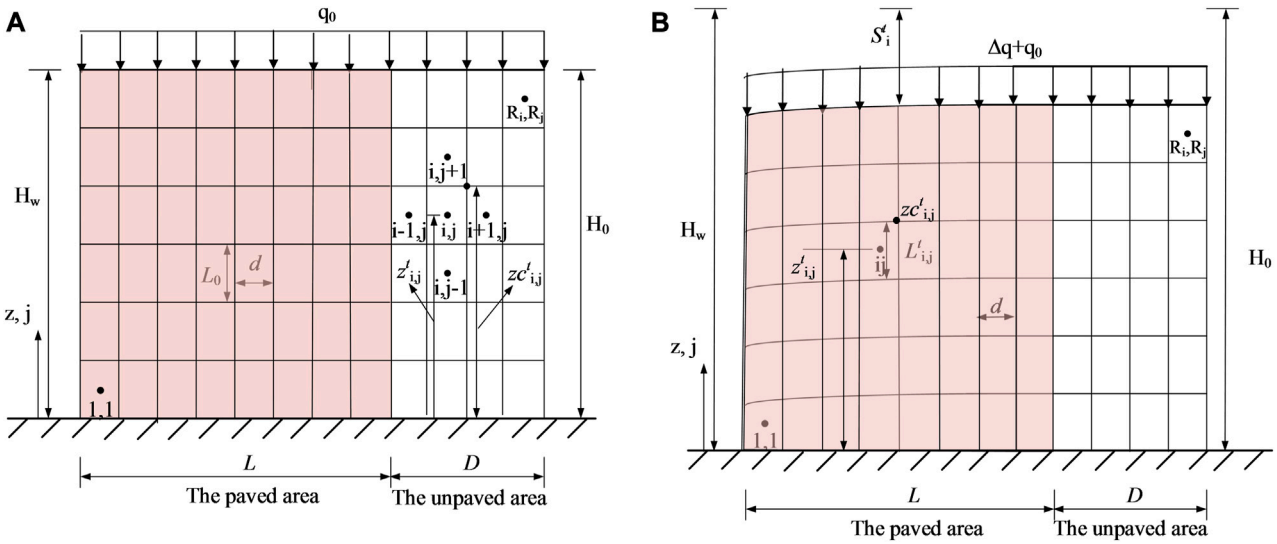

FIGURE 2
Geometry for MPSC model: **(A)** initial configuration; **(B)** during consolidation.

a.The soil is always saturated, and soil particles and pore water will not be compressed.
b.The deformation of the soil only occurs in the vertical direction, and it can be described by the UH constitutive model considering the time effect (Yao et al., 2020).
c.The top surface of the soil is a drainage surface, and can be described by distributed drainage boundaries (Fan and Mei, 2016), and other boundaries are impervious.
d.The flow of pore water in the soil conforms to Darcy's law.

2.3 MPSC model

When studying the consolidation process of distributed drainage boundary foundations, scholars (Yao et al., 2019; Chen et al., 2020b) usually choose the characteristic element (i.e., Figure 1B) for modeling. Among them, the width of the characteristic element includes two parts: a paved area with a width of L and a unpaved area with a width of D. Similar to the existing research, the MPSC model also uses the above method, and the schematic diagram is shown in Figure 2. As shown in Figure 2A, the thickness of the soil layer is H_0, and it is always in saturated state (i.e., the height of the static water surface is always H_w). At the initial moment (see Figure 2A), the soil layer is divided into $R_i \times R_j$ elements. Among them, the horizontal direction is R_i elements of equal width (d); the vertical direction is R_j elements of equal thickness (L_0). In the analysis, the center point of the element is used as the research object. In order to facilitate the calculation of the position of the corresponding element, z coordinate system with the positive direction upward is established here, and the coordinates of the center point of the element (i.e., $z^t_{i,j}$) and the coordinates of the right vertex of the

element (i.e., $z^t_{c,i,j}$) are given. Among them, $z^t_{c,i,j}$ is related to the cross-sectional area of the element (i.e., $A^t_{i,j}$), and the corresponding relationship is shown in Eq. 1. Moreover, $z^t_{i,j}$ and the thickness of the consolidated element (i.e., $L^t_{i,j}$) are related to $z^t_{c,i,j}$, and the corresponding relationship is shown in Eqs 2, 3. At the initial moment (see Figure 2A), the soil layer has been consolidated and stabilized under the original load q_0 and its own weight. When the new load Δq is applied, the soil layer enters a new consolidation stage (see Figure 2B). During the consolidation process, the deformation only occurs in the vertical direction, and the width of element in the horizontal direction is always the same. Regarding the drainage surface of the foundation, it is assumed that only the top surface is drained, and it can be described by a distributed drainage boundary. That is to say, the paved area is drainage area, and the corresponding hydraulic gradient is not equal to 0; the unpaved area is undrained area, and the corresponding hydraulic gradient is 0.

$$z^t_{c,i,j} = z^t_{c,i-1,j} + z^t_{c,i,j-1} - z^t_{c,i-1,j-1} + \frac{A^t_{i,j} - \left(z^t_{c,i-1,j} - z^t_{c,i-1,j-1}\right)d}{d/2} \quad (1)$$

$$z^t_{i,j} = \frac{z^t_{c,i-1,j} + z^t_{c,i-1,j-1} + z^t_{c,i,j} + z^t_{c,i,j-1}}{4} \quad (2)$$

$$L^t_{i,j} = \frac{z^t_{c,i-1,j} - z^t_{c,i-1,j-1} + z^t_{c,i,j} - z^t_{c,i,j-1}}{2} \quad (3)$$

2.4 Total stress of element

Regarding the plane-strain consolidation problem, (Deng and Zhou, 2016a; Deng and Zhou, 2016b) carried out corresponding research based on the piecewise-linear method. With reference to the research of Deng et al. (2016a), Deng et al. (2016b), the total stress of the corresponding element can be expressed as:

$$\sigma^t_{i,j} = \left(H_w - \frac{z^t_{c,i-1,Rj} + z^t_{c,i,Rj}}{2}\right)\gamma_w + q_0 + \Delta q + \frac{A^t_{i,j}\gamma^t_{i,j}}{2d} + \sum_{n=j+1}^{Rj}\frac{A^t_{i,n}\gamma^t_{i,n}}{d} \quad (4)$$

Where γ_w represents the specific gravity of water; $\gamma^t_{i,j}[= [G_s + e^t_{i,j})\gamma_w]/(1 + e^t_{i,j})]$ represents the saturated weight for element (i, j). The parameter G_s is the specific gravity of soil particles. Based on previous research (Fox et al., 1997) on piecewise-linear consolidation methods, the value of G_s can be defined as follows: when the self-weight of the soil is not considered, $G_s = 1$; when the self-weight of the soil is considered, the magnitude of G_s depends on the category of the soil.

2.5 Constitutive relationship

In MPSC model, it is assumed that the deformation of the soil has rheological characteristics, and the UH constitutive model considering the time effect (Yao et al., 2013; Hu and Yao, 2015) can be used to describe the above-mentioned characteristics of the soil. Regarding the UH constitutive model considering the time effect

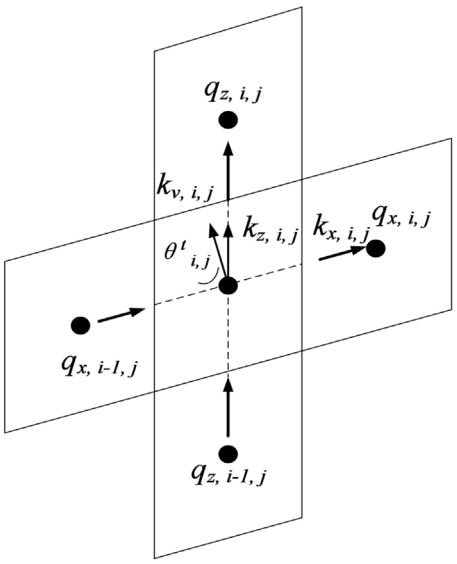

FIGURE 3
Fluid flow between contiguous elements (Deng and Zhou, 2016a).

(Yao et al., 2013; Hu and Yao, 2015), existing studies (Liu et al., 2020) have introduced it into the one-dimensional consolidation process for corresponding discussion. Among them, the relationship between effective stress and void ratio can be expressed by Eqs 5, 6). Regarding the seepage process, it is considered that the seepage process is isotropic. And, the process conforms to Darcy's law.

$$\sigma'^{t+\Delta t}_{i,j} = \frac{\sigma'^{t}_{i,j}}{1 - \frac{\left(e^t_{i,j} - e^{t+\Delta t}_{i,j}\right)\ln 10 - C_\alpha\left(R^t_{i,j}\right)^\alpha \Delta t}{C_s + \frac{(C_c - C_s)M^4}{M_f^4}}}, \quad \sigma'^{t+\Delta t}_{i,j} > \sigma'^{t}_{i,j} \quad (5)$$

$$\sigma'^{t+\Delta t}_{i,j} = \frac{C_s\sigma'^{t}_{i,j}}{C_s - \left[\left(e^t_{i,j} - e^{t+\Delta t}_{i,j}\right)\ln 10 - C_\alpha\left(R^t_{i,j}\right)^\alpha \Delta t\right]}, \quad \sigma'^{t+\Delta t}_{i,j} \le \sigma'^{t}_{i,j} \quad (6)$$

Where C_c, C_s and C_α are the compression index, the swelling index and the secondary consolidation coefficient, respectively; Δt is the time increment; M、 M_f are the stress ratio at the critical state and the potential failure stress ratio, respectively. $R^t_{i,j}$ is the over-consolidation parameter of the corresponding element at time t. The corresponding expressions for the above parameters are as follows:

$$M = 6\sin\varphi/(3 - \sin\varphi) \quad (7)$$

$$M_f = 6\left[\sqrt{\chi/R(1 + \chi/R)} - \chi/R\right] \quad (8)$$

$$R = \sigma'/\sigma'_0\exp\left[-\ln 10\varepsilon^p_v(1 + e_0)/(C_c - C_s)\right] \quad (9)$$

Where $\chi = M^2/[12(3 - M)]$; φ is the effective internal friction angle of the soil; σ'_0 is the initial effective stress adapted to the initial void ratio e_0; It is worth noting that R_0 is the initial value of the over-consolidation parameter R, and it has a reciprocal relationship with the over-consolidation ratio OCR; ε^p_v is plastic deformation.

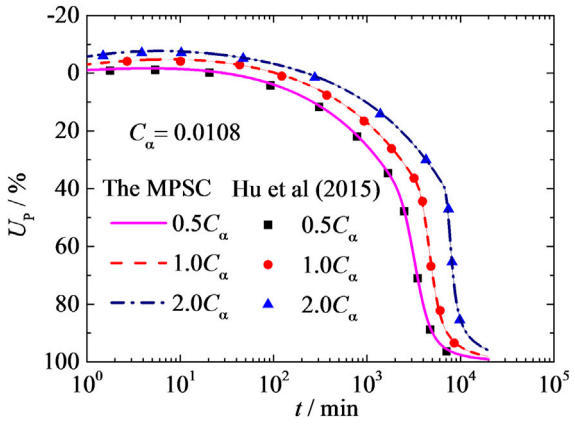

FIGURE 4
Comparison results of the average consolidation degree U_P under rheological effect.

2.6 Seepage process and settlement

After solving the total stress and effective stress, the corresponding pore pressure can be expressed as:

$$u_{i,j}^t = \sigma_{i,j}^t - \sigma'^t_{i,j} \tag{10}$$

For the seepage process, Figure 3 shows a schematic diagram of the seepage flow. It can be seen from Figure 3 that the seepage process is divided into vertical seepage and horizontal seepage. First, the vertical seepage process is introduced here. Among them, the vertical equivalent permeability coefficient can be expressed as:

$$K_{zs,i,j}^t = \frac{k_{z,i,j+1}^t k_{z,i,j}^t \left(L_{i,j+1}^t + L_{i,j}^t\right)}{L_{i,j+1}^t k_{z,i,j}^t + L_{i,j}^t k_{z,i,j+1}^t} \tag{11}$$

Where $k_{z,i,j}^t$ is the vertical permeability coefficient, and its relation to void ratio can be described by e-lg$k$ (Liu et al., 2020).

$$e = e_0 - C_k \lg(k_0/k) \tag{12}$$

Where C_k is the permeability index, which can reflect the speed of change of the permeability coefficient with void ratio.

For the upper and lower boundaries, the equivalent permeability coefficients are defined as $k_{zs,i,Rj}^t [= k_{v,i,Rj}^t]$ and $k_{zs,i,0}^t [= k_{z,i,1}^t]$.

In addition to the permeability coefficient, the vertical hydraulic gradient is

$$i_{z,i,j}^t = \frac{h_{i,j+1}^t - h_{i,j}^t}{z_{i,j+1}^t - z_{i,j}^t} \tag{13}$$

Where $h_{i,j}^t$ is the head of element (i, j) at time t, which is composed of two parts, namely the head generated $[u_{i,j}^t/\gamma_w]$ by the pore pressure and the position head $z_{i,j}^t$.

In the paper, the boundary of the top surface of the soil layer can be described by distributed drainage boundary conditions, which is composed of paved area and unpaved area. In unpaved area, the top boundary of the soil layer is impervious, that is, the vertical component of the hydraulic gradient is 0. In paved area, the vertical component of the corresponding hydraulic gradient can be expressed by Eq. 14, namely:

$$i_{z,i,Rj}^t = \frac{2\left(H_w - h_{i,Rj}^t\right)}{L_{i,Rj}^t \sin\theta_{i,Rj}^t} \tag{14}$$

For horizontal seepage, the corresponding hydraulic gradient and equivalent permeability coefficient can be expressed as:

$$i_{x,i,j}^t = \frac{h_{i+1,j}^t - h_{i,j}^t}{\sqrt{d^2 + \left(z_{i+1,j}^t - z_{i,j}^t\right)^2}} \tag{15}$$

$$K_{xs,i,j}^t = \frac{2k_{x,i,j}^t k_{x,i+1,j}^t}{k_{x,i+1,j}^t + k_{x,i,j}^t} \tag{16}$$

Where $k_{x,i,j}^t$ is horizontal permeability coefficient, which is equal to the vertical permeability coefficient $k_{z,i,j}^t$.

Then, the flow at the boundary of the element in the corresponding direction can be expressed as:

$$q_{x,i,j}^t = -K_{xs,i,j}^t i_{x,i,j}^t \left(z_{c,i,j}^t - z_{c,i,j-1}^t\right) \sin\theta_{i,j}^t \tag{17}$$

$$q_{z,i,j}^t = -K_{zs,i,j}^t i_{z,i,j}^t d \tag{18}$$

After solving the corresponding flow, related indicators (i.e., the area $A_{i,j}^{t+\Delta t}$, void ratio $e_{i,j}^{t+\Delta t}$, top surface settlement $S_i^{t+\Delta t}$, Average settlement $S_{avg}^{t+\Delta t}$) of the corresponding element at time $t + \Delta t$ can be expressed as:

$$A_{i,j}^{t+\Delta t} = A_{i,j}^t + \left(q_{x,i-1,j}^t + q_{z,i,j-1}^t - q_{x,i,j}^t - q_{z,i,j}^t\right)\Delta t \tag{19}$$

$$e_{i,j}^{t+\Delta t} = \frac{A_{i,j}^{t+\Delta t}\left(1 + e_{0,i,j}\right)}{A_{0,i}} - 1 \tag{20}$$

$$S_i^{t+\Delta t} = H_0 - z_{c,i,Rj}^{t+\Delta t} \tag{21}$$

$$S_{avg}^{t+\Delta t} = \frac{\sum_{i=1}^{Ri} S_i^{t+\Delta t}}{Ri} \tag{22}$$

Where $A_{0,j}$ is the cell cross-sectional area at the initial moment; $e_{0,i,j}$ is the void ratio of the corresponding element at the initial moment, which is judged according to the initial stress.

In order to observe the dissipation of pore pressure in the foundation, the calculation formula of excess pore pressure is given here, namely:

$$u_{ex,i,j}^t = u_{i,j}^t - u_{0,i,j} \tag{23}$$

Where $u_{0,i,j}$ is the pore pressure of the corresponding element at the initial moment.

Then, the average excess pore pressure in the foundation can be expressed as:

$$u_{ex,avg}^t = \frac{\sum_{i=1}^{Ri}\sum_{j=1}^{Rj} dL_{i,j}^t u_{ex,i,j}^t}{(L + D)H_0} \tag{24}$$

3 Model verification

3.1 Comparison considering the rheological effect of soil

In order to simulate the rheology of soil, many scholars have proposed corresponding constitutive relations. Among them, Yao

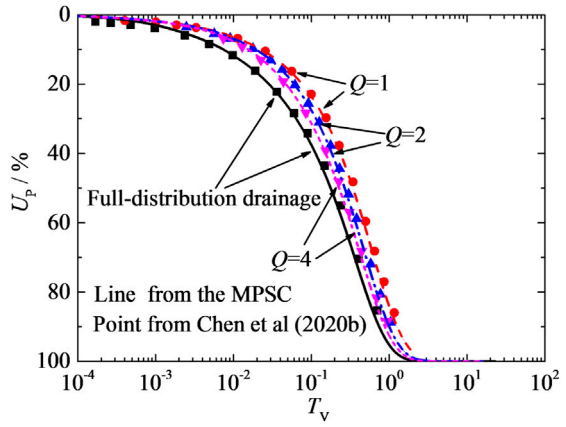

FIGURE 5
Comparison of U_P under distributed drainage boundary.

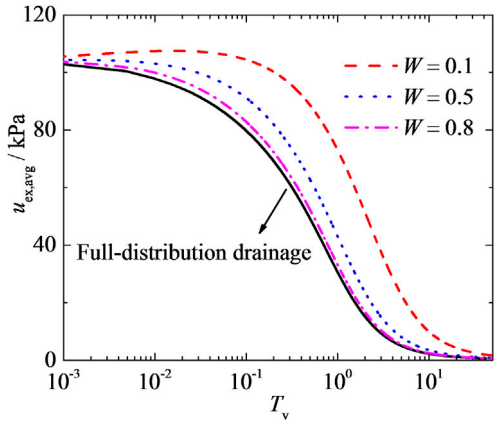

FIGURE 6
Influence of pave rate W on average excess pore pressure.

et al. (2013) proposed the UH model considering the time effect. Later, Hu and Yao, (2015) introduced its one-dimensional form into the classic Terzaghi consolidation theory and studied the effect of rheology on the consolidation process. In order to verify the validity of the MPSC model in this paper, the case provided by Hu and Yao, (2015) is used for comparison. When making comparison, the MPSC model needs to be degenerated into a one-dimensional form. The specific method is: the number of horizontal units is 1, and the top drainage boundary is a completely permeable boundary. What's more, the values of other parameters are: the soil thickness H_0=1m, H_w=1m, G_s =1.0, q_0=10kPa, e_0=0.53, Δq =90 kPa. Regarding the constitutive model, the corresponding parameter value is as follows: C_c =0.0217, C_s =0.0131, M =1.112, R_0=0.95. For the secondary consolidation coefficient, the corresponding values are 0.5 C_α, C_α and 2 C_α. Among them, C_α =0.0108. Regarding the seepage process, Darcy's law is considered to be applicable, and the permeability coefficient k=3.63 × 10^{-7} m/min and remains unchanged.

Figure 4 shows the comparison results of the average consolidation degree U_P obtained by Hu and Yao, (2015) and MPSC model in this paper. By comparing the data in Figure 4, it is found that the maximum error between the calculated results of the two methods is 2.6%. That is to say, the calculation results in this paper can better match the results of Hu and Yao, (2015). This also indicates that the calculation model in this paper is effective for the rheological consolidation calculation process.

3.2 Comparison under distributed drainage boundary

In order to optimize the layout of horizontal drainage bodies, scholars (Fan and Mei, 2016) proposed the distributed drainage boundary. Existing studies (Yao et al., 2019; Chen et al. (2020a), Chen et al. (2020b) have shown that the boundary can achieve the purpose of drainage and resource utilization. In previous studies, Chen et al. (2020b) used analytical solutions to explore the influence of the width-thickness ratio Q on the pore pressure dissipation process under the linear elastic constitutive relationship. Among them, time is expressed in a dimensionless way, and the corresponding expression is

$$T_v = \frac{C_v t}{H_0^2} = \frac{k(1+e_0)}{a\gamma_w H_0^2} t \tag{25}$$

Where a is the compression factor; e_0 is the initial void ratio.

In order to verify the correctness of the MPSC model in this paper, the above case is selected for comparison. When making comparison, the flow process of water in soil pores conforms to Darcy's law, and the UH model considering the time effect in MPSC model needs to replaced by the elastic constitutive relationship (i.e., $\Delta e = a\Delta p$) as Chen et al. (2020b). Additionally, the other conditions set in this paper in the comparison are consistent with those used by Chen et al. (2020b). The comparison results are shown in Figure 5, and the maximum error between the calculated results of the two methods is 3.4%. This indicates that the MPSC model is capable of simulating soil consolidation problems under distributed drainage boundary conditions.

4 Analysis of the consolidation behaviour

In this section, the consolidation behavior of the foundation under the combined action of the distributed drainage boundary and the rheological effect is analyzed. Among them, the indicators describing the consolidation process of the foundation include the average excess pore pressure $u_{ex,avg}$ and the average settlement S_{avg}. In the analysis, the dimensionless time is used to reflect the consolidation process, namely:

$$T_v = \frac{\sigma_0 k_0 (1+e_0)\ln 10}{C_c \gamma_w H_0^2} t \tag{26}$$

Where σ_0 is the reference stress, and e_0 and k_0 are the reference void ratio and reference permeability coefficient

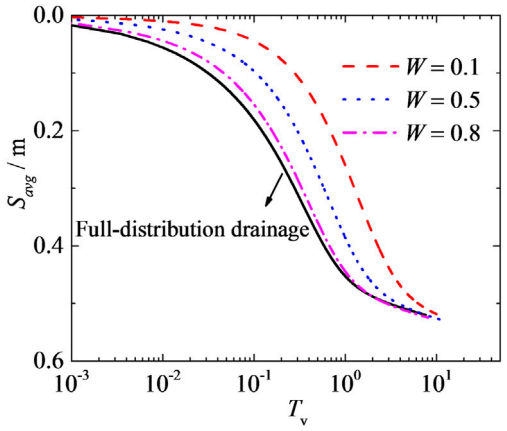

FIGURE 7
Influence of pave rate W on average settlement.

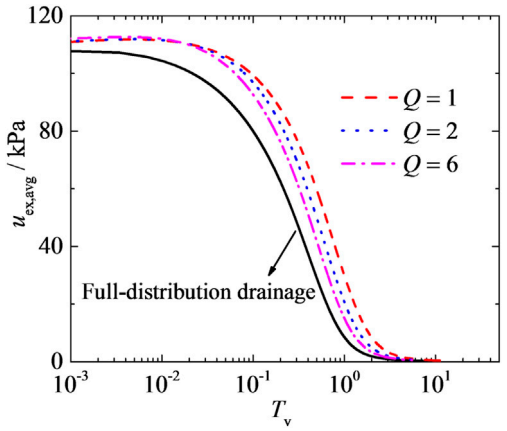

FIGURE 8
Influence of thickness-width ratio Q on average excess pore pressure.

corresponding to σ_0. In addition, the values of the parameters in the analysis are as follows: H_0=6m, H_w=6m, G_s =2.75, L+D=6 m (i.e., horizontal width), C_c =0.45, C_s =0.1, C_k =0.6, C_α =0.012, R_0=0.9, M =0.5665, the pave rate W=0.5, the thickness-width ratio Q=5.0. Regarding the load, the original load on the top of the soil is q_0 =100kPa, the new load Δq =100kPa, e_0=1.0, k_0=2.0×10^{-7} m/min. It is worth noting that when analyzing the influence of related parameters on consolidation properties, the corresponding parameters can be changed.

4.1 Influence of the pave rate on consolidation behavior

In the study of distributed drainage boundary, the pave rate W is a key parameter. Generally, the pave rate refers to the ratio of the width of the paving drainage body to the total width of the soil layer. In this case, the pave rate W is taken as 0.1, 0.5 and 0.8 in sequence. Figure 6 shows the effect of the pave rate W on the average excess pore pressure $u_{ex,avg}$. It can be found from this figure that at the initial stage of consolidation (such T_v=0.001), the average excess pore pressure $u_{ex,avg}$ is greater than the applied load (i.e., new load Δq). This is a phenomenon that has not been discovered by existing studies (Fan and Mei, 2016; Yao et al., 2019; Chen et al., 2020b) under distributed drainage boundary. Regarding the cause of this phenomenon, most one-dimensional studies (Hu and Yao, 2015; Liu et al., 2020) attribute it to rheological effects. Besides, when the boundary is a distributed drainage boundary (that is, the pave rate W is less than 1.0), the pore pressure curve is always above the full-distribution drainage boundary. This shows that the pave rate can delay the dissipation of pore pressure in the foundation. Moreover, the degree of delay will increase as the pave rate decreases. For example, at T_v = 0.4, the average excess pore pressure $u_{ex,avg}$ with the pave rates of 0.1, 0.5 and 0.8 are 95.01 kPa, 68.18 kPa, and 46.28 kPa, respectively. However, when the pave rate is 0.8, the pore pressure curve will gradually approach the pore pressure curve at the boundary of the completely arranged drainage body. This also shows that reasonable laying of horizontal drainage materials can achieve the effect of both drainage and resource conservation.

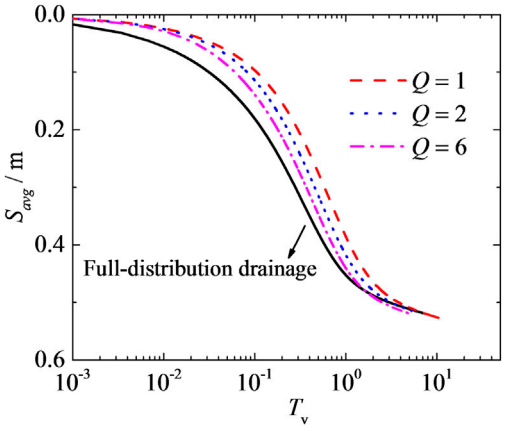

FIGURE 9
Influence of thickness-width ratio Q on average settlement.

Figure 7 shows the influence of the pave rate W on the average settlement S_{avg}. On the whole, the smaller the pave rate, the smaller the settlement at the same time. For instance, at T_v = 0.2, when the pave rate is 0.1, 0.5 and 0.8, the values of S_{avg} are 0.072 m, 0.156 m, 0.226 m, respectively. Moreover, they are respectively 0.28 times, 0.61 times, and 0.88 times of the corresponding settlement under the full-distributed drainage boundary. In other words, to reach the same value of settlement, the greater the pave rate, the shorter the time consumed. Taking S_{avg} = 0.3 m as an example, the time required for the pave rate equal to 0.8 when the settlement value is reached is only 0.26 times the pave rate equal to 0.1.

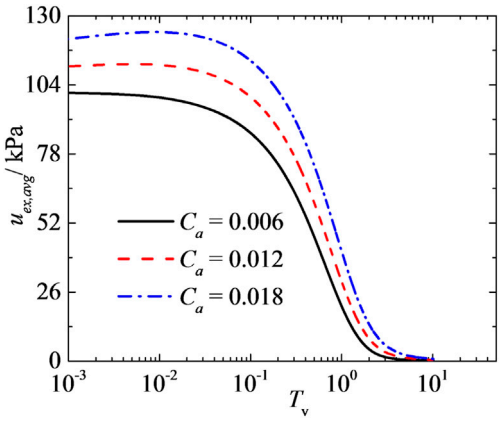

FIGURE 10
Influence of secondary consolidation coefficient on average excess pore pressure.

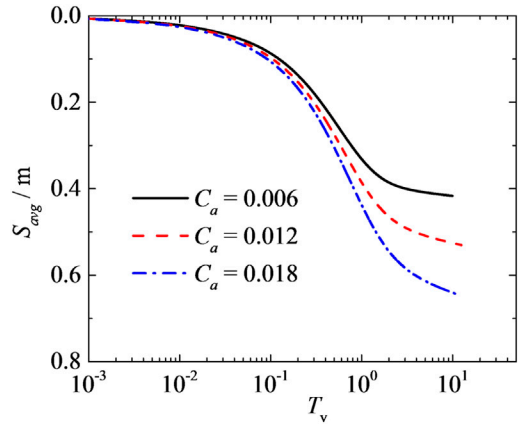

FIGURE 11
Influence of secondary consolidation coefficient on the average settlement.

4.2 Influence of thickness-width ratio *Q* on consolidation

In addition to the pave rate, the thickness-width ratio Q is also an important parameter in the study of distributed drainage boundaries. In this case, the thickness-to-width ratio is 1, 2, and 6 respectively to carry out the corresponding research. Figure 8 shows the effect of Q on $u_{ex,avg}$. Similar to the above results, after considering the effect of thickness-to-width ratio, the average pore pressure dissipation curve is also located above the pore pressure curve of the full-distributed drainage boundary. This also means that the thickness-to-width ratio can also delay the dissipation of pore pressure. Moreover, the smaller the thickness-to-width ratio, the more obvious the above-mentioned delay effect. For example, when T_v= 0.5, the average excess pore pressure when the thickness-to-width ratio is 1 is still 1.42 times the corresponding pore pressure when the value of Q is 6. It can be seen that the influence of the thickness-to-width ratio on the dissipation of pore water pressure cannot be ignored.

Figure 9 shows the thickness-to-width ratio on the average settlement S_{avg}. It can be found from this figure that the ratio mainly affects the middle and late stages of consolidation. And, as the thickness-to-width ratio decreases, the value of settlement at the same time is smaller. For example, when T_v = 0.3, the settlement when the thickness-to-width ratio is equal to 1 is only 0.73 times the corresponding settlement when the thickness-to-width ratio is equal to 6. Furthermore, it can be found from the figure that the corresponding curves considering the thickness-to-width ratio are all located above the settlement curve of the full-distribution drainage boundary. In other words, the settlement process of the foundation after considering the thickness-to-width ratio will be slower than the settlement process under the full-distributed drainage boundary.

4.3 Influence of secondary consolidation coefficient on consolidation behavior

The rheological properties of cohesive soil is an important feature that distinguishes it from other soils. The existing researches (Liu et al., 2020; Zhou et al., 2020) indicate that the coefficient of secondary consolidation is an important indicator for describing the rheological characteristics of soil. Based on this, with the secondary consolidation coefficient C_α as the representative, the influence of the rheology on the consolidation process under the distributed drainage boundary is analyzed here. In the analysis, the value of C_α is taken as 0.006, 0.012, and 0.018 in sequence.

Figure 10 shows the effect of the secondary consolidation coefficient on the average excess pore pressure. It can be found from this figure that the greater the secondary consolidation coefficient, the greater the peak average of the excess pore pressure. For example, the peak of the pore pressure when C_α = 0.018 is 1.23 times the corresponding peak of C_α =0.006. The above phenomenon has been discovered by scholars (Hu and Yao, 2015; Liu et al., 2020) in one-dimensional consolidation analysis. Moreover, scholars (Hu and Yao, 2015; Liu et al., 2020) have also provided corresponding explanations, that is, the rheological characteristics of soil cause obstruction in the discharge of pore water in the soil.

Figure 11 shows the effect of secondary consolidation coefficient on the average settlement S_{avg}. It can be seen from this figure that the larger the secondary consolidation coefficient (that is, the stronger the rheological effect), the larger the value of settlement at the same time. For example, at T_v =1.0, with the increase of the secondary consolidation coefficient, the value of the average settlement is 0.334 m, 0.391 m, 0.443 m, respectively. From this result, the settlement when the secondary consolidation coefficient is equal to 0.018 is 1.33 times the settlement when the secondary consolidation coefficient is 0.006. It can be seen that the rheological effect has a significant influence on the settlement of the distributed drainage boundary foundation. Besides, it can also be seen from Figure 11 that the greater the secondary consolidation coefficient, the greater the slope of the end of the deformation curve, and the longer it takes for the settlement of the foundation to reach a stable state. From the above analysis, it can be seen that it is very necessary to accurately measure the secondary

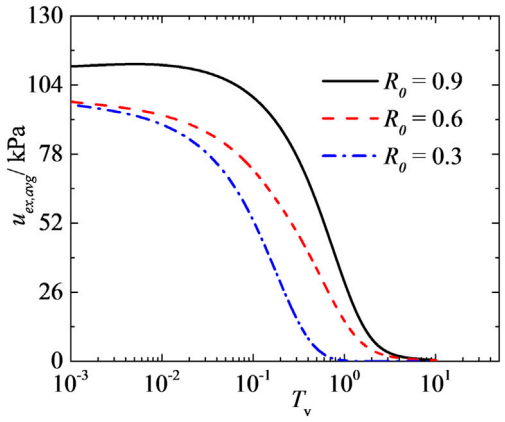

FIGURE 12
Influence of initial over-consolidation parameter R_0 on average excess pore pressure.

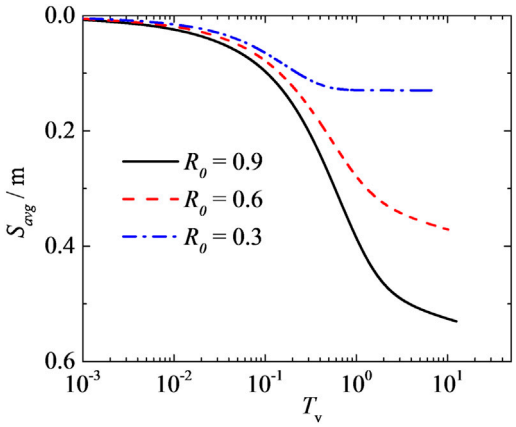

FIGURE 13
Influence of initial over-consolidation parameter R_0 on average settlement.

consolidation coefficient of soil when predicting the settlement of soil in practical engineering.

4.4 Influence of the initial over-consolidation state on consolidation behavior

The over-consolidation of soil is an important branch of consolidation research. In the UH model considering the time effect (Yao et al., 2013; Hu and Yao, 2015; Liu et al., 2020), the initial over-consolidation parameter R_0 reflect the initial over-consolidation state of the soil. In the study, the initial over-consolidation parameter R_0 is 0.3, 0.6 and 0.9 in turn. Figure 12 shows the effect of the parameter R_0 on the average excess pore pressure. From this figure, the initial over-consolidation state has significant effect on the dissipation process of the excess pore pressure in the distributed drainage boundary foundation. On the whole, the larger the value of R_0 (that is, the weaker the initial over-consolidation state), the slower the average pore pressure will dissipate. For example, at T_v = 0.2, with the increase of R_0, the corresponding average pore pressures are 28.62 kPa, 58.60 kPa and 88.25 kPa. In other words, when it dissipates to the same pore pressure value, the stronger the initial over-consolidation of the soil, the shorter the time it takes. For example, when the average excess pore pressure dissipates to 52 kPa, the dimensionless time taken when the initial over-consolidation parameters are 0.3, 0.6, and 0.9 are 0.10, 0.26, and 0.60, respectively.

Figure 13 shows the influence of the parameter R_0 on average settlement. Figure 13 shows that the initial over-consolidation state of the soil has a significant impact on the settlement process of the foundation. For the same moment, the smaller the initial over-consolidation parameter R_0, the smaller the corresponding average settlement. For example, when the dimensionless time T_v = 1, as the initial over-consolidation parameter increases, the corresponding settlement values are 0.129 m, 0.281 m, and 0.389 m. It can be seen that the settlement at this moment when the initial over-consolidation parameter is 0.9 is 3.02 times the corresponding settlement when the initial over-consolidation parameter is 0.3. In addition, it can also be seen from the figure that the stronger the degree of initial over-consolidation, the shorter the time it takes for the foundation to enter a stable state. For example, when the dimensionless time T_v is equal to 1, the foundation has reached a stable state when the initial over-consolidation parameter is equal to 0.3, but the deformation of the foundation when the initial over-consolidation parameter is equal to 0.6 and 0.9 is still in progress. This also indicates that preloading is an effective method to reduce post construction settlement.

5 Conclusion

Considering soil's rheology and the distributed drainage boundary, this paper presents a modified piecewise-linear model for plane-strain consolidation. By comparing with the existing research, the validity of the consolidation model in this paper was verified. Finally, several calculation examples were used to discuss the consolidation behavior of the foundation under the combined action of distributed drainage boundaries and rheological effects. The main conclusions are as follows:

1. After considering the rheological behavior of the soil, there is an increase in pore pressure in the soil layer. Moreover, other factors (i.e., the initial over-consolidation parameter, the pave rate and the thickness-to-width ratio) can have a further impact on above phenomenon.
2. Distributed drainage boundaries can delay the consolidation process of soil. Moreover, reasonable selection of the pave rate and the thickness-to-width ratio can achieve the purpose of consolidation drainage and resource saving.
3. With the increase of rheological effect, the dissipation of pore pressure of distributed drainage boundary foundation slows down at the same time, but the process of foundation settlement speeds up.
4. The larger initial over-consolidation parameter, the slower the pore pressure dissipation in the distributed drainage boundary foundation, but the faster the foundation settlement.

Data availability statement

The original contributions presented in the study are included in the article/supplementary material, further inquiries can be directed to the corresponding author.

Author contributions

Conceptualization: YX, JZ; Methodology: ZL; Writing and editing: YX, JZ; Verification and editing: PC. All authors contributed to the article and approved the submitted version.

Funding

This work is supported by the National Natural Science Foundation of China (Grant No. 51578511), and the support is gratefully acknowledged. All the authors are highly thankful to the reviewers for their fruitful comments to improve the quality of the paper.

Conflict of interest

The authors declare that the research was conducted in the absence of any commercial or financial relationships that could be construed as a potential conflict of interest.

Publisher's note

All claims expressed in this article are solely those of the authors and do not necessarily represent those of their affiliated organizations, or those of the publisher, the editors and the reviewers. Any product that may be evaluated in this article, or claim that may be made by its manufacturer, is not guaranteed or endorsed by the publisher.

References

Chai, J. C., Horpibulsuk, S., Shen, S. L., and Carter, J. P. (2014). Consolidation analysis of clayey deposits under vacuum pressure with horizontal drains. *Geotext. Geomembranes* 42 (5), 437–444. doi:10.1016/j.geotexmem.2014.07.001

Chen, Y. T., Wang, G. J., Meng, F. Q., and Xu, Y. (2016a). Application and analysis of the geotextile composite cushion in the ground improvement of the new dredger fill. *Chin. J. Geotech. Eng.* 38 (S1), 169–172. doi:10.11779/CJGE2016S1032

Chen, Z. B., Kong, Q. P., Zhu, J. G., and Zhang, S. F. (2016b). Experimental study on behavior of secondary consolidation of soft soils considering upper soil layers' stress under repeated cyclic loading. *J. Cent. South Univ. Sci. Tech.* 47 (10), 3507–3514. doi:10.11817/j.issn.1672-7207.2016.10.030

Chen, Z., Ni, P. P., Chen, Y. F., and Mei, G. X. (2020b). Plane-strain consolidation theory with distributed drainage boundary. *Acta Geotech.* 15 (2), 489–508. doi:10.1007/s11440-018-0712-z

Chen, Z., Zhang, F., Chen, Y. F., Hu, S. W., Mei, G. X., Zhang, H., et al. (2020a). Pituitary-derived circular RNAs expression and regulatory network prediction during the onset of puberty in landrace × yorkshire crossbred pigs. *Eng. Mech.* 37 (1), 135–144. doi:10.3389/fgene.2020.00135

Deng, A., and Zhou, Y. D. (2016a). Modeling electroosmosis and surcharge preloading consolidation I: Model formulation. *J. Geotech. Geoenviron.* 142 (2), 04015093. doi:10.1061/(ASCE)GT.1943-5606.0001417

Deng, A., and Zhou, Y. D. (2016b). Modeling electroosmosis and surcharge preloading consolidation II: Validation and simulation results. *J. Geotech. Geoenviron.* 142 (2), 04015094. doi:10.1061/(ASCE)GT.1943-5606.0001418

Ding, P., Xu, R. Q., Zhu, Y. H., and Wen, M. J. (2022). Fractional derivative modelling for rheological consolidation of multilayered soil under time-dependent loadings and continuous permeable boundary conditions. *Acta Geotech.* 17, 2287–2304. doi:10.1007/S11440-021-01417-0

Fan, H. B., and Mei, G. X. (2016). Finite element consolidation analysis with distributed drainage boundaries in homogeneous ground. *J. PLA. Univ. Sci. Tech.* 17 (5), 438–444. doi:10.12018/j.issn.1009-3443.20160519002

Fox, P. J., and Berles, J. D. (1997). CS2: A piecewise-linear model for large strain consolidation. *Int. J. Numer. Anal. Metall.* 21 (7), 453–475. doi:10.1002/(SICI)1096-9853(199707)21:7<453::AID-NAG887>3.0.CO;2-B

Fox, P. J., Pu, H. F., and Berles, J. D. (2014). CS3: Large strain consolidation model for layered soils. *J. Geotech. Geoenviron.* 140 (8), 04014041. doi:10.1061/(ASCE)GT.1943-5606.0001128

Gao, Y., Yu, Z., Chen, W., Yin, Q., Wu, J., and Wang, W. (2023). Recognition of rock materials after high-temperature deterioration based on SEM images via deep learning. *J. Mater Res. Technol.* 25, 273–284. doi:10.1016/j.jmrt.2023.05.271

Gray, H. (1944). Simultaneous consolidation of contiguous layers of unlike compressible soils. *Trans. ASCE* 70 (2), 149–166.

Gui, Y., Yu, Z. H., Liu, H. M., Cao, J., and Wang, Z. C. (2015). Secondary consolidation properties and mechanism of plateau lacustrine peaty soil. *Chin. J. Geotech. Eng.* 37 (08), 1390–1398. doi:10.11779/CJGE201508005

Hu, J., and Yao, Y. P. (2015). One-dimensional consolidation analysis of UH model considering time effect. *J. B. Univ. Aeronaut. Astronaut.* 41 (8), 1492–1498. doi:10.13700/j.bh.1001-5965.2014.0583

Joseph, P. G. (2014). Viscosity and secondary consolidation in one-dimensional loading. *Geotech. Res.* 1 (3), 90–98. doi:10.1680/gr.14.00008

Li, X. L., Zhang, X. Y., Shen, W. L., Wang, Y., Qin, Q., Lu, X., et al. (2023). Abutment pressure distribution law and support analysis of super large mining height face. *Int. J. Env. Res. Pub He* 20 (2), 227. doi:10.3390/ijerph20010227

Liu, J. C., and Lei, G. H. (2013). One-dimensional consolidation of layered soils with exponentially time-growing drainage boundaries. *Comput. Geotech.* 54 (10), 202–209. doi:10.1016/j.compgeo.2013.07.009

Liu, J. C., Lei, G. H., and Wang, X. D. (2015). One-dimensional consolidation of visco-elastic marine clay under depth-varying and time-dependent load. *Mar. Georesour. Geotec.* 33 (4), 337–347. doi:10.1080/1064119X.2013.877109

Liu, J. F. (2008). Requirements of thickness of sand mats for consolidation method. *Chin. J. Geotech. Eng.* 30 (3), 366–371. doi:10.3321/j.issn:1000-4548.2008.03.010

Liu, S. M., and Li, X. L. (2023a). Experimental study on the effect of cold soaking with liquid nitrogen on the coal chemical and microstructural characteristics. *Environ. Sci. Pollut. R.* 30 (3), 36080–36097. doi:10.1007/s11356-022-24821-9

Liu, S. M., Sun, H. T., Zhang, D. M., Yang, K., Li, X., Wang, D., et al. (2023c). Experimental study of effect of liquid nitrogen cold soaking on coal pore structure and fractal characteristics. *Energy* 275 (7), 127470. doi:10.1016/j.energy.2023.127470

Liu, S. M., Sun, H. T., Zhang, D. M., Yang, K., Wang, D., Li, X., et al. (2023b). Nuclear magnetic resonance study on the influence of liquid nitrogen cold soaking on the pore structure of different coals. *Phys. Fluids* 35 (1), 012009. doi:10.1063/5.0135290

Liu, Z. Y., Zhang, J. C., Duan, S. Q., Xia, Y. Y., and Cui, P. L. (2020). A consolidation modelling algorithm based on the unified hardening constitutive relation and Hansbo's flow rule. *Comput. Geotech.* 117, 103233. doi:10.1016/j.compgeo.2019.103233

Liu, Z. Y., Zhang, J. C., Yang, C. Y., and Xu, C. Y. (2021). Piecewise-linear model for one-dimensional consolidation considering Non-Darcian flow under continuous drainage boundary. *Int. J. Geomech.* 21 (5), 06021011. doi:10.1061/(ASCE)GM.1943-5622.0002017

Mei, G. X., Feng, J. X., Xu, M. J., and Ni, P. P. (2022). Estimation of interface parameter for one-dimensional consolidation with continuous drainage boundary conditions. *Int. J. Geomech.* 22 (3), 04021292. doi:10.1061/(ASCE)GM.1943-5622.0002300

Nagahara, H., Fujiyama, T., Ishiguro, T., and Ohta, H. (2004). FEM analysis of high airport embankment with horizontal drains. *Geotext. Geomembranes* 22 (1), 49–62. doi:10.1016/S0266-1144(03)00051-7

Shi, J. S., Ling, D. S., and Niu, J. J. (2021). SCS: A one-dimensional piecewise-linear large strain consolidation model for structured soils. *Int. J. Numer. Anal. Metall.* 45 (17), 2541–2564. doi:10.1002/nag.3276

Terzaghi, K., Peck, R. B., and Mesri, G. (1996). *Soil mechanics in engineering practice*. New York, NY, USA: John Wiley and Sons, 229–231.

Wang, L., Sun, D. A., Li, P. C., and Xie, Y. (2017). Semi-analytical solution for one-dimensional consolidation of fractional derivative viscoelastic saturated soils. *Comput. Geotech.* 83, 30–39. doi:10.1016/j.compgeo.2016.10.020

Xu, L. D., and Lei, G. H. (2016). Effect of horizontal sand drainage cushion on consolidation efficiency of natural ground. *J. Hehai Univ. Nat. Sci.* 44 (1), 78–83. doi:10.3876/j.issn.1000-1980.2016.01.013

Xu, L. D., and Lei, G. H. (2017). Effect of sand blanket on efficiency of ground consolidation with prefabricated vertical drains and its design method. *J. Cent. South. Univ. Sci. Tech.* 48 (4), 1035–1043. doi:10.11817/j.issn.1672–7207.2017.04.025

Yan, B. Q., Guo, Q. F., Ren, F. H., and Cai, M. F. (2017). Modified Nishihara model and experimental verification of deep rock mass under the water-rock interaction. *Int. J. Rock. Mech. Min.* 83, 104250–104339. doi:10.1016/j.ijrmms.2020.104250

Yao, R. D., Ni, P. P., Mei, G. X., and Zhao, Y. L. (2019). Numerical analysis of surcharge preloading consolidation of layered soils via distributed sand blankets. *Mar. Georesour. Geotec.* 37 (8), 902–914. doi:10.1080/1064119X.2018.1506529

Yao, Y. P., Huang, J., Zhang, K., and Cui, G. Z. (2020). Numerical back-analysis of creep settlement of airport high fill. *Rock Soil Mech.* 41 (10), 3395–3404+3414. doi:10.16285/j.rsm.2020.0402

Yao, Y. P., Kong, L. M., and Hu, J. (2013). An elastic-viscous-plastic model for over-consolidated clays. *Sci. China Technol. Sc.* 56 (2), 441–457. doi:10.1007/s11431-012-5108-y

Zhang, J. C., Li, X. L., Qin, Q. Z., Wang, Y. B., and Gao, X. (2023b). Study on overlying strata movement patterns and mechanisms in super-large mining height stopes. *B Eng. Geol. Environ.* 82 (3), 142. doi:10.1007/s10064-023-03185-5

Zhang, L. B., Shen, W. L., Li, X. L., Wang, Y., Qin, Q., Lu, X., et al. (2023a). Abutment pressure distribution law and support analysis of super large mining height face. *Int. J. Env. Res. Pub He* 20 (1), 227. doi:10.3390/ijerph20010227

Zhou, F. X., Wang, L. Y., and Liu, H. B. (2020). A fractional elasto-viscoplastic model for describing creep behavior of soft soil. *Acta Geotech.* 16 (1), 67–76. doi:10.1007/s11440-020-01008-5

Zhou, Q. J., and Chen, X. P. (2006). Test study on properties of secondary consolidation of soft soil. *Rock Soil Mech.* 27 (3), 404–408. doi:10.16285/j.rsm.2006.03.014

frontiers | Frontiers in Earth Science

TYPE Original Research
PUBLISHED 01 September 2023
DOI 10.3389/feart.2023.1222959

OPEN ACCESS

EDITED BY
Chao Liu,
Nanjing University of Information Science and Technology, China

REVIEWED BY
Shiwen Teng,
Ocean University of China, China
Markus Olin,
VTT Technical Research Centre of Finland Ltd., Finland

*CORRESPONDENCE
Jiabing Zhang,
zjb22@mails.jlu.edu.cn

RECEIVED 23 May 2023
ACCEPTED 17 August 2023
PUBLISHED 01 September 2023

CITATION
Zhang X, Zhang J, Li X and Ren X (2023), Stochastic dynamics construction of a three-dimensional microstructure of red clay.
Front. Earth Sci. 11:1222959.
doi: 10.3389/feart.2023.1222959

Stochastic dynamics construction of a three-dimensional microstructure of red clay

Xiaohu Zhang[1], Jiabing Zhang[2]*, Xin Li[1] and Xiao Ren[3]

[1]School of Civil Engineering, Guizhou University of Engineering Science, Bijie, China, [2]College of Construction Engineering, Jilin University, Changchun, China, [3]Library, Guizhou University of Engineering Science, Bijie, China

Constructing a microstructure of red clay is an important part of studying the physical and mechanical properties of red clay. The study of red clay microstructure is generalized. The red clay matrix and pores are regarded as two types of randomly moving particles, and the microstructure model of three-dimensional red clay random porous media is established from the Langevin equation of the phase separation process in stochastic dynamics, using the separation and aggregation of the two particles. The model controls the evolution process of the porous medium by artificially controlling the particle placement. Here, the trends of porosity, average pore length, Euler's number, and the fractal dimension of the porous medium during the evolution process under different parameter conditions (smooth length Δ and rise and fall term η) are calculated, and a feasible method for surviving the microstructure of red clay is summarized. Due to the consideration of the interaction forces between the solid- and void-phase particles, the porous media generated by this model are more similar to the real porous media in nature, with connected and unconnected pore structures and tortuous pore channels. Finally, the red clay of Bijie, Guizhou, is modeled as an example to prove the feasibility of the method.

KEYWORDS

red clay, porosity, stochastic dynamics, numerical simulation, microstructure

1 Introduction

Red clay is reddish-brown, highly plastic clay formed by the weathering of carbonate rocks in a hot and humid climate. Red clay is widely distributed in Bijie, Guizhou, an area rich in karst landscapes. Red clay has strong sensitivity to water; its strength weakens when it is exposed to water and shrinks and cracks when it is dry, so water has a strong influence on red clay in terms of seasonal alternation. Rainfall and dryness can lead to the loss and destruction of the red clay surface layer, causing large economic losses and affecting the survival and safety of local residents (Tan et al., 2015).

Because of the strong sensitivity of red clay to water, the loss of water will form a large number of microscopic pores in red clay (Tang et al., 2007). At present, scholars' research on the microscopic pore structure of red clay is mainly focused on the following two aspects: microstructure evolution law and microstructure model construction.

First, in terms of the microstructure evolution law of red clay, many scholars have studied the change law of its microstructure under different influencing factors. Pan et al. (2021) studied the effect of acidity and alkalinity on the microstructure of red clay, and acidic and alkaline solutions erode the structure of the clay matrix and destroy its internal pore structure distribution, which in turn reduces the shear strength, cohesion,

and internal friction angle. Li (2021) used microorganisms to improve red clay and found that the mineral composition of red clay changed significantly under the action of microorganisms, and there was a significant amount of precipitation of calcium carbonate on the surface of the particles, which was cemented by calcium carbonate. The soil particles filled the pore spaces of soil, enhanced the connection between soil particles, and obviously improved the shear strength of red clay. Mou et al. (2021) studied the microstructural evolution pattern of red clay under alkali contamination conditions and found that ammonia contamination could change the surface of soil particles from smooth to rough, accompanied by the pattern of pore enlargement and diffusion, and explored the reasons for the occurrence of the pattern. Cai et al. (2021) studied the evolution law of red clay microstructure under dry and wet cycles and found that its pore size distribution curve showed the characteristics of bimodal and single peak distributions. Wang (2020) studied the microstructural characteristics of artificially cemented red clay and found that the size law of lateritization followed the order colloidal content >dry and wet cycles >maintenance time, and the maximum growth rate of the pore volume of these three factors in the process of red clay lateritization was 31%, 5.6%, and 0.35%, respectively. Jiaming et al. (2020) studied the microstructure of zinc-contaminated red clay and found that red clay particles under the condition of doping with zinc ions were mainly observed in the structural skeleton of stacked flakes and blocks, and the doping of zinc ions reduced the strength of red clay, increased the matrix porosity and fractal dimension, and formed an unstable structure. Ke et al. (2019) studied the effect of freezing on the microstructure of red clay and found that after freezing occurred, the ice crystal action had an extrusion effect on soil particles, leading to the destruction of the surrounding soil particles and causing an increase in large pores and reduction of small pores. Overall, the soil porosity decreases after freezing. He et al. (2018) studied the effect of an external admixture on the microstructure of red clay, prepared a comparative analysis of the microstructure via electron microscopy scanning, and established a model to quantify the brittleness index of red clay. Jun et al. (2018) found that with the increase in shear force, the particles in the soil were elongated and the pore directionality was better, while in the case of soaked alkali solution, the particles in the soil maintained their roundness, and their pore directionality was poor. Jinghe et al. (2018) found that mixing sand and fly ash in red clay can fundamentally change the soil structure and improve its stability and strength. Qi et al. (2017) found that the changes in the specific physical properties of red clay under high alkali contamination conditions were caused by a combination of microscopic pore area, particle number, new salt filling inside the microscopic pores, and the adsorption of substances in the solution by clay minerals.

Second, in terms of microstructure models, Taixu et al. (2019) used image analysis software to extract and process the SEM image of red clay soils and quantitatively analyzed the morphological characteristics of the pore structure in red clay soils using the fractal dimension. Cai et al. (2018) analyzed the relationship between evolution parameters and the pore ratio on the macroscopic and microscopic scales of red clay soils and proposed a microstructure model of unsaturated soils with a double pore structure and verified its feasibility. Tao et al. (2011) analyzed the mineral composition and microstructural characteristics of red clay, proposed a soil microstructure model, analyzed the influence of the microstructure on the physical properties of this type of red clay, and obtained a pore ratio consistent with the experimental results. Jie et al. (2021) extended the DDA algorithm to study large pores and cementation effects of clay, constructed a microstructure model with a pore ratio close to that of the as-built soil, and performed numerical calculations. Zhi-Tian Qiao established a two-dimensional microstructure model for clayey soils using the Monte Carlo random placement, which provided a prototype for studying the micromechanical behavior of clay (Ping et al., 2020). Zuo et al. (2019) used a fractal model of porous media in geotechnical bodies to reasonably predict the macroscopic physical characteristics, such as porosity, and concluded that red clay particles and their pore distributions exhibit fractal characteristics. Guo et al. (2017) established a microstructural model for the discontinuous deformation analysis of soil samples based on numerical graphical analysis and particle morphology extraction, which was verified by compression tests. Zhou et al. (2012) established a microscopic "grain collection" model of red clay, used the model to analyze and interpret the theoretical analysis results under engineering conditions, and conducted a 3-week compression simulation to prove that the model can better reflect the macroscopic mechanical effects of red clay. Liu et al. (2011) introduced structural elements describing the properties of chalky particles into the clay mineral structure model, proposed a microstructure combination element model for soft rocks, established a reformation model for soft rock softening using the reformation group method, and analyzed the critical criterion for the microstructure evolution of the soft rock softening process. Tan and Kong (2001) proposed a structural model for soil gel cementation, which reasonably explained the high water content of red clay. The contradictory phenomena of high water content, high porosity ratio, and high plasticity with high bearing capacity and low compressibility of red clay soils were explained reasonably.

The aforementioned studies on red clay microstructural models are based on the structural evolution process under the action of exogenous factors or the establishment of macroscopic physical models. Meanwhile, the theoretical construction of the physical model of red clay microstructure is universal, and however, the structural model established cannot be applied to all types of red clay. The formation of a red clay microstructure results from the joint action of microcluster particle polymerization and granulation process. To elucidate the formation characteristics of red clay microstructure, this paper aims to establish a numerical model of the microstructure of red clay porous media, describe the polymerization and separation process of red clay microclusters by using the phase separation equation, and estimate the approximation of the microstructure model of red clay by using the multi-parameter coupling method. The article also investigates the change process of the parameters such as porosity, Euler's number, fractal dimension, and feature length during the iterative approximation process, which proves the usability of the method in constructing the red clay microstructure model.

2 Model establishment

2.1 Hypotheses on the evolution of the microporous structure of red clay

Red clay refers to a type of red clay soil containing more clay particles and rich in iron and aluminum oxide cementation formed under hot and humid climatic conditions after a certain type of red clay soil formation. In the formation process of red clay, the carbonate rock undergoes weathering, micro-granulation, and later modification of microgranules, and when the parent rock undergoes this complete process of soil formation, red clay is formed.

In the weathering process, iron sulfide, oxide, carbonate, etc., in the rock will form free iron and acidic aqueous solution after oxidation, carbonation, and hydrolysis. In the acidic aqueous medium, free iron, aluminum colloids, kaolinite, etc., under the action of the electrostatic force, were linked to a porous, water-containing, rough surface and irregularly shaped structural units. Moreover, in the acidic aqueous solution, free iron, aluminum, and silica gel are adsorbed together to form a double electric layer, which is linked to a colloid in combination with water, and this colloid binds the structural units into larger aggregates.

In the process of micro-granulation, when red clay, which is in the overall cemented state mentioned previously, encounters high temperature and dry climate conditions, cracks appear in its internal contraction due to water loss. When it rains, water penetrates along the cracks and wedges through the transfer of water from the film, weakening the cementation bond. Certainly, it is not excluded that free iron, aluminum, silica gel, etc., that leached out due to prolonged rainwater soaking will coalesce to form a new adhesive linkage. The continuous drying and wetting cycle promoted the breakdown of the cementation of the whole red clay block into fine particles and structural units composed of bulk red clay.

In the middle-to-late Pleistocene, the bulk red clay formed through micro-cluster granulation; since there was no hot and humid climatic conditions, the leaching effect was weak, the structural unit body showed a certain degree of solidification and compaction, and a small amount of free iron, aluminum, and silica re-gelatinized, followed by the formation of the modern sense of the honeycomb red clay, with a small natural density, high water content, large pore ratio, high liquid and plastic limit, medium-to-low compression, and a medium-to-high strength of the characteristics.

The formation process of red clay involves the aforementioned three steps; weathering carries out rock decomposition and the formation of particles; the hydrolysis of these particles and metal ions is carried out under the action of the electrostatic force of the combination of aggregates. Micro-granulation further breaks down these aggregates. The soil-forming action of the free elements and the granulation and formation of particles results in the solidification and compaction under the action of re-cementation. The effect of the aforementioned three processes on the microscopic pore structure of red clay can be attributed to the polymerization and separation of the cementing compounds. The collodion can either be externally or internally added to the structure. With a fixed computational region, the porosity of the system decreases with the continuous addition of the externally added binders whereas increases if the binders are continuously reduced.

The Langevin equation can better simulate the polymerization and separation process of the two-phase or multi-phase system, and it can also better simulate the polymerization and separation process of the binder in the microstructure of red clay, so as to realize the simulation of the microporosity structure of red clay. In fact, the pore structure characteristics of various types of red clay can be simulated by modifying the control equation.

2.2 Langevin process

The original Langevin equation describes Brownian motion, which describes the irregular motion of particles in a liquid due to collisions of liquid molecules. The Langevin equation has many forms but is usually expressed as follows: the rate of a slow-moving physical quantity is the sum of the minimum coarse free energy F of the system and a random noise term (Zhang et al., 2019), which is mathematically expressed as follows:

$$\frac{d\phi}{dt} = -M\left(-\nabla^2\right)^a \frac{\delta F}{\delta \phi} + H, \tag{1}$$

where ϕ represents the computational region, M represents the kinetic energy, t represents the time, and H represents the random noise term, i.e., the rise and fall term, which satisfies the following equation:

$$\langle H(\mathbf{r}_1, t_1)\rangle\langle H(\mathbf{r}_2, t_1)\rangle = 2k_B T M \nabla^{2a}\delta(t_1 - t_2), \tag{2}$$

$$\langle H(\mathbf{r}, t)\rangle = 0, \tag{3}$$

where $\boldsymbol{r}$, $\boldsymbol{r}_1$, and $\boldsymbol{r}_2$ denote the position vectors; t, t_1, and t_2 denote time; δ denotes the Dirac δ-function; k_B denotes the Boltzmann constant; and T denotes the Kelvin temperature.

If ϕ represents a non-conservative field, then Eq. 1 and Eq. 2 have $a = 0$; if ϕ represents a conservative field, then we have $a = 1$. The rise and fall term η is a quantity that is independent of the time space but increases with the temperature. As mentioned previously, the kinetics of Langevin depends on the form of the free energy in the form of F. Usually, the minimum free energy F consists of two components, the surface energy and the volume energy, given as follows:

$$F(\phi) = \int d\mathbf{r}\left[f(\phi) + h\left(\nabla\phi, \nabla^2\phi, \ldots\right)\right], \tag{4}$$

where f and h denote the volume free energy and the surface free energy, respectively; the simplest form of the volume free energy and the surface free energy of a two-phase system is given as follows:

$$\begin{aligned} f &= \frac{1}{2}\mu\phi^2 + \frac{1}{4}w\phi^4, \\ h &= \frac{1}{2}\kappa\left|\nabla\phi^2\right|. \end{aligned} \tag{5}$$

Here, μ, w, and κ denote the constants, and for a two-phase system, $\mu > 0$ and $w > 0$.

Figure 1 shows that the function f has two energy minima corresponding to the energy equilibrium states of the two phases, and if the volume energies of the two phases are equal, the depths of the two minima are also equal. This property can be used to model

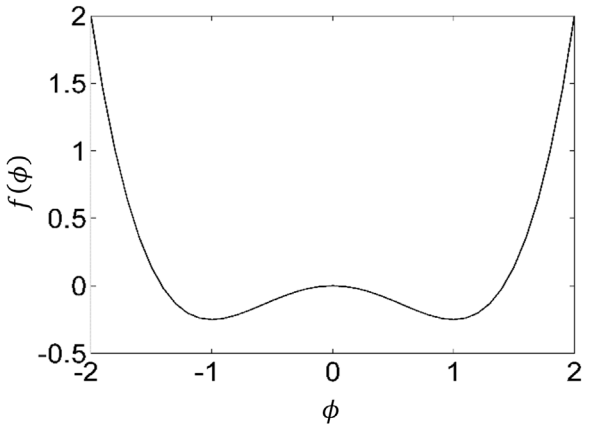

FIGURE 1
Volume free energy characterization of two-phase systems.

the kinetic process of the transition between the disorder and order, while φ can represent the lattice density of the phase:

$$\frac{d\phi}{dt} = -M\left(\mu\phi + w\phi^3 - \kappa\nabla^2\phi\right) + H. \tag{6}$$

The aforementioned kinetic process includes the growth evolution of each phase in the region, and the values of the two phases correspond to $\phi = \pm\text{sqrt}(|\kappa|w)$, respectively, while the values near the interface between the two phases vary continuously from $\phi = -\text{sqrt}(|\kappa|w)$ to $\phi = +\text{sqrt}(|\kappa|w)$, and the value of $\phi = 0$ can be considered as the boundary between the two phases.

If we assume that the initial region of pore structure generation is randomly filled with pore particles and solid particles, there is only a repulsive force and no attractive force between these two particles; the volume free energy between them follows the simple form of F mentioned previously. Then, the dynamic phase separation process between pore particles and solid particles can be understood as the evolutionary process of solid skeleton and pore structure formation, in which homogeneous particles accumulate together because of the gravitational force and the heterogeneous particles separate because of the repulsive force. Therefore, to some extent, the physical characteristics of this two-phase separation process can be used to model the microstructure of the generated porous media, that is, the solid phase when $\phi > 0$ and the pore phase when $\phi < 0$.

For the aforementioned Langevin dynamics process, the statistical mean value of its noise term $<H(\boldsymbol{r},t)\geq 0$, i.e., the number of solid-phase particles and pore-phase particles applied to the computational region is equal at each iteration of the system, so that the percentage of pores will eventually converge to 50%. To obtain a smaller porosity in the dynamic evolution in order to reach the porosity range of an ordinary porous medium, the mean value of the noise is taken to be greater than zero in this paper, which means that more solid-phase noise is randomly applied to the computational region in each iteration. $<H(\boldsymbol{r},t)\geq 0$ ensures that the porosity of the system decreases continuously during the iterative process, as shown in Figure 3.

In this paper, the Box–Muller algorithm is used to generate random numbers, y_1 and y_2, with the mean value of 1, where the two random numbers (n_1 and n_2) are any numbers between 0 and 1 and are expressed as follows:

$$\left.\begin{matrix} y_1 \\ y_2 \end{matrix}\right\} = \sqrt{-2\ln n_1}\cos 2\pi n_2. \tag{7}$$

Thus, we have

$$\langle H(\mathbf{r},t)\rangle = y_1 y_2\sqrt{2k_B TM/\Delta t}\Big/\Delta + \eta. \tag{8}$$

In Eq. 8, Δ denotes the smooth length of the differential computation process, which is a size-dependent quantity. Substituting Eq. 8 into Eq. 6, we have

$$\frac{d\phi}{dt} = -M\left(\mu\phi + w\phi^3 - \kappa\nabla^2\phi\right) + y_1 y_2\sqrt{2k_B TM/\Delta t}\Big/\Delta + \eta. \tag{9}$$

The computational area is selected to be a 100 × 100 × 100 lattice (the two-dimensional calculation area is 100 × 100), and the following simpler parameters are selected: $\mu = 1$, $k_B T = 0.01$, $\kappa = 1$, $w = 1$, and M = 1, considering Δ and η as control variables.

2.3 Indicators for the characterization of the microscopic pore structure

a. The phase function determines the distribution characteristics of the solid and pore phases in the back of the pore medium, i.e., $\phi > 0$ for the solid phase and $\phi < 0$ for the pore phase.
b. Euler's number of the porous media: Euler's number is a scalar quantity, numerically equal to the difference between the number of solid connected domains and the number of holes. It is a description of the spatial integrity of porous media, i.e., $E = C\text{-}H$, where E, C, and H denote Euler's number, the number of connections, and the number of holes, respectively. In the geometric theory, the macroscopic form of a closed region can be measured by its topological properties. The connectivity of an image is a topological property, which is invariant after translation, rotation, stretching, compression, and torsion, so the number of holes in the region H and the number of connected regions C are the topological properties that can be measured by Euler's number. Euler's number is a topological measure of an image and is equal to the total number of all objects minus the number of holes in those objects. In this paper, we use the 4-neighborhood structure for calculation.
c. Pore fractal dimension: As a practical and potential tool, the fractal dimensional characteristics of porous media materials have been studied by many researchers. For a fractal structure, $F(L)$ is the scale-dependent quantity; then, according to the scalar law, we obtain the following:

$$F(L) \sim LD. \tag{10}$$

Here, $F(L)$ denotes the surface area of the pores and D denotes the pore fractional dimensional value of this porous medium. For a three-dimensional object, when measured according to the length parameter δ_0, it can be partitioned into N squares with self-

similarity. Therefore, the pore fractional dimensional value D can be calculated according to the following equation:

$$D = \lim_{x \longrightarrow 0} \frac{\ln\left(N_{\delta_0}(F)\right)}{-\ln(\delta_0)}. \tag{11}$$

The larger the pore fractional dimension value is, the more complex the boundary of the pore structure is.

3 Simulated evolutionary results of the characterization parameters

In this numerical experiment, the evolution of the two-phase structure is calculated separately for nine parameter cases with a target porosity equal to 5% at the end of the set iteration. The topology of the two-phase structure (such as the basic size of the pores, pore fractal dimension, porosity, and Euler's number) is analyzed using the variation law of the control parameters Δ and η of the system.

Figure 2 shows the variation in the Euler's number of the two-phase structure with the number of iterations, and it can be seen that Euler's number first decreases, then increases, and finally tends to 0 (Euler's number equal to 0 means all solid phases), and the minimum Euler's number reaches −87929 at the beginning of the iteration, which indicates that the number of pores is much larger than the number of solid objects at the beginning of the iteration. Because the solid and pore phases are randomly distributed at the beginning of the iteration, a higher Euler's number indicates that the connectivity of the structure is poor.

During the iterative calculation, the two phases repel each other, while the same phases attract each other internally. Along with the applied noise (constant input of two-phase particles and more solid-phase particles when η >0), the phases separate from each other, smaller clusters are merged with larger clusters, and the number of solid objects slowly exceeds the number of pores. Because the mean value of the applied noise η is greater than 0, the pore phase shrinks continuously because of the increase in the solid-phase particles, and, finally, Euler's number approaches 0, which means that the solid particles in the material are merged into one.

From Figure 2, it can be seen that the larger the η value is, the faster the rise in Euler's number for Δ=1.2. This is because the larger the η value is, the more the solid-phase particles are added to the system and the faster the system evolves. When Δ = 1.6, Euler's number of the system tends to fall and then rise rapidly at the beginning of the evolution because the larger the Δ value is, the larger the smoothing length is and the easier it is to swallow up the tiny pores or particles. It can be seen that this change is more obvious when Δ = 2. After reaching a very small value, the larger the Δ value is, the slower the rise in Euler's number with a constant η value. In general, the smaller the smoothing length Δ, the larger the η value and the faster the approximation speed, while the larger the smoothing length Δ, the smaller the η value and the slower the approximation speed.

The variation curves of two-phase porosity with the number of iterations are given in Figure 3. The figure shows that the porosity decreases with the increase in the number of iterations, and the smaller

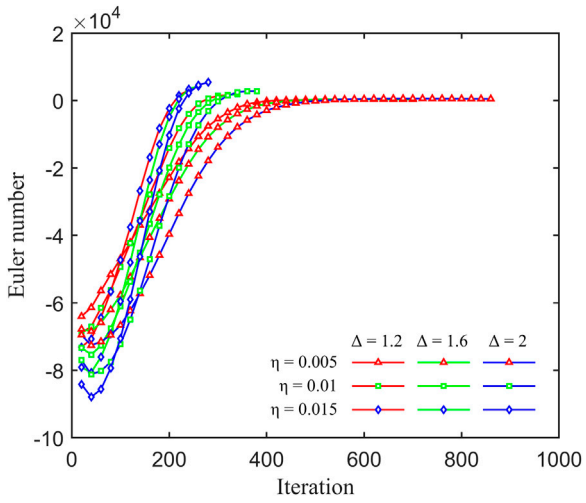

FIGURE 2
Euler's number evaluation of the porous system.

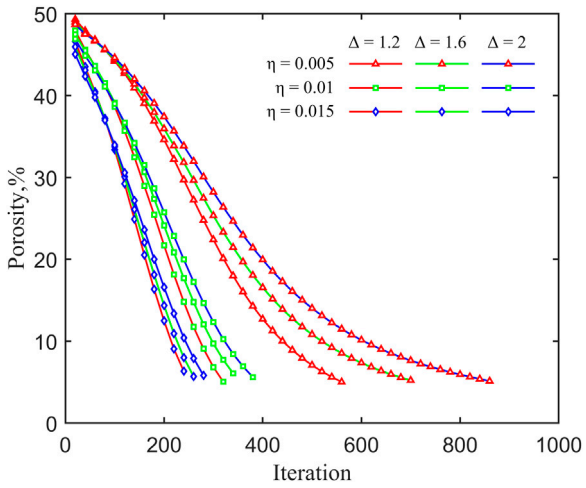

FIGURE 3
Porosity evaluation of the porous system.

the η value is, the slower the iteration converges, while the larger the Δ value is, the slower the porosity decreases for the same η value. Overall, it can be seen that the effect of η on porosity is greater than that of Δ.

Figure 4 shows the trend of the average pore length in the X-direction with the number of iterations in the 3D model. It can be seen that when η = 0.005, the average pore length in the X-direction increases with the number of iterations; when η = 0.01, the average pore length in the X-direction first decreases slowly with the number of iterations and then increases slowly after it reaches the minimum value; and when η = 0.015, the average pore length in the X-direction decreases rapidly with the number of iterations. When the target porosity is reached, the average pore length in the X-direction,

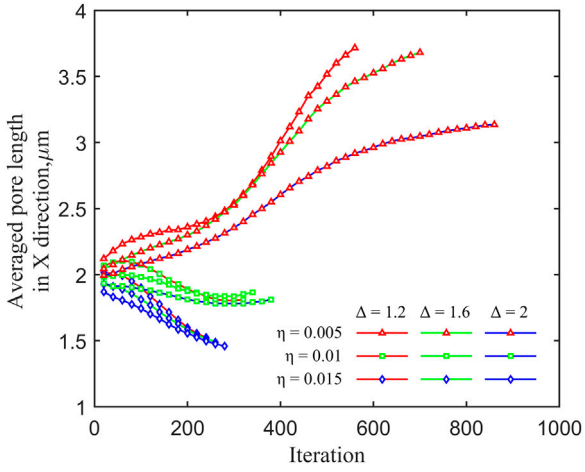

FIGURE 4
Averaged pore length in the X-direction evaluation of the porous system.

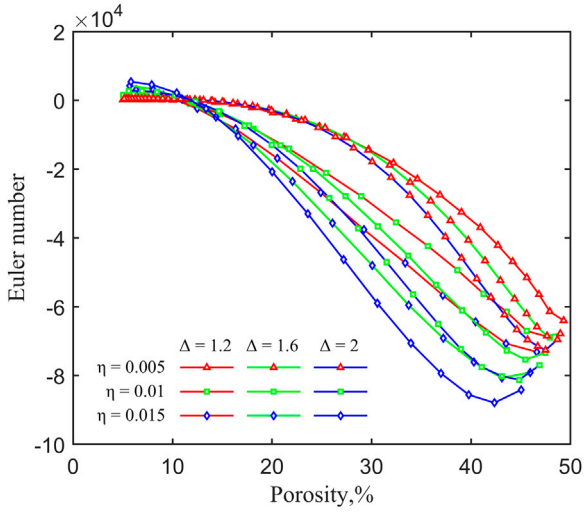

FIGURE 6
Euler's number evaluation vs. porosity.

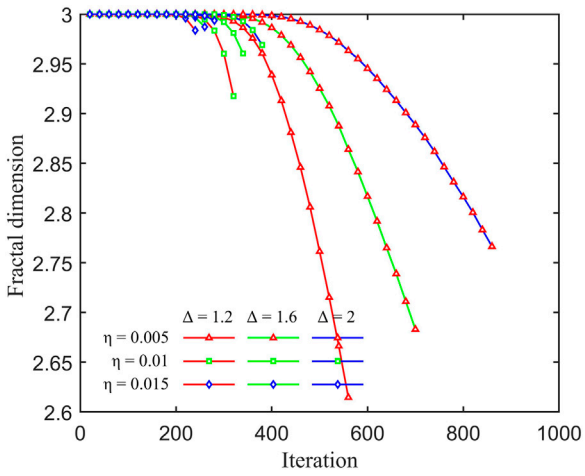

FIGURE 5
Fractal dimension evaluation of the porous system.

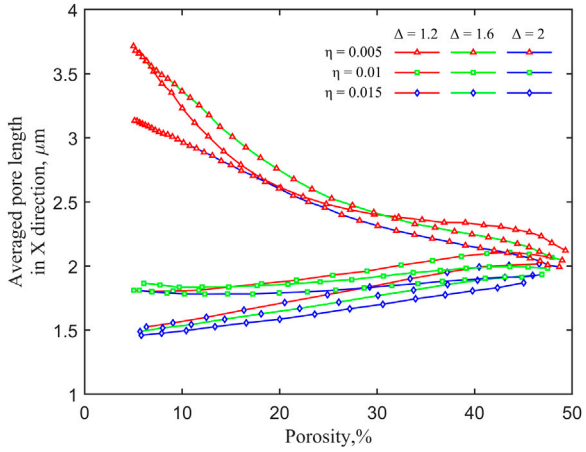

FIGURE 7
Characteristic length evaluation in the X-direction vs. porosity.

corresponding to $\Delta = 1.2$ and $\eta = 0.005$, is the largest, with a value of 3.71 μm, and the average pore length in the X-direction, corresponding to $\Delta = 2$ and $\eta = 0.015$, is the smallest, with a value of 1.46 μm.

The variation curves of the 3D pore fractal dimension with the number of iterations are shown in Figure 5. It can be seen that at the beginning of the iteration, both the solid and pore phases are in the state of haphazard distribution due to the high structural Euler's number. Therefore, the pore geometry is extremely complex, and the fractal dimension of the pore structure tends to be close to 3. When the target porosity is reached, the fractal dimension is 2.615 for a Δ value of 1.2, 2.683 for a Δ value of 1.6, and 2.766 for a Δ value of 2; when the target porosity is reached, the fractal dimension is 2.615 for a η value of 0.005.

The relationship curves between Euler's number and porosity are given in Figure 6. It can be seen from the figure that Euler's number tends to decrease and then increase as the porosity decreases, and Euler's number finally has positive values. The model with the η value of 0.005 and the Δ value of 1.2 has the slowest increase in Euler's number, and the model with the η value of 0.015 and the Δ value of 2 has the highest increase in Euler's number. The higher the Δ value, the slower the increase in Euler's number with porosity when η is kept constant. The larger the η value, the slower the increase in Euler's number with porosity when Δ is kept constant.

The curves of the variation in the average length of pores with the porosity in the *X*-, *Y*-, and *Z*-directions in the three-dimensional structure are given in Figure 7, Figure 8, and

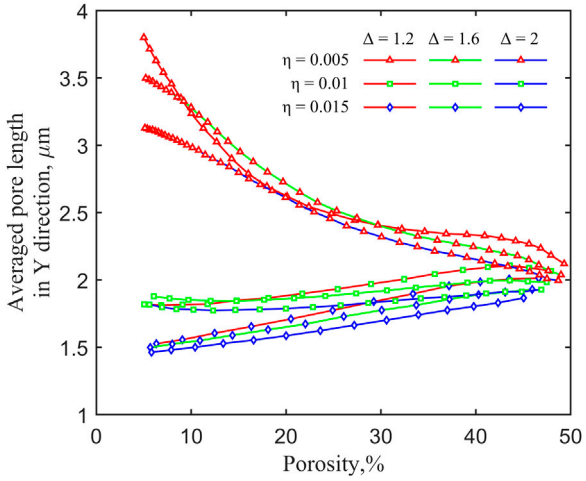

FIGURE 8
Characteristic length evaluation in the Y-direction vs. porosity.

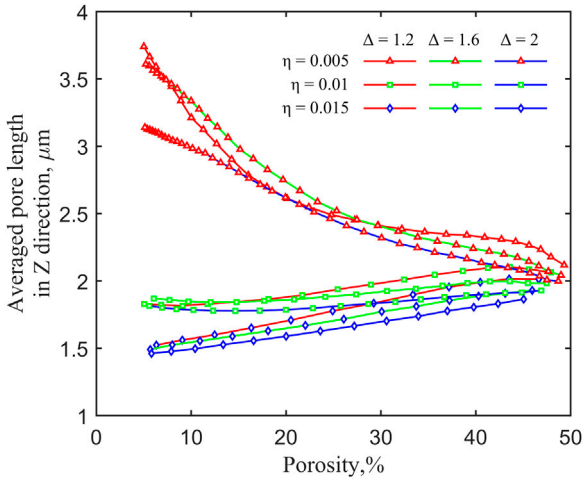

FIGURE 9
Characteristic length evaluation in the Z-direction vs. porosity.

Figure 9, respectively. As can be seen from the figures, the trends of the average pore length in the three directions are basically the same, and the example of the X-direction is as follows: when η is 0.005, the average pore length in the X-direction decreases with the increase in the Δ value; the value is 3.72 μm when Δ is 1.2 and 3.13 μm when Δ is 2. When η is 0.015, the average pore length in the X-direction decreases with the increase in the Δ value; the value is 1.52 μm when Δ is 1.2 and 1.46 μm when Δ is 2. The average length of the pore in the X-direction decreases with the increase in the Δ value; the value is 1.46 μm when Δ is 2. In the same case, the average length of pores in the X-direction decreases essentially with increasing values of Δ, and the average length in the X-direction decreases essentially with increasing values of η.

Therefore, the generation of 2D/3D pore structures is intervened and controlled by controlling the values of η and Δ in order to obtain the complex geometrical structure of predicted red clay through mathematical iterations and image processing techniques.

4 Example of red clay 2D model construction

Due to the lack of experimental conditions, 3D red clay microstructure data acquisition could not be carried out. In order to facilitate the aim of this study, the experiment was carried out based on the existing digital images of a certain red clay samples collected from Qixingguan, Bijie (e.g., Figure 10A), which has a more complex structural distribution. Its binarized pore structure image was obtained via the image processing technique; as shown in Figure 10B, the black part is the pore, and the white part is the clay matrix; its porosity is 9.48%, fractal dimension is 1.36, and Euler's number is −92. Figure 10C shows that statistical histograms of pore diameters were carried out on the binarized pore image, and the pore is as long as the distribution of the pore, which is less than 4 μm. Figure 10D shows the microscopic pore structure image ($\Delta = 2$ and $\eta = 0.005$) of red clay obtained by the simulation of the proposed method, with a simulated porosity of 9.53%, pore fractal dimension of 1.34, and Euler's number of −85, and the histogram of its simulated microscopic pore distribution is shown in Figure 10E. Through comparisons, it is found that the method can better realize the simulation of the microscopic pore structure of red clay, and the simulated results can be well consistent with the real results obtained via electron microscope scanning and better describe its connectivity, porosity, and fractal dimension.

5 Example of red clay 3D model construction

Although the microstructure of red clay is very complex and it is very difficult to obtain its real microstructural parameters, numerical modeling is a useful method. Previous modeling methods approximate the real porous medium by porosity and correlation function and do not consider other pore parameters. The proposed method can generate a micro-geometric model of the porous medium by controlling two parameters, Δ and η. Since the connectivity parameters of red clay samples are not available, this example is approximated according to a single parameter, porosity, in order to obtain an equivalent red clay microstructure model.

The numerical simulation results of the red clay microstructure are given in Figures 11–14 for four porosities (4.98%, 24.5%, 37.1, and 41.5% porosities, respectively). It can be seen that the three-dimensional red clay microstructure obtained from the simulation can be seen in green color for the red clay matrix, and the pores inside it are clearly visible. The red clay models with different microscopic pore structure characteristics

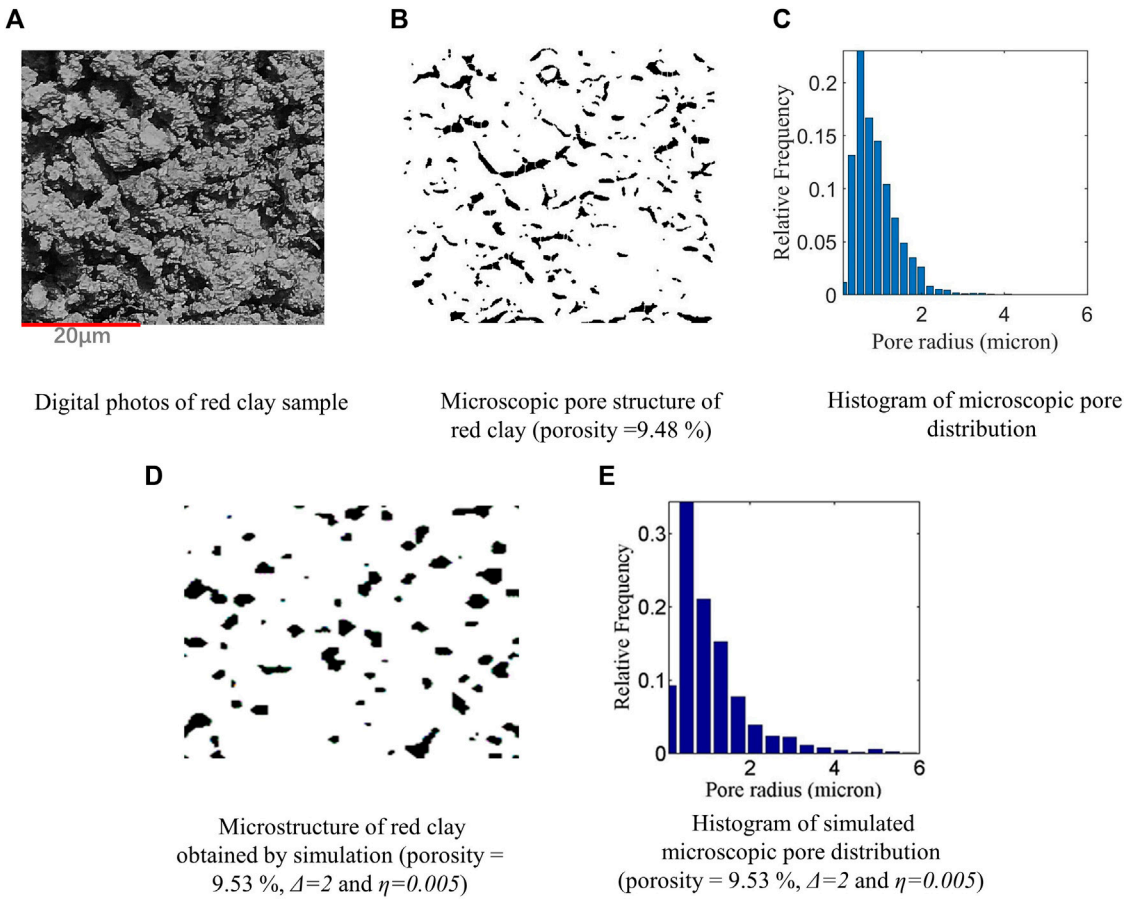

FIGURE 10
Pore structure of the red clay sample and the simulation result. **(A)** Digital photographs of red clay. **(B)** Microscopic pore structure of red clay (porosity = 9.48%). **(C)** Histogram of microscopic pore distribution. **(D)** Microstructure of red clay obtained by simulation (porosity = 9.53%, Δ = 2, and η = 0.005). **(E)** Histogram of simulated microscopic pore distribution (porosity = 9.53%, Δ = 2, and η = 0.005).

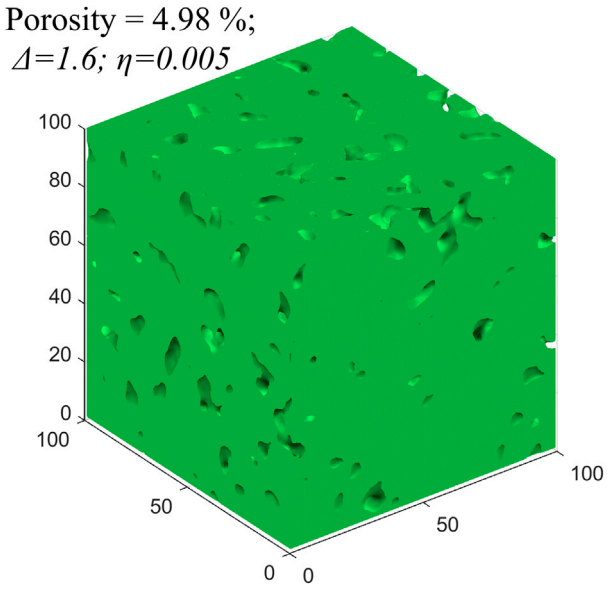

FIGURE 11
Three-dimensional simulation of the microporous structure of red clay (example 1).

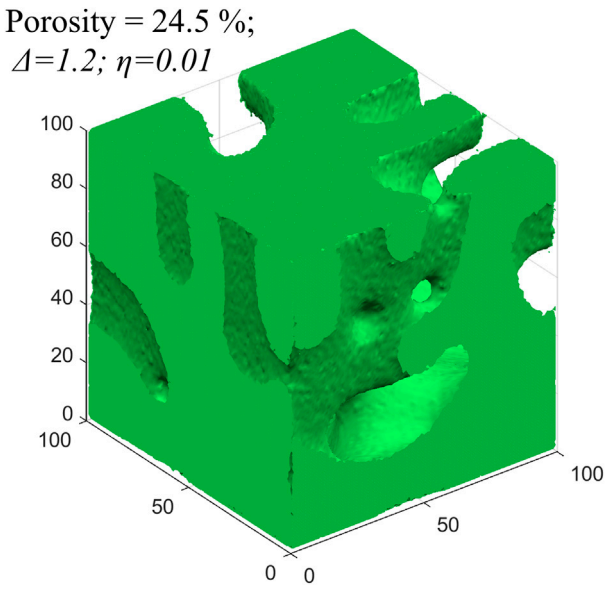

FIGURE 12
Three-dimensional simulation of the microporous structure of red clay (example 2).

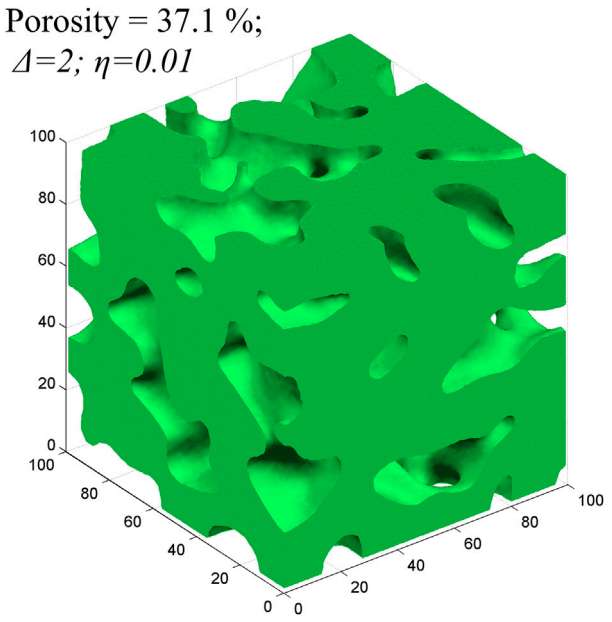

FIGURE 13
Three-dimensional simulation of the microporous structure of red clay (example 3).

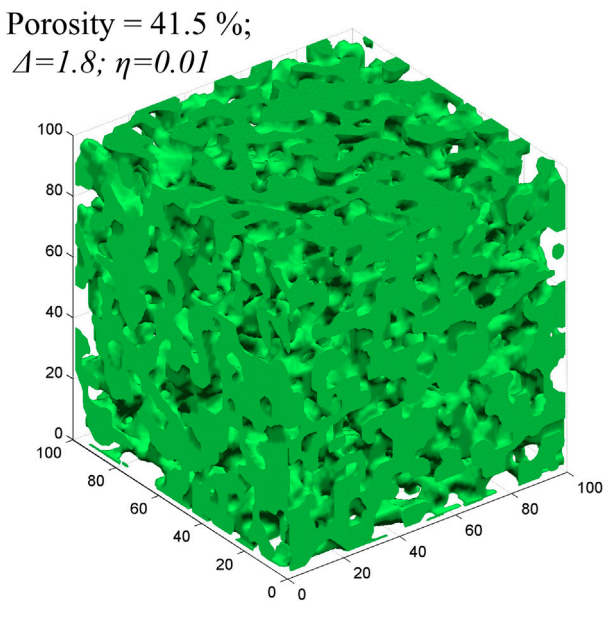

FIGURE 14
Three-dimensional simulation of the microporous structure of red clay (example 4).

can be obtained under different initial conditions as well as for different Δ and η values. The generated models better reproduce the high porosity ratio characteristics of red clay, and various mechanical calculations can be performed based on these characteristics.

It can be seen that the proposed method can better simulate the randomness of the red clay porous media structure; this method is not only limited to the simulation of a three-dimensional red clay pore structure; in fact, the smaller the η and Δ values are, the larger the size of the pore will be; in contrast, the larger the Δ and η values are, the smaller the size of the pore will be; with the increase in the number of iterations, the pore structure will gradually be replaced by the solid phase and, at the same time, because the η value itself shows a random rise and fall, it can reflect the random fractal characteristics of the pore structure. Therefore, it is possible to generate porous media models with different pore structures by controlling the magnitude of these two parameters.

6 Conclusion

The presence of the red clay terrain in Guizhou Province, China, and the inherent characteristics of red clay and the complexity of its structure have forced the development and refinement of new models to describe it. In this paper, a new stochastic dynamics method for simulating the generation of microstructures of such porous media is proposed. The conclusions are as follows:

(1) Starting from the formation process of red clay, it is found that its microstructure is the result of the joint action of aggregation and granulation of its internal microcluster particles, and its microporous structure can be described by the Langevin process, and a relevant model is established. By changing two control parameters (Δ and η), the changes in the pore structure-related parameters such as porosity, pore characteristic length, Euler's number, and pore fractal dimension, during this stochastic kinetic process, were investigated, and their interrelationships were compared and analyzed.
(2) It is found that the reduction in porosity of the porous media can be accelerated by controlling the average value of the random rise and fall phase, and the size of the pore structure can be increased by reducing the value of Δ.
(3) Through the approximation of porosity, the microscopic pore structure of red clay in Bijie, Guizhou, was simulated numerically, and the proposed method can better simulate the microscopic structure of real samples.

Data availability statement

The original contributions presented in the study are included in the article/Supplementary Material; further inquiries can be directed to the corresponding author.

Author contributions

XZ conceptualized and devised the methodology. JZ prepared the original draft. XL and XR reviewed and edited the manuscript.

XZ supervised the study. All authors contributed to the article and approved the submitted version.

Funding

This work was supported by the funding from the Basic Research Program of Guizhou Province (ZK [2022] General 166), the Teaching Content and Curriculum Reform Project of Higher Education Institutions in Guizhou Province (2022304), the Technology Top Talent Support Project of the Guizhou Provincial Education Department ([2020]155), the Research and Development Project of the Guizhou University of Engineering Science (G2018016), the University Student Innovation and Entrepreneurship Training Program Project (s202210668178), the Bijie City Science and Technology Project, and the Joint Fund Project ([2023] 54).

Conflict of interest

The authors declare that the research was conducted in the absence of any commercial or financial relationships that could be construed as a potential conflict of interest.

Publisher's note

References

Cai, G. Q., Wang, Y. N., Zhou, A. N., and Zhao, C. G. (2018). A microstructure-dependent hydro-mechanical coupled constitutive model for unsaturated soils. *Yantu Gongcheng Xuebao/Chinese J. Geotechnical Eng.* 40 (4), 618–624. doi:10.11779/CJGE201804005

Cai, G., Liu, Y., Xu, R., Li, S., and Zhao, C. (2021). Microstructural changes in red clay on drying-wetting paths. *Chin. Sci. Tech. Sci.* 51 (2), 221–230. doi:10.1360/sst-2020-0203

Guo, L. X., Zhang, C. L., Yang, D. G., and Li, T. L. (2017). Discontinuous deformation analysis with microstructural model for axial odometer test of loess. *J. Yangtze River Sci. Res. Inst.* 34 (3), 80–84. doi:10.11988/ckyyb.20151103

He, W., Xue-jun, C., Yu, S., Li-jie, C., and Xiang, H. (2018). Effect of external admixture on microstructure and brittleness index of red clay. *Sci. Technol. Eng.* 18 (035), 212–216. doi:10.3969/j.issn.1671-1815.2018.35.036

Jiaming, L., Xuejun, C., Xiang, H., Yicheng, C., and Sizhe, Y. (2020). Mechanical properties and microstructure tests of zinc-contaminated red clay. *J. Henan Univ. Sci. Technol. Sci.* 41 (2), 99–97. doi:10.15926/j.cnki.issn1672-6871.2020.02.017

Jie, Z., Changliang, Z., Ping, L., Tonglu, L., Zhitian, Q., and Qiang, L. (2021). Microscopic discontinuous deformation of structured loess under compression. *J. Yangtze River Sci. Res. Inst.* 38 (5), 123–128. doi:10.11988/ckyyb.20200506

Jinghe, T., Jiansen, S., and Huiqiang, L. (2018). Influence of sand and fly ash contents on the properties of guilin red clay mixtures. *Soil Eng. Found.* 32 (5), 524–524.

Jun, C., Qi, W., Mingyuan, Y., Minghu, W., Bin, G., and Ji, D. (2018). Laboratory tests for shear strength and fracture surface microstructure of alkali contaminated red clay. *J. Eng. Geol.* 26 (05), 1300–1310. doi:10.13544/j.cnki.jeg.2018158

Ke, X., Zhi, W., Xiaohan, M., Mingli, Z., Qiang, G., and Nan, S. (2019). Effect of freezing on the microstructure of Qinghai-Tibet red clay and Lanzhou silt. *J. Glaciol. Geocryol.* 41 (5), 1122–1128. doi:10.7522/j.issn.1000-0240.2019.0327

Li, X. (2021). *Study on microstructure and mechanical properties of microbially modified expansive soils*. M.S. Central South University of Forestry Science and Technology. Changsha, China.

Liu, Z., Zhou, C. Y., Zhu, F. X., Zhang, L., and Yu, R. J. (2011). Critical criterion for microstructure evolution of soft rocks in softening process. *Yantu Lixue/Rock Soil Mech.* 32 (3), 661–665. doi:10.3969/j.issn.1000-7598.2011.03.004

Mou, Chunmei, Zhang, Lu, Yuxi, Wei, and Fu, Qing (2021). Microstructural evolution of the red clay contaminated by NH3 ·H2 O in Guilin. *J. Guangxi Univ. Nat. Sci. Ed.* (2), 259–259. doi:10.13624/j.cnki.issn.1001-7445.2021.0259

Pan, Tai, Zhao, Guitao, and Huang, Ying (2021). Effect of pH value on mechanical properties and microstructure of yunnan laterite. *Silic. Bull.* 40 (10), 3427–3429. doi:10.16552/j.cnki.issn1001-1625.20210609.004

Ping, L., Qiang, L., Tong-lu, L., Zhi-tian, Q., Wei, S., and Jie, Z. (2020). A method for generating two-dimensional microstructure model of loess based on Monte Carlo method. *J. Yangtze River Sci. Res. Inst.* 37 (4), 79–84. doi:10.11988/ckyyb.20190035

Qi, W., Jun, C., Peng, Z., Pengchao, S., and Yunbin, S. (2017). Experimental study on physical properties and microstructure of red clay polluted by alkali. *Tunn. Undergr. Space Technol.* 13 (6), 1483–1492.

Taixu, C., Yun, C., Yunbin, S., Wensheng, B., Zhonghu, W., and Tingting, W. (2019). Study of microstructure and fractal characteristics of existing foundation red clay particles based on SEM images. *Carsologica Sin.* 38 (4), 635–638. doi:10.11932/karst20190424

Tan, L. R., and Kong, L. W. (2001). Fundamental property and microstructure model of red clay. *Chin. Jounal Geotechnical Eng.* 23 (4), 458–462. doi:10.3321/j.issn:1000-4548.2001.04.016

Tan, Y., Yu, B., Liu, X., Wan, Z., and Wang, H. (2015). Pore size evolution of compacted laterite under desiccation shrinkage process effects. *Geotechnics* 36 (2), 369–367. doi:10.16285/j.rsm.2015.02.010

Tang, C., Shi, B., Chun, L., Wang, B., and Gao, W. (2007). Developing law and morphological analysis of shrinkage cracks of clayey soil under different temperatures. *J. Geotechnical Eng.* 29 (5), 743–749. doi:10.1142/9789812709455_0004

Tao, L. I., Liu, B., Yan, L. I., and Peng, L. I. (2011). The void ratio of saturated red clay calculated from a micro-structure model. *J. China Univ. Min. Technol.* 40 (5), 720–725. doi:10.1007/s10565-010-9168-0

Wang, Y. (2020). *Microstructure and mechanical properties of artificially cemented red clay*. PhD. Guilin University of Technology. Guilin, China.

Zhang, X., Li, L., and Han, L. (2019). Microporous media model generated by using Langerin's equation. *Sci. Technol. Eng.* 19 (6), 222–230. doi:10.3969/j.issn.1671-1815.2019.06.035

Zhou, Y., Liu, X., Liang, Z., and Zhang, D. (2012). Study of micro-structure model of red clay and its engineering mechanical effect. *Chin. J. Undergr. Space Eng.* 8 (4), 726–721. doi:10.11835/j.issn.1000-582X.2014.06.003

Zuo, S., Zhang, Y., Zhao, R., and Zhang, J. (2019). Study on fractal characteristics of meso-microstructure of red clay in Guiyang. *J. Beijing Jiaot. Univ.* 43 (3), 122–128. doi:10.11860/j.issn.1673-0291.20180172

frontiers | Frontiers in Earth Science

TYPE Original Research
PUBLISHED 06 September 2023
DOI 10.3389/feart.2023.1266649

OPEN ACCESS

EDITED BY
Xuelong Li,
Shandong University of Science and Technology, China

REVIEWED BY
Lei Shi,
China University of Mining and Technology, China
Yu Xuguang,
Tangshan Vocational and Technical College, China

*CORRESPONDENCE
Xiangdong Niu,
niuxiangdong@stu.kust.edu.cn

RECEIVED 25 July 2023
ACCEPTED 25 August 2023
PUBLISHED 06 September 2023

CITATION
Zhe Y, Hou K, Niu X and Liang W (2023), Early warning technique research of surface subsidence for safe mining in underground goaf in Karst Plateau zone. *Front. Earth Sci.* 11:1266649. doi: 10.3389/feart.2023.1266649

Early warning technique research of surface subsidence for safe mining in underground goaf in Karst Plateau zone

Yalei Zhe[1], Kepeng Hou[1], Xiangdong Niu[1]* and Wei Liang[2]

[1]Faculty of Land Resources Engineering, Kunming University of Science and Technology, Kunming, China, [2]Institute of Mining Engineering, Guizhou Institute of Technology, Guiyang, China

Underground mining in Karst Plateau landform area may cause the loss of support for the upper rock stratum, resulting in rock collapse and large-scale subsidence of the ground surface. Also, the formation of a large-scale goafs may further lead to geo-hazards such as collapse, water gushing, slope instability and so on in the area. To reduce the impact of goaf settlement on local strata stability, this paper established a standardized safe mining detection model for goafs based on the geological safety characteristics of mining goafs. With reference to the statistical analysis of the geological conditions in the mining area, a numerical model with 358 goafs and the proposed mining area was established using FLAC^{3D} numerical software. The surface subsidence and variations of plastic zone in the mining area were comprehensively analyzed. The results indicated that there was a correlation between the stability of the mining area and the geological occurrence conditions of the goafs. By quantitatively taking the values from standardized safety mining detection models, the standardized safety mining detection and warning technique was finally established. The findings can provide technical guidance for safety detection and early warning in the whole process of underground goaf mining in Karst Plateau karst development zone.

KEYWORDS

Karst Plateau zone, surface subsidence, security detection, numerical model, early warning technique

1 Introduction

Due to the historical reasons such as poor mine supervision and unstandardized mining, many metal and non-metal mines in China have abandoned a large number of unprocessed goafs of various sizes and shapes. Especially since the 1980s, indiscriminate mining under chaotic mining order has created numerous unidentified goafs, which have emerged as one of the most significant risk sources affecting the safe mining and the safety of the lives and property of the inhabitants around the goafs (liao et al., 2008; He et al., 2020; Liu and Li, 2023). Elimination of threats to resource extraction requires surveying and mapping of the goafs to identify their distribution, scale and risk levels.

Extensive studies on the goafs have been conducted by scholars worldwide from the remote sensing and survey perspective to validate the reliability of the resistivity tomography (ERT) method. (Martínez-Pagán et al., 2013) conducted experiments in the semiarid climatic region of La Sierra Minera. Since the space of the cave was occupied by air, one might expect a high electrical resistivity contrast between the cave itself and the host rock. (Yu et al., 2018) utilized the large-loop transient electromagnetic approach to detect the water-rich goaf. The

inversion results confirmed that the resistivity of water-rich goaf often exhibited a very low resistivity, and the resistivity contour line behaved as a sharp closed circle. (Chen et al., 2021) examined the developmental characteristics of the goafs in the working zone through the layout of the Transient Electromagnetic Method(TEM) survey line. Subsequently, based on this working zone, the magnetotelluric sounding method was adopted to verify the delineated goafs by TEM, and the anomalous apparent resistivity surface obtained by these two methods was basically constant. In view of the problems of existing methods for solving the parameters of goaf spatial features, (Wei et al., 2022) proposed a method of identifying the spatial location of underground coal goafs by using the minimum unit probability integration merging method and optimized quantum annealing.

Regarding the studies on the goaf stability issues, (Ma, 2021) investigated the creep failure law of coal pillars in the room pillar goaf under overburden loading, where the critical instability state in the dynamic instability process of coal pillars was determined, and the pillar goaf stability evaluation system with multiple indices was established based on the fuzzy exhaustive evaluation method. (Ning et al., 2019). used Mathews stability diagram method to calculate the allowable hydrological radius of rocks in the goaf of Huanggang iron ore mining, and then determined the stability grade of the goaf. Based on 110 goaf samples, (Huang and Chu, 2019) combined random forest algorithm with recursive feature elimination theory to screen out the indexes that contribute more information to the hazard grading of the goafs, and they realized the streamlined dimensionality reduction of the evaluation index system of the goaf. In addition, a large number of researchers also performed computational analysis on goaf stability with the finite difference method or the finite element method (Zhang et al., 2010; Sariandi et al., 2018; Wang et al., 2018; Jia and Xue, 2021).

In terms of quarry area management, (Wang et al., 2023) dealt with goaf-related hazards in advance at specific working faces by enhancing continuous monitoring of water levels and volumes. The most widely available approach for ground pressure management is to use the waste rock, tailings sand, concrete and other materials to fill the goafs (Deng et al., 2009; Feng and Huang, 2020; Liu et al., 2022; Yu et al., 2022; Zu et al., 2023).

In summary, previous studies on goaf detection methods and stability evaluation have mostly focused on goaf detection timing management. Currently, there are no scholars studying goaf detection timing management. The geological conditions of underground goaf in karst development zone are complex, the changing morphology of the ore body, the historical legacy of mining, the disorder and chaos of the early mining, the intemperate mapping, the lack of detailed information and goaf management and the collapse or closure of roadways and goafs in some cases have made it difficult to verify the distributional status of some goafs, resulting in the original hidden goafs becoming even more mysterious (Chun et al., 2020; Li et al., 2021; Li et al., 2021). Therefore, it is difficult to carry out surface subsidence stability warning technology for safe mining in goaf. This article is the first to apply the Eisenhower Rule, Priority Formula and Monte Carlo method of operations research to the construction of a standardized model for goaf safety detection. The simulation results of the whole mining process using the FLAC^{3D} were applied to the standardized model, which realized the goaf classification and efficient detection at different periods. The findings can make the use of human and financial resources to deal with goaf detection and safety hazards more reasonable, scientific and proactive. The research results can provide useful references for the subsequent monitoring and warning of goaf disasters in mines, and provide guarantees for the safety production of mines.

2 Standardized safety detection model

In the process of mine production and construction, the safety problems brought by the potential hazards of the goafs to the production and the surrounding environment should be correctly addressed, while the safety management policy of prevention oriented and comprehensive treatment should be adhered to. In this paper, by adopting the Eisenhower Rule, the Priority Formula and Monte Carlo method and combining the safety characteristics of the goafs themselves, four safety quadrants for goaf detection grading were classified, and finally a standardized safety detection model for goaf was developed, as shown in Figure 1.

The specific construction method of the standardized safety detection model for goafs in Figure 1, as well as the adopted Eisenhower Rule, Priority Formula and Monte Carlo method are described in detail in Sections 3 and 4.

3 Eisenhower Rule time series management

3.1 Eisenhower Rule

Eisenhower Rule, also known as 'the Four Quadrant Rule', was introduced by Dwight David Eisenhower. The division of things to be done into four quadrants based on the urgent, non-urgent, important and unimportant arrangement helps us to gain a deep understanding of time and efficient management (Henjewele et al., 2013; Dai, 2019; Li et al., 2020; Luo et al., 2021).

Quadrant 1: this quadrant contains urgent and important matters that should be addressed on a priority basis. The goaf in this quadrant belongs to the high risk and susceptible category. On the one hand, the goaf in this quadrant leads to the deterioration of mining conditions, and directly threaten the production safety of underground operations. On the other hand, it severely affects the life and property safety of surrounding residents, while the degree of detection directly determines the safety of the mine production and the production cycle. Therefore, the level of exploration requires a high level of over 90%.

Quadrant 2: this quadrant contains urgent but unimportant events, so events in this quadrant are very deceptive and tend to take up a lot of valuable time of many people. The goaf in this quadrant falls into the category of low-risk and high-sensitivity. If the goaf is close to the production zone but relatively spatially independent, it will be in relative stable state. Detection work in this quadrant is needed, but the degree of detection can be appropriately reduced, above 50% is sufficient; while appropriate methods could be chosen to categorize the goaf types.

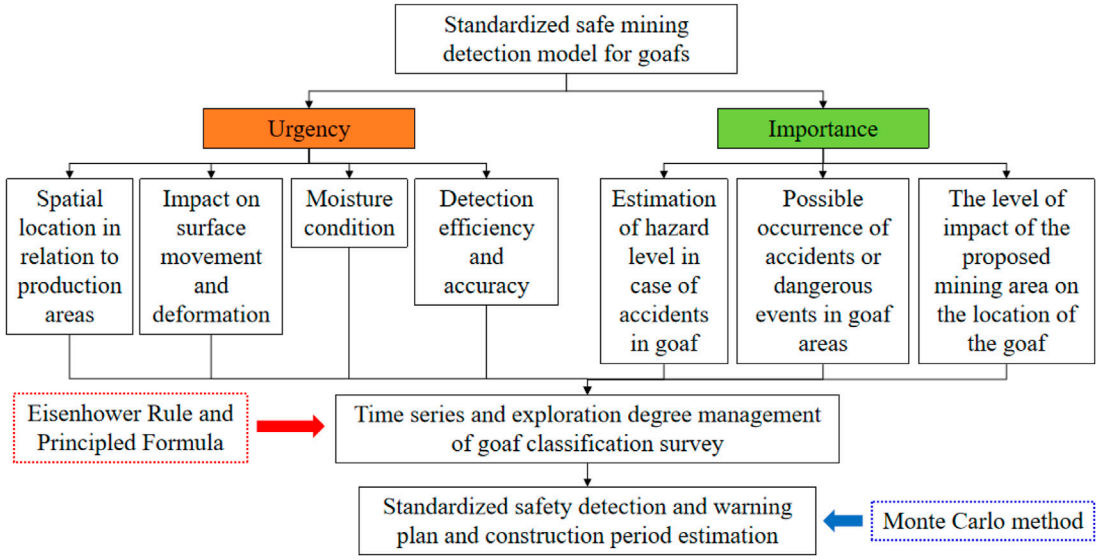

FIGURE 1
Standardized safety detection model for goaf.

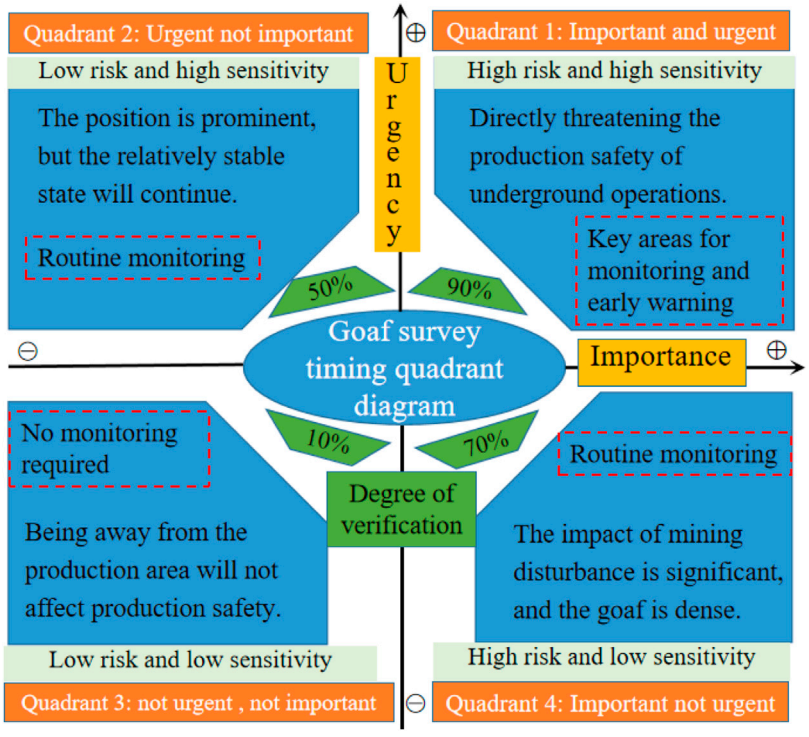

FIGURE 2
Eisenhower diagram of managing the timing of goaf investigations and the degree of exploration.

Quadrant 3: this quadrant contains events that are mostly trivial tasks, with no time urgency and no importance. It is manifested by the fact that the goaf in the quadrant is in the low-risk and low-sensitivity category, where the goaf is far away from the production zone, and has good stability and anti-interference. Even if the goaf is destroyed, the safety of production will not be affected. The detection of the goaf in this region is the icing on the cake, only need to reach over 10%, and may favor the detection tasks.

Quadrant 4: this quadrant differs from Quadrant 1 in that the events in this quadrant are not time-critical; however, they have

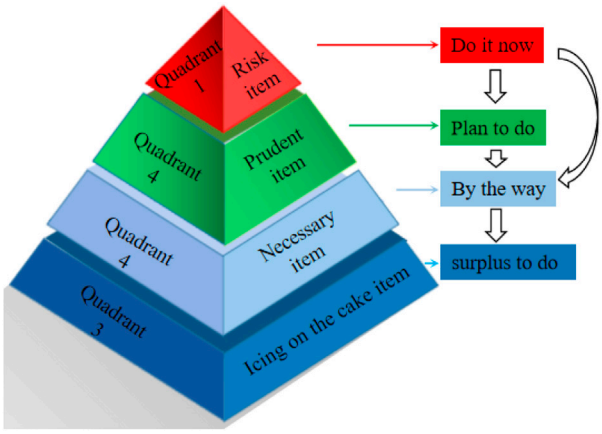

FIGURE 3
The order of detection of each quadrant goaf.

significant impacts. It is manifested by the fact that the goaf in this region falls into the category of high-risk and low-sensitivity, while the goaf is normally in a stable state. There are spatial overlap, denser void areas, thin pinched walls of the endowment and high mining disturbance, which can easily cause large-scale catastrophic accidents. The extent and capacity of the next mine design can be more strongly influenced by the area of the mine goaf. The goaf in this region requires detection with a high degree, must reach over 70%, and they belong to the conservative object.

Based on the above elaboration of the four quadrants, the time management of the goaf survey and the degree of detection of the Eisenhower schematic diagram is drawn in Figure 2, and the goaf detection sequence in the quadrant is shown in Figure 3.

3.2 Method of quantifying the temporal sequence of goaf detection and investigation

3.2.1 The degree of emergency

Based on the relationship between the goaf and the mine engineering layout, and with respect to the urgency of the goaf detection survey, the time of surface deformation and stabilization, the accuracy of detection and the accumulation of water in the former hole were evaluated, and the specific values were.

(1) The area close to the proposed project was characterized by a concentration of personnel, equipment and frequent activities. Therefore, the closer the midsection to the proposed goaf of production resumption at this time, the greater the impact of leftover goaf on production, therefore the investigation and detection should be performed first with respect to temporal urgency (Guo et al., 2014; Liu et al., 2023a; Liu et al., 2023b). We denoted this urgency by *J*, which took the range of values [1 - Number of middle sections from the proposed goaf] = [1 - n].

(2) In general, the impact of goaf on surface deformation can be divided into three stages. The initial period was the occurrence of subsidence of 10 mm in the main section of the surface displacement basin. The surface subsidence rate was greater than 50 mm/month (the dip angle of the ore body $\alpha \leq 45^{\circ}$) or the surface subsidence rate was greater than 30 mm/month (the dip angle of the ore body $\alpha > 45^{\circ}$), which can be regarded as the active period. In six consecutive months, the subsidence value did not exceed 30 mm was considered as the end of the period of surface movement and as the recession period, i.e., the stabilization period. This tightness is denoted by *T*, which takes the values of [0 - the time needed for the surface movement deformation to stabilize] = [0-n]. The approximate continuation time of the surface deformation in the project area can be deduced from Equation 1, if the surface deformation of the mine is not monitored (Wang and Zhen, 2021):

$$T_d = 1000 \exp\left(1 - \frac{400}{H_0}\right) \quad (1)$$

where T_d is the time taken to stabilize a region inside the moving basin, d; H_0 is the mining depth, m. By subtracting the time of the formation of the goaf, the time needed to stabilize the surface movement deformation can be gained. Subtracting T_d from the time of goaf formation can determine the remaining stable time for surface movement and deformation.

(3) The detection depth has a great impact on the efficiency and accuracy of goaf detection, a number of commonly used and matured means of physical prospecting can be divided into several levels: very shallow goaf (<40 m), shallow goaf (50–150 m), medium-deep goaf (150–400 m), deep goaf (>400 m). Tightness was denoted by *S* and took values in the range of [very shallow, shallow, medium-deep, deep] = (liao et al., 2008; He et al., 2020; Liu and Li, 2023; Martínez-Pagán et al., 2013).

(4) The water damage caused by the old holes in the goaf was characterised by the strong suddenness, large volume of water in initial stage and great difficulty in prevention and control. The occurrence of water damage in the old holes of the same layer usually causes great damages and enormous economic losses. Therefore, there is a urgent need to utilize advanced sensing means to identify the distribution and size of the goafs and to obtain their water storage capacities (Gui et al., 2016; Qiu et al., 2018). We denoted this tightness by *W*, which took the following range of values:

3.2.2 Significance

To determine the significance of the goaf detection survey based on the degree of deterioration in mining conditions caused by the goaf, the impact of several aspects on mine production and safety was assessed. These aspects involve the large-scale bubble fall and rock offset, surface collapse, hazards endangering agricultural land and buildings, as well as casualties and equipment damage in underground connected workplace caused by high-speed air waves and shock waves of goaf sudden collapse, etc. (Zhang et al., 2023; Zhang et al., 2023; Gao et al., 2023; Li et al., 2023) Specific values were taken as follows:

1) The valuation of the risk level in case of an accident in the extraction zone was indicated by *P* (Jiang et al., 2021; Pei et al., 2021). The larger, more numerous and denser the midsection goafs were, the more serious the consequences of destabilization damage would

TABLE 1 Estimation of hazard level for accidents in goafs.

Harmful consequences		1			2	3	4
The level and value of accidents in goaf		Extraordinary accident	Major accidents	Larger accidents	General accidents	Serious injury accidents	Minor injury accidents
Maximum potential casualties	Deaths (people)	Over 30	10–29	9–3	2–1	0	0
	Injured (people)	Over 100	99–50	10–49	9–2	1	0
Maximum potential economic loss	(Million yuan)	10,000 or more	10,000–5,000	5,000–1,000	1,000–100	100–1	Below 1
MIL-STD-882D System Safety Program Requirements		I			II	III	IV
		Disaster			Danger	Vigilance	Ignore

TABLE 2 The probability value of accidents or dangerous events occurring in the goaf.

Value	Displacement of surrounding rock in goaf and distribution of plastic zone
1	Large deformation occurs, with plastic zones appearing and penetrating
2	Large displacement, partially connected plastic zone
3	The displacement is small, with a small amount of plastic zone appearing and not penetrating
4	Small displacement, no plastic zone

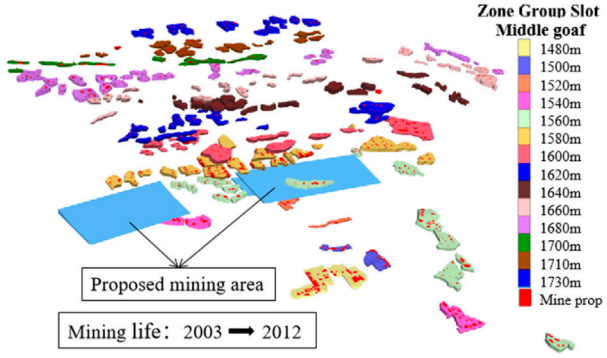

FIGURE 4
Distribution of empty areas in Baiyang mine section.

be. With reference to the internationally accepted risk evaluation standard 'System Safety Standard Practice' (U.S. military standard MIL-STD-882D), a four-level control relationship was established based on the characteristics of the goafs, as shown in Table 1, which was then utilized to estimate the occurrence level of accidents for each midsection goaf assignment.

2) The possibility fraction of the accidents or hazardous events occurring in the goafs was expressed by G. The value was selected according to the displacement and deformation of the surrounding rock in the goaf and the distribution of the plastic zone. If the displacement in the middle section is small and there is no plastic zone, it indicates that the goaf is relatively stable. Otherwise, it means that the goafs were very prone to deformation damage. The range of probability values is shown in Table 2.

3) The grade of the part where the mining goafs were located that was affected by the mining movement of the proposed mining area was expressed by I. Its value was selected based on the deformation results of the rock masses in each midsection of the ore body quarry from the numerical simulation calculation described above. The value range [critical impact area, less impact area] = [1, 0]. If the midsection of the rock movement did not change with the increase of the mining depth, the midsection was considered to be less disturbed by the lower ore body mining. The value of 0 was taken where it was in the less affected part, and the value of 1 was taken in the opposite case.

Considering the importance of the parameters, it is expressed as Equation 2, which is called the 'Priority Formula'.

$$\begin{cases} X = \dfrac{0.6}{P} + \dfrac{0.3}{G} + 0.1I \\ Y = \dfrac{0.4}{J} + 0.2T_d + \dfrac{0.15}{S} + \dfrac{0.25}{W} \end{cases} \tag{2}$$

The Eisenhower Rule is a direct expression of Operations Research and is effective in improving efficiency. However, its shortcomings are also more obvious, whereas it is not possible to plan quantitatively and finely for many complicated matters. In this paper, the Eisenhower Rule and Priority Formula were adopted, and the end point was taken as the origin of the "十" quadrant. The upper right quadrant was for important and urgent events, the upper left quadrant was for unimportant but urgent events, the lower right quadrant was for important but not urgent events, and the lower left quadrant was for unimportant and not urgent events. The orders of priority were: upper right, upper left, lower right, lower left. If there were fewer hidden problems in the same quadrant, it can be simplified to prioritize the problems from largest to smallest using the $\sqrt{X^2 + Y^2}$. However, if the Eisenhower Rule was skipped and the priority of

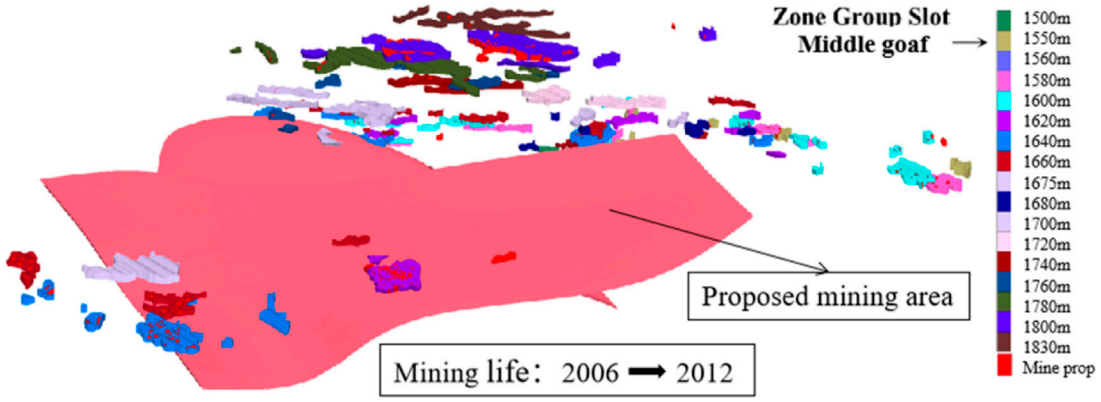

FIGURE 5
Distribution map of the goafs in the Duimenshan section.

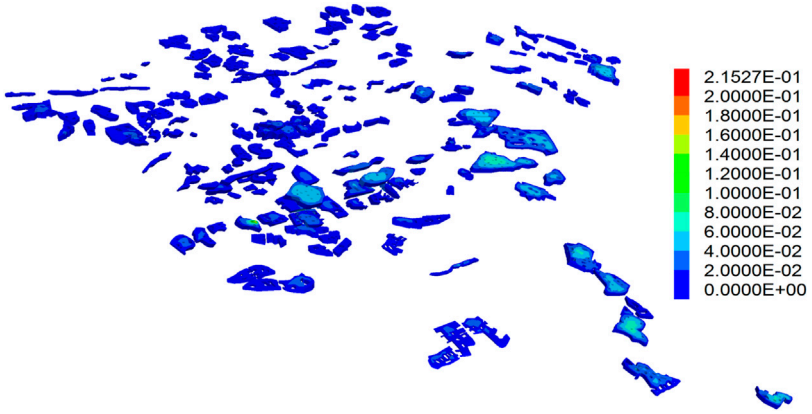

FIGURE 6
Displacement distribution nephogram of Baiyang mine Section induced by the current mining (Unit: m).

hidden problems was measured only by $\sqrt{X^2+Y^2}$, there may be a single influence of X or Y, which may lead to unreasonable planning.

Therefore, according to the Eisenhower Rule and the 'Priority Formula' derived from quantitative values of urgency and importance, a new perspective on the detection management of the goaf was proposed. Not all goafs must be detected, and those that were left over from history and were not verified in a short period of time can be classified as the category of 'black box'. For those goafs that had no impact on production safety and the surrounding environment, there was no need to make great efforts to perform the detection and investigation, whereas the risk control could be conducted based on the past information.

4 Monte Carlo method duration estimation

The calculation of project duration using the traditional critical path (CPM) and plan review technique (PERT) in the planning stage will be affected by various uncertainties, so the calculated duration is bound to have some errors. In this paper, the Monte Carlo method and computer programming were utilized to realize the multiple cycles of the duration of the goaf exploration and investigation.

Monte Carlo method is also known as computerized stochastic simulation method (Niu et al., 2020). Using a random number generator to generate the cumulative probability value of a variable, the corresponding variable value can be calculated through the cumulative probability, which is equivalent to a randomly generated variable value. The random benefit index is then calculated by the randomly generated variable. Repeating this process N times yields N sets of benefit indexes. When the number of repetitions N is large enough, the probability distribution of the benefit index can be obtained.

Following the operational idea, the procedures of the Monte Carlo simulation method in project time management in this paper are as follows.

(1) Determine the type of probability distribution of the random variable, which can be assumed to be a modified triangular distribution.

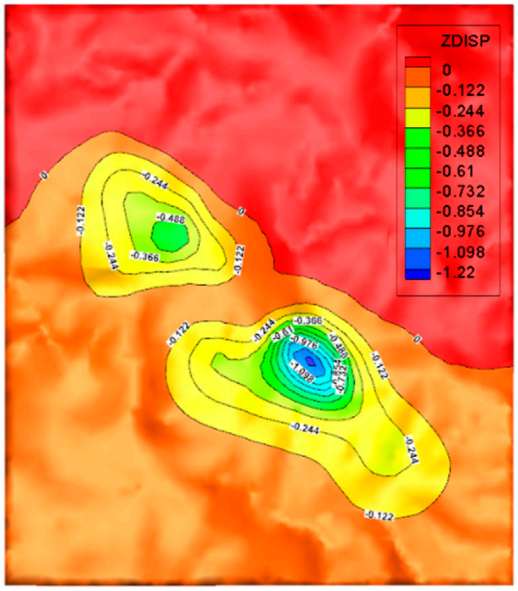

FIGURE 7
Nephogram of surface subsidence due to current mining in Baiyang mine section (unit: cm).

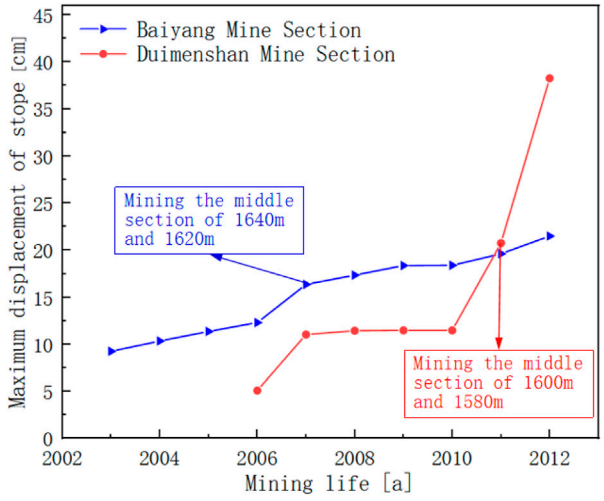

FIGURE 8
The change tend of the rock mass in goaf.

(2) Generation of random numbers. The Rand function was adopted to generate random numbers between 0 and 1.
(3) Obtain statistical data. Considering that the plan review technique used the three-time estimation to calculate the process time, the triangular distribution formula was introduced and coded into the program, After running the program, the value of the duration X_i for each process would be randomly generated as the duration of this process, so that the total duration of the project can be calculated. The triangular distribution formula is as follows:

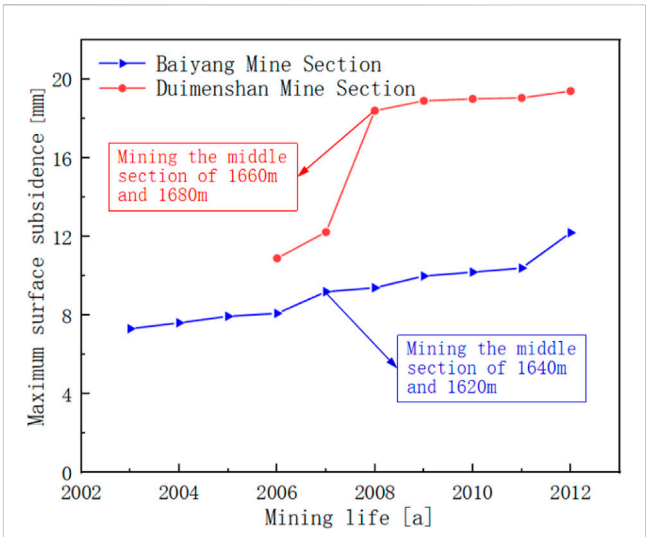

FIGURE 9
The change trend of surface subsidence.

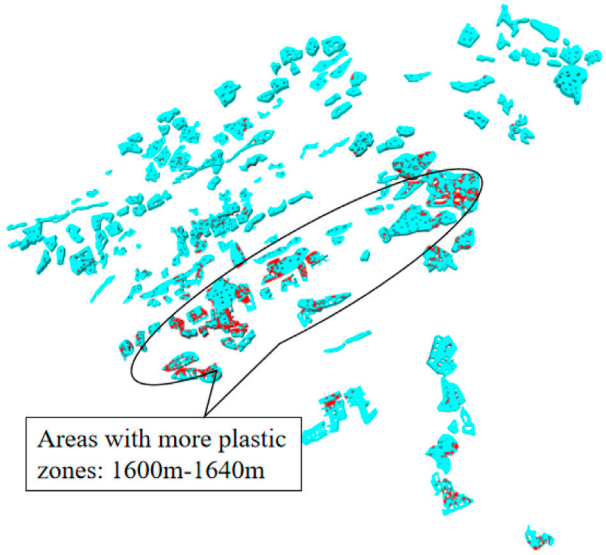

FIGURE 10
The distribution of the plastic zone in the current goafs in the Baiyang mine section.

$$\begin{cases} B_i = \dfrac{c_i - a_i}{b_i - a_i} \\ X_i = a_i + \sqrt{R_i (c_i - a_i)(b_i - a_i)} & R_i < B_i \\ X_i = b_i - \sqrt{(1 - R_i)(b_i - c_i)(b_i - a_i)} & R_i \geq B_i \end{cases} \tag{3}$$

where B_i is the random critical value; R_i is a uniformly distributed random number between 0 and 1, generated by the Rand function; X_i is the duration of each process; and a_i, b_i, c_i are the three time parameters in the three-time estimation table, which are the most optimistic duration, the most pessimistic duration and the most likely duration, respectively.

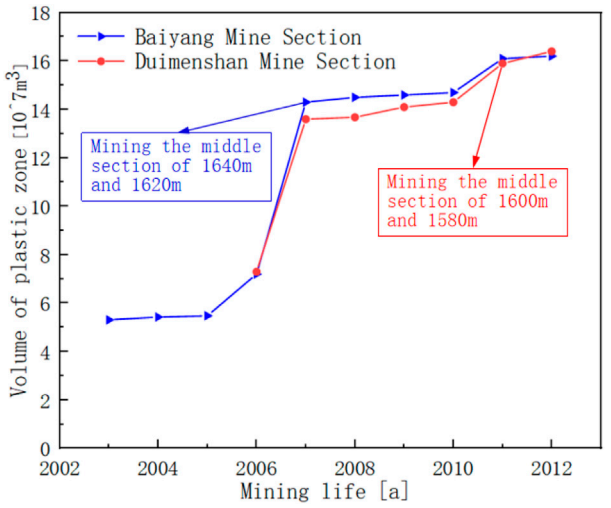

FIGURE 11
Volume variations of the plastic zone in quarry rock masses in two mining sections.

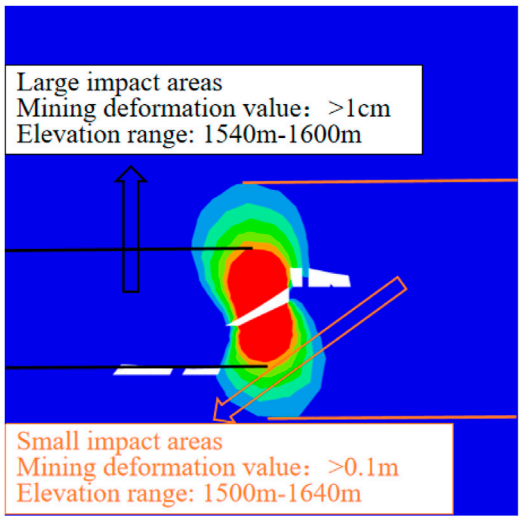

FIGURE 13
The impact range on two sections in vertical direction.

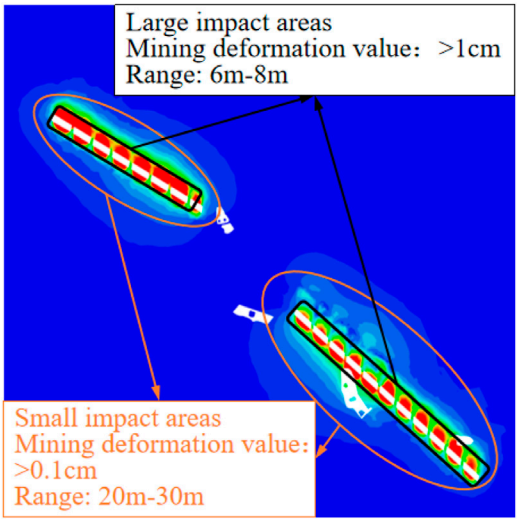

FIGURE 12
The impact range on two sections in horizontal direction.

(4) Determine the type of probability distribution. Once enough statistical data were obtained, a probability statistical chart can be plotted using Excel to make a qualitative assumption about the probability distribution of the activity.
(5) Determine the distribution parameters for the project duration.

5 Engineering applications

After decades of mining in Baiyang and Duimenshan mine sections of Bainiuchang mining area in Mengzi City, Yunnan Province, there are many hidden dangers in safety production. The priority task of mine recovery is to analyse the stability of the current goafs and to investigate the relationship between the mining of the lower ore body and the original goafs, so as to ensure the safe exploitation of the mine resources. However, the disorderly mining activities within the mining area under the influence of historical reasons did not yet form a more complete graph data for the scope of exploration/mining, and also there was a lack of systematic planning for exploration/mining activities. There is a lack of comprehensive research on exploration projects. The 'shape' (the morphological characteristics of the ore body), 'quality' (the distribution characteristics and the change law of the mine grade) and the 'symbiosis' (ore type, the law of mineral symbiosis) was not clear. The large proportion of low-grade mineral reserves, the serious imbalance of tertiary ore quantity as well as the serious blindness of project construction had resulted in a large number of goafs left in the mining (exploration) midsection at various elevations, with different sizes and shapes. Some of the roadways and goafs collapsed and were inaccessible to personnel, bringing greater difficulties to the survey and detection of the goafs.

5.1 Detection survey timing management

On the basis of the preliminary results of the mine engineering geology and goaf investigation, the FLAC3D was utilized to develop a three-dimensional numerical model to compute and analyze the mining process. For the scientific and reasonable survey of goafs and the detection level classification, the stress-strain laws of the rock masses in both the Baiyang and Duimenshan mine sections were investigated, which realized the purpose of highlighting the key goafs, graded detection and comprehensive processing, and guided the resumption of mining work and production. The model size of the two ore sections is the same. The *X* direction is perpendicular to the ore body and the length is 3500 m. Direction Y is the ore body trend, 4000 m long; The *Z* direction is vertical, the bottom elevation

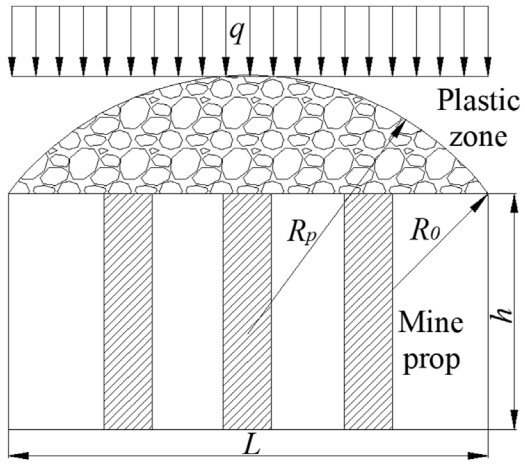

FIGURE 14
Schematic diagram of pillar bearing mechanism.

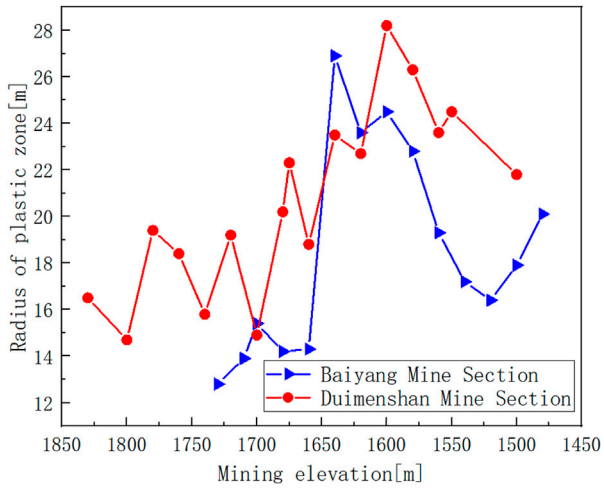

FIGURE 15
Maximum plastic radius of overlying surrounding rock at each mining level stope.

of the model is 900 m, and the top elevation simulates the actual terrain of the mine.

5.1.1 Numerical modeling of the goaf

The two mining sections are far away from each other, and are in no interactive influence. Therefore, the two mining sections were modeled separately, where the distributions of goafs are presented in Figures 4, 5.

5.1.2 Analysis of the current situation

The site survey shows that the mining time of the goafs between the 1,480 m and 1730 m midsections in the Baiyang mine section were from year 2003–2012, and those between the 1,500 m and 1830 m midsections in the Duimenshan mine section were from year 2006–2012. Under the comprehensive consideration of the accuracy of the computational results and computational workload, the actual back-mining steps were simplified to facilitate numerical analysis of the entire excavated goafs during the simulation computation. The mining site in the same mining time was excavated and finished at one time, while each goaf at midsection was sequentially excavated from top to bottom. Due to the large number of nephograms of the calculation results, some of the calculation results of the Baiyang mine section are selected for presentation, and the rest of the calculation results are displayed in graphs.

(1) Rock mass displacement

The Baiyang mine section after 10 years of mining formed the current situation of the goafs. Numerical simulation results of the displacement nephogram of the current mining are shown in Figure 6, where the maximum displacement was 21.5 cm. The subsidence of the goaf roof was basically proportional to the exposed area of the goaf, whereas a larger exposed area of the goaf led to a greater roof subsidence. Some of the goafs were in a continuous state with an overall poor stability. Due to the large exposed area, the roof falling, pillar destabilization and other hazards may occur in some individual goafs.

Figure 7 illustrates the nephogram of surface subsidence caused by the current mining. The range and value of the subsidence were both small, with a maximum value of 12.2 mm, which indicated that the current surface was in a stable state.

With the increase of the mining age, the trends of surface subsidence and rock mass displacement of the quarry in the Baiyang and Duimenshan mine sections are shown in Figures 8, 9. When the midsections at 1,640 m and 1,620 m of Baiyang mine section were mined in 2007, the slope of the displacement curve was steeper, indicating a greater impact on rock mass displacement and surface subsidence of the quarry.

When the midsections at 1,660 m and 1,680 m of Duimenshan mine section were mined in 2008, the surface subsidence curve became steeper, which indicated that the mining had a greater impact on surface subsidence. When the ore body below 1,600 m was mined in 2010, the displacement curve became steeper, indicating that mining of the lower ore body had a more significant impact on the movement and deformation of the rock masses.

(2) Plastic zone

Figure 10 shows the distribution of the plastic zone in the rock mass of the goafs that obtained by the numerical simulation after 10 years of mining in the Baiyang mine section. In the region where the exposed area was large and the goafs were densely packed, a large area of plastic zone occurred, and the rock mass may be deformed and damaged.

Figure 11 shows the variations of the plastic zone volume in the quarry rock mass in the Baiyang and Duimenshan mine sections with the increasing mining age. When the midsections at 1,640 m and 1,620 m of the Baiyang mine section as well as the ore body below 1,600 m of the Duimenshan mine section were mined in 2007, the volume curve of the plastic zone steepened, which indicated that

TABLE 3 Quantification of urgency and importance.

Mine section	Midsection elevation/m	Tightness				Importance			X	Y	$\sqrt{X^2+Y^2}$
		J	T	S	W	P	G	I			
Baiyang mine section	1730	9	0	3	3	4	4	0	0.23	0.18	0.29
	1710	8	0	3	3	4	4	0	0.23	0.18	0.29
	1700	7	0	3	3	4	4	0	0.23	0.19	0.29
	1,680	6	0	3	3	4	3	0	0.25	0.20	0.32
	1,660	5	0	3	3	3	2	0	0.35	0.21	0.41
	1,640	4	0	3	2	4	1	0	0.45	0.28	0.53
	1,620	3	0	3	2	3	1	0	0.50	0.31	0.59
	1,600	2	0	4	2	2	1	1	0.70	0.36	0.79
	1,580	1	0	4	2	1	1	1	1.00	0.56	1.15
	1,560	1	0	4	1	1	1	1	1.00	0.69	1.21
	1,540	2	0	4	1	2	2	1	0.55	0.49	0.73
	1,520	3	0	4	1	2	2	0	0.45	0.42	0.62
	1,500	4	0	4	2	3	2	0	0.35	0.26	0.44
	1,480	5	0	4	1	4	2	0	0.30	0.37	0.47
Duimenshan mine section	1830	4	0	3	3	4	4	0	0.23	0.23	0.32
	1800	3	0	3	3	4	4	0	0.23	0.27	0.35
	1780	2	0	3	2	4	4	1	0.33	0.38	0.50
	1760	1	0	3	2	3	4	1	0.38	0.58	0.69
	1740	1	0	3	2	2	3	1	0.50	0.58	0.76
	1720	1	0	3	2	2	2	1	0.55	0.58	0.80
	1700	1	0	3	2	1	2	1	0.85	0.58	1.03
	1,680	1	0	3	1	1	1	1	1.00	0.70	1.22
	1,675	1	0	3	1	1	1	1	1.00	0.70	1.22
	1,660	1	0	3	2	2	1	1	0.70	0.58	0.91
	1,640	2	0	3	2	3	1	1	0.60	0.38	0.71
	1,620	3	0	3	1	3	1	1	0.60	0.43	0.74
	1,600	4	0	4	1	3	2	1	0.45	0.39	0.59
	1,580	5	0	4	2	4	2	0	0.30	0.24	0.39
	1,560	6	0	4	1	4	1	0	0.45	0.35	0.57
	1,550	7	0	4	2	4	1	0	0.45	0.22	0.50
	1,500	8	0	4	1	4	1	0	0.45	0.34	0.56

the stability of the goafs formed by the mining in these midsections was relatively poor.

5.1.3 Analysis of the impact of mining on the proposed goaf

The proposed mining areas in the Baiyang and Duimenshan mine sections were between 1,560 m and 1,580 m midsections, as well as 1,660 m and 1760 m midsections, respectively. The regions with the mining deformation values greater than 1 cm, greater than 0.1 cm and smaller than 1 cm and less than 0.1 cm were defined as the regions of greater impact, less impact and no impact, respectively. The degree and range of impacts on these two sections of the mine are circled as presented in Figures 12, 13 in both the horizontal and vertical directions.

As indicated in the circled range of the impact, after the proposed goaf of the Baiyang mine section was mined, the range

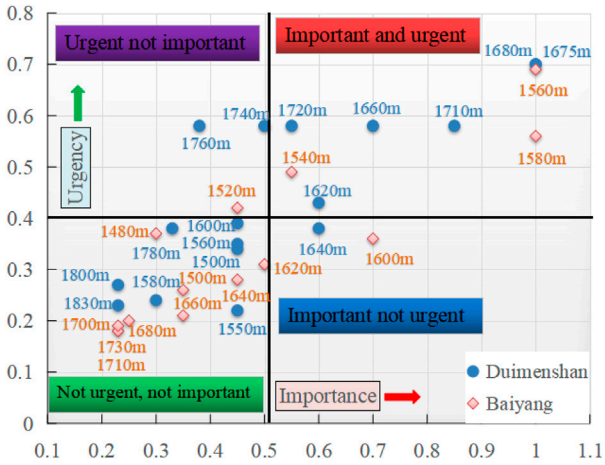

FIGURE 16
Survey time sequence management chart.

of the greatest impact was 6–8 m in horizontal direction while that was about 20 m in vertical direction, i.e., from the midsection of 1,540 m to the midsection of 1,600 m. After the proposed goaf of Duimenshan mine section was mined, the range of the greatest impact was 100 m in horizontal direction while that was approximately 180 m in vertical direction, i.e., the 1,600 m midsection to the 1780 m midsection.

5.1.4 Theoretical calculation of plastic zone radius

Modern ground pressure theory believes that the load borne by the support is the total gravity of the rock in the upper plastic zone, independent of the overlying rock layer. Therefore, as long as the pillar can withstand the gravity of the rock in the plastic zone of the roof surrounding rock after mining, the long-term stability of the roof and pillar system can be ensured. The bearing mechanism of the pillar is shown in Figure 14.

After mining the ore block, ignoring the influence of the pillar on the range of plastic zone in the roof surrounding rock, solving the Kastner formula can obtain the radius of the plastic zone in the roof surrounding rock, which is:

$$R_p = R_0\left[\frac{(P_0 + c\cot\varphi)(1-\sin\varphi)}{c\cot\varphi}\right]^{\frac{(1-\sin\varphi)}{2\sin\varphi}} \tag{4}$$

Where R_p is radius of the plastic zone at the excavation site, m; R_0 is excavation radius, m; P_0 is the vertical self weight stress of the overlying rock layer at the excavation site, MPa; c is cohesive force of rock mass, MPa; φ is internal friction angle of rock mass, °.

Practice has shown that the radius of the plastic zone is less affected by the shape of the excavation section, and can be approximated as the equivalent excavation radius, which is replaced by the outer circle radius of different shapes in calculation. For ore blocks, the equivalent excavation radius R_0 is:

$$R_0 = \sqrt{\left(\frac{L'}{2}\right)^2 + \left(\frac{h}{2}\right)^2} \tag{5}$$

Where L' is the mining space span, m; h is the height of the mining space, m.

The vertical self weight stress at the excavation site is:

$$P_0 = \gamma H \tag{6}$$

Where γ is the unit weight of the overlying rock layer, N/m3; H is the thickness of the overlying rock layer, m.

The bulk density $\gamma = 27.6KN/m^3$, cohesion $c = 0.79MPa$, internal friction angle $\varphi = 36.69°$. Based on the detailed

TABLE 4 The urgency of water damage detection in the goaf is taken.

Value	Water status in goaf
4	Dried without water or with a small amount of water entrained by water vapour
3	Drenching, seepage and drainage are smooth, and there is no obvious water
2	Long term drenching, drainage blockage, local flooding
1	With high water storage and good mobile water recharge

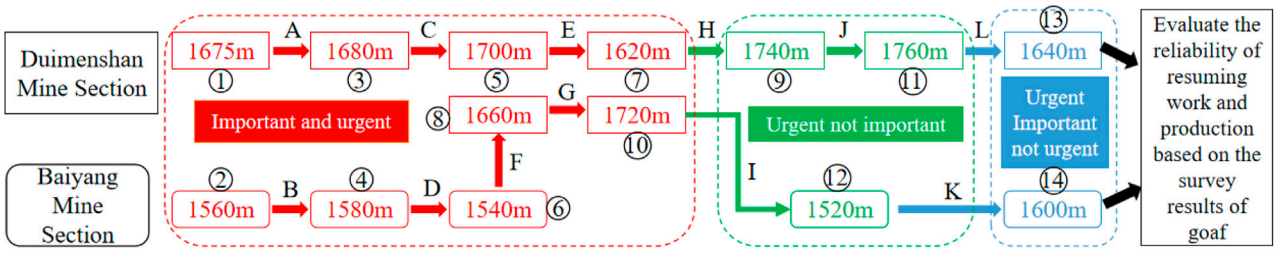

FIGURE 17
Time series network diagram of goaf detection survey.

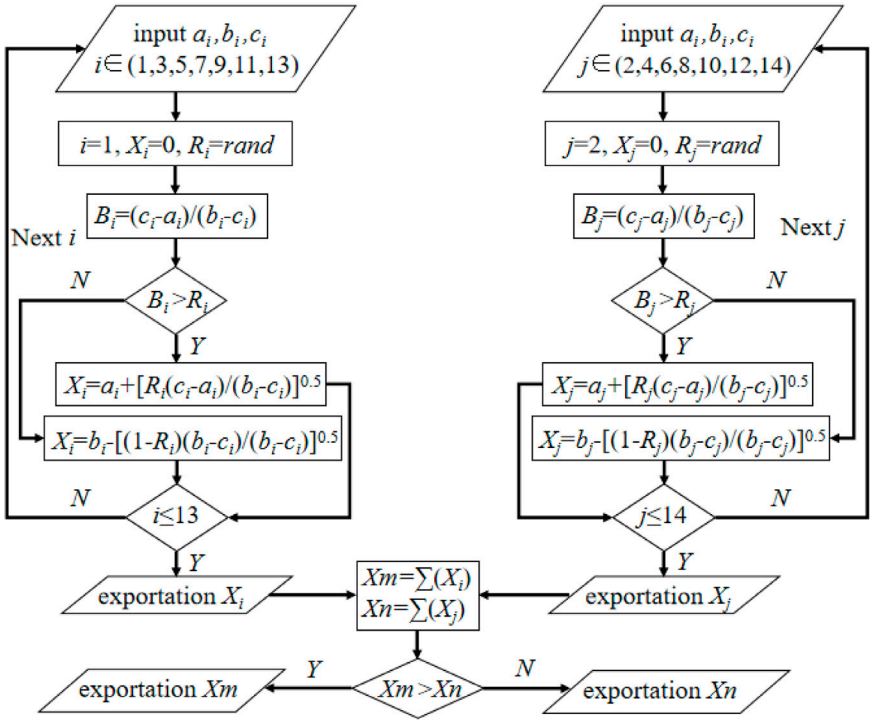

FIGURE 18
Block diagram of the calculation program.

TABLE 5 Estimation of the operation 3.

Process	Argument		
	a	b	c
A (1, 3)	4	12	5
B (2, 4)	3	11	7
C (3, 5)	2	8	4
D (4, 6)	4	13	8
E (5, 7)	7	15	10
F (6, 8)	2	9	5
G (8, 10)	6	14	10
H (7, 9)	5	14	9
I (10, 12)	4	9	6
J (9, 11)	2	10	6
K (12, 14)	2	7	5
L (11, 13)	3	12	5

survey of the size of the goaf and the results of drone scanning detection, the maximum plastic zone radius of the overlying surrounding rock of each mining level can be obtained by calculating equations (4) to 6). The calculation results are shown in Figure 15.

From Figure 15, it can be seen that during the mining of 1640 m in the Baiyang ore section, the radius of the plastic zone is the largest, at 26.9 m. However, during the mining of 1600 m in Damenshan, the radius of the plastic zone is the largest, at 28.2 m, which is in good agreement with the numerical simulation results.

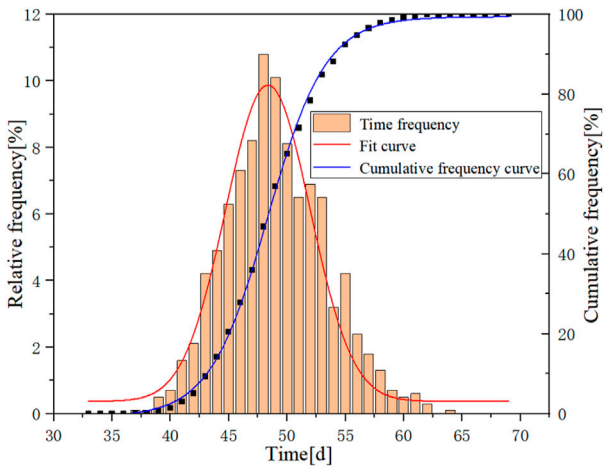

FIGURE 19
Probability distribution chart.

5.1.5 Timing management

The indicators of importance and urgency proposed in the previous section were quantified based on the results of the investigation and numerical simulation of the goafs in the Baiyang and Duimenshan mine sections of the Mengzi mine. The impact of the current goafs on the surface subsidence was determined by Equation 2, and the maximum duration of surface displacement was 3.5 years. Considering that it has been more than 10 years since the mine ceased production in 2012, the urgency value T was therefore set to be 0, and the values of the rest parameters are shown in Table 3.

The results are plotted in a four-quadrant Eisenhower Rule diagram, where the midpoint of the four quadrant division is the average of the calculated results of urgency X and importance Y in Table 3, as illustrated in Figure 16.

It can be seen from the figure above that, prior to the resumption of production activities in the mine, the most primary and core detection areas for the goafs were as follows: midsections of the 1,540 m, 1,560 m and 1,580 m of the Baiyang mine section, midsections of the 1,620 m, 1,660 m, 1,675 m, 1,680 m, 1710 m and 1720 m of the Duimenshan mine section. The results of this study are presented in Table 4, it can be seen that there was a higher requirement for the degree of investigation and detection of the goafs. The secondary ones were the midsections of the 1,520 m, 1740 m, and 1760 m of the Duimenshan mine section. The final ones were 1,600 m midsection of Baiyang mine section and 1,640 m midsection of Duimenshan mine section. Except for the above-mentioned goaf, all other goaf areas belong to the "black box" category, with a total of 18 midsections. These goaf areas will be supplemented with exploration in the remaining time after the above investigation is completed.

5.2 Duration estimation

Section 5.1 specifies the scope and priority of the detection survey that must be carried out before the resumption of work and production in the mine, in addition to the goafs within the scope of the 'black box'. Two groups of personnel were arranged to carry out the detection survey at the same time, the detection work is mainly carried out using TEM, the network diagram is shown in Figure 17.

5.2.1 Monte Carlo simulation process

The 14 investigation processes in the network diagram were distributed over 2 paths L_m and L_n, each of which had 7 investigation processes. The serial numbers on path L_m were 1, 3, 5, 7, 9, 11 and 13, while these on the path L_n were 2, 4, 6, 8, 10, 12 and 14. The calculation procedure is represented by the program block diagram, which was cycled n times to get the process duration and then to calculate the duration of each path. The duration of the path with the longest was the total duration. The more cycles, the closer the total duration was to the actual value. One of the cycles is shown in Figure 18.

The time parameters of each investigated process with specific three-time estimation data are shown in Table 5.

5.2.2 Simulation results

Statistical analysis of the 1,000 sets of calculation results after 1,000 cycles of the Monte Carlo calculation program was performed to obtain a probability distribution graph about the survey duration for goaf detection, as indicated in Figure 19. By connecting the histogram into a smooth curve, it can be qualitatively determined that the construction duration of the project fully conformed to the Normal distribution. There was a 90% probability that the construction duration was between 43 and 56 d, and it can be determined that the most probable construction duration of the project was 48 d.

6 Discussion

There are many factors that affect the stability of goaf and the safety of production areas. The construction of a standardized safety mining detection model for goaf in this article considers a total of 7 factors in terms of urgency and importance, which may not be comprehensive enough. In terms of detection, different detection methods have different advantages, disadvantages, and applicable conditions, which requires a lot of space to discuss. The construction of the model is only based on the analysis of conventional detection methods, without fully considering the impact of various methods.

The construction of the model in this article is applicable to mines that use open pit mining. During the analysis process, it is necessary to quantify the various parameters of urgency and importance. Therefore, it is necessary to have some basic data on the remaining goaf of the mine. In the early stage, it is necessary to conduct a review of production design data and the actual situation on site.

7 Conclusion

(1) This article is the first to apply the three important theories of operational research, Eisenhower Rule, Priority Formula and Monte Carlo method, to the construction of a standardized model for goaf safety detection, which can provide technical guidance for the entire process of safety detection and early warning in underground goaf mining.

(2) Quantifying the urgency and importance of goaf detection and investigation, achieving hierarchical, phased, and time series management, can highlight key goaf areas and drive comprehensive goaf detection work in mines.
(3) Applying the FLAC^{3D} numerical simulation results of the mine to the model saves a lot of manpower and material resources in the exploration work, and accelerates the pace of resuming work and production.

Data availability statement

The original contributions presented in the study are included in the article/supplementary material, further inquiries can be directed to the corresponding author.

Author contributions

YZ: Conceptualization, Data curation, Formal Analysis, Methodology, Writing–original draft. KH: Funding acquisition, Methodology, Resources, Supervision, writing–review and editing. XN: Investigation, Methodology, Software, Writing–review and editing. WL: Funding acquisition, Methodology, Supervision, Writing–review and editing.

Funding

The author(s) declare financial support was received for the research, authorship, and/or publication of this article. The work described in this paper was supported by the Guizhou Provincial Science and Technology Project [No. QKHZC (2021) General 407] and the New Talent Training Project of the Guizhou Institute of Technology (No. GZLGXM-29).

Conflict of interest

The authors declare that the research was conducted in the absence of any commercial or financial relationships that could be construed as a potential conflict of interest.

Publisher's note

References

Chen, F., Wang, X., Wang, Z., and Zheng, J. (2021). Study on the application of comprehensive geophysical prospecting technology for the goaf detection in coal mine. *IOP Conf. Ser. Earth Environ. Sci.* 660 (1), 012109. doi:10.1088/1755-1315/660/1/012109

Chun, B., Meng, X., and Jun, M. (2020). Hazards of environmental disruption in mine goafs and stability evaluation in gaofeng mining area. *Nat. Environ. Pollut. Technol.* 19 (3), 005. doi:10.46488/NEPT.2020.V19I03.005

Dai, Y. (2019). A preliminary study on the disposal sequence of a gate safety hazard. *Municipal·Traffic·Water Resour. Eng. Des.* 3, 149–150+153. doi:10.13616/j.cnki.gcjsysj.2019.02.050

Deng, J., Meng, Z., and Mao, J. (2009). Potential hazard evaluation and treatment of mine goaf in orebody. *Metal. Mine* 8, 126–129.

Feng, P., and Huang, D. (2020). Study on application of goaf management and residual mining technology in niujuan deposit. *E3S Web Conf.* 165, 03041. doi:10.1051/e3sconf/202016503041

Gao, Y., Yu, Z., Chen, W., Yin, Q., Wu, J., and Wang, W. (2023). Recognition of rock materials after high-temperature deterioration based on SEM images via deep learning. *J. Mater. Res. Technol.* 05, 273–284. doi:10.1016/j.jmrt.2023.05.271

Gui, H., Sun, L., and Chen, S. (2016). Research on goaf water features and disaster formation mechanism in China coalmines. *IOP Conf. Ser. Earth Environ. Sci.* 44 (4), 042036. doi:10.1088/1755-1315/44/4/042036

Guo, X., Dou, L., Xu, B., Tang, S., Wen, X., and Wu, B. (2014). Metagenomic profiles and antibiotic resistance genes in gut microbiota of mice exposed to arsenic and iron. *Coal Sci. Technol.* 42 (02), 1–8. doi:10.1016/j.chemosphere.2014.03.068

He, R., Han, Z., Zhou, Y., Liu, H., and Liu, Y. (2020). Analysis on disaster characteristics and preventive measures of goaf in metal and non-metal mines. *Min. Res. Dev.* 40 (9), 33–38. doi:10.13827/j.cnki.kyyk.2020.09.007

Henjewele, C., Fewings, P., and Pantaleo, D. (2013). De-marginalising the public in PPP projects through multi-stakeholders management. *J. Financial Manag. Prop. Constr.* 1 8 (2), 210–231. doi:10.1108/jfmpc-05-2013-0021

Huang, X., and Chu, F. (2019). Risk grade evaluation model of goaf based on logical regression and clustering algorithm. *Ment. Mine* 8, 179–184. doi:10.19614/j.cnki.jsks.201908030

Jia, H., and Xue, J. (2021). The stability study of goaf based on C-ALS data point cloud and FLAC3D Coupled modeling. *E3S Web Conf.* 261, 03053. doi:10.1051/e3sconf/202126103053

Jiang, H., Ye, Y., Hu, N., Wang, Q., Chen, H., and Wu, M. (2021). The risk assessment of goaf based on the ariable weight synthesizing weights grey target model. *China Min. Mag.* 30 (10), 106–113.

Li, L., Wu, D., and Liu, Y. (2020). Study on permanent basic farmland demarcation around the city with the fourquadrant method. *Chin. J. Agric. Resour. Regional Plan.* 41 (5), 87–97.

Li, X., Wang, J., and Guo, X. (2021a). Analysis and Practice of detection methods for goafs in complex coal mines. *J. Phys. Conf. Ser.* 2006 (1), 012056. doi:10.1088/1742-6596/2006/1/012056

Li, X., Zhang, X., Shen, W., Zeng, Q., Chen, P., Qin, Q., et al. (2023). Research on the mechanism and control technology of coal wall sloughing in the ultra-large mining height working face. *Int. J. Environ. Res. Public Health* 20 (2), 868. doi:10.3390/ijerph20010868

Li, Z., Xu, Y., Liu, H., Zhai, X., Zhao, S., and Yu, Z. (2021b). Numerical analysis on the potential danger zone of compound hazard in gob under mining condition. *Process Saf. Environ. Prot.* 147, 1125–1134. doi:10.1016/j.psep.2021.01.043

liao, G., Peng, X., Wang, Y., Hu, J., Li, Q., and Ma, H. (2008). Practice about evaluation technology in disposing the hidden trouble in large complicated group mined-out stope. *J. Saf. Sci. Technol.* 4 (1), 15–20.

Liu, S., and Li, X. (2023). Experimental study on the effect of cold soaking with liquid nitrogen on the coal chemical and microstructural characteristics. *Environ. Sci. Pollut. Res.* 30 (3), 36080–36097. doi:10.1007/s11356-022-24821-9

Liu, S., Sun, H., Zhang, D., Yang, K., Li, X., Wang, D., et al. (2023b). Experimental study of effect of liquid nitrogen cold soaking on coal pore structure and fractal characteristics. *Energy* 275 (7), 127470. doi:10.1016/j.energy.2023.127470

Liu, S., Sun, H., Zhang, D., Yang, K., Wang, D., Li, X., et al. (2023a). Nuclear magnetic resonance study on the influence of liquid nitrogen cold soaking on the pore structure of different coals. *Phys. Fluids* 35 (1), 012009. doi:10.1063/5.0135290

Liu, Z., Deng, D., Feng, J., Wang, R., Fan, J., and Ma, Y. (2022). Study on natural settlement index characteristics of iron-bearing tailings applied to goaf filling treatment. *Sustainability* 14 (17), 10739. doi:10.3390/su141710739

Luo, Y., He, L., Ma, Z., Chen, Z., and Zhou, L. (2021). Clearing the design barriers of international EPC project via the technique of project stakeholders management and quadrant method. *J. Eng. Manag.* 35 (1), 55–59. doi:10.13991/j.cnki.jem.2021.01.010

Ma, H. (2021). *Coupling effect of coal pillar-roofand stability evaluation of pillar goaf*. Xuzhou: China University of Mining and Technology.

Martínez-Pagán, P., Gómez-Ortiz, D., Martín-Crespo, T., Manteca, J. I., and Rosique, M. (2013). The electrical resistivity tomography method in the detection of shallow mining cavities. A case study on the Victoria Cave, Cartagena (SE Spain). *Eng. Geol.* 156, 1–10. doi:10.1016/j.enggeo.2013.01.013

Ning, Y., Jiang, F., and Lin, W. (2019). Study on stability evaluation and treatment scheme of goaf in Huanggang iron mine. *Min. Res. Dev.* 39 (8), 74–77. doi:10.13827/j.cnki.kyyk.2019.08.015

Niu, Q., Song, X., and Zhang, H. (2020). Risk AssessmentofBuildingsatServiceStage basedon Monte Carlo method. *J. Xuzhou Inst. Technol. (Nat. Sci. Ed.)* 35 (2), 86–92. doi:10.15873/j.cnki.jxit.000357

Pei, Y., Wu, J., Sun, Q., Zhang, Z., and Yang, X. (2021). Improved GA-BP risk level evaluation model for complex goaf in mines. *Chin. J. Undergr. Space Eng.* 17, 979–984.

Qiu, H., Qiu, W., Tong, S., and Zhang, H. (2018). Overview of goaf water hazards control in China coalmines. *Arabian J. Geosciences* 11 (3), 12517. doi:10.1007/s12517-018-3391-z

Sariandi, F., Putra, G. V., Setyorini, G. V., and Saptono, S. (2018). Stope stability analysis of limestone ex-mined area at Ponjong sub-district Special Region of Yogyakarta using finite element method. *IOP Conf. Ser. Earth Environ. Sci.* 212, 012037. doi:10.1088/1755-1315/212/1/012037

Wang, C., Lu, Y., Cui, B., Hao, G., and Zhang, X. (2018). Stability evaluation of old goaf treated with grouting under building load. *Geotechnical Geol. Eng.* 36 (4), 2553–2564. doi:10.1007/s10706-018-0482-2

Wang, N., Wang, Z., Sun, Q., and Hui, J. (2023). Coal mine goaf interpretation: survey, passive electromagnetic methods and case study. *Minerals* 13 (3), 422. doi:10.3390/min13030422

Wang, Y., and Zhen, Z. (2021). Study on the law of surface subsidence and deformation in goaf. *Sci. Technol. Innovation* 6, 35–37.

Wei, T., Guo, G., Li, H., Wang, L., Yang, X., and Wang, Y. (2022). Fusing minimal unit probability integration method and optimized quantum annealing for spatial location of coal goafs. *KSCE J. Civ. Eng.* 26 (5), 2381–2391. doi:10.1007/s12205-022-1034-0

Yu, C., Liu, X., Liu, J., Li, E., Yue, P., and Yan, S. (2018). Application of transient electromagnetic method for investigating the water-enriched mined-out area. *Appl. Sci.* 8 (10), 1800. doi:10.3390/app8101800

Yu, H., Li, S., and Wang, X. (2022). The recent progress China has made in the backfill mining method, Part III: practical engineering problems in stope and goaf backfill. *Minerals* 12 (1), 88. doi:10.3390/min12010088

Zhang, J., Li, X., Qin, Q., Wang, Y., and Gao, X. (2023b). Study on overlying strata movement patterns and mechanisms in super-large mining height stopes. *Bull. Eng. Geol. Environ.* 82 (3), 142. doi:10.1007/s10064-023-03185-5

Zhang, L., Shen, W., Li, X., Wang, Y., Qin, Q., Lu, X., et al. (2023a). Abutment pressure distribution law and support analysis of super large mining height face. *Int. J. Environ. Res. Public Health* 20 (1), 227. doi:10.3390/ijerph20010227

Zhang, Y., Cao, P., Yuan, H., and Dong, L. (2010). *Numer. Simul. Stab. Complicat. Goaf* 27 (2), 233–238.

Zu, F., Du, C., Han, C., Xu, L., and Peng, Q. (2023). Applicable conditions of room-and-pillar mining goaf treatment methods under a traffic load. *Appl. Sci.* 13 (3), 2024. doi:10.3390/app13032024

frontiers | Frontiers in Ecology and Evolution

TYPE Original Research
PUBLISHED 07 September 2023
DOI 10.3389/fevo.2023.1265883

OPEN ACCESS

EDITED BY
Xuelong Li,
Shandong University of Science and Technology, China

REVIEWED BY
Wenda Wu,
Taiyuan University of Technology, China
G. L. Guo,
Eastern Institute of Advanced Study, China

*CORRESPONDENCE
Wenlong Shen
shenwenlong.888@163.com

RECEIVED 24 July 2023
ACCEPTED 17 August 2023
PUBLISHED 07 September 2023

CITATION
Liu J, Shen W, Bai J, Shan C and Liu X (2023) Experiment on separated layer rock failure technology for stress reduction of entry under coal pillar in mining conditions. *Front. Ecol. Evol.* 11:1265883. doi: 10.3389/fevo.2023.1265883

Experiment on separated layer rock failure technology for stress reduction of entry under coal pillar in mining conditions

Juntao Liu[1], Wenlong Shen[2,3]*, Jianbiao Bai[1], Chengfang Shan[1,4] and Xudong Liu[1]

[1]State Key Laboratory of Coal Resources and Safe Mining, China University of Mining and Technology, Xuzhou, Jiangsu, China, [2]School of Energy Science and Engineering, Henan Polytechnic University, Jiaozuo, China, [3]Collaborative Innovation Center of Coal Work Safety and Clean High Efficiency Utilization, Henan Polytechnic University, Jiaozuo, China, [4]Chief Engineer Office, Kuqa Yushuling Coal Mine Limited Liability Company, Kuqa, China

Longwall entrance is especially vulnerable to the combined mining of nearby coal seams because of the substantial deformation disaster loaded by the abutment stress caused by the mining disturbance. Changes to the fracture characteristics, movement behavior, and structural morphology of the bearing structure above the coal pillar are recommended using the separated layer rock failure technology (SLRFT) to safeguard the entry beneath the coal pillar from high abutment stress. To simulate the impacts of the SLRFT on the decrease of the abutment stress surrounding the entry under the coal pillar under the plane–stress circumstances, two experimental models were created. Abutment stress revolution, roof movement laws, and fracture features were all tracked using three identical monitoring systems in each experimental model. The experimental results indicate that SLRFT generates the shorter caving step length, more layered collapse, and higher caving height of the immediate roof, which improves the dilatancy of caving rock mass, the filling rate, and the compaction degree of the worked-out area. In the ceiling above the worked-out area, the fracture progresses from a non-penetrating horizontal and oblique gaping fracture to stepped closed fractures and piercing fractures. The main roof's subsidence shifts from a linear, slow tendency to a stepped, fast one. The bearing structure changes from two-side cantilever structure with a T type into one-side cantilever structure with a basin type. Because the compacted worked-out region has a bigger support area, more of the overburden load is transferred there, weakening the abutment stress around the longwall entry from 12.5 kPa to 3.7 kPa. The stress reduction degree increases with the reduction of the cantilever length of the bearing structure and the increasing of the support coefficient of the compacted worked-out area. These findings illustrate the effectiveness of SLRFT in lowering entrance stress. With the established experimental model, it is possible to evaluate the viability, efficiency, and design of SLRFT under various engineering and geological circumstances.

KEYWORDS

separated layer rock failure technology, abutment stress reduction, longwall entry under coal pillar, combined mining of close distance coal seams, bearing structure above the coal pillar

1 Introduction

The stability of the longwall entry is affected by the stress, the materials, and the support surrounding it (Kang et al., 2019; Xia et al., 2022; Li et al., 2023; Zhang et al., 2023a). The longwall entry will serve as the subterranean space's access point for ventilation, transit, pedestrian, and other production systems. It will encounter multiple disturbances of the mining abutment stress when it is located under the coal pillar in the combined mining of close distance coal seams (Ning et al., 2020). According to Liu et al. (2021), these multiple disturbances will result in supporting body failure, significant deformation, roof collapsing, or even rock burst, endangering the stability control of the longwall entry under a specific geological and technical condition. These specific geological and technical conditions always concentrate on temperature, air pressure, hydraulic pressure, and the ground pressure (Liu and Li, 2023; Liu et al., 2023b; Ye et al., 2023; Zhang et al., 2023b). According to Zhang et al. (2022b), locating the abutment stress's origin is helpful for stress reduction.

According to Wang et al. (2015), the abutment stress in the upper close-distance coal pillar is the main source of the abutment stress near the longwall entry. When the neighboring working face retreats, this coal pillar will experience loading and unloading action, which alters how the abutment stress is distributed in the coal pillar (Shen et al., 2016). This change is induced from the partial overburden weight above the worked-out area loading on the unworked-out area by the bearing structure, which results in the stress redistribution around the longwall entry under the coal pillar and makes the rock around the longwall entry suffer from loading and unloading action either (Shen et al., 2021; Zhang et al., 2023c). Under this type of action, the plastic, crushing, and rupture failure zones will spread into the deeper rock surrounding the longwall entry, which is the cause of the longwall entry's significant deformation (Bai et al., 2015; Liu et al., 2023a; Zhang et al., 2020; Liu et al., 2022). To lessen the failure zone indicated above and keep this longwall entrance stable, it is effective to weaken the abutment stress.

To reduce abutment stress, one can either eliminate the source of the stress, avoid situations with high abutment stress, or move the stress to a location remote from the longwall entry (Shen et al., 2020). Solid backfilling technology is used to eliminate the generation of the abutment stress by preventing the movement of the roofs, which needs to consume a lot of filling materials and is hard to reach 100% of filling rate (Zhang et al., 2016; Zhang et al., 2022c; Meng et al., 2023). When the location of the longwall entry is permissible for adjustment (Wilson and Ashwin, 1972; Hou and Ma, 1989; Li et al., 2015; Yuan et al., 2023), entry layout technology can protect the longwall entry from high abutment stress. Cutting roof technology can transfer the abutment stress from the longwall entry to the far away area by changing the bearing structure above the coal pillar, which always ignores the effects of the nearby thick rock strata's movement, the upper hard roof structure movement, the structure plane along the rock plane, and the preset crack mechanical behavior (Huang et al., 2018; Wang et al., 2021; Wang et al., 2020; Sun et al., 2022; Zhang et al., 2022a). It is necessary to conduct more research to determine whether the hard roof would crack, slip, cave along the predicted crack plane, and produce a suitable bearing structure above the coal pillar.

In this work, separated layer rock failure technology (SLRFT) is proposed to weaken the multiple disturbances of the abutment stress and improve the stability of the longwall entry. The initial step in determining its stress reduction method is to analyze the fracture characteristics, movement behavior, and structural morphology of the bearing structure above the coal pillar. For the purpose of revealing the process for stress reduction and subsequently proving the viability of SLRFT, two physical simulation models with plane–stress circumstances are created. SLRFT's effectiveness and influencing elements are ultimately explored and determined.

2 Method of SLRFT

A technique for altering rock structure while mining disturbs it is shown in Figure 1. It is known as SLRFT. The artificial structure plane parallel to the lower thick rock stratum plane (ASPP), the artificial structure plane intersecting in the upper thick hard roof (ASPI), and the mining extra loading and unloading impact on ASPP and ASPI (MALU) make up its three interaction aspects. In the SLRFT, ASPP is an artificial discontinuous structural plane that needs to be parallel to the thick rock stratum plane and can be generated with hydrofracturing or high-pressure water jet technology in the field application. Its main function is

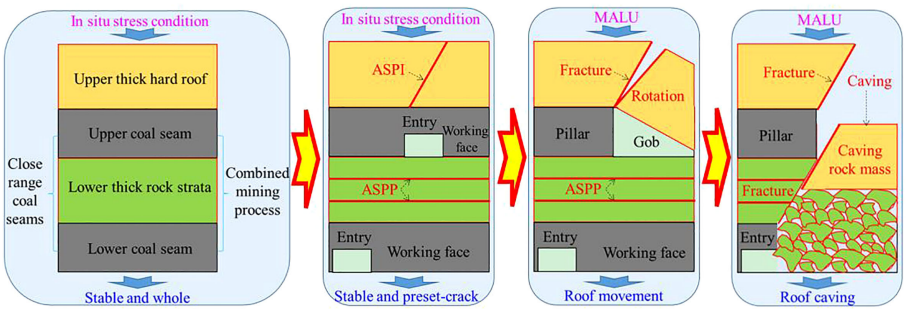

FIGURE 1
Method of SLRFT.

accelerating the movement of lower thick rock strata by separating the lower thick rock strata into multiple straticulate rock structures along ASPP under MALU. By dividing the upper thick hard roof into two portions along ASPI under MALU, ASPI plays a crucial function in identifying the site of the fracture of the upper thick hard roof. MALU is experiencing temporal and spatial variation during the ASPP and ASPI processes. In addition, the time-varying MALU will respond to the ASPP and ASPI processes. Finally, SLRFT will achieve the reduction of abutment stress around the longwall entry by changing the bearing structure of the fracture thick roof strata with ASPP, ASPI, and MALU.

Before MALU and ASPP may have an impact, ASPI must be created in the upper thick hard roof. Under the first in-place load, the hard roof maintains its stability and completeness. The hard roof's internal load will transform into a new equilibrium state after ASPI is created, whereas the hard roof's external load will remain in its initial state. The exterior load of the hard roof will change into a different state during the MALU process due to the mining impact; thus, it maintains stability because the internal change cannot affect the external condition. When the worked-out area is covered by the hard roof, this external load will decrease. However, it will rise if the neighboring undeveloped area is covered by a hard roof. In addition, as the mining working face advances, it will go through a rising and decreasing procedure. Finally, with the influence of MALU, the hard roof will fracture along the preset structure plane and changes into a reasonable bearing structure by a different way of movement behavior and fracture characteristics.

Prior to the impact of MALU, ASPP must be created in the lower, thicker rock strata. The thick rock strata maintain their stability under the initial *in situ* stress before the influence of MALU. After ASPP is established, it is separated into multiple straticulate rock structures. The straticulate rock structures are susceptible to bending, fracturing, caving, and expanding under the impact of MALU. The thick rock strata's movement behavior, fracture characteristics, and structural morphology will alter as a result of ASPP. Finally, the caving-expansion rock mass is beneficial to the filling of the underground mined area, which will affect the behavior of the upper thick hard roof

3 Experimental models for SLRFT

3.1 Geological and mining conditions

In the Chinese province of Shanxi, Jinzhong is home to the Lingshihuayuan coal mine. In this coal mine, the nearby coal seams are mined using a combined mining technique to provide coal resources. The coal seams at numbers 8, 9, 10, and 11 are the closest to the surface as shown in Figure 2A. Among the coal seams, the thickness of the numbers 8 and 11 cannot meet the mining requirement under the current mining technology. Nearly 390 m below the surface of the earth, there is a coal seam known as number 9. Its average thickness is 1.12 m, and its average dip angle is 2°. Limestone, sandstone, and fine sandstone make up the underlying strata above coal seam number 9. Moreover, the roof strata of the number 10 coal seam are composed of sandy mudstone, which is located beneath the number 9 coal seam. This roof strata's average thickness is 5.32 m, which corresponds to the distance between coal seam numbers 9 and 10. The number 10 coal seam has an average thickness of 4.23 m and a 2° dip angle. Sandstone, the number 11 coal seam, mudstone, and sandstone are among the geological types found in its nether regions.

Each coal seam uses a two-entry method, as indicated in Figure 2B, for every longwall full-seam operation. The length of the longwall panel is 164 m in the coal seam number 9 and 199 m in coal seam number 10. To recycle more than 378,872 tons of coal resources, the entry of the longwall panel in coal seam number 10 must be positioned below the coal pillar of the longwall panel in coal seam number 9. The entry must be made to withstand the abutment stress brought on by the upper coal pillar and mining working face in coal seam numbers 9 and 10.

3.2 Physical models

As illustrated in Figure 3, two physical models were developed to assess the SLRFT's reliability at the State Key Laboratory of Coal Resources in China. Each model has a length, a width, and a height of 2.50 m, 0.20 m, and 0.73 m, respectively. The shape, density, and strength should be consistent with the connection as Equation (1), according to the similarity theory (Fumagalli, 1973). In this experiment, C_L, C_ρ, C_σ, and C_t's similarity ratios were calculated to be 100, 1.5, 150, and 10, respectively. With the help of this model design, it is possible to simulate the mechanical behavior of the higher coal pillar and lower entry and lower mining operating activities in the lower coal seam. To replicate the SLRFT effects in the two models, various ASPP and ASPI numbers were set up. In model 1's sandy mudstone, one ASPP was placed in the center, and, in model 2's sandy mudstone, two ASPPs were placed, as shown in Figure 3. In addition, two ASPIs were placed in the limestone in model 2, whereas zero ASPIs were placed in model 1, as seen in Figure 3.

$$\begin{cases} C_\sigma / C_\rho / C_L = 1 \\ C_L = L_\rho / L_m \\ C_\sigma = \sigma_p / \sigma_m \\ C_\rho = \rho_p / \rho_m \\ C_t = /C_L / \sqrt{C_L} \end{cases} \quad (1)$$

where C_L, C_σ, and C_t are the similarity ratios of geometry, strength, and time, respectively. C_ρ is the density similarity ratio between the prototype and the model. L_p, σ_p, and ρ_p represent the dimension, strength, and density of the rock strata in the field, respectively; L_m, σ_m, and ρ_m represent the dimension, strength, and density of the rock strata in the model, respectively.

3.3 Physical materials

Table 1 lists the 21 materials that were utilized to mimic the mechanical behavior of rock strata, coal seams, ASPP, ASPI, and structure plane for each model. Sand, gypsum, calcium carbonate,

A

Lithology	Thickness (m)	Depth (m)	Remarks
Sandy mudstone	6.00	354.79	Nearby Overburden rock strata in the roof
Mudstone	6.15	360.94	
Limestone	4.15	365.09	
Mudstone	2.50	367.59	
Sandy mudstone	1.50	369.09	
Sandstone	2.80	371.89	
Sandy mudstone	1.00	372.89	
Limestone	3.15	376.04	
Coal seam 8	0.50	376.54	
Sandy mudstone	2.00	378.54	
Fine sandstone	1.23	379.77	
Sandy mudstone	2.31	382.08	
Limestone	6.80	388.88	Upper thick hard roof
Coal seam 9	1.12	390.00	Upper coal seam
Sandy mudstone	5.32	395.32	Lower thick rock strata
Coal seam 10	4.23	399.55	Lower coal seam
Sandy Mudstone	2.23	401.78	Nearby supporting rock strata in the floor
Coal seam 11	0.63	402.41	
Sandy mudstone	11.00	413.41	
Sandstone	2.14	415.55	
Mudstone	5.94	421.49	

B

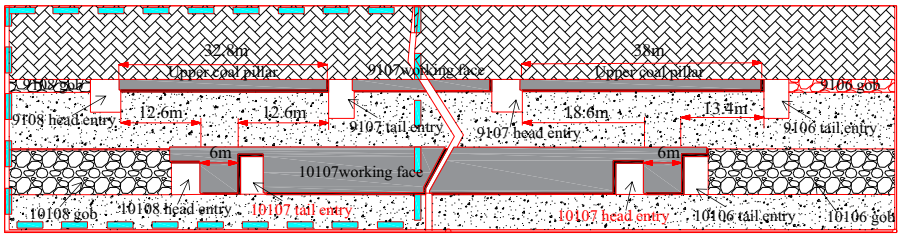

FIGURE 2
Generalized stratigraphic column and entry layout condition. **(A)** Coal seam histogram. **(B)** Entry layout profile.

water, mica powder, and other materials are mixed together. According to the strength similarity ratio and the uniaxial compression strength of each rock stratum, the ratio of each type of simulation material contents is established by the current material ratio (Tu, 2010). For each model, a total of 809.64 kg of sand, 61.09 kg of calcium carbonate, 115.75 kg of gypsum, 98.6 L of water, and 20 kg of mica powder are utilized.

3.4 Monitoring instruments and scheme

Evaluating the indices of the SLRFT effect during the combined mining activity of upper and lower working faces, the vertical displacement, structure morphology, and abutment stress are identified. To track the development of the abutment stress in the rock at the longwall entry, a ZC40YL data acquisition system with a

A B

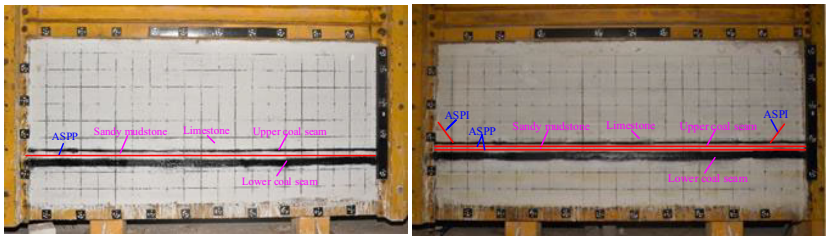

FIGURE 3
Physical models for SLRFT. **(A)** Model 1 with ASPP and without ASPI. **(B)** Model 2 with ASPP and ASPI.

TABLE 1 Materials used in each physical model.

Lithology	Thickness (cm)	Uniaxial compressive strength of prototype (MPa)	Uniaxial compressive strength of model (kPa)	Sand (kg)	Calcium carbonate (kg)	Gypsum (kg)	Water (L)
Sandy mudstone	6.00	26.00	173.33	65.57	3.28	7.65	7.70
Mudstone	6.15	23.00	153.33	63.75	3.83	8.93	7.70
Limestone	4.15	50.00	333.33	38.25	3.83	8.93	5.10
Mudstone	2.50	23.00	153.33	31.88	3.19	3.19	3.80
Sandy mudstone	1.50	26.00	173.33	21.86	1.09	2.55	2.60
Sandstone	2.80	30.00	200.00	28.68	2.87	6.69	3.80
Sandy mudstone	1.00	26.00	173.33	10.93	0.55	1.27	1.30
Limestone	3.15	50.00	333.33	47.81	4.78	11.16	6.40
Coal seam 8	0.50	12.52	83.47	11.15	3.18	3.18	1.30
Sandy mudstone	2.00	26.00	173.33	21.86	1.09	2.55	2.60
Fine sandstone	1.23	35.00	233.33	20.4	1.53	3.57	2.60
Sandy mudstone	2.31	26.00	173.33	32.78	1.64	3.83	3.80
Limestone	6.80	50.00	333.33	66.94	6.69	15.62	8.90
Coal seam 9	1.12	12.52	83.47	11.15	0.80	0.80	1.30
Sandy mudstone	5.32	18.45	123.00	54.64	2.73	6.37	6.40
Coal seam 10	4.23	14.09	93.93	44.63	3.19	3.19	5.10
Sandy mudstone	2.23	22.25	148.33	21.86	1.10	2.55	2.60
Coal seam 11	0.63	14.09	93.93	11.15	0.80	0.80	1.30
Sandy mudstone	11.00	26.00	173.33	120.21	6.00	14.00	14.00
Sandstone	2.14	34.67	231.13	20.40	2.55	2.55	2.60
Mudstone	5.94	23.00	153.33	63.75	6.38	6.38	7.70

BW flat earth pressure box was used. The progression of the vertical displacement was documented using a three-dimensional digital photogrammetry system called CoordMeasis that included white gauge points, encoding points, and scale plates. The structure morphology was also captured using the high-definition camera. In the physical model, 189 gauge points and six flat earth pressure boxes are placed. According to Figure 4, the specific monitoring settings are set up.

The sandy mudstone above the lower coal seam and the limestone above the upper coal seam are chosen as the focus of the analysis to highlight the impacts of SLRFT on the vertical displacement. Six monitoring locations have been chosen in total to track the limestone and sandstone's vertical displacement over time. Points 1 and 2 are situated at the sandy mudstone and limestone, respectively, and are separated from the lower coal seam's lateral end of the gob by a horizontal distance of 11.5 cm. At a horizontal distance of 57.5 cm from the lateral termination of the gob in the lower coal seam, points 3 and 4 are situated at the sandy mudstone and limestone, respectively. With a horizontal distance of 102.9 cm from the lateral endpoint of the gob in the lower coal seam, points 5 and 6 are situated at the sandy mudstone and limestone, respectively.

The sandstone above the lower coal seam and the sandstone below the lower coal seam are chosen to study the bearing properties of rock strata beneath the upper coal pillar to reveal the impacts of SLRFT on the abutment stress. Three monitoring locations have been chosen in total to track the development of the rock below the top coal pillar's abutment stress. Underneath the lower coal pillar, at point A, is the sandy mudstone. The location of point B is at the sandy mudstone beneath the center of the lower

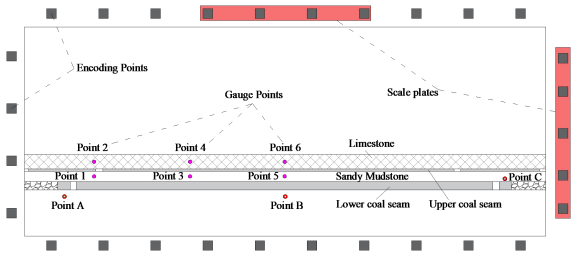

FIGURE 4
Monitoring points layout in the physical models.

working face. Above the lower coal pillar, point C is situated at the sandy mudstone.

3.5 Experimental procedures

Seven steps make up the entire experimental process. The first phase involves setting up the experimental equipment and supplies. The two tall, stiff loading frames, the electricity-powered mixing barrel, the electronic scale, the monitoring systems, the simulation materials, and other necessary equipment are among them. For each model, 21 actual rock strata can be built individually in the second stage. A variety of mica powders were employed to replicate ASPP in the sandy mudstone, ASPI in the limestone, and the structural plane between two neighboring rock strata. In the third step, 20 loading rams in the top frame were subjected to a vertical load of 0.06 MPa to approximate the overburden loads after 1 week. The normal displacement in the floor and side boundaries was fixed with the frame. In the fourth step, excavation was conducted to generate the entries, coal pillars, gobs, and working faces in the upper and lower coal seams under the condition of the design in Figure 2. The order of excavation in the upper coal seam is as follows: 9106 tail entry, 9106 gob, 9108 head entry, 9108 gob, 9107 head entry, and 9107 tail entry. The lower coal seam has the following order: 10107 head entry, 10107 tail entry, 10108 head entry, 10108 gob, 10106 tail entry, 10106 gob, and 10108 head entry. The working face was retreated in the fifth step, moving from the upper coal seam's 9107 head entry to 9107 tail entry stage by stage every 30 min. A miniature shovel was used in each stage to dig out coal that was 10 mm long. After the working face had been excavated by 50 cm in the higher coal seam, the working face was retreated from 10107 head entrance to 10107 tail entry stage by stage every 30 min in the lower coal seam. The distance between the bottom and upper working faces, measured horizontally, is 50 cm. A small shovel was also used at each stage to dig out coal that was 10 mm long. The excavation continues through the final working face in the lower coal seam in the final stage. The monitoring systems should be functioning normally during excavation so that they can record data until the completion of excavation.

In the experimental procedures, the mining activities are divided into three stages: stage I, stage II, and stage III. The upper working face is retreating in stage I, whereas the lower working face remains stationary. Once the upper working face has retreated 50 cm, the lower working face also starts to regress, and the mining operation shifts to stage II, which is a simultaneous retreat of the upper and lower working faces. After the top working face retreats to the finishing line position, 150 cm from the start, the mining activity transitions into stage III, which involves the retreating of the bottom working face.

4 Results

4.1 Effects of SLRFT on the movement behavior of rock strata

SLRFT primarily accelerates the roof subsidence close to the lateral gob termination in the lower coal seam, as seen in Figure 5A. In stage I, roof sinking at point 1 remains at zero, whereas it steadily increases at point 2 as the top working face retreats. In this stage, there is little and a gradual increase in the subsidence difference between the SLRFT effect and the ASPP effect. As the upper and lower working faces combine to retreat, roof sinking at point 1 grows gradually in stage II, then accelerates quickly later, and eventually stabilizes gradually. The end value that SLRFT has an impact on is almost the same as the final value that ASPP has an impact on, and the velocity that SLRFT has an impact on is greater than that of ASPP. More definitely, the combined retreating of the upper and lower working faces is indicated by the roof sinking of point 2 increasing slowly with a linear trend under the impact of ASPP and increasing slowly under the influence of SLRFT. Its final value and velocity influenced by SLRFT are significantly larger than them influenced by ASPP. Because the lower working face is receding in stage III, roof subsidence at points 1 and 2 remains steady and barely changes. This suggests that stage II is when SLRFT and ASPP have the most impact on roof subsidence.

As depicted in Figure 5B, SLRFT mostly contributes to the acceleration of roof sinking toward the location 57.5 cm from the lateral end of the gob in the lower coal seam. The roof subsidence of point 3 is remaining zero in stage I. The top working face's retreat causes point 4's roof subsidence to increase quickly after remaining zero at first. SLRFT has a smaller early influence on subsidence velocity than ASPP but a bigger late one. In stage II, roof subsidence of point 3 keeps zero initially, increases slowly later, increases rapidly, and then finally stabilizes, as the retreating of the combined retreating of the upper and lower working face. The

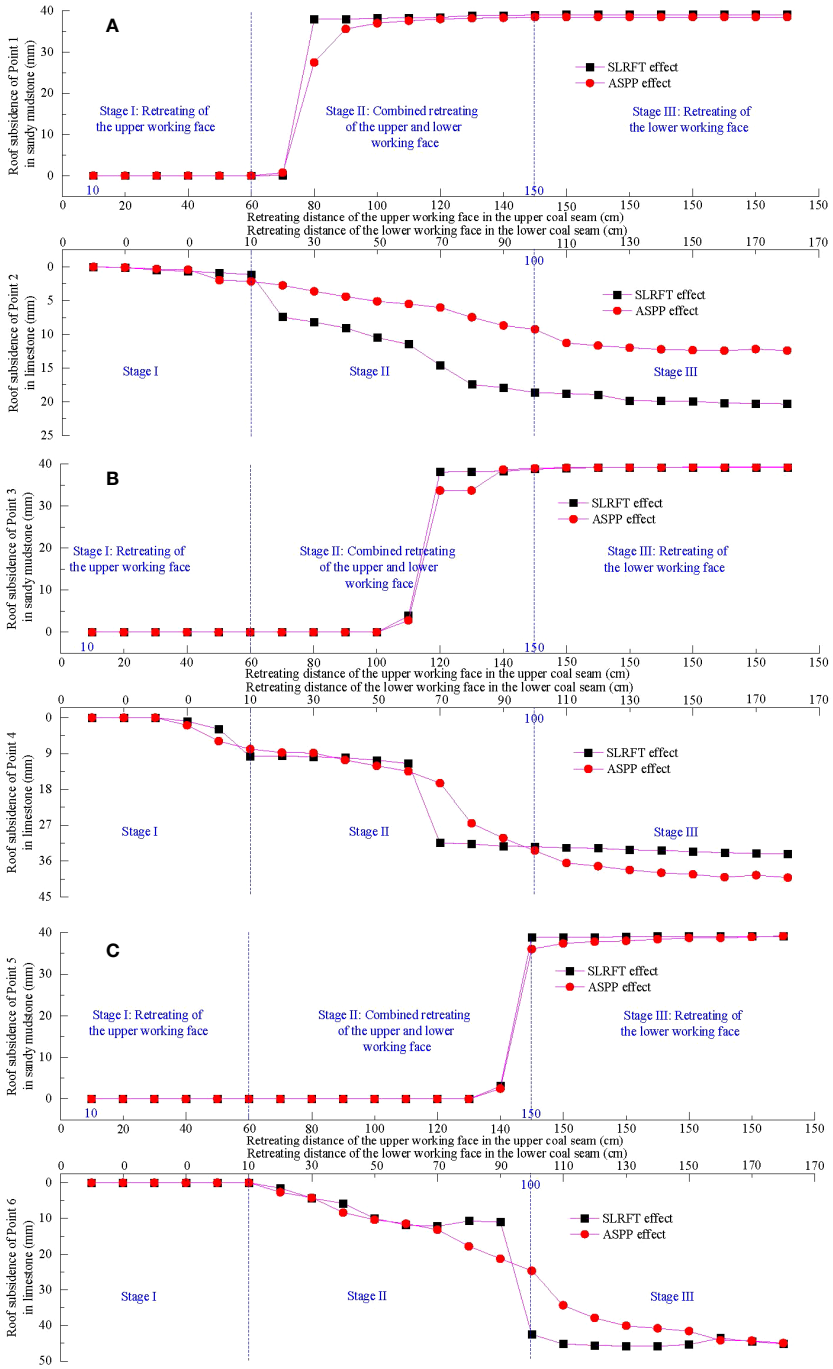

FIGURE 5
Movement behavior of roofs influenced by SLRFT and ASPP. **(A)** Roofs above the position 11.5 cm away from the lateral end of gob in the lower coal seam. **(B)** Roofs above the position 57.5 cm away from the lateral end of gob in the lower coal seam. **(C)** Roofs above the position 102.9 cm away from the lateral end of gob in the lower coal seam.

end value that SLRFT has an impact on is almost the same as the final value that ASPP has an impact on, and the velocity that SLRFT has an impact on is greater than that of ASPP. Notably, the combined retreating of the upper and lower working faces causes roof subsidence at point 4 to develop slowly at first, quickly later, and then suddenly stabilize. This is also true for ASPP, which causes roof subsidence to increase slowly at first, quickly later. Its velocity that SLRFT has an impact on is much more than that of ASPP. The fact that the lower working face is receding throughout stage III, whereas the roof subsidence at points 3 and 4 remains stable or barely increases, suggests that stage II is when the impacts of SLRFT and ASPP on roof subsidence are most noticeable.

As demonstrated in Figure 5C, SLRFT mostly contributes to the acceleration of roof sinking near the location 102.9 cm from the lateral end of the gob in the lower coal seam. In stage I, the top working face is retreating by zero, whereas the roof subsidence of

points 5 and 6 continues. In stage II, the ceiling subsidence of point 5 remains 0 at first, climbs gradually later, increases quickly, and then stabilizes as the combined retreat of the top and lower working faces. SLRFT has a greater impact on the object's final value and velocity than ASPP does. Notably, the combined retreating of the upper and lower working faces causes the roof subsidence of point 6 to increase with three distinct linear steps when influenced by SLRFT and with practically a single linear trend when impacted by ASPP. Its velocity that SLRFT has an impact on is much more than that of ASPP. In stage III, point 5's roof sinking, which is influenced by SLRFT and ASPP, remains steady and barely grows because of the lower working face receding. The final value is about the same. In addition, as the lower working face retreats, the roof sinking at point 6 experiences a progressive stabilization phase before increasing swiftly at first, increasing slowly afterward, and finally stabilizing. The final value is practically the same as well. It needs to be clarified that the fractural rock mass in limestone experiences slight up-and-down rotation under SLRFT in stage III, and this slight rotation behavior results in the slight reduction of the roof subsidence at monitoring point 6 within the 130 cm to 170 cm.

4.2 Effects of SLRFT on the bearing structure above the longwall entry

As shown in Figure 6, where the working face is retreating into nearby coal seams, the bearing structure caused by SLRFT above the longwall entry differs significantly from that impacted by ASPP in terms of fracture distribution, structural morphology, caving height, and gob filling behavior.

Roofs above the gob that are affected by ASPP in stage I produce non-penetrating oblique and horizontal gaping fractures, whereas those that are affected by SLRFT produce stepped closed fractures and piercing fractures. When there are fracture differences, two-sided cantilever structures rise above the longwall entry and are influenced by ASPP, whereas one-sided cantilever structures rise above the longwall entry and are influenced by SLRFT. These structures include suspended structures and caving rock mass structures. When the roofs are dealt with SLRFT, the caving zone can completely cover the lower and upper gobs for the roofs above the lower gob and extends to the limestone above the upper coal seam. However, when the roofs are dealt with ASPP, caving zone only reaches the lower coal seam and cannot fill the bottom gob.

Stage II is characterized by the coupled retreating process in which sandy mudstone gradually caves to the lower gob floor. One ASPP has a greater effect on the duration of a caving step than two ASPPs do. The caving zone divides into two layers under the impact of one ASPP and into three layers under the influence of two ASPPs. The caving rock mass structure is simple to fracture and fill the gob due to the influence of SLRFT. However, the SLRFT has no effect on the masonry construction, which remains stable and suspended. The two-sided cantilever structure transforms into a single-sided cantilever structure with an oblique closed fracture and an uncompacted bottom gob. In contrast, the bottom gob of the one-side cantilever construction is still present and in the condition of compacting. The hanging structure sags and forces the caving rock mass structure to become more compressed.

In stage III, the gob was gradually compacted in certain areas, and the bearing structure remained steady above the longwall entry. Small caving height and partial filling cause the oblique fracture to form above the gob's terminating side and spread to the higher roofs under the impact of ASPP. In contrast, the roofs above the terminating side of the gob gradually produce bending subsidence, and the prior cracks were compacted under the influence of significant caving height and the majority of filling brought on by SLRFT. The cantilever structure and the masonry structure, meanwhile, maintain stability and support the weight on the coal pillar and longwall entry under ASPP. Nevertheless, even in the presence of SLRFT, the cantilever structure maintains its stability and supports stresses on the longwall entry, the coal pillar, and the compacted gobs.

4.3 Effects of SLRFT on the abutment stress around the longwall entry

As can be seen in Figure 7A, SLRFT primarily works to reduce the rock's abutment stress in the sandy mudstone beneath the lower coal pillar. In stage I, the top working face begins to retreat, and the abutment stress at point A gradually increases at first and then grows rapidly step by step later. SLRFT has a greater impact on it than ASPP does on its maximum value and growing velocity. The largest difference, roughly, is 2.57 kPa. In stage II, the abutment stress at point A, which is driven by ASPP, eventually stabilizes after a steady increase in fluctuation. Nevertheless, it drops quickly at first under the influence of SLRFT, then experiences enormous fluctuations, increases very slowly, decreases quickly afterward, and ultimately increases slowly and gradually. Approximately 10.88 kPa separates the final value. With a fluctuation between 12.5 kPa and 14.6 kPa in stage III, point A's abutment stress under the impact of ASPP virtually stabilizes. However, it is affected by SLRFT, which causes it to climb gradually at first, decline quickly subsequently, and then stabilize gradually. SLRFT has a much smaller impact on the final value, 3.7 kPa, than ASPP, which has a much larger impact.

SLRFT is most effective, as demonstrated in Figure 7B, at reducing the rock's abutment stress in the sandy mudstone beneath the middle portion of the lower working face. The abutment stress of point B grows gradually in stage I, then increases quickly, and eventually stabilizes. Its highest value under the impact of ASPP is 3.0 kPa, which is higher than 1.7 kPa under the influence of SLRFT. In stage II, the abutment stress at point B that is affected by the ASPP varies initially with a slight fluctuation, then reduces linearly step by step after that, then grows slowly step by step after that, and eventually increases extremely rapidly to the peak. It maintains stability at first under the impact of SLRFT, declines quickly after that, declines slowly after that, and eventually climbs quickly until it reaches its peak. The peak value affected by ASPP is 18.2 kPa, which is significantly higher than 2.6 kPa that was affected by SLRFT. In stage III, the abutment stress at point B rapidly drops to zero and then remains constant. The velocity that ASPP has caused is more than the velocity that SLRFT has altered.

The abutment stress of the rock in the sandy mudstone above the lower coal pillar is significantly influenced by SLRFT, as illustrated in Figure 7C. Abutment stress at point C under the influence of ASPP

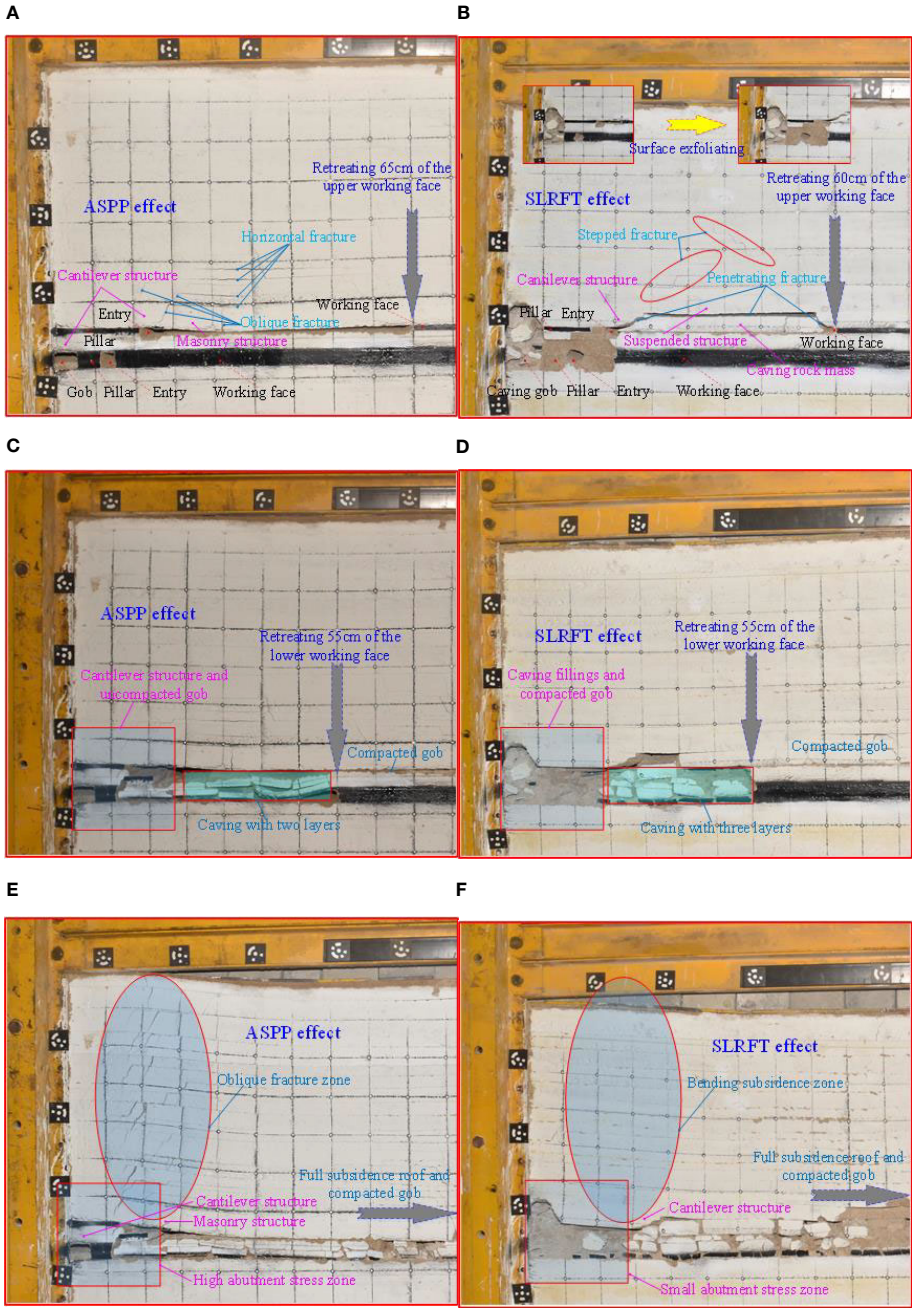

FIGURE 6
Structural morphology of bearing structure influenced by SLRFT and ASPP. **(A)** ASPP effect in stage I. **(B)** SLRFT effect in stage I. **(C)** ASPP effect in stage II. **(D)** SLRFT effect in stage II. **(E)** ASPP effect in stage III. **(F)** SLRFT effect in stage III.

remains zero during stage I before increasing quickly and then decreasing quickly at the end. Whereas, the SLRFT-influenced variable maintains zero at first, increases gradually later, increases quickly after that, increases gradually after that, and stabilizes at last. Its greatest value affected by SLRFT is 9.7 kPa, a much higher amount than 3.6 kPa that was affected by ASPP. In stage II, the ASPP-influenced abutment stress at point C grows gently at first with variability, then quickly in the middle, and slowly toward the end. The SLRFT, however, causes it to decline quickly at first, remain stable afterward, and then grow gradually over time. Its maximum value that is affected by SLRFT is 10.1 kPa, a far lower amount than 14.2 kPa that is affected by ASPP. In stage III, the ASPP-influenced abutment stress of point C initially rises and then falls over time. In contrast, it is impacted by SLRFT and initially remains stable before decelerating quickly, increasing slowly, and eventually stabilizing. Its highest value that SLRFT can alter is 11.8 kPa, which is less than 18.0 kPa that ASPP may impact.

5 Discussion

SLRFT is an effective way to weaken the abutment stress around the longwall entry under the close distance coal pillar during the

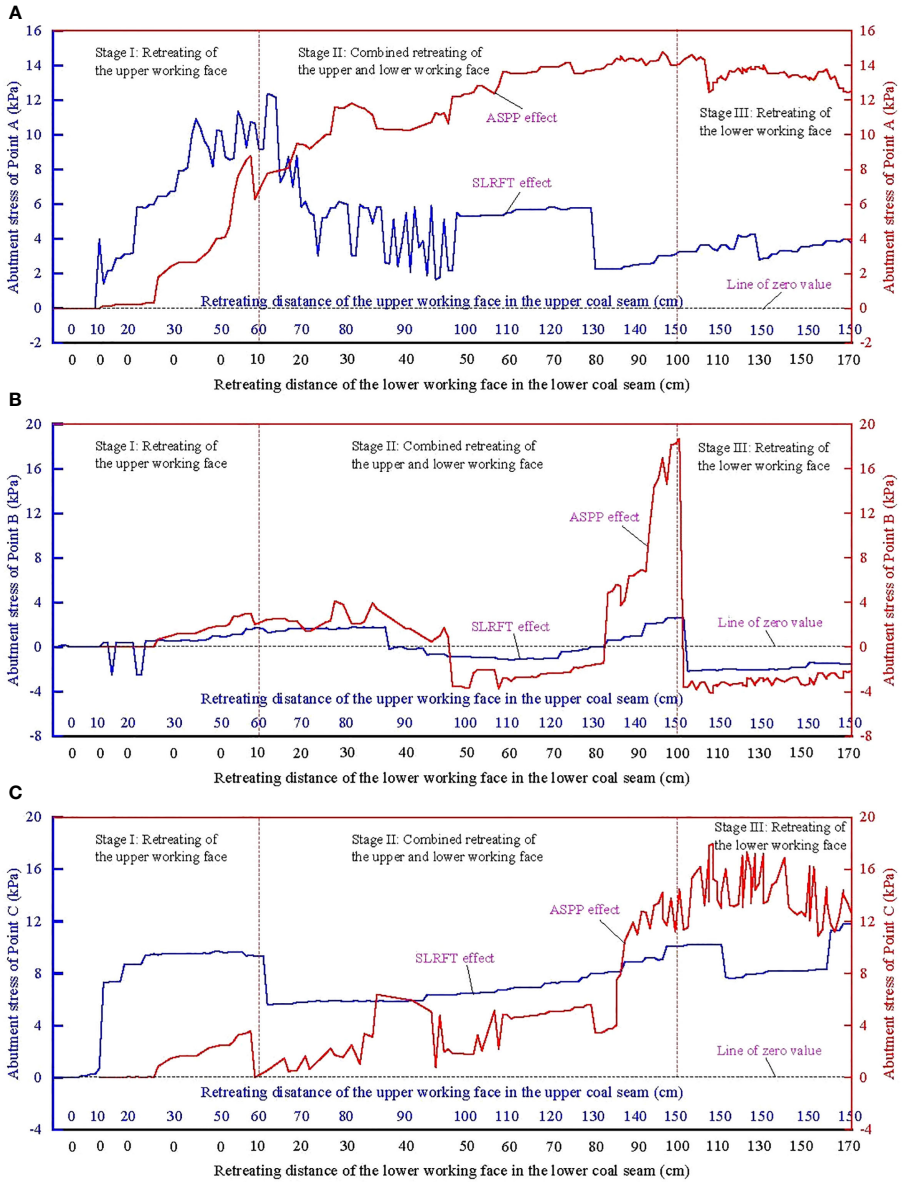

FIGURE 7
Abutment stress of rock influenced by SLRFT and ASPP. **(A)** Point A in the sandy mudstone below the lower coal pillar. **(B)** Point B in the sandy mudstone below the middle location of the lower working face. **(C)** Point C in the sandy mudstone above the lower coal pillar.

combined retreating process of the upper and lower working face, although the partial overburden weight above the worked-out area still loads on the unworked-out area by the bearing structure (Jirankova et al., 2012). Compared with the traditional natural caving method (Wen et al., 2019), SLRFT weakens the abutment stress mainly through changing the stress transfer mechanism in a way of varying the structural morphology, fracture characteristics, and the movement behavior of the bearing structure above the worked-out area.

During the course of its use in the conventional natural caving method, the mining-induced abutment stress primarily passes through the upper coal pillar into the longwall entry. It primarily maintains stability and results from the stable abutment stress in the upper coal pillar before the upper working face retreats (Kang et al., 2017). The variational abutment stress in the higher coal pillar causes it to rise quickly as the upper working face retreats (Colwell et al., 1999). In the top coal pillar during the combined retreating of the upper and lower working faces, the variational abutment stress causes it to increase quickly once more (Liu et al., 2021).

According to Shen et al. (2019), SLRFT initially reduces the variational abutment stress in the coal pillar by altering the structural morphology of the bearing structure above the coal pillar. This is because the variational abutment stress in the coal pillar is primarily caused by the activation of the bearing structure above the coal pillar. In stage I, the bearing structure transitions from a two-sided T-shaped cantilever structure to a one-sided basin-shaped cantilever structure above the upper coal pillar, as well as from a masonry structure to a suspended structure and a

caving rock mass next to the cantilever structure. With or without the help of SLRFT, it will produce rotational subsidence, new masonry structures, and one-side cantilever structures, but, in stages II and III, it only produces rotary subsidence.

SLRFT, which can lead to the various bearing structures discussed above, weakens the abutment stress surrounding the longwall entry under close distance coal pillar by altering the fracture characteristics of the bearing structure above the upper coal pillar. Stage I of the fracture involves non-penetrating horizontal and oblique gaping fractures that transition into stepped closed fractures and penetrating fractures in the roof above the worked-out area. In stage II, they will display behavior such as closure, extension, opening, and piercing. After then, without the help of SLRFT in stage III, a new oblique opening fracture develops and extends to the higher roofs. The effect of SLRFT in stage III compacted the earlier cracks into closure.

SLRFT alters the movement behavior of the bearing structure above the upper coal pillar, which can lead to the various fractures described above, weakening the abutment stress surrounding the longwall entry under close distance coal pillar. The main roof's sinking changes from a moderate, linear trend to a rapid, stepped trend in stage II due to the immediate roof's higher subsidence velocity under the effect of SLRFT than it would be without it. The primary cause is an improvement in stage II and stage III filling rates, compaction levels, and dilatancy of the caving rock mass due to shorter caving step lengths, more layered collapse, and greater caving heights of the immediate ceiling. As part of the overburden load is transferred into the worked-out area from the compacted worked-out area, the upper coal pillar's loading may be compromised because of the worked-out area's increased support area for the bearing structure.

Under the condition of the discussion, the bearing structure above the upper coal pillar is shown in Figure 8. $A\gamma H$ is the weight of the rock above the bearing structure. A is the abutment stress coefficient in the bearing structure. γ is the average volume weight. H is the buried depth of the rock strata. q is the support stress of the coal pillar. k is the support coefficient of the compacted worked-out area. kq is the support stress of the compacted worked-out area. x_1 is the cantilever length of the bearing structure. x_2 is the compacted length of the bearing structure. M is the bending moment of rock around the bearing structure. According to static equilibrium, the support stress of the coal pillar can be calculated using Equation (2). Its bearing capacity coefficient ζ can be calculated by Equation (3) for the determined geological and engineering conditions.

$$q = \frac{x_1 + x_2}{kx_1 + x_2} A\gamma H \tag{2}$$

$$\zeta = \frac{x_1 + x_2}{kx_1 + x_2} \tag{3}$$

To evaluate the loading impact of the bearing structure on the coal pillar, the bearing capacity coefficient can be used. As shown in Figure 9, it will vary depending on the cantilever length of the bearing structure and the support coefficient of the compacted worked-out region. Shorter cantilever length and higher support coefficient may be able to reduce the abutment stress in the coal pillar. This is because the bearing capacity coefficient will rise as the cantilever length of the bearing structure increases and will fall as the support coefficient of the compacted worked-out area increases. This may help to explain how SLRFT is able to reduce the abutment stress surrounding the longwall entry when the coal pillar is situated close by.

When there are deep rock strata beneath the coal pillar, hard roofs above the coal pillar, and wide caving rock mass in the worked-out area in nearby coal seams, SLRFT can be employed to lessen the abutment stress surrounding the longwall entry. The implications of the vertical separation in the stress propagation path between the close-proximity coal seams and the discontinuous interface on the SLRFT, however, need to be further investigated in the future.

6 Conclusion

When the longwall entry encounters the evolution of the abutment stress brought on by numerous mining activities, it is challenging to prevent the close-proximity coal pillar from experiencing significant deformation. SLRFT was proposed to lessen the abutment stress surrounding longwall entry and lessen the significant distortion of this type of entry.

SLRFT, a technique for remodeling roof-bearing structures under mining disturbance, consists of three interactive

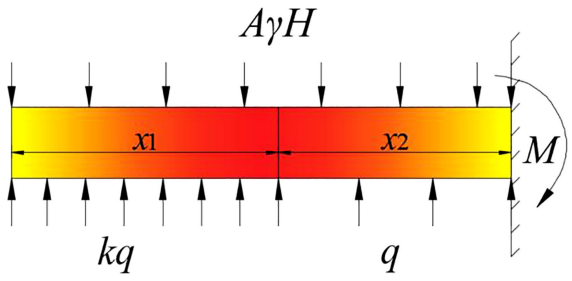

FIGURE 8
Mechanical condition of the bearing structure above the upper coal pillar.

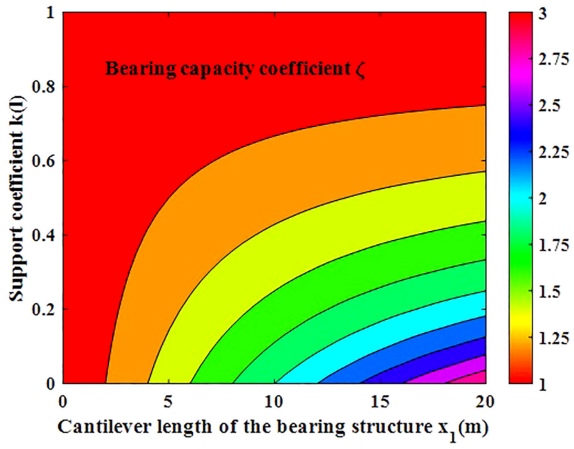

FIGURE 9
Evolution of the bearing capacity coefficient.

components: the ASPP, the ASPI, and the MALU. By dividing the lower thick rock stratum into numerous straticulate rock structures along ASPP under MALU, ASPP significantly contributes to the acceleration of the lower thick rock strata's movement. By dividing the upper thick hard roof into two portions along ASPI under MALU, ASPI plays a crucial function in identifying the site of the fracture of the upper thick hard roof.

The mechanism for the lowering of abutment stress was shown using two physical simulation models with plane–stress circumstances. SLRFT lengthens the stress transmission path by altering the bearing structure's movement patterns, fracture characteristics, and structural morphology above the coal pillar. First, the fracture in the ceiling above the worked-out area shifts from a non-penetrating horizontal and oblique gaping fracture to stepped closed fractures and piercing fractures. Second, the main roof's subsidence changed from having a steady, linear pattern to one that was swift and stepped. The bearing structure finally switches from a two-sided cantilever structure with a T type to a single-sided cantilever structure with a basin type.

SLRFT results in a shorter step length, a more stratified collapse, and a higher caving height of the immediate roof, which enhances the dilatancy of the caving rock mass, the filling rate, and the degree of compaction of the worked-out region. Because the compacted worked-out region has a bigger support area, more of the overburden load is transferred there, weakening the abutment stress around the longwall entry from 12.5 kPa to 3.7 kPa. The degree of stress reduction increases when the cantilever length of the bearing structure is decreased and the support coefficient of the compacted worked-out area is increased.

When there are deep rock strata beneath the coal pillar, hard roofs above the coal pillar, or wide caving rock masses in the worked-out area in close-by coal seams, SLRFT is an effective approach to reduce the abutment stress around the longwall entry. The implications of the vertical separation in the stress propagation path between the close-proximity coal seams and the discontinuous interface on the SLRFT, however, need to be further investigated in the future. A feasibility, efficacy, and design analysis of SLRFT in various engineering geological settings can be done using the established experimental model.

Data availability statement

The original contributions presented in the study are included in the article/supplementary material. Further inquiries can be directed to the corresponding author.

Author contributions

JL: Conceptualization, Investigation, Writing – review & editing. WS: Funding acquisition, Methodology, Writing – original draft. JB: Conceptualization, Supervision, Writing – review & editing. CS: Data curation, Validation, Writing – review & editing. XL: Data curation, Visualization, Writing – review & editing.

Funding

The authors declare financial support was received for the research, authorship, and/or publication of this article. This work is supported by the National Natural Science Foundation of China (contract 52274077), the Fundamental Research Funds for the Universities of Henan Province (NSFRF220440), the Funds for Distinguished Young Scholars of Henan Polytechnic University (J2023-3), and the Funds for Establishment Project of Double First-Class Disciplines of Safety and Energy Engineering Department (AQ20230736).

Conflict of interest

The authors declare that the research was conducted in the absence of any commercial or financial relationships that could be construed as a potential conflict of interest.

Publisher's note

References

Bai, J. B., Shen, W. L., Guo, G. L., Wang, X. Y., and Yu, Y. (2015). Roof deformation, failure characteristics, and preventive techniques of gob-side entry driving heading adjacent to the advancing working face. *Rock Mechanics Rock Eng.* 48 (6), 2447–2458. doi: 10.1007/s00603-015-0713-2

Colwell, M., Frith, R., and Mark, C. (1999). Analysis of longwall tailgate serviceability (ALTS): a chain pillar design methodology for Australian conditions. *Coal Pillar Mech. Des.*, 33–48.

Fumagalli, E. (1973). *Statical and geomechanical models* (New York, NY, USA: Springer).

Hou, C. J., and Ma, N. J. (1989). Stress in in-seam roadway sides and limit equilibrium zone. *J. China Coal Soc.* 4, 21–29. doi: 10.13225/j.cnki.jccs.1989.04.003

Huang, B. X., Liu, J. W., and Zhang, Q. (2018). The reasonable breaking location of overhanging hard roof for directional hydraulic fracturing to control strong strata behaviors of gob-side entry. *Int. J. Rock Mechanics Min. Sci.* 103, 1–11. doi: 10.1016/j.ijrmms.2018.01.013

Jirankova, E., Petros, V., and Sancer, J. (2012). The assessment of stress in an exploited rock mass based on the disturbance of the rigid overlying strata. *Int. J. Rock Mechanics Min. Sci.* 50, 77–82. doi: 10.1016/j.ijrmms.2012.01.004

Kang, J. Z., Shen, W. L., Bai, J. B., Yan, S., Wang, X. Y., Li, W. F., et al. (2017). Influence of abnormal stress under a residual bearing coal pillar on the stability of a mine entry. *Int. J. Min. Sci. Technol.* 27 (6), 945–954. doi: 10.1016/j.ijmst.2017.06.012

Kang, H. P., Wu, L., Gao, F. Q., Lv, H. W., and Li, J. Z. (2019). Field study on the load transfer mechanics associated with longwall coal retreat mining. *Int. J. Rock Mechanics Min. Sci.* 124, 1–10. doi: 10.1016/j.ijrmms.2019.104141

Li, W. F., Bai, J. B., Peng, S., Wang, X. Y., and Xu, Y. (2015). Numerical modeling for yield pillar design: A case study. *Rock Mechanics Rock Eng.* 48 (1), 305–318. doi: 10.1007/s00603-013-0539-8

Li, H. T., Li, X. L., Fu, J. H., Zhu, N. Q., Chen, Y. W., Ding, S., et al. (2023). Experimental study on compressive behavior and failure characteristics of imitation steel fiber concrete under uniaxial load imitation steel fiber concrete under uniaxial load. *Construction Building Materials* 399 (8), 132599. doi: 10.1016/j.conbuildmat.2023.132599

Liu, S. M., and Li, X. L. (2023). Experimental study on the effect of cold soaking with liquid nitrogen on the coal chemical and microstructural characteristics. *Environ. Sci. pollut. Res.* 30 (3), 36080–36097. doi: 10.1007/s11356-022-24821-9

Liu, H. M., Li, X. L., and Yu, Z. Y. (2023a). Influence of hole diameter on mechanical properties and stability of granite rock surrounding tunnels. *Phys. Fluids* 35 (6), 064121. doi: 10.1063/5.0154872

Liu, X. D., Shen, W. L., Bai, J. B., Wang, R., Kang, J. Z., and Wang, X. Y. (2021). Mining-induced redistribution of the abnormal stress under the close bearing coal pillar for entry design. *Adv. Civil Eng.* 2021, 1–13. doi: 10.1155/2021/5595372

Liu, S. M., Sun, H. T., and Zhang, D. M. (2023b). Experimental study of effect of liquid nitrogen cold soaking on coal pore structure and fractal characteristics. *Energy* 275 (7), 127470. doi: 10.1016/j.energy.2023.127470

Liu, H. Y., Zhang, B. Y., Li, X. L., Liu, C. W., Wang, C., Wang, F., et al. (2022). Research on roof damage mechanism and control technology of gob-side entry retaining under close distance gob. *Eng. Failure Anal.* 138, 1–16. doi: 10.1016/j.engfailanal.2022.106331

Meng, Z. X., Dong, Y., Zhang, X. G., Jiao, F. S., Fan, Y. Q., and Thammavongsa, C. (2023). Short-wall paste continuous mining and continuous backfilling for controlling industrial square surface subsidence. *Front. Earth Sci.* 10. doi: 10.3389/feart.2022.1009617

Ning, J. G., Wang, J., Tan, Y. L., and Xu, Q. (2020). Mechanical mechanism of overlying strata breaking and development of fractured zone during close-distance coal seam group mining. *Int. J. Min. Sci. Technol.* 30 (2), 207–215. doi: 10.1016/j.ijmst.2019.03.001

Shen, W. L., Bai, J. B., Wang, X. Y., and Yu, Y. (2016). Response and control technology for entry loaded by mining abutment stress of a thick hard roof. *Int. J. Rock Mechanics Min. Sci.* 90, 26–34. doi: 10.1016/j.ijrmms.2016.10.001

Shen, W. L., Shi, G. C., Wang, Y. G., Bai, J. B. A., Zhang, R. F., and Wang, X. Y. (2021). Tomography of the dynamic stress coefficient for stress wave prediction in sedimentary rock layer under the mining additional stress. *Int. J. Min. Sci. Technol.* 31 (4), 653–663. doi: 10.1016/j.ijmst.2021.04.003

Shen, W. L., Shi, G. C., Wang, M., Rong, T. L., Wang, Y. G., Zhang, R. F., et al. (2020). Method of entry layout under synergistic effects of abutment stress and dynamic stress. *Shock Vibration* 2020, 1–16. doi: 10.1155/2020/6655293

Shen, W. L., Wang, M., Cao, Z. Z., Su, F. Q., Nan, H., and Li, X. L. (2019). Mining-induced failure criteria of interactional hard roof structures: A case study. *Energies* 12 (15), 1–17. doi: 10.3390/en12153016

Sun, Y. T., Bi, R. Y., Sun, J. B., Zhang, J. F., Taherdangkoo, R., Huang, J. D., et al. (2022). Stability of roadway along hard roof goaf by stress relief technique in deep mines: a theoretical, numerical and field study. *Geomechanics Geophysics Geo-Energy Geo-Resources* 8 (2), 1–16. doi: 10.1007/s40948-022-00356-8

Tu, S. H. (2010). *Experimental method and measurement technique of rock control* (Xuzhou, China: China University of Mining and Technology Press).

Wang, X. Y., Bai, J. B., Wang, R. F., and Sheng, W. L. (2015). Bearing characteristics of coal pillars based on modified limit equilibrium theory. *Int. J. Min. Sci. Technol.* 25 (6), 943–947. doi: 10.1016/j.ijmst.2015.09.010

Wang, Q., He, M. C., Li, S. C., Jiang, Z. H., Wang, Y., Qin, Q., et al. (2021). Comparative study of model tests on automatically formed roadway and gob-side entry driving in deep coal mines. *Int. J. Min. Sci. Technol.* 31 (4), 591–601. doi: 10.1016/j.ijmst.2021.04.004

Wang, Y. J., He, M. C., Yang, J., Wang, Q., Liu, J. N., Tian, X. C., et al. (2020). Case study on pressure-relief mining technology without advance tunneling and coal pillars in longwall mining. *Tunnelling Underground Space Technol.* 97, 1–13. doi: 10.1016/j.tust.2019.103236

Wen, J. H., Cheng, W. M., Chen, L. J., Shi, S. S., and Wen, Z. J. (2019). A study of the dynamic movement rule of overlying strata combinations using a short-wall continuous mining and full-caving method. *Energy Sci. Eng.* 7 (6), 2984–3004. doi: 10.1002/ese3.474

Wilson, A. H., and Ashwin, D. P. (1972). Research into the determination of pillar size. *Min. Eng.* 131 (141), 409–417.

Xia, K. Z., Chen, C. X., Wang, T. L., Zheng, Y., and Wang, Y. (2022). Estimating the geological strength index and disturbance factor in the Hoek-Brown criterion using the acoustic wave velocity in the rock mass. *Eng. Geol.* 306, 106745. doi: 10.1016/j.enggeo.2022.106745

Ye, D. Y., Liu, G. N., Wang, F. T., Gao, F., Yang, T. T., and Zhu, J. Y. (2023). Fractal hydrological-thermal-mechanical analysis of unconventional reservoir: A fracture-matrix structure model for gas extraction. *Int. J. Heat Mass Transfer* 202, 123670. doi: 10.1016/j.ijheatmasstransfer.2022.123670

Yuan, F., Tang, J. X., Kong, L. R., and Li, C. (2023). Layout timing of mining roadways considering goaf and roof stability. *Front. Earth Sci.* 10. doi: 10.3389/feart.2022.1092585

Zhang, Z. Z., Deng, M., Bai, J. B., Yu, X. Y., Wu, Q. H., and Jiang, L. S. (2020). Strain energy evolution and conversion under triaxial unloading confining pressure tests due to gob-side entry retained. *Int. J. Rock Mechanics Min. Sci.* 126, 1–10. doi: 10.1016/j.ijrmms.2019.104184

Zhang, J. X., Li, B. Y., Zhou, N., and Zhang, Q. (2016). Application of solid backfilling to reduce hard-roof caving and longwall coal face burst potential. *Int. J. Rock Mechanics Min. Sci.* 88, 197–205. doi: 10.1016/j.ijrmms.2016.07.025

Zhang, L., Shen, W., Li, X., Wang, Y., Qin, Q., Lu, X., et al. (2022b). Abutment pressure distribution law and support analysis of super large mining height face. *Int. J. Environ. Res. Public Health* 20 (1), 1–16. doi: 10.3390/ijerph20010227

Zhang, F. T., Wang, X. Y., Bai, J. B., Wu, W. D., Wu, B. W., and Wang, G. H. (2022a). Fixed-length roof cutting with vertical hydraulic fracture based on the stress shadow effect: A case study. *Int. J. Min. Sci. Technol.* 32 (2), 295–308. doi: 10.1016/j.ijmst.2021.09.007

Zhang, Z. B., Wang, E. Y., Li, N., Zhang, H. T., Bai, Z. M., and Zhang, Y. H. (2023a). Research on macroscopic mechanical properties and microscopic evolution characteristic of sandstone in thermal environment. *Construction Building Materials* 366, 130152. doi: 10.1016/j.conbuildmat.2022.130152

Zhang, Z. B., Wang, E. Y., Zhang, H. T., Bai, Z. M., Zhang, Y. H., and Chen, X. (2023b). Research on nonlinear variation of elastic wave velocity dispersion characteristic in limestone dynamic fracture process. *Fractals* 31 (1), 2350008. doi: 10.1142/S0218348X23500081

Zhang, J. C., Li, X. L., and Qin, Q. Z. (2023c). Study on overlying strata movement patterns and mechanisms in super-large mining height stopes. *Bull. Eng. Geology Environ.* 82 (3), 142. doi: 10.1007/s10064-023-03185-5

Zhang, Q., Yang, K., Zhang, J. X., Wang, Q., Yuan, L. F., Shi, Z. Z., et al. (2022c). A theoretical model of roof self-stability in solid backfilling mining and its engineering verification. *Appl. Sciences-Basel* 12 (23), 1–19. doi: 10.3390/app122312114

frontiers | Frontiers in Environmental Science

TYPE Original Research
PUBLISHED 11 September 2023
DOI 10.3389/fenvs.2023.1252206

OPEN ACCESS

EDITED BY
Xuelong Li,
Shandong University of Science and Technology, China

REVIEWED BY
Jianwen Shao,
Tianjin University, China
Rulong Bn,
Guilin University of Technology, China

*CORRESPONDENCE
Xing-Yu Ding,
dingxingyu@hncu.edu.cn
Wen-Jun Hu,
list07@mails.jlu.edu.cn

RECEIVED 03 July 2023
ACCEPTED 23 August 2023
PUBLISHED 11 September 2023

CITATION
Ding X-Y, Hu W-J, Liu F and Yang X (2023), Risk assessment of debris flow disaster in mountainous area of northern Yunnan province based on FLO-2D under the influence of extreme rainfall. *Front. Environ. Sci.* 11:1252206. doi: 10.3389/fenvs.2023.1252206

Risk assessment of debris flow disaster in mountainous area of northern Yunnan province based on FLO-2D under the influence of extreme rainfall

Xing-Yu Ding[1]*, Wen-Jun Hu[2,3]*, Fang Liu[2,3] and Xian Yang[1]

[1]School of Civil Engineering, Hunan City University, Yiyang, Hunan, China, [2]Yunnan Institute of Geo-Environment Monitoring, Kunming, Yunnan, China, [3]Key Laboratory of Geohazard Forecast and Geoecological Restoration in Plateau Mountainous Area, Kunming, Yunnan, China

The stratum in Yunlong mountain area is unstable, and it is more likely to have extreme damage to the mountain in extreme rainfall weather, and even cause the occurrence of mountain disasters such as debris flow. This paper conducted field geological surveys and used the FLO-2D professional simulation system to scientifically evaluate the risk probability of three debris flow in Yunlong County. The risk prediction before and after engineering control was compared for the county's urban areas.This paper uses construction drawings and remote sensing images to assist in positioning methods for debris flow simulation. After dividing the debris flow simulation grid, the control project is added to the simulation project in the form of a plug-in, and specific engineering parameters are imported into the simulation project file by modifying its properties. The setting of the control project in numerical simulation is completed, solving the problem of setting engineering measures. By this method, the probability analysis of debris flow under three different rainfall frequencies of 1%, 2% and 5%, namely once in 20 years, once in 50 years and once in 100 years, is simulated, and the flow and sedimentation characteristics of debris flow before and after engineering control are compared. The results show that under 5% rainfall frequency, the simulated results before engineering control were compared with the actual deposition range, and the evaluation accuracy is within a reasonable error range. After debris flow engineering control, the proportion of high risk areas of debris flow in urban areas decreased significantly, especially when the frequency of rainfall was once in 100 years, and the area of non-danger areas increased by 5.92% compared with that before control. In the end, this paper combines the depth of mud, the velocity of mud and the outbreak frequency to get the debris flow risk assessment map before and after engineering treatment, and puts forward suggestions for further prevention and control measures of debris flow disaster. The research results of this paper will provide good guidance for the occurrence and control of debris flow hazards under the influence of extreme rainfall in the mountainous area of northern Yunnan.

KEYWORDS

debris flow, FLO-2D, numerical simulation, rainfall frequency, risk assessment

1 Introduction

The northern Yunnan region of China is located near the extinction boundary of the Eurasian Plate and the Indian Ocean Plate, where faults are developed and the crusts are broken. In addition, this region is one of the most seriously damaged areas in China where debris flow is densely distributed, as well as one of the most typical areas of debris flow activity in the world because of its numerous mountain and canyon landforms, large slope and abundant precipitation (Tang, 1995; Xu, 2018a). According to the field survey, a total of 12 counties and cities in northern Yunnan suffered debris flow disasters with different degrees (Shang, 1993; Yang et al., 2017), bringing a huge threat to the safety of people's lives and property. The risk evaluation of debris flow disaster not only has reference value for engineering design and construction in debris flow activity area but also has guiding significance for the implementation of debris flow prevention and control measures; besides, it is also an important means to improve the efficiency of debris flow prevention and control.

Debris-2D, FLO-2D and Geoflow are mature numerical simulation software in the world, which can carry out large-scale engineering problem analysis (Peng et al., 2017). Among them, the FLO-2D software establishes the mass conservation and momentum conservation equations in differential form, and uses the explicit central difference method to solve them, which can calculate the change of flow depth, velocity and influence range with time. As a two-dimensional software, FLO-2D can analyze the movement characteristics of debris flow in detail and has been widely used in debris flow disaster research (Brien, 2009a; Liang et al., 2016; Cao et al., 2021). Bertolo et al. (Bertolo and Wicezorek, 2005) used FLO-2D to simulate the sedimentation process of debris flow movement in small watershed. Huang et al. (Xun and Chuang, 2016) used FLO-2D to simulate the influence range of debris flow in the experimental area and found that the simulation results were consistent with the actual range. Jia et al. (Jia et al., 2015) simulated the debris flow accumulation process using FLO-2D, and built a danger zone zoning model based on the momentum of the debris flow to quantify the debris flow accumulation fan. Ling et al. (Wang and Ling, 2011) simulated the debris flow in the Songhe area based on FLO-2D software and conducted risk evaluation in this area based on the flow depth, flow velocity, and sediment accumulation characteristics. Zhang et al. (Zhang et al., 2019) used FLO-2D to simulate the outbreak process of the debris flow in Ruoru village under rainfall frequencies of 5%, 2%, and 1%, and obtain a risk assessment chart based on the mud depth, flow velocity, and outbreak frequency. It can be seen that many scholars have tried to apply FLO-2D to the risk assessment of debris flow, and the assessment results are highly consistent with the on-site investigation.

The prevention and control of debris flow in the mountainous area of northern Yunnan province were first proposed in the mid-1960s; So far, to some extent, various engineering measures for controlling the debris flow gullies that may threaten people's lives and properties have been implemented, including various interception measures, slope stabilization measures, drainage measures, water control measures, and siltation detention measures (Yan, 2016; Gao et al., 2023). Although these engineering prevention measures have achieved varying degrees of effectiveness, most of the risk assessment of debris flow disasters mainly focused on evaluating their pre-treatment risk, and trarely consider risk assessment of debris flow disasters under the influence of engineering measures (Jakob et al., 2012; Liu and Li, 2023). In this paper, based on detailed field investigation data (Dong and Hu, 2021) and FLO-2D numerical simulation software, this paper assisted positioning by construction drawings and remote sensing images of the treatment project. After the mesh division of debris flow simulation was completed, the treatment project was added to the simulation project in the form of plug-in, and specific engineering parameters were imported into the simulation project file by modifying its attributes. The setting of the management project in the numerical simulation is completed, and the difficult problem of the setting of engineering measures is solved. The risk assessment after the prevention and control of three debris flow gulches in Yunlong County has been studied. The risk assessment of debris flow refers to the evaluation of the possibility of all people or objects suffering debris flow damage within the scope of debris flow basin (Ortiz-Giraldo et al., 2023; Yang et al., 2023). This assessment mainly evaluates the spatial distribution, development environment, development degree, disaster type and other factors of debris flow, so as to determine the probability of its occurrence, and provide a reference for the subsequent prevention and control of debris flow.

2 Research background

Yunlong County, Yunnan Province, is located in the northern part of Yunnan; Its landscape features highly eroded mountains and canyons, with an unusually developed "V"-shaped valley (Figure 1; Figure 2) that exhibits strong cutting and fractured rock layers (Calista et al., 2020). The formation of debris flows in the area is related to special climatic conditions, terrain, and lithology, as well as human engineering activities also play an important role in the occurrence of debris flows. The structural system within Yunlong County is complex, there are various structural systems intersecting and accommodating each other, thus a composite property with multi-stage and long-term activity is possessed. In its composite parts (Huang et al., 2019; Gan and Luo, 2020), fractures crisscross, rocks are broken, rock is severely

FIGURE 1
Steep terrain on both sides of the Bijiang River.

FIGURE 2
Bijiang valley.

weathered, and geological disasters such as landslides, collapses, and potentially unstable slopes are easily formed. The gully erosion is extremely developed in the slope zone of the assessment area. The upper and middle reaches of the valley often form high and steep banks due to headward erosion, downstream erosion, and lateral erosion. In addition, human activities such as road excavation have led to a high incidence of landslides and collapse, providing a large amount of material for debris flows.

In this area, the steep slope topography and the continuous action of strong downcutting erosion of gully water lead to the gradual unloading, tipping, collapse and surface landslide of gully bank slope, which provide material sources for the formation of debris flow (Hou et al., 2021). The rock mass exposed in Yunlong County has different resistance to weathering because of different lithology and different degree of joint fissure development. The stratigraphic lithology is shown in Table 1. The feldspar quartz sandstone of Hutousi Formation and the sandstone of the lower part of Jingxin Formation, which have strong wind resistance in the area, are mainly formed by collapsing blocks, gravel, or masonry destroyed along joints and cracks, which provide solid material with coarse particles for debris flow (Liu et al., 2023a; Liu et al., 2023b).

Through detailed field investigation (Dong and Hu, 2021), the basic situation of the three debris flow gullies in the area and the relevant control engineering measures in the gullies are obtained, as shown in Table 2. The basic characteristics of the three debris flow trenches are as follows:Shiwei River, the lithology of the stratigraphic rocks is third-order mudstone and siltstone, and the slope erosion is severe, resulting in serious soil erosion. In the Shili River basin, landslides, collapses,slope, collapses, potentially unstable slopes, and artificial abandoned soil provide material sources for debris flows. The reserve of loose solid materials is about 2912.93 × 104 m^3, and the reserve of loose solid materials for debris flow activity is 291.293 × 104 m^3. The accumulation area at the mouth of the gully is fan-shaped, with a

TABLE 1 Regional comprehensive stratigraphic list of Yunlong county.

Erathem	System	Series	Formation	Code	Thickness (m)	Lithology description
mesozoic erathem	cretaceous system	Upper Series	Hutousi	K_2h	138	Light gray, brown, gray white giant thick layer, massive feldspathic quartz sandstone, local copper
			nanxin	K_1n	861–1496	Purplish red medium and coarse-grained sandstone are mainly mixed with mudstone, silty mudstone and siltstone
		Lower Series		upper section	K_1j^2 182–385	Purplish red mudstone, silty mudstone, argillaceous siltstone with fine sandstone
			jingxing	Lower section	K_1j^1 468	Gray-green, gray-white fine-grained quartz sandstone and purplish red mudstone, silty mudstone, local copper

TABLE 2 Characteristics of the three debris flow gullies in Yunlong county.

Name	Drainage area (km^2)	Length of main ditch (km)	Average longitudinal gradient (‰)	Scale	Development phase	Engineering measures
Shiwei River	42.03	13.08	101.4	Large	Exuberant	There are 16 check dams, 2check landmarks and 1 sand barrier built in Gouni. In order to control floods and landslides,a complex of V-shaped flumes and anti-slip piles and retaining walls are used in the landslide area of the flood prevention dam ditch at the source
Suolichangqing	16.5	8.02	147.5	Large	Development	The severely affected area by debris flows, Shimen Community, hasbuilt a 400 m channel for diversion and discharge
Nuodeng River	10.4	7.5	162.7	Large	Development	There are two valley -dammed reservoirs located in Gounei

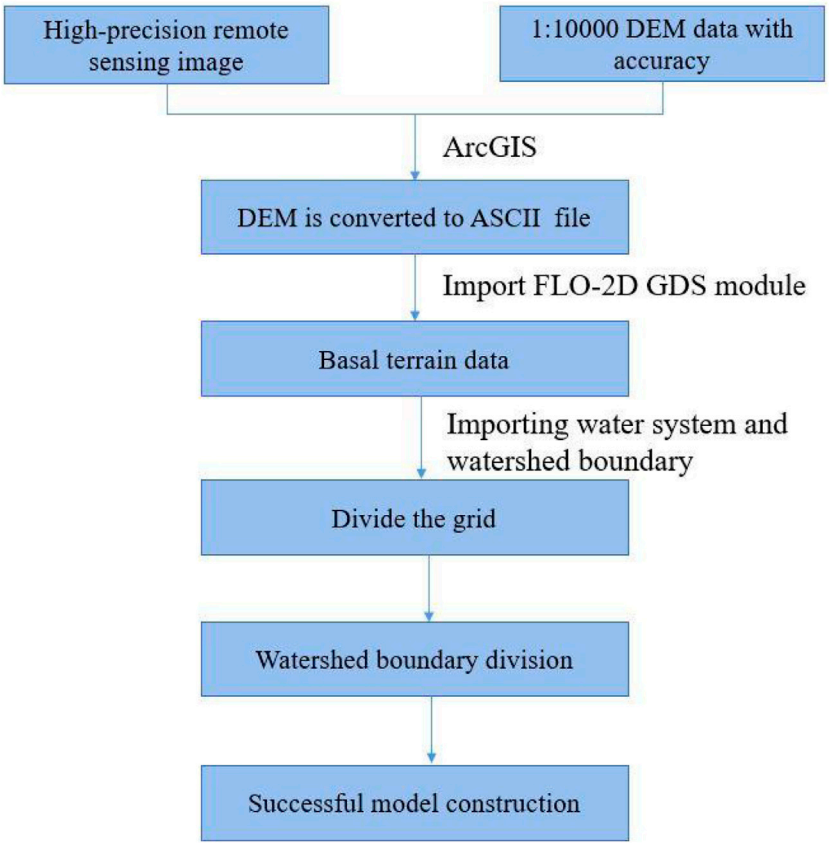

FIGURE 3
Numerical model construction process.

TABLE 3 Values of various parameters for debris flow channels.

Name	Shiwei river	Suolichangqing	Nuodeng river
Debris flow density r (g/cm^3)	1.56	1.62	1.58
Sediment density r_s (g/cm^3)	2.60	2.65	2.66
volume concentration Cv	0.35	0.38	0.35
Simulated burst time t (h)	2	1.5	1.5
Manning coefficient	0.1		
Laminar flow retarding coefficient K	2280		
Rheological parameter α_1	0.811		
Rheological parameter β_1	13.72		
Rheological parameter α_2	0.0046		
Rheological parameter β_2	11.24		

length of about 1240 m and a width of about 1000 m. Suolichangqing, the lithology consists of Neogene mudstone and siltstone, and the slope erosion is strong, causing serious soil erosion. The weathered layer thickness in the Zhukelijing debris flow basin is relatively large, and the loose solid material mainly comes from landslides, erosion and abrasion-type material sources, and debris flow channel deposits. The amount of loose solid material source is about 2136.76 × 104 m^3, and the movable loose material source is about 106.838 × 104 m^3. Nuodeng River, the lithology of the strata is mainly comprised of Neogene mudstone and siltstone, with strong slope erosion and severe soil and water loss. The loose solid material source is mainly

TABLE 4 Calculation parameters of peak flow of debris flow.

Name	Shiwei river main channel	Shiwei river tributary channel (Qingshiyanqing)	Suolichangqing	Nuodeng river
Sediment correction factor	0.538	0.538	0.60	0.537
Gross blockage factor	1.3	1.3	1.4	1.3

TABLE 5 Peak flow meter of outlet point cross section.

Name	Rainstorm peak flow under different frequencies (m^3/s)			Peak flow of debris flow under different frequencies (m^3/s)		
	p = 1%	p = 2%	p = 5%	p = 1%	p = 2%	p = 5%
Shiwei River main channel	417.46	361.10	289.27	834.92	722.20	578.54
Shiwei River tributary channel (Qingshiyanqing)	101.38	87.78	70.58	202.76	175.56	141.16
Suolichangqing	216.80	187.31	149.36	486.22	420.08	334.97
Nuodeng River	138.63	119.68	95.29	277.00	239.14	190.40

from landslides and channel deposits, with the volume of the large landslide body in the loose slope area being about 1160.0 × 104 m^3. The source of loose solid materials is about 2027.7 × 104 m^3, and the movable loose material source is about 101.38 × 104 m^3. The accumulation area at the mouth of the gully is fan-shaped, with a length of about 230 m and a width of about 240 m.

3 Construction and parameter values of FLO-2D numerical model

The FLO-2D software model was proposed by Brien in 1988, in which the digital elevation model (DEM) is divided into the same size and regular topographic grid to solve the control equation of debris flow movement by using non-Newtonian fluid and central finite difference method, while the flow process, accumulation range and dangerous area of debris flows can be simulated by numerical quantitative method. Related literature (Brien, 2009b; Castelli et al., 2017; Cong et al., 2019) had discussed in detail the theoretical model of the numerical simulation software and the assumptions to be met.

In this article, combined with various parameters such as rainfall, flow data, and digital terrain data, FLO-2D numerical simulation software was used to simulate the movement process and status of debris flows, including flow velocity, deposition depth, and deposition range, to restore the movement process of debris flows. After obtaining the numerical simulation parameters of debris flows occurring every 20 years, 50 years, and 100 years, the potential impact and deposition situation of debris flows under rainfall conditions with a recurrence interval of 20, 50, and 100 years in Yunlong County were predicted. By combining the motion parameters with the danger of debris flows, an appropriate debris flow hazard zoning model is selected to classify the debris flows into different levels of danger.

3.1 Numerical model construction

This article collects 1:10000 contour lines and high-precision remote sensing image maps of Yunlong County (Dong and Hu, 2021). The construction process of the numerical model is shown in Figure 3.

When conducting a numerical simulation of debris flow engineering after treatment, it is necessary to add the treatment engineering to the simulation project in the form of a plugin after the grid division of debris flow simulation is completed, and the position of the treatment engineering in the watershed is very important, which can be assisted using the construction drawings of the treatment engineering and remote sensing images. By creating a series of corresponding grids for the treatment projects and importing the specific project parameters into the simulation project file by modifying their properties, the setting of the treatment engineering in the numerical simulation can be completed.

3.2 Parameter choice

The main parameters selected for FL0-2D numerical simulation (FLO-2D Software Inc, 2004) include debris flow density, volume concentration, laminar retarding coefficient and rheological parameters.

3.2.1 Input parameters

Based on on-site surveys and collected design reports of debris flow, and combined with the FL0-2D User Manual and relevant literature, various calculation parameters except rainfall intensity were obtained and analyzed, as shown in Table 3.

The calculation of debris flow volume concentration can refer to the calculation formula in reference (Zhang et al., 2022).

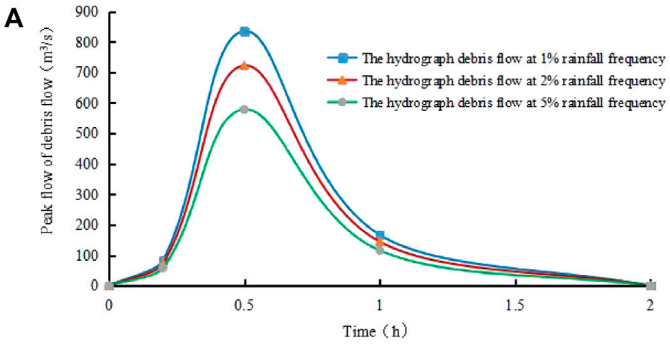

Under different rainfall frequencies flow process line of debris flow in the main channel of Shiwei River

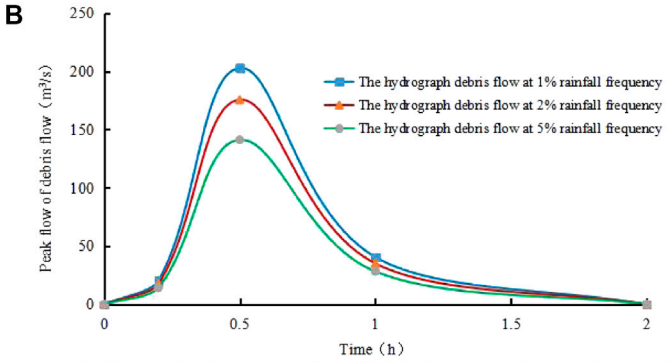

Under different rainfall frequencies flow process line of debris flow in the tributary channel of Shiwei River

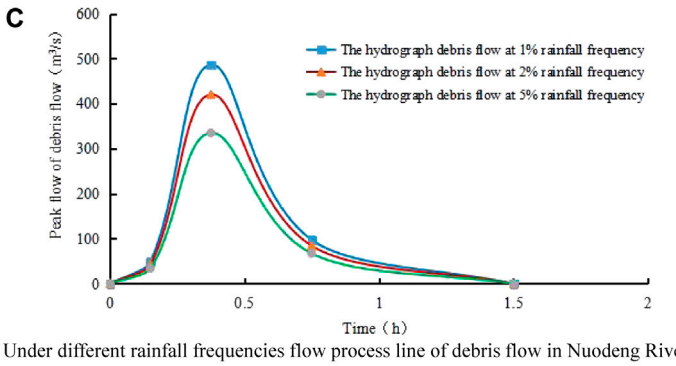

Under different rainfall frequencies flow process line of debris flow in Nuodeng River

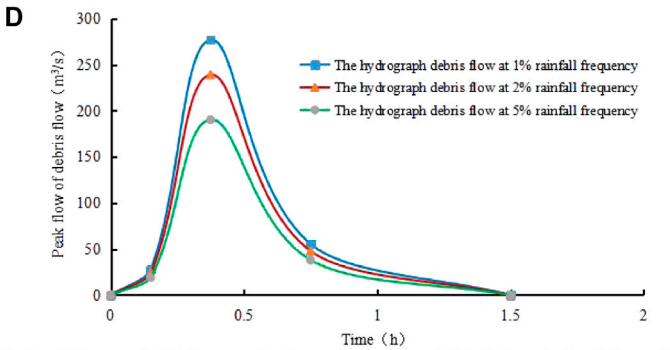

Under different rainfall frequencies flow process line of debris flow in Suolichangqing

FIGURE 4
Flow process lines of debris flow for each debris flow channel in Yunlong County.

TABLE 6 Simulation data of Shiwei River blocking engineering.

Dam construction	Dam height (m)	Dam length (m)	Width of the dam cross-section at the top (m)	Width of the dam cross-section at the bottom (m)
Shiwei River rock dam LS1	7	47.54	2.68	10.56
Shiwei River valley township GF5	5	42.85	2.00	6.70
Qingshiyanqing valley township GF6	5	78.29	2.00	6.70
Qingshiyanqing valley township GF7	5	43.77	2.00	6.70
Qingshiyanqing valley township GF8	5	28.09	2.00	6.70
Qingshiyanqing valley township GF9	5	50.89	2.00	6.70
Shiwei River Fixed Bed Dam GC1	2.5	24.30	1.00	4.60
Shiwei River Fixed Bed Dam GC2	3	39.53	1.00	4.60
Shiwei River Fixed Bed Dam GC3	3	17.85	1.00	4.60
Shiwei River valley township GF12	5	43.60	2.00	6.70
Shiwei River valley township GF13	5	45.15	2.00	6.70
Shiwei River valley township GF14	5	46.98	2.00	6.70
Shiwei River valley township GF16	5	56.83	2.00	6.70

$$C_V = \frac{r - r_w}{r_s - r_w} \quad (1)$$

r is the density of debris flow (g/cm^3),r_s is the density of fluid sediment (g/cm^3) and r_w is the density of water (g/cm^3).

The rheological parameters α_1 and β_1 are related to the viscosity coefficient η, and the rheological parameters α_2 and β_2 are related to the yield stress τ_y, as detailed in the formula in the FL0-2D User Manual.

$$\eta = \alpha_1 e^{\beta_1 C_V} \quad (2)$$

$$\tau_y = \alpha_2 e^{\beta_2 C_V} \quad (3)$$

3.2.2 Debris flow process line design

Numerical simulation of debris flow using FLO-2D software requires the calculation of the flow process line of the debris flow (XU, 2018b; Li et al., 2022; Zhang LB. et al., 2023). After obtaining the peak flow of the rainstorm with the rainfall-hydrological method, the runoff flow at the outlet can be calculated according to relevant specifications (Hu, 1993; China University of Geosciences, 2018; Li et al., 2023) under different rainfall frequencies, and the peak flow of the debris flow at the outlet can be obtained. The calculation parameters for the peak flow of debris flow are shown in Table 4, and the peak flow of the outlet section is shown in Table 5.

$$Q_c = (1 + \varphi)Qd \quad (4)$$

$$\varphi = (\gamma - \gamma_W)/(\gamma_S - \gamma) \quad (5)$$

Qc is the peak flow of the debris flow section (m^3/s), Q is the peak flow of the flood section (m^3/s), ψ is the sediment correction coefficient, and d is the blockage coefficient.

The flow process line of debris flow can be obtained by using the generalized pentagon method (Gong et al., 2017; Wang et al., 2020; Zhang JC. et al., 2023), as shown in Figures 4A–D.

3.2.3 Selection of catchment points

The effectiveness of the simulation is determined by the reasonable selection of catchment points. Through field investigations and comparisons of collected data, loose material accumulation sites where a large amount of debris flow in each debris flow channel forming area existed were selected as the catchment points to serve as the starting points for numerical simulation. The catchment point for the main channel of Shiwei River was located at the convergence of the tributaries in the upstream forming area, while the catchment point for the tributary channel of Shiwei River was located at the foot of the front edge slope of the Guanzhuangdian landslide. The catchment point for Suolichangqing was located at the confluence point of the upstream tributaries, and the catchment point for Nuodeng River was located at the foot of the slope of the large landslide of Songpodigu in the forming area.

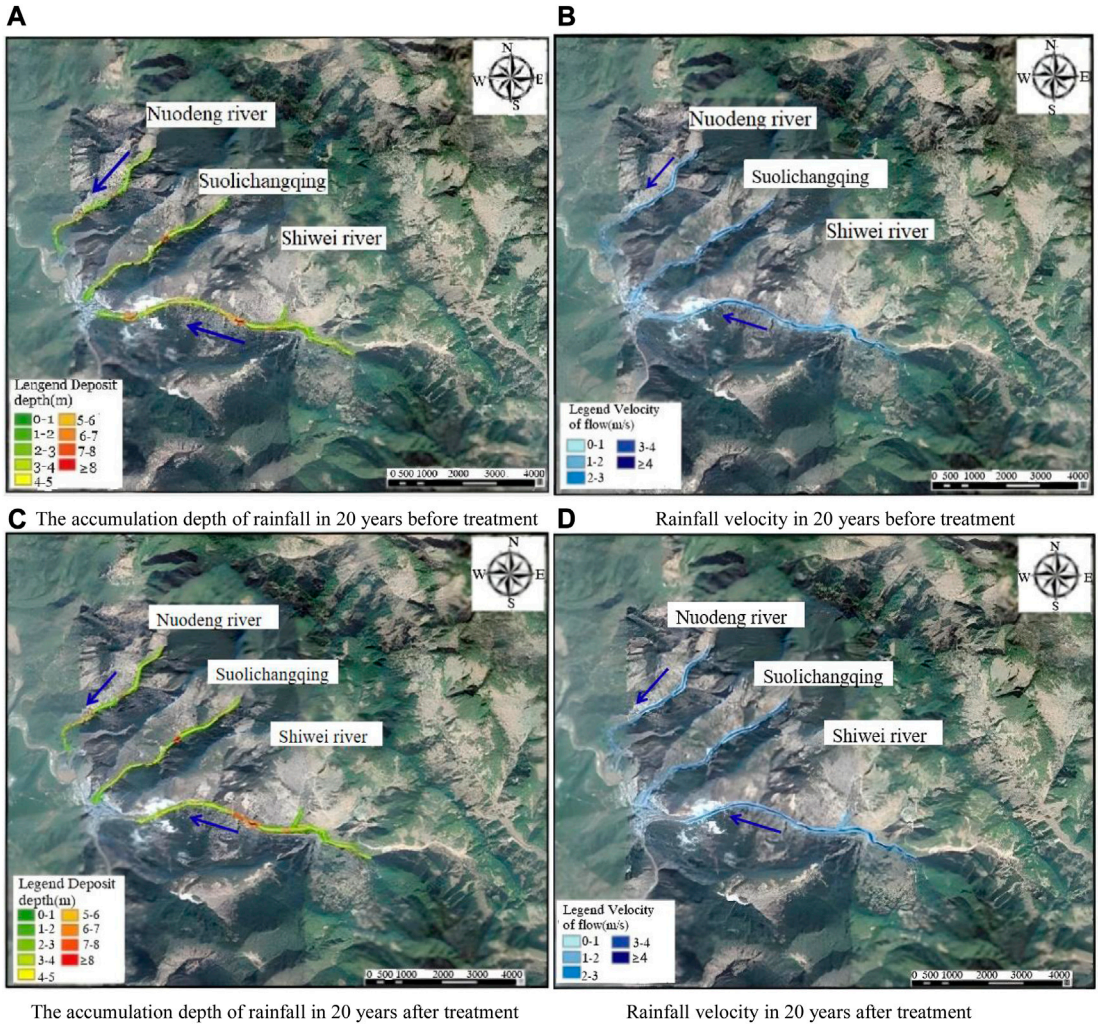

FIGURE 5
Simulation results of 20 years before and after treatment.

4 Risk assessment before and after performing debris flow control

4.1 Field investigation results of debris flow control engineering

The reasonable selection of catchment points determines the effectiveness of the simulation. Based on field investigations and comparisons of collected data, loose material accumulation sites where a large amount of debris flow in each debris flow channel forming area existed were selected as the catchment points to be seen as the starting points for numerical simulation. The catchment point for the main channel of Shiwei River was located at the confluence of the tributaries in the forming area upstream, while the catchment point for the tributary channel of Shiwei River was located at the slope foot of the front edge of the Guanzhuangdian landslide. The catchment point for Suolichangqing was located at the confluence point of the upstream tributaries, and the catchment point for Nuodeng River was located at the foot of the slope of the large landslide of Songpodigu in the forming area.

The early debris flow control engineering for the Suolichangqing and Nuodeng River debris flows in the study area nearly failed, resulting in the post-control movement processes being consistent with natural conditions. This simulation mainly focuses on simulating the blocking engineering of the main channel and tributary channel of Shiwei River at the Qingshiyanqiong blocking site. The statistical data of the blocking engineering can be found in Table 6.

4.2 Numerical simulation results before and after debris flow control

Numerical simulations after the implementation of control measures were conducted, the movement and accumulation of debris flows in three gullies in Yunlong County under three recurrence intervals (p = 5%, p = 2%, p = 1%) were obtained. The simulation results are shown in Figures 5–7.

In this study, the simulated data of debris flow fan areas occurring once every 20 years in the study area was compared with the actual measured fan area data. According to the simulation results, the

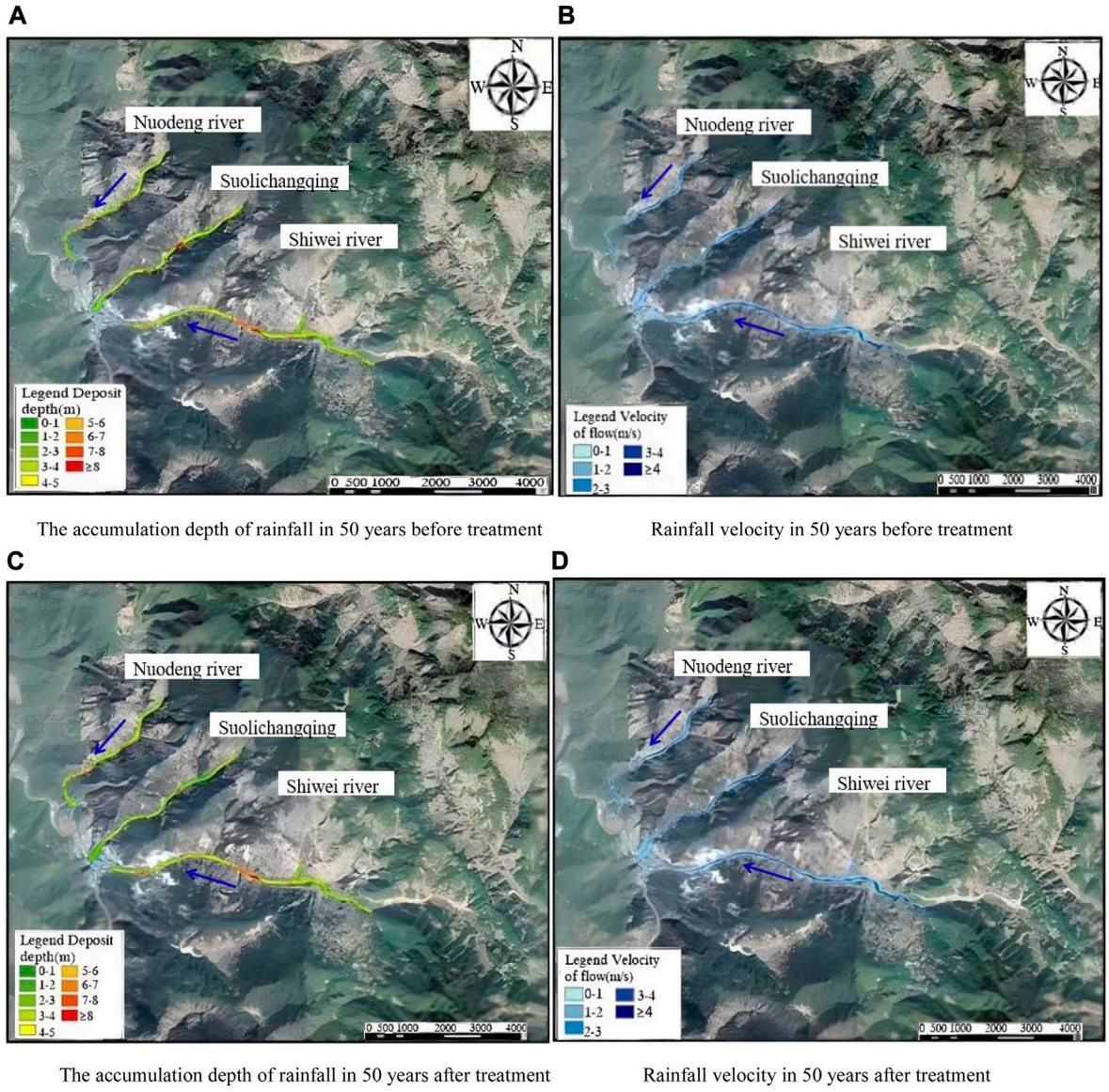

FIGURE 6
Simulation results of 50 years before and after treatment.

accuracy of the 20-year recurrence interval fan area for Lion Rock River in Yunlong County was 79.8%, for Suolichangqing in Yunlong County was 77.7%, and for Nuodeng River in Yunlong County was 79.4%. The numerical simulation results before and after debris flow control in Yunlong County are shown in Table 7.

Based on the FLO-2D numerical simulation results, it is known that due to the failure of the early debris flow control engineering in Suolichangqing and Nuodeng River, the movement process of debris flow is consistent with the natural situation. However, the trapping function of the control engineering in Shiwei River significantly reduced the area of the accumulation fan, the average accumulation depth, the maximum accumulation depth and the outburst volume. Under the conditions of a 20-year or 50-year rainfall, there is no debris flow reaching the current accumulation fan position, and after being controlled, the area, average depth, maximum depth, and outburst volume of the accumulation fan all tend to be zero, with loose materials accumulating in the channel. Under the conditions of a 100-year rainfall, some debris flows reach the current accumulation fan position, the area of the accumulation fan is 21.3% of the pre-construction value, and the outburst volume is 19.6% of the pre-construction value.

4.3 Verification of numerical simulation results

In this paper, the simulation data of debris flow gully accumulative fan range in the study area once every 20 years are compared with the actual data of debris flow gully accumulative fan range in the study area. The specific formula is as follows.

$$A = \left\{ \frac{S_1}{S_2} \times \frac{S_1}{S_3} \right\} \times 100\% \quad (6)$$

TABLE 7 Numerical simulation results before and after regulation engineering.

Name	Recurrence period (Year)	Accumulative fan area (m^2)	Average accumulation depth (m)	Maximum deposit depth (m)	Discharge volume (m^3)
Shiwei River	Before treatment p = 5%	53200	2.33	4.76	123956
	Before treatment p = 2%	99600	2.35	5.08	234060
	Before treatment p = 1%	178000	2.42	5.47	430760
	After treatment p = 5%	0	0	0	0
	After treatment p = 2%	0	0	0	0
	After treatment p = 1%	38000	2.22	4.89	84360
Suoli changqing	Before treatment p = 5%	42400	1.04	2.44	44096
	Before treatment p = 2%	64400	1.11	2.64	71484
	Before treatment p = 1%	99200	1.23	2.87	122016
	After treatment p = 5%	42400	1.04	2.44	44096
	After treatment p = 2%	64400	1.11	2.64	71484
	After treatment p = 3%	99200	1.23	2.87	122016
Nuodeng River	Before treatment p = 5%	12400	1.18	2.15	14632
	Before treatment p = 2%	19600	1.2	2.48	23560
	Before treatment p = 1%	28800	1.31	3.31	37728
	After treatment p = 5%	12400	1.18	2.15	14632
	After treatment p = 2%	19600	1.2	2.48	23560
	After treatment p = 1%	28800	1.31	3.31	37728

TABLE 8 Accuracy assessment of numerical simulation.

p = 5%	Debris flow accumulation area			
Name	Measured value (10^4m^2)	Simulation value (10^4m^2)	Overlap (10^4m^2)	Accuracy
Shiwei River	5.38	5.32	4.78	79.8
Suolichangqing	4.29	4.24	3.76	77.7
Nuodeng River	1.32	1.24	1.14	79.4

TABLE 9 Standard for classifying the danger of debris flow.

Intensity of debris flow	Depth of mud(m)	Relationship formula	Product of depth of mud and flow velocity
High	H ≥ 2.5	OR	VH ≥ 2.5
Medium	0.5 ≤ H < 2.5	AND	0.5≤VH < 2.5
Low	0 ≤ H < 0.5	AND	VH < 0.5

The degree of accuracy in formula A; S_1 is the overlap area between the measured and simulated accumulations. S_2 is the accumulation area of debris flow measured in field survey. S_3 is the accumulation area of numerical simulation debris flow. The result value for precision A is 0–1, and the closer it is to 1, the more accurate the final simulation result will be. The accuracy of each ditch calculated by formula 6 is shown in Table 8, which is consistent with the above simulation results, thus verifying the accuracy of this numerical simulation.

4.4 The risk assessment before and after debris flow control

Risk evaluation of the Yulong County urban area with high human activity was conducted based on the depth and velocity of mud and debris flow obtained through numerical simulations. The classification standard for the risk of mud and debris flow refers to the standards used for the Wenchuan debris flow, as shown in Table 9.

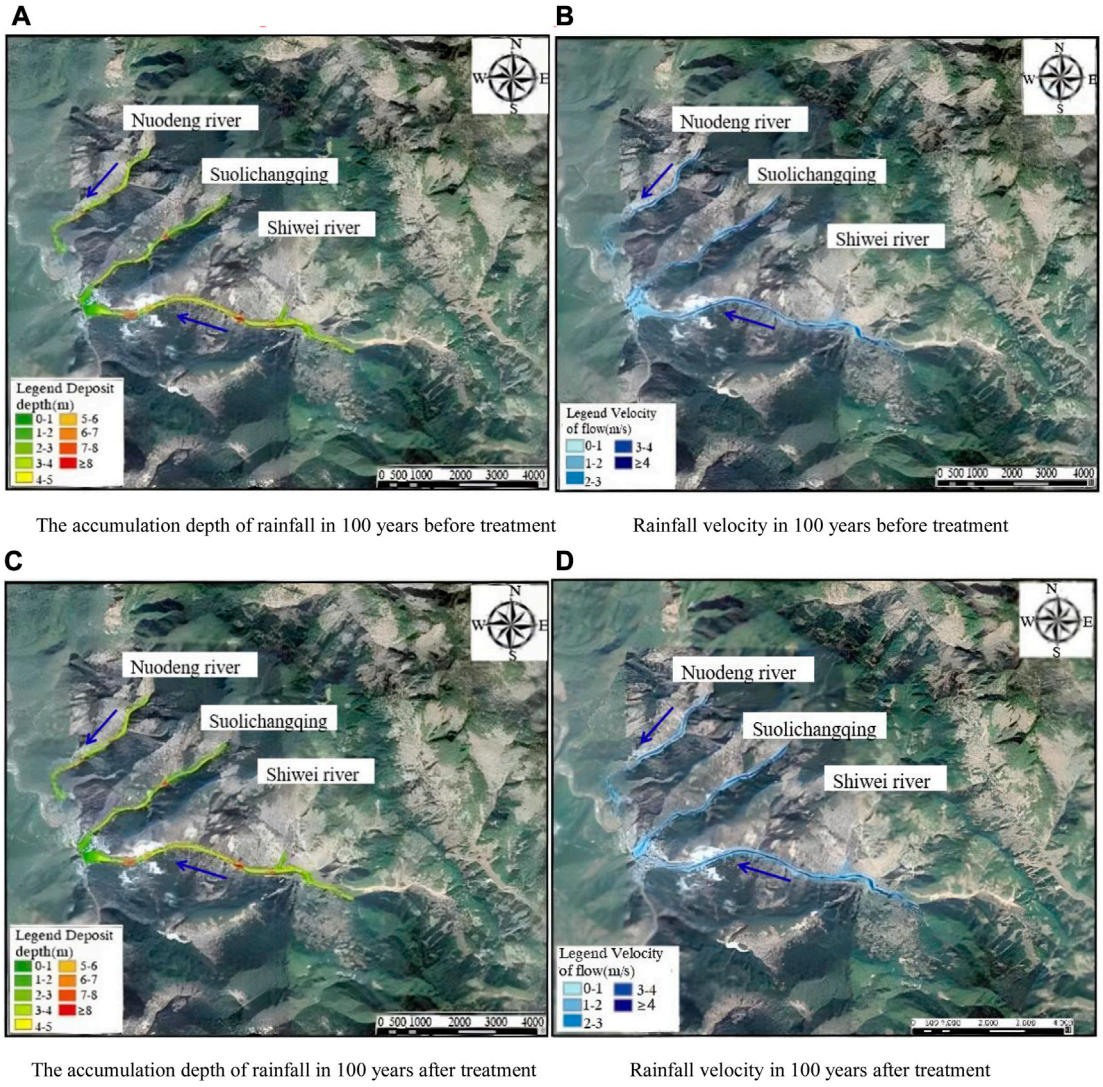

FIGURE 7
Simulation results of 100 years before and after treatment.

According to the current urban area range of Yunlong County and the overall development plan (2013–2030), the urban area of Yunlong County is approximately 2.5075 square kilometres. Based on the qualitative evaluation and FLO-2D numerical simulation results, a risk assessment was conducted for geological hazards in the urban area of Yunlong County before and after geological disaster management. The evaluation results are divided into high-risk areas, medium-risk areas, low-risk areas, and zero-risk areas, as shown in Figure 8.

"Safe zones" indicate that the area is not at risk of being affected by debris flows; "Low-risk zones" indicate that debris flows may cause slight damage to buildings in the area; "Medium risk zones" indicate that some buildings in the area may be destroyed, and personnel may be injured or killed; "High-risk zones" indicate that debris flows will destroy buildings and cause significant loss of life. As shown in Figure 8, the high-risk zones in the county's urban area are mainly divided into two regions; The first high-risk zone is located in the whole Shiwei River flowing through the urban area of Yunlong County, which although has been rehabilitated with drainage facilities to timely evacuate small-scale debris flows, there may be risks of slow drainage or blockages in case of rainfalls with a frequency of once every 100 years, and there are risks inside and around the drainage facilities. The second high-risk zone is located at the Suolichang Canyon in the urban area of Yunlong County, which has risks of debris flows with a frequency of once every 20 years.

The results of the geological hazard risk assessment for different rainfall frequencies, including $p = 5\%$, $p = 2\%$, and $p = 1\%$, were used to analyze the statistics of the area of each risk zone before and after engineering treatment, as shown in Table 10.

According to the above analysis, it can be known that after the implementation of engineering measures for debris flow disasters, the proportion of high-risk areas in the urban area of Yunlong County was significantly decreased, especially under the condition of 20-year rainfall. The area of high-risk areas decreased the most. Under rainfall conditions of 50 years and 100 years, the area of medium-

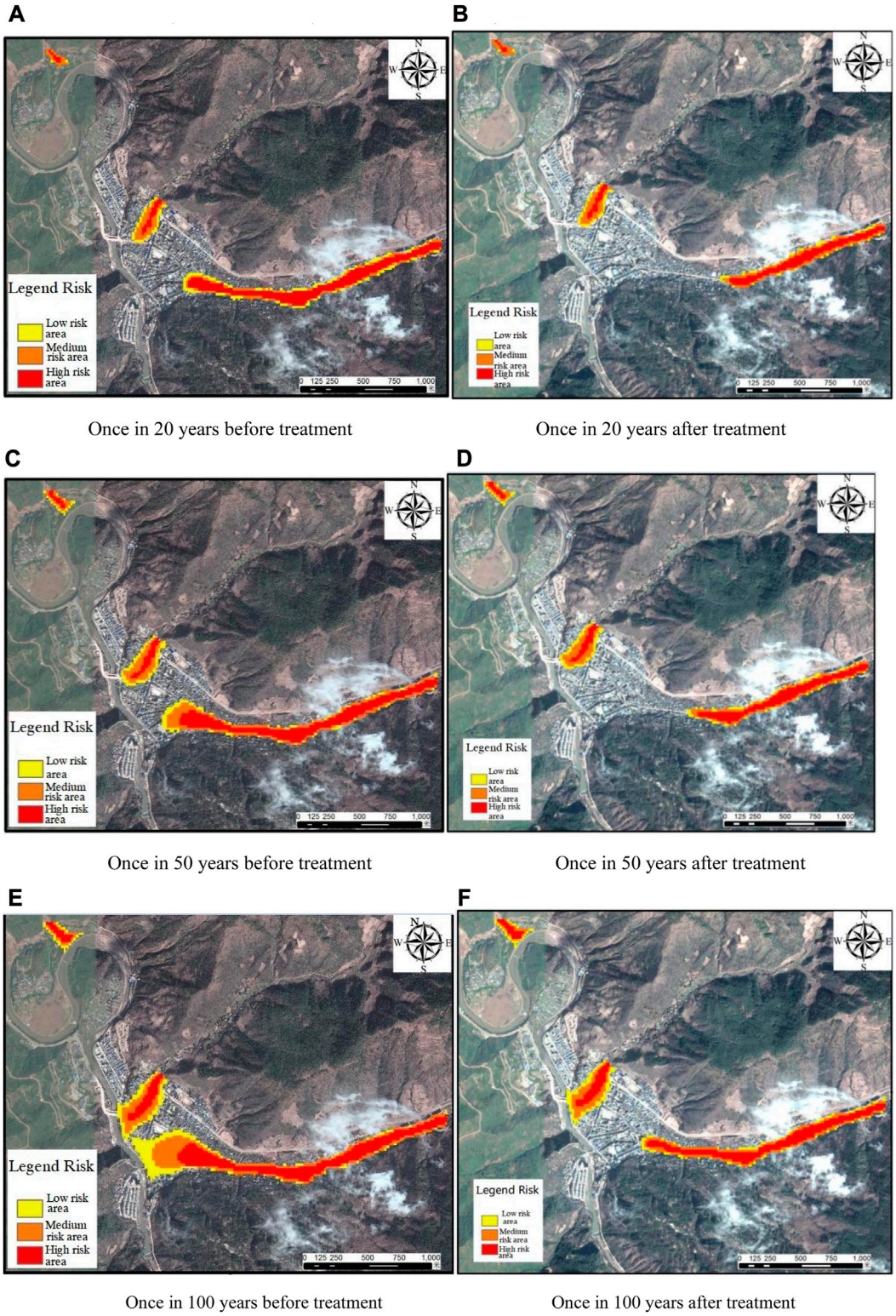

FIGURE 8
The danger zonation map of the urban area of Yunlong County.

risk areas decreased significantly, but under the condition of 20-year rainfall, the area of medium-risk areas increased slightly, this is mainly because some high-risk areas are transformed into medium-risk areas. Under different rainfall frequencies, the proportion of low-risk areas decreased. Overall, after implementing engineering measures for debris flow disasters, the area of no-risk areas increased, especially the area of no-risk areas increased by 5.92% when the rainfall frequency was 100 years, which greatly ensures the safety of densely populated areas.

TABLE 10 Statistical of the hazardous zoning area in the urban area of Yunlong County before and after governance.

	Zone	High danger zone	Medium danger zone	Low danger zone	No danger zone	Aggregate
Before treatment	p = 5% area (km^2)	0.1528	0.0788	0.0688	2.2071	2.5075
	p = 5% percentage (%)	6.09	3.14	2.74	88.03	100
	p = 2% area (km^2)	0.1776	0.1364	0.0656	2.1279	2.5075
	p = 2% percentage (%)	7.08	5.44	2.62	84.86	100
	p = 1% area (km^2)	0.2108	0.1728	0.122	2.0019	2.5075
	p = 1% percentage (%)	8.41	6.89	4.87	79.83	100
After treatment	p = 5% area (km^2)	0.162	0.12	0.0752	2.1503	2.5075
	p = 5% percentage (%)	3.41	3.22	1.33	92.04	100
	p = 2% area (km^2)	0.1128	0.094	0.0532	2.2475	2.5075
	p = 2% percentage (%)	4.5	3.75	2.12	89.63	100
	p = 1% area (km^2)	0.162	0.12	0.0752	2.1503	2.5075
	p = 1% percentage (%)	6.46	4.79	3	85.75	100

The setting up of the Shiwei River debris flow interception project plays a great role in reducing the harm caused by debris flows. In the later period, a comprehensive prevention and control project can be considered, which includes a "composite V-shaped drainage chute + fish mouth project + sand-collecting dam + valley-distributed dam + rigid dam + flood control dike" to further improve the prevention and control effect. Suolichangqing and Nuodeng River have lower prevention and control levels and longer construction times. At present, they are in a saturated state and require the addition of appropriate treatment measures to ensure safety.

5 Conclusion

Based on various parameters of rainfall, flow data, and digital terrain data, this article used the FLO-2D numerical simulation software to simulate the movement process of the three debris flow gullies in Yunlong County before and after treatment. Based on the debris flow movement state, the danger and zoning of the county town area were evaluated, and the following conclusions were drawn:

1) This paper assisted positioning by construction drawings and remote sensing images of the treatment project. After the mesh division of debris flow simulation was completed, the treatment project was added to the simulation project in the form of plug-in, and specific engineering parameters were imported into the simulation project file by modifying its attributes. The setting of the management project in the numerical simulation is completed, and the difficult problem of the setting of engineering measures is solved.
2) Under the rainfall conditions of a return period of 20 years and 50 years, the Shiwei River did not reach the current debris flow deposit fan position, and loose materials were piled up in the gorge. Under the rainfall conditions of a return period of 100 years, some of the debris flow reached the current deposit fan position, and the area of the deposit fan was 21.3% of that before treatment, and the volume of the scouring was 19.6% of that before treatment.
3) After the implementation of engineering treatment for debris flow disasters, the proportion of high-risk areas in the urban area of Yunlong County was substantially decreased, especially under the condition of once-in-twenty-year rainfall, the area of high-risk regions was reduced the most. Especially when the rainfall frequency is once in a hundred years, the area of non-dangerous zones has increased by 5.92% compared to before the treatment.

Data availability statement

The original contributions presented in the study are included in the article/supplementary material, further inquiries can be directed to the corresponding authors.

Author contributions

X-YD: Writing—original draft, W-JH: review and editing, XY: Conceptualization, FL: Data curation.

Funding

This research was supported by the Hunan Provincial Natural Science Foundation of China (No. 2023JJ50339), and the Natural Science Foundation of Hunan Province, China (No. 2023JJ30212).

Conflict of interest

The authors declare that the research was conducted in the absence of any commercial or financial relationships that could be construed as a potential conflict of interest.

Publisher's note

References

Bertolo, P., and Wicezorek, G. F. (2005). Calibration of numerical models for small debris flows in Yosemite Valley,California,USA. *Nat. Hazards Earth Syst. Sci.* 5 (6), 993–1001. doi:10.5194/nhess-5-993-2005

Brien, J. S. (2009a). *FLO-2D reference manual*. Arizona, United States: FLO-2D Software Inc, 10–11.

Brien, J. S. (2009b). *FLO-2D reference manual*. Arizona, United States: FLO-2D Software Inc, 10–11.

Calista, M., Menna, V., Mancinelli, V., Nicola, S., and Enrico, M. (2020). Rockfall and debris flow hazard assessment in the SW escarpment of montagna del morrone ridge (Abruzzo, Central Italy). *Water* 12 (4), 1206–1215. doi:10.3390/w12041206

Cao, P., Hou, S. S., and Chen, L. (2021). Risk assessment of mass debris flow based on numerical simulation: An example from the Malu River basin in Min County. *Chin. J. Geol. Hazard Control* 32 (2), 100–109. doi:10.16031/j.cnki.issn.1003-8035.2021.02.14

Castelli, F., Freni, G., Lentini, V., and Fichera, A. (2017). Modelling of a debris flow event in the Enna area for hazard assessment. *Procedia Eng.* 175, 287–292. doi:10.1016/j.proeng.2017.01.026

China University of Geosciences (2018). *Code for debris flow disaster prevention and control engineering survey*. Beijing: China University of Geosciences.

Cong, K., Li, R. D., and Bi, Y. H. (2019). Benefit evaluation of debris flow control project based on FLO-2D model. *Northwest Geol.* 52 (3), 209–216.

Dong, Y., and Hu, W. J. (2021). *Investigation and risk assessment report of geological disaster prevention and control effect in Yunlong County and planning area of Yunnan Province*. Yunnan: Yunnan geological Survey.

FLO-2D Software Inc (2004). *FLO-2D,2Dimensional flood routine model manual: Version 10*. Arizona: Nutrioso, AZ85932.

Gan, J. L., and Luo, C. T. (2020). Runout and process simulation of gully debris flow in middle and low mountains. *J. Nat. Disasters* 29 (2), 97–110.

Gao, Y., Yu, Z., Chen, W., Yin, Q., Wu, J., and Wang, W. (2023). Recognition of rock materialsafter high-temperature deterioration based on SEM images via deep learning. *J. MaterialsResearch Technol.* 25, 273–284. doi:10.1016/j.jmrt.2023.05.271

Gong, K., Yang, T., Xia, C. H., and Yang, Y. (2017). Assessment of landslide hazard based on FLO-2D-a case study in mianxun town, mianxian county, wenchuan province. *J. Water Resour. Water Eng.* 28 (6), 134–138. doi:10.11705/j.issn.1672-643X.2017.06.23

Hou, S. S., Cao, P., Chen, L., Feng, Z., Wang, C., and Li, A. (2021). Risk assessment of debris flow disaster in eryang River Basin Based on numerical simulation. *Hydrogeology& Eng. Geol.* 48 (2), 143–151. doi:10.16030/j.cnki.issn.1000-3665.20200305

Hu, G. B. (1993). The analytical calculation of flood regulation based on the pentagonal flood process line. *Jiangxi Hydraulic Sci. Technol.* 19 (3), 198–201.

Huang, X., Tang, C., Li, Y. L., He, J. Y., Zhang, K. S., Liu, T., et al. (2019). Morphology-tunable WMoO nanowire catalysts for the extremely efficient elimination of tetracycline: Kinetics, mechanisms and intermediates. *Adv. Earth Sci.* 31 (10), 1047–1057. doi:10.1039/c8nr08162j

Jakob, M., Stein, D., and Ulmi, M. (2012). Vulnerability of buildings todebris flow impact. *Nat. Hazards* 60 (2), 241–261. doi:10.1007/s11069-011-0007-2

Jia, T., Tang, C., and Wang, N. N. (2015). Method and application of debris flow hazard zoning Based on FLO-2D and impulse model. *Water Resourse Power* 33 (2), 152–155. doi:10.16030/j.cnki.issn.1000-3665.202003057

Li, B. X., Cai, Q., Song, J., Cheng, L., and Liu, J. K. (2022). Risk assessment of debris flow hazard based on FLO-2D:A case study of debris flow in Maiduo Gully. *J. Natuerl Disastres* 31 (4), 256–265. doi:10.16031/j.cnki.issn.1003-8035.2021.02.14

Li, X. L., Zhang, X. Y., Shen, W. L., Zeng, Q., Chen, P., Qin, Q., et al. (2023). Research on the mechanism and control technology of coal wall sloughing in the ultra-large mining height working face. *Int. J. Environ. Res. Public Health* 20 (2), 868. doi:10.3390/ijerph20010868

Liang, H. X., Shang, M., and Xu, X. (2016). Research on the influence factors of flow and deposition of debris flow based on the FLO-2D simulation. *J. Eng. Geol.* 24 (2), 228–234. doi:10.1007/s12665-014-3865-6

Liu, S. M., and Li, X. L. (2023). Experimental study on the effect of cold soaking with liquid nitrogen on the coal chemical and microstructural characteristics. *Environ. Sci. Pollut. Res.* 30 (3), 36080–36097. doi:10.1007/s11356-022-24821-9

Liu, S. M., Sun, H. T., Zhang, D. M., Yang, K., Wang, D., Li, X., et al. (2023a). Nuclear magnetic resonance study on the influence of liquid nitrogen cold soaking on the pore structure of different coals. *Phys. Fluids* 35 (1), 012009. doi:10.1063/5.0135290

Liu, S. M., Sun, H. T., ZhangYang, D. M. K., Li, X., Wang, D., et al. (2023b). Experimental study of effect of liquid nitrogen cold soaking on coal pore structure and fractal characteristics. *Energy* 275 (7), 127470. doi:10.1016/j.energy.2023.127470

Ortiz-Giraldo, L., Botero, B. A., and Vega, J. (2023). An integral assessment of landslide dams generated by the occurrence of rainfall-induced landslide and debris flow hazard chain. *Front. Earth Sci.* 11, 1157881. doi:10.3389/feart.2023.1157881

Peng, S. Y., Li, G. J., and Qin, S. W. (2017). Review of research on dynamic processes and erosion of debris flow. *Yangtze River* 48 (3), 53–56. 101. doi:10.16232/j.cnki.1001-4179.2017.03.011

Shang, W. A. (1993). Landslide and debris flow disasters in Yunnan's towns and their prevention and control. *First Natl. Conf. Landslide Debris Flow Prev. Control*, 323–328.

Tang, X. C. (1995). Debris flow control and its future in mountain of south west China. *Mar. Quat.* 15 (3), 105–112.

Wang, J. J., and Ling, H. I. (2011). Developing a risk assessment model for typhoon-triggered debris flows[J]. *J. Mt. Sci.* 8 (1), 14. doi:10.1007/s11629-011-2065-z

Wang, G. F., Yang, Q., Chen, Z. L., Jia, L., and Mao, J. R. (2020). Risk assessment of debris flow in the ganjia gully of the bailongjiang basin. *J. Sediment Res.* 45 (4), 66–73. doi:10.16239/j.cnki.0468-155x.2020.04.011

Xu, H. L. (2018a). *The run-out scal prediction of the rapid-steep channel debris-flow base on FLO-2D*. Chengdu: Chengdu University of Technology.

Xu, Huiliang (2018b). *The run-out scal prediction of the rapid-steep channel debris-flow base on FLO-2D*. Chengdu: Chengdu University of Technology.

Xun, H., and Chuang, T. (2016). Quantitative risk assessment of catastrophic debris flows through numerical simulation. *Adv. Earth Sci.* 31 (10), 1047–1055.

Yan, H. M. (2016). *Risk assessment of debris flow in main gully based on FLO-2D*. Chengdu: Southwest Jiaotong University.

Yang, H. L., Fan, X. Y., and Jiang, Y. J. (2017). Analysis of engineering treatment effect of debris flow based on FLO-2D:Case of Yindongzi gully in Dujiangyan City. *Yangtze River* 48 (17), 66–71. 95. doi:10.1016/j.csite.2023.103325

Yang, W., Wan, F., Ma, S., Qu, J., Zhang, C., and Tang, H. (2023). Hazard assessment and formation mechanism of debris flow outbursts in a small watershed of the Linxia Basin. *Front. Earth Sci.* 10, 994593. doi:10.3389/feart.2022.994593

Zhang, F. X., Zhang, L. Q., Zhou, J., and Yang, Z. Y. (2019). Risk assessment of debris flow in Ruoru village,Tibet based on FLO-2D. *J. Water Resour. Water Eng.* 30 (5), 95–102. doi:10.1007/s11629-020-6448-x

Zhang, H. W., Liu, F. Z., and Wang, J. C. H. (2022). Hazard assessment of debris flows in Kongpo Gyamda,Tibet based on FLO-2D numericalsimulation. *J. Geomechanics* 28 (2), 306–318. doi:10.3969/j.issn.1006-6616.2008.03.009

Zhang, J. C., Li, X. L., Qin, Q. Z., and Zuo, Z. (2023b). Study on overlying strata movement patterns and mechanisms in super-large mining height stopes. *Bull. Eng. Geol. Environ.* 82 (3), 142. doi:10.1007/s10064-023-03185-5

Zhang, L. B., Shen, W. L., Li, X. L., Wang, Y., Qin, Q., Lu, X., et al. (2023a). Abutment pressure distribution law and support analysis of super large mining height face. *Int. J. Environ. Res. Public Health* 20 (1), 227. doi:10.3390/ijerph20010227

frontiers | Frontiers in Earth Science

TYPE Original Research
PUBLISHED 14 September 2023
DOI 10.3389/feart.2023.1254042

OPEN ACCESS

EDITED BY
Xuelong Li,
Shandong University of Science and Technology, China

REVIEWED BY
Chaoyu Chang,
Institute of Disaster Prevention, China
Anquan Xu,
Tianjin University, China

*CORRESPONDENCE
Zhongfa Guo,
xjr2458023298@sina.com
Dewen Liu,
civil_liudewen@sina.com
Weiwei Sun,
861981546@qq.com

RECEIVED 06 July 2023
ACCEPTED 09 August 2023
PUBLISHED 14 September 2023

CITATION
Xu J, Gao H, Guo Z, Zhao J, Yang Z, Zhao G, Guo Z, Liu D and Sun W (2023), Key technologies research on of soil-structure interaction base story isolated structure response in 3D seismic zone. *Front. Earth Sci.* 11:1254042.
doi: 10.3389/feart.2023.1254042

Key technologies research on of soil-structure interaction base story isolated structure response in 3D seismic zone

Jingran Xu[1], Haolun Gao[1], Zihan Guo[1], Jie Zhao[1], Zhuoxin Yang[1], Guangxing Zhao[1], Zhongfa Guo[2]*, Dewen Liu[1]* and Weiwei Sun[1]*

[1]Southwest Forestry University, Kunming, Yunnan Province, China, [2]Rattana Bundit University, Bangkok, Thailand

The development of karst in Karst area leads to poor stability of stratum. If earthquake occurs, the area will produce destructive disaster. In order to improve the stability capacity of the grassroots in the region, this study investigates the seismic response of inter-story isolation structures considering soil-structure interaction (SSI) in three-dimensional earthquakes. A model of the inter-story isolation structure incorporating SSI was developed, and one-dimensional, two-dimensional, and three-dimensional ground motions were applied to compare the seismic response under different input conditions. A three-dimensional isolation system was introduced and compared with traditional horizontal isolation structures to address excessive tensile and compressive stresses on the isolation structure during three-dimensional ground motion. The results demonstrate that the seismic response to three-dimensional earthquakes surpasses one-dimensional and two-dimensional inputs. Furthermore, adding a three-dimensional isolation structure effectively isolates vertical ground motion and reduces structural seismic response. Moreover, it minimizes soil stresses on the foundation compared to traditional horizontal isolation structure, enhancing foundation stability. This study will provide theoretical value and practical guidance for the research on key technology of SSI base story isolation structure response in Karst Plateau 3D Seismic zone.

KEYWORDS

karst, three-dimensional seismic zone, soil structure interaction, vibration isolation structure, key technology

1 Introduction

Inter-story seismic isolation is a novel technology developed based on base isolation principles, which has shown progress (Peng and Dong, 2023; Ehsan and Toopchi-Nezhad, 2023; Wan et al., 2023; Fan et al., 2023; Liang et al., 2023; Davide and Kalfas Konstantinos, 2023; Zhang et al., 2021; Zhang et al., 2021; Basili and Angelis, 2022; Hur and Park, 2022; Li et al., 2022). The Tokyo Shiodome Sumitomo Mansion (Toshiyuki et al., 2008), utilizing an inter-story isolated structure, effectively mitigates seismic response by incorporating an isolation story within the middle of the building. Bernardi et al. (2023) introduced a multi-objective optimization method to consider the overall structural response. They investigated the application of Inter-Story Isolation (IIS) as a Tuned Mass Damper (TMD) for structural tuning and derived new design equations accordingly. Three structural cases

underwent time history analysis to evaluate the optimization effects of this approach. The findings demonstrated that IIS improved the lower structural performance to some extent while also restraining isolation displacement and upper structural acceleration during seismic events. Zhou et al. (2016) developed a simple two-degree-of-freedom model using a streamlined reduction method based on modal synthesis. This model effectively captures the response characteristics of the entire system and facilitates the development of an analysis method for optimizing the parameters of the inter-story isolation system. Numerical examples were employed to explore the impact of different floor placements of the best inter-story isolation system within the same building, confirming the capability of isolation devices to reduce the structure's seismic response.

Zhang et al. (2017) proposed using Real-Time Hybrid Simulation (RTHS) to study the performance of buildings equipped with inter-story isolation. The shaking table serves as a means to establish essential boundary conditions. This study conducted experimental tests and numerical simulations on the substructures above and below the isolation story. Specifically, a 14-story building with inter-story isolation was subjected to a shaking table experiment controlled using an acceleration tracking method. The results demonstrated the accuracy and reliability of RTHS in investigating buildings with inter-story isolation. Tasaka et al. (2008) presented examples of base and inter-story isolation systems designed and refurbished by NIKKEN, a Japanese architectural and engineering company. The renovation project focused on retrofitting the base-isolation system while retaining the original structure, thereby enhancing its seismic performance. Furthermore, inter-story isolation systems can be applied to mid to high-rise buildings. Faiella et al. (2022) examined a three-story brick and stone building with an irregular structural configuration. The study addressed identifying dynamic parameters associated with the upper structure on the isolation story and required a comprehensive analysis of the lumped mass model to minimize the earthquake response. To establish standardized guidelines for the overall seismic response of buildings equipped with inter-story isolation structures, a detailed analysis of the Inter-Story Isolation (IIS) structure was conducted using a three-dimensional finite element model. The research findings were the basis for drawing conclusive opinions and proposing general design guidelines. Jin et al. (2012), Song et al. (2023) conducted experimental investigations into the seismic response and effectiveness of the mid-story isolation system in a four-story steel frame model. Various placements of the isolation story were considered, including the bottom of the first floor, the top of the first floor, the top of the second floor, and the top of the third floor.

The research outcomes revealed that the mid-story isolation system generally reduces seismic response, although it may amplify the acceleration of the lower structure of the isolation story. Additionally, applying mid-story isolated structures in reinforcing existing structures (Toshiyuki et al., 2008; Basili and Angelis, 2022; Zhang et al., 2022; Davide and Kalfas Konstantinos, 2023; Ehsan and Toopchi-Nezhad, 2023; Liu et al., 2023a; Liu et al., 2023a; Liu et al., 2023b; Li et al., 2023) effectively lowers the seismic response. Furthermore, machine learning methods have been employed to predict disaster occurrences in different environments (Huang et al., 2020a; Gao et al., 2023; Zhang et al., 2023). The structure development process (Liao et al., 2001; Li et al., 2014; Huang et al., 2020b; Zhang et al., 2021; Huang et al., 2022; Li et al., 2022; Liu et al., 2022) has undergone significant advancements. Ryan and Earl, (2010) conducted a systematic study on the relationship between the effectiveness of inter-story isolation systems and their locations. They extensively explored the selection of isolation system parameters to achieve optimal performance. The research revealed that the single-story isolation system responds distinctively to the overall structure, effectively mitigating forces from above the isolation system but showing lesser effectiveness in reducing the strength of the structure below. To address practical challenges and ensure commercial feasibility, the study aimed to alleviate the forces acting on the structure below the isolation system by designing an inter-story isolation system suitable for light loads. Bolvardi et al. (2018) investigated the utilization of inter-story isolation systems in platform-type figure-rise Cross-Laminated Timber (CLT) buildings. Modifications were made to the displacement-based Generalized Direct Design (DDD) program to identify key design parameters of the inter-story isolation system required to achieve pre-selected displacement targets for the building. The proposed design program was applied to a 12-story CLT building design example using seismic hazard parameters specific to Los Angeles, California. The building's performance was numerically validated through nonlinear time history simulation.

Basili and Angelis, (2022), Liu and Li, (2023) conducted shaking table experiments on frame structures using a multi-degree-of-freedom setup. Three different structural configurations were tested, including a four-story, three-story intermediate, and three-story structure equipped with an unconventional Tuned Mass Damper (TMD). The experiments subjected the structures to input motion conditions such as white noise, sine sweep, and natural earthquake excitations. The study observed different dynamic behaviors for each test configuration, and the employed isolators demonstrated significant dissipation capacity across a wide range of excitation amplitudes. Moreover, the study highlighted the controlling effect of unconventional TMD in enhancing structural vibration reduction. The studies above have primarily focused on the structural response to horizontal ground motion. However, there is a research gap regarding the investigation of the seismic response of inter-story seismic isolation systems considering the Soil-Structure Interaction (SSI) effect under three-dimensional ground motion, which still needs to be explored by scholars. To address this gap, we establish a model for inter-story seismic isolation that accounts for the SSI effect. One-dimensional, two-dimensional, and three-dimensional ground motions are separately applied as input parameters. By comparing the seismic responses of inter-story seismic isolation under different dimensional seismic wave inputs, we aim to address the research questions and provide solutions to the identified challenges.

2 Methods and materials

2.1 Methods

2.1.1 Centrally concentrated viscoelastic artificial boundary with fixed base

In the study considering Soil-Structure Interaction (SSI) effects, a continuous distribution of viscoelastic artificial boundaries is employed. When discretizing the problem using finite element

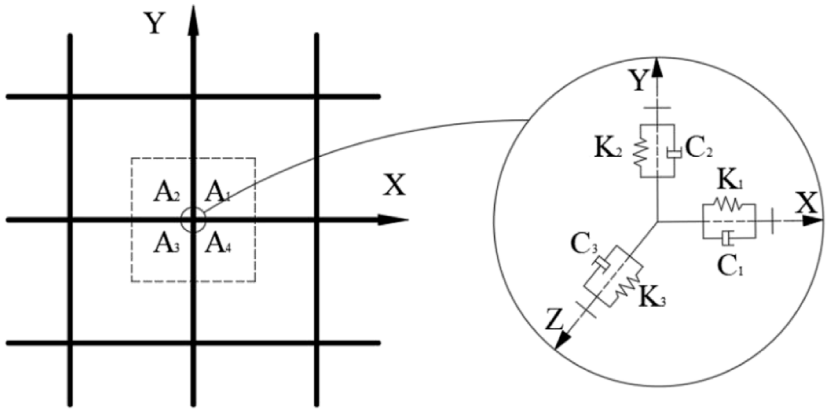

FIGURE 1
The sketch map of a three-dimensional viscoelastic artificial boundary.

TABLE 1 Section and reinforcement of frame beam and column.

Member	Story	Sectional dimension (mm×mm)	Arrangement of bars (C)
Frame column	1–3	700 × 700	1,625
	4–8	700 × 700	1,225
Frame beam	1–4	300 × 700	525
			422
	5–8	300 × 700	425
			322
Secondary beam	1–8	300 × 600	422
			322

analysis, the computational domain is also discretized along with the boundaries. To simplify the implementation of the viscoelastic artificial boundary, a centrally concentrated approach is utilized. As illustrated in Figure 1, coordinates X and Y represent the tangential directions, while Z represents the normal direction for the boundary.

The formulas for spring stiffness and damping coefficient are given by the following expressions:

$$K_1 = K_2 = \frac{2G}{R}\sum_{I=1}^{4} A_i, \quad C_1 = C_2\rho c_s\sum_{I=1}^{n} A_i \tag{2–1}$$

$$K_3 = \frac{4G}{R}\sum_{I=1}^{4} A_i, \quad C_3 = \rho c_P\sum_{I=1}^{n} A_i \tag{2–2}$$

Where,

ρ——Mass density;

c_s——Shear wave velocity;

c_P——Compressional wave velocity;

G——Shear modulus;

R——Distance from the wave source to the artificial boundary

The shear wave velocity and compressional wave velocity of the soil layers can be determined using the following formulas:

$$c_s = \sqrt{\frac{G}{\rho}} \tag{2–3}$$

$$c_P = \sqrt{\frac{\lambda + 2G}{\rho}} \tag{2–4}$$

$$\lambda = \frac{E\mu}{(1+\mu)(1-2\mu)} \tag{2–5}$$

Where,

μ——Poisson's ratio;

E——Elastic modulus;

λ——Lamé constant, which remains consistent with the previous descriptions.

2.2 Project overview

An 8-story reinforced concrete frame structure is established with a seismic fortification intensity of 8° and a structural damping

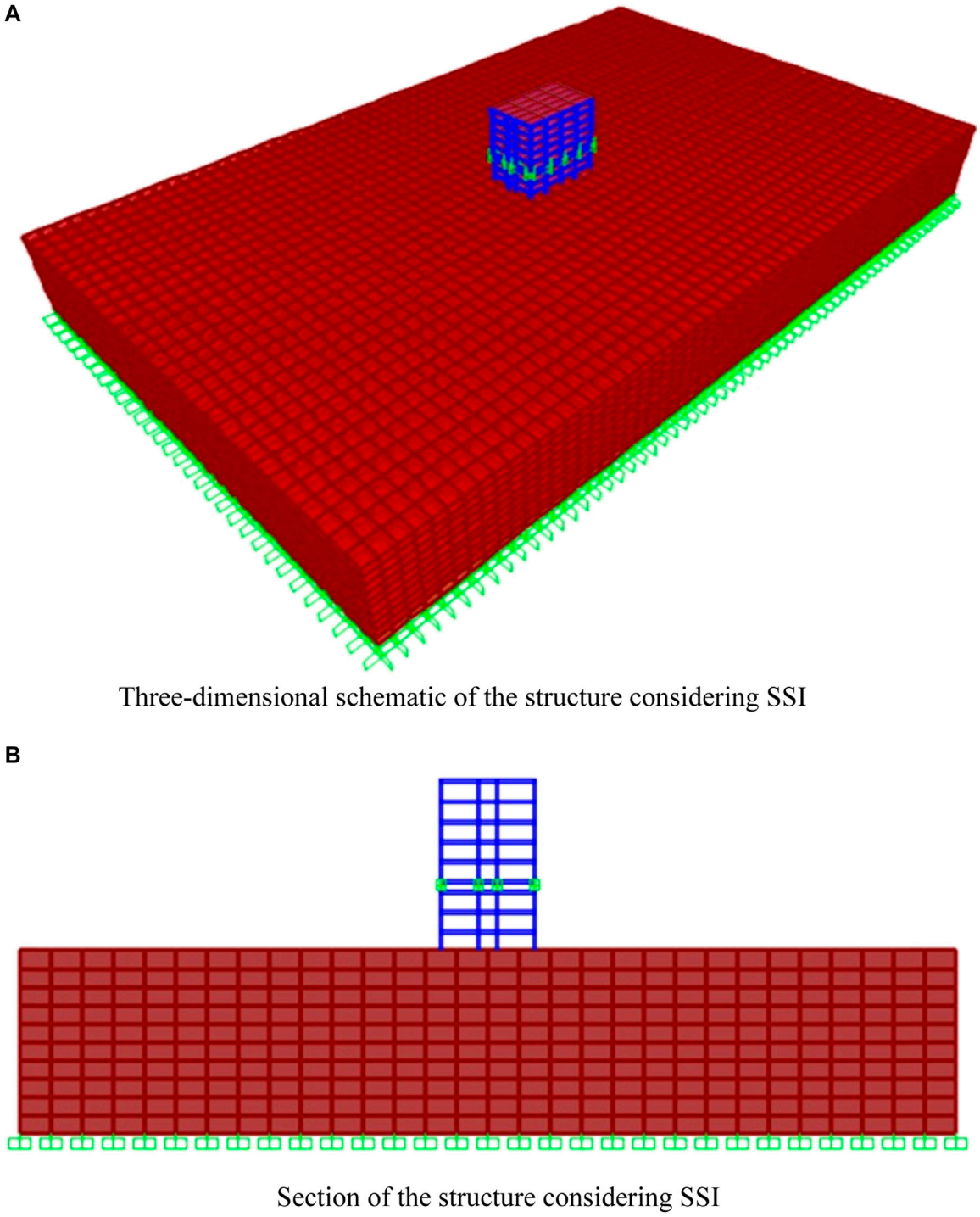

FIGURE 2
Schematic diagram of the isolated structure considering the SSI effect. **(A)** Three-dimensional schematic of the structure considering SSI. **(B)** Section of the structure considering SSI.

ratio of 0.05. The isolation story is positioned at the top of the three stories. The building structure has a plane size of 24 m × 15 m, and each story has a height of 3.3 m. The slab thickness measures 150 mm, while the beam and slab have a concrete strength grade of C30. The column's concrete strength grade is C40, and the reinforcement is of strength grade HRB400 for the main bars and HPB300 for the stirrups. The concrete cover has a thickness of 30 mm. Nonlinear material properties are assigned to the concrete with a strength grade of C40 using the Takeda hysteresis type. At the same time, HRB400 steel reinforcement is defined with the Kinematic hysteresis type. The frame columns are designated PMM plastic hinges, whereas the frame beams and beam

TABLE 2 (A) Parameters of foundation soil story.

Soil story name	Thickness (m)	Density (kg/m^3)	Poisson ratio	Shear modulus (10^8N/m^2)	Bulk modulus (10^8N/m^2)	Angle of internal friction (°)
Soft soil	3	2000	0.2	3.89	9.80	26
Medium soft soil	3	2,100	0.2	4.69	11.81	30
Hard soil	24	2,200	0.2	5.57	14.08	34

TABLE 3 Parameters of isolation bearing.

Model	Effective diameter	The total thickness of rubber (mm)	Initial shear stiffness (kN/m)	Equivalent stiffness (kN/m)	Vertical stiffness (kN/mm)	Yield force (kN)
LRB600	600	110	13,110	1,580	2,800	63.0

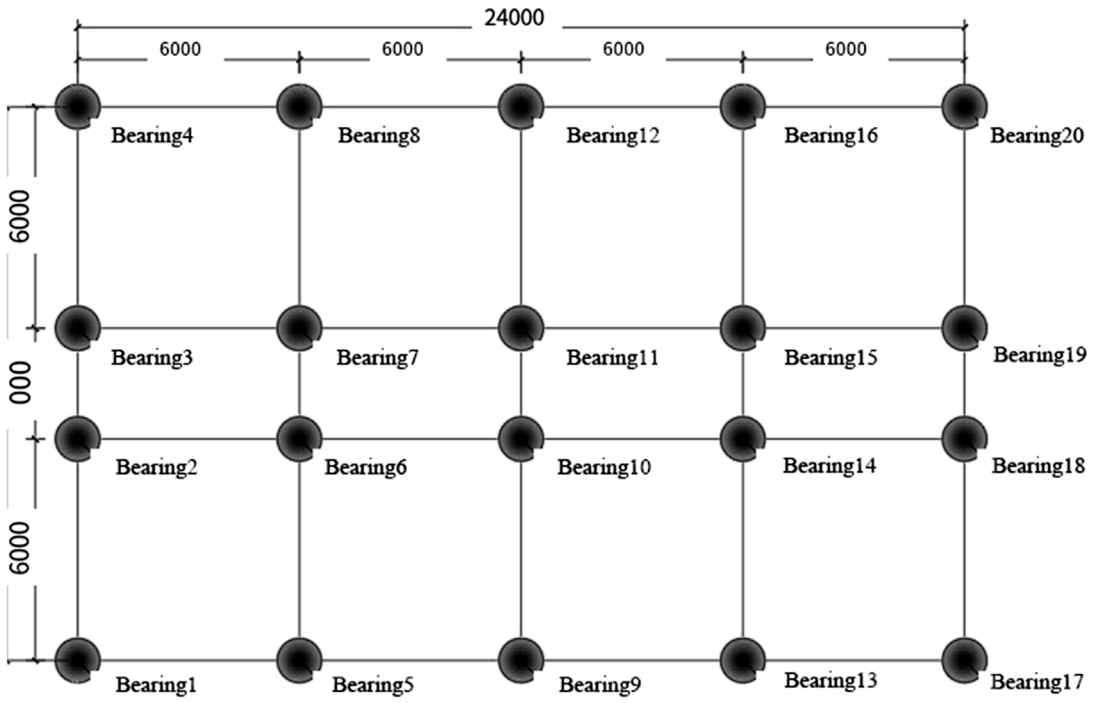

FIGURE 3
Number and layout of isolation bearing.

connections are labeled M3 plastic hinges. Table 1 provides detailed information on each story's section dimensions and reinforcement of the beams and columns.

2.3 Modeling

The finite element model of the inter-story isolation structure considering the SSI effect is established using SAP2000 software. Figure 2 illustrates the model, where the upper structure is simulated using frame elements, thick shell elements represent the raft foundation, and the foundation soil is modeled using solid elements. The foundation size is ten times the structure size, with a plane size of 240 m × 150 m. The upper structure's raft foundation is embedded in the soil layer, and a layered model with a thickness of 30 m is employed to capture the foundation soil's characteristics better. Table 2 presents the parameters of the foundation soil, and an artificial viscoelastic boundary is set around the foundation soil boundary.

The SAP2000 software extracts the column bottom reaction f under the standard gravity load to determine the number and type of isolation support. The total horizontal yield force is estimated as 2% of the column bottom reaction under the standard gravity load, which helps determine the required isolation supports. The inter-

TABLE 4 Base-isolation seismic information Table.

Seismic wave name	Earthquake name	Time	Location	Focal depth/km	Magnitude	PGA/cm·s^{-2}
Kobe	Port Island	1995-01-16	Japan	17.9	6.9	289.8
						347.9
						566.8
El centro	Imperial valley	1940-05-19	California	8.8	6.9	210.1
						341.7
						206.4
Hollister	Hollister city hall annex	1974-11-28	California	6.1	5.2	174.6
						361.9
						193.2

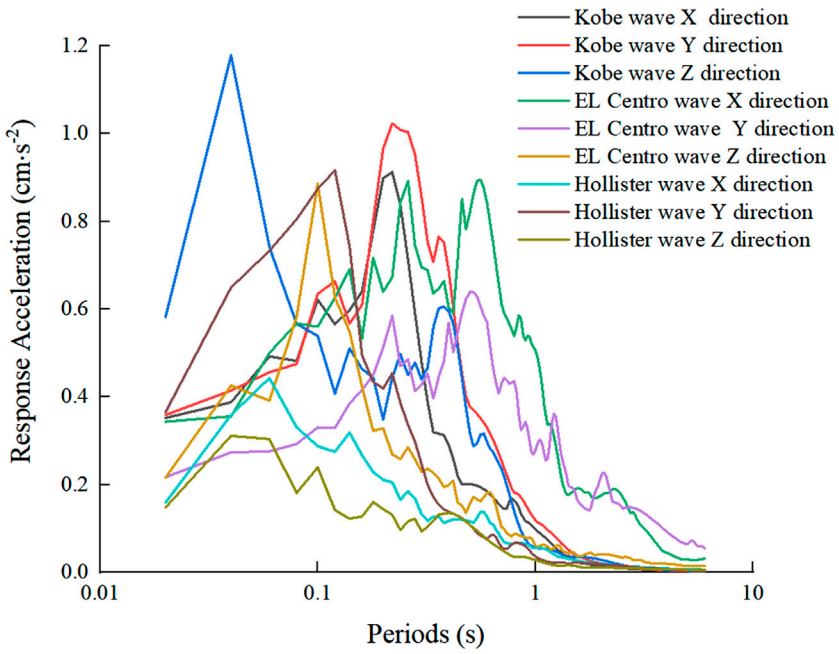

FIGURE 4
Seismic wave response spectrum.

story isolation structure employs LRB600 isolation bearings; their parameters are listed in Table 3. The arrangement of the isolation bearings can be seen in Figure 3. The rubber isolator and gap elements are used in the isolation bearings to capture the vertical tension and compression nonlinear stiffness. To accurately represent the restoring force characteristics of the isolation story in the subsequent time history analysis, the Bouc-Wen model is employed.

2.4 Selection of seismic waves

This paper investigates the response of the inter-story isolation structure to three selected seismic waves. Table 4 provides the ground motion information, while Figure 4 illustrates the acceleration response spectrum of these seismic waves. The maximum acceleration input of the three-dimensional seismic wave is adjusted based on the ratio of *X* direction, *Y* direction, and *Z* direction, set explicitly at 1:0.85:0.65. To align with the base-isolation seismic intensity of 8° during rare earthquakes, the peak acceleration of the seismic wave is adjusted to 400 cm/s^2.

The research on dynamic characteristics of isolated structures primarily focuses on inter-story displacement and inter-story shear. Assessing a building's seismic capability involves examining the shear force variation between floors, which accurately reflects the seismic performance of each floor in the seismic isolation structure. To analyze the effects of soil-structure interaction (SSI), elastic-plastic time-history analysis is conducted on both staggered

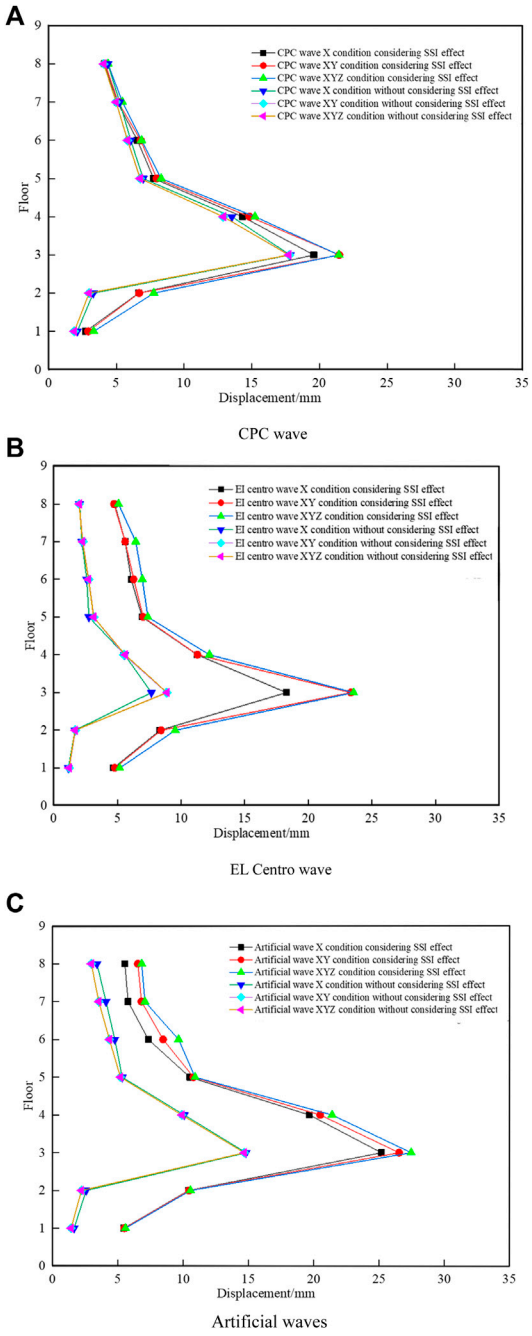

FIGURE 5
The mid-story displacement and mid-story shear forces of different seismic waves subjected to different input dimensional working conditions. **(A)** CPC wave. **(B)** EL Centro wave. **(C)** Artificial waves.

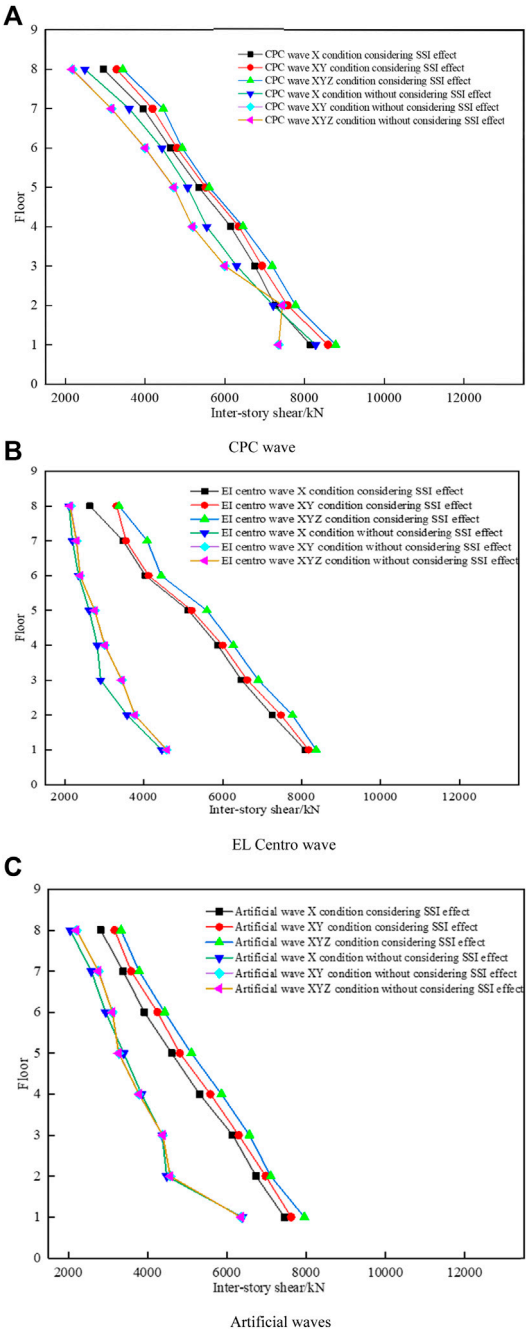

FIGURE 6
The mid-story shear forces of different seismic waves subjected to different input dimensional working conditions. **(A)** CPC wave. **(B)** EL Centro wave. **(C)** Artificial waves.

structures with and without SSI. Figure 6 compares inter-story displacement values between these two isolated structures.

Figure 5 reveals that the inter-story displacements of both types of inter-story isolated structures, subjected to three-dimensional seismic wave input, are greater than those under one-dimensional and two-dimensional seismic input. Additionally, considering the SSI effect, the inter-story seismic structure's inter-story displacement values show more significant variations across different seismic wave input dimensions compared to the results of the inter-story seismic structure without considering SSI.

Figure 6 compares inter-story shear values between the two isolated structures. It can be observed that the inter-story shear values of structures with varying story intervals under the influence of three-dimensional seismic wave input are consistently more extensive than those under one-dimensional and two-dimensional seismic inputs. Furthermore, the inter-

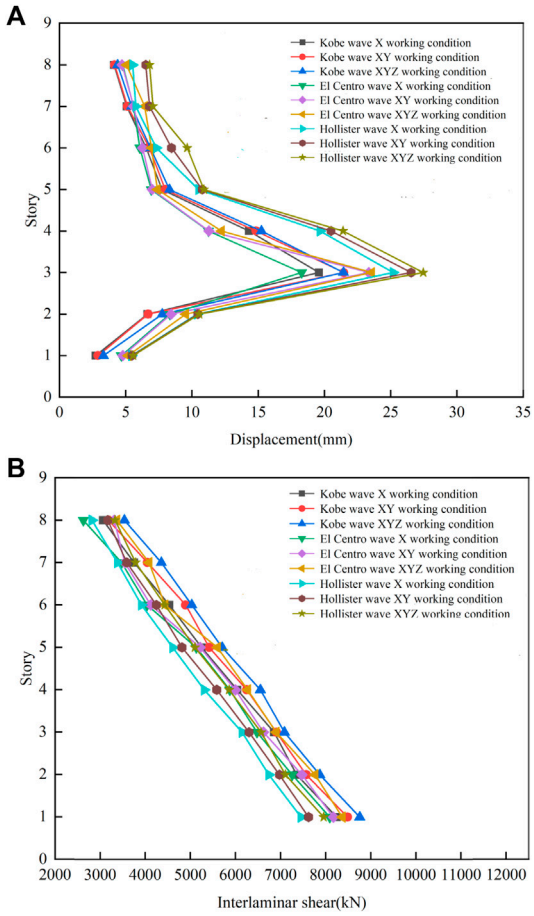

FIGURE 7
(A) Displacements between lower stories under different seismic wave input dimensions. **(B)** Inter-story shear forces under different seismic wave input dimensions.

story shear value of the inter-story seismic structure considering the SSI effect is greater than that of the inter-story seismic structure without considering SSI across different seismic wave input conditions. Please refer to Figure 7 for a visual representation.

3 Seismic response analysis of inter-story isolation structure

3.1 Structural response analysis

An elastic-plastic time history analysis is conducted on the inter-story isolation structure, considering the SSI effect. The outcomes of story displacement and story shear are illustrated in Figures 7A, B, respectively. It is evident from both figures that when considering the SSI effect, the seismic response of the lower isolation structure under three-dimensional ground motion exhibits greater significance compared to that under one-dimensional and two-dimensional seismic inputs.

3.2 Response of the isolated bearing

Figure 8A illustrates the hysteresis curve of the recovery force-displacement for the isolation bearing subjected to underground motion input. The figure demonstrates that the hysteresis curve exhibits chaotic behavior when subjected to ground motion input. Along with the distinct hysteretic characteristics, it also displays specific viscous properties, indicating a correlation between the anisotropic responses following ground motion input. Consequently, the hysteresis curve of the support assumes an irregular shape. The restoring force model employed for the isolation bearing is depicted as a bilinear relationship, as illustrated in Figure 8B.

3.3 Isolation bearing analysis

In accordance with the seismic design code for buildings (Code for Seismic Design of Buildings, 2010), the maximum horizontal displacement of isolation bearings during rare earthquakes should not exceed the smaller value between 0.55 times the bearing diameter and three times the total thickness of rubber layers. For this study, LRB600 bearings are utilized, resulting in a horizontal displacement limit of 330 mm (600 × 0.55). Based on the time history analysis results, the maximum horizontal displacement of the inter-story isolation structure bearing, considering the SSI effect under different input conditions, is measured at 249.98 mm, which falls within the prescribed limit.

To ensure the effective performance of the inter-story isolation structure's bearings under an 8-degree rare earthquake, it is essential to evaluate both the tensile and compressive stress experienced by the approaches. As per the specifications, the tensile stress of the isolation bearing should not exceed 1 MPa, while the compressive stress should not exceed 30 MPa.

Figure 9A illustrates the compressive stress curve of the inter-story isolation structure's bearings. It is evident from the figure that the compressive stress generated by the Kobe and Hollister waves remains below 30 MPa. However, some bearings experienced compressive stress exceeding 30 MPa during the El Centro wave earthquake, and notably, bearing 18 exhibited the highest compressive stress, measuring 39.7 MPa, surpassing the specified limit.

The tensile stress curve of the bearings in the story isolation structure is presented in Figure 9B. Analysis of Figure 9B reveals that several bearings surpass the standard limit for tensile stress under each seismic wave. Notably, bearing 18 experienced maximum tensile stress of 2.2 MPa during the Kobe wave earthquake, exceeding the standard limit by more than twice. Similarly, under the El Centro wave earthquake, bearing 15 reaches a maximum tensile stress of 1.4 MPa, while under the Hollister wave earthquake, support 15 exhibits an ultimate tensile stress of 1.5 MPa.

Based on the analysis of the bearing stress curve, it can be concluded that when considering the SSI effect under three-dimensional ground motion, the conventional horizontal isolation bearing used in the story isolation structure fails to isolate vertical ground motion effectively. Furthermore, specific bearings encounter issues of tensile and compressive stress exceeding the limits. To address this problem, the implementation of a vertical isolation device is proposed.

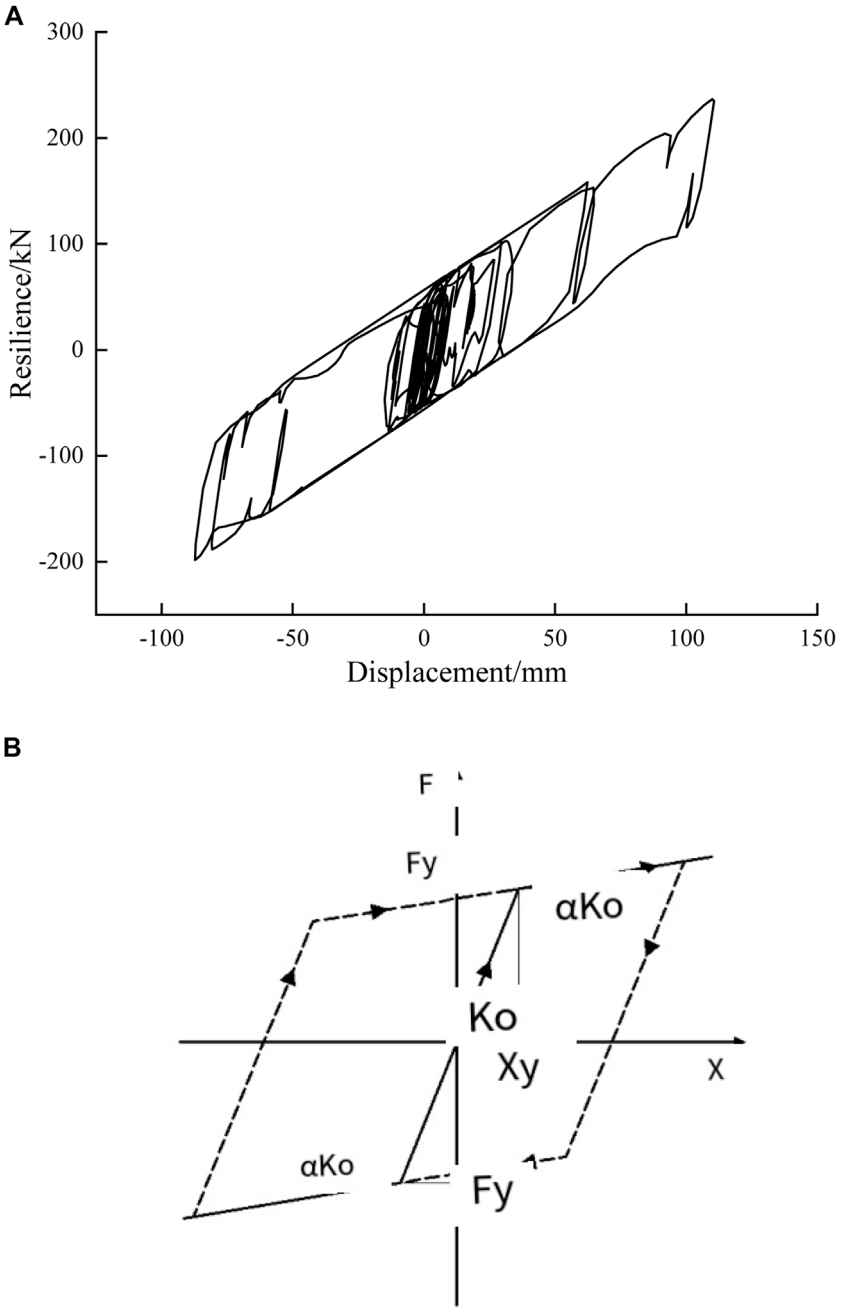

FIGURE 8
(A) Force-displacement hysteresis curve. **(B)** Recovery force model of isolation bearing.

4 Seismic response analysis of inter-story isolation structure with three-dimensional isolation bearing

4.1 Three-dimensional isolation bearing modeling

A three-dimensional isolation structure model incorporating a vertical isolation bearing is constructed in this study. For the vertical isolation story, a steel spring with a stiffness of 8×10^3 kN/m is chosen as the vertical isolation bearing. It is complemented by parallel viscous dampers, represented by the Damper element. The seismic response of traditional horizontal and three-dimensional isolation structures is compared and analyzed under three-dimensional ground motion excitations.

4.2 Modal analysis

Modal analysis is performed on both the three-dimensional and traditional horizontal isolation structures, and the results for the first six natural vibration periods are presented in Table 5. It is evident

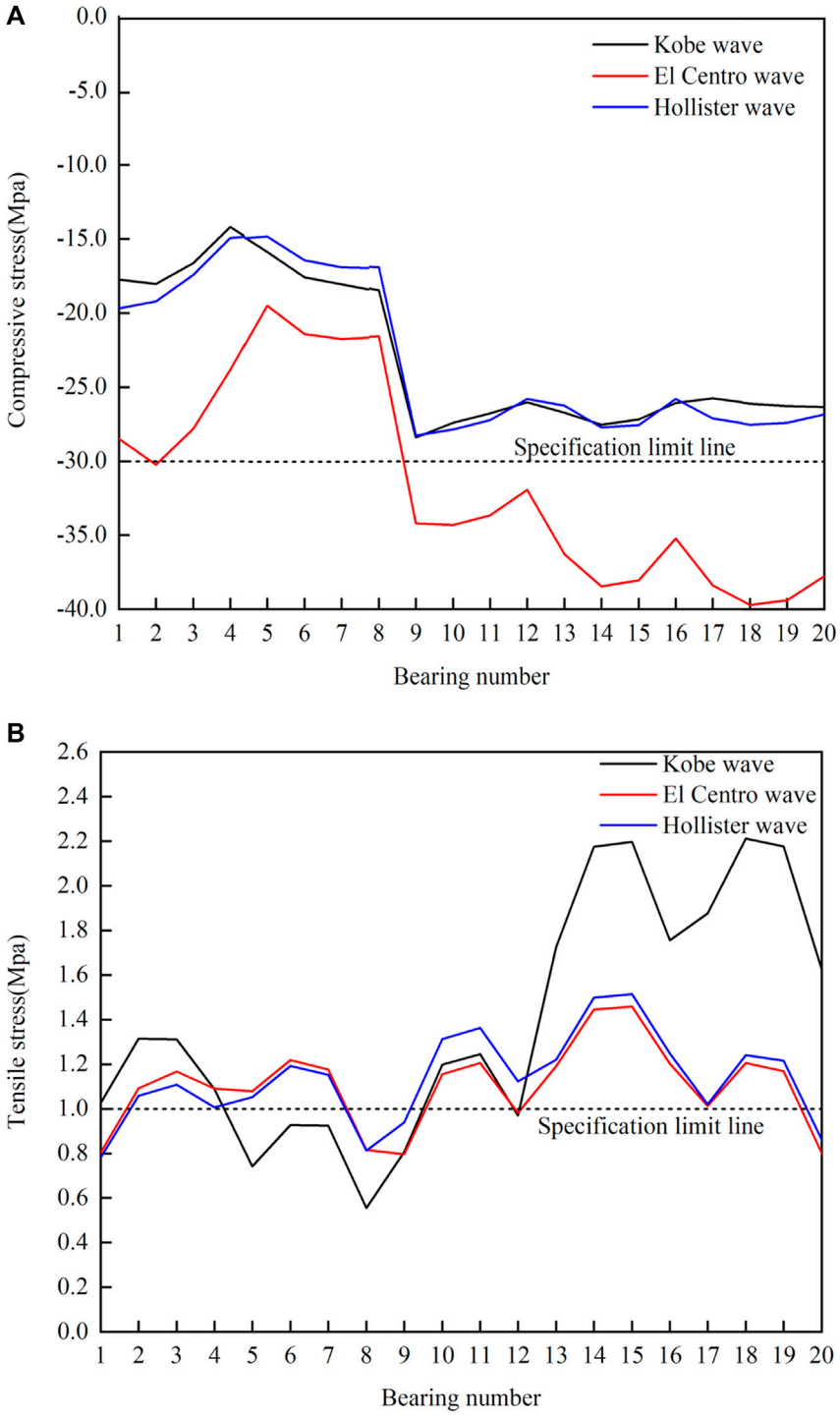

FIGURE 9
(A) Compression stress curve of isolation bearing. **(B)** Tensile stress curve of isolation bearing.

from Table 5 that the three-dimensional isolation structure exhibits longer natural vibration periods compared to the traditional horizontal isolation structure. This can be attributed to the presence of an additional vertical isolation device in the three-dimensional structure, which enhances the system's flexibility and further extends the natural vibration period of the structure.

Moreover, the three-dimensional isolation structure's fourth, fifth, and sixth modes experience a more pronounced increase in their natural vibration periods when compared to the traditional horizontal isolation structure. This significant extension of the natural vibration periods for these modes contributes to an enhanced damping effect within the isolation structure, particularly for the respective methods mentioned.

TABLE 5 Natural vibration periods of different isolated structures (s).

Mode order	Traditional horizontal isolation structure	Three-dimensional seismic isolation structure
1	3.064	3.161
2	3.025	3.143
3	2.878	2.898
4	0.475	0.685
5	0.425	0.651
6	0.421	0.634

TABLE 6 Comparison of maximum displacement between different isolation structures under different seismic input conditions (mm).

Seismic wave	Input direction	Traditional horizontal isolation structure	Three-dimensional seismic isolation structure
Kobe wave	X	19.59	21.45
	XY	21.47	22.28
	XYZ	21.44	23.35
El centro wave	X	18.28	19.29
	XY	23.35	25.16
	XYZ	23.57	25.40
Hollister wave	X	25.20	26.02
	XY	26.54	26.41
	XYZ	27.46	28.58

4.3 Isolation effect analysis

4.3.1 Displacement comparison

The maximum inter-story displacement of the three-dimensional isolation structure is compared to that of the traditional horizontal isolation structure, and the results are presented in Table 6. The findings in Table 6 reveal that the additional three-dimensional isolation bearing leads to a more significant displacement in the isolation story, particularly noticeable when subjected to three-dimensional ground motion.

The maximum horizontal displacement of the three-dimensional seismic isolation structure under various input conditions is measured at 306.49 mm. While this value exceeds the displacement observed in the traditional horizontal isolation structure, it remains within the acceptable limit specified by the regulations.

4.3.2 Base shear comparison

The comparison of base shear between the three-dimensional isolation structure and the traditional horizontal isolation structure under three-dimensional seismic input is depicted in Figure 10A. As observed in Figure 10A, the base shear force of the three-dimensional isolation structure is smaller than that of the traditional horizontal isolation structure when subjected to seismic waves. This observation indicates that the presence of the vertical isolation device helps further attenuate the energy transmitted to the superstructure.

4.3.3 Vertex vertical acceleration comparison

The comparison of vertical acceleration between the three-dimensional seismic isolation structure and the traditional horizontal seismic isolation structure under three-dimensional seismic input is presented in Figure 10B. Figure 10B shows that the three-dimensional seismic isolation structure exhibits superior control over the vertical acceleration of the vertex compared to the traditional horizontal seismic isolation structure. The three-dimensional seismic isolation approach effectively mitigates the vertical acceleration at the top of the structure, thereby minimizing the transmission of vertical seismic forces to the upper structure and demonstrating an excellent vertical isolation effect.

4.4 Stress comparison of isolation bearing

The bearing pressure stress curve of the three-dimensional isolation structure is illustrated in Figure 11A. It is evident from Figure 11A that the maximum compressive stress experienced by the three-dimensional isolated structure under different seismic waves is 28.9 MPa, which is below the allowable limit specified in the code.

Figure 11B depicts the tensile stress of the isolation bearing. Figure 11B shows that the maximum tensile stress of the

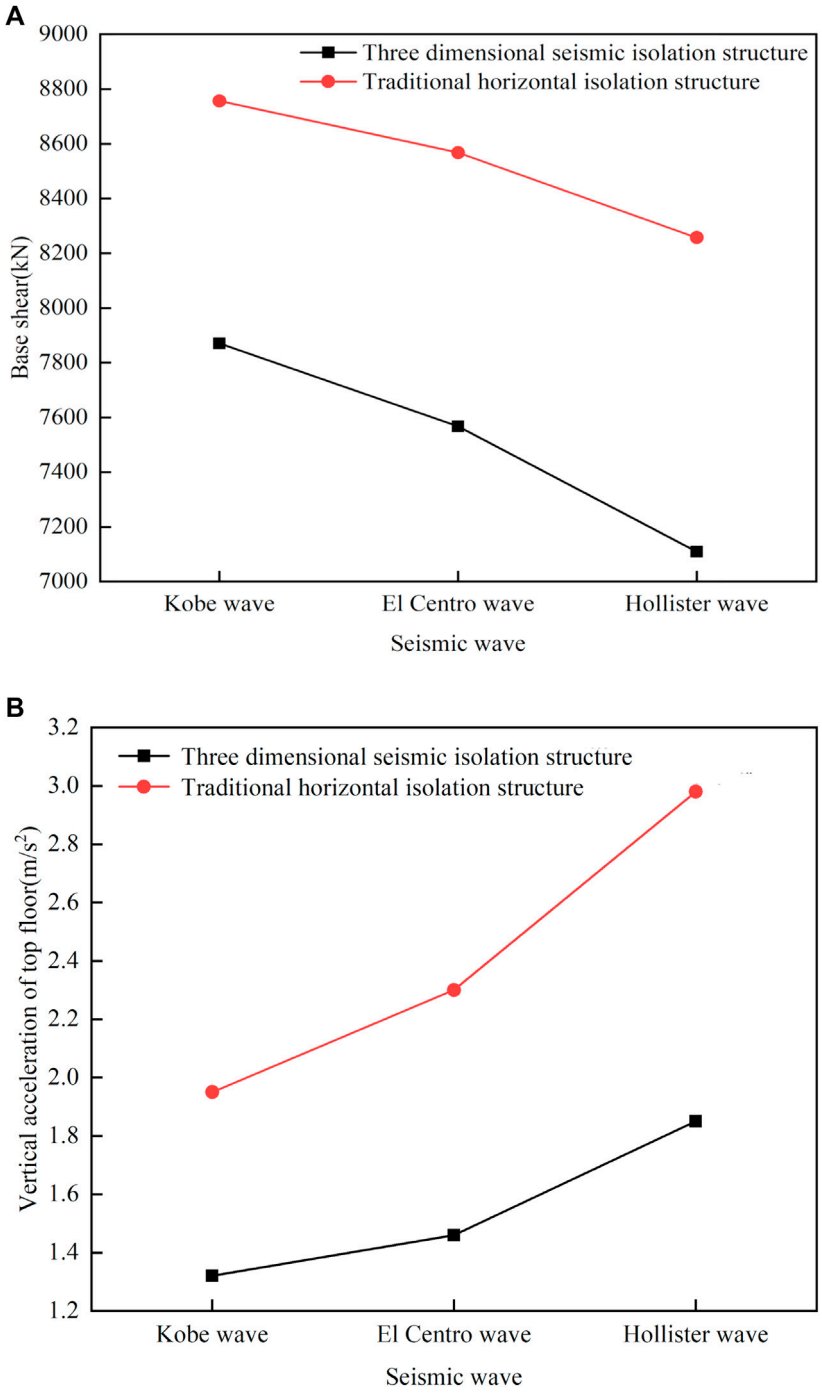

FIGURE 10
(A) Base shear force under XYZ seismic waves. **(B)** Vertical acceleration of top floor under XYZ seismic waves.

three-dimensional isolation structure under various seismic waves is 0.9 MPa, lower than the ultimate tensile stress the specifications allow. Furthermore, the maximum tensile stress of the bearing after incorporating the vertical isolation device is reduced by 59% compared to the maximum tensile stress of the isolation bearing in the traditional horizontal isolation structure. This optimization of stress in isolation bearing effectively addresses the issue of tensile stress exceeding limits in the conventional horizontal isolation structure under three-dimensional ground motion, thereby achieving the desired damping effect.

4.5 Stress comparison of foundation soil

A three-dimensional isolation structure's effectiveness lies in its superior damping effect and in considering the stress imposed

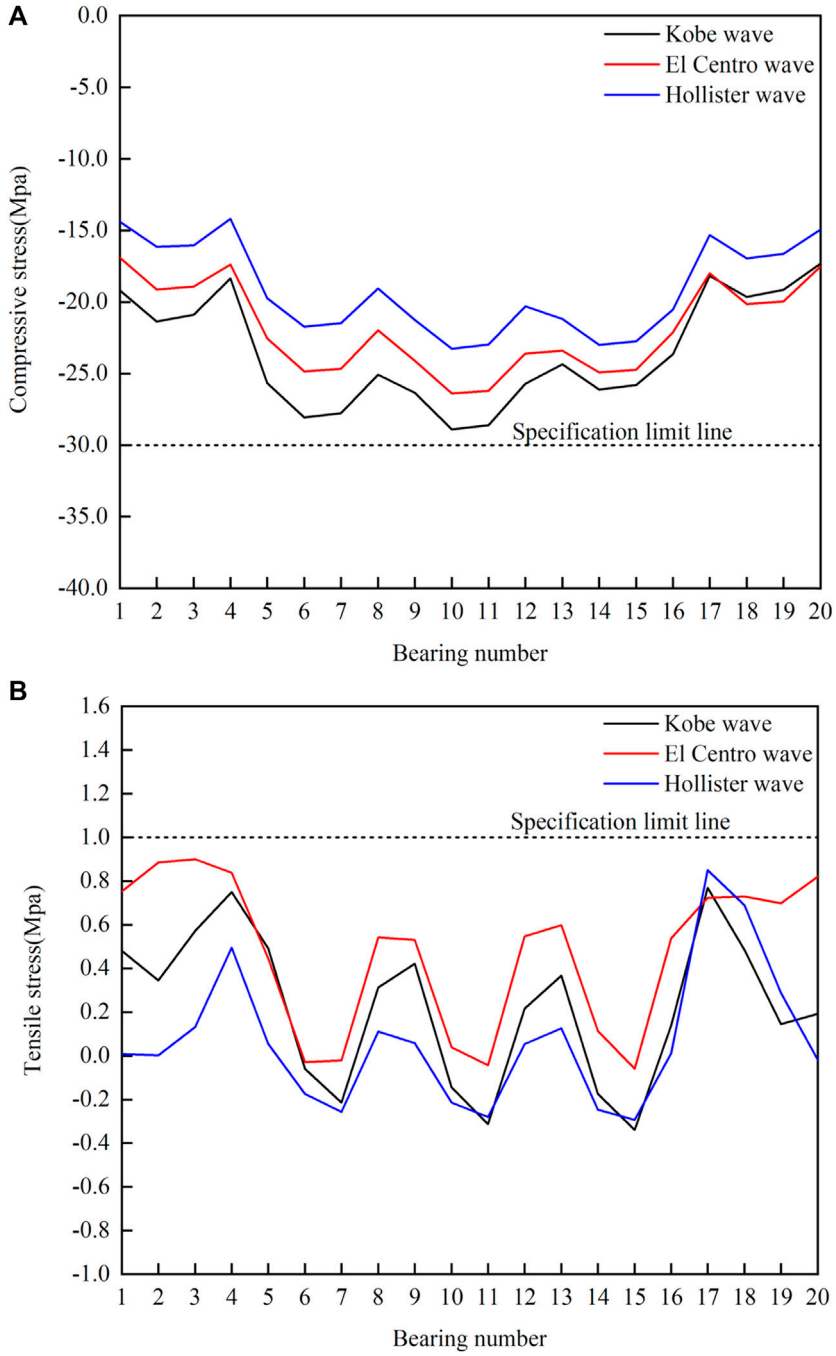

FIGURE 11
(A) Compression stress curve of isolation bearing for three-dimensional isolated structure. **(B)** Tensile stress curve of three-dimensional isolation structure isolation bearing.

on the foundation soil as a crucial criterion for evaluating its overall isolation performance. Figure 12 illustrates the comparison of the maximum soil stress between the two isolation structures under three-dimensional ground motion input. As depicted in Figure 12, incorporating the three-dimensional isolation bearing results in lower soil stress on the foundation than the traditional horizontal isolation bearing. Reducing soil stress is advantageous for the foundation and facilitates better design.

5 Analysis and comparison of the response of inter-story seismic structures considering SSI effect in different soil stories to 3D earthquakes

5.1 Setting of different soil stories

Based on the soil characteristics of the stories, two distinct sites are established in the inter-story seismic model that

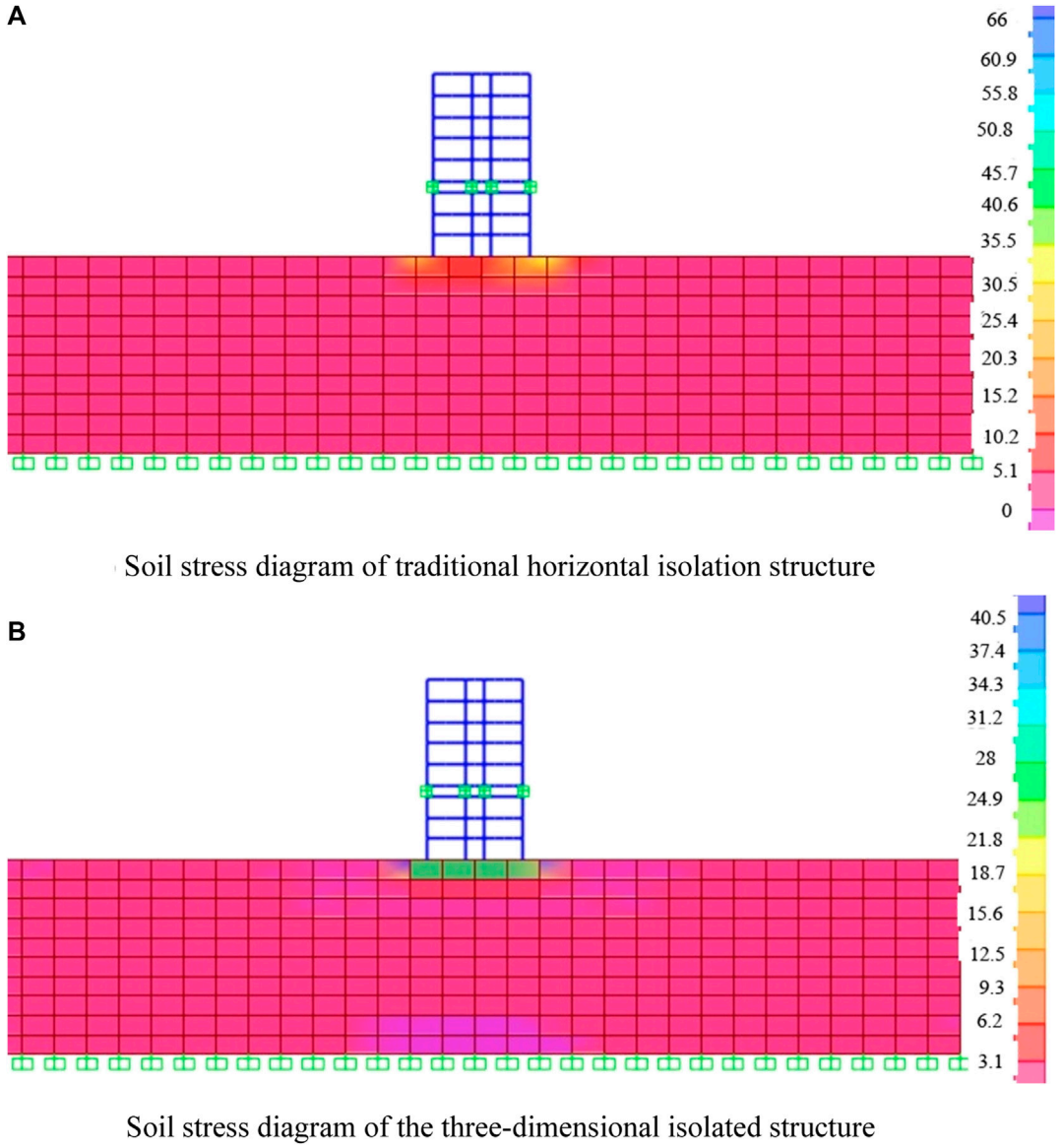

FIGURE 12
Comparison of soil stress of two isolation structures. **(A)** Soil stress diagram of traditional horizontal isolation structure. **(B)** Soil stress diagram of the three-dimensional isolated structure.

TABLE 7 Different soil parameters.

Site number	Soil story properties	Soil story number	Soil story thickness (m)	Shear modulus (Mpa)	Modulus of elasticity (Mpa)	Poisson's ratio	Shear wave velocity (m/s)
Site 1	Hard soil	1	3	125	325	0.3	250
		2	3	259.2	622.1	0.2	360
		3	24	445.5	1,069.2	0.2	450
Site 2	Soft soil	1	3	14.6	40.8	0.4	90
		2	3	58.3	151.6	0.3	180
		3	24	352.8	846.7	0.2	420

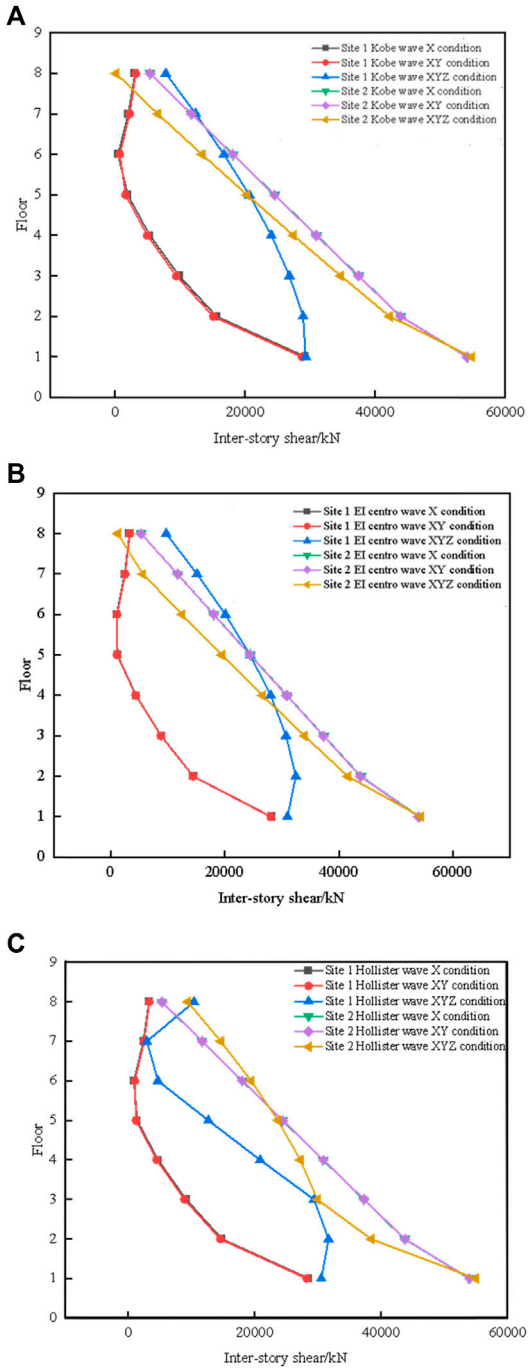

FIGURE 13
Interlaminar shear value of traditional horizontal isolation structure subjected to different seismic waves in two soil stories. **(A)** Traditional horizontal isolation structure under Kobe wave. **(B)** Horizontal isolation structure under EL Centro wave. **(C)** Horizontal isolation structure under the Hollister wave.

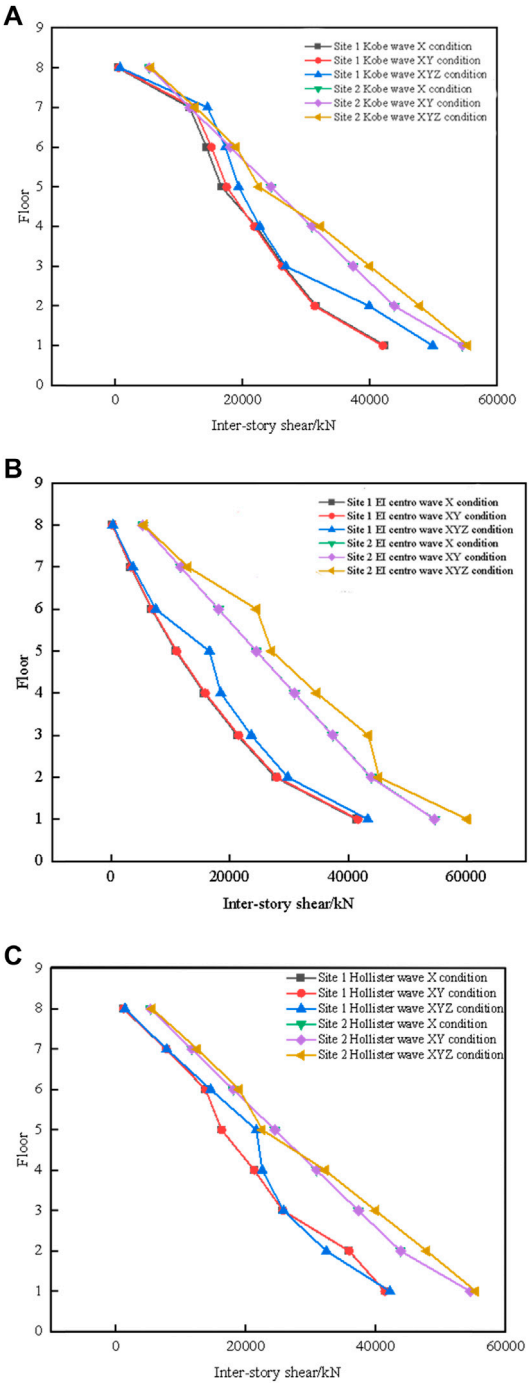

FIGURE 14
Inter-story shear force values of horizontal isolated structures in two soil stories subjected to different seismic waves. **(A)** Three-dimensional seismic isolation structure under Kobe waves. **(B)** three-dimensional isolation structure under EL Centro wave. **(C)** Three-dimensional isolation structure under the Hollister wave.

accounts for the soil-structure interaction (SSI) effect. Site 1 represents hard soil, while Site 2 represents soft soil. The selected parameters for the soils at these two sites are presented in Table 7. The subsequent analysis focuses on examining the disparity in response and isolation effectiveness between traditional horizontal isolation structures and three-dimensional isolation structures when considering the SSI effect at each site.

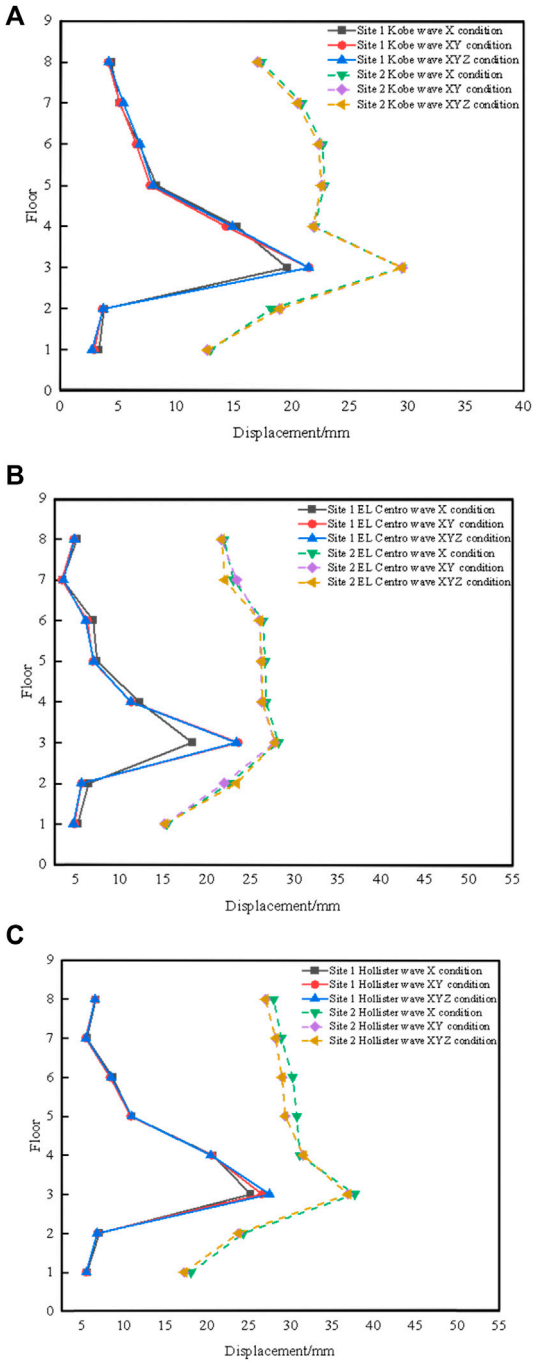

FIGURE 15
Inter-story displacement of horizontal isolation structure subjected to different seismic waves. **(A)** Traditional horizontal isolation structure under Kobe wave. **(B)** Traditional horizontal isolation structure under EL Centro wave. **(C)** Traditional horizontal isolation structure under the Hollister wave.

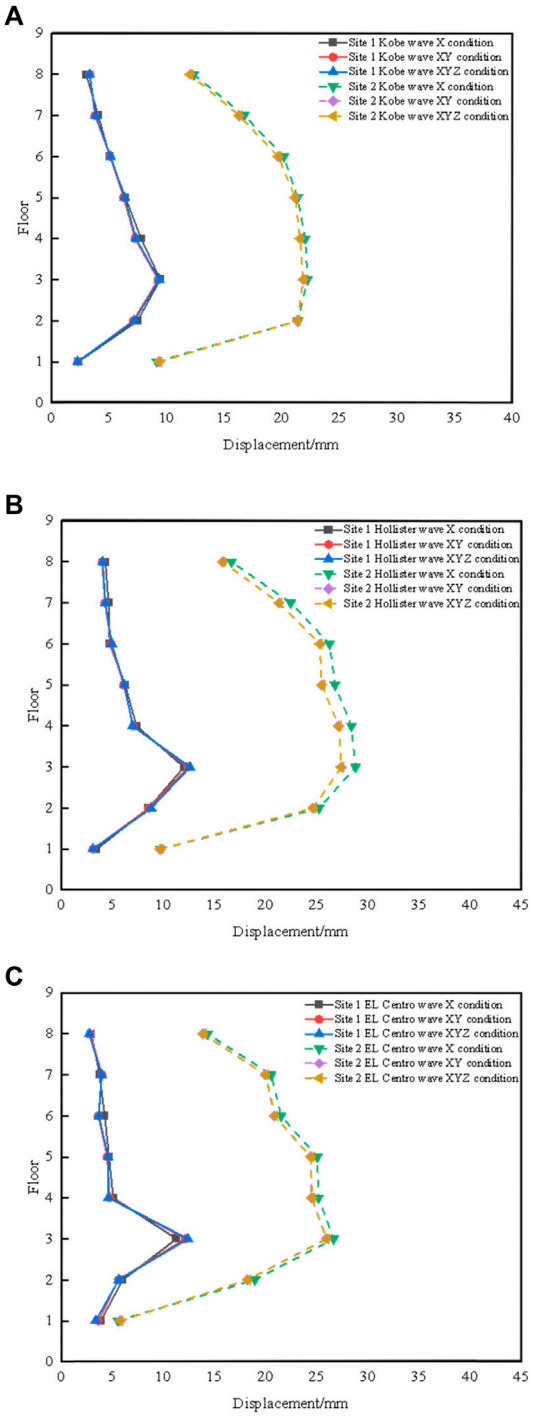

FIGURE 16
The inter-story displacement values of three-dimensional isolated structures subjected to different seismic waves in two soil stories. **(A)** Three-dimensional seismic isolation structure under Kobe waves. **(B)** three-dimensional isolation structure under EL Centro wave. **(C)** Horizontal isolation structure under the Hollister wave.

5.2 Comparative analysis of the structural response

5.2.1 Comparative analysis of shear forces between stories

Based on the results obtained from the time history analysis, the inter-story shear forces of both traditional horizontal isolation structures and three-dimensional isolation structures were investigated under different soil stories. The inter-story shear forces of the horizontal isolation structures, accounting for the soil-structure interaction (SSI) effect, are depicted in Figure 13. As observed in Figure 13, the inter-story shear

TABLE 8 Maximum vertex acceleration of traditional horizontal isolation structure subjected to different seismic wave inputs in different soil stories ($m \cdot s^{-2}$).

Seismic wave input condition	Site 1	Field 2	Field 2/Field 1
Kobe wave X condition	4.06	7.17	1.77
Kobe wave XY condition	3.71	6.96	1.88
Kobe waves XYZ condition	3.34	6.94	2.08
Hollister wave X condition	7.46	10.33	1.38
Hollister wave XY condition	6.99	10.10	1.44
Hollister wave XYZ condition	6.83	10.02	1.47
EL centro wave X condition	6.27	9.54	1.52
EL centro wave XY condition	5.72	9.38	1.64
EL centro wave XYZ condition	5.66	9.39	1.66

value of the traditional horizontal isolation structure, considering the SSI effect at site 2, surpasses that at site 1 under the same multi-dimensional seismic input conditions. Similarly, Figure 14 illustrates the inter-story shear of the three-dimensional seismic isolation structure, incorporating the SSI effect, for different soil stories. It is evident from Figure 14 that, like the traditional horizontal isolation structure, the inter-story shear value of the three-dimensional isolation structure, considering the SSI effect at site 2, exceeds that at site 1 under the same multi-dimensional seismic input conditions. The findings from Figures 13, 14 demonstrate that both the horizontal isolation structure and three-dimensional isolation structure, considering the SSI effect, result in larger shear forces in the soft soil story compared to the hard soil story.

5.2.2 Comparative analysis of inter-story displacement

Based on the results obtained from the time history analysis, the inter-story displacements of two types of isolation structures were extracted under different soil stories. Figure 15 illustrates a comparison of the inter-story displacements of traditional horizontal isolation structures under different soil stories, considering the soil-structure interaction (SSI) effect. As depicted in Figure 15, the horizontal isolation structure at site 2, regarding the SSI effect, exhibits significantly larger inter-story displacement values than at site 1 under the same multi-dimensional seismic input conditions. Similarly, Figure 16 displays the inter-story displacements of three-dimensional seismic isolation structures considering the SSI effect for different soil stories. It can be observed from Figure 16 that, akin to the horizontal isolation structure, the three-dimensional isolation structure considering the SSI effect at site 2, still demonstrates greater inter-story displacement than at site 1 under the same multi-dimensional seismic input conditions. Combining the findings from Figures 15, 16, it becomes evident that both the horizontal isolation structure and three-dimensional isolation structure, considering the SSI effect, generate larger inter-story displacements in soft soil compared to hard soil. Furthermore, when considering different isolation structures with the SSI effect, it is noted that the softer the soil story, the greater the structural displacement response.

5.3 Comparative analysis of isolation effect

5.3.1 Comparative analysis of vertex acceleration

Table 8 present the vertex acceleration values for the traditional horizontal and three-dimensional isolation structures. The data indicate that both structures exhibit significantly higher vertex accelerations on the soft soil story at site 2 compared to the isolation structure on the complex soil story. Notably, the three-dimensional isolation structure shows a greater increase in vertex acceleration on the soft soil story than the horizontal isolation structure. These findings suggest that the isolation effect of the three-dimensional structure is less pronounced on the soft soil story in comparison to the hard soil story.

5.3.2 Comparative analysis of support stress

The bearing stress envelope values of three seismic wave time histories were analyzed to investigate the influence of soil story properties on the isolation effect of both the traditional horizontal isolation structure and the three-dimensional isolation structure. These structures' tensile and compressive stress values were compared and examined on different soil stories. The results of the tensile stress comparison are presented in Figure 17A, while Figure 17B illustrates the compressive stress comparison. As depicted in Figure 17A, the tensile stress experienced by the supports of the same isolation structure on the soft soil story at site 2 is significantly higher than that at site 1. The traditional horizontal isolation structure exhibits tensile stress exceeding the limit on both soil stories at site 1 and site 2. Meanwhile, the three-dimensional isolation structure shows no tensile stress exceeding the limit at site 1 but does encounter this issue on the soft soil story. Turning to Figure 17B, it is evident that the compressive stress experienced by both the traditional horizontal isolation structure and the three-dimensional isolation structure is greater on the soft soil story at site 2 compared to site 1. However, the compressive stress values for both structures remain within acceptable limits.

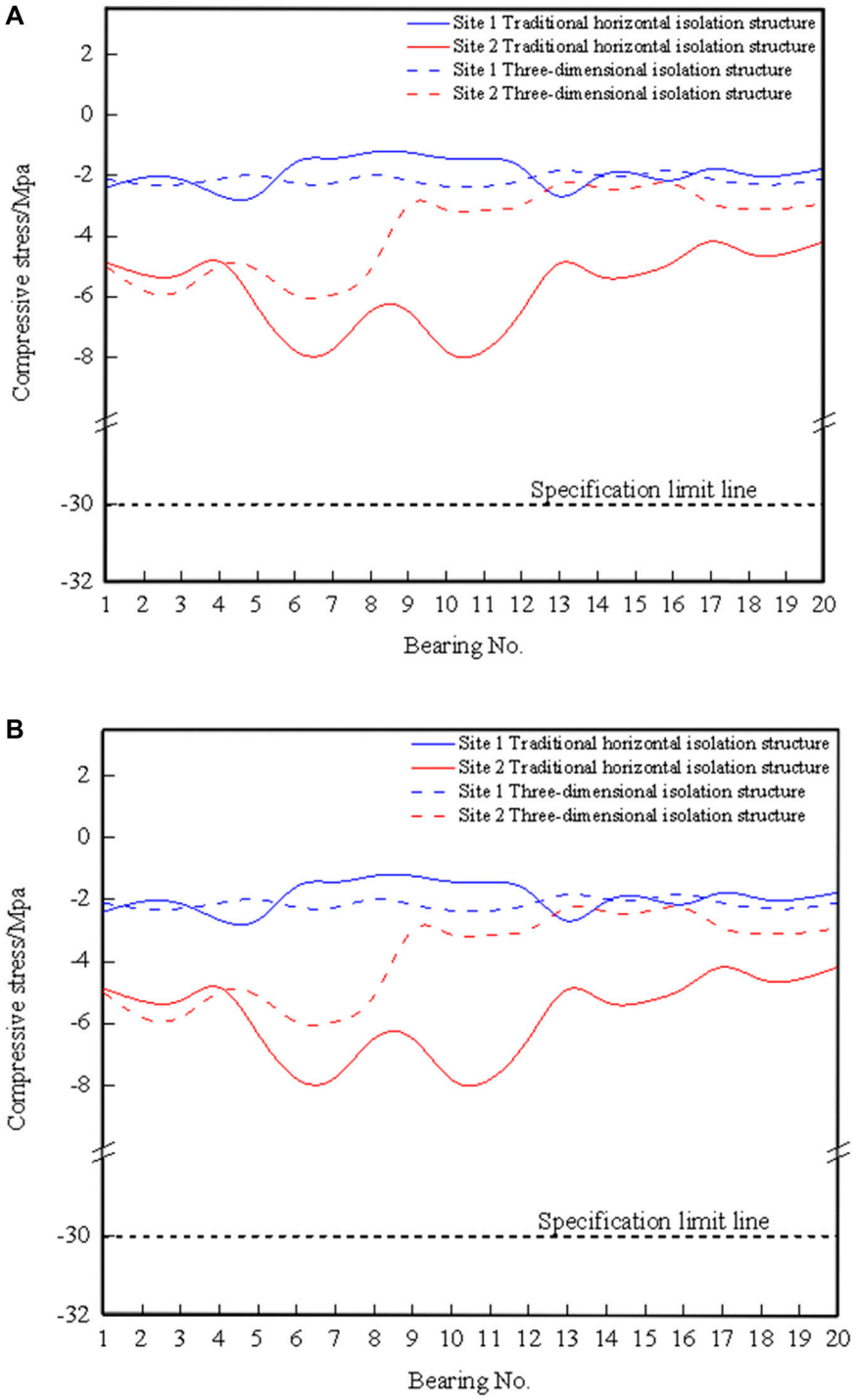

FIGURE 17
(A) Tensile stress of isolation structure bearing in different soil stories. **(B)** Bearing Pressure Stress of Isolated Structures in Different Soil Stories.

6 Conclusion and discussion

6.1 Conclusion

This paper establishes an inter-story isolation structure model considering the soil-structure interaction (SSI) effect. Various ground motion scenarios, including one-dimensional, two-dimensional, and three-dimensional inputs, are applied to compare the seismic responses of inter-story isolation structures. A three-dimensional isolation device is introduced to address the issue of tensile and compressive stress exceeding the limits in isolation bearings under three-dimensional seismic input. The

seismic response results of traditional horizontal isolation structures are analyzed and compared. The following conclusions are drawn from the study.

(1) considering the SSI effect, the inter-story isolation structure exhibits larger inter-story displacement and inter-story shear values than the two-dimensional and one-dimensional seismic inputs under three-dimensional seismic conditions.
(2) The inclusion of three-dimensional isolation bearings in the three-dimensional isolation structure effectively reduces the transmission of vertical seismic waves to the upper structure, thereby achieving excellent vertical isolation.
(3) The use of three-dimensional isolation significantly mitigates the tension and compression stress in the isolation structure bearings, effectively addressing the issue of excessive stress observed in traditional horizontal isolation structures under three-dimensional seismic actions. This optimization of bearing forces results in the expected damping effect.
(4) The introduction of three-dimensional isolation bearings leads to lower soil stress in the foundation compared to the traditional horizontal isolation bearings, which has positive implications for foundation design considerations.

6.2 Discussion

Inter-story isolation, as an emerging seismic isolation technology, has been implemented in numerous inter-story isolation engineering examples both domestically and internationally. However, the theoretical framework for this system is still not sufficiently developed, and the relevant literature is relatively scarce. Furthermore, there has been no research on inter-story isolation considering the Soil-Structure Interaction (SSI) effects under three-dimensional seismic conditions. This paper focuses on the response of inter-story isolated structures considering SSI effects during three-dimensional seismic events. Numerical simulation analysis is conducted to investigate the seismic response under four influencing factors: SSI effects, the dimension of seismic input, the type of seismic input, and the type of isolation bearings. Modal analysis and time-history analysis are employed for seismic response comparison. The impact of both stiff and soft soil layers on the response of inter-story isolated structures considering SSI effects under three-dimensional seismic input conditions is explored, offering valuable insights for further in-depth research on inter-story isolation structures.

In comparison to base isolation, inter-story isolation may lead to severe consequences and significant losses if the isolation layers are damaged, potentially resulting in the overall collapse of the superstructure. Thus, further exploration and protection measures regarding the performance requirements of isolation layers are necessary. The scope of this study is limited to the response of regular framed inter-story isolation structures considering SSI effects. If the structural configuration is altered, the response of irregular structures with inter-story isolation under three-dimensional seismic conditions and their effectiveness in reducing seismic effects warrant further investigation. Additionally, the seismic input for inter-story isolation structures consists of two horizontal components and one vertical component. However, real seismic effects also include torsional components, and it remains a subject of further research to examine the changes in response patterns when considering torsional effects in inter-story isolated structures.

Data availability statement

The original contributions presented in the study are included in the article/supplementary material, further inquiries can be directed to the corresponding authors.

Author contributions

JX: Data curation, Software, Writing–original draft. HG: Writing–review and editing. ZiG: Data curation, Writing–review and editing. JZ: Software, Writing–original draft. ZY: Data curation, Writing–review and editing. GZ: Writing–review and editing. ZhG: Methodology, Writing–review and editing. DL: Methodology, Writing–review and editing. WS: Writing–review and editing.

Conflict of interest

The authors declare that the research was conducted in the absence of any commercial or financial relationships that could be construed as a potential conflict of interest.

Publisher's note

References

Basili, M., and Angelis, M. D. (2022). Experimental dynamic response of a multi-story frame structure equipped with non-conventional TMD implemented via inter-story isolation. *Appl. Sci.* 12 (18), 9153. doi:10.3390/app12189153

Bernardi, E., Donà, M., and Tan, P. (2023). Multi-objective optimization of the inter-story isolation system used as a structural TMD. *Bull. Earthq. Eng.* 21 (5), 3041–3065. doi:10.1007/s10518-022-01592-9

Bolvardi, V., Pei, S., van de Lindt, J. W., and Dolan, J. D. (2018). Direct displacement design of tall cross-laminated timber platform buildings with inter-story isolation. *Eng. Struct.* 167, 740–749. doi:10.1016/j.engstruct.2017.09.054

Davide, F., and Kalfas Konstantinos, N. (2023). Inter-story seismic isolation for Figure-rise buildings. *Eng. Struct.* doi:10.1016/J.ENGSTRUCT.2022.115175

Ehsan, G., and Toopchi-Nezhad, H. (2023). Annular fiber-reinforced elastomeric bearings for seismic isolation of lightweight structures. *Soil Dyn. Earthq. Eng.* 166, 107764. doi:10.1016/J.SOILDYN.2023.107764

Faiella, D., Calderoni, B., and Mele, E. (2022). Seismic retrofit of existing masonry buildings through inter-story isolation system: a case study and general design criteria. *J. Earthq. Eng.* 26 (4), 2051–2087. doi:10.1080/13632469.2020.1752854

Fan, Y., Liu, D., Lei, M., Zheng, Y., Zhao, T., and Gao, L. (2023). Seismic fragility analysis of the inter-story isolated structure for the influence of main-aftershock sequences. *Adv. Mech. Eng.* 1, 168781322211457. doi:10.1177/16878132221145791

Gao, Y., Yu, Z., Chen, W., Yin, Q., Wu, J., and Wang, W. (2023). Recognition of rock materials after high-temperature deterioration based on SEM images via deep learning. *J. Mater. Res. Technol.* 25, 273–284. doi:10.1016/j.jmrt.2023.05.271

Huang, F., Cao, Z., Guo, J., Jiang, S. H., Li, S., and Guo, Z. (2020a). Comparisons of heuristic, general statistical, and machine learning models for landslide susceptibility prediction and mapping. *Catena* 191, 104580. doi:10.1016/j.catena.2020.104580

Huang, F., Cao, Z., Jiang, S. H., Zhou, C., Huang, J., and Guo, Z. (2020b). Landslide susceptibility prediction based on a semi-supervised multiple-layer perceptron model. *Landslides* 17, 2919–2930. doi:10.1007/s10346-020-01473-9

Huang, F., Chen, J., Liu, W., Huang, J., Hong, H., and Chen, W. (2022). Regional rainfall-induced landslide hazard warning based on landslide susceptibility mapping and a critical rainfall threshold. *Geomorphology* 408, 108236. doi:10.1016/j.geomorph.2022.108236

Hur, M. W., and Park, T. W. (2022). Seismic performance of story-added type buildings remodeled with story seismic isolation systems. *Buildings* 3, 270. doi:10.3390/BUILDINGS12030270

Jin, J. M., Tan, P., Zhou, F. L., Ma, Y. H., and Shen, C. Y. (2012). Shaking table test study on mid-story isolation structures. *Adv. Mater. Res.* 446, 378–381. Trans Tech Publications Ltd. doi:10.4028/scientific5/amr.446-449.378

Li, W. F., Wang, S. G., and Miao, Q. S. (2014). Nonlinear simulation of reinforced masonry structure and adding-story isolation model. *China Civ. Eng. J.* 47 (S2), 35–40.

Li, X., Zhang, X., Shen, W., Zeng, Q., Chen, P., Qin, Q., et al. (2023). Research on the mechanism and control technology of coal wall sloughing in the ultra-large mining height working face. *Int. J. Environ. Res. Public Health* 20 (1), 868. doi:10.3390/ijerph20010868

Li, Z., Huang, G., Chen, X., and Zhou, X. (2022). Seismic response and parametric analysis of inter-story isolated tall buildings based on enhanced simplified dynamic model. *Int. J. Struct. Stab. Dyn.* 22, 03n04. doi:10.1142/S0219455422400089

Li, Z., Huang, G., Chen, X., and Zhou, X. (2022). Seismic response and parametric analysis of inter-story isolated tall buildings based on the enhanced simplified dynamic model. *Int. J. Struct. Stab. Dyn.* 22 (03n04), 2240008. doi:10.1142/S0219455422400089

Liang, Q., Jinyuan, W., and Li, L. (2023). Seismic control of story isolation system using tuned mass damper inerter. *J. Eng. Mech.* 149 (3). doi:10.1061/JENMDT.EMENG-6850

Liao, W. I., Loh, C. H., and Wan, S. (2001). Earthquake responses of RC moment frames subjected to near-fault ground motions. *Struct. Des. Tall Build.* 10 (3), 219–229. doi:10.1002/tal.178

Liu, D., Li, L., Zhang, Y., Chen, L., Wan, F., and Yang, F. (2022). Study on seismic response of a new staggered story isolated structure considering SSI effect. *J. Civ. Eng. Manag.* 28 (5), 397–407. doi:10.3846/jcem.2022.16825

Liu, S., and Li, X. (2023). Experimental study on the effect of cold soaking with liquid nitrogen on the coal chemical and microstructural characteristics. *Environ. Sci. Pollut. Res.* 30 (13), 36080–36097. doi:10.1007/s11356-022-24821-9

Liu, S., Sun, H., Zhang, D., Yang, K., Li, X., Wang, D., et al. (2023a). Experimental study of effect of liquid nitrogen cold soaking on coal pore structure and fractal characteristics. *Energy* 275, 127470. doi:10.1016/j.energy.2023.127470

Liu, S., Sun, H., Zhang, D., Yang, K., Wang, D., Li, X., et al. (2023b). Nuclear magnetic resonance study on the influence of liquid nitrogen cold soaking on the pore structure of different coals. *Phys. Fluids* 35 (1), 012009. doi:10.1063/5.0135290

Peng, T., and Dong, Y. (2023). Seismic responses of aqueducts using a new type of self-centering seismic isolation bearing. *Sustainability* 3, 2402. doi:10.3390/SU15032402

Ryan, K. L., and Earl, C. L. (2010). Analysis and design of inter-story isolation systems with nonlinear devices. *J. Earthq. Eng.* 14 (7), 1044–1062. doi:10.1080/13632461003668020

Song, L. U. O., Gong, F. Q., Li, L. L., and Peng, K. (2023). Linear energy storage and dissipation laws and damage evolution characteristics of rock under triaxial cyclic compression with different confining pressures. *Transactions of Nonferrous Metals Society of China* 33 (7), 2168–2182

Toshiyuki, S., Shingo, T., and Yasuhiro, T. (2008). Response control design of Tokyo Shiodome Sumitomo mansion with seismic isolation interface at mid building. *Prog. Build. steel Struct.* (03), 36–41.

Tasaka, M., Mori, N., Yamamoto, H., Murakami, K., and Sueoka, T. (2008). "Applying seismic isolation to buildings in Japan—Retrofitting and middle-story isolation". In Structures Congress 2008: 18th Analysis and Computation Specialty Conference, 1–11.

Wan, F., Cheng, L., Hong, L., Liu, D., Yao, S., and Lei, M. (2023). Seismic response of a mid-story-isolated structure considering soil–Structure interaction in sloping ground under three-dimensional earthquakes. *Front. Earth Sci.* 10. doi:10.3389/FEART.2022.1098711

Zhang, J., Li, X., Qin, Q., Wang, Y., and Gao, X. (2023). Study on overlying strata movement patterns and mechanisms in super-large mining height stopes. *Bull. Eng. Geol. Environ.* 82 (4), 142. doi:10.1007/s10064-023-03185-5

Zhang, L., Shen, W., Li, X., Wang, Y., Qin, Q., Lu, X., et al. (2022). Abutment pressure distribution law and support analysis of super large mining height face. *Int. J. Environ. Res. Public Health* 20 (1), 227. doi:10.3390/ijerph20010227

Zhang, R., Phillips, B. M., Taniguchi, S., Ikenaga, M., and Ikago, K. (2017). Shake table real-time hybrid simulation techniques for the performance evaluation of buildings with inter-story isolation. *Struct. Control Health Monit.* 24 (10), e1971. doi:10.1002/stc.1971

Zhang, S., Liu, F., Hu, Y., Li, S., and Zhu, L. (2021). Study on seismic response characteristics of the interlayer isolation structure. *J. Vibroengineering* 23 (8), 1765–1784. doi:10.21595/jve.2021.22003

Zhou, Q., Singh, M. P., and Huang, X. Y. (2016). Model reduction and optimal parameters of mid-story isolation systems. *Eng. Struct.* 124, 36–48. doi:10.1016/j.engstruct.2016.06.011

frontiers | Frontiers in Earth Science

TYPE Original Research
PUBLISHED 26 October 2023
DOI 10.3389/feart.2023.1278308

OPEN ACCESS

EDITED BY
Xuelong Li,
Shandong University of Science and Technology, China

REVIEWED BY
Qiguang Di,
China Railway 12th Bureau Group Co., Ltd., China
Yanpeng He,
Xi'an University of Science and Technology, China
Jinlong Zhou,
China Coal Research Institute, China

*CORRESPONDENCE
Honghao Shen,
shenhonghao@cbtgc.com

RECEIVED 16 August 2023
ACCEPTED 28 September 2023
PUBLISHED 26 October 2023

CITATION
Sun X, Shen H, Jiang T, Zhang P, Peng S and Zhang S (2023), 6G-enabled open-pit mine security: toward wise evaluation, monitoring, and early warning. *Front. Earth Sci.* 11:1278308. doi: 10.3389/feart.2023.1278308

6G-enabled open-pit mine security: toward wise evaluation, monitoring, and early warning

Xiaokun Sun[1], Honghao Shen[2]*, Tingting Jiang[2], Peng Zhang[2], Simiao Peng[3] and Shupeng Zhang[4]

[1]School of Mechanics and Civil Engineering, China University of Mining and Technology, Beijing, China, [2]China Building Technique Group Co., Ltd., Beijing, China, [3]Beijing University of Civil Engineering and Architecture, Beijing, China, [4]North Blasting Technology Co., Ltd., Beijing, China

The mining of open pit can easily cause geological disasters such as landslide and debris flow. It is widely acknowledged that communication technology could solve the existing problems in engineering practice from the aspects of disaster monitoring, deformation monitoring, landslide warning and emergency communication. This research paper introduces a fully integrated monitoring and early warning solution tailored for mining regions. By synergizing 6G and Global Navigation Satellite System (GNSS) technologies, the system effectively addresses signal transmission challenges in complex environments. The utilization of 6G's high-speed, low-latency, and extensive connectivity capabilities enables efficient communication in these settings. The study focuses on a specific open-pit mine located in a cold region of China, utilizing it as a case study to demonstrate the system's effectiveness in enhancing slope safety through comprehensive monitoring and early warning mechanisms. Apart from considering traditional dump characteristics and external factors, the system also introduces an innovative early warning index for detecting slope changes. Applying the Analytic Hierarchy Process (AHP) and Fuzzy comprehensive evaluation method ensures reliable evaluation results, facilitating slope assessment, monitoring, and early warning procedures in water-rich open-pit mines situated in cold areas.

KEYWORDS

AHP-fuzzy comprehensive evaluation, 6G, GNSS, mine monitoring and warning, open-pit mine

1 Introduction

6G communication technology has garnered significant attention in the engineering industry due to its remarkable advantages in key technologies and performance, setting it apart from other communication technologies. Addressing existing challenges in engineering practice, such as disaster monitoring, deformation monitoring, landslide warning, and emergency communication, can be effectively achieved through the adoption of this new generation communication technology. The "14th Five-Year Plan for Mine Safety Production" in China emphasizes the prioritization of deepening "Internet + supervision and regulation" to enhance mine safety production. This supervisory approach encompasses slope stability evaluation, slope monitoring, early warning, and related aspects.

One prominent application scenario of 6G communication technology lies in slope disaster monitoring, early warning, and safety assessment. Globally, geological disasters, including landslides, have become a significant concern (Lavigne et al., 2014; Anua´rio Brasileiro de Desastres Naturais, 2012; Guadagno et al., 2001; Jafari et al., 2013; Merry et al.,

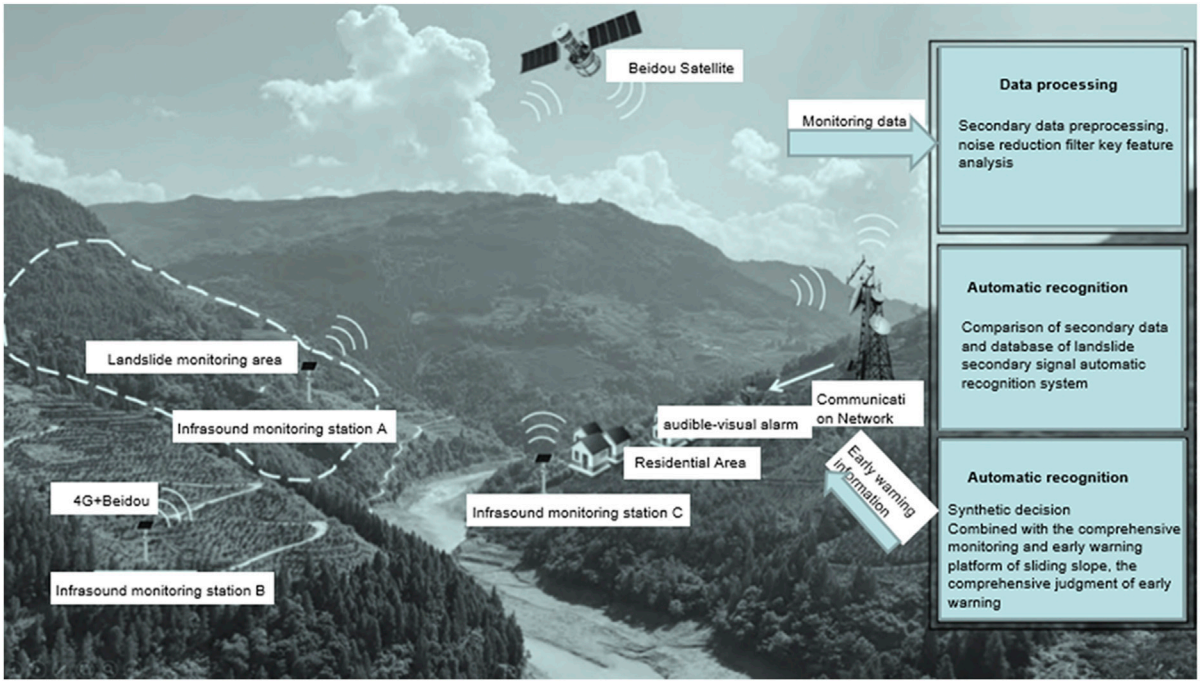

FIGURE 1
Technical diagram of a landslide infrasonic monitoring and warning system.

2005). The demand for coal resources often leads to long-term and intensive mining practices in coal mining areas, involving large-scale operations across multiple working surfaces. Consequently, the geological environment in these mining regions suffers varying degrees of damage, resulting in occasional geological disasters (Liu et al., 2023; Zhang et al., 2023). Open-pit coal mining, in particular, can lead to large-scale mines affected by interactions between surface water and groundwater. Combined with geological structure changes and the nature of slope rock mass, these factors increase the likelihood of collapse, landslides, debris flow, and other geological disasters (Wang et al., 2021; Jiang et al., 2023). Such occurrences not only severely impact the normal production and livelihood of residents in the vicinity of mining areas but also cause economic losses while posing threats to the surrounding geological and ecological environment.

So as to better reflect the stability and safety of slopes, more and more attention has been paid to the monitoring and warning systems of slopes. Especially with the development and progress of science and technology, the main monitoring of geological disasters such as landslides has been inferred from manual observation of surface change characteristics and surrounding landform changes (Xia and Zhu, 1999; Chen, 2022; Liu and Li, 2023a; Liu et al., 2023) to some measuring tools such as total station GPS mobile phone monitoring and InSAR technology, and now it is being combined with 6G communication technology (Wang, 2020; Liu et al., 2021; Yuan and Guo, 2021; Zhang et al., 2021; Zhou, 2022). Compared with other communication technologies, 6G communication technology has great advantages in key technologies and performance, especially in the application of intelligent industrial systems. For example, 6G communication technology has significant advantages in natural disaster warning, 6G wireless communication system architecture, construction high-precision positioning, and application services based on 6G communication systems, remote control of equipment, and construction safety monitoring information collection (Ma, 2020). The effective dynamic monitoring of a mining area and timely acquisition and analysis of the mining area surface settlement law can provide a strong basis for reasonable development and planning management of the mining area in the later period (Xia et al., 2001). Based on the characteristics of mining areas, through the application of 6G communication technology, we can easily solve the existing problems in engineering practices from the aspects of disaster monitoring, deformation monitoring, landslide warning, emergency communication, and so on.

At present, landslide monitoring mainly uses displacement and deformation as early warning indicators, and the effect is not ideal for sudden and strong rock landslide early warning. Infrasound in fixed frequency bands are generated by the damage and structural changes of rock and soil in a landslide before the instability failure, which makes landslide monitoring and warning technology based on infrasound possible (in Figure 1) (Hu and Shulin, 2002; Yin et al., 2021; Wang et al., 2022; Xiong et al., 2023).

The emergency communication technology and systems for mine disaster rescue scenarios generally adopt Wi-Fi as the relay and coverage scheme. Due to the legal restrictions of continuous channel occupancy time and the legal requirements of pre-access monitoring in unauthorized frequency bands, it is difficult to achieve a communication index with extremely low delay. Simultaneous relay networking of multiple emergency communication devices in the same frequency band has the same frequency interference, which will affect the communication quality. For public safety and vehicle

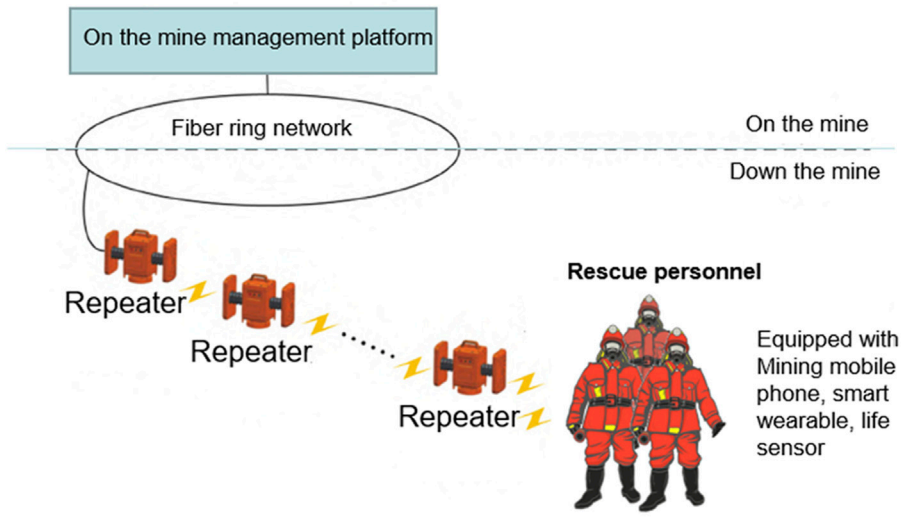

FIGURE 2
Structure diagram of the mine emergency communication system based on 6G direct communication.

networking application scenarios, 6G technology defines Sidelink direct link communication technology, which can achieve low time delay and high reliability direct communication between terminal devices (Wu and Tu, 2002). Aiming at the technical requirements of mine emergency communication systems for low delay and high reliable communication, a mine emergency communication system architecture based on 6G direct communication is proposed, and a mapping method of equipment identification and time-frequency resource location of the direct communication link is designed (Figure 2). The device transmits resource locations through pre-configured forward and back links, and can communicate with adjacent front-end and back-end devices without establishing routing connections. The device uses time-domain resource cyclic multiplexing to realize resource space division multiplexing and same-frequency interference avoidance between neighboring relay devices. The proposed method can realize the relay network mechanism without scheduling permission and minimal routing to avoid the same-frequency interference under the space division multiplexing of transmission resources, effectively improve the utilization efficiency of transmission resources, and the average air interface delay under conventional baseband parameters and network configuration can reach 25 ms, significantly reducing the transmission delay.

In this study, 6G transmission technology is applied to the field of open mine safety, and high-speed and low-delay data transmission and communication are realized. Through 6G technology, real-time monitoring and data transmission of various locations in mining areas can be realized, improving the efficiency and accuracy of mine safety monitoring. The research team has developed a set of intelligent assessment and monitoring systems to conduct the intelligent assessment and monitoring of mine safety through comprehensive analysis of real-time data and monitoring results of the mine. The system can detect abnormal situations quickly and give early warning in time, which improves the level of mine safety management.

The eastern part of the Inner Mongolia Autonomous Region, located in an extremely cold region, has the largest number of open-pit coal mines and the largest output in China. The slope stability of open-pit mines in this region is greatly affected by water because the precipitation is very concentrated in summer and winter, and the slopes are also hit by meltwater in spring, which can easily cause flooding. Therefore, wise evaluation, monitoring, and early warning are urgently needed regarding the slope stability of open-pit mines. Taking the Dongming open-pit mine as an example in the first section, this paper constructs the stability evaluation–monitoring–early-warning system of the inner dump. The second part introduces the geometeorological and hydrogeological conditions of the Dongming open-pit mine. The third part uses AHP-fuzzy comprehensive evaluation to evaluate the stability of the inner dump from 19 indexes in three aspects: characteristics of the inner dump, external influences, and early warning of slope change. The fourth part introduces the landslide monitoring and warning system based on 6G Internet of things technology in detail. The fifth part summarizes the thesis briefly.

2 Research background

In order to achieve high quality mine emergency communication with low delay and no co-frequency interference, the repeater adopts intelligent transport systems (ITS) dedicated frequency band 5,855–5,925 MHz (band 47) and 6G direct communication technology to establish and transmit wireless links. The diagram of the 6G direct connection communication is shown in Figure 3, where N is the number of interval devices that can reuse the same transmission resources.

In addition to the early warning of mining landslides and rescue, etc., as well as the early warning of some electrical fires, 6G technology (Wan et al., 2021) designed an electrical fire monitoring system based on wireless transmission technology. The system uses the heat (temperature) and threshold (current) generated by the monitoring

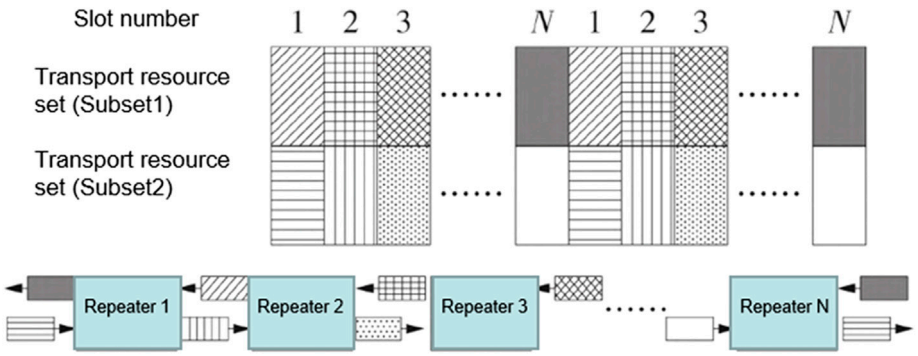

FIGURE 3
Schematic diagram of 6G direct connection communication.

line, adopts wireless communication technology to transmit the alarm information to the monitoring host, and the monitoring host issues instructions, and the information is transmitted to the personnel on duty, so as to prevent the occurrence of electrical fires. Through the test, the system has good stability, a strong ability to penetrate walls, and far-reaching transmission. In addition, the new generation of communication technology has further improved the application of unmanned driving in various environments (Wu and Tu, 2001) and emergency communication in rescue and disaster relief (Zhou et al., 2004).

At present, there are roughly four analysis methods for slope stability, which are the limit equilibrium method, engineering geological analysis method, numerical analysis method, and modern mathematical analysis method (Perski et al., 2009). The research object of slope engineering in inner dump is rock and soil mass in complex geological environment. Because the working face is advancing all the time, the mechanical properties of rock and soil mass are jointly affected by various complex factors such as the cause of stacking part, structure, and the environment in which it is located. The rock and soil mass in the inner dump shows characteristics such as non-uniformity, discontinuity, and time variation. The evaluation of slope stability of the inner dump is inevitably fuzzy. The fuzzy comprehensive evaluation method based on fuzzy set theory can better evaluate the hierarchical and fuzzy problems of influencing factors such as slope stability (Zhang, 2008a), such as rock slope stability evaluation (Wang and Tong, 2007a), two-level comprehensive evaluation model of slope stability (Li, 1992a), and multi-level fuzzy comprehensive evaluation model of rock slope stability (Li, 1997a). At present, the evaluation indexes of stability tend to focus more on the mechanical characteristics and external influences of the inner dump (Li, 1992b; Zhou et al., 1995; Li, 1997b; Zhang and Shi, 2000a; Zhang and Shi, 2000b; Wang and Tong, 2007b; Zhang, 2008b; Liu and Li, 2023b) and lack slope change warning.

3 Case situation

The Dongming open-pit mine is located in the eastern part of the Inner Mongolia Autonomous Region in China (Figure 4; Figure 5), located on the Hulunbuir High Plain, with Hailar City to the southeast and Chenbahu Banner to the west. The administrative division is subordinate to Chenbahu Banner. It is 20 km from Hyrule. The geographical coordinates of the mining area are 119°38′27″-119° 40′32″east longitude, 49°24′22″-49°25′37″north latitude, and the area of the mining area is 4 km^2.

The Dongming open-pit coal mine is located on the north bank of the Hailar River on the western slope of the Great Khingan Mountains. It is a slightly undulating high plain, connected with low mountains and hills in the north and northeast, with an elevation of $+605m \sim +630m$. The terrain is gentle and there are no rivers or lakes. There are three aquifers in the coalfield area. One is a fissure aquifer, which is distributed in the northeast and east of the coalfield. The lithology is the clastic zone of the Longshan Formation. The second is a fissure and pore aquifer, which is distributed in the wavy plateau area in the middle of coalfield. The lithology is mainly sandstone, conglomerate, and coal seam. A pore aquifer is distributed in the gully or lowland between Hailar, Molleger River Valley, and the undulating high plain. The lithology is Quaternary alluvial sand, gravel layer, and pebble. Due to the small surface mine area, there are only two aquifers in the hydrogeological unit, namely, the Quaternary pore water-bearing rock group and the fissure water-bearing rock group. It belongs to water-rich coal mine.

This region is a subcold continental climate, winter cold and long snowy; Summer is hot and short, seasonal rainy, spring and autumn monsoon drought; The average annual temperature is −2.6℃, the highest temperature is 37.7℃, and the lowest temperature is −48℃. Snowmelt in spring and seasonal precipitation in summer can easily cause floods and damage the slope stability of the dump.

According to the geological engineering characteristics of the Dongming open-pit mine, the slope instability mode, the type of landslide, as well as the overall analysis of mining engineering conditions, it is necessary to have inner dump slope safety evaluation and monitoring to ensure safe production, considering that rain water is prone to producing gullies in spring and summer.

4 Stability evaluation of inner dump

The occurrence of landslide accidents in dump sites is a gradual process. The change is usually slow at the beginning, but with the passage of time, the deformation of slopes accelerate gradually, and

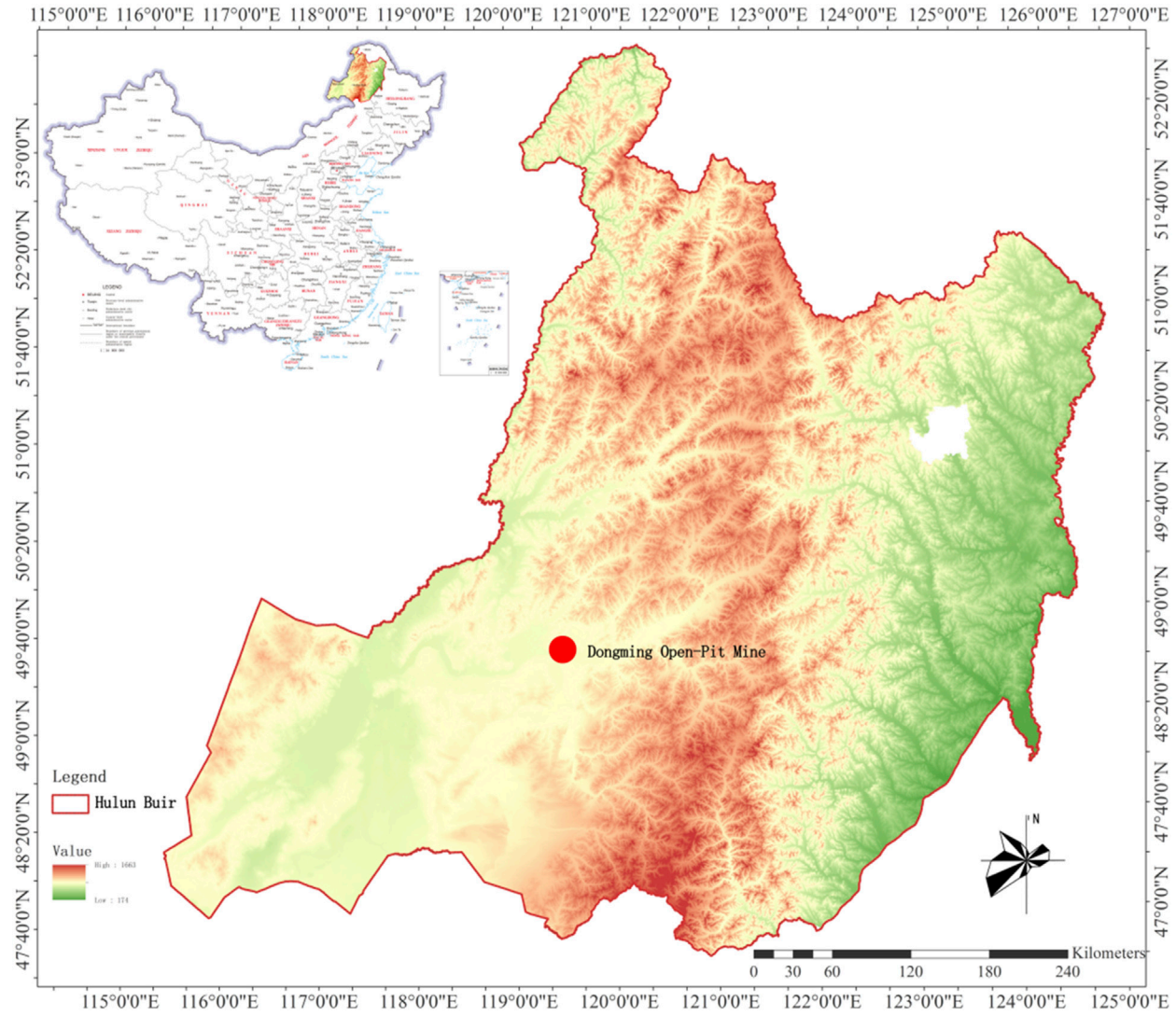

FIGURE 4
The Dongming open-pit mine site map.

the development speed is faster when closed to landslide accident. According to the landslide mechanism of dumps, the stability evaluation of the inner dump is divided into three aspects, namely, the characteristics of the inner dump, the external influences, and the early warning of slope changes.

4.1 Establishment of evaluation model

Based on the previous monitoring data, research reports, and characteristics of the Dongming open-pit slope stability in water-rich mining areas in cold areas, comprehensive research and analysis of various conditions, the stability evaluation of the inner dump is formed, and the system is divided into three levels. On the basis of the preliminary evaluation system framework, 30 geoscience and geotechnical engineering experts were invited to refine and determine the evaluation system structure and index selection. Finally, the system was divided into three levels with 19 indicators.

The first layer is the objective layer (A), which is the stability evaluation of the inner dump and the top level and ultimate goal of the system.

The second layer is the criterion layer (B), which mainly focuses on the comprehensive evaluation of the stability of the internal dump from three aspects: characteristics of the internal dump (B1), external influences (B2), and slope changes (B3).

The third layer is the index layer (C), which is the concrete expansion of the criterion layer.

To sum up, the stability evaluation system of the inner dump consists of one target layer, three criterion layers, and 19 indicator layers, as shown in Figure 6.

In terms of the characteristics of the inner dump, various factors that may affect the characteristics of the dump in the open pit are comprehensively considered in the inner dump characteristics' part, including the foundation bed, basement bedrock, internal friction angle, slope, height, step height, platform width as inner dump features, and cohesive force moisture content, permeability coefficient and porosity as

FIGURE 5
Inner dump in the Dongming open-pit mine.

stacking material. For the external part, rain is the main factor that causes landslide disasters in open pit mines in cold areas. Therefore, two indexes of rainfall intensity and rainfall duration, as well as the maximum seismic intensity related to earthquakes and the weathering alterations related to soil discharge were selected. In the newly added change of side slope section, indicators that can be measured in real time were mainly added: surface displacement, internal displacement, pore water pressure, and the internal stress of rock and soil.

Index quantification and grade are determined by Expert ratings based on Dongming Open-pit geoscience and geotechnical engineering feature, Engineering rock mass classification standard and Codes such as Code for waste dump design of metal mine (GB 51119-2015).

$$P = K\left(f_0^2 - f_i^2\right) \tag{1}$$

where P is the void water pressure and K is the calibration coefficient of the measured pore water pressure gauge. f_i is the average frequency of the pore water pressure gauge at the time of measurement and f_0 measures the average initial frequency of the pore water pressure gauge before installation.

The internal stress of rock and soil takes the formula for calculating the original rock stress given by Kinnick in 1925 in the hypothesis of homogeneous isotropic linear elastomers: the vertical principal stress is equal to the weight of the rock and soil body on the unit base area, that is,

$$\sigma z = \alpha z \tag{2}$$

where α is the average volume weight of the overlying rock and Z is the depth.

There are also two horizontal principal stress σx and σy, which is equal to side stress coefficient λ multiply vertical principal stress, that is,

$$\sigma x = \sigma y = \lambda \sigma z \tag{3}$$

while side stress coefficient is related to Poisson ration, that is

$$\lambda = \mu/(1-\mu) \tag{4}$$

General speaking μ≈0.2–0.3 as μ is Poisson ratio if object is rock mass, and then λ≈0.25 here.

4.2 AHP weight calculation and consistency test

4.2.1 Single hierarchical sorting

Single hierarchical ranking refers to the ranking of the importance of each factor at this level relative to the factor at the previous level.

The method of determining the maximum eigenroot of a matrix and corresponding eigenvectors is.

1) The matrix is normalized by column

$$\frac{b_{ij}}{\sum_{i=1}^{n} b_{ij}}; \tag{5}$$

2) Sum the normalized matrix by row to get

$$\bar{w} = \left(\overline{w_1}, \overline{w_2}, \cdots, \overline{w_n}\right)^T; \tag{6}$$

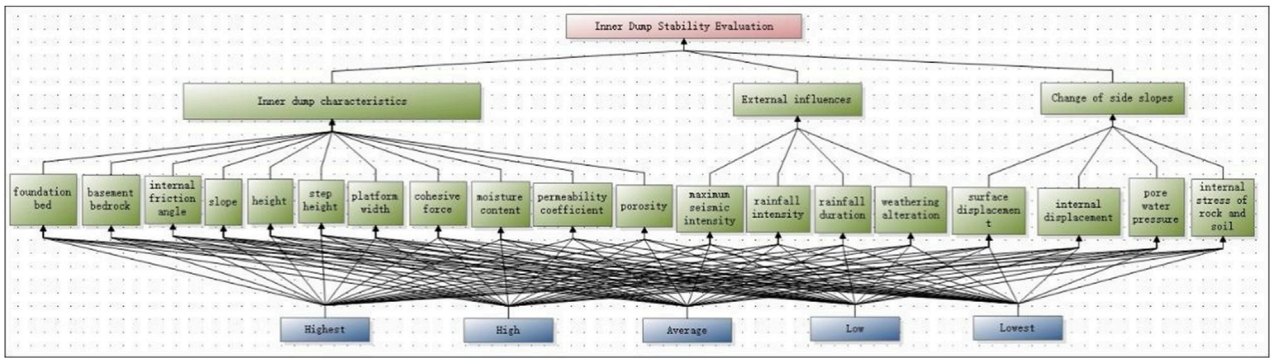

FIGURE 6
Evaluation system of inner dump stability.

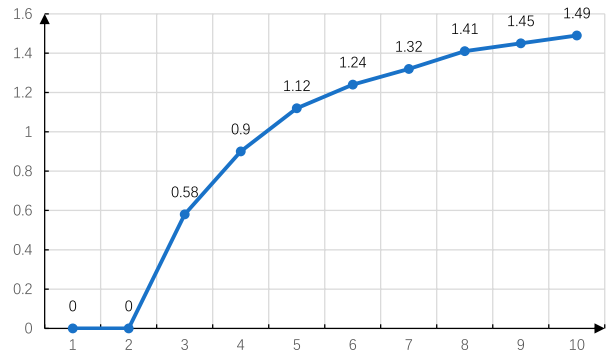

FIGURE 7
Matrix consistency.

3) Normalize the vector

$$w_i = \frac{\bar{w}_i}{\sum_{i=1}^{n} \bar{w}_i}; \tag{7}$$

4) Calculate the maximum feature root

$$\lambda_{max} = \sum_{i=1}^{n} \frac{(BW)_i}{nW_i}; \tag{8}$$

5) Get the weight vector

$$AW = \lambda W; \tag{9}$$

6) Questionnaires were sent to experts in civil engineering, who judged the relative importance of factors under the same index layer by pairwise comparison between factors, and scored the importance of factors in the questionnaire using the form of 1-9 and its reciprocal. Therefore, it is easy to get the importance rankings of criterion layer: B1 internal characteristics >B2 External influences>>B3 Slope variations. Among criterion layers, the importance rankings of index layer of B1 layer show that C3 Internal friction angle>C8 Cohesive force>C1 Foundation bed>C9 Moisture content>C4 Slope>C5 Height>C6 Step height>C7 Platform width>C11 Porosity>C10 Permeability coefficient>C2 Basement bedrock. Moreover, the importance rankings of B2 layer are C13 Rainfall intensity>C14 Duration of rainfall>C12 Maximum seismic intensity>C15 Weathering alterations; and C17 Internal displacement>C18 Pore water pressure>C16 Surface displacement>C19 Internal stress of rock and soil in B3 layer.

4.2.2 Determine the index membership degree

To determine the membership degree relationships related to evaluation, questionnaire surveys were sent to experts in related fields, and the data results of the questionnaire were analyzed after evaluation and scoring. Membership was represented by R, and the absolute value reduction method was used to calculate:

$$R_{ij} = \begin{cases} 1 (i = j) \\ 1 - \sum_{k=1} |x_{ik} - x_{jk}|, (i \neq j) \end{cases} \tag{10}$$

According to the value r_{ij} obtained by absolute subtraction method, the membership degree matrix was established on the basis of the obtained value. The matrix is as follows:

$$R = [r_{ij}] = \begin{bmatrix} r_{11} & \cdots & r_{1j} \\ \vdots & \ddots & \vdots \\ r_{i1} & \cdots & r_{ij} \end{bmatrix} \tag{11}$$

The i th index of the evaluation factor U corresponds to the evaluation value generated by the j item in the index set V, which is represented by rij.

For example, the proportion of C1 with high stability, average stability, and low stability is 0.2, 0.7, and 0.1, respectively. Therefore, the C1 membership degree is {0 0.2 0.7 0}.

4.2.3 Consistency check

$$CI = \frac{\lambda_{max-n}}{n-1} \tag{12}$$

$$\lambda_{max} = \sum_{i=1}^{n} \frac{[CW]_i}{nW_i} \tag{13}$$

where CI is the consistency index and λmax is the largest characteristic root. [CW]i is the *I*th component of the matrix [CW]. Define conformance metrics

$$CR = \frac{CI}{RI} \tag{14}$$

RI is the value of the random consistency index, as shown in Figure 7.

CR is the consistency ratio; RI is a random consistency index.

Criterion layer and index layers all passed the conformance test, with the judgment matrix shown in Tables 1–5.

4.3 Fuzzy comprehensive evaluation

Fuzzy comprehensive evaluation is similar to analytic hierarchy process (AHP), but it does not evaluate which specific plan is better, but which of the ratings of very bad, bad, good, and very good is more consistent with the overall situation of medium our overall index A. In this project, it is of great significance to know the grade of slope safety in inner dump, and evaluating grades of each indicator is shown in Table 6.

4.3.1 Membership degree of the qualitative index

The standard of the qualitative index membership degree can be determined by statistical method. The calculation formula is adopted:

$$r_{i,k}^{s} = f_{i,k} \Big/ \sum_{k=1}^{s} f_{i,k} \tag{15}$$

where i is the index and k is the evaluation level (k = 1, 2 . . . , s)

TABLE 1 Criterion layer judgment matrix.

B	B1	B2	B3
B1	1	4	3
B2	1/4	1	2
B3	1/3	1/2	1

Then, the consistency test was carried out, and the result was CI, 0.0539, CR, 0.093. The CR, was less than 0.1, which passes the consistency test.

4.3.2 Membership degree of quantitative indicators

The membership degree of quantitative indicators can be determined thanks to the grade standard, that is to say, if the obtained survey results are in a certain standard value or within a certain interval, the membership degree is 1, and the others are 0. Get the index layer weight. Among them.

B1-B11; B12-B15;

$$w_1 = (0.1531\ 0.0115\ 0.2763\ 0.0791\ 0.0563\ 0.0401\ 0.0287\ 0.2086\ 0.1106\ 0.0152\ 0.0207)$$

$$w_2 = \{0.1603\ 0.4668\ 0.2776\ 0.0953\}$$

B16-B19.

4.3.3 Membership matrix

The membership matrices of the characteristics of B1 inner dump, B2 external influences, and B3 slope changes are presented in Figures 8-10, respectively.

Firstly, the weight of the index layer is calculated, and then the first-order fuzzy evaluation can be obtained by multiplying the right weight vector with the membership matrix, and the following formula is used:

$$k_i = w_i \times B_i \tag{16}$$

For example,:

$$k_2 = \mathbf{w}_2 \times B_2 = \{0.16030.4680.27760.0953\} \times \begin{pmatrix} 0.2\ 0.6\ 0.2\ 0.0\ 0.0 \\ 1.0\ 0.0\ 0.0\ 0.0\ 0.0 \\ 0.0\ 0.2\ 0.6\ 0.2\ 0.0 \end{pmatrix}$$

$$= \{0.6654\ 0.1985\ 0.1170\} \tag{17}$$

By the same token, you get k1, k2, k3, and you get K as follows, as shown in Figure 11.

The weight of the criterion layer is written as follows:

$$w = \{0.6301\ 0.2184\ 0.1515\}$$

Then the weight of criterion layer is used to multiply the membership matrix:

$$k = w \times K \tag{18}$$

The second-order fuzzy evaluation can be obtained as follows:

$$\{0.8411\ 0.1163\ 0.0333\ 0.0067\ 0.0013\}$$

The five indexes respectively correspond to high suitability, high suitability, average suitability, low suitability, and low suitability. The highest value of fuzzy evaluation was 0.8411,

TABLE 2 Characteristic judgment matrix of internal waste dump.

B1	C1	C2	C3	C4	C5	C6	C7	C8	C9	C10	C11
C1	1	9	1/3	3	4	5	6	1/2	2	8	7
C2	1/9	1	1/11	1/7	1/6	1/5	1/4	1/10	1/8	1/2	1/3
C3	3	11	1	5	6	7	8	2	4	10	9
C4	1/3	7	1/5	1	2	3	4	1/4	1/2	6	5
C5	1/4	6	1/6	1/2	1	2	3	1/5	1/3	5	4
C6	1/5	5	1/7	1/3	1/2	1	2	1/6	1/4	4	3
C7	1/6	4	1/8	1/4	1/3	1/2	1	1/7	1/5	3	2
C8	2	10	1/2	4	5	6	7	1	3	9	8
C9	1/2	8	1/4	2	3	4	5	1/3	1	7	6
C10	1/8	2	1/10	1/6	1/5	1/4	1/3	1/9	1/7	1	1/2
C11	1/7	3	1/9	1/5	1/4	1/3	1/2	1/8	1/6	2	1

λmax=11.688, CI, 0.0688, CR, 0.0456. The CR, was less than 0.1, which passes the consistency test.

TABLE 3 External influence judgment matrix B12-B15.

B2	C12	C13	C14	C15
C12	1	1/3	1/2	2
C13	3	1	2	4
C14	2	1/2	1	3
C15	1/2	1/4	1/3	1

λmax=3.0309, CI, 0.0103, CR, 0.0115. The CR, was less than 0.1, which passes the consistency test.

TABLE 4 External influence judgment matrix B16-B19.

B3	C16	C17	C18	C19
C16	1	1/3	1/2	2
C17	3	1	2	4
C18	2	1/2	1	3
C19	1/2	1/4	1/3	1

λmax=3.0309, CI, 0.0103, CR, 0.0115. The CR, was less than 0.1, which passes the consistency test.

TABLE 5 Weight of criterion layer and scheme layer.

			B1	B2	B3	Weight	Sequence
			0.6301	0.2184	0.1515	—	—
A	B1 Internal characteristics	C1 Foundation bed	0.1531	—	—	0.0965	4
		C2 Basement bedrock	0.0115	—	—	0.0072	19
		C3 Internal friction angle (°)	0.2763	—	—	0.1741	1
		C4 Slope (°)	0.0791	—	—	0.0498	8
		C5 Height (m)	0.0563	—	—	0.0355	10
		C6 Step height	0.0401	—	—	0.0253	12
		C7 Platform width	0.0287	—	—	0.0181	15
		C8 Cohesive force/Mpa	0.2086	—	—	0.1314	2
		C9 Moisture content/%	0.1106	—	—	0.0697	6
		C10 Permeability coefficient	0.0152	—	—	0.0096	18
		C11 Porosity	0.0207	—	—	0.0130	17
	B2 External influences	C12 Maximum seismic intensity	—	0.1603	—	0.0350	11
		C13 Rainfall intensity	—	0.4668	—	0.1019	3
		C14 Duration of rainfall	—	0.2776	—	0.0606	7
		C15 Weathering alterations	—	0.0953	—	0.0208	14
	B3 Slope variations	C16 Surface displacement(mm)	—	—	0.1603	0.0243	13
		C17 Internal displacement	—	—	0.4668	0.0707	5
		C18 Pore water pressure(kpa)	—	—	0.2776	0.0421	9
		C19 Internal stress of rock and soil	—	—	0.0953	0.0144	16

TABLE 6 Inner dump slope stability evaluation system.

Criterion layer	Index layer	Index quantization	Grade standards				
			I	II	III	IV	V
B1 Internal characteristics	C1 Foundation bed	Soil layer thickness	<2 m	2–5 m	5–8 m	8–10 m	>10 m
	C2 Basement bedrock	Basement bedrock thickness	>30 m	30-15 m	15–10 m	10-5 m	<5 m
	C3 Internal friction angle (°)	Engineering rock mass classification standard	>19	19–15	15–10	10–5	<5
	C4 Slope (°)		<15	15–20	20–25	25–30	>30
	C5 Height (m)		<100	100–120	120–180	180–240	>240
	C6 Step height		10–15 m	15–20 m	20–25 m	25–30 m	30–35 m
	C7 Platform width		40–50 m	30–40 m	20–30 m	10–20 m	0–10 m
	C8 Cohesive force/Mpa	—	5.1–7	5.1–2.1	2.1–1.5	01.5–0.7	0–0.7
	C9 Moisture content/%	—	0–16	16–21	21–26	26–31	31–100
	C10 Permeability coefficient	—	35–40 m/d	40–50 m/d	50–60 m/d	60–70 m/d	70–80 m/d
	C11 Porosity	—	0%-10%	10%-20%	20%-25%	25%-30%	30%-35%
B2 External influences	C12 Maximum seismic intensity	—	0–3	3–5	5–7	7–9	—
	C13 Rainfall intensity	—	0–25 mm	25–50 mm	50–100 mm	100–200 mm	>200 mm
	C14 Duration of rainfall	Engineering rock mass classification standard	<6 h	6–12 h	12–18 h	18–24 h	>24 h
	C15 Weathering alterations		>80	80–60	60–40	40–20	<20
B3 Slope variations	C16 Surface displacement(mm)		15<	15–25	25–35	35–55	>55
	C17 Internal displacement		10<	10–20	20–30	30–40	>40
	C18 Pore water pressure(kpa)		<50	50–100	100–200	200–300	>40
	C19 Internal stress of rock and soil		<960	960–1,920	1,920–2,300	2,300–3,260	>3,260

Change of slope slide was added in this paper as an early warning index, and data of surface displacement and internal displacement depend on field monitoring. The pore water pressure is equal to the hydrostatic pressure without the action of water flow, and the formula is.

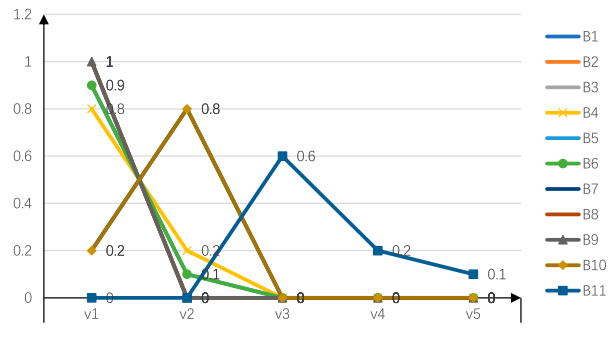

FIGURE 8
Membership matrix of inner dump characteristics.

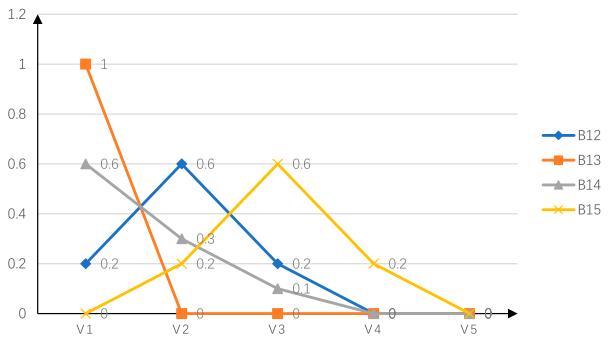

FIGURE 9
Membership matrix of external influences.

indicating that it is in the high suitability rating on the whole. In order to obtain the final score, the evaluation set is assigned 1 to 5 points, by the formula:

$$G_A = k_A \times V \tag{19}$$

The total score was 4.7853, which belongs to the high security level. This is mainly attributed to internal characteristics, including the current stacking material and stacking methods, but the impact of rain intensity and duration as well as ground water welling cause tremendous impact as the main disaster-

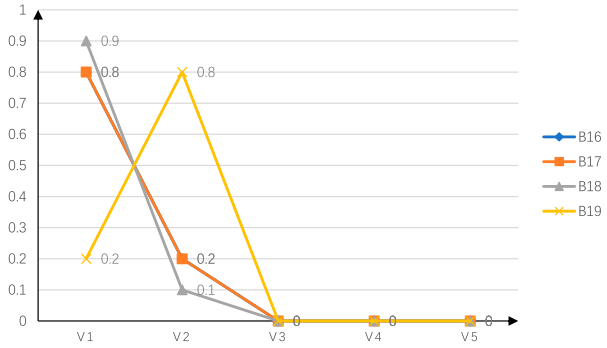

FIGURE 10
Membership matrix of slope changes.

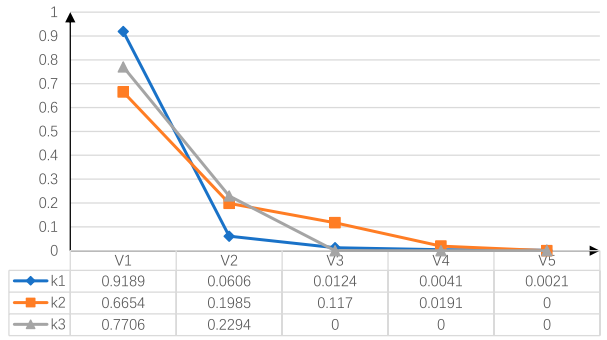

	V1	V2	V3	V4	V5
k1	0.9189	0.0606	0.0124	0.0041	0.0021
k2	0.6654	0.1985	0.117	0.0191	0
k3	0.7706	0.2294	0	0	0

FIGURE 11
First-level fuzzy evaluation.

inducing factors. With the advance of the working surface, the inner dump characteristics change, which affect stability. Therefore, it is necessary to monitor rainfall and surface deformation for early warning. Based on the 6G Internet of things, real-time monitoring and transmission of rainfall and displacement in various locations on the slope can be realized, improving the efficiency and accuracy of mine safety monitoring.

5 Application of monitoring and warning system based on the 6G internet of things

Combined with the latest 6G Internet of things technology, a remote landslide monitoring and early warning system can be established for long-term monitoring and early warning, and real-time tracking of the deformation and failure trend of landslides, timely discovery and prediction of dangerous situations, and corresponding measures are taken to prevent the loss of life and property caused by sudden disasters.

The main difference between monitoring and early warning is to judge monitoring data due to early warning criteria, and to issue timely early warning and risk response, as shown in Figure 12. This requires the landslide monitoring and early warning system to have an automatic identification and judgment function thanks to the early warning criteria, and send out early warning information. The monitoring and early warning system organically combines 6G, the Internet of things, and landslide early warning technology. Taking rainfall and surface deformation as the key monitoring objects, data of rainfall, surface cracks, and GNSS surface displacement through monitoring stations are transmitted through 6G technology and analyzed and processed on the server, and finally advanced warning is conducted thanks to the effective early warning criteria.

Using the latest 6G Internet of things technology, a remote landslide monitoring and early warning system can be established for long-term monitoring and early warning of landslides. The system can track the deformation and failure trends of landslides in real time, judge the monitoring data according to the early warning criteria, and issue early warning and hedge responses in time to prevent the loss of life and property caused by sudden disasters. The system uses 6G technology to transmit monitoring data. Since the main cause

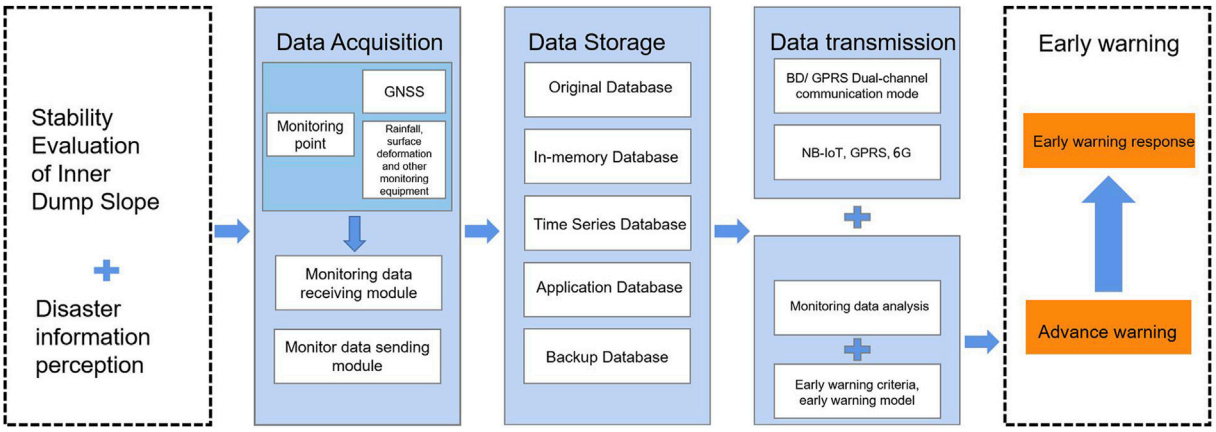

FIGURE 12
Landslide monitoring and early warning process.

of disasters in the inner dump is precipitation, data are collected by sensing and sensing monitoring stations such as rainfall, surface cracks, and GNSS surface displacement, and the data are analyzed and processed on a server to realize automatic identification and judgment functions, and advance warning is carried out depending on effective warning criteria. Therefore, the monitoring and early warning system plays an important role in landslide early warning technology, which can improve the efficiency of monitoring and management and contribute to the sustainable development of society.

5.1 Data collection

Data acquisition is one of the core steps of the monitoring and early warning system. Since water is the main disaster factor of water-rich open-pit mines in cold regions, landslide disaster field monitoring stations are arranged, equipped with a combination of machine vision monitoring systems, GNSS monitoring systems, rainfall gauges, groundwater level monitoring equipment, second-order work monitoring equipment, and other related monitoring equipment to perceive the slope and environmental state data depending on the specific slope monitoring needs. These devices collect monitoring data periodically, communicate directly with the server on the device side, and transmit the collected data to the server on the device side over the network.

5.1.1 GNSS

GNSS mobile stations and self-calibration cooperative targets are installed on the rods of monitoring equipment. GNSS data acquired by receivers' collecting data, and temporary storage and fixed time interval transmission are realized by transmission control boxes. The displacement observation platforms can simultaneously obtain the surface displacement data calculated by real-time difference decomposition of the difference processing program of GNSS mobile station data and the three-dimensional displacement data obtained by the machine vision surface displacement monitoring system. By comparing the two sets of displacement data, the accuracy analysis function of the field monitoring test system of slope surface displacement monitoring based on binocular vision can be realized.

A rainfall monitoring point should be set up every 20 km^2 catchment area in the monitoring area, and the measuring point should be arranged in an open position away from people. The rainfall monitor can be installed next to the GNSS reference station to facilitate site construction and maintenance.

The point layout density of the integrated surface displacement observation station should refer to the layout requirements of the GNSS displacement monitoring system in the Survey Code for Landslide Prevention and Control Engineering. According to the geological conditions of the monitoring points, a monitoring section should be arranged along the vertical and horizontal axis of the the potential landslide area, and each section should have no less than three measuring points.

5.1.2 Rainfall monitoring subsystem

Rainfall is an important inducing factor of landslide disasters in this study area. The selection of rainfall monitoring points should be based on the "watershed control principle, elevation control principle, communication smooth principle, terrain open principle, and area control principle" in order to study the rainfall characteristics of landslides induced.

The initial threshold is divided according to the corresponding rainfall level of the National Meteorological Administration (after the monitoring system runs steadily, the early warning parameters can be optimized and adjusted due to the local hydrological rainfall data and actual monitoring data), in which: the first-level warning value consists of a rainfall rate of 1.0 mm/min, an hourly rainfall of 15 mm, and a daily rainfall of 50 mm; the second-level warning value is a rainfall rate of 2.0 mm/min, an hourly rainfall of 30 mm, and a daily rainfall of 100 mm; and the third-level warning value is a rainfall rate of 4.0 mm/min, an hourly rainfall of 60 mm, and a daily rainfall of 200 mm.

5.2 Data storage

To facilitate data exchange with the application server, the server on the device uses a cache database and periodically pushes data to the application server due to the data request specifications of the application server. After receiving the data pushed by the device server, the application server preprocesses the data before storing it, and then stores the data in the database of the storage center. It can realize the real-time monitoring and early warning of landslides. The collected data can be directly transmitted to the server for analysis and processing, and advance warning can be carried out thanks to effective warning criteria. Thus, the accuracy and timeliness of early warnings are greatly improved, and the reliability and precision of landslide early warning are guaranteed. At the same time, the cache database and data push technology can realize the rapid transmission and processing of data and improve the efficiency and stability of the system.

5.3 Data storage layer

The built-in data parsing function is used to analyze and store the data on the database according to the professional data protocol of the data acquisition layer. The original database and backup database are used to store the monitoring perceived data values.

5.4 Data transmission

In the Internet of things, 6G communication, as a high-quality and real-time monitoring data transmission system, has many advantages, such as high speed, large capacity, and low delay. In the Dongming inner dump detection project, the corresponding Internet of things terminal is used to monitor rainfall, ground cracks, and surface deformation in real time, and then the 6G communication channel is selected for data transmission.

Based on the data output interface and communication protocol of high-precision mechanical sensors, an automatic data acquisition device was developed. The equipment includes a data acquisition module, data storage module, and data transmission module, and is equipped with solar power supply equipment. The data acquisition

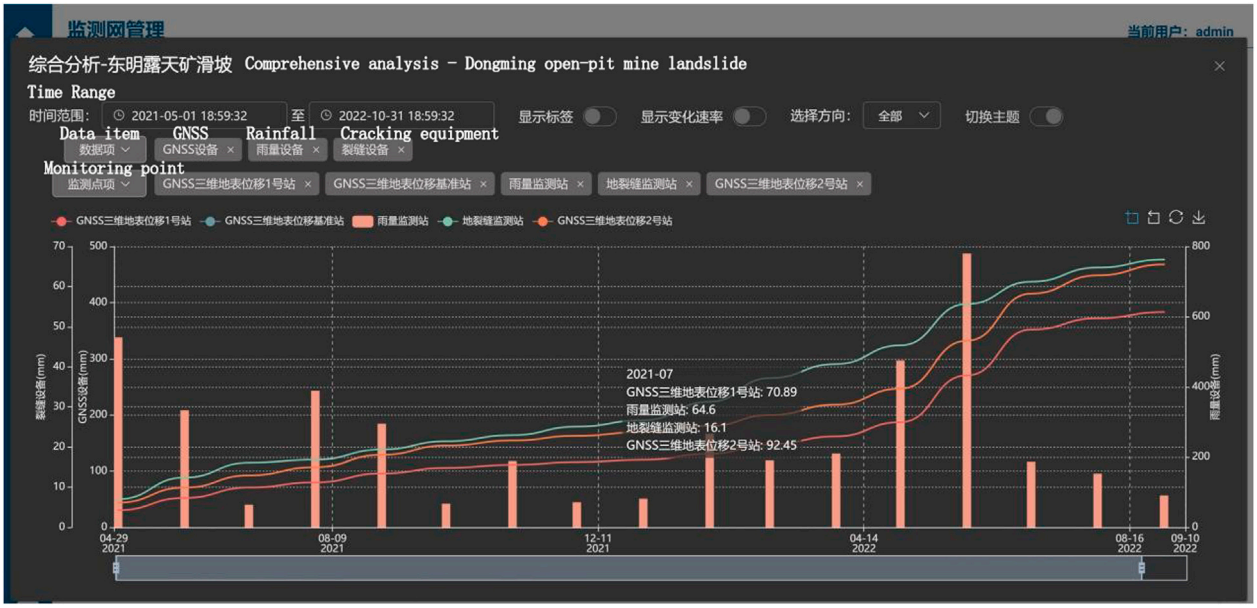

FIGURE 13
Landslide monitoring and warning in the Dongming inner dump.

device is connected with the sensor and the solar power supply system through shielded cables to form a complete data acquisition system. The system adopts the Beidou satellite and GPRS dual communication mode (BD/GPRS mode) after data acquisition to transfer the data from the site to the indoor monitoring center, which can realize the rapid transmission and processing of data. At the same time, the system collects the data of the monitoring points in two modes: network networking and line networking, and can select the appropriate data transmission mode according to different monitoring areas and transmission distances, which improves the flexibility and adaptability of the system.

5.5 Data monitoring and early warning

The monitoring and early warning platform can provide comprehensive analysis of monitoring data. Users can specify the time range of data generation and visually display the data of all monitoring points monitoring landslides. This can help users better understand the change trends and stability of the slope, and take appropriate measures in time. The method of Li et al. (2021) was adopted to improve the tangent Angle warning criterion for landslide warning. By analyzing real-time monitoring data and warnings, landslide velocity and deformation trends could be judged more accurately, and corresponding measures could be taken in time to ensure slope safety (Figure 13).

6 Conclusion

This research paper introduces an advanced integrated monitoring and early warning system designed for mining areas, utilizing cutting-edge 6G communication technology. The system employs a novel AHP-fuzzy comprehensive evaluation method with a three-layer model and 19 indicators to assess and monitor the stability of water-rich inner dump slopes in open-pit mines. The evaluation results indicate a high safety level score of 4.7853. To ensure the long-term safety of slopes, a geological disaster monitoring and early warning system is implemented, leveraging the capabilities of the 6G communication network. This system takes advantage of low-power consumption, long-distance communication, and multi-channel data return facilitated by differential chirp modulation technology. With its broad coverage, the system effectively guarantees slope stability throughout the entire process of evaluation, monitoring, and warning. The research outcomes offer valuable insights for slope assessment and monitoring in cold regions housing water-rich open-pit mines.

Data availability statement

The datasets presented in this study can be found in online repositories. The names of the repository/repositories and accession number(s) can be found in the article/Supplementary material.

Author contributions

XS: Writing–original draft, Writing–review and editing. HS: Data curation, Writing–original draft, Conceptualization. TJ: Formal Analysis, Supervision, Conceptualization, Writing–original draft. PZ: Visualization, Conceptualization, Writing–original draft. SP: Investigation, Data curation, Validation, Writing–original draft. SZ: Project administration, Resources, Writing–original draft.

Funding

The author(s) declare financial support was received for the research, authorship, and/or publication of this article. This work was supported by the National Natural Science Foundation of China (Grant number: 41772335).

Conflict of interest

Authors HS, TJ, and PZ were employed by the China Building Technique Group Co., Ltd. Author SZ was employed by the North Blasting Technology Co Ltd.

The remaining authors declare that the research was conducted in the absence of any commercial or financial relationships that could be construed as a potential conflict of interest.

Publisher's note

All claims expressed in this article are solely those of the authors and do not necessarily represent those of their affiliated organizations, or those of the publisher, the editors and the reviewers. Any product that may be evaluated in this article, or claim that may be made by its manufacturer, is not guaranteed or endorsed by the publisher.

References

Anua´rio Brasileiro de Desastres Naturais, (2012). *Ministery of national integration*. Brası´lia: National Center for Management of Risks and Disasters, 78.

Chen, P. (2022). Stability analysis and safety evaluation of west Dump slope in Anjialing open-pit Mine. *Open-pit Min. Technol.* 37 (01), 36–38. (in Chinese).

Guadagno, F. M., Revellino, P., and Grelle, G. (2001). "The 1998 Sarnolandslides: conflicting interpretations of a natural event," in *International conference on debris-flow hazards mitigation: mechanics*. doi:10.4408/IJEGE.2011-03.B-009

Hu, W., and Shulin, L. (2002). A study on the acoustic emission technology in the analysis of rock slope stability. *Min. Res. Dev.* 22 (3), 9–11. (in Chinese).

Jafari, N. H., Stark, T. D., and Merry, S. (2013). The July 10, 2000 Payatas landfill slope failure. *Int. J. Geoeng Case Hist.* 2 (3), 208–228. doi:10.4417/IJGCH-02-03-03

Jiang, B., Xin, Z., Zhang, X., Deng, Y., Wang, M., Li, S., et al. (2023). Mechanical properties and influence mechanism of confined concrete arches in high-stress tunnels. *Int. J. Min. Sci. Technol.* 33, 829–841. doi:10.1016/j.ijmst.2023.03.008

Lavigne, F., Wassmer, P., Gomez, C., Davies, T. A., Hadoko, D. S., Yan, T., et al. (2014). The 21 February 2005, catastrophic waste avalanche at Leuwigajah dumpsite, Bandung, Indonesia. *Geoenviron Disasters* 1 (1), 10. doi:10.1186/s40677-014-0010-5

Li, J. (1992a). Hierarchical fuzzy comprehensive evaluation method for rock slope stability. *J. Guizhou Inst. Technol.* 21 (4), 27–35. (in Chinese).

Li, J. (1992b). Hierarchical fuzzy comprehensive evaluation method for rock slope stability. *J. Guizhou Inst. Technol.* 21 (4), 27–35. (in Chinese).

Li, Z. (1997a). Application of fuzzy analysis in slope stability evaluation. *Chin. J. Rock Mech. Eng.* 16 (5), 490–495. (in Chinese).

Li, Z. (1997b). Application of fuzzy analysis in slope stability evaluation. *Chin. J. Rock Mech. Eng.* 16 (5), 490–495. (in Chinese).

Li, Z., Fang, L., Sun, X., and Peng, W. (2021). 5G IoT-based geohazard monitoring and early warning system and its application. *EURASIP J. Wirel. Commun. Netw.* 2021 (1), 160. doi:10.1186/s13638-021-02033-y

Liu, H. M., Li, X. L., and Yu, Z. Y. (2023a). Influence of hole diameter on mechanical properties and stability of granite rock surrounding tunnels. *Phys. Fluids* 35 (6), 064121.

Liu, J., Wang, X., and Guobin, S. (2021). Study on slope disaster mechanism of inner dump in Yimin open-pit Mine. *Saf. Coal Mine* 52 (03), 234–236.

Liu, S. M., and Li, X. L. (2023a). Experimental study on the effect of cold soaking with liquid nitrogen on the coal chemical and microstructural characteristics. *Environ. Sci. Pollut. Res.* 30 (3), 36080–36097. doi:10.1007/s11356-022-24821-9

Liu, S. M., and Li, X. L. (2023b). Experimental study on the effect of cold soaking with liquid nitrogen on the coal chemical and microstructural characteristics. *Environ. Sci. Pollut. Res.* 30 (3), 36080–36097. doi:10.1007/s11356-022-24821-9

Liu, S. M., Sun, H. T., Zhang, D. M., Yang, K., Li, X., Wang, D., et al. (2023b). Experimental study of effect of liquid nitrogen cold soaking on coal pore structure and fractal characteristics. *Energy* 275 (7), 127470. doi:10.1016/j.energy.2023.127470

Ma, Y. (2020). Stability analysis and Safety evaluation analysis of dump slope. *World Nonferrous Met.* (05), 193–194. (in Chinese).

Merry, S., Kavazanjian, E., Jr, and Fritz, W. U. (2005). Reconnaissance of the july 10, 2000, payatas landfill failure. *J. Perform. Constr. Facil.* 19 (2), 100–107. doi:10.1061/(asce)0887-3828(2005)19:2(100)

Perski, Z., Ramon, H., Wojcik, A., and Wojciechowski, T. (2009). InSAR analyses of terrain deformation near the Wieliczka Salt Mine,Poland. *Eng. Geol.* 106, 58–67. doi:10.1016/j.enggeo.2009.02.014

Wan, H., Cai, D., He, X., et al. (2021). Experimental research on monitoring deep deformation of high-steep slopes by using optical fiber sensing. *J. China Three Gorges Univ. Sci.* 23 (1), 20–23. (in Chinese).

Wang, F. N., Guo, Z. B., Qiao, X. B., Fan, J., Li, W., Mi, M., et al. (2021). Large deformation mechanism of thin-layered carbonaceous slate and energy coupling support technology of NPR anchor cable in Minxian Tunnel: a case study. *Tunn. Undergr. Space Technol.* 117, 104151. doi:10.1016/j.tust.2021.104151

Wang, Q., Xu, S., Xin, Z., He, M., Huayong, W., and Jiang, B. (2022). Mechanical properties and field application of constant resistance energy-absorbing anchor cable. *Tunn. Undergr. Space Technol.* 125, 104526. doi:10.1016/j.tust.2022.104526

Wang, Q., and Tong, R. (2007a). Analysis and application of fuzzy comprehensive evaluation method in Enterprise safety evaluation. *J. North China Inst. Sci. Technol.* 3 (4), 26–31. (in Chinese).

Wang, Q., and Tong, R. (2007b). Analysis and application of fuzzy comprehensive evaluation method in Enterprise safety evaluation. *J. North China Inst. Sci. Technol.* 3 (4), 26–31. (in Chinese).

Wang, T. (2020). An open mined-out area in mine slope stability analysis. *Chin. Min. Eng.* 49 (02), 9–11. (in Chinese).

Wu, X., and Tu, Y. (2001). Methods and new development of landslide activity monitoring. *China Instrum.* (1), 10–12. (in Chinese).

Wu, X., and Tu, Y. (2002). New approach of landslide activity monitoring—probing into TDR technology. *Chin. J. Rock Mech. Eng.* 21 (5), 740–744. (in Chinese).

Xia, B., Zhang, Y., Yu, L., et al. (2001). Monitoring and treatment technology of landslide geological disasters in China. *Explor. Eng. Tunneling*, 87–90. (in Chinese).

Xia, Y., and Zhu, R. (1999). Multilevel Fuzzy Comprehensive evaluation System for rock slope stability. *J. Eng. Geol.* 7 (1).

Xiong, F., Zhu, C., Feng, G., Zheng, J., and Sun, H. (2023). A three-dimensional coupled thermo-hydro model for geothermal development in discrete fracture networks of hot dry rock reservoirs. *Gondwana Res.* 122, 331–347. doi:10.1016/j.gr.2022.12.002

Yin, Q., Wu, J. Y., Zhu, C., He, M. C., Meng, Q. X., and Jing, H. W. (2021). Shear mechanical responses of sandstone exposed to high temperature under constant normal stiffness boundary conditions. *Geomechanics Geophys. Geo-Energy Geo-Resources* 7, 35. doi:10.1007/s40948-021-00234-9

Yuan, Y., and Guo, X. (2021). Analysis on slope stability of Antaibao open-pit Mine. *Open-pit Min. Technol.* 36 (01), 76–78+82. (in Chinese).

Zhang, J. C., Li, X. L., Qin, Q. Z., Wang, Y., and Gao, X. (2023). Study on overlying strata movement patterns and mechanisms in super-large mining height stopes. *Bull. Eng. Geol. Environ.* 82 (3), 142. doi:10.1007/s10064-023-03185-5

Zhang, L., Lu, Z., Tang, S., Zhang, M., Zhang, R., Huang, Y., et al. (2021). Vegetation composition and community stability evaluation of open-pit coal mine slope. *Acta Ecol. Sin.* 41 (14), 5764–5774.

Zhang, Y., and Shi, H. (2000a). Two-stage fuzzy comprehensive evaluation of slope stability. *J. Eng. Geol.* 8 (1), 31–34.

Zhang, Y., and Shi, H. (2000b). Two-stage fuzzy comprehensive evaluation of slope stability. *J. Eng. Geol.* 8 (1), 31–34.

Zhang, Y. (2008a). *Slope engineering*. Beijing: China Architecture and Building Press, 4–8. (in Chinese).

Zhang, Y. (2008b). *Slope engineering*. Beijing: China Architecture and Building Press, 4–8. (in Chinese).

Zhou, C., Chen, W., and Guoqi, T. (2004). Study on rock body thrust monitoring system with OTDR distributing optical fiber. *Explor. Eng. Drill. Tunneling* (1), 43–46. (in Chinese).

Zhou, J. (2022). *Study on slope stability of dump in the first mining area of huolin hebei open-pit mine*. Liaoning Technical University. (in Chinese).

Zhou, J., and Tang, C. (1995). Application of fuzzy evaluation model in qualitative evaluation of centennial stability. *J. Nat. Disasters* 4 (3), 73–82.

frontiers | Frontiers in Earth Science

TYPE Original Research
PUBLISHED 31 October 2023
DOI 10.3389/feart.2023.1277147

OPEN ACCESS

EDITED BY
Zhibo Zhang,
University of Science and Technology Beijing, China

REVIEWED BY
Depeng Ma,
Shandong Agricultural University, China
Guangtan Cheng,
Shandong Agricultural University, China

*CORRESPONDENCE
Gang Huang,
tb23020009a41@cumt.edu.cn

RECEIVED 14 August 2023
ACCEPTED 26 September 2023
PUBLISHED 31 October 2023

CITATION
Yang Y, Huang G, Zhang Y and Yuan L (2023), An improved Burgers creep model of coal based on fractional-order. *Front. Earth Sci.* 11:1277147. doi: 10.3389/feart.2023.1277147

An improved Burgers creep model of coal based on fractional-order

Yongjie Yang[1], Gang Huang[2]*, Yangqiang Zhang[3] and Lei Yuan[1]

[1]State Key Laboratory of Strata Intelligent Control and Green Mining Co-Founded by Shandong Province and the Ministry of Science and Technology, Shandong University of Science and Technology, Qingdao, China, [2]State Key Laboratory of Coal Resources and Safe Mining, China University of Mining and Technology, Xuzhou, China, [3]State Key Laboratory of Gas Disaster Monitoring and Emergency Technology, China Coal Technology and Engineering Group Chongqing Research Institute, Chongqing, China

The instability and destruction of various types of coal pillars left in deep underground mining are frequently attributed to cumulative creep deformation exceeding the permissible limit, with high *in situ* stress playing a critical role in this phenomenon. To understand the complicated creep behavior of coal, triaxial compression creep tests were conducted. It has been proven that the coal specimens subjected to high confining pressure exhibit typical three-stage creep characteristics. Furthermore, with the increase in confining pressure, the creep threshold value increases while the creep threshold coefficient decreases. By fitting the creep strain-time results, an improved Burgers creep model based on fractional-order was proposed. This model can describe the primary, secondary, and tertiary stages and reflect the nonlinear behavior, contributing to the understanding of the long-term stability evaluation of deep coal pillars.

KEYWORDS

coal, triaxial creep, constitutive model, fractional-order, rheology

1 Introduction

In underground coal mining, various coal pillars are often left under surface buildings and around main entries. These pillars remain in place for an extended period, and their long-term stability is critical for the movement of the overburden and the protection of surface structures (Zhang et al., 2023a). In most cases, the failure of coal mass is not primarily due to insufficient strength but rather instability caused by long-term accumulation of creep deformation beyond the limit before reaching ultimate failure.

With the increasing mining depth, the *in situ* stress is greatly increased. In this case, coal undergoes a transition from brittle to ductile behavior, posing challenges for stability control in underground engineering(Zhang et al., 2022; Zhang et al., 2023b). One of the main challenges is the influence of rheological properties of the rock mass and the prominent creep deformation characteristics of coal pillars. These challenges are particularly pronounced in deep mines where the effects of creep are more significant. For entries with a long service life in deep mines, such as rise or dip entries, their long-term stability is directly related to mine safety and production. When determining the width of protected coal pillars, the time effect should be taken into consideration. Therefore, studying the creep behaviors of coal under high *in situ* stress, especially the triaxial creep behaviors, holds certain importance in the stability control of deep coal pillars.

In recent years, there have been many research achievements on the creep behaviors and constitutive models of rocks. For example, by adjusting the combination of units, improved creep models and corresponding constitutive equations are proposed. Some scholars have also improved some units or unit parameters in existing creep models so that the model can describe the tertiary stage. Recent studies have developed various creep models for rocks and

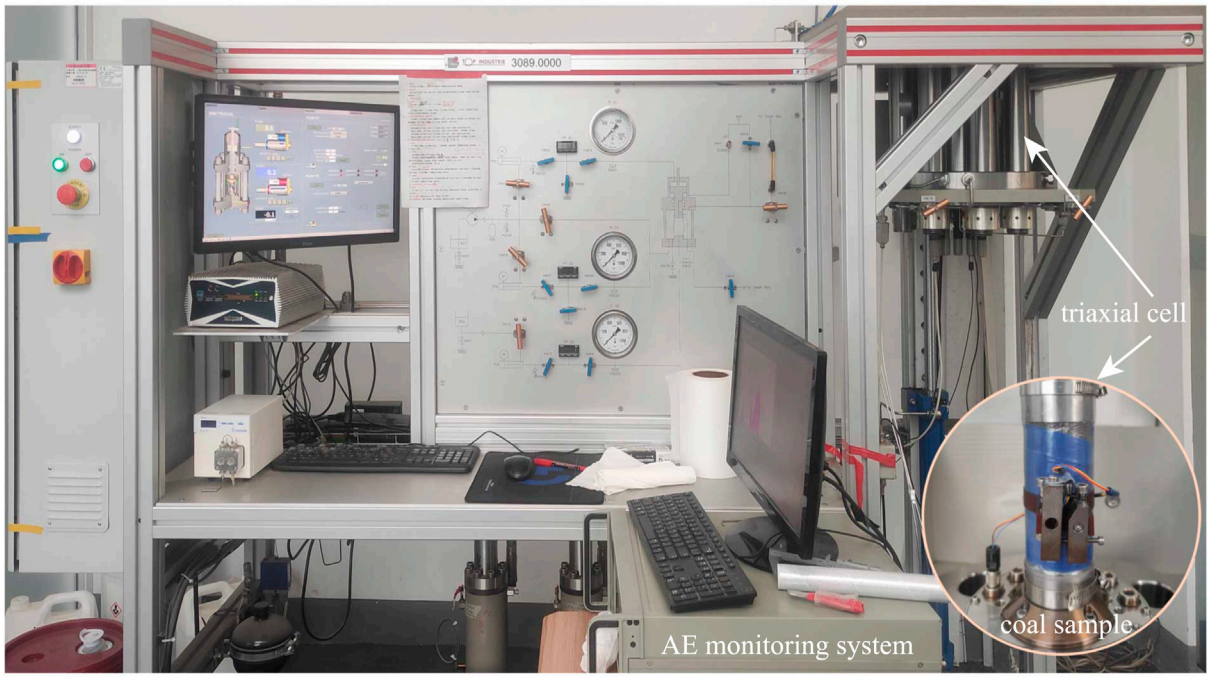

FIGURE 1
Multi-function rock triaxial testing system.

TABLE 1 Design of uniaxial and triaxial creep compression tests of coal specimens.

No.	Confining pressure (MPa)	Applied stress level (MPa)				
UCC1	0	4.0	5.0	6.0	7.0	8.0
TCC1	5	6.0	8.0	10.0	12.0	14.0
TCC2	10	10.0	12.0	14.0	16.0	18.0
TCC3	15	16.0	18.0	20.0	22.0	24.0

Note: In the coal specimen numbering, "UCC" represents uniaxial creep compression tests, and "TCC" represents triaxial creep compression tests.

minerals. Li and Yin (2021) modified the Nishihara model by incorporating an accelerating element to characterize sandstone creep. Similarly, Yan et al. (2023) established a creep model for hard flint limestone. However, Liu et al. (2017) and Shao et al. (2023) adopted an improved damage Nishihara model to simulate creep in their materials. Multi-stage creep tests on sandstone by Hou et al. (2019) led to a model with elastic, viscous and damage components. For high soft rocks, Ping et al. (2016) combined improved Burgers, Hookean and Saint Venant elements. Fractal derivative theory was applied by Yin et al. (2023) to develop a viscoelastic-plastic creep model with damage. Wu et al. (2020) and Lyu et al. (2021) used fractional Maxwell approaches, Abel dashpots and damage factors for salt rock and other materials. Li et al. (2017) compared Burgers, Nishihara and extended Nishihara models for coal under varying gas conditions. Other recent work includes modified Burgers (Ran et al., 2021) and pore pressure-based (Zhang et al., 2023c) models. Short-term nonlinear creep with damage was analyzed by Yang et al. (2015) using the Burgers equation. Zhang et al. (2019) introduced a negative elastic modulus and a non-Newtonian component into the classical Nishihara model based on the theoretical analysis of the experimental results. Cheng et al. (2020) established a creep hardening damage model considering the viscosity damage factor of coal. In summary, a range of improved constitutive relationships have been proposed through integrating additional elements and mechanisms.

Through existing literature, it is known that the research scope of rock rheology is wide. Researchers, based on traditional sciences such as material mechanics, fracture damage mechanics, elastoplastic theory, and rheological principles, analyze existing rheological models, or develop improved mechanical models based on test data. However, most of the literature studying the creep constitutive relationship of rocks has focused on rock and soil materials such as sandstone, shale, mudstone, soil, and filling materials. There are relatively few studies involving the creep constitutive relationships of coal, and many issues remain unclear, particularly regarding coal's triaxial creep constitutive relationships.

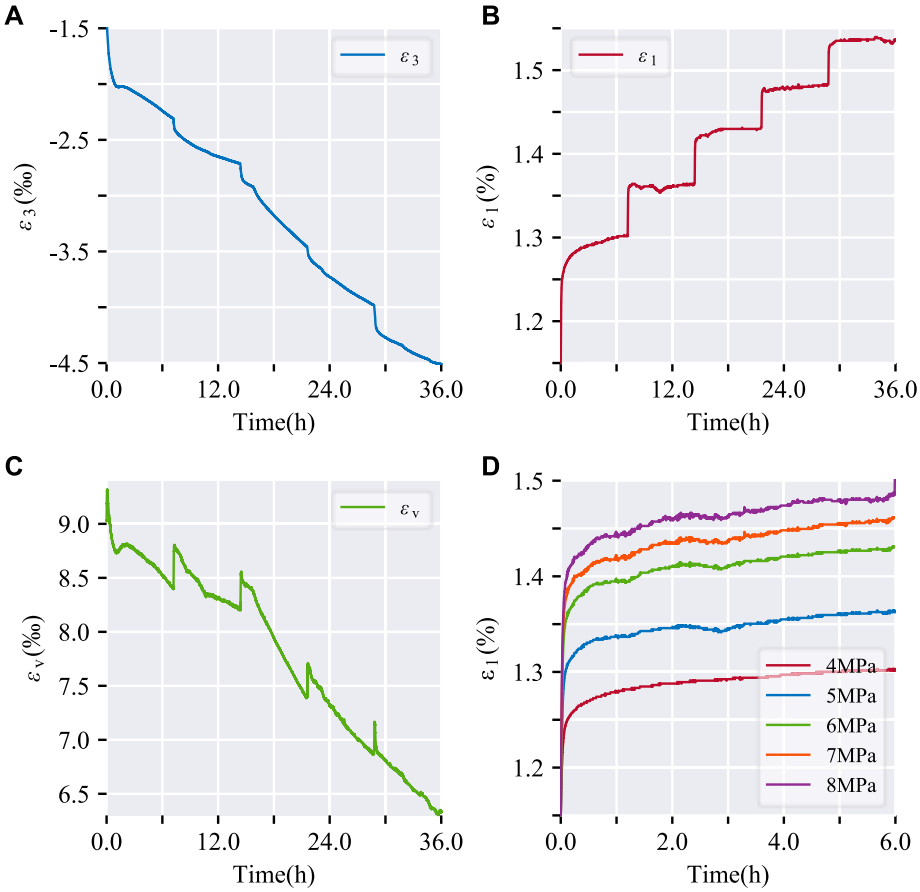

FIGURE 2
Strain-time curves of coal specimen (No.UCC1) under uniaxial compression creep. **(A)** diametric strain over time; **(B)** axial strain over time; **(C)** volumetric strain over time; **(D)** axial strain over time at different applied stress level.

This paper conducted triaxial compression creep tests on coal, by fitting the test results, the adaptability of Burgers equation was verified. Then an improved Burgers creep model based on fractional-order was proposed, which can describe the primary, secondary and tertiary stages of triaxial creep of coal specimens and reflect nonlinear behaviors.

2 Triaxial compression creep test of coal

2.1 Specimen preparation

The coal specimens tested in this work were extracted from the No. 3 seam at Yangcheng Coal Mine, Jining City, Shandong Province, China. This coal seam ranges between 5.54 and 7.78 m thick with a bulk density of 1.35 kN/m^3. Intact coal blocks lacking substantial joints were chosen for specimen preparation (Liu et al., 2023; Liu and Li, 2023). Vertical coring techniques were utilized to obtain cylindrical specimens, which were processed to standard dimensions (diameter × height = 50 × 100 mm) based on International Society of Rock Mechanics (ISRM) recommended practice(ISRM, 1978; Bieniawski and Bernede, 1979; ISRM, 1983). This ensured consistent sample geometry and conditions across the testing program.

2.2 Apparatus

The traditional triaxial compression ($\sigma_2 = \sigma_3$) creep test of the coal specimens was conducted using the TOP INDUSTRIE STAC 600-600 multifunctional rock triaxial testing system (Figure 1). This testing system can perform uniaxial compression, traditional triaxial compression tests, as well as uniaxial and triaxial compression creep tests on rocks. It enables the investigation of the short-term and long-term deformation and strength properties of rocks, as well as the evolution of permeability properties during the deformation process of rocks.

2.3 Triaxial compression creep test plan

2.3.1 Loading mode

The loading methods for creep tests on coal specimens generally include single-step loading, stepwise loading, and cyclic loading/unloading. For different applied stress levels,

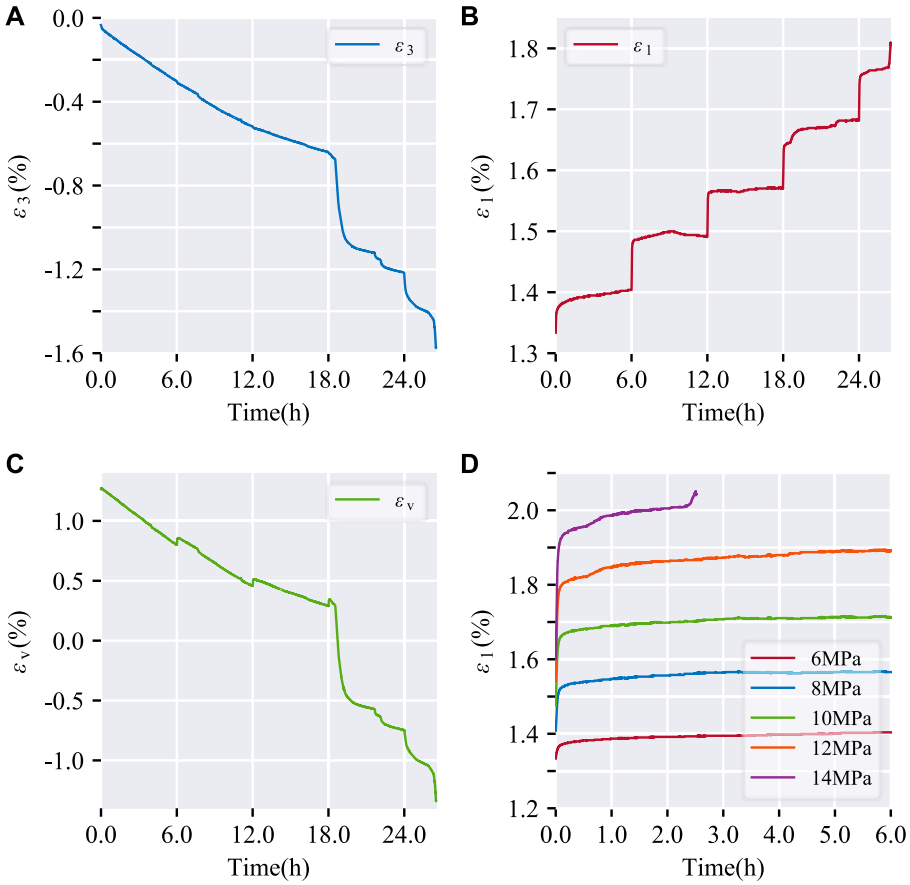

FIGURE 3
Strain-time curves of coal specimen (No.TCC1) under triaxial compression creep (σ_3=5 MPa). **(A)** diametric strain over time; **(B)** axial strain over time; **(C)** volumetric strain over time; **(D)** axial strain over time at different applied stress level.

single-step loading requires conducting separate tests for each specimen, which clearly consumes more time, demands a larger number of coal specimens, and imposes higher requirements on the testing equipment. Due to the significant variability among coal specimens, the use of single-step loading is not advisable. On the other hand, stepwise loading involves testing the same coal specimen, with the next applied stress level loaded after the specimen reaches stable creep deformation at the previous stress level. Compared to single-step loading, stepwise loading effectively mitigates the impact of specimen variability on test results (Tan and Kang, 1980).

2.3.2 Applied stress level

The magnitude of the applied stress is typically set between 12.5% and 80% (Griggs, 1939) of the compressive strength. The triaxial compressive strength of the coal specimens at different confining pressures (0 MPa, 5 MPa, 10 MPa, and 15 MPa) is as follows: 10.2 MPa, 12.3 MPa, 14.5 MPa, and 17.8 MPa, respectively. Based on the results of compression tests on the specimens, the applied stress was divided into five levels at 40%, 50%, 60%, 70%, and 80% of their respective compressive strengths.

2.3.3 Test duration

To avoid excessive equipment consumption, it is not possible to load for too long test duration. At the same time, the triaxial compression strength of the coal specimens is relatively low, so the creep time for each applied stress level was determined to be 6 h. This duration allows for the manifestation of creep characteristics within a short period of time.

2.3.4 Test design

As shown in Table 1, a uniaxial compression creep test and three triaxial compression creep tests were designed for coal specimens under different confining pressures (5 MPa, 10 MPa, and 15 MPa).

2.4 Test results

2.4.1 Macroscopic deformation characteristics

Figures 2–5 show the creep deformation results of each coal specimen under different confining pressures (0 MPa, 5 MPa, 10 MPa, and 15 MPa), ε_1, ε_3, and ε_v represent axial strain, circumferential strain, and volumetric strain, respectively.

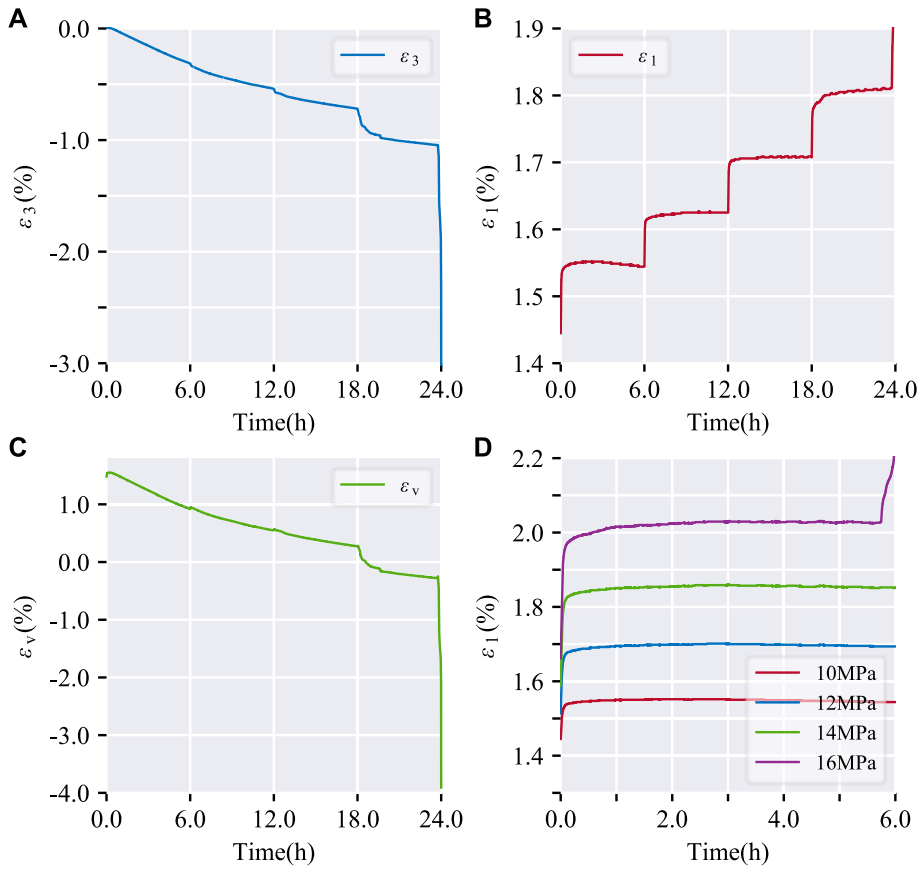

FIGURE 4
Strain-time curves of coal specimen (No.TCC2) under triaxial compression creep (σ_3=10 MPa). **(A)** diametric strain over time; **(B)** axial strain over time; **(C)** volumetric strain over time; **(D)** axial strain over time at different applied stress level.

From Figures 2–5, it can be observed that the diametric strain-time curve, axial strain-time curve, and volumetric strain-time curve all exhibit a stepped pattern. The circumferential strain, axial strain, and volumetric strain increase continuously with the prolongation of loading time, indicating a clear creep behavior of the coal specimens.

Uniaxial creep tests displayed stable time-dependent deformation without tertiary creep (Figure 2D). Under triaxial conditions, moderate stress levels induced stable creep with distinguishable primary and secondary regimes (Figures 3D, 4D, 5D). However, the highest stress state resulted in unstable tertiary creep characterized by acceleration after secondary creep. Coal specimen No.TCC3 exemplified the stress-controlled transition at 20 MPa–below this axial level, the creep rate gradually declined and stabilized over time. Beyond 20 MPa, significant creep rate increase emerged following the secondary stage, indicative of tertiary creep onset.

2.4.2 Creep strength characteristics

It can be seen from Section 2.4.1 that there are obvious stress thresholds during the deformation process of coal specimens, such as the minimum stress level for creep deformation, and the stress level where tertiary creep occurs. Table 2 shows the calculated results of the creep strength characteristics parameters.

(1) Coal specimens exhibit a creep threshold under varying confining pressures. Below this threshold axial stress, no creep occurs. At the threshold stress, significant creep phenomena emerge, with distinct primary and secondary creep stages observed. Furthermore, increasing confining pressure elevates the creep threshold continuously for two reasons: first, higher confinement corresponds to greater uniaxial strength, necessitating larger applied creep stresses; second, stronger circumferential constraints impose a larger threshold for creep initiation.
(2) In terms of the creep threshold coefficient, the values are 0.50, 0.47, 0.63 and 0.64 under 0 MPa, 5 MPa, 10 MPa and 15 MPa confining pressures, respectively, which are lower than the general creep threshold coefficient for rocks.
(3) Regarding the creep strength, the creep strength of coal specimens under different confining pressures is less than their uniaxial compressive strength, exhibiting significant creep characteristics. Under 0 MPa, 5 MPa, 10 MPa, and 15 MPa confining pressures, the creep strengths are 0.78, 0.74, 0.65, and 0.56 times the corresponding uniaxial

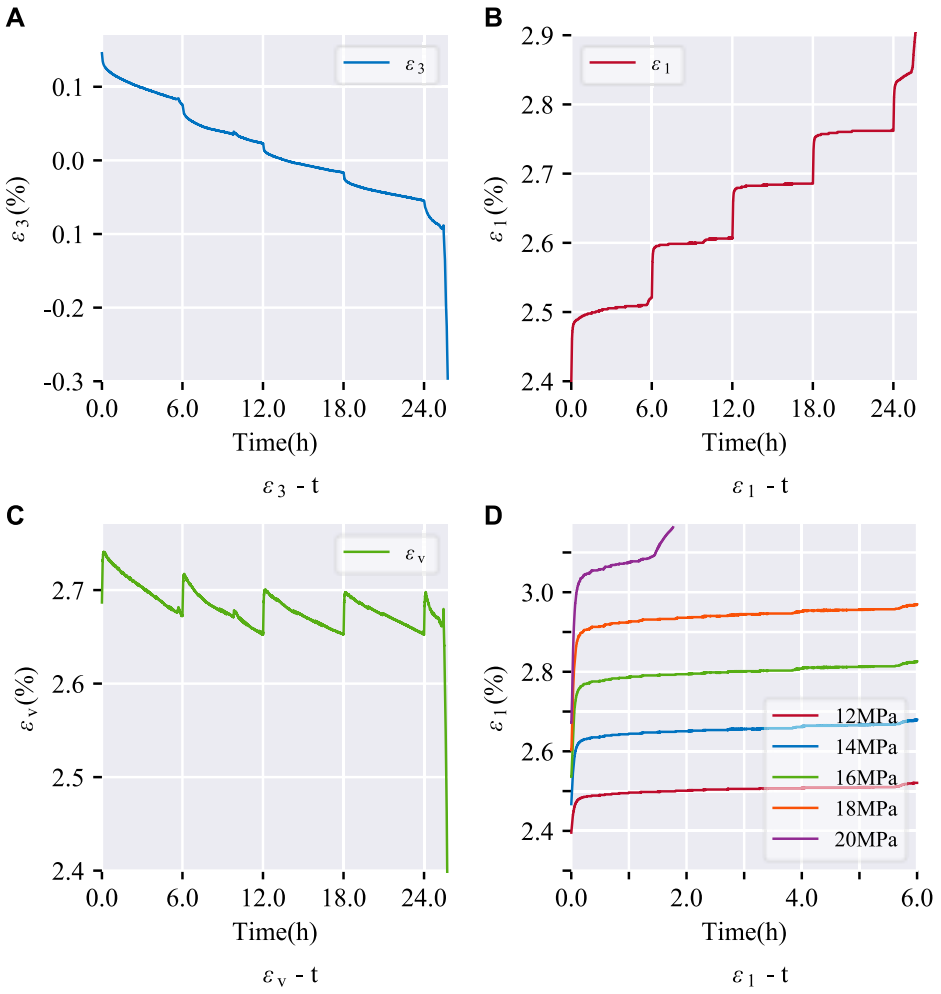

FIGURE 5
Strain-time curves of coal specimen (No.TCC3) under triaxial compression creep (σ_3=15 MPa). **(A)** diametric strain over time; **(B)** axial strain over time; **(C)** volumetric strain over time; **(D)** axial strain over time at different applied stress level.

TABLE 2 Calculation results of creep strength characteristics parameters for coal specimens.

No.	σ_3 (MPa)	Creep threshold (MPa)	Creep threshold coefficient	Creep strength (MPa)	Creep coefficient
UCC1	0	4.0	0.50	8.0	0.78
TCC1	5	6.0	0.47	12.83	0.74
TCC2	10	10.0	0.63	15.90	0.65
TCC3	15	12.0	0.64	18.47	0.56

Note: The creep threshold refers to the minimum stress level at which creep deformation begins to occur in the coal specimen. Creep strength corresponds to the maximum stress at which creep failure occurs in the coal specimen during a creep test. The creep threshold coefficient is defined as the ratio of the creep threshold value to the creep strength. The creep coefficient is defined as the ratio of creep strength to the peak stress attained during a triaxial compression test.

compressive strengths, decreasing with increasing confining pressure.

(4) At the final stress level, tertiary creep occurred under 5 MPa, 10 MPa, and 15 MPa confining pressures, resulting in considerable deformation that severely weakened the mechanical properties of the coal specimens, leading to unstable failure.

3 Improved Burgers creep model based on fractional-order

The previous section conducted triaxial compression creep tests on coal. From the creep curves, it can be observed that coal exhibits mechanical behaviors such as elasticity and plasticity. Therefore, it is feasible to approximate the creep characteristics of coal using

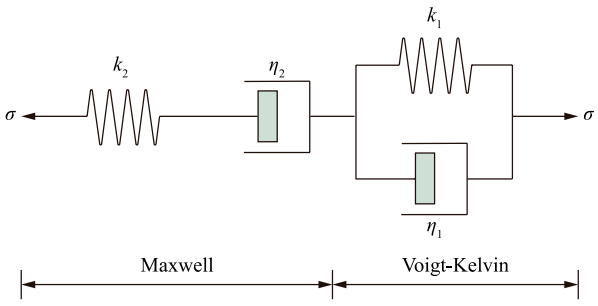

FIGURE 6
Burgers model.

abstract mechanical models and establish its constitutive relationship.

3.1 Fitting of the Burgers model

Based on Li's research Li et al. (2017), it was determined that the Burgers model provides a superior representation of the three stages of the creep process in coal compared to other models. Consequently, the Burgers model was chosen for fitting. The Burgers model consists of Maxwell and Voigt-Kelvin elements connected in series, as depicted in Figure 6. The constitutive relationship for creep of this model is presented in Equation 1.

$$\varepsilon = \frac{\sigma}{k_2} + \frac{\sigma}{\eta_2} + \frac{\sigma}{k_1}\left(1 - e^{-\frac{k_1}{\eta_1}t}\right) \tag{1}$$

where k_1, k_2 are the stiffness of the springs in the Maxwell and Voigt-Kelvin model, respectively; η_1, η_2 are the viscosity coefficients of the dashpots in the Maxwell and Voigt-Kelvin model, respectively.

The fitting curve of the Burgers model is shown in Figure 7. It can be observed that the Burgers model exhibits instantaneous deformation and a primary creep stage. It includes a linear term, allowing it to reflect steady creep characteristics. However, a limitation of the model is that it has only one inflection point and cannot capture accelerated creep behavior.

3.2 Fractional-order improved Burgers model

As mentioned in Section 3.1, the main limitation of the Burgers model is its inability to capture tertiary creep behavior in coal specimens. The Newtonian unit in the model has purely linear and extremely viscous characteristics, making it difficult to reflect the nonlinear creep features of coal specimens. Therefore, improving the Burgers model is necessary.

3.2.1 Introduction to fractional calculus

In classical calculus, the German mathematician Leibniz used $d^n y(x)/dx^n$ (where n is a positive integer) to represent derivatives of different orders. Fractional-order calculus (non-integer calculus) directly extends integer-order calculus (Hassouna et al., 2022), where n is expanded from positive integers to fractions, complex numbers, and other levels.

Hence, when $n \in (0,1)$, it indicates the medium's properties lie between those of an ideal solid and fluid. As shown in Figure 8, in fractional-order models, the Abel dashpot in fractional-order models represents this behavior (Koeller, 1984), with the constitutive relationship:

$$\sigma(t) = \eta \frac{d^n \varepsilon}{dt^n} \tag{2}$$

where n is the order, $n \in (0,1)$; η is the viscosity coefficient of the Abel dashpot.

3.2.2 Fractional-order Burgers model

The one-dimensional fractional-order Burgers model comprises fractional-order Maxwell and Voigt-Kelvin elements connected in series (Figure 9). The governing creep equation is:

$$\varepsilon = \frac{\sigma}{k_2} + \frac{\sigma}{\eta_2} \cdot \frac{t^\beta}{\Gamma(1+\beta)} + \frac{\sigma}{k_1}\left[1 - E_\alpha\left(-\left(\frac{k_1}{\eta_1}t\right)^\alpha\right)\right] \tag{3}$$

where α, β are the orders of the Abel dashpot in the fractional-order Maxwell and Voigt-Kelvin model, respectively. E_α represents the single-parameter Mittag-Leffler function in fractional-order calculus, and $\Gamma(1+\beta)$ denotes the Gamma Function.

As observed in Figure 10, the fractional-order Burgers model can accurately capture the nonlinear characteristics of coal specimens during the primary and secondary creep stages. The fitting results are more precise, as exemplified under 6 MPa axial stress (Figure 10B). The experimental data largely falls within the 95% confidence interval.

Underground coal formations are mostly subjected to a triaxial stress state. Therefore, it is necessary to extend the fractional-order Burgers model from one-dimensional to three-dimensional to reflect the creep characteristics of coal more accurately. The creep equation for the three-dimensional fractional-order Burgers model is given by:

$$\varepsilon_1 = \begin{aligned} &\frac{\sigma_1 + 2\sigma_3}{9K} + \frac{\sigma_1 - \sigma_3}{3G_2} + \frac{\sigma_1 - \sigma_3}{3\eta_2} \cdot \frac{t^\beta}{\Gamma(1+\beta)} \\ &+ \frac{\sigma_1 - \sigma_3}{3G_1}\left[1 - E_\alpha\left(-\left(\frac{k_1}{\eta_1}t\right)^\alpha\right)\right] \end{aligned} \tag{4}$$

where K is the volumetric modulus of the coal specimen, G_1, G_2 are the shear modulus of the Abel dashpot in the fractional-order Maxwell and Voigt-Kelvin model, respectively.

The triaxial creep response was modeled using a 3D fractional-order Burgers formulation. As shown in Figure 11, good agreement was obtained between the primary and secondary creep stages experimentally observed for coal specimens and the theoretical fit. The nonlinear creep behavior was effectively captured within a 95% confidence interval under representative conditions of 15 MPa confinement and 18 MPa axial stress. However, limitations were evident under sustained loading approaching failure, where the model deviated from

measured tertiary creep characterized by accelerating strain accumulation.

3.2.3 Improved fractional-order Burgers model

3.2.3.1 Property of Abel dashpot

From the constitutive equation of the Abel dashpot (Eq. 2), the creep equation can be derived as follows:

$$\varepsilon = \frac{\sigma}{\eta} \cdot \frac{t^n}{\Gamma(1+n)} \tag{5}$$

In this study, with a reference condition of σ = 15 MPa and ξ = 3 GPa s, the characteristics of strain with respect to the order n in the Abel dashpot are discussed. As shown in Figure 12, changing the order of the Abel dashpot results in different curves. When the order n is less than 1.0, the curve exhibits a concave shape. When the order n is greater than 1.0, the creep curve shows a convex shape, resembling a tertiary creep curve. Therefore, an Abel dashpot with an order greater than 1.0 can be used to reflect the tertiary creep characteristics of the coal specimen.

3.2.3.2 Improved fractional-order ideal viscoplastic model

From the results of the triaxial compression creep tests, it can be observed that prior to the final stage of stress loading, the coal specimen undergoes primary creep and then enters the stage of secondary creep. Only after a certain period following the final loading stage does the coal specimen exhibit tertiary creep. This indicates two conditions must be met for tertiary creep to occur: first, the applied stress level magnitude must exceed the threshold for tertiary creep; second, the loading time must reach the initiation time for tertiary creep. In the presence of Coulomb elements, the fractional viscoplastic model exhibits distinct behavior. When the applied stress level is below the critical stress value (σ_s), the model initially experiences rapid deformation, which then gradually stabilizes over time. Conversely, when the applied stress level exceeds the critical stress value (σ_s), the fractional viscoplastic model enters an unstable creep phase, clearly fulfilling the first condition for tertiary creep. However, it's important to note that this model lacks time-related components, and therefore, it does not satisfy the second condition for tertiary creep as per the requirements of fractional viscoplastic models.

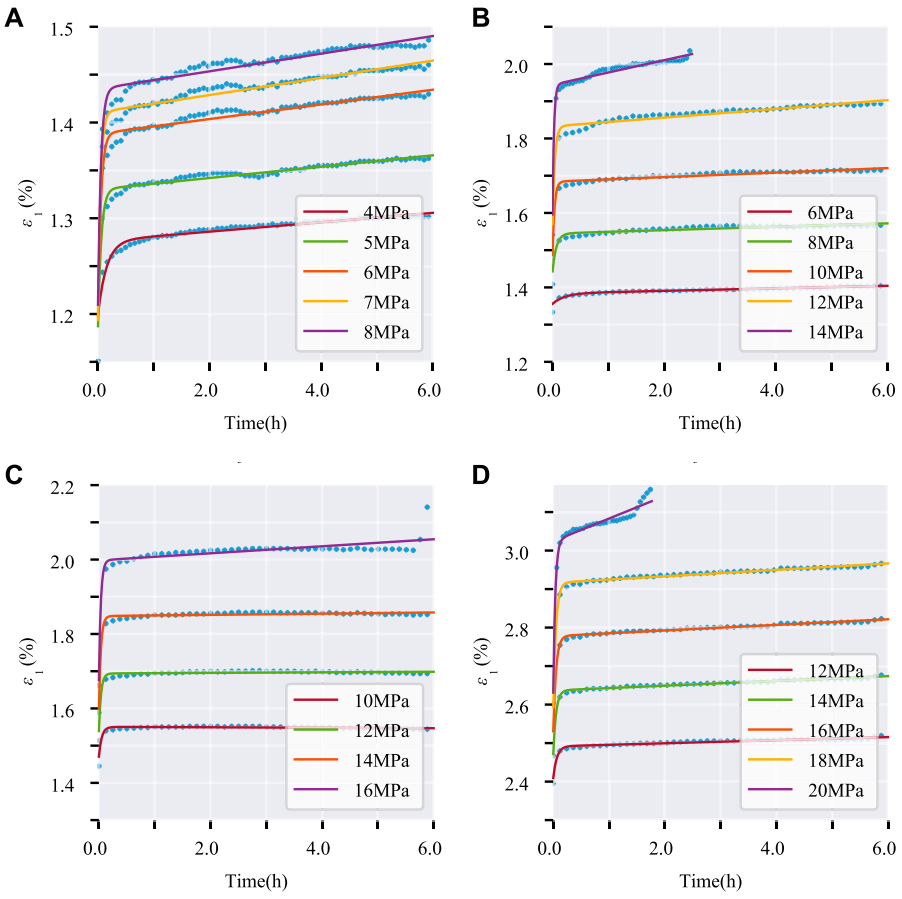

FIGURE 7
Burgers model fitting. **(A)** axial creep curve fitting; **(B)** triaxial creep curve fitting (σ_3=5 MPa); **(C)** triaxial creep curve fitting (σ_3=10 MPa); **(D)** triaxial creep curve fitting (σ_3=15 MPa).

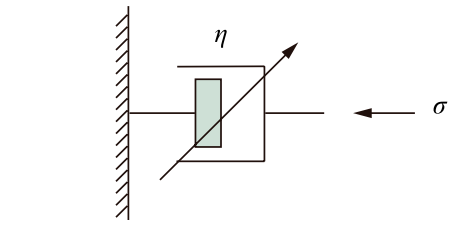

FIGURE 8
Abel dashpot.

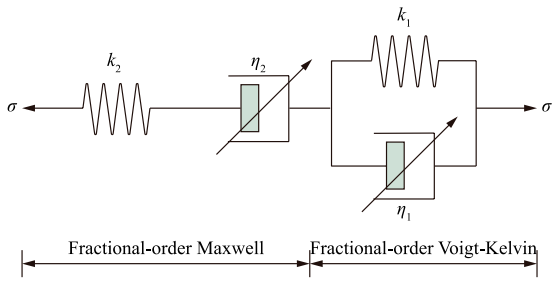

FIGURE 9
Fractional-order Burgers model.

3.2.3.3 Improved fractional-order Burgers model

In order to capture the tertiary creep characteristics of the coal specimen, as shown in Figure 13, an additional "switch" unit is introduced into the fractional-order ideal viscoplastic model. The tertiary creep only occurs when the loading time reaches the initiation time for tertiary creep (t_a) and the applied stress level exceeds the critical stress level. When $t > t_a$, the constitutive equation for fractional-order ideal viscoplastic model can be derived as follows:

$$\varepsilon = \frac{\sigma - \sigma_s}{\eta} \cdot \frac{(t - t_a)^{\gamma}}{\Gamma(1+\gamma)} \tag{6}$$

where, γ is the order of the Abel dashpot in the fractional-order ideal viscoplastic model, γ >1.0; t_a is the initiation time for tertiary creep; σ_s is the initiation applied stress level for tertiary creep.

An enhanced fractional-order Burgers model was developed by incorporating an improved fractional-order viscoelastic component, as illustrated in Figure 14.

In a uniaxial stress state, when $t < t_a$, the creep equation is given by:

$$\varepsilon = \frac{\sigma}{k_2} + \frac{\sigma}{\eta_2} \cdot \frac{t^{\beta}}{\Gamma(1+\beta)} + \frac{\sigma}{k_1}\left[1 - E_{\alpha}\left(-\left(\frac{k_1}{\eta_1}t\right)^{\alpha}\right)\right] \tag{7}$$

In a uniaxial stress state, when $t \geq t_a$ and $\sigma \geq \sigma_s$, the creep equation is given by:

$$\varepsilon = \frac{\sigma}{k_2} + \frac{\sigma}{\eta_2} \cdot \frac{t^{\beta}}{\Gamma(1+\beta)} + \frac{\sigma}{k_1}\left[1 - E_{\alpha}\left(-\left(\frac{k_1}{\eta_1}t\right)^{\alpha}\right)\right] + \frac{\sigma - \sigma_s}{\eta_3} \cdot \frac{(t - t_a)^{\gamma}}{\Gamma(1+\gamma)} \tag{8}$$

In a triaxial stress state, based on Eq. 7, when $t \geq t_a$ and σ_1-$\sigma_3 < \sigma_s$, we have:

$$\varepsilon_1 = \frac{\sigma_1 + 2\sigma_3}{9K} + \frac{\sigma_1 - \sigma_3}{3G_2} + \frac{\sigma_1 - \sigma_3}{3\eta_2} \cdot \frac{t^{\beta}}{\Gamma(1+\beta)} + \frac{\sigma_1 - \sigma_3}{3G_1}\left[1 - E_{\alpha}\left(-\left(\frac{k_1}{\eta_1}t\right)^{\alpha}\right)\right] \tag{9}$$

In a triaxial stress state, based on Eq. 8, when $t \geq t_a$ and σ_1-$\sigma_3 \geq \sigma_s$, we have:

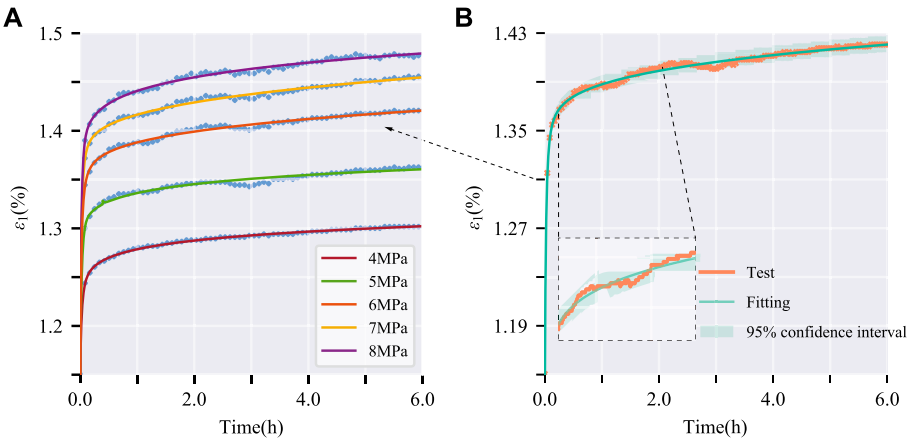

FIGURE 10
Fitting of uniaxial creep curve based on fractional-order Burgers model. **(A)** Fitting curve at different applied stress level; **(B)** Zoomed in fitting curve at 6 MPa applied stress level.

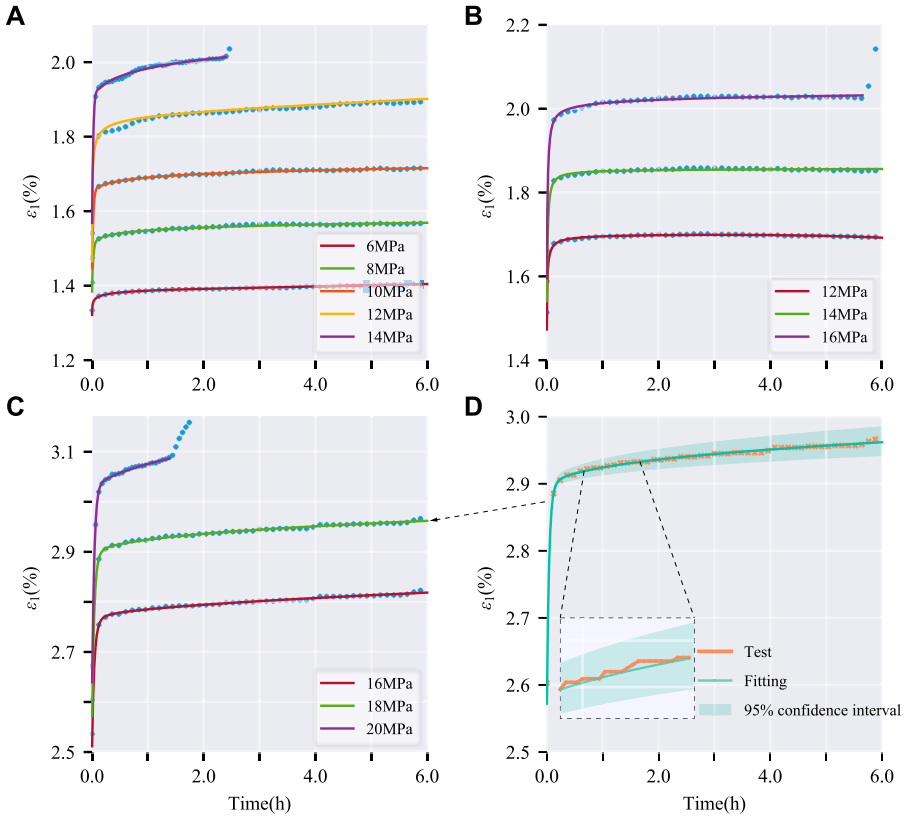

FIGURE 11
Fitting of triaxial creep curve based on fractional-order Burgers model. **(A)** σ_3=5 MPa; **(B)** σ_3=10 MPa; **(C)** σ_3=15 MPa; **(D)** Zoomed in fitting curve at 18MPa applied stress level.

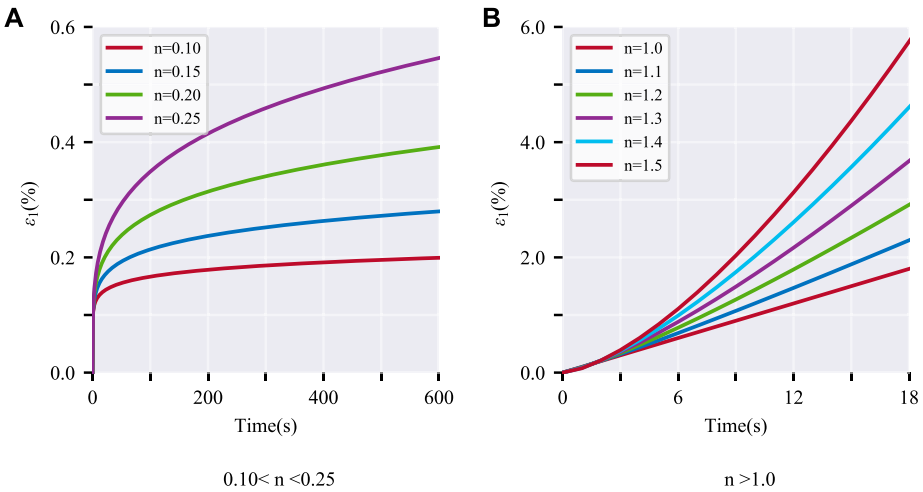

FIGURE 12
Abel dashpot creep curves at different orders. **(A)** 0.10 < n < 0.25; **(B)** n > 1.

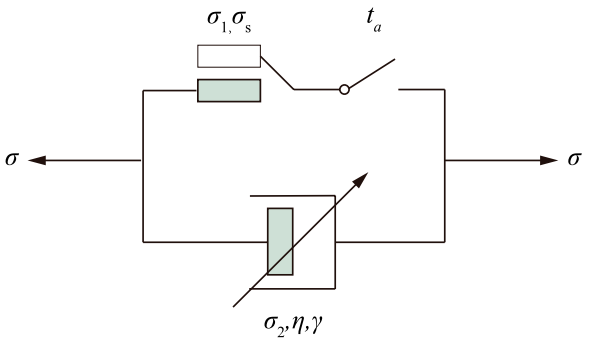

FIGURE 13
Improved fractional-order ideal viscoplastic model. σ_1 is the stress on the Coulomb element, and σ_2 is the stress on the Abel dashpot.

$$\varepsilon_1 = \frac{\sigma_1 + 2\sigma_3}{9K} + \frac{\sigma_1 - \sigma_3}{3G_2} + \frac{\sigma_1 - \sigma_3}{3\eta_2} \cdot \frac{t^{\beta}}{\Gamma(1+\beta)} + \frac{\sigma_1 - \sigma_3}{3G_1}\left[1 - E_{\alpha}\left(-\left(\frac{k_1}{\eta_1}t\right)^{\alpha}\right)\right] + \frac{\sigma_1 - \sigma_3 - \sigma_s}{3\eta_3} \cdot \frac{(t - t_a)^{\gamma}}{\Gamma(1+\gamma)} \quad (10)$$

3.2.3.4 Parameter identification of improved fractional-order Burgers creep model

According to Eqs 7–10, the improved fractional-order Burgers model has a total of 13 parameters: α, β, γ, k_1, k_2, K, G_1, G_2, η_1, η_2, η_3, t_a, and σ_s. These parameters can be roughly divided into two categories:

The first parameter group comprises values readily obtained from experimental creep tests. Examples are the volumetric modulus K, the initiation time t_a for tertiary creep onset, and the critical applied stress σ_s inducing instability.

The second group contains parameters derived by model optimization to experimental data. Examples include the order of Abel dashpots (α, β, γ), viscosity coefficients (η_1, η_2, η_3), spring stiffness values (k_1, k_2), and shear moduli of springs (G_1, G_2).

Fitting of the triaxial creep curve of coal specimens was carried out using Eq. 10, and the results are shown in Figure 15 below.

Model calibration was conducted by fitting Eq. 10 to experimental triaxial creep curves obtained for the coal specimens, with results depicted in Figure 15.

The triaxial creep response modeled by the enhanced fractional Burgers formulation showed good agreement with experimental coal data across the entire creep process, as evidenced in Figure 15. In particular, the nonlinear primary and tertiary creep regimes were well captured, demonstrating adaptability of the improved model.

4 Discussion

This work implemented triaxial creep testing on coal specimens and developed an enhanced fractional-order Burgers formulation capable of representing primary, secondary and tertiary creep regimes. The nonlinear creep-time behavior was well characterized, improving constitutive modeling of coal creep with implications for deep coal pillar stability assessments. Compared to traditional creep models, the tertiary stage was better captured by the modified approach. Limitations remain, as damage mechanisms and stress-dependent effects were not incorporated, while the physical basis of the accelerating component requires further elucidation.

5 Conclusion

The creep-time curve of the coal specimen exhibits typical three-stage characteristics, namely primary creep, secondary creep, and tertiary creep stages. At higher confining pressures, the duration of the applied stress level corresponding to tertiary creep is shorter.

Through curve fitting procedures, the adaptability of the Burgers model to the test results was validated. The Burgers model demonstrated capacity to adequately characterize the primary and secondary creep regimes in triaxial creep tests on coal specimens. However, a limitation was evident in the model's inability to capture tertiary creep phenomena.

In response to the restrictions of the Burgers model, this study presents an enhanced fractional-order Burgers creep model, which has been expanded from one dimension to three dimensions. In order to better account for the acceleration tendencies observed in

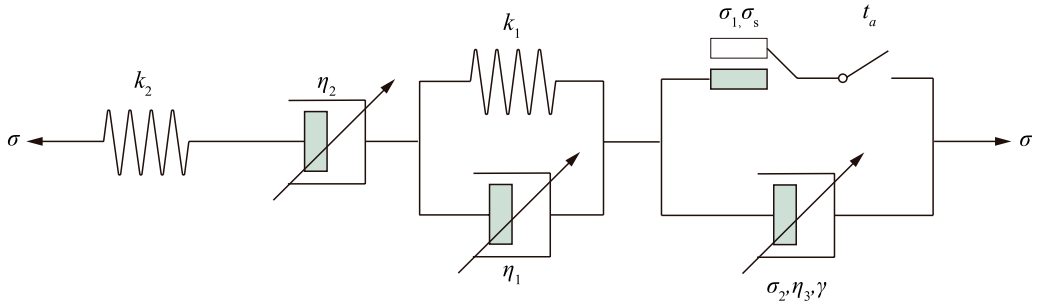

FIGURE 14
Improved fractional-order Burgers model.

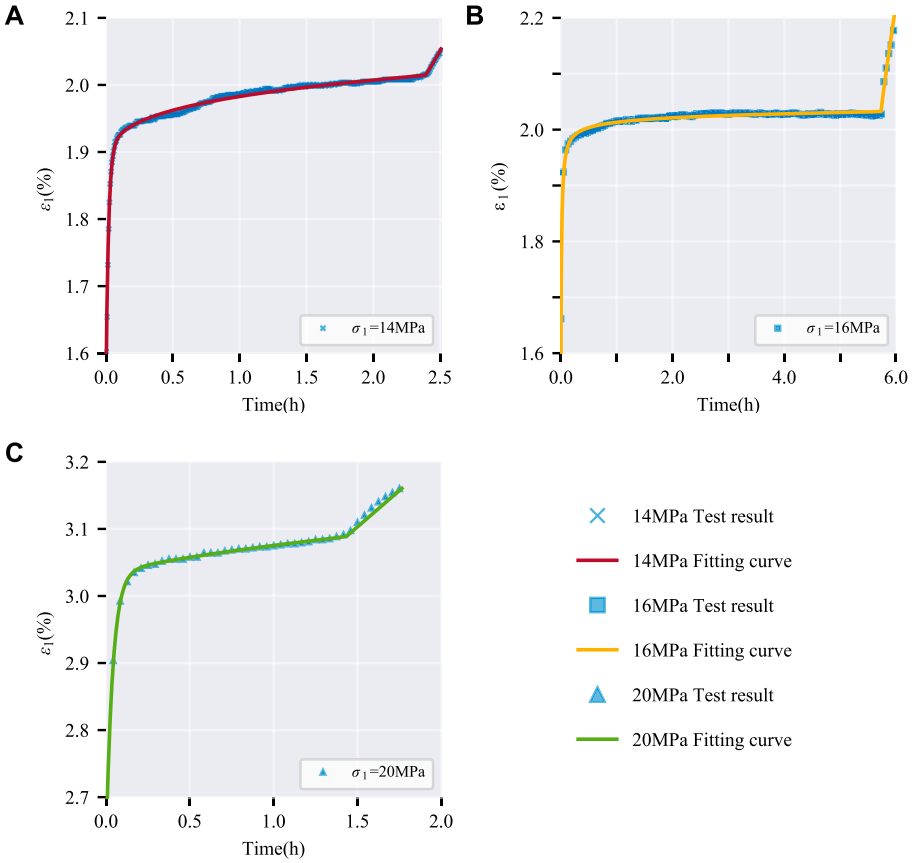

FIGURE 15
Tertiary creep curve fitting of improved fractional-order Burgers model. **(A)** σ_3=5 MPa; **(B)** σ_3=10 MPa; **(C)** σ_3=15 MPa.

the triaxial creep behavior of coal samples, the fractional-order ideal viscoplastic model was adapted with the inclusion of a time-dependent switching mechanism. This modified model effectively captures the complete triaxial creep progression in coal, demonstrating substantial fitting capability and accurately portraying the nonlinear attributes inherent to coal specimen triaxial creep.

Data availability statement

The raw data supporting the conclusions of this article will be made available by the authors, without undue reservation.

Author contributions

YY: Writing–original draft, Funding acquisition, Writing–review and editing. GH: Writing–original draft, Writing–review and editing. YZ: Writing–review and editing, Data curation, Formal Analysis. LY: Data curation, Formal Analysis, Writing–review and editing.

Funding

The authors declare financial support was received for the research, authorship, and/or publication of this article. This research was funded by the Natural Science Foundation of Shandong Provincial (Grant Nos. ZR2022ME195).

Conflict of interest

The authors declare that the research was conducted in the absence of any commercial or financial relationships that could be construed as a potential conflict of interest.

Publisher's note

References

Bieniawski, Z. T., and Bernede, M. J. (1979). Suggested methods for determining the uniaxial compressive strength and deformability of rock materials. *Int. J. Rock Mech. Min. Sci. Geomech. Abstr.* 16, 138–140. doi:10.1016/0148-9062(79)91451-7

Cheng, Q., Li, H., Huang, B., and Zhao, X. (2020). Creep hardening damage constitutive model of coal with fracture proppant. *J. Geophys. Eng.* 17, 1026–1036. doi:10.1093/jge/gxaa061

Griggs, D. (1939). Creep of rocks. *J. Geol.* 47, 225–251. doi:10.1086/624775

Hassouna, M., El Kinani, E. H., and Ouhadan, A. (2022). "Chapter thirteen - fractional calculus: applications in rheology," in *Fractional order systems*. Editors A. G. Radwan, F. A. Khanday, and L. A. Said (Cambridge, Massachusetts, United States: Academic Press), 513–549.

Hou, R. B., Zhang, K., Tao, J., Xue, X., and Chen, Y. (2019). A nonlinear creep damage coupled model for rock considering the effect of initial damage. *Rock Mech. Rock Eng.* 52, 1275–1285. doi:10.1007/s00603-018-1626-7

ISRM (1978). Suggested methods for determining the strength of rock materials in triaxial compression. *Int. J. Rock Mech. Min. Sci. Geomech. Abstr.* 15, 47–51. doi:10.1016/0148-9062(78)91677-7

ISRM (1983). Suggested methods for determining the strength of rock materials in triaxial compression: revised version. *Int. J. Rock Mech. Min. Sci. Geomech. Abstr.* 20, 285–290. doi:10.1016/0148-9062(83)90598-3

Koeller, R. C. (1984). Applications of fractional calculus to the theory of viscoelasticity. *J. Appl. Mech.* 51, 299–307. doi:10.1115/1.3167616

Li, X. C., Yang, C. L., Ren, T., Nie, B., Zhao, C., Liu, S., et al. (2017). Creep behaviour and constitutive model of coal filled with gas. *Int. J. Min. Sci. Technol.* 27, 847–851. doi:10.1016/j.ijmst.2017.07.017

Li, X. F., and Yin, Z. X. (2021). Study of creep mechanical properties and a rheological model of sandstone under disturbance loads. *Processes* 9, 1291. doi:10.3390/pr9081291

Liu, H. Z., Xie, H. Q., He, J. D., Xiao, M. L., and Zhuo, L. (2017). Nonlinear creep damage constitutive model for soft rocks. *Mech. Time-Dependent Mater*, 21, 73–96. doi:10.1007/s11043-016-9319-7

Liu, S. M., and Li, X. L. (2023). Experimental study on the effect of cold soaking with liquid nitrogen on the coal chemical and microstructural characteristics. *Environ. Sci. Pollut. Res.* 30, 36080–36097. doi:10.1007/s11356-022-24821-9

Liu, S., Sun, H., Zhang, D., Yang, K., Li, X., Wang, D., et al. (2023). Experimental study of effect of liquid nitrogen cold soaking on coal pore structure and fractal characteristics. *Energy* 275, 127470. doi:10.1016/j.energy.2023.127470

Lyu, C., Liu, J. F., Ren, Y., Liang, C., and Liao, Y. (2021). Study on very long-term creep tests and nonlinear creep-damage constitutive model of salt rock. *Int. J. Rock Mech. Min. Sci.* 146, 104873. doi:10.1016/j.ijrmms.2021.104873

Ping, C., Wen, Y. D., Wang, Y. X., Haiping, Y., and Bingxiang, Y. (2016). Study on nonlinear damage creep constitutive model for high-stress soft rock. *Environ. Earth Sci.* 75, 900. doi:10.1007/s12665-016-5699-x

Ran, H. Y., Guo, Y. X., Feng, G. R., Qi, T., and Du, X. (2021). Creep properties and resistivity-ultrasonic-AE responses of cemented gangue backfill column under high-stress area. *Int. J. Min. Sci. Technol.* 31, 401–412. doi:10.1016/j.ijmst.2021.01.008

Shao, Y. W., Suo, Y. L., Xiao, J., Bai, Y., and Yang, T. (2023). Creep characteristic test and creep model of frozen soil. *Sustainability* 15, 3984. doi:10.3390/su15053984

Tan, T. K., and Kang, W. F. (1980). Locked in stresses, creep and dilatancy of rocks, and constitutive equations. *Rock Mech.* 13, 5–22. doi:10.1007/BF01257895

Wu, F., Gao, R. B., Liu, J., and Li, C. (2020). New fractional variable-order creep model with short memory. *Appl. Math. Comput.* 380, 125278. doi:10.1016/j.amc.2020.125278

Yan, Q., Qin, S. F., Sang, X. F., Luo, Z., and Liang, M. (2023). Research on creep characteristics of loading and unloading of hard Flint limestone. *Front. Mater*, 10. doi:10.3389/fmats.2023.1177733

Yang, S. Q., Xu, P., and Ranjith, P. G. (2015). Damage model of coal under creep and triaxial compression. *Int. J. Rock Mech. Min. Sci.* 80, 337–345. doi:10.1016/j.ijrmms.2015.10.006

Yin, Q., Zhao, Y., Gong, W. M., Dai, G., Zhu, M., Zhu, W., et al. (2023). A fractal order creep-damage constitutive model of silty clay. *Acta Geotech.* 18, 3997–4016. doi:10.1007/s11440-023-01815-6

Zhang, F. M., Zhang, D. F., and Huang, S. J. (2023a). Creep characteristics and creep model of coal based on pore water pressure. *Processes* 11, 638. doi:10.3390/pr11020638

Zhang, J. C., Li, X. L., Qin, Q. Z., Wang, Y., and Gao, X. (2023b). Study on overlying strata movement patterns and mechanisms in super-large mining height stopes. *Bull. Eng. Geol. Environ.* 82, 142. doi:10.1007/s10064-023-03185-5

Zhang, J., Li, B., Zhang, C., and Li, P. (2019). Nonlinear viscoelastic–plastic creep model based on coal multistage creep tests and experimental validation. *Energies* 12, 3468. doi:10.3390/en12183468

Zhang, Z. B., Wang, E. Y., Li, N., Zhang, H., Bai, Z., and Zhang, Y. (2023c). Research on macroscopic mechanical properties and microscopic evolution characteristic of sandstone in thermal environment. *Constr. Build. Mater*, 366, 130152. doi:10.1016/j.conbuildmat.2022.130152

Zhang, Z. B., Wang, E. Y., Zhang, H. T., Bai, Z., and Chen, X. (2022). Research on nonlinear variation of elastic wave velocity dispersion characteristic in limestone dynamic fracture process. *Fractals* 31, 2350008. doi:10.1142/S0218348X23500081

frontiers | Frontiers in Earth Science

TYPE Original Research
PUBLISHED 01 November 2023
DOI 10.3389/feart.2023.1283184

OPEN ACCESS

EDITED BY
Xuelong Li,
Shandong University of Science and Technology, China

REVIEWED BY
Cai Peichen,
Chang'an University, China
Junbiao Yan,
Chinese Academy of Sciences (CAS), China

*CORRESPONDENCE
Zhaorui Lin,
1006161072@qq.com

RECEIVED 25 August 2023
ACCEPTED 20 October 2023
PUBLISHED 01 November 2023

CITATION
Li B, Lin Z, Chen Y, Xu C, Li P and Ding H (2023), Numerical analysis for supporting and deformation of complex foundation pit groups in unstable areas of karst strata. *Front. Earth Sci.* 11:1283184. doi: 10.3389/feart.2023.1283184

Numerical analysis for supporting and deformation of complex foundation pit groups in unstable areas of karst strata

Bin Li[1], Zhaorui Lin[2]*, Yonggang Chen[1], Changjie Xu[2,3], Peng Li[1] and Haibin Ding[2]

[1]China Railway Construction Group Co., Ltd., Beijing, China, [2]Institute of Geotechnical Engineering, School of Civil Engineering and Architecture, East China Jiaotong University, Nanchang, Jiangxi, China, [3]State Key Laboratory of Performance MonitoringProtecting of Rail Transit Infrastructure, East China Jiaotong University, Nanchang, Jiangxi, China

Due to the extensive karst development zone in karst areas, the stability of the underground soil layer is poor. The support of foundation pits in this area will be affected by complex environmental factors, and if not handled properly, it will cause significant safety hazards and economic losses. In this paper, the three-dimensional finite element model of the complex foundation pit and adjacent foundation pit group was established with the help of Midas GTS NX numerical software, and numerical simulation was carried out for the whole foundation pit excavation and construction process, and the deformation results of the adjacent foundation pit support structure of the complex foundation pit group and the soil outside the foundation pit were obtained. The results show that the underground wall of the complex foundation pit shifted to the north under the action of buttresses, with a similar "cantilever" displacement pattern on the south side of the underground wall in the center, a "push-back displacement" on the north side of the underground wall in the center, and a "ventral" displacement pattern at the corners of the grounded wall and on the east and west sides. Combined with the field measurement data, the support piles in the internal support system have a "cantilever" displacement pattern under the condition of massive soil unloading in the vicinity of the foundation pit, while the supporting piles show a "parabolic" displacement pattern under the action of the corner internal support. The deformation characteristics of the foundation pit in the presence of adjacent pits are significantly different from the results based on empirical laws. The results of the above study will provide useful technical guidance for the safety of excavation support for foundation pit groups in complex environments and the reasonable control of the surrounding environment.

KEYWORDS

karst, stratum instability zone, foundation pit group, deformation, numerical simulation

1 Introduction

Due to the extensive karst development zone in karst areas, the stability of the underground soil layer is poor. The support of foundation pits in this area will be affected by complex environmental factors, and if not handled properly, it will cause significant safety hazards and economic losses (Liu et al., 2011; Liu and Li, 2023; Tan and Li, 2011).

Typical profiles in a foundation pit are frequently taken and calculated using methods such as the equivalent beam method or the elastic foundation beam method in traditional pit design theory. Many researchers have expanded and extracted typical profiles containing the foundation pit and the surrounding environment on this basis. A representative theoretical model is formed by simplifying these complex operating conditions, which can then be designed or theoretically derived (Chen et al., 2023; Liu et al., 2019; Liu et al., 2023a; Shouhua et al., 2019; Xu et al., 2013a; Xu et al., 2013b; Xu et al., 2022). These works have a guiding significance for the foundation pit design. These theoretical results, however, frequently fail to consider the impact of foundation pit construction on the surrounding environment. Hsieh and Ou (Pio-Go and Chang-Yu, 1998) proposed the "concave settlement profile" and "spandrel-type settlement profile" soil settlement models and applied them to the prediction calculation of foundation excavation on the environment outside the pit. Many researchers have praised the findings of their studies. Based on their findings, additional theoretical models have been promoted and developed to deal with more complex geological conditions and to improve working conditions (Chen et al., 2022; Dan and Sahu, 2012; Fan et al., 2021; Gao et al., 2023; NG et al., 2012; Ou and Hsieh, 2011; Son and Cording, 2011; Zhang et al., 2023). These calculation models typically only consider soil deformation, and the conditions of adjacent structures are not fully explored.

Some cases of damage to surrounding structures caused by foundation excavation (Li et al., 2023; Shen et al., 2023; Zhang and Wu, 2014; Zhang et al., 2018) highlight the need for monitoring and specific consideration of deep foundation pits with complex surroundings in practical engineering. Deformation monitoring of foundation pits, as an important means of preventing and controlling foundation pit construction risks, plays a critical role in avoiding foundation pit accidents. Tan and Wei (2012) conducted monitoring for narrow-shaped foundation pits in soft soil areas. Their findings highlighted the importance of the bottom slab in preventing pit deformation in soft soil areas. Scholars have also emphasized the importance of monitoring the surrounding environment (Liu et al., 2020; Song et al., 2020); however, monitoring after the engineering begins is insufficient, and the lack of effective prediction of deformation may result in delays and material waste. Numerical simulation methods are frequently used in engineering projects that are difficult to predict using traditional theories. The case discussed by Guo et al. (Guo et al., 2019) is influenced by three adjacent buildings and the river, and the "T" excavation with varying depths adds to the project's complexity. In this case, the finite difference method was used to provide effective support for project execution and risk assessment. In this type of analysis work, the finite element method is also widely used. These studies provide a foundation for the protection of existing structures such as subway tunnels (Ye et al., 2021), buildings (Dong et al., 2016; Liu et al., 2023b; Mangushev et al., 2016), and adjacent pile foundations (Zhang et al., 2021). Furthermore, some researchers have established procedures for assessing and predicting possible deformation of foundation pits based on mathematical frameworks such as probabilistic models, using monitoring data from previous projects and numerical simulation results (Juang et al., 2011; Schuster et al., 2009; Wang et al., 2014; Yan et al., 2023a). Unfortunately, due to the complexities of soil properties, these works are difficult to apply in a wide range of geological conditions.

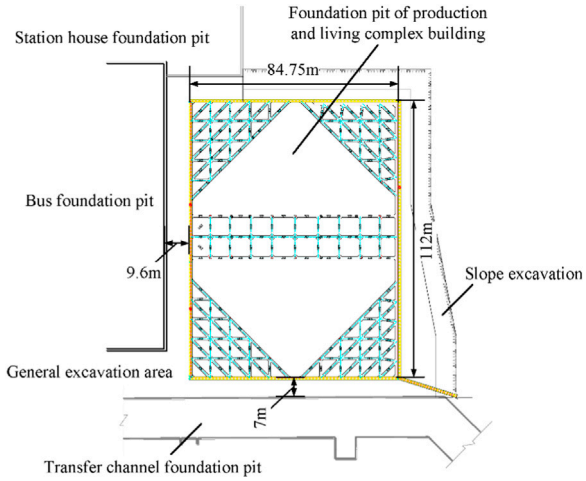

FIGURE 1
Foundation pit plan.

In recent years, the simultaneous construction of groups of foundation pits has been reported in the literature in the context of urban land constraints (Li, 2021; Yan et al., 2023b; Zeng et al., 2018). Because of the proximity of a large amount of soil unloading, this construction situation has a stronger specificity as a special case of the interaction between the foundation pit and the surrounding environment. The complicated surrounding environment complicates foundation pit deformation prediction work. At the same time, the narrow working surface caused by the foundation pit's proximity, as well as the coordination of work between different units in charge of the pit, pose serious challenges to the monitoring work performed in the foundation pit.

This paper is based on the foundation pit of the Guangzhou Baiyun Station Project's production and living complex building, as well as the complex construction environment formed by this foundation pit and the three deep foundation pits surrounding it. The 3D finite element software Midas GTS NX is used to simulate the mutual position relationship between the four foundation pits and establish the 3D finite element model. The influence of foundation pit construction on the adjacent foundation pit and the surrounding soil is studied by construction simulation, which ensures safety and stability in the construction process. Meanwhile, the deformation of the supporting structure under the influence of excavation and adjacent foundation pit is monitored by laying inclined pipes around the representative positions of the foundation pit of the production and living complex building. The security problems in the project are effectively found in the simulation and monitoring, which ensures the availability of the support structure and the sustainability of the project. The development of the foundation pit and the reasonable control of its surrounding deformation are summarized qualitatively, which provides the necessary experience for the stable design, construction, and research of similar projects.

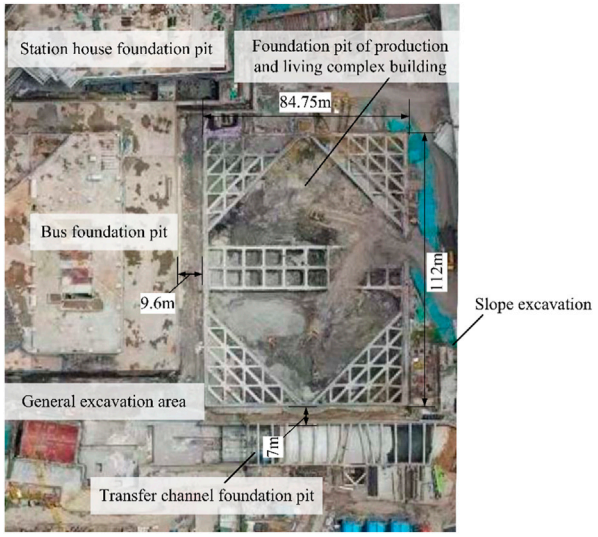

FIGURE 2
Top view of the construction site.

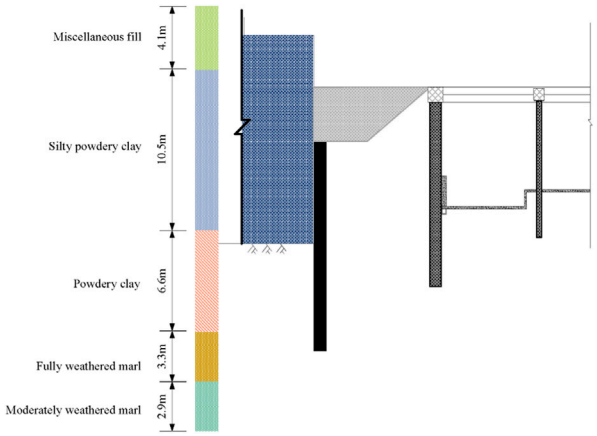

FIGURE 3
Typical soil profile.

2 Project overview

The new Guangzhou Baiyun Station integrated transportation hub building, with a total scale of approximately 453,000 square meters, is located in the south of Baiyun District, Guangzhou City. One of the most complicated surrounding environments and the most diverse support forms in the new Baiyun Station project is the basement pit group of the production and living complex building (Figure 1). Baiyun District of Guangzhou belongs to karst landform, and the area where the foundation pit of production and living buildings is located contains a complex environment such as karst. The complex surrounding environment makes it necessary to analyze the sustainability of the pit to ensure that the project is safe and sustainable and that the adjacent buildings are adequately secured. The top view of the construction site in Figure 2 depicts the complex environment surrounding the project site. The foundation pit is a three-story basement pit of the production and living complex building, with an outer border of a regular rectangle 110.2 m from north to south and 83.0 m from east to west. The perimeter is approximately 386.4 m, with an area of approximately 9,146.6 m^2. Furthermore, the south side of the first floor is partially wedge-shaped pick-out, with an area of approximately 769.3 m^2. The foundation pit is surrounded by a railway station house foundation pit (hereinafter referred to as the station house foundation pit), a tourist bus foundation pit (hereinafter referred to as the bus foundation pit), and a subway reserved transfer channel foundation pit (hereinafter referred to as the transfer channel foundation pit), and the surrounding environment is very complicated, so the mutual influence between foundation pit excavation and the surrounding environment must be considered. The pit's north side is adjacent to the bus pit (excavation depth 17.90 m), and the distance between the two pit support structures is approximately 9.04 m. The east side of the pit is adjacent to the station house pit (excavation depth 14.40 m), with a distance of about 8.97 m between the two pit support structures. The transfer channel pit is adjacent to the west side of the pit (excavation depth 10.20 m), and the distance between the two pit support structures is approximately 7.21 m.

TABLE 1 Parameters of each soil layer.

Soil layer	ρ (g/cm^3)	c (kPa)	φ (°)
Miscellaneous fill	1.90	6.80	12.00
Silty powdery clay	1.68	8.00	6.00
Powdery clay	1.90	26.25	9.21
Fully weathered marl	1.89	44.20	24.60
Moderately weathered marl	2.59	300.00	30.00

Numerical simulation studies are necessary to ensure that deformation is effectively controlled during foundation pit construction, to avoid affecting the construction of adjacent pits and the use of existing structures, and to improve construction safety and sustainability.

The production and living complex's foundation pit uses a comprehensive support system that combines slope release, grouting pile, and internal support. The ground connection wall supports the adjacent bus foundation pit and station house foundation pit, while the interchange channel foundation pit is supported by the ground connection wall and internal support. The three adjacent foundation pits all finished the support structure construction before the production and living complex foundation pit, with the underground main structure of the bus foundation pit and station house foundation pit being completed during the excavation and support of the production and living complex foundation pit.

3 Finite element simulation

3.1 Selection of typical profiles and determination of model calculation parameters

According to pertinent drilling data and ground investigation findings, the typical section is depicted in Figure 3. In this paper, the

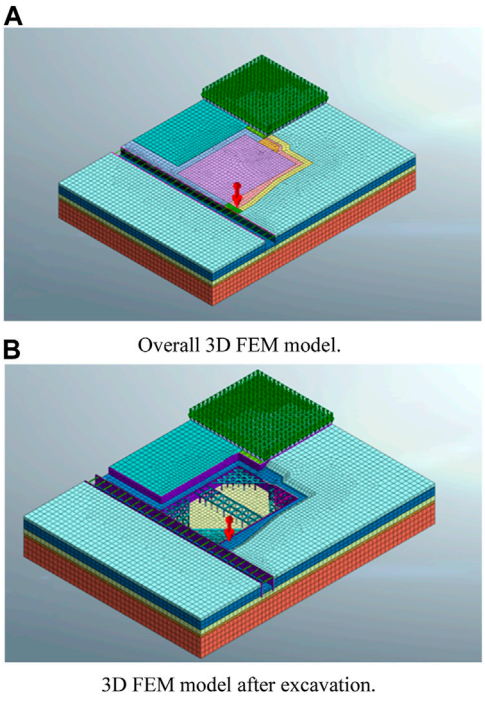

FIGURE 4
3D FEM model. **(A)** Overall 3D FEM model. **(B)** 3D FEM model after excavation.

soil distribution in the foundation pit area of the production and living complex is represented by the number. Miscellaneous fill, silty silt-powdered clay, powdery clay, fully weathered marl, and moderately weathered marl are the principal soil layers that extend from the ground to the impact area under consideration. Based on the elevation displayed in the soil profile, it is possible to calculate the thickness of each layer. Table 1 provides an overview of the soil parameters for each layer that were discovered through field and laboratory tests.

3.2 Establishment of finite element model

The length, width, and thickness of the three-dimensional finite element model in this paper are 340 m, 160 m, and 50 m respectively, and they are created using the finite element software Midas GTS NX in accordance with the actual engineering situation (Figure 4). The model is surrounded by simulations of the existing transfer channel pit, bus pit, and station house pit. Applied surface loads are used to simulate the loads brought on by above-ground structures.

The adoption of an appropriate soil ontological model for simulation is essential for the application of the finite element model. The modified Moore-Coulomb model is employed to simulate the stress-strain behavior of the soil from the standpoint of satisfying engineering requirements and convenience. To simulate the ground link wall and bored bite pile, the model uses a 2D plate unit. According to the actual working conditions, a bored bite pile with a pile diameter of 1,000 mm and a ground link wall with a thickness of 800 and 1,000 mm are set, respectively. The stiffness equivalence principle then converts the bite pile's thickness to the cross-sectional thickness of the plate. The internal support, crown beam, and lattice column were each simulated using a 1D beam unit, with model parameters set by the actual size of the construction site. The underground bus station and station house structures were modeled using solid units.

3.3 Construction process simulation

The project used in this paper required 150 days to complete, starting with the boring of the occluded piles and ending with the excavation of the foundation pit. The corresponding construction steps were set up by the construction progress plan, as shown in Table 2, to accurately simulate the actual situation. The slope release excavation for steps 2 and 4 was completed in two steps, and the fill between the pits for the production and living complex, the bus, and the interchange channel was also excavated and leveled in accordance with the excavation elevation in these two steps.

It should be noted that construction work on the underground structure, the superstructure of the surrounding station house pit, and the bus pit are all being done concurrently with the excavation of the foundation pit and construction of the support structure. The model activated the station house's underground solid model in step 3 of the construction of the foundation pit of the production and living complex and activated the surface load acting on this part of the solid model in step 4 to simulate the effects of the station house's superstructure to fully account for the effects of these factors. The bus station's subsurface solid model was turned on in steps three and four of the production and living complex's pit construction.

4 Data analysis

4.1 Analysis of horizontal deformation of foundation pit support structure of production and living complex building

Figure 5 depicts the piles' horizontal displacement clouds in the production and living complex's foundation pit under the condition of foundation pit bottom excavation. The clouds of the piles on the side near the transfer channel are depicted in Figures 5A (west side). The pile's displacement in this instance exhibits a "parabolic" pattern of displacement along the vertical axis. There is a distinct demarcation on the horizontal scale between the displacement values on the side closest to the bus foundation pit (north side) and the side of the secondary release slope (south side). The area with the greatest displacement is shown by the blue box in the figure, and it is all located close to the side of the bus pit. The demarcation of the horizontal displacement is shown in the area denoted by the black box, which is situated at the intersection of the corner's two inner supports. The action of the bus foundation pit, which is transmitted by the force of the inner support of the corner, may have caused a significant displacement to that side, which is the likely cause of this phenomenon. The blue-boxed areas of the northern grouting pile (Figures 5B) and the southern grouting pile (Figures 5D) both produced a significant displacement toward the northern side for the same reason. The results of the

TABLE 2 Construction steps.

Excavation stage no.	Description
1	Ground stress initialization and self-weight load application
2	Excavation to elevation ±0.00 m (total excavation 5 m)
3	Part I Structural Construction
4	Excavation to elevation −3.00 m (total excavation 8 m)
5	Part II Structural Construction
6	Excavation to elevation −7.50 m (total excavation 12.5 m)
7	Excavation to elevation −12.00 m (total excavation 17 m)

model are similar to the calculation and monitoring results of Guo et al. (2019). Different from the research results of Guo et al. (2019), due to the particularity of the joint excavation of the foundation pit group, the symmetrical area of the foundation pit of the production and living complex building shows a significant "push back displacement".

4.2 Analysis of the horizontal deformation of the support structure of the adjacent foundation pit

Figure 6 depicts the ground connection wall of the transfer channel foundation pit's lateral deformation. According to morphology, the deformation of the ground connection wall of the foundation pit can be roughly divided into three areas, the region shown by the red box in Figure 6, where the ground connection wall deforms in a "parabolic" shape toward the foundation pit while disregarding the influence of surrounding foundation pits and structures. In this project, the part marked by the red box is buried underground. Due to the division of the project site, no site pictures have been obtained. The active soil pressure zone of the ground connection wall close to the side of the adjacent pit was excavated and leveled in the area denoted by the blue box and the area denoted by the black box, leaving the portion of the interchange pit elevation above −3 m exposed on the ground (Figure 7). Due to this reason, the areas indicated by the blue box and the black box have both experienced overall horizontal displacement towards the direction adjacent to the foundation pit. The area indicated by the black box is adjacent to the integrated tourism bus foundation pit, and its excavation depth is greater than the production and living complex foundation pit adjacent to the area indicated by the blue box. Therefore, the horizontal displacement value indicated by the black box is greater than that indicated by the blue box.

Figure 8 extracts the typical curve of the transfer channel foundation pit's ground connection wall deformation. In line with what is depicted in Figure 8, the wall that is connected to the ground exhibits two common deformation patterns. The displacement pattern of the red box area, which displays a "parabolic" displacement pattern toward the pit, is represented by the red curve. The maximum value of the displacement of the ground connection wall is less than 25 mm, but it is slightly larger on the side closest to the production and living complex. The larger displacement on this site may be due to the complex environment surrounding the production and living complex side and the complex stress field. The ground connection wall in the area of the blue and black lines exhibits a "cantilever" displacement pattern toward the side of the foundation pit of production and living complex building. The blue and black curves in Figure 8 demonstrate typical displacements in this region. By using the number, we can determine that the ground connection wall's horizontal displacement in this area has increased beyond the typical engineering warning threshold, potentially posing a serious safety risk to the project. If such construction continues, the support structure may become unstable and the surrounding soil may crack and collapse. The construction site quickly backfilled the backpressure soil in the middle of the two foundation pits in the general excavation area after receiving the early warning from the model calculation results of this paper and monitoring and warning at the site, and accelerated the bottom slab-pouring operation of the transfer channel foundation pit (Figure 7). This action successfully controlled the deformation of this foundation pit and prevented the occurrence of safety accidents. This reflects the significance of this research for the safe and stabilized operation of this project.

4.3 Bending moment analysis of the foundation pit enclosure structure of the production and living complex building

Figure 9 extracts the typical curve of the transfer channel foundation pit's ground connection wall bending moment of the production and living complex building at each construction step. The variation of bending moment shows that as the excavation depth of the foundation pit increases, the amplitude of bending moment significantly increases. The bending moment shapes in Figures 9A, B are similar. The surrounding structure generates negative bending moments towards the outside of the pit below the bottom. Above the bottom of the pit, the main positive bending moment is towards the pit, and a small amount of negative bending moment may occur near the top of the support pile. Figures 9C The negative bending moment generated near the top of the support pile is relatively large. Two layers of internal support were used for support at this location, which may be the reason for this internal force situation. The position shown in Figures 9D shows that due to the "pusback displacement" caused by the support, the deformation of the support pile at this position is relatively small, and the bending moment value is significantly smaller than the other three profiles.

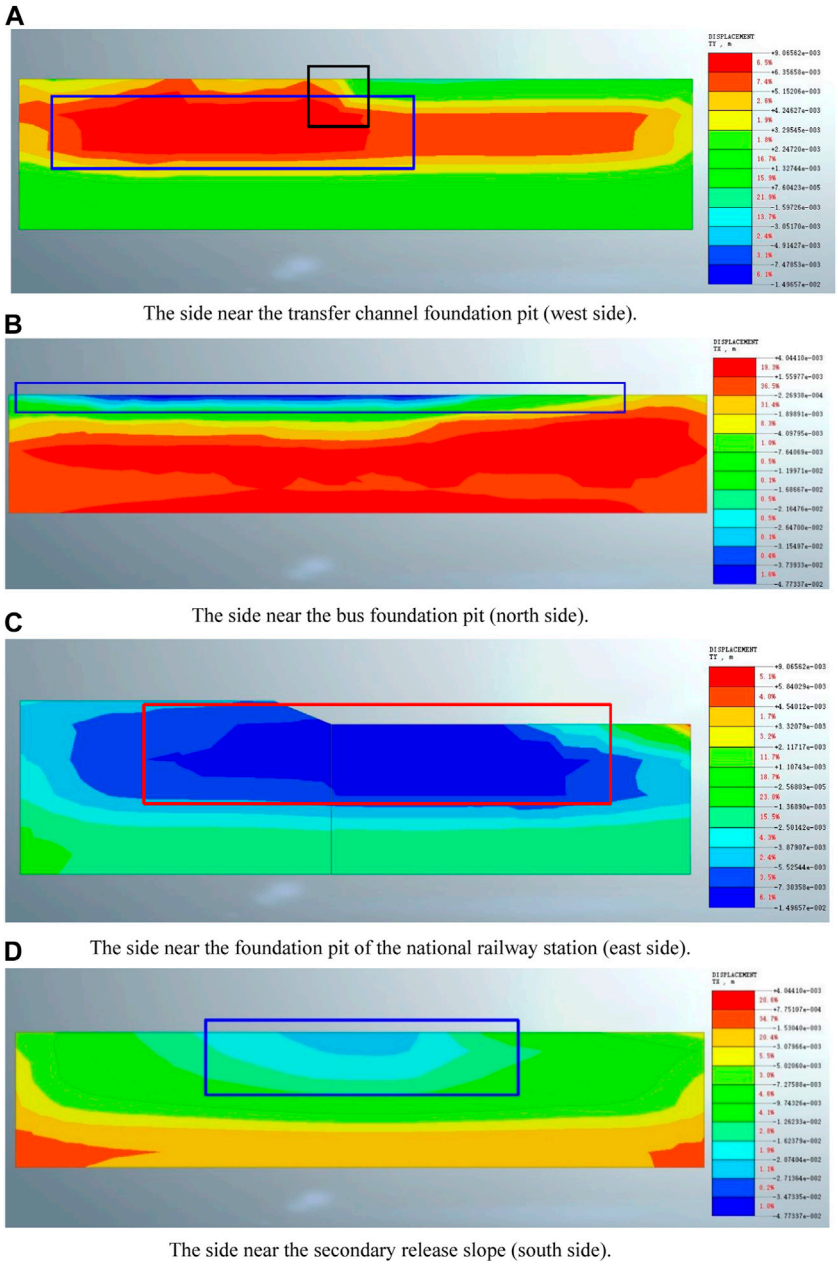

FIGURE 5
Horizontal deformation cloud map of the foundation support structure of production and living complex building. **(A)** The side near the transfer channel foundation pit (west side). **(B)** The side near the bus foundation pit (north side). **(C)** The side near the foundation pit of the national railway station (east side). **(D)** The side near the secondary release slope (south side).

4.4 Analysis of the vertical deformation of the foundation pit and surrounding soil of the production and living complex

Figure 10 depicts the vertical displacement of the production and living complex building foundation pit and the surrounding environment. The vertical direction shows a bulge deformation at the bottom of the foundation pit of the production and living complex. Among them, the position of the infill pile near the pit's perimeter has the least vertical deformation, while the middle of the pit has the most. The overall uplift deformation pattern exhibits elastic uplift deformation. The overall uplift trend is shown in the platform area where the slope is released, which may be caused by the unloading of soil excavation. There is a settlement trend in the soil between the pit of the production and living complex and the foundation pit of the bus. The supporting structures of both foundation pits are generally displaced toward the foundation pit, resulting in a settlement pattern of low in the middle and high on both sides.

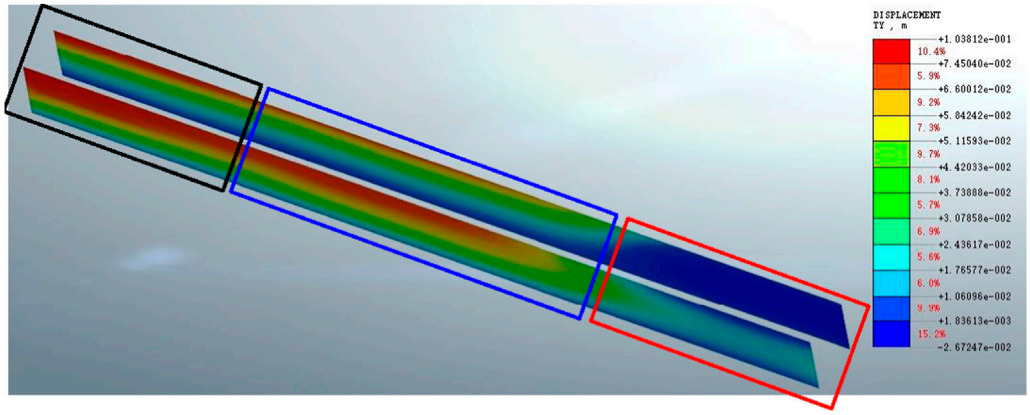

FIGURE 6
Horizontal deformation cloud map of the support structure of the transfer channel foundation pit.

FIGURE 7
Site photo of the ground connection wall of the transfer channel foundation pit after general excavation.

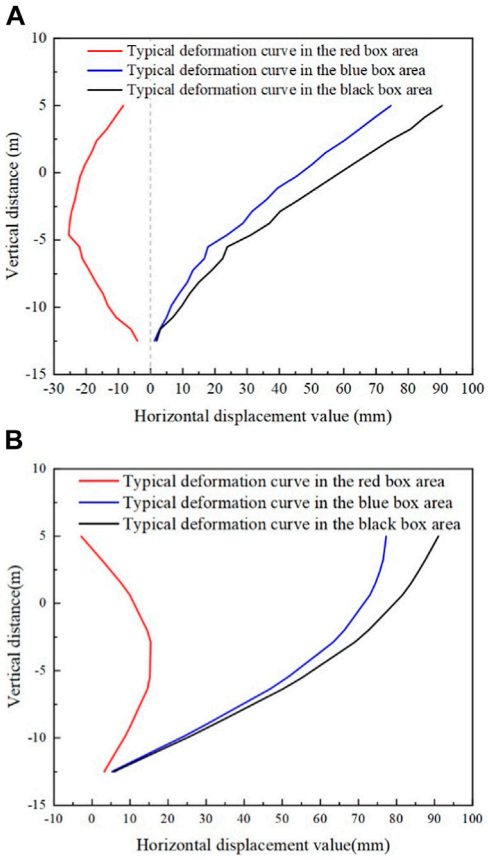

FIGURE 8
Typical curve of horizontal displacement of foundation connection wall of transfer channel foundation pit. **(A)** The ground connecting wall on the side of the building near the production and living complex. **(B)** Away from the production and living complex building side of the ground connecting wall.

Figure 11 shows the typical surface settlement data outside the pit after excavation. There are some differences between the surface settlement pattern outside the secondary release slope (Figures 11A) and the "concave settlement profile" settlement model proposed by Pio-Go and Chang-Yu, (1998). According to the construction process simulation, the finite element model excavated a total of 17 m and obtained the maximum settlement value at 7.2 m, which is 0.42 times the excavation depth. The surface settlement value was 0.64 times the maximum settlement value at the start of the settlement profile, whereas the "concave settlement profile" settlement model was only 0.5 times the maximum settlement value at the start of the settlement profile. Meanwhile, in the secondary settlement area, the surface settlement value eventually converges to a settlement value of approximately 27 m but does not converge to 0. This difference could be attributed to the stratum and soil's unique properties on the one hand, and the support mode of slope release followed by enclosure on the other, which differs from the simple internal support system.

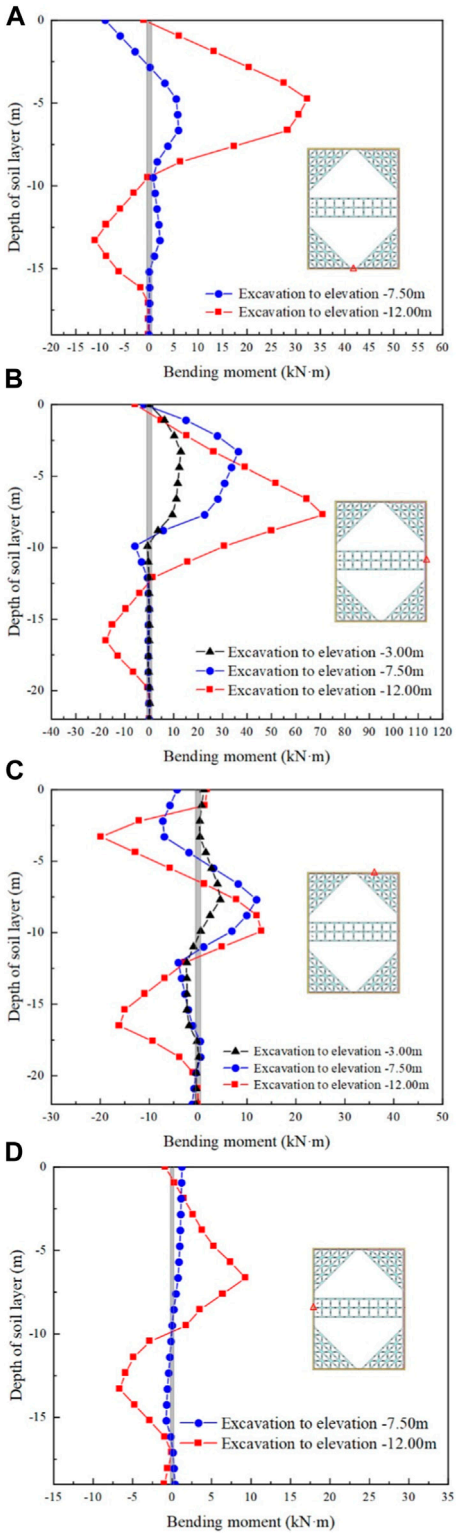

FIGURE 9
Typical bending moment of foundation pit connecting wall. **(A)** Bending moment situation on the side near the transfer channel foundation pit (west side). **(B)** Bending moment situation on the side near the secondary release slope (south side). **(C)** Bending moment situation on the side (east side) near the foundation pit of the National Railway Station. **(D)** Bending moment situation on the side near the bus foundation pit (north side).

The soil between the foundation pit of the production and living complex and the foundation pit of the transfer channel, on the other hand, showed an uplift deformation pattern, with a larger uplift on the side close to the foundation pit of the production and living complex. The general excavated and leveled soil being unloaded causes the soil body in this area to rise as a whole. This uplift trend was exacerbated by the overall deformation of the support system of the transfer channel foundation pit toward the foundation pit of the production and living complex. Under the effect of the internal support of the corner, the support system of the production and living complex played a significant role, and its lateral deformation was significantly smaller than that of the pit of the interchange access building. However, this exacerbated the ground uplift near the production and living complex's foundation pit.

The above soil deformation analysis reveals that the vertical deformation of surface soil in deep foundation pits with complex surrounding environments, particularly the foundation pit group, differs from the commonly used "concave settlement profile" and "spandrel-type settlement profiles. The deformation pattern of the adjacent foundation support structure is frequently related to the deformation pattern of the soil. Vertical deformation of the soil body between adjacent pits should be closely monitored to avoid excessive deformation.

4.5 Field monitoring set-up

Four inclined tubes were buried to measure the horizontal deformation of the foundation pit enclosure system in order to study the real deformation characteristics of the support structure in the context of the project site. Figure 12 depicts the actual monitoring points. The tilting pipe's burial on the property is captured in Figure 13.

The final formed pile top elevation has a significant difference between them due to the crown beam elevation gradient, so the inclined tubes CX3 and CX4 were placed on that side to observe the corresponding deformation. The need for soil treatment between the two adjacent pits made it impossible to deploy monitoring equipment on the side closest to the bus foundation pit.

4.6 Comparison analysis of finite element calculation results and field measurement data

The foundation pit support structure's horizontal deformation warrants close attention and monitoring in real-world engineering. Comparing the monitoring data with the numerical simulation calculation results is a common means to verify the validity of the numerical simulation results. The data for the inclined tube after the foundation pit was built and the outcomes of the corresponding finite element analysis are extracted in Figure 14.

The three monitoring points CX1, CX3, and CX4 all exhibit a "parabolic" horizontal displacement pattern when the two deformations are compared. The maximum calculated displacement value appears at a depth of −8.55 m, and the maximum horizontal displacement value is 5.86 mm, while the

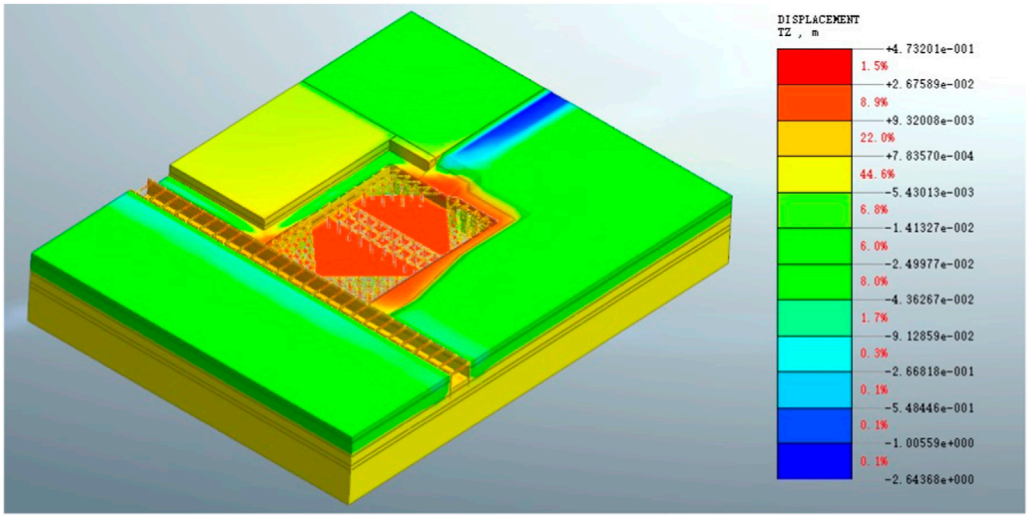

FIGURE 10
Vertical deformation cloud map of foundation pit and surrounding environment. **(A)** Typical curve of surface settlement outside the secondary release slope. **(B)** Typical vertical deformation of the soil between the pit of the production and living complex and the pit of the transfer channel.

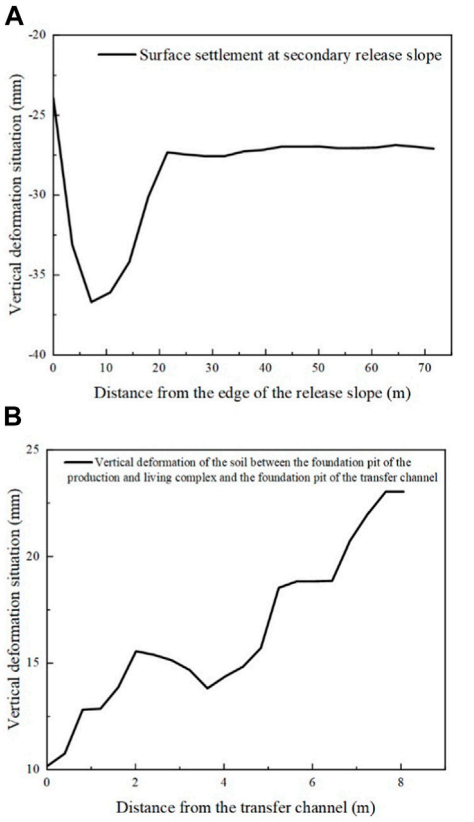

FIGURE 11
Typical vertical deformation curve of soil between pits. **(A)** Typical curve of surface settlement outside the secondary release slope. **(B)** Typical vertical deformation of the soil between the pit of the production and living complex and the pit of the transfer channel.

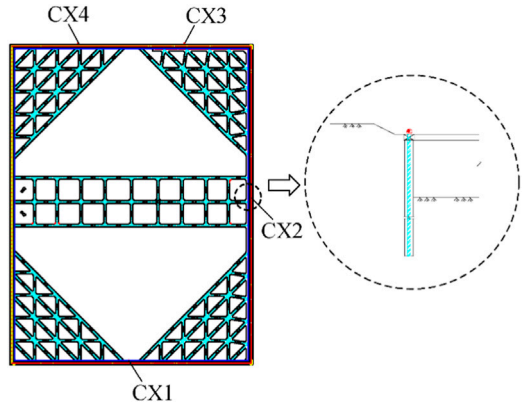

FIGURE 12
Foundation pit monitoring plan layout.

maximum monitoring value of CX1 displacement appears at −8 m, and the maximum horizontal displacement value is 5.32 mm. The maximum calculated displacement value appeared at a depth of −4.75 m, while the maximum monitoring value of CX4 displacement appeared at a depth of −2.5 m, with a maximum horizontal displacement value of 7.94 mm. The occurrence height at CX1 and the maximum monitored horizontal displacement value are very close to the predicted results. The maximum displacement emergence locations are higher than the predicted results, even though the horizontal displacement amplitudes at CX3 and CX4 are close to each other. In CX1 and CX4, the "belly bulge" area of the monitoring data is larger than that of the calculation results, and CX1, CX3, and CX4 all have a primary amplitude in the area closer to the pile top,

10.3389/feart.2023.1283184

FIGURE 13
Burial of inclined tubes at the construction site.

which also makes their displacement shapes show an “R" shape. These shapes are not reflected in the calculation results. There are two main reasons for this error. On the one hand, the more typical stratum in the foundation pit area is used in the finite element calculation model, and the area in the model is regarded as the mean soil layer. However, there are still some differences between the actual stratum and the assumption of the model. This may bring some error to the calculation results. On the other hand, the additional load brought by the earthwork transportation path and construction machinery cannot be effectively reflected in the calculation, which also affects the accuracy of the calculation to a certain extent. The maximum monitoring value for CX2 is at depth −2 m and has a maximum horizontal displacement value of 23.76 mm; the maximum calculated value for CX2 is at depth 0 m and has a maximum horizontal displacement value of 22.91 mm. The large degree of fit between the monitoring data and the calculated results proves the reliability of the finite element simulation method and model simplification to a certain extent.

The existence of the nearby bus foundation pit may be the cause of the “cantilevered” displacement pattern at this location. The formed soil wedge was not complete because the support structure of the bus foundation pit prevented the slip crack surface from developing in the active soil wedge. Due to the low active earth pressure acting on the production and living complex pit’s support structure, the overall foundation pit support was offset in the direction of the bus foundation pit. The two-stage slope release support adds more load to the side opposite monitoring point CX2, intensifying the braced structure’s deflection on that side. Since CX2 has a larger displacement amplitude than the other three monitoring points, it also deviates significantly from the typical internally braced support structure in terms of support displacement pattern.

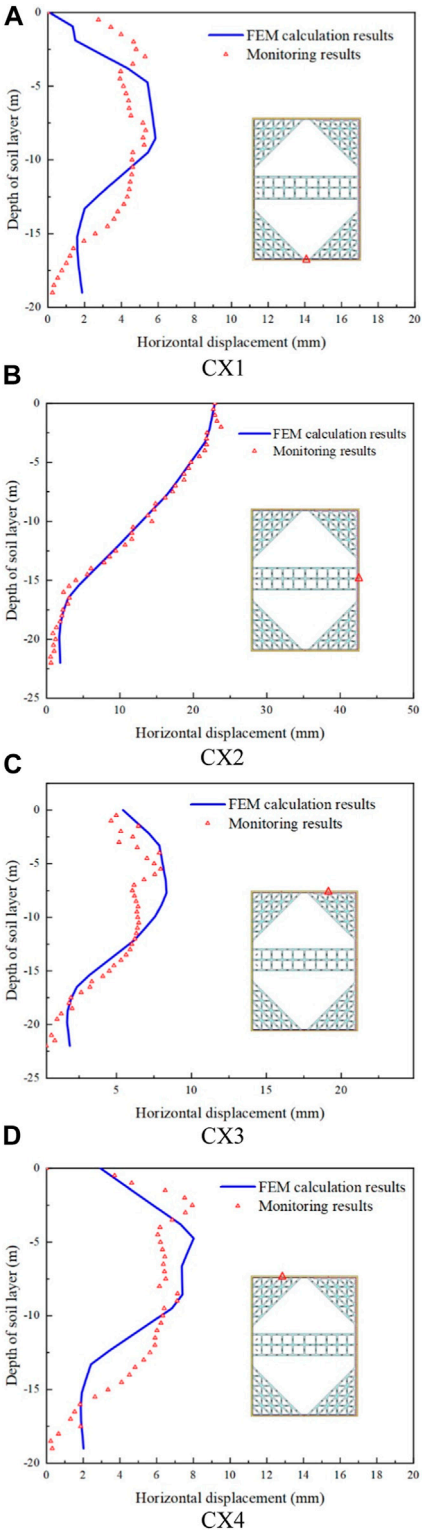

FIGURE 14
Comparison of foundation pit monitoring data and finite element calculation results. **(A)** CX1. **(B)** CX2. **(C)** CX3. **(D)** CX4.

5 Conclusion

In this article, numerical modeling is utilized to examine the deformation of the foundation pit and the surrounding adjacent foundation pits during the excavation and support of the foundation pit of Guangzhou Baiyun Station's production and living complex, and verify the numerical simulation results based on field monitoring data. The following primary findings are made from the analysis results.

(1) When designing deep foundation pits with a high number of excavations near a foundation group or a deep foundation pit, the usage of internal support forms must be carefully evaluated. The unloading induced by the adjacent pit or excavation may force the entire support structure to shift in the unloading direction. The magnitude of this overall movement was not quantitatively assessed in this study.
(2) The deformation of the foundation support structure is frequently related to the form of the support. Under the action of the internal support system, the foundation pit of the production and living complex building was displaced by 23 mm from the top of the support structure of the adjacent foundation pit, which indicated that the foundation pit support system may produce a displacement pattern similar to "cantilever" in the asymmetric case. Under the action of the internal suppor, the top of the retaining structure adjacent to the pit will have a smaller displacement, or even a "push-back displacement" towards the edge of the pit.
(3) The shape of vertical deformation of the surface soil outside the pits differs substantially from the previously listed rules due to the reciprocal influence of the support systems of the nearby foundation pits. Because of the total deformation of the supporting structure, the soil body between foundation pits may swell. Because of the deformation of other pits, the maximum surface settlement of the foundation pit at a depth of 0.42 times the excavation depth outside the pit, and the surface settlement value was 0.64 times the maximum settlement value at the start of the settlement profile.

Data availability statement

The original contributions presented in the study are included in the article/supplementary material, further inquiries can be directed to the corresponding author.

Author contributions

BL: Data curation, Funding acquisition, Methodology, Project administration, Writing–original draft. ZL: Data curation, Software, Writing–original draft. YC: Software, Validation, Writing–original draft. CX: Funding acquisition, Methodology, Project administration, Writing–review and editing. PL: Investigation, Software, Writing–review and editing. HD: Software, Supervision, Writing–review and editing.

Funding

The authors declare financial support was received for the research, authorship, and/or publication of this article. This work was supported by National Natural Science Foundation of China (NSFC Grant No. 52238009) and the National Science Fund of Jiangxi Province (No. 20223BBG71018).

Conflict of interest

Authors BL, YC, and PL were employed by China Railway Construction Group Co., Ltd.

The remaining authors declare that the research was conducted in the absence of any commercial or financial relationships that could be construed as a potential conflict of interest.

Publisher's note

References

Chen, H., Li, J., Yang, C., and Feng, C. (2022). A theoretical study on ground surface settlement induced by a braced deep excavation. *Eur. J. Environ. Civ. Eng.* 26 (5), 1897–1916. doi:10.1080/19648189.2020.1739563

Chen, Y., Tang, L., Ye, Y., Cheng, Z., and Zhou, Z. (2023). Effects of different chloride salts on granite residual soil: properties and water–soil chemical interaction mechanisms. *J. Soils Sediments.* 23 (4), 1844–1856. doi:10.1007/s11368-023-03445-7

Dan, K., and Sahu, R. (2012). A theoretical study on ground movement prediction for braced excavation in soft clay. *Int. J. Geotech. Eng.* 6 (1), 53–64. doi:10.3328/IJGE.2012.06.01.53-64

Dong, Y. P., Burd, H. J., and Houlsby, G. T. (2016). Finite-element analysis of a deep excavation case history. *Géotechnique.* 66 (1), 1–15. doi:10.1680/jgeot.14.P.234

Fan, X., Phoon, K., Xu, C., and Tang, C. (2021). Closed-form solution for excavation-induced ground settlement profile in clay. *Comput. Geotech.* 137, 104266. doi:10.1016/j.compgeo.2021.104266

Gao, Y., Yu, Z., Chen, W., Yin, Q., Wu, J., and Wang, W. (2023). Recognition of rock materials after hightemperature deterioration based on sem images via deep learning. *J. Mater. Res. Technol.* 25, 273–284. doi:10.1016/j.jmrt.2023.05.271

Guo, P., Gong, X., and Wang, Y. (2019). Displacement and force analyses of braced structure of deep excavation considering unsymmetrical surcharge effect. *Comput. Geotech.* 113, 103102. doi:10.1016/j.compgeo.2019.103102

Juang, C. H., Schuster, M., Ou, C., and Phoon, K. K. (2011). Fully probabilistic framework for evaluating excavation-induced damage potential of adjacent buildings. *J. Geotech. Geoenviron. Eng.* 137 (2), 130–139. doi:10.1061/(ASCE)GT.1943-5606.0000413

Li, H., Li, X., Fu, J., Zhu, N., Chen, D., Wang, Y., et al. (2023). Experimental study on compressive behavior and failure characteristics of imitation steel fiber concrete under uniaxial load. *Constr. Build. Mater.* 399, 132599. doi:10.1016/j.conbuildmat.2023.132599

Li, Z. (2021). Displacement monitoring during the excavation and support of deep foundation pit in complex environment. *Adv. Civ. Eng.* 2021, 1–7. doi:10.1155/2021/5715306

Liu, B., Zhang, D., and Xi, P. (2019). Influence of vehicle load mode on the response of an asymmetrically-loaded deep excavation. *Ksce J. Civ. Eng.* 23 (8), 3315–3329. doi:10.1007/s12205-019-0511-6

Liu, B., Zhang, D., Yang, C., and Zhang, Q. (2020). Long-term performance of metro tunnels induced by adjacent large deep excavation and protective measures in nanjing silty clay. *Tunn. Undergr. Space Technol.* 95, 103147. doi:10.1016/j.tust.2019.103147

Liu, G. B., Jiang, R. J., Ng, C. W. W., and Hong, Y. (2011). Deformation characteristics of a 38 m deep excavation in soft clay. *Can. Geotech. J.* 48 (12), 1817–1828. doi:10.1139/t11-075

Liu, H., Li, X., Yu, Z., Tan, Y., Ding, Y., Chen, D., et al. (2023a). Influence of hole diameter on mechanical properties and stability of granite rock surrounding tunnels. *Phys. Fluids* 35 (6). doi:10.1063/5.0154872

Liu, S., and Li, X. (2023). Experimental study on the effect of cold soaking with liquid nitrogen on the coal chemical and microstructural characteristics. *Environ. Sci. Pollut. Res. Int.* 30 (13), 36080–36097. doi:10.1007/s11356-022-24821-9

Liu, S., Sun, H., Zhang, D., Yang, K., Li, X., Wang, D., et al. (2023b). Experimental study of effect of liquid nitrogen cold soaking on coal pore structure and fractal characteristics. *Energy* 275, 127470. doi:10.1016/j.energy.2023.127470

Mangushev, R. A., Osokin, A. I., and Garnyk, L. V. (2016). Experience in preserving adjacent buildings during excavation of large foundation pits under conditions of dense development. *Soil Mech. Found. Eng.* 53 (5), 291–297. doi:10.1007/s11204-016-9401-9

Ng, C. W. W., Hong, Y., Liu, G. B., and Liu, T. (2012). Ground deformations and soil–structure interaction of a multi-propped excavation in shanghai soft clays. *Géotechnique.* 62 (10), 907–921. doi:10.1680/geot.10.P.072

Ou, C., and Hsieh, P. (2011). A simplified method for predicting ground settlement profiles induced by excavation in soft clay. *Comput. Geotech.* 38 (8), 987–997. doi:10.1016/j.compgeo.2011.06.008

Pio-Go, H., and Chang-Yu, O. (1998). Shape of ground surface settlement profiles caused by excavation. *Can. Geotech. J.* 35 (6), 1004–1017. doi:10.1139/t98-056

Schuster, M., Kung, G. T., Juang, C. H., and Hashash, Y. M. A. (2009). Simplified model for evaluating damage potential of buildings adjacent to a braced excavation. *J. Geotech. Geoenviron. Eng.* 135 (12), 1823–1835. doi:10.1061/(ASCE)GT.1943-5606.0000161

Shen, Y., Zhang, D., Wang, R., Li, J., and Huang, Z. (2023). Sbd-k-medoids-based long-term settlement analysis of shield tunnel. *Transp. Geotech.* 42, 101053. doi:10.1016/j.trgeo.2023.101053

Shouhua, L., Junsheng, Y., Jinyang, F., and Xiangcou, Z. (2019). Performance of a deep excavation irregular supporting structure subjected to asymmetric loading. *Int. J. Geomech.* 19 (7). doi:10.1061/(asce)gm.1943-5622.0001468

Son, M., and Cording, E. J. (2011). Responses of buildings with different structural types to excavation-induced ground settlements. *J. Geotech. Geoenviron. Eng.* 137 (4), 323–333. doi:10.1061/(ASCE)GT.1943-5606.0000448

Song, D., Chen, Z., Dong, L., Tang, G., Zhang, K., and Wang, H. (2020). Monitoring analysis of influence of extra-large complex deep foundation pit on adjacent environment: a case study of zhengzhou city, China. *Geomatics, Nat. Hazards Risk* 11 (1), 2036–2057. doi:10.1080/19475705.2020.1823492

Tan, Y., and Li, M. (2011). Measured performance of a 26 m deep top-down excavation in downtown shanghai. *Can. Geotech. J.* 48 (5), 704–719. doi:10.1139/t10-100

Tan, Y., and Wei, B. (2012). Observed behaviors of a long and deep excavation constructed by cut-and-cover technique in shanghai soft clay. *J. Geotech. Geoenviron. Eng.* 138 (1), 69–88. doi:10.1061/(ASCE)GT.1943-5606.0000553

Wang, L., Luo, Z., Xiao, J., and Juang, C. H. (2014). Probabilistic inverse analysis of excavation-induced wall and ground responses for assessing damage potential of adjacent buildings. *Geotech. Geol. Eng.* 32 (2), 273–285. doi:10.1007/s10706-013-9709-4

Xu, C., Lin, Z., Jiang, Y., Shi, Y., Fan, X., Xiong, Z., et al. (2022). Research on the spatial effect of foundation pit under asymmetric loads. *Front. Mater.* 9. doi:10.3389/fmats.2022.976696

Xu, C. J., Xu, Y. L., Lin, H. H., and Sun, F. M. (2013a). Influences of vehicle loads on braced excavation in soft clay. *Appl. Mech. Mater.* 353-356, 146–151. doi:10.4028/www.scientific.net/AMM.353-356.146

Xu, C. J., Yin, M., and Lin, G. (2013b). Characters analysis of the retaining structure of the foundation pit under local load. *Appl. Mech. Mater.* 477-478, 448–452. doi:10.4028/www.scientific.net/amm.477-478.448

Yan, J., Kong, L., and Wang, J. (2023a). Evolution law of small strain shear modulus of expansive soil: from a damage perspective. *Eng. Geol.* 315, 107017. doi:10.1016/j.enggeo.2023.107017

Yan, J., Kong, L., Xiong, C., and Xu, G. (2023b). Damage analysis of shear mechanical behavior of pile–structural soil interface considering shear rate effect. *Acta Geotech.* 18, 5369–5383. doi:10.1007/s11440-023-01912-6

Ye, S., Zhao, Z., and Wang, D. (2021). Deformation analysis and safety assessment of existing metro tunnels affected by excavation of a foundation pit. *Undergr. Space.* 6 (4), 421–431. doi:10.1016/j.undsp.2020.06.002

Zeng, F., Zhang, Z., Wang, J., and Li, M. (2018). Observed performance of two adjacent and concurrently excavated deep foundation pits in soft clay. *J. Perform. Constr. Facil.* 32 (4), 4018040. doi:10.1061/(ASCE)CF.1943-5509.0001184

Zhang, G., and Wu, D. X. (2014). Analysis of foundation pit accidents due to expansive soil in hefei district. *Appl. Mech. Mater.* 501-504, 331–335. doi:10.4028/www.scientific.net/AMM.501-504.331

Zhang, J., Li, X., Qin, Q., Wang, Y., and Gao, X. (2023). Study on overlying strata movement patterns and mechanisms in super-large mining height stopes. *Bull. Eng. Geol. Environ.* 82 (4), 142. doi:10.1007/s10064-023-03185-5

Zhang, R., Zhang, W., and Goh, A. T. C. (2021). Numerical investigation of pile responses caused by adjacent braced excavation in soft clays. *Int. J. Geotech. Eng.* 15 (7), 783–797. doi:10.1080/19386362.2018.1515810

Zhang, X., Yang, J., Zhang, Y., and Gao, Y. (2018). Cause investigation of damages in existing building adjacent to foundation pit in construction. *Eng. Fail. Anal.* 83, 117–124. doi:10.1016/j.engfailanal.2017.09.016

frontiers | Frontiers in Earth Science

TYPE Original Research
PUBLISHED 03 November 2023
DOI 10.3389/feart.2023.1292945

OPEN ACCESS

EDITED BY
Xuelong Li,
Shandong University of Science and Technology, China

REVIEWED BY
Dong Duan,
Taiyuan University of Technology, China
Fei Wu,
Chongqing University, China
Xiaoshaung Li,
Shaoxing University, China

*CORRESPONDENCE
Chengheng Hou,
492674382@qq.com

RECEIVED 12 September 2023
ACCEPTED 20 October 2023
PUBLISHED 03 November 2023

CITATION
Hou C (2023), Study on slope stability under excavation and water storage based on physical model tests.
Front. Earth Sci. 11:1292945.
doi: 10.3389/feart.2023.1292945

Study on slope stability under excavation and water storage based on physical model tests

Chengheng Hou[1,2]*

[1]China Coal Technology and Engineering Group Shenyang Research Institute Co, Ltd, Fushun, Liaoning, China, [2]State Key Laboratory of Coal Mine Safety Technology, Fushun, China

Understanding the characteristics and mechanism of slope deformation caused by slope excavation and water storage is very important in the stability analysis of slope engineering. Therefore, based on similarity theory, a physical model test of excavation and water storage was established, and the deformation characteristics of the slope (three-stage excavation and five-stage water storage) were studied by using the monitoring technology of multiple measuring devices. The variation characteristics of the displacement, stress and pore water pressure in the slope were revealed. The results show that the contents of cement and yellow sand can regulate the physical, mechanical and hydrological properties and that gypsum and hydraulic oil have an effect on the permeability. Excavation leads to deformation of the rock mass in the middle and lower slope to the outside of the slope. This is attributed to the stress release, and local stress concentration occurs at the foot of the slope after redistribution. Moreover, the rock mass located in the fault zone shows nonglobal movement because the hanging wall rock mass will produce relative dislocation along the fault zone under self-gravity. Under water storage, the slope body is affected by the hydrostatic pressure, and transient compaction deformation occurs first. As water permeates into the slope body, the water weakens the rock mass, resulting in the gradual deformation of the rock mass near the slope surface to the outside of the slope. The above model test results can provide a valuable reference for slopes stability analysis in construction and subsequent operation.

KEYWORDS

physical model, slope excavation, water storage, deformation, similar material

1 Introduction

In the process of excavation and water storage of underground structures, the deformation and sliding damage of rock will bring serious economic losses and personnel safety accidents (Tang et al., 2016; Yin et al., 2019; Yu et al., 2019; Yin et al., 2021a; Yang et al., 2022). To study the cause and formation process of these hazards, a large number of indoor physical model tests based on the physical and mechanical properties of similar materials have appeared (Zhang et al., 2007; Tang et al., 2017; Yang et al., 2019; Prodan et al., 2023). These physical model tests have great guiding value for simulating the deformation process and failure of complex structures in hydraulic slope engineering the field. A large number of monitoring values from model tests can intuitively provide the deformation characteristics of the slope in different environments and reveal its influencing factors (Tang et al., 2018b; Zheng et al., 2018; Tao et al., 2020; Yin et al., 2021b). And numerical simulation methods are also used to study the failure and deformation process of rock (Tang et al., 2006; Tang and Tang, 2015; Tang et al., 2020). Many scholars have

established physical models under different geological conditions to identify and monitor the stress and strain field data inside a slope and the change law of the pore water pressure to study the deformation mechanism and instability process of the slope during excavation and water storage.

Zhu et al. (2020) established a physical model of slope excavation in anti-dip strata and studied the evolution characteristics of the displacement field and strain field of the excavation process model by using a variety of monitoring methods. Adhikary et al. (1997) used a sand-gypsum mixture and a fiber cement board to carry out centrifugal experiments on a horizontal slope with a jointed appearance to study the bending failure mechanism of the slope. Ding et al. (2020) simulated the deformation law of slope rock mass by constructing a geological engineering model, defined the main influencing factors of slope instability, and analyzed the movement and failure characteristics of the rock mass. Huang et al. (2023) carried out model tests to monitor the whole displacement field and failure sequence of the slope and analysed the influence mechanism of a water level change on the slope deformation and failure mechanism under excavation. Cao et al. (2022) used formal simulation materials to construct a similar shape of a dump and studied the failure characteristics and model landslide mechanism under different loads based on the monitoring data. Sun and Zhao (2014) established different physical models of a slope and studied different evolution stages of the slope according to the proposed simplified geomechanical model. Lo and Weng (2017) studied the deformation process and failure characteristics of fractured slopes under complex conditions through field investigation and physical model experiments and believed that the facet dip angle was the key factor determining slope deformation.

Wu et al. (2015) employed a series of physical models to simulate experiments of water infiltration into slopes under different conditions and analysed the main factors leading to slope instability and failure. Hu et al. (2019) studied the influence mechanism of slope deformation and stability under reservoir filling and believed that the increase in the pore water pressure was a critical period in the occurrence of large deformation of landslides based on physical model tests. (Tang, 2018; Tang et al., 2018a; Tang et al., 2022) analysed the influence of water on rock failure characteristics and damage mechanism in the long-term and short-term environment. Tang et al. (2021) also studied the influence relationship of water on rock fracture toughness based on the edge-cracked semicircular bend (SCB) testing. Liang et al. (2021) and Liang et al. (2023) Liang et al. studied the triaxial and shear characteristics of sandstone, and established an empirical equation for the change of mechanical characteristics of sandstone with water content and immersion time. Chen et al. (2021) analyzed the long-term and short-term failure mechanism of rock caused by water level height. Ding et al. (2023) studied the failure characteristics and damage mechanism of sandstone under different water absorption time. In recent years, the model tests of slopes under the common conditions of slope excavation and water storage have been different from the actual working conditions, and most of them only include surface deformation observation. Moreover, the understanding of the deformation mechanism and instability failure of slopes under different conditions needs to be further improved. To better guide the construction and later operation of actual engineering projects, it is necessary to study the variation characteristics of the deformation, stress and pore water pressure of the slope and internal broken body under unloading and water storage conditions.

Based on the selection principle of similar materials and similarity theory, this study determines the appropriate model materials and the optimal material ratio through physical and mechanical tests. First, a physical model of slope excavation is established based on the geological structure of the on-site rock stratum and fault zone, and the three excavation processes of the slope are simulated. The slope stability (deformation, surface settlement and internal stress) by each excavation disturbance are monitored and analysed. Then, the whole process of water storage is simulated by changing the water storage level (five water levels), and the slope deformation, surface subsidence, slope internal stress and pore water pressure changes in each storage period are studied and discussed.

2 Determination of model parameters and materials

2.1 Model parameters

In a simulated geomechanical model, three main factors affect the results of the test: the geometric size of the physical simulation test, the mechanical properties of the rock mass material and the boundary conditions of the physical model. In the model test, it is necessary to ensure that the physical model is similar to the original structure in physical phenomena to ensure that the results obtained by the test can be replicated by the prototype. According to similarity theory, geometric similarity of the model is a prerequisite for similar physical phenomena (Wu et al., 2020a; Wu et al., 2020b), so the geometrically similar condition is a key in the design of the structural model. The similarity scale is obtained by comparing the sizes of the model and the prototype, and the corresponding proportions of the mechanical parameters between the physical model materials and the prototype slope materials should also be equal or proportional (Shi et al., 2015). Therefore, according to the similarity principle and test requirements, the length of the model, the bulk density of the materials, the uniaxial compressive strength, the tensile strength, the cohesion, the internal friction angle, the Poisson's ratio, and the displacement and stress, which reflect physical phenomena, are selected to describe the change process in slope excavation and water storage.

In this study, considering the accuracy of the test, the workload and economic indicators in making the model and performing the test, the difficulty of finding the model materials and the scope of the simulated prototype (Huang et al., 2013), the geometric similarity ratio of rock and soil mass was selected as 1000 in the excavation and water storage test (C_l=1000). At the same time, to ensure that the landslide thrust generated by the rock and soil mass under the action of the self-gravity stress field was highly consistent with the actual situation, the similarity ratio of the rock and soil mass was 1.3 (C_γ=C_ρ=1000). Therefore, the theoretical physical and mechanical parameters of the corresponding model test materials were calculated as shown in Table 1.

2.2 Model similar materials and ratio

Based on the elastic modulus, Poisson's ratio, creep, thermal conductivity and other factors, similar materials are generally

TABLE 1 Model parameters in the excavation and water storage simulation test.

	Bulk density (kN/m^3)	Cohesion (kPa)	Internal friction angle (°)	Elastic modulus (GPa)	Poisson's ratio	Tensile strength (MPa)	Compressive strength (MPa)	Permeability coefficient (m/s)
Similarity ratio	1.3	1300	1	1300	1	1300	1300	31.6
Quaternary system	13.85	0.023	28					
Brown shale	16.92	0.076	25	0.0009	0.3	0.00023	0.002	$6.3*10^{-9}$–$6.3*10^{-8}$
Oil shale	16.15	0.154	35	0.0026	0.26	0.00026	0.0026	$3.2*10^{-11}$–$9.6*10^{-9}$
Coal seam	11.54	0.107	35	0.0009	0.24	0.00018	0.0018	$3.2*10^{-9}$–$3.2*10^{-8}$
Backfill material	15.38	0	29	0.0006	0.3	0.000003	0.00003	
Basalt	21.54	0.138	40	0.0055	0.14	0.00385	0.0385	$3.2*10^{-9}$
Fault F1	15.38	0.009	20	0.00155	0.3	0.00069	0.0069	
Fault F4	15.38	0.009	7	0.00038	0.3	0.0002	0.002	
Cretaceous sandstone	17.69	0.1	45	0.00308	0.25	0.00077	0.0077	

FIGURE 1
Similar materials of samples for physical models.

composed of three components: aggregate, adhesive and additive (Zuo et al., 2004; Zhang et al., 2008). Based on the comparison of the performance, advantages and disadvantages of similar material combinations (Cheng et al., 2016; Zhang et al., 2019), the selection principle and physical-mechanical parameters of similar materials are also considered for the model test object of this study. Finally, yellow sand, gypsum, cement and water were used as raw materials of similar materials, as shown in Figure 1. Different materials play different roles, for example, yellow sand, as a filling material, is used to adjust the weight, with a certain cohesion; gypsum and cement, as cementing materials, are used to control the material mechanical properties; water, with a mixing function, is used to meet the process requirements; hydraulic oil, as a regulator, is used to adjust the permeability, which does not affect the other material properties; and coloured iron powder dye is used to distinguish different rock and soil layers.

According to the materials selected above and previous studies (Wen et al., 2020; Shi et al., 2021), we designed 24 groups of ratio tests and made samples for uniaxial compressive strength tests (50 mm × 100 mm), standard samples for direct shear tests (61.8 mm × 20 mm) and standard samples for percolation tests (61.8 mm × 40 mm) with different ratios, as shown in Figure 2. The process of making standard specimens of similar materials was as follows:

1. Preparation of raw materials: Yellow sand was screened with a standard screen of 2.36 mm, and cement, gypsum, water and hydraulic oil were accurately weighed according to the test scheme.
2. Preparation of the mould: The tray and cylinder of the mould were installed, and whether the mould was installed in place and whether the cylinder and tray were tightly clamped were checked. At the same time, for convenience of demoulding, the inner wall of the mould needed to be coated with hydraulic oil and allowed to sit for a period of time before being coated with petroleum jelly.
3. Mixing of materials: The proportionally weighed yellow sand was poured into the mixing container and evenly stirred. Then, cement and gypsum were evenly added, and water and hydraulic oil were added. The mixture was evenly stirred during addition of the materials, fully stirred and set aside.
4. Weighing and feeding: An electronic balance was used to weigh a certain quantity of the mixed material, and a funnel was used to add the material into the mould cylinder. Material falling was avoided in the process of feeding.
5. Material pounding: The materials were crushed in layers with a compactor after adding the materials into the cylinder.

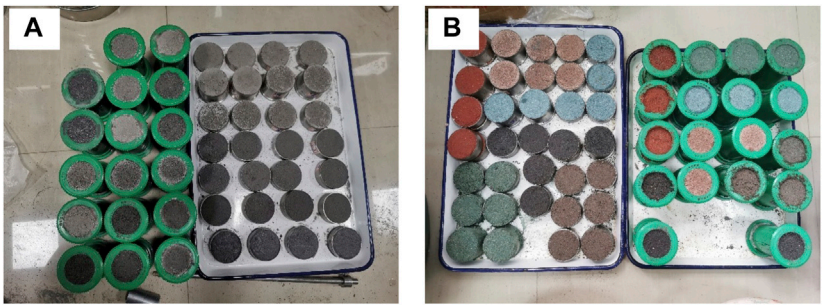

FIGURE 2
Mechanical sample preparation of similar materials with different ratios.

TABLE 2 Similar material ratios in excavation and water storage simulation tests.

Prototype lithology	Cement (%)	Gypsum (%)	Sand (%)	Water (%)	Oil (%)	Iron dye (%)
Oil shale	3	1	81	15	1.5	0.5
Basalt	8.75	3.75	75	12.5	1.25	
Coal seam	5	22.5	67.5	5	1	
Backfill material	5	30	60	5	1	3.5
Brown shale	5	15	75	5	1	0.5
Fault F1	10	10	70	10	1	0.5
Fault F4	5	15	70	10	1	0.5
Cretaceous sandstone	10	5	75	10	1	0.5

6. Demoulding and labelling: After 2 days of natural drying, the sample was demoulded. After completion of the mould, the specimen was carefully removed, and each specimen was labelled.
7. Natural curing: The moulded specimen was placed indoors for natural curing, and the curing time was 2 days.

After curing, the uniaxial compressive strength, elastic modulus, Poisson's ratio, tensile strength, permeability, heavy weight, cohesion and internal friction angle of similar materials with different proportions were measured by laboratory tests. Referring to the above, the relative ratios of the physical and mechanical parameters of the corresponding model test materials were calculated, and the similar material ratio schemes of the final excavation and water storage physical models are shown in Table 2.

3 Model test scheme design

3.1 Physical simulation assembly and data acquisition system

The size of the model box in this study is 200 cm × 50 cm × 100 cm. The box is composed of five 2.5 cm thick transparent acrylic plates, a fixed frame and angle steel fixtures. The highly transparent acrylic plate can withstand the heavy filling of the model, and because of its high transparency, it is easy to observe and record the deformation of the model from all angles during the test. The fixed frame is made of aluminium alloy and fixed through screws to the angle steel fixtures, which are used to fix four stress plates. Considering the compression of the model body and mutual interference caused by the loading process between the adjacent loading plates. Angle steel is placed between the adjacent loading plates to close the gap between the loading plates during the filling of the model. So that the force plate neither expands outwards nor overturns in the filling and compaction of the material, which is conducive to filling of the material. At the same time, three beams are added at the bottom. They are used to support the deformation of the bottom bearing plate when the model is loaded.

In this physical simulation test, the geometric similarity ratio is determined according to the similarity relationship between the original slope and the test model, and the geometric similarity ratio of the excavation and water storage simulation test model is 1:1000. The model slope design is shown in Figures 3A, B. After the preliminary preparation of the test model is completed, the packing is started, the thickness of each rock and soil layer is converted to the model box according to similarity theory, and different matching schemes are determined according to the physical and mechanical parameters of different rock layers after the similarity theory conversion. According to the required

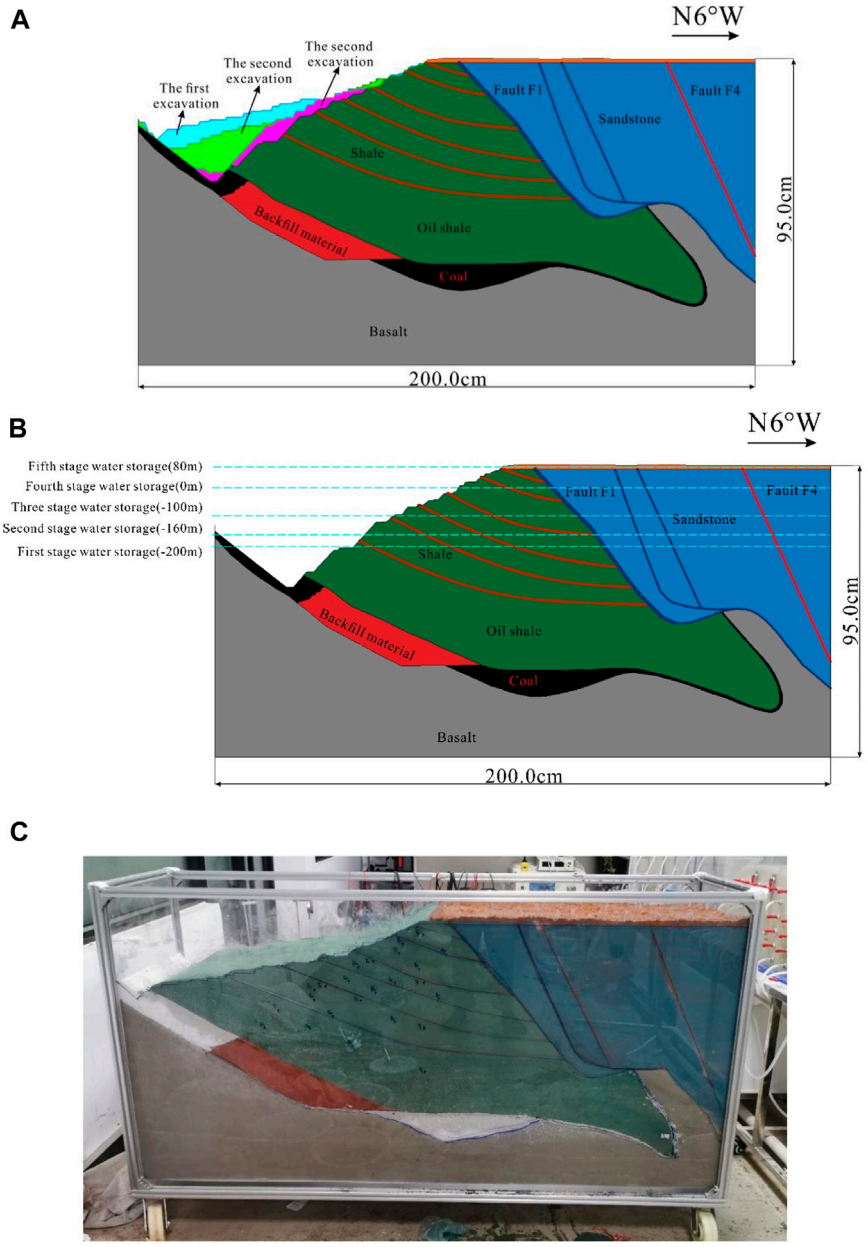

FIGURE 3
Design drawing of the simulation test and slope model: **(A)** excavation, **(B)** water storage, **(C)** slope physical model.

proportions of similar materials in each layer, the similar materials are weighed in proportion by an electronic balance and evenly stirred. The mixed materials are loaded into the filling box and crushed. Sensors are installed at the corresponding positions according to the test requirements during the filling process. After the filling is completed, the test can be carried out after a week of maintenance in the natural state (Figure 3C).

In this study, a TST3827E static strain acquisition instrument is used to monitor the stress (Figure 4A), and a sensor system composed of dial indicator displacement meters, earth pressure boxes, seepage meters and a digital image detection device is used to collect the stress change and deformation data of the slope model. The dial indicator displacement meters and ZBL-V6O0 multipoint digital image detection device are used to observe the macroscopic deformation characteristics (Figures 4B, C). YLH17 miniature earth pressure boxes (with a size of 17*10 mm, a range of 30 kPa and 0.05% Fs) and KXYL20-type pore water lysimeters (with a size of 20*13 mm, a range of 30 kPa and 0.5%–0.05% Fs) are used to collect soil pressure and pore water pressure data of different parts, respectively (Figures 4D, E). To simulate the slope water storage test and keep the water storage level stable, a stable head water supply device was made. The device comprises a pumping tank, a simple connector and two pumping pumps. The water level is controlled by changing the height of the water supply tank (Figure 4F).

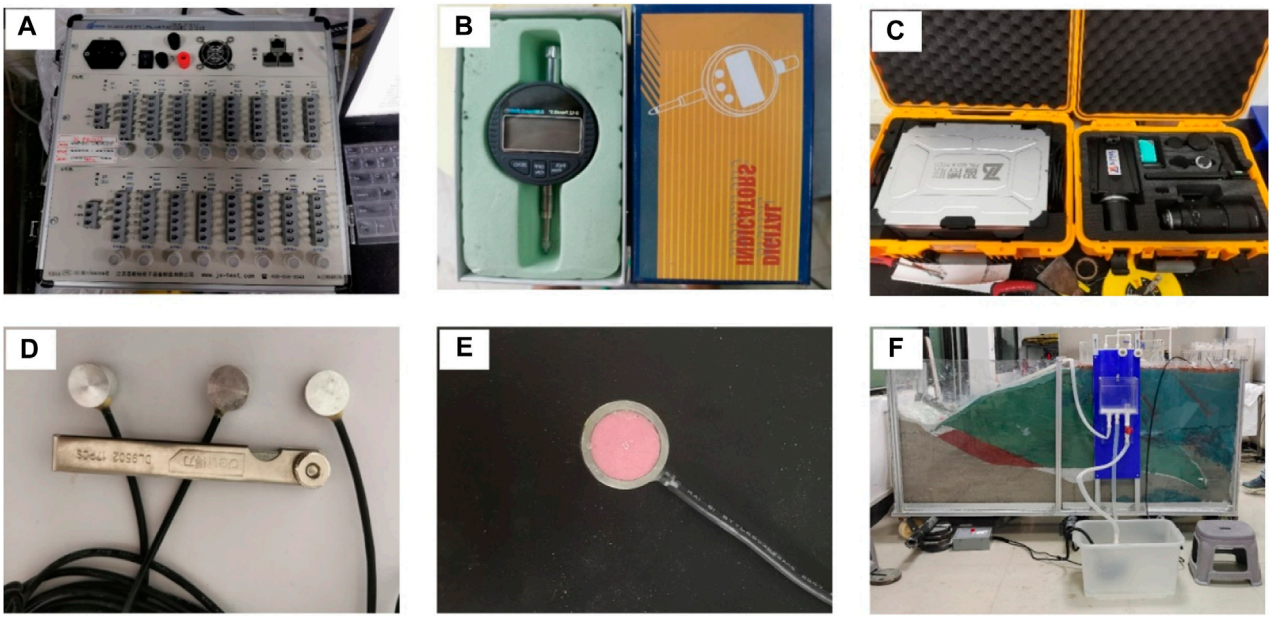

FIGURE 4
Data acquisition system: **(A)** TST3827E static strain acquisition instrument, **(B)** dial indicator displacement meter, **(C)** ZBL-V6O0 multipoint digital image detection device, **(D)** YLH17 miniature earth pressure box, **(E)** KXYL20-type pore water lysimeter, **(F)** stable head water supply device.

3.2 Excavation model test

3.2.1 Test scheme

According to the annual slope contour, excavation was carried out three times in this test (Figure 3A). The excavation simulation test was mainly performed to observe the slope deformation, ground surface settlement and slope stress changes during and after the excavation.

3.2.1.1 Slope deformation observation

A digital image detection device is used for slope deformation observation. The arrangement of measurement points is shown in Figure 5A, where observation points M1-5 are parallel to the slope and mainly observe the displacement of the lower part of the excavation slope. Observation points M6-10 are parallel to the surface and mainly observe surface subsidence. Observation points M11-13 are located in the interior of the slope and mainly observe the change in the weak interlayer in the interior of the slope. Observation points M14 to 18 are located on both sides of fault F1 and fault F4 and mainly observe the difference in the displacement change on both sides of fault F1 and fault F4.

3.2.1.2 Ground surface settlement monitoring

Five dial indicator displacement meters are arranged in the model slope, among which two dial indicator displacement meters are arranged on the upper slope of the slope body, located at the central axis of the slope body; the spacing is 10 cm, and the numbers are W1 and W2. Three dial indicator displacement meters are arranged at the top of the slope, located at the central axis of the slope body, with a spacing of 20 cm, which are numbered W3-W5 (Figure 5B).

3.2.1.3 Slope stress monitoring

Seven earth pressure boxes are arranged in the model slope, all of which are arranged on the longitudinal section of the central axis of the slope body (see Figure 5B). Among them, the pressure surfaces of T5 and T7 face the surface, and the other five earth pressure boxes are buried with their surfaces facing the normal direction outside the stratum plane. Four earth pressure boxes are arranged parallel to the slope surface, with a transverse interval of 15.7 cm–16.0 cm, numbered T1-T4. Three earth pressure boxes are arranged perpendicular to the top of the slope from top to bottom, with an interval of 15.0 cm, numbered T5 to T7. Since the earth pressure boxes have a certain size and thickness, embedded parts with the same size as the earth pressure boxes are placed at the corresponding positions, fixed, packed, and compacted twice during the installation process. Before tamping the lower material, the embedded parts are slowly dug out, and the earth pressure boxes are placed, fixed, packed and gently tamped.

3.2.2 Test procedure

In the test preparation stage, the earth pressure boxes and the dynamic and static strain acquisition instruments are connected, the data acquisition frequency is 0.1 Hz, and the connection mode is full bridge. After the normal debugging operation of the instruments, the initial value is set to zero. After confirming that the dial indicator is set to zero, the displacement monitoring device can work normally and collect data, formal monitoring is started, and the slope is excavated. After the excavation, dial indicator displacement meter readings are first recorded every 1 min. After 1 h, dial indicator displacement meter readings are recorded every 5 min. After 2 hours, dial indicator displacement meter readings are recorded every 10 min, and to confirm that the model reaches a completely stable state inside, the actual single monitoring duration is more

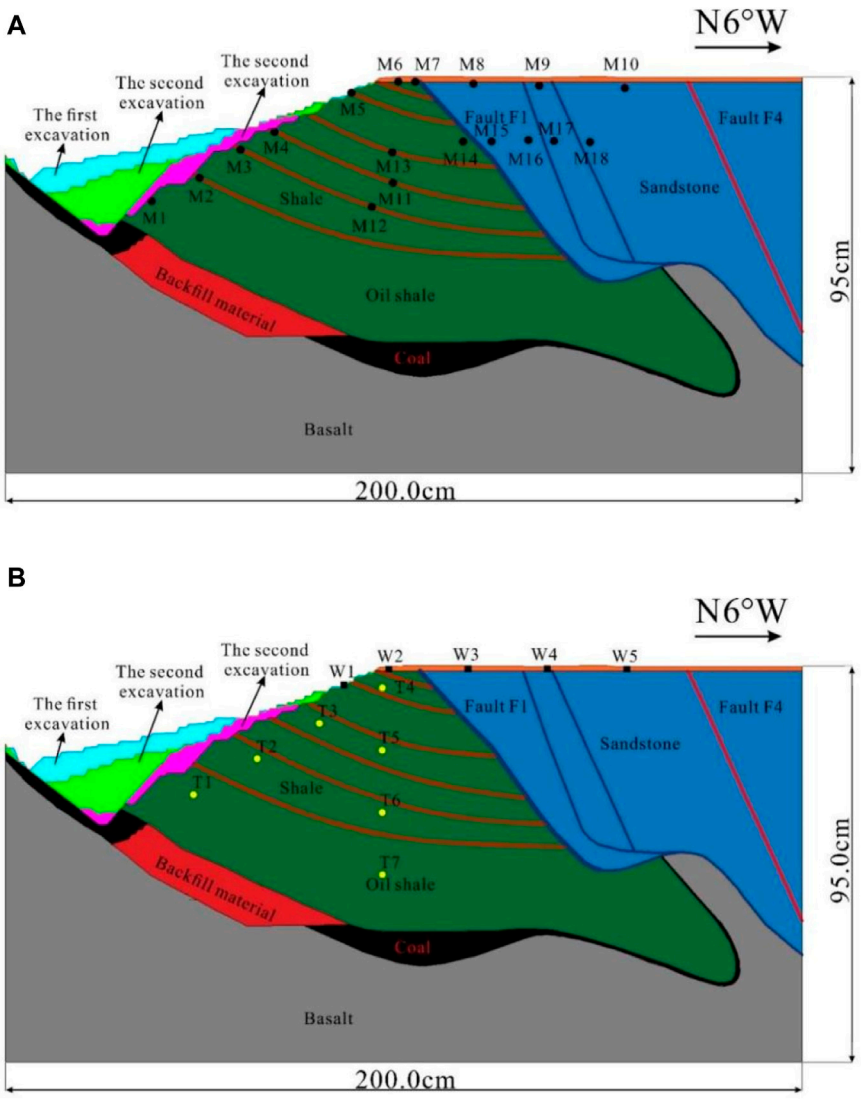

FIGURE 5
Layout diagram of slope deformation observation points in the excavation simulation test: **(A)** observation schematic diagram, **(B)** monitoring device layout.

than 3 h. After the data of the sensors and the dial indicator displacement meters are stable, the next excavation is carried out, and the test is finished when the data of the three excavation simulation tests are stable.

3.3 Water storage model test

3.3.1 Test scheme

This test was mainly performed to study the slope deformation, surface settlement, slope stress and pore water pressure in the process of water storage. Water storage was mainly divided into five stages, and the specific scheme was designed as follows:

First stage of water storage: Water is stored at the foot of the slope up to 28 cm from the surface (equivalent to the prototype level of −200 m), and the water level is kept stable. Continuous observation and monitoring are carried out for 6 h to record the changes in slope deformation, surface settlement, slope stress and pore water pressure.

Second stage of water storage: On the basis of the first-stage water level, the second-stage water level is increased by 4 cm–24 cm from the surface (equivalent to the prototype level of −160 m), and the water level is kept stable. Continuous observation and monitoring are carried out for 18 h to record the changes in slope deformation, surface settlement, slope stress and pore water pressure.

Third stage of water storage: On the basis of the second-stage water level, the third-stage water level is increased by 6 cm–18 cm from the surface (equivalent to the prototype level of −100 m), and the water level is kept stable. Continuous observation and monitoring are carried out for 36 h to record the changes in slope deformation, surface settlement, slope stress and pore water pressure.

Fourth stage of water storage: On the basis of the third-stage water level, the fourth-stage water level is increased 10 cm–8 cm

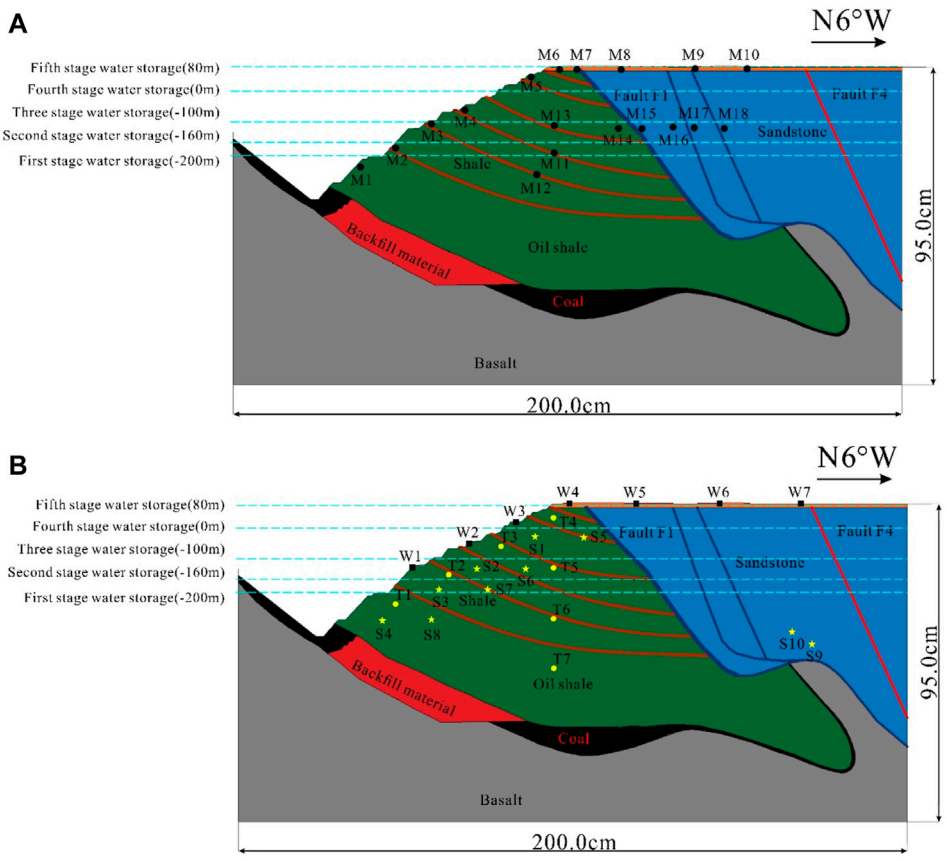

FIGURE 6
Layout diagram of slope deformation observation points in the water storage simulation test: **(A)** observation schematic diagram, **(B)** monitoring device layout.

from the surface (equivalent to the original ±0 m level), and the water level is kept stable. Continuous observation and monitoring are carried out for 60 h to record the changes in slope deformation, surface settlement, slope stress and pore water pressure.

Fifth stage of water storage: On the basis of the fourth-stage water level, the fifth-stage water level is increased by 8 cm–0 cm from the surface (equivalent to the prototype Quaternary system level), and the water level is kept stable. Continuous observation and monitoring are carried out for 96 h to record the changes in slope deformation, surface settlement, slope stress and pore water pressure.

The stable head water supply system was used in the test to realize raising and stability of the storage water level. The water storage simulation test was mainly performed to observe the slope deformation and surface settlement under different water storage levels and to monitor slope stress and pore water pressure changes.

3.3.1.1 Slope deformation observation

The slope deformation observation adopts a multipoint digital image detection device, and the arrangement of measurement points is shown in Figure 6A. Observation points M1-5 are parallel to the slope and mainly observe the displacement of the lower part of the excavation slope. Observation points M6-10 are parallel to the surface and mainly observe surface subsidence. Observation points M11-13 are located in the interior of the slope and mainly observe the change in the weak interlayer in the interior of the slope. Observation points M14-18 are located on both sides of fault F1 and fault F4 and mainly observe the difference in the displacement change on both sides of fault F1 and fault F4.

3.3.1.2 Ground surface settlement monitoring

A total of 7 dial indicator displacement meters are arranged in the model slope, among which 3 dial indicator displacement meters are arranged on the surface of the slope body, located at the central axis of the slope body. The spacings are 17 cm and 14 cm, and the numbers are W1, W2 and W3. Four dial indicator displacement meters are arranged at the top of the slope, located at the central axis of the slope body. The spacings are 19.7 cm, 25.5 cm, and 24.6 cm, and the numbers are W4-W7 (Figure 6B). Because the water storage level rises to above the dial indicator displacement meter, W1 is removed from the third stage of water storage, W2 is removed from the fourth stage of water storage, and W3 is removed from the fifth stage of water storage.

3.3.1.3 Slope stress monitoring

A total of 7 earth pressure boxes are arranged in the model slope, all of which are arranged on the longitudinal section of the central

axis of the slope body (Figure 6B). Among them, the T5 and T7 compression surfaces are towards the surface, and the other 5 earth pressure boxes are buried with their surfaces facing the normal direction outside the rock plane. Among them, four earth pressure boxes are arranged parallel to the slope surface, with a transverse interval of 15.7 cm–16.0 cm, numbered T1-T4. Three earth pressure boxes are arranged perpendicular to the top of the slope from top to bottom with an interval of 15.0 cm, numbered T5-T7. Since the earth pressure boxes have a certain size and thickness, embedded parts with the same size as the earth pressure boxes are placed at the corresponding positions, fixed, packed, and compacted twice during the installation process. Before tamping the lower material, the embedded parts are slowly dug out, and the earth pressure boxes are placed, fixed, packed and gently tamped.

3.3.1.4 Pore water pressure of the slope

A total of 10 seepage gauges are arranged in the model slope, all of which are arranged below the periodically changing water level elevation. S1-S4 and S5-S8 are alternately arranged on both sides of the longitudinal section of the central axis of the slope body, 12 cm from the central axis. The longitudinal spacings are 9.4 cm, 6.2 cm, and 9.3 cm. Two seepage gauges are arranged at the same horizontal position. S9 and S10 are arranged on both sides of the longitudinal section of the central axis of the slope body, 12 cm from the central axis, and the longitudinal spacings are 25.8 cm and 21.3 cm, respectively (Figure 6B). The lysimeters are saturated in water before burial, and the burial method is the same as that of the earth pressure boxes.

3.3.2 Test procedure

According to the design of the water storage simulation test scheme, the water level of the first stage of water storage is controlled at 280 m below the surface of the prototype, which is 28 cm below the surface of the model. After confirming that the dial indicator displacement meters are set to 0, the acquisition system, sensors and displacement detection devices can work normally and collect data. The stable head water supply device is turned on for water storage. The observation time of each stage of the water storage simulation test is successively increased and is 6 h, 18 h, 36 h, 60 h and 96 h. After reaching the required observation time, the numerical changes in the sensors and dial indicator displacement meters are observed. After the changes in the sensors and dial indicator displacement meters tend to be stable, the height of the water supply tank is changed to the water storage level of the next stage, and the next stage of water storage is carried out. When the observation time of the last stage of the water storage simulation test is reached and the values of the sensors and dial indicator displacement meters are stable, the water storage simulation test is finished.

4 Physical simulation test results and discussion

4.1 Excavation model

4.1.1 Slope deformation characteristics

The collected observation point deformation data are processed by MATLAB to obtain the relationship curve between the horizontal displacement, vertical displacement and time, as shown in Figure 7, where the horizontal displacement is positive when the observation point moves to the left and negative when it moves to the right. The horizontal and vertical displacements of M1-18 indicate obvious deformation in the same direction in both the horizontal and vertical directions, indicating the overall load unloading deformation of the slope to the outside of the slope.

After each excavation, unloading deformation occurs at M4with the largest changes, and then the deformation gradually increased and the amplitude gradually decreased due to the continuous adjustment of the stress of slope. M1 is deformed first, and M2-18 begin to respond to deformation later because M1 is located at the foot of the slope and has an obvious response to the excavation disturbance stress concentration. The horizontal deformation (Figure 7A) in the area near the slope surface is greater than the vertical deformation (Figure 7B), the side slope angle formed by excavation is small, the horizontal stress change of the excavated slope surface is greater than the vertical stress change, and the horizontal deformation in the area near the oil shale in the slope is greater than the vertical deformation. These phenomena all occur in the weak layer of brown shale, and the horizontal stress change is greater than the vertical stress change.

The excessive excavation of rock mass in the middle and lower parts of the slope makes the slope angle in this area the largest, resulting in the largest deformation near the slope surface. In the interbed area of oil shale and brown shale in the slope body, the overall deformation is small, and the deformation is minimal near the fault F1 and fault F4. With increasing excavation depth, deformation of the internal rock mass to the slope surface is generated, and the variation range is gradually expanded. The deformation of the slope surface is much larger than that of the internal rock mass, and the deformation is significantly reduced with extension into the interior of the slope. The influence zone of slope excavation is located on the left side of the fault F1 from the slope to the interior of the slope body. The deformation zone on the surface of the slope body is within a certain range. With increasing excavation depth, the redistribution of unloading stress caused by excavation produces macroscopic creep deformation on the surface of the slope body. Due to the excavation, the surface of the slope rock mass in the region has been displaced to different degrees over a large range, and the initial displacement is small and then increases.

According to the cumulative deformation in the excavation test (Figure 7). The origin is at the lower left corner (Figure 3A), and the coordinates are (N200, -875). The horizontal deformation near the middle of the slope (N890, 817) reaches the maximum (0.3973 mm). This area is above the excavation line and in the soft brown shale rock layer, so the maximum horizontal deformation occurs here. The rock mass located in the compound fold structure area below the fracture zone of the F1 fault has a large vertical displacement, which indicates that this part of the rock mass is misaligned along the weak plane under the action of the self-gravity stress and the self-gravity of the toppling rock mass of the hanging wall. The deformation curves of M14 and 15 on the two sides of the hanging wall and footwall zones of fault F1 show a great difference. The vertical displacement of the hanging wall zone is larger than that of the footwall zone, and overall dislocation occurs compared with the footwall rock mass. This trend is also observed at M17 and 18 on the two sides of the hanging wall and footwall zones of fault F4. The deformation direction of the footwall

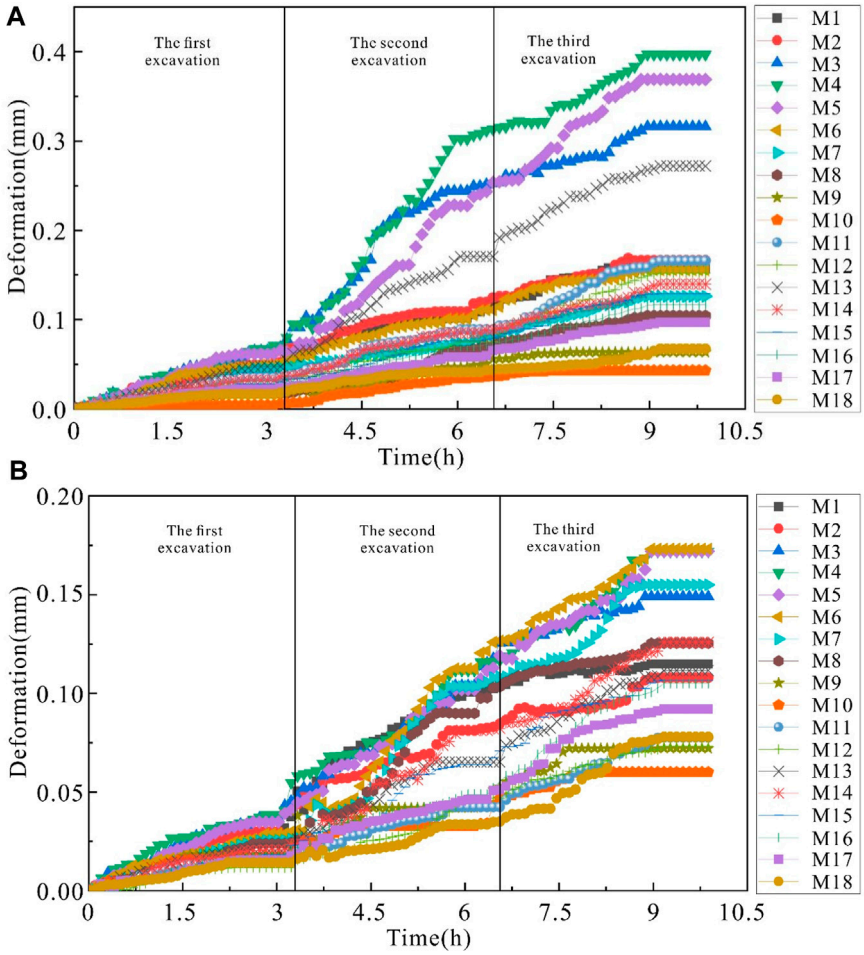

FIGURE 7
Change in the deformation at M1-18 during excavation: **(A)** horizontal deformation, **(B)** vertical deformation.

zone of the fault is roughly the same, but the fault does not move as a whole. The vertical displacement of the footwall zone is larger than that of the hanging wall zone, and overall stagger sliding occurs compared with the hanging wall rock mass. It can be considered that the fault fracture zone has an obvious influence on the slope deformation in the whole study area, resulting in compressive dislocation deformation.

4.1.2 Ground surface settlement characteristics

The surface cumulative settlement deformation curves of the three excavation tests are shown in Figure 8. The surface of the ground is uniformly decreased during excavation, the deformation trends of the dial indicator displacement meters are the same as the vertical deformation at M6-10, and the deformation amounts are similar. After the first excavation, the initial deformation of W1 at the shoulder and W2 at the top of the slope is small and then rapidly increases, which is caused by the increase in the slope angle due to slope excavation and the unloading deformation at the top of the slope. W4 and W5 are basically not deformed, and they are located furthest from the excavated slope surface and are minimally affected. In the second excavation test, overall subsidence deformation occurs. W1 at the shoulder and W2 at the top of the slope begin to exhibit a decline first, and the change is the largest near the slope surface to the top of the slope. During the excavation process, the lower part of the slope forms a large slope angle, the middle of the slope surface forms part of the void, and the upper slope body undergoes large deformation towards the foot of the slope. Since this excavation has the largest depth and the largest slope angle, the surface settlement changes the fastest. In the third excavation test, the same W1 at the shoulder and W2 at the top of the slope first begin to exhibit a decline, the excavation produces an overhead surface, and the shoulder and top of the slope undergo unloading deformation. W4 and W5 are basically unchanged because they are located at the furthest distance from the excavation slope and are least affected by the excavation.

In this excavation simulation test, after sorting the data observed in the three excavation simulation tests, the final surface settlement of the geological prototype after the three excavations can be deduced according to the similarity ratio. Among them, the cumulative settlement at the slope shoulder (N1043,900) is the largest at 0.1782 mm. The farther the surface is from the slope surface, the smaller the surface settlement.

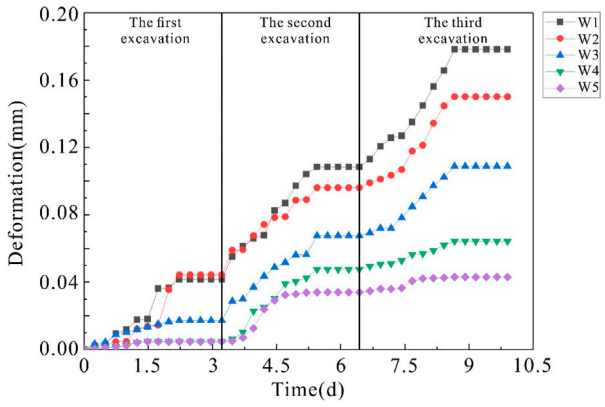

FIGURE 8
Change in the ground surface settlement deformation in excavation.

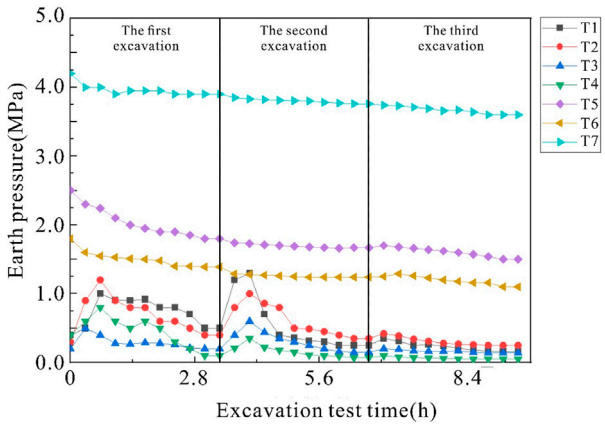

FIGURE 9
Change in stress at T1-7 in excavation.

4.1.3 Stress characteristics

The stress changes during excavation are shown in Figure 9. It can be seen that at T5, T6 and T7, which are buried deep inside the slope, the earth pressure values are relatively large, and the overall change trend is relatively stable. The maximum earth pressure value of T7 (N1143,450) is 3.77 MPa. While the T6 compression surface faces the outer normal direction of the rock stratum plane, the T5 and T7 compression surfaces are towards the surface, and the earth pressure values are larger than that of T6. A data drop phenomenon of T1-T4 located below the slope surface is found. There is a short-term increase in stress at the three times of the three excavation processes, indicating that the slope surface is affected by excavation, and the reason is due to the stress adjustment of each point in the slope. The stress at the measurement point temporarily increases, but over time, the overall stress in the slope is reduced. The largest stress release is mainly near the excavation slope, and although there are changes at other places, the changes are not large. The variation range of earth pressure values from T1-T4 is larger than that from T5-T7, indicating that with increasing depth, the pressure is increasingly less affected by excavation. Among T1-T4, the minimum earth pressure is 0.05 MPa for T4 (N1143,900), indicating that the foot of the slope is the most affected and that the change is the largest. In the slope excavation process, the stress change in the slope is a complex process. After the excavation is completed, the stress at the measurement point near the empty surface of the slope is not instantly released, and this release is not completed in a short time such as displacement but is a long-term process.

4.2 Water storage model

4.2.1 Slope deformation characteristics

Similar to the excavation model, the cumulative deformation curve of M1-18 in the five-stage water storage test is shown in Figure 10. The deformation rapidly changes near the water storage level adjustment time, slows down as time goes by, and finally enters a plateau area with a relatively small displacement change. For each water storage period, M1 exhibits a change first, and M2-18 begin to respond to deformation later. Because M1 is located at the foot of the slope, the stress changes first. In the early stage of water storage, the slope is squeezed by the hydrostatic pressure of the surface water, and the stress decreases. The stress change at M5 is the largest, and the amplitude is the largest. Then, because of the continuous adjustment of the stress in the slope, the deformation gradually increases, but the amplitude decreases. The horizontal deformation (Figure 10A) near the slope surface is greater than the vertical deformation (Figure 10B), which is caused by the surface water flowing into the internal slope and squeezing the slope to hinder vertical deformation. The vertical deformation of the near-ground surface is greater than the horizontal deformation, the surface is affected by gravity stress, and the vertical stress change is greater than the horizontal stress change.

In the early stage of water level change, the pore water inside the slope is constantly adjusted. The hydrodynamic pressure generated by pore water flow has a stronger influence on slope deformation than the hydrostatic pressure of relatively stable water. That is, large deformation of the slope is often caused by hydrodynamic pressure, that is, is driven by hydrodynamic pressure, and then, progressive failure occurs under hydrostatic pressure. At the same time, observing the occurrence time of the maximum displacement at each observation point (Figure 10), it can be seen that the rock mass deformation at the low elevation of the slope is earlier than that at the high elevation, indicating that the failure of the slope caused by water storage starts from the foot of the slope and gradually moves to the middle part of the slope, forming progressive failure. In the early stage, the rock mass below the water level is subjected to the load inside the slope body, and the deformation is mainly compaction deformation, which enhances the stability of the slope body to a certain extent. However, this phenomenon is only temporary. After that, the rock mass is damaged under the action of dynamic and hydrostatic pressure, and each data point tends to stabilize, indicating that the slope deformation tends to converge. In particular, the deformation direction of the area near the slope in the fifth stage is opposite to that in the previous four stages (Figure 10A), indicating that when the water level is raised to the surface (80 m), the pore water pressure exerts a greater

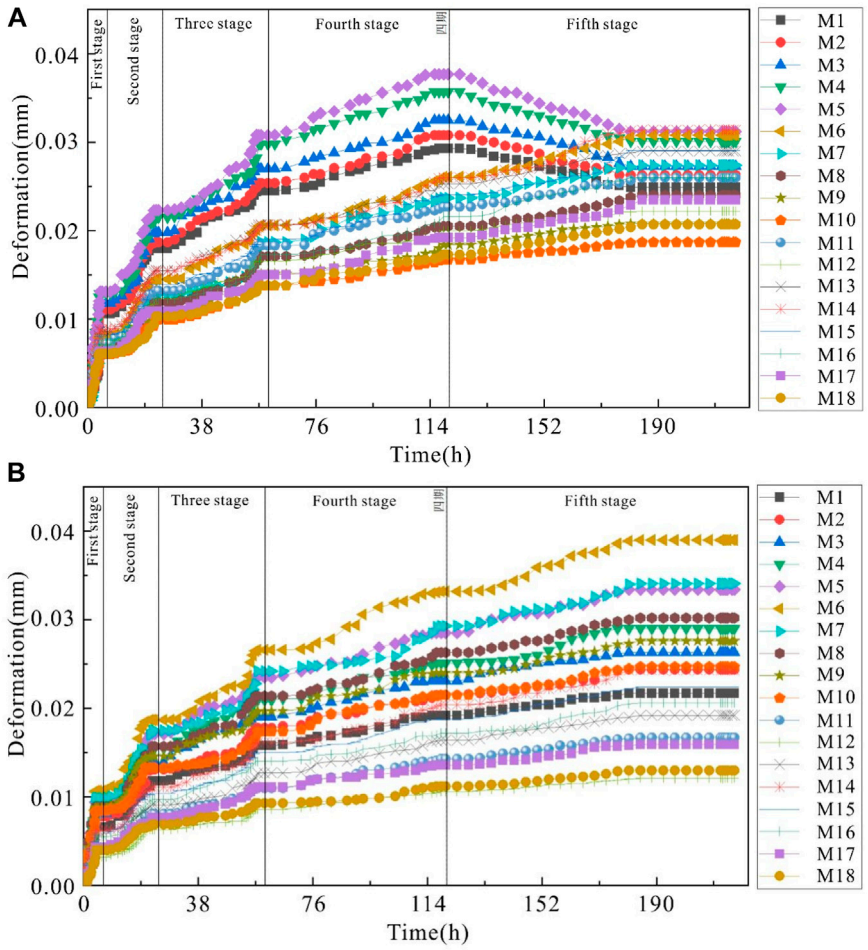

FIGURE 10
Change in deformation at M1-18 in water storage: **(A)** horizontal deformation, **(B)** vertical deformation.

extrusion effect on the surface of the slope body. As a result, the slope body produces a slanting downward edge, and the horizontal cumulative deformation decreases. The cumulative vertical deformation data in the near-surface area are similar to the surface subsidence data.

According to the cumulative deformation in the water storage test (Figure 10). The origin is at the lower left corner (Figure 3A), and the coordinates are (N200, -875). Under the action of staged water storage, the surface of the slope (M4-6) is subjected to greater tensile and compressive stress due to the total dynamic and hydrostatic pressure, so the maximum deformation occurs. The horizontal cumulative deformation in the interbed zone within the slope body is greater than the vertical deformation (M1-M13), and the horizontal slip in this zone is mainly along the weak brown shale layer. The vertical deformation near fault F1 and F4 in the slope body is greater than the horizontal deformation (M14-M18), indicating that settlement deformation mainly occurs in this zone.

4.2.2 Ground surface settlement characteristics

The ground surface settlement deformation curve of the five-stage water storage test is shown in Figure 11. W1-W3 were removed before the third, fourth, and fifth stages of the storage test, respectively. During the water storage process, the monitoring point nearest to the water level (W1 in figure A, W2 in figure B, W3 in figureC, and W4 in figure D) exhibits a change first. The deformation continues to increase but the amplitude of variation gradually decreases as the test proceeds. The monitoring point at the farthest distance from the slope surface shows the smallest stress change, so the deformations at W5, W6, and W7 decrease in turn. In the early stage (Figures 11A, B), the surface water flows along the pores of the slope to the interior of the slope body, resulting in large deformation. The subsequent deformation is progressive deformation, which is transmitted from the deformation at the foot of the slope. In the later stage (Figures 11C, D), the pore water pressure in the middle part of the slope body increases, the internal stress of the slope body decreases, and the stress in the slope body is redistributed, leading to deformation at the top of the slope. The deformation starts from the middle part and is progressive, with the maximum deformation occurring at the top of the slope. This result is the same as the observed results of slope deformation and the same as the data collected by the digital

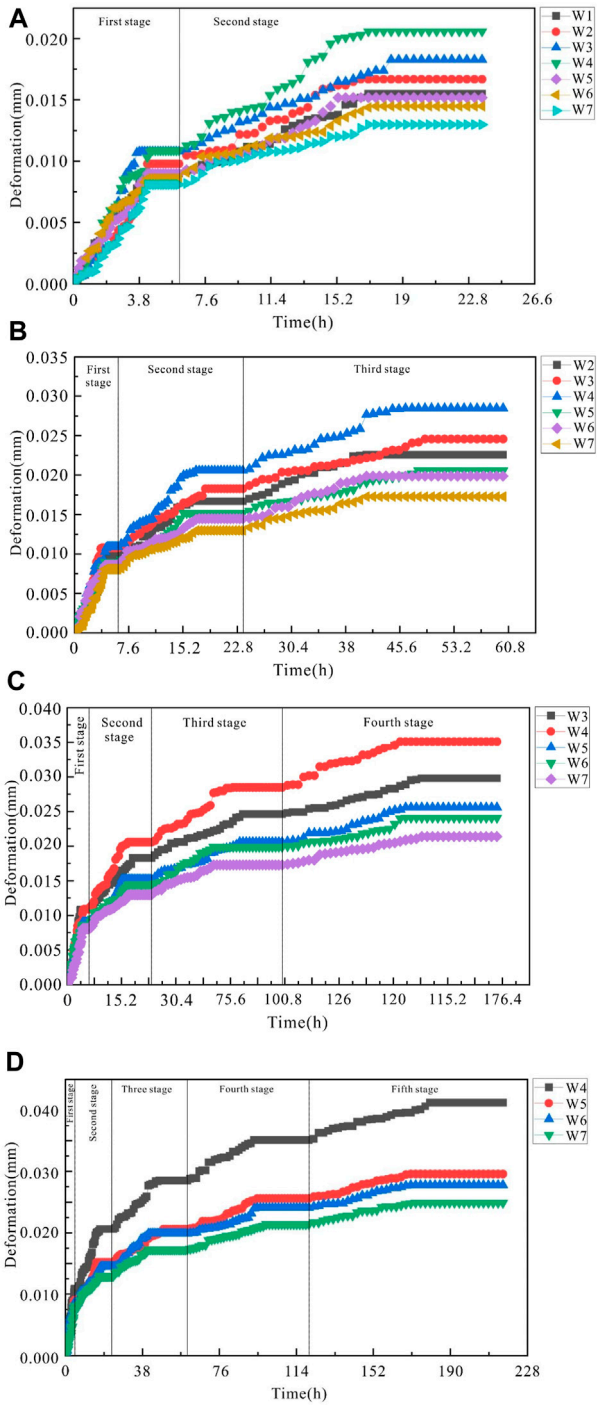

FIGURE 11
Change in the ground surface settlement deformation in water storage: **(A)** second stage, **(B)** third stage, **(C)** fourth stage, **(D)** fifth stage.

image monitoring device (Figure 10), indicating that the fault affects the ground surface settlement, and the settlement at the foot is larger.

According to Figure 11, the final settlement of the ground surface was obtained. Since W1, W2, and W3 were removed before the third, fourth, and fifth stages of the storage test, respectively, their values cannot represent the final deformation. The maximum cumulative settlement of W4 (N1190,950) located at the top of the slope is 0.0412 mm. Due to the rise in the water storage level, the hydrostatic pressure on the surface of the slope body increases, and the stress inside the slope body is redistributed. Finally, under the action of hydrostatic pressure and hydrodynamic pressure, slope top subsidence deformation occurs. W5 (N1390, 950), W6 (N1640, 950) and W7 (N1890, 950) are farther from the slope surface, and the settlement amounts at the three places are 0.0296 mm, 0.0278 mm and 0.0249 mm, respectively. The surface deformation of the slope body is much larger than the internal deformation of the slope body, and the deformation far from the slope surface is significantly reduced.

4.2.3 Pore water pressure characteristics

The changes in the pore water pressure are shown in Figure 12. The change in the pore pressure in the whole process basically maintains synchronization with the progress of the water storage stage, while the monitoring points located in the depth of the slope slightly lag, and the overall curves present a step-like feature. The change order of the pore water pressure is consistent with the rule that the values change from the slope surface to the deep slope body, from bottom to top. The stability of the pore water pressure is consistent with the trend of gradually decreasing from low elevation to high elevation and from the slope surface to the deep slope body.

In the first stage, the values at S4 and S8-S10 gradually increase and remain stable in order. The pore water pressure at S4 near the foot of the slope increases first, and the pressure at S8-S10 near the water level elevation of the first stage also gradually increase. In the second stage, S4 and S8, which are located at the lowest location, are the first to respond after a period of time. S3, S7, S9, and S10 slightly lag behind the S4 and S8 responses, and the increase is small. In the third stage, the increase in the pore pressure at S3 and S7 is greater than the response in the second stage. S2 and S6 show a small increase due to the water level exceeding their embedding height. In the fourth stage, the change in the pore pressures of S2 and S6 in the middle is greater than the response in the third stage. S1 and S5 show a small increase because the water level exceeds the embedding height. In the fifth stage, the increase in the pore pressure of S1 and S5 in the middle is greater than the response in the fourth stage. Finally, S4 has the largest pore pressure value, reaching 3.11 MPa, which is in the region closest to the slope surface. The minimum is at S10, only 0.21 MPa, which is the farthest point from the slope surface. This indicates that the pore water pressure decreases when extending into the slope body interior.

4.2.4 Stress characteristics

The variation in earth pressure is shown in Figure 13. By observing the change characteristics of the curve, it is found that the values at T1-T4 in the shallow surface of the slope foot decrease in the early stage of water level rise, corresponding to the same time point as the pore pressure rise. This is because with the rise in the reservoir level, the dry rock mass at the foot of the slope is submerged by water. The buoyance of the water will make the rock mass below the water level subject to the buoyance force, and the water penetrates into the interior of the slope body from the slope surface. Therefore, the pore water pressure between the rock plate and the cracks at the slope foot

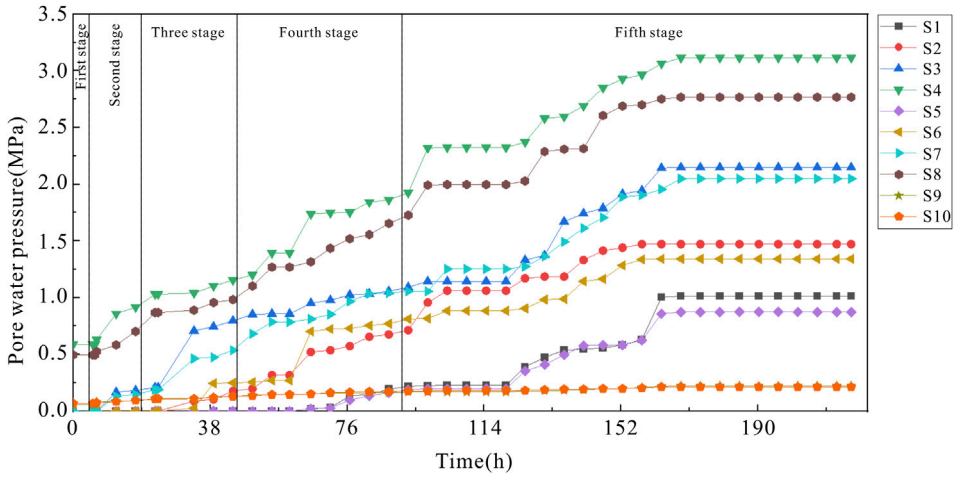

FIGURE 12
Change in the pore water pressure in water storage.

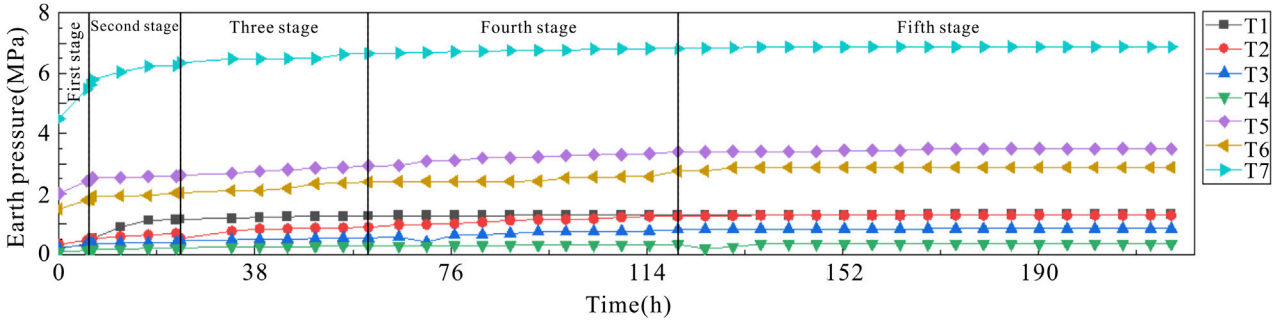

FIGURE 13
Change in stress at T1-7 in water storage.

increases, which reduces the effective stress at the slope foot. According to the distribution of the earth pressure, the value in the slope is 0.34–6.88 MPa. The earth pressures at T1 and T2 located at a lower elevation of the slope body and T5-T7 located in a deeper part of the slope body are relatively large, with a maximum value of 6.88 MPa at T7 (N1143,450) and a minimum value of 0.34 MPa at T4 (N1143,900). This shows that under the effect of water storage, the rock mass at the slope foot supports the upper rock mass, the pressure is the largest, and the stress concentration phenomenon exists. With the stress release of the rock mass at the foot of the slope and the loss of support of the upper rock mass, the stress concentration site gradually shifts to the high rock mass. The internal stress of the slope body finally stabilizes, slightly slower than the pore water pressure.

5 Conclusion

Based on an analysis of the engineering geological conditions of the slope, this study carries out a simulation test of slope excavation disturbance and water storage according to the similarity principle and similarity criterion. The stability of the slope body and fault structural zone are analysed and discussed, and the following conclusions are obtained:

1. According to the principle of similar material selection, yellow sand is selected as an aggregate, gypsum and cement are used as cementing agents, water is used as a solvent, hydraulic oil is used as a filling agent, and coloured iron powder is used to distinguish different rock layers. The contents of cement and yellow sand can regulate the physical and mechanical properties and hydrological properties. Gypsum has a certain regulation effect on the strength and permeability. Hydraulic oil has a great regulatory effect on the permeability.
2. Excavation causes stress release of the slope and unloading deformation of the slope rock mass. The local slope rock mass deforms to the outside of the slope body, and the deformation is mainly concentrated near the middle and lower parts of the slope surface. This is caused by the excavation and unloading of the rock mass, which causes stress redistribution of the slope rock mass. The stress greatly changes near the slope surface, and the stress is locally concentrated at the foot of the slope.

3. During excavation, the rock mass located in the fault structural zone shows nonglobal movement, and the vertical displacement of the footwall rock mass is larger than that of the hanging wall rock mass, indicating that the rock mass at this place has a tendency to produce relative dislocation along the fault fracture zone under the action of excavation disturbance and self-gravity of the hanging wall rock mass.
4. In the early stage of water storage, the surface rock mass of the slope body below the water level is subjected to dynamic and hydrostatic pressure inside the slope body, resulting in transient compaction deformation. However, with the infiltration of water into the slope body, the pore water pressure inside the slope body increases, the water weakens the slope rock mass, the rock mass near the slope surface gradually deforms to the outside of the slope, and the slope top shows a certain settlement trend. According to the simulation model, the maximum deformation of the slope can reach 0.0312 mm, and the surface settlement can reach 0.0412 mm.

Data availability statement

The data analyzed in this study is subject to the following licenses/restrictions: The data sets are proprietary and subject to a confidentiality agreement. Requests to access these datasets should be directed to Chengheng Hou, 492674382@qq.com.

Author contributions

CH: Formal Analysis, Investigation, Methodology, Writing–original draft, Writing–review and editing.

Funding

The author declare that no financial support was received for the research, authorship, and/or publication of this article.

Conflict of interest

Author CH was employed by China Coal Technology and Engineering Group Shenyang Research Institute Co, Ltd.

Publisher's note

References

Adhikary, D. P., Dyskin, A. V., Jewell, R. J., and Stewart, D. P. (1997). A study of the mechanism of flexural toppling failure of rock slopes. *Rock Mech. Rock Eng.* 30, 75–93. doi:10.1007/BF01020126

Cao, C., Feng, J., Zhang, Z., Lu, L., and Tao, Z. (2022). Characteristics and mechanism of dump landslides under compound loads based on physical model test. *Bull. Eng. Geol. Enviro* 81, 350. doi:10.1007/s10064-022-02825-6

Chen, P., Tang, S., Liang, X., Zhang, Y., and Tang, C. (2021). The influence of immersed water level on the short-and long-term mechanical behavior of sandstone. *Int. J. Rock Mech. Min.* 138, 104631. doi:10.1016/j.ijrmms.2021.104631

Cheng, W. M., Sun, L. L., Wang, G., Du, W. Z., and Qu, H. Y. (2016). Experimental research on coal seam similar material proportion and its application. *Int. J. Min. Sci. Technol.* 26, 913–918. doi:10.1016/j.ijmst.2016.05.034

Ding, S., Tang, S., Jia, H., and Li, Y. (2023). The influence of water on the failure characteristics of sandstone under uniaxial compression conditions by acoustic emission and NMR observation. *Eng. Geol.* 322, 107173. doi:10.1016/j.enggeo.2023.107173

Ding, X., Li, F., Wang, Z., Sang, S., and Cao, M. (2020). Physical model experimental study on the coalface overburden movement law on the end slope of an open-pit mine. *Geotech. Geol. Eng.* 40, 4859–4877. doi:10.1007/s10706-022-02206-6

Hu, X., He, C., Zhou, C., Xu, C., Zhang, H., Wang, Q., et al. (2019). Model test and numerical analysis on the deformation and stability of a landslide subjected to reservoir filling. *Geofluids* 2019, 1–15. doi:10.1155/2019/5924580

Huang, B. L., Wang, S. C., and Chen, X. T. (2013). Prototype physical similarity experimental study of impulsive wave generated by cataclastic rockmass failure. *Chin. J. Rock. Mech. Eng.* 32, 1417–1425.

Huang, H., Zhao, J., Liu, S., and Ke, H. (2023). Centrifuge model test study on the mutual effect of water level variation and excavation on the deformation and failure of slopes. *KSCE J. Civ. Eng.* 27, 521–534. doi:10.1007/s12205-022-2082-1

Liang, X., Tang, S., Tang, C., and Wang, J. (2021). The influence of water on the shear behaviors of intact sandstone. *Bull. Eng. Geol. Environ.* 80 (8), 6077–6091. doi:10.1007/s10064-021-02315-1

Liang, X., Tang, S., Tang, C. A., Hu, L., and Chen, F. (2023). Influence of water on the mechanical properties and failure behaviors of sandstone under triaxial compression. *Rock Mech. Rock Eng.* 56 (2), 1131–1162. doi:10.1007/s00603-022-03121-1

Lo, C. M., and Weng, M. C. (2017). Identification of deformation and failure characteristics in cataclinal slopes using physical modeling. *Landslides* 14, 499–515. doi:10.1007/s10346-016-0735-1

Prodan, M. V., Peranić, J., Pajalić, S., and Arbanas, Ž. (2023). Physical modelling of rainfall-induced sandy and clay-like slope failures. *Adv. Mater. Sci. Eng.* 3234542. doi:10.1155/2023/3234542

Shi, X. M., Liu, B. G., and Xiao, J. (2015). A method for determining the ratio of similar materials with cement and plaster as bonding agents. *Rock Soil Mech.* 36, 1357–1362. doi:10.16285/j.rsm.2015.05.017

Shi, Y. B., Ye, Y. C., Hu, N. Y., Huang, X., and Wang, X. H. (2021). Experiments on material proportions for similar materials with high similarity ratio and low strength in multilayer shale deposits. *Appl. Sci.* 11, 9620. doi:10.3390/app11209620

Sun, L. N., and Zhao, Z. H. (2014). The Study on movement of underground water and its effect on the stability of surrounding rocks. *Adv. Mater. Res.* 838, 726–732. doi:10.4028/www.scientific.net/AMR.838-841.726

Tang, S., Huang, R., Wang, S., Bao, C., and Tang, C. (2017). Study of the fracture process in heterogeneous materials around boreholes filled with expansion cement. *Int. J. Solids. Struct.* 112, 1–15. doi:10.1016/j.ijsolstr.2017.03.002

Tang, S., Li, J., Ding, S., and Zhang, L. (2022). The influence of water-stress loading sequences on the creep behavior of granite. *Bull. Eng. Geol. Environ.* 81 (11), 482. doi:10.1007/s10064-022-02987-3

Tang, S., Li, J., Zhang, L., Liu, Z., Wang, S., Dong, L., et al. (2021). Study on the static critical stress intensity factors of sandstone in a water environment based on semicircular bending specimens. *Theor. Appl. Fract. Mec.* 116, 103106. doi:10.1016/j.tafmec.2021.103106

Tang, S., and Tang, C. (2015). Crack propagation and coalescence in quasi-brittle materials at high temperatures. *Eng. Fract. Mech.* 134, 404–432. doi:10.1016/j.engfracmech.2015.01.001

Tang, S., Tang, C., Zhu, W., Wang, S., and Yu, Q. (2006). Numerical investigation on rock failure process induced by thermal stress. *Chin. J. Rock. Mech. Eng.* 25 (10), 2071. doi:10.3321/j.issn:1000-6915.2006.10.019

Tang, S., Wang, J., and Chen, P. (2020). Theoretical and numerical studies of cryogenic fracturing induced by thermal shock for reservoir stimulation. *Int. J. Rock. Mech. Min.* 125, 104160. doi:10.1016/j.ijrmms.2019.104160

Tang, S., Zhang, H., Tang, C., and Liu, H. (2016). Numerical model for the cracking behavior of heterogeneous brittle solids subjected to thermal shock. *Int. J. Solids. Struct.* 80, 520–531. doi:10.1016/j.ijsolstr.2015.10.012

Tang, S. (2018). The effects of water on the strength of black sandstone in a brittle regime. *Eng. Geol.* 239, 167–178. doi:10.1016/j.enggeo.2018.03.025

Tang, S. B., Yu, C. Y., Heap, M. J., Chen, P. Z., and Ren, Y. G. (2018a). The influence of water saturation on the short-and long-term mechanical behavior of red sandstone. *Rock Mech. Rock Eng.* 51, 2669–2687. doi:10.1007/s00603-018-1492-3

Tang, S., Yu, C., and Tang, C. (2018b). Numerical modeling of the time-dependent development of the damage zone around a tunnel under high humidity conditions. *Tunn. Undergr. Sp. Tech.* 76, 48–63. doi:10.1016/j.tust.2018.03.012

Tao, Z., Shu, Y., Yang, X., Peng, Y., Chen, Q., and Zhang, H. (2020). Physical model test study on shear strength characteristics of slope sliding surface in Nanfen open-pit mine. *Int. J. Min. Sci. Technol.* 30, 421–429. doi:10.1016/j.ijmst.2020.05.006

Wen, C. X., Jia, S. P., Fu, X. F., Meng, L. D., Zhao, Z. Y., and Riccio, A. (2020). Experimental research and sensitivity analysis of mudstone similar materials based on orthogonal design. *Adv. Mater. Sci. Eng.* 9, 1–14. doi:10.1155/2020/2031276

Wu, L. Z., Huang, R. Q., Xu, Q., Zhang, L. M., and Li, H. L. (2015). Analysis of physical testing of rainfall-induced soil slope failures. *Environ. Earth Sci.* 73, 8519–8531. doi:10.1007/s12665-014-4009-8

Wu, T., Chuanbo, Z., Nan, J., Yuqing, X., and Zhu, B. (2020a). Study on the mechanical cumulative damage model of slope fault fracture zone under the cumulative effect of blasting vibration. *Polytech. Civ. Eng.* 64, 845–858. doi:10.3311/PPci.16030

Wu, T., Zhou, C., Jiang, N., Xia, Y., and Zhang, Y. (2020b). Stability analysis for high-steep slope subjected to repeated blasting vibration. *Arab. J. Geosci.* 13, 828. doi:10.1007/s12517-020-05857-y

Yang, G., Leung, A. K., Xu, N., Zhang, K., and Gao, K. (2019). Three-dimensional physical and numerical modelling of fracturing and deformation behaviour of mining-induced rock slopes. *Appl. Sci.* 9, 1360. doi:10.3390/app9071360

Yang, Z. Q., Fan, X. L., Yang, Y., Hou, K. P., Du, J., Chen, X. G., et al. (2022). Deformation patterns and failure mechanism of high and steep stratified rock slopes with upper steep and lower gentle style induced by step-by-step excavations. *Environ. Earth Sci.* 81, 229. doi:10.1007/s12665-022-10327-7

Yin, Q., Liu, R., Jing, H., Su, H., Yu, L., and He, L. (2019). Experimental study of nonlinear flow behaviors through fractured rock samples after high-temperature exposure. *Rock Mech. Rock Eng.* 52, 2963–2983. doi:10.1007/s00603-019-1741-0

Yin, Q., Wu, J., Zhu, C., He, M., Meng, Q., and Jing, H. (2021a). Shear mechanical responses of sandstone exposed to high temperature under constant normal stiffness boundary conditions. *Geomech. Geophys. Geo.* 7, 35–17. doi:10.1007/s40948-021-00234-9

Yin, Q., Wu, J., Zhu, C., Wang, Q., Zhang, Q., Jing, H., et al. (2021b). The role of multiple heating and water cooling cycles on physical and mechanical responses of granite rocks. *Geomech. Geophys. Geo.* 7 (3), 69. doi:10.1007/s40948-021-00267-0

Yu, C., Tang, S., Duan, D., Zhang, Y., Liang, Z., Ma, K., et al. (2019). The effect of water on the creep behavior of red sandstone. *Eng. Geol.* 253, 64–74. doi:10.1016/j.enggeo.2019.03.016

Zhang, J., Chen, Z., and Wang, X. (2007). Centrifuge modeling of rock slopes susceptible to block toppling. *Rock Mech. Rock Eng.* 40, 363–382. doi:10.1007/s00603-006-0112-9

Zhang, Q. Y., Li, S. C., Guo, X. H., Li, Y., and Wang, H. P. (2008). Research and development of new typed cementitious geotechnical similar material for iron crystal sand and its application. *Rock Soil Mech.* 29, 2126–2130.

Zhang, S., Fan, G., Zhang, D., Chen, M., and Zhang, C. (2019). Study on material properties and similar material proportion of weakly cemented water-resisting strata. *Arab. J. Geosci.* 12, 340. doi:10.1007/s12517-019-4521-y

Zheng, Y., Chen, C. X., Liu, T. T., Zhang, W., and Song, Y. F. (2018). Slope failure mechanisms in dipping interbedded sandstone and mudstone revealed by model testing and distinct–element analysis. *Bull. Eng. Geol. Environ.* 77, 49–68. doi:10.1007/s10064-017-1007-6

Zhu, C., He, M., Karakus, M., Cui, X., and Tao, Z. (2020). Investigating toppling failure mechanism of anti-dip layered slope due to excavation by physical modelling. *Rock Mech. Rock Eng.* 53, 5029–5050. doi:10.1007/s00603-020-02207-y

Zuo, B. C., Chen, C. X., Liu, C. H., Shen, Q., Xiao, G. F., and Liu, X. W. (2004). Research on similar material of slope simulation experiment. *Rock Soil Mech.* 25, 1085–1088. doi:10.16285/j.rsm.2004.11.028

frontiers | Frontiers in Earth Science

TYPE Original Research
PUBLISHED 06 November 2023
DOI 10.3389/feart.2023.1273637

OPEN ACCESS

EDITED BY
Zhibo Zhang,
University of Science and Technology Beijing, China

REVIEWED BY
Xin Cai,
Central South University, China
Pengfei Shan,
Xi'an University of Science and Technology, China
Dingding Zhang,
Xi'an University of Science and Technology, China

*CORRESPONDENCE
Yuxin Da,
imliangjie@163.com

RECEIVED 07 August 2023
ACCEPTED 28 September 2023
PUBLISHED 06 November 2023

CITATION
Da Y, Ning Z, Huang Z, Du Q, Liu Q, Zhao J and Li Q (2023), Improvement of the separation evolution law and separation position determination method of mining overburden strata. *Front. Earth Sci.* 11:1273637. doi: 10.3389/feart.2023.1273637

Improvement of the separation evolution law and separation position determination method of mining overburden strata

Yuxin Da[1]*, Zhiyuan Ning[2], Zilong Huang[3], Qirui Du[4], Qi Liu[1], Jinhai Zhao[1] and Qinghai Li[1]

[1]College of Energy and Mining Engineering, Shandong University of Science and Technology, Qingdao, China, [2]School of Civil Engineering, Chongqing Jiaotong University, Chongqing, China, [3]School of Urban Construction and Safety Engineering, Shanghai Institute of Technology, Shanghai, China, [4]College of Geoscience, China University of Petroleum, Beijing, China

In view of the shortcomings of the traditional method of determining the position of the separation layer, according to the actual movement of the pressure balance arch and the rock layer in the overburden, the concept of the triangular separation domain is proposed, and the relationship between the range of the triangular separation domain and the mining distance and the mining fracture angle is established. The calculation method of rock load is modified. By analyzing the stress mode in the pressure arch of the separation zone, the mechanical model of the deflection calculation of each rock stratum is established. Combining the triangular separation zone with the new mechanical model, the calculation model of the dynamic evolution analysis of the separation zone and the calculation model of the composite beam in the separation zone are established. The traditional method and the improved method are used to determine the separation position in an actual mining example. The field exploration proves that the results of the improved method described in this paper are more accurate. The model predicts the position of overburden separation by comparing the deflection between adjacent strata on the same horizontal contact surface, and can accurately predict the position of separation above the working face.

KEYWORDS

coal seam mining, separation domain, rock load, rock deflection, mechanical model, prediction of overburden separation position

1 Introduction

1.1 Research status

In the process of coal seam mining, the overlying rock will deform, break, and form a large number of cracks (Liu et al., 2023a). The cracks that are pulled along the bedding direction between or within the rock layers are called separation cracks (referred to as separation). With the increase in coal mining depth, multi-seam mining, thick and extra-thick coal seam mining, the difference in engineering geological characteristics of overlying strata and complex hydrogeological conditions, the overlying bed separation water damage occurs from time to time and has the characteristics of large instantaneous water volume, periodicity, and no obvious signs of water inrush, which is extremely harmful (Wu et al., 2014). At present, there are a wide range of mines with separated layer water disasters,

involving a complete range of coal measures, and there are differences in the formation conditions and influencing factors, causes, and intensity of water disasters in different coal mines (Liu et al., 2023b), which shows the complexity of the problem of separated layer water disasters. Therefore, accurate prediction of the development of the separation of the overlying strata is very essential for preventing and controlling the water inrush caused by these separations.

Many scholars have carried out relevant theoretical and practical research studies on the development of high separation layer and the water disaster of the separation layer. Ning et al. (2017) used digital photography and multi-position monitoring of boreholes to study rock movement and overburden failure caused by long-wall mining and proposed a statistical formula for predicting the maximum height of overburden failure in close-distance multi-seam mining. By analyzing the fracture of WKS in multi-seam mining, Ma et al. (2022) established a 'long beam' hydraulic model and calculated the fracture position of WKS in the Xiqu mine. Through the physical simulation of the water and sand gushing test system, Li et al. (2022) studied and explored the spatial distribution and dynamic evolution law of the mining overburden fracture zone under the coupling effect of stress and seepage. Based on the key stratum theory, Hu et al. (2021) used the plate theory to reveal the relationship between the fracture of the overlying strata and the influx of bed separation water. Shu et al. (2020) used the cusp catastrophe model to explain the energy transition mode of key layer breaking in the separation layer and proposed two water inrush modes of fracturing and splitting. Peng et al. (2019) comprehensively analyzed the mechanism of this type of disaster from the aspects of water channel, water filling source, material source, water storage space, power source, and geological structure in view of the water inrush and sand inrush accident in the Zhaojin Coal Mine of the Huanglong Coalfield. Through the discrete element particle flow PFC3D software, Shi (2020) simulated the possibility of water and sand inrush under different mining thicknesses under the condition of weakly cemented overburden. He et al. (2018) proposed a method for determining the contact state of rock strata based on the step-by-step comparison and merging method and proposed a mechanical model of stepped composite beams that can be used to study and calculate the dynamic evolution of separation. Fan et al. (2019), combined with the Winkler foundation beam model, established the mechanical model of water damage above the water-conducting fracture zone and derived the theoretical discriminant of the first and periodic water-conducting form separated layers. Chu (2013) put forward the prevention and control technology of water disaster according to the spatial development position, hydrogeological characteristics, and periodic weighting step of the working face in the Hongliu Coal Mine. Li et al. (2009) thought that the water filling source of the water inrush accident in S1818 and S1821 fully mechanized the mining face of Datong No. 1 Coal Mine was the separated layer water of the overlying strata. Taking the Beizao Coal Mine in Shandong Province as an example, Sun et al. (2012) studied the mechanism of roof separation and water inrush in soft rock strata. Wang et al. (2021) developed a new type of similar material to simulate strata separation. Combined with the evolution characteristics of acoustic emission events, Zhang et al. qualitatively and quantitatively discussed the influence of fracture degree on velocity dispersion characteristics (Zhang et al., 2023a) and established a quantitative relationship model between macroscopic mechanical properties and treatment temperature (Zhang et al., 2023b). PALCHIK (2003) located bed separation in the overburden strata, revealed the influence of coal seam thickness, separation development position, overburden thickness and other factors on horizontal fractures, and studied the mechanical properties of upper and lower strata in the bed separation space. Zhou et al. (2023) revealed the internal mechanism of rock mass watering to inhibit rock burst and carried out a series of uniaxial compression tests on sandstone samples with different water contents. Cai et al. (2023) verified by the uniaxial compression test that the localization of compressive stress dominates the macroscopic failure of pre-holed rock. Other scholars have carried out research on the determination of overburden failure height (PALCHIK, 2015) and longwall mining speeds (Zhang et al., 2021). The aforementioned research study has played a positive role in understanding the movement law of mining overburden, the evolution process of bed separation, and the prediction of bed separation position.

However, the current determination of the separation position is mostly based on the traditional separation position determination formula (Yue et al., 2015; Yan et al., 2018) or its derived formula through macro analysis (Liang and Sun, 2002; Yang et al., 2014; Ji et al., 2022) or empirical approximation (Qiao et al., 2014; Yan et al., 2016). However, the traditional composite beam theory ignores the influence of the rock strata outside the calculation range on the rock strata within the calculation range. It neither judges in advance which range of rock strata can be used as composite beams nor considers the essence of the deformation of the separated rock strata under the action of the horizontal stress and gravity stress as a whole. Only the more common longitudinal superposition model is analyzed, and the results obtained are often inconsistent with the actual separation position. Therefore, in view of the characteristics of the abscission zone in the overlying strata of the goaf, the author simplifies the abscission zone pressure arch into a triangular abscission zone. At the same time, for the composite beam in the abscission zone, considering the influence of the horizontal *in situ* stress of deep mining, the rock beam load solution model is established according to the mechanical model of the rock deflection calculation and the geometric relationship of the deformation of the composite beam. Finally, it is applied to the judgment of the abscission position in the field.

1.2 Overview of engineering geology in the study area

The study area is the 22207 fully mechanized mining face in the Shendong mining area of China (Figure 1). The designed strike length of the working face is 4544.7 m, the recoverable strike length is 4538 m, the buried depth is 285.2–398.8 m, the average is 363.6 m, the coal thickness is 2.8–6.6 m, the average is 4.82 m, and the average dip angle is 1–3°. The coal-bearing strata in the field are the Middle–Lower Jurassic Yan'an Formation, and the sedimentary basement of the coal measures is the Upper Triassic Yanchang Formation. The Yan'an Formation in the area is intact and has not been eroded later. The thickness of the coal-bearing strata is 157.34 (B99 Borehole)–325.06 m (B107 Borehole) with an average of 212.48 m.

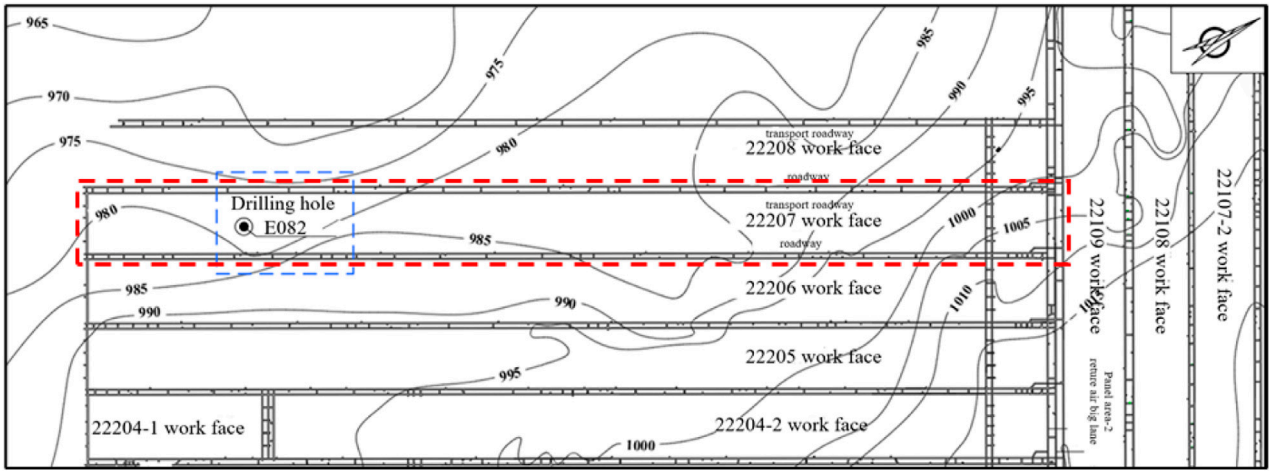

FIGURE 1
Burtai mine mining engineering plan (22,207 working face surrounding).

The coal-bearing strata in the field are the Middle–Lower Jurassic Yan'an Formation, and the sedimentary basement of the coal measures is the Upper Triassic extension group. According to the lithology, lithofacies combination characteristics, and coal-bearing characteristics of the formation, the coalfield can be divided into three rock sections. The three rock sections are divided into one rock section (J1-2y1 + 2), two rock sections (J1-2y3), and three rock sections (K1I-Q) (Table 1). The Yan'an Formation in the area is well preserved and has not been eroded in the later stage. The lithology of the three rock sections is mainly composed of gray–white, deep gray, gray–black medium-fine-grained sandstone, siltstone, sandy mudstone, mudstone, and coal seam, which is easy to deform. Due to the uneven settlement of the overlying strata in the process of coal mining, the separation space is often formed in the second and third rock sections. The water accumulation in these separations leads to frequent catastrophic water inrush accidents. Therefore, it is necessary to further optimize the separation identification method based on the existing separation identification method to prevent similar roof water inrush events after the mining of the 22,207 working face.

2 Simplifying the shape of the separated layer domain

For any size of the goaf, there is a pressure balance arch in the overlying strata above it (Figure 2). The load of the rock strata outside the balance arch is transmitted to the arch foot by the balance arch without affecting the rock strata in the balance arch. The rock strata in the balance arch will bend and sink under the action of self-weight due to the loss of support. When the subsidence of adjacent rock strata is not balanced, it will separate from the contact surface of rock strata and form separation. Therefore, the area of the balanced arch is the area that forms the separation layer, which is called the separation layer domain. In the vertical direction, the separation layer cannot be formed in the whole overburden rock. The span of the separation layer at the same position in the horizontal direction is not fixed. The load borne by the upper strata of the separation layer under different footage conditions is not fixed. With the continuous expansion of the goaf area, the old and small balance arches are destroyed, and new and large balance arches will be generated. The front foot of the arch moves forward with the increase in the mining footage, and the range of the arch is also expanding. With the progress of this process, the separation area is also expanding, and the roof separation of the stope is also dynamically developed in the horizontal and vertical directions of the working face. Therefore, when calculating the development of bed separation in roof overburden under a certain mining size, the range and shape of the bed separation domain should be determined first.

Influenced by many factors such as buried depth, mining thickness and lithology, the shape equation of the balanced arch is very complex and not easy to apply. Combined with the similar material simulation experiment and numerical simulation experiment observation results of some scholars (Figure 3), it is found that only the rock layer between the two rock fracture lines (red diagonal in the following figure) will bend, sink, and produce separation due to the loss of support. Based on this, it is proposed that the triangular area trapped by two rock fracture lines and the coal seam roof can be approximately used as the separation zone (that is, the range trapped by two red oblique lines and one green horizontal line in the following diagram). This not only takes into account the fact that the separation domain exists and the general morphological characteristics of the separation domain but also reduces the computational difficulty and enhances the operability.

According to the geometric shape of the development of the separation domain, it can be known that the advancing distance of the working face (S_i), the height of the separation domain (H_i), the fracture angle of the rock stratum on the side of the open-off cut (α_1), and the fracture angle of the rock stratum on the side of the working face (α_2) have the following relationship:

TABLE 1 Formation characteristics and rock mechanics parameters of the 22,207 mining face.

Stratigraphic position	Number of rock layer *i*	Lithology	Volume-weight	Thickness *hi* (m)	Accumulated burial depth	Elastic modulus
			γi (KN/m^3)		*Hi* (m)	*Ei* (GPa)
Three rock sections (K1I-Q)	20	Medium	22.2	14.1	339.3	13.7
	19	Coarse sandstone	21.9	12.9	315.2	8.8
	18	Fine sandstone	22.4	107.6	296.35	13.9
	17	Sandy mudstone	21.8	7.4	269.28	13.8
	16	Fine sandstone	22.4	72.6	248.8	21.4
	15	Sandy mudstone	23.2	5.3	224.11	14.1
	14	Medium	24.3	46.1	218.78	18.2
	13	Siltstone	22.9	9.1	202.68	23.1
	12	Medium	21.4	33.8	193.63	21.1
Two rock sections (J1-2y3)	11	Sandy mudstone	22.5	14.3	179.87	22.6
	10	Fine sandstone	23.7	21.7	139.18	23.2
	9	Sandy mudstone	23.8	3.8	111.91	18.9
	8	Medium	22.1	5.1	98.11	16.4
	7	Sandy mudstone	23.9	4.7	89.01	27.8
	6	Fine sandstone	23.5	4.3	84331	28.7
One rock section (J1-2y1 + 2)	5	Sandy mudstone	23.5	7.8	79.93	30.4
	4	Medium	21.6	5.2	70.82	52.8
	3	Mudstone	23.3	4.3	52.28	22.9
	2	Fine sandstone	23.6	2.9	47.92	57.5
	1	Coal	12.3	5	24	18.2
	0	Bottom plate	23.1	4	16	56.1

$$H_i/\tan\alpha_1 + H_i/\tan\alpha_2 = S_i. \quad (1)$$

According Xu et al. (2018), the fracture shape of the rock stratum is symmetrical, and the fracture angle of the rock stratum on the side of the open-off cut and working face is basically equal. According to the calculation formula of the fracture angle of the key stratum,

$$\alpha = \alpha_1 = \alpha_2 = 45° - \frac{1}{2}\varphi + \frac{1}{2}\arctan\sqrt[3]{\frac{R_t}{2q}}, \quad (2)$$

where φ is the internal friction angle of the rock, °; R_t is the tensile strength of rock, MPa; and q is the load of the rock stratum, MPa.

The value range of the two bottom angles of the triangular off-layer domain is generally 40°–80°. This relationship can quickly determine the size of the separation zone of the overlying strata in the goaf. In order to better describe the problem, default $\alpha = \alpha_1 = \alpha_2$.

3 Traditional method for determining the position of separated strata

3.1 Origin of the traditional determination method

In addition to its own weight, the load of any rock stratum in the mining overburden is also usually affected by the interaction of the overlying adjacent rock strata. Generally speaking, the load of mining strata is non-uniformly distributed, but for practical engineering problems, in order to be convenient and simple, it is usually assumed that the rock load is uniformly distributed. In order to modify the calculation method of mining overburden rock load, the conventional calculation method of rock load is briefly described here.

The calculation model of the composite rock beam is shown in Figure 4. There are n rock layers above the immediate roof, and the

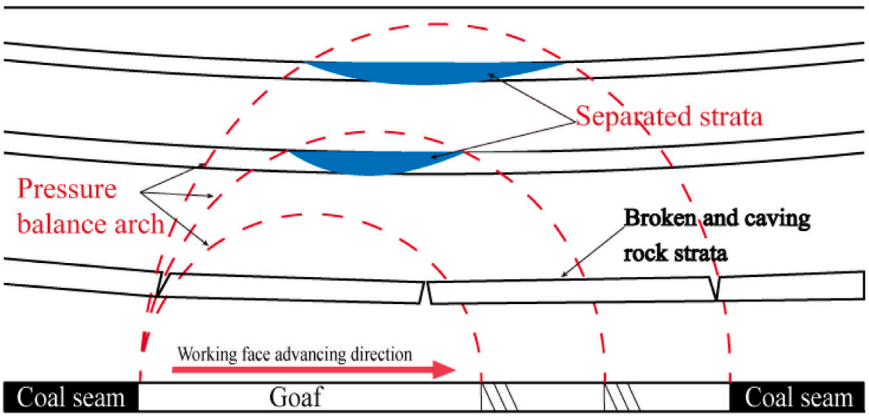

FIGURE 2
Mechanical structure of overburden bed separation.

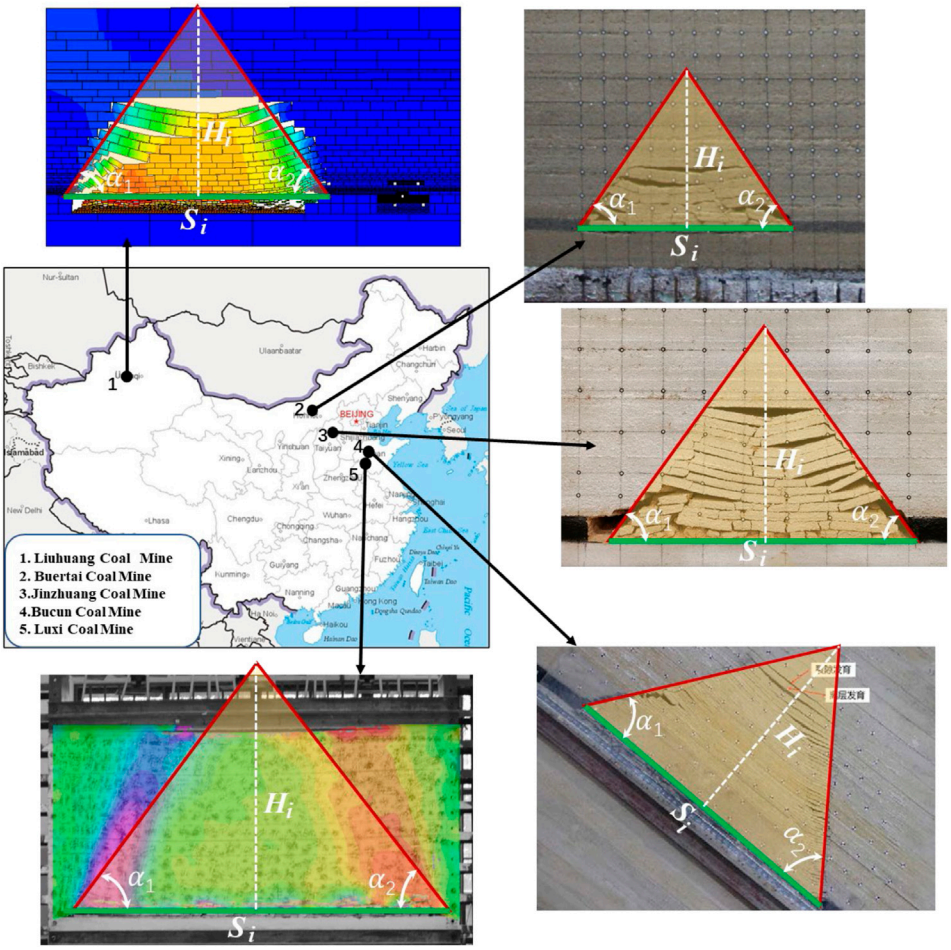

FIGURE 3
Multiple tests to simulate the deformation and failure process of overburden rock.

thickness of each rock layer is h_i (i=1,2, . . . ,n); the volume force is γ_i (i=1,2, . . . ,n); and the elastic modulus is E_i (i=1,2, . . . ,n). When the key stratum moves, the overlying strata controlled by the key stratum will move synchronously and coordinately to form a structure similar to the composite beam. According to the principle of composite beams, the load of composite beams will

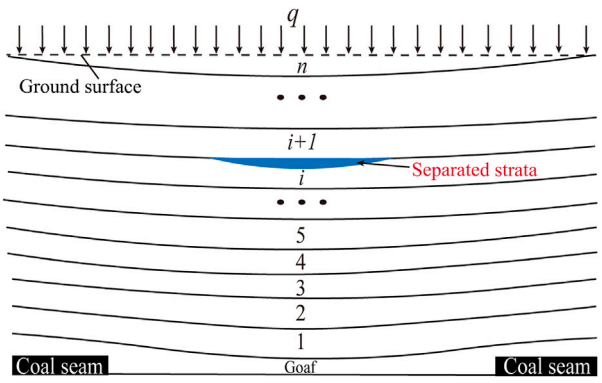

FIGURE 4
Composite beam theory research layer schematic diagram.

be shared by each beam, and the shear force, bending moment, and load will be redistributed. The relationship is as follows:

$$\begin{aligned}(M_n) &= (M_n)_1 + (M_n)_2 + \cdots + (M_n)_n,\\ (Q_n) &= (Q_n)_1 + (Q_n)_2 + \cdots + (Q_n)_n,\\ (q_n) &= (q_n)_1 + (q_n)_2 + \cdots + (q_n)_n.\end{aligned} \tag{3}$$

According to the mechanics of materials, the curvature of each rock beam is $(C_n)_i = 1/p_i$ (p_i is the radius of curvature, i=1,2, . . . ,n, the same below). Its relationship with the bending moment M_i and bending modulus E_iI_i (I_i is the moment of inertia of the section) is

$$(C_n)_i = \frac{(M_n)_i}{E_iI_i}. \tag{4}$$

By using the condition that the curvature $(C_n)_i$ of each rock beam is equal, the load $(q_n)_1$ formed by the influence of the n-layer rock on the first layer and the load $(q_n)_i$ of any ith layer can be obtained, which are

$$(q_n)_1 = \frac{E_1I_1}{E_1I_1 + E_2I_2 + E_3I_3 + \cdots + E_nI_n}(q_n), \tag{5}$$

$$(q_n)_i = \frac{E_iI_i}{E_1I_1 + E_2I_2 + E_3I_3 + \cdots + E_nI_n}(q_n). \tag{6}$$

Because the section of each rock stratum is a rectangle, the moment of inertia I_i can be expressed as follows:

$$I_i = \frac{bh_i^3}{12}, \quad (i = 1, 2, \ldots, n). \tag{7}$$

Equations 5 and (6) can be combined to obtain

$$(q_n)_1 = \frac{E_1h_1^3(\gamma_1h_1 + \gamma_2h_2 + \cdots + \gamma_nh_n)}{E_1h_1^3 + E_2h_2^3 + \cdots + E_nh_n^3}, \tag{8}$$

$$(q_n)_i = \frac{E_ih_i^3(\gamma_1h_1 + \gamma_2h_2 + \cdots + \gamma_nh_n)}{E_1h_1^3 + E_2h_2^3 + \cdots + E_nh_n^3}. \tag{9}$$

The essence of using the key stratum theory to determine the location of bed separation development is the comparison between the bending stiffness EI of the rock stratum and its own load. When the bending stiffness of the rock stratum (n+1 rock layer) is enough to support its own load, it will not transfer the load to the lower rock stratum. It is judged that the lower part will develop the bed separation space and *vice versa*.

3.2 Mechanical model analysis of separation domain load

When calculating the fracture distance of the upper strata of the separation layer, the calculation range should be delineated in advance, and the calculation range is the range of the strata that apply load to the upper strata of the separation layer. The traditional calculation method does not take into account the change in the actual load, and the default actual load is still the original ground stress. In fact, due to the existence of the pressure balance arch after excavation, the range of rock strata that can apply load to the upper strata of the separation layer is limited and variable. Only the rock strata in the pressure balance arch (Figure 5A) apply load to the upper strata of the separation layer. After determining the scope and shape of the abscission zone in the overburden under a certain footage condition, in order to facilitate the calculation and analysis, it is assumed that the calculation range is a triangular abscission zone, and the length of the suspension span of each rock layer involved in the calculation is different and the rock span decreases from bottom to top. At the same time, the calculation process must be carried out on the premise that no rock layers in the abscission zone are broken. Because the breaking of rock strata is developed from bottom to top, it is generally only necessary to ensure that the bottom strata are not broken. If the lower strata in the separation domain are broken, the calculation object only includes the upper unbroken strata in the separation domain. The simplified overlying strata model is shown in Figure 5B.

In the triangular separation domain, the rock strata involved in the calculation are no longer assumed to be of equal span, and the actual span of each rock stratum is determined by the thickness of the rock stratum and the height of the rock stratum in the separation domain. The core problem is to calculate the curvature (or bending moment) of each rock stratum in its middle position. However, due to the unequal span of each rock stratum, the actual load range of each rock stratum will change, and the relevant calculation formula will be adjusted.

When the rock beam is sinking and bending, the fracture length of the rock beam in different layers is different, and the fracture length of the upper rock beam is smaller. Clearly, the curvature of the rock beam breaking bending is larger and the radius of curvature is smaller. It can be considered that the curvature of the rock beam breaking increases with the decrease in the length of the rock beam. This way, the curvature of the rock beam after mining should be related to the buried depth of the rock layer in addition to its internal force-bending moment and bending stiffness. The triangular relationship can be established by the rock breaking angle α, the buried depth of the rock layer, and the breaking length of the rock beam, as shown in Figure 6:

$$S_{i+1} = S_i - h_i{*}2\cot\alpha, \tag{10}$$

$$H_i = \sum_{k=1}^{i} h_k. \tag{11}$$

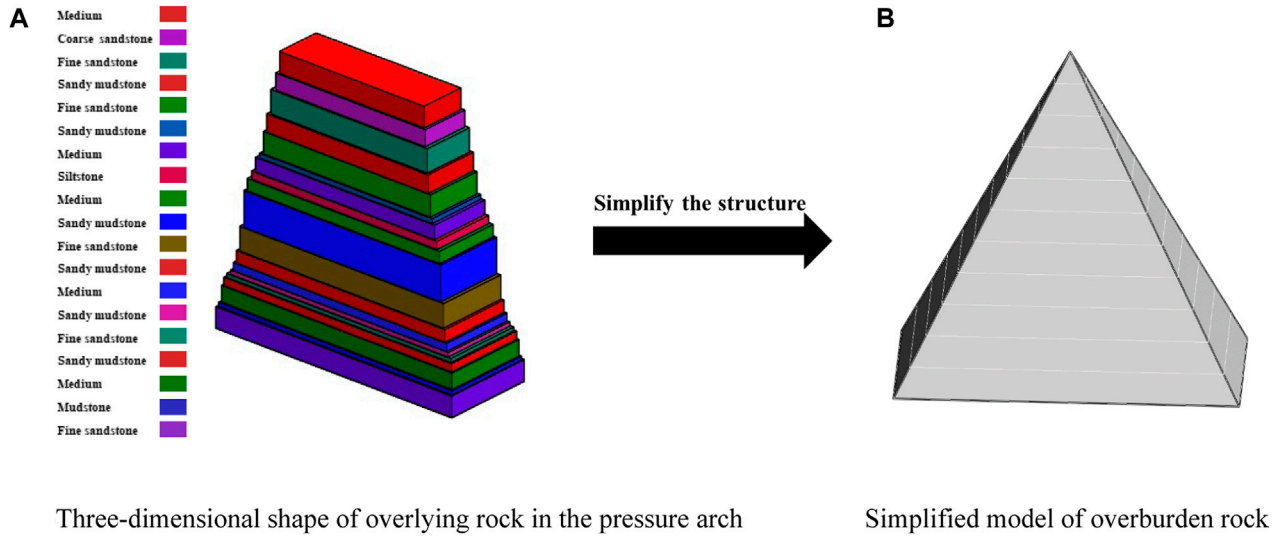

FIGURE 5
Distribution form of overburden rock in the pressure arch.

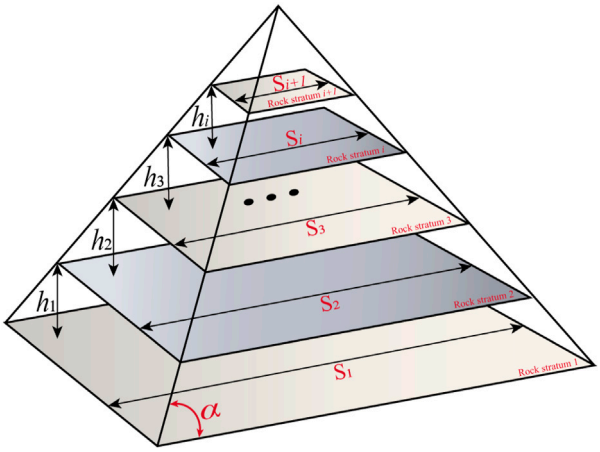

FIGURE 6
Variable curvature rock load calculation model.

The ratio of the curvature of each rock layer to the first layer can be expressed as

$$\begin{cases} \dfrac{C_2'}{C_1'} = \dfrac{1}{1 - h_1' \cot\alpha} \\ \dfrac{C_3'}{C_1'} = \dfrac{1}{1 - (h_1' + h_2')\cot\alpha} \\ \vdots \\ \dfrac{C_n'}{C_1'} = \dfrac{1}{1 - (h_1' + h_2' + \cdots + h_{n-1}')\cot\alpha} \end{cases} \tag{12}$$

where $h_i' = \frac{2h_i}{S_i}$.

Equations 8, 9, and 12 can be combined to obtain

$$\begin{cases} (q_n)_1' = \dfrac{E_1 h_1^3 (\gamma_1 h_1 + \gamma_2 h_2 + \cdots + \gamma_n h_n)}{E_1 h_1^3 + \dfrac{E_2' h_2^3}{1 - h_1' \cot\alpha} + \dfrac{E_3' h_3^3}{1 - (h_1' + h_2')\cot\alpha} + \cdots + \dfrac{E_n' h_n^3}{1 - (h_1' + h_2' \cdots + h_{n-1}')\cot\alpha}} \\ (q_n)_i' = \dfrac{\dfrac{E_i h_i^3 (\gamma_1 h_1 + \gamma_2 h_2 + \cdots + \gamma_n h_n)}{1 - (h_1' + h_2' \cdots + h_{i-1}')\cot\alpha}}{E_1 h_1^3 + \dfrac{E_2' h_2^3}{1 - h_1' \cot\alpha} + \dfrac{E_3' h_3^3}{1 - (h_1' + h_2')\cot\alpha} + \cdots + \dfrac{E_n' h_n^3}{1 - (h_1' + h_2' \cdots + h_{n-1}')\cot\alpha}} \end{cases} \tag{13}$$

The lower the rock stratum is, the larger the length of the rock beam is, and the more load will be shared accordingly. In fact, by comparison, it can also be seen that under the same conditions, the old top load obtained by modified Eq. 13 is smaller than that of conventional Eqs. 8, 9.

The influence of the horizontal stress field on the separation of overlying strata and roof instability in goaf has been confirmed in mines in Australia, Britain, the United States, China, New Zealand, and Japan (Kang et al., 2010). Therefore, the theoretical model used to calculate and predict the separation position of overlying strata should consider the comprehensive influence of vertical stress and horizontal stress, as shown in Figure 7. Among them, λ is the lateral pressure coefficient, $\lambda = \sigma_H/\sigma_V$, and σ_H and σ_V are the maximum horizontal stress and the maximum vertical stress, respectively. Under normal conditions, the lateral pressure coefficient λ is 0.5–3.0.

On the basis of the aforementioned analysis, we select one layer of the overlying strata to calculate the deflection and maximum tensile stress under the combined action of vertical and horizontal stress, as shown in Figure 8: the maximum deflection occurs in the middle of the rock beam, where N is the horizontal stress, $N = h^*\sigma h$, l is the width of the rock beam, and h is the thickness of the rock layer. The mid-span deflection

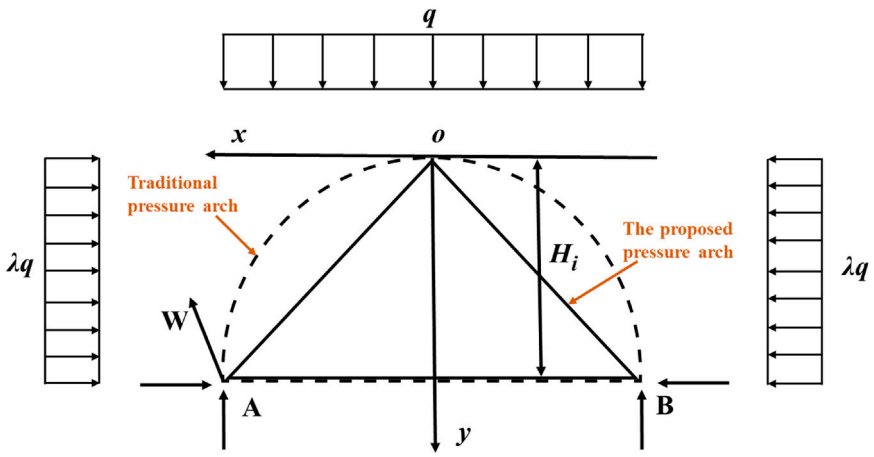

FIGURE 7
Stress analysis of the pressure arch.

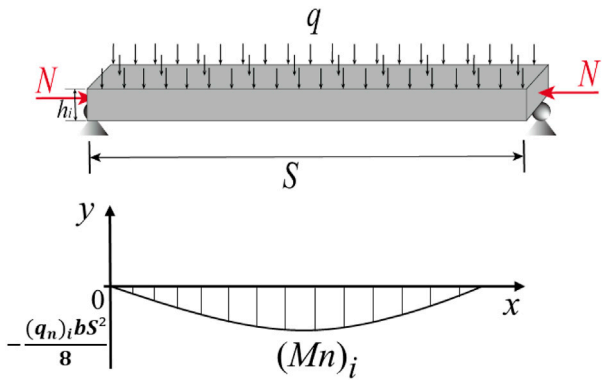

FIGURE 8
Mechanical model of a single-layer rock simply supported beam.

of the rock beam and its corresponding bending moment are as follows:

$$\begin{cases} \delta = \dfrac{4S^4 q}{\pi} \dfrac{1}{EI\pi^4 - N\pi^2 S^2} = \dfrac{5qS^4}{384EI} \dfrac{1536}{5\pi^5} \dfrac{1}{1-\dfrac{N}{N_e}} \approx \dfrac{5qS^4}{384EI} \dfrac{1}{1-\dfrac{N}{N_e}} \\ N_e = \pi^2 EI/S^2 \\ I = \dfrac{1 \cdot h^3}{12} = \dfrac{h^3}{12} \end{cases}, \tag{14}$$

$$M_{\max} = \frac{qS^2}{8} + N\delta = \frac{qS^2}{8}\left[1 + \frac{1 + 0.03\frac{N}{N_e}}{1 - \frac{N}{N_e}}\right]. \tag{15}$$

The position where the maximum tensile stress appears is also the position where the bending moment is the largest. The calculation formula of the maximum tensile stress is as follows:

$$\sigma_{\max} = \frac{M_{\max}}{\frac{1-h^2}{6}} = \frac{6}{h^2} M_{\max}. \tag{16}$$

Then, for the overlying multilayer rock strata, combined with Eq. 13, the mid-span deflection of the *i*th-layer rock beam and its corresponding bending moment can be obtained as

$$\begin{cases} \delta_i = \dfrac{5S_i^4}{384E_iI_i} \dfrac{1}{1-\dfrac{N_i}{(N_e)_i}} \dfrac{\dfrac{E_ih_i^3(\gamma_1h_1 + \gamma_2h_2 + \cdots + \gamma_nh_n)}{1-(h_1' + h_2' \cdots + h_i')_1 \cot\alpha}}{E_1h_1^3 + \dfrac{E_2'h_2^3}{1-h_1'\cot\alpha} + \dfrac{E_3'h_3^3}{1-(h_1'+h_2')\cot\alpha} + \cdots + \dfrac{E_n'h_n^3}{1-(h_1'+h_2' \cdots + h_{n-1}')\cot\alpha}} \\ (N_e)_i = \pi^2 E_i I_i / S_i^2 \\ N_i = \sigma_h \cdot h_i \\ I_i = \dfrac{1 \cdot h_i^3}{12} = \dfrac{h_i^3}{12} \end{cases} \tag{17}$$

Through this formula, the deflection of each rock stratum can be calculated. When the deflection of the *i*th layer is less than that of the *i*-1th layer, that is $\delta_i \le \delta_i - 1$, there is a separation between the two layers. On the contrary, the upper and lower strata will deform together without bedding separation.

3.3 Areas of improvement

This method combines the knowledge of the triangular separation domain, traditional composite beam principle, lateral pressure theory, and maximum deflection calculation of a simply supported beam to create a calculation model that can be used for dynamic evolution analysis of the separation layer. It not only calculates the influence of rock strata outside the range on the rock strata within the calculation range but also determines in advance which rock strata can be used as composite beams. Considering the essence of deformation of separated rock strata under the action of horizontal stress and self-weight stress as a whole, it overcomes the limitations of traditional methods that only analyze common longitudinal superposition models.

By comparing the maximum deflection of rock strata, the actual combination state of rock strata can be presented, which makes the contact state of rock strata (whether there is separation between adjacent rock strata) easy to operate. Therefore, the improved separation position discrimination method is more in line with the actual situation.

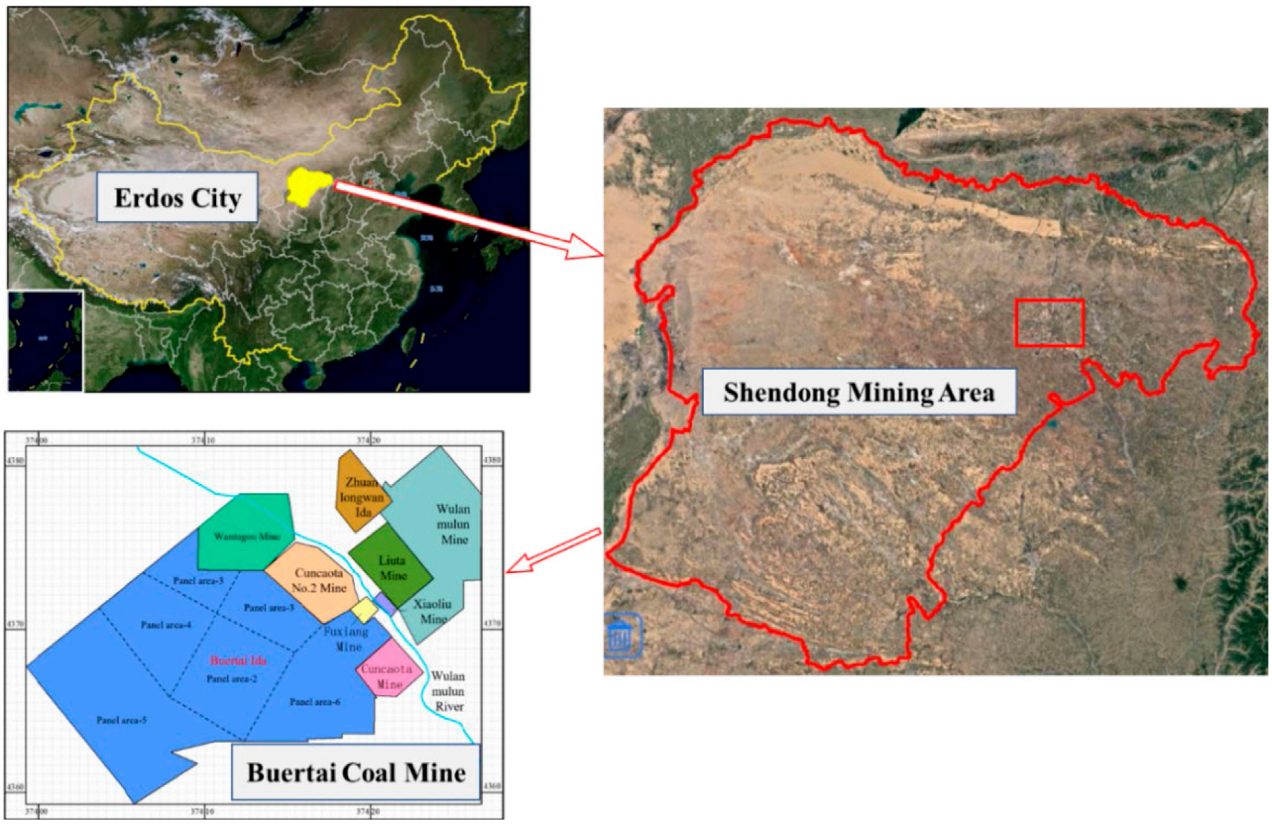

FIGURE 9
Site location map: Buertai Coal Mine.

4 Application and verification

In order to show the use method of the correction formula and to compare the accuracy of the discrimination results of the improved and traditional methods, the traditional and improved methods are used to discriminate the position of the overburden separation layer in the 22207 working face (Figure 9) of the Shendong Buertai Coal Mine. The relative accuracy of the two methods is assessed by comparing the predicted locations of separated strata from the two methods with field measurements.

4.1 Application

The overlying strata have uneven settlement due to mining damage, and the caving zone, fracture zone, and bending subsidence zone are formed from the bottom up. Caving and fracture zones are commonly referred to as water flowing fractured zones (Figure 10). The degree of rock fragmentation in the caving zone is high; the degree of rock mass fragmentation in the fracture zone is small, forming a certain amount of rock cracks; the fracture distribution in the range of the bending subsidence zone is obviously different from that of the water-conducting fracture zone. It is difficult to accumulate a large amount of groundwater in the separation layer in the range of the water-conducting fracture zone, and the rock and soil structures in the bending subsidence zone are relatively complete. The integrity of the separation layer in this range is better, and it can better accumulate the separation layer water. The separation layer water forms a water-conducting channel through the load and eventually leads to the occurrence of the separation layer water inrush event. Therefore, this paper focuses on the separation space formed above the water-conducting fracture zone.

According to the field operation of the Buertai Coal Mine in the Shendong mining area, the ratio of the height of the water flowing fractured zone to mining height (RFM) is 21, the mining height of the 22,207 working face is 5 m, and the development height of the water flowing fractured zone above the 22,207 working face is 105 m. Table 1 shows that the total thickness of the overburden rock in the 1–12 layers is 107.9 m, indicating that the water-conducting fracture has developed in the 12th layer. Therefore, the calculation of the separation space of 1–12 layers is meaningless. The following only needs to determine the separation position of the 12–20 layers of the overburden rock.

4.1.1 The determining process and results of the traditional method

There are eight layers of overburden rock from the 12th layer to the 20th layer, so the value range of n in Eq. 9 is 1–9 and i is 12. The 12th layer of the overburden rock is the first layer in the traditional calculation model.

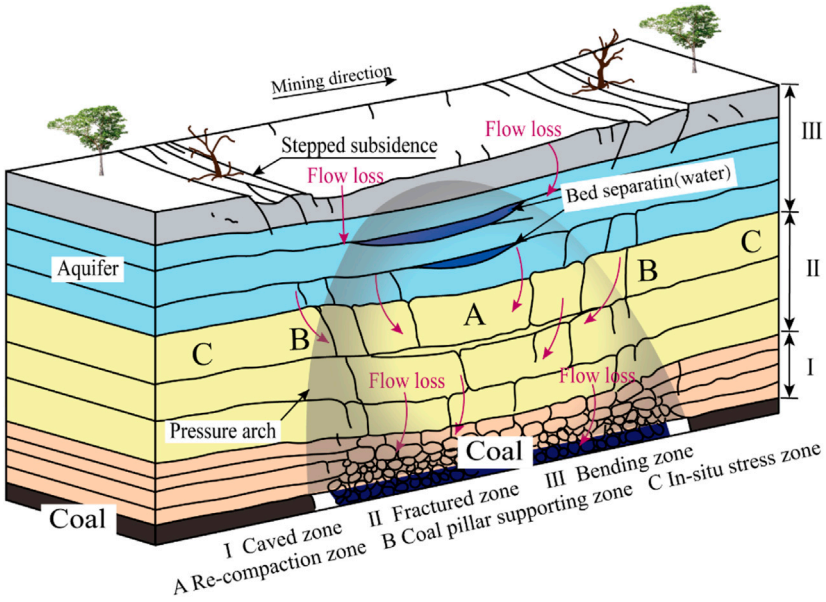

FIGURE 10
Post-mining overburden 'three zone' divisions.

TABLE 2 Position determination results for separated strata in the 22,207 mining face using the traditional method.

Number of rock layer i	Lithology	Volume-weight	Thickness *hi* (m)	Accumulated burial depth	Elastic modulus	(qn) 12	Are there separated strata below this layer?
		γ_i (KN/m^3)		*Hi* (m)	*Ei* (GPa)	(KPa)	
20	Medium	22.2	14.1	339.3	13.7	202.39	N
19	Coarse sandstone	21.9	12.9	315.2	8.8	192.65	N
18	Fine sandstone	22.4	107.6	296.35	13.9	184.59	Y
17	Sandy mudstone	21.8	7.4	269.28	13.8	298.61	N
16	Fine sandstone	22.4	72.6	248.8	21.4	286.59	Y
15	Sandy mudstone	23.2	5.3	224.11	14.1	677.03	N
14	Medium	24.3	46.1	218.78	18.2	639.27	Y
13	Siltstone	22.9	9.1	202.68	23.1	912.22	N
12	Medium	21.4	33.8	193.63	21.1	723.32	-
				...			
1	Coal	12.3	5	24	18.2		

When $n = 1$,

$$(q_1)_{12} = (q)_{12} = \gamma_{12}h_{12} = 21.4 \times 33.8 = 723.32.$$

When $n = 2$,

$$(q_2)_{12} = \frac{E_{12}h_{12}^3(\gamma_{12}h_{12} + \gamma_{13}h_{13})}{E_{12}h_{12}^3 + E_{13}h_{13}^3} = \frac{21.1 \times 33.8^3(21.4 \times 33.8 + 22.9 \times 9.1)}{21.1 \times 33.8^3 + 23.1 \times 9.1^3} = 912.22.$$

The calculation steps of n taking 3–8 are similar, which will not be repeated here.

When $n = 9$,

$$(q_9)_{12} = \frac{E_{12}h_{12}^3(\gamma_{12}h_{12} + \gamma_{13}h_{13} + \cdots + \gamma_{20}h_{20})}{E_{12}h_{12}^3 + E_{13}h_{13}^3 + \cdots + E_{20}h_{20}^3},$$

$$= \frac{21.1 \times 33.8^3(21.4 \times 33.8 + 22.9 \times 9.1 + \cdots + 22.2 \times 14.1)}{21.1 \times 33.8^3 + 23.1 \times 9.1^3 + \cdots + 13.7 \times 14.1^3},$$

$$= 202.39.$$

TABLE 3 Relationship between rock load, mining distance, and fracture angle.

S/m	n	$(q_n)'_{12}$/(KPa)			$(q_n)_{12}$ (KPa)
		α=45°	α=60°	α=75°	
500	9	47.61	176.21	165.43	202.39
	8	45.45	115.53	158.32	192.65
	7	43.51	111.03	151.75	184.59
	6	194.11	239.81	271.56	298.61
	5	186.49	230.22	260.66	286.59
	4	591.66	628.85	654.91	677.03
	3	558.84	593.93	618.42	639.27
	2	909.12	910.56	911.48	912.22
	1	723.32	723.32	723.32	723.32
1000	9	89.13	142.50	175.31	202.39
	8	85.51	136.31	167.68	192.65
	7	81.95	130.63	160.67	184.59
	6	254.18	273.18	286.79	298.61
	5	244.01	262.22	275.26	286.59
	4	635.55	653.36	666.05	677.03
	3	600.18	616.96	628.92	639.27
	2	910.84	911.45	911.87	912.22
	1	723.32	732.32	732.32	723.32

The calculation results of $(q_n)_{12}$ are shown in Table 2. The results show that $(q_3)_{12} < (q_2)_{12}$, $(q_5)_{12} < (q_4)_{12}$, and $(q_7)_{12} < (q_6)_{12}$. Therefore, through the calculation results of traditional methods, after mining, there are three layers of separated strata in layers 13–14, 15–16, and 17–18 above the water flowing fractured zone.

4.1.2 Analysis and discussion of the calculated load in the separation range

According to Eq. 9, the conventional load $(q_n)_{12}$ formed by the influence of 12–20 layers of rock on the 12th layer can be obtained. Given the range of separation domain, according to Eq. 13, the corresponding correction load $(q_n)'_{12}$can be obtained (n takes 1–9). For the sake of generality, the mining overburden rock breaking angle α is 75°, 60°, and 45°, respectively, and the mining distance is S=500 m and S=1000 m for analysis. The corresponding load is shown in Table 3.

Table 3 shows that when the rock mining breaking angle α is 45°, 60°, and 75°, there are $(q_3)'_{12} < (q_2)'_{12}$, $(q_5)'_{12} < (q_4)'_{12}$, and $(q_7)'_{12} < (q_6)'_{12}$, which is consistent with the calculation results of the conventional rock load, which indicates that the 14th, 16th, and 18th strata can still be determined as the key strata. When the mining width S is 500 m and 1000 m and the mining fracture angle α is 45°, 60°, and 75°, the modified load $(q_9)'_{12}$ of the rock stratum is 76.5%, 12.9%, and 18.3% and 55.9%, 29.6%, and 13.4% lower than its conventional load $(q_n)_{12}$, respectively. This indicates that the simplified triangular separation domain has a significant effect on the modified rock load but the effect of the separation pressure arch slows down as the curvature of the upper rock beam increases.

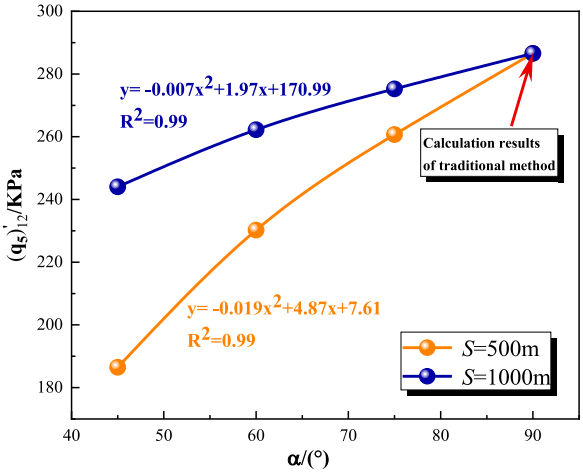

FIGURE 11
Curve of the modified load $(q_5)'_{12}$ of the rock stratum with α.

The variation of rock load $(q_5)'_{12}$ with the mining breaking angle is shown in Figure 11.

Figure 4 and Table 2 show that the mining breaking angle α and the mining width S of the rock stratum have an obvious influence on the rock stratum load, while the conventional load of the rock stratum, that is, Eq. 9, is the case of the corresponding mining breaking angle $\alpha = 90°$, which is only related to the density, thickness, and elastic modulus of the rock stratum but has nothing to do with the mining width. The rock load increases with the decrease in rock breaking angle α, and the increase law is close to the linear law. The rock load decreases with the increase in mining width S. This conclusion can explain the reason why the calculated step distance of rock fracture after mining of the No. 36 coal seam in the Buertai Coal Mine is larger than the actual fracture step distance.

4.1.3 The determining process and the results of the improved method

Because the settlement of the rock stratum occurs from bottom to top, the comparative analysis of rock beam deflection should also be carried out from bottom to top. Combined with Table 1 and Table 3, for the convenience of calculation, taking $S = 5.0cm$, $\alpha = 60°$, and $\sigma_h = 2.5*2500*9.8*220 = 13.47MPa$ into Eq. 17, we obtain

$$(\delta_1)_{12} = \frac{5S_{12}^4}{384E_{12}I_{12}} \frac{1}{1-\frac{N_{12}}{(N_e)_{12}}} (q_1)'_{12}$$

$$= \frac{5 \times 5^4}{384 \times 21.1 \times \frac{33.8^3}{12}} \times \frac{1}{1-\frac{13.47 \times 33.8}{\frac{\pi^2 \times 21.1 \times 33.8^3}{12 \times 5^2}}} \times 732.32 \approx 0.09.$$

Using the same calculation method, we calculate the deflection of each rock layer in the range of the separation zone, as shown in Table 4. The excessive deflection of the rock beam or the generation of the separation layer is mainly related to the softer and thinner rock layer, but the effective rock beam length and effective load involved in the deflection calculation in the range of the separation zone will make the generation of the separation

TABLE 4 22,207 working face overlying strata deflection calculation results.

Number of rock layer	$(\delta_1)_{12}$	$(\delta_2)_{12}$	$(\delta_3)_{12}$	$(\delta_4)_{12}$	$(\delta_5)_{12}$	$(\delta_6)_{12}$	$(\delta_7)_{12}$	$(\delta_8)_{12}$	$(\delta_9)_{12}$
Deflection (m)	0.087	4.468	0.022	12.019	0.001	0.779	0.011	0.005	0.000

TABLE 5 Improved method was used to determine the separation position of the 22,207 stope.

Number of rock layer *i*	Lithology	Are there separated strata below this layer?
20	Medium	N
19	Coarse sandstone	N
18	Fine sandstone	N
17	Sandy mudstone	N
16	Fine sandstone	Y
15	Sandy mudstone	N
14	Medium	Y
13	Siltstone	N
12	Medium	-
...		
1	Coal	

TABLE 6 Comparison of different methods to determine the position of stratification in the 22207 working face.

Number of rock layer *i*	Lithology	Are there separated strata below this layer?		
		Traditional method	Improved method	DTIO
20	Medium	N	N	N
19	Coarse sandstone	N	N	N
18	Fine sandstone	Y	N	N
17	Sandy mudstone	N	N	N
16	Fine sandstone	Y	Y	Y
15	Sandy mudstone	N	N	N
14	Medium	Y	Y	Y
13	Siltstone	N	N	N
12	Medium	-	-	-
		...		
1	Coal			

layer more complicated. The relationship between the rock beam disturbances in the adjacent separation domain is $(\delta_3)_{12} < (\delta_2)_{12}$, $(\delta_5)_{12} < (\delta_4)_{12}$, and $(\delta_7)_{12} < (\delta_6)_{12}$. At the same time, considering the reason of calculating the minimum dividing range, the deflection gap between the sixth layer and the seventh layer can be ignored. In summary, the main location of the separation layer is between the 13th layer and the 14th layer, the 15th layer, and the 16th layer (Table 5).

4.2 Measurement and verification

Before the mining of the 22,207 working face, a borehole (E082) was installed at a distance of 93.4 m from the open-off cut position of the 22,207 working face. The drilling TV imaging observation (DTIO) was carried out after mining on 25 August 2020. The position of the separation layer can be determined by the fracture development at different depths shown by the drilling TV image. The borehole images

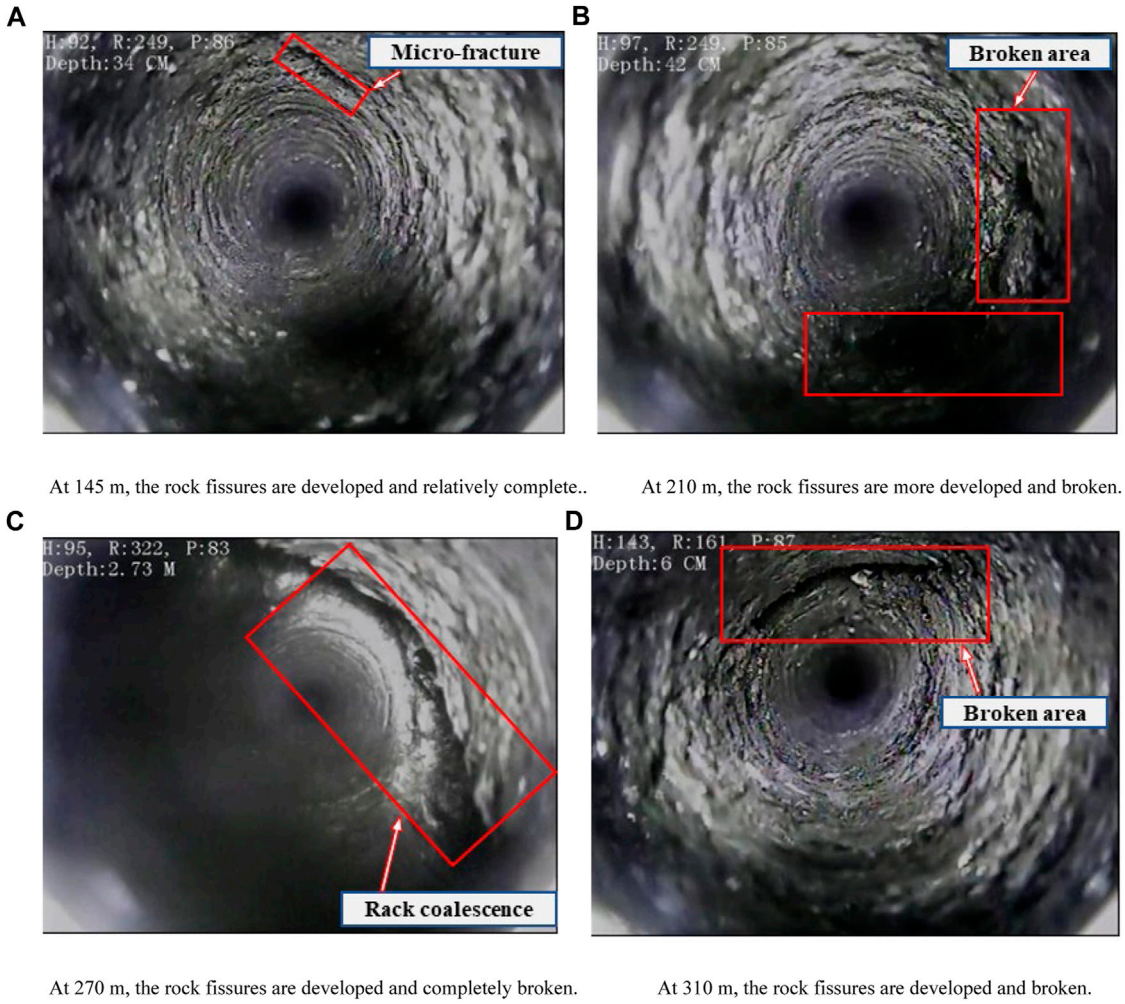

FIGURE 12
Borehole TV images of different depths in the 22,207 working face.

of 145 m (the bottom of the 17th overburden), 210 m (the bottom of the 16th overburden), 270 m (the middle of the 13th overburden), and 310 m (the bottom of the 12th overburden) are shown in Figure 12.

Figure 12A shows that between the 16th and 17th layers, although the cracks have developed to this height, the rock layer is still relatively complete, and there is no separation. Figure 12B shows that the fractures between the 16th and 15th layers are relatively broken, and the separation layer appears. Figure 12C shows that the overlying strata in the middle of the 13th layer are completely broken, and the contact surface between the 14th layer and the 13th layer has a large horizontal fracture, including the separation space caused by uneven settlement. In Figure 12D, the horizontal fracture has developed to the bottom of the 12th layer, but the rock layer has only small cracks and still maintains a complete block structure, probably because the 11th layer is sandy mudstone (Table 1). Sandy mudstone is a soft rock that can withstand greater deformation without fracturing and softens after saturation, so the cracks can be partially refilled.

In summary, there is no separation space between the 17th and 18th layers, but the separation occurred between the 13th and 14th layers, the 15th and 16th layers, and the 11th and lower layers are completely broken.

These observations are different from the results of the traditional separation layer calculation method described in Section 4.1.1 because the traditional method does not consider the influence of the separation layer on the load of the traditional composite beam overburden when calculating the load of the composite beam overburden between the 17th and 18th layers. The distribution of bed separation in the overlying strata measured on the site is in good agreement with the distribution of bed separation identified by the improved method (Section 4.1.3), which indicates that the results of the improved method are more accurate than those of the traditional method for the strata deeply affected by complex geological conditions, as shown in Table 6.

5 Conclusion

1) In view of the traditional method, there is no influence of rock strata outside the calculation range on the rock strata within the calculation range, and there is no limitation of judging which rock strata can be used as composite beams in advance.

According to the actual movement of rock strata and the concept of triangular-separation domain, considering the linear change in the curvature of the rock beam instead of constant value, the modified calculation formula of corresponding rock strata load is established, and the influence of mining distance and fracture angle of mining overburden on rock strata load is calculated and analyzed.

2) Considering the nature of the deformation of the separated strata under the action of horizontal stress and self-weight stress, combined with the knowledge of the triangular separation domain, traditional composite beam principle, lateral pressure theory, and maximum deflection calculation of simply supported beams, a mechanical calculation model for comparing the maximum deflection of the rock strata is proposed. It overcomes the limitation of the traditional method that only analyzes the more common longitudinal superposition model, can present the actual combination state of the rock strata, and more accurately determine the location of any separated strata.
3) A calculation model based on the comparative analysis of the maximum deflection of rock strata is established. The field exploration results show that the improved method has more accurate calculation results, which provides effective theoretical support for the prevention and control of roof water inrush caused by water accumulation in bed separation space and has practical engineering value.

Data availability statement

The original contributions presented in the study are included in the article/Supplementary Material; further inquiries can be directed to the corresponding author.

Author contributions

YD: methodology, writing–original draft, and writing–review and editing. ZN: writing–original draft, data curation, methodology. ZH: writing–review and editing, formal analysis, validation. QD: writing–review and editing, formal analysis, funding acquisition, software. QL: funding acquisition, writing–original draft, and writing–review and editing. JZ: writing–review and editing. QL: writing–review and editing.

Funding

The authors declare that financial support was received for the research, authorship, and/or publication of this article. This work was supported by the National Natural Science Foundation of China (Project No. 51904168), the Anhui Province Key Laboratory of Building Structure and Underground Engineering (KLBSUE-2022-07), and the Scientific Research Foundation of Key Laboratory of Mining Disaster Prevention and Control (MDPC202012).

Acknowledgments

The authors would like to express their gratitude to everyone who helped with the present study.

Conflict of interest

The authors declare that the research was conducted in the absence of any commercial or financial relationships that could be construed as a potential conflict of interest.

Publisher's note

References

Cai, X., Yuan, J. F., Zhou, Z. L., Pi, Z., Tan, L., Wang, P., et al. (2023). Effects of hole shape on mechanical behavior and fracturing mechanism of rock: implications for instability of underground openings. *Tunn. Undergr. Space Technol.* 141, 105361. doi:10.1016/j.tust.2023.105361

Chu, Y. D. (2013). Analysis of roof sandstone water bursting mechanism in Hongliu coalmine, yuanyanghu mining area, eastern ningxia. *Coal Geol. China* 25 (4), 34–39. doi:10.3969/j.issn.1674-1803.2013.04.09

Fan, K. F., Li, W., Wang, Q., Liu, S., Xue, S., Xie, C., et al. (2019). Formation mechanism and prediction method of water inrush from separated layers within coal seam mining: a case study in the Shilawusu mining area, China. *Eng. Fail. Anal.* 103, 158–172. doi:10.1016/j.engfailanal.2019.04.057

He, J. H., Li, W., Liu, Y., Yang, Z., Liu, S. L., and Li, L. F. (2018). An improved method for determining the position of overlying separated strata in mining. *Eng. Fail. Anal.* 83, 17–29. doi:10.1016/j.engfailanal.2017.09.015

Hu, R., Wu, J. W., Zhai, X., and Liu, W. (2021). Recognition and prevention of bed separation water: based on trapezoid platform model. *Geofluids* 2021, 1–10. doi:10.1155/2021/6626268

Ji, J. S., Li, Z. H., Yang, K., Zhou, G., Ma, G., Liu, C., et al. (2022). Research on formation mechanism and evolution pattern of bed separation zone during repeated mining in multiple coal seams. *Geofluids* 2022, 1–19. doi:10.1155/2022/4290063

Kang, H., Zhang, X., Si, L., Wu, Y., and Gao, F. (2010). *In-situ* stress measurements and stress distribution characteristics in underground coal mines in China. *Eng. Geol.* 116, 333–345. doi:10.1016/j.enggeo.2010.09.015

Li, W. B., Wu, P., and Wang, X. J. (2009). Probe into gently dipping strata roof separation water jeopardizing on fully mechanized mining face and controlling. *Coal Geol. China* 21 (10), 42–45. doi:10.3969/j.issn.1674-1803.2009.10.012

Li, Y., Zhang, S., Yang, Y., Chen, H., Li, Z., and Ma, Q. (2022). Study on the water bursting law and spatial distribution of fractures of mining overlying strata in weakly cemented strata in West China. *Geomechanics Eng.* 28 (6), 613–624. doi:10.12989/gae.2022.28.6.613

Liang, Y., and Sun, D. (2002). Study on the composed rock beam theory of strata movement and its application. *Chin. J. Rock Mech. Eng.* 21, 654–657. doi:10.3321/j.issn:1000-6915.2002.05.010

Liu, S. M., Sun, H. T., Zhang, D., Yang, K., Wang, D., Li, X., et al. (2023a). Nuclear magnetic resonance study on the influence of liquid nitrogen cold soaking on the pore structure of different coals. *Phys. Fluids* 35 (1). doi:10.1063/5.0135290

Liu, S. M., Sun, H. T., Zhang, D. M., Yang, K., Li, X., Wang, D., et al. (2023b). Experimental study of effect of liquid nitrogen cold soaking on coal pore structure and fractal characteristics. *J. **Energy*** 275 (7), 127470. doi:10.1016/j.energy.2023.127470

Ma, K., Yang, T. H., Zhao, Y., Hou, X., Liu, Y., Hou, J., et al. (2022). Mechanical model for analyzing the water-resisting key stratum to evaluate water inrush from goaf in roof. *Geomechanics Eng.* 28 (3), 299–311. doi:10.12989/gae.2022.28.3.299

Ning, J. G., Wang, J., Tan, Y., Zhang, L., and Bu, T. (2017). *In situ* investigations into mining-induced overburden failures in close multiple-seam longwall mining: a case study. *JJ, Geomechanics Eng.* 12 (4), 657–673. doi:10.12989/gae.2017.12.4.657

Palchik, V. (2003). Formation of fractured zones in overburden due to longwall mining. *Environ. Goel* 44 (1), 28–38. doi:10.1007/s00254-002-0732-7

Palchik, V. (2015). Bulking factors and extents of caved zones in weathered overburden of shallow abandoned underground workings. *Int. J. Rock Mech. Min. Sci.* 79, 227–240. doi:10.1016/j.ijrmms.2015.07.005

Peng, T., Feng, X. H., and Liang-liang, L. (2019). Study on mechanism of water inrush and sand inrush in mining of coal seam with thick overlying bedrock. *Coal Sci. Technol.* 47 (7), 260–264. doi:10.13199/j.cnki.cst.2019.07.035

Qiao, W., Yang, H., Yuan, Z.-B., and Guo, W. (2014). Formation and prevention of water inrush from roof bed separation with full-mechanized caving mining of ultra thick coal seam. *Chin. J. Rock Mech. Eng.* 33, 2077–2084. doi:10.13722/j.cnki.jrme.2014.10.014

Shi, L. (2020). Numerical simulation study on law of water and sand in-rush in working face under condition of weakly cemented stratum. *Coal Sci. Technol.* 48 (7), 347–353. doi:10.13199/j.cnki.cst.2020.07.039

Shu, Z. Y., He, B. Q., and Ling, L. (2020). Study on mechanism of separation strata water-inrush induced by impact energy of key strata abrupt breaking. *Coal Sci. Technol.* 48 (5), 149–156. doi:10.13199/j.cnki.cst.2020.05.021

Sun, Z. F., Yan, S. J., and Wang, Y. Q. (2012). Primary investigation of water inrush from separation layer over mining face of soft rock stratum. *Coal Sci. Technol. Mag.* (3), 27–31. doi:10.19896/j.cnki.mtkj.2012.03.014

Wang, Z. Y., Zhang, Q., Shao, J., Zhang, W., Wu, X., and Zhu, X. (2021). New type of similar material for simulating the processes of water inrush from roof bed separation. *ACS Omega* 5 (47), 30405–30415. doi:10.1021/acsomega.0c03535

Wu, Q., Fan, Z. L., Zhang, Z., and Zhou, W. (2014). Evaluation and zoning of groundwater hazards in Pingshuo No. 1 underground coal mine, Shanxi Province, China, Shanxi Province. *Hydrogeology J.* 22 (7), 1693–1705. doi:10.1007/s10040-014-1138-9

Xu, B., Jin-quan, J., Jin, D., and Pengqiang, Z. (2018). Mechanical derivation and experimental simulation of fracture angle of overlying key strata in stope. *J. China Coal Soc.* 43 (03), 599–606. doi:10.13225/j.cnki.jccs.2017.1346

Yan, H., He, F.-l., Yang, T., Li, L., Zhang, S., and Zhang, J. (2016). The mechanism of bedding separation in roof strata overlying a roadway within a thick coal seam: a case study from the Pingshuo Coalfield, China. *Eng. Fail. Anal.* 62, 75–92. doi:10.1016/j.engfailanal.2015.12.006

Yan, H., Zhang, J. X., Li, L. y., Feng, R. m., and Li, T. T. (2018). Prediction of upper limit position of bedding separation overlying a coal roadway within an extra-thick coal seam. *J. central south Univ.* 25 (2), 448–460. doi:10.1007/s11771-018-3749-0

Yang, Q., Qiao, W., and Le, J. (2014). Analysis on formation condition of water in roof bed separation in fully mechanized face of extra-thick seam and evaluation of its risk. *Min. Saf. Environ. Prot.* 41, 64–66. doi:10.3969/j.issn.1008-4495.2014.03.018

Yue, J. G., Yang, W. F., and Gu, C. S. (2015). Formation mechanism and identification method of super-high seam by fully mechanized caving method. *Environ. Goel* 23, 603–610. (Suppl). doi:10.13544/j.cnki.jeg.2015.s1.092

Zhang, S. Z., Fan, G. W., Zhang, D., Li, S., Chen, M., Fan, Y., et al. (2021). Impacts of longwall mining speeds on permeability of weakly cemented strata and subsurface watertable: a case study. *Geomatics Nat. Hazards Risk* 12 (1), 3063–3088. doi:10.1080/19475705.2021.1993354

Zhang, Z. B., Wang, E. Y., Zhang, H., Bai, Z., and Zhang, Y. (2023b). Research on macroscopic mechanical properties and microscopic evolution characteristic of sandstone in thermal environment. *Constr. Build. Mater.* 366, 130152. n. pag. doi:10.1016/j.conbuildmat.2022.130152

Zhang, Z. B., Wang, E. Y., Zhang, H., Bai, Z., Zhang, Y., Chen, X., et al. (2023a). Research on nonlinear variation of elastic wave velocity dispersion characteristic in limestone dynamic fracture process. *Fractals-complex Geometry Patterns Scaling Nat. Soc.* 31 (1), 2350008. doi:10.1142/S0218348X2350008,

Zhou, Z. L., Wang, P. Y., Cai, X., and Cao, W. (2023). Influence of water content on energy partition and release in rock failure: implications for water-weakening on rock-burst proneness. *Rock Mech. Rock Eng.* 56, 6189–6205. doi:10.1007/s00603-023-03379-z

frontiers | Frontiers in Earth Science

TYPE Original Research
PUBLISHED 27 December 2023
DOI 10.3389/feart.2023.1301595

OPEN ACCESS

EDITED BY
Xuelong Li,
Shandong University of Science and Technology, China

REVIEWED BY
Kaizong Xia,
Chinese Academy of Sciences (CAS), China
Shupeng Zhang,
North Blasting Technology Co.Ltd., China
Kang Yi,
Taiyuan University of Technology, China

*CORRESPONDENCE
Jing Chai,
1319071878@qq.com

RECEIVED 25 September 2023
ACCEPTED 20 October 2023
PUBLISHED 27 December 2023

CITATION
Gao S, Du W, Liu Y, Chai J, Gao D, Ma C and Chen J (2023), Reasonable top coal thickness for large cross-section open-off cut in lower-layer mining.
Front. Earth Sci. 11:1301595.
doi: 10.3389/feart.2023.1301595

Reasonable top coal thickness for large cross-section open-off cut in lower-layer mining

Shigang Gao[1,2], Wengang Du[1], Yongliang Liu[1], Jing Chai[1,2]*, Dengyan Gao[2], Chenyang Ma[1] and Jianhua Chen[2]

[1]College of Energy Engineering, Xi 'an University of Science and Technology, Xi'an, China, [2]Shenhua Shendong Coal Group Corporation Limited, China Energy Group, Yulin, China

The thickness of top coal is the main factor affecting the stability of the large cross section open-off cut under the goaf. The 1^{-2} lower 203 cross section open-off cut of the Huojitu Coal Mine was used as the background to investigate the top coal rational thickness of the large cross section open-off cut under the goaf in slicing mining. The top coal above the cut was simplified into a beam model to calculate its plastic zone range with the elastoplastic theory under the influence of the upper slicing mining and the lower slicing cut excavating. The deformation law of the top coal of the large cross section open-off cut under different top coal thicknesses was studied with both a simulation experiment and numerical simulation. The displacement, stress, and top coal structure of the surrounding rock of the cut were observed *in situ* using several observation methods. The results show that the plastic zone of the floor in the upper slicing face and the influence of the cut excavation are 2.02 m and 1.43 m, and the maximum plastic zone of the top coal is 3.45 m. A top coal thickness of more than 3.45 m is conducive to maintaining the stability of the large cross section open-off cut. The top coal of the cut can be divided into the roof-fall hazard zone and roof-fall warning zone according to the results monitored by distributed optical fiber. When the top coal thickness is 3.0 m, 3.5 m, and 4.0 m, the deformation law changes from an exponential deformation to a linear and then to a logarithmic relationship in the roof-fall hazard zone and from a linear to a logarithmic relationship in the roof-fall warning zone. When the thickness of top coal is 3.5 m and 4.0 m, the subsidence trend of the top coal visibly decreases, and the subsidence is only 56% and 39% of the subsidence of that of a thickness of 3 m. The deformation law of top coal measured using the DIC (Digital Image Correlation, DIC) is consistent with that of distributed optical fiber. The average thickness of the top coal reserved in the 1^{-2} lower 203 large cross section open-off cut is 4.0 m. The maximum surface subsidence of the top coal cut hole is 12 mm in the field monitoring. The maximum internal subsidence is 6 mm, and the maximum shed beam strain is −416 με. The deformation of the top coal is slight, indicating that the top coal thickness of 3.5–4.0 m is reasonable.

KEYWORDS

slicing mining, large cross-section open-off cut, top coal thickness, optical fiber sensor, field monitoring

1 Introduction

The cumulative proven coal reserves in northern Shaanxi are 138.8 billion tons, and the remaining coal reserves are 131.5 billion tons, making it rich in resources. Among them, the maximum recoverable thickness of a single layer in the Jurassic coalfield in the Shenfu mining area is 12.5 m. In the early days, due to technical limitations, many mines adopted layered mining technology for mining. When mining in the lower coal seam, due to the influence of small kilns, etc., the production roadway of the working face is laid out under the goaf of the upper layer. The thickness of the top coal and the support technology have become the main technical problems in the mining of the lower coal seam (LIU et al., 2013; CHAI et al., 2022a; HE and HUANG, 2022; XIA et al., 2022; XIA et al., 2023).

The research on the layered mining of thick coal seams and the top coal retention and support technology of the roadway in the lower coal seam mainly focuses on the tunnel excavation and supporting technology in the goaf area of close coal seams (DONG et al., 2013; GAO and ZHANG, 2014; Qi, 2018). WANG et al. (2020) studied the position and support method of the tunnel at the lower working face in the goaf area of the coal seam at a very close distance and reasonably offset it from the upper residual coal pillar by 9 m, effectively avoiding the influence of the residual coal pillar in the upper goaf area, and proposed this method of supporting the roadway under similar conditions. CAO (2015) used theoretical analysis and proposed a very close coal seam support scheme that used the top coal thickness of 3 m as the dividing line to carry out segmented support and improve the strength and pre-tightening force of the anchor bolts. The size of the large section cut hole of 1^{-2} coal seam in the Shigetai Mine is 7.9 × 3 m. It adopts an "anchor rod + steel mesh + anchor cable + steel beam shed + single pillar" approach. The joint support scheme has a maximum moving distance of 42 mm for the roof and bottom plates and a maximum moving distance of 26 mm for the two gangs, which can meet the requirements of working face installation and normal mining (ZHAO, 2018). In view of the disturbance caused by working adjacent faces under the goaf, Yang et al. (2019) suggested the technology of combining pressure relief with bolt support to control the stability of the surrounding rock of the roadway under the goaf after analyzing the fracture mechanism and stress distribution of the key strata of the overlying rock and the deformation distribution characteristics of the rock surrounding the roadway on the side of the goaf. GAO et al. (2021) simulated the deformation and stress of the surrounding rock and supporting structure during the tunneling process under the goaf, compared the deformation and stress concentration states of the tunnel-surrounding rock under different support row spacings, and verified the rationality of the support scheme.

In the theoretical research of the stability of a lower stratified mining roadway, scholars have studied the failure factors and failure rules of large-section tunnels and cut-hole surrounding rocks (CHAI et al., 2008; NIU et al., 2014). HE et al. (2014) used numerical simulation to analyze the zoning characteristics and crack evolution rules of the surrounding rock fissure fields when the hole width was 6–10 m. Anchor belt nets and double truss anchor cables were used to support the joint during excavation, resulting in completion of the hole in 10 days. The movement of the roof and floor of the tunnel and the two sides was small, and the surrounding rock control effect was good. ZHANG et al. (2004) studied the anchor network cable support scheme for the surrounding rock of fully mechanized caving in thick coal seams. They used Timoshenko beams to analyze the roof-like connectors and the side coal mass and determined the factors that affect the stability of the opening. The support plan was optimized, and specific support parameters were determined. Jiang et al. (2021) established a mechanical model of the roof under the goaf and deduced its internal force according to the failure characteristics of the surrounding rock of the stope roof. The shear and compression safety factors of the open-off cut roof were given, and the factors affecting the stability of the roof were the span of the open-off cut and the thickness of the roof. In order to solve the problem of roof coal support for large-span openings under goafs in layered mining of thick coal seams, CHAI et al. (2022b) and CHAI et al. (2022c) analyzed the load-bearing deformation and failure characteristics of large-span roof coals, derived the extreme value conditions of instability, and analyzed the deformation laws of the top coal with the hole peek device.

The roof of the cut hole in the lower coal seam was damaged before tunneling. The roof structure changed, cracks developed, stability was poor, and the risk of roof falling increased, which brought many technical difficulties to the lower coal seam tunneling (Yan et al., 2015; Xinjie et al., 2016; He et al., 2023). Scholars calculated the initial breaking distance and periodic breaking distance of the roof by constructing a plate model and used the beam model to analyze the stability of the tunnel roof (Xiao et al., 2011; Tulu et al., 2016). In terms of the broken load-bearing structure of the tunnel roof, JIANG et al. (2016) established a continuous deep beam mechanical structure model under uniform load and obtained the stress distribution law of the roof rock layer under tunnel mining. YAO (2014) analyzed the mining tunnel of the Hexi Mine and deduced the deep-seated reasons for the breakage of the roof anchor cables. The maximum deflection and angle under three different combination structures of the broken roof rock layer block beam, fixed beam, and composite beam of the roadway were discussed. Factors such as the roadway width, interburden thickness, upper coal seam mining height, and relationship with roof deformation were discussed. Through UDEC (Universal Distinct Element Code, UDEC), Liu et al. (2021) analyzed the fracture evolution law and failure form of the surrounding rock of the open-off cut roof during the first excavation and the second excavation. Xie et al. (2020) used numerical simulation software to analyze the distribution characteristics of effective prestress in the roof of the goaf and concluded that it can form an anchored rock beam structure. Few scholars have constructed a mechanical model of the tunnel roof to analyze the deformation laws of the top coal under the goaf, and there are few studies on related support technologies.

In summary, most of the existing research results are research on the support technology of large-section hole cutting under the goaf area of close coal seams. There are few reports on the thickness of the top coal left for large cross-section cut holes under the goaf and the coupling relationship between the surrounding rock and the supporting structure under layered mining conditions (Gong et al., 2019). Ensuring the stability of the surrounding rock of the cut holes while maximizing the reduction of the thickness of top coal can both improve the recovery rate of legacy coal resources and

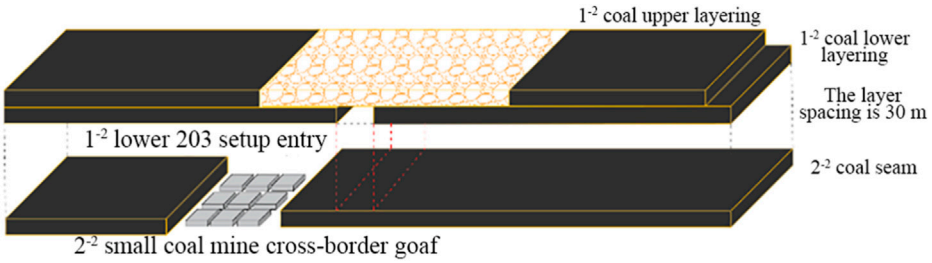

FIGURE 1
Cut selection scheme of the 1-2 lower 203 working face in the Huojitu mine.

reduce the amount of tunneling work (undercover amount). This has become the focus of current research. This paper uses theoretical calculations to obtain the depth of damage to the upper-layer mining floor and the plastic damage range of the top coal caused by the lower coal seam cutting tunneling. Both physically similar simulation tests and numerical simulations were carried out to study the deformation of three groups of top coal thickness conditions. The work is expected to provide a scientific and reasonable basis for large cross-section open-off cut under similar working conditions.

2 Theoretical analysis of the plastic zone range of top coal of the cut hole

2.1 Engineering background

The average coal thickness of the 1-2 203 coal seam composite area in the Huojitu Coal Mine is 10 m, the buried depth is 63–87 m, and the average buried depth is 80 m. Due to the limitations of the manufacturing level of mechanized mining equipment at that time, this panel adopted the layered mining method for mining. The upper-layer working face was designed to have a mining height of 4.5–5 m, and a remaining 5-m-thick coal seam was retained in the upper-layer goaf area. Under this situation, more than 30 million tons of coal resources have not been mined. In order to avoid the small kiln cross-border area, it is planned to arrange the 1-2 lower 203 large cross section open-off cut under the 1-2 upper 203 goaf area, as shown in Figure 1.

The 1-2 lower 203 working face excavation tunnel includes the 1-2 lower 203 tunnel, the shunting chamber, the end frame nest, and the shearer machine nest. The design length of the cutout is 251.4 m, the width is 9.0 m, and the height is 3.9 m. The cross-section of the cut is large. In order to prevent the roof from connecting with the goaf above during the excavation process, leaving a reasonable thickness of top coal becomes the main issue to ensure safe production on the working face.

2.2 Scope of the plastic zone of top coal of the cut hole

The 1-2 lower 203 working face is located below the goaf of the 1-2 upper 203 working face. After the working face is mined, the top coal plastic zone consists of two parts affected by the mining of the upper-layer working face. As shown in Figure 2, one part is calculated through elastic–plastic theory, which determines the maximum damage depth, h_{max}, of the floor after the upper layer is mined. The other part is the plastic state after the coal and rock mass is stressed during the tunneling process; its thickness is h_1. The sum of the two thicknesses is regarded as the maximum range of the plastic zone H of the coal beam.

2.2.1 Plastic zone of floor in the upper-layer working face

A goaf is formed behind the longwall working face, and it has a rectangular cross section. The mining height of the coal seam will be very small compared with the width of the longwall working face. Assume that the mining length of the working face is L, the vertical stress is γH, the horizontal stress is xyH (x is the lateral stress coefficient), and r_0 is the maximum damage distance in front of the stope. Using elastic theory (Schenato et al., 2017), the horizontal

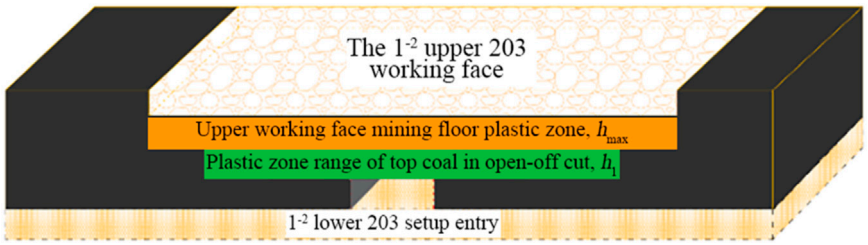

FIGURE 2
Composition of the plastic zone of cut top coal.

stress, vertical stress, and shear stress near the stope can be obtained as follows:

$$\begin{cases} \sigma_x = \gamma H\sqrt{\frac{L}{2r}}\cos\frac{\theta}{2}\left(1-\sin\frac{\theta}{2}\sin\frac{3\theta}{2}\right)-(1-x)\gamma H, \\ \sigma_y = \gamma H\sqrt{\frac{L}{2r}}\cos\frac{\theta}{2}\left(1+\sin\frac{\theta}{2}\sin\frac{3\theta}{2}\right), \\ \tau_{yy} = \gamma H\sqrt{\frac{L}{2r}}\cos\frac{\theta}{2}\sin\frac{\theta}{2}\cos\frac{3\theta}{2}. \end{cases} \tag{1}$$

Here, r is the boundary of the failure zone and θ is the angle between the edge and the horizontal direction at the maximum yield depth, h.

Analysis of Equation 1 shows that if the point (r, θ) is known, the stress of the surrounding rock of the stope is directly proportional to the buried depth of the working face and the length of the working face. Based on the actual mining conditions of the Huojitu Coal Mine, the boundary of the damage area is $r<L$, and the lateral pressure coefficient x is generally 1. Substituting these values into Equation 1, the principal stress of the stope edge is obtained as follows:

$$\begin{aligned} \sigma_1 &= \frac{\gamma H}{2}\sqrt{\frac{L}{r}}\cos\frac{\theta}{2}\left(1+\sin\frac{\theta}{2}\right), \\ \sigma_2 &= \frac{\gamma H}{2}\sqrt{\frac{L}{r}}\cos\frac{\theta}{2}\left(1-\sin\frac{\theta}{2}\right), \\ \sigma_3 &= 0. \end{aligned} \tag{2}$$

Here, r is the boundary of the failure zone, γ is the bulk density of the rock formation, H is the buried depth, L is the mining length of the working face, and θ is the angle between the edge and the horizontal direction at the maximum yield depth, h.

Assuming that the surrounding rock failure obeys the Mohr–Coulomb criterion, the following formula can be obtained:

$$\sigma_1 - \xi\sigma_3 = R_c, \tag{3}$$

$$\xi = \frac{1+\sin\varphi}{1-\sin\varphi}. \tag{4}$$

Here, R_c represents the uniaxial compressive strength and ϕ represents the internal friction angle.

Substituting Equation 1 into Equation 3, the yield failure depth h of the floor caused by stress concentration below the edge of the mining layer can be calculated as

$$h = \frac{\gamma^2 H^2 L}{4R_c^2}\cos^2\frac{\theta}{2}\left(1+\sin\frac{\theta}{2}\right)^2\sin\theta. \tag{5}$$

After finding the first-order derivative of θ in the aforementioned formula and allowing the derivative to be zero, the maximum value of the base plate failure depth under the plane stress state can be obtained:

$$h_{\max} = \frac{1.57\gamma^2 H^2 L}{(4R_c^2)}. \tag{6}$$

This maximum value is obtained when θ is approximately −75°. According to the aforementioned formula, it can be seen that the damage depth of the floor is positively related to the square of the inclination length of the working face and the buried depth. It is negatively related to the square of the compressive strength of the floor. When calculating the thickness of floor failure, we use the elastic–plastic theory and take into account the factors affecting the joint cracks existing in the floor. Then, Equation 6 becomes

$$h_{\max} = \frac{1.57\gamma^2 H^2 L}{(4R_c^2\cdot\delta^2)}. \tag{7}$$

Here, δ is the influence coefficient of joints and fissures in the floor rock layer, γ is the average bulk density of the overlying rock layer of the mined coal seam in kN/m^3, H is the average buried depth of the mined coal seam in m, L is the inclination length of the mining coal seam working surface in m, and R_c represents the compressive strength of the floor rock layer in MPa.

2.2.2 Plastic zone of roof during the lower coal seam large cross section open-off cut excavation

During the lower coal seam cut hole excavation process, without being disturbed by the mining of the upper layer, the top coal of the cut near the upper coal seam will first undergo elastic deformation and then plastic damage. According to the analysis of the stress characteristics of beam structures in elastic–plastic mechanics, the strain at the x-axis section is

$$\varepsilon = \frac{y}{\rho}. \tag{8}$$

Here, ρ is the radius of curvature of the beam, and the relationship with the deflection is

$$\frac{y}{\rho} = -\frac{d^2\omega}{dx^2}. \tag{9}$$

According to the elastic theory, the stress is

$$\sigma = E\varepsilon = E\frac{y}{\rho}. \tag{10}$$

In the elastic stage, the relationship between curvature and bending moment is

$$\frac{1}{\rho} = \frac{M}{EI}. \tag{11}$$

It can be seen that the normal stress of elastic bending is distributed linearly in the direction, taking the maximum absolute value at $y=\pm h/2$:

$$|\sigma|_{\max} = \frac{M\frac{h}{2}}{\frac{bh_1^3}{12}} = \frac{6M}{bh_1^2}. \tag{12}$$

According to the yield condition of the uniaxial stress state, when $|\sigma|_{\max} < \sigma_s$, the cross section is all in the elastic state; when $|\sigma|_{\max} = \sigma_s$, the elastic stage reaches the limit, and the elastic limit bending moment M_e is

$$M_e = \frac{\sigma_s b h_1^2}{6}. \tag{13}$$

When $M>M_e$, the cross section enters the plastic stage from the elastic stage, and the corresponding normal stress approaches the ultimate stress at $y=\pm h/2$. Forming a plastic zone in which the normal stress is evenly distributed, the area near the neutral axis is

still an elastic zone, and the normal stress is still linearly distributed. Using the static equilibrium relationship, we can get

$$M = 2b\int_0^{\frac{h_1}{2}} \sigma y dy = 2b\left(\int_0^{\zeta} \sigma_s \frac{y}{\zeta} y dy + \int_0^{\frac{h_1}{2}} \sigma_s y dy\right) = \frac{\sigma_s b h_1^2}{4}\left(1 - \frac{4\zeta^2}{3h_1^2}\right). \tag{14}$$

As M increases, ξ decreases; that is, the plastic zone continues to expand, and the elastic zone continues to shrink until $\xi = 0$, and the cross section completely enters the plastic state. At this time, the plastic limit bending moment M_s is

$$M_s = \frac{\sigma_s b h_1^2}{4}. \tag{15}$$

From the aforementioned formula, it can be seen that the plastic ultimate bending moment of the roof coal beam is related to the yield strength, span, and height of the coal beam. Therefore, measures can be taken to increase the thickness of the roof coal, improve its resistance to damage, and prevent the cut hole roof coal from entering a plastic state. The coal beam is stable before it is damaged by mining. According to material mechanics calculations, the maximum bending moment under a vertical load is

$$M_{\max} = \frac{q l_0^2}{24}. \tag{16}$$

To ensure that all coal beams do not enter the plastic state, $M_s \geq M_{\max}$ must exist, that is,

$$\frac{\sigma_s b h_1^2}{4} \geq \frac{q l_0^2}{24}, \tag{17}$$

$$h_1 \geq l_0 \sqrt{\frac{q}{6\sigma_s b}}. \tag{18}$$

The average buried depth of the 1^{-2} coal seam in the Huojitu Coal Mine is 76 m, the coal seam thickness is 9.5–10.6 m, the average mining height of the upper layer is 4 m, and the length of the 1^{-2} upper 203 working face is 210 m. The uniaxial compressive strength Rc of the 1^{-2} coal is 9.2 MPa, the influence coefficient δ of floor joint cracks is 0.95, the average bulk density of the overlying rock layer γ = 0.018 kN/m^3, and the highest stress concentration coefficient K_1 = 3.5. Substituting the aforementioned geological parameters into Equation 5, the specific calculation results are as follows:

$$h_{\max} = \frac{1.57\gamma^2 H^2 L}{(4R_c^2 \cdot \delta^2)} = \frac{1.57 \times 0.018^2 \times 76^2 \times 210}{4 \times 9.2^2 \times 0.95^2} \approx 2.02 \text{ m}.$$

The maximum damage depth of the upper layer mining floor is 2.02 m, and the range of plastic damage of the coal beam is 0–2.02 m.

According to the actual situation on site, the uniform load q=1.4 Mpa and σ_s=9.2 Mpa overlying the cut-out eye are substituted to obtain $h_1 \geq 1.43$ m. That is, when the hole is tunneled, the maximum plastic range of the top coal is 1.43 m. The maximum range of the plastic zone of the top coal of the cut hole is

$$H = h_{\max} + h_1 = 2.02 + 1.43 = 3.45m. \tag{19}$$

That is, when the thickness of the top coal of the cutting hole is greater than 3.45 m, it is beneficial to maintain the stability of the cutting hole.

3 Similar simulation test analysis of cut hole top coal thickness

A simulation was conducted to determine the reasonable top coal thickness for cut hole in the 1^{-2} lower 203 coal seam working face using a simulation test platform with a length of 3,000 mm, a width of 200 mm, and a height of 2,000 mm. The geometric similarity ratio of the simulation experiment is 1:50, the stress similarity ratio is 78, and the time similarity ratio is 7.1. The model ratios are shown in Table 1.

According to the theoretical analysis results, the thickness of the top coal at cut hole No.1, No.2, and No.3 is 3 m, 3.5 m, and 4 m, respectively. During the model building process, the acrylic mold is pre-embedded and cut. According to the actual situation, the 1^{-2} upper 203 coal seam working face was mined to form the goaf, and then the die was pulled to simulate the cut hole mining process. The simulation was run six times.

Fiber optic sensing technology has the advantages of wide distribution and high precision and has been applied in similar simulation experiments to monitor overlying rock deformation and working face pressure (Xie et al., 2020). This article applies distributed fiber optic technology to similar simulation experiments. As shown in Figure 3, the experiment monitored the deformation of the top coal from the inside and the surface of the model. In this test, the layers were under the 1^{-2} coal, and a 2 mm horizontal optical fiber was arranged on the cut hole roof with a strain coefficient of 0.0497 MHz/με. In the test, the NBX6055 spatial resolution was set to 1 cm, and the monitoring accuracy was 50 με. A distributed optical fiber sensing system based on BOTDA (Brillouin Optical Time Domain Analysis, BOTDA) technology was used to monitor the internal deformation of the top coal of the cut hole. The equipment was an NBX-6055 photometer. During the test process, the spatial resolution of the instrument was 5 cm, the sampling interval was 1 cm, and the sensing distance was 20 km. The optical fiber was implanted into the physical model using pre-embedding. When the model was laid to the height of the sensor position, the optical fiber was horizontally laid into the center of the model. After the model was laid, tension was applied to the two segments of the optical fiber to maintain the horizontal state of the optical fiber in the model.

After the model was built, speckle spots were arranged on the top coal above the cut holes and the two coal bodies. The digital speckle system camera has 12 million pixels and a strain measurement range of 0.005%–2,000%. During the experiment, the shooting frequency was 1 Hz, the strain measurement accuracy was 0.005%, and the displacement measurement accuracy was 10 μm (0.01 pixels). Data were collected for cut holes No.1, No.2, and No.3 for each excavation. The open-off cut process of the 1^{-2} coal seam is shown in Figure 4 a. The caving characteristics of overlying strata after the mining of the upper layer working face are shown in Figure 4b.

TABLE 1 Physical similarity simulation experiment material ratio.

No.	Lithology	Proportion number	Layer thickness/cm	Cumulative thickness/cm	River sand/kg	Gypsum/kg	White powder/kg	Coal/kg	Water/kg
12	Fine-grained sandstone	837	3.1	126	24.6	0.9	2.2		2.77
11	Siltstone	728	12.2	122.9	96.4	2.8	10.8		11
10	Siltstone	728	1.5	110.7	12.1	0.3	1.4		1.39
9	Siltstone	728	6.9	109.2	54.1	1.5	6.3		6.21
8	Coarse-grained sandstone	973	17.1	102.3	137.9	10.5	4.9		15.4
7	1^{-1} coal seam		5.1	85.2	19.8	1	5	19.8	4.6
6	Fine-grained sandstone	837	25.8	80.1	206.1	8.1	18		23.4
5	Siltstone	728	7.2	54.3	56.4	1.5	6.3		6.3
4	1^{-2} coal seam		19.9	47.1	78	3.9	19.5	78	18
3	Siltstone	728	6.6	27.2	52.2	1.5	6		6
2	Fine-grained sandstone	837	5.2	20.6	41.9	1.6	3.7		4.7
1	Siltstone	728	15.4	15.4	121.2	3.6	13.8		13.8

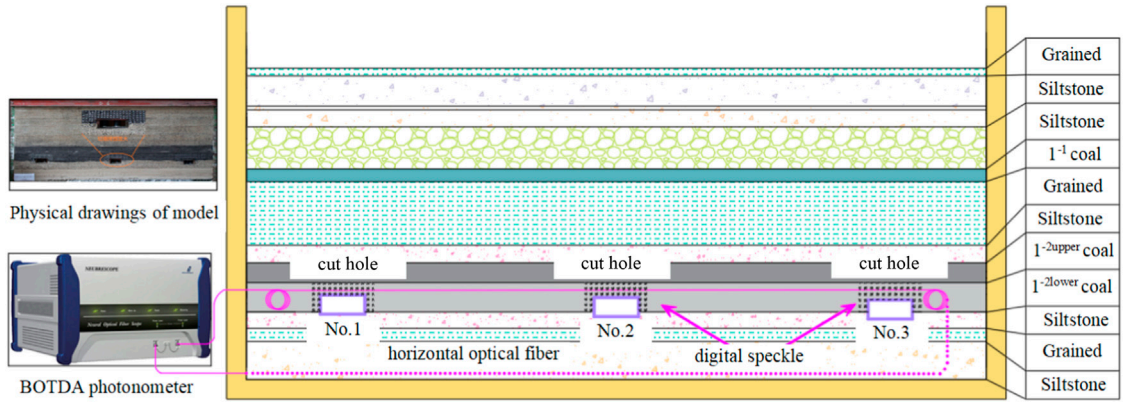

FIGURE 3
Model monitoring system.

3.1 Analysis of top coal deformation results

3.1.1 Internal deformation zoning characteristics of top coal

The optical fiber monitoring results of top coal deformation during the excavation process of entries No.1, No.2, and No.3 are shown in Figure 5, with the center of the top coal as the 0 point. It can be seen that the deformation of the top coal is distributed in a "W" shape. The deformation characteristics of positive fiber-optic sensing tension and negative pressure indicate that the middle part of the top coal appears to sink significantly due to the influence of its own weight and the load of the overlying goaf. With the tunneling, the subsidence within the ±50 mm range of the center of the top coal of cut holes No.1, No.2, and No.3 is significantly greater than that of the two sides, showing the zoning characteristics of a large deformation in the middle and small deformation on both sides. The area within ±50 mm of the center of the top coal can be divided into roof-fall hazard areas. It shows that when the cut hole width of the 1^{-2} 203 working face is 9.96 m, the roof deformation is large within 5 m of the center of the cutout. If the support is not placed in a timely manner, there is a greater risk of top coal falling.

Within the range of ±50–100 mm on both sides of the cut holes No.1, No.2, and No.3, the horizontal optical fiber test results gradually changed from positive strain to negative strain, indicating that the subsidence of the top coal gradually decreased near the two sides of the cut hole. As the tunneling distance increases, the subsidence of the top coal in the area of cut holes No.1, No.2, and No.3 also gradually increases, but the peak deformation is only 7%–

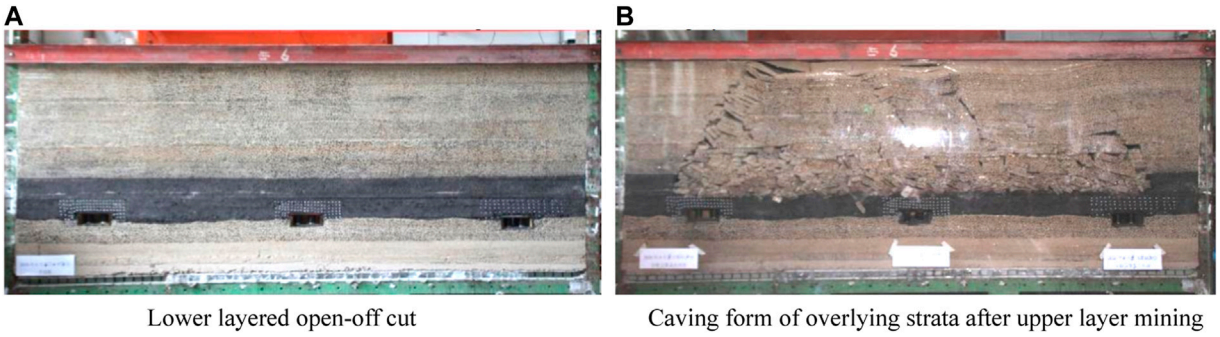

FIGURE 4
Physical similarity simulation experiment result diagram. **(A)** Lower layer open-off cut. **(B)** Caving form of overlying strata after upper-layer mining.

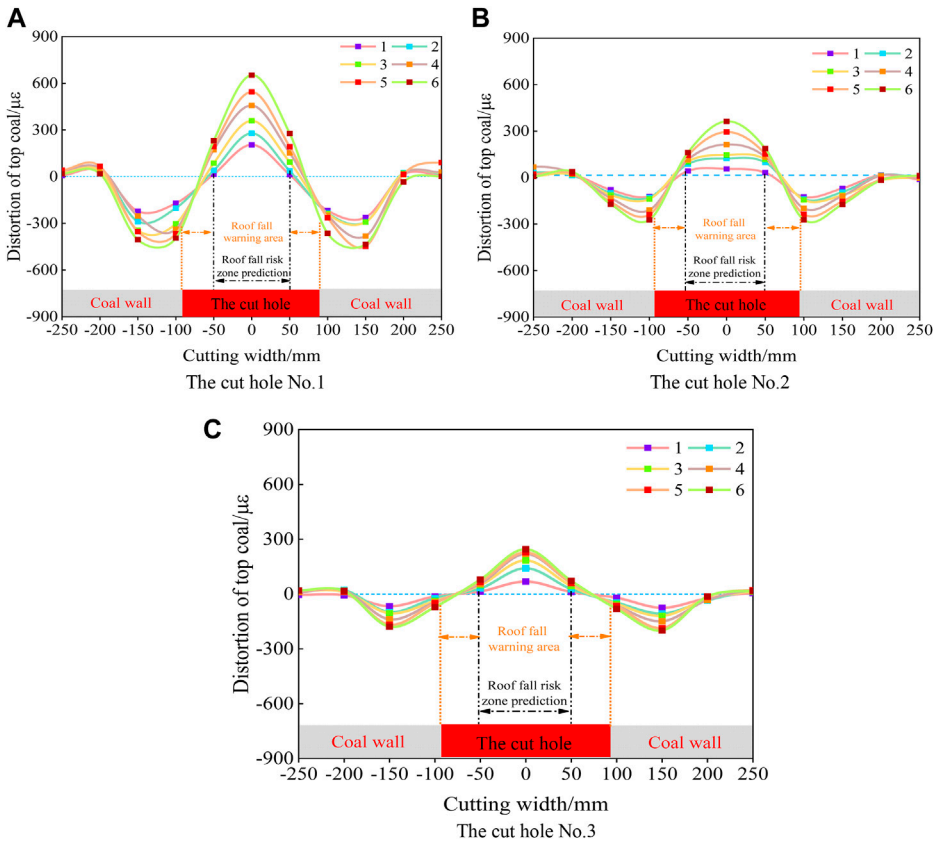

FIGURE 5
Deformation results of top coal monitored with the horizontal optical fiber. **(A)** cut hole No.1 **(B)** cut hole No.2. **(C)** cut hole No.3.

37% of the deformation in the center of the tunnel, indicating high stability. Therefore, within the range of 2.5 m between the two sides of the cut hole, the possibility of roof coal caving is small, and this area can be identified as a roof caving warning area.

3.1.2 Internal deformation rules of top coal

The deformation characteristics of the roof risk zone during the excavation process of cut holes No.1, No.2, and No.3 are shown in Figure 6. Comparing the optical fiber test results of cut holes No.1, No.2, and No.3, the center subsidence of the top coal of cut hole 1 in the roof collapse danger zone was significantly greater than that of setup No.2 and No.3 at each excavation stage. After the cut hole was penetrated, it reached 652 με; the center of cut hole No.2 was 363 με, and the deformation amount was approximately 56% of that of cut hole No.1; the deformation of cut hole No.3 was the smallest, and the subsidence amount of the top coal after the cut hole was penetrated was only 228 με, which was approximately 35% of that of cut hole No.1. Fitting the deformation results of the top coal center points of cut holes No.1, No.2, and No.3 found that as the cut hole is tunneled to penetration, when the top coal thickness is 3 m, the subsidence

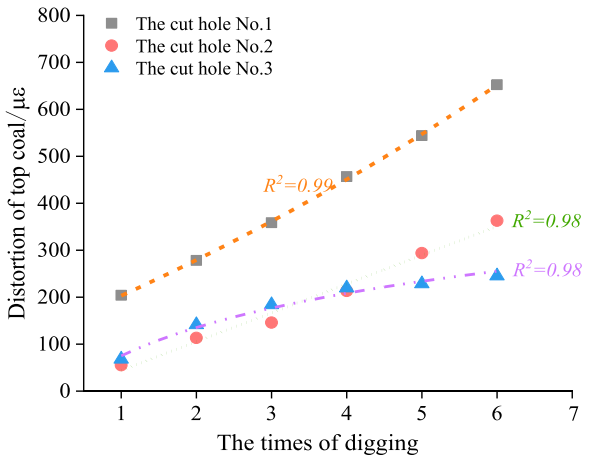

FIGURE 6
Deformation law of roof-fall hazard area.

amount of the top coal roof risk area of the cut hole increases approximately exponentially. When the thickness of the top coal is 3.5 m, the deformation amount in the risk zone of roof coal collapse increases approximately linearly. When the thickness of the top coal is 4 m, the deformation amount in the risk zone of roof coal collapse increases approximately logarithmically. These results show that when the width of the cut hole is constant and the thickness of the top coal of the cut hole in the 1^{-2} 203 working face is set to 3 m, the stability of the top coal is poor, the subsidence of the roof collapse danger zone increases exponentially, the deformation of the top coal is large, and the maintenance of the cut hole is difficult. When the thickness of the top coal is set to 3.5 m, the stability of the top coal is moderate, the subsidence in the risk area of roof collapse increases linearly, and the deformation of the top coal is between that of the 3.0 m and the 4.0 thicknesses. When the thickness of the top coal is set to 4 m, the stability of the top coal is high, and the risk area width of roof collapse is minimum. The amount of subsidence increases with an approximate logarithmic law, and within a certain period of time after the hole is cut through, the amount of deformation of the top coal changes little.

As the hole is tunneled, the deformation patterns of the roof collapse warning zones with different top coal thicknesses are shown in Figure 7. Figure 7A shows the deformation characteristics of the roof collapse warning area on the left side of the cut holes No.1, No.2, and No.3, and Figure 7B shows the deformation characteristics of the roof collapse warning area on the right side of the cut holes No.1, No.2, and No.3. As the number of excavations increases, the subsidence of the roof collapse warning area on the left and right sides of the No.1 cut eye increases approximately linearly. When the tunnel is penetrated, the deformation of the roof collapse warning area on the left side of the No.1 cut eye reaches 231 με, and the roof collapse danger area on the right side reaches 278 με. The subsidence in the roof collapse warning area on the left and right sides of cut holes No.2 and No.3 increases logarithmically, and the growth rate of the top coal subsidence gradually decreases after the third tunneling. After the penetration, the subsidence amount of the roof collapse warning area on the left side of the cut hole No.2 is 161 με, and the subsidence amount on the right side is 187 με. The subsidence amount of the roof collapse warning area on the left side of the cut hole No.3 is 79 με and that on the right side is 72 με. The roof collapse warning areas of the cut hole No.2 and No.3 are significantly smaller than that of the cut hole No.1.

In summary, when the thickness of the top coal of the cut hole is 3.0 m, the subsidence of the roof collapse warning area increases linearly with the cut hole tunneling, the stability of the top coal is poor, and the probability of roof collapse risk is relatively high within a certain period of time after the breakthrough. When the thickness of the top coal is 3.5 m and 4.0 m, the subsidence amount in the roof collapse warning area increases logarithmically as the hole is tunneled. During the fourth to sixth tunneling process, the growth rate of the roof coal deformation in the roof collapse warning area slows down significantly; the top coal has better stability.

Comparative analysis of Figures 5 and 6 shows that under different top coal thicknesses, during the tunneling process, the deformation of the top coal roof collapse danger zone in the span direction of the borehole is significantly greater than the roof

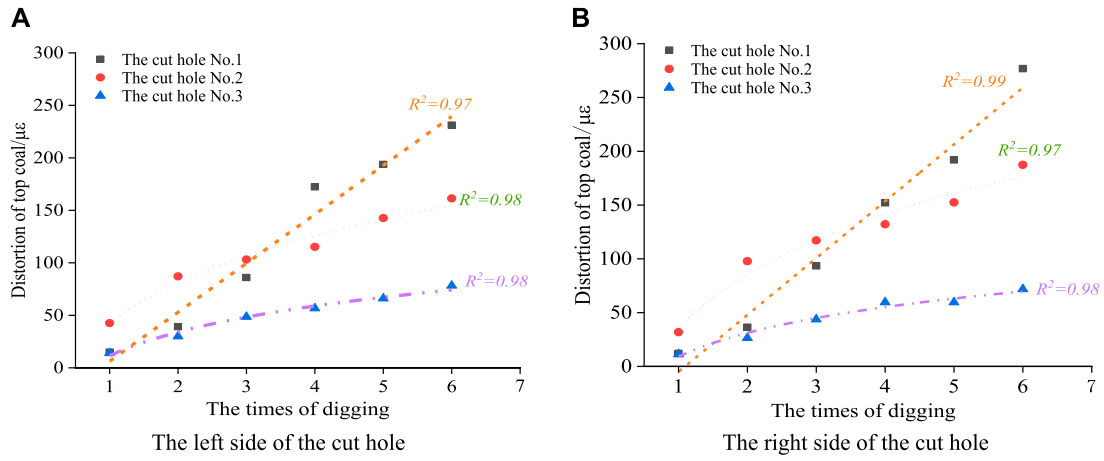

FIGURE 7
Deformation law of roof-fall warning area. **(A)** Left side of the cut hole. **(B)** Right side of the cut hole.

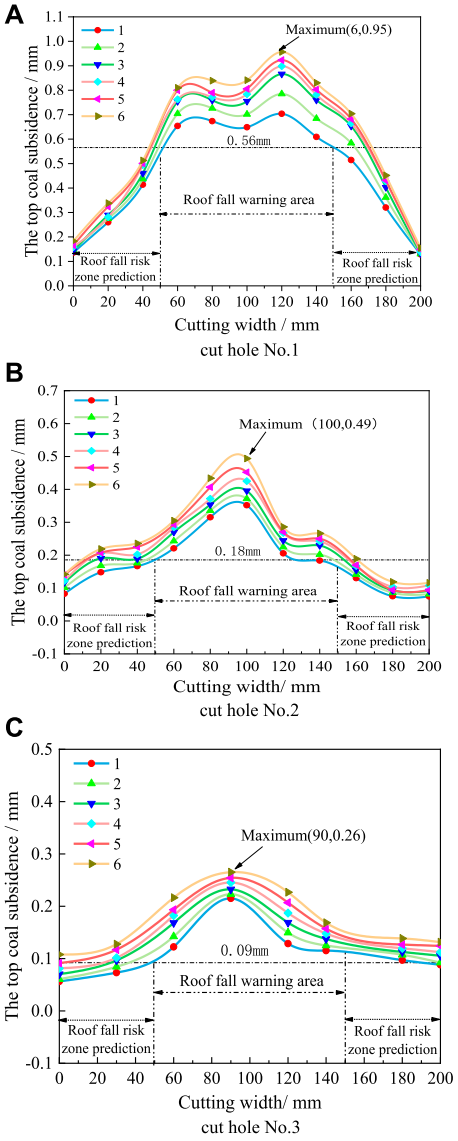

FIGURE 8
DIC monitoring data of cut hole roof subsidence. **(A)** cut hole No.1, **(B)** cut hole No.2, and **(C)** cut hole No.3.

collapse warning areas on both sides. When the thickness of the top coal is 3.0 m, the deformation pattern of the top coal changes from exponential deformation to linear deformation from the top coal roof risk area to the roof collapse warning areas on both sides. The stability of the top coal is poor, and the risk of roof collapse is high. When the thickness of the top coal is 3.5 m, the deformation pattern of the top coal changes from linear deformation to logarithmic deformation from the roof collapse danger zone in the center of the top coal to the roof collapse warning areas on both sides. The top coal shows a certain self-stabilization ability and good stability. When the thickness of the top coal is 4.0 m, the subsidence law of the top coal is logarithmic within the width of the cut hole for both the roof collapse danger area and the roof collapse warning area. The top coal shows good self-stabilization ability, and the top coal is more stable.

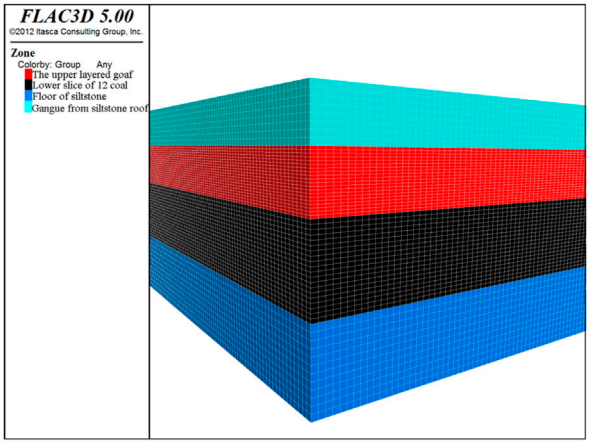

FIGURE 9
Design scheme of the local model.

3.1.3 Analysis of surface deformation of surrounding rock of cut hole

The vertical displacement of the top coal measured using the DIC testing system at the 10 mm horizontal layer above the roof during the tunneling process of each cut was extracted, as shown in Figure 8. The top coal deformation measured using DIC in cut holes No.1, No.2, and No.3 is similar to the distributed optical fiber monitoring results. During the tunneling process, the deformation of the center of the top coal is significantly greater than that of the two sides, showing obvious zoning characteristics. It can still be divided into a roof collapse danger area and a roof collapse warning area. Among them, 45–145 mm is a roof collapse danger area, and the remaining areas are roof collapse warning areas. When the top coal thickness is 3.0 m, after the hole is cut through, the maximum subsidence of the roof collapse danger zone is 0.95 mm. When the top coal thickness is 3.5 m, the maximum subsidence is 0.49 mm. When the top coal thickness is 4.0 m, the maximum subsidence amount is only 0.26 mm. As the top coal thickness increases, the maximum subsidence amount in the roof collapse danger zone gradually decreases. When the top coal thickness is 3.5 m and 4.0 m, the subsidence amount is 52% and 27% of the subsidence at 3 m, respectively. Thicker coal yields higher stability.

The thickness of the top coal increases from 3.0 m to 4.0 m, and the maximum subsidence amounts in the roof collapse warning areas are 0.56 mm, 0.18 mm, and 0.09 mm, respectively. When the top coal thickness is 3.5 m and 4.0 m, the deformation is only 32% and 16% of that found with a 3.0 m thickness, and the subsidence amount is small. As the hole is cut, the subsidence of the top coal changes little. It shows that when the top coal thickness is greater than 3.5 m, the stability is better.

4 Numerical simulation analysis of reasonable thickness of top coal of cut hole

In order to study the deformation of the surrounding rock in the large-section cut hole under the goaf and verify the reliability of the cut hole support scheme, a local model of the cut hole was

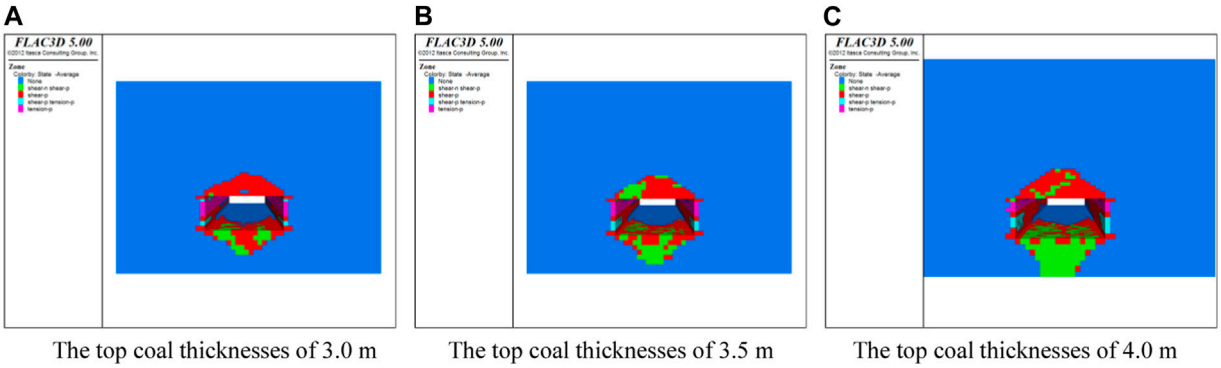

FIGURE 10
Roof caving of cut hole with different top coal thicknesses. **(A)** Top coal thickness of 3.0 m, **(B)** top coal thickness of 3.5 m, and **(C)** top coal thickness of 4.0 m.

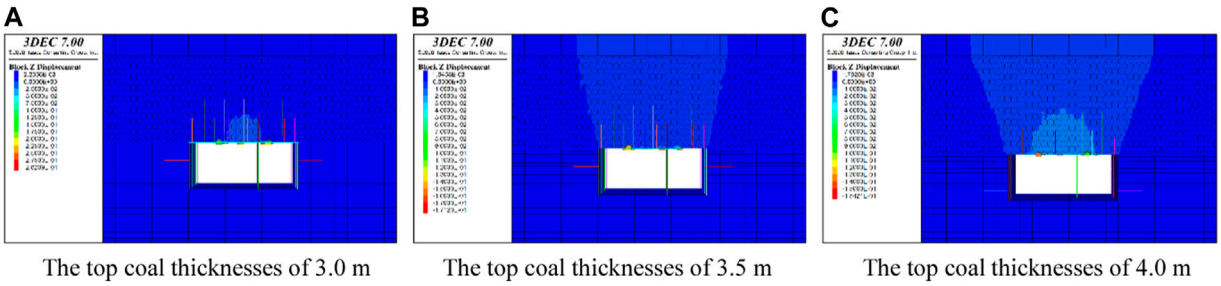

FIGURE 11
Roof subsidence of cut hole with different top coal thicknesses under a support condition. **(A)** Top coal thickness of 3.0 m, **(B)** top coal thickness of 3.5 m, and **(C)** top coal thickness of 4.0 m.

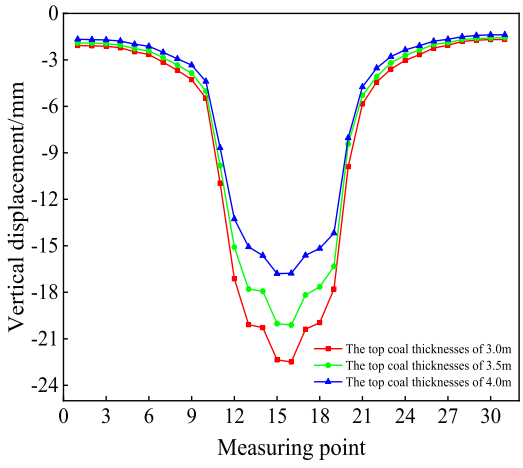

FIGURE 12
Roof subsidence of cut hole with different top coal thicknesses under a support condition.

established, and different top coal thicknesses were set up, with and without support. The established numerical calculation model is shown in Figure 9. In order to be consistent with the onsite mining conditions, the model adopts the internal excavation method; that is, the working face is inside the model, and the front and back, left and right, and upper and lower parts of the working face are solid coal and rock masses. The stability of a hole cut with top coal thicknesses of 3.0 m, 3.5 m, and 4.0 m was analyzed under various conditions. 3DEC was used to compare and analyze the roof collapse of the hole and tunnel under different top coal thicknesses, and FLAC3D was used to analyze the plastic state and stress distribution characteristics of the surrounding rock mass of the excavation.

4.1 Stability analysis of surrounding rock for hole cutting without support

Figure 10 shows the plastic zone distribution characteristics of cut holes with top coal thicknesses of 3.0 m, 3.5 m, and 4.0 m without support. The plastic zone of the rock surrounding the cut hole is symmetrically distributed. The coal walls on both the front and auxiliary sides of the cut hole with different top coal thicknesses are damaged by tension-shear mixing. There is no obvious change in the damage range. The damage range of the plastic zone of the coal wall is small. The damage depth of the left coal wall is 1 m, and the damage depth of the right coal wall is 0.9 m. The failure mode of the roof rock layer above the cut hole is mainly tensile failure. When the top coal thickness is 4 m, the plastic zone directly above the center of

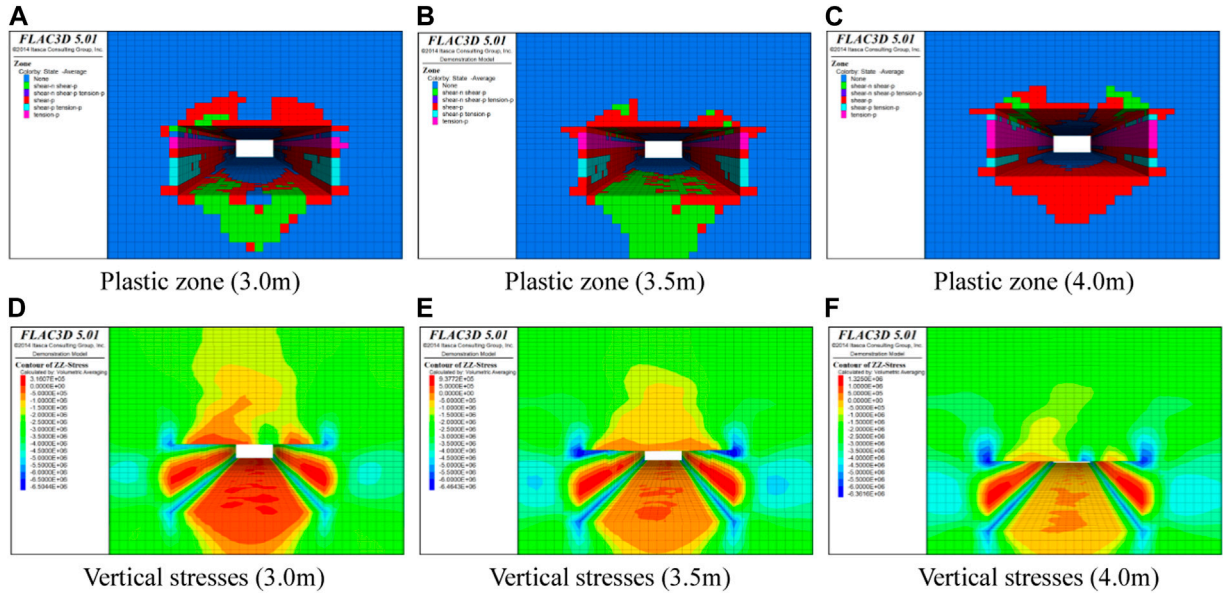

FIGURE 13
Plastic zone and stress field distribution of cut hole with different top coal thicknesses under support conditions. **(A)** Plastic zone (3.0 m), **(B)** plastic zone (3.5 m), **(C)** plastic zone (4.0 m), **(D)** vertical stresses (3.0 m), **(E)** vertical stresses (3.5 m), and **(F)** vertical stresses (4.0 m).

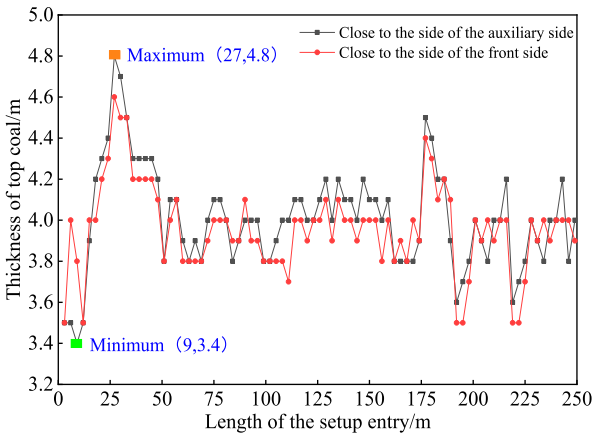

FIGURE 14
Top coal thickness distribution.

the cut hole reaches 2.9 m. When the top coal thickness is 3.5 m, the plastic zone is 2.5 m. When the thickness is 3 m, the plastic zone is 2.65 m. A "Λ" shaped shear failure area is formed with the cut hole as the center.

4.2 Stability analysis of rock surrounding cut hole under supporting conditions

Figure 11 shows the vertical displacement cloud diagrams of top coal thicknesses of 3.0 m, 3.5 m, and 4.0 m after support. No large-scale roof collapse was found after support was added, and some blocks were broken. When the top coal thickness is 3.0 m, 3.5 m, and 4.0 m, the maximum subsidence values of the roof are 282 mm, 171 mm, and 154 mm, respectively. Because some blocks have a large breakage subsidence value and the roof subsidence is not obvious at other locations, measuring lines were arranged at two height positions of the roof (0 m and 0.2 m), and the roof subsidence curve was drawn as shown in Figure 12.

It can be seen from Figure 10 that the subsidence values of the two height positions of the cut-out roof are small. When the top coal thickness is 3.0 m, 3.5 m, and 4.0 m, the maximum subsidence values of the roof are 23 mm, 20 mm, and 17 mm, respectively, and the support effect is obvious.

Figure 12 show the distribution of plastic zones with top coal thicknesses of 3.0 m, 3.5 m, and 4.0 m after support. The rock formation failure mode in the roof of the cut hole is mainly shear failure. Different top coal thicknesses also have certain damage range differences. When the top coal thickness is 3.0 m, the range of the plastic zone directly above the center of the cut hole reaches 2.58 m. The plastic zone changes less than that without support. The plastic zone is 1.95 m at 3.5 m and 1.31 m at 4.0 m. The range of the plastic zone for top coal thicknesses of 3.5 m and 4.0 m is significantly reduced after support. The effect is obvious.

Figures 13D, E, and 13f show the vertical stress distribution cloud diagrams of top coal thicknesses of 3.0 m, 3.5 m, and 4.0 m after support. When the top coal thickness is 3.0 m, the maximum stress value directly above the cut hole reaches 0.087 MPa; when the top coal thickness is 3.5 m, the maximum stress value is 0.69 MPa; when the top coal thickness is 4.0 m, the maximum stress value is 0.98 MPa. Compared with the no-support condition, the vertical stress cloud diagram changes from a symmetrical distribution to an asymmetrical distribution. Two pressure relief areas are formed with the middle single pillar as the boundary, a 5.4 m pressure relief area on the left and a 3.6 m pressure relief area on the right. The top and bottom plates at the central single pillar position form a certain degree of stress

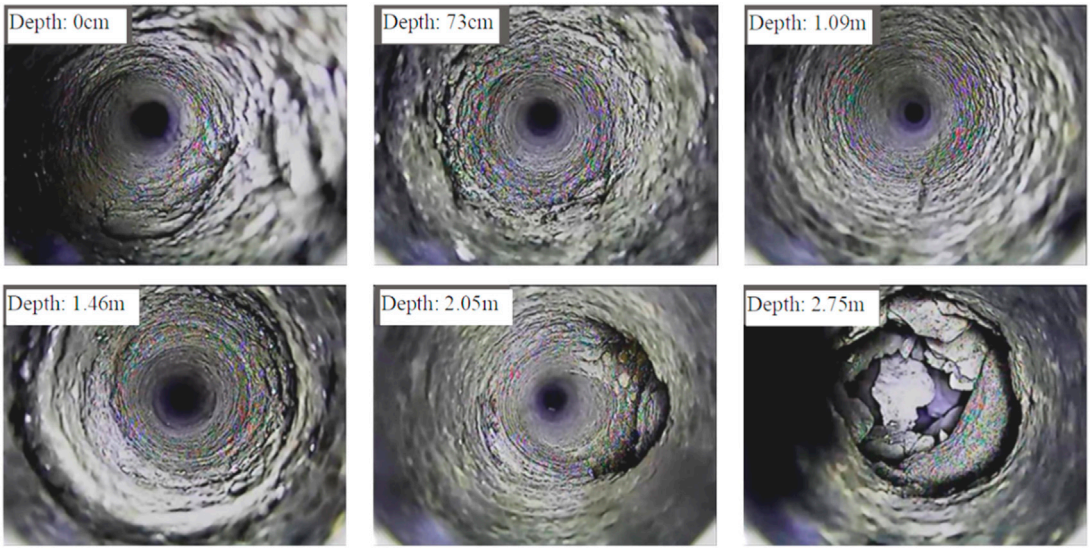

FIGURE 15
Characteristics of top coal failure of cut hole.

concentration. The degree of compressive stress concentration in the stress concentration areas of the coal walls and bottom corners on both sides is significantly reduced, and a new stress concentration area is formed on the top and bottom plates of the central single pillar. The supporting structure effectively improves the stress concentration of the surrounding rock, and the overall stress distribution of the surrounding rock is more balanced.

5 Engineering verification of reasonable thickness of top coal of cut hole

5.1 The actual thickness of the top coal left in the cut hole

According to the theoretical and experimental results, the cut hole height of the 1^{-2} 203 coal seam is 3.9 m, the thickness of the remaining top coal is 4.0 m. After the cut hole is penetrated, top coal thickness detection boreholes are arranged along the top coal of the cut hole. The thickness of the top coal of the cut hole is shown in Figure 14. The top coal thickness is between 3.4 m and 4.8 m, mainly concentrated in 3.7–3.9 m and 3.9–4.1 m within these two intervals, and the top coal is relatively thick on the side near the main gang. The design height of the cutting hole is 3.9 m, and the average thickness of the top coal is 4.0 m.

5.2 Structure and failure characteristics of top coal with cut hole

The internal failure characteristics of top coal at different depths are monitored by a borehole peeper, as shown in Figure 15. The total length of the peephole is 2.80 m, and cracks develop in the coal and rock mass near the cut hole area. Some cracks appear in the coal and rock mass at 0.73 m; long longitudinal cracks appear in the coal and rock mass at 1.09 m, and circumferential cracks in the coal and rock mass develop at 1.46 m. The coal mass is relatively broken; at 2.05 m, the coal and rock mass cracks develop and appear to be falling off; at 2.75 m, the crack reaches the goaf area of the overlying rock layer, and accumulated gangue can be observed. Among them, the surrounding coal rock mass shedding area at 2.05 m may be affected by the mining disturbance of the upper coal seam. After drilling 2.05 m, the integrity of the top coal is better, and the cracks are concentrated between 1.0 and 2.0 m. The integrity of the top plate can be determined by drilling and observing the results.

Affected by the cut hole excavation, the opening sections of the boreholes at the three measuring stations are relatively broken. Among the three boreholes, the integrity of the No.1 borehole is worse. This is mainly due to the thin thickness of the top coal at the eye-cutting and is within the scope of the double damage caused by layered mining.

Observing the surface displacement of the surrounding rock of the cut hole and the stress changes of the support body and roof coal structure shows that the maximum displacement of the roof and bottom plates is 12 mm, the maximum displacement of the two pillars is 6 mm, the maximum displacement of the deep part is 6 mm, and the support force of the pillars exceeds 15 MPa. The maximum displacement accounts for a small proportion, and the stress on the pillars is small. The maximum strain of the shed beam is −416 με, and no major deformation occurs. The maximum change in the axial force of the anchor cable is 20.625 kN. A peek at the drill hole shows that a small part of the drill hole in the roof plate is cut. There is fragmentation in the area, but the top coal structure in the remaining areas is relatively complete, and no collapse has occurred. The thickness of the top coal in the drilling hole is between 3.4 m and 4.8 m, mainly concentrated in the range of 3.7 m and 4.1 m, and the top coal is relatively thick on the side near the side of workface plant. The average thickness of the top coal is 4.0 m. Combined with the stability of the eye-cutting site, it shows that the top coal thickness is 3.5–4.0 m, which is reasonable and can meet production requirements after the required support has been added.

6 Conclusion

(1) The scope of the plastic zone of the top coal of the large cross-section under the goaf in layered mining consists of the plastic zone of the floor caused by the mining of the upper layer and the plastic zone of the top coal caused by the tunneling. According to elastic–plastic theory calculations, the depth of destruction of the upper layer mining floor is 2.02 m, the plastic range under the influence of tunneling is 1.43 m, the plastic zone of the top coal is 3.45 m, and the thickness of the top coal of the tunnel is greater than 3.45 m, which is conducive to maintaining the stability of the tunnel.

(2) The deformation of large cross-section roof coal can be divided into a roof collapse danger area and a roof collapse warning area. When the top coal thickness is 3.0, 3.5, and 4.0 m, the roof collapse danger zone decreases exponentially, linearly, and logarithmically, respectively. When the top coal thickness is 3.5–4.0 m, the sinking trend is slower, and the top coal support has higher stability. The roof collapse warning area decreases linearly and logarithmically, respectively. When the top coal thickness is 3.5–4.0 m, it has better self-stabilizing ability and higher stability.

(3) Under the condition of no support, when the thickness of the top coal of the cut hole is 3.5–4.0 m, the plastic zone range is significantly smaller than that of the top coal of 3.0 m; under the condition of support, the range of the plastic zone of the top coal is significantly smaller, and the stability is better. On-site monitoring shows that the thickness of the top coal is between 3.4 and 4.8 m, with an average remaining thickness of 4.0 m. The drill hole peek results and the shed beam deformation results show that the thickness of the top coal is 3.5–4.0 m, which is more reasonable.

Data availability statement

The datasets presented in this study can be found in online repositories. The names of the repository/repositories and accession number(s) can be found in the article/Supplementary Material.

Author contributions

GS: data curation, formal analysis, funding acquisition, investigation, methodology, project administration, resources, writing–original draft, and writing–review and editing. DW: data curation, formal analysis, resources, software, writing–original draft, and writing–review and editing. LY: formal analysis, investigation, methodology, project administration, software, and writing–original draft. CJ: conceptualization, formal analysis, investigation, methodology, project administration, writing–original draft, and writing–review and editing. GD: data curation, investigation, project administration, resources, supervision, writing–original draft, and writing–review and editing. MC: formal analysis, investigation, validation, writing–original draft, and writing–review and editing. CJ: data curation, resources, validation, and writing–original draft.

Funding

The author(s) declare that financial support was received for the research, authorship, and/or publication of this article. This study was supported by the Key Program of the National Natural Science Foundation of China (No. 41027002).

Acknowledgments

We thank the National Natural Science Foundation of China. We thank the academic editors and reviewers for their kind suggestions and valuable comments.

Conflict of interest

Authors GS, CJ, GD, and CJ were employed by Shenhua Shendong Coal Group Corporation Limited, China Energy Group.

The remaining authors declare that the research was conducted in the absence of any commercial or financial relationships that could be construed as a potential conflict of interest.

Publisher's note

References

Cao, D. (2015). Roadway supporting technology practice under extremely contiguous seams goaf in Yungang Mine. *Coal Sci. Technol.* 43 (S1), 73–75.

Chai, J., Han, Z., and Qiao, Yu (2022b). Top coal stability of long-span opening under goaf in layered mining. *J. Min. Saf. Eng.* 39 (02), 282–291. doi:10.13545/j.cnki.jmse.2021.0315

Chai, J., Liu, Y., and Wang, Z. (2022a). Pressure relief effect of protective layer mining and its optical fiber monitoring. *J. China Coal Soc.* 47 (8), 2896–2906. doi:10.13225/j.cnki.jccs.2022.0448

Chai, J., Qiao, Yu, and Gao, S. (2022c). Roof stability evaluation of large section cut hole in lower slice of slicing mining. *J. Mine Automation* 48 (5), 21–31. doi:10.13272/j.issn.1671-251x.2021110029

Chai, Z., Kang, T., and Li, Y. (2008). Anchoring effect of extre mely thick coal seam large section roadway for cable bolts supporting. *J. China Coal Soc.* 33 (7), 732–737.

Dong, Yu, Xie, W., and Jing, S. (2013). High strength stable type support technology of mining gateway under goaf in contiguous seams. *Coal Sci. Technol.* 41 (2), 19–23. doi:10.13199/j.cst.2013.02.25.dongy.007

Gao, J., and Zhang, Z. (2014). Study on support technology of gateway in contiguous seams under mining goaf in Pingshuo mining area. *Coal Sci. Technol.* 42 (5), 1–4. doi:10.13199/j.cnki.cst.2014.05.001

Gao, S., Chen, S., and Chai, J. (2021). Study on optimization of supporting technology for large cross section open-off cut under contigous gob. *Coal Sci. Technol.* 49 (12), 20–28. doi:10.13199/j.cnki.cst.2021.12.003

Gong, P., Zhao, T., and YetilmezsoyYi, K. K. (2019). Mechanical modeling of roof fracture instability mechanism and its control in top-coal caving mining under thin topsoil of shallow coal seam. *Adv. Civ. Eng.* 2019, 1–10. doi:10.1155/2019/1986050

He, Y. P., Huang, Q. X., Wei, Y. H., and Du, J. (2023). Research on roof load transfer by passing coal pillar of working face in shallow buried closely multiple-seam. *Minerals* 13 (1), 118. doi:10.3390/min13010118

He, F., Xu, L., and Wu, H. (2014). Fracture field evolution and stability analysis of surrounding rock in thick coal roof large-section cut hole. *J. China Coal Soc.* 39 (02), 336–346. doi:10.13225/j.cnki.jccs.2013.0307

He, Y., and Huang, Q. (2022). Research on roof structure and determination of working resistance of shallow buried Single key stratum based on grid-drillhole field method. *Lithosphere* S4, 4328618. doi:10.2113/2022/4328618

Jiang, L., Jiao, H., Wang, Y., and Wang, G. g. (2021). Comprehensive safety factor of roof in goaf underdeep high stress. *J. Central South Univ. Springer* 28 (2), 595–603. doi:10.1007/s11771-021-4624-y

Jiang, Y., Yang, Y., and Ma, Z. (2016). Breakage mechnism of roof strata above widespread mined-out area with roadway mining method and feasibility analysis of upward mining. *J. China Coal Soc.* 41 (04), 801–807. doi:10.13225/j.cnki.jccs.2015.0775

Liu, S., Bai, J., Wang, X., Wu, B., Wang, G., Li, Y., et al. (2021). Study on dynamic evolution of roof crack and support timing of secondary tunneling for large section Open-off cut in deep mines. *Adv. Civ. Eng.* 2021, 1–16. doi:10.1155/2021/9918470

Liu, J., Shen, B., and Jiang, P. (2013). Technical countermeasures of improving China coal production capacity. *Coal Sci. Technol.* 41 (1), 21–24. doi:10.13199/j.cst.2013.01.24.liujzh.006

Niu, S., Yang, S., and Yi, L. I. (2014). Shear instability mechanism and support methods of laminated roof and floor strata in roadway. *J. China Coal Soc.* 39 (S2), 325–331. doi:10.13225/j.cnki.jccs.2013.1404

Qi, S. (2018). *Study on the stress field distribution & sup-porting technology for miing roadway under goaf in 1 M close distance coal seams mining*. Taiyuan: Tai-yuan University of Technology.

Schenato, L., Palmieri, L., Camporese, M., Bersan, S., Cola, S., Pasuto, A., et al. (2017). Distributed optical fibre sensing for early detection of shallow landslides triggering. *Rep* 7 (1), 14686–14687. doi:10.1038/s41598-017-12610-1

Tulu, I. B., Esterhuizen, G. S., Klemetti, T., Murphy, M. M., Sumner, J., and Sloan, M. (2016). A case study of multi-seam coal mine entry stability analysis with strength reduction method. *Int. J. Min. Sci. Technol.* 26 (2), 193–198. doi:10.1016/j.ijmst.2015.12.003

Wang, Z., Fang, L. O. U., and Jin, S. (2020). Roadway position and surrounding rock control technology under mining goaf in extremely close coal seam. *Coal Eng.* 52 (02), 1–4.

Xia, K., Chen, C., Liu, X., Yuan, J., and Dang, S. (2023). Assessing the stability of high-level pillars in deeply-buried metal mines stabilized using cemented backfill. *Int. J. Rock Mech. Min. Sci.* 170, 105489. doi:10.1016/j.ijrmms.2023.105489

Xia, K., Chen, C., Wang, T., Zheng, Y., and Wang, Y. (2022). Estimating the geological strength index and disturbance factor in the Hoek-Brown criterion using the acoustic wave velocity in the rock mass. *Eng. Geol.* 306, 106745. doi:10.1016/j.enggeo.2022.106745

Xiao, T., Bai, J., Xu, L., and Xuebin, Z. (2011). Characteristics of stress distribution in floor strata and control of roadway stability under coal pillars. *Min. Sci. Technol. (China)* 21 (2), 243–247. doi:10.1016/j.mstc.2011.02.016

Xie, S., Zhang, Q., Chen, D., Wang, E., Zeng, J., Ji, C., et al. (2020). Research of roof anchorage rock beam bearing structure model of Extra-Large width Open-off cut and its engineering application in a coal mine, China. *Adv. Civ. Eng.* 2020, 1–19. doi:10.1155/2020/3093294

Xinjie, L., Xiaomeng, L., and Weidong, P. (2016). Analysis on the floor stress distribution and roadway position in the close distance coal seams. *Arabian J. Geosciences* 9 (2), 83. doi:10.1007/s12517-015-2035-9

Yan, H., Weng, M., Feng, R., and Li, W. K. (2015). Layout and support design of a coal roadway in ultra-close multiple-seams. *J. Central South Univ.* 22 (11), 4385–4395. doi:10.1007/s11771-015-2987-7

Yang, H., Han, C., Zhang, N., Sun, C., Pan, D., and Dong, M. (2019). Stability control of a Goaf-side roadway under the mining disturbance of an adjacent coal working face in an under-ground mine. *Sustainability* 11 (22), 6398. doi:10.3390/su11226398

Yao, B. (2014). *Failure mechanism and control technology of surrounding rock of Roadway under Goaf*. Beijing: China University of mining and Technology.

Zhang, Y., Xie, K., and He, F. (2004). Study on surrounding rock stability of working face supported by bolt-mesh-anchor in soft and thick coal seam. *Chin. J. Rock Mechnics Eng.* (19), 3298–3304. doi:10.3390/en13020305

Zhao, X. (2018). Study on excavation technology of large section cut hole under overlying mining goaf in close distance seams. *Coal Technol.* 37 (12), 77–80.

frontiers | Frontiers in Earth Science

TYPE Original Research
PUBLISHED 28 December 2023
DOI 10.3389/feart.2023.1287151

OPEN ACCESS

EDITED BY
Xuelong Li,
Shandong University of Science and Technology, China

REVIEWED BY
Jinbo Miao,
Hebei University of Engineering, China
Zhenbo Zhang,
Shijiazhuang Tiedao University, China
Zhitian Xie,
Beijing Municipal Engineering Research Institute, China
Xiaopu Cui,
Beijing University of Technology Beijing, China, in collaboration with reviewer ZX

*CORRESPONDENCE
Fengnian Wang,
wangfn_bj@163.com

RECEIVED 01 September 2023
ACCEPTED 19 October 2023
PUBLISHED 28 December 2023

CITATION
Qiang S, Zhao L, Wang X, Li X and Wang F (2023), Analysis of face stability for shallow shield tunnels in sand. *Front. Earth Sci.* 11:1287151. doi: 10.3389/feart.2023.1287151

Analysis of face stability for shallow shield tunnels in sand

Sihan Qiang[1], Lizhi Zhao[1], Xuehai Wang[1], Xiaoming Li[1] and Fengnian Wang[2,3]*

[1]5TH Engineering LTD. of the First Highway Engineering Bureau CCCC, Beijing, China, [2]Shanxi Transportation Technology Research and Development Co., Ltd., Taiyuan, China, [3]School of Earth Sciences and Engineering, Hohai University, Nanjing, China

The stability of the tunnel face is the key problem in shield tunnel construction. This paper focuses on the face stability of a shallow tunnel in sand. Numerical simulation and theoretical analysis are combined to study the limit support pressure and failure zone. Firstly, numerical simulation is employed to study the collapse of the tunnel face, obtaining the limit support pressure and collapse zone. A new failure model suitable for shallow tunnels is constructed based on these numerical simulations. Then, an analytic solution for the limit support pressure is derived using limit analysis upper bound theory. The accuracy and applicability of this proposed model are verified by comparing it with numerical results and classical analytical models. Through this research, it is found that the proposed model provides a more accurate description of situations where soil arches cannot be formed for shallow tunnels in sand, leading to higher accuracy in calculating the limit support pressure. The influence of various factors on stability of the tunnel face is analyzed, revealing mechanisms of tunnel face collapse.

KEYWORDS

shallow tunnel, sand stratum, tunnel face stability, limit analysis method, sand

1 Introduction

Recently, tunnels have been constructed mainly using the shield method. During shield construction, tunnel face is usually stabilized by controlling the pressure in soil or slurry chamber. The stability of the tunnel face is typically ensured by controlling the pressure in the soil chamber or slurry chamber during shield tunneling (Chen et al., 2018; Wang et al., 2021a). Insufficient support pressure can easily lead to collapse of the excavation face, resulting in significant economic losses. Therefore, determining the values of soil chamber pressure and slurry chamber pressure is crucial for the control of shield tunneling (Liao et al., 2009). Currently, many researchers have employed a combination of model test, numerical simulations, and theoretical analysis to study the limit support pressure (σ_T) of collapse, the minimum support pressure to maintain stability of excavation face.

Researchers have conducted various physical experiments to study σ_T and the failure zone shapes (Kirsch, 2010; Messerli et al., 2010; Chen et al., 2013; Wang et al., 2021b). Some researchers have also conducted centrifuge model tests to study collapse mechanism of tunnel face, yielding significant research outcomes (Atkinson et al., 1977; Chambon and Corte, 1994; Meguid et al., 2008; Idinger et al., 2011; Li et al., 2023). Physical model tests not only provide validation for numerical simulation results but also establish a solid foundation for theoretical models. Numerical simulation, due to their advantages of low cost, high efficiency, and repeatability, are often used as a complement to model experiments and are widely applied in tunnel engineering. Currently, the main numerical models used are the continuum models (Senent et al., 2013; Li et al., 2019; Li et al., 2020; Liu H. et al., 2023) and the discrete element models. The

10.3389/feart.2023.1287151

TABLE 1 Calculation parameters.

Cases	Tunnel diameter D (m)	Cover ratio C/D	Unit weight γ (kN/m^3)	Elastic modulus E (MPa)	Poisson ratio ν	Friction angle φ(°)	Cohesion c(kPa)
1~4	6	0.5	18	20	0.35	25,30,35,40	0
5~8		0.75				25,30,35,40	
9~12		1.0				25,30,35,40	
12~16		1.25				25,30,35,40	

discrete element method has also been extensively employed to investigate tunnel face instability (Funatsu et al., 2008; Chen et al., 2011; Zhang et al., 2011; Liu and Li, 2023), since its capability to handle mechanics problems involving discontinuous materials. Scholars have made significant achievements in various aspects, including the calculation of σ_T and definition of collapse zone.

Theoretical analysis is an essential approach to obtain the σ_T of excavation face, and scholars have been devoted themselves to proposing theoretical solutions for calculating the σ_T. Currently, there are two main methods. The limit equilibrium method assumes a failure mode and solves the σ_T based on the equilibrium conditions of forces. Scholars have proposed different failure models and obtained σ_T for different soil layers (Horn, 1961; Murayama et al., 1966; Anagnostou and Kovári, 1994; Arthur et al., 1994; Yu et al., 2020; Zhang et al., 2020; Liu S. et al., 2023; Zhang et al., 2023). The limit analysis method mainly acquire the limit support pressure from an energy perspective. (Leca and Dormieux, 1990) proposed failure mechanisms consisting of a single truncated cone or double truncated cones and derived the theoretical solutions of σ_T based on the limit analysis upper bound theory. Based on the model proposed by (Leca and Dormieux, 1990; Soubra et al., 2008) proposed a 3D failure model with multiple truncated cones and found that increasing the number of truncated cones beyond five had little effect on computational accuracy. This failure model has been widely cited by scholars. (Mollon et al., 2011b) using a logarithmic spiral model and spatial discretization technique, established a new 2*D* failure model that further improved the calculation accuracy. In addition, (Mollon et al., 2011a) proposed a 3*D* horn-shaped collapse model based on a multi-block model and spatial discretization technique, which overcame non-overlap of the multi-truncated cones model at excavation face and further improves the accuracy of the model.

Based on model tests and numerical simulations, researchers have abstracted failure models of excavation face instability during shield tunneling and derived analytical solutions for the σ_T. However, there are still some unresolved issues that deserve attention. For shallow tunnels, the σ_T obtained by the limit equilibrium theory tends to be higher than the experimental values, which can easily lead to passive instability of tunnel face. On the other hand, models based on limit analysis theory can form soil arching even in case of shallow tunnels. However, in experiments, the failure zone may still extend to the ground surface for loose sand with cover ratio greater than 2.0, resulting in underestimated soil pressures (Di et al., 2022a).

In this paper, based on the numerical models, a new collapse model for shallow tunnel in sand is proposed. The analytical solutions are derived using the limit analysis method. The proposed theoretical model is compared with numerical models and existing models to validate its applicability and accuracy. Finally, using the proposed model, the influence of various factors on stability of tunnel face is analyzed, and the mechanism of collapse of tunnel face is revealed.

2 Numerical simulation

2.1 Numerical models

The finite difference software FLCA3D is used to study limit support pressure σ_T and failure zone for shallow tunnel in this section. A total of 16 cases were considered in Table 1 to investigate the effect of cover ratio C/D and friction angle φ on tunnel face stability. The soil

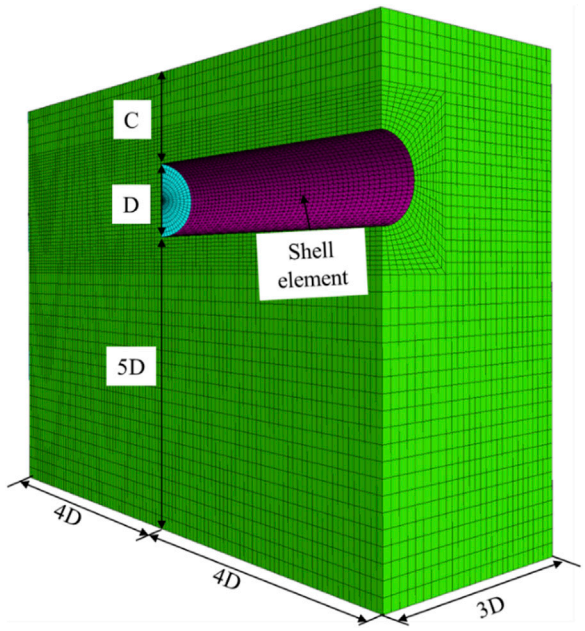

FIGURE 1
Numerical model.

parameters are as described below: Unit weight $\gamma = 18$ kN/m^3, Young's modulus $E = 20$ MPa, Poisson's ratio $\nu = 0.35$, and cohesion $c = 0$ kPa.

As shown in Figure 1, a semi-model approach was adopted, taking into account computational efficiency. The dimensions of the model are the following: width 3D, length 8D, height 6D + C, where D is tunnel diameter and C is the tunnel burial depth. The boundary conditions of the model are as follows: fixed at the bottom, constrained normal displacement at the sides, and free at the top. The soil material was modeled using solid elements, assuming it follows the Mohr-Coulomb criterion. To simulate the lining, shell elements with $E = 20$ GPa, $\nu = 0.17$ and a thickening of 0.35 m were used.

To simulate, proceed as follows:

(1) Create soils layers and initialize the soil stress.
(2) To simplify the simulation process, a one-step excavation method is used, with lining applied simultaneously.
(3) Apply a support pressure (P_T) to the tunnel face, where the value of the P_T is equal to the horizontal stress in the center of the tunnel face.
(4) Reduce the P_T and plot the curve of P_T versus horizontal displacement (Δ_h) of the center of the excavation face.
(5) When the P_T sharply increases, the corresponding support pressure is considered as the limit support pressure (σ_T) (Li et al., 2022).

2.2 Numerical results

2.2.1 Limit support pressure

In the simulation, when the support pressure sharply increases, the corresponding support pressure is considered as the limit support pressure. The double tangent method proposed by Li et al. (2019) is used to determine the limit support pressure. The specific method is as follows: make the curve of support pressure and excavation face displacement, make the tangent line of the descending section and the horizontal section respectively, and the intersection point of the two is the limit support pressure. Figures 2A–D shows the relationship between Δ_h and P_T for varying cover ratios C/D. Under varying cover ratios, the support pressure gradually decreases with increasing φ. From the results shown in Figure 2A, it can be observed that at $C/D = 0.5$ and $\varphi = 25^\circ$, the $\sigma_T = 17.85$ kPa. When the $\varphi = 30^\circ$, 35°, and 40°, the σ_T = 12.75 kPa, 9.35 kPa, and 7 kPa, respectively. Figure 2B demonstrates that for $C/D = 0.75$, and $\varphi = 25^\circ$, 30°, 35°, and 40°, the $\sigma_T = 18.85$ kPa, 13.50 kPa, 9.85 kPa, and 7.00 kPa, respectively. Similarly, from Figures 2C, D, the σ_T can be obtained for cover ratios of 1.0 and 1.25, respectively.

Figure 3 illustrates the relationship between the σ_T and the φ (in radians) for different C/D. By comparing, it can be observed that there is an exponential relationship between the σ_T and the φ. The exponential function $\sigma_T = e^{a+b\varphi+c\varphi 2}$ was used to fit the data, resulting in the following relationships: for $C/D = 0.5$, $\sigma_T = e^{4.91-5.32\varphi+1.54\varphi^2}$, R^2=0.995; for C/D = 0.75, $\sigma_T = e^{4.50-3.47\varphi-0.25\varphi 2}$, $R^2 = 0.992$; for $C/D = 1.0$, $\sigma_T = e^{4.11-1.74\varphi-1.94\varphi 2}$, R^2 = 0.987; for $C/D = 1.25$, $\sigma_T = e^{3.88-0.561\varphi+3.15\varphi 2}$, R^2=0.981.

The fitting results show that the coefficients a, b, and c have a strong linear relationship with the cover ratio C/D, as illustrated in Figure 4. The correlation between the coefficient a and the C/D can be expressed as $a = 5.57–1.39C/D$, R^2=0.978. The correlation between the coefficient b and the C/D is as follows: $b = -8.38 + 6.42C/D$, R^2=0.983. The correlation between coefficient c and C/D is as follows: $c = 4.51–6.09C/D$, R^2= 0.989. Therefore, the correlation between the σ_T and C/D and φ is as follows:

$$\sigma_T(C/D, \varphi) = e^{(5.57-1.39C/D)+(-8.38+6.42C/D)\varphi+(4.51-6.09C/D)\varphi 2} \quad (1)$$

The validity range of Formula (1) is $C/D \leq 1.25$ and friction angle $25^\circ \leq \varphi \leq 40^\circ$.

Figure 5 shows the variation of σ_T with respect to the C/D. The solid line represents the results calculated based on Formula (1), while the dashed line presents the values obtained from numerical simulations. From the graph, it is obvious that in the range of C/D≤1.25, the σ_T obtained from the numerical simulations shows an approximately linear increase with the increase of the C/D. Similarly, the σ_T calculated based on the fitted equation also shows an approximately linear increase with the cover ratio. A comparison between the two reveals that the calculated results from the Formula (1) are larger than the numerical results, and the discrepancy between them increases as the C/D increases. For instance, when φ=25° and $C/D = 0.5$, the fitted result is approximately 1.62% higher than the numerical simulation result. When $\varphi = 30^\circ$ and $C/D = 1.25$, the fitted result is approximately 4.98% higher, and at φ=30° and C/D=1.25, the difference reaches a maximum of approximately 9.2%. It is worth noting that the results from Formula (1) are relatively conservative compared to the numerical calculation results, and the difference is within an acceptable range, indicating a relatively safe approach for engineering applications.

2.2.2 Failure zone

Figure 6 illustrates the shapes of the failure zone under different cover ratios C/D for an internal friction angle of 35°. The boundary of the failure zone is defined by the abrupt change in the displacement gradient (Zhang et al., 2015). It is obvious that when the C/D≤1.0, the collapse zone extends to ground surface. The failure zone can be divided into two parts: the lower failure zone and the upper failure zone. The

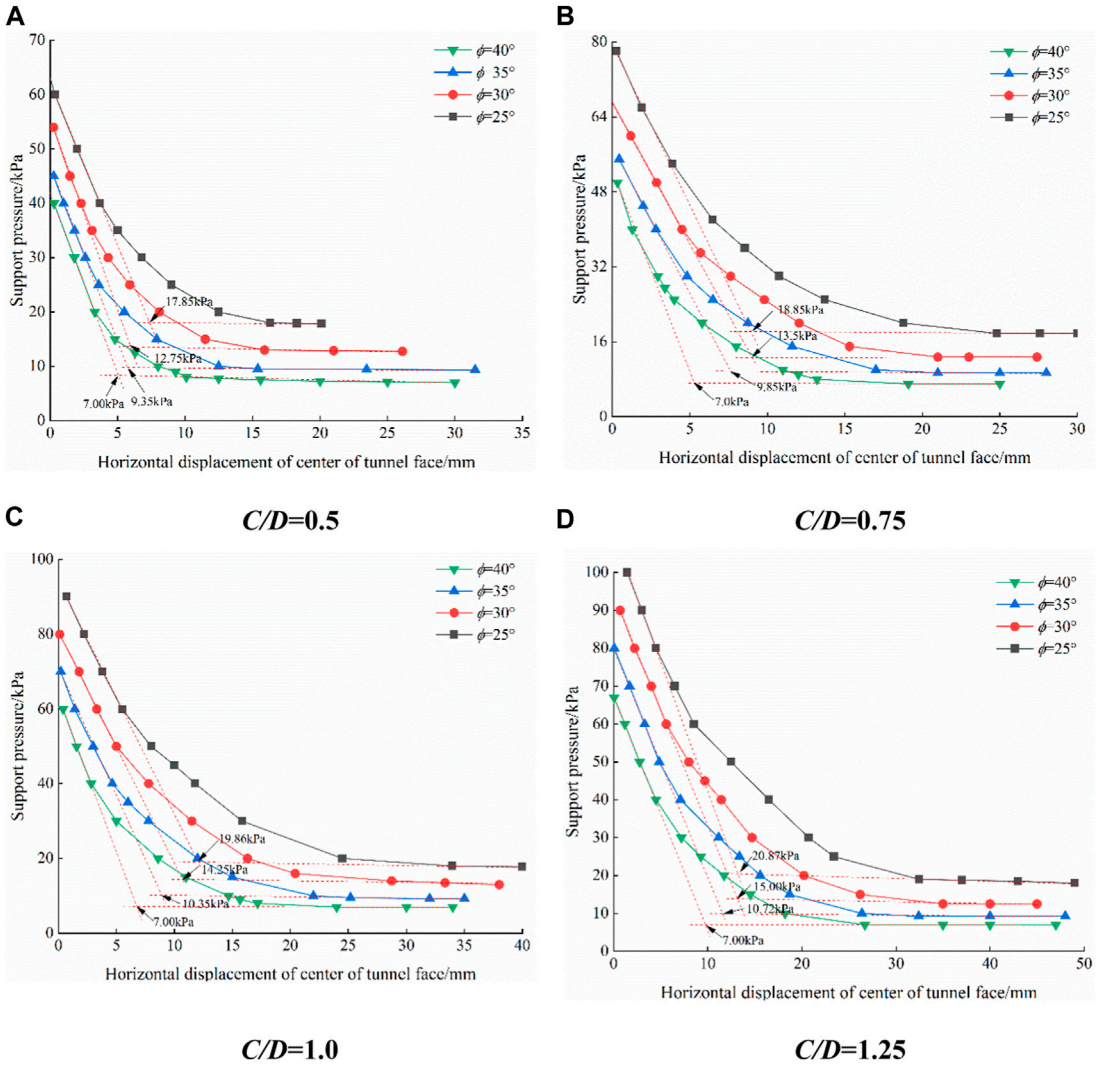

FIGURE 2
Relation curve of support pressure and horizontal displacement under different *C/D*. **(A)** C/D=0.5. **(B)** C/D=0.75. **(C)** C/D=1.0. **(D)** C/D=1.25.

lower failure zone exhibits a logarithmic curve shape, while the upper failure zone can be considered as an inverted round table shape (although the numerical simulation results are not apparent due to the stronger lining parameters near the tunnel face). The inverted round table can be further divided into a cylindrical-shaped failure core and a disturbed zone, which is consistent with the findings of (Li et al., 2018). When *C/D*>1.0, The collapse zone no longer extends to the surface; its shape consists mainly of the logarithmic curve-shaped lower failure zone and the upper soil arch zone.

3 Analytical model

3.1 Failure mechanism

Based on the numerical simulations, model tests (Di et al., 2022b), and engineering experience, a new *3D* collapse model for shallow shield tunnels has been proposed. As shown in Figure 7, tunnel diameter is D, cover depth is C, and support pressure is applied uniformly on the tunnel face. The failure zone is divided into upper and lower parts. The lower part adopts the classical five-cone model (Soubra et al., 2008): it assumes that the lower part consists of five rigid truncated cones, with each cone having a vertex angle of 2φ. The cones move along the axis of the cone and are constrained by the associated flow rules. The first truncated cone is formed by a rigid cone whose axis is at an Angle of α to the tunnel axis and a plane I which is at an angle of β_1 to the tunnel face. To ensure that the second cone completely coincides with the first cone at section I, the second cone is generated as a mirror image of the first cone and is cut by plane II, and so on for the third to fifth cones. The upper part of the collapse zone has a shape similar to an inverted round table. The core of the failure zone is in the shape of a cylinder, and the portion excluding the failure core is the disturbed zone. The boundary of the disturbed zone forms an angle θ with the horizontal direction. There is friction between the disturbed zone and the failure core, which reduces the vertical soil pressure.

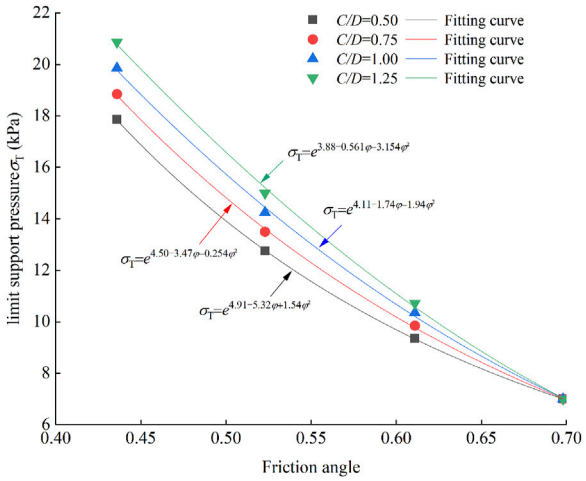

FIGURE 3
Relationship between limit support pressure and friction angle under different *C/D*.

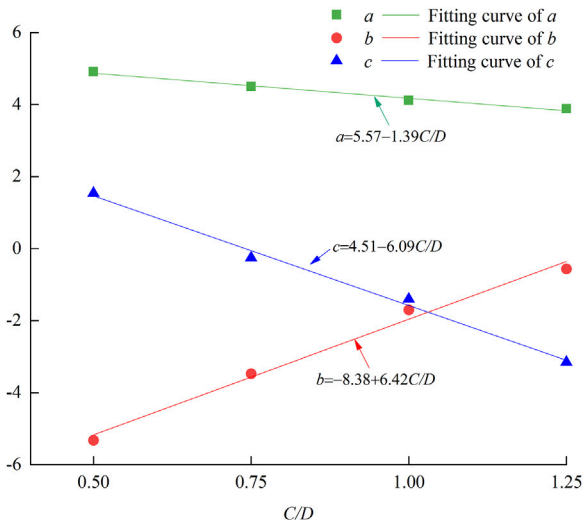

FIGURE 4
Relationship between coefficient (*a*,*b*,*c*) and *C/D*.

3.2 The vertical earth pressure σ_v

The effect of the upper collapse zone can be equivalently represented as a vertical earth pressure σ_v (Han et al., 2016). Based on geometric relationships, it is found that the intersection plane between the fifth truncated cone and the upper failure zone has an elliptical shape, with major axis a_6 and minor axis b_6. To simplify the calculation, we can approximate it as a circular shape with radius *r*, as proposed by (Li et al., 2020). The equivalent formula is given below:

$$r = \sqrt{a_6 b_6} \tag{2}$$

As shown in Figure 8, the upper failure zone is considered as an inverted round table, where the failure core is a cylindrical shape with a radius of *r*, and the remaining part is the disturbed zone. During the occurrence of failure, the disturbed zone forms an angle θ with the horizontal plane, exhibiting a tendency to slide downward, resulting in friction along the slip surface. The core of collapse zone tends to move downward and is constrained by the disturbed zone. Here, P_s represents the surface overload, and σ'_v represents the reactive force of σ_v.

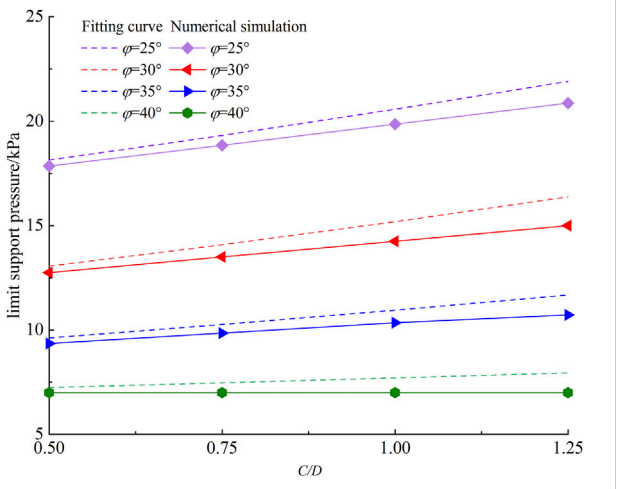

FIGURE 5
Relationship between limit support pressure and *C/D*.

To determine the magnitude of vertical soil pressure, we select any vertical plane passing through the axis of the truncated cone as the calculation diagram, such as Figure 9. The following assumptions are made: The soil follows the Mohr-Coulomb strength criterion. Coefficient of friction of the sliding surface *AD* and *BE* is tanφ. Due to soil disturbed, the friction angle between the failure core and the disturbed zone is given by η ($\eta \leq \varphi$). The ground overload P_s and the vertical soil pressure σ_s are both uniformly distributed loads.

The *ADF* section is taken as the object of force analysis, and the vertical equilibrium equation and the horizontal equilibrium equation are formulated to obtain the following equations:

$$\begin{cases} N\sin(\theta-\varphi) - T'\cos\eta - cC\cot\theta = 0 \\ W_2 + P_s C\cot\theta + T\sin\eta - N\cos(\varphi-\theta) = 0 \end{cases} \tag{3}$$

Where:

$$W_2 = \frac{\gamma C^2}{2}\cot\theta \tag{4}$$

The vertical equilibrium equation is formulated for the *ABFG* section as the object of study, yielding the following equation.

$$W_1 + P_s r - 2cC - 2T\sin\eta - \sigma_v r = 0 \tag{5}$$

Where:

$$W_1 = \frac{\gamma r C}{2} \tag{6}$$

When active failure occurs, the angle θ is given by $\theta = \pi/4 + \varphi/2$ by the Mohr-Coulomb criterion. The friction angle η can be obtained from Table 2 (Li et al., 2018). For sandy soil classified as VI rock mass, its range of values is between 0.3φ and 0.5φ.

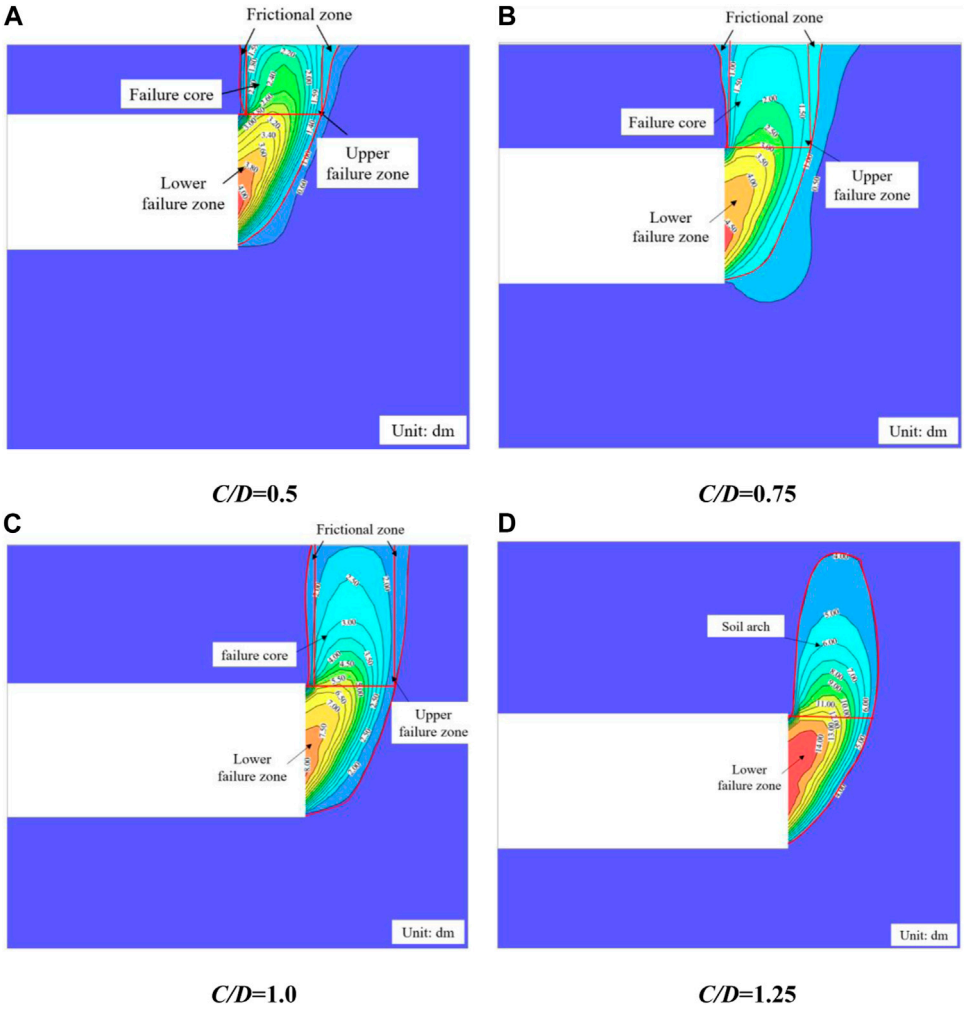

FIGURE 6
Failure zone under different *C/D* (φ = 35°unit:dm). **(A)** C/D=0.5. **(B)** C/D = 0.75. **(C)** C/D = 1.0. **(D)** C/D = 1.25.

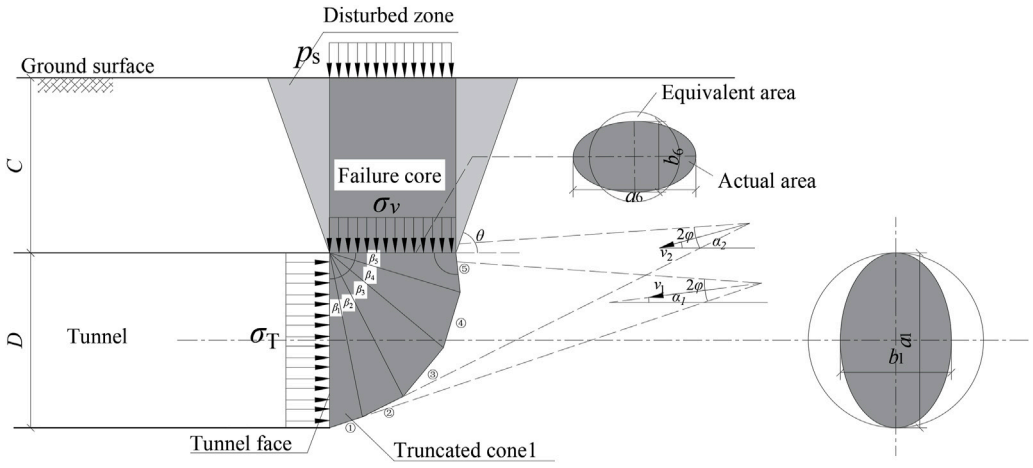

FIGURE 7
Proposed failure mechanism.

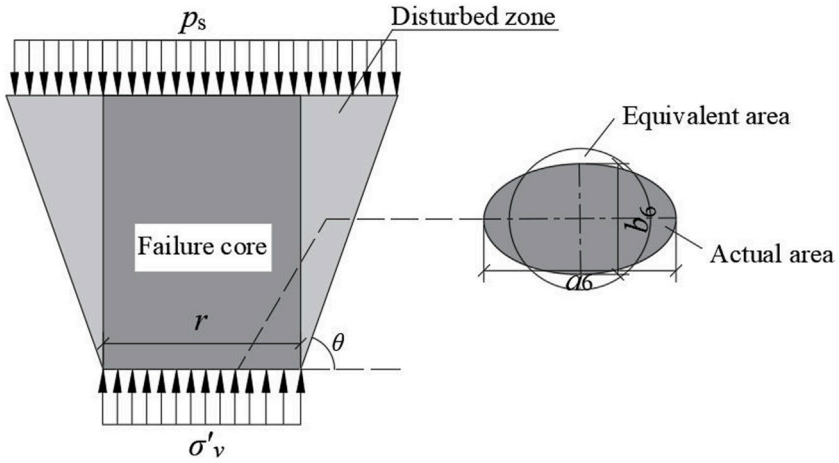

FIGURE 8
Upper failure mechanism.

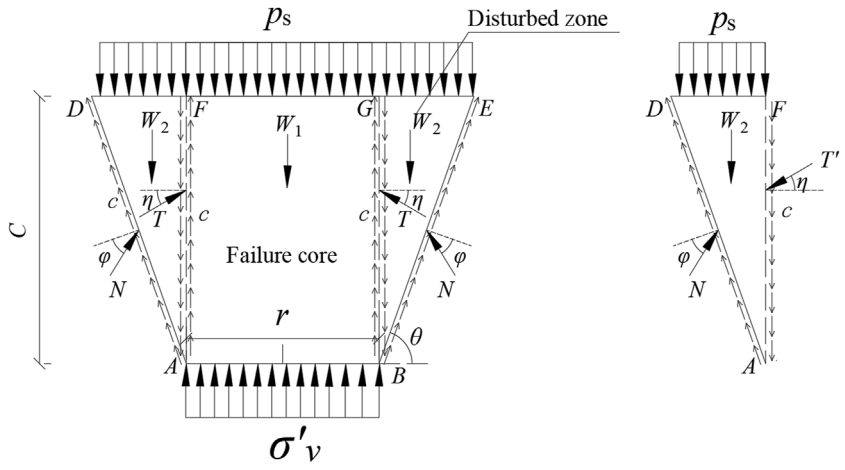

FIGURE 9
Calculation diagram of upper failure zone.

TABLE 2 η **value of all grades of surrounding rock.**

Grades of surrounding rock	I~III	IV	V	VI
η	0.9φ	$(0.7\sim0.9)\varphi$	$(0.5\sim0.7)\varphi$	$(0.3\sim0.5)\varphi$

By simultaneously solving Eqs 3–6, the vertical soil pressure σ_v can be obtained.

3.3 Limit support pressure

3.3.1 Limit analysis method

The limit analysis method derives the limit load from an energy perspective. An upper bound estimate of such loads is found by considering a kinematically admissible failure mechanism for which the power of the loads applied to the system is larger than the power that can be dissipated inside the system during its movement (Chen, 1975). Thus, When the tunnel face is stable, the following equation should satisfy:

$$P_e \le P_v \tag{7}$$

Where P_e is the power of external forces and P_v is the dissipated power in the failure zone.

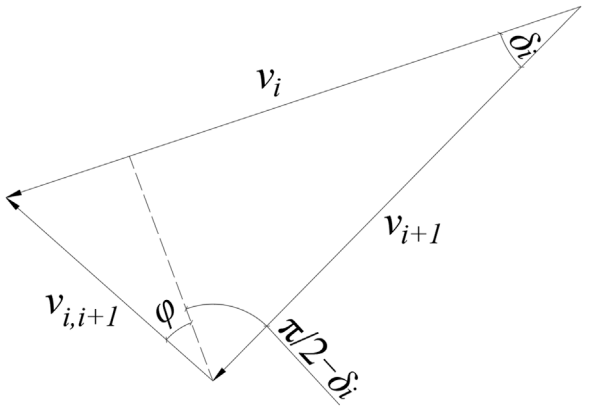

FIGURE 10
Velocity field of the proposed mechanism.

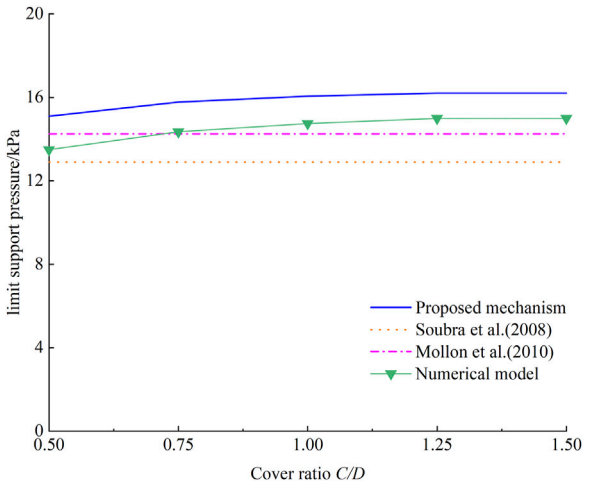

FIGURE 11
Comparison of proposed model with other models under different *C/D*.

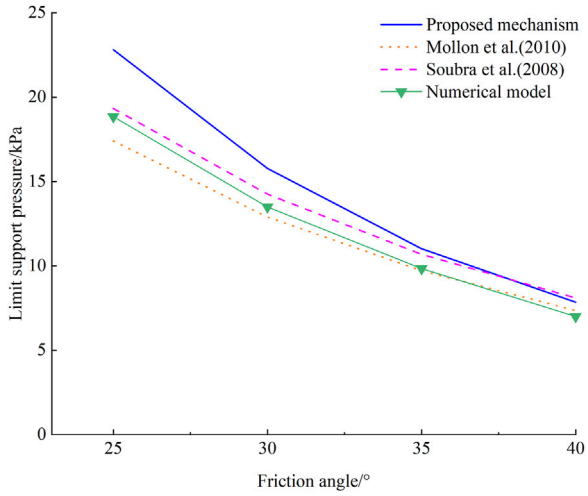

FIGURE 12
Comparison of proposed model with other models under different φ.

3.3.2 Geometric relationship

To calculate the internal and external powers in the failure zone, it is necessary to derive the geometric relationships. Based on these relationships, the angle α_i between the axis of the *i-the* truncated cone and the tunnel axis is given by Formula (8):

$$\alpha_i = \sum_{j=1}^{i-1} \beta_i + \delta_i \, (i = 2, 3, 4, 5) \tag{8}$$

The angles δ_i are as follows:

$$\delta_i = \begin{cases} \alpha, i = 1 \\ \beta_i - \delta_{i-1}, i = 2, 3, 4, 5 \end{cases} \tag{9}$$

Through analysis, it can be determined that the section obtained by the oblique intersection of each cone with the plane is an ellipse. The long axis, short axis, and area of the ellipse obtained by the *i-th* cone are denoted by a_i, b_i, and A_i, respectively, as given by Eqs 10–12.

$$a_i = \begin{cases} \frac{D}{2}, i = 1 \\ \frac{D}{2} \prod_{k=1}^{i} \frac{\cos(\delta_k + \varphi)}{\cos(\delta_{k+1} - \varphi)}, i = 2, 3, 4, 5 \\ a_5 \frac{\cos(\beta_4 - \beta_3 + \beta_2 - \beta_1 + \alpha_1 + \varphi)}{\sin(2\beta_4 + 2\beta_2 + \alpha_1 + \varphi)}, i = 6 \end{cases} \tag{10}$$

$$b_i = \begin{cases} a_i \frac{\sqrt{\cos(\delta_i + \varphi)\cos(\delta_i - \varphi)}}{\cos\varphi}, i = 1, 2, 3, 4, 5 \\ a_6 \frac{\sqrt{\sin\left(\sum_{j=1}^{5} \delta_i + \varphi\right) \sin\left(\sum_{j=1}^{5} \delta_i - \varphi\right)}}{\cos\varphi}, i = 6 \end{cases} \tag{11}$$

$$A_i = \pi a_i b_i \tag{12}$$

The volumes of *i-th* cones, denoted as V_i, can be expressed by formula (13):

$$V_i = \begin{cases} \frac{A_i h_i - A_{i+1} h_{i+1}}{3}, i = 1, 2, 3, 4 \\ \frac{A_5 h_5 - A_5 h_5'}{3}, i = 5 \end{cases} \tag{13}$$

Where:

$$\begin{cases} h_1 = \frac{D\cos(\alpha_1 + \varphi)\cos(\alpha_1 - \varphi)}{\sin 2\varphi} \\ h_2 = \frac{D\cos(\alpha_1 + \varphi)\cos(\beta_1 - \alpha_1 + \varphi)}{\sin 2\varphi} \\ h_i = h_2 \prod_{j=2}^{i-1} \frac{\cos(\delta_{j+1} + \varphi)}{\cos(\delta_j - \varphi)}, i = 3, 4, 5 \\ h_5' = h_5 \frac{\sin(2\beta_4 + 2\beta_2 + \alpha_1 - \varphi)}{\cos(\delta_5 - \varphi)} \end{cases} \tag{14}$$

10.3389/feart.2023.1287151

TABLE 3 Comparison between model test results and analytical solutions of limit support pressure.

c (kPa)	φ (°)	γ (kN/m³)	D (m)	C/D	Test result	Proposed mechanism			
					kPa	c = 0kPa, φ = 38°	c = 5kPa, φ = 38°	c = 0kPa, φ = 42°	c = 5kPa, φ = 42°
0–5	38–42	16.1	5	0.5	3.6	6.65	0.1	5.13	stable
				0.5	3.5				
				1	3.5	6.71	0.02	5.14	stable
				1	3.0				
				1	3.3				
0–5	38–42	15.3	5	0.5	4.2	6.32	0.3	4.87	stable
				1	5.5	6.37	0.3	4.88	stable
0–5	38–42	16.0	10	1	7.4	13.44	6.76	10.32	4.62

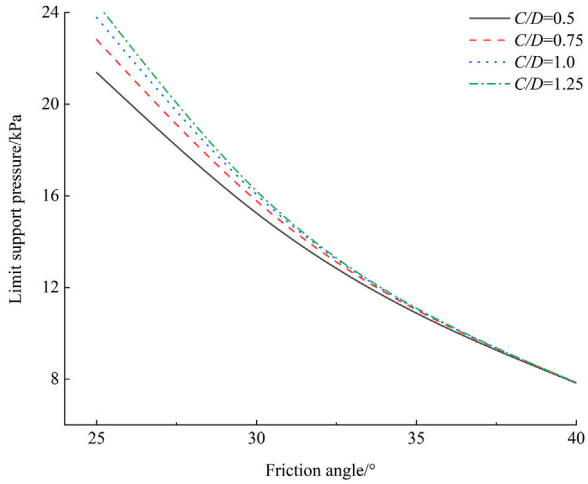

FIGURE 13
Influence of friction angle on limit support pressure under different *C/D*.

It is assumed that the velocity of each cone is parallel to its axis. The velocity of the *i-th* cone is denoted as v_i, and the relative velocity between the *i-th* cone and the *(i+1)-th* cone is denoted as $v_{i,i+1}$. The relationship between v_i, v_{i+1}, and $v_{i,i+1}$ is illustrated in Figure 10. the v_i, v_{i+1}, and $v_{i,i+1}$ can be expressed by formula (15) and (16).

$$v_i = v_1 \prod_{j=2}^{i} \frac{\cos\left(\delta_j + \varphi\right)}{\cos\left(\delta_{j+1} - \varphi\right)}, i \geq 2 \tag{15}$$

$$v_{i,i+1} = v_i \frac{\sin\left(2\delta_{j+1}\right)}{\cos\left(\delta_{j+1} - \varphi\right)}, i \geq 1 \tag{16}$$

3.3.3 Optimization of limit support pressure

The P_e is mainly composed of three parts: the power of support pressure P_T, the power of gravity in the failure zone P_γ, and the power of vertical load $P_{\sigma v}$, which can be expressed as follows:

$$P_e = P_T + P_\gamma + P_{\sigma_v} \tag{17}$$

P_T can be calculated using Eq. 18:

$$P_T = -A_1 \cos\alpha_1 \sigma_T v_1 \tag{18}$$

The power of gravity P_γ can be expressed using the following equation:

$$P_\gamma = \left[V_1 \sin\alpha_1 v_1 + V_2 \sin\left(2\beta_1 - \alpha_1\right)v_2 + V_3 \sin\left(2\beta_2 + \alpha_1\right)v_3 + V_4 \sin\left(2\beta_1 + 2\beta_3 - \alpha_1\right)v_4 + V_5 \sin\left(2\beta_2 + 2\beta_4 + \alpha_1\right)v_5\right]\gamma \tag{19}$$

The power of equivalent vertical pressure $P_{\sigma v}$ can be expressed using the following equation:

$$P_{\sigma_v} = A_6 \sin\left(2\beta_2 + 2\beta_4 + \alpha_1\right)\sigma_v v_5 \tag{20}$$

The dissipated power occurs mainly at the boundary of the collapse zone and between the truncated cones, which can be expressed by Formula (21):

$$P_v = \left[\frac{A_1 \cos\alpha_1}{\sin\varphi} v_1 - \frac{A_5 \sin\left(2\beta_2 + 2\beta_4 + \alpha_1\right)}{\sin\varphi} v_5\right] c \cos\varphi \tag{21}$$

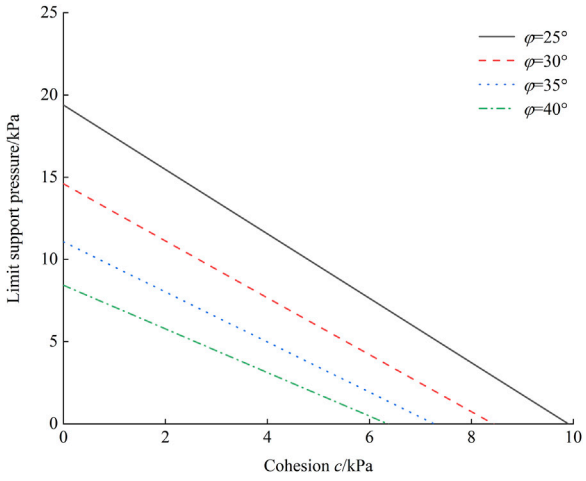

FIGURE 14
Influence of cohesion on limit support pressure under different φ.

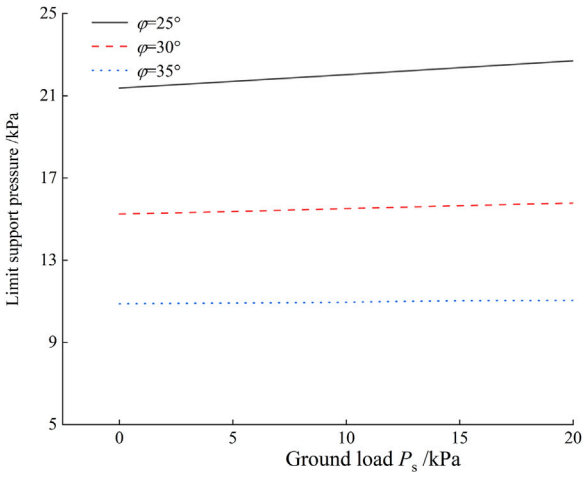

FIGURE 15
Influence of Ground load on limit support pressure under different.

By substituting Eqs 17–21 into Eq. 7, the following expression can be derived:

$$\sigma_T \geq \sigma_v N_{\sigma_v} + \gamma D N_\gamma + c N_c \tag{22}$$

Where:

$$\begin{cases} N_{\sigma_v} = \dfrac{A_6 \sin(2\beta_2 + 2\beta_4 + \alpha_1)}{A_1 \cos\alpha_1} \dfrac{v_5}{v_1} \\ N_\gamma = \left[V_1 \sin\alpha_1 v_1 + V_2 \sin(2\beta_1 - \alpha_1) v_2 + V_3 \sin(2\beta_2 + \alpha_1) v_3 \right. \\ \left. + V_4 \sin(2\beta_1 + 2\beta_3 - \alpha_1) v_4 + V_5 \sin(2\beta_2 + 2\beta_4 + \alpha_1) v_5 \right] / (D A_1 \cos\alpha_1 v_1) \\ N_c = \dfrac{N_{\sigma_v} - 1}{\tan\varphi} \end{cases} \tag{23}$$

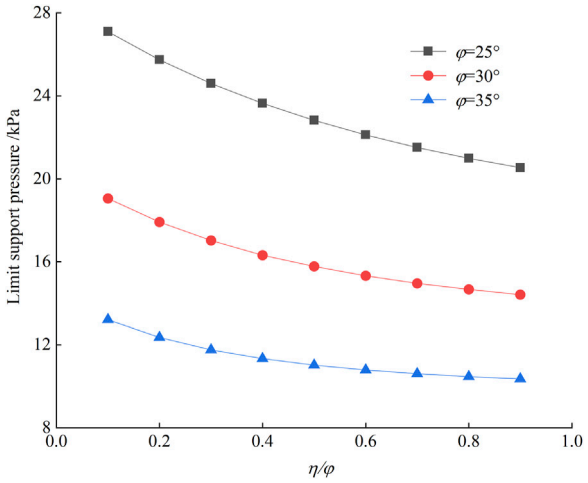

FIGURE 16
Influence of η/φ on limit support pressure under different φ.

Formula (23) reveals that the σ_T depends on the geometric characteristics of the failure model (α_1, β_1 to β_5, C, D) and the soil parameters (c, φ). Therefore, the upper-bound method of the σ_T can be obtained through optimization theory. By considering the geometric characteristics of the failure model (α_1, β_1 to β_5) as optimization variables and maximizing the σ_T as the optimization objective, the value of σ_T can be determined:

$$\sigma_T = \max_{\alpha_1,\beta_1,\beta_2,\beta_3,\beta_4,\beta_5} \sigma_v N_{\sigma_v} + \gamma D N_\gamma + c N_c \tag{24}$$

4 Comparison

To verify the accuracy of the proposed model in the paper, it is compared with numerical models, classical analytical models, and model tests.

4.1 Comparing with numerical model and existing models

In Figure 11, a comparison is made between the proposed theoretical model, existing theoretical and numerical models, and model tests under the condition of an internal friction angle of 30° and η/φ = 0.5. From the graph, it can be observed that both the proposed model and the numerical model show an increase in the σ_T with an increase in the cover ratio, and the trends are similar. When the cover ratio reaches 1.25, the increase in the σ_T becomes less significant. (Soubra et al., 2008; Mollon et al., 2011a) also found that the σ_T does not change significantly beyond a cover ratio of 0.5. A comparison reveals that when the cover ratio is 0.5, the σ_T obtained from the proposed model is approximately 18% higher than the numerical results. As the cover ratio increases, the difference between the two approaches becomes smaller. When the cover ratio is 1.5, the proposed model yields approximately 8% higher results compared to the numerical simulation. The main reason for

these discrepancies is that, based on model tests and engineering practice, the soil arch cannot form an arch for shallow tunnels, resulting in soil collapse to the ground and an increased vertical soil pressure. However, this phenomenon cannot be accurately simulated using a continuous medium model, leading to an underestimation of the vertical soil pressure. As the embedment ratio increases, the difference between the two models diminishes gradually due to the gradual emergence of the arching effect. Comparison with (Soubra et al., 2008; Mollon et al., 2011a), the proposed model yields approximately 13.7% and 25% higher results, respectively. The main reason for these differences is that (Soubra et al., 2008; Mollon et al., 2011a) prematurely assume the formation of an arching effect in soil with smaller friction angles, which contradicts experimental results and engineering practices.

In Figure 12, the results of different theoretical calculations for the variation of σ_T with φ are given for cover ratio $C/D = 0.75$ and $\eta/\varphi = 0.5$. It can be observed that all the results exhibit a nonlinear decrease with the increase of the φ. In terms of numerical values, when the $\varphi = 25^\circ$, the differences in σ_T obtained by the four models are the largest, while the differences are the smallest when the $\varphi = 40^\circ$. In addition, compared to the other models the proposed model gives higher σ_T. The main reason for these phenomena is that when the φ is small, the soil arch can't be formed, resulting in a higher vertical soil pressure. As the φ increases, the formation of the soil arch becomes easier, and the limit support pressure calculated by different models tend to converge.

4.2 Comparing with model experiments

Centrifuge tests results conducted by (Chambon and Corte, 1994) using sand are shown in Table 3. The sand parameters are as follows: $\varphi = 38^\circ$–42°, $c = 0$~5 kPa. As shown in the table, when the $\varphi = 38^\circ$ and the $c = 0$ kPa, the σ_T proposed in the paper is significantly higher than that obtained experimentally. With an increase in cohesion, the reduction in ultimate support force becomes more pronounced. When the cohesive strength reaches 5 kPa, the excavation face can stabilize itself. It should be noted that the soil parameters provided by (Chambon and Corte, 1994) are given as ranges, making it difficult to make accurate comparisons. However, the calculated results in this study include the experimental values, which demonstrates the validity of the proposed model.

5 Analysis

By comparison, it is found that the proposed model in this study is agrees well with numerical models and classical models. Especially in terms of shallow tunnel in sand, this model can more accurately describe the failure mode and provide more precise solutions. This section focuses on analyzing the influence of various factors on the σ_T.

5.1 Cover ratio C/D and friction angle φ

In the case of $C/D = 0.5$~1.25, Figure 13 shows the variation of σ_T with φ. It can be observed that the σ_T increases gradually with the increase of C/D when the φ is low. However, as the φ increases, the effect of cover ratio on σ_T becomes insignificant. The reason for this phenomenon is due to the following: At small friction angle, the frictional effect along the sliding surface is not apparent, resulting in an increase in σ_T with increasing depth. As the φ gradually increases, the soil arch effect becomes more prominent, leading to a decrease in the effect of C/D on σ_T.

5.2 Cohesion c

The influence of the c on the σ_T at different φ is illustrated in Figure 14. It can be seen that the σ_T decreases linearly with the increase of c, and the smaller the φ is, the more sensitive the σ_T is to the change of c. The main reasons for this phenomenon are as follows: Numerical simulations and theoretical studies have shown that the φ plays an important role in the area of collapse zone, and the smaller the φ, the larger the area of the collapse zone and the sliding surface. The energy dissipation of the cohesion occurs mainly at the sliding surface, so the larger the sliding surface area, the more obvious is the reduction of the σ_T as the cohesion increases.

5.3 Surface load P_s

The influence of the P_s on the σ_T for various φ is shown in Figure 15. It is apparent that the σ_T increases linearly as the P_s increases. The increase in the σ_T is small in comparison with the increase in the P_s, and the increase in the σ_T is smaller and smaller with the increase in the φ. At a friction angle of 35°, the surface load will have little effect on the σ_T due to the soil arch effect.

5.4 Friction angle ratio η/φ

The friction angle ratio η/φ is the ratio of the friction angle between the disturbed zone and failure core to the soil friction angle, which is important for the formation of the soil arch. The influence of η/φ on the σ_T is investigated in this section. As shown in Figure 16, for small η/φ the frictional effect of the disturbed zone on the failure core is less and the σ_v is closer to the vertical earth pressure, resulting in a larger σ_T. As η/φ increases, the σ_T gradually decreases. Beyond a certain value, the effect of η/φ on the σ_T is not apparent due to the soil arch effect.

6 Conclusion

Numerical simulation and theoretical Analysis are combined to study the face stability of shallow shield tunnel in sand. Firstly, numerical simulation is used to study the tunnel collapse in sand to obtain the σ_T and shape of collapse zone. The new failure model suitable for shallow tunnel is constructed based on numerical simulations, and the σ_T is solved by upper-bound method. The following conclusions are mainly obtained:

(1) Through numerical simulation, it is found that the σ_T decreases exponentially with the increase of the φ in the range of φ =

25°~40° and C/D = 0.5~1.25. The σ_T increases approximately linearly with the increase of the C/D. And the regression equation is obtained by regression analysis.

(2) Through numerical simulation, it is found that for the sandy soil layer, when the $C/D \leq 1$, the can zone can reach ground surface, and the shape of the collapse zone is an inverted round table, which includes a columnar failure core and the rest of the disturbed zone.

(3) A new failure model based on five truncated cones with inverted circular table is proposed. By comparison, it is found that the proposed model is consistent with the numerical model and exiting modes. In addition, the proposed model is more accurate in describing the phenomenon that no soil arch can be formed for shallow tunnel in sand, and it has higher accuracy in solving the σ_T of shallow shield tunnel in sand.

(4) Through the theoretical analysis, it is found that the σ_T decreases nonlinearly with the increase of the φ, and the larger φ is, the more obvious soil arch effect is, and the smaller the effect of C/D on the σ_T is. In addition, the σ_T decreases linearly with the increase of cohesion c, and the smaller φ, the more σ_T sensitive is to the cohesion. The increase of P_S will cause the σ_T to increase, but when the soil arch forms, the effect of P_s on the σ_T is smaller.

Data availability statement

The original contributions presented in the study are included in the article/Supplementary Material, further inquiries can be directed to the corresponding author.

Author contributions

SQ: Project administration, Resources, Writing–original draft. LZ: Conceptualization, Investigation, Writing–original draft. XW: Data curation, Investigation, Writing–original draft. XL: Investigation, Project administration, Writing–original draft. FW: Data curation, Writing–original draft, Writing–review and editing.

Funding

The authors declare financial support was received for the research, authorship, and/or publication of this article. The authors declare financial support was received for the research, authorship, and/or publication of this article. Youth Fund Project of Shanxi Provincial Science and Technology Department, "Research on Flexibility Regulation Mechanism and Engineering Application of NPR Anchor Cables in High Geostress Soft Rock Tunnels.

Conflict of interest

Authors SQ, LZ, XW, and XL were employed by 5TH Engineering LTD. of the First Highway Engineering Bureau CCCC.

Author FW was employed by Shanxi Transportation Technology Research and Development Co., Ltd.

The authors declare that this study received funding from the Science and Technology Project of Shanxi Province Transportation Holding Group Co., Ltd, "Research on Disaster-Causing Mechanism of Coal Mine Subsidence and Prevention and Control of NPR Anchor Cables for Operating Tunnels in Mountainous Areas", Project No.: 2022-JKKJ-6. The funder had the following involvement in the study: decision to publish and preparation of the manuscript.

Publisher's note

References

Anagnostou, G., and Kovári, K. (1994). The face stability of slurry-shield-driven tunnels. *Tunn. Undergr. space Technol.* 9 (2), 165–174. doi:10.1016/0886-7798(94)90028-0

Arthur, L., Darby, A., Rafoneke, B., Daws, G., MacDonald, D., Innaurato, N., et al. (July, 1994). "Face support for a large mix-shield in heterogeneous ground conditions," in Tunnelling'94: Papers presented at the seventh international symposium,'Tunnelling'94' (Springer), London, UK, 531–550.

Atkinson, J., Potts, D., and Schofield, A. (1977). Centrifugal model tests on shallow tunnels in sand. *Tunn. Tunnlng.* 9 (1), 59–64

Chambon, P., and Corte, J.-F. (1994). Shallow tunnels in cohesionless soil: stability of tunnel face. *J. geotechnical Eng.* 120 (7), 1148–1165. doi:10.1061/(asce)0733-9410(1994)120:7(1148)

Chen, R., Tang, L., Ling, D., and Chen, Y. (2011). Face stability analysis of shallow shield tunnels in dry sandy ground using the discrete element method. *Comput. Geotechnics* 38 (2), 187–195. doi:10.1016/j.compgeo.2010.11.003

Chen, R., Yin, X., Tang, L., and Chen, Y. (2018). Centrifugal model tests on face failure of earth pressure balance shield induced by steady state seepage in saturated sandy silt ground. *Tunn. Undergr. Space Technol.* 81, 315–325. doi:10.1016/j.tust.2018.06.031

Chen, R.-P., Li, J., Kong, L.-G., and Tang, L.-J. (2013). Experimental study on face instability of shield tunnel in sand. *Tunn. Undergr. Space Technol.* 33, 12–21. doi:10.1016/j.tust.2012.08.001

Chen, W. F. (1975). *Limit analysis and soil plasticity*. Amsterdam, The Netherlands: Elsevier Science, 1–15.

Di, Q., Li, P., Zhang, M., and Cui, X. (2022a). Influence of relative density on deformation and failure characteristics induced by tunnel face instability in sandy cobble strata. *Eng. Fail. Anal.* 141, 106641. doi:10.1016/j.engfailanal.2022.106641

Di, Q., Li, P., Zhang, M., and Cui, X. (2022b). Investigation of progressive settlement of sandy cobble strata for shield tunnels with different burial depths. *Eng. Fail. Anal.* 141, 106708. doi:10.1016/j.engfailanal.2022.106708

Funatsu, T., Hoshino, T., Sawae, H., and Shimizu, N. (2008). Numerical analysis to better understand the mechanism of the effects of ground supports and reinforcements on the stability of tunnels using the distinct element method. *Tunn. Undergr. Space Technol.* 23 (5), 561–573. doi:10.1016/j.tust.2007.10.003

Han, K., Zhang, C., and Zhang, D. (2016). Upper-bound solutions for the face stability of a shield tunnel in multilayered cohesive–frictional soils. *Comput. Geotechnics* 79, 1–9. doi:10.1016/j.compgeo.2016.05.018

Horn, N. (1961). "Horizontal earth pressure on perpendicular tunnel face," in Proceedings of the Hungarian National Conference of the Foundation Engineer Industry. Budapest

Idinger, G., Aklik, P., Wu, W., and Borja, R. I. (2011). Centrifuge model test on the face stability of shallow tunnel. *Acta Geotech.* 6, 105–117. doi:10.1007/s11440-011-0139-2

Kirsch, A. (2010). Experimental investigation of the face stability of shallow tunnels in sand. *Acta Geotech.* 5, 43–62. doi:10.1007/s11440-010-0110-7

Leca, E., and Dormieux, L. (1990). Upper and lower bound solutions for the face stability of shallow circular tunnels in frictional material. *Géotechnique* 40 (4), 581–606. doi:10.1680/geot.1990.40.4.581

Li, H., Li, X., Fu, J., Zhu, N., Chen, D., Wang, Y., et al. (2023). Experimental study on compressive behavior and failure characteristics of imitation steel fiber concrete under uniaxial load. *Constr. Build. Mater.* 399, 132599. doi:10.1016/j.conbuildmat.2023.132599

Li, H., Tian, X., Song, Z., Wang, J., and Zhou, G. (2018). Study on calculaiton method of digging length for shallow tunnel based on Xie Jiajie's Sourrounding Rock Pressure Formula. *J. Xi'an Univ. Arch. Tech. Nat. Sci. Ed.* 50 (05), 662–667. doi:10.15986/j.1006-7930.2018.05.007

Li, P., Chen, K., Wang, F., and Li, Z. (2019). An upper-bound analytical model of blow-out for a shallow tunnel in sand considering the partial failure within the face. *Tunn. Undergr. Space Technol.* 91, 102989. doi:10.1016/j.tust.2019.05.019

Li, P., Wei, Y., Zhang, M., Huang, Q., and Wang, F. (2022). Influence of non-associated flow rule on passive face instability for shallow shield tunnels. *Tunn. Undergr. Space Technol.* 119, 104202. doi:10.1016/j.tust.2021.104202

Li, P., Zou, H., Wang, F., and Xiong, H. (2020). An analytical mechanism of limit support pressure on cutting face for deep tunnels in the sand. *Comput. Geotechnics* 119, 103372. doi:10.1016/j.compgeo.2019.103372

Liao, S.-M., Liu, J.-H., Wang, R.-L., and Li, Z.-M. (2009). Shield tunneling and environment protection in Shanghai soft ground. *Tunn. Undergr. Space Technol.* 24 (4), 454–465. doi:10.1016/j.tust.2008.12.005

Liu, H., Li, X., Yu, Z., Tan, Y., Ding, Y., Chen, D., et al. (2023a). Influence of hole diameter on mechanical properties and stability of granite rock surrounding tunnels. *Phys. Fluids* 35 (6). doi:10.1063/5.0154872

Liu, S., and Li, X. (2023). Experimental study on the effect of cold soaking with liquid nitrogen on the coal chemical and microstructural characteristics. *Environ. Sci. Pollut. Res.* 30 (13), 36080–36097. doi:10.1007/s11356-022-24821-9

Liu, S., Sun, H., Zhang, D., Yang, K., Li, X., Wang, D., et al. (2023b). Experimental study of effect of liquid nitrogen cold soaking on coal pore structure and fractal characteristics. *Energy* 275, 127470. doi:10.1016/j.energy.2023.127470

Meguid, M., Saada, O., Nunes, M., and Mattar, J. (2008). Physical modeling of tunnels in soft ground: a review. *Tunn. Undergr. Space Technol.* 23 (2), 185–198. doi:10.1016/j.tust.2007.02.003

Messerli, J., Pimentel, E., and Anagnostou, G. (2010). "Experimental study into tunnel face collapse in sand," in *Physical modelling in geotechnics, two volume set* (CRC Press), Boca Raton, FL, USA, 601–606.

Mollon, G., Dias, D., and Soubra, A. H. (2011a). Rotational failure mechanisms for the face stability analysis of tunnels driven by a pressurized shield. *Int. J. Numer. Anal. Methods Geomechanics* 35 (12), 1363–1388. doi:10.1002/nag.962

Mollon, G., Phoon, K. K., Dias, D., and Soubra, A.-H. (2011b). Validation of a new 2D failure mechanism for the stability analysis of a pressurized tunnel face in a spatially varying sand. *J. Eng. Mech.* 137 (1), 8–21. doi:10.1061/(asce)em.1943-7889.0000196

Murayama, S., Endo, M., Hashiba, T., Yamamoto, K., and Sasaki, H. (August, 1996). "Geotechnical aspects for the excavating performance of the shield machines," in The 21st annual lecture in meeting of Japan Society of Civil Engineers). Japan.

Senent, S., Mollon, G., and Jimenez, R. (2013). Tunnel face stability in heavily fractured rock masses that follow the Hoek–Brown failure criterion. *Int. J. Rock Mech. Min. Sci.* 60, 440–451. doi:10.1016/j.ijrmms.2013.01.004

Soubra, A.-H., Dias, D., Emeriault, F., and Kastner, R. (March, 2008). "Three-dimensional face stability analysis of circular tunnels by a kinematical approach," in GeoCongress 2008: characterization, monitoring, and modeling of GeoSystems, New Orleans, LA, USA, 894–901.

Wang, F. N., Guo, Z., Qiao, X., Fan, J., Li, W., Mi, M., et al. (2021a). Large deformation mechanism of thin-layered carbonaceous slate and energy coupling support technology of NPR anchor cable in Minxian Tunnel: a case study. *Tunn. Undergr. Space Technol.* 117, 104151. doi:10.1016/j.tust.2021.104151

Wang, F. N., Yin, S., Guo, A., Wang, Z., Mi, M., Qi, G., et al. (2021b). Frame structure and engineering applications of the multisource system cloud service platform of monitoring of the soft rock tunnel. *Geofluids* 2021, 1–15. doi:10.1155/2021/6672732

Yu, L., Zhang, D., Fang, Q., Cao, L., Zhang, Y., and Xu, T. (2020). Face stability of shallow tunnelling in sandy soil considering unsupported length. *Tunn. Undergr. Space Technol.* 102, 103445. doi:10.1016/j.tust.2020.103445

Zhang, J., Li, X., Qin, Q., Wang, Y., and Gao, X. (2023). Study on overlying strata movement patterns and mechanisms in super-large mining height stopes. *Bull. Eng. Geol. Environ.* 82 (4), 142. doi:10.1007/s10064-023-03185-5

Zhang, X., Wang, M., Wang, Z., Li, J., Tong, J., and Liu, D. (2020). A limit equilibrium model for the reinforced face stability analysis of a shallow tunnel in cohesive-frictional soils. *Tunn. Undergr. Space Technol.* 105, 103562. doi:10.1016/j.tust.2020.103562

Zhang, C., Han, K., and Zhang, D. (2015). Face stability analysis of shallow circular tunnels in cohesive-frictional soils. *Tunn. Undergr. Space Technol.* 50, 345–357.

Zhang, Z., Hu, X., and Scott, K. D. (2011). A discrete numerical approach for modeling face stability in slurry shield tunnelling in soft soils. *Comput. Geotechnics* 38 (1), 94–104. doi:10.1016/j.compgeo.2010.10.011

frontiers | Frontiers in Earth Science

TYPE Original Research
PUBLISHED 29 December 2023
DOI 10.3389/feart.2023.1303996

OPEN ACCESS

EDITED BY
Zhibo Zhang,
University of Science and Technology Beijing, China

REVIEWED BY
Geng Jiabo,
Jiangxi University of Science and Technology, China
Kaizong Xia,
Chinese Academy of Sciences (CAS), China

*CORRESPONDENCE
Enyuan Wang,
eywangcumt@163.com

RECEIVED 28 September 2023
ACCEPTED 12 December 2023
PUBLISHED 29 December 2023

CITATION
Ou J, Wang E, Li Z, Li N, Liu H and Wang X (2023), Experimental study of coal and gas outburst processes influenced by gas pressure, ground stress and coal properties.
Front. Earth Sci. 11:1303996.
doi: 10.3389/feart.2023.1303996

Experimental study of coal and gas outburst processes influenced by gas pressure, ground stress and coal properties

Jianchun Ou[1], Enyuan Wang[2]*, Zhonghui Li[2], Nan Li[1], He Liu[2] and Xinyu Wang[2]

[1]State Key Laboratory for Fine Exploration and Intelligent Development of Coal Resources, China University of Mining and Technology, Xuzhou, China, [2]School of Safety Engineering, China University of Mining and Technology, Xuzhou, China

With the continuous increase of mining depth, coal and gas outburst poses a significant threat to mining safety. Conducting research on the mechanisms of coal and gas outbursts contributes to understanding the evolutionary process of such incidents, thus enabling accurate prediction and prevention of coal and gas outbursts during mining operations. This paper has developed a comprehensive visual experimental system that is specifically tailored to simulate diverse coal body conditions, ground stress and gas pressures. By monitoring and analyzing the real-time progression of coal fissures during the outburst process, we can obtain valuable insights into the evolution and mechanisms of coal and gas outbursts. Additionally, this study introduces a method to determine the critical threshold for predicting coal and gas outbursts, and the critical gas pressure threshold for Jiulishan Coal Mine (Jiaozuo City, Henan Province, China) is established at 0.6 MPa.

KEYWORDS

coal and gas outburst, spatio-temporal evolution, ground stress, gas pressure, coal properties

1 Introduction

Coal and gas outbursts are geological hazards characterized by the sudden ejection of fractured coal, rock and gas from the coal seam into the mining space, resulting from the combined effects of ground stress and gas (Li et al., 2023; Liu et al., 2023; Soleimani et al., 2023). The occurrence of coal and gas outbursts generates strong shockwaves with tremendous destructive power, posing significant threats to the safety of miners and mining facilities (Black, 2019a; Mekhtiev et al., 2021). With the continuous growth in energy demand and the increase in mining intensity and depth, the complex interactions among stress, gas, coal and rock have made the geological conditions of mines increasingly complicated, the probability of coal and gas outburst events increases (Li et al., 2019; Kursunoglu and Onder, 2019; Ul'yanova et al., 2019). The intricate mining conditions in deep mines give rise to distinct features of coal and gas outbursts, which are marked by heightened energy levels, intensity, and challenges in prevention and control efforts (Odintsev and Makarov, 2020; Gawor and Wasilewski, 2021; Remennikov et al., 2022; Shang et al., 2023). Therefore, studying the evolutionary processes and mechanisms of coal and gas outbursts holds significant importance for the safe operation of coal mines.

Previous research has conducted extensive research on the mechanisms of coal and gas outbursts and have proposed a range of hypotheses, including the "rheological hypothesis,"

"failure of the coal shell hypothesis," "unified instability theory," "fluid-solid coupling instability theory," and the composite hypothesis (Jiang et al., 2015; Yuan, 2017; Jin et al., 2018). These studies still have important guiding significance for current research. In recent years, with the advancement of experimental methods, research on the outburst mechanisms has continued to deepen. Koziel et al. (2022) conducted a study to investigate the prominent energy source in the porous structure of rocks, which is due to the presence of high-pressure gas. The prominence of this energy source is determined by the type of transformation that occurs during the decompression process. Zhao et al. (2022) conducted coal and gas outburst experiments under deep high-stress conditions and studied the stress-gas-pressure-temperature response characteristics of coal and rock around the outburst hole. The experimental findings indicate a significant stress response in the vicinity of the blast hole, with diminishing stress changes as the distance from the blast hole position increases. Based on these observations, one can deduce that the principal energy source for coal and gas outbursts originates from the internal energy of gas.

Coal possesses a complex fractured morphology, cracks and the finely porous structure (Ul'yanova et al., 2019; Godyn and Kozusnikova, 2019), experiences the formation of gas-bearing fractures due to the extension and convergence of microcracks under the ground stress. The cracks act as direct indicators of coal damage, and a comprehensive analysis of their attributes and formations can unveil the processes and mechanisms behind the onset and development of disasters (Odintsev and Makarov, 2020; Gao et al., 2021). Feldman et al. (2017) proposed a model to describe the development of primary fractures in coal seams under rapid unloading conditions, along with criteria for fracture occurrence and fracture timing in the edge areas of the coal seams. The study revealed that in virgin gas-bearing coal seams, fractures are influenced by both rock pressure and gas pressure within the coal seam fissures. Zhu et al. (2022) used mercury intrusion porosimetry and gas adsorption methods to investigate the pore structure characteristics of coal samples from highly gassy coal seams. The results indicated that during the initial stage of crack propagation, the main cracks on the coal samples extended along the direction of natural fractures. As the cracks expanded, the surface fractal dimension of the main cracks increased, and their degree of curvature intensified. The propagation path of the main crack is mainly affected by natural fractures and loads. Odintsev and Shipovskii. (2019) investigated the mechanisms underlying the formation of dynamic fracture in outburst-hazardous coal band under the influence of coal seam explosions. Furthermore, the researchers made estimations regarding the initial timing of crack development under the pressure exerted by liberated methane. The results indicate that the onset of crack development varies significantly, ranging from several tens of seconds to several hours, depending on the distinct mechanical characteristics exhibited by different coal samples.

Obviously, extensive literatures have carried out the coal and gas outburst simulation experiments. However, the interaction mechanism between various influencing factors is still controversial in the process of prominent events. Therefore, the design of a simulated experimental device for real-time dynamic observation of the fracture evolution of coal during coal and gas outbursts is of great significance for investigating the mechanisms of coal and gas outbursts and improving prevention measures. Meanwhile, the variations in gas pressure, ground stress, and mechanical characteristics of coal are substantial across different mining areas. The complex interaction of various influencing factors greatly impacts the occurrence of coal and gas outbursts, rendering their prediction challenging (Black, 2019b; Amani et al., 2021; Shadrin et al., 2022). Therefore, it is indispensable to formulate an accurate approach to anticipate the crucial thresholds of indicators related to coal and gas outbursts in different mining areas (Agrawal et al., 2023; Zheng et al., 2023).

In this paper, a comprehensive simulation experiment system was designed. The simulation experiments were conducted to investigate the effects of ground stress, gas pressure and coal properties on the occurrence of outbursts. Real-time observation and analysis of the generation, expansion and movement of coal fractures during coal and gas outbursts were conducted, and the experimental data were fitted. The interaction among ground stress, gas pressure and coal properties during coal and gas outbursts was analyzed, and the process of coal cracks during the outburst evolution was determined was analyzed. Additionally, a method was proposed for determining the critical values to predict coal and gas outbursts, and the critical value for gas pressure was found to be 0.6 MPa for the Jiusan Mine (Jiaozuo City, Henan Province, China).

2 Experimental section

2.1 Experimental system

As shown in Figure 1, the coal and gas outburst experiment system consist of a pressure loading device, gas loading device and observation device. The pressure loading device is primarily composed of a computer-controlled electro-hydraulic servo pressure testing machine, which applies stress to the coal to simulate the ground stress by the coal underground. The gas loading device is used to fill the coal samples in the apparatus with gas, and the observation device includes a high-speed camera and a transparent organic glass window. The high-speed camera is positioned facing the transparent window to capture the fracture evolution process of the coal during the outburst. In order to capture and analyze coal and gas outburst processes, the frame rate of the high-speed camera was set to 2,000 frames per second.

2.2 Sample preparation

In coal and gas outburst simulation experiments, the physical and mechanical conditions of the coal body are important factors affecting the outburst process. To compare the impact of different coal types on the outburst, this experiment used both coal briquette and lump coal as the coal samples. By controlling the ratio of coal powder to coal tar, the coal briquette was prepared with different physical and mechanical properties. The preparation of coal briquette was performed directly in the outburst experiment apparatus, the pre-prepared coal powder was loaded into the apparatus in three stages, with each stage being pressurized at 20 MPa. The pressurization was done using a hydraulic press at a rate of 300 N/s, and once the predefined pressure was reached, it was maintained for 30 min. Before pressing the coal briquette, the outburst opening needed to be sealed to ensure proper bonding between the prepared coal and the container wall. For

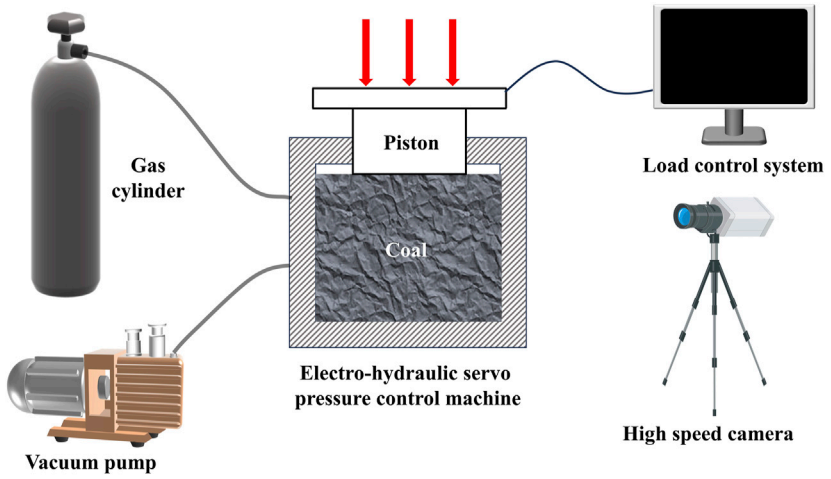

FIGURE 1
The coal and gas outburst simulation experiment system.

TABLE 1 The results of outburst experiment under different coal properties.

Sample	Content of coal tar (%)	Gas pressure (MPa)	Pressure of briquette (MPa)	Ground stress (MPa)	Result
1	0	0.20	20	10	No outburst
2	0	0.22	20	10	Outburst
3	7	0.49	20	10	No outburst
4	7	0.72	20	10	Outburst
5	15	0.58	20	10	No outburst
6	15	1.25	20	10	Outburst

the lump coal outburst experiments, large coal samples were selected from the field and then cut into pieces that matched the volume of the experimental container. These coal pieces were placed in the experimental apparatus, and coal powder was used to fill the gaps between the coal samples and the container wall.

3 Experimental results

3.1 Results of simulation experiments on coal and gas outburst

Different physical and mechanical properties of coal briquette were prepared by changing the ratio of coal powder to coal tar. A stress of 10 MPa was applied to the coal samples to simulate ground stress, and the minimum gas pressure required for coal outburst under this stress was measured. The experimental results are presented in Table 1.

In the absence of coal tar additives, after directly applying pressure to the coal samples, no outbursts occurred at a gas pressure of 0.20 MPa, and only minor fissures appeared. When the gas pressure increases to 0.22 MPa, the outburst phenomenon occurs. However, when a coal briquette made of 7% coal tar was added, no outbursts occurred at a gas pressure of 0.49 MPa, and the outbursts occurred when the gas pressure increased to 0.72 MPa. Similarly, when a coal briquette made of 15% coal tar was added, no outbursts occurred at a gas pressure of 0.58 MPa. The outbursts occurred when the gas pressure increased to 1.25 MPa.

Coal and gas outbursts often occur in coal seams with soft layers, however, with the increase of mining depth, the ground stress and gas pressure increase correspondingly, and the probability of hard coal outburst increases significantly (Yuan et al., 2021; Kursunoglu and Onder, 2023). In the hard coal outburst experiment, when the flap of the outburst mouth is suddenly opened, the coal undergoes a transition from being subjected to three-dimensional forces to being subjected to two-dimensional forces, resulting in the rapid release of stored elastic energy. Table 2 displays the outburst conditions of hard coal. Figure 2 illustrates the distribution of coal fractures after an experiment with a gas pressure of 0.65 MPa and a ground stress of 15 MPa. Multiple fractures appear near the outburst mouth, with small widths and primarily in the vertical direction. Furthermore, the upper part of the coal body experiences more severe damage, resulting in the fragmentation into several larger coal chunks.

Figure 3 illustrates the distribution of coal fractures after an experiment with a gas pressure of 0.75 MPa and a ground stress of 20 MPa. The outburst mouth exhibits two significant connected and branched shear fractures, with a noticeable increase in width. From the side cracks, it can be observed that the coal near the outburst mouth experiences further damage, resulting in the fragmentation into smaller particles. Furthermore, the fractures of coal located farther from the

TABLE 2 Incidents of hard coal outburst.

Sample	Gas pressure (MPa)	Bottom coal seam	Ground stress (MPa)	Result
1	0.65	Soft coal seam	15	No outburst
2	0.75	Soft coal seam	20	No outburst
3	0.60	None	20	Outburst

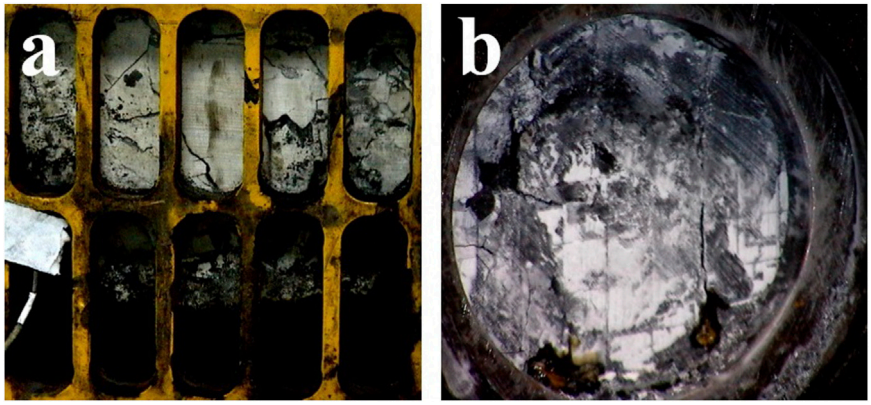

FIGURE 2
Hard coal sample after outburst in 0.65 MPa of gas pressure and 15 MPa of ground stress: **(A)** The crack fracture of flank, **(B)** The crack fracture of outburst mouth.

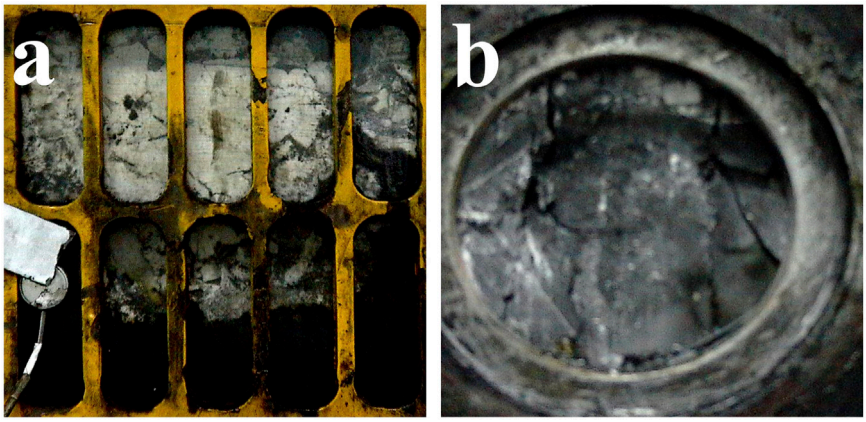

FIGURE 3
Hard coal sample after outburst in 0.75 Mpa of gas pressure and 20 Mpa of ground stress: **(A)** The crack fracture of flank, **(B)** The crack fracture of outburst mouth.

outburst mouth have certain closure. By considering the results of the side crack observations, it can be concluded that the corner position of the coal block undergoes the most severe damage.

Figure 4 illustrates the distribution of coal fractures after an experiment with a gas pressure of 0.6 MPa and a ground stress of 20 MPa. Under the gas pressure of 0.6 MPa and the *in-situ* stress of 20 MPa, the outburst of hard coal occurred, the dynamic characteristics during the outburst were not significant. The hard coal did not exhibit a pronounced ejection phenomenon, resulting in relatively large coal particles left after the outburst. After the outburst occurs, a hole with a large opening and a small cavity formed inside the coal body, and the coal surrounding the cavity became quite loose. Under this experimental condition, the coal located below the outburst mouth was mostly unaffected by the outburst, and the degree of fragmentation was minimal. The coal located below the outburst mouth was not subjected to a change in stress state when the outburst mouth opened, and the elastic energy in the coal was not rapidly released in a short time, thus not providing a rapid release pathway for the gas within the coal, resulting in minimal damage to the coal. As shown in Table 2, in the case of the same ground stress, when the gas pressure increases, the

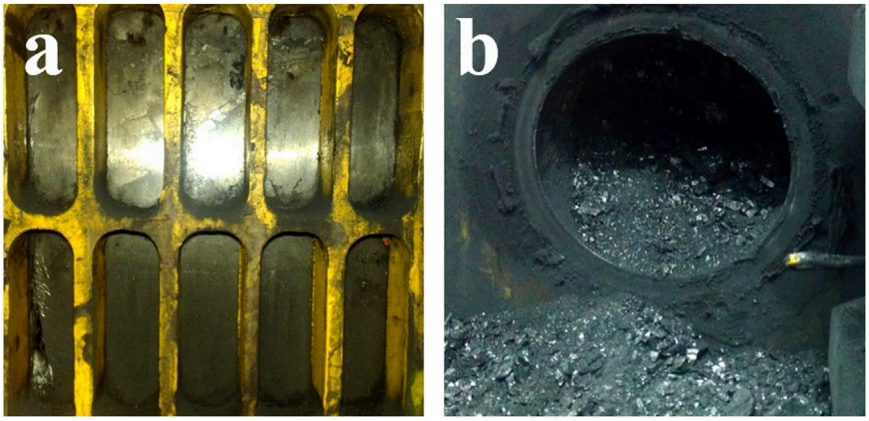

FIGURE 4
Hard coal sample after outburst in 0.6 Mpa of gas pressure and 20 Mpa of ground stress: **(A)** The crack fracture of flank, **(B)** The crack fracture of outburst mouth.

TABLE 3 The results of outburst experiment under the different ground stress.

Sample	Content of coal tar (%)	Gas pressure (MPa)	Pressure of briquette (MPa)	Ground stress (MPa)	Result
1	7	0.37	20	5	No outburst
2	7	0.37	20	7.5	No outburst
3	7	0.37	20	10.41	Outburst
4	7	0.46	20	2	No outburst
5	7	0.46	20	3.12	No outburst
6	7	0.46	20	5.38	Outburst

outburst phenomenon does not occur. This is due to the outburst mouth baffle and the coal block inside the device do not come into contact with each other, and when the outburst occurs and the protruding mouth baffle opens, the coal body is not completely and quickly depressurized, and the stored elastic energy cannot be released quickly.

The impact of ground stress on the outburst of coal briquette is illustrated in Table 3, indicating that no outbursts occurred under the ground stress of 5 MPa and 7.5 MPa. However, when the ground stress increased to 10.41 MPa, an outburst phenomenon occurred, with a mass of 3.2 kg, accounting for 45.7% of the total coal mass. This indicates that coal briquette containing 7% coal tar exhibit outburst phenomena within a certain range of critical stress threshold under a gas pressure of 0.37 MPa.

3.2 The distribution of coal cracks in the outburst process

Coal and gas outbursts are rapid processes that can be completed in just a few seconds. In order to analyze the evolution of cracks during the outburst process, this study conducted continuous observations using a high-speed camera system. Figure 5 presents the evolution of coal cracks captured by the high-speed camera during the moment of outburst, the entire outburst process is less than 0.1 s. After the outburst occurs, the coal in the outburst area is quickly expelled, followed by the emergence of cracks. Initially, the cracks appear at the top of the coal and gradually propagate towards the interior. The crack propagation speed is first fast and then slow, and finally tends to stop. Additionally, when the gas pressure exceeds 0.48 MPa, no cracks were observed during the outburst process.

Figure 6A illustrates the evolution process of coal fractures during the outburst process, while Figures 6B, C depict the displacement and velocity plots of the marked particles in Figure 6A. From Figure 6B, it can be observed that the trajectory of the coal particle motion also approximates a parabolic shape. The particle exhibits significant displacement, moving approximately 0.06 m along the *x*-axis according to the recorded observations on the graph. After outburst, the motion velocity of the coal particle rapidly increases, reaching a maximum speed of 1.1 m per second, and gradually decreases, reaching its maximum value at 0.15 s. Once the outburst occurs, the coal was expelled rapidly under the driving force of gas pressure.

4 Discussion

4.1 The analysis of coal and gas outburst laws and influencing factors

In the coal briquette outburst experiment, the occurrence of coal and gas outburst phenomena in the coal body under low coal tar

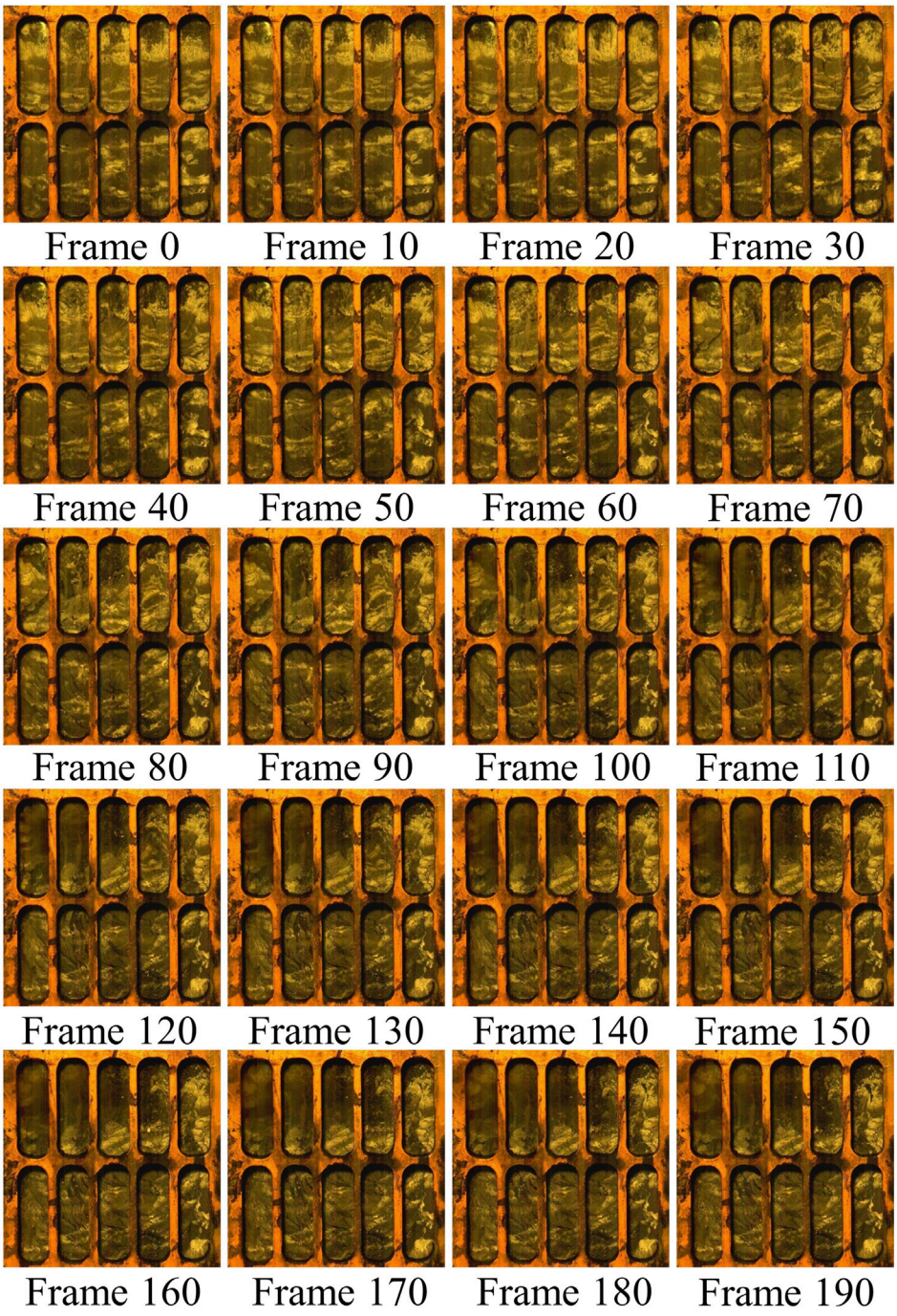

FIGURE 5
Schematic diagram of evolution process of coal fracture in outburst process.

content and small gas pressure was observed, and the frequency of coal outbursts increased as the gas pressure increased. Furthermore, the ability of coal bodies with different intensities to resist outburst varied, resulting in different minimum values of gas pressure required for outburst. During the outburst experiment with hard coal, the *in-situ* stress led to the continuous accumulation of elastic energy within the coal body. The critical factor for outbursts in hard coal is the release of elastic energy during the decompression process (Rudakov and Sobolev, 2019; Soleimani et al., 2023).

As shown in Table 3, conclusions can be drawn from the results of the 4th, 5th, and 6th experimental groups, where coal samples containing 7% coal tar exhibit a range of critical ground stress thresholds for outburst phenomena under a gas pressure of 0.46 MPa. In summary, the Eq. 1 and Eq. 2 can be derived:

$$p = 0.37MPa, 7.5MPa \leq \sigma \leq 10.41MPa \quad (1)$$

$$p = 0.46MPa, 3.12MPa \leq \sigma \leq 5.38MPa \quad (2)$$

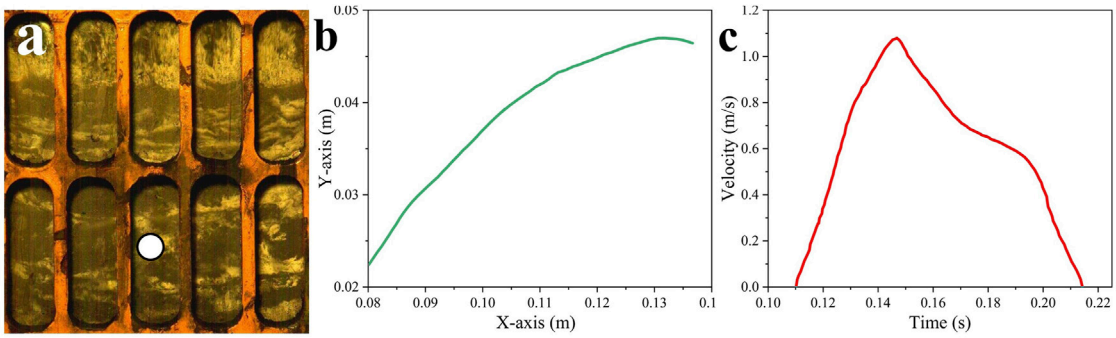

FIGURE 6
(A) Schematic diagram of particle trajectories taken from coal relative position, **(B)** The trajectory of particle motion, **(C)** The velocity of particle motion.

TABLE 4 The results of outburst experiment under the different outburst mouth.

Sample	Content of coal tar (%)	Gas pressure (MPa)	Pressure of briquette (MPa)	Ground stress (MPa)	Outburst mouth	Result
1	7	0.49	20	10	No special treatment	No outburst
2	7	0.49	30	10	Add rubber sheet	No outburst
3	7	0.49	20	10	Baffle does not contact the coal body	Outburst

To further analyze the impact of pressure of briquette and gas coupling on outbursts, the influence mechanisms of the outburst occurrence was researched under the different outburst mouth when the gas pressure was 0.49 MPa, the experimental findings are presented in Table 4. A layer of sealing rubber film was added to the outburst mouth while maintaining the experimental conditions unchanged. After the induction step of the outburst, the coal mass did not experience an outburst but exhibited a certain degree of swelling. At the moment of the outburst occurrence, the barrier plate on the outburst opening was suddenly removed, resulting in deformation and fragmentation of the coal mass near the opening under the influence of stress, causing it to move towards the outburst mouth. However, due to the obstructive effect of the thin film, no pressure differential was formed around the outburst opening, preventing the outburst of the coal. According to the report of Wang et al. (2018), the release of a certain level of coal stress alone cannot lead to an outburst without the involvement of gas. In the third group of experiments, while keeping other conditions unchanged, there was no contact between the coal mass near the outburst opening and the barrier plate. Therefore, during the outburst moment, when the outburst barrier plate was removed, there was no depressurization, fragmentation, or deformation of the coal mass near the outburst opening. Although there was a pressure difference between the coal seam gas and the atmosphere at this time, the resistance of the coal mass prevented the occurrence of an outburst. The analysis mentioned above leads to the conclusion that the impact of ground stress on outbursts is primarily evident during the occurrence of the outburst, if the ground stress cannot be rapidly released at that moment, its influence on the outburst will be significantly reduced. For instance, when the outburst baffle does not contact with the coal body, even a slight increase in gas pressure will not occur. Similar conclusion has also been obtained in previous studies (Du and Wang, 2019; Wu et al., 2020), further confirming the rationality of this study.

During the excavation of the coal roadway, three zones persist in front of the working face, including the pressure relief zone, the stress concentration zone, and the original stress zone (Zhang et al., 2020). The pressure relief zone consistently exists during subsequent excavation cycles. Therefore, under equivalent conditions of coal strength and ground stress, a greater gas pressure value is required in the original coal seam for conditions conducive to outbursts as compared to the pressure during rock cross-cut coal. To investigate the impact of original gas pressure in the coal seam on coal and gas outbursts during tunnel excavation, this study conducted 7 sets of coal and gas outburst experiments under varying gas pressures. The experimental parameters are presented in Table 5. Under the conditions of coal tar content of 7%, pressure of briquette of 20 MPa, and ground stress of 10 MPa, a low gas pressure will not induce coal outbursts. However, when the gas pressure increases to 0.72 MPa, the outburst phenomenon occurs, and the outburst coal accounts for about 29.3% of the total coal.

The occurrence of coal and gas outburst is affected by many factors. It is of great significance to establish a method to accurately predict the critical value of coal and gas outburst index in different mining areas to reduce the risk of coal and gas outburst in coal mine production (Amani et al., 2021; Soleimani et al., 2023). Taking Jiulishan Coal Mine (Jiaozuo City, Henan Province, China) as an example, the critical value of mine gas pressure for outburst was determined by experiments. The coal

TABLE 5 The results of outburst experiment under different gas pressure.

Sample	Content of coal tar (%)	Gas pressure (MPa)	Pressure of briquette (MPa)	Ground stress (MPa)	Result
1	7	0.3	20	10	No outburst
2	7	0.37	20	10	No outburst
3	7	0.43	20	10	No outburst
4	7	0.48	20	10	No outburst
5	7	0.49	20	10	No outburst
6	7	0.58	20	10	No outburst
7	7	0.72	20	10	Outburst

briquette containing 7% coal tar was used as the coal sample to meet the requirement of similarity in the physical and mechanical properties of the coal body in the Jiulishan Coal Mine, and the ground stress was approximately 10 MPa calculated based on the burial depth. Preliminary estimation was conducted based on the possible occurrence of gas pressure, starting from 0.30 MPa in the experiments, and no outbursts were observed. Continuing the use of the original coal sample, experiments were conducted with an additional 0.2 MPa of gas pressure under unchanged conditions, and no outbursts occurred. The gas pressure was further increased by 0.2 MPa until reaching 0.72 MPa when an outburst occurred. Then, experiments were continued using the midpoint between the values of gas pressure causing outburst and non-outburst until an outburst occurred. This process continued iteratively until reaching an accuracy of 0.01 MPa. Through experimentation, the critical gas pressure for coal and gas outbursts in the Jiulishan Coal Mine was determined to be 0.6 MPa. The specific experimental steps and methods are shown in Table 6. According to relevant literature data (Zhang, 1995), the gas pressure critical value in the Jiaozuo mining area is 0.6 MPa, which is consistent with the gas pressure critical value determined in this experiment, indicating the accuracy of method used in determining the gas pressure critical value in this experiment.

4.2 The analysis of distribution law of coal cracks in the process of protrusion evolution

The experimental results show that the duration of the coal and gas outburst process is very short, and the time from the beginning to the end of the outburst is less than 0.1 s. After the outburst starts, the coal near the outburst mouth first peels off and pulverizes, and then develops from the surface to the interior and from the shallow to the deep. In order to describe the trajectory of coal ejection from the hole during the outburst, the coal in the experimental device can be divided into three parts: upper, middle, and lower. The upper part refers to the coal section that corresponds to the horizontal height where the outburst mouth is located, the middle part refers to the coal section at the same horizontal height as the outburst mouth, the lower part refers to the coal section below the horizontal height where the outburst mouth is located. The coal in the upper part near the outburst section is directly ejected from the outburst mouth after stripping off the coal wall. The coal far away from the outburst mouth is affected by the combined force of gas pressure and radial stress, and the trajectory of its movement is parabolic ejection, while under the obstruction of the coal in front, the coal that is unable to be ejected falls down under the influence of gravity in the lower part. The coal corresponding to the height of the outburst mouth moves towards the outburst mouth in a near-horizontal manner. The coal in the lower part moves towards the outburst mouth under the influence of gas pressure, and due to the inability to eject horizontally, its trajectory of movement near the outburst head is approximately arched and upward, and it is finally expelled rapidly after reaching the outburst mouth.

After the outburst starts, the outburst mouth of the coal body opens, the coal body is thrown out, and the broken coal accumulates near the outburst hole. A slight movement towards the outburst mouth can be observed in the accumulated coal after a short interval following the first outburst. This is because the crushed coal accumulated after the first outburst obstructs the gas outflow channel, leading to an increase in gas pressure inside the hole. When the gas pressure within the hole reaches a high level, the broken coal in the hole will be forcefully expelled by the gas pressure, resulting in a decrease in the gas pressure within the hole. The broken coal in the cavity will be forcefully ejected when the gas pressure reaches a high level. As the difference between the gas pressure inside the hole and the gas pressure in the coal wall increases, when the pressure difference reaches a certain level, another outburst may occur. Therefore, coal and gas outbursts are not completed in a single occurrence, but rather in an intermittent development process, and similar results were also observed by Cheng et al. (2023).

4.3 The analysis of the interaction of stress, gas pressure and coal body in the process of protrusion

The interaction of stress, gas pressure and coal body in the process of protrusion is a complex problem, in order to analyze this interaction in depth, this paper carries out several sets of experiments and selects the typical experimental results to illustrate them.

According to Figure 7, the relationship between the coal solidity coefficient and gas pressure can be obtained as shown in Eq. 3:

$$f = 0.066e^{1.893p} \tag{3}$$

In Eq. 3, it can be seen that the gas pressure required to reach the protrusion condition increases as the coal body firmness coefficient increases.

Also, Eq. 4 can be obtained from Figure 8:

$$p = -0.019\sigma + 0.538 \tag{4}$$

TABLE 6 Determination of the critical value of gas pressure in Jiulishan Coal Mine.

Sample	Content of coal tar (%)	Gas pressure (MPa)	Pressure of briquette (MPa)	Ground stress (MPa)	Result
1	7	0.30	20	10	No outburst
2	7	0.49	20	10	No outburst
3	7	0.72	20	10	Outburst
4	7	0.58	20	10	No outburst
5	7	0.65	20	10	Outburst
6	7	0.615	20	10	Outburst
7	7	0.6	20	10	Outburst

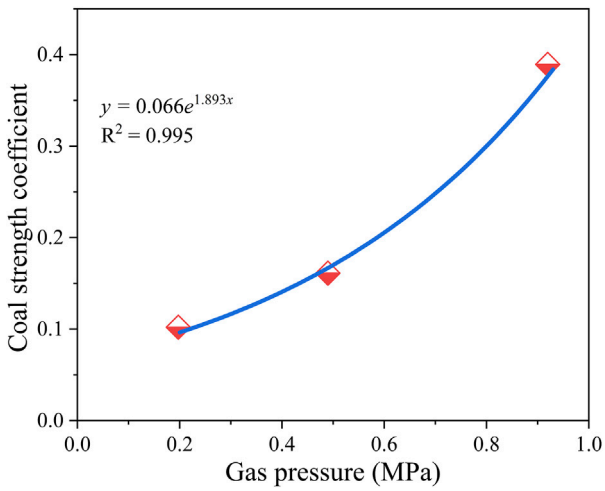

FIGURE 7
Fitting of gas pressure and coal properties.

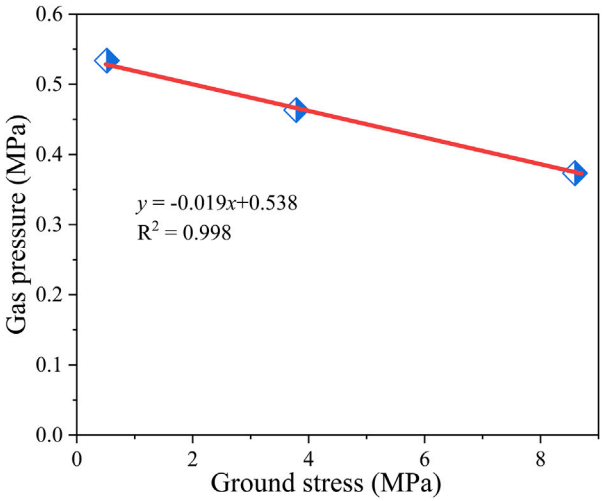

FIGURE 8
Fitting of ground stress and gas pressure.

According to Eq. 4, it can be seen that the gas pressure required for protrusion decreases as the ground stress increases. However, when the gas pressure reaches a certain value, protrusion may still occur even if the ground stress is small. Specifically, whether or not protrusion occurs also depends on the physical and mechanical properties of the coal body.

Eq. 5 can be obtained by substituting Eq. 3 into Eq. 4:

$$f = 0.183e^{-0.036\sigma} \tag{5}$$

It follows that the relationship between the three elements that determine the critical value is shown in Eq. 6.

$$\begin{cases} f = 0.066e^{1.893p} \\ p = -0.019\sigma + 0.538 \\ f = 0.183e^{-0.036\sigma} \end{cases} \tag{6}$$

5 Conclusion

In this paper, a protrusion simulation experiment system that integrates ground stress, gas pressure and coal properties is developed. Through the simulation experiment, the roles of ground stress, gas pressure and coal properties in outburst were studied, and the outburst experiment result data are fitted. With the increase of coal hardness, the gas pressure and ground stress required for outburst increase. In addition, the relationship between gas pressure and ground stress is also found, that is, increasing ground stress will lead to a decrease in the gas pressure required for outburst. It is worth noting that when the gas pressure reaches a certain value, protrusion is able to occur even if the ground stress is small. In addition, this paper proposes a method to determine the critical value for coal and gas protrusion prediction, and studies and determines the critical value of gas pressure of 0.6 MPa in Jiulishan Coal Mine (Jiaozuo City, Henan Province, China).

Data availability statement

The raw data supporting the conclusion of this article will be made available by the authors, without undue reservation.

Author contributions

JO: Conceptualization, Data curation, Formal Analysis, Funding acquisition, Investigation, Methodology, Project administration, Software, Writing–original draft, Writing–review and editing. EW: Funding acquisition, Writing–review and editing. ZL: Conceptualization, Data curation, Formal Analysis, Investigation, Writing–review and editing. NL: Methodology, Project administration, Resources, Writing–review and editing. HL: Software, Supervision, Validation, Visualization, Writing–review and editing. XW: Formal Analysis, Resources, Visualization, Writing–review and editing.

Funding

The author(s) declare financial support was received for the research, authorship, and/or publication of this article. This work was supported by the National Natural Science Foundation of China (No. 51974305) and the National Key R&D Program of China (2022YFC3004705).

Conflict of interest

The authors declare that the research was conducted in the absence of any commercial or financial relationships that could be construed as a potential conflict of interest.

Publisher's note

All claims expressed in this article are solely those of the authors and do not necessarily represent those of their affiliated organizations, or those of the publisher, the editors and the reviewers. Any product that may be evaluated in this article, or claim that may be made by its manufacturer, is not guaranteed or endorsed by the publisher.

References

Agrawal, H., Durucan, S., Cao, W., Korre, A., and Shi, J.-Q. (2023). Rockburst and gas outburst forecasting using a probabilistic risk assessment framework in longwall top coal caving faces. *Rock Mech. Rock Eng.* 56 (10), 6929–6958. doi:10.1007/s00603-022-03076-3

Amani, K., Najafi, M., and Rafiee, R. (2021). Prediction of coal and gas outburst risk by fuzzy rock engineering system. *Environ. Earth Sci.* 80 (15), 491. doi:10.1007/s12665-021-09782-5

Black, D. J. (2019a). Review of coal and gas outburst in australian underground coal mines. *Int. J. Min. Sci. Technol.* 29 (6), 815–824. doi:10.1016/j.ijmst.2019.01.007

Black, D. J. (2019b). Review of current method to determine outburst threshold limits in Australian underground coal mines. *Int. J. Min. Sci. Technol.* 29 (6), 859–865. doi:10.1016/j.ijmst.2019.03.002

Cheng, L., Xu, J., Peng, S., Yang, H., Jiao, F., Zhou, B., et al. (2023). Dynamic behavior of outburst two-phase flow in a coal mine t-shaped roadway: the formation of impact airflow and its disaster-causing effect. *Int. J. Min. Sci. Technol.* 33 (8), 1001–1017. doi:10.1016/j.ijmst.2023.03.011

Du, F., and Wang, K. (2019). Unstable failure of gas-bearing coal-rock combination bodies: insights from physical experiments and numerical simulations. *Process Saf. Environ. Prot.* 129, 264–279. doi:10.1016/j.psep.2019.06.029

Feldman, E. P., Kalugina, N. A., and Meln'ik, T. N. (2017). Role of unloading and filtration of gas in the development of main cracks in coal seams. *J. Appl. Mech. Tech. Phys.* 58 (1), 155–164. doi:10.1134/s0021894417010175

Gao, K., Huang, P., Liu, Z., Liu, J., Shu, C., and Qiao, G. (2021). Coal-rock damage characteristics caused by blasting within a reverse fault and its resultant effects on coal and gas outburst. *Sci. Rep.* 11 (1), 19158. doi:10.1038/s41598-021-98581-w

Gawor, M., and Wasilewski, S. l. (2021). Investigations of dynamic properties of an integrated methane and rock outburst sensor. *Measurement* 186, 110178. doi:10.1016/j.measurement.2021.110178

Godyn, K., and Kozusnikova, A. (2019). Microhardness of coal from near-fault zones in coal seams threatened with gas-geodynamic phenomena, upper silesian coal basin, Poland. *Energies* 12 (9), 1756. doi:10.3390/en12091756

Jiang, C., Xu, L., Li, X., Tang, J., Chen, Y., Tian, S., et al. (2015). Identification model and indicator of outburst-prone coal seams. *Rock Mech. Rock Eng.* 48 (1), 409–415. doi:10.1007/s00603-014-0558-0

Jin, K., Cheng, Y., Ren, T., Zhao, W., Tu, Q., Dong, J., et al. (2018). Experimental investigation on the formation and transport mechanism of outburst coal-gas flow: implications for the role of gas desorption in the development stage of outburst. *Int. J. Coal Geol.* 194, 45–58. doi:10.1016/j.coal.2018.05.012

Koziel, K., Nowakowski, A., Sitek, L., and Skoczylas, N. (2022). Rock and gas outbursts in copper mines: use of brazilian tests to evaluate the work of disintegration of rock resulting from stresses produced by gas present in its porous structure. *Rock Mech. Rock Eng.* 55 (10), 6209–6225. doi:10.1007/s00603-022-02955-z

Kursunoglu, N., and Onder, M. (2019). Application of structural equation modeling to evaluate coal and gas outbursts. *Tunn. Undergr. Space Technol.* 88, 63–72. doi:10.1016/j.tust.2019.02.017

Kursunoglu, N., and Onder, M. (2023). Coal and gas outburst risk assessment using cluster analysis method. *Acta Montan. Slovaca* 28 (2), 325–343. doi:10.46544/AMS.v28i2.06

Li, H., Li, X., Fu, J., Zhu, N., Chen, D., Wang, Y., et al. (2023). Experimental study on compressive behavior and failure characteristics of imitation steel fiber concrete under uniaxial load. *Constr. Build. Mater.* 399 (8), 132599. doi:10.1016/j.conbuildmat.2023.132599

Li, J., Hu, Q., Yu, M., Li, X., Hu, J., and Yang, H. (2019). Acoustic emission monitoring technology for coal and gas outburst. *Energy Sci. Eng.* 7 (2), 443–456. doi:10.1002/ese3.289

Liu, H., Li, X., Yu, Z., Tan, Y., Ding, Y., Chen, D., et al. (2023). Influence of hole diameter on mechanical properties and stability of granite rock surrounding tunnels. *Phys. Fluids* 35 (6), 064121. doi:10.46544/AMS.v28i2.06

Mekhtiev, A. D., Yurchenko, A. V., Ozhigin, S. G., Neshina, E. G., and Al'kina, A. D. (2021). Quasi-distributed fiber-optic monitoring system for overlying rock mass pressure on roofs of underground excavations. *J. Min. Sci.* 57 (2), 354–360. doi:10.1134/s1062739121020198

Odintsev, V. N., and Makarov, V. V. (2020). Dynamic fracture of gas-bearing coal seam during zonal disintegration. *J. Min. Sci.* 56 (6), 932–946. doi:10.1134/s106273912006006x

Odintsev, V. N., and Shipovskii, I. E. (2019). Simulating explosive effect on gas-dynamic state of outburst-hazardous coal band. *J. Min. Sci.* 55 (4), 556–566. doi:10.1134/s1062739119045904

Remennikov, A., Kalubadanage, D. M., Yang, X., and Ren, T. (2022). The development of specialised modular protective structure on continuous miners against coal burst hazards. *Int. J. Prot. Struct.* 13 (2), 182–208. doi:10.1177/20414196211069574

Rudakov, D., and Sobolev, V. (2019). A mathematical model of gas flow during coal outburst initiation. *Int. J. Min. Sci. Technol.* 29 (5), 791–796. doi:10.1016/j.ijmst.2019.02.002

Shadrin, A. V., Diyuk, Y. A., and Teleguz, A. S. (2022). Substantiation of informational system for coal seam outburst danger continuous prediction with high level of the result veracity. *Russ. J. Earth Sci.* 22 (4), ES4001–21. doi:10.2205/2022es000799

Shang, S., Zhang, Q., Zhao, Y., Diao, Y., Yin, J., Che, Y., et al. (2023). Experimental research of the geo-stress evolution law and effect in the intact coal and gas outburst process. *Front. Earth Sci.* 10, 1036165. doi:10.3389/feart.2022.1036165

Soleimani, F., Si, G., Roshan, H., and Zhang, Z. (2023). Numerical modelling of coal and gas outburst initiation using energy balance principles. *Fuel* 334, 126687. doi:10.1016/j.fuel.2022.126687

Ul'yanova, E. V., Malinnikova, O. N., Pashichev, B. N., and Malinnikova, E. V. (2019). Microstructure of coal before and after gas-dynamic phenomena. *J. Min. Sci.* 55 (5), 701–707. doi:10.1134/s1062739119056063

Wang, H., Zhang, B., Yuan, L., Yu, G., and Wang, W. (2018). Gas release characteristics in coal under different stresses and their impact on outbursts. *Energies* 11 (10), 2661. doi:10.3390/en11102661

Wu, X., Peng, Y., Xu, J., Yan, Q., Nie, W., and Zhang, T. (2020). Experimental study on evolution law for particle breakage during coal and gas outburst. *Int. J. Coal Sci. Technol.* 7 (1), 97–106. doi:10.1007/s40789-019-00284-1

Yuan, A., Fu, G., and Hou, J. (2021). A multiscale structural analysis of soft and hard coal deposits in deep high-gas coal seams. *Adv. Civ. Eng.* 2021, 1–11. doi:10.1155/2021/8865038

Yuan, L. (2017). Scientific conception of precision coal mining. *J. China Coal Soc.* 42 (1), 1–7. doi:10.13225/j.cnki.jccs.2016.1661

Zhang, G. (1995). The prediction of coal and gas outburst in Jiaozuo mining area. *J. Jiaozuo Min. Inst.* 14 (1), 71–75.

Zhang, H., Wen, Z., Yao, B., and Chen, X. (2020). Numerical simulation on stress evolution and deformation of overlying coal seam in lower protective layer mining. *Alexandria Eng. J.* 59 (5), 3623–3633. doi:10.1016/j.aej.2020.06.011

Zhao, B., Wen, G., Ma, Q., Sun, H., Yan, F., and Nian, J. (2022). Distribution characteristics of pulverized coal and stress-gas pressure-temperature response laws in coal and gas outburst under deep mining conditions. *Energy Sci. Eng.* 10 (7), 2205–2223. doi:10.1002/ese3.1129

Zheng, X., Lai, W., Lei, Z., and Sheng, X. (2023). Quantitative evaluation of the indexes contribution to coal and gas outburst prediction based on machine learning. *Fuel* 338, 127389. doi:10.1016/j.fuel.2023.127389

Zhu, J., Shao, T., Li, G., Yang, Y., Chen, Z., Lan, T., et al. (2022). Multiscale pore structure characteristics and crack propagation behavior of coal samples from high gas seam. *Materials* 15 (13), 4500. doi:10.3390/ma15134500

frontiers | Frontiers in Earth Science

TYPE Original Research
PUBLISHED 08 January 2024
DOI 10.3389/feart.2023.1297690

OPEN ACCESS

EDITED BY
Zhibo Zhang,
University of Science and Technology Beijing, China

REVIEWED BY
Guo-Feng Liu,
Chang'an University, China
Wenjing Niu,
Guangxi University, China

*CORRESPONDENCE
Juan Wang,
juanwang618@126.com

RECEIVED 20 September 2023
ACCEPTED 23 November 2023
PUBLISHED 08 January 2024

CITATION
Sun P, Wang J and Yan Z (2024), Enhancing rock and soil hazard monitoring in open-pit mining operations through ultra-short-term wind speed prediction.
Front. Earth Sci. 11:1297690.
doi: 10.3389/feart.2023.1297690

Enhancing rock and soil hazard monitoring in open-pit mining operations through ultra-short-term wind speed prediction

Pengxiang Sun, Juan Wang* and Zhenguo Yan

Shaanxi Key Laboratory of Nanomaterials and Nanotechnology, Xi'an University of Architecture and Technology, Xi'an, Shaanxi, China

Wind speed exacerbates challenges associated with rock stability, introducing factors such as heightened erosion and the possibility of particle loosening. This increased sensitivity to erosion can result in material displacement, thereby compromising the overall stability of rock layers within the open-pit mining site. Therefore, accurate wind speed predictions are crucial for understanding the impact on rock stability, ensuring the safety and efficiency of open-pit mining operations. While most existing studies on wind speed prediction primarily focus on making overall predictions from the entire wind speed sequence, with limited consideration for the stationarity characteristics of the sequence, This paper introduces a novel approach for effective monitoring and early warning of geotechnical hazards. Our proposed method involves dividing wind speed data into stationary and non-stationary segments using the sliding window average method within the threshold method, validated by the Augmented Dickey-Fuller test. Subsequently, we use temporal convolutional networks (TCN) with dilated causal convolution and long short-term memory to predict the stationary segment of wind speed, effectively improving prediction accuracy for this segment. For the non-stationary segment, we implement complete ensemble empirical mode decomposition with adaptive noise (CEEMDAN) to reduce sequence complexity, followed by TCN with an attention mechanism (ATTENTION) to forecast wind speed one step ahead. Finally, we overlay the predictions of these two segments to obtain the final prediction. Our proposed model, tested with data from an open-pit mining area in western China, achieved promising results with an average absolute error of 0.14 knots, mean squared error of 0.05 knots^2, and root mean squared error of 0.20 knots. These findings signify a significant advancement in the accuracy of short-term wind speed

Abbreviations: TCN, Temporal Convolutional Network; ADF, Augmented Dickey-Fuller; LSTM, Long Short Term Memory; CEEMDAN, Complete Ensemble Empirical Mode Decomposition with Adaptive Noise; GPR, Gaussian Process Regression; GA, Genetic Algorithm; ANN, Artificial Neural Network; VMD, Variational Mode Decomposition; NWP, Numerical Weather Prediction; MOS, Mos Forecasting Method; WRF, Weather Research and Forecasting Model; NWP, Numerical Weather Prediction; ARIMA, Autoregressive Integrated Moving Average Model; SVM, SupportVectorMachine; ANN, Artificial Neural Network; MLP, Multilayer Perceptron; SAM, Segment Anything Model; RBFN, Radial basis function network; GWO, Grey Wolf Optimization; GRU, Gate Recurrent Unit.

prediction. This advancement not only enables the rapid assessment and proactive response to imminent risks but also contributes to geotechnical hazard monitoring in open-pit mining operations.

KEYWORDS

geotechnical disaster warning, TCN, LSTM, CEEMDAN, attention mechanism

1 Introduction

Despite the changing landscape of energy sources, coal remains a vital resource for meeting global energy demands. However, particularly in open-pit settings, face unique challenges related to wind-induced geological hazards (Chen et al., 2019; Wang and Du, 2020; Sun and Wang, 2022; Zhang et al., 2009) found that air flow has a significant impact on the stability of soil slopes (Vardon, 2015). Showed the importance of predicting climate characteristics, especially changes in wind speed, temperature, precipitation, *etc.*, for geotechnical infrastructure. So strong winds in open-pit mining areas significantly elevate the risks associated with rockfalls and mountainous landslides, presenting serious safety concerns for both miners and equipment. These natural hazards, exacerbated by powerful winds, can lead to accidents, damages, and disruptions in mining activities. Addressing these challenges is of utmost importance to ensure the safety and efficiency of coal mining operations (Hepbasli, 2008). The use of wind speed data offers an effective solution for mitigating these risks. By seamlessly integrating wind speed information into geotechnical hazard monitoring systems, mining companies can bolster their capacity to identify and respond to impending geological instabilities triggered or exacerbated by high winds. This integration enables early warnings and the automatic activation of safety protocols, thereby minimizing the potential for accidents and damages (Khazaei et al., 2022). Wind speed prediction emerges as a pivotal component within geotechnical hazard monitoring systems. Providing accurate and real-time wind speed forecasts empowers mining operators to make swift and well-informed decisions, safeguarding the welfare of workers and the integrity of mining operations (Parra et al., 2021). Linked forest coverage, wind speed, and soil stability, and the results showed that higher canopy opening and wind speed can reliably predict a higher probability of landslide detection, although it is much better at lower order channels and mid slope positions than on open slopes. In areas affected by recent volcanic eruptions causing volcanic ash, the predictive ability of wind speed is relatively low, and the impact of forest coverage on canopy openness still exists. Even though scientists already know the effect of wind speed on the stability of open pit soil, the current relevant literature only inputs wind speed as a variable to conduct correlation analysis of the stability of open pit soil. For example, adding wind speed factor to the stability prediction of open-pit slope (Nie et al., 2017), proposed a short and medium term polynomial prediction (MsTPLP) model for landslides based on Levenberg-Marquardt (LM) algorithm. The experimental results show that the proposed model failure time is very accurate, demonstrating the potential of this method in landslide prediction (Kunyan and Meihong, 2019). Proposed an improved BP neural network based on genetic algorithm and proposed a prediction model for open-pit slope stability. The prediction results of the model show that GA-BP model is effective in predicting the stability of open-pit slope, and has the advantages of small error and high calculation accuracy, providing a new method for accurately predicting the stability of open-pit slope. Although wind speed is important for open-pit slope stability, few scientists have applied wind speed prediction alone to mine sites. Hence, the incorporation of wind speed prediction into geotechnical hazard monitoring systems stands as a paramount measure to ensure the safety and sustained success of coal mining operations in open-pit environments (Peng and Lu, 1995; Mölders and Physics, 1999).

Wind speed forecasting can be roughly divided into long-term, short-term, and ultra-short-term wind speed forecasting, each of which has different uses. Long-term wind speed forecasting typically covers extended timeframes, ranging from days to weeks into the future. Its primary purpose is to help plan and manage wind energy resources, assess the feasibility of wind power projects, and inform long-term decision-making in various industries. While it is not directly related to immediate geotechnical hazard monitoring, long-term trends in wind patterns can inform broader risk assessments (Yu et al., 2013)., developed a global Gaussian process regression (GPR) method based on Gaussian mixture copula model (GMCM) and Bayesian inference strategy, using a new aggregated GPR model within the Bayesian framework to explain the stochastic uncertainty in long-term wind speed time series. Short-term wind speed forecasting focuses on predicting wind speeds within a timeframe of hours to days ahead. It plays a crucial role in real-time operation and dispatch of wind power plants, helping to optimize energy production and grid integration. While not directly linked to geotechnical hazard monitoring, short-term forecasts can indirectly impact safety by influencing power plant operation and energy distribution in areas where wind-related hazards are a concern (Zhang et al., 2020). Proposed a short-term wind speed prediction model based on genetic algorithm-artificial neural network (GA-ANN) improved by variational mode decomposition (VMD), which can effectively improve the accuracy of wind speed prediction and greatly promote the development of green energy. Ultra-short-term wind speed forecasting functions within significantly compressed timeframes, often spanning mere minutes to a few hours ahead. Its primary role is to facilitate real-time control, support operational decision-making, and provide immediate hazard monitoring across diverse applications, encompassing both the wind energy sector and critical safety systems. In the realm of geotechnical hazard monitoring, the significance of ultra-short-term wind speed predictions cannot be overstated, as they serve as a linchpin for the swift evaluation and proactive response to imminent risks. These risks encompass a spectrum of perils, ranging from the potential for rockfalls to the looming threat of landslides, all of which may be incited by the forceful influence of high winds. The precision inherent in ultra-

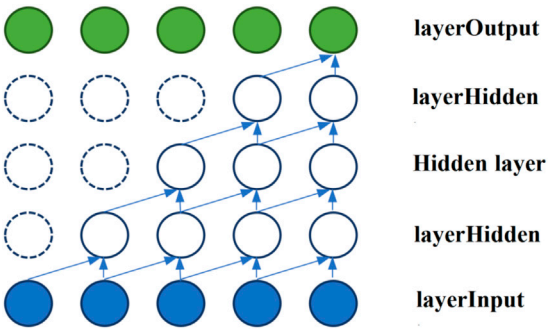

FIGURE 1
Causal convolution in TCN.

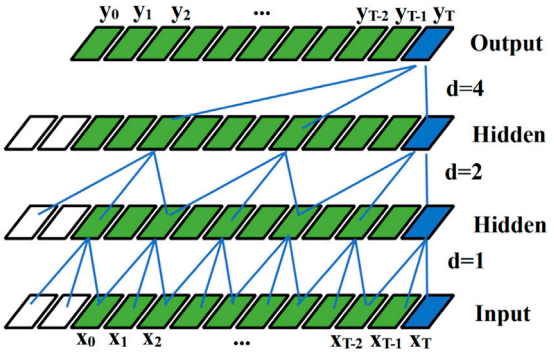

FIGURE 2
Expansion causal convolution.

short-term forecasts empowers stakeholders to issue early warnings and promptly initiate safety protocols, underpinning the resilience and protection of lives, infrastructure, and assets (Chandra et al., 2013; Tascikaraoglu et al., 2014; Ssekulima et al., 2016; Shobana Devi et al., 2020). Accordingly, this study focused on ultra-short-term wind speed prediction.

Existing forecasting models can be generally divided into three categories. The first type covers physical models, which use weather forecasting parameters (NWP) such as terrain, atmosphere, and temperature as input variables, and model output statistics (MOS) or various relatively simple statistical techniques to arrive at the best estimate of the local wind speed before applying physical considerations to reduce the residual error (Giebel et al., 2011; Cheng et al., 2013; Zhang et al., 2019a). Xu et al. used the WRF model to effectively improve the accuracy of short-term wind speed prediction (Xu et al., 2021). Al-Yahyai et al. proposed a NWP prediction method based on physical principles (Al-Yahyai et al., 2010). Through comparisons with measured wind speeds under different wind conditions, they reported that the prediction results can essentially meet the requirements of prediction accuracy. However, their physical model involves complex calculation and long calculation time, and has relatively low accuracy, making it unsuitable for ultra-short-term wind speed prediction (Al-Yahyai et al., 2010).

The second type covers statistical methods. They are widely used because wind speed changes show certain regularity and similarity in the ultra-short term, and the cycle of ultra-short-term wind speed prediction is short. Statistical methods mainly include autoregressive integrated moving average model (ARIMA), support vector machine (SVM), and artificial neural network (ANN) methods (Erdem and Shi, 2011; Liu et al., 2013; Ranganayaki and Deepa, 2019). Liu et al. used the ARIMA model to develop univariate models and evaluated the performance of the method using large amounts of forecasting data (Liu et al., 2021). Kavasseri and Seetharaman predicted wind speed series using the proposed f-ARIMA model and compared its performance with the continuous method, and reported that the proposed model can significantly improve the prediction accuracy (Kavasseri and Seetharaman, 2009). Mohandes et al. introduced the SVM into wind speed prediction, and compared its performance with the multi-layer perceptron (MLP) neural network, and the results showed that SVM has stronger predictive ability (Mohandes et al., 2004). Although the use of statistical methods can enhance the accuracy of wind speed prediction compared with physical model methods, the overall prediction performance of a single statistical method in wind speed prediction is not ideal (Zhang et al., 2019b).

The third type covers hybrid prediction models. It has gradually become the main method among current prediction models owing to its high prediction accuracy and high model applicability. Wang et al. (Wang et al., 2014) proposed a hybrid model for wind speed forecasting based on SAM, ESM, and RBFN, and experiments proved that the proposed model can capture different modes to improve forecasting performance. Kulkarni et al. (Kulkarni et al., 2008) used periodic curve fitting and artificial neural network extrapolation to predict wind speed with reasonable accuracy. Although the above hybrid models can achieve highly accurate wind speed prediction, they are rarely used because the overall models are extremely complex and the prediction time is too long. Instead, decomposition-prediction-combination models and models based on optimization algorithms are most widely used because of their efficiency and accuracy. Wang et al. (Wang et al., 2010). used the variational modal method to decompose the wind speed sequence into a series of different sub-modes to reduce the complexity of the original data and the impact of non-stationarity on the prediction accuracy; subsequently, they performed long short-term memory network (LSTM) modeling predictions separately and finally combined the models to obtain the prediction results. Xiang et al. and Zhang et al. (Zhang et al., 2019c; Xiang et al., 2019) used the wind speed signal preprocessing method based on variational mode decomposition and showed that the proposed method could achieve high prediction accuracy and operating efficiency. Regarding optimization, algorithms such as the whale optimization algorithm (CGWOA), GWO, and bat optimization algorithm (BAT) are widely used to optimize the convergence factor, iteration number, and other related parameters in a single model, so as to obtain better results (Sun et al., 2015; Fu et al., 2019; Zhang et al., 2022a; Li et al., 2022). However, these two hybrid models do not consider the modal aliasing phenomenon produced by recursive

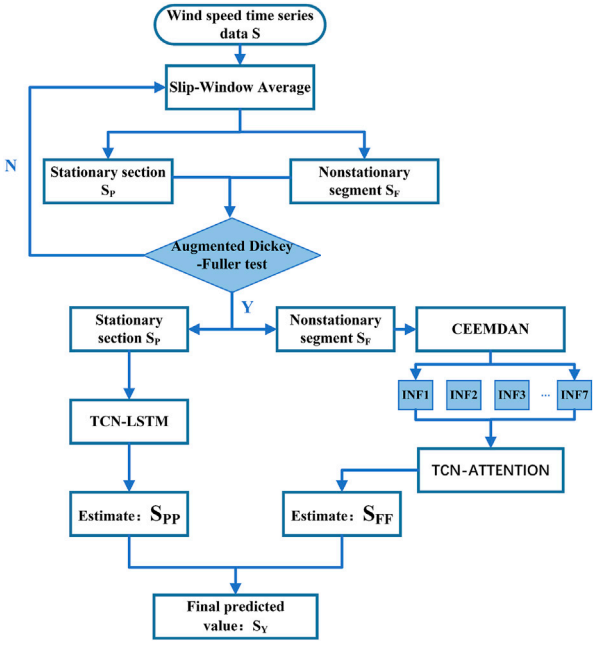

FIGURE 3
Forecast model flowchart.

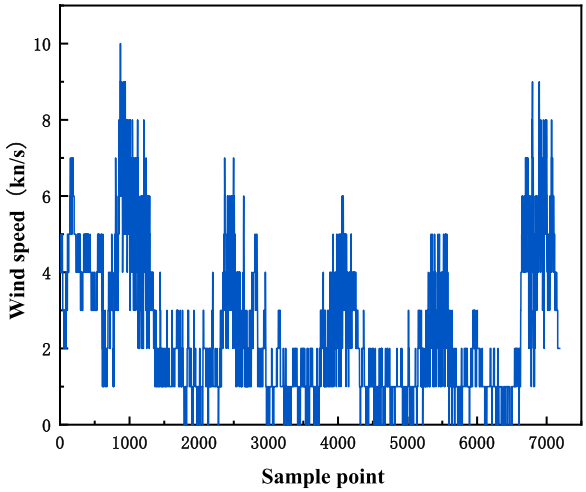

FIGURE 4
Raw wind speed time series.

decomposition algorithms such as empirical mode decomposition, nor do they consider the characteristics of wind speed data in different stationary segments. This leads to problems such as the loss of specific physical meaning of IMF and model-data mismatch.

Based on existing research, this paper proposes a combined prediction model of CEEMDAN, temporal convolutional network (TCN), and LSTM with the introduction of the attention mechanism (ATTENTION). First, the correlation judgment was used to assess the factors affecting wind speed. Then, the wind speed data were divided into stationary and non-stationary segments by using the characteristics of the most relevant factors affecting wind speed. Thereafter, the wind speed in the stationary segment was predicted using the TCN-LSTM combined model, the wind speed in the non-stationary segment was divided into reasonable wind speed components using CEEMDAN, the wind speed components of each part were predicted using the TCN-ATTENTION model, and the wind speed component predictions of each part were combined to obtain the overall wind speed forecast. The model prediction results of the stationary and non-stationary segments were then combined to obtain the final prediction result. Compared with other classical models, this model has better prediction ability and better prediction processing efficiency.

2 Algorithm principle

2.1 TCN algorithm

TCN is a new type of algorithm that can be used to solve time series forecasting. TCN models consist of causal convolutions, dilated/dilated convolutions, and residual blocks (Luo et al., 2021a). Compared with traditional models, such as CNN, LSTM, and GRU, it has a lighter network structure. At the same time, it can effectively avoid common problems of recursive models such as gradient explosion/vanishing problems or lack of memory retention (Luo et al., 2021b). The salient features of TCN are the randomness of convolution architecture design and sequence length. In addition, through the combination of residual networks and expanded convolution, it is also very convenient for constructing deep and wide networks (Huang et al., 1998).

The overall principle of causal convolution is shown in Figure 1. The causal convolution at time t is only affected by the value of the lower layer at time t. It is a one-way structure rather than a two-way structure.

The main structure of TCN is the expansion causal convolution based on causal convolution, which reduces the number of layers used by the convolutional network and increases the receptive field by inputting larger intervals of sampling data. The receptive field is affected by parameter d of the dilated convolution and the number of layers k. For the filter f: (f1, f2 · · · fk), the operation formula of the expansion causal convolution is:

$$F(X) = \sum_{i=0}^{k-1} f(i) \cdot x_{t-i \cdot d} \tag{1}$$

The principle of dilated causal convolution is shown in Figure 2. As shown in the schematic diagram, increasing K or d can increase the receptive field. In general, as the number of layers increases, the dilated convolution parameters will increase according to the exponent of 2. In this paper, the expansion coefficient d is 1, 2, and 4, the expansion causal convolution with the number of layers k is 3, and the one-dimensional convolutional network is used to obtain the information of the previous layer by changing the parameters, so as to flexibly adjust the receptive field size. The TCN gradient does not have the problem of gradient disappearance/explosion because it is different from the time direction. It can be used for ultra-short-term wind speed forecasting with good clarity and simplicity.

TABLE 1 Data parameters.

Serial number	0	1	2	3	4	5	6
Title letter	WS	DIR	DIR 5S	TEMP	DPT	WS 5S	PRESS
Parameter (Unit)	Wind speed (knots)	wind direction	Five second gust wind direction	Temperature (F)	Dew point temperature (F)	Five second gust wind speed (knots)	Pressure (pa)

TABLE 2 Missing data situation.

Norm	Date	Time	WS	DIR	DIR 5S	TEMP	DPT	WS 5S	PRESS
Missing	False	False	True	True	True	False	False	True	False
Missing quantity	0	0	5	5	5	0	0	5	0
Percentage missing	0	0	0.000694	0.000694	0.000694	0	0	0.000694	0

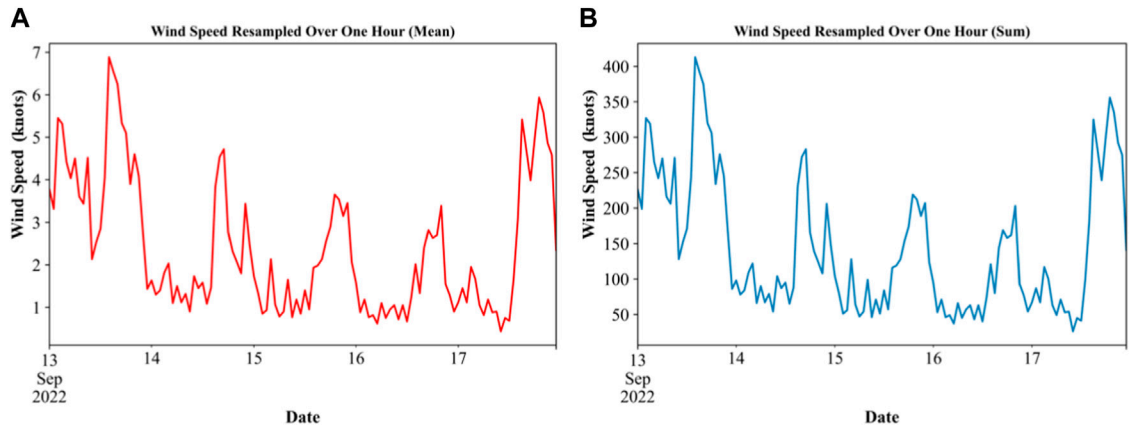

FIGURE 5
Hourly resampling of wind speed. **(A)**: Hourly resampling sum of wind speed over time, **(B)**: Hourly resampled mean wind speed over time.

2.2 CEEDMEAN algorithm

Empirical mode decomposition (EMD) is a means of smoothing non-stationary signals by converting a signal sequence into multiple intrinsic mode functions (IMFs) and residuals. EMD has been widely used in various fields but it still involves the problems of the mode aliasing phenomenon and end effect (Zhang et al., 2019b). These problems can be effectively suppressed by CEEMD.

The specific operation steps are as follows: first, the original signal x(t) to be decomposed is added to K times of Gaussian white noise with an average value of 0, and k times of sequences to be decomposed are constructed, i=1,2,3 . . . k.

$$x_i(t) = x(t) + \varepsilon\delta_i(t) \tag{2}$$

Where ε is the weight coefficient of Gaussian white noise; $\delta_i(t)$ is the Gaussian white noise generated during the ith processing.

Then, decompose the empirical mode $x_i(t)$ and take the mean value of the first modal component obtained as the first modal component obtained $\mathrm{IMF}_1(t)$ by CEEMDAN decomposition. Subsequently, obtain the margin signal of the first decomposition $\mathrm{IMF}_1(t)$.

$$IMF_1(t) = \frac{1}{K}\sum_{i=1}^{K} IMF_1^i(t) \tag{3}$$

$$r_1(t) = x(t) - IMF_1(t) \tag{4}$$

Add specific noise to the margin signal at the jth stage and continue the EMD.

$$IMF_j(t) = \frac{1}{K}\sum_{i=1}^{K} IMF_1^i(t) \tag{5}$$

$$r_1(t) = x(t) - IMF_1(t) \tag{6}$$

Finally, if the EMD stops, the iteration stops and the CEEMDAN decomposition ends.

In this paper, CEEMDAN is mainly used to decompose the wind speed fluctuation segment, thereby reducing the complexity of the data, stabilizing the data, and preparing for the subsequent TCN-ATTENTION prediction.

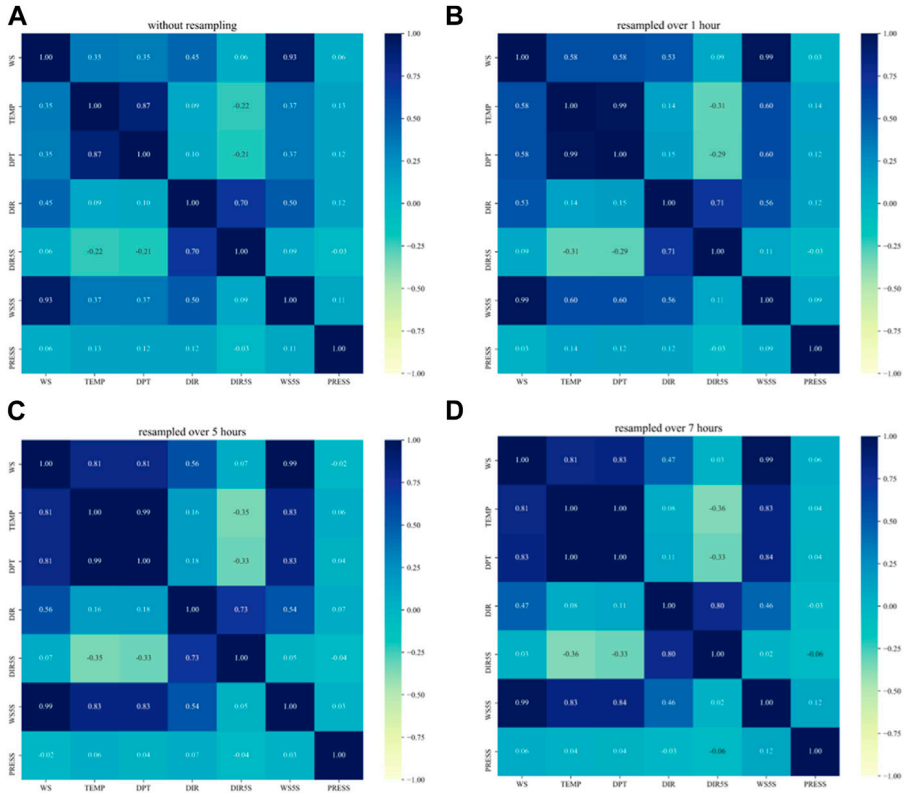

FIGURE 6
Data correlation test. **(A)**: Correlation of variables in raw data, **(B)**: Correlation of variables after 1-h resampling, **(C)**: Correlation of variables after 5-h resampling, **(D)**: Correlation of variables after 7-h resampling.

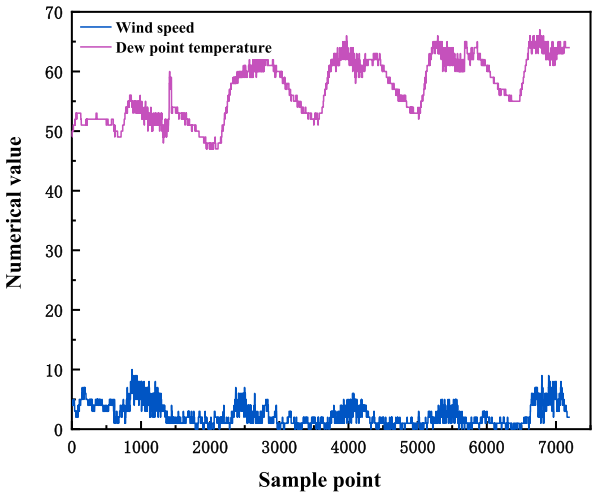

FIGURE 7
Sequence diagram of wind speed and dew point temperature.

2.3 Combined model of TCN-LSTM-CEEMDAN-ATTENTION

The TCN-LSTM-CEEMDAN-ATTENTION model (Figure 3) was established to predict the wind speed. As mentioned earlier, the wind speed data included the stationary and non-stationary segments. The LSTM model optimized by TCN has a strong ability to analyze and predict the data of the stationary segment. Furthermore, the TCN model after CEEMDAN decomposition and the subsequent addition of the attention mechanism has good performance for the separate prediction of the non-stationary segment.

Assuming the wind speed time series data S, firstly, the sliding window averaging method is used to distinguish the stationary segment S_P and the non-stationary segment S_F, and secondly, the TCN-LSTM model is used to predict the stationary segment S_P to obtain S_{PP}. Thereafter, the non-stationary segment S_F is decomposed by CEEMDAN to get INF={infi,i=1,2, . . .,7}. Then, each part of INF is predicted using TCN-ATTENTION to obtain S_{FF}. Finally, the two parts are combined and merged to obtain the final prediction result of the target sequence data $S_Y = S_{PP} + S_{FF}$.

The stationary segment S_P is an input sequence of length, where represents the input of the th time step. The first layer convolution operation of the TCN model can be expressed as:

$$z_t^{(l)} = \phi\left(W^{(l)x_t^{(l)}} + b^{(l)}\right) \tag{7}$$

Where $x^{(l)}t = [ht - k^{(l)} + 1, h_{t-k^{(l)}+2}, \ldots, h_t]$ represents the output vector of the current time step t and its previous time step $k^{(l)} - 1$, $W^{(l)} \in R^{F^{(l)} \times k^{(l)}}$ is a convolution kernel, $b^{(l)} \in R^{F^{(l)}}$ is a bias vector, and ϕ is a nonlinear activation function, usually ReLU. $z_t^{(l)} \in R^{F^{(l)}}$ represents the output vector of the convolutional operation of layer.

TABLE 3 Threshold selection.

Threshold	1.0	1.1	1.2	1.3	1.4	1.5	1.6	1.7	1.8	1.9	2.0
MSE	0.1435	0.2541	0.1298	0.1023	0.1134	0.1145	0.1435	0.1531	0.1083	0.1032	0.0971
Threshold	2.1	2.2	2.3	2.4	2.5	2.6	2.7	2.8	2.9	3.0	3.1
MSE	0.0990	0.0931	0.1221	0.1264	0.1647	0.2633	0.2311	0.2653	0.2835	0.2648	0.2532

TABLE 4 Smooth sequence delineation of timing nodes.

Parameters	2022.9.13	2022.9.14	2022.9.15	2022.9.15
Data Segmentation Node	14:09	15:20	15:20	16:19

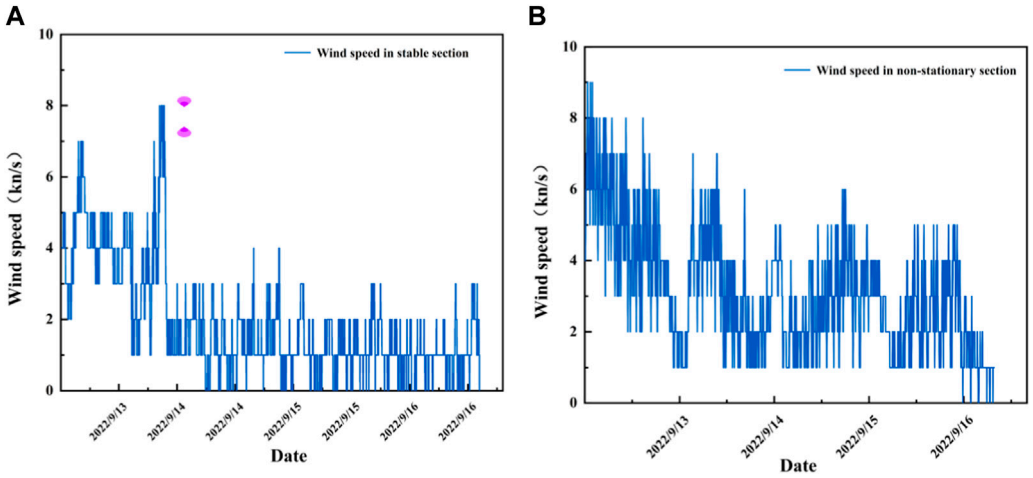

FIGURE 8
Stability division of wind speed training data. **(A)**: Smooth sequence segment of training data, **(B)**Training data non-stationary sequence segments.

TABLE 5 Using ADF test to partition data.

Sequences / parameters	First paragraph	Second paragraph	Sequences / parameters	First paragraph	Second paragraph
Adt test (T-value)	−4.2045	−3.0680	Value of critical ADF test at 99% confidence interval	−3.4322	−3.4334
p-value	0.00064	0.02901	Value of critical ADF test at 95% confidence interv	−2.8623	−2.8629
Procrastinate	16	23	Value of critical ADF test at 90% confidence interv	−2.5671	−2.56749
Number of tests	3,582	2,127	Smoothness judgment	smoothly	non-stationary

The layer l convolution operation of the TCN model can be concatenated to form the output vector z_t of the entire TCN model:

$$z_t = \left[z_t^{(1)}, z_t^{(2)}, \ldots, z_t^{(L)}\right] \tag{8}$$

Where L is the number of layers in the TCN model, 1 represents the output vector of the TCN model.

The hidden state vector of the LSTM model h_t can be expressed as:

$$i_t = \sigma\left(W_{ix_t} + U_{ih_{t-1}} + b_i\right) \tag{9}$$

$$f_t = \sigma\left(W_{fx_t} + U_{fh_{t-1}} + b_f\right) \tag{10}$$

$$o_t = \sigma\left(W_{ox_t} + U_{oh_{t-1}} + b_o\right) \tag{11}$$

$$\tilde{c_t} = \tanh\left(W_{cx_t} + U_{ch_{t-1}} + b_c\right) \tag{12}$$

$$\mathrm{c_t} = \mathrm{f_t} \odot \mathrm{c_{t-1}} + \mathrm{i_t} \odot \tilde{\mathrm{c}}_\mathrm{t} \tag{13}$$

$$\mathrm{h_t} = \mathrm{o_t} \odot \tanh\left(\mathrm{c_t}\right) \tag{14}$$

Here, $\mathbf{i_t}$, $\mathbf{f_t}$, and $\mathbf{o_t}$ respectively represent the activation vectors of the input gate, forget gate, and output gate; $\tilde{c_t}$ represents the

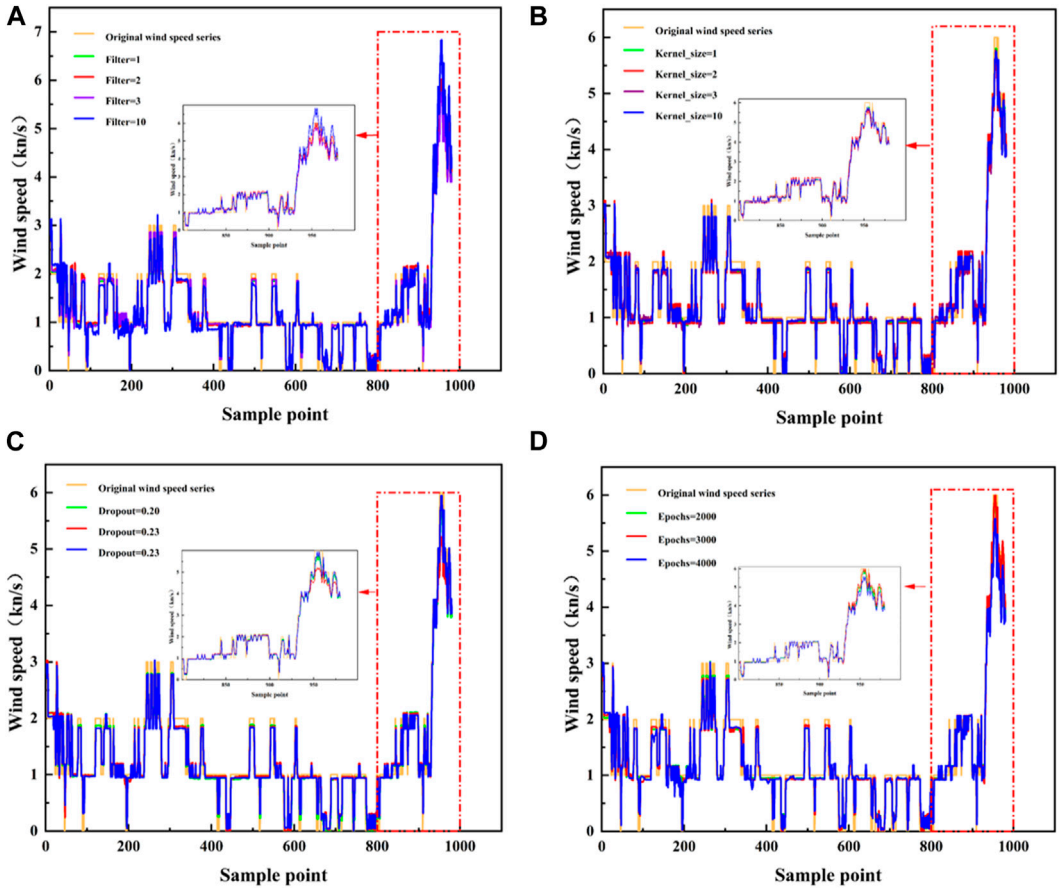

FIGURE 9
TCN-LSTM model tuning. **(A)** Comparison of predictions of different Filter value models, **(B)** Comparison of model predictions for different Kernel_ size values, **(C)** Comparison of model predictions for different Dropout values, **(D)** Comparison of model predictions for different Epochs values.

candidate cell state vector at the current moment; $\mathbf{c_t}$ represents the cell state vector at the current moment; and $\mathbf{h_t}$ represents the hidden state vector at the current moment. $\mathbf{W_i}, \mathbf{W_f}, \mathbf{W_o}, \mathbf{W_c}$ is the weight matrix of the input gate, forget gate, output gate and candidate cell states, $\mathbf{U_i}, \mathbf{U_f}, \mathbf{U_o}, \mathbf{U_c}$ is the weight matrix of the corresponding hidden state, and $\mathbf{b_i}, \mathbf{b_f}, \mathbf{b_o}, \mathbf{b_c}$ is the bias vector. σ represents the sigmoid function, and $\odot$ represents element-wise multiplication.

The non-stationary segment S_F is decomposed into several IMFs using formula (15).

$$s(t) = \sum_{i=1}^{n} c_i(t) + r_n(t) \tag{15}$$

where $s(t)$ is the non-stationary segment sequence S_F, $c_i(t)$ is the ith IMF, $r_n(t)$ is the remaining item, and n is the number of IMFs.

Then, TCN is applied, that is, formulas (16–18) are applied to better capture long-term dependencies.

$$y = f(x) + g(x) \tag{16}$$

$$f(x) = \sigma(W_1 x + b_1) \tag{17}$$

$$g(x) = \sigma\left(W_2(\delta(x) * x) + b_2\right) \tag{18}$$

where, x is the input sequence, y is the output sequence, σ is the Activation function, W_1, W_2 is the weight matrix, b_1, b_2 is the bias vector, * represents convolution operation, $\delta(x)$ is an extensible Dilated Revolution operation。

Finally, by combining CEEMDAN and TCN, and adding the Attention mechanism, the CEEMDAN-TCNN Attention model (Formula 19) is obtained:

$$h_t = \sum_{i=1}^{n} \alpha_i \cdot T^N\left(C^N(x_{1:T})\right)[i,t] \tag{19}$$

Where, $\boldsymbol{h_t}$ is the output of the first time step, C^N is a CEEMDAN operation, T^N is TCN operation, α_i is the Attention weight.

3 Experimental process

3.1 Data sources

The data was collected from a mining site in western China,specifically an open-pit mining area, spanning from September 13 to 17, 2022, totaling 5 days. A set of 7,200 data points was gathered, each spaced at 1-min intervals, There are six parameters in the data set (Table 1), serving as the focus of our research (see Figure 4). As depicted in the figure, it is evident that the wind speed data exhibits irregular and unstable patterns.

TABLE 6 TCN-LSTM model parameter adjustment evaluation form.

Filters	MAE (knots)	MSE (knots^2)	RMSE (knots)	R^2
2	0.1855	0.0971	0.3116	0.9061
3	0.1927	0.0968	0.3112	0.9063
4	0.1856	0.0980	0.3130	0.9052
10	0.2243	0.1126	0.3356	0.9011
Kernel_size				
1	0.2003	0.0967	0.3114	0.9062
2	0.2276	0.1005	0.3169	0.9028
3	0.1916	0.0999	0.3162	0.9033
10	0.1872	0.09767	0.3125	0.9055
Dropout				
0.20	0.1867	0.0982	0.3134	0.9050
0.23	0.1955	0.1049	0.3239	0.8986
0.26	0.1853	0.0953	0.3087	0.9108
Epochs				
2000	0.1913	0.0953	0.3087	0.9108
3,000	0.1938	0.0970	0.3115	0.9062
4,000	0.2095	0.1041	0.3227	0.8993

3.2 Data stationarity and non-stationarity division

In this study, 7,200 sets of data were used, of which 5,760 were used as the training sequence set of the overall model and the remaining 1,440 were used as the test sequence set to test and verify the generalization ability of the model. First, the shadow matrix method of the original data set was used to assess the lack of data in the data set. The shadow matrix is a copy of the weight matrix, and its value is updated by the main weight matrix. Moreover, its historical information is maintained to a certain extent. If the value of the shadow matrix element is 1, the corresponding position value of the original dataset is a missing state; otherwise, if the value of the shadow matrix element is 0, the corresponding value in the original data set exists. A description of the statistics of missing raw data is provided in Table 2. Considering the low proportion of missing data, the impact of missing data on the integrity of the model is small, and deleting missing data will not cause data deviation. Accordingly, the direct deletion method was used for data preprocessing.

After data preprocessing, the data were resampled at 1-h intervals in order to rapidly and intuitively extract information on the structural kernel properties of the data in the population distribution (Li et al., 2016). Figure 5A presents a graph of the time-varying sum of resampled wind speed for 1 hour, and Figure 5B presents a graph of the time-varying graph of the resampled average value of wind speed for 1 hour. According to the change graph, the average value and sum of the resampled data set have a similar structure, and the overall volatility has certain rules. To improve the accuracy of the data analysis, the original wind speed data and the 1-h, 5-h, and 7-h re-sampling data were tested for correlation. As shown in Figure 6, with increasing the sampling time, the correlation between the wind direction and the 5-s gust wind direction first increases and then decreases, and the correlation characteristics between other variables become more prominent. The reason is that when the resampling interval increases from a smaller value, the correlation will increase because the relationship between data points becomes clearer and more salient. However, after reaching a certain resampling interval, the variation between data points becomes irregular and chaotic, weakening the correlations. This is because the interactions between data points become more difficult to capture and analyze. Therefore, the relationship between resampling interval and correlation usually presents a curve of initial rise followed by a fall.

In the heat map, the correlation trend of wind speed and wind direction, and the wind direction of the 5-s gust all increase first and then decrease, with the highest values of 0.56 and 0.09 respectively. The overall correlation is low. However, the temperature and dew point temperature do not exhibit any downward trend with increasing sampling time. As a result, their correlation is more prominent in the 7-h resampling. For the 7-h interval, the top three variables most correlated with wind speed are 5-s gust wind speed (correlation parameter 1.00), dew point temperature (correlation parameter 0.83), and air temperature (correlation parameter 0.81). As the 5-s gust wind speed was obtained from wind speed data, it is not a factor affecting the wind speed sequence. Moreover, as the dew

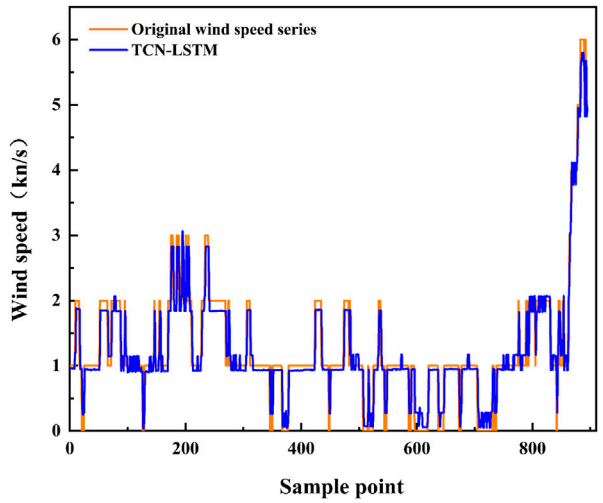

FIGURE 10
Prediction of stationary wind speed data using TCN-LSTM model.

point temperature was calculated from air temperature, humidity, and atmospheric pressure, the reflected data characteristics are more comprehensive. Therefore, the dew point temperature was selected as the largest variable affecting the wind speed. Figure 7 presents a sequence diagram of wind speed and dew point temperature. As shown in the figure, when the dew point temperature is a trough, the wind speed sequence is a stationary segment. The larger the trough span, the longer the duration of the stationary segment of the wind speed sequence.

The preprocessed data were divided using the sliding window average method in the threshold method. First, the time series data were divided into fixed-size sliding windows, and then for each window, the average value of all data in the window was calculated. Using the average value as the representative value of the window, the window was slid forward by one unit, and the average value was continuously calculated until the window slid to the end of the sequence. The optimal threshold range was determined using the grid search method, which is a hyperparameter tuning method for automatically selecting the optimal parameters in the model. It evaluates and compares all possible hyperparameter combinations to find the optimal hyperparameter combination by performing an exhaustive search on a specified parameter grid. The sliding window average method in the threshold method is used to segment the preprocessed data. The time series data is first divided into fixed-size sliding Windows, and then the average of all the data within the window is calculated for each window. Using the mean as the representative value of the window, slide the window forward one unit and continuously calculate the mean until the window slides to the end of the sequence. The optimal threshold range is determined by the grid search method, which is a hyperparameter tuning method that automatically selects the optimal parameters in the model. It evaluates and compares all possible hyperparameter combinations, and finds the optimal hyperparameter combination through exhaustive search of the specified parameter grid. The MyModel class calculates the mean and variance in the time series data. It then traverses the data points to find the first point that breaks the threshold, marking it as non-stationary. This non-stationary point is used to cut the time series data. The program creates a Pipeline with the MyModel class as one of the steps. Define the param_grid parameter, which includes a range of different thresholds. GridSearchCV was used for grid search, and the model performance under different thresholds was evaluated through cross-validation, with MSE as the evaluation index. Finally, the threshold with the best performance was found, the optimal threshold was set to 2.2 (Table 3), and the sliding window average method was used to obtain the time nodes of the stationarity and non-stationarity of the wind speed series on the training day (Table 4). In order to ensure reasonable data segmentation, the average value of time node 15:17 is taken as the segmentation point.

After dividing the data, the unit root (Augmented Dickey-Fuller test, ADF) test was used to conduct time series division test, and the stability of the data was assessed according to the occurrence of ADF in the time series. The presence of ADF indicates unstable data and *vice versa*. In the ADF test, the *p*-value is evaluated against the 0.05 confidence interval. If the *p*-value is less than 0.05, it can be considered that the null hypothesis is rejected, the data does not have a unit root, and the sequence is stable; if it is greater than or equal to 0.05, the null hypothesis cannot be significantly rejected. In this case, further significant test statistics are required. If the significant test statistic is less than three confidence levels (10%, 5%, 1%), then there is (90%, 95, 99%) certainty to reject the null hypothesis, otherwise the data are considered to be non-stationary. The stationary and non-stationary sequences were extracted from the divided training set (Figure 8).

The ADF test results of the extracted data are shown in Table 5. The T value of the first sequence was -4.2045 and less than 1%, 5%, and 10%, indicating rejection of the hypothesis. Moreover, the *p*-value of 0.00064 is significant at 5%, verifying the rejection of the null hypothesis, and thus the stationarity of the data. The T value of the second sequence was -3.0680, and it was not less than 1%, 5%, and 10% at the same time, indicating that the hypothesis cannot be rejected, and that the data is non-stationary. These results proved that partitioning of the data according to stationarity was successful.

3.3 Wind speed prediction and fitting effect

Through the division of data described in the previous section, the stationary and non-stationary data sequences were successfully obtained. Next, TCN-LSTM was used to process the stationary data, and CEEMDAN-TCN-ATTENTION was used to process the non-stationary data.

3.3.1 TCN-LSTM model prediction

Before model training, the wind speed and dew point temperature in the stationary segment and the non-stationary segment sequence were aligned according to the time axis, and the wind speed and dew point temperature at each time point were used as multivariate data at that time point, thereby obtaining a multivariate time series. The model was trained using this multivariate time series.

The TCN-LSTM model was trained with 3,600 sets of data and used to predict the stationary part of the wind speed time series. The sample sequence was converted into a supervised learning sequence and then normalized. The model first defines the TCN model. Then,

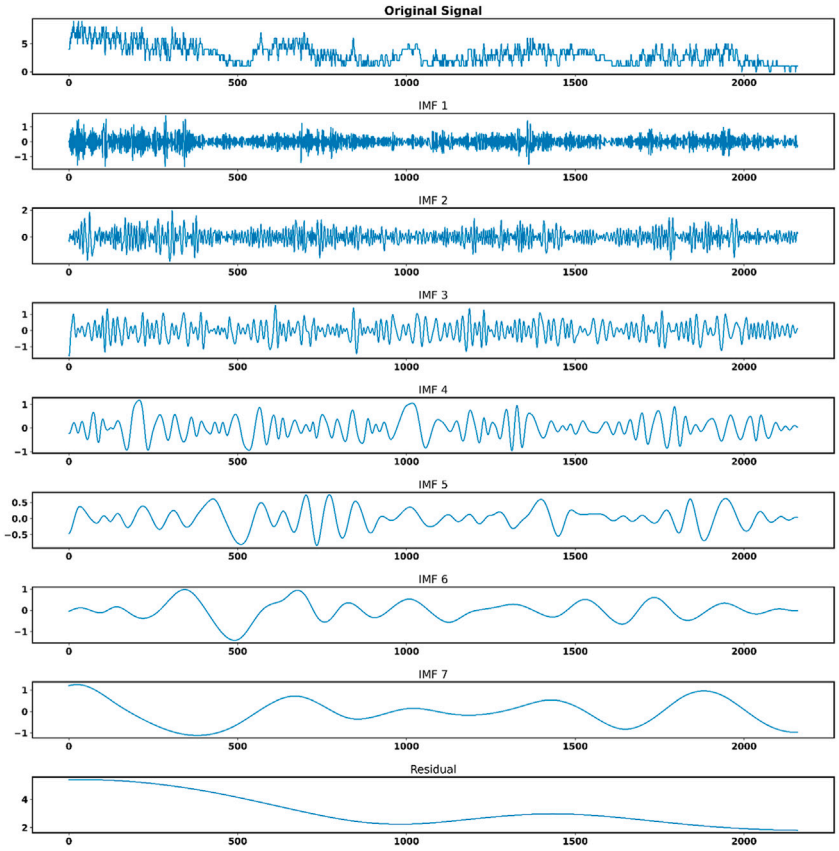

FIGURE 11
CEEMDAN decomposition diagram.

the parameters are optimized using the following evaluation indicators: mean absolute error (MAE), mean squared error (MSE), root mean squared error (RMSE) and R squared error (R2).

The initial parameters were set as follows: loss function MSE, filters=2, Kernel_size=2, Dropout=0.23, Epochs=4,000.

(1) Filter optimization

Filters refer to the number of convolution kernels used in the convolution layer, and each convolution kernel can extract a specific feature. Therefore, the size of filters affects the number and complexity of features learned by the model. With Kernel_size=3, Dropout=0.2, and Epochs=2000, the test sets were compared among Filters of 2, 3, and 4.

As shown in Figure 9 (a) and Table 6, MAE, MSE, RMSE, and R^2 did not exhibit large numerical changes with increasing values of filters. The reason is that the feature space of the input data set is not very complicated, and the use of more filters will not bring significant improvements. In order to obtain more accurate predictions, the filter value was set at 3.

(2) Kernel_size optimization

With Filters=3, Dropout=0.2, and Epochs=2000, the test sets were compared among Kernel_sizes of 1, 2, and 3.

Kernel_size refers to the size of the convolution kernel, which is usually a square or rectangular matrix. The convolution kernel slides and extracts features during the convolution process. Kernel_size will affect the size and shape of the features learned by the model. A larger Kernel_size can usually capture a wider range of features, but it will increase the amount of calculation and the complexity. As shown in Figure 9 (b) and Table 6, the increase in the value of Kernel_size did not cause much change. The reason is that the features in the data set are small, and more useful features cannot be learnt by increasing Kernel_size. To improve the prediction accuracy, the Kernel_size was set at 1.

(3) Dropout optimization

With Filters=3, Kernel_size=10, and Epochs=2000, the test sets were compared among Dropouts of 0.20, 0.23, and 0.26.

As shown in Figure 9 (c), and Table 6, the best results were obtained at Dropout=0.26, with MAE=0.1853 knots, MSE=0.0953 knots^2, RMSE=0.3087 knots, and R2=0.9108.

(4) Epoch optimization

With Filters=3, Kernel_size=10, and Dropout=0.26, the test sets were compared among Epochs of 2000, 3,000 and 4,000.

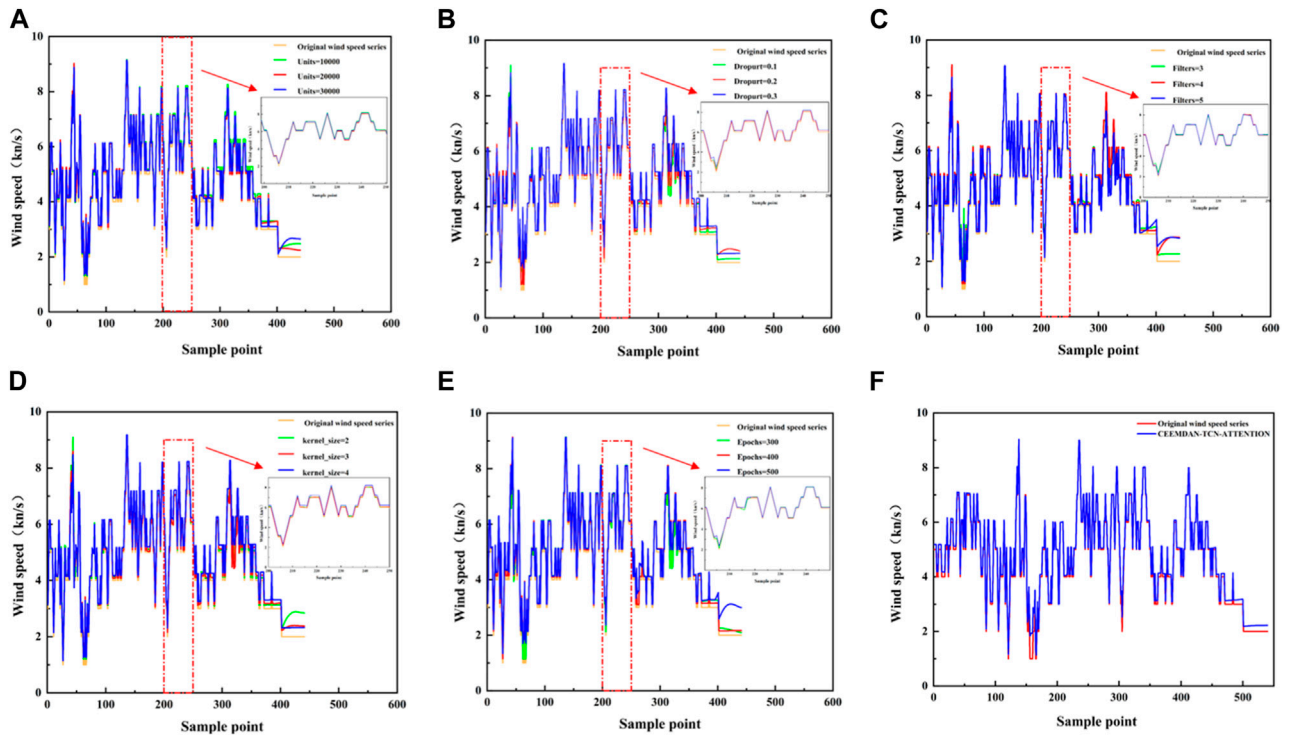

FIGURE 12
CEEMDAN-TCN-ATTENTION model tuning. **(A)** Comparison of model predictions for different Units values, **(B)** Comparison of model predictions for different Dropurt values, **(C)** Comparison of model predictions for different Filters values, **(D)** Comparison of model predictions for different Kernel_size values, **(E)** Comparison of model predictions for different Epochs values, **(F)** Prediction of non-stationary wind speed data.

As shown in Figure 9 (d), and Table 6, the best results were obtained at Epochs=2000, with MAE=0.1913 knots, MSE=0.0953 knots^2, RMSE=0.3087 knots, and R2=0.9108.

Considering these results, the main parameters of the TCN-LSTM wind speed plateau sequence model were set as follows: Filters=3, Kernel_size=10, Dropout=0.26, and Epochs=2000. The comparison between the prediction and actual situation is shown in Figure 10.

3.3.2 CEEMDAN-TCN-ATTENTION model prediction

The CEEMDAN-TCN-ATTENTION model was used to predict the non-stationary segment of the wind speed time series, and 2,160 sets of data were used for training. As shown in Figure 11, CEEMDAN divided the wind speed data were divided into modal components (IMF1–IMF7) and residual sequence (Res), arranged in order of frequency from high to low. In CEEMDAN, each IMF is obtained by extracting and interpolating a series of local mean and extreme points from the original data. Each IMF represents a specific vibrational mode in the data, with distinct time-scale and frequency signatures. Residual series are leftover data, usually considered noise or random disturbances. As shown in Figure 11, IMF1 usually represents high-frequency noise or the trend of high-frequency changes, and may have negligible relationship with independent variables, but IMF2 to IMF7 represent lower and lower frequency components, and the change patterns of these IMFs can reflect each independent variable. Therefore, IMF2 to IMF7 respectively represent the influence of sknt(wind speed), drct(wind direction), gust_drct(5-s gust wind direction), Tmpf,(temperature) Dwpf(dewpoint temperature), gust_sknt(5-s gust wind speed), and pres1(pressure) on wind speed. IMF5 and the original data exhibit the same trend.

Combined with the correlation analysis in Figure 6, the dew point temperature was verified to be the main influencing factor of wind speed, with a positive correlation between them. The TCN-ATTENTION model was then run for each IMF separately.

The model first defines the TCN model, then adds the self-attention layer, and then optimizes related parameters. The following evaluation indicators were used: MAE, MSE, RMSE, and R2.

(1) Unit optimization

In self-attention, the unit parameter is usually used to specify the vector dimension of the input sequence. First, the basic parameters in the combined model were set. In actual use, the size of units can be adjusted according to the application scenario and the complexity of the model. A larger value of units may increase the representation ability of the model, but it will also increase the calculation time and training complexity of the model. The initial parameters were set as follows: loss function MSE, Dropout=0.3, Filters=5, Kernel_size=2, Epochs=300. The performance of the test set was compared with unit sizes of 10,000, 20,000, and 30,000.

TABLE 7 CEEMDAN-TCN-ATTENTION model parameter adjustment evaluation form.

Units	MAE (knots)	MSE (knots^2)	RMSE (knots)	R^2
10,000	0.2231	0.0582	0.2412	0.9792
20,000	0.1602	0.0340	0.1844	0.9879
30,000	0.1767	0.0516	0.2272	0.9816
Dropout	MAE (knots)	MSE (knots^2)	RMSE (knots)	R^2
0.1	0.1509	0.0346	0.1861	0.9877
0.2	0.1096	0.0143	0.1194	0.9929
0.3	0.2294	0.0663	0.2574	0.9764
Filters	MAE (knots)	MSE (knots^2)	RMSE (knots)	R^2
3	0.1499	0.0363	0.1906	0.9870
4	0.1737	0.0661	0.2571	0.9764
5	0.1698	0.0829	0.2879	0.9705
kernel_size	MAE (knots)	MSE (knots^2)	RMSE (knots)	R^2
2	0.1776	0.0696	0.2638	0.9752
3	0.1546	0.0384	0.1959	0.9863
4	0.2366	0.0616	0.2481	0.9781
Epochs	MAE (knots)	MSE (knots^2)	RMSE (knots)	R^2
300	0.2533	0.1377	0.3711	0.9509
400	0.0860	0.1338	0.1157	0.9940
500	0.1705	0.0370	0.1923	0.9868

As shown in Figure 12A and Table 7, the best performance was achieved at the unit size of 20,000, with MAE, MSE, RMSE, and R2 of 0.1602 knots, 0.0340 knots ^{2}, 0.1844 knots, and 0.9879, respectively.

(2) Dropout optimization

With Units=20,000, Filters=5, Kernel_size=2, and Epochs=300, the test sets with Dropout of 0.1, 0.2, and 0.3 were compared.

As shown in Figure 12Band Table 7, the best performance was achieved at the dropout of 0.2, with MAE, MSE, RMSE, and R2 of 0.1096 knots, 0.0143 knots^2, 0.1194 knots, and 0.9949, respectively.

(3) Filter optimization

With Units=20,000, Dropout=0.2, Kernel_size=2, and Epochs=300, the test sets were compared among Filters of 3, 4, and 5.

As shown in Figure 12C and Table 7, the best performance was achieved at the Filter value of 3, with MAE, MSE, RMSE, and R2 of 0.1499 knots, 0.0363 knots^2, 0.1906 knots, and 0.9870, respectively.

(4) Kernel_size optimization

With Units=20,000, Dropout=0.2, Filters=4, and Epochs=300, the test sets were compared among Kernel_size of 2, 3 and 4.

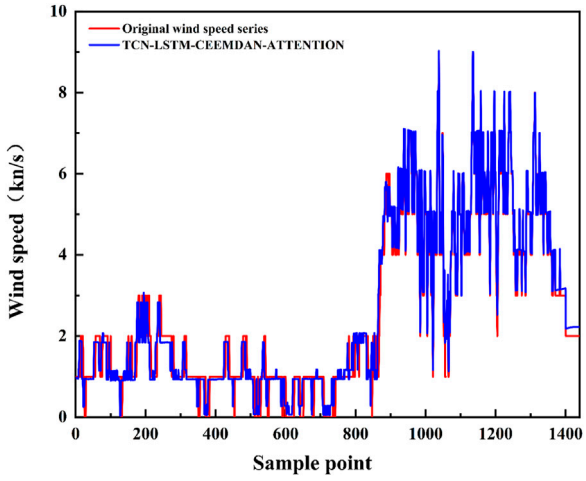

FIGURE 13
Overall model wind speed data prediction.

As shown in Figure 12D and Table 7, the best performance was achieved at the Kernel_size of 3, with MAE, MSE, RMSE, and R2 of 0.1546 knots, 0.0384 knots^2, 0.1959 knots, and 0.9863, respectively.

(5) Epoch optimization

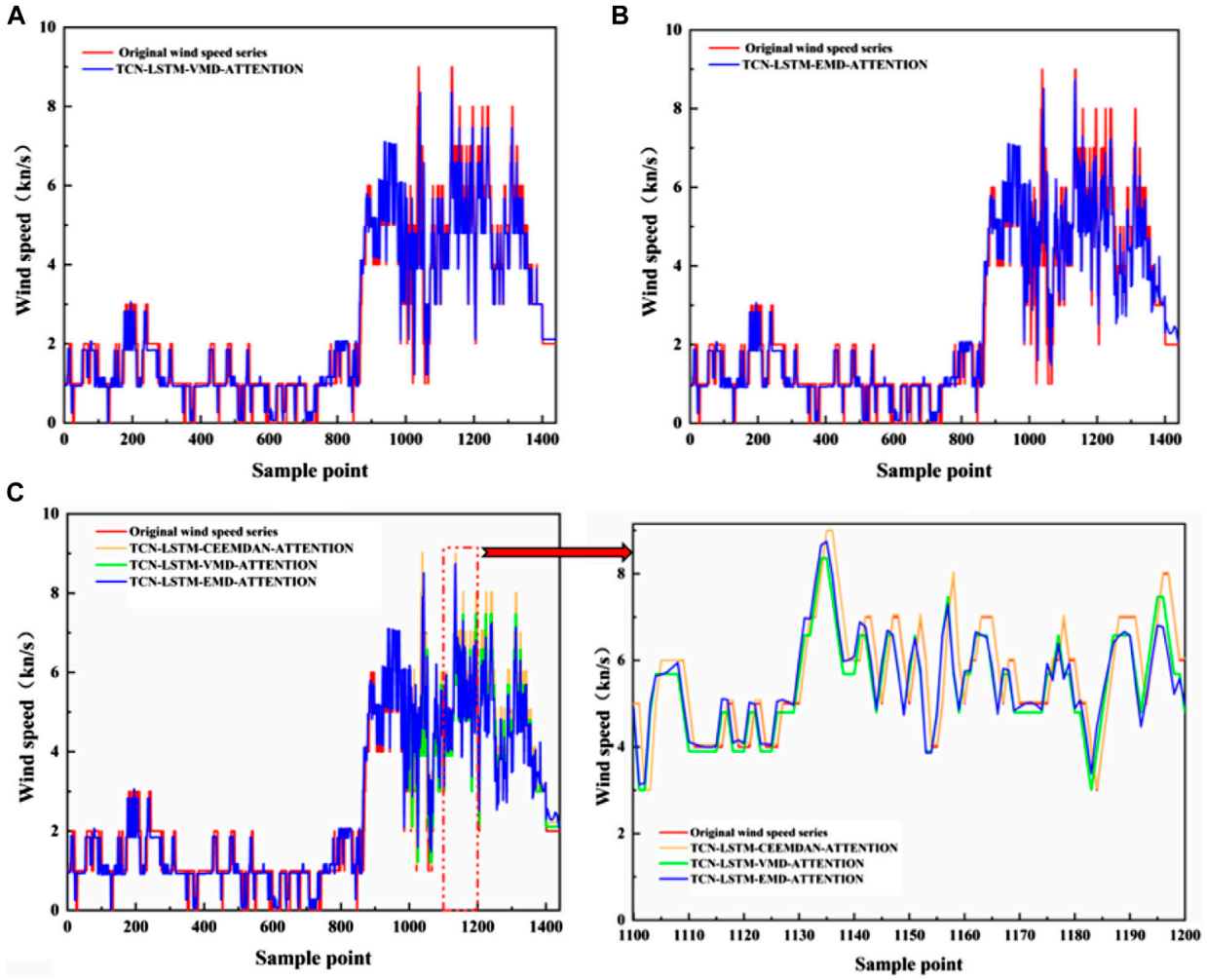

FIGURE 14
Comparison of the prediction results of each decomposition model. **(A)** TCN-LSTM-VMD-ATTENTION Forecast Comparison Chart, **(B)** TCN-LSTM-EMD-ATTENTION Forecast Comparison Chart. **(C)** Comparison of prediction results of different decomposition models.

The same method was used to optimize the Epochs parameter. With Units=20,000, Dropout=0.2, Filters=4, and Kernel_size=1, the test sets were compared among Epochs of 300, 400, and 500.

As shown in Figure 12E and Table 7, the CEEMDAN-TCN-ATTENTION model showed the best performance for the non-stationary segment at the Epoch value of 400, with MAE, MSE, RMSE, and R2 of 0.0860 knots, 0.1338 knots^2, 0.1157 knots, and 0.9950, respectively. The prediction graph is shown in Figure 12F.

3.3.3 Combined model of TCN-LSTM-CEEMDAN-ATTENTION

A total of 18,800 sets of data from a wind farm in western China September 13 to 16, 2022 were used to train the combined model. TCN-LSTM was used to predict stationary sequences, and CEEMDAN-TCN-ATTENTION was used to predict non-stationary sequences. Finally, the TCN-LSTM -CEEMDAN-ATTENTION combined model was used to predict 1,440 sets of data on September 17. The main parameters of the TCN-LSTM model for the stationary segment were set as follows: Filters=3, Kernel_size=10, Dropout=0.26, and Epochs=2000. The main parameters of the CEEMDAN-LSTM-ATTENTION model for the non-stationary segment sequence were set as follows: Units=20,000, Dropout=0.2, Filters=4, Kernel_size=1, and Epochs=400. The overall prediction plot of the model is shown in Figure 13.

4 Discussion

The TCN-LSTM-CEEMDAN-ATTENTION model was compared with the TCN-LSTM-VMD-ATTENTION and TCN-LSTM-EMD-ATTENTION models. Figures 14A,B show prediction comparison charts of the TCN-LSTM-CEEMDAN-ATTENTION model with the TCN-LSTM-VMD-ATTENTION and TCN-LSTM-EMD-ATTENTION models, respectively. Figure 14C presents a comparison diagram of the three different decomposition algorithms. Table 8 lists the evaluation indicators of the three different decomposition algorithms. As shown in Figures 14, 15 and Table 8, the overall MAE, MSE, and RMSE of the model

TABLE 8 Analysis of prediction results of different decomposition models.

Mould	MAE (knots)	MSE (knots2)	RMSE (knots)
TCN-LSTM-CEEMDAN-ATTENTION	0.1381	0.0499	0.2048
TCN-LSTM-VMD-ATTENTION	0.2001	0.0801	0.2461
TCN-LSTM-EMD-ATTENTION	0.4902	0.2967	0.5447

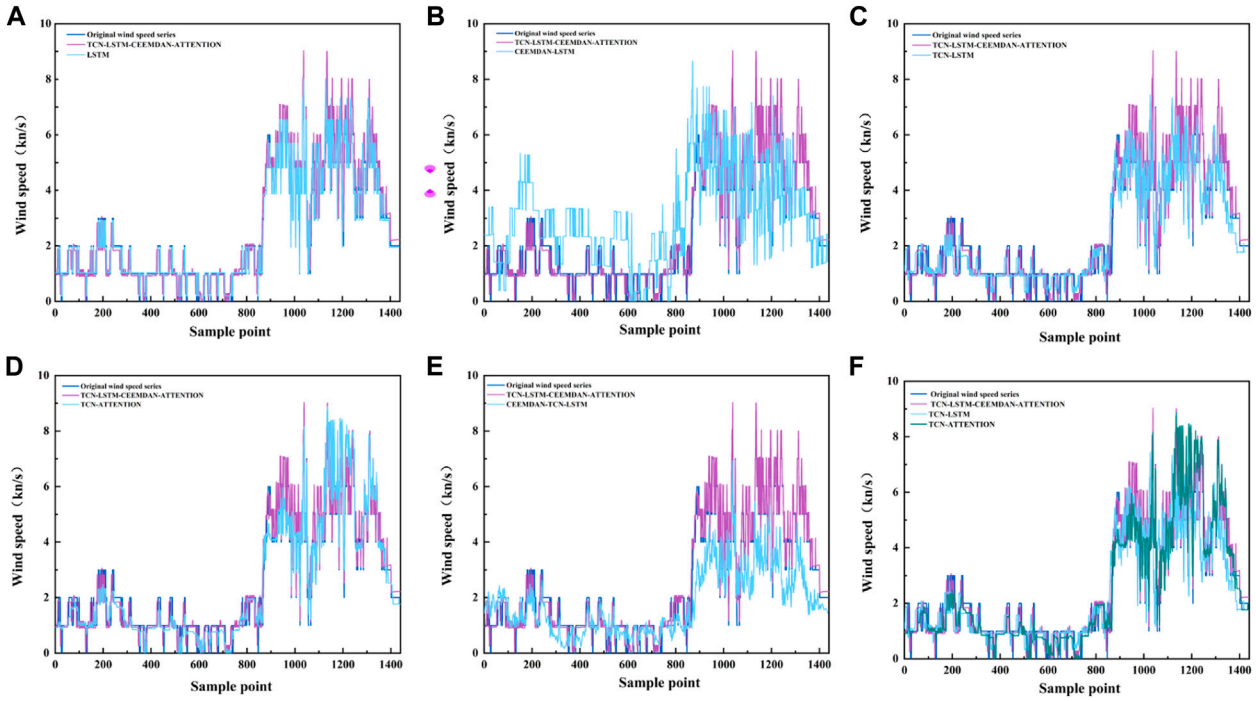

FIGURE 15
Comparison of the results of the predictions of the models. **(A)** Comparison between the model and LSTM prediction in this article, **(B)** Comparison between the model and CEEMDAN-LSTM prediction in this article, **(C)** Comparison between the model and TCN-LSTM prediction in this article, **(D)** Comparison between the model and TCN-ATTENTION in this article, **(E)** Comparison between the model and CEEMDAN-TCN-LSTM prediction in this article, **(F)** Comparison between the model in this article and some models' predictions.

with CEEMDAN are better than those with the other two algorithms. The model predicted data and the actual value fit well. These results prove that the use of CEEMDAN in the decomposition process of this model is optimal.

The TCN-LSTM-CEEMDAN-ATTENTION model was compared with the LSTM model alone, CEEMDAN-LSTM model, TCN-LSTM model, TCN-ATTENTION model, and CEEMDAN-TCN-ATTENTION model. A comparison chart is shown in Figure 15. In order to evaluate the prediction accuracy of each model more accurately, three indicators were used: MAE, MSE, and RMSE. The prediction results of each model are listed in Table 9.

Table 9 shows that the MAE, MSE, and RMSE of the TCN-LSTM-CEEMDAN-ATTENTION model are the smallest at 0.1381 knots, 0.0499 knots^2, and 0.2048 knots, respectively. Accordingly, it can be concluded that the TCN-LSTM-CEEMDAN-ATTENTION model has superior prediction performance, and is thus more suitable for ultra-short-term wind speed prediction.

In this experiment, the time consumed by each model (TCN-LSTM-CEEMDAN-ATTENTION, LSTM, CEEMDAN-LSTM, TCN-LSTM, TCN-ATTENTION, and CEEMDAN-TCN-ATTENTION) throughout the run was recorded. As shown in Table 9, the overall runtime of the TCN-LSTM-CEEMDAN-ATTENTION model is smaller than that of the other models. Therefore, it can be concluded that the efficiency of the TCN-LSTM and CEEMDAN-TCN-ATTENTION processes improve after the data are divided by stationarity.

We also compared the evaluation parameters of the ultra short term wind speed prediction models established by other researchers, including Yan et al.'s article "Wind speed prediction using a hybrid model of EEMD and LSTM considering seasonal features" (Yan et al., 2022), Zhang et al.'s article"A comprehensive wind speed prediction system based on Monte Carlo and artificial intelligence algorithms" (Zhang et al., 2022b), Wang et al.'s article "Wind speed prediction using measurements from neighboring locations and combining the extreme learning machine and the AdaBoost algorithm" (Wang et al., 2022), Ji et al.'s article "Short-Term

TABLE 9 Comparison of prediction results of different models.

Mould	MAE (knots)	MSE (knots2)	RMSE (knots)	Elapsed time(s)
TCN-LSTM-CEEMDAN-ATTENTION	0.1381	0.0499	0.2048	1,000.2007
LSTM	0.3130	0.2897	0.5382	1,430.1756
CEEMDAN-LSTM	1.4871	3.3649	1.8343	1,482.3360
TCN-LSTM	0.4083	0.3386	0.5819	2,750.3588
TCN-ATTENTION	0.4529	0.4206	0.6485	1,634.7742
CEEMDAN-TCN-LSTM	0.9781	1.8512	1.3606	1,354.9698

TABLE 10 Comparison of models in similar types of articles.

Mould	MAE (knots)	MSE (knots2)	RMSE (knots)	R2
TCN-LSTM-CEEMDAN-ATTENTION	0.1381	0.0499	0.2048	0.9940
SARIMA-EEMD-LSTM	0.3027	—	0.4102	0.9848
VMD-SCCS-BP-ARMA	0.4220	—	0.3548	—
Multiple-point-AdaBoost-ELM	0.2474	—	0.3212	0.7384
TL-CNN-GRU	1.0390	—	1.5690	—

Canyon Wind Speed Prediction Based on CNN—GRU Transfer Learning" (Ji et al., 2022). The comparative data is shown in Table 10. After comparing models in similar articles, the model established in this article still has significant advantages and is suitable for ultra short term wind speed prediction.

5 Conclusion

This study introduces and validates a state-of-the-art real-time prediction model for ultra-short-term wind speeds using a dual-model framework consisting of the TCN-LSTM and CEEMDAN-TCN-ATTENTION architectures. The main objective of this study is to improve the efficiency of geotechnical hazard monitoring and early warning systems, with a special focus on open pit mining areas. The excellent predictive accuracy and efficiency of the model in predicting ultra-short-term wind speeds highlights its key role in advancing smart geotechnical hazard monitoring.

A noteworthy contribution of this investigation lies in its methodical treatment of the distinctive characteristics inherent in stationary and non-stationary sequences within ultra-short-term wind speed time series. The application of the sliding window averaging method facilitated the categorization of wind speed series into stationary and non-stationary components. The TCN-LSTM model demonstrated proficiency in predicting the stationary sequence, leveraging its dilated causal convolution and LSTM units for discerning time correlations and maintaining temporal continuity. Concurrently, for the non-stationary sequence, the CEEMDAN-TCN-ATTENTION model, incorporating CEEMDAN for data simplification and ATTENTION for enhanced TCN data capture, proved effective. The amalgamation of these models yielded the robust TCN-LSTM-CEEMDAN-ATTENTION model.

The comparative analysis involving various decomposition algorithms and five distinct single and combined models accentuated the superior predictive capabilities of our proposed integrated model. With minimal Mean Absolute Error (MAE) of 0.1381, Mean Squared Error (MSE) of 0.0499, and Root Mean Squared Error (RMSE) of 0.2048, our model surpassed alternative approaches. Its prediction fit outperformed other models, reinforcing its suitability for ultra-short-term wind speed prediction.

The model is important for geotechnical hazard monitoring, especially in open pit mining areas. The validated model not only improves our understanding of ultrashort-term wind speed dynamics, but also provides a practical and efficient tool for real-time prediction. The success of our approach highlights its potential for wider application in geotechnical monitoring systems, promising improved safety and operational efficiency in high-risk environments. Integrating this advanced predictive model into an operating system is a key step towards a more resilient and responsive approach to geotechnical disaster management.

Data availability statement

The datasets presented in this study can be found in online repositories. The names of the repository/repositories and accession number(s) can be found below: https://mesonet.agron.iastate.edu/COOP/extremes.php.

Author contributions

PS: Writing–original draft, Writing–review and editing. JW: Writing–review and editing, Supervision. ZY: Writing–review and editing.

Funding

The author(s) declare that financial support was received for the research, authorship, and/or publication of this article. This work was supported by Shaanxi Province key industrial chain project (2023-ZDLGY-24).

Acknowledgments

We are very grateful for the support of Shaanxi Nano Research Laboratory and Shaanxi Province (2023-ZDLGY-24) for this project. We also appreciate the feedback from reviewers, which has been very helpful in improving the manuscript.

Conflict of interest

The authors declare that the research was conducted in the absence of any commercial or financial relationships that could be construed as a potential conflict of interest.

Publisher's note

All claims expressed in this article are solely those of the authors and do not necessarily represent those of their affiliated organizations, or those of the publisher, the editors and the reviewers. Any product that may be evaluated in this article, or claim that may be made by its manufacturer, is not guaranteed or endorsed by the publisher.

References

Al-Yahyai, S., Charabi, Y., Gastli, A. J. R., and Reviews, S. E. (2010). Review of the use of numerical weather prediction (NWP) models for wind energy assessment. *Renew. Sustain. Energy Rev.* 14, 3192–3198. doi:10.1016/j.rser.2010.07.001

Chandra, D. R., Kumari, M. S., and Sydulu, M. (2013). "A detailed literature review on wind forecasting," in Proceedings of the 2013 International Conference on Power, Energy and Control (ICPEC), Dindigul, India, February 2013 (IEEE), 630–634.

Chen, X., Li, L., Wang, L., and Qi, L. (2019). The current situation and prevention and control countermeasures for typical dynamic disasters in kilometer-deep mines in China. *Saf. Sci.* 115, 229–236. doi:10.1016/j.ssci.2019.02.010

Cheng, W. Y., Liu, Y., Liu, Y., Zhang, Y., Mahoney, W. P., and Warner, T. T. (2013). The impact of model physics on numerical wind forecasts. *Renew. Energy* 55, 347–356. doi:10.1016/j.renene.2012.12.041

Erdem, E., and Shi, J. (2011). ARMA based approaches for forecasting the tuple of wind speed and direction. *Appl. Energy* 88, 1405–1414. doi:10.1016/j.apenergy.2010.10.031

Fu, W., Wang, K., Li, C., and Tan, JJEC (2019). Multi-step short-term wind speed forecasting approach based on multi-scale dominant ingredient chaotic analysis, improved hybrid GWO-SCA optimization and ELM. *Energy Convers. Manag.* 187, 356–377. doi:10.1016/j.enconman.2019.02.086

Giebel, G., Draxl, C., Brownsword, R., Kariniotakis, G., and Denhard, M. (2011). The state-of-the-art in short-term prediction of wind power. *A lit. Overv.* doi:10.13140/RG.2.1.2581.4485

Hepbasli, A. J. R. (2008). A key review on exergetic analysis and assessment of renewable energy resources for a sustainable future. *Renew. Sustain. Energy Rev.* 12, 593–661. doi:10.1016/j.rser.2006.10.001

Huang, N. E., Shen, Z., Long, S. R., Wu, M. C., Shih, H. H., Zheng, Q., et al. (1998). The empirical mode decomposition and the Hilbert spectrum for nonlinear and non-stationary time series analysis. *Proc. R. Soc. Lond. A* 454, 903–995. doi:10.1098/rspa.1998.0193

Ji, L., Fu, C., Ju, Z., Shi, Y., Wu, S., and Tao, L. J. A. (2022). Short-Term canyon wind speed prediction based on CNN—GRU transfer learning. *Atmos. (Basel).* 13, 813. doi:10.3390/atmos13050813

Kavasseri, R. G., and Seetharaman, K. J. (2009). Day-ahead wind speed forecasting using f-ARIMA models. *Renew. Energy* 34, 1388–1393. doi:10.1016/j.renene.2008.09.006

Khazaei, S., Ehsan, M., Soleymani, S., and Mohammadnezhad-Shourkaei, H. J. E. (2022). A high-accuracy hybrid method for short-term wind power forecasting. *Energy* 238, 122020. doi:10.1016/j.energy.2021.122020

Kulkarni, M. A., Patil, S., Rama, G., and Sen, P. J. (2008). Wind speed prediction using statistical regression and neural network. *J. Earth Syst. Sci.* 117, 457–463. doi:10.1007/s12040-008-0045-7

Kunyan, Z., and Meihong, LJCMM (2019). Slope stability prediction of open-pit mine based on GA-BP model. *CHINA Min. Mag.* 28, 144–148. doi:10.12075/j.issn.1004-4051.2019.06.023

Li, W., Qiao, S., Zhang, H., Zheng, Q., and Yang, S. (2022). "Ultra-short-term wind power forecasting model based on improved whale algorithm and LSTM neural network," in Proceedings of the 4th International Conference on Information Science, Electrical, and Automation Engineering (ISEAE 2022), Beijing, China, September 2019 (SPIE), 153–159.

Li, Y., Zhao, Y., Wang, L., Zhang, M., and Zhou, M. (2016). Variance estimation considering multistage sampling design in multistage complex sample analysis. *Zhonghua liu xing bing xue za zhi = Zhonghua liuxingbingxue zazhi* 37, 425–429. doi:10.3760/cma.j.issn.0254-6450.2016.03.028

Liu, H. P., Shi, J., and Erdem, E. (2013). An integrated wind power forecasting methodology: interval estimation of wind speed, operation probability of wind turbine, and conditional expected wind power output of A wind farm. *Int. J. Green Energy* 10, 151–176. doi:10.1080/15435075.2011.647170

Liu, M.-D., Ding, L., and Bai, Y.-LJEC (2021). Application of hybrid model based on empirical mode decomposition, novel recurrent neural networks and the ARIMA to wind speed prediction. *Energy Convers. Manag.* 233, 113917. doi:10.1016/j.enconman.2021.113917

Luo, H., Dou, X., Sun, R., and Wu, S. J. (2021a). A multi-step prediction method for wind power based on improved TCN to correct cumulative error. *Front. Energy Res.* 9, 723319. doi:10.3389/fenrg.2021.723319

Luo, H. F., Dou, X., Sun, R., and Wu, S. J. (2021b). A multi-step prediction method for wind power based on improved TCN to correct cumulative error. *Front. Energy Res.* 9. doi:10.3389/fenrg.2021.723319

Mohandes, M. A., Halawani, T. O., Rehman, S., and Hussain, A. A. (2004). Support vector machines for wind speed prediction. *Renew. Energy* 29, 939–947. doi:10.1016/j.renene.2003.11.009

Mölders, N. J. M., and Physics, A. (1999). On the atmospheric response to urbanization and open-pit mining under various geostrophic wind conditions. *Meteorol. Atmos. Phys.* 71, 205–228. doi:10.1007/s007030050056

Nie, L., Li, Z., Lv, Y., Wang, H. J., and Environment, t (2017). A new prediction model for rock slope failure time: a case study in West Open-Pit mine, Fushun, China. *Bull. Eng. Geol. Environ.* 76 (3), 975–988. doi:10.1007/s10064-016-0900-8

Parra, E., Mohr, C. H., and Korup, OJGRL (2021). Predicting Patagonian landslides: roles of forest cover and wind speed. *Geophys. Res. Lett.* 48, e2021GL095224. doi:10.1029/2021gl095224

Peng, X., and Lu, G. J. (1995). Physical modelling of natural wind and its guide in a large open pit mine. *J. Wind Eng. Industrial Aerodynamics* 54, 473–481. doi:10.1016/0167-6105(94)00060-q

Ranganayaki, V., and Deepa, S. N. (2019). Linear and non-linear proximal support vector machine classifiers for wind speed prediction. *Clust. Computing-the J. Netw. Softw. Tools Appl.* 22, 379–390. doi:10.1007/s10586-018-2005-6

Shobana Devi, A., Maragatham, G., Boopathi, K., Lavanya, M., and Saranya, R. (2020). "Long-term wind speed forecasting—a review," in Proceedings of the Artificial Intelligence Techniques for Advanced Computing Applications, Singapore, July 2020 (Springer), 79–99.

Ssekulima, E. B., Anwar, M. B., Al Hinai, A., and El Moursi, M. S. (2016). Wind speed and solar irradiance forecasting techniques for enhanced renewable energy integration with the grid: a review. *IET Renew. Power Gener.* 10, 885–989. doi:10.1049/iet-rpg.2015.0477

Sun, W., Liu, M., and Liang, Y. J. E. (2015). Wind speed forecasting based on FEEMD and LSSVM optimized by the bat algorithm. *Energies (Basel).* 8, 6585–6607. doi:10.3390/en8076585

Sun, W., and Wang, X. (2022). Improved chimpanzee algorithm based on CEEMDAN combination to optimize ELM short-term wind speed prediction. *Environ. Sci. Pollut. Res.* 30, 35115–35126. doi:10.1007/s11356-022-24586-1

Tascikaraoglu, A., Uzunoglu, M. J. R., and Reviews, S. E. (2014). A review of combined approaches for prediction of short-term wind speed and power. *Renew. Sustain. Energy Rev.* 34, 243–254. doi:10.1016/j.rser.2014.03.033

Vardon, P. J. (2015). Climatic influence on geotechnical infrastructure: a review. *Environ. Geotech.* 2 (3), 166–174. doi:10.1680/envgeo.13.00055

Wang, J., Li, X., Zhou, X., and Zhang, K. J. P. (2010). Ultra-short-term wind speed prediction based on VMD-LSTM. *Earth Environ. Sci.* 48, 45–52. doi:10.19783/j.cnki.pspc.190860

Wang, J., Zhang, W., Wang, J., Han, T., and Kong, LJIS (2014). A novel hybrid approach for wind speed prediction. *Inf. Sci.* 273, 304–318. doi:10.1016/j.ins.2014.02.159

Wang, K., and Du, F. (2020). Coal-gas compound dynamic disasters in China: a review. *Process Saf. Environ. Prot.* 133, 1–17. doi:10.1016/j.psep.2019.10.006

Wang, L., Guo, Y., Fan, M., and Li, X. J. (2022). Wind speed prediction using measurements from neighboring locations and combining the extreme learning machine and the AdaBoost algorithm. *Adab. algorithm* 8, 1508–1518. doi:10.1016/j.egyr.2021.12.062

Xiang, L., Deng, Z., and Zhao, Y. (2019). Multi-step wind speed prediction model based on LPF-VMD and KELM. *Power Syst. Technol.* 43, 4461–4467.

Xu, W., Liu, P., Cheng, L., Zhou, Y., Xia, Q., Gong, Y., et al. (2021). Multi-step wind speed prediction by combining a WRF simulation and an error correction strategy. *Renew. Energy* 163, 772–782. doi:10.1016/j.renene.2020.09.032

Yan, Y., Wang, X., Ren, F., Shao, Z., and Tian, CJER (2022). Wind speed prediction using a hybrid model of EEMD and LSTM considering seasonal features. *Energy Rep.* 8, 8965–8980. doi:10.1016/j.egyr.2022.07.007

Yu, J., Chen, K., Mori, J., and Rashid, MMJE (2013). A Gaussian mixture copula model based localized Gaussian process regression approach for long-term wind speed prediction. *Energy* 61, 673–686. doi:10.1016/j.energy.2013.09.013

Zhang, J., Yang, C., Niu, F., Sun, Y., and Wang, R. (2022a). "Combined wind speed prediction model considering the spatio-temporal features of wind farm," in Proceedings of the 4 2022 2nd International Conference on Computer, Control and Robotics (ICCCR), Shanghai, China, March 2022 (IEEE), 132–138.

Zhang, X.-y., Zhu, Y.-m., and Fang, C.-h. (2009). The role fore air flow in soil slope stability analysis. *J. Hydrodyn.* 21, 640–646. doi:10.1016/s1001-6058(08)60195-x

Zhang, Y., Pan, G., Chen, B., Han, J., Zhao, Y., and Zhang, CJRE (2020). Short-term wind speed prediction model based on GA-ANN improved by VMD. *Renew. Energy* 156, 1373–1388. doi:10.1016/j.renene.2019.12.047

Zhang, Y., Zhao, Y., Pan, G., and Zhang, J. J. (2019a). Wind speed interval prediction based on lorenz disturbance distribution. *IEEE Trans. Sustain. Energy* 11, 807–816. doi:10.1109/tste.2019.2907699

Zhang, Y., Zhao, Y., Shen, X., and Zhang, JJAE (2022b). A comprehensive wind speed prediction system based on Monte Carlo and artificial intelligence algorithms. *Appl. Energy* 305, 117815. doi:10.1016/j.apenergy.2021.117815

Zhang, Y. G., Chen, B., Pan, G. F., and Zhao, Y. (2019c). A novel hybrid model based on VMD-WT and PCA-BP-RBF neural network for short-term wind speed forecasting. *Energy Convers. Manag.* 195, 180–197. doi:10.1016/j.enconman.2019.05.005

Zhang, Y. G., Gao, S., Ban, M. H., and Sun, Y. (2019b). A method based on lorenz disturbance and variational mode decomposition for wind speed prediction. *Adv. Electr. Comput. Eng.* 19, 3–12. doi:10.4316/aece.2019.02001

Frontiers in Earth Science

Investigates the processes operating within the major spheres of our planet

Advances our understanding across the earth sciences, providing a theoretical background for better use of our planet's resources and equipping us to face major environmental challenges.

Discover the latest Research Topics

See more →

Frontiers

Avenue du Tribunal-Fédéral 34
1005 Lausanne, Switzerland
frontiersin.org

Contact us

+41 (0)21 510 17 00
frontiersin.org/about/contact